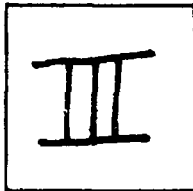


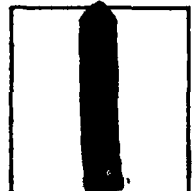
PHOTOGRAPH THIS SHEET

AD A094294

DTIC ACCESSION NUMBER



LEVEL



INVENTORY

**FEDERAL ELECTRIC CO. CINCINNATI OHIO ALTERNATE  
ENGINE GROUP  
HIGH VELOCITY JET NOISE SOURCE LOCATION AND  
REDUCTION** TASK 3. EXPERIMENTAL INVESTIGATION OF SUPPRESSION  
PRINCIPLES VOLUME II - PARAMETRIC TESTING and SOURCE MEASUR-  
EMENTS. FINAL REPT., DEC."78, REPT. NO. R78AEG627  
CONTRACT DOT-OS-30634 FAA-RD-76-79-3-2

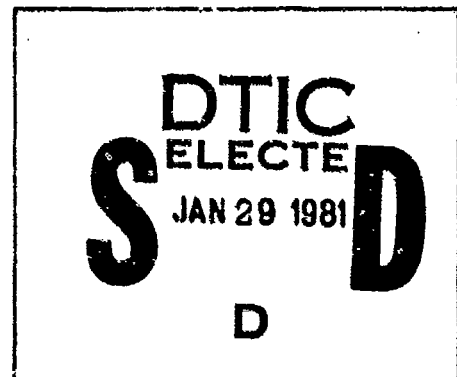
**DISTRIBUTION STATEMENT A**

Approved for public release  
Distribution Unlimited

**DISTRIBUTION STATEMENT**

ACCESSION FOR	
NTIS	GRA&I
DTIC	TAB
UNANNOUNCED	
JUSTIFICATION	
BY	
DISTRIBUTION /	
AVAILABILITY CODES	
DIST	AVAIL AND/OR SPECIAL
A	

DISTRIBUTION STAMP



DATE ACCESSIONED

81 1 27 008

DATE RECEIVED IN DTIC

PHOTOGRAPH THIS SHEET AND RETURN TO DTIC-DDA-2

# **HIGH VELOCITY JET NOISE SOURCE LOCATION AND REDUCTION**

## **TASK 3 - EXPERIMENTAL INVESTIGATION OF SUPPRESSION PRINCIPLES**

**Volume II - Parametric Testing and Source Measurements**

### **TECHNICAL CONTRIBUTORS:**

**J.F. Brausch**

**M.A. Smith**

**W.S. Clapper**

**E.J. Stringas**

**P.F. Scott**

**R.W. Whittaker**

**GENERAL ELECTRIC COMPANY  
AIRCRAFT ENGINE GROUP  
CINCINNATI, OHIO 45215**



**DECEMBER 1978**

**FINAL REPORT**

Document is available to the U.S. public through  
the National Technical Information Service,  
Springfield, Virginia 22161.

**Prepared for**

**U.S. DEPARTMENT OF TRANSPORTATION  
FEDERAL AVIATION ADMINISTRATION  
Systems Research & Development Service  
Washington, D.C. 20590**

**AD A094294**



NOTICE

The contents of this report reflect the views of the General Electric Company which is responsible for the facts and the accuracy of the data presented herein. The contents do not necessarily reflect the official views or policy of the Department of Transportation. This report does not constitute a standard, specification or regulation.

1. Report No. FAA-RD-76-79, III - II		2. Government Accession No.		3. Recipient's Catalog No.	
4. Title and Subtitle High Velocity Jet Noise Source Location and Reduction, Task 3 - Experimental Investigation of Suppression Principles Volume II - Parametric Testing and Source Measurements				5. Report Date December 1978	
				6. Performing Organization Code	
7. Author(s). J.F. Brausch, W.S. Clapper, R.J. Stringas, R. Whittaker. W.S. Clapper (Task 3 Technical Director and Editor) E.J. Stringas (Technical Project Manager)				8. Performing Organization Report No. R78ABG627	
				10. Work Unit No.	
9. Performing Organization Name and Address General Electric Company Group Advanced Engineering Division Aircraft Engine Group Cincinnati, Ohio 45215				11. Contract or Grant No. DOT-OS-30034	
				13. Type of Report and Period Covered Technical Report October 1974-April 1978	
12. Sponsoring Agency Name and Address U.S. Department of Transportation Federal Aviation Administration Systems Research and Development Service Washington, D.C. 20590				14. Sponsoring Agency Code ARD-550	
15. Supplementary Notes This report is in partial fulfillment of the subject program. Related documents to be issued in the course of the program include final reports of the following Tasks: Task 1 - Activation of Facilities and Validation of Source Location Techniques; Task 1 Supplement - Certification of the General Electric Jet Noise Anechoic Test Facility; Task 2 - Theoretical Developments and Basic Experiments; Task 4 - Development/Evaluation of Techniques for "Inflight" Investigation; Task 5 - Investigation of "Inflight" Aero-Acoustic Effects; Task 6 - Noise Abatement Nozzle Design Guide. FAA Program Monitor, R.S. Zuckerman.					
16. Abstract  Experimental investigations were conducted of suppression principles, including developing an experimental data base, developing a better understanding of jet noise suppression principles, and formulating empirical methods for the acoustic design of jet noise suppressors. Acoustic scaling has been experimentally demonstrated, and five "optimum" nozzles have been selected for subsequent anechoic free-jet testing.  A series of experimental tests was conducted to provide farfield acoustic data on 47 baseline and suppressor nozzle configurations and to provide aerodynamic nozzle performance on 18 of the configurations. Suppressor design parameters evaluated experimentally included: suppressor area ratio, radius ratio, flow management, inner stream geometry, element number and type, treated ejectors on multielement and unsuppressed inverted-coannular-flow nozzles.  Parametric testing established suppression levels for single and dual flow nozzles during static operation. Selective free-jet tests conducted on eight configurations were utilized to establish flight suppression levels for plug, chute, tube and hole nozzles. The aerodynamic performance test program illustrated that suppressed exhaust nozzles which incorporate elemental base areas as an integral part of the design are sensitive to external Mach number. In general suppressor element base drag was the most significant loss mechanism.  This volume is part of the four volume set that constitutes the Task 3 final report. The other volumes are: Volume I - Verification of Suppression Principles and Development of Suppression Prediction Methods, Volume III - Suppressor Concepts Optimization, and Volume IV - Laser Velocimeter Time Dependent Cross Correlation Measurements.					
17. Key Words (Suggested by Author(s)) Jet Noise, Suppression, Aerodynamic Performance, Freejet, Jet Plume Characteristics			18. Distribution Statement  Document is available to the U.S. public through the National Technical Information Service, Springfield, Virginia 22161.		
19. Security Class. (of this report) Unclassified		20. Security Class. (of this page) Unclassified		21. No. of Pages 823	
				22. Price*	

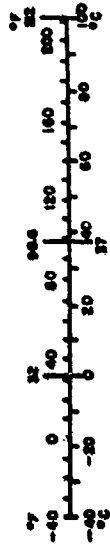
\* For sale by the National Technical Information Service, Springfield, Virginia 22151

# METRIC CONVERSION FACTORS

Approximate Conversions to Metric Measures			
Symbol	When You Know	Multiply by	To Find
<b>LENGTH</b>			
m	inches	2.5	centimeters
cm	feet	30	centimeters
mm	yards	0.9	meters
m	miles	1.6	kilometers
<b>AREA</b>			
m <sup>2</sup>	square inches	6.5	square centimeters
cm <sup>2</sup>	square feet	11	square centimeters
in <sup>2</sup>	square yards	0.8	square meters
ft <sup>2</sup>	square miles	2.6	square kilometers
mi <sup>2</sup>	acres	0.4	hectares
<b>MASS (weight)</b>			
kg	grams	2.2	kilograms
g	ounces	0.7	grams
lb	pounds	0.45	kilograms
oz	short tons	0.9	kilograms
<b>VOLUME</b>			
l	liters	1.05	quarts
qt	quarts	0.95	liters
gal	gallons	3.8	liters
cu ft	cubic feet	28	liters
cu yd	cubic yards	7.6	cubic meters
m <sup>3</sup>	cubic meters	1.35	cubic feet
ft <sup>3</sup>	cubic feet	0.028	cubic meters
mi <sup>3</sup>	cubic miles	4.0	cubic kilometers
<b>TEMPERATURE (temp)</b>			
°C	Fahrenheit temperature	5/9 (then add 32)	Celsius temperature

\* 1 in = 2.54 centimeters. For other exact conversions and more data, see Metric, Pub. 750, U.S. GPO: 1969 O-350-000. For other exact conversions and more data, see Metric, Pub. 750, U.S. GPO: 1969 O-350-000.

Approximate Conversions from Metric Measures			
Symbol	When You Know	Multiply by	To Find
<b>LENGTH</b>			
m	centimeters	0.04	inches
cm	centimeters	0.4	inches
m	meters	3.3	feet
mm	meters	1.1	yards
m	kilometers	0.6	miles
<b>AREA</b>			
cm <sup>2</sup>	square centimeters	0.16	square inches
in <sup>2</sup>	square centimeters	1.2	square inches
cm <sup>2</sup>	square meters	0.4	square yards
in <sup>2</sup>	square meters	2.5	square miles
ha	hectares (10,000 m <sup>2</sup> )	2.5	acres
<b>MASS (weight)</b>			
kg	grams	0.035	ounces
g	kilograms	2.2	pounds
lb	grams (1000 kg)	1.1	short tons
<b>VOLUME</b>			
l	liters	0.95	quarts
qt	quarts	1.05	liters
gal	gallons	0.26	quarts
cu ft	cubic feet	35	cubic feet
cu yd	cubic yards	1.3	cubic yards
<b>TEMPERATURE (temp)</b>			
°C	Celsius temperature	9/5 (then add 32)	Fahrenheit temperature



## PREFACE

This report describes the work performed under Task 3 of the DOT/FAA High Velocity Jet Noise Source Location and Reduction Program (Contract DOT-OS-30034). The objectives of the contract were:

- Investigation, including scaling effects, of the aerodynamic and acoustic mechanisms of various jet noise suppressors.
- Analytical and experimental studies of the acoustic source distribution in such suppressors, including identification of source location, nature, and strength and noise reduction potential.
- Investigation of in-flight effects on the aerodynamic and acoustic performance of these suppressors.

These investigations are expected to lead to the preparation of a design guide report for predicting the overall characteristics of suppressor concepts, from models to full scale, static to in-flight conditions, as well as a quantitative and qualitative prediction of the phenomena involved.

The work effort in this program was organized under the following major Tasks, each of which is reported in a separate Final Report:

Task 1 - Activation of Facilities and Validation of Source Location Techniques.

Task 2 - Theoretical Developments and Basic Experiments.

Task 3 - Experimental Investigation of Suppression Principles.

Task 4 - Development and Evaluation of Techniques for "In flight" Investigation.

Task 5 - Investigation of "In flight" Aero-Acoustic Effects on Suppressed Exhausts.

Task 6 - Preparation of Noise Abatement Nozzle Design Guide Report.

Task 1 was an investigative and survey effort designed to identify acoustic facilities and test methods best suited to jet noise studies. Task 2 was a theoretical effort complemented by theory verification experiments which extended across the entire contract period of performance.

The subject of the present, Task 3, report series (FAA-RD-76-79 III - I, II, III, and IV) was formulated as a substantial part of the contract effort to gather various test data on a wide range of high velocity jet nozzle suppressors. These data, together with supporting theoretical advances from Task 2, have led to a better understanding of jet noise and jet noise

suppression mechanisms, as well as to a validation of scaling methods. Task 3 helped to identify several "optimum" nozzles for simulated in-flight testing under Task 5, and to provide a extensive, high-quality, data bank leading to formulation of methods and techniques useful for designing jet noise suppressors for application in the Task 6 design guide as well as in future studies.

Task 4 was similar to Task 1, except that it dealt with the specific test facility requirements, measurement techniques, and analytical methods necessary to evaluate the "in flight" noise characteristics of simple and complex suppressor nozzles. This effort provided the capability to conduct the "flight" effects test program of Task 5.

## TABLE OF CONTENTS

<u>Section</u>		<u>Page</u>
1.0	SUMMARY	1
2.0	INTRODUCTION	10
3.0	PARAMETRIC ACOUSTIC TESTING AND SOURCE MEASUREMENTS	12
3.1	Description of Test Models	14
3.2	Definition of Test Matrices	34
3.2.1	Acoustic Test Matrices	34
3.2.2	Laser Velocimeter Test Matrix	45
3.2.3	Ellipsoidal Mirror Test Matrices	48
3.3	Data Acquisition and Data Reduction Procedures	49
3.3.1	Acoustic Data	49
3.3.1.1	Acoustic Data Acquisition	49
3.3.1.2	Acoustic Data Reduction	52
3.3.1.3	Air Attenuation Corrections	54
3.3.1.4	Data Corrections to a Free-Field Environment JENOTS	54
3.3.1.5	Data Scaling Procedure	55
3.3.1.6	Power Level Calculations	55
3.3.1.7	Acoustic Data Normalization	55
3.3.2	Laser Velocimeter Data	57
3.3.3	Ellipsoidal Mirror Data	63
3.4	Data Analysis	57
3.4.1	Tests Related to Baseline Nozzle Configurations	67
3.4.1.1	Baseline Conical Nozzles (Models 1, 14)	67
3.4.1.2	Convergent-Divergent Plug Nozzle Study	85
3.4.1.3	Plug Nozzle Radius Ratio Study	96
3.4.1.4	Baseline Dual-Flow Study	107
3.4.1.5	Dual Flow Parametric Study	124
3.4.1.6	Unsuppressed Annular Jet Study	135
3.4.1.7	Summary	150
3.4.2	Tests Related to Suppressors Influenced by Geometric and Cycle Variations, Single- and Dual-Flow Nozzles	150
3.4.2.1	Chute Area Ratio and Radius Ratio Studies	151
3.4.2.2	Flow Management and Inner Stream Geometry Studies	199
3.4.2.3	Flow Segment	282
3.4.2.4	Element Type Studies	301
3.4.2.5	Treated Ejector Applications	321
3.4.2.6	Summary of Suppression Levels	358

## TABLE OF CONTENTS (Continued)

<u>Section</u>		<u>Page</u>
	3.4.3 Tests to Evaluate the Influence of Simulated Flight	358
	3.4.3.1 Simulated Flight Investigation for Several Configurations	358
	3.4.3.2 Shock Noise Studies	405
	3.4.4 Laser Velocimeter Results	411
	3.4.5 Ellipsoidal Mirror (EM) Testing	432
	3.4.5.1 Data Analysis	432
4.0	AERODYNAMIC PERFORMANCE TEST PROGRAM	445
4.1	General Program Objectives and Scope	445
4.2	Test Facility Description	446
4.3	Model Description	450
	4.3.1 Annular Suppressed Models	450
	4.3.2 104-Tube Model	457
	4.3.3 Eight-Lobe Suppressor Model	457
	4.3.4 Reference Nozzle	457
4.4	Data Reduction Procedures	463
	4.4.1 Flow Rates	463
	4.4.2 Flow Coefficients	463
	4.4.3 Thrust Measurements	464
	4.4.4 Thrust Coefficient	466
	4.4.5 Pressure Data	466
4.5	Test Results and Discussion	467
	4.5.1 Data Quality	467
	4.5.2 Annular Nozzle Thrust Coefficients	472
	4.5.3 Effect of Suppressor Element Number	472
	4.5.4 Effect of Suppressor Area Ratio	477
	4.5.5 Effect of Inner Nozzle Area (Inner Radius Ratio)	477
	4.5.6 Effect of Inner Plug Axial Location	482
	4.5.7 Effect of Inner Nozzle Area (Radius Ratio) and Plug Location on Element Base Pressure	482
	4.5.8 Effect of Suppressor Ventilation on Performance	488
	4.5.9 Effect of External Mach Number	488
	4.5.10 104-Tube Nozzle Test Results	488
	4.5.11 Eight Lobe Nozzle Test Results	488
	4.5.12 Suppressor Flow Coefficients	495
4.6	Conclusions	495
5.0	RESULTS AND CONCLUSIONS	497

TABLE OF CONTENTS (Concluded)

<u>Section</u>		<u>Page</u>
Appendix A	Test Model Definitions	501
Appendix B	Acoustic Test Matrices, Aerodynamic Test Conditions	543
Appendix C	General Electric Air-Attenuation Model	586
Appendix D	Summary of the Ellipsoidal Mirror Development	597
Appendix E	Error Analysis of the Ellipsoidal Mirror Technique	635
Appendix F	Aerodynamic Performance Details	654
References		821



# LIST OF SYMBOLS

## Symbols

A	Nozzle Exhaust Area, ft <sup>2</sup>
a <sub>0</sub>	Ambient Speed of Sound, ft/sec
AR	Suppressor Area-Ratio; Determined by the Total Nozzle Area, Excluding Any Plug, to the Flow Area of the Nozzle
C <sub>D</sub> , CD	Flow Coefficient
C <sub>f</sub>	Skin Friction Coefficient
C <sub>f<sub>g</sub></sub> , C <sub>T</sub>	Thrust Coefficient
C <sub>v</sub>	Peak Thrust Coefficient
D	Diameter, ft or Chute-Base Drag, lbf
d	Chute Ventilation Depth, ft
D <sub>Ei</sub>	Ejector Inlet Diameter, ft
D <sub>eq</sub>	$\sqrt{(4 \text{ Area}/\pi)}$
D <sub>f</sub>	Friction Drag, lbf
D <sub>s</sub>	Shroud Diameter at Tip, ft
DBTF	Duct-Burning Turbofan
EPNL	Effective Perceived Noise Level, EPNdB
F	Force or Thrust, lbf
f	Frequency, Hz
F <sub>p</sub>	Pressure Force, lbf
F <sub>S</sub>	Ideal Gross Thrust, lbf
F <sub>g</sub>	Stream Thrust Parameters, lbf
f <sub>g</sub>	Dimensionless Stream Thrust Parameter
G	Ellipsoidal Mirror Gain, dB
H	Diffraction Window Function
h	Annulus Height, ft
L <sub>g</sub>	Ejector Length, ft
M	Mach Number; Jet or Free Stream
m	Known Value of a Parameter
N	Number of Elements
n	Number of Samples Taken of a Given Parameter
N <sub>0</sub>	Velocity Index

## LIST OF SYMBOLS

### Symbols

$N_{SH}$	Normalized Shock Cell Noise, dB
OAPWL	Overall Sound Power Level, dB
OASPL	Overall Sound Pressure Level, dB
$P$	Pressure, lbf/in. <sup>2</sup>
PNL	Perceived Noise Level, PNdB
$P_T/P_a$ , $P_T/P_o$ , PR	Nozzle total Pressure Ratio
$R$ , $r$	Radius, ft
$R_p$	Plug Radius, ft
$R_r$	Radius Ratio, determined by the ratio of the inner radius to the outer radius for the particular flow passage.
$R/R_o$ , $r/r_o$	Normalized Radial Location when referring to Jet Plume Laser Velocimeter Surveys
SPL	Sound Pressure Level, dB
$T$	Temperature, ° R
$t$	Time, Seconds
TF	Turbofan
$U$ , $V$	Mean Velocity, ft/sec, Jet or Free stream
$U'$ $u'$	Local Turbulent Velocity, ft/sec
VCE	Variable Cycle Engine
$W$	Weight Flow Rate, lbm/sec
$W_{C/S^* P}$	Chute or Spoke Width at Plug, ft
$W_{C/S^* S}$	Chute or Spoke Width at Shroud, ft
$W_F$ , $S$	Flow Width at Shroud, ft
$W_F$ , $P$	Flow Width at Plug, ft
$X$	Axial Distance, ft
$\bar{X}$	mean of measured Values of a Parameter
$X_{peak}$	Peak Axial Noise Source Location For a Given Frequency, ft
$X_s$	Ejector Axial Spacing, ft
1/3 OBSPL	One-Third-Octave-Band SPL, dB
$\theta$	Shock Cell Noise Parameter, $\sqrt{N^2-1}$ or Bypass Ratio, $W_o/W_i$
$\gamma$	Plug half Angle, degrees

## LIST OF SYMBOLS

### Symbols

$\theta$	Element Orientation Angle, Degrees
$\theta_I$	Angle Relative to Inlet Axis, Degrees
$\lambda$	Wavelength, ft
$\rho$	Density, lbm/ft <sup>3</sup>
$w, w$	Jet Density Exponent

### Subscript

a, o	Ambient
a, a/c, FS	Aircraft, Tunnel, Free stream or External
B, ch	Chute Base
c, i	Core or Inner Stream
ISA	International Standard Atmosphere
j	Jet
m, ma, mix	Mass-Averaged Conditions
o, f	Outer Stream or Fan Duct
s	Static Conditions
T	Total Conditions
1, 2, 3, 4	Control Planes Associated with Thrust Measurement Test Setup
8	Condition at Core (Inner) Flow Throat
9	Nozzle Exit Conditions of Inner (Core) Flow
18	Condition at Outer (Fan/Duct) Flow Throat

### Superscript

i	Inner (Core) Stream
o	Outer (Fan/Duct) Stream
*	Denotes Sonic Conditions

## LIST OF ILLUSTRATIONS

<u>Figure</u>		<u>Page</u>
1-1.	Evaluation of Noise Mechanisms for a Conical Nozzle.	2
1-2.	Correlation Between Measured and Predicted Effective Perceived Noise Level, EPNL, for All Types of Suppressor Nozzles.	4
1-3.	Typical Peak Static Noise Suppression Characteristics.	6
1-4.	Summary of Range and Noise Characteristics for Several Baseline and Suppression Levels.	9
3-1.	Description of Geometric Parameters.	28
3-2(a).	Far-Field Acoustic Test Matrix, Model 1, JENOTS.	36
3-2(b).	Far-Field Acoustic Test Matrix, Model 14, Cell 41 Anechoic Facility.	36
3-3.	Far-Field Acoustic Test Matrix, Model 2, JENOTS.	37
3-4.	Far-Field Acoustic Test Matrix, Models 3, 4, and 5, JENOTS.	37
3-5.	Far-Field Acoustic Test Matrix, Models 6 and 8, JENOTS.	39
3-6.	Far-Field Acoustic Test Matrix, Model 8, JENOTS.	40
3-7(a).	Far-Field Acoustic Test Matrix, Model 9, JENOTS.	41
3-7(b).	Far-Field Acoustic Test Matrix, Models 10, 11, 12, and 13, JENOTS.	41
3-8.	Far-Field Acoustic Test Matrix, Models 14 Through 19, Cell 41 Anechoic Facility.	42
3-9.	Far-Field Acoustic Test Matrix, Models 20 and 21, Cell 41 Anechoic Facility.	42
3-10.	Far-Field Acoustic Test Matrix, Models 22 Through 32 and 36, Cell 41 Anechoic Facility.	43
3-11.	Far-Field Acoustic Test Matrix, Models 39 Through 45 and 47, JENOT: Free Jet.	46
3-12.	Schematic of Acoustic Data Acquisition Systems.	50

LIST OF ILLUSTRATIONS (Continued)

<u>Figure</u>		<u>Page</u>
3-13.	Data Reduction System, JENOTS and Cell 41.	53
3-14.	Schematic of Laser Velocimeter Optics Package.	59
3-15(a).	Laser Velocimeter and Ellipsoidal Mirror at JENOTS.	60
3-15(b).	Laser Velocimeter in Cell 41 Anechoic Facility.	60
3-16.	Schematic of Laser Velocity Measurements.	62
3-17.	Schematics and Summary of Ellipsoidal Mirror Characteristics.	65
3-18.	Summary of Conical (Models 1 and 14) Nozzle Peak OASPL Characteristics.	69
3-19.	Summary of Conical Nozzle (Models 1 and 14) Peak PNL Characteristics.	69
3-20.	Summary of Conical Nozzle (Models 1 and 14) 90° OASPL Characteristics.	70
3-21.	Summary of Conical Nozzle (Models 1 and 14) 90° PNL Characteristics.	70
3-22.	Summary of Conical Nozzle (Models 1 and 14) 50° OASPL Characteristics.	71
3-23.	Summary of Conical Nozzle (Models 1 and 14) 50° PNL Characteristics.	71
3-24.	Summary of Conical Nozzle (Models 1 and 14) Power Level Characteristics.	72
3-25.	Supersonic Jet OASPL Correlation with Shock Strength Parameter $\beta$ , Conical Nozzle (Model 14).	74
3-26.	Supersonic Jet PNL Correlation with Shock Strength Parameter $\beta$ , Conical Nozzle (Model 14).	75
3-27.	Impact of Shock Noise on OASPL and PNL Directivity Conical Nozzle (Model 14), $V_{ma} = V_j = 1600$ ft/sec.	77
3-28.	Impact of Shock Noise on Spectra Conical Nozzle (Model 14), $V_{ma} = V_j = 1600$ ft/sec.	78

# LIST OF ILLUSTRATIONS (Continued)

<u>Figure</u>		<u>Page</u>
3-29.	Impact of Shock Noise on OASPL and PNL Directivity, Conical Nozzle (Model 14), $V_{ma} = V_j = 2000$ ft/sec.	79
3-30.	Impact of Shock Noise on Spectra, Conical Nozzle (Model 14), $V_{ma} = V_j = 2000$ ft/sec.	80
3-31.	Impact of Cycle Variation at Ambient Temperature on OASPL and PNL Directivity, Conical Nozzle (Model 1).	81
3-32.	Impact of Cycle Variation at Ambient Temperature on Spectra, Conical Nozzle (Model 1).	82
3-33.	Impact of Cycle Variation at 1500° R on OASPL and PNL Directivity, Conical Nozzle (Model 14).	83
3-34.	Impact of Cycle Variation at 1500° R on Spectra, Conical Nozzle (Model 14).	84
3-35.	Summary of C-D Plug Nozzle (Model 2) Peak Noise Characteristics.	86
3-36.	Summary of C-D Plug Nozzle (Model 2) 90° Noise Characteristics.	87
3-37.	Summary of C-D Plug Nozzle (Model 2) 50° Noise Characteristics.	88
3-38.	Summary of C-D Plug Nozzle (Model 2) Power Level Noise Characteristics.	89
3-39.	Correlation of Peak OASPL with Pressure Ratio for a C-D Plug Nozzle (Model 2).	93
3-40.	Polar OASPL Distributions at $V_{ma} = 1000, 1250, 1640,$ and $2090$ ft/sec.	94
3-41.	150° Spectra at $V_{ma} = 1000, 1250, 1640,$ and $2090$ ft/sec.	95
3-42.	Jet Density Exponent Correlation.	97
3-43.	Model Hardware for Parametric Nozzle Radius Ratio Study.	99
3-44.	Summary of Plug Nozzle Peak OASPL and Suppression Levels.	100
3-45.	Summary of Plug Nozzle Peak PNL and Suppression Levels.	101

# LIST OF ILLUSTRATIONS (Continued)

<u>Figure</u>		<u>Page</u>
3-46.	Summary of Plug Nozzle 90° OASPL and Suppression Levels.	102
3-47.	Summary of Plug Nozzle 90° PNL and Suppression Levels.	103
3-48.	Summary of Plug Nozzle 50° OASPL and PNL Characteristics.	104
3-49.	Summary of Plug Nozzle OAPWL and Suppression Levels.	105
3-50.	Impact of Plug Radius Ratio on OASPL and PNL Directivity, $V_{ma} = 1490$ ft/sec.	108
3-51.	Impact of Plug Radius Ratio on OASPL and PNL Directivity, $V_{ma} = 1490$ ft/sec.	109
3-52.	Impact of Plug Radius Ratio on OASPL and PNL Directivity, $V_{ma} = 1950$ ft/sec.	110
3-53.	Impact of Plug Radius Ratio on Spectra, $V_{ma} = 1950$ ft/sec.	111
3-54.	Impact of Plug Radius Ratio on OASPL and PNL Directivity, $V_{ma} = 2350$ ft/sec.	112
3-55.	Impact of Plug Radius Ratio on Spectra, $V_{ma} = 2350$ ft/sec.	113
3-56.	Jet Density Exponent Correlation.	114
3-57.	Impact of Velocity Ratio on Spectra, $AR = 2.0$ Coplanar- Coannular Nozzle (Model 6).	116
3-58.	Impact of Velocity Ratio on Spectra, $AR = 2.0$ Coplanar- Coannular Nozzle (Model 6).	117
3-59.	Impact of Velocity Ratio on OASPL and PNL Directivity.	118
3-60.	Impact of Velocity Ratio on Spectra.	119
3-61.	Comparison of OASPL and PNL Directivity at $V_o/V_i = 1.25$ , $AR = 2.0$ Coplanar-Coannular Nozzle (Model 6).	120
3-62.	Comparison of OASPL and PNL Directivity, $V_o/V_i = 2.0$ , $AR = 2.0$ Coplanar-Coannular Nozzle (Model 6).	121
3-63(a).	Normalized Spectra, $V_o/V_i = 1.25$ , $AR = 2.0$ Coplanar- Coannular Nozzle (Model 6).	122
3-63(b).	Normalized Spectra, $V_o/V_i = 2.0$ , $AR = 2.0$ Coplanar- Coannular Nozzle (Model 6).	123

# LIST OF ILLUSTRATIONS (Continued)

<u>Figure</u>		<u>Page</u>
3-64.	Peak PNL Coplanar-Coannular Nozzle Area Ratio Variation.	125
3-65.	Peak OASPL Coplanar-Coannular Nozzle Area Ratio Variation.	126
3-66.	90° PNL and OASPL Coplanar-Coannular Nozzle Area Ratio Variation.	127
3-67.	50° PNL and OASPL Coplanar-Coannular Nozzle Area Ratio Variation.	128
3-68.	OASPL and PNL Directivity Variation with Area Ratio, $V_o/V_i = 2.0$ .	129
3-69.	OASPL and PNL Directivity Variation with Area Ratio, $V_o/V_i = 1.5$ .	130
3-70.	OASPL and PNL Directivity Variation with Area Ratio, $V_o/V_i = 2.0$ .	131
3-71.	Spectra Variation with Area Ratio, $V_o/V_i = 1.0$ .	132
3-72.	Spectra Variation with Area Ratio, $V_o/V_i = 1.5$ .	133
3-73.	Spectra Variation with Area Ratio, $V_o/V_i = 2.0$	134
3-74.	Coannular-Coplanar Nozzle Suppression Characteristics with Varying Nozzle Area Ratio.	136
3-75.	Impact of Cycle Variation on Suppression Characteristics of $A_o/A_i = 0.4$ Coplanar-Coannular Nozzle (Models 12 and 13).	137
3-76.	Impact of Cycle Variation on Suppression Characteristics of $A_o/A_i = 0.65$ Coplanar-Coannular Nozzle (Models 10 and 11).	138
3-77.	OASPL Directivity Variation with Area Ratio, $W_i/W_o < 0.1$ .	139
3-78.	PNL Directivity Variation with Area Ratio, $W_i/W_o < 0.1$ .	140
3-79.	Spectra Variation with Area Ratio, $V_{ma} = 2350$ ft/sec.	141
3-80.	Spectra Variation with Area Ratio, $V_{ma} = 1800$ ft/sec.	142
3-81.	Impact of Inner Flow Variation, $A_o/A_i = 0.4$ , PNL and OASPL Directivity.	143
3-82.	Impact of Inner Flow Variation, $A_o/A_i = 0.65$ , PNL and OASPL Directivity.	144



LIST OF ILLUSTRATIONS (Continued)

<u>Figure</u>		<u>Page</u>
3-83.	Impact of Inner Flow Variation on Spectra, $A_o/A_i = 0.4$ $V_{ma} = 2400$ ft/sec.	145
3-84.	Impact of Inner Flow Variation on Spectra, $A_o/A_i = 0.4$ , $V_{ma} = 1800$ ft/sec.	146
3-85.	Impact of Inner Flow Variation on Spectra, $A_o/A_i = 0.65$ $V_{ma} = 2400$ ft/sec.	147
3-86.	Impact of Inner Flow Variation on Spectra, $A_o/A_i = 0.65$ $V_{ma} = 1800$ ft/sec.	148
3-87.	Summary of Plug Nozzle and Coplanar-Coannular Nozzle Peak PNL Suppression Levels.	149
3-88.	Annular Suppressor Area Ratio and Radius Ratio Variation on Turbojet.	152
3-89.	Impact of Area Ratio and Radius Ratio on Peak OASPL.	153
3-90.	Impact of Area Ratio and Radius Ratio on Peak PNL.	154
3-91.	Impact of Area Ratio and Radius Ratio on $90^\circ$ PNL and OASPL.	155
3-92.	Impact of Area Ratio and Radius Ratio on $50^\circ$ PNL and OASPL.	156
3-93.	Impact of Area Ratio and Radius Ratio on OAPWL.	157
3-94.	Impact of Area Ratio and Radius Ratio on PNL and OASPL Directivity, $V_{ma} = 2625$ ft/sec.	159
3-95.	Impact of Area Ratio and Radius Ratio on Spectra, $V_{ma} =$ $2625$ ft/sec.	160
3-96.	Impact of Area Ratio and Radius Ratio on PNL and OASPL Directivity, $V_{ma} = 2150$ ft/sec.	162
3-97.	Impact of Area Ratio and Radius Ratio on Spectra, $V_{ma} =$ $2150$ ft/sec.	163
3-98.	Impact of Area Ratio and Radius Ratio on PNL and OASPL Directivity, $V_{ma} = 1400$ ft/sec.	165

LIST OF ILLUSTRATION (Continued)

<u>Figure</u>		<u>Page</u>
3-99.	Impact of Area Ratio and Radius Ratio on Spectra, $V_{ma} = 1400$ ft/sec.	166
3-100.	Half-Span Suppressor Area Ratio and Radius Ratio Variation on Dual Flow.	167
3-101.	Impact of Area Ratio and Radius Ratio on Peak PNL, Dual Flow.	169
3-102.	Impact of Area Ratio and Radius Ratio on Peak OASPL, Dual Flow.	170
3-103.	Impact of Area Ratio and Radius Ratio on $90^\circ$ PNL, Dual Flow.	172
3-104.	Impact of Area Ratio and Radius Ratio on $90^\circ$ OASPL, Dual Flow.	173
3-105.	Impact of Area Ratio and Radius Ratio on $50^\circ$ PNL, Dual Flow.	174
3-106.	Impact of Area Ratio and Radius Ratio on $50^\circ$ OASPL, Dual Flow.	175
3-107.	Impact of Area Ratio and Radius Ratio on OAPWL, Dual Flow.	177
3-108.	Impact of Area Ratio and Radius Ratio on OASPL and PNL Directivity, $V_{ma} = 2425$ ft/sec, Dual Flow.	178
3-109.	Impact of Area Ratio and Radius Ratio on Spectra, $V_{ma} = 2425$ ft/sec, Dual Flow.	179
3-110.	Impact of Area Ratio and Radius Ratio on OASPL and PNL Directivity, $V_{ma} = 1200$ ft/sec, Dual Flow.	180
3-111.	Impact of Area Ratio and Radius Ratio on Spectra, $V_{ma} = 1200$ ft/sec, Dual Flow.	181
3-112.	Impact of Area Ratio and Radius Ratio on PNL and OASPL Directivity, $V_{ma} = 1945$ ft/sec, Dual Flow.	182
3-113.	Impact of Area Ratio and Radius Ratio on Spectra, $V_{ma} = 1945$ ft/sec, Dual Flow.	183

# LIST OF ILLUSTRATIONS (Continued)

<u>Figure</u>		<u>Page</u>
3-114.	Annular Suppressor Area Ratio Variation at Constant Radius Ratio, Dual Flow.	185
3-115.	Area Ratio Variation at Constant Radius Ratio, Peak OASPL.	187
3-116.	Area Ratio Variation at Constant Radius Ratio, Peak PNL.	188
3-117.	Area Ratio Variation at Constant Radius Ratio, 90° OASPL.	189
3-118.	Area Ratio Variation at Constant Radius Ratio, 90° PNL.	189
3-119.	Area Ratio Variation at Constant Radius Ratio, 50° OASPL.	190
3-120.	Area Ratio Variation at Constant Radius Ratio, 50° PNL.	190
3-121.	Area Ratio Variation at Constant Radius Ratio, OAPWL.	191
3-122.	Area Ratio Variation at Constant Velocity Ratio, Peak OASPL.	192
3-123.	Area Ratio Variation at Constant Velocity Ratio, Peak PNL.	193
3-124.	Area Ratio Variation at Constant Radius Ratio, OASPL and PNL Directivity, $V_{ma} = 2075$ ft/sec.	194
3-125.	Area Ratio Variation at Constant Radius Ratio, Spectra, $V_{ma} = 2075$ ft/sec.	195
3-126.	Area Ratio Variation at Constant Radius Ratio, OASPL and PNL Directivity, $V_{ma} = 1340$ ft/sec.	196
3-127.	Area Ratio Variation at Constant Radius Ratio, Spectra, $V_{ma} = 1340$ ft/sec.	197
3-128.	Dual Flow Models for Velocity Ratio Investigation at $A_0/A_1 = 0.65$ .	202
3-129.	Dual Flow Models for Velocity Ratio Investigation at $A_0/A_1 = 0.65$ .	203
3-130.	Dual Flow Models for Velocity Ratio Investigation at $A_0/A_1 = 1.92$ and $3.61$ .	204
3-131.	Peak PNL and OASPL Variation with $V_0/V_1$ , Model 33.	205

# LIST OF ILLUSTRATIONS (Continued)

<u>Figure</u>		<u>Page</u>
3-132.	90° PNL and OASPL Variation with $V_o/V_i$ , Model 33.	206
3-133.	50° PNL and OASPL Variation with $V_o/V_i$ , Model 33.	207
3-134.	Peak PNL and OASPL Variation with $V_o/V_i$ , Model 34.	208
3-135.	90° PNL and OASPL Variation $V_o/V_i$ , Model 34.	209
3-136.	50° PNL and OASPL Variation with $V_o/V_i$ , Model 34.	210
3-137.	Peak PNL and OASPL Variation with $V_o/V_i$ , Model 35.	211
3-138.	90° PNL and OASPL Variation with $V_o/V_i$ , Model 35.	212
3-139.	50° PNL and OASPL Variation with $V_o/V_i$ , Model 35.	213
3-140.	Impact of $V/V_i$ on PNL and OASPL Directivity, Model 33, $V_{ma} = 2010$ to 2050 ft/sec.	216
3-141.	Impact of $V_o/V_i$ on Spectra, Model 33, $V_{ma} = 2010$ to 2050 ft/sec.	217
3-142.	Impact of $V/V_i$ on PNL and OASPL Directivity, Model 33, $V_{ma} = 1685$ to 1840 ft/sec.	218
3-143.	Impact of $V_o/V_i$ on Spectra, Model 33, $V_{ma} = 1685 - 1840$ ft/sec.	219
3-144.	Impact of $V_o/V_i$ on PNL and OASPL Directivity, Model 34, $V_{ma} = 2250 - 2390$ ft/sec.	220
3-145.	Impact of $V_o/V_i$ on Spectra, Model 34, $V_{ma} = 2250 - 2390$ ft/sec.	221
3-146.	Impact of $V/V_i$ on PNL and OASPL Directivity, Model 34, $V_{ma} = 1720$ to 1830 ft/sec.	222
3-147.	Impact of $V_o/V_i$ on Spectra, Model 34, $V_{ma} = 1720 - 1830$ ft/sec.	223
3-148.	Peak PNL and OASPL Variation with $V_o/V_i$ , Model 31.	225
3-149.	90° PNL and OASPL Variation with $V_o/V_i$ , Model 31.	226
3-150.	50° PNL and OASPL Variation with $V_o/V_i$ , Model 31.	227

# LIST OF ILLUSTRATIONS (Continued)

<u>Figure</u>		<u>Page</u>
3-151.	Peak PNL and OASPL Variation with $V_o/V_1$ , Model 31.	228
3-152.	90° PNL and OASPL Variation with $V_o/V_1$ , Model 27.	229
3-153.	50° PNL and OASPL Variation with $V_o/V_1$ , Model 27.	230
3-154.	Peak PNL and OASPL Variation with $V_o/V_1$ , Model 26.	231
3-155.	90° PNL and OASPL Variation with $V_o/V_1$ , Model 26.	232
3-156.	50° PNL and OASPL Variation with $V_o/V_1$ , Model 26.	233
3-157.	Dual Flow Model for $\beta$ Investigation at $A_o/A_1 = 1.92$ .	235
3-158.	Peak PNL Variation with $\beta$ , Model 33.	237
3-159.	Peak OASPL Variation with $\beta$ , Model 33.	238
3-160.	90° PNL and OASPL Variation with $\beta$ , Model 33.	239
3-161.	50° PNL and OASPL Variation with $\beta$ , Model 33.	240
3-162.	Peak PNL Variation with $\beta$ , Model 34.	241
3-163.	Peak OASPL Variation with $\beta$ , Model 34.	242
3-164.	90° PNL and OASPL Variation with $\beta$ , Model 34.	243
3-165.	50° PNL and OASPL Variation with $\beta$ , Model 34.	244
3-166.	Peak PNL Variation with $\beta$ , Model 31.	245
3-167.	Peak OASPL Variation with $\beta$ , Model 31.	246
3-168.	90° PNL and OASPL Variation with $\beta$ , Model 31.	247
3-169.	50° PNL and OASPL Variation with $\beta$ , Model 31.	248
3-170.	Peak PNL Variation with $\beta$ , Model 23.	249
3-171.	Peak OASPL Variation with $\beta$ , Model 23.	250
3-172.	90° PNL and OASPL Variation with $\beta$ , Model 23.	251

# LIST OF ILLUSTRATIONS (Continued)

<u>Figure</u>		<u>Page</u>
3-173.	50° PNL and OASPL Variation with $\beta$ , Model 23.	252
3-174.	Dual Flow Models 23, 24, 25, and 26 for $A_o/A_i$ and Inner Plug Geometry Variation.	255
3-175.	Dual Flow Models 28 and 29 for $A_o/A_i$ and Inner Plug Geometry Variation.	256
3-176.	Schematic of Inner Plug Geometry Variations.	257
3-177.	Peak PNL Variation with $A_o/A_i$ and Inner Plug Geometry, Models 23 - 26, $W_{Inner} = 15\% W_{Outer}$ Cycle.	258
3-178.	Peak OASPL Variation with $A_o/A_i$ and Inner Plug Geometry, Models 23 - 26, $W_{Inner} = 15\% W_{Outer}$ Cycle.	259
3-179.	90° PNL and OASPL Variation with $A_o/A_i$ and Inner Plug Geometry, Models 23 - 26, $W_{Inner} = 15\% W_{Outer}$ Cycle.	260
3-180.	50° PNL and OASPL Variation with $A_o/A_i$ and Inner Plug Geometry, Models 23 - 26, $W_{Inner} = 15\% W_{Outer}$ .	261
3-181.	Peak PNL Variation with $A_o/A_i$ and Inner Plug Geometry, Models 23 - 26, $W_{Inner} = 30\% W_{Outer}$ Cycle.	262
3-182.	Peak OASPL Variation with $A_o/A_i$ and Inner Plug Geometry, Models 23 - 26, $W_{Inner} = 30\% W_{Outer}$ Cycle.	263
3-183.	90° PNL and OASPL Variation with $A_o/A_i$ and Inner Plug Geometry, Models 23 - 26, $W_{Inner} = 30\% W_{Outer}$ Cycle.	264
3-184.	50° PNL and OASPL Variation with $A_o/A_i$ and Inner Plug Geometry, Models 23 - 26, $W_{Inner} = 30\% W_{Outer}$ Cycle.	265
3-185.	Peak PNL Variation with $A_o/A_i$ and Inner Plug Geometry, Models 23 - 26, DBTF/Inverted Dual Flow Cycle.	266
3-186.	Peak OASPL Variation with $A_o/A_i$ and Inner Plug Geometry, Models 23 - 26, DBTF/Inverted Dual Flow Cycle.	267
3-187.	90° PNL and OASPL Variation with $A_o/A_i$ and Inner Plug Geometry, Models 23 - 26, DBTF/Inverted Dual Flow Cycle.	268
3-188.	50° PNL and OASPL Variation with $A_o/A_i$ and Inner Plug Geometry, Models 23 - 26, DBTF/Inverted Dual Flow Cycle.	269

# LIST OF ILLUSTRATIONS (Continued)

<u>Figure</u>		<u>Page</u>
3-189.	Peak PNL and OASPL Variation with Inner Plug Geometry, Models 28 and 29, DBTF/Inverted Dual Flow Cycle.	270
3-190.	90° PNL and OASPL Variation with Inner Plug Geometry, Models 28 and 29, DBTF/Inverted Dual Flow Cycle.	271
3-191.	50° PNL and OASPL Variation with Inner Plug Geometry, Models 28 and 29, DBTF/Inverted Dual Flow Cycle.	272
3-192.	Impact of $A/A_1$ and Inner Plug Geometry on PNL and OASPL Directivity, Models 23 - 26, $W_{Inner} = 30\% W_{Outer}$ Cycle, $V_{ma} = 2300$ ft/sec.	275
3-193.	Impact of $A/A_1$ and Inner Plug Geometry on Spectra, Models 23 - 26, $W_{Inner} = 30\% W_{Outer}$ Cycle, $V_{ma} = 2300$ ft/sec.	276
3-194.	Impact of $A/A_1$ and Inner Plug Geometry on PNL and OASPL Directivity, Models 23 - 26, $W_{Inner} = 30\% W_{Outer}$ Cycle, $V_{ma} = 1875$ ft/sec.	277
3-195.	Impact of $A/A_1$ and Inner Plug Geometry on Spectra, Models 23 - 26, $W_{Inner} = 30\% W_{Outer}$ Cycle, $V_{ma} = 1875$ ft/sec.	278
3-196.	Impact of $A/A_1$ and Inner Plug Geometry on PNL and OASPL Directivity, Models 23 - 26, $W_{Inner} = 30\% W_{Outer}$ Cycle, $V_{ma} = 1380$ ft/sec.	279
3-197.	Impact of $A/A_1$ and Inner Plug Geometry on Spectra, Models 23 - 26, $W_{Inner} = 30\% W_{Outer}$ Cycle, $V_{ma} = 1380$ ft/sec.	280
3-198.	Summary of Comparison of Suppressed Dual Flow with No Inner Flow to Full-Plug Turbojets.	281
3-199.	Half-Span Suppressor Element Number Variation on Dual Flow.	283
3-200.	Suppressor Element Number Variation, Peak Noise and Suppression Levels.	285
3-201.	Suppressor Element Number Variation, Peak PNL and Suppression Levels.	286

# LIST OF ILLUSTRATIONS (Continued)

<u>Figure</u>		<u>Page</u>
3-202.	Suppressor Element Number Variation, Peak OASPL and Suppression Levels.	287
3-203.	Suppressor Element Number Variation, 90° PNL.	288
3-204.	Suppressor Element Number Variation, 90° OASPL.	289
3-205.	Suppressor Element Number Variation, 50° PNL.	290
3-206.	Suppressor Element Number Variation, 50° OASPL.	291
3-207.	Suppressor Element Number Variation, OAPWL.	292
3-208.	Suppressor Element Number Variation, OASPL and PNL Directivity, $V_{ma} = 2425$ ft/sec.	294
3-209.	Suppressor Element Number Variation, Spectra, $V_{ma} = 2425$ ft/sec.	295
3-210.	Suppressor Element Number Variation, OASPL and PNL Directivity, $V_{ma} = 2100$ ft/sec.	296
3-211.	Suppressor Element Number Variation, Spectra, $V_{ma} = 2100$ ft/sec.	297
3-212.	Suppressor Element Number Variation, OASPL and PNL Directivity, $V_{ma} = 1200$ ft/sec.	298
3-213.	Suppressor Element Number Variation, Spectra, $V_{ma} = 1200$ ft/sec.	299
3-214.	Element Type Variation on Turbojet.	302
3-215.	Variation of Element Type, Turbojet, Peak OASPL and Suppression Levels.	303
3-216.	Variation of Element Type, Turbojet, Peak PNL and Suppression Levels.	304
3-217.	Variation of Element Type, Turbojet, 90° OASPL and PNL.	306
3-218.	Variation of Element Type, Turbojet, 50° OASPL and PNL.	307
3-219.	Variation of Element Type, Turbojet, OAPWL and Suppression Levels.	308



LIST OF ILLUSTRATIONS (Continued)

<u>Figure</u>		<u>Page</u>
3-220.	Variation of Element Type, Turbojet, OASPL and PNL Directivity, $V_{ma} = 2380$ ft/sec.	309
3-221.	Variation of Element Type, Turbojet, Spectra, $V_{ma} = 2380$ ft/sec.	310
3-222.	Variation of Element Type, Turbojet, OASPL and PNL Directivity, $V_{ma} = 2620$ ft/sec.	311
3-223.	Variation of Element Type, Turbojet, Spectra, $V_{ma} = 2620$ ft/sec.	312
3-224.	Conversion of Half-Span Suppressor from Chutes to Spokes.	314
3-225.	Element Type Variation, Dual Flow, Peak PNL and Suppression Levels.	315
3-226.	Element Type Variation, Dual Flow, Peak OASPL and Suppression Levels.	316
3-227.	Element Type Variation, Dual Flow, 90° OASPL and PNL.	317
3-228.	Element Type Variation, Dual Flow, 50° OASPL and PNL.	318
3-229.	Element Type Variation, Dual Flow, Low System Area Ratio.	320
3-230.	Element Type Study, Dual Flow, Low System Area Ratio, Peak PNL.	322
3-231.	Element Type Study, Dual Flow, Low System Area Ratio, Peak OASPL.	323
3-232.	Acoustically Treated Ejector Application to Annular Suppressor, Turbojet.	324
3-233.	Details of the Acoustically Treated Ejector.	326
3-234.	Impact of Acoustically Treated Ejector, Turbojet, Peak PNL.	328
3-235.	Impact of Acoustically Treated Ejector, Turbojet, Peak OASPL.	329
3-236.	Impact of Acoustically Treated Ejector, Turbojet, 90° OASPL, PNL, and Suppression Levels.	330

# LIST OF ILLUSTRATIONS (Continued)

<u>Figure</u>		<u>Page</u>
3-237.	Impact of Acoustically Treated Ejector, Turbojet, 50° OASPL, PNL, and Suppression Levels.	331
3-238.	Impact of Acoustically Treated Ejector, Turbojet, OAPWL and Suppression Levels.	332
3-239.	Impact of Acoustically Treated Ejector, Turbojet, OASPL, and PNL Directivity, $V_{ma} = 2005$ ft/sec.	334
3-240.	Impact of Acoustically Treated Ejector, Turbojet, Spectra, $V_{ma} = 2005$ ft/sec.	335
3-241.	Impact of Acoustically Treated Ejector, Turbojet, OASPL, and PNL Directivity, $V_{ma} = 2625$ ft/sec.	336
3-242.	Impact of Acoustically Treated Ejector, Turbojet, Spectra, $V_{ma} = 2625$ ft/sec.	337
3-243.	Acoustically Treated Ejector Application to Annular Suppressor, Dual Flow.	338
3-244.	Treated Ejector Application to Dual Flow, Peak PNL and Suppression Levels.	340
3-245.	Treated Ejector Application to Dual Flow, Peak OASPL and Suppression Levels.	341
3-246.	Treated Ejector Application to Dual Flow, DBTF Cycle, Peak OASPL, PNL, and Suppression Levels.	342
3-247.	Treated Ejector Application to Dual Flow, 90° OASPL, PNL, and Suppression Levels.	343
3-248.	Treated Ejector Application to Dual Flow, 50° OASPL, PNL, and Suppression Levels.	344
3-249.	Treated Ejector Application to Dual Flow, OAPWL and Suppression Levels.	345
3-250.	Treated Ejector Application to Dual Flow, OASPL and PNL Directivity, $V_{ma} = 2095$ ft/sec.	346
3-251.	Treated Ejector Application to Dual Flow, Spectra, $V_{ma} = 2095$ ft/sec.	347

LIST OF ILLUSTRATIONS (Continued)

<u>Figure</u>		<u>Page</u>
3-252.	Unsuppressed Coannular Nozzles with Acoustically Treated Ejector.	349
3-253.	Unsuppressed Coannular Nozzles with Treated Ejectors, Peak OASPL, PNL, and Suppression Levels.	350
3-254.	Unsuppressed Coannular Nozzles with Treated Ejectors, 90° OASPL and PNL.	351
3-255.	Unsuppressed Coannular Nozzles with Treated Ejectors, 50° OASPL and PNL.	352
3-256.	Unsuppressed Coannular Nozzle with Treated Ejectors, OAPWL and Suppression Levels.	353
3-257.	Summary of Results for Treated Ejector Application to Unsuppressed Coannular Systems.	355
3-258.	Unsuppressed Coannular Nozzles with Treated Ejectors, OASPL and PNL Directivity.	356
3-259.	Unsuppressed Coannular Nozzles with Treated Ejectors, Spectra.	357
3-260.	Typical Peak Static Noise Suppression Characteristics.	359
3-261.	Tests to Evaluate the Influence of Simulated Flight, Summary of Suppressor Nozzle Families.	360
3-262.	Static and Flight Peak PNL Levels.	362
3-263.	Static and Flight PNL Suppression Levels.	363
3-264.	Static and Flight Peak PNL Levels.	365
3-265.	Static and Flight 90° PNL Levels.	366
3-266.	Conical Nozzle (Model 47) Velocity Indices.	368
3-267.	Plug Nozzle (Models 39 and 40) Velocity Indices	369
3-268.	Chute Nozzle (Models 41, 42, and 43) Velocity Indices.	370
3-269.	104-Tube (Model 44) and 104-Hole (Model 45) Nozzle Velocity Indices.	371
3-270.	Velocity Indices for Several Nozzles.	372

LIST OF ILLUSTRATIONS (Continued)

<u>Figure</u>		<u>Page</u>
3-271.	Comparison of Static and Flight Spectra, 104-Tube and 36-Chute Nozzles (Models 44 and 41).	373
3-272.	A Comparison of Flight Spectra for 104-Tube (Model 44) and 36-Chute (Model 42) Nozzles.	374
3-273.	Summary of Static and Flight PNL Suppression Characteristics (Models 39 and 40).	375
3-274.	Summary of Static and Flight Suppression Characteristics (Models 41 and 42).	376
3-275.	Summary of Static and Flight Suppression Characteristics (Models 44 and 45).	377
3-276.	0.35 Radius Ratio Plug Nozzle (Model 40) PNL and OASPL Directivity, $V_{ma} = 2400$ ft/sec.	378
3-277.	0.85 Radius Ratio Plug Nozzle (Model 40) PNL and OASPL Directivity, $V_{ma} = 2000$ ft/sec.	379
3-278.	0.85 Radius Ratio Plug Nozzle (Model 40) Spectra, $V_{ma} = 2400$ ft/sec.	380
3-279.	0.85 Radius Ratio Plug Nozzle (Model 40) Spectra, $V_{ma} = 2000$ ft/sec.	381
3-280.	0.789 Radius Ratio Plug Nozzle (Model 39) PNL and OASPL Directivity, $V_{ma} = 2400$ ft/sec.	382
3-281.	0.789 Radius Ratio Plug Nozzle (Model 39) PNL and OASPL Directivity, $V_{ma} = 2000$ ft/sec.	383
3-282.	0.789 Radius Ratio Plug Nozzle (Model 39) Spectra, $V_{ma} = 2000$ ft/sec.	384
3-283.	0.789 Radius Ratio Plug Nozzle (Model 39) Spectra, $V_{ma} = 2000$ ft/sec.	385
3-284.	AR = 2.5 36-Chute, Turbojet (Model 41), PNL and OASPL Directivity, $V_{ma} = 2400$ ft/sec.	386
3-285.	AR = 2.5 36-Chute, Turbojet (Model 41), PNL and OASPL Directivity, $V_{ma} = 2400$ ft/sec.	387
3-286.	AR = 2.5 36-Chute, Turbojet (Model 41), Spectra, $V_{ma} = 2400$ ft/sec.	388

LIST OF ILLUSTRATIONS (Continued)

<u>Figure</u>		<u>Page</u>
3-287.	AR = 2.5 36-Chute, Turbojet (Model 41) Spectra, $V_{ma} = 2000$ ft/sec.	389
3-288.	AR = 2.5 36-Chute with Auxiliary Flow (Model 42), PNL and OASPL Directivity, $V_{ma} = 2000$ ft/sec.	390
3-289.	AR = 2.5 36-Chute with Auxiliary Flow (Model 42), PNL and OASPL Directivity, $V_{ma} = 2000$ ft/sec.	391
3-290.	AR = 2.5 36-Chute with Auxiliary Flow (Model 42), Spectra, $V_{ma} = 2400$ ft/sec.	392
3-291.	AR = 2.5 36-Chute with Auxiliary Flow (Model 42), Spectra, $V_{ma} = 2000$ ft/sec.	393
3-292.	AR = 2.5 36-Chute with Abrupt Step (Model 43), PNL and OASPL Directivity, $V_{ma} = 2400$ ft/sec.	394
3-293.	AR = 2.5 36-Chute with Abrupt Step, (Model 43) PNL and OASPL Directivity, $V_{ma} = 2000$ ft/sec.	395
3-294.	AR = 2.5 36-Chute with Abrupt Step (Model 43), Spectra, $V_{ma} = 2400$ ft/sec.	396
3-295.	AR = 3.5 36-Chute with Abrupt Step (Model 43), Spectra, $V_{ma} = 2000$ ft/sec.	397
3-296.	104-Tube Nozzle (Model 44), PNL and OASPL Directivity, $V_{ma} = 2400$ ft/sec.	398
3-297.	104-Tube Nozzle (Model 44), Spectra, $V_{ma} = 2400$ ft/sec.	399
3-298.	104-Hole Nozzle (Model 45), PNL and OASPL Directivity, $V_{ma} = 2400$ ft/sec.	400
3-299.	104-Hole Nozzle (Model 45), PNL and OASPL Directivity, $V_{ma} = 2080$ ft/sec.	401
3-300.	104-Hole Nozzle (Model 45), Spectra, $V_{ma} = 2400$ ft/sec.	402
3-301.	104-Hole Nozzle (Model 45), Spectra, $V_{ma} = 2080$ ft/sec.	403
3-302.	Summary of Conical Nozzle (Model 47) Forward Quadrant Noise Trends.	406
3-303.	Summary of 50° Spectra Characteristics.	407

LIST OF ILLUSTRATIONS (Continued)

<u>Figure</u>		<u>Page</u>
3-304.	0.85 Radius Ratio Plug Nozzle (Model 40) 50° Spectra at Constant Pressure Ratio.	408
3-305.	0.85 Radius Ratio Plug Nozzle (Model 40) Directivity at Constant Pressure Ratio.	409
3-306.	The Effect of Pressure Ratio Variation on the Directivity and Spectra Characteristics of a 104-Hole Nozzle (Model 45).	410
3-307.	Summary of Peak Mean Velocity Decay Characteristics.	413
3-308.	Turbulence Intensity Levels at Location of Peak Mean Velocity.	414
3-309.	Peak Turbulence Intensity Levels.	415
3-310.	Centerline Velocity Decay Characteristics.	416
3-311.	Centerline Velocity Decay Characteristics.	417
3-312.	AR = 2.0 36-Chute (Model 16) and 36-Spoke (Model 18) Nozzles, Mean Velocity and Turbulence Profiles.	418
3-313.	AR = 2.0 36-Chute (Model 16) and 36-Spoke (Model 18) Nozzles, Mean Velocity and Turbulence Profiles.	419
3-314.	Effect of Area Ratio on Peak Axial Velocity Decay Characteristics.	421
3-315.	Impact of Suppression Area Ratio on Radial Mean Velocity and Turbulence Intensity Profiles.	422
3-316.	Impact of Suppressor Area Ratio on Mean Velocity and Turbulence Intensity Profiles.	423
3-317.	Impact of a Treated Ejector on the Mean Velocity and Turbulence Profiles of a 36-Chute Nozzle.	424
3-318.	Centerline Velocity Decay for 3.56-inch Conical Nozzle (Reference 12) $V_{ref} = 2200$ ft/sec.	425
3-319.	0.85 Radius Ratio Plug Nozzle (Model 40) Centerline Mean Velocity Decay Characteristics.	427
3-320.	8-Spoke Nozzle (Model 46), Static and Flight.	428

# LIST OF ILLUSTRATIONS (Continued)

<u>Figure</u>		<u>Page</u>
3-321.	36-Chute Nozzle (Model 41) Mean Velocity Decay Characteristics, Static and Flight.	429
3-322.	104-tube Nozzle (Model 44) Mean Velocity Characteristics, Static and Flight.	430
3-323.	104-Tube Nozzle (Model 44) Turbulence Intensity Characteristics, Static and Flight.	431
3-324.	Integral Closure Check for AR = 2.0 36-Chute Nozzle, $V_o = 2384$ ft/sec, $V_i = 1187$ ft/sec.	433
3-325.	Integral Closure Check for AR = 1.75 20-Shallow-Chute Nozzle, $V_o = 2375$ ft/sec, $V_i = 1167$ ft/sec.	433
3-326.	Integral Closure Check for AR = 2.0 36-Chute Nozzle with Treated Ejector, $V_o = 1803$ ft/sec, $V_i = 1173$ ft/sec.	434
3-327.	Integral Closure Check for AR = 2.0 36-Chute Nozzle, $V_i = 2378$ ft/sec.	434
3-328.	Integral Closure Check for AR = 2.5 36-Spoke Nozzle, $V_o = 2382$ ft/sec, $V_i = 1269$ ft/sec.	435
3-329.	Effect of Element Number of Multispoke (Shallow Chute) Dual-Flow Suppressor Noise Source Distributions.	437
3-330.	Effect of Chute Area Ratio on Multichute Dual-Flow Suppressor Noise Source Distributions.	438
3-331.	Comparison of Noise Source Distributions for Multichute and Multispoke Dual-Flow Suppressors.	439
3-332.	Comparison of Noise Source Distributions for Multichute Dual-Flow and Turbojet Suppressors.	440
3-333.	Comparison of Noise Source Distributions for Multichute Dual-Flow and Turbojet Suppressors with Ejectors.	441
3-334.	Effect of an Ejector on Multichute Dual-Flow Suppressor Noise Source Distributions.	442
3-335.	Effect of an Ejector on Multichute Turbojet Suppressor Noise Source Distributions.	443
3-336.	Axial Distributions of Sound Source Intensity for a 40-Shallow-Chute Dual-Flow Suppressor (Model 32).	444

LIST OF ILLUSTRATIONS (Continued)

<u>Figure</u>		<u>Page</u>
4-1.	Typical Model Installation.	447
4-2.	Schematic of Model Air Supply.	448
4-3.	Schematic of Model Thrust-Measuring System.	449
4-4.	Schematic of Annular Suppressed Nozzle Showing Key Geometric Variables.	451
4-5.	Summary of Annular Suppressor Models Tested.	453
4-6.	Schematic of Dual-Flow Suppressor Installation.	458
4-7.	104-Tube Nozzle.	459
4-8.	104-Tube Nozzle Geometric Details.	460
4-9.	8-Lobe Nozzle.	461
4-10.	Supersonic Tunnel Association (STA) Nozzle.	462
4-11.	Control Volume Applied to Model Test Setup.	465
4-12.	STA Static Performance with the 1.248-in.-Diameter Outer Flowmeter.	469
4-13.	STA Static Performance with the 1.1398-in.-Diameter Inner Flowmeter.	470
4-14.	Wind-On STA Nozzle Thrust Coefficients.	471
4-15.	STA Nozzle Bias and Standard Deviation on Static Thrust Coefficient.	473
4-16.	STA Nozzle Bias and Standard Deviation on Flow Coefficient.	474
4-17.	Effect of Suppressor Element Number and Inner Flow on Nozzle Gross Thrust Coefficients of Shallow-Chute Nozzles.	476
4-18.	Effect of Suppressor Element Number and Free-Stream Mach Number on Nozzle Performance of Shallow-Chute Nozzles.	478
4-19.	Effect of Suppressor Element Number and Outer Flow on Nozzle Gross Thrust Coefficients of Shallow-Chute Nozzles.	479



# LIST OF ILLUSTRATIONS (Continued)

<u>Figure</u>		<u>Page</u>
4-20.	Effect of Suppressor Area Ratio and Inner Flow on Nozzle Gross Thrust Coefficients of Deep-Chute Nozzles.	480
4-21.	Effect of Suppressor Area Ratio and Free-Stream Mach Number on Nozzle Performance of Deep-Chute Nozzles.	481
4-22.	Effect of Inner Radius Ratio and Free-Stream Mach Number on Nozzle Performance of Shallow-Chute Nozzles.	483
4-23.	Inner Radius Ratio Performance Trends, Deep-Chute Models.	484
4-24.	Inner Plug Axial Position Performance Trends, Shallow-Chute Models.	485
4-25.	Inner Plug Axial Location Performance Trends, Deep-Chute Models.	486
4-26.	Inner Plug Effects on Suppressor Base Pressures, $M_0 = 0.36$ , $P_{T_i}/P_a = 2.5$ .	487
4-27.	Comparison of Chute and Spoke Model Performance.	489
4-28.	Performance Trends with External Mach Number Shallow-Chute Models.	490
4-29.	Performance Trends with External Mach Number, Deep Chutes.	491
4-30.	104-Tube Nozzle Performance Trends.	492
4-31.	104-Tube Nozzle Base Drag Losses.	493
4-32.	Eight-Lobe Performance Characteristics.	494
A-1.	Model 1 - 4.64-in.-Diameter Conical Nozzle, Adapted to JENOTS. Model 14 - 4.64-in.-Diameter Conical Nozzle, Adapted to Cell 41, Anechoic.	502
A-2.	Model 2 - Convergent-Divergent Plug, Single Flow.	503
A-3.	Model 3 - Converging Plug, $R_T = 0.59$ , Single Flow.	504
A-4.	Model 4 - Converging Plug, $R_T = 0.789$ , Single Flow.	505
A-5.	Model 5 - Converging Plug, $R_T = 0.853$ , Single Flow.	506

# LIST OF ILLUSTRATIONS (Continued)

<u>Figure</u>		<u>Page</u>
A-6.	Model 6 - Dual-Flow Coannular Coplanar, $A_o/A_i = 2.0$ . Model 9 - Coannular Coplanar, $A_o/A_i = 2.0$ , Normal Fan Operation, Low Inner Flow.	507
A-7.	Model 7 - Dual-Flow Coannular Coplanar, $A_o/A_i = 0.65$ . Models 10 and 11 Coannular Coplanar, $A_o/A_i = 0.65$ , Normal Fan Operation, Low Inner Flow and No Inner Flow, Respectively.	508
A-8.	Model 8 - Dual-Flow Coannular Coplanar, $A_o/A_i = 0.4$ . Models 12 and 13 - Coannular Coplanar, $A_o/A_i = 0.4$ , Normal Fan Operation, Low Inner Flow and No Inner Flow, Respectively.	509
A-9.	Model 15 - 36 Chute, $AR = 2.5$ , $R_T = 0.653$ Turbojet.	510
A-10.	Model 16 - 36 Chute, $AR = 2.0$ , $R_T = 0.716$ Turbojet.	511
A-11.	Model 17 - 36 Chute, $AR = 1.5$ , $R_T = 0.782$ Turbojet	512
A-12.	Model 18 - 36 Spoke, $AR = 2.0$ , $R_T = 0.716$ Turbojet.	513
A-13.	Model 19 - 36 Chute, $AR = 2.0$ , $R_T = 0.716$ Turbojet with Acoustically Treated Secondary Ejector.	514
A-14.	Model 20 - 62 Tube/Plug, $AR = 2.95$ Turbojet.	515
A-15.	Model 21 - 32 Chute, $AR = 210$ , $R_T = 0.498$ Turbojet.	516
A-16.	Model 22 - 36 Chute, $AR = 2.5$ , $R_o^o = 0.653$ Outer Suppressor; $A_o/A_i = 1.92$ , $R_o^i = 0.779$ Inner Plug, Retracted.	517
A-17.	Model 23 - 36 Chute, $AR = 2.0$ , $R_o^o = 0.716$ Outer Suppressor; $A_o/A_i = 1.92$ , $R_o^i = 0.779$ Inner Plug, In-Line.	518
A-18.	Model 24 - 36 Chute, $AR = 2.0$ , $R_o^o = 0.716$ Outer Suppressor; $A_o/A_i = 1.92$ , $R_T^i = 0.779$ Inner Plug, Retracted.	519
A-19.	Model 25 - 36 Chute, $AR = 2.0$ , $R_o^o = 0.716$ Outer Suppressor; $A_o/A_i = 3.61$ , $R_T^i = 0.89$ Inner Plug, In-Line.	520

# LIST OF ILLUSTRATIONS (Continued)

<u>Figure</u>		<u>Page</u>
A-20.	Model 26 - 36 Chute, $AR = 2.0$ , $R_o^o = 0.716$ Outer Suppressor; $A_o/A_i = 3.61$ , $R_r^i = 0.89$ Inner Plug, Retracted.	521
A-21.	Model 27 - 36 Chute, $AR = 1.5$ , $R_o^o = 0.782$ Outer Suppressor; $A_o/A_i = 1.92$ , $R_r^i = 0.779$ Inner Plug, Retracted.	522
A-22.	Model 28 - 36 Spoke, $AR = 2.0$ , $R_o^o = 0.716$ Outer Suppressor; $A_o/A_i = 1.92$ , $R_r^i = 0.779$ Inner Plug, Retracted.	523
A-23.	Model 29 - 36 Spoke, $AR = 2.0$ , $R_o^o = 0.716$ Outer Suppressor; $A_o/A_i = 1.92$ , $R_r^i = 0.779$ Inner Plug, In-Line.	524
A-24.	Model 30 - 20 Shallow Chute, $AR = 1.75$ , $R_o^o = 0.717$ Outer Suppressor; $A_o/A_i = 1.92$ , $R_r^i = 0.779$ Inner Plug, Retracted.	525
A-25.	Model 31 - 30 Shallow Chute, $AR = 1.75$ , $R_o^o = 0.717$ Outer Suppressor; $A_o/A_i = 1.92$ , $R_r^i = 0.779$ Inner Plug, Retracted.	526
A-26.	Model 32 - 40 Shallow Chute, $AR = 1.75$ , $R_o^o = 0.717$ Outer Suppressor; $A_o/A_i = 1.92$ , $R_r^i = 0.779$ Inner Plug, Retracted.	527
A-27.	Model 33 - 36 Chute, $AR = 2.5$ , $R_o^o = 0.783$ Outer Suppressor; $A_o/A_i = 0.65$ , $R_r^i = 0.674$ Inner Plug, Retracted.	528
A-28.	Model 34 - 36 Chute, $AR = 3.0$ , $R_o^o = 0.783$ Outer Suppressor; $A_o/A_i = 0.65$ , $R_r^i = 0.674$ Inner Plug, Retracted.	529
A-29.	Model 35 - 36 Spoke, $AR = 2.5$ , $R_o^o = 0.783$ Outer Suppressor; $A_o/A_i = 0.65$ , $R_r^i = 0.674$ Inner Plug, Retracted.	530
A-30.	Model 36 - 36 Chute, $AR = 2.0$ , $R_o^o = 0.716$ Outer Suppressor; $A_o/A_i = 1.92$ , $R_r^i = 0.779$ Inner Plug, Retracted with Acoustically Treated Ejector.	531

# LIST OF ILLUSTRATIONS (Continued)

<u>Figure</u>		<u>Page</u>
A-31.	Model 37 - Coannular-Noncoplanar Dual Plug Nozzle, $R_r^o = 0.853$ , $A_o/A_i = 1.59$ , $R_r^i = 0.800$ with Acoustically Treated Secondary Ejector.	532
A-32.	Model 38 - Coannular-Noncoplanar Dual Plug Nozzle, $R_r^o = 0.926$ , $A_o/A_i = 0.71$ , $R_r^i = 0.800$ with Acoustically Treated Secondary Ejector.	533
A-33.	Model 39 - Converging Plug, Single Flow, $R_r = 0.789$ .	534
A-34.	Model 40 - Converging Plug, Single Flow, $R_r = 0.85$ .	535
A-35.	Model 41 - 36 Chute, $AR = 2.5$ , $R_r = 0.78$ Turbojet.	536
A-36.	Model 42 - 36 Chute, $AR = 2.5$ , $R_r^o = 0.78$ Outer Suppressor with Induced Flow Through $A_o/A_i = 0.65$ , $R_r^i = 0.674$ Inner Plug, Retracted.	537
A-37.	Model 43 - 36 Chute, $AR = 2.5$ , $R_r^o = 0.78$ Outer Suppressor with Abrupt Step Over $A_o/A_i = 0.65$ , $R_r^i = 0.674$ Inner Plug, Retracted.	538
A-38.	Model 44 - 104 Elliptical Tubes, $AR = 2.8$ .	539
A-39.	Model 45 - 104 Elliptical Holes, $AR = 2.8$ .	540
A-40.	Model 46 - 8-Lobe Daisy, $AR = 2.1$ .	541
A-41.	Model 47 - 4.0-in.-Diameter Conical.	542
C-1.	JENOTS Data: SPL Spectra, FSDR Program Calculation.	587
C-2.	JENOTS Data: SPL Spectra, FSDR Program Calculation.	588
C-3.	Revised Atmospheric Correction Factors.	589
C-4.	Revised Atmospheric Absorption.	590
C-5.	Atmospheric Attenuation Factors.	591
C-6.	Total Absorption of Sound in Air as a Function of Frequency.	592
D-1.	Test Set-Up for Ellipsoidal Mirror Surveys.	598

LIST OF ILLUSTRATIONS (Continued)

<u>Figure</u>		<u>Page</u>
D-2.	18-inch-Diameter Shallow-Disk EM with 9-foot Working Distance.	599
D-3.	34.654-inch-Diameter Deep-Dish EM with 15-foot Working Distance.	600
D-4.	"Reverse Mounting" Microphone Fixture for Deep-Dish Ellipsoidal Mirror.	601
D-5.	Ellipsoidal Mirror Set-Up of JENOTS.	602
D-6.	Ellipsoidal Mirror Set-Up in the Anechoic Facility.	602
D-7.	Set-Up of Mirror and Noise Source for Calibration of 18-inch EM.	605
D-8.	Set-Up of Reference Microphone and Noise Source for Calibration of 18-inch EM.	606
D-9.	Gain of the 18-inch-Diameter Ellipsoidal Mirror.	607
D-10.	Normalized Window Function Width for the 18-inch-Diameter Ellipsoidal Mirror.	603
D-11.	Gain of the Deep-Dish Ellipsoidal Mirror.	609
D-12.	Normalized Window Function Width for the Deep-Dish Ellipsoidal Mirror.	610
D-13.	Equipment Schematic for EM Data Processing, General Electric Acoustic Vane.	612
D-14.	95% Confidence Interval Curves as a Function of Frequency and Integration Time.	613
D-15.	Typical Brush Chart from EM Data Reduction.	614
D-16.	Integral Closure Check for 3.56-inch Conical Nozzle, $V = 2253$ ft/sec, $V_a/c = 0$ .	621
D-17.	Axial Distribution of Sound Source Intensity (16,000 Hz, 1/3 Octave Band).	622

LIST OF ILLUSTRATIONS (Continued)

<u>Figure</u>		<u>Page</u>
D-18.	Axial Distribution of Sound Source Intensity (6300 Hz, 1/3 Octave Band).	623
D-19.	Axial Distribution of Sound Source Intensity (2500 Hz, 1/3 Octave Band).	624
D-20.	Axial Distribution of Sound Source Intensity (1000 Hz, 1/3 Octave Band).	625
D-21.	Axial Location of Peak Sound Source Intensity.	627
D-22.	Source Spectrum at Station 18 ( $x/D = 5.9$ ).	628
D-23.	Source Spectrum at Station 46 ( $x/D = 30.6$ ).	629
D-24.	Resolution of the Deep-Dish Ellipsoidal Mirror (Point Source Measurement), 4000 Hz.	633
D-25.	Resolution of the Deep-Dish Ellipsoidal Mirror (Point Source Measurement).	634
E-1.	Assumed Measurement Geometry.	636
E-2.	95% Confidence Interval Curves as a Function of Data Record Number.	645
E-3.	Details of Test Cases Used in Numerical Analysis.	651
F-1.	Geometric Details of Configuration SC-1, $N = 20$ , Baseline Plug.	661
F-2.	Geometric Details of Configuration SC-2, $N = 30$ , Baseline Plug.	662
F-3.	Geometric Details of Configuration SC-3, Modified Baseline Plug.	663
F-4.	Geometric Details of Configuration SC-4, $N = 30$ , Full Plug.	664
F-5.	Geometric Details of Configuration SC-5, $N = 30$ , Forward Baseline Plug.	665

LIST OF ILLUSTRATIONS (Continued)

<u>Figure</u>		<u>Page</u>
F-6.	Geometric Details of Configuration SC-6, $N = 40$ , Baseline Plug.	666
F-7.	Geometric Details of Configuration DC-1, $AR = 1.5$ , Baseline Plug.	667
F-8.	Geometric Details of Configuration DC-2, $AR = 1.5$ , Full Plug.	668
F-9.	Geometric Details of Configuration DC-3, $AR = 2.0$ , Baseline Plug.	669
F-10.	Geometric Details of Configuration DC-4, $AR = 2.0$ , Modified Baseline Plug.	670
F-11.	Geometric Details of Configuration DC-5, $AR = 2.0$ , Full Plug.	671
F-12.	Geometric Details of Configuration DC-6, $AR = 2.0$ , Forward Plug.	672
F-13.	Geometric Details of Configuration DC-7, $AR = 2.5$ , Baseline Plug.	673
F-14.	Geometric Details of Configuration DC-8, $AR = 2.5$ , Full Plug.	674
F-15.	Geometric Details of Configuration DC-3 (Spoke), $N = 36$ , $AR = 2.0$ , Baseline Plug.	675
F-16.	Supersonic Tunnel Association (STA) Boattail Static- Pressure Instrumentation.	677
F-17.	Annular Nozzle Outer Shroud Static Pressures.	678
F-18.	Outer Plug Static Pressures.	679
F-19.	Inner Plug Static Pressures.	680
F-20.	Suppressor Element Base Static Pressures.	681
F-21.	104-Tube Nozzle Instrumentation.	682
F-22.	Configuration SC-1 Performance.	684

LIST OF ILLUSTRATIONS (Concluded)

<u>Figure</u>		<u>Page</u>
F-23.	Configuration SC-2 Performance.	685
F-24.	Configuration SC-3 Performance.	686
F-25.	Configuration SC-4 Performance.	687
F-26.	Configuration SC-5 Performance.	688
F-27.	Configuration SC-6 Performance.	689
F-28.	Configuration DC-1 Performance.	690
F-29.	Configuration DC-2 Performance.	691
F-30.	Configuration DC-3 Performance.	692
F-31.	Configuration DC-4 Performance.	693
F-32.	Configuration DC-5 Performance.	694
F-33.	Configuration DC-6 Performance.	695
F-34.	Configuration DC-7 Performance.	696
F-35.	Configuration DC-8 Performance.	697
F-36.	Configuration DC-3 (Spoke) Performance.	698



# LIST OF TABLES

<u>Table</u>		<u>Page</u>
1-1.	Summary of Nozzle Static and Projected Flight Peak PNL Suppression Characteristics.	7
3-1.	Description of Test Models and Test Types.	15
3-2.	Test Model Comparisons Summary.	30
3-3.	Far-Field Acoustic Test Matrix Description, Models 22-32 and 36, Cell 41 Anechoic Facility.	44
3-4.	Laser Velocimeter Test Matrix, Aero Cycle Conditions.	47
3-5.	JENOTS Ground Reflections Corrections ( $\Delta dB$ 's to be Added to SPL's).	56
3-6.	Summary of Nozzle Static and Projected Flight Peak PNL Suppression Characteristics.	364
4-1.	Nozzle Configuration Description.	452
4-2.	Annular Nozzle Performance Summary.	475
B-1.	Model No. 1: 4.64-inch-Diameter Conical, Adapted to JENOTS.	544
B-2.	Model No. 2: Convergent-Divergent Plug, Single Flow.	546
B-3.	Model No. 3: Convergent Plug, $R_r = 0.59$ , Single Flow.	547
B-4.	Model No. 4: Convergent Plug, $R_r = 0.789$ , Single Flow.	548
B-5.	Model No. 5: Convergent Plug, $R_r = 0.853$ , Single Flow.	549
B-6.	Model No. 6: Dual-Flow Coannular-Coplanar, $A_o/A_i = 2.0$ .	550
B-7.	Model No. 7: Dual-Flow Coannular-Coplanar, $A_o/A_i = 0.5$ .	552
B-8.	Model No. 8: Dual-Flow Coannular-Coplanar, $A_o/A_i = 0.4$ .	553
B-9.	Model No. 9: Coannular-Coplanar, $A_o/A_i = 2.0$ , Low Inner Flow.	553
B-10.	Model No. 10: Dual-Flow Coannular-Coplanar, $A_o/A_i = 0.65$ , Low Inner Flow.	554
B-11.	Model No. 11: Coannular-Coplanar, $A_o/A_i = 0.65$ , No Inner Flow.	555

# LIST OF TABLES (Continued)

<u>Table</u>		<u>Page</u>
B-12.	Model No. 12: Coannular-Coplanar, $A_o/A_i = 0.4$ , Low Inner Flow.	555
B-13.	Model No. 13: Coannular-Coplanar, $A_o/A_i = 0.4$ , No Flow.	556
B-14.	Model No. 14: 4.64-inch-Diameter Conical, Adapted to Cell 41, Anechoic.	557
B-15.	Model No. 15: 36 Chute, $AR = 2.5$ , $R_r = 0.653$ , Turbojet.	558
B-16.	Model No. 16: 36 Chute, $AR = 2.0$ , $R_r = 0.716$ , Turbojet.	559
B-17.	Model No. 17: 36 Chute, $AR = 1.5$ , $R_r = 0.782$ , Turbojet.	559
B-18.	Model No. 18: 36 Spoke, $AR = 2.0$ , $R_r = 0.716$ , Turbojet.	560
B-19.	Model No. 19: 36 Chute, $AR = 2.0$ , $R_r = 0.716$ , Turbojet with Acoustically Treated Secondary Ejector.	560
B-20.	Model No. 20: 72 Tube/Plug, $AR = 2.95$ , Turbojet.	561
B-21.	Model No. 21: 32 Chute, $AR = 2.0$ , $R_r = 0.498$ , Turbojet.	561
B-22.	Model No. 22: 36 Chute, $AR_i = 2.5$ , $R_r^o = 0.653$ Outer Suppressor; $A_o/A_i = 1.92$ , $R_r^i = 0.779$ Inner Plug, Retracted.	562
B-23.	Model No. 23: 36 Chute, $AR_i = 2.0$ , $R_r^o = 0.716$ Outer Suppressor; $A_o/A_i = 1.92$ , $R_r^i = 0.779$ Inner Plug, In-Line.	563
B-24.	Model No. 24: 36 Chute, $AR_i = 2.0$ , $R_r^o = 0.716$ Outer Suppressor; $A_o/A_i = 1.92$ , $R_r^i = 0.779$ Inner Plug, Retracted.	564
B-25.	Model No. 25: 36 Chute, $AR_i = 2.0$ , $R_r^o = 0.716$ Outer Suppressor; $A_o/A_i = 3.61$ , $R_r^i = 0.89$ Inner Plug, In-Line.	565
B-26.	Model No. 26: 36 Chute, $AR_i = 2.0$ , $R_r^o = 0.716$ Outer Suppressor; $A_o/A_i = 3.61$ , $R_r^i = 0.89$ Inner Plug, Retracted.	566
B-27.	Model No. 27: 36 Chute, $AR_i = 1.5$ , $R_r^o = 0.782$ Outer Suppressor; $A_o/A_i = 1.92$ , $R_r^i = 0.779$ Inner Plug, Retracted.	567
B-28.	Model No. 28: 36 Spoke, $AR_i = 2.0$ , $R_r^o = 0.716$ Outer Suppressor; $A_o/A_i = 1.92$ , $R_r^i = 0.779$ Inner Plug, Retracted.	568
B-29.	Model No. 29: 36 Spoke, $AR_i = 2.0$ , $R_r^o = 0.716$ Outer Suppressor; $A_o/A_i = 1.92$ , $R_r^i = 0.779$ Inner Plug, In-Line.	569

LIST OF TABLES (Continued)

<u>Table</u>		<u>Page</u>
B-30.	Model No. 30: 20 Shallow Chute, $AR = 1.75$ , $R_r^O = 0.717$ Outer Suppressor; $A_o/A_i = 1.92$ , $R_r^I = 0.779$ Inner Plug, Retracted.	570
B-31.	Model No. 31: 30 Shallow Chute, $AR = 1.75$ , $R_r^O = 0.717$ Outer Suppressor; $A_o/A_i = 1.92$ , $R_r^I = 0.779$ Inner Plug, Retracted.	571
B-32.	Model No. 32: 40 Shallow Chute, $AR = 1.75$ , $R_r^O = 0.717$ Outer Suppressor; $A_o/A_i = 1.92$ , $R_r^I = 0.779$ Inner Plug, Retracted.	572
B-33.	Model No. 33: 36 Chute, $AR = 2.5$ , $R_r^O = 0.783$ Outer Suppressor; $A_o/A_i = 0.65$ , $R_r^I = 0.674$ Inner Plug, Retracted.	573
B-34.	Model No. 34: 36 Chute, $AR = 3.0$ , $R_r^O = 0.783$ Outer Suppressor; $A_o/A_i = 0.65$ , $R_r^I = 0.674$ Inner Plug, Retracted.	574
B-35.	Model No. 35: 36 Spoke, $AR = 2.5$ , $R_r^O = 0.783$ Outer Suppressor; $A_o/A_i = 0.65$ ; $R_r^I = 0.647$ Inner Plug, Retracted.	575
B-36.	Model No. 36: 36 Chute, $AR = 2.0$ , $R_r^O = 0.716$ Outer Suppressor; $A_o/A_i = 1.92$ ; $R_r^I = 0.779$ Inner Plug, Retracted with Acoustically Treated Secondary Ejector.	576
B-37.	Model No. 37: Coannular-Noncoplanar Dual Plug Nozzle, $R_r^O = 0.853$ , $A_o/A_i = 1.59$ , $R_r^I = 0.800$ with Acoustically Treated Secondary Ejector.	577
B-38.	Model No. 38: Coannular-Noncoplanar Dual Plug Nozzle, $R_r^O = 0.926$ , $A_o/A_i = 0.71$ , $R_r^I = 0.800$ with Acoustically Treated Secondary Ejector.	577
B-39.	Model No. 39: Converging Plug, Single-Flow, $R_r = 0.789$ .	578
B-40.	Model No. 40: Converging Plug, Single-Flow, $R_r = 0.85$ .	579
B-41.	Model No. 41: 36 Chute, $AR = 2.5$ , $R_r = 0.78$ Turbojet.	580
B-42.	Model No. 42: 36 Chute, $AR = 2.5$ , $R_r^O = 0.78$ Outer Suppressor with Induced Flow Through $A_o/A_i = 0.65$ , $R_r^I = 0.674$ Inner Plug, Retracted.	581
B-43.	Model No. 43: 36 Chute, $AR = 2.5$ , $R_r^O = 0.78$ Outer Suppressor with Abrupt Step Over $A_o/A_i = 0.65$ , $R_r^I = 0.674$ Inner Plug, Retracted.	582
B-44.	Model No. 44: 104 Elliptical Tube, $AR = 2.8$ .	583

LIST OF TABLES (Concluded)

<u>Table</u>		<u>Page</u>
B-45.	Model No. 45: 104 Elliptical Hole, AR = 2.8.	584
B-46.	Model No. 47: 4.0-inch-Diameter Conical.	585
C-1.	Listing of the GE Air-Attenuation Correction Computer Program.	593
E-1.	Sum and Sum of Squares of Row Elements of Typical A <sup>-1</sup> EM Matrices.	646
E-2.	Theoretical Statistical Errors for a Single Point Source at Center of Measurement Set - 18-inch Elliptical Mirror.	653

## 1.0 SUMMARY

The High Velocity Jet Noise Source Location and Reduction Program (Contract DOT-OS-30034) was conceived to bring analytical and experimental knowledge to bear on understanding the fundamentals of jet noise for simple and complex suppressors.

Task 3, the subject of this report, involved the experimental investigation of suppression principles, including developing an experimental data base, developing a better understanding of jet noise suppression principles, and formulating empirical methods for the acoustic design of jet noise suppressors. Acoustic scaling has been experimentally demonstrated, and five "optimum" nozzles were selected for anechoic, free-jet testing in Task 5.

Volume I - Verification of Suppression Principles and Development of Suppression Prediction Methods - Some of the experimental studies (reported in Volume II) involved acquisition of detailed, far-field, acoustic data and of aerodynamic jet-flow-field data on several baseline and noise-abatement nozzles. These data were analyzed and used to validate the theoretical jet noise prediction method of Task 2 (referred to as M\*G\*B, designating the authors' initials) and to develop and validate the empirical noise-prediction method presented herein (referred to as M\*S, designating the last name initials of the authors).\*

The Task 2 theoretical studies conclude that four primary mechanisms influence jet noise suppression: fluid shielding, convective amplification, turbulent mixing, and shock noise. A series of seven suppressor configurations (ranging from geometrically simple to complex) were evaluated in Task 3 to establish the relative importance of each of the four mechanisms. Typical results of this evaluation of noise mechanisms are summarized in Figure 1-1 in terms of perceived noise level (PNL) directivity for a conical nozzle. In general, mechanical suppressors exhibit a significant reduction in shock noise relative to a baseline conical nozzle, reduce the effectiveness of fluid shielding (increase rather than suppress noise), reduce the effectiveness of convective amplification (reduce noise), and produce a modest reduction in turbulent mixing noise. The largest amount of shock noise reduction correlates with the suppressor which has the smallest characteristic dimension. Fluid shielding decreases because suppressors cause the mean velocity and temperature of the jet plume to decay faster than the conical baseline. A reduction in convection Mach number (and hence in convective amplification) occurs because a suppressor plume decays very rapidly. Turbulent mixing noise is reduced through alteration of the mixing process that results from segmenting the exhaust jet.

\*The Task 3 empirical (M\*S) method was initially intended for nozzle geometries which could not be modeled in the purely analytical Task 2 (M\*G\*B) method (a multielement nozzle with a treated ejector, for example).

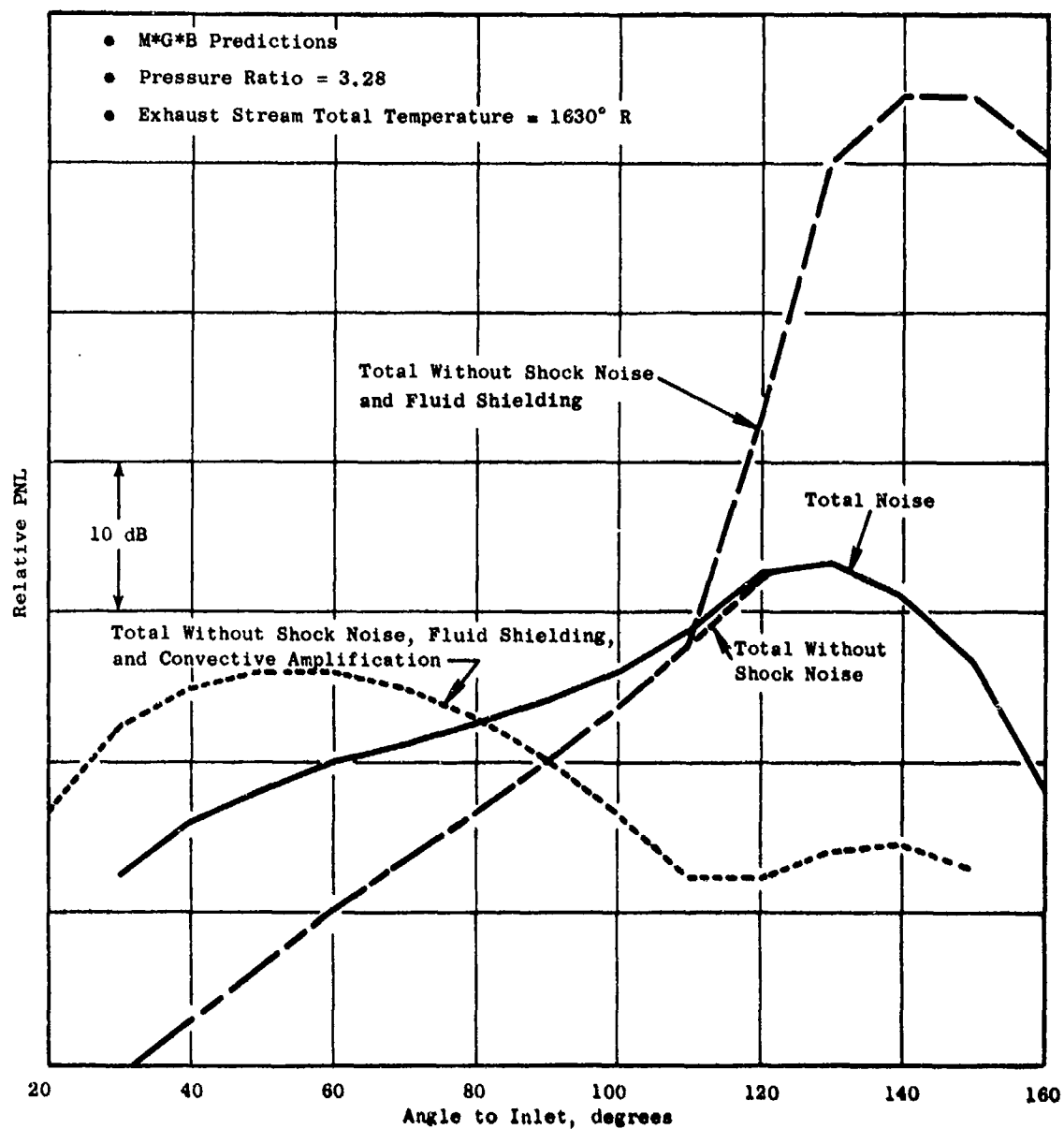


Figure 1-1. Evaluation of Noise Mechanisms for a Conical Nozzle.

Aerodynamic flow-field measurements (mean-velocity profiles) were demonstrated to be useful in verifying the flow-field predictions which were calculated by the M\*G\*B (theoretical) noise-prediction program. Noise source location devices such as the Ellipsoidal Mirror (EM) were demonstrated to be less useful than the Laser Velocimeter (LV) for the M\*G\*B theory verification studies because the LV provides data which may be directly compared with predictions made using the M\*G\*B program. Axial and radial mean-velocity profiles are typical examples of such comparisons.

The empirical M\*S jet noise prediction method has been developed to predict the static acoustic characteristics of multielement suppressors applicable to both advanced turbojets and variable-cycle engines (which are representative of power plants for future supersonic cruise aircraft). The effect of external flow on the M\*S jet noise prediction is discussed in the Task 6 Design Guide Report. Inputs required to use the M\*S computational procedure include: element type, element number, suppressor area ratio and radius ratio, chute-spoke planform and cant angle plus pulg contour. The prediction accuracy is estimated to be +3.3 Effective Perceived Noise Decibels (EPNdB) at a 95% confidence level. Figure 1-2 illustrates the correlation between measured and predicted EPNLs for all types of suppressors.

The merits of both the M\*S and M\*G\*B computational techniques can be stated as follows. The empirical (M\*S) jet noise prediction method, based on correlations of scale-model jet data, serves as a useful preliminary design and prediction tool for selecting the basic nozzle type (chute, spoke, multi-tube, etc.) and primary geometric parameters (element number, area ratio, etc.) for a given application. It is also useful in evaluating the acoustic performance of a given suppressor nozzle, provided the nozzle is one of the types from which the correlation was derived. Further, the method is useful for doing parametric studies since the computation procedure is relatively simple and economical of both computer time and cost. The theoretical (M\*G\*B) prediction method, on the other hand, is more suited to detailed design and analysis of a suppressor nozzle. It can supply detailed information on the jet plume flow development as well as the far-field acoustic characteristics. It is also capable of evaluating changes in nozzle planform shape, element placement and spacing, etc. In addition, the theoretical prediction model is a useful diagnostic tool, capable of assessing the relative roles the various mechanisms play in the noise suppression process, and can also serve as a source location analysis tool.

Volume II - Parametric Testing and Source Measurements - A parametric experimental series was conducted to provide far-field acoustic data on 47 baseline and suppressor nozzle configurations and to provide aerodynamic nozzle performance on 18 of the configurations. The data presented in this volume were taken for use in the current program as well as to provide an extensive, high-quality, data base for future studies. The impact of varying the area ratio and velocity ratio of dual-flow, baseline nozzle configurations was investigated, and the importance of shock noise was assessed. The impact of varying area ratio and element number was parametrically studied for both single and dual-flow suppressors; core plug geometry, velocity ratio, and

- Flyover calculation using static data corrected to free-field conditions.
- The "Reference" level is the predicted value of noise for each nozzle, at a specified set of thermodynamic conditions, plus an arbitrary value of 100 dB.

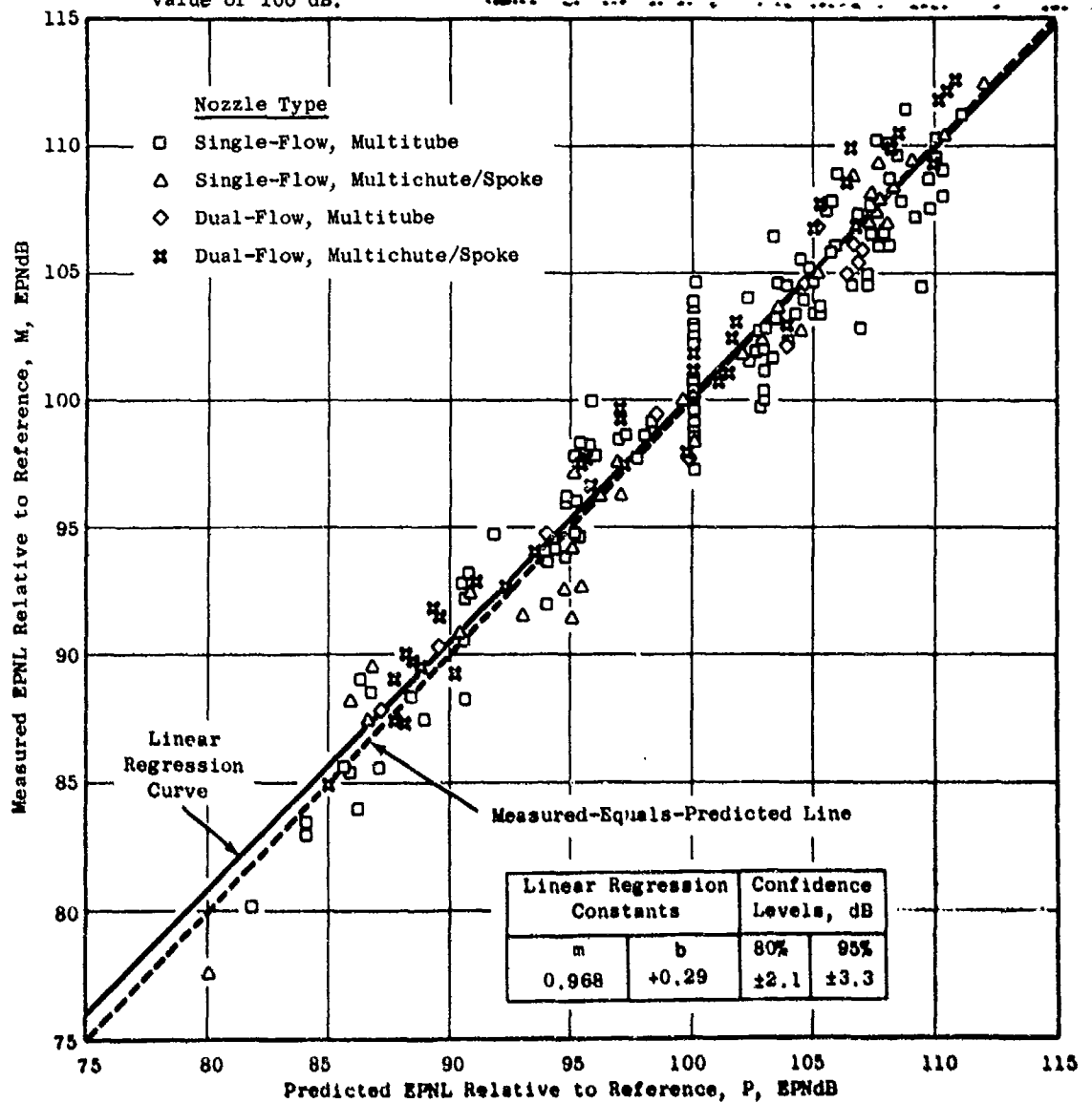


Figure 1-2. Correlation Between Measured and Predicted Effective Perceived Noise Level, EPNL, for all Types of Suppressor Nozzles.



weight flow ratio were evaluated for dual-flow suppressors. These studies establish absolute static suppression levels on the basis of normalized maximum PNL, for several families of suppressor nozzles, as illustrated in Figure 1-3.

Parametric testing identified the following primary trends for single-flow and for dual-flow suppressors during static operation:

#### Single Flow

- Suppression increases with increasing area ratio at high jet velocity.
- Suppression decreases with increasing area ratio at low jet velocity.
- Suppression level is affected by element type (spoke systems suppress slightly better than chutes).

#### Dual Flow

- Suppression increases with increasing area ratio.
- Suppression increases with increasing element number at high jet velocity.
- Suppression level is affected by core plug geometry [by 2 to 3 decibels (dB)].
- Suppression increases 3 to 4 dB when a treated ejector is added to a suppressor configuration.

Selective, free-jet tests conducted on eight configurations indicate that suppression generally decreases in flight. Typical static versus free-jet results are shown in Table 1-1.

The aerodynamic performance test data recorded on 18 of the configurations at both static and wind-on conditions is also included in this volume. Base pressure measurements were taken on several of the models in order to determine base drag (which is thought to be responsible for the poor aerodynamic performance of most mechanical suppressors in flight). These wind tunnel tests identified the following primary trends in aerodynamic performance:

- Performance decreases with increasing element number.
- Performance increases with increasing chute depth.
- Performance increases with increasing ratio of inner flow area to outer flow area.

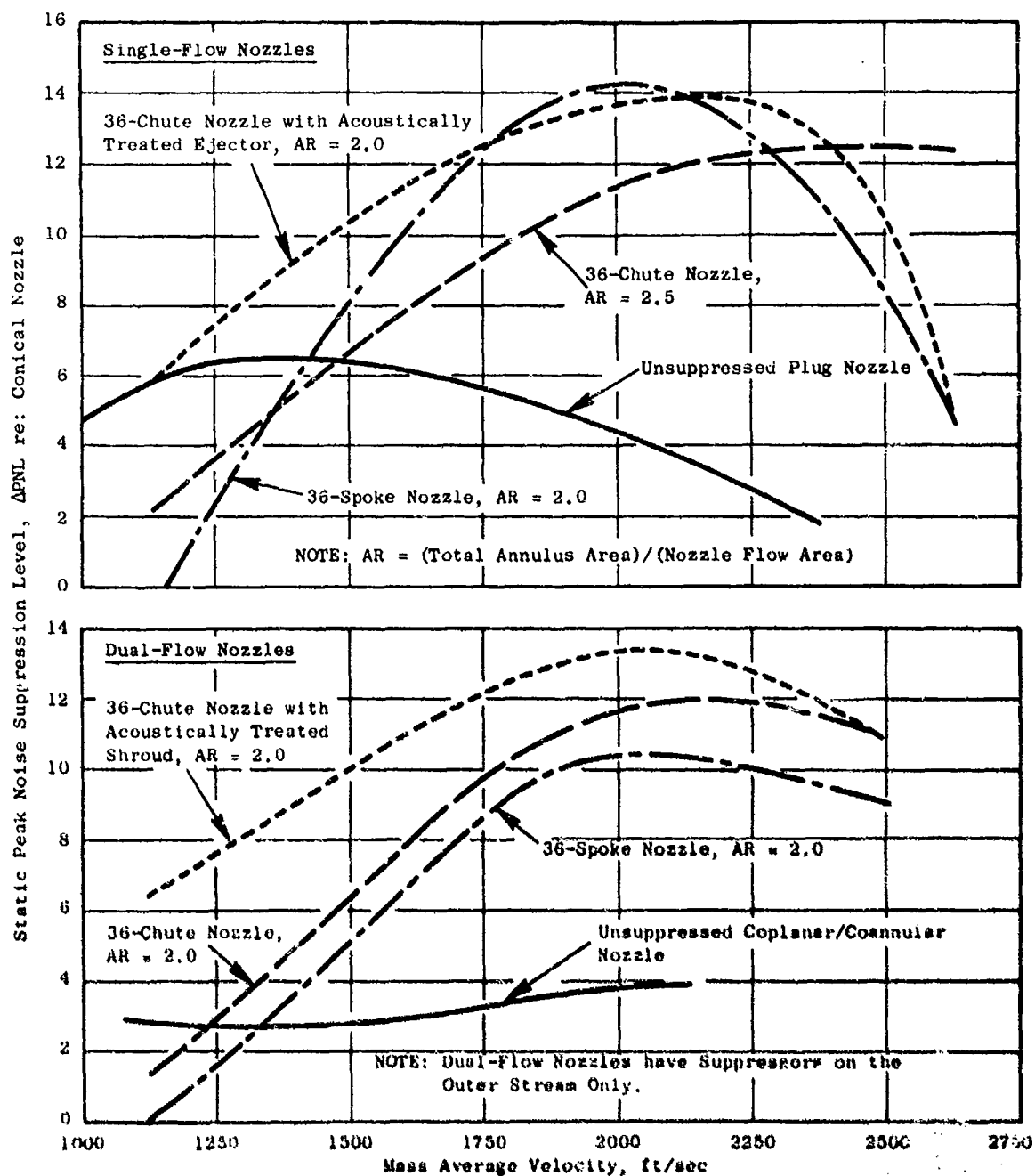


Figure 1-3. Typical Peak Static Noise Suppression Characteristics.

- Performance is affected by element type (chutes perform better than spokes because spokes have higher base drag).

The base pressure correlations provide a procedure for predicting suppressor nozzle aerodynamic performance.

Table 1-1. Typical Summary of Nozzle Static and Projected Flight Peak PNL Suppression Characteristics.

- Suppression Levels are Relative to a Conical Nozzle at Equivalent Flight Conditions
- $V_j = 2500$  ft/sec

<u>Configuration</u>	<u>Suppression Level, db</u>	
	<u>Static</u>	<u>Flight</u>
Plug Nozzle - 0.789 Radius Ratio	1.3	3.0
Plug Nozzle - 0.85 Radius Ratio	2.3	3.7
8-Lobe Nozzle	5.6	5.6
AR = 2.5 36-Chute Nozzle	13.5	10.9
AR = 2.5 36-Chute Nozzle with Auxiliary Flow	12.5	9.4
104-Tube Nozzle	12.0	12.0

Volume III - Suppressor Concepts Optimization - Several studies were conducted to attempt an optimization of suppressor concepts. The end product of this overall effort was to design five nozzles for static and free-jet testing in Task 5. Trade studies of performance versus suppression, aircraft integration studies, and development of a figure of merit method of analysis all make up the activities in this "optimization" process.

Trade studies of suppression versus aerodynamic performance indicate that a properly selected and designed mechanical suppressor can attain a delta suppression to delta thrust coefficient ratio ( $\Delta PNL/\Delta C_F$ ) of almost 3.0 (based on static suppression and wind-on aerodynamic performance).

The aircraft integration study consisted of ranking nine baseline and suppressor nozzles with respect to performance level, suppression level, weight, impact on aircraft mission range, and noise footprint. In general, suppression level was found to be the most important design variable, with performance and weight ranking second and third, respectively.

The appropriate figure of merit, considering all the design variables, was found to be aircraft range. However, use of range as the figure of merit requires that the aircraft mission be specified, and several techniques for cursorily ranking the suppressors based solely on suppression level, performance, and weight may also be identified. A summary of the range versus noise

characteristics of typical nozzle configurations is presented in Figure 1-4. Once a noise goal is specified, adding a suppressor provides a significant range improvement over an unsuppressed system because adding a suppressor is less costly than reducing noise by enlarging the engine to reduce jet velocity....

The design of the five optimum nozzles was based on data from previous studies, performed by government and industry, on the M\*G\*B and M\*S models discussed above and on the parametric data obtained in the acoustic and aerodynamic performance test series reported in Volume II. The configurations were designed and fabricated for open-throat, anechoic, free-jet testing in Task 5. The configurations chosen for evaluation were: (1) a 32-chute, single-flow nozzle; (2) a 40-shallow-chute, dual-flow nozzle; (3 and 4) a 36-chute, dual-flow nozzle, with and without a treated ejector; and (5) a 54-element, coplanar-mixer, plug nozzle.

Demonstration of acoustic scaling for several suppressor configurations was conducted to assure the adequacy of using scale-model results to project full-scale suppression levels. Full-scale data were obtained on several suppressor configurations using J79 and J85 engines. The suppressors evaluated were: (1) a baseline conical nozzle, (2) a 32-chute nozzle with and without a treated ejector, (3) an 8-lobe nozzle, and (4) a 104-tube nozzle. Scale-model data were obtained for these same configurations to allow comparison of scale-model and full-scale results. In general, peak full-scale suppression levels projected from scale-model data were verified by the full-scale engine results. Directivity patterns were duplicated within  $\pm 2$  PNdB (the largest differences occurring with the conical nozzle configuration). Some spectral anomalies were observed for select cases; however, they were not of sufficient magnitude to invalidate the scale-model results. The conclusion resulting from this study is that full-scale noise levels can be predicted from scale-model test results using Strouhal scaling laws.

Volume IV - Laser Velocimeter Time Dependent Cross Correlation Measurements - In-jet/in-jet and in-jet/far-field exhaust noise diagnostic measurements conducted using a Laser Velocimeter (LV) are reported in this volume. Measurements were performed on a conical nozzle and a coannular plug nozzle. Two-point, space/time measurement using a two-LV system were completed for the conical nozzle. Measurements of mean velocity, turbulent velocity, eddy convection speed, and turbulent length scale were made for a subsonic ambient jet and for a sonic heated jet. For the coannular plug nozzle, a similar series of two-point, laser-correlation measurements were performed. In addition, cross correlations between the laser axial component of turbulence and a far-field acoustic microphone were performed.

Volumes I, II, III, and IV contain the results of a comprehensive effort to identify and integrate the theoretical studies, parametric test data, acoustic and performance diagnostic measurements, and system studies. A logical procedure has evolved for conducting suppressor design trade-offs.

- Four Engines
- 12,500-ft Balance Field Length; 53,500-lbf Thrust Engine
- NASA Aircraft

#### VARIABLE-CYCLE ENGINE

- Nozzle Type
- Fully Mixed, Conical
  - - - 36-Chute, AR = 2.5
  - - - 40-Shallow-Chute
  - - - Optimum Projection

#### TURBOJET ENGINE

- Nozzle Type
- Baseline, Conical
  - - - 32-Chute
  - - - 57-Tube + Ejector

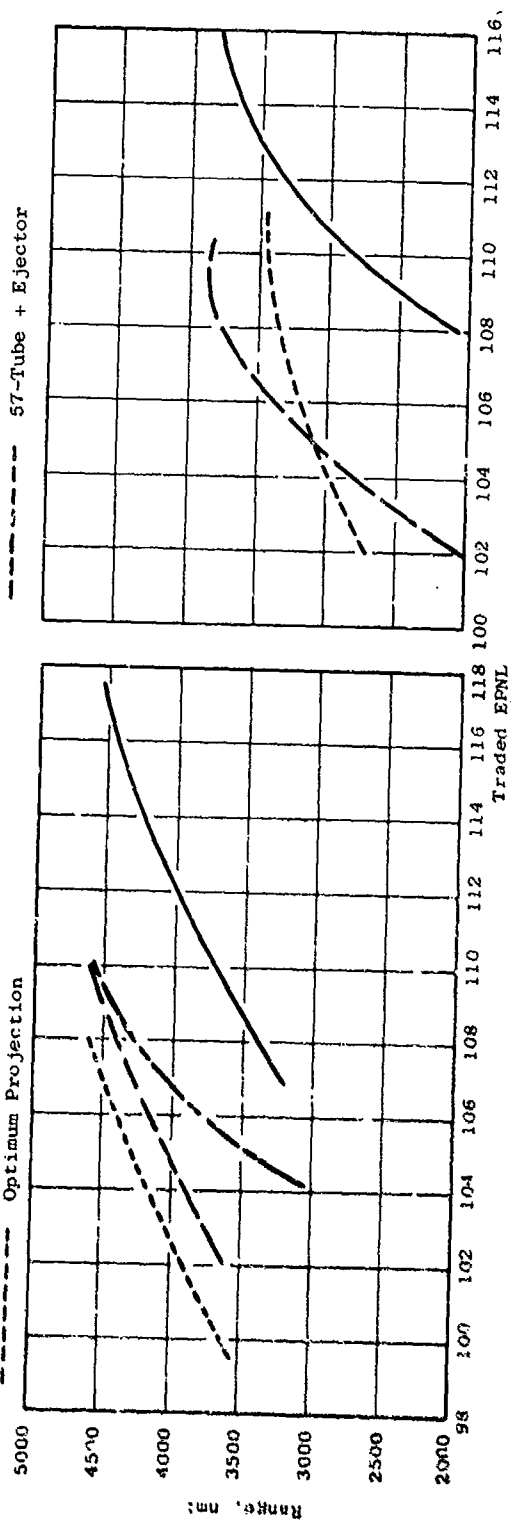


Figure 1-4. Summary of Range and Noise Characteristics for Several Baseline and Suppression Levels.

## 2.0 INTRODUCTION

The first 20 years of commercial aircraft operation with jet propulsion have clearly demonstrated the need for effective high velocity jet noise suppression technology in order to meet community acceptance. Aircraft system studies show that an efficient jet noise suppression device is required if a commercial supersonic aircraft is to be economically viable as well as environmentally acceptable. The current state of the art of high velocity jet noise suppression would make a supersonic transport (SST), with advanced technology engines, meet 1969 noise rules (at best). This state of the art is represented by the material in References 1 through 6.

Reference 1 describes analytical and experimental investigations which were conducted in the early 1960's. This study established a basis for development of mathematical and empirical methods for the predictions of jet-flow-field, aerodynamic characteristics and for determining the directional characteristics of jet noise suppressors. This work was limited in the sense that the suppressors evaluated had only modest suppression potential, and the measurement techniques available did not allow the acquisition of high-frequency, spectral data necessary to establish full-scale, PNL suppression levels.

The development of commercial SST vehicles by the U.S. and by the British-French multinational corporation in the 1960's placed extreme emphasis on the need for effective and efficient noise suppression devices. Phase I of work, conducted by the Boeing and General Electric companies, is summarized in References 2 and 3. Primary emphasis was on jet noise suppressor development through model and engine testing applicable to an afterburning turbojet engine. Suppressor designs were based primarily on empirical methods. Phase II of this effort, References 4 and 5, continued the suppressor development with a stronger emphasis placed on the integration of analytical studies and experimental test data. Specifically, the Boeing Company concentrated on optimization of tube-type suppressor systems and related semiempirical prediction methods. General Electric focused on the development both of chute and of tube-type suppressor systems with primary emphasis placed on optimization of chute-type suppressor nozzles.

Similar studies were conducted by the British and French in development of the Concorde, and typical results are summarized in Reference 6.

The design technology represented in References 1 through 6 is primarily semiempirical. The absence of general design rules based on engineering principles led to the government's formulation of the High Velocity Jet Noise Program, Contract DOT-OS-30034, in 1973. The purpose has been to achieve fundamental understanding, on a quantitative basis, of the mechanisms of jet noise generation and suppression and to develop design methods.

This report presents the results of Task 3 of the contract. It provides the experimental data base which was used in conjunction with the supporting

theories from Task 2 to develop a better understanding of jet noise and jet noise suppression.

The report is organized into four volumes (FAA-RD-76-79, III - I, II, III, IV) and is presented in a format consistent with the Task 3 work plan division of subtasks. Volume I is entitled "Verification of Suppression Principles and Development of Suppression Prediction Methods." Volume II, under this cover, is a data report entitled "Parametric Testing and Source Measurements," and Volume III is an analysis report entitled "Suppressor Concepts Optimization." Volume IV is an analysis report entitled "Laser Velocimeter Time Dependent Cross Correlation Measurement."

Volume I uses the data base (Volume II) and the Task 2 theoretical model (Reference 7) to postulate the suppression mechanisms. Volume I also presents an independent, empirical, static-jet-noise-prediction method which was developed from engineering correlations of the test data. Volume II presents the data and results of the parametric acoustic tests, the aerodynamic performance tests, and the Laser Velocimeter tests. Volume III presents the results of a trade study of performance versus suppression, an aircraft integration study, a "figure of merit" methodology, and a summary of the five "optimum" nozzles selected for testing in Task 5. An acoustic-scaling investigation was conducted to support the suppressor concepts optimization activities and is presented as an Appendix to Volume III. Volume IV presents the results of the in-jet/in-jet and in-jet/far-field cross correlation investigations.

The work reported in the present volume represents the experimental data base obtained to accomplish the general objectives of Volume I, "Verification of Suppression Principles and Development of Suppression Prediction Methods." Far-field acoustic data and select flow field, source characteristics, and aerodynamic performance data were obtained for a series of baseline nozzles and for several families of noise-abatement nozzles. Section 3.0 presents the Acoustic Test Program, and Section 4.0 presents the Aerodynamic Performance Test Program.

Schematics and pertinent dimensions for each of the nozzles evaluated for noise level are summarized in Appendix A. Appendix B contains a summary of the acoustic data and corresponding thermodynamic conditions. The air-attenuation model used for correcting acoustic data to standard-day conditions is summarized in Appendix C. Appendices D and E summarize the development of the ellipsoidal mirror and the results of an error-analysis study. Appendix F contains schematics of the models tested for aerodynamic performance and a detailed summary of the test data.

### 3.0 PARAMETERIC ACOUSTIC TESTING AND SOURCE MEASUREMENTS

This study consists of the selection, design, and procurement of test nozzles plus test and measurement efforts. Primarily, it provided the following data for analysis and evaluation during the Verification of Suppression Principles and Development of Suppression Prediction Methods studies presented in Volume I and the Suppressor Concepts Optimization studies presented in Volume III.

- A. Detailed acoustic data were obtained on seven generic nozzles for data/theory comparison and verification of suppression principles and the initial development of the suppression prediction methods. These nozzles represented baselines and several families of noise-abatement suppressors. They started with simple, unsuppressed single-flow nozzles (conical and annular with plug), progressed in complexity to an unsuppressed coannular-coplanar dual-flow nozzle and culminated in four suppressor nozzle families of complex geometry, i.e., lobed, multitube, multichute, and high radius-ratio annular nozzle with multichute suppressor and plug. Measurements of both flow-field details and limited noise-source characteristics were obtained in addition to the far-field acoustic measurements.
- B. Detailed static far-field acoustic data and select flow-field and source-characteristic data were obtained on an additional 32 models (models within A above, not included). Primary purpose was to amass the parametric design data required to experimentally establish the effect of varying geometric parameters for several groups of baseline and noise-abatement nozzles. The nozzles and parametric geometry variations were selected to adequately develop data applicable to (1) advanced suppression concepts appropriate for a future dual-flow variable cycle engine (VCE), and (2) the more conventional multielement suppressor concepts in conjunction with turbojet cycle applications. The data bank was used also in developing, checking, and improving the suppression prediction/correlation method described in Volume I.
- C. Far-field acoustic data plus select flow-field and source characteristic data were obtained (where appropriate) on eight baseline and suppressor configurations within a static and simulated flight environment, free-jet, for the following purposes:
  - 1. To provide flight effect data to guide the designs of the five "optimum suppressors" described in Volume III.
  - 2. To evaluate the impact of "flight" on shock noise generation.



- D. Wind tunnel static and simulated flight aerodynamic performance data (see Section 4.0) were obtained on a select group of baseline and noise-abatement nozzles. A total of 18 configurations was evaluated, through a joint NASA/GE effort, in the Lewis Research Center's 6 x 8-foot wind tunnel. These aerodynamic performance data were also used to perform the aircraft integration studies and to guide the designs of the five optimum suppressors described in Volume III.

The following criteria were used to influence selection of the models for parametric testing.

- A. Configurations were made representative of several types of engine exhaust systems, i.e., turbojet, turbofan, and variable cycle (VCE) high-speed aircraft engines.
- B. Designs were selected to achieve varying levels of suppression, anticipating the need to develop trend relationships among suppression, thrust decrement, and overall system impact. Increasing levels of achievable suppression were anticipated in the following nozzle configuration progression: plugs, lobed, turbojet multichute, turbojet multitube, VCE multichute, duct burning turbofan (DBTF) multichute, and VCE/DBTF multichute/ejector.
- C. Design parameters were varied to influence noise generation, and configurations were selected to shed light on critical points in suppression theory. Among the major design parameters were radius ratio, area ratio, degree of segmentation, element characteristic dimensions, plug geometry, base design, treated ejector application, and flow management (bypass ratio, velocity ratio, isothermal and isovelocity cycle management).
- D. Models were developed and tests were structured to establish the following effects on noise generation: equivalence of chute-to-spoke and tube-to-hole elements, dual-flow influences, flight effects on suppression, and the importance of shock noise under flight conditions.

Fulfilling the general scope of this study, and meeting the design criteria and key elements listed above, required a total of 47 model configurations structured around the following list of nozzle families and design considerations:

- Conical (convergent) baseline nozzles
- Simplistic single-flow plug nozzle (convergent, convergent-divergent, and varying plug radius ratio)
- Unsuppressed dual-flow (coannular-coplanar) nozzles

- Unsuppressed annular jet nozzles (with ventilated and nonventilated base)
- Chute area ratio, segmentation (element number), and spoke-versus-chute studies for turbojet suppression
- Influence of flow management on chute suppressor and base design studies for VCE suppression
- Dual-flow chute suppressors for turbofan systems
- Acoustically treated ejector applications
- Simulated flight investigations

### 3.1 DESCRIPTION OF TEST MODELS

Within this study, 47 test model configurations were evaluated, 34 with new test hardware and 13 with previously manufactured hardware from DOT/FAA Contracts DOT-FA72 WA-2894 and FA-SS-71-13 as well as from NASA-Lewis Contract NAS3-18008. (This does not include the models reported in Volume III, Suppressor Concepts Optimization). All model hardware was of high manufacturing quality, normally designed to be subjected to gas stream conditions up to, or in excess of,  $T_T = 1800^\circ \text{ R}$  and  $P_T/P_0 = 4.0$ . Most configurations used Hastelloy X as base material and higher strength alloys for the suppressor elements. Particular attention was addressed to producing high-quality flowpath lines and to sealing against leakage, whether from stream-to-stream or from stream-to-ambient environment. Many of the configurations were designed using a modular building-block approach, with interchangeable parts, so that consistency of physical flowpath geometry was maintained and only geometric parameters under study were physically varied. Model hardware was of fixed-point (nonvariable) design. Duplication of typical engine flow lines was normally maintained for one to two equivalent flow diameters upstream of the exit plane before transitioning adaptive hardware. Abrupt changes in internal flow lines were avoided and engine obstructions such as turbine struts were not simulated.

Turbojet simulation models ranged in size from 3.8 to 6.9-inch equivalent flow diameter. Dual-flow outer nozzles ranged from 3.2 to 6.5-inch equivalent diameter and inner nozzles from 2.9 to 4.7 inch. Each was selected to allow efficient operation of the individual acoustic facility burners over a wide range of planned cycle conditions and to allow incorporation of multielement suppressors whose characteristic frequency range of interest falls within the 80-KHz measuring capability of facility equipment. This allowed accomplishment of proper scaling of acoustic spectra data to engine size.

Table 3-1 organizes the test models. Each configuration is identified with its proper model number, model title, flowpath line schematic and photograph. These numbers and titles will serve as consistent identification

Table 3-1. Description of Test Models and Test Types.





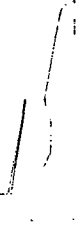

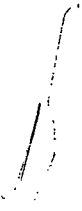

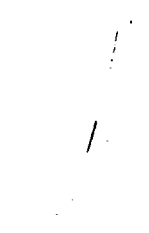







Model No.	Title	Flowpath Schematic	Model Photograph	Design Flow Areas		Type of Test Performed				Model Details Appendix A Figure Number
				A <sub>0</sub> , in. <sup>2</sup>	A <sub>1</sub> , in. <sup>2</sup>	JFJ = JENOTS Free Jet, J = JENOTS, C = Cell 41			EM	
						Far-Field Acoustics	LV			
1	4.64-in.-Diameter Conical Adapted to JENOTS			--	16.82	J	J	--	A-1	
2	Convergent-Divergent Plug, Single Flow			--	37.40	J	J	J	A-2	
3	Converging Plug, R <sub>T</sub> = 0.59, Single Flow			--	33.63	J	--	--	A-3	
4	Converging Plug, R <sub>T</sub> = 0.789, Single Flow			--	10.85	J	--	--	A-4	

Table 3-1. Description of Test Models and Test Types (Continued).

Model No.	Title	Flowpath Schematic	Model Photograph	Design Flow Areas		Type of Test Performed			Model Details Appendix A Figure Number
				A <sub>0</sub> , in. <sup>2</sup>	A <sub>1</sub> , in. <sup>2</sup>	JFJ = JENOTS Free Jet, J = JENOTS, C = Cell 41			
						Far-Field Acoustics	LV	EM	
5	Converging Plug, R <sub>r</sub> = 0.853, Single Flow			-- ----- 6.73	J	--	--	A-5	
6	Dual-Flow Coannular Coplanar, A <sub>0</sub> /A <sub>1</sub> = 2.0			33.63 ----- 16.82	J	J	J	A-6	
7	Dual-Flow Coannular Coplanar, A <sub>0</sub> /A <sub>1</sub> = 0.65			10.85 ----- 16.82	J*	J	--	A-7	
8	Dual-Flow Coannular Coplanar, A <sub>0</sub> /A <sub>1</sub> = 0.4			6.73 ----- 16.82	J	--	J	A-8	

\* Data from NASA-Lewis DBTF Program Contract No. NAS3-18008  
(Applies Only to Model No. 7)

Table 3-1. Description of Test Models and Test Types (Continued).


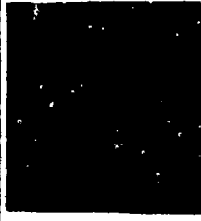



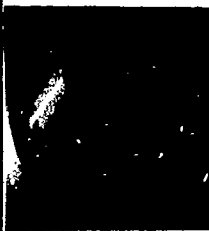


Model No.	Title	Flowpath Schematic	Model Photograph	Design Flow Areas		Type of Test Performed			Model Details Appendix A Figure Number
				$A_0$ , in. <sup>2</sup>	$A_1$ , in. <sup>2</sup>	Far-Field Acoustics	LV	EM	
9	Coannular Coplanar, $A_0/A_1 = 2.0$ , Low Inner Flow			33.63	-----	J	--	--	A-6
10	Coannular Coplanar, $A_0/A_1 = 0.65$ , Low Inner Flow			10.85	-----	J	J	--	A-7
11	Coannular Coplanar, $A_0/A_1 = 0.65$ , No Inner Flow			10.85	-----	J	J	--	A-7
12	Coannular Coplanar, $A_0/A_1 = 0.4$ , Low Inner Flow			6.73	-----	J	--	J	A-8
				16.82	-----				

Table 3-1. Description of Test Models and Test Types (Continued).





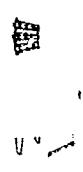
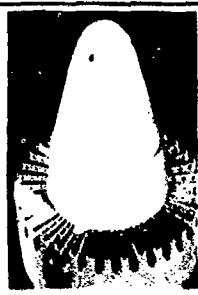

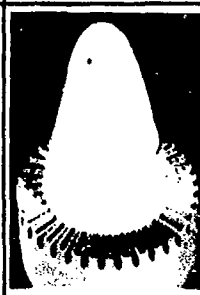
Model No.	Title	Flowpath Schematic	Model Photograph	Design Flow Areas		Type of Test Performed				Model Details Appendix A Figure Number
				$A_0$ , in. <sup>2</sup>	$A_1$ , in. <sup>2</sup>	JFJ = JENOTS Free Jet, J = JENOTS, C = Cell 41				
						Far-Field Acoustics	LV	EM		
13	Coannular Coplanar, $A_0/A_1 = 0.4$ , No Inner Flow			6.73 ----- 16.82		J		--	--	A-8
14	4.64-in.-Diameter Conical, Adapted to Cell 41, Anechoic			-- ----- 16.82		C		--	--	A-1
15	36 Chute, AR = 2.5, $R_T = 0.653$ Turbojet			-- ----- 23.76		C		--	--	A-9
16	36 Chute, AR = 2.0, $R_T = 0.716$ Turbojet			-- ----- 23.76		C		C	C	A-10

Table 3-1. Description of Test Models and Test Types (Continued).


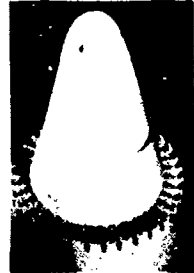

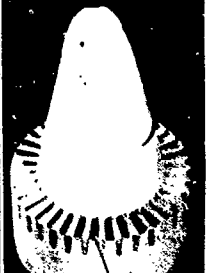




Model No.	Title	Flowpath Schematic	Model Photograph	Design Flow Areas		Type of Test Performed				Model Details Appendix A Figure Number
				A <sub>0</sub> , in. <sup>2</sup>	A <sub>1</sub> , in. <sup>2</sup>	JFJ = JENOTS Free Jet, J = JENOTS, C = Cell 41				
						Far-Field Acoustics	LV	EM		
17	36 Chute, AR = 1.5, R <sub>f</sub> = 0.752 Turbojet			-- ----- 23.76	C	--	--		A-11	
18	36 Spoke, AR = 2.0, R <sub>f</sub> = 0.716 Turbojet			-- ----- 23.76	C	C	--		A-12	
19	36 Chute, AR = 2.0, R <sub>f</sub> = 0.716 Turbojet with Acoustically Treated Secondary Ejector			-- ----- 23.76	C	--	C		A-13	
20	72 Tube/Plug, AR = 2.95 Turbojet			-- ----- 30.87	C	C	C		A-14	

Table 3-1. Description of Test Models and Test Types (Continued).

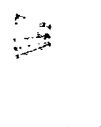
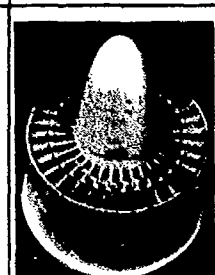



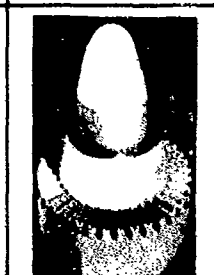

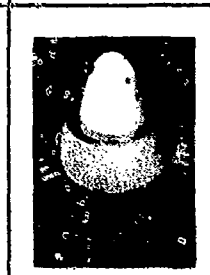
Model No.	Title	Flowpath Schematic	Model Photograph	Design Flow Areas		Type of Test Performed				Model Details Appendix A Figure Number	
				A <sub>0</sub> , in. <sup>2</sup>	A <sub>1</sub> , in. <sup>2</sup>	JFJ = JENOTS Free Jet, J = JENOTS, C = Cell 41			EM		
						Far-Field Acoustics	LV				
21	32 Chute, AR = 2.0, R <sub>0</sub> = 0.498 Turbojet			--	30.83	C	--	C	--	C	A-15
22	36 Chute, AR = 2.5, R <sub>0</sub> = 0.653 Outer Suppressor; A <sub>0</sub> /A <sub>1</sub> = 1.92, R <sub>1</sub> = 0.779 Inner Plug, Retracted			23.76	12.39	C	C	C	--	--	A-16
23	36 Chute, AR = 2.0, R <sub>0</sub> = 0.716 Outer Suppressor; A <sub>0</sub> /A <sub>1</sub> = 1.92, R <sub>1</sub> = 0.779 Inner Plug, In-Line			23.76	12.39	C	--	C	--	C	A-17
24	36 Chute, AR = 2.0, R <sub>0</sub> = 0.716 Outer Suppressor; A <sub>0</sub> /A <sub>1</sub> = 1.92, R <sub>1</sub> = 0.779 Inner Plug, Retracted			23.76	12.39	C	C	C	C	C	A-18



Table 3-1 Description of Test Models and Test Types (Continued).

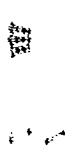



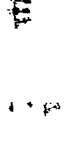

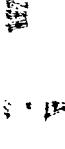

Model No.	Title	Flowpath Schematic	Model Photograph	Design Flow Areas		Type of Test Performed			Model Details Appendix A Figure Number
				$A_0$ , in. <sup>2</sup>	$A_1$ , in. <sup>2</sup>	Far-Field Acoustics	LV	EM	
25	36 Chute, AR = 2.0, $R_F$ = 0.716 Outer Suppressor; $A_0/A_1$ = 3.61, $R_F$ = 0.89 Inner Plug, In-Line			23.76	-----	C	--	C	A-19
				6.58					
26	36 Chute, AR = 2.0, $R_F$ = 0.716 Outer Suppressor; $A_0/A_1$ = 3.61, $R_F$ = 0.89 Inner Plug, Retracted			23.76	-----	C	--	--	A-20
				6.58					
27	36 Chute, AR = 1.5, $R_F$ = 0.72 Outer Suppressor; $A_0/A_1$ = 1.92, $R_F$ = 0.779 Inner Plug, Retracted			25.76	-----	C	C	--	A-21
				12.39					
28	36 Spoke, AR = 2.0, $R_F$ = 0.716 Outer Suppressor; $A_0/A_1$ = 1.92, $R_F$ = 0.779 Inner Plug, Retracted			23.76	-----	C	--	--	A-22
				12.39					

Table 3-1. Description of Test Models and Test Types (Continued).

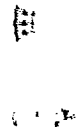
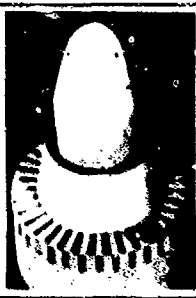
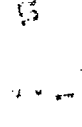

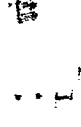

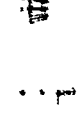

Model No.	Title	Flowpath Schematic	Model Photograph	Design Flow Areas		Type of Test Performed			Model Details Appendix A Figure Number
				$A_0$ , in. <sup>2</sup>	$A_1$ , in. <sup>2</sup>	JFJ = JENOTS Free Jet, J = JENOTS, C = Cell 41			
						Far-Field Acoustics	LV	EM	
29	36 Spoke, AR = 2.0, $R_0$ = 0.716 Outer Suppressor, $A_0/A_1$ = 1.92, $R_1$ = 0.779 Inner Plug, In-Line			23.76 ----- 12.39	C	--	--	A-23	
30	20 Shallow Chute, AR = 1.75, $R_0$ = 0.717 Outer Suppressor, $A_0/A_1$ = 1.92, $R_1$ = 0.779 Inner Plug, Retracted			23.76 ----- 12.39	C	--	C	A-24	
31	30 Shallow Chute, AR = 1.75, $R_0$ = 0.717 Outer Suppressor, $A_0/A_1$ = 1.92, $R_1$ = 0.779 Inner Plug, Retracted			23.76 ----- 12.39	C	--	C	A-25	
32	40 Shallow Chute, AR = 1.75, $R_0$ = 0.717 Outer Suppressor, $A_0/A_1$ = 1.92, $R_1$ = 0.779 Inner Plug, Retracted			23.76 ----- 12.39	C	--	C	A-26	

Table 3-1. Description of Test Models and Test Types (Continued).


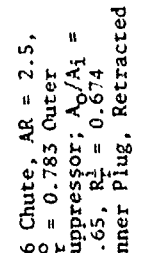
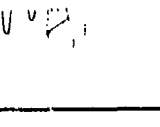
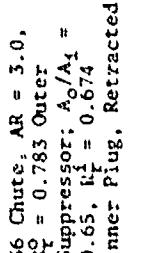
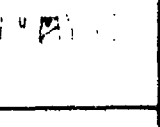
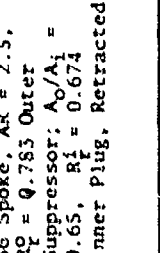
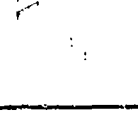
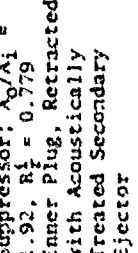
Model No.	Title	Flowpath Schematic	Model Photograph	Design Flow Areas		Type of Test Performed			Model Details Appendix A Figure Number
				$A_0$ , in. <sup>2</sup>	$A_1$ , in. <sup>2</sup>	JFJ = JENOTS Free Jet, J = JENOTS, C = Cell 41			
						Far-Field Acoustics	LV	EM	
33	36 Chute, AR = 2.5, $R_0 = 0.783$ Outer Suppressor; $A_0/A_1 = 0.65$ , $R_1 = 0.674$ Inner Plug, Retracted			11.12 ----- 17.21	C	--	C	A-27	
34	36 Chute, AR = 3.0, $R_0 = 0.783$ Outer Suppressor; $A_0/A_1 = 0.65$ , $R_1 = 0.674$ Inner Plug, Retracted			11.12 ----- 17.21	C	--	C	A-28	
35	36 Spoke, AR = 2.5, $R_0 = 0.783$ Outer Suppressor; $A_0/A_1 = 0.65$ , $R_1 = 0.674$ Inner Plug, Retracted			11.12 ----- 17.21	C	--	C	A-29	
36	36 Chute, AR = 2.0, $R_0 = 0.715$ Outer Suppressor; $A_0/A_1 = 1.92$ , $R_1 = 0.779$ Inner Plug, Retracted with Acoustically Treated Secondary Ejector			23.76 ----- 12.39	C	C	C	A-30	

Table 3-1. Description of Test Models and Test Types (Continued).









Model No.	Title	Flowpath Schematic	Model Photograph	Design Flow Areas		Type of Test Performed			Model Details Appendix A Figure Number
				$A_0$ , in. <sup>2</sup>	$A_1$ , in. <sup>2</sup>	Far-Field Acoustics	LV	EM	
37	Coannular-Noncoplanar Dual Plug Nozzle, $p_0 = 0.853$ , $A_0/A_1 = 1.59$ , $R_f = 0.800$ , with Acoustically Treated Secondary Ejector			18.05	---	C	--	--	A-31
38	Coannular-Noncoplanar Dual Plug Nozzle, $p_0 = 0.926$ , $A_0/A_1 = 0.71$ , $R_f = 0.800$ , with Acoustically Treated Secondary Ejector			8.01	---	C	--	--	A-32
39	Converging Plug, Single Flow, $R_f = 0.789$			--	---	JFJ	JFJ	JFJ	A-33
40	Converging Plug, Single Flow, $R_f = 0.85$			--	---	JFJ	JFJ	JFJ	A-34

Table 3-1. Description of Test Models and Test Types (Continued).

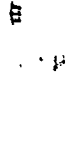

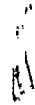





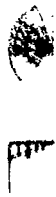
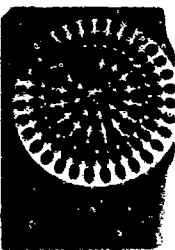




Model No.	Title	Flowpath Schematic	Model Photograph	Design Flow Areas		Type of Test Performed			Model Details Appendix A Figure Number
				$A_0, \text{ in.}^2$	$A_1, \text{ in.}^2$	Far-Field Acoustics	LV	EM	
41	36 Chute, AR = 2.5. $R_0 = 0.78$ Turbojet			-- ----- 11.12	-- ----- 11.12	JFJ	JFJ	JFJ	A-35
42	36 Chute, AR = 2.5. $R_0 = 0.78$ Outer Suppressor with Induced Flow Through $A_0/A_1 = 0.65$ , $R_1 = 0.674$ Inner Plug, Retracted			11.12 ----- 17.21	11.12 ----- 17.21	JFJ	JFJ	JFJ	A-36
43	36 Chute, AR = 2.5, $R_0 = 0.78$ Outer Suppressor with Abrupt Step Over $A_0/A_1 = 0.65$ , $R_1 = 0.674$ Inner Plug, Retracted			11.12 ----- 17.21	11.12 ----- 17.21	JFJ	JFJ	JFJ	A-37
44	104 Tube, AR = 2.8			-- ----- 13.03	-- ----- 13.03	JFJ	JFJ	JFJ	A-38

Table 3-1. Description of Test Models and Test Types (Concluded).

Model No.	Title	Flowpath Schematic	Model Photograph	Design Flow Areas		Type of Test Performed				Model Details Appendix A Figure Number
				$A_0$ , in. <sup>2</sup>	$A_1$ , in. <sup>2</sup>	JFJ = JENOTS Free Jet, J = JENOTS, C = Cell 41				
						Far-Field Acoustics	LV	EM		
45	104 Hole, AR = 2.8			-- ----- 13.03	-- ----- 13.03	JFJ	JFJ	JFJ	A-39	
46	8 Lobe, AR = 2.1			-- ----- 12.63	-- ----- 12.63	--	JFJ	--	A-40	
47	4.0-in.-Diameter Conical			-- ----- 12.57	-- ----- 12.57	JFJ	--	JFJ	A-41	

throughout the volume. Each configuration was subjected to far-field acoustic testing plus select laser velocimeter plume documentation and/or ellipsoidal mirror microphone source measurement on GE-Evendale facilities according to the following codes, as shown on the tables.

- J = JENOTS (Jet Engine Noise Outdoor Test Stand)
- JFJ = JENOTS Free Jet
- C = Cell 41 Anechoic Facility

Select configuration designs were also evaluated for aerodynamic performance in the joint GE/NASA-Lewis test program discussed in Section 4.0. Independent, but identical, aerodynamic hardware sets were manufactured in proper wind tunnel size.

Figure 3-1 defines geometric parameters associated with the overall model systems, the individual outer and inner streams, the multielement suppressors, and the ejectors.

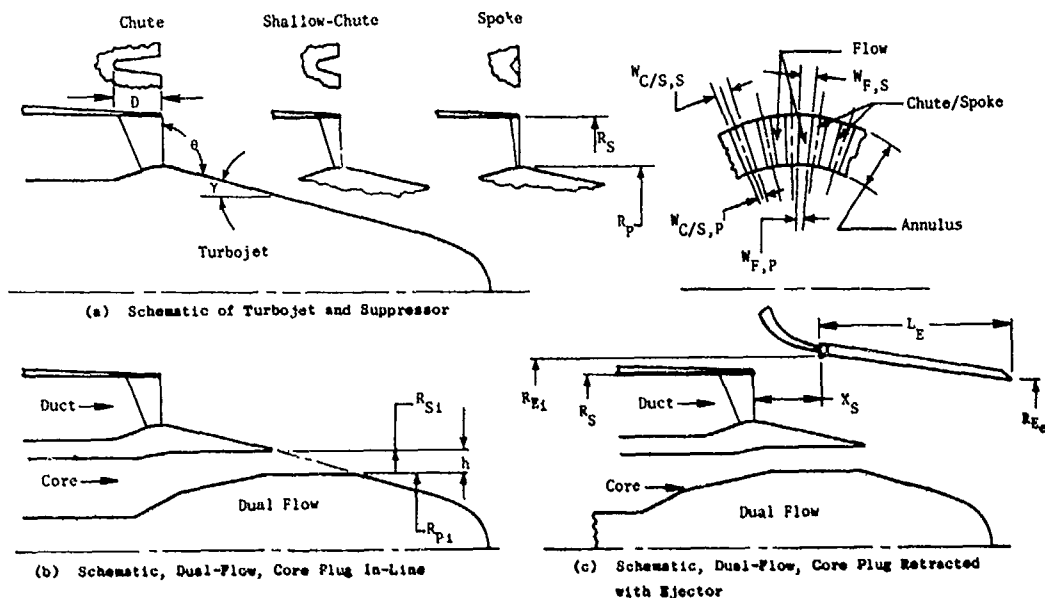
The last column of Table 3-1 identifies Figures A-1 through A-41 of Appendix A which show in detail the physical dimensions of each model component. The individual models are categorized and discussed in the following paragraphs.

Models 1 through 13 in Table 3-1 were tested statically in the JENOTS facility, validated within this program's Task 1 (Reference 8). Model 1 is a 4.64-inch-diameter conical nozzle which established the baseline to which suppression levels were referenced.

Models 2 through 5 are single-flow plug nozzles. Model 2 has a convergent-divergent internal flowpath with an expansion area ratio of 1.22. Models 3, 4, and 5 establish a series of convergent plug nozzles for which radius ratio varies at values of 0.59, 0.789 and 0.853, respectively. The core plug is maintained consistent for the three models and the shroud is changed; therefore, a true plug radius ratio effect is established.

Models 6 through 13 are versions of coannular-coplanar geometries with variations in groups as follows:

- A. Models 6, 7, and 8 maintain core geometry and vary fan shrouds to accomplish  $A_0/A_1$  values of 2.0, 0.65, and 0.4, respectively. These were tested at typical dual-flow cycle conditions.
- B. Models 9, 10, and 12 are similar in geometry to Models 6, 7, and 8; however, inner flow was regulated to rates of  $\leq 10\%$  of the outer flow.
- C. Models 11 and 13 are similar in geometry to Model sets 7/10 and 8/12, respectively; however, core blank-off hardware was installed



#### System

- Turbojet; Single Flow
- Dual Flow; Turbofan (TF), Duct-Burning Turbofan (DBTF), Variable Cycle Engine (VCE)
  - Outer Stream/Duct/Fan Used Interchangeably
  - Inner Stream/Core Used Interchangeably
  - Area Ratio,  $A_0/A_1$ , Duct Area/Core Area
  - Bypass Ratio,  $W_0/W_1$ , Duct Weight Flow/Core Weight Flow
  - Velocity Ratio,  $V_0/V_1$ , Duct Ideal Velocity/Core Ideal Velocity

#### Duct Suppressor

- Chute - Good Ventilation Capability, Stowage within Plug Required
- Shallow Chute - Moderate Ventilation Capability - Stowage on Plug Surface
- Spoke - No Ventilation Capability - Stowage on Plug Surface
- Segmentation,  $N$ , Number of Elements
- Area Ratio,  $AR$ , Full Annular Area/Flow Area
- Radius Ratio,  $R_P^0$ , Plug Radius ( $R_P$  at Hub)/Shroud Radius ( $R_S$  at Tip)
- Chute or Spoke Width Ratio,  $W_{C/S,S}/W_{C/S,P}$ , Width at Shroud/Width at Plug
- Flow Width Ratio,  $W_{F,S}/W_{F,P}$ , Width at Shroud/Width at Plug
- Depth to Width Ratio,  $D/W_{C/S,S}$ , Chute Depth/Chute Width at Shroud
- Plug Half Angle,  $\gamma$
- Element Orientation Angle,  $\theta$

#### Core

- Radius Ratio,  $R_P^1$ , Plug Radius ( $R_P$ )/Shroud Radius ( $R_S$ )
- Annulus Height,  $h$
- Plug Location: In-Line (Schematic b), Retracted (Schematic c)

#### Ejector (Single and Dual Flow)

- Ejector Inlet Radius,  $R_{E1}$
- Ejector Exit Radius,  $R_{E2}$
- Ejector Length,  $L_E$
- Ejector Axial Spacing,  $X_S$

Figure 3-1. Description of Geometric Parameters.



so that positive flow shut-off was accomplished. The system, therefore, reverts to a single annular flow exiting over an inner cavity of low base pressure.

Table 3-2 summarizes the comparisons which can be made through use of the test data acquired on Models 3 through 13.

Models 14 through 38 (Table 3-1) were tested statically in the General Electric Anechoic Chamber (Evendale, Ohio) which was also validated within Task 1 (Reference 9). Model 14 is a 4.64-inch-diameter conical nozzle (same geometry as Model 1) but adapted to the anechoic chamber. Models 15 through 21 are single-flow turbojet configurations with annular multielement suppressors around a plug geometry and are categorized as follows:

- A. Models 15, 16, and 17 maintain 36-element segmentation and vary area ratio and radius ratio through values of 2.5/0.653, 2.0/0.716 and 1.5/0.782, respectively.
- B. Model 18 maintains similar geometry to Model 16 except the chutes are converted to zero-ventilation spokes.
- C. Model 19 maintains the suppressor/plug geometry of Model 16 but adds an acoustically treated secondary ejector.
- D. Models 20 and 21 were previously designed and tested under DOT/FAA Supersonic Transport Noise Reduction Technology Contracts DOT-FA72WA-2894 and FA-SS-71-13, respectively, (References 3 and 4). In this program they were adapted to the anechoic facility and selected for test to fill identified data voids in turbojet suppression technology of generic multielement/plug systems of low radius ratio.

Models 22 through 38 are dual-flow nozzle configurations with geometries typical in application to DBTF/VCE systems. They are categorized as follows:

- A. Models 22, 24, and 27 maintain 36-element segmentation and common inner flowpath geometry which maintain  $A_0/A_1$  at 1.92, but vary suppressor area ratio and radius ratio through values of 2.5/0.653, 2.0/0.716 & 1.5/0.782, respectively, similar to the same parametric variations on the turbojet systems of Models 15, 16, and 17 above.
- B. Models 23, 24, 25 and 26 maintain 36-element segmentation and suppressor area ratio of 2.0 but vary system  $A_0/A_1$  with values of 1.92 and 3.61, plus alter inner plug positioning from an in-line geometry (Models 23 and 25) to a retracted geometry (Models 24 and 26). These inner plug geometry changes assess the impact of varying the inner stream flow injection method within the dual-flow system.

Table 3-2. Test Model Comparisons Summary.

Variable Parameter	Mode	Model No.	$A_o/A_i$	Annulus $R_r$	Description
Radius Ratio	Single Flow	3	---	0.59	Convergent Flowpath-Plug Centerbody
		4	---	0.789	Convergent Flowpath-Plug Centerbody
		5	---	0.853	Convergent Flowpath-Plug Centerbody
$A_o/A_i$	Conventional Dual Flow	6	2.0	0.59	Coannular Coplanar
		7	0.65	0.789	Coannular Coplanar
		8	0.4	0.853	Coannular Coplanar
	Low Inner Flow $W_i < 0.1 W_o$	9	2.0	0.59	Coannular Coplanar
		10	0.65	0.789	Coannular Coplanar
		12	0.4	0.853	Coannular Coplanar
	No Inner Flow	11	0.65	0.789	Coannular Coplanar
		13	0.4	0.853	Coannular Coplanar
	Constant $A_o/A_i$ and $R_r$	6 9 3	2.0 2.0 2.0	0.59 0.59 0.59	Conventional Dual Flow Low Inner Flow Plug Centerbody
Variation Through Conventional Dual Flow/ Low Inner Flow/ No Inner Flow/ Plug	Constant $A_o/A_i$ and $R_r$	7	0.65	0.789	Conventional Dual Flow
		10	0.65	0.789	Low Inner Flow
		11	0.65	0.789	No Inner Flow
		4	0.65	0.789	Plug Centerbody
	Constant $A_o/A_i$ and $R_r$	8	0.4	0.853	Conventional Dual Flow
		12	0.4	0.853	Low Inner Flow
		13	0.4	0.853	No Inner Flow
		5	0.4	0.853	Plug Centerbody

Table 3-2. Test Model Comparisons Summary (Concluded).

Variable Parameter	Mode	Model No.	Outer		Inner			System	
			Element Description	Area Ratio, AR	Radius Ratio, $R_o/R_i$	Annulus Height, h	Radius Ratio, $R_r/R_i$		Plug Geometry
Suppressor Area Ratio and Radius Ratio	• Turbojet	15	36 Chute	2.5	0.653	Not Applicable			Area Ratio, $A_o/A_i$
		16	36 Chute	2.0	0.716				
		17	36 Chute	1.5	0.782				
	• Dual Flow	22	36 Chute	2.5	0.653	0.70	0.779	Retracted	1.92
		24	36 Chute	2.0	0.716	0.70	0.779	Retracted	1.92
		27	36 Chute	1.5	0.782	0.70	0.779	Retracted	1.92
Suppressor Area Ratio	• Dual Flow • Constant Radius Ratio	34	36 Chute	3.0	0.783	1.034	0.674	Retracted	0.65
		33	36 Chute	2.5	0.783	1.034	0.674	Retracted	0.65
		27	36 Chute	1.5	0.782	0.70	0.779	Retracted	1.92
Flow Management, Auxiliary Injection Geometry	• Dual Flow • Chutes	23	36 Chute	2.0	0.716	0.70	0.779	In-Line	1.92
		24	36 Chute	2.0	0.716	0.70	0.779	Retracted	1.92
		25	36 Chute	2.0	0.716	0.35	0.89	In-Line	3.61
	• Dual Flow • Spokes	26	36 Chute	2.0	0.716	0.35	0.89	Retracted	3.61
		28	36 Spoke	2.0	0.716	0.70	0.779	Retracted	1.92
		29	36 Spoke	2.0	0.716	0.70	0.779	In-Line	1.92
Flow Management, Auxiliary Injection Rate	• Dual Flow	23	36 Chute	2.0	0.716	0.70	0.779	In-Line	1.92
		24	36 Chute	2.0	0.716	0.70	0.779	Retracted	1.92
		28	36 Spoke	2.0	0.716	0.70	0.779	Retracted	1.92
	• Dual Flow	31	36 Shallow Chute	1.75	0.717	0.70	0.779	Retracted	1.92
		30	20 Shallow Chute	1.75	0.719	0.70	0.779	Retracted	1.92
		32	40 Shallow Chute	1.75	0.719	0.70	0.779	Retracted	1.92
Segmentation, Element Number	• Dual Flow	24	36 Chute	2.0	0.716	0.70	0.779	Retracted	1.92
		28	36 Spoke	2.0	0.716	0.70	0.779	Retracted	1.92
		23	36 Chute	2.0	0.716	0.70	0.779	In-Line	1.92
Suppressor Element Type	• Turbojet	29	36 Spoke	2.0	0.716	0.70	0.779	In-Line	1.92
		16	36 Chute	2.0	0.716	Not Applicable			
		18	36 Spoke	2.0	0.716				
	• Dual Flow	33	36 Chute	2.5	0.783	1.034	0.674	Retracted	0.65
		35	36 Spoke	2.5	0.783	1.034	0.674	Retracted	0.65
		Application of Acoustically Treated Effector	• Dual Flow	24	36 Chute	2.0	0.716	0.70	0.779
36	36 Chute			2.0	0.716	0.70	0.779	Retracted	1.92
16	36 Chute			2.0	0.716	Not Applicable			
19	36 Chute	2.0	0.716						
	• Turbojet	37	Annular	---	0.853	0.634	0.800	Retracted	1.59
		38	Annular	---	0.926	0.634	0.800	Retracted	0.71

- C. Models 28 and 29 maintain the same annular suppressor geometry of Model 23 except the chutes are converted to zero-ventilation spokes. This model set was designed to further assess the impact of inner plug geometry changes within a dual-flow system but now with an outer stream suppressor utilizing spokes.
- D. Models 30, 31, and 32 comprise a nozzle set designed to evaluate the impact of degree of segmentation, using 20, 30 and 40 shallow chutes. Suppressor area ratio and radius ratio are common at 1.75 and 0.717, respectively. Inner plug geometry is held with  $R_T^1 = 0.779$  and the plug in the retracted position. System area ratio is constant at  $A_0/A_1 = 1.92$ .
- E. Models 33, 34, and 35 form a set of configurations evolved around the basic geometry of Model 33, which comes from the NASA-Lewis Duct Burning Turbofan Contract NAS3-18008 (Reference 10). The model was upgraded to adapt to the anechoic test rig. Model 35 is Model 33 converted to a zero-ventilation spoke configuration, and Model 34 adds a new area ratio = 3.0 annular chute suppressor. System area ratio is consistent with  $A_0/A_1 = 0.65$ , and  $R_T^1 = 0.674$  inner plug is common in the retracted position.
- F. Model 36 adds an acoustically treated secondary ejector to the basic geometry of Model 24, similar on this dual-flow model set to the turbojet set of Models 16 and 19.
- G. Models 37 and 38 are acoustically treated ejector applications to coannular, noncoplanar dual-flow plug nozzles, the basic nozzle without ejector being previously evaluated under NASA-Lewis Contract NAS3-19777 (Reference 11). Inner plug geometry is maintained at  $R_T^1 = 0.800$  and outer shrouds are interchanged to affect  $R_T^0$  and  $A_0/A_1$  values of 0.853/1.159 and 0.926/0.71, respectively.

Table 3-2 summarizes the comparisons which can be made through use of test data acquired on Models 15 through 38. The general categories of variable parameters investigated are grouped as follows:

- Suppressor area ratio and radius ratio - each varying but not independently: applicable to turbojet Models 15, 16, and 17 and to dual-flow system Models 22, 24, and 27.
- Suppressor area ratio variation with constant radius ratio, Models 27, 33, and 34, applicable to dual-flow systems.
- Flow management with respect to inner stream injection geometry, assessing impact of inner plug location and inner plug radius ratio with accompanying variation in system area ratio: on dual-flow systems, relative chute suppressors (Models 23 through 26), and relative to spoke suppressor (Models 28 and 29).

- Flow management with respect to inner stream injection rate, meaning inner flow nominally equal to 0, 15, and 30% of outer flow on four select independent geometry nozzles: Models 23, 24, 28, and 31.
- Degree of segmentation of suppressed annulus of dual-flow system: Models 30, 31, and 32.
- Suppressor element type in terms of chute versus spoke on dual-flow systems, Model sets 24/28, 23/29, and 33/35 and on turbojet. Model set 16/18.
- Application of acoustically treated secondary ejector to suppressed dual flow (Model set 24/36) to suppressed turbojet (Model set 16/19) and to unsuppressed annular dual flow (Model set 37/38).

The Model Series 39 through 47 in Table 3-1 was tested statically and in the free-jet mode in the JENOTS facility to gain an early assessment of the influence of simulated flight for several baseline and suppressor configurations and to evaluate shock noise within a simulated flight environment. The models can be categorized as follows:

- Models 39 and 40 are single-flow plug nozzles of convergent flow-path geometry and with radius ratios of 0.789 and 0.85, respectively.
- Model set 41, 42, and 43 share a 36-chute annular suppressor of  $AR = 2.5$  and  $R_r = 0.78$ . Model 41 is a single-flow turbojet configuration. Model 42 utilizes induced tertiary flow ducted through hollow struts to simulate a dual-flow system having an inner plug with retracted position geometry and with  $R_r = 0.674$  and  $A_0/A_1 = 0.65$ . Model 43 closes off the induced flow passage of Model 42 and allows the annular suppressed jet to dump over the abrupt step of the inner plug geometry.
- Models 44 and 45 are 104 elliptical tube and hole configurations, respectively, to evaluate the influence of tube base ventilation within a wind-on environment.
- Model 46 is an 8-lobe daisy configuration of  $AR = 2.1$ .
- Model 47 is a 4-inch-diameter conical nozzle with both internal and external contoured flow lines.

Models 44, 46, and 47 are direct scale-model versions of J85-size nozzles tested within the joint GE/SNECMA\* moving-frame validation test program on the Bertin Aerotrain. The full-size 8-lobe nozzle and the 104-tube nozzle were also tested on the Gates Learjet-25C and F-106 aircraft, respectively (Reference 12).

\*SNECMA - Société Nationale D'Etude et De Construction de Moteurs D'Aviation.

### 3.2 DEFINITION OF TEST MATRICES

#### 3.2.1 Acoustic Test Matrices

Of the 47 models enumerated in Table 3-1, 45 were tested for far-field acoustic data within this study. The nozzles represent various system applications, i.e., turbojet, turbofan, duct burning turbofan, and variable cycle engine. The systems range in complexity from simple conical and coplanar coannular baselines, to complex dual-flow plug nozzles with multielement suppressors and acoustically-treated secondary ejectors. Additionally, the purposes for test varied with individual nozzles and nozzle sets to:

- 1) Develop a detailed data base for use in Volume 1, "Verification of Suppression Principles and Development of Suppression Prediction Methods."
- 2) Develop parametric data for systematic variations in suppressor geometry.
- 3) Evaluate shock noise.
- 4) Establish noise dependency on flow-management parameters such as  $W_o/W_i$ ,  $A_o/A_i$ , inner flow injection geometry and velocity/temperature control.
- 5) Obtain an early evaluation of simulated free-jet environment influence, etc.

The test matrices for the nozzles varied extensively in order to best develop the data base required to fulfill the specific objectives for the particular configuration. These test matrices are discussed in this section in terms of "nominal" values of aerodynamic parameters; i.e., ranges of  $P_T/P_o$ ,  $T_T$ ,  $V_j$ ,  $V_o/V_i$ ,  $W_o/W_i$ , etc., and in terms of their applicability to individual models or sets. However, to make the test results presented more meaningful, and the data acquired more useful, "specific" aerodynamic test values are necessary. These "as-measured" test values are tabulated in Appendix B, one table for each nozzle configuration. The tables also list pertinent acoustic data (scaled to an engine size of 338 in.<sup>2</sup> as discussed in Section 3.3.1.5) and conventionally-used data-normalization parameters.

The models are grouped, and test matrices discussed in the following ten sets:

<u>Set</u>	<u>Model No.'s</u>	<u>Set Description</u>
A	1 and 14	Conical Baseline - JENOTS and Cell 41 Anechoic Facility Adaptations
B	2	Convergent/Divergent Plug - JENOTS
C	3-5	Single-flow plug nozzle parametric radius ratio study - JENOTS

<u>Set</u>	<u>Model No.'s</u>	<u>Set Description</u>
D	6 and 8-13	Coannular coplanar nozzle geometries tested as dual flow, nominal outer stream operation with low inner flow, and nominal outer stream operation with no inner flow - JENOTS
E	15-19	Suppressed turbojet configurations studying suppressor area ratio, radius ratio, element type, and application of acoustically treated ejector - Cell 41 Anechoic Facility
F	20 and 21	Multielement annular suppressors on turbojet/plug system of low radius ratio - Cell 41 Anechoic Facility
G	22-32 and 36	Suppressed dual-flow configurations studying suppressor area ratio, radius ratio, element type, variation of inner stream geometry, flow management, and application of acoustically-treated ejector; all on systems of moderate to high radius ratio - Cell 41 Anechoic Facility
H	33, 34 and 35	Suppressed dual-flow configurations studying suppressor area ratio and element type on models of low system area ratio ( $A_0/A_1 = 0.65$ ) - Cell 41 Anechoic Facility
I	37 and 38	Acoustically-treated ejector application to coannular non-coplanar dual-flow plug nozzles - Cell 41 Anechoic Facility
J	39-45 and 47	Free-jet assessment of the influence of simulated flight on several baseline and suppressor configurations: conical, plug, chute, tube, and hole - JENOTS free jet

Set A - The 4.64-inch-diameter conical nozzle, as adapted to JENOTS (Model 1), was tested per the matrix of Figure 3-2(a) and as adapted to Cell 41 Anechoic Facility (Model 14) was tested per the matrix of Figure 3-2(b). Lines of constant total temperature at values of ambient, 700°, 850°, 1000°, 1250°, 1300°, 1450°, and 1500° R were primarily used. Constant stagnation temperature lines at 1000° and 1500° R also were used on Model 14.

Set B - Model 2, convergent-divergent flowpath plug, used the matrix of Figure 3-3 following (a) a typical turbojet operating line; (b) isovelocity lines at 1000, 1250, 1640, and 2090 ft/sec to establish noise dependency on jet density/temperature; (c) isothermperature lines of 1000°, 1250°, 1500°, 1750° and 2000° R to establish noise/velocity dependency.

Set C - Models 3, 4, and 5 (plug parametric radius ratio study) utilized the test matrix of Figure 3-4. Each of the three models was tested along the simulated turbojet engine cycle line. Additionally, Model 4 ( $R_r = 0.789$ ) was subjected to a more detailed parametric matrix of (a) isovelocity lines

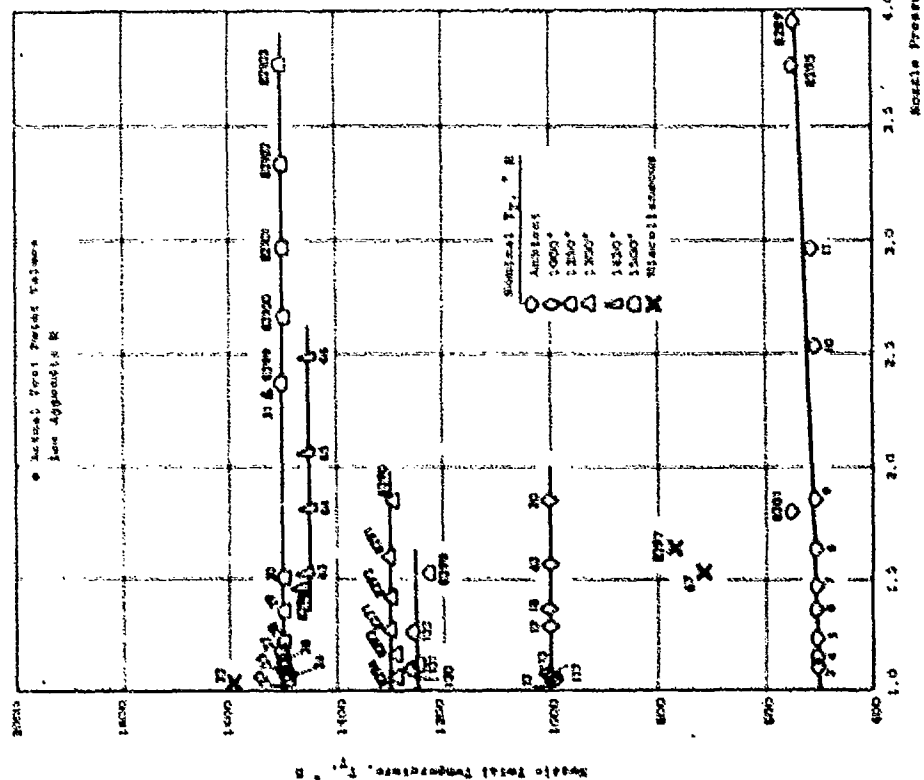


Figure 3-2(a). Far-Field Acoustic Test Matrix,  
Model 1, JENOTS.

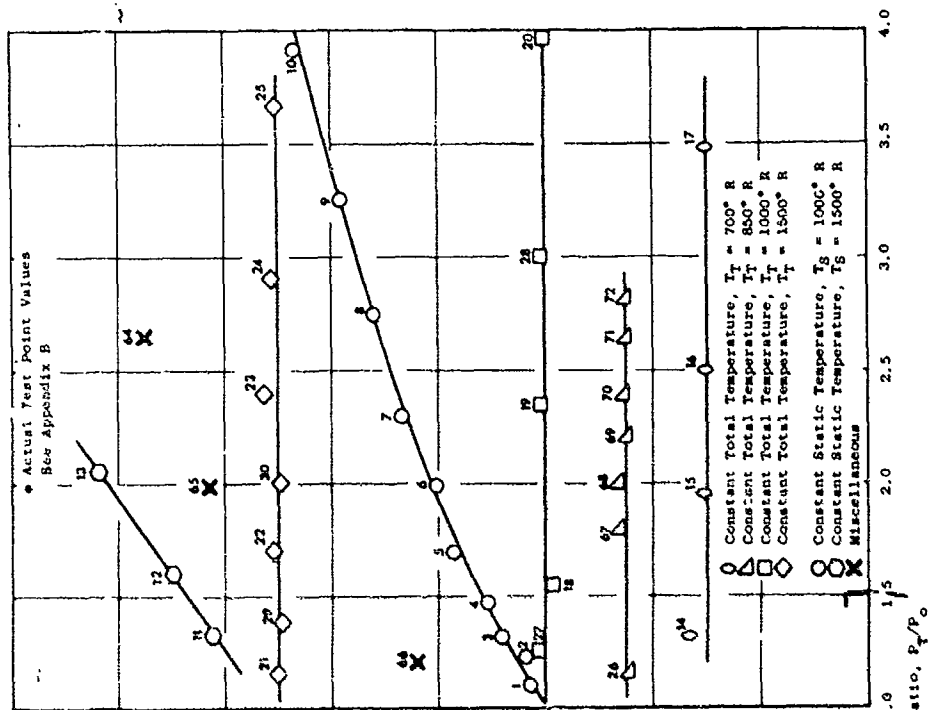


Figure 3-2(b). Far-Field Acoustic Test  
Matrix, Model 14, Cell 41  
Anechoic Facility.



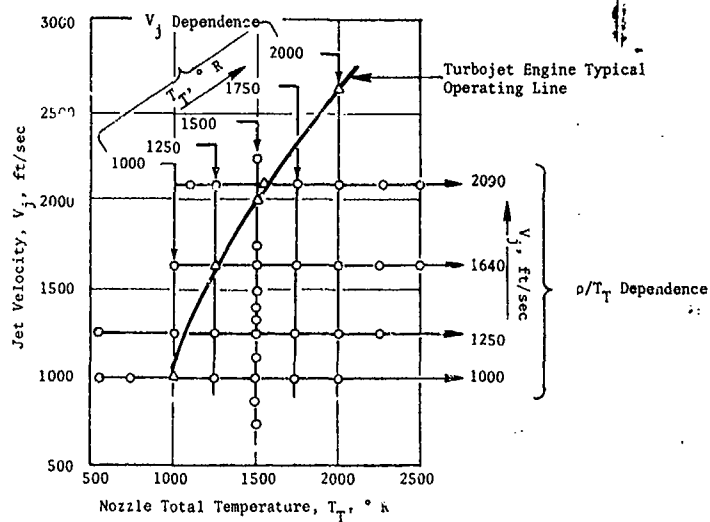


Figure 3-3. Far-Field Acoustic Test Matrix, Model 2, JENOTS.

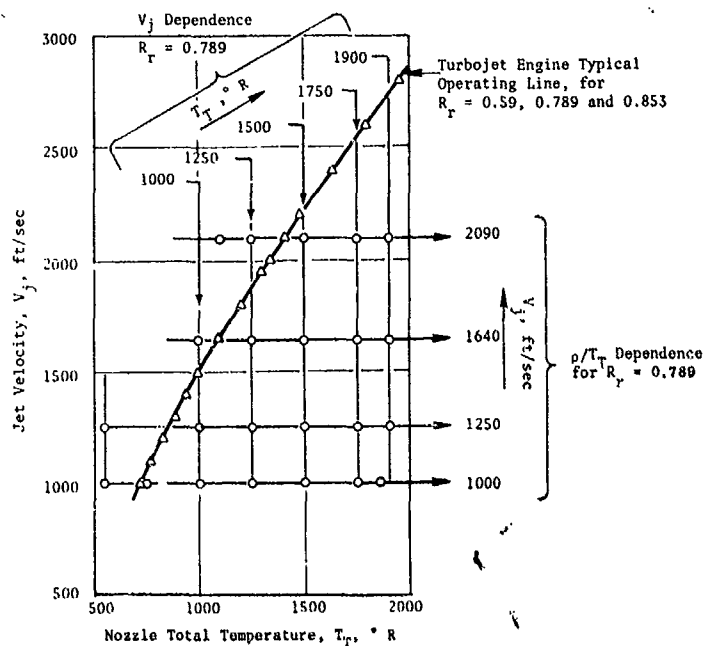


Figure 3-4. Far-Field Acoustic Test Matrix, Models 3, 4, and 5, JENOTS.

at 1000, 1250, 1640, and 2090 ft/sec to establish noise dependency on jet density/temperature, and (b) isothermperature lines of 1000°, 1250°, 1500°, 1750° and 1900° R to establish noise/velocity dependency.

Set D - Models 6 and 8 are dual-flow coannular-coplanar configurations of  $A_0/A_1 = 2.0$  and  $0.4$ , respectively. They were tested using the nominal matrix of Figure 3-5. The inner stream was maintained at specific temperature/velocity conditions while the outer stream varied to effect a range of  $1.0 \leq V_0/V_1 \leq 2.0$ . (Match symbols and data points of "inner velocity", left of figure, to those of "outer velocity", right of figure.) The test matrix was patterned along that of the duct burning turbofan matrix of Reference 10. Model 7 (of  $A_0/A_1 = 0.65$ ) was acoustically tested within the referenced program and the available far-field data will be used for comparisons within this report. Model 8 was further tested using the matrix of Figure 3-6 which maintained equal inner and outer stream temperatures at ambient and 1500° R and varied  $V_0/V_1$  from 0 to 5.0

Models 9, 10, and 12 of  $A_0/A_1 = 2.0$ ,  $0.65$ , and  $0.4$  respectively, used the same physical hardware as Models 6, 7, and 8. The outer stream was operated in the conventional high-flow velocity mode but the inner weight flow and velocity were substantially reduced to determine the effect of low inner flow on generated noise. Matrices for the outer stream cycle are in Figure 3-7(a) for Model 9 and in Figure 3-7(b) for Models 10 and 12. While utilizing these outer stream cycles, the inner stream parameters ranged within ambient  $\leq T_{t1}$ , ° R,  $\leq 1000$ ;  $50 \leq V_{t1}$ , ft/sec  $\leq 320$  and  $W_{t1} \leq 10\%$  of  $W_0$ .

Models 11 and 13 (of  $A_0/A_1 = 0.65$  and  $0.4$ ) again used the same physical hardware as Models 7 and 8 but provided positive shut-off of the inner flow. These models utilized the test matrix of Figure 3-7(b).

Set E - Models 15 through 19, single-flow turbojets, used conventional and advanced turbojet cycle lines as per Figure 3-8. The 16-point matrix had parameters of  $1.7 \leq P_{t1}/P_0 \leq 3.9$ ,  $730 \leq T_{t1}$ , ° R  $\leq 1760$  and  $1200 \leq V_{t1}$ , ft/sec  $\leq 2650$ .

Set F - Models 20 and 21, conventional single-flow low radius ratio multitube and multichute annular plug suppressors, used the test matrix of Figure 3-9.

Set G - The suppressed dual-flow configurations, Models 22 through 32 and 36, normally used a 37 test point matrix depicted graphically in Figure 3-10 and based on the description within Table 3-3. Data points 1 through 20 were used to evaluate noise variation with flow management. Points 1-8 (for Models 23, 24, 28, and 31, only) used no inner flow; therefore, the outer flow exited over an abrupt step in the inner flowpath and the nozzle essentially reverted to a single-flow system. Positive shut-off of the inner flow was assured by using blank-off hardware within the inner stream. Points 9 through 14 metered the inner flow to be approximately 15% of the outer flow rate and points 15 through 20 raised that percentage to 30.

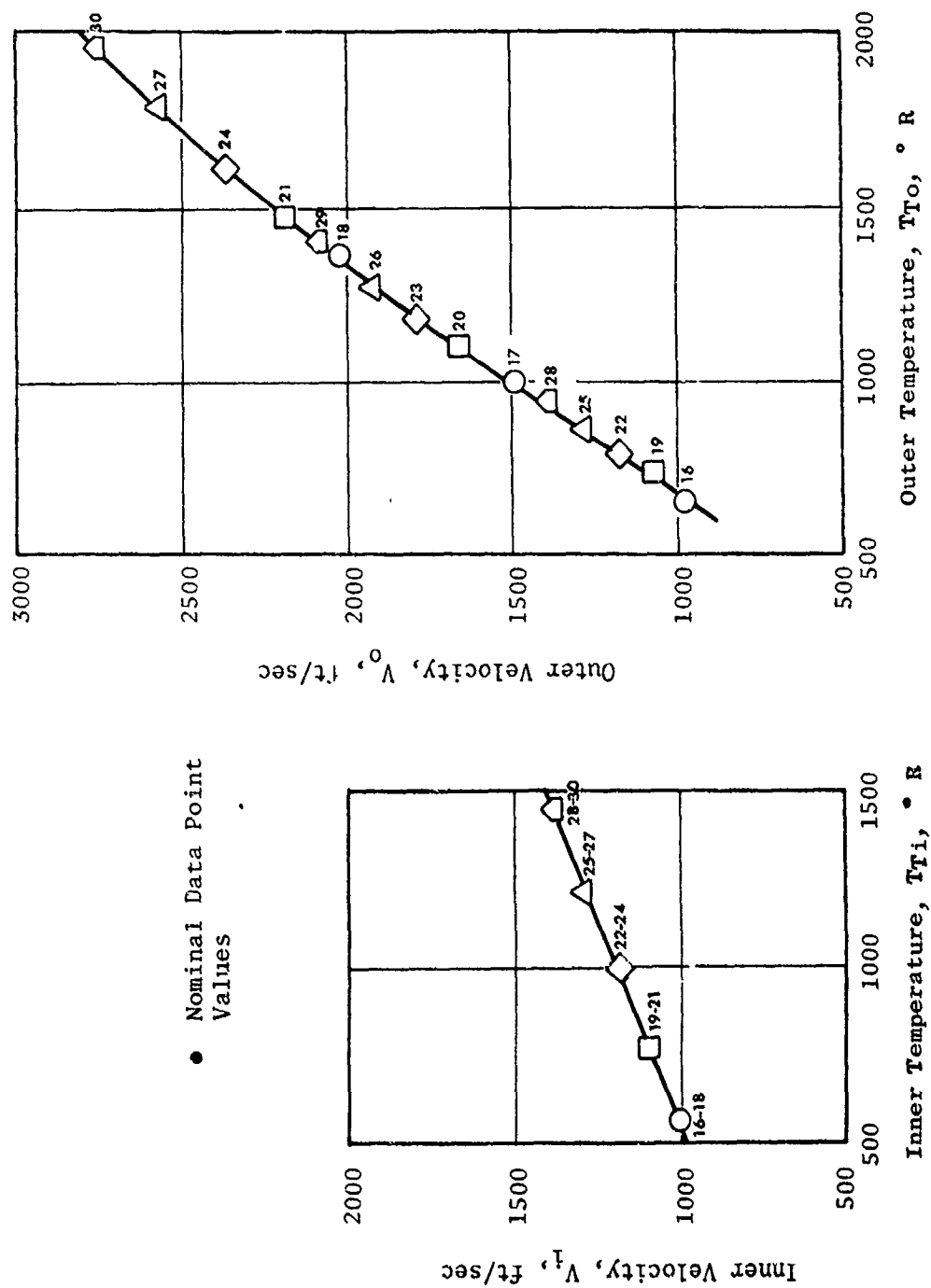


Figure 3-5. Far-Field Acoustic Test Matrix, Models 6 and 8, JENOTS.

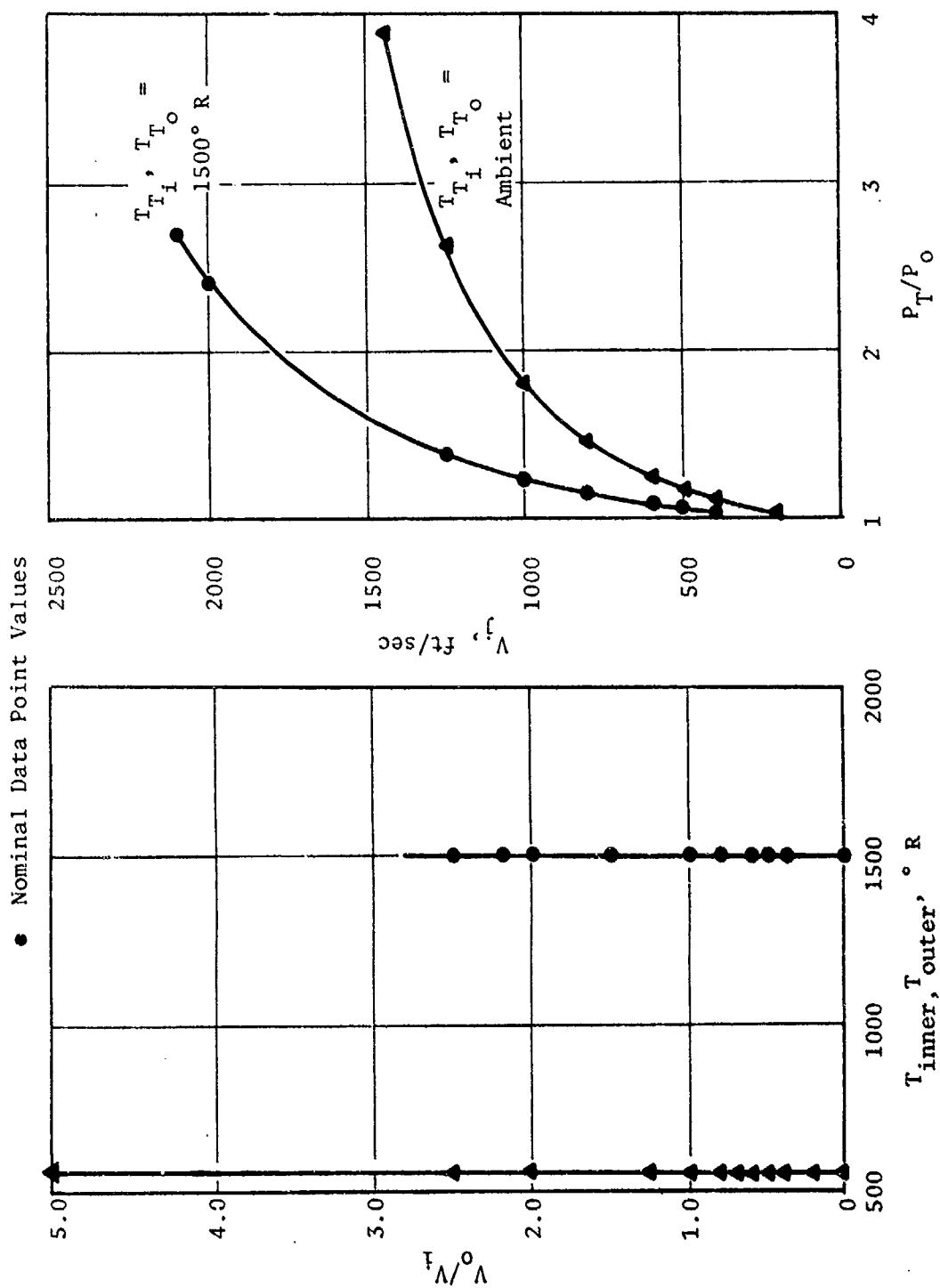


Figure 3-6. Far-Field Acoustic Test Matrix, Model 8, JENOTS.

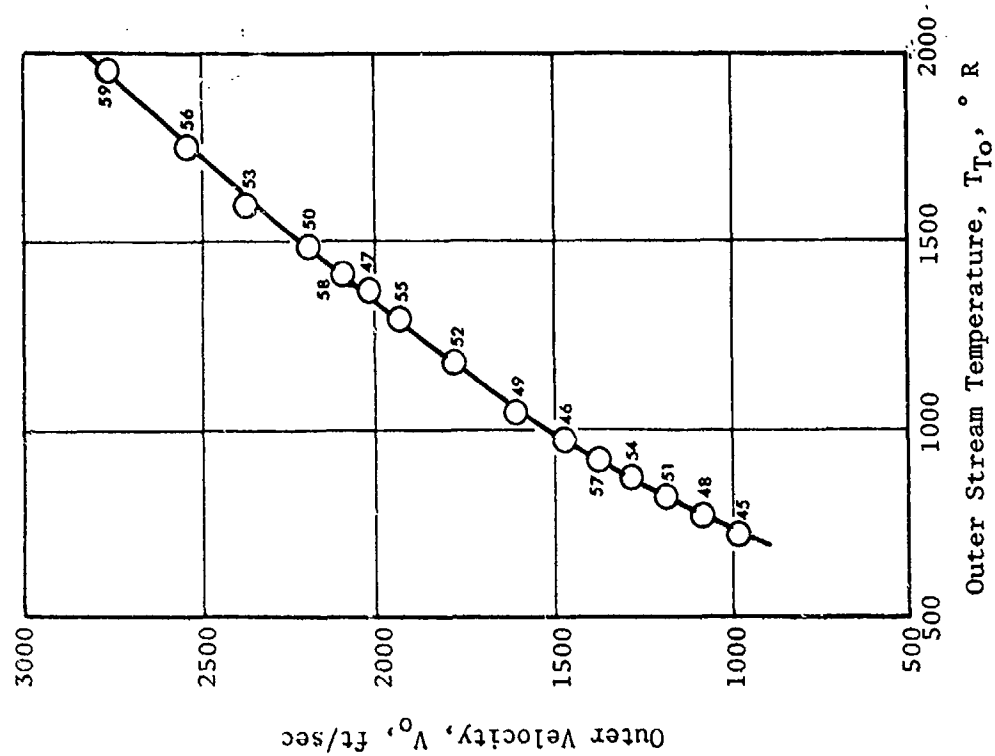


Figure 3-7(b). Far-Field Acoustic Test Matrix, Models 10, 11, 12, and 13, JENOTS.

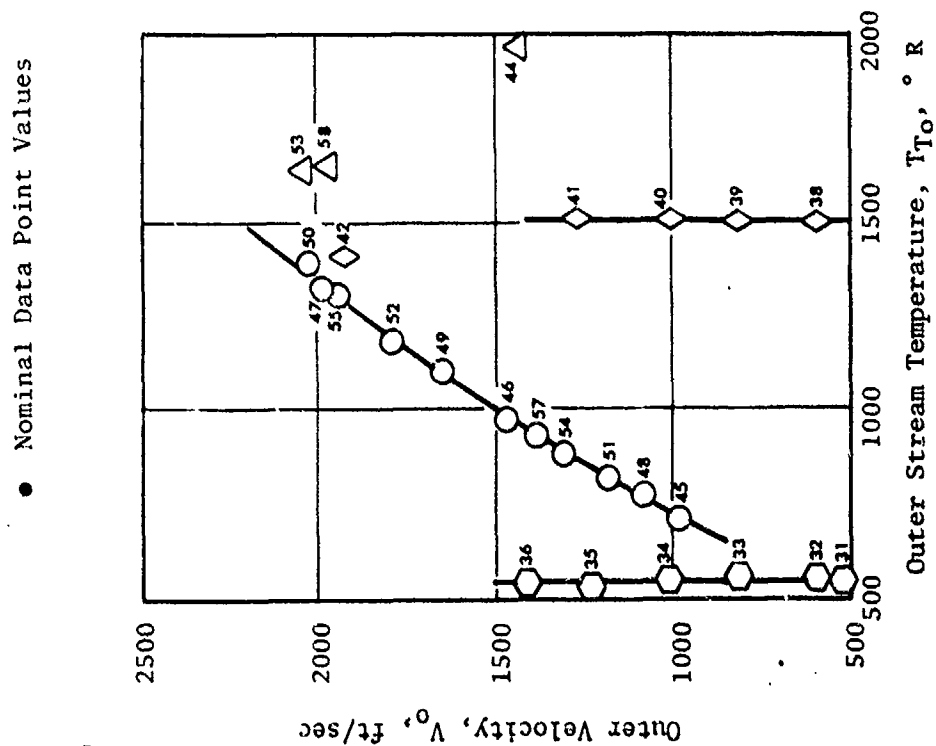


Figure 3-7(a). Far-Field Acoustic Test Matrix, Model 9, JENOTS.

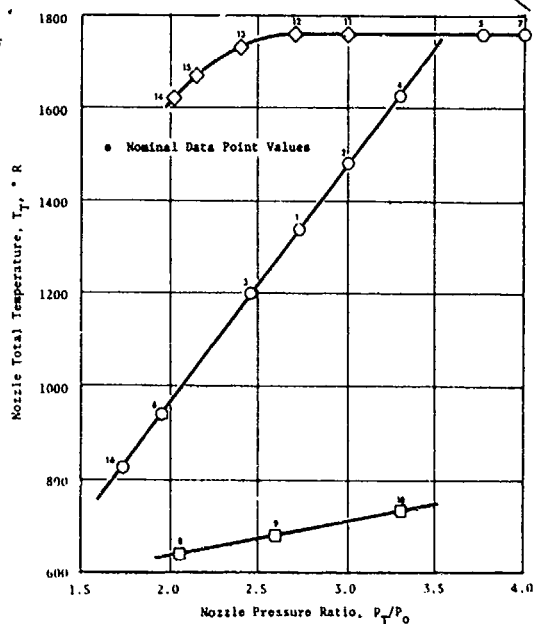


Figure 3-8. Far-Field Acoustic Test Matrix, Models 15 Through 19, Cell 41 Anechoic Facility.

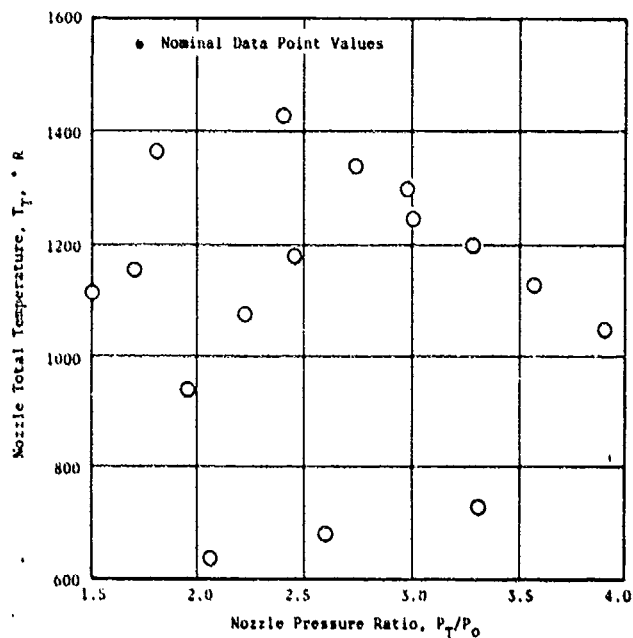


Figure 3-9. Far-Field Acoustic Test Matrix, Models 20 and 21, Cell 41 Anechoic Facility.

• Nominal Values of Outer and Inner Stream Aerodynamic Test Conditions Interrelating  $(T_T)_{o, 1}$ ;  $(P_T/P_o)_{o, 1}$ ; and  $V_{o, 1}$

NOTE: Large Symbols = Inner

Small Symbols = Outer

Test Point Numbers are Indicated with the Plot Symbol

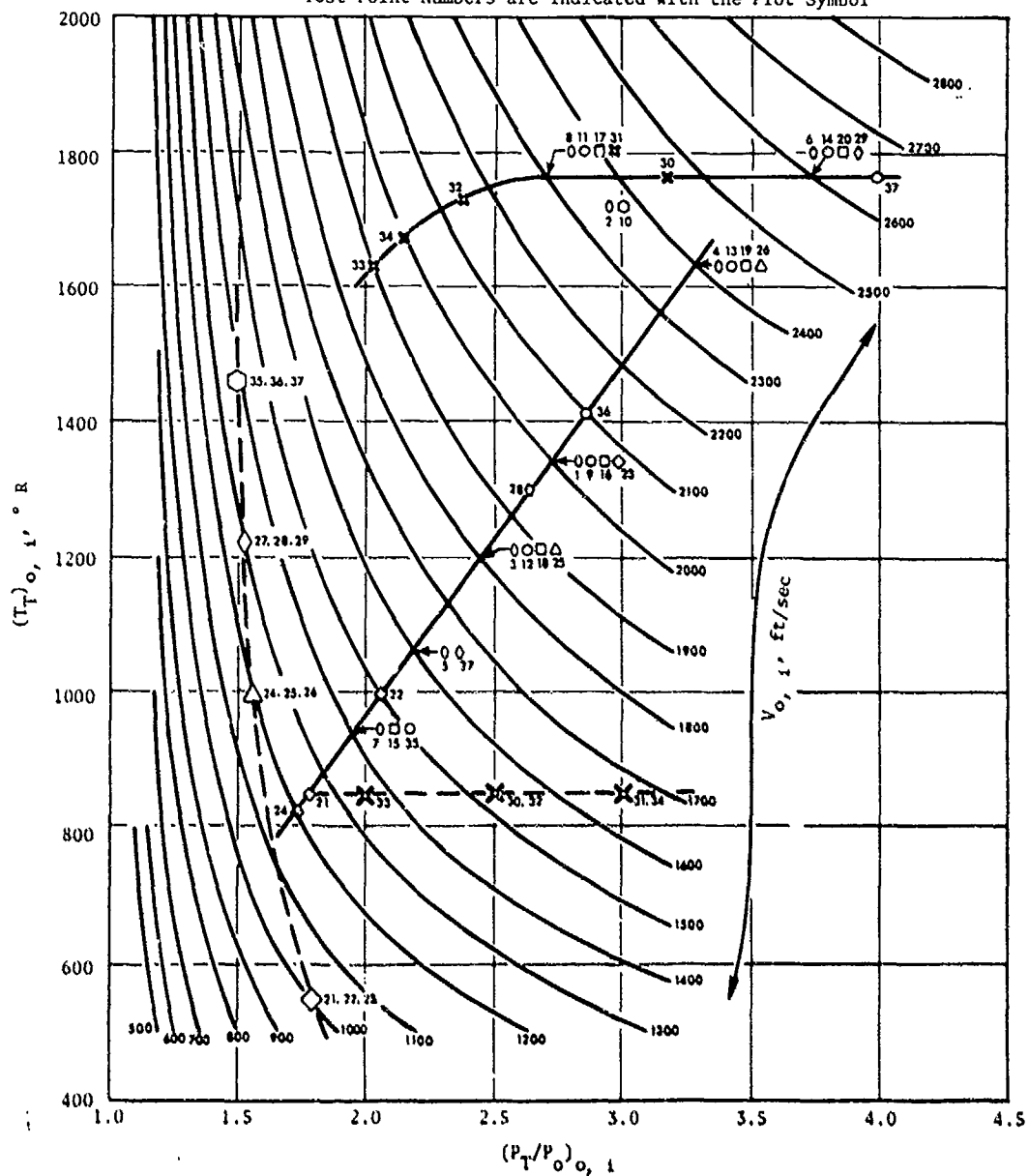


Figure 3-10. Far-Field Acoustic Test Matrix, Models 22 Through 32 and 36, Cell 41 Anechoic Facility.

Table 3-3. Far-field Acoustic Test Matrix Description - Models 22-32 and 36 -  
Cell 41 Anechoic Facility.

Objective	Data Point Nos.	Outer Stream				Inner Stream
D J A L F L O W	1-8	2.2-3.75	940-1760	1400-2300	High	No inner flow - abrupt step
	9-11	2.45-3.75	1340-1760	2000-2600		Inner flow metered to 15% of outer flow
	15-20	1.95-3.75	940-1760	1400-2600	High	Inner flow metered to 30% of outer flow
Inverted dual flow and DBF cycles	21-29 and 35-37	1.73-3.99	825-1760	1200-2680	1.0-2.0	Inner stream at 1000, 1200, 1300, and 1400 ft/sec
	30-34	2.0-3.2	1625-1760	1900-2450	1.2-1.6	Inner stream at 850° R and 1350-1660 ft/sec
		$P_T/P_0$	$T_T, ° R$	$V_0, \text{ft/sec}$	$\frac{V_0}{V_1}$	



Simulation of inverted dual flow and DBTF cycles was accomplished with Points 21 through 29 plus 35 through 37, within a  $V_0/V_1$  range of 1.0-2.0. Points 30 through 34 simulated Advanced Supersonic Transport/Variable Cycle Engine (AST/VCE) cycles.

Set H - Models 33, 34, and 35 followed a matrix similar to that of Set G; however, it was expanded to be more consistent with the test matrix of Reference 10 (DBTF program). Additionally, the data point series which simulates the 0, 15, and 30% inner flow cases was expanded from the matrix of Set G (see Appendix B for details).

Set I - Models 37 and 38 applied an acoustically treated secondary ejector to basic coannular/noncoplanar dual-flow plug nozzles; an abbreviated form of the Set G matrix was utilized. Basically, parts of the inverted dual-flow/DBTF cycle matrix (Points 22, 23, and 27-29) and the AST/VCE cycle matrix were used (see Figure 3-10 and Table 3-3). Several other data points were added; see the detailed tables in Appendix B.

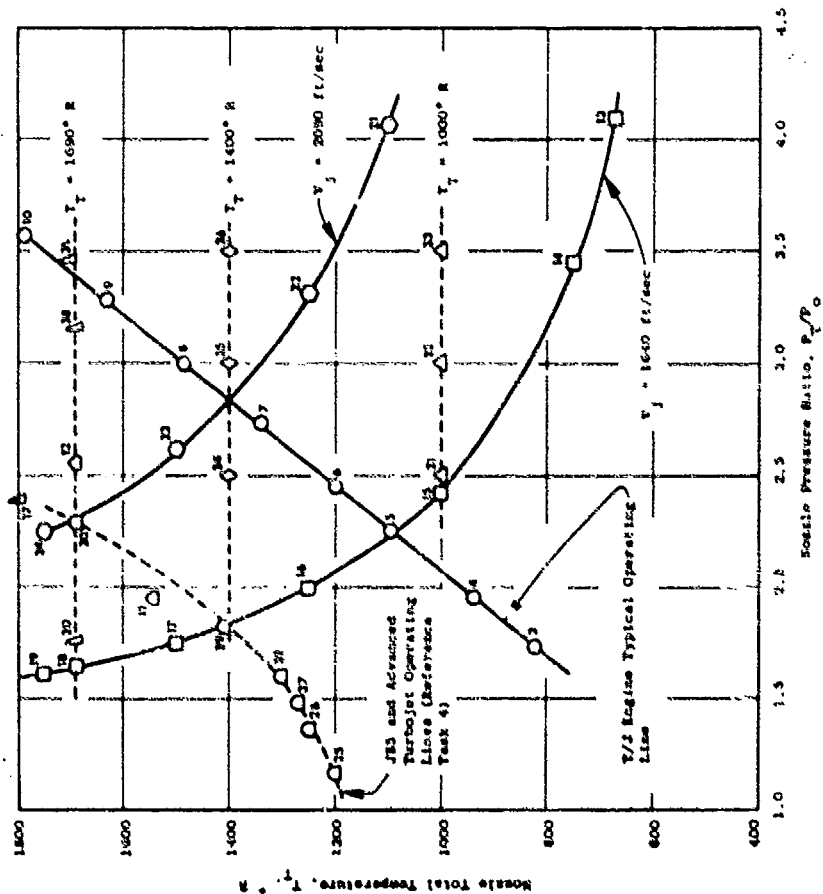
Set J - Configurations within this set, Models 39-45 and 47, utilized the overall test matrix of Figure 3-11 but with data points selectively chosen for each individual configuration. The overall matrix primarily followed: (a) a typical turbojet engine operating line; (b) isovelocity lines at 1640 and 2090 ft/sec; (c) isothermperature lines at 1000°, 1400°, and 1690° R; (d) simulation of the J85 and advanced turbojet operating lines to tie in with tests performed in Task 4 (Reference 12).

In referring to the individual model data tabulations in Appendix B, many of the data points were tested at free-stream velocities of 150 and 275 ft/sec, in addition to the normal static test. Itemization of specific data points for each model is as follows:

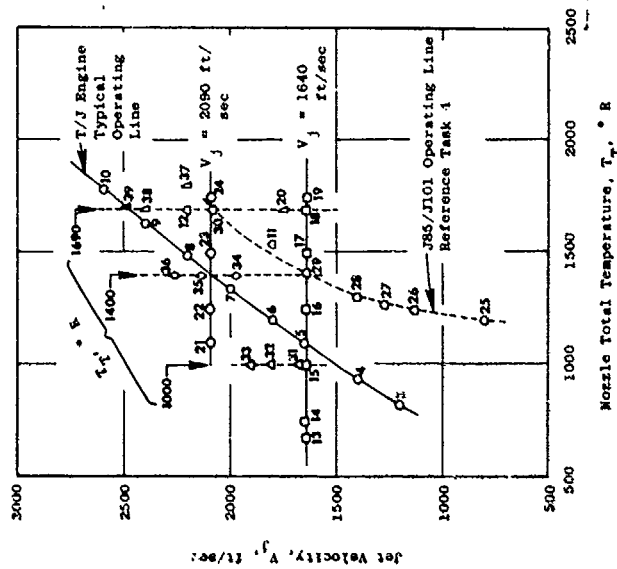
- Models 39 and 40, plug nozzles of  $R_p = 0.789$  and 0.85, used test points 3 through 12, primarily the turbojet operating line. Additionally, Model 40 used points 15-17, 19, and 21-24, forming isovelocity lines at 1640 and 2090 ft/sec.
- Models 41, 42, and 43 used data points 3, 4, 6, 7, and 9-12, again primarily the turbojet operating line.
- Models 44 and 45, the 104-tube and 104-hole nozzle nozzles, used points 9, 11-18, and 20. Model 45 also used points 25-30.
- Model 47, 4.0-inch conical nozzle, used data points 12 and 30 through 37, basically for shock noise evaluation within static and wind-on environments.

### 3.2.2 Laser Velocimeter Test Matrix

Laser velocimeter measurements of jet plumes were conducted on a total of 21 different model configurations as indicated in Table 3-1. Table 3-4



a) Cycle Matrix Shown as a Function of  $P_0/P_{00}$  and  $T_t$



b) Cycle Matrix Shown as a Function of  $T_t$  and  $V_j$

Figure 3-11. Far-Field Acoustic Test Matrix, Models 39 Through 45 and 47, JENOTS Free Jet.

Table 3-4. Laser Velocimeter Test Matrix;  
Aero Cycle Conditions.

Model No.	Inner			Outer			Free Stream $V_{FS}$ (ft/sec)	
	$(P_T/P_O)_i$	$T_i$ (°R)	$V_i$ (ft/sec)	$(P_T/P_O)_o$	$T_o$ (°R)	$V_o$ (ft/sec)		
1	1.79	545	1000	Not Applicable				
1	1.56	1000	1200					
1	1.221	1500	1000					
2	2.52	1550	2090					
2	1.99	1250	1640					
2	1.36	1000	1000					
6	1.77	555	1000	1.022	550	200		
6	1.77	555	1000	1.09	555	400		
6	1.81	555	1000	1.224	555	600		
6	1.78	550	1000	1.43	550	800		
6	1.79	545	1000	1.79	545	1000		
6	1.62	650	1000	2.19	650	1250		
6	1.51	530	500	1.82	530	1000		
6	1.22	1500	1000	1.032	1500	400		
6	1.22	1500	1000	1.073	1500	600		
6	1.22	1500	1000	1.22	1500	1000		
6	1.22	1500	1000	2.36	1500	2000		
7	1.56	1000	1200	1.73	825	1200		
7	1.56	1000	1200	2.45	1200	1800		
7	1.56	1000	1200	3.28	1630	2400		
10	$M_i = 10; M_o$			1.73	825	1200		
10				2.45	1200	1800		
10				3.28	1630	2400		
11	Not Applicable			2.45	1200	1800		
16	1.73	825	1200	Not Applicable				
16	3.28	1630	2400					
16	1.73	825	1200					
16	3.28	1630	2400					
16	1.93	940	1800					
16	2.33	1200	1800					
20	1.43	1116	1200	Not Applicable				
20	3.28	1630	2400					
22	1.56	1000	1200					
24	1.56	1000	1200					
27	1.56	1000	1200					
28	1.56	1000	1200					
39	2.25	825	1200					
39	3.28	1630	2400					
40	1.73	825	1200					
40	3.28	1630	2400					
43	1.73	825	1200				275	
40	3.28	1630	2400				275	
41	1.73	825	1200				275	
41	3.28	1630	2400					
41	1.73	825	1200					
41	3.28	1630	2400					
42	1.73	825	1200	Not Applicable			275	
42	3.28	1630	2400					
47	1.73	825	1200					
47	3.28	1630	2400					
47	1.73	825	1200					
47	3.28	1630	2400					
47	1.73	825	1200					
47	3.28	1630	2400					
47	1.73	825	1200					
47	3.28	1630	2400					
47	1.73	825	1200					
47	3.28	1630	2400					
48	2.32	1630	2200	Not Applicable			275	
48	2.32	1630	2200					
48	3.28	1630	2400					
48	3.28	1630	2400					

summarizes these configurations as well as the aerodynamic test conditions for each model at which LV measurements were taken. Of the 21 total models, 14 were tested at the JENOTS Facility and the remaining 7 within the Cell 41 Anechoic Facility. Thirteen of the models were single flow (simulating turbojet systems) and eight were dual flow. Models progressed in complexity from simple baseline conical to unsuppressed annular plug; to annular flow over a blunt base; to dual-flow coannular coplanar; to mechanical suppressors of the lobe, chute/spoke, and tube/hole families. Table 3-4 also shows that seven of the JENOTS configurations were tested under static ( $V_{FS} = 0$ ) as well as free stream ( $V_{FS} = 150$  or  $275$  ft/sec) environments.

### 3.2.3 Ellipsoidal Mirror Test Matrices

Ellipsoidal mirror measurements of source intensity distributions in Task 3 were conducted on a total of 26 different nozzle configurations as shown in Table 3-1. Of these, 14 configurations were tested at the Cell 41 Anechoic Facility using the 34.654-inch-diameter deep-dish mirror, and 12 were tested at the JENOTS Facility using the 18-inch-diameter shallow-dish mirror. The ellipsoidal mirror test matrix was planned to allow an assessment of various geometric and operating parameters on the jet noise source distributions of suppressor nozzles by comparison of measured source distributions for specific data points. Results can be expressed as Strouhal Number ( $fDeq/V_0$ ) versus normalized axial distance ( $X_{peak}/Deq$ ) where  $Deq$  is the equivalent circular diameter based on nozzle area,  $V_0$  is the ideally expanded jet velocity and  $X_{peak}$  is the peak source location for a given frequency,  $f$ . For dual-flow configurations  $Deq$  is calculated from total area (inner plus outer streams) and  $V_0$  is based on the higher velocity of the outer stream. Comparisons of data can be made for the following parameters: (a) degree of segmentation using 20/30/40 shallow chutes, (b) area ratio impact on dual-flow 36-chute suppressors, (c) element-type comparison of spoke versus chute on 36-element dual-flow suppressor, (d) 36-element or dual-flow versus on single-flow turbojet, and (e) application of treated ejector on turbojet and dual-flow systems.

Results of EM tests are discussed in Section 3.4.5, Ellipsoidal Mirror Microphone Measurements.

### 3.3 DATA ACQUISITION AND DATA REDUCTION PROCEDURES

#### 3.3.1 Acoustic Data

As shown in Table 3-1, 21 models were tested on the General Electric JENOTS Scale-model acoustic test facility and 26 were tested in the Cell 41 Anechoic Facility. The JENOTS facility is described in detail in the Task 1 final report (Reference 8) and includes the acoustic arena, burner systems, single and coannular flow systems, aerodynamic instrumentation and data acquisition, and acoustic data acquisition and reduction.

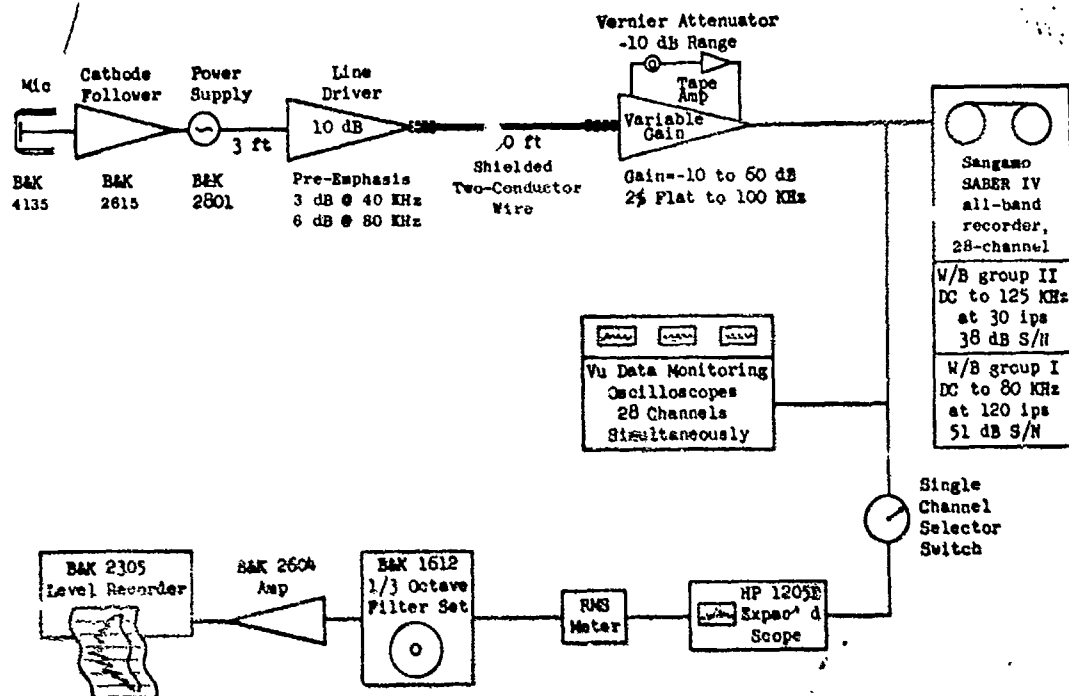
The sound field consists of 14 microphones arranged at  $10^\circ$  intervals around a  $40'$  arc from  $30^\circ$  -  $160^\circ$ . The microphones are elevated  $16'$  above the ground on specially designed "gooseneck" mounts to minimize the influence of reflections. Nozzle centerline height is  $55''$  above the concrete pad. Test Model No. 2 used the single-flow with afterburner setup and all others used the coannular flow system with the acoustically-treated plenum section.

The Cell 41 Anechoic Facility is described in detail in the Task 1 Supplement Report (Reference 9). Reference 9 includes the facility operational domain, the burner systems, acoustic plenum/silencer system, microphone system, anechoic quality of the facility, contamination of measurements, analysis of variance - overall precision of the acoustic measurements, and general certification of the facility. Model numbers 14 through 38 of this study were tested in this facility.

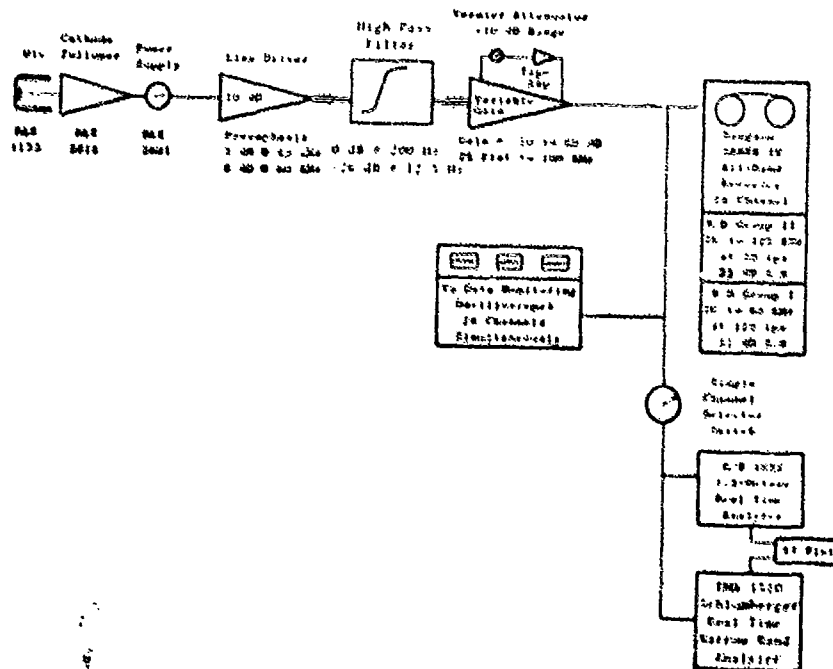
##### 3.3.1.1 Acoustic Data Acquisition

The acoustic data acquisition systems for JENOTS and Cell 41 are shown schematically in Figure 3-12. The JENOTS system is composed of B&K microphone/cathode follower powered and conditioned by a B&K 2801 power supply, followed by 3 feet of line to a specially designed 10-dB, fixed-gain pre-amplifier which drive 150 feet of cable terminating at the variable-gain differential input amplifiers to the Sangamo Sabre IV tape recorder. The signal is recorded on tape for future playback in the data reduction room. The microphone type used to obtain 80-KHz data is the B&K 4135 without grid caps. The cathode follower used most often is the B&K 2615 preamplifier although B&K 2619 is also used. The purpose of the cathode follower is to give a very high input impedance with small load to the microphone and a low-output impedance allowing the connection of long cables between the pre-amplifier and relatively low impedance amplifiers in the circuit. The B&K 2619 uses a field-effect transistor to give higher input impedance and lower inherent noise than Type B&K 2615. The cathode follower also supplies the microphone with a 200-volt polarization from the power supply.

The B&K 2801 power supply is operated in the direct-output mode to avoid sensitivity loss. The frequency response of the various preamplifiers is not influenced by the power supply when used in this position. This power supply does have optional 50-ohm and 200-ohm transformer outputs for use in eliminating amplifier oscillation and dampening RC resonance. The JENOTS systems,



(a) JENOTS Data Acquisition System.



(b) Cell 41 Acoustic Facility Data Acquisition System.

Figure 3-12. Schematics of Acoustic Data Acquisition Systems.

however, are free of such problems due to the unloading of the power supply by the preamplifier. Three feet from the output of the power supply is a fixed 10-dB amplifier for driving the signal to the tape recorder amplifier. In anticipation of the low sound levels experienced at high frequency, the circuitry was designed with a frequency response that "preemphasized" the high-frequency signals such that it has a 3 dB increase at 40 KHz and an additional 3 dB between 40 KHz to 80 KHz. This increases the ability to measure low-amplitude high-frequency data. Two-conductor shielded wires were chosen for the 150 feet of lead from the line driver to the tape recorder amplifier to eliminate stray signal pickup. The cable introduces an effective 0.0458- $\mu$ f capacitance to the circuit.

The amplifier at the tape recorder was designed by GE and has a variable gain from -10 dB to +60 dB. The amplifier delivers a 4-volt, peak-to-peak signal to the tape recorder electronics at the normal calibration signal level. This setting will allow a 6 dB over range without distortion. The amplifiers are flat within 5% from 5 Hz to 100 KHz. Each amplifier has an adjustable vernier attenuator which can give any desired measure of attenuation between 0 and 10 dB. During test calibration, this vernier is usually adjusted to make the 124-dB pistonphone calibration signal the full-scale (1.4 V/rms) input to the tape recorder. The 10-dB steps in the tape recorder amplifier then directly correspond to 10-dB steps in OASPL from 124 dB. The vernier can be moved to the fixed position, in which case, the signal goes directly into the 10-dB-step tape recorder amplifier. The output of each amplifier channel has a V-Data Monitoring oscilloscope for continual inspection of all signals for any clipping or deterioration of the signal due to excessive crest factor (peak value/rms).

The Sangamo Sabre IV 4930 magnetic tape recorder/reproducer has IRIG wideband and RM wideband Group I and Group II capability. In normal JENOTS operation all data are recorded on 1-inch in Wideband Group II at 30 ips, having a flat frequency response in excess of 100 KHz when used in conjunction with the B&K 4135 microphone. The voice channel is recorded direct.

The JENOTS recorder was modified to record 28 tracks and to improve its signal-to-noise dynamic range from the normal 32 dB to 39 dB over all frequencies. This lower noise floor was obtained by individual channel tuning by the Sangamo Electric Company at the factory. Playback capability of two data channels plus voice for on-site data investigation is also available.

The Cell 41 Anechoic Facility data acquisition is similar to that of JENOTS, utilizing B&K 4135 condenser microphones without grid caps, transistorized 2619 cathode followers and 2801 power supplies; obtaining acoustic data through the 80 KHz 1/3-octave center frequency. The output of the power supply is similarly connected to a line driver adding 10 dB of amplification to the signal. Preemphasis to the high-frequency portion of the signal is also used. In order to remove low-frequency noise, high-pass filters with attenuations of approximately 26 dB at 12.5 KHz decreasing to 0 dB at 200 Hz were installed in the system.

The tape recorder's amplifying characteristics are similar to those of JENOTS. The prime system used for recording acoustic data is a Sangamo Sabre IV 28-track FM recorder. The system is set up for Wideband Group I (intermediate band double extended) at 120-ips tape speed. Operating at 120-ips tape speed provides the improved dynamic range necessary for obtaining the high-frequency/low-amplitude portion of the acoustic signal. The tape recorder is set up for  $\pm 40\%$  carrier deviation with a recording level of 8 volts peak-to-peak. During recording, the signal is displayed on a calibrated master oscilloscope, and signal gain is adjusted to maximum without exceeding the 8-volt peak-to-peak level.

High-pass filters were incorporated in the acoustic data acquisition systems to enhance high-frequency data previously lost in the tape recorder electronic noise floor for microphones from  $110^\circ$  to  $160^\circ$ . The microphone signal below the 20 KHz 1/3-octave band was filtered out, and the gain was increased to boost the signal to noise ratio. For microphones from  $110^\circ$  to  $160^\circ$ , both the filtered and unfiltered signals were recorded on tape. For data below 20 KHz the unfiltered signal was used to calculate the sound pressure levels while for high frequencies the filtered signal was used. The entire jet noise spectra at a given angle was then obtained by computationally merging these two spectra.

#### 3.3.1.2 Acoustic Data Reduction

Acoustic data reduction is conducted in the General Electric AEG Instrumentation and Data Room (IDR) and is similar for both JENOTS and Cell 41 Anechoic systems as shown schematically in Figure 3-13. The data tapes are played back on a CEC3700B tape deck with electronics capable of reproducing signal characteristics with the specifications indicated for Wideband Group I and Group II. During acoustic testing, a tone is inserted on the tape recorder to mark the point on the tape where recording of the microphone signal for a given acoustic test point is initiated. During the data-reduction phase a tape control unit automatically shuttles the tape, initiating an integration-start signal to the analyzer at this tone as the tape moves in its forward motion. This motion continues until an integration-complete signal is received. Then the tape control unit switches to the next channel, the tape rewinds, and the process is repeated. When all channels are complete, the tape moves forward to the next data point on the magnetic tape.

All 1/3-octave analyses are performed on a General Radio 1921 1/3-octave analyzer. Normal integration time is set for 32 seconds to ensure good integration for the low-frequency content. The analyzer has a 1/3-octave filter set for 12.5 Hz to 100 KHz and has a rated accuracy of  $\pm 1/4$  dB in each band. Each data channel is passed through an interface to the CEPAC 30 computer where the data are corrected for the frequency response of the microphone and the data acquisition system and corrected to standard day ( $59^\circ$  F, 70% relative humidity) atmospheric attenuation conditions per methods discussed in Section 3.3.1.3 for JENOTS and Cell 41 Anechoic Facilities. The output of the computer is passed to a Terminet 300 console where the corrected sound pressure level (SPL) can be printed out on sheets for "quick look"



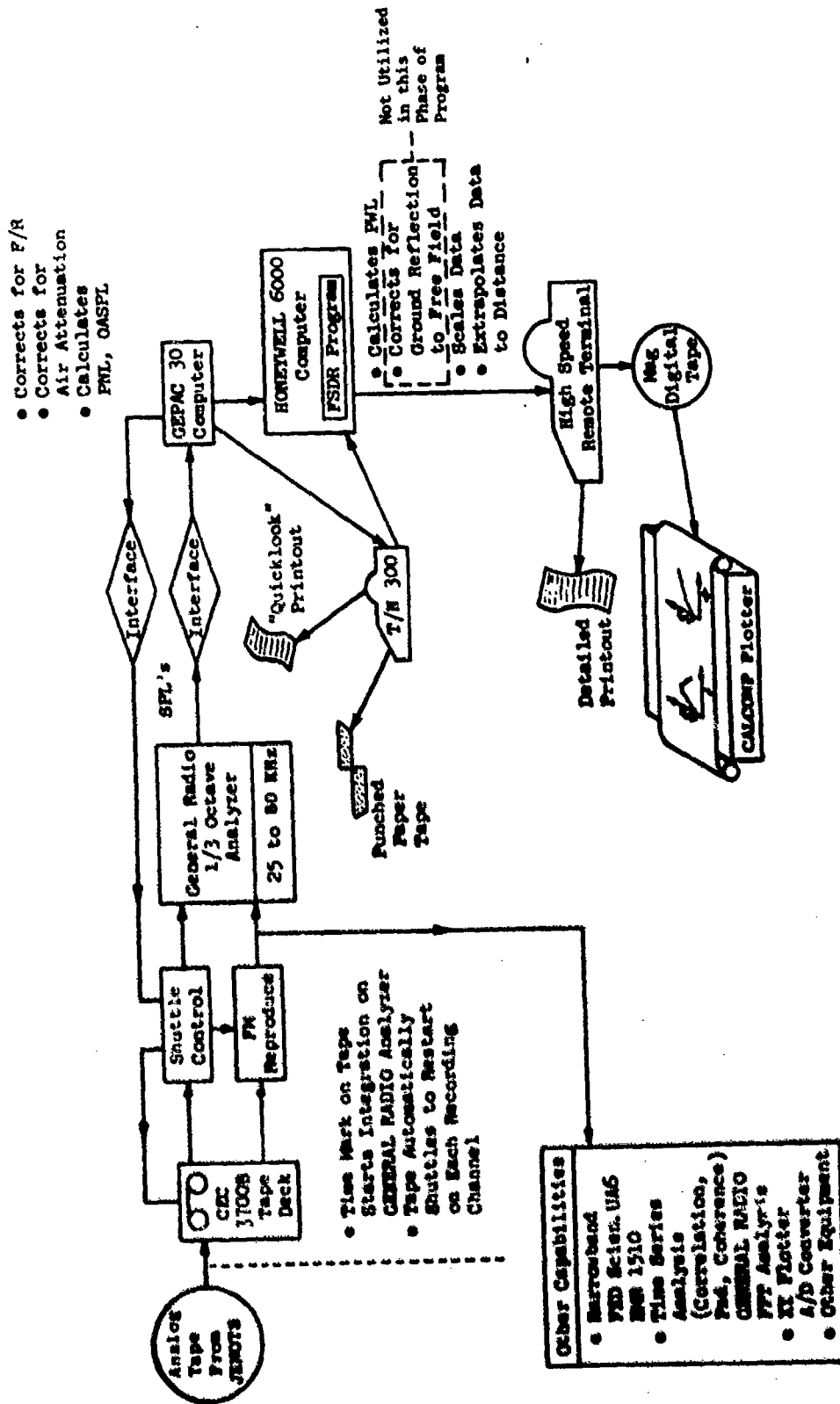


Figure 3-13. Data Reduction System, JENOTS and Cell 41.

analysis. For calculation of acoustic power, corrections for ground reflections to free field, scaling to other nozzle sizes, or extrapolations to different far-field distances, the data are sent to the Honeywell 6000 computer for processing through the full-scale data reduction (FSDR) program where the appropriate calculations are performed. This step is accomplished by accessing the SPL's stored on magnetic tape in the 6000 computer through a 1200-band Modem. The data printout is accomplished on a high-speed "remote" terminal. A magnetic tape is also written for CALCOMP plotting of the data.

#### 3.3.1.3 Air Attenuation Corrections

Acoustic testing is subject to continual changes in meteorological conditions. Correspondingly, the attenuation of sound over the distance from the jet source to the microphone will vary with the environmental fluctuations of temperature and humidity due to differences in atmospheric absorption. It is common practice to attempt to account for these differences by either (1) correcting the data for air attenuation from the measured day values to a "standard day" of 59° F and 70% relative humidity (as has been done for data within this study) or by (2) removing all the air attenuation from the data. These corrections have been calculated using References 13 and 14. This work extended the experimental data of Reference 15 (Harris) taken at 68° F to other temperatures using the theoretical work of Reference 16 (Knesner). Reference 15 experiments, however, were only performed to the 12.5-KHz narrowband, and its corrections are limited to the 8-KHz 1/3-octave band. The need for corrections at higher frequencies led to an extension to 80 KHz (Reference 17). These corrections were developed by extrapolations of the Reference 13 and 14 (ARP866) curves, tempered by the continual experience of comparing scaled jet spectra of nozzles ranging from 1 inch to 4 feet in diameter. The Reference 17 air attenuation model was found to be best suited to the JENOTS outdoor test data and was applied to all data taken on that facility. The model, developed using References 13, 15, and 20, is discussed in Appendix C and also is presented in the form of a computer program listing which is used to generate the high frequency correction factors. Reference 10 discusses the air attenuation correction status in more detail, with particular application to the JENOTS facility data, and presents comparisons of data corrected by use of several techniques. To develop air attenuation corrections for application to acoustic data taken in the more controlled environment of the Cell 41 Anechoic Facility, an extension of Reference 14 to the 80-KHz 1/3 octave band was programmed and used.

#### 3.3.1.4 Data Corrections to a Free-Field Environment-JENOTS

The ground presence at JENOTS affects the propagation of noise reflection/absorption. The approach taken to convert the measured noise data to the "free field" was based on theoretical analysis of the ideal case of an infinitely hard surface, a point source of broadband noise, and a stable homogenous medium (Reference 18). The analysis was modified by a series of tests and parametric studies conducted in Task 1 of this program (Reference 8). This involved the determination of the ground impedance phase factor and

reflection coefficient, an estimate of the scattering phenomenon, and a correction for the distributed source effects of the jet. The results of the calculations are shown in Table 3-5. These values were incorporated into the data reduction program as standard ground reflection corrections for all JENOTS data.

#### 3.3.1.5 Data-Scaling Procedure

The primary function of a scaling procedure is to present test data in a useful form for engineering evaluation. Prior to scaling, the model SPL's are conditioned as described in Section 3.3.1.2 for frequency response of the microphone and the data acquisition system. The JENOTS data are corrected to "free field" per Section 3.3.1.4. These model SPL's are then corrected to the source by removal of extra ground attenuation (per Reference 19) and air attenuations based on the measured ambient meteorological conditions, per Section 3.3.1.3. The spectrum frequencies are shifted on a  $1/3$ -octave basis as a function of nozzle diameter ratio (e.g.,  $\sqrt{A_{\text{full scale}}/A_{\text{model scale}}}$ ). For all data within this study, a full-scale area of 338 in.<sup>2</sup> is used; that of the J79 engine's fixed area exhaust nozzle, used for the Acoustic Scaling Demonstration in Volume III. The absolute level is adjusted by the weight flow ratio (which is assumed equal to the square of the diameter ratio). The resultant spectrum is extrapolated to the desired arc or sideline using the inverse square law (20 log distance) and standard day atmospheric absorption as per Section 3.3.1.3. Extra ground attenuation (EGA) is not used in the extrapolation procedure. For most configurations within this study, "full-scale" data were developed at a 160-ft arc and a 2400-ft sideline.

#### 3.3.1.6 Power Level Calculations

The method used to calculate sound power levels from the corrected SPL's is to integrate sound pressure levels assigned to strip areas based on the input microphone radius and acoustic angles of interest. The method used in the computer program is detailed in Appendix B of Reference 10. All levels are corrected to represent full-spherical radiation.

#### 3.3.1.7 Acoustic Data Normalization

For presentation of acoustic results, the data normalization technique developed in Reference 11, modified for inclusion of static ideal gross thrust, was adopted. Reference 11 concluded that the mixed stream properties best govern the overall noise levels (OAPWL, OASPL, PNL<sub>max</sub>). Selection of mixed stream velocity as the basis for data comparisons has a strong physical attractiveness as it expresses the noise in terms of a velocity calculation based on the thermodynamic conditions of both streams. It also allows comparison of noise values at the same ideal thrust and total mass flow which are meaningful propulsion performance parameters.

Table 3-5. JENOTS Ground Reflections Corrections (AaB's to be Added to SPL's).

Frequency (Hz)	θ Angle Referenced Inlet													
	30	40	50	60	70	80	90	100	110	120	130	140	150	160
50	-4.99	-4.97	-4.93	-4.88	-4.82	-4.75	-4.66	-4.55	-4.41	-4.24	-4.03	-3.77	-3.46	-3.1
63	-4.45	-4.41	-4.35	-4.29	-4.21	-4.1	-3.98	-3.82	-3.64	-3.42	-3.16	-2.86	-2.52	-2.19
80	-4.0	-4.0	-3.94	-3.87	-3.79	-3.69	-3.56	-3.42	-3.27	-3.06	-2.79	-2.46	-2.11	-1.76
100	-4.0	-4.0	-3.9	-3.8	-3.69	-3.56	-3.42	-3.27	-3.06	-2.79	-2.46	-2.11	-1.76	-1.41
125	-3.5	-4.0	-3.5	-3.0	-2.5	-2.0	-1.7	-1.0	1.0	2.0	2.0	2.9	3.8	2.8
160	0	0	-1.5	-0.5	-1.0	1.5	2.7	1.5	1.0	3.0	2.0	3.0	3.2	2.2
200	-2.0	-1.5	-1.5	-1.0	-1.0	0.5	0	0	0.5	1.0	-0.17	-0.65	-1.03	0
250	0	0	0	-0.5	-1.5	-1.5	-2.5	-2.5	1.5	-1.0	-2.0	-4.48	-4.58	-2.39
315	1.5	0	-1.5	-1.5	-1.5	-1.8	-4.0	-1.5	-3.0	-3.0	-3.0	-4.9	-5.09	-2.0
400	-2.0	-4.2	-4.1	-3.5	-2.5	-3.2	-3.1	-2.34	-1.85	-1.34	-4.9	-0.37	-0.7	-4.3
500	-1.0	-1.0	0	-1.3	-1.1	-1.2	-1.1	-1.35	-1.14	-1.87	-2.1	+1.8	-0.5	-0.5
630	-1.64	-1.5	-1.0	-2.5	-2.0	-3.2	-2.1	-2.09	-2.03	-3.5	-3.5	-1.64	-1.3	-0.9
800	-1.55	-1.35	-1.12	-1.0	-1.0	-2.0	-2.1	-0.88	-1.22	-0.5	-1.05	-0.5	-0.8	+2.2
1000	-1.0	-2.44	-1.3	-2.36	-2.3	-2.13	-1.9	-1.72	-1.47	-1.22	-2.1	-1.9	-0.71	-0.8
1250	-1.97	-2.03	-2.10	-2.17	-2.24	-2.28	-2.3	-2.28	-2.24	-2.18	-2.12	-2.08	-2.04	-2.2
1600	-2.17	-1.5	-2.06	-1.98	-1.90	-1.83	-1.8	-1.83	-1.93	-2.07	-2.23	-2.36	-2.45	-2.5
2000	-0.74	-2.0	-2.6	-0.92	-1.11	-1.37	-1.7	-1.90	-2.05	-2.10	-2.06	-1.97	-1.88	-1.8
2500	-1.5	-2.0	-1.8	-2.84	-2.70	-2.52	-2.35	-2.29	-2.31	-2.37	-2.45	-2.51	-2.54	-2.56
3150	-2.5	-2.57	-2.60	-2.66	-2.78	-2.93	-3.1	-3.14	-3.07	-2.91	-2.75	-2.65	-2.6	-2.59
4000	-2.80	-2.78	-2.74	-2.66	-2.58	-2.55	-2.60	-2.67	-2.72	-2.72	-2.72	-2.72	-2.72	-2.71
5000	-2.6	-2.72	-2.77	-2.84	-2.90	-2.95	-2.60	-2.41	-2.36	-2.44	-2.52	-2.56	-2.58	-2.59
6300	-2.70	-2.68	-2.64	-2.59	-2.56	-2.64	-2.90	-2.97	-2.85	-2.72	-2.68	-2.66	-2.66	-2.66
8000	-2.76	-2.76	-2.75	-2.73	-2.67	-2.60	-2.70	-2.80	-2.78	-2.74	-2.72	-2.71	-2.7	-2.7
10000	-2.69	-2.69	-2.68	-2.67	-2.67	-2.71	-2.80	-2.70	-2.60	-2.63	-2.65	-2.65	-2.65	-2.65
12500	-2.70	-2.70	-2.71	-2.69	-2.69	-2.71	-2.70	-2.70	-2.66	-2.66	-2.66	-2.66	-2.66	-2.66
16000	-2.61	-2.61	-2.61	-2.60	-2.58	-2.56	-2.70	-2.60	-2.57	-2.57	-2.57	-2.57	-2.57	-2.57
20000	-2.63	-2.63	-2.63	-2.62	-2.61	-2.61	-2.70	-2.56	-2.60	-2.60	-2.59	-2.59	-2.59	-2.59
25000	-2.71	-2.71	-2.71	-2.70	-2.70	-2.69	-2.70	-2.68	-2.68	-2.67	-2.67	-2.67	-2.67	-2.67
31500	-2.74	-2.73	-2.73	-2.73	-2.72	-2.72	-2.70	-2.68	-2.71	-2.70	-2.70	-2.69	-2.69	-2.69
40000	-2.71	-2.71	-2.71	-2.71	-2.70	-2.70	-2.70	-2.69	-2.68	-2.68	-2.68	-2.67	-2.67	-2.67
50000	-2.73	-2.73	-2.73	-2.73	-2.72	-2.72	-2.72	-2.71	-2.70	-2.70	-2.70	-2.69	-2.69	-2.69
63000	-2.70	-2.70	-2.70	-2.69	-2.69	-2.68	-2.70	-2.68	-2.67	-2.67	-2.66	-2.66	-2.66	-2.65
80000	-2.72	-2.72	-2.72	-2.71	-2.71	-2.71	-2.70	-2.70	-2.69	-2.69	-2.68	-2.68	-2.68	-2.68

In general, acoustic data will be presented as:

$$\text{Noise value} = 10 \log_{10} [F_s (T_o/T_{sm})^{\omega-1}] \text{ vs. } V_{ma}, f, \text{ or } \theta$$

where:

Noise value = PNL, OASPL, OAPWL, OR 1/3 OBSPL

$F_s$  = Static ideal gross thrust (sum of inner and outer streams)

$T_o$  = Ambient temperature, ° R

$T_{sm}$  = Static temperature corresponding to mass averaged velocity,  $V_{ma}$ , and total temperature,  $T_{Tma}$ , ° R.

$\omega$  = Jet density exponent (per SAE ARP 876) based on mass-averaged velocity,  $V_{ma}$

$$V_{ma} = \frac{W_i V_i + W_o V_o}{W_i + W_o} \quad (\text{Mass-Averaged Jet Velocity, ft/sec})$$

$$T_{Tma} = \frac{W_i T_{T_i} + W_o T_{T_o}}{W_i + W_o} \quad (\text{Mass-Averaged Total Temperature, ° R})$$

where  $W$  and  $T_T$  are the exit plane values of mass flow and total temperature for the inner and outer (subscript  $i$  &  $o$ ) streams, respectively, and  $f$  &  $\theta$  are 1/3-octave-band center frequency and angle relative to inlet axis. In the case of turbojet test data, the flow parameters revert to the single-stream notation.

On occasion, for ease of data handling and presentation, the normalization seen on graphs will be:

Noise value -N, where:

$$N = 10 \log_{10} [F_s / 10,000 (T_o/T_{sm})^{\omega-1}]$$

The introduction of a 10,000-lb reference thrust shifts noise levels by 40 dB and allows plotting of all positive values of the low-level sideline noise data.

### 3.3.2 Laser Velocimeter Data

The laser velocimeter system was developed by General Electric during the AF/DOT Supersonic Jet Exhaust Noise Investigation (Reference 21) for measurement of mean and rms turbulent velocities in high-temperature, high-

velocity jets. The basic optics system is a differential Doppler, back-scatter, single-package arrangement that has the proven feature of ruggedness for the severe acoustic environment. The LV is a noncontacting optical system in which the velocities of the seed particles are measured (in a single direction) as they pass through the fringes of an interference pattern created by two intersecting beams of coherent radiation. Figure 3-14 shows a schematic arrangement of the laser package used on this program. The laser beams are projected from below the lens, forming an angle,  $\alpha$ , that keeps the major axis of the control volume ellipsoid to a minimum. The dimensions of the control volume are 0.25 inch for the major axis and 0.020 inch for the minor axis. The range of the LV control volume from the laser hardware was 85 inches. At this distance from the jet, a protective enclosure is not necessary. The three steering mirrors and the beam splitter are mounted on adjustable supports, all of the same aluminum alloy which eliminates temperature-alignment problems. References 21, 22, and 23 contain detailed descriptions of the system and its validation, as well as results for measurements on scale-model nozzles under static conditions.

The setup of the laser velocimeter (and ellipsoidal mirror) at JENOTS is shown in Figure 3-15(a) and the LV within the Cell 41 Anechoic Facility in Figure 3-15(b). At JENOTS the LV optics package is mounted on a remotely actuated platform on tracks parallel to the jet axis. Since the LV has a fixed working range of 85 inches, measurements at different points in the jet are accomplished by traversing the platform along three axes: horizontal, vertical, and axial (jet axis). Travel capabilities along the three axes are 32, 32, and 240 inches, respectively. Resolution is  $\pm 1/16$  inch for each axis except for the last 208 inches of axial travel which has a resolution of  $\pm 1/8$  inch.

Within the anechoic facility, the track is located on the northwest side of the chamber at a position approximately 13 feet from the nozzle axis. The traverse span ranges from approximately 2 feet below the nozzle discharge plane to approximately 17 feet above the nozzle discharge plane (see Reference 8).

The cart and lift have a rated load capacity of 3600 pounds. It rides on precision-aligned rails made of hardened steel for wear resistance and accurate positioning. The track extends through a sliding concrete hatch, via a hinged section of track, to the floor of the auxiliary room to permit interchanging the EN and LV systems as required. Traversing operation of the cart on the track can be accomplished from either the test chamber, auxiliary room, or control console. Remote position indication is provided by means of a 10-turn potentiometer driven off the winch shaft, with readout at the control console. The ability to record the position signal on magnetic tape in conjunction with the acoustic data for subsequent correlation is provided.

At both facilities the LV can be operated in a traversing mode to obtain continuous profiles of mean axial velocity, or it can be operated in a stationary mode to construct velocity histograms for determination of both mean and rms turbulent axial velocities at discrete points.

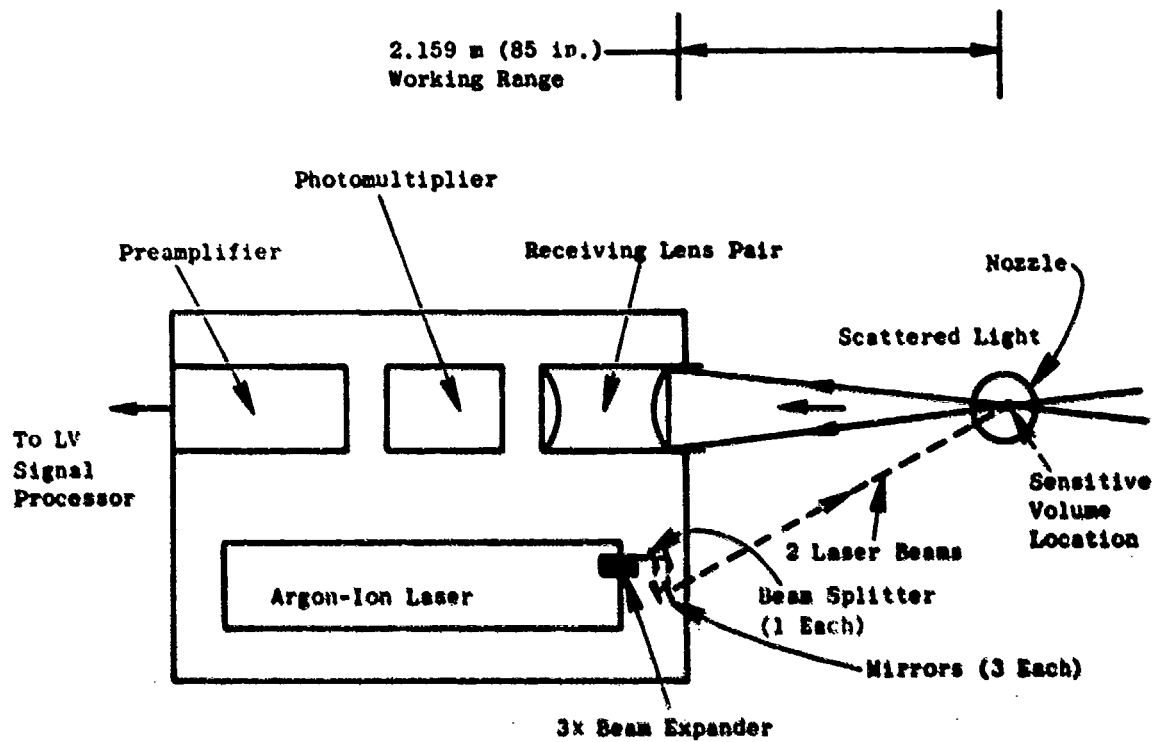


Figure 3-14. Schematic of Laser Velocimeter Optics Package.

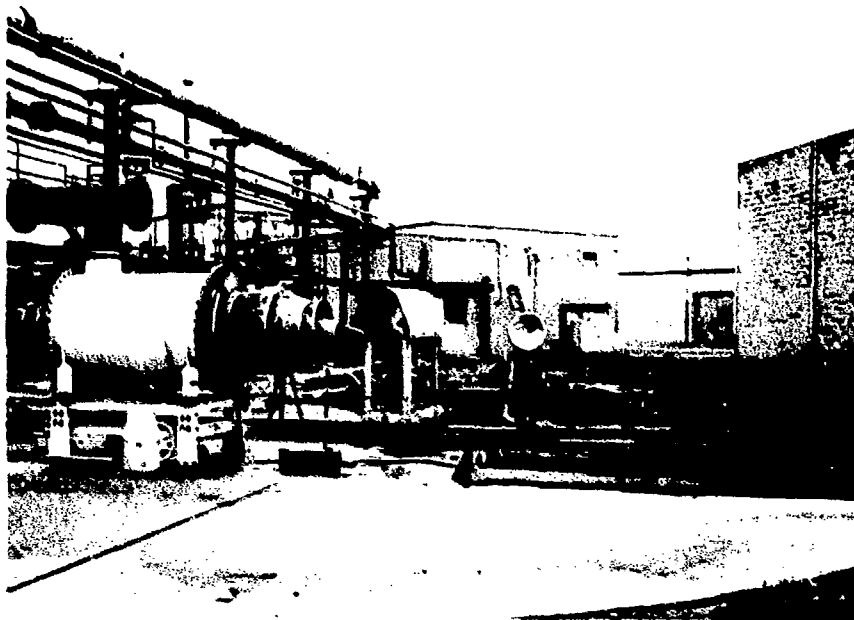


Figure 3-15(a). Laser Velocimeter and Ellipsoidal Mirror at JENOTS.

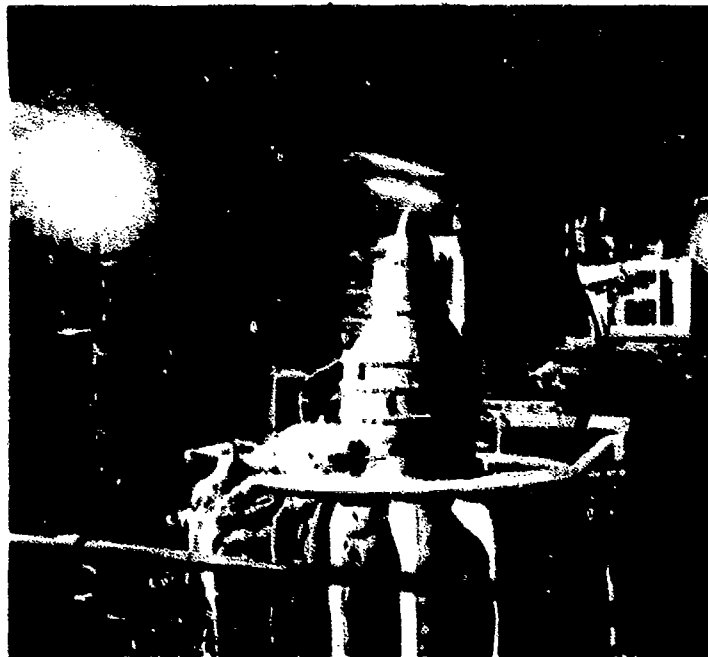


Figure 3-15(b). Laser Velocimeter in Cell 41 Anechoic Facility.



Traverses can be made along any of the three LV axes. In this mode of operation, the velocity levels and positions of incoming data are continuously recorded by an x-y plotter. Sampling rates on the order of at least 250 samples per inch of travel are typical for good definition. If data rates are low or details of a profile are not clear, the traversing speed can be reduced or portions of the traverse can be repeated one or more times. Better definition also can be obtained by executing the traverse as a series of "stutter" steps, with short pauses interspersed to accumulate additional data.

Histograms are located at strategic points to verify details from the mean velocity traverses and to obtain rms turbulence levels. The histogram is formed from a large number of samples, typically 500 to 1000.

Seeding is by injection of aluminum oxide ( $Al_2O_3$ ) powder, a nominal 1- $\mu$ m diameter, into the supply air to the burner and into the region of the nozzle so as to seed the entrained air. The powder-feeder equipment used is described in Reference 23 except that the fluidized bed column supply air was heated to about 250° F to prevent powder aggregation by moisture absorption.

This LV setup is used only for exhaust plume surveys and is removed during acoustic tests.

The concept of using laser velocimeter measurements for obtaining routine mean and turbulent-velocity profiles may be described in the following simple fashion. Two beams of monochromatic light intersect at a point in space and set up a fringe pattern of known spacing (see Figure 3-16). The flow is seeded with small particles which pass through the measuring volume; the light scattered from the particles is collected, and the laser signal processor measures the time it takes for the particles to pass through each fringe. Knowing the distance and the time for each validated particle enables the construction of the usual histogram (see insert on Figure 3-16). Then, by statistical techniques, the mean value (which corresponds to the mean velocity) and standard deviation (which corresponds to the turbulent velocity) are constructed. The method of calculation used to obtain the mean velocity and turbulent velocity from laser velocimeter measurements is described below.

A histogram is an estimate of the first-order probability density of the amplitude of a given sample. To obtain a velocity histogram, the time-dependent laser velocimeter velocity,  $V(t)$ , is accumulated and divided into classes bounded by values of velocity increments,  $V_i$ . For each independent sample of velocity, a class interval is formed such that  $V_i \leq V(t) < V_{i+1}$ . During a measurement period,  $k_i$  number of velocity samples accumulated in each sample class,  $V_i$ . From the total sample of measured velocity points, the histogram is constructed as shown in Figure 3-16.

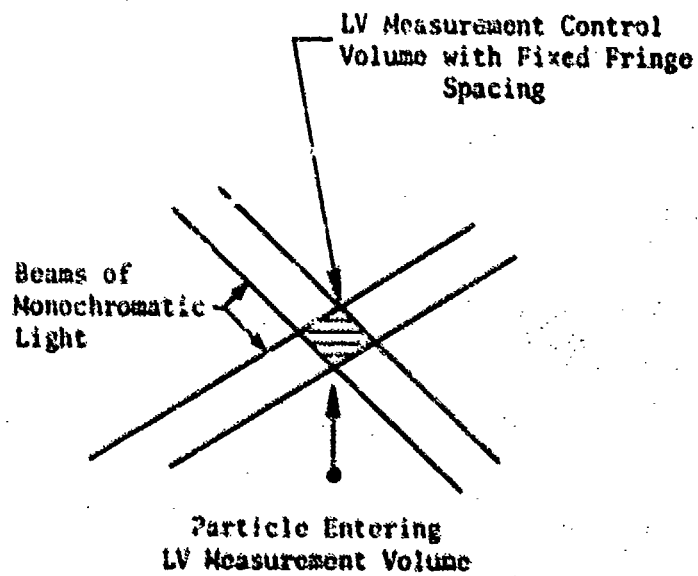
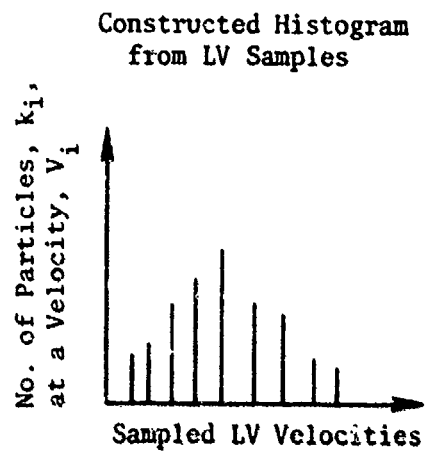


Figure 3-16. Schematic of Laser Velocity Measurements.

The mean velocity of the jet,  $\bar{v}_j$ , obtained from the discrete velocity samples is calculated by:

$$\bar{v}_j = \sum_{\text{All Class Intervals}} \left( \frac{v_{i+1} + v_i}{2} \right) \frac{k_i}{N}$$

where

$\frac{v_{i+1} + v_i}{2}$  is the value of the sampled axial velocity component at the center of the class interval.

$K_i$  is the number of velocity samples in the class interval.

$N$  is the total number of velocity samples ( $\sum_i k_i$ ) in the histogram.

To obtain the axial turbulent velocity,  $u'$ , from the sampled data contained in the histogram, the standard square root of the statistical variance is performed. This calculation is performed using the following equation:

$$u' = \left[ \sum_{\text{All Class Intervals}} \left( \frac{\frac{v_{i+1} + v_i}{2} - \bar{v}_j}{N} \right)^2 k_i \right]^{1/2}$$

Reference 10 discusses the statistical errors for LV mean and turbulent velocity measurements. Discussions of LV turbulence spectra and in-jet far-field cross correlation measurements are treated in Reference 8.

### 3.3.3 Ellipsoidal Mirror Data

The ellipsoidal mirror (EM) was identified in Task 1 of this program (Reference 8) as a fast, flexible method of obtaining macroscopic noise source location information for a jet plume. Measurements were made on cold-flow, round, static jets to establish the basic capabilities of the technique. Measurements taken within Task 4 of this program (Reference 12) demonstrated the ability of the EM to detect variations of source distributions among different geometric nozzle configurations and between various levels of free-stream velocity for heated-flow jets. Task 3 continued the development of EM data acquisition and processing systems and further evaluated the accuracy of the technique. Appendix D is a comprehensive "Summary of Ellipsoidal Mirror Development" and treats in detail the development and evaluation of the EM technique. Task 3 additionally acquired heated-flow source location data on a total of 26 base-line and suppressor model configurations of the single (TJ) and dual-flow families. For the

test work, an 18-inch shallow-dish mirror and a 34.654-inch deep-dish mirror were used for the JENOTS and Cell 41 Anechoic Facility, respectively. Schematics and a summary of EM characteristics are presented in Figure 3-17. The mirror systems were calibrated for window function and gain; the window function representing the sensitivity of the system to discriminate between adjacent sources. Calibration results for the two systems in terms of gain and normalized window function width are also discussed in Appendix D. The deep-dish mirror, while not showing as good agreement with theoretical trends, showed higher gain and slightly narrower window function relative to the 18-inch shallow-dish mirror.

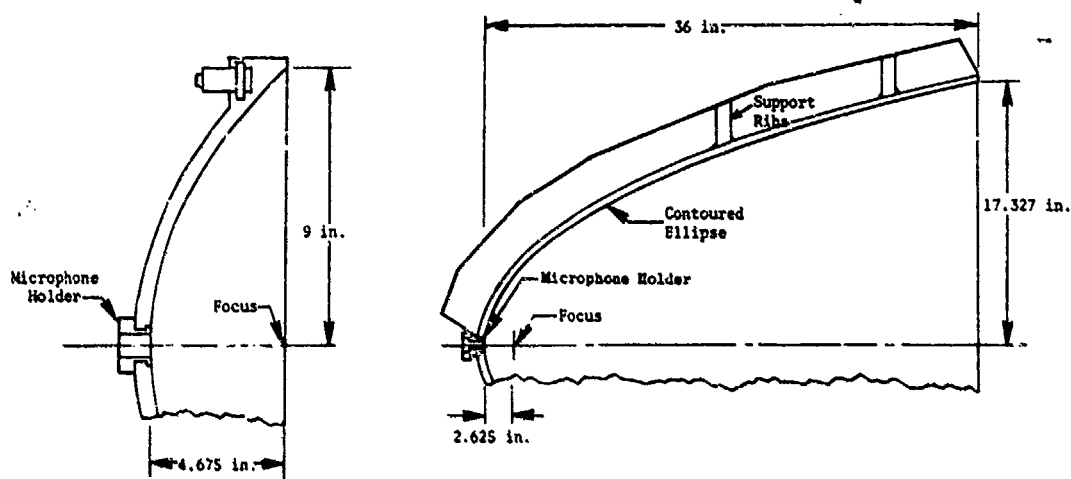
For each EM system, data are recorded on magnetic tape over a full length of "outbound" traverse. The microphone signal, DC cart position, and time code signals are all recorded using the standard acoustic data acquisition systems of the facilities discussed in Section 3.3.1.

Data reduction is a two-phase procedure consisting of (1) conversion of the raw analog data to digitized spectral distributions and (2) numerical processing (deconvolution procedure) of these results to correct for the effects of mirror gain and diffraction window function. After deconvolution, the distributions represent total source contributions at each axial position (i.e., a slice of jet measurements). Studies were performed for selection of the best deconvolution technique (the relaxation technique was selected) and for the effect of presmoothing data. These studies led to the adoption of improved data reduction procedures and also assessed the limitations and sources of errors from three areas: (1) theoretical limitations, (2) data acquisition errors, and (3) data processing errors and limitations. The major sources of errors encountered in processing EM data are:

1. Statistical errors due to insufficient averaging time.
2. Enhancement of ambient or electronic noise, or of statistical measurement errors, due to an ill-conditioned window function matrix.
3. Limits on achievable resolution due to numerical instabilities in the solution of an ill-conditioned set of equations.
4. Errors induced by uncertainty in window function measurements.

Data analysis can be interpreted as (1) axial source intensity distributions for individual 1/3-octave bands or (2) source spectra at discrete axial positions. The results are most readily summarized in terms of the axial location of the peak intensity for each frequency band: i.e.,  $fD/V$  versus  $x/D$ .

For 1/3-octave band analyses, two processing cycles normally are performed using 1 and 4 second integration times for the JENOTS 18-inch mirror and 2 and 8 second times for the anechoic facility deep-dish mirror. The two cycles accommodate high and low frequency requirements over the 500 Hz to 40 KHz frequency range used.



(a) 18-inch-Diameter Shallow-Dish EM with 9-foot Working Distance.

(b) 34.654-inch-Diameter Deep-Dish EM with 15-foot Working Distance.

(c) Summary of Ellipsoidal Mirror Characteristics.

Facility	Anechoic	JENOTS
Mirror Diameter	34.654 in.	18.0 in.
Mirror Length	36.0 in.	4.675 in.
Focal Length	2.625 in.	4.675 in.
Working Distance	180.0 in.	106.0 in.
Mirror Aperture	3° 44'	4° 48'
Eccentricity	0.971	0.930
Traverse Speed (Approximate)	1.8 ft/min	3.8 ft/min
Traverse Distance (Approximate)	20 ft	20 ft
Traverse Direction (Jet Axis)	Vertical	Horizontal
Microphone Type	1/4 in. B&K 4136 Without Grid	1/4 in. B&K 4136 Without Grid
Microphone Orientation	Toward Mirror	Toward Source

Figure 3-17. Schematics and Summary of Ellipsoidal Mirror Characteristics.

Mirror cart position is gaged from brush chart reduction of cart position signal, overall sound level, and time code.

Integral closure checks can be performed to see if the measured far-field noise signature can be calculated from the measured source distribution. This check does not guarantee that the source measurements are correct but establishes a confidence level in the results which can be used to identify ranges of variables for which a given technique is definitely not valid. Integral closure checks have shown (as a minimum) that the deconvolved source distributions generally appear to be valid over the 1-KHz to 20-KHz and 500-Hz to 10-KHz frequency ranges for the 18-inch shallow-dish and the 34.654-inch deep-dish mirrors, respectively.

An error analysis of the EM technique was also performed as a part of Task 3's continued evaluation of source measurements techniques and is treated in detail in Appendix E. This appendix evaluates the window function removal technique, or the way in which the acoustic sources are combined by the mirror to yield the measurement values. The appendix describes (1) the model for EM error analysis, (2) the technique for computing the estimate and invertability of the A-matrix, (3) estimator variance and bias, (4) errors induced by window function measurement uncertainty, and (5) a numerical evaluation study. The following conclusions were suggested.

1. A small elliptical mirror, such as the 18-inch mirror developed for this program, is capable of obtaining useful data when:
  - The source frequency is greater than 1000 Hz
  - The source dynamic range is less than 25 dB
  - The source spacing is greater than 0.5 inch
  - The measurement accuracy required is more than  $\pm 2.5$  dB
2. The window function removal procedure is very sensitive to any error.
3. The presence of errors in analyzed data may be difficult to detect due to high correlation between adjacent errors. Check procedures should be included in the data reduction procedure to guarantee the data quality.

### 3.4 DATA ANALYSIS

The preceding sections have described the test models, test matrices, facilities, and data reduction procedures utilized in performing this study. This section will present the acoustic results in terms of noise characteristics as a function of velocity, directivity, and spectra. The data presented will, in most cases, be normalized per the parameters discussed in Section 3.3.1.7.

Section 3.4.1 presents the acoustic results of tests related to baseline nozzle configurations, e.g., conical, plug, and coplanar-coannular nozzles. Section 3.4.2 presents the acoustic results of tests designed to define the influence of geometric and cycle variations on the suppression characteristics of single- and dual-flow suppressor nozzles. Parameters investigated include chute area ratio, radius ratio, inner stream flow management and geometric variations, flow segmentation, element-type variation, and the application of treated ejectors. Section 3.4.3 presents the suppression levels which occur in flight based on a series of scale-model free-jet measurements. Conical, plug, chute, and tube nozzle suppression characteristics are discussed. Sections 3.4.4 and 3.4.5 present the results of laser velocimeter and ellipsoidal mirror diagnostic measurements on several baseline and suppressor nozzles.

#### 3.4.1 Tests Related to Baseline Nozzle Configurations

This section presents the acoustic results of tests related to baseline nozzle configurations. PNL, OASPL, and spectra acoustic characteristics are established for conical, plug, and coplanar-coannular nozzles. Sections 3.4.1.1 and 3.4.1.2 establish the noise characteristics of conical and convergent-divergent plug nozzles. The conical nozzle data are used as a reference to establish suppression levels throughout the rest of this report. Section 3.4.1.3 discusses the impact of plug radius ratio variation on the various noise parameters. Section 3.4.1.4 discusses the acoustic characteristics of a coplanar-coannular nozzle having an outer to inner flow area ratio,  $A_0/A_1$ , of 2.0. Section 3.4.1.5 presents the acoustic results of parametric test series using coplanar-coannular nozzles of  $A_0/A_1 = 0.4, 0.65$ , and 2.0. The acoustic changes caused by reducing the inner flow to zero or less than 10% of the outer stream are discussed in Section 3.4.1.6.

##### 3.4.1.1 Baseline Conical Nozzles (Models 1, 14)

This study was conducted to establish baseline noise levels using a conical nozzle, tested at both the JENOTS and Cell 41 Anechoic Facility. Subsequent test data for other baseline systems (i.e., C-D plug, high radius ratio plug, annular nozzles, and dual-flow coannular-coplanar nozzles) and for mechanically suppressed systems (i.e., single- and dual-flow multielement suppressors) are referenced to these conical nozzle data for gaging overall system acoustic effectiveness and to identify dominant regions of suppression. Since both JENOTS and the Cell 41 Anechoic Facility were used at

various stages of the Task 3 program (see Section 3.1, Table 3-1) to generate parametric noise data, a common baseline test for each facility was conducted. A 4.64-inch exit diameter conical nozzle was selected with a  $2.3^\circ$  internal converging flowpath angle, as per Appendix A, Figure 1. Adapted to the JENOTS facility, the nozzle is designated Model 1. The same nozzle adapted to the Cell 41 Anechoic Facility is designated Model 14.

To develop a referee data base across a wide span of cycle conditions, Models 1 and 14 were tested using the matrices of Section 3.2.1 Figure 3-2(a) and 3-2(b), respectively. The JENOTS test matrix included constant total temperature lines at  $T_t = \text{amb}, 1000^\circ, 1250^\circ, 1300^\circ, 1450^\circ$  and  $1500^\circ$  R. The Cell 41 Anechoic Facility matrix included (a) constant total temperature lines at  $700^\circ, 850^\circ, 1000^\circ$  and  $1500^\circ$  R, and (b) constant static temperature lines at  $1000^\circ$  and  $1500^\circ$  R. The matrices were developed to span the cycle conditions intended for subsequent suppressed nozzle tests. Additionally, the Model 14 matrix included sufficient test points to acquire parametric data influenced by shock cell noise. These data were used in Volume 1, Section 4.1 (Jet Noise Mechanisms) and within the subsequent studies of this volume in comparing nonconical nozzles to determine effectiveness of shock noise suppression. Details of the aerodynamic cycle data, along with basic noise information for both models, are included in the Appendix B tabulations.

Acoustic test results for the conical nozzles are presented in terms of normalized OASPL, PNL, and OAPWL versus mass-averaged velocity ( $V_{ma}$ ). The mass-averaged velocity for a single-flow nozzle coincides with the fully expanded isentropic velocity. This is the format for most other baseline and suppressed nozzle configurations. See Section 3.3.1.7 (Acoustic Data Normalization) for definition of the normalization technique. The following data sets are included:

Figures 3-18 and 3-19	Peak OASPL and PNL
Figures 3-20 and 3-21	$90^\circ$ OASPL and PNL
Figures 3-22 and 3-23	$50^\circ$ OASPL and PNL
Figure 3-24	OAPWL

Part (a) of each graph is Model 1 (JENOTS) data corrected to free-field, and part (b) is Model 14 (Cell 41 Anechoic Facility) data. Each of the data sets have data-fitted curves applied. These data-fitted curves are used as the primary basis of comparing the PNL, OASPL, and OAPWL distributions with  $V_{ma}$ . For Figures 3-18, 3-19, and 3-24, i.e., peak OASPL, peak PNL and OAPWL, the data-averaged curves are transferred to part (c) of the graph where they are compared to predicted noise levels. For the  $90^\circ$  and  $50^\circ$  data sets, Figures 3-20 through 3-23, part (c) has only predicted noise levels and associated data-fitted curves generated using the Model 14 aero cycle data. To predict these noise levels, the method adopted in Volume 1, Section 3.3.2 (Conical Nozzles) was utilized. The method consists of the SAE ARP 876 proposed revision (see Volume 1, Appendix C) for predicting single-stream jet-mixing noise modified by increasing the predicted levels by 1.0 dB to bring it in line with the unapproved revision being considered in early 1978 by the SAE Jet Noise A-21 Subcommittee. The single-stream, shock-cell noise prediction procedure, Reference 24, proposed to the SAE Subcommittee, was also adopted.



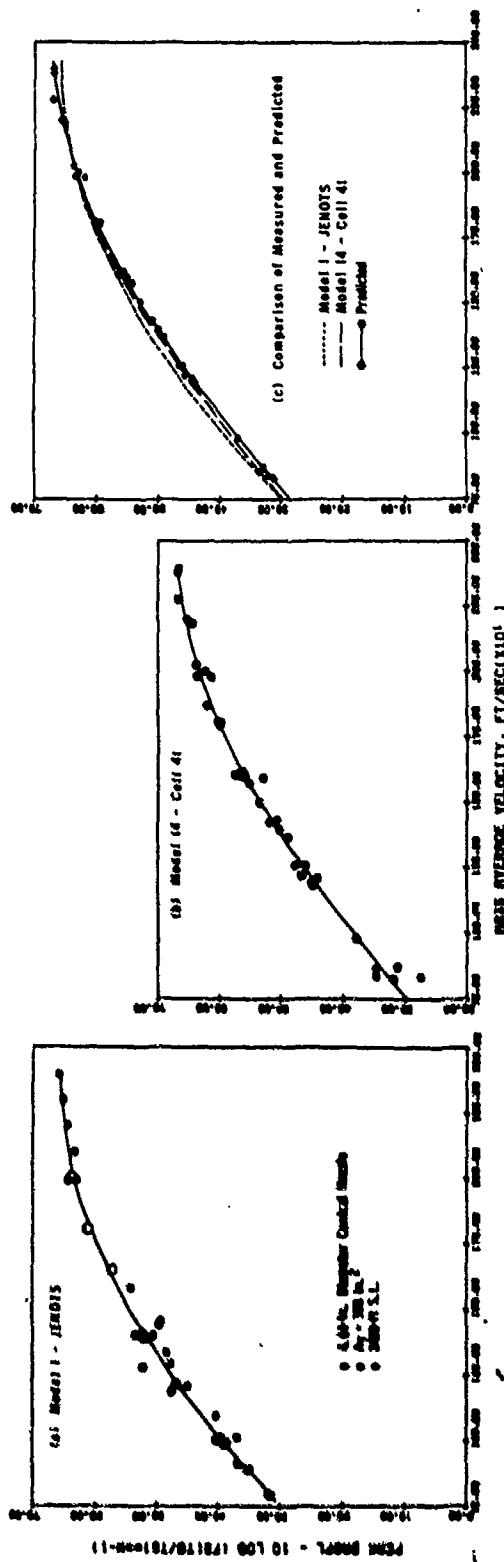


Figure 3-18. Summary of Conical Nozzle (Models 1 and 14) Peak OASPL Characteristics.

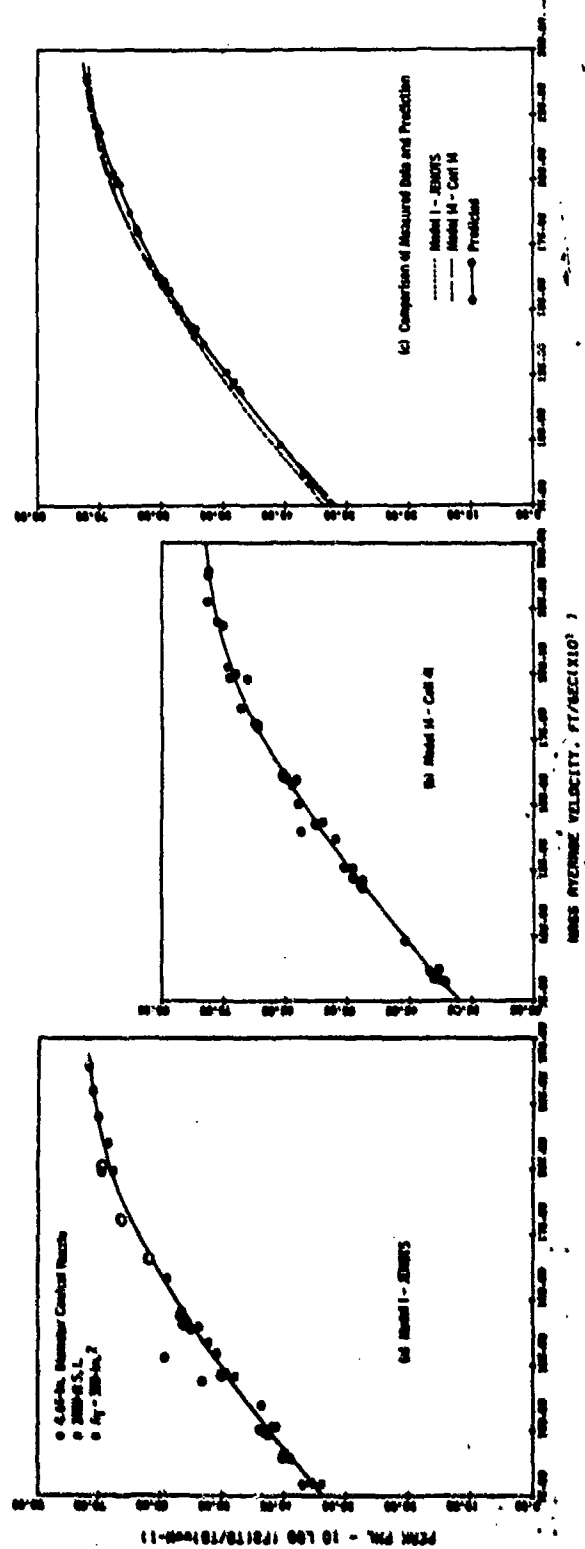


Figure 3-19. Summary of Conical Nozzle (Models 1 and 14) Peak PNL Characteristics.

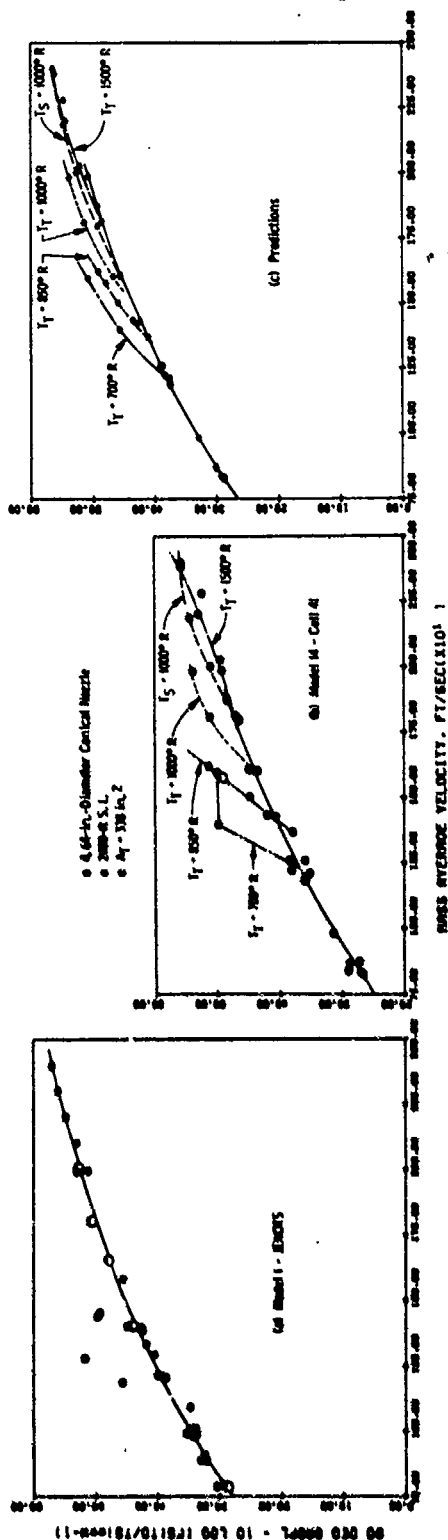


Figure 3-20. Summary of Conical Nozzle (Models 1 and 14) 90° OASPL Characteristics.

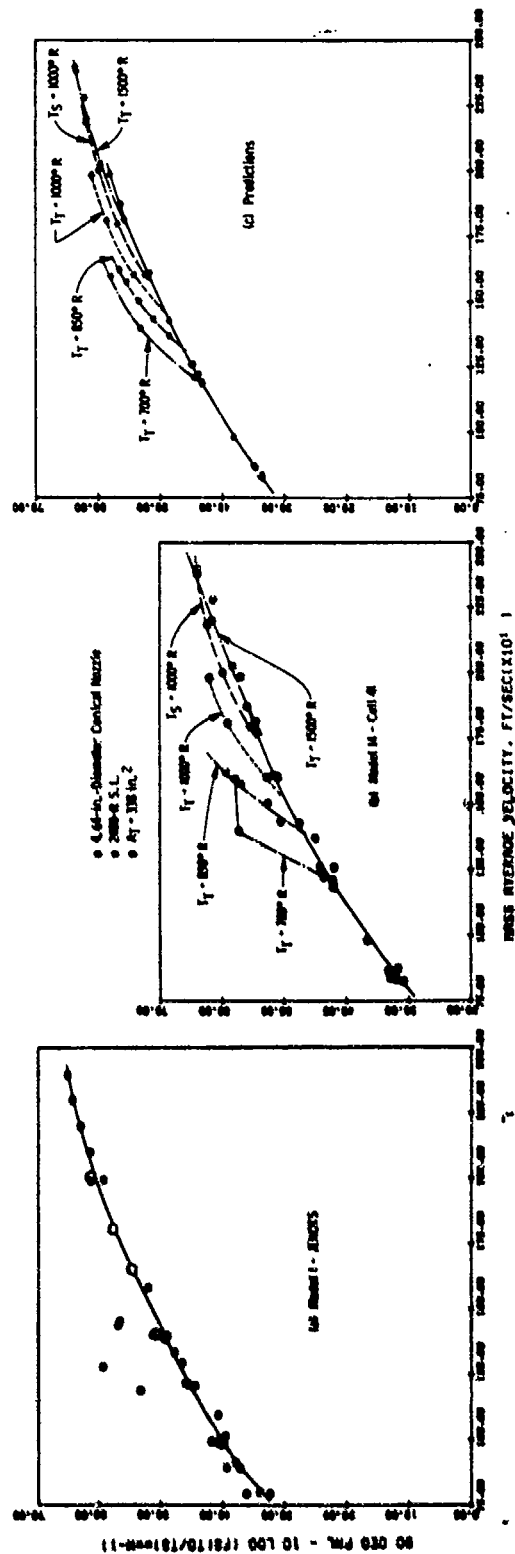


Figure 3-21. Summary of Conical Nozzle (Models 1 and 14) 90° PNL Characteristics.

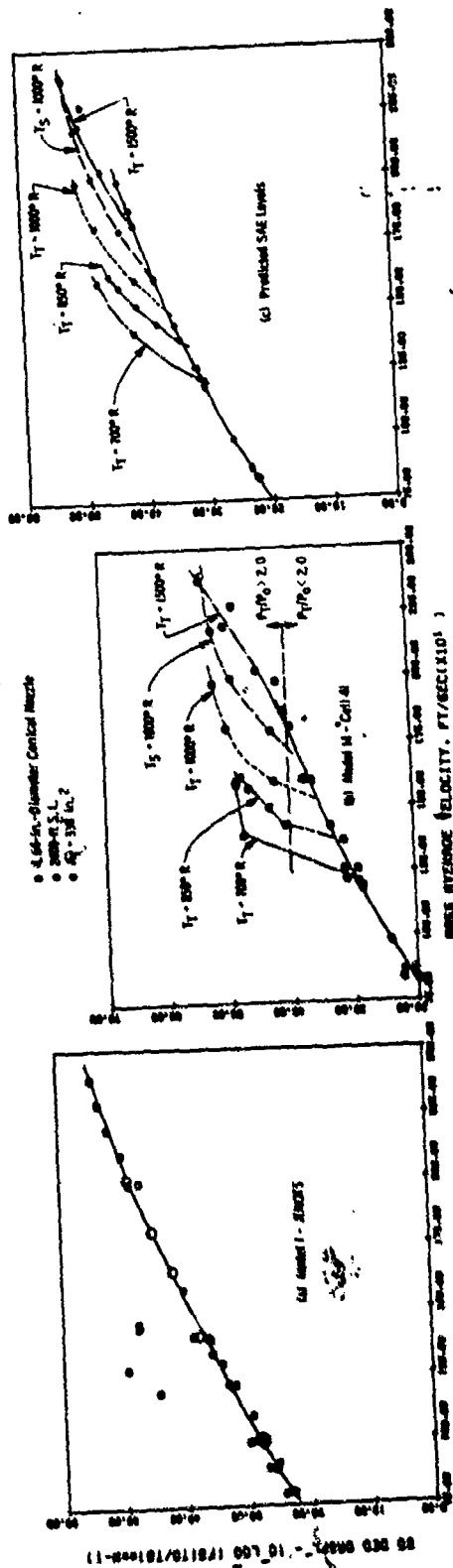


Figure 3-22. Summary of Conical Nozzle (Models 1 and 14) 50° OASPL Characteristics.

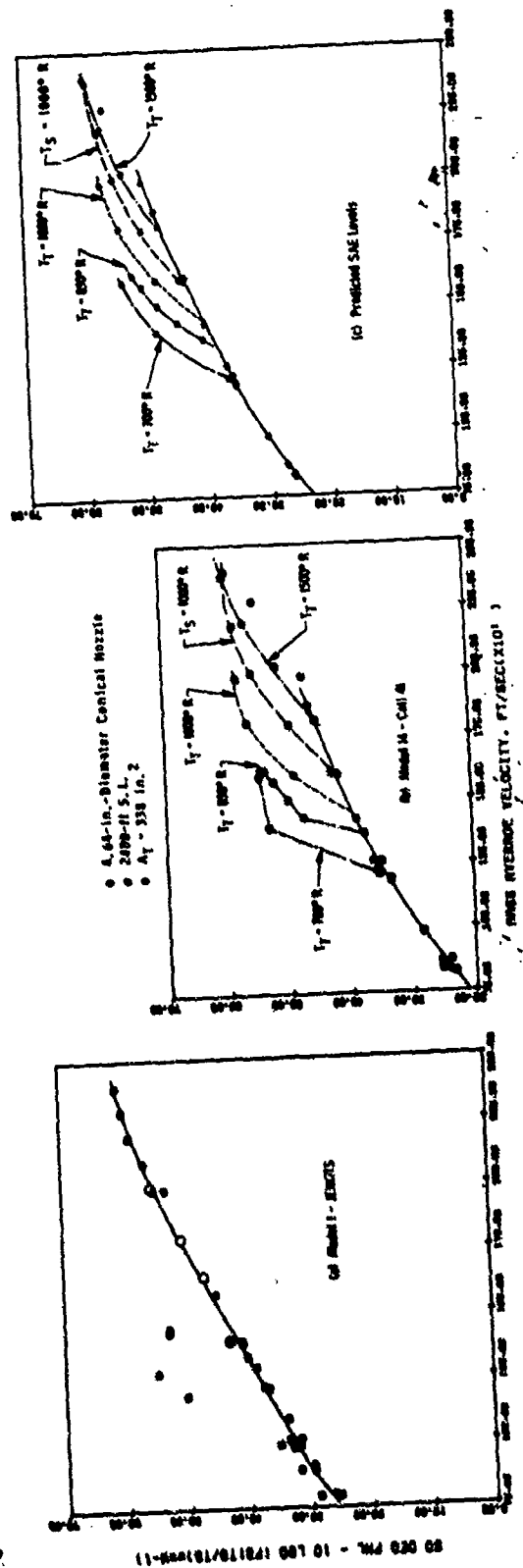


Figure 3-23. Summary of Conical Nozzle (Models 1 and 14) 50° PNL Characteristics.

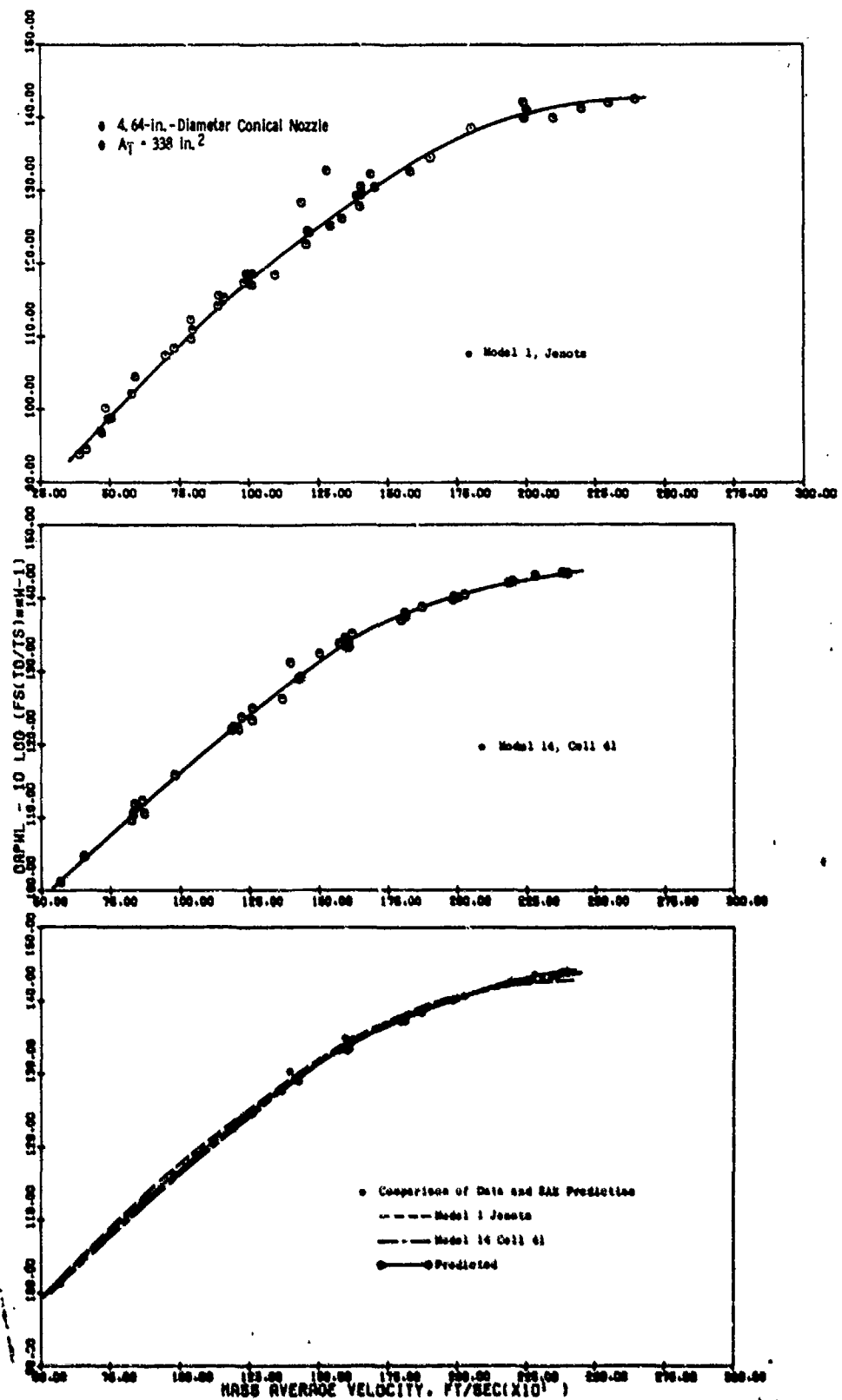


Figure 3-24. Summary of Conical Nozzle (Models 1 and 14) Power Level Characteristics.

The comparisons made in Figures 3-19 and 3-20, part (c), for peak OASPL and PNL show very good agreement among data from the two facilities, the data-averaged curves normally agreeing within  $\pm 0.5$  dB. Relative to predicted data curves, the maximum deviation is about 1 to 2 dB in the midvelocity region, measured data falling above predicted.

Although the peak-noise variance for the two facilities is small, the individual facility conical nozzle data are used for comparing other test model results, rather than using a composite average. Similarly, when comparing individual data point PNL, OASPL, directivity, spectra, etc., single-point conical nozzle data from the same facility are used.

At  $90^\circ$  and  $50^\circ$  (Figures 3-20 through 3-23), deviations between the two baselines are more significant, particularly in the supercritical operational regime where Model 14 cycle conditions primarily followed a shock-cell noise evaluation matrix. For Model 14, variation of shock-cell influenced noise with  $V_{ma}$ , as a function of  $T_T = 700^\circ$ ,  $850^\circ$ ,  $1000^\circ$ , and  $1500^\circ$  R and  $T_g = 1000^\circ$  R, is distinctly identifiable in the broadside ( $90^\circ$ ) and forward quadrant ( $50^\circ$ ) data. Part (c) of Figures 3-20 through 3-23 shows predicted noise values based on the aero cycle data of Model 14. They, too, follow similar distinct trends associated with turbulent mixing noise at low velocity and with shock-cell generated noise in the supercritical regime of operation. Note that the data are all normalized with respect to temperature and the low-velocity (turbulent mixing noise dominated) points correlated well around the mean data line. The higher velocity supercritical pressure ratio points (dominated by shock-cell noise, which is independent of temperature) do not collapse around the mean line. An approximate distinction between points above and below  $P_T/P_O = 2.0$  is included on Figure 3-22. The predicted and measured power levels are summarized on Figure 3-24.

Shock-cell noise and its importance as a noise mechanism for supersonic choked jets is discussed in detail in Volume 1, Section 4.1 (Jet Noise Mechanisms), and in Task 2 (Reference 7) Section 4.6 (Shock-Cell Noise). According to experimental correlations for conical nozzles, it was shown that the OASPL should be only a function of the pressure ratio parameter as given by  $\beta = \sqrt{M^2 - 1}$ . Model 14  $90^\circ$  and  $50^\circ$  OASPL data from Figures 3-20 and 3-22 are replotted as a function of  $\beta$  in Figure 3-25, now unnormalized for temperature. The data for all temperature values now collapse close to a line which varies as  $\beta^4$ . Deviation from this line occurs at low values of  $\beta$  as the mixing noise begins to dominate the spectrum when shock strength diminishes. As an extension of this empirical correlation to the subjective PNL basis, Model 14  $90^\circ$  and  $50^\circ$  data from Figures 3-21 and 3-23 are replotted in Figure 3-26 versus the  $\beta$  parameter. They, too, show insensitivity to temperature and collapse well around the  $\beta^4$  line.

To illustrate the acoustic characteristics of the conical baseline over isovelocity and isothermperature lines of cycle operation, the following OASPL and PNL directivity sets, plus spectra at  $50^\circ$ ,  $70^\circ$ ,  $90^\circ$ ,  $110^\circ$ ,  $130^\circ$  and  $150^\circ$ , are included:

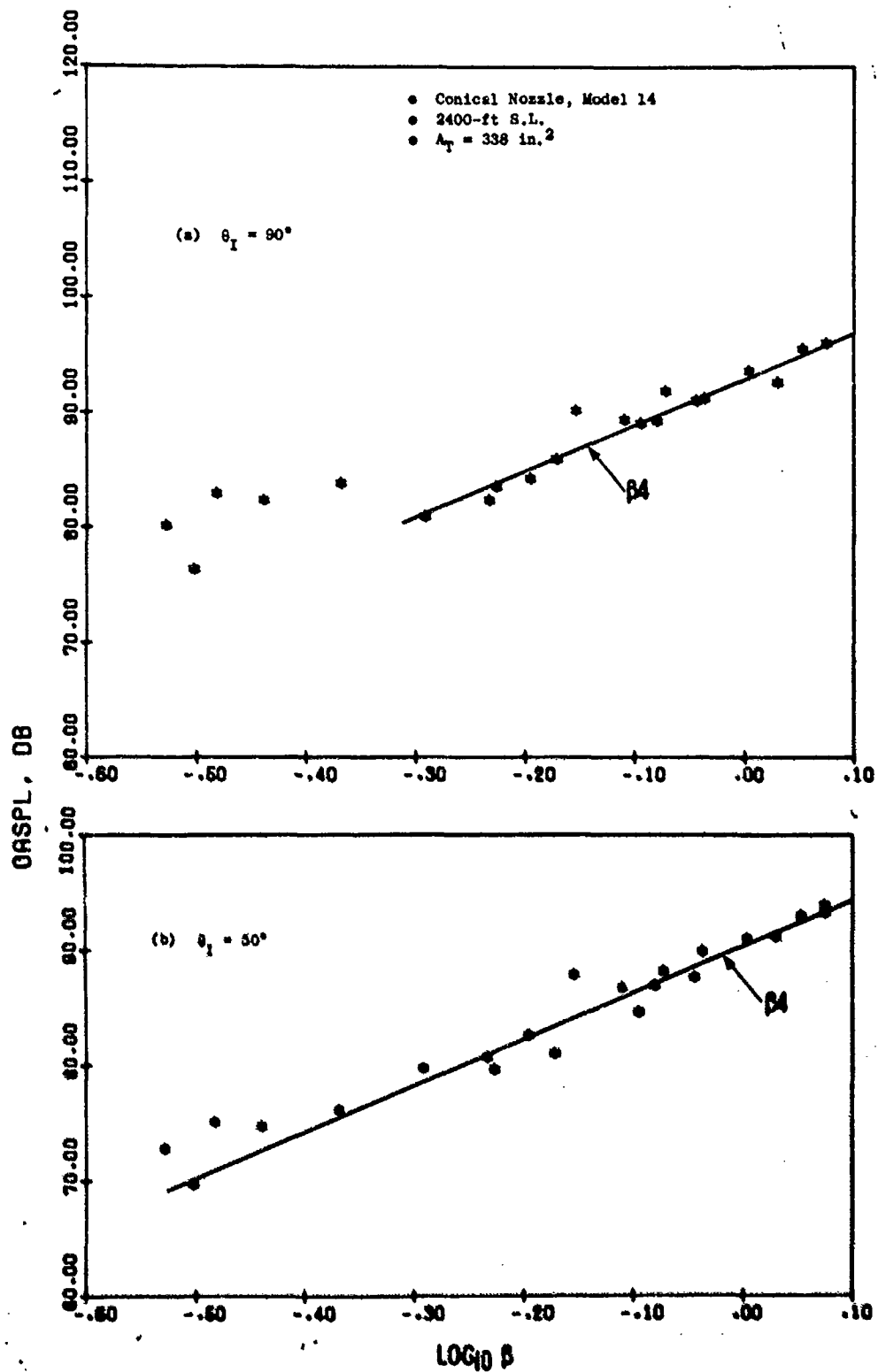


Figure 3-25. Supersonic Jet OASPL Correlation with Shock Strength Parameter  $\beta$ , Conical Nozzle (Model 14).

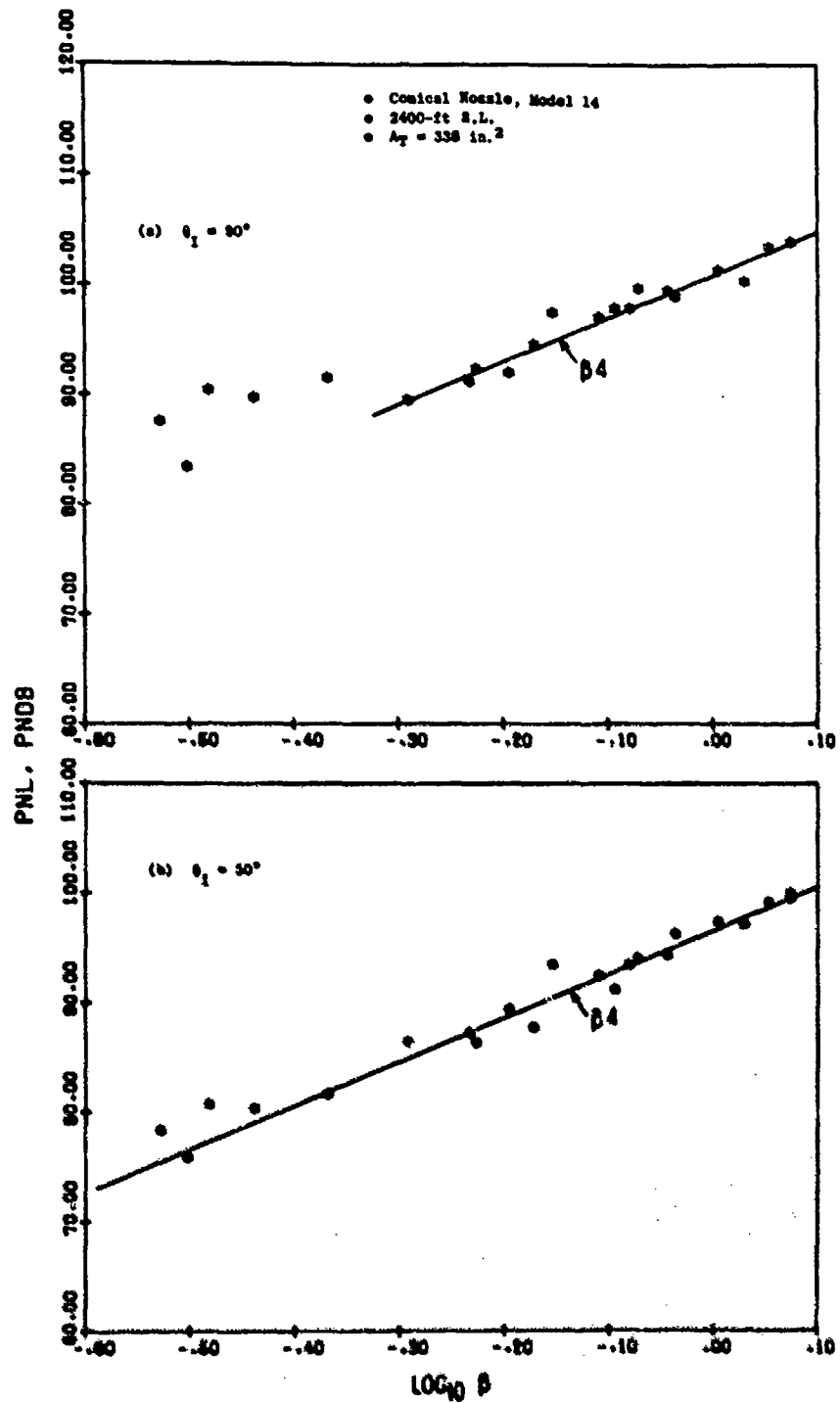


Figure 3-26. Supersonic Jet PNL Correlation with Shock Strength Parameter  $\beta$ , Conical Nozzle (Model 14).

### Isovelocity

Figures 3-27 and 3-28,  $V_j = V_{ma} = 1600$  fps;  $1.6 \leq P_T/P_0 \leq 3.49$ ;  $1697 \geq T_T, ^\circ R \geq 705$

Figures 3-29 and 3-30,  $V_j = V_{ma} = 2000$  fps;  $2.06 \leq P_T/P_0 \leq 3.96$ ;  $1736 \geq T_T, ^\circ R \geq 1004$

### Isotemperature

Figures 3-31 and 3-32,  $T_T = \text{AMB}$ ;  $1.10 \leq P_T/P_0 \leq 3.94$ ;  $402 \leq V_j = V_{ma}, \text{fps} \leq 1453$

Figures 3-33 and 3-34,  $T_T = 1500^\circ R$ ;  $1.15 \leq P_T/P_0 \leq 3.67$ ;  $836 \leq V_j = V_{ma}, \text{fps} \leq 2380$

The results given in Figures 3-27 through 3-30 for isovelocity data elicit the following observations:

- The data are not normalized for  $T_T$ , therefore, a wide variance in peak noise level is seen. If the data were normalized, closer agreement would result, similar to the Figure 3-18 and 3-19 peak noise plots. Normalization parameters for each data point are tabulated in Appendix B.
- For each data set, the transition is seen from the regions where noise is predominately influenced by turbulent mixing to where shock-cell noise dominates. For the 1600 fps data, the OASPL and PNL directivity patterns (Figure 3-27) follow standard turbulent-mixing noise distributions at low pressure ratio levels, particularly for the points with  $P_T/P_0 \leq 1.96$ . Above that level, the directivity patterns show increasing influence of shock-cell noise: the  $P_T/P_0 = 2.30$  points showing influence at  $120^\circ$  and forward, and the higher  $P_T/P_0$  data being influenced even in the far aft sector. The spectra plots bear this out even through  $130^\circ$ .

For the  $V_j = 2000$  fps data set, slight shock-cell noise influence is seen even at the lowest  $P_T/P_0 = 2.06$  point, borne out in the  $50^\circ$  spectra. As  $P_T/P_0$  increases, the onset of influence moves further aft until, at highest  $P_T/P_0 = 3.96$ , influence is seen at least to the  $110^\circ$  angular location.

- Shock-cell noise is quite broadband from mid to high frequency and clearly dominates the jet noise spectrum in the forward quadrant, as illustrated quantitatively in the spectra plots.

From the Figure 3-31 through 3-34 plots for isotemperature data lines, further observations can be made:

- Within the  $T_T = \text{amb}$  data set, for highly supercritical data points at low to mid-velocity (1200 to 1450 fps), shock-cell noise totally



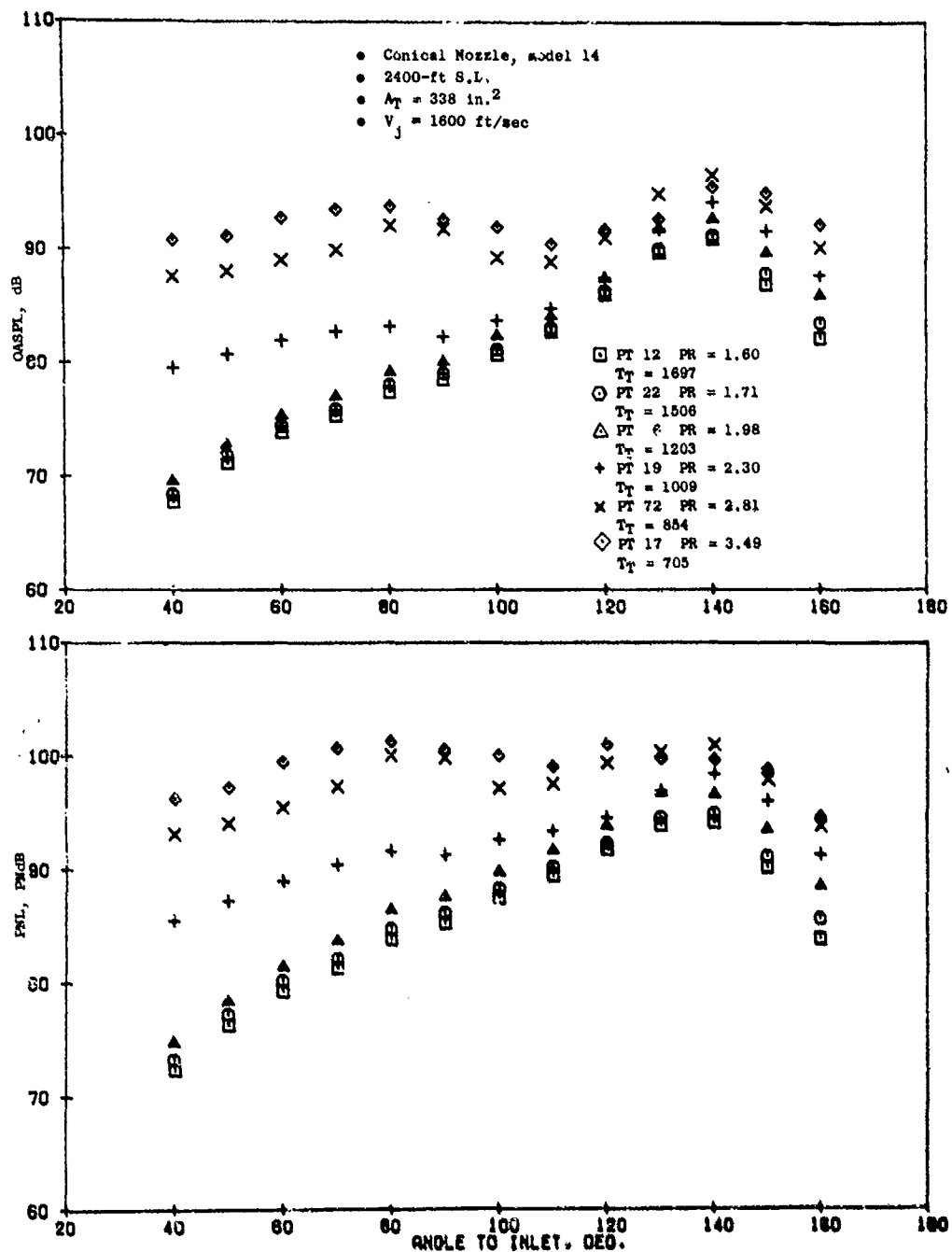


Figure 3-27. Impact of Shock Noise on OASPL and PNL Directivity. Conical Nozzle (Model 14),  $V_{ma} = V_j = 1300 \text{ ft/sec}$ .

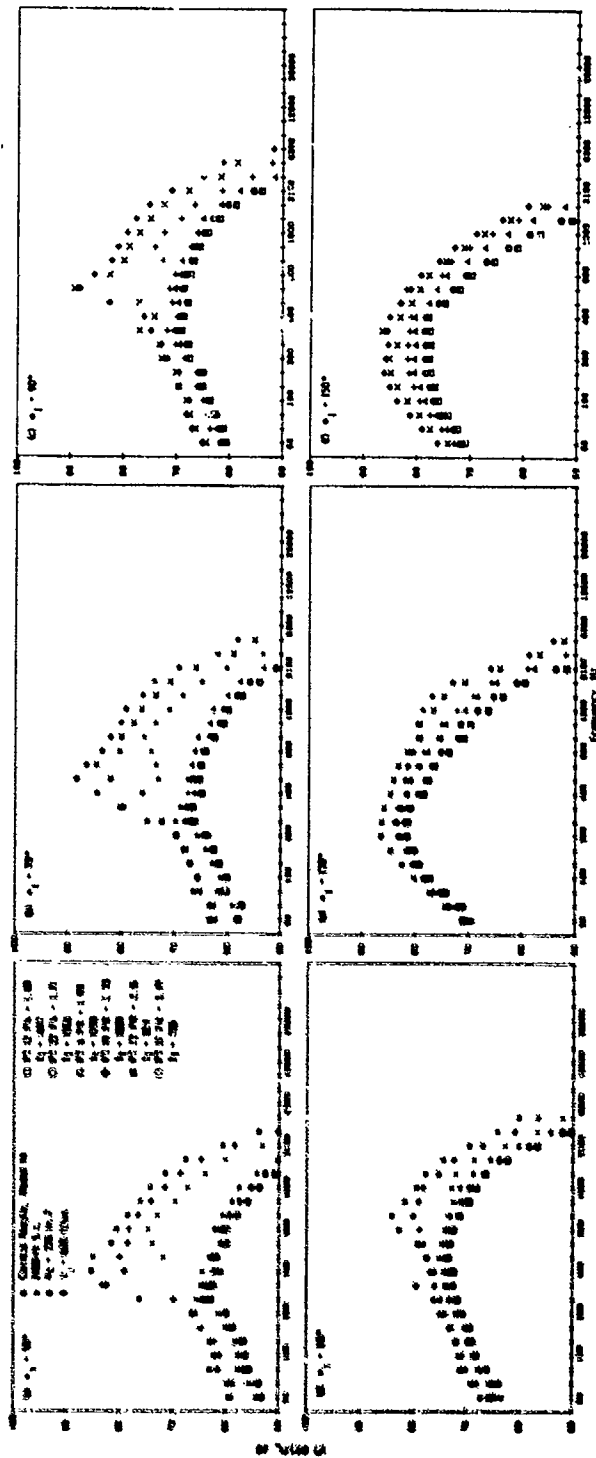
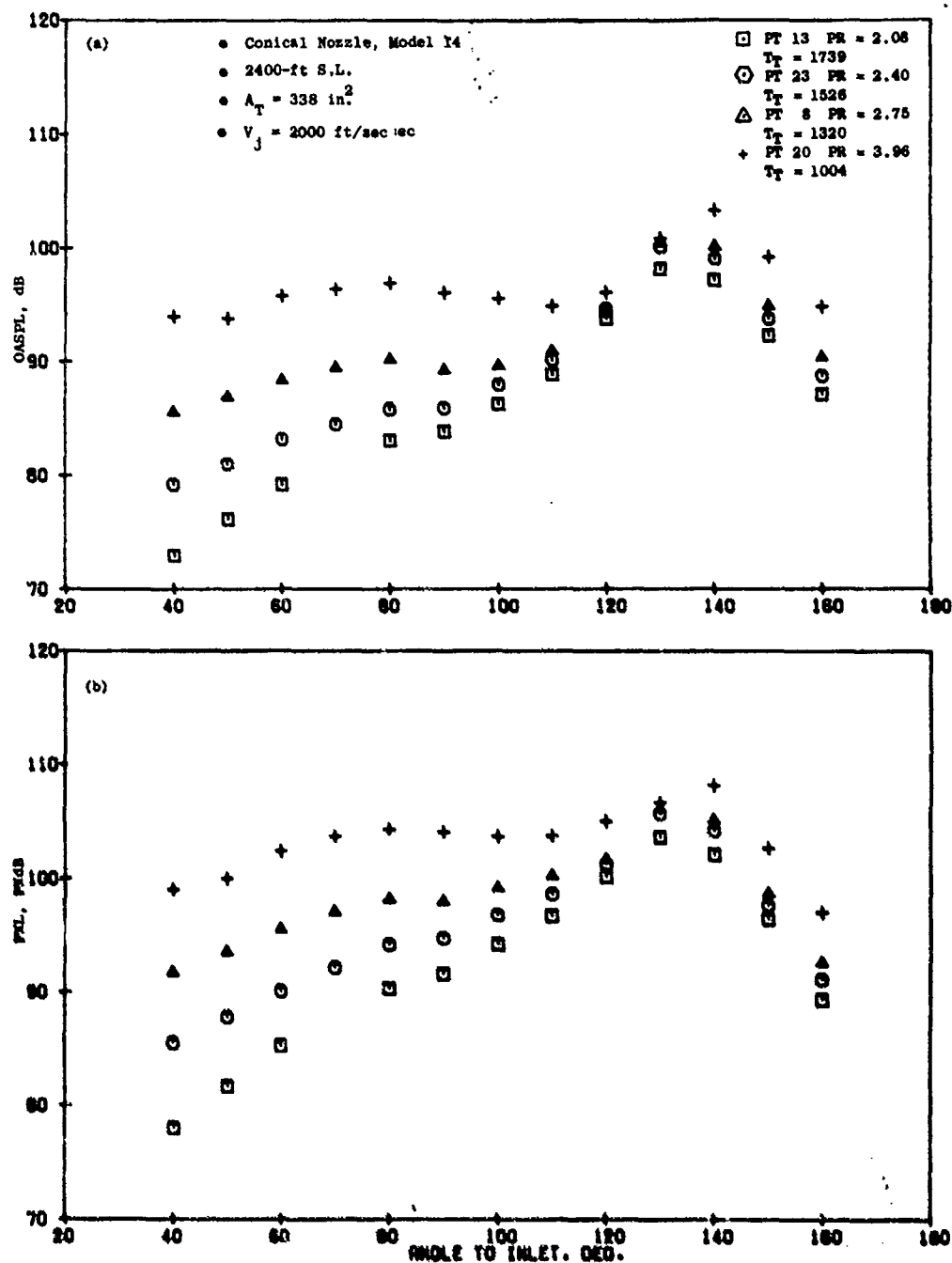
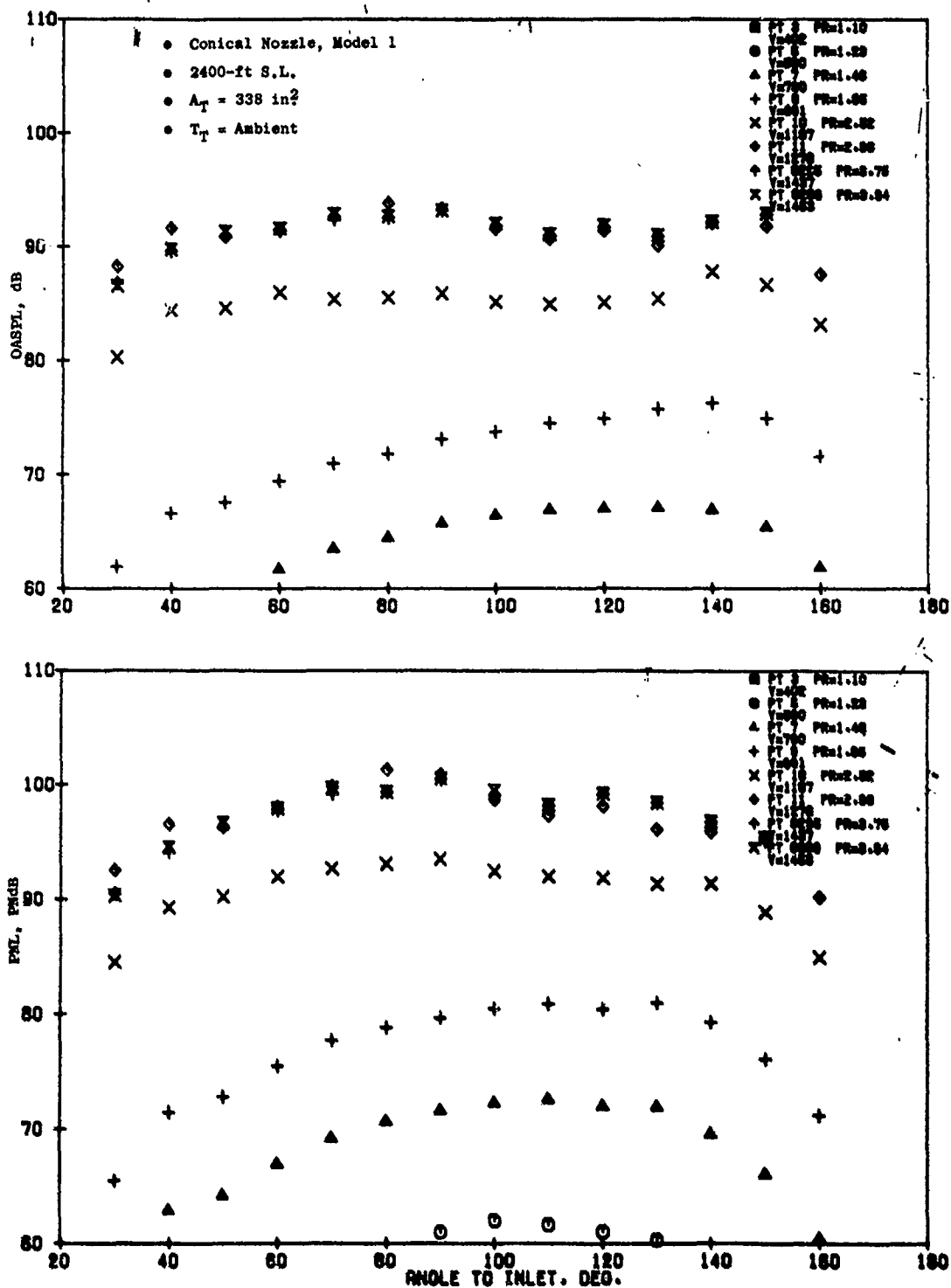


Figure 3-28. Impact of Shock Noise on Spectra Conical Nozzle (Model 14),  $V_{ma} = V_j = 1600$  ft/sec.





**Figure 3-30. Impact of Shock Noise on Spectra, Conical Nozzle (Model 14),**  
 $V_{na} = V_j = 2000 \text{ ft/sec.}$



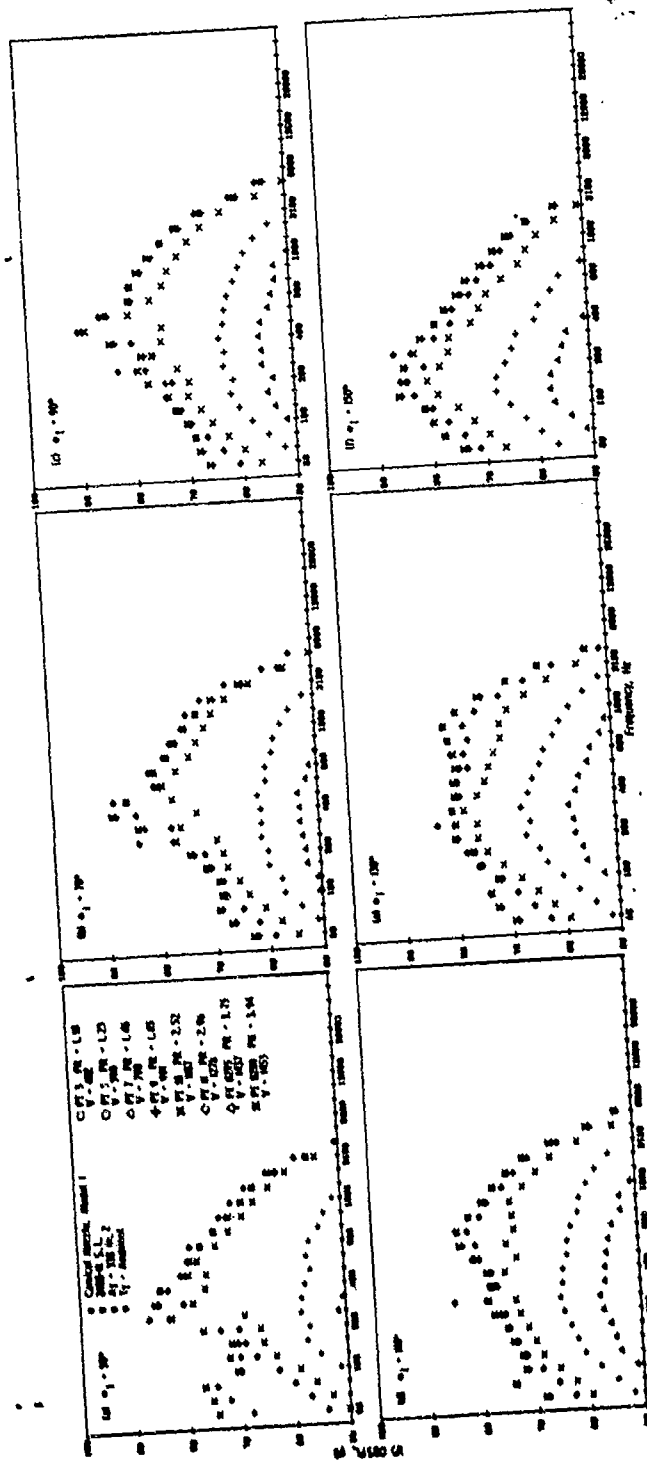


Figure 3-32. Impact of Cycle Variation at Ambient Temperature on Spectra, Conical Nozzle (Model 1).

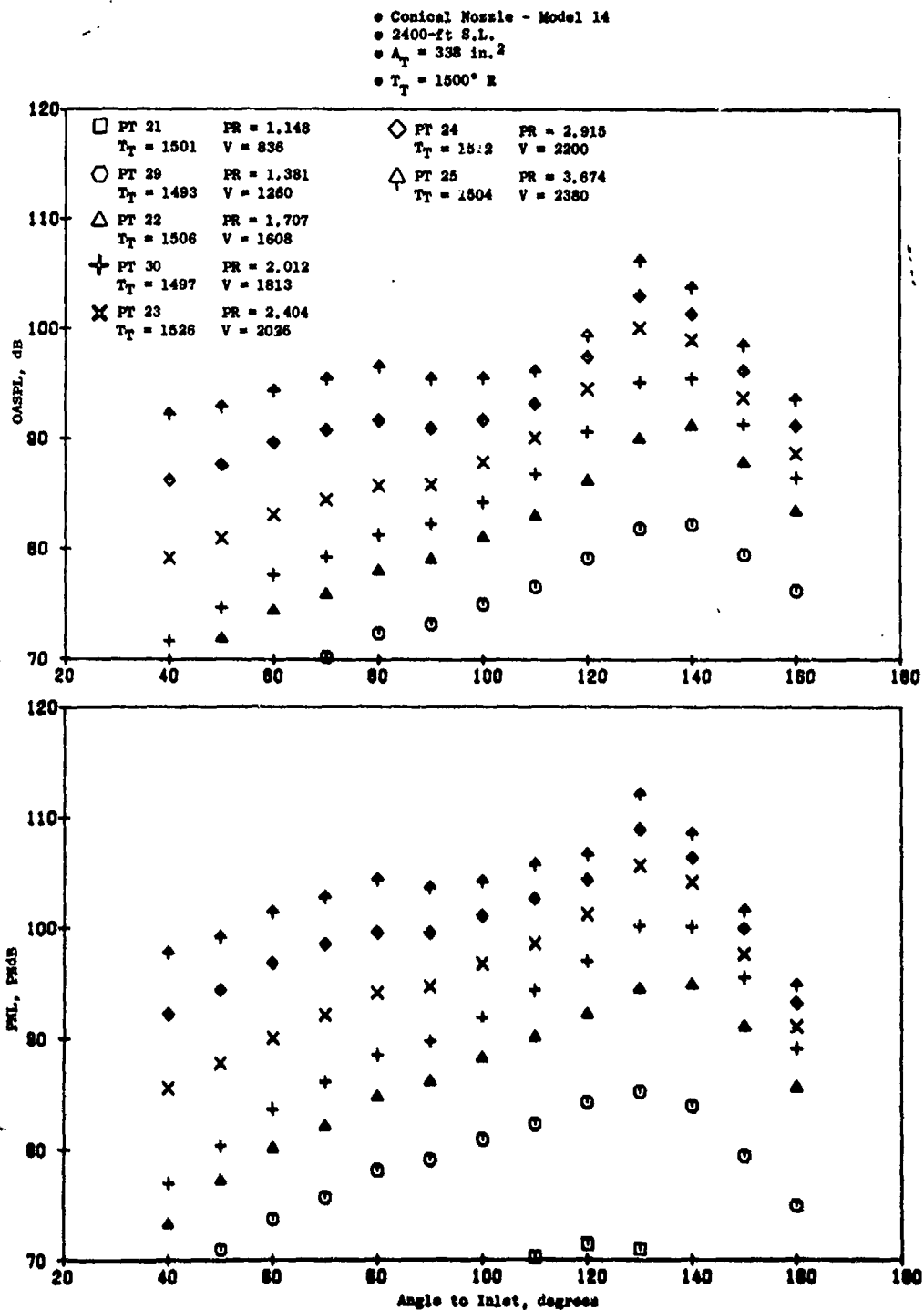


Figure 3-33. Impact of Cycle Variation at  $1500^\circ \text{ R}$  on OASPL and PNL Directivity, Conical Nozzle (Model 14).

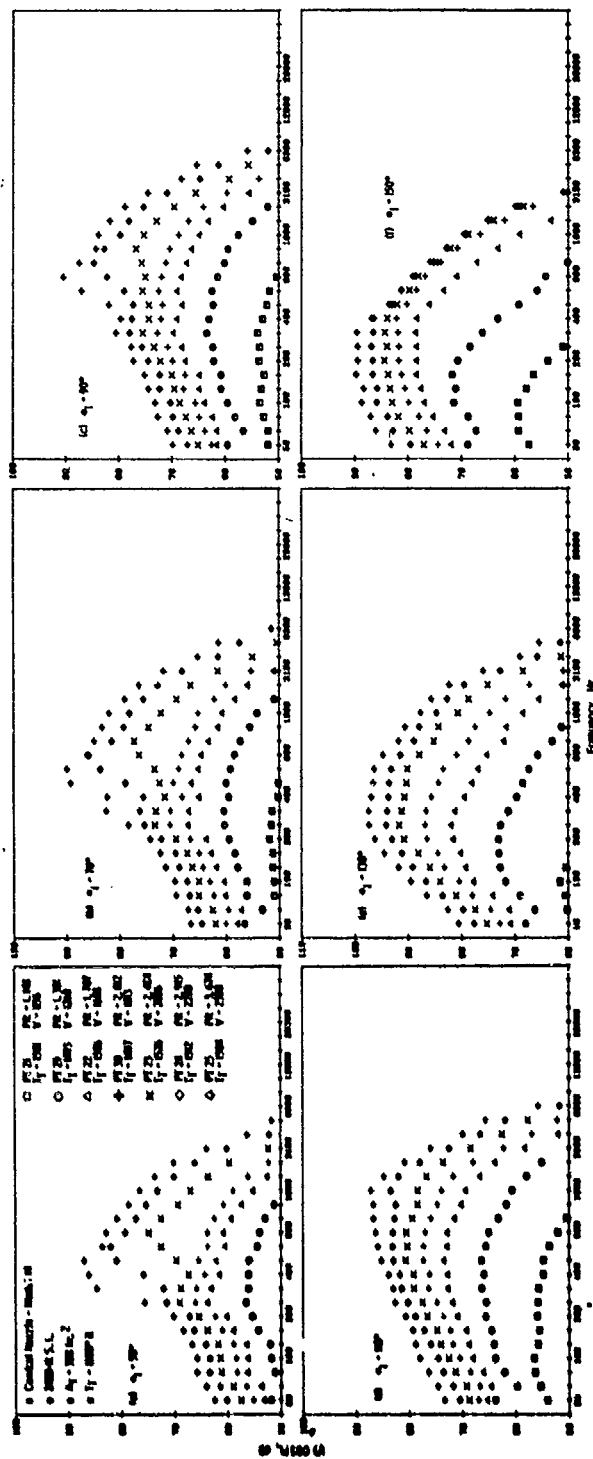


Figure 3-34. Impact of Cycle Variation at 1500° R on Spectra, Conical Nozzle (Model 14).



-dominates all but the most aft noise angles. The OASPL is nearly omnidirectional, i.e., independent of observer angle,  $\theta_1$ . The very low velocity points ( $P_T/P_0 \leq 1.85$ ) also show fairly flat directivity patterns; however, this is characteristic of low-velocity turbulent-mixing noise.

- At higher  $T_T = 1500^\circ \text{ R}$ , again shock-cell noise dominates the forward quadrant angles at supercritical  $P_T/P_0$ ; however, the regime of dominance is not as distinct as with the isovelocity data set.

For comparisons of baseline spectra and directivity to other models within later studies of this volume, individual conical nozzle data points are selected to best match the  $P_T/P_0$ ,  $T_T$  and  $V_j$  cycle of the particular nozzle in study. By doing so, a true measure of suppressor effectiveness can be made.

#### 3.4.1.2 Convergent-Divergent Plug Nozzle Study (Model 2)

An investigation of the acoustic characteristics of a convergent-divergent (C-D) internal flowpath plug nozzle was conducted in this study. This nozzle system represents a realistic turbojet engine configuration with a geometry significantly different than a conical nozzle or simple converging plug nozzle. The nozzle, Model 2, is shown in Figure 3-1 and details are in Appendix A, Figure 2. The C-D flowpath has an exit-to-throat area ratio of 1.22 and equivalent flow diameter ratio of 1.10. At the throat, the plug-to-shroud radius ratio is 0.66, and at the exit plane it is 0.55. The plug has a  $3^\circ$  half-angle within the area of the straight cylindrical shroud, followed by a  $10^\circ$  half angle flowpath extending to the contoured plug end.

Acoustic testing was performed at JENOTS and followed the matrix of Section 3.2.1, Figure 3-3, including the following:

- Turbojet engine typical operating line
- Isotemperature lines at  $T_T = 1000^\circ, 1250^\circ, 1500^\circ, 1750^\circ, 2000^\circ$ , and  $2250^\circ \text{ R}$
- Isovelocity lines at  $V_j = V_{ma} = 1000, 1250, 1640$ , and  $2090 \text{ ft/sec}$ .

The isovelocity lines were established primarily to derive the temperature dependency of noise for this type of nozzle, similar to that established for a conical nozzle by Hoch, et.al. (Reference 25).

Acoustic test results on a normalized overall basis versus jet velocity are presented for the following:

Figure 3-35 Peak OASPL & PNL  
Figure 3-36  $90^\circ$  OASPL & PNL  
Figure 3-37  $50^\circ$  OASPL & PNL  
Figure 3-38 OAPWL

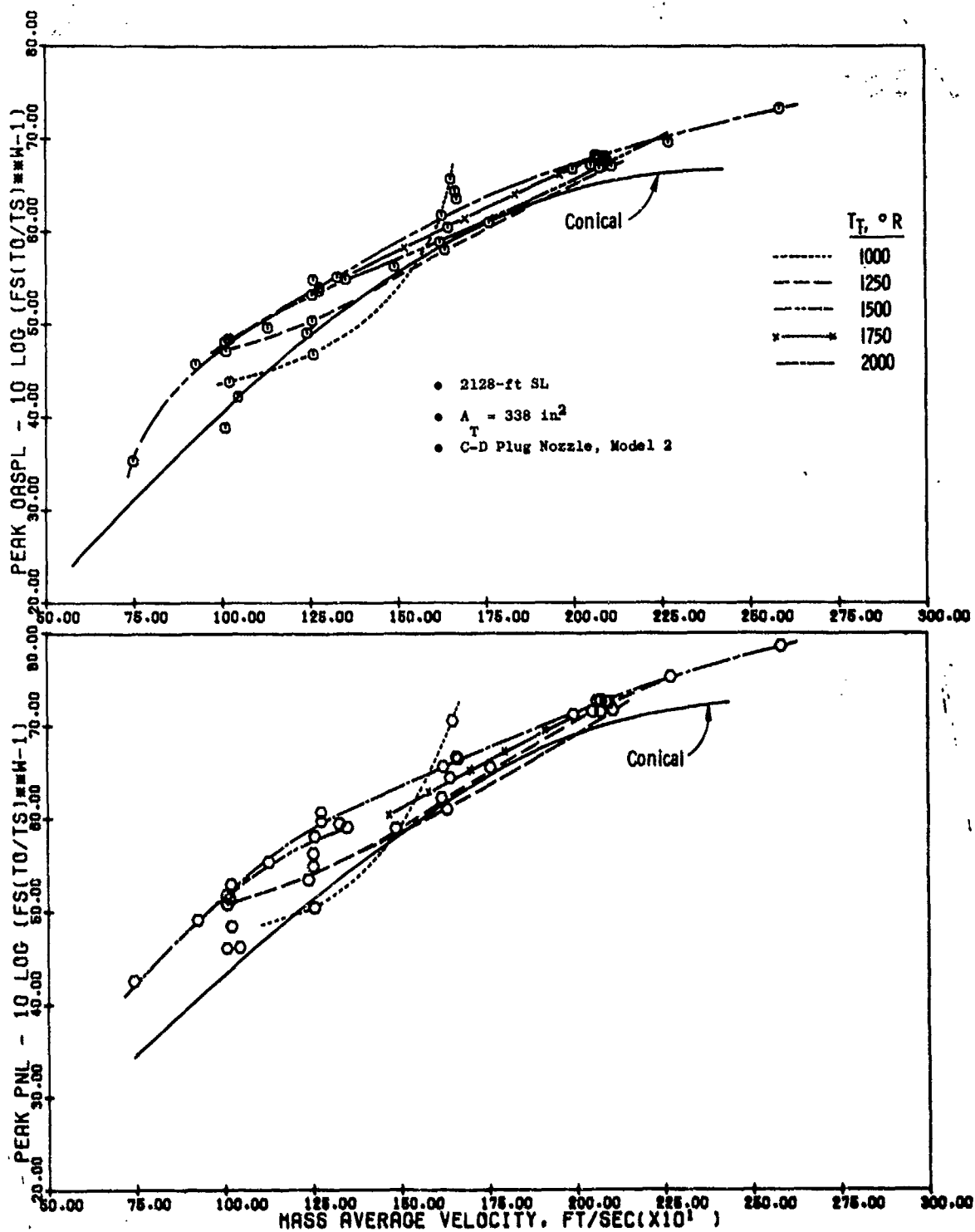


Figure 3-35. Summary of C-D Plug Nozzle (Model 2) Peak Noise Characteristics.

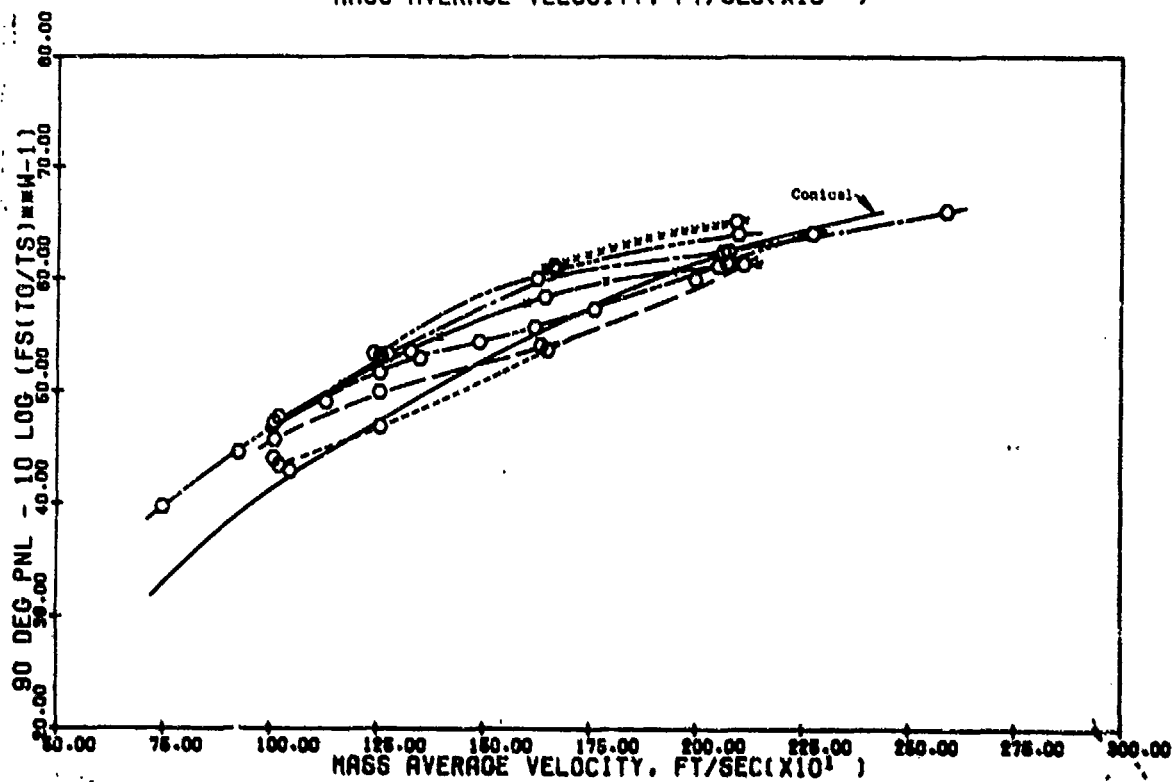
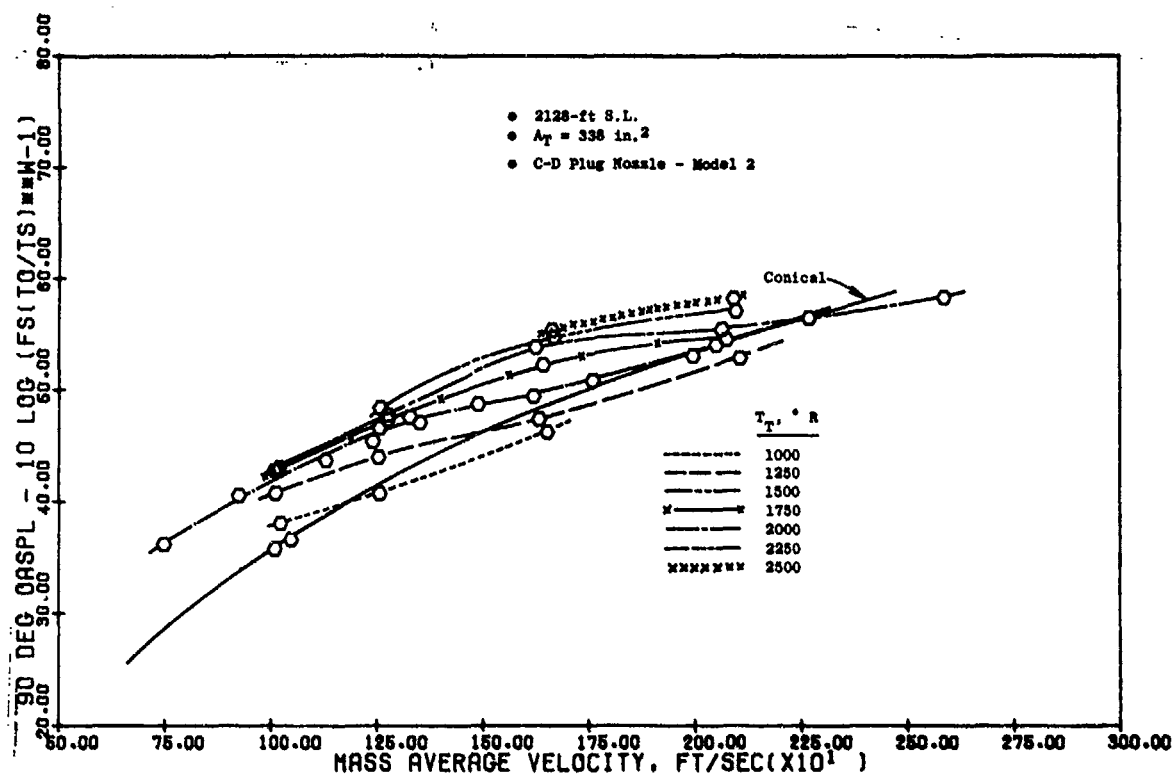


Figure 3-36. Summary of C-D Plug Nozzle (Model 2) 90° Noise Characteristics.

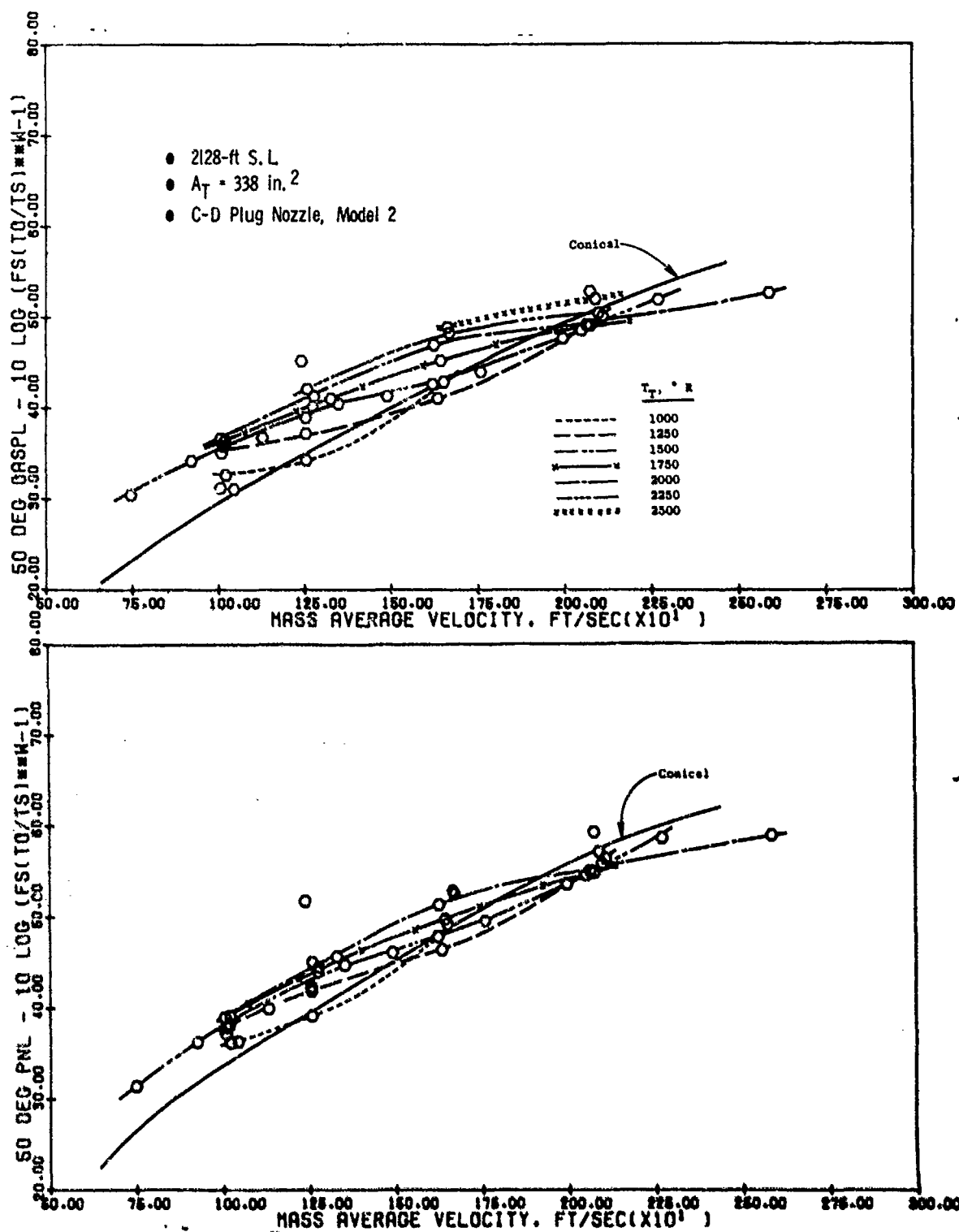


Figure 3-37. Summary of C-D Plug Nozzle (Model 2) 50° Noise Characteristics.

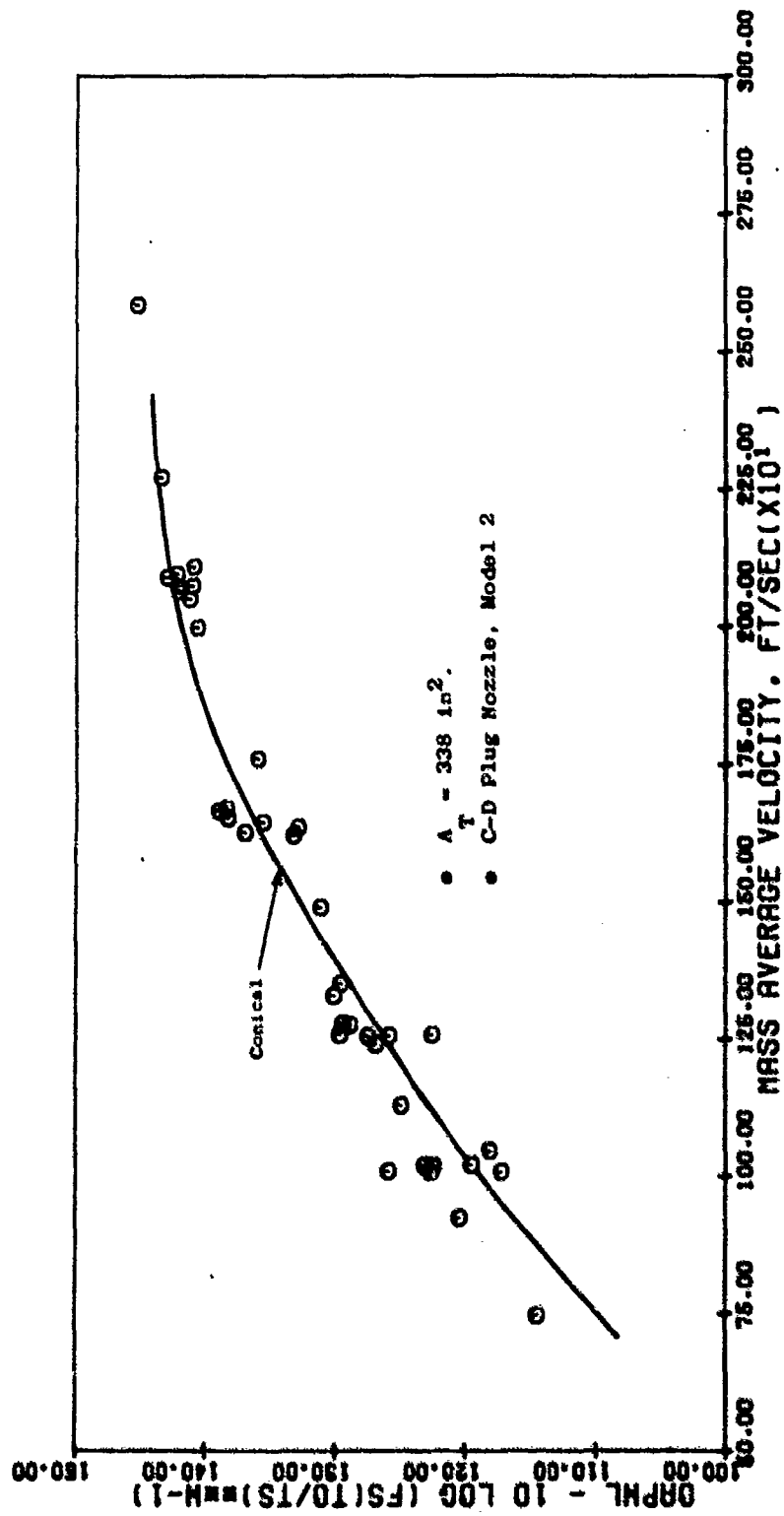


Figure 3-38. Summary of C-D Plug Nozzle (Model 2) Power Level Noise Characteristics.

The above data are presented on a 2128-foot sideline rather than at the standard of 2400-foot sideline, adopted for this report because initial data reduction for this nozzle was at 2128-feet. The conical nozzle data-fitted curves are, therefore, also corrected to the 2128-foot sideline.

Acoustic data trends are observed to be quite dissimilar to those of other model series in that:

- a. Collapse of the data with use of the temperature (density) normalization is not observed even at peak noise angles suggesting a strong influence of other than turbulent mixing noise.
- b. Noise levels at low velocity (1000 ft/sec) vary as much or more than at high velocity (2090 ft/sec), exactly opposite to the trend of the Section 3.4.1.1 Baseline Conical Nozzles.
- c. Normalized noise levels at a particular jet velocity show trends with temperature. Constant temperature lines can be derived, as seen in each data plot.
- d. Most noise levels are above the referee conical baseline, at all velocity values, also indicative of other than turbulent mixing noise influence.

Operation above supercritical pressure ratio begins to introduce shock-cell associated noise in puretone and broadband form in conical nozzle data. The resulting noise levels do not correlate with conventional temperature scaling methods because shock cell noise is nontemperature dependent. Operation of a conical nozzle near and below choking pressure ratio generates turbulent mixing noise, which, when normalized with temperature (density), collapses well around a single mean curve.

The flowpath design and operational characteristics must be examined more closely to understand the noise levels of the C-D nozzle. Assuming a one-dimensional flow approximation, flow conditions within and aft of the C-D system are established as a function of nozzle area ratio ( $A_{\text{exit}}/A_{\text{throat}}$  or  $A_g/A_g$ ) and nozzle pressure ratio,  $P_T/P_0$ . For Model 2's C-D flowpath, the nozzle should be shock-free at  $M = 1.55$  or  $P_T/P_0 = 3.90$ . Subsonic Mach number and  $P_T/P_0$  corresponding to this  $A_g/A_g$  are 0.58 and 1.24, respectively. Therefore, the following flow patterns are anticipated for the range of nozzle pressure ratios evaluated:

- (a) For  $P_T/P_0 < 1.24$ , the flow throughout the nozzle is subsonic, the velocity and Mach number are maximum at the throat plane.
- (b) For  $P_T/P_0 = 1.24$ , the flow is accelerated to  $M = 1$  at the throat plane and subsequently decays to a subsonic velocity at the exit plane.

- (c) For  $1.24 < P_T/P_0 < 2.61$ , the flow is accelerated to  $M = 1$  at the throat and to supersonic conditions within the divergent section. A normal shock wave is formed within the divergent part of the nozzle, across which total pressure and velocity of the flow decreases. The flow at the exit from the nozzle is subsonic.
- (d) At  $P_T/P_0 = 2.61$ , the location of the normal shock wave is at the exit plane of the divergent section. This pressure ratio is calculated from the expression:

$$P_T/P_0 = \frac{2\gamma}{\gamma+1} (M_{\text{exit}}^2)^{\frac{\gamma-1}{\gamma+1}} ;$$

where  $M_{\text{exit}}$  corresponds to supersonic isentropic expansion from  $M = 1$  at  $A_8$  to  $M = M_{\text{exit}}$  at  $A_9$ .

- (e) For  $2.54 < P_T/P_0 < 3.90$ , the flow attains  $M = 1$  at the throat and accelerates to supersonic in the divergent section. As the flow leaves the nozzle supersonically, shock patterns (oblique and normal) form outside the nozzle, across which the flow is decelerated.
- (f) At  $P_T/P_0 = 3.90$ , the flow attains  $M = 1$  at the throat and is accelerated isentropically to supersonic velocity, attaining  $M = 1.54$  at the exit plane. The flow ideally is without shock structure throughout.
- (g) Above  $P_T/P_0 = 3.90$ , the flow can again become shock infested.

The following observations aid in understanding the generated noise patterns:

- (a) Only (b) and (f) of the above flow patterns (at  $P_T/P_0 = 1.24$  and  $3.90$ ) expand the flow isentropically, corresponding to the normal flow pattern associated with a convergent nozzle for which the isentropic fully expanded velocity is calculated as  $V_{\text{ma}}$ . This is the main parameter against which noise is plotted for comparison to the conical nozzle data. Flow stream characteristics of a C-D system may not lend to correlation using the isentropic velocity calculation based on nozzle  $P_T/P_0$  and  $T_T$ . Operation between  $P_T/P_0$  of  $1.24$  to  $2.61$  results in an internal normal shock which reduces velocity, the loss dependent on shock strength. The exit plane velocity will not correspond to the isentropic expansion velocity calculation.
- (b) Since a shock structure can be generated within the nozzle diverging section for  $1.24 < P_T/P_0 < 2.61$ , low velocity noise can be influenced by shock-cell formations. In contrast, conical nozzle shock-cell noise influence is not observed until  $P_T/P_0 > 1.86$ .

- ...
- (c) For the  $P_T/P_0 = 1.24$  to  $2.61$  range of operation, dominance of either turbulent mixing noise or shock-associated noise depends on the competitive influence of: (a) increased shock-strength associated with higher operating pressure ratio and, (b) relative change in exit velocity associated with the increase in  $P_T/P_0$ , tempered by greater loss across the stronger internal normal shock.
  - (d) Shock-associated noise generated internally may not exhibit the same characteristics as externally generated shock-cell noise for convergent nozzles.
  - (e) Other sources of noise may exist, i.e., internally generated noise associated with an interaction of the shock structure and flow disturbances such as those associated with turbulence of combustion, upstream support strut wakes, or from nozzle wall boundary layers. This interaction may also significantly boost jet mixing noise levels.
  - (f) For operation in the  $2.61 < P_T/P_0 < 3.90$  regime, where external shock structure is expected to be present, the more omnidirectional characteristic of shock-cell noise associated with convergent flow nozzles should be present and shock-cell noise will compete with turbulent mixing noise for predominance.

Changes in noise characteristics are expected to be pressure ratio dependent, of significant magnitude, and broadband in content, based on the above considerations.

As a preliminary attempt at correlation of peak noise, 120-foot arc peak OASPL and 2128-foot sideline peak OASPL are plotted versus nozzle  $P_T/P_0$  at the isovelocity lines of 1000, 1250, 1640 and 2090 ft/sec in Figure 3-39. Pressure ratio ranges corresponding to anticipated flow regimes are indicated. Additionally, Figure 3-40 presents 120-foot polar OASPL distributions for the four isovelocity lines and Figure 3-41 contains 1/3 OBSPL spectra at  $150^\circ$  relative to the inlet (normally the peak noise angle for each of the four velocity points).

The following observations are noted based on a review of the above data figures, consistent with the previous observations (a) through (f):

- For  $P_T/P_0 \leq 1.24$ , peak OASPL levels vary within 1 dB (at 1000 ft/sec) on a nonnormalized basis. When normalized for  $T_T$ , the variance drops to 0.3 dB; the closer correlation anticipated for turbulent mixing noise.
- For pressure ratio range of operation where an internal shock is expected, i.e.,  $1.24 < P_T/P_0 < 2.61$ , Figure 3-39, correlation of Peak OASPL with  $P_T/P_0$ , indicates a changing trend with velocity change. At 1000 and 1250 ft/sec noise decreases as  $P_T/P_0$  increases at 1640 ft/sec the level remains near constant, and at 2090 ft/sec the peak OASPL increases. This may be in line with the





- 120-ft Arc
- $A_1 = 238 \text{ in.}^2$
- C-D Plug Nozzle - Model 2

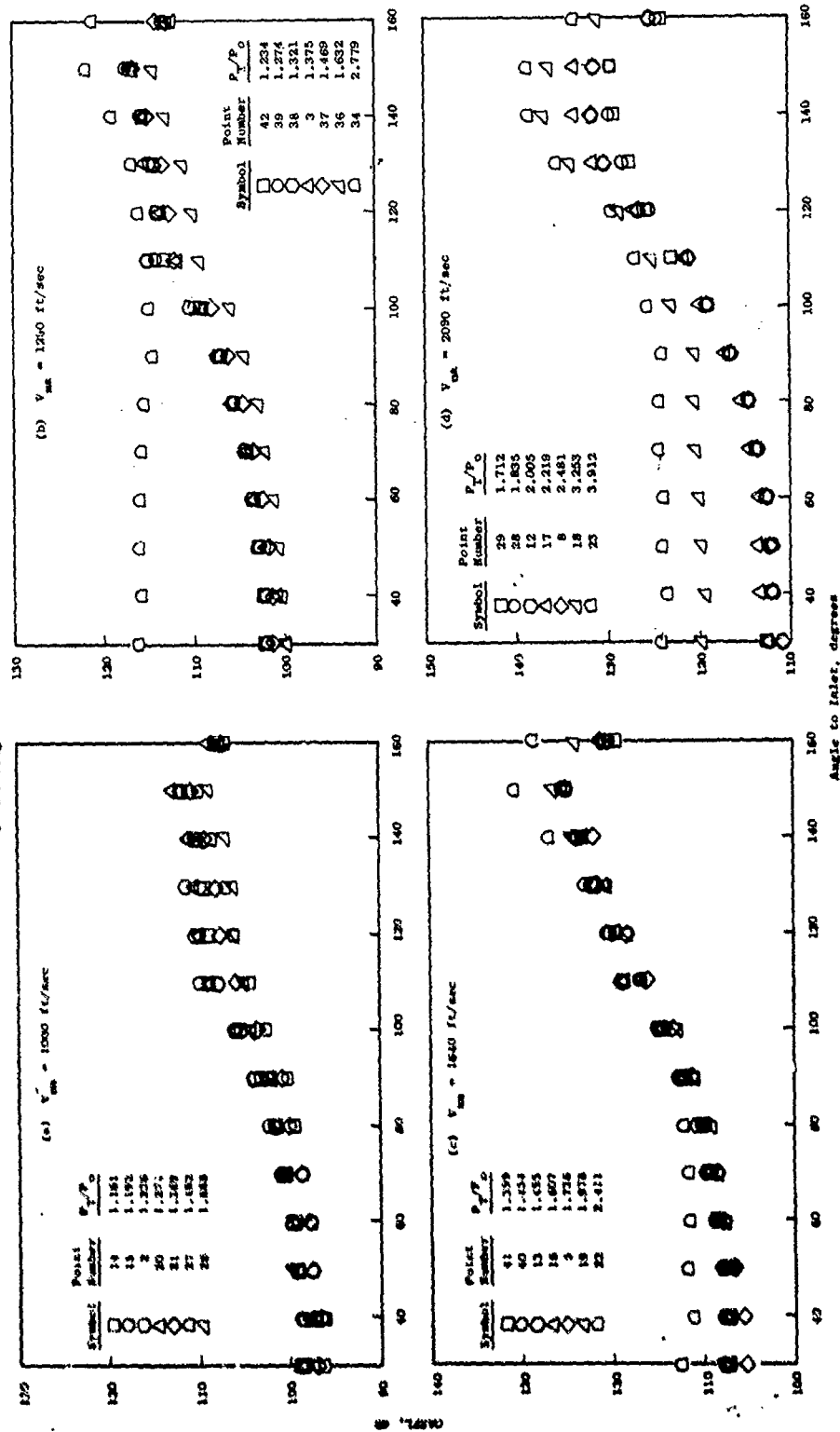


Figure 3-40. Polar OASPL Distributions at  $V_{\infty} = 1000, 1250, 1640, \text{ and } 2090 \text{ ft/sec.}$

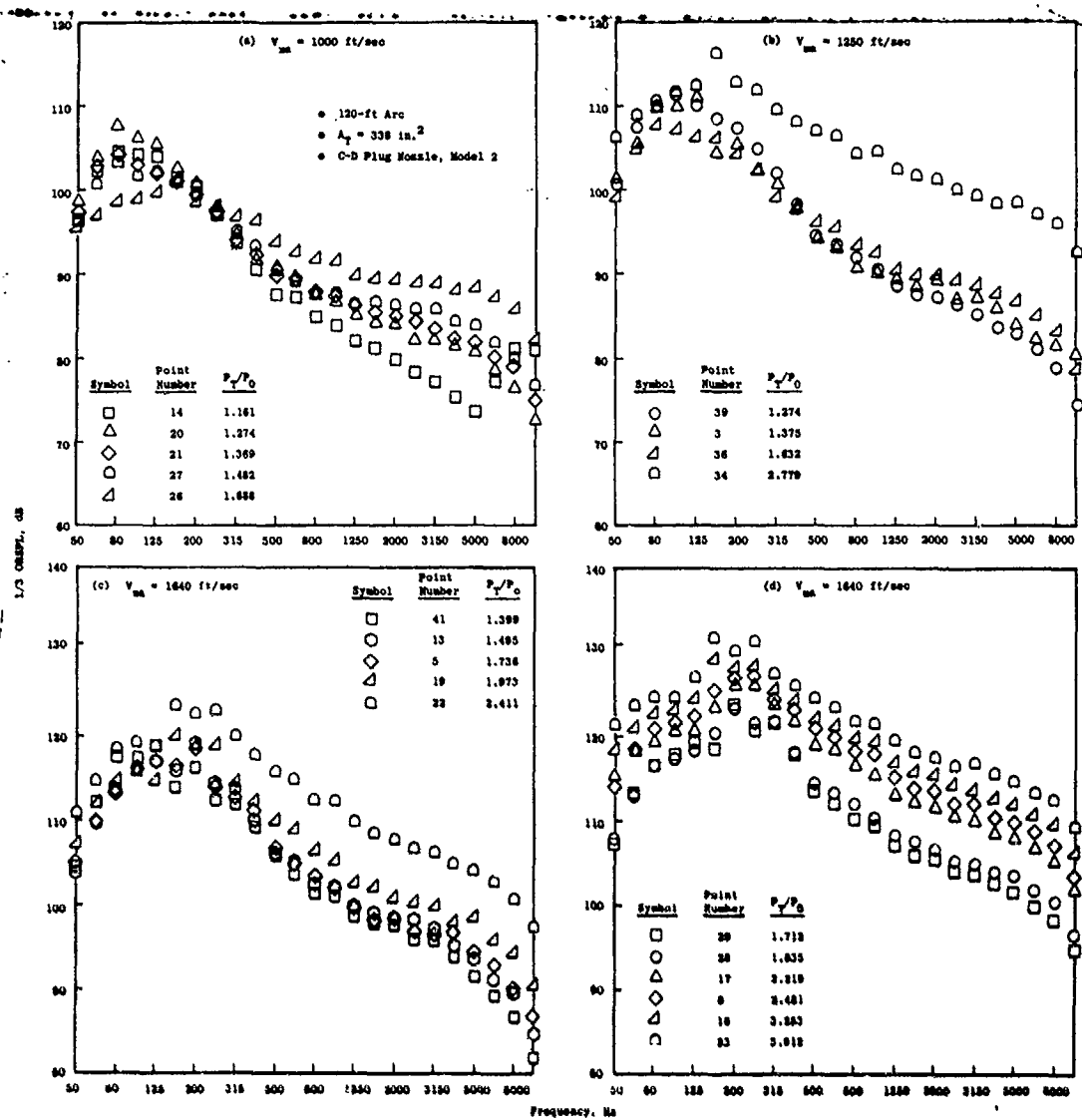


Figure 3-41. 150° Spectra at  $V_{ma} = 1000, 1250, 1640, \text{ and } 2090$  ft/sec.

previous observation (c). The OASPL and 1/3 OBSPL data of Figures 3-40 and 3-41, within this range of operation, indicate smooth transition in levels at all angles. Spectrum changes are mostly broadband in content.

- For the pressure ratio range of operation where an external shock structure is anticipated,  $2.61 < P_T/P_0 < 3.90$ , the more omnidirectional characteristic associated with conical nozzle shock-cell noise persists [previous observation (f)], and competition for dominance of either turbulent mixing or shock noise is more pronounced. At 1000 ft/sec all points are below  $P_T/P_0 = 2.54$  and no external shock structure is expected; therefore, directivity and spectra changes are all uniform. At 1250 ft/sec, for the  $P_T/P_0 = 2.79$  point, inlet and broadside noise levels are raised substantially while aft-to-peak levels increase moderately. Spectra at  $150^\circ$  show noise increases to be very broadband from  $\approx 160$  Hz through 10KHz. At 1640 ft/sec, where maximum  $P_T/P_0 = 2.41 (< 2.54$  where shock sits at the exit plane) OASPL directivity shows no abrupt rise in the forward quadrant; however, aft angle  $150^\circ$  spectra still shows a fairly broadband increase in noise levels, indicating possibility of strong aft directed shock noise. At 2090 ft/sec, the  $P_T/P_0 = 2.48$  point maintains low forward quadrant noise whereas the  $P_T/P_0 = 3.25$  and  $3.91$  points increase forward quadrant and broadside OASPL proportionately with  $P_T/P_0$  change. Spectra changes at  $150^\circ$  are again broadband and consistent with  $P_T/P_0$  changes.

A jet density correlation was derived using the isovelocity data lines at  $V_{ma} = 1000, 1250, 1640$  and  $2090$  ft/sec obtained through systematic variation of  $P_T/P_0$  and  $T_T$ . Nonnormalized OAPWL and peak OASPL values are plotted versus  $10 \log_{10} (\rho_j/\rho_{isa})$  in Figure 3-42. Straight lines are fitted through each velocity set by least squares curve fit. The resulting line slopes yield the density exponent ( $\omega$ ) for the correlation of jet noise dependence on density. Each line of data, therefore, establishes the value of  $\omega$  for that particular velocity and these  $\omega$  values versus  $\log_{10} V_{ma}/a_0$  are also plotted in Figure 3-42 for both OAPWL and peak OASPL. The figures also show comparison to the conical nozzle  $\omega$  dependency established by Hoch, et.al. (Reference 25). Differences are quite substantial and again illustrate the distinctly different noise characteristics of a C-D nozzle (Model 2) system.

#### 3.4.1.3 Plug Nozzle Radius Ratio Study (Models 3, 4, and 5)

The plug nozzle may be thought of as a basic building block. In its simplest form, it is the basic propulsion nozzle geometry normally used for increasing aerodynamic efficiency. In its more complex form, it is the base structure around which multielement annular suppressors are incorporated. Through use of a translating cylindrical shroud, it reverts to geometry similar to that of the convergent-divergent system of the previous section. The C-D flowpath is essential for proper flow expansion guidance in cruise flight mode, necessary to optimize aerodynamic performance.

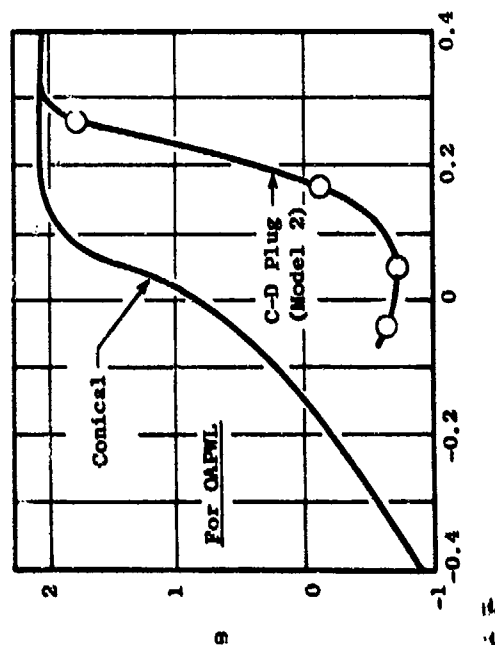
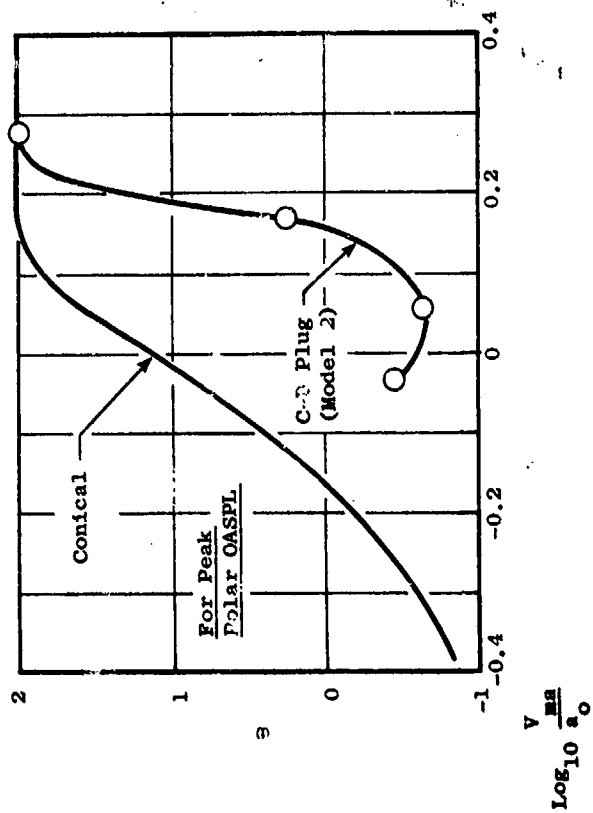
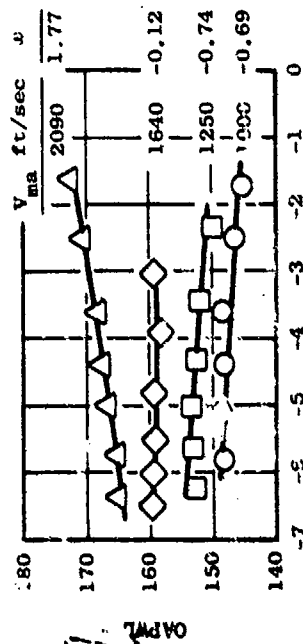
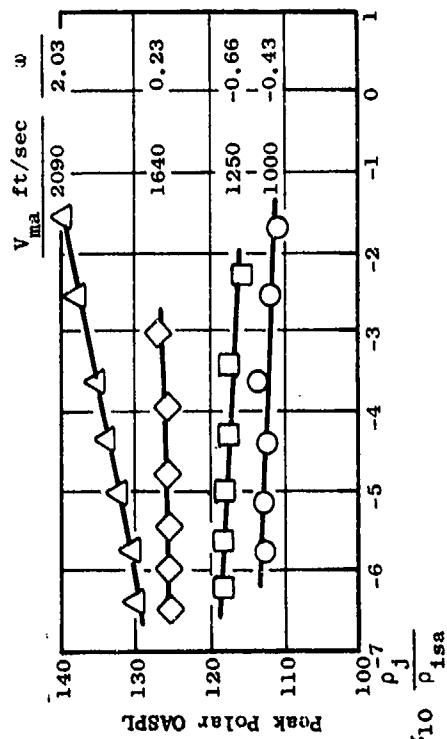


Figure 3-42. Jet Density Exponent Correlation.

The far-field acoustic characteristics of three different annular plug nozzles were measured within this study to establish noise level variation as a function of plug geometry, primarily plug radius ratio. Additionally, information was obtained for use in Task 2, Section 4.6.7, "Experimental Evaluation of Annular Plug Nozzle Shock Cell Noise Characteristics," and Section 4.7.8, "Data Theory Comparisons." Temperature (density) dependence information was also obtained to establish noise  $\omega$  dependency similar to that done by Hoch, et al. (Reference 25) for conical nozzles and to that of the previous section for the C-D plug (Model 2). This noise data allows documentation of the dependency of the plug system in a general manner similar to the conical nozzle.

The three configurations tested are shown in Figure 3-43 with details in Appendix A, Figures 3, 4, and 5. The models maintain the  $10^\circ$  half-angle core plug of 2.40" radius over the plug peak. The plug flowpath is contoured to simulate conventional engine flowlines. Interchangeable converging shrouds of  $R_g = 4.071, 3.041$  and  $2.815$ " are used to effect plug-to-shroud radius ratios ( $R_r$ ) of 0.59, 0.789 and 0.853 for Models 3, 4, and 5, respectively.

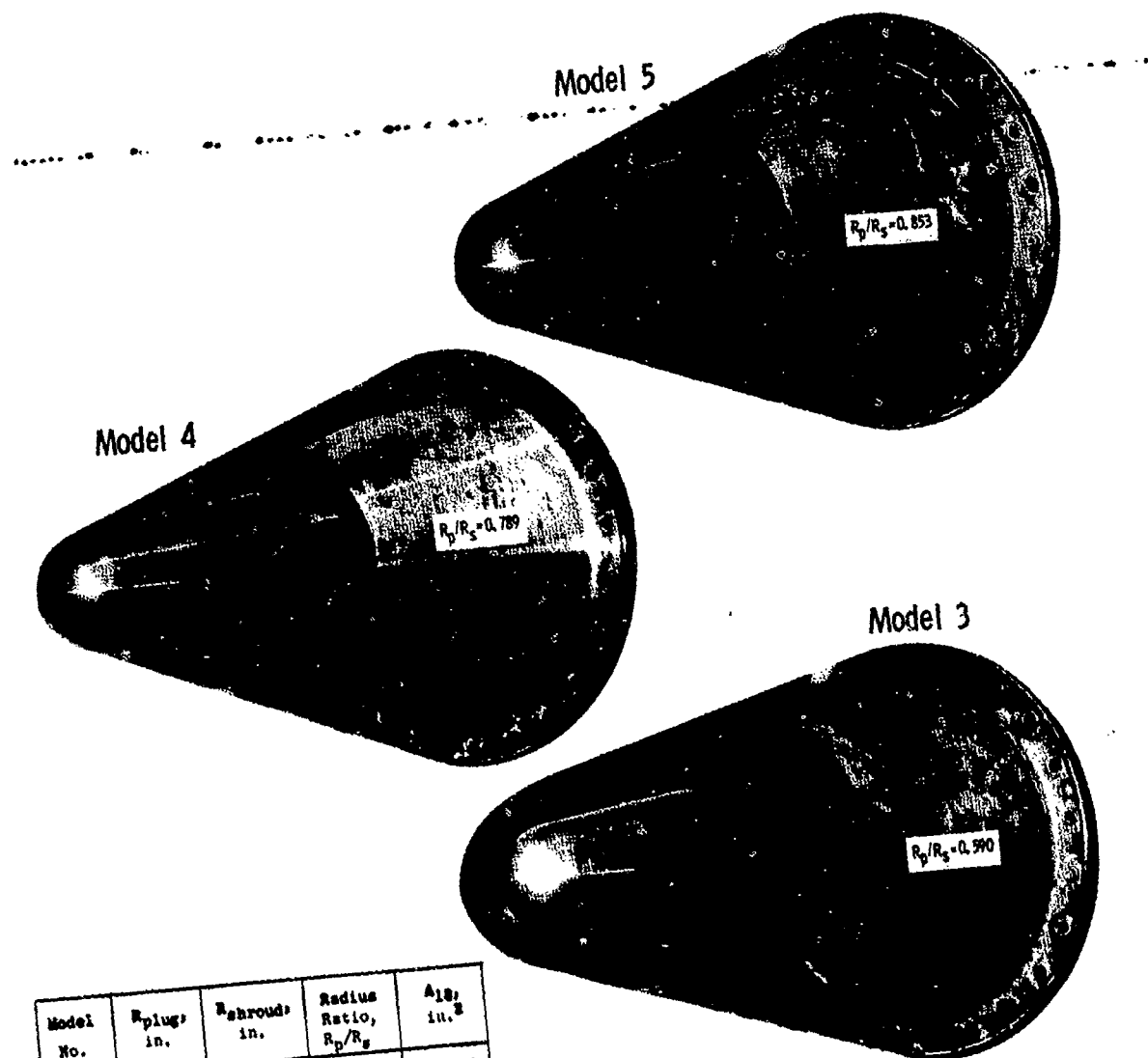
The models were tested at JENOTS with the far-field acoustic matrix of Section 3.2.1, Figure 3-4. Each used the simulated turbojet engine cycle line, and Model 4, of representative  $R_r = 0.789$ , was selected for a more detailed parametric test matrix consisting of:

- Isovelocity lines at 1000, 1250, 1640, and 2090 ft/sec, similar to that of Model 2 of the previous section to establish noise dependency on jet density/temperature.
- Isotemperature lines of  $1000^\circ, 1250^\circ, 1500^\circ, 1750^\circ$ , and  $1900^\circ$  R, to establish noise/velocity dependency.

Previous suppression levels associated with plug nozzles were low to moderate (1 to 3  $\Delta$ PNL) in level, primarily associated with plugs of low radius ratio. The current plug-baseline systems were developed to evaluate several design principles. An increase in plug radius ratio for a fixed area nozzle pushes the flow to a smaller annulus, further removed from the nozzle centerline and should, therefore, increase peripheral mixing area. Smaller annulus slit height (higher radius ratio) is associated with reduction in shock-cell noise. The smaller annulus height, relative to a fixed plug length, enhances the possibility for greater physical shielding of high-frequency noise.

Data results for the parametric radius ratio study, along the simulated turbojet engine cycle line, are presented as follows; each scaled and normalized per Section 3.3.1.7 then plotted versus  $V_{ma}$  with  $\Delta$  suppression plots included as appropriate:

Figure 3-44 and 3-45	Peak OASPL and PNL
Figure 3-46 and 3-47	$90^\circ$ OASPL and PNL
Figure 3-48	$50^\circ$ OASPL and PNL
Figure 3-49	OAPWL



Model No.	$R_{\text{plug}}$ in.	$R_{\text{shroud}}$ in.	Radius Ratio, $R_p/R_s$	$A_{18}$ , in. <sup>2</sup>
5	2.40	2.815	0.853	6.794
4	2.40	3.041	0.789	10.857
3	2.40	4.071	0.590	33.970

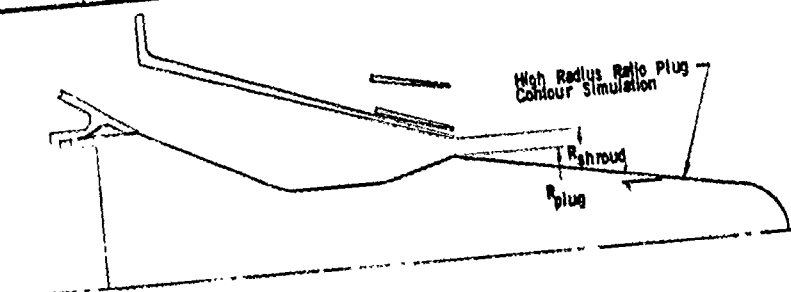


Figure 3-43. Model Hardware for Parametric Nozzle Radius Ratio Study.

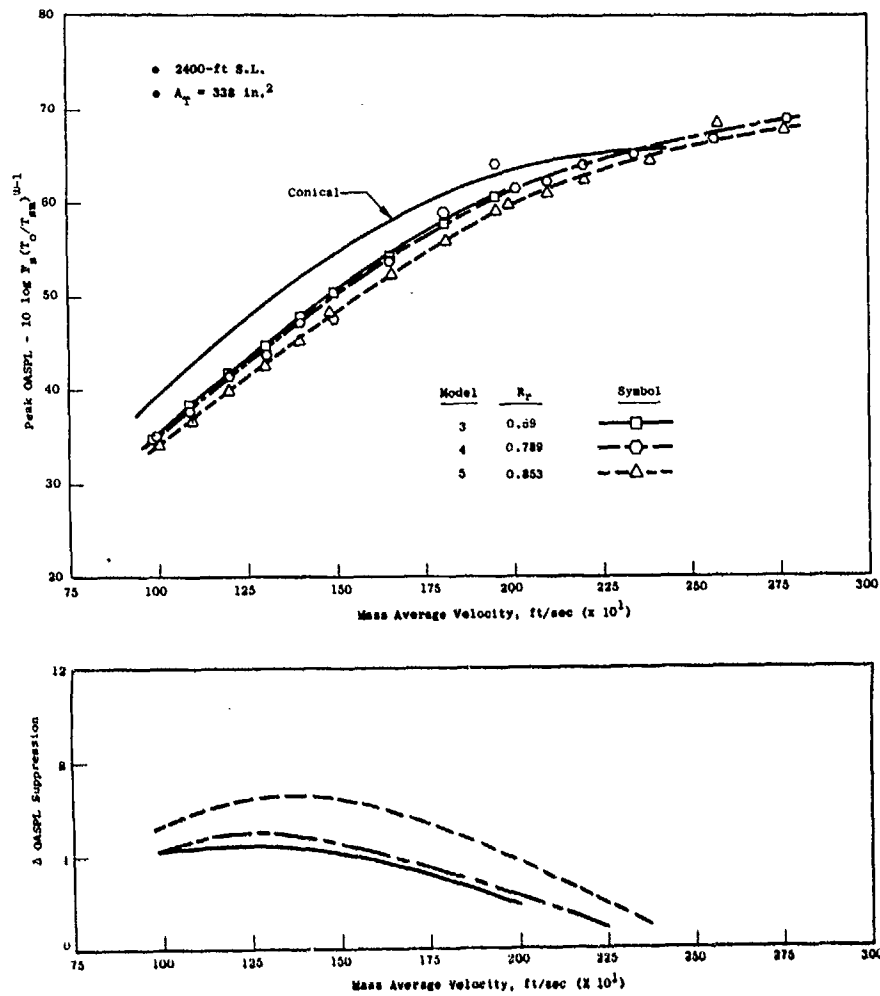


Figure 3-44. Summary of Plug Nozzle Peak OASPL and Suppression Levels.



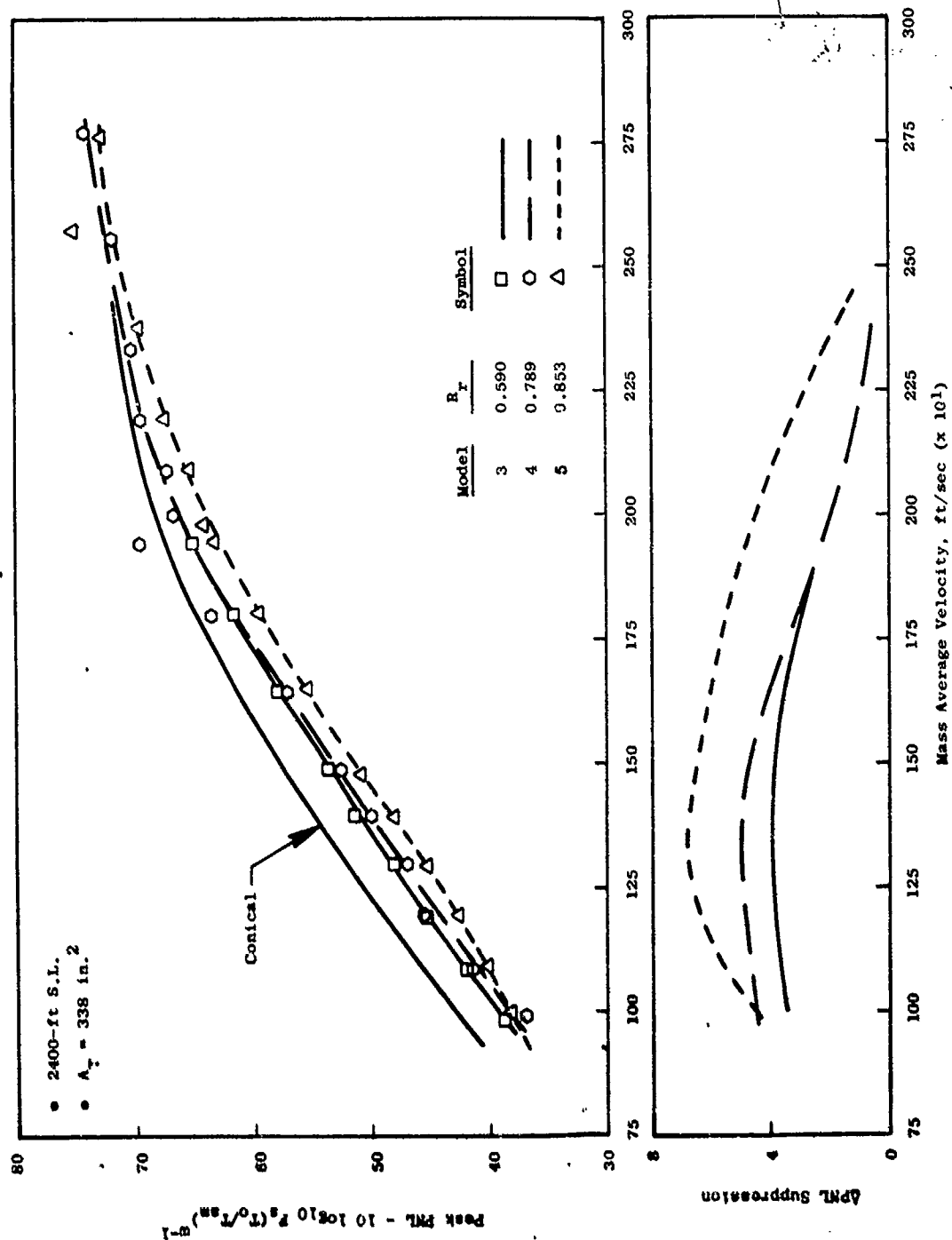


Figure 3-45. Summary of Plug Nozzle Peak PNL and Suppression Levels.

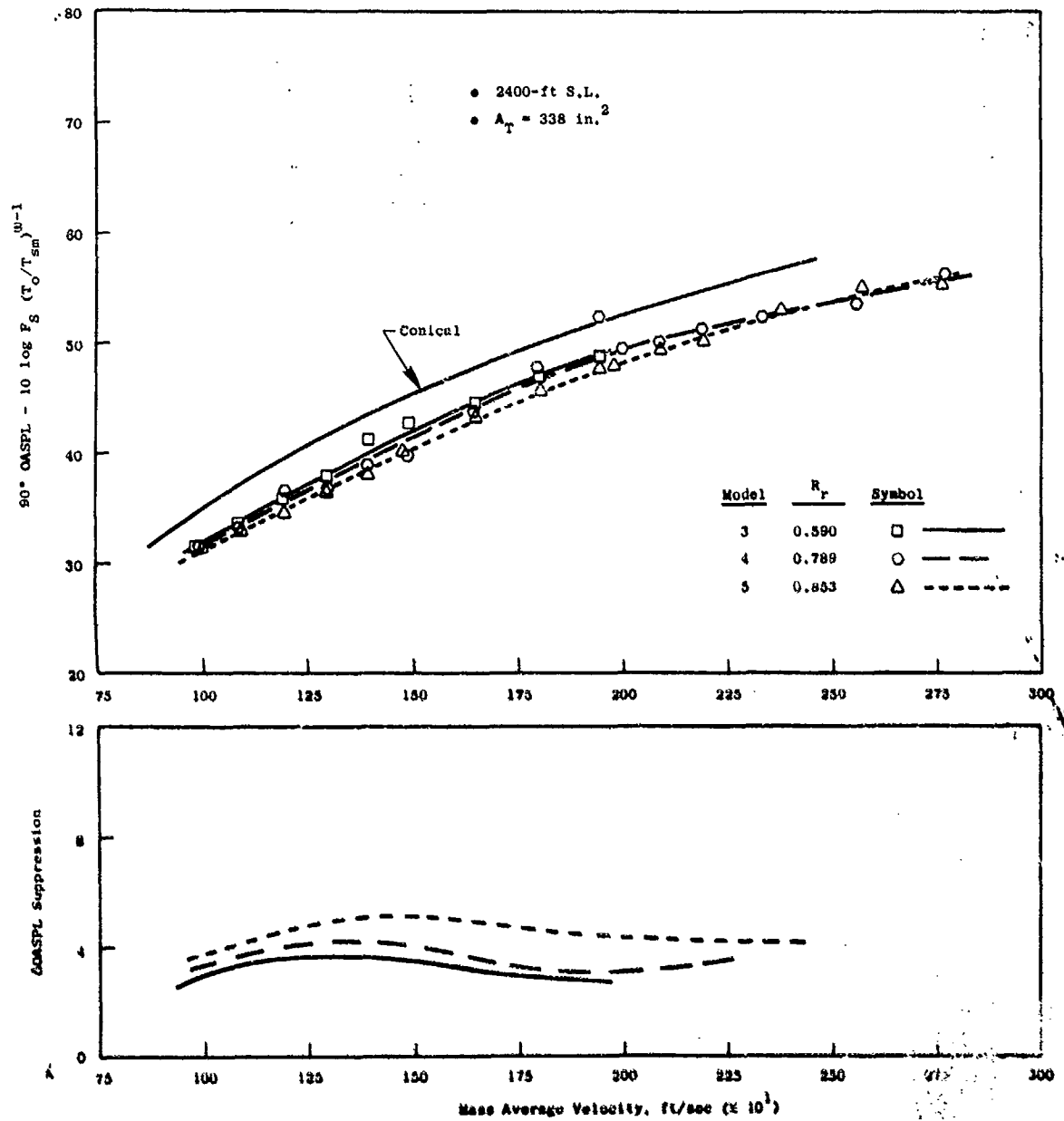


Figure 3-46. Summary of Plug Nozzle 90° QASPL and Suppression Levels.

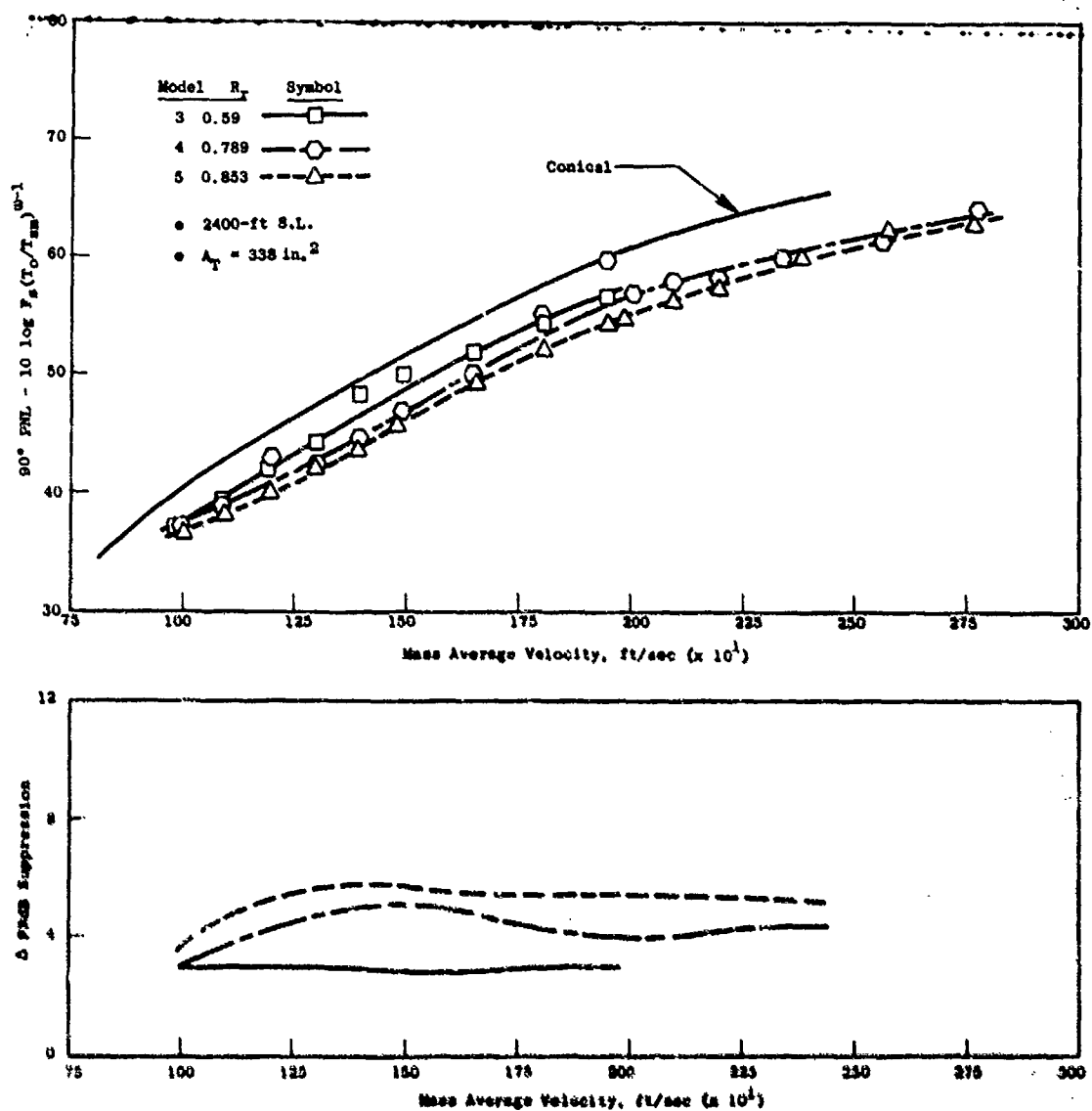


Figure 3-47. Summary of Plug Nozzle  $90^\circ$  PNL and Suppression Levels.

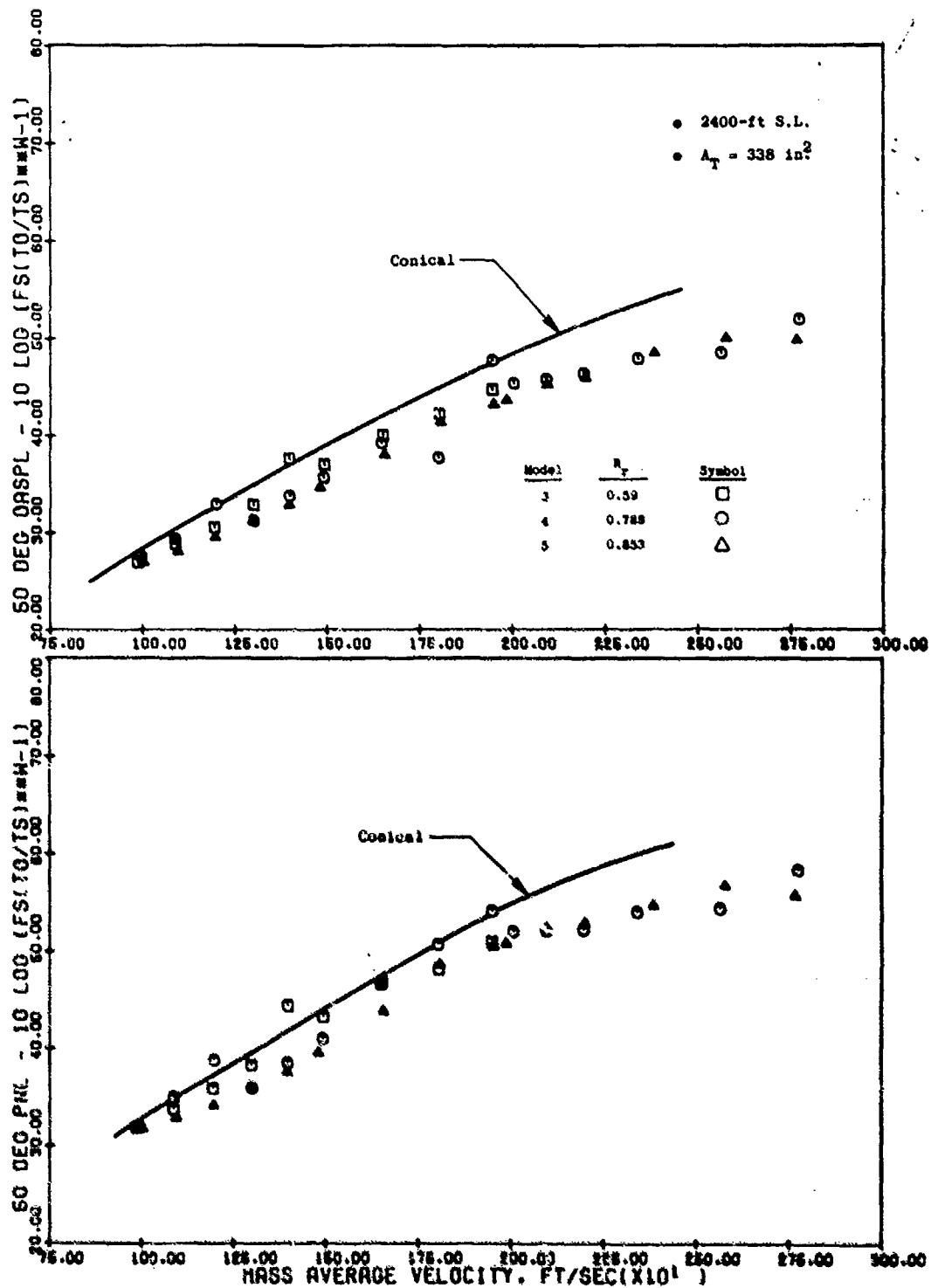


Figure 3-48. Summary of Plug Nozzle 50° OASPL and PNL Characteristics.

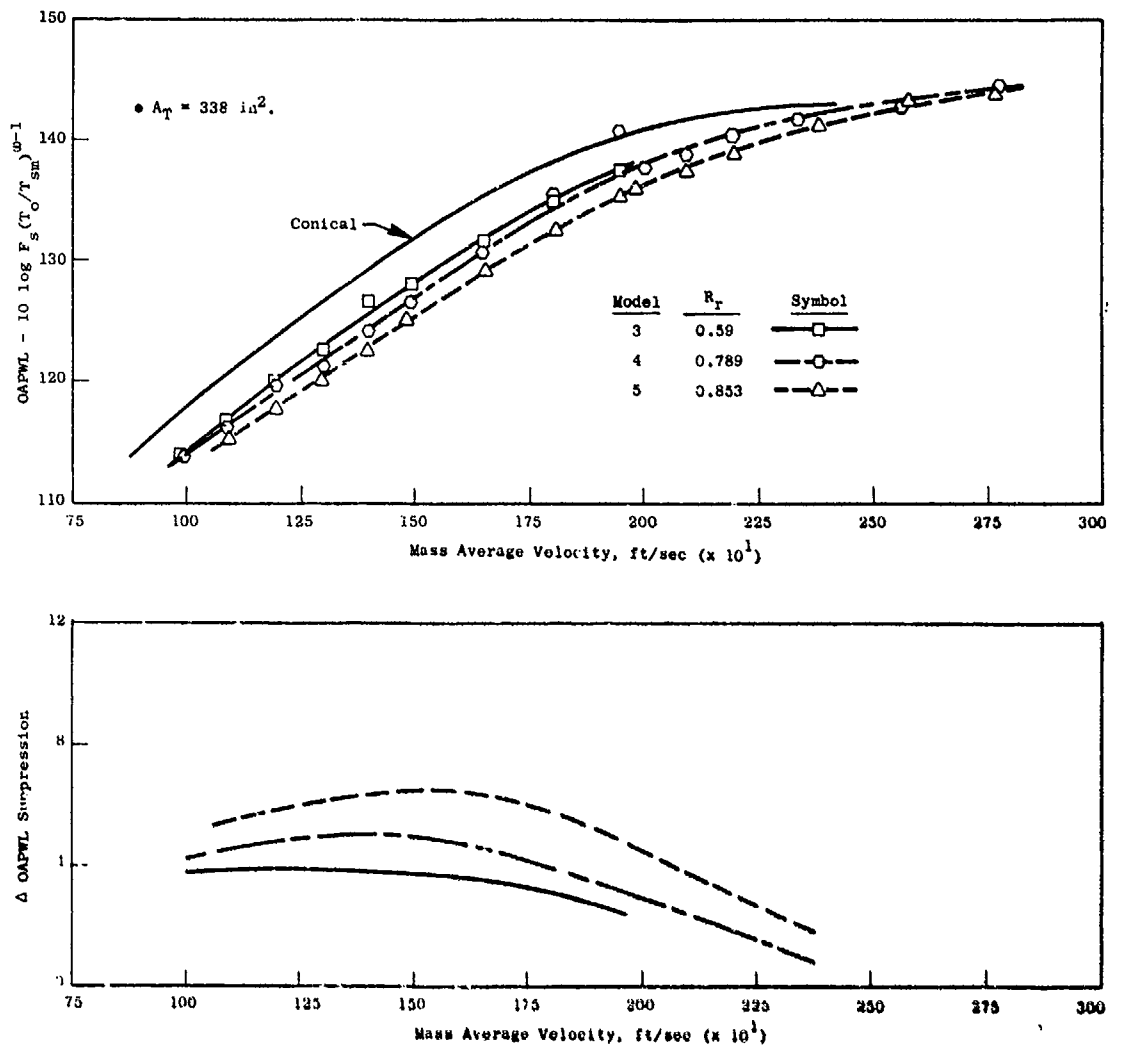


Figure 3-49. Summary of Plug Nozzle OAPWL and Suppression Levels.

Figures 3-44 through 3-47 show definite trends of suppression increase with higher radius ratio at peak and 90° for both OASPL and PNL. Maximum suppressions of 6.6 ΔPNL/6.8 ΔOASPL are seen at peak and 5.7 ΔPNL/5.1 ΔOASPL at 90° attained by the  $R_T = 0.853$  plug (Model 5). Velocity region of max. suppression occurs at 1200 to 1500 ft/sec, considerably different than the higher velocity range for suppressors. Peak noise level suppression drops off considerably at high velocity; however, 90° suppression is fairly constant across the test velocity range. Since the 90° suppression levels are fairly well carried over to peak angles in the aft quadrant for low velocity, it is an indicator that a reduction in turbulent mixing noise is the primary suppression mechanism. A total variance of approximately 2.0 Δpeak OASPL and 3 Δpeak PNL is seen from the  $R_T = 0.59$  to 0.853 excursion, maximum change occurring between the 0.789 (Model 4) and 0.853 (Model 5) plugs.

Data collapse quite consistently around the mean data-fitted curves, except for several points above the mean lines which possibly contain some shock-cell noise influence. At 50°, the PNL and OASPL levels are not as conducive to curve fitting, again indicating the presence of other than turbulent-mixing noise. Section 4.6.7 of Task 2 addresses shock-cell noise characteristics and correlations for these three annular plug nozzles. It has indicated that the annular jet formed between the nozzle shroud and plug centerbody may produce significantly different shock-cell patterns than an equivalent-flow-area conical nozzle when operating at underexpanded pressure ratios. The presence of the plug or centerbody provides a guided-expansion surface for the supersonic expansion/compression process. Additionally, the turbulent boundary layer on the plug surface may interact with the impinging shocks, modifying their characteristics.

Measured OASPL values for all supercritical nozzle pressure ratios correlate well at  $\theta_i = 30^\circ$  and  $50^\circ$  (where shock-cell noise is expected to dominate) when plotted versus  $\beta$  following typical conical nozzle  $\beta^4$  dependency. A method of normalizing shock cell noise ( $N_{sh}$ ) was formulated as:

$$N_{sh} = OASPL - 40 \log_{10} (\beta) - 20 \log_{10} (D_{eq}/r_o) \quad \text{Task 2 Report, Equation 263 (Reference 7)}$$

Data correlated very well at 30°, 50° and 70° when normalized in this manner and plotted versus  $\beta$ . A consistent trend of lower shock-cell noise (from 3 to 5 dB below conical) is observed as radius ratio is increased. As mentioned previously, this can be associated with decreasing annulus slit height as  $R_T$  increases and, subsequently, reduces the potential for strong shock structure development.

Comparisons of 50° nonnormalized spectra at  $P_T/P_o = 2.65, 3.28, \text{ and } 3.55$  were also done in the Task 2, Section 4.6.7, and showed that conical nozzle spectra shape is not maintained for a plug nozzle. A tendency to form two peaks was seen, their separation increasing with increasing radius ratio. The spectra were also more broadband in character than equivalent conical nozzle spectra.

For a more detailed comparison of PNL, OASPL and 1/3 OBSPL characteristics for the three radius ratio models tested along the simulated turbojet operating cycle line, the following are included:

- Figures 3-50 and 3-51  $P_T/P_O = 2.07$ ,  $T_T = 985^\circ \text{ R}$ ,  $V_{ma} = 1490 \text{ ft/sec}$
- Figures 3-52 and 3-53  $P_T/P_O = 2.65$ ,  $T_T = 1295^\circ \text{ R}$ ,  $V_{ma} = 1950 \text{ ft/sec}$
- Figures 3-54 and 3-55  $P_T/P_O = 3.27$ ,  $T_T = 1535^\circ \text{ R}$ ,  $V_{ma} = 2350 \text{ ft/sec}$

Observations from the data plots include:

- Directivity patterns are quite consistent among the three radius ratio models with a general lowering of levels across all angles as  $R_T$  increases.
- Broadside and forward quadrant noise levels, even at high  $P_T/P_O$ , are quite low compared to shock-cell infested conical nozzle patterns.
- A tendency is observed toward double-humped spectra, particularly for low velocity data.
- Some shock-cell tones are present in the forward quadrant angle's spectra and occasionally at  $90^\circ$  to  $110^\circ$ .
- Changes in spectra levels from model to model occur fairly well broadband, particularly at low  $V_{ma}$ . At high velocity, spectra are quite similar in level and shape, bearing out the little change seen in PNL and OASPL at high  $V_{ma}$ .

Jet-density correlation, using data acquired at  $V_{ma} = 1000, 1250, 1640$  and  $2090 \text{ ft/sec}$  on Model 4, was done similar to the procedure described in the previous section for the C-D plug (Model 2). Nonnormalized OAPWL and peak OASPL are plotted versus  $10 \log_{10} (\rho_O/\rho_{isa})$  in Figure 3-56. Values of  $\omega$  are tabulated and plotted versus  $\log_{10} V_{ma}/a_O$ . Curves are shown through the data points to compare to the conical nozzle density dependence established by Hoch, et al. (Reference 25). Minor variations relative to the conical nozzle are seen, indicating that the choice of the conical nozzle curve for data correlation is sound.

#### 3.4.1.4 Baseline Dual Flow Study

An  $AR = 2.0$  coplanar-coannular nozzle, Model 6, was tested on JENOTS to establish the acoustic characteristics of a typical dual flow coplanar-coannular nozzle. Appendix A, Figure A-6 should be referred to for detailed geometric characteristics. The acoustic test matrix included cold inner and outer flow streams having a velocity ratio range of  $V_O/V_I = 0$  to  $5.0$ , plus hot inner and outer streams ( $\approx 1500^\circ \text{ R}$ ) over a  $V_O/V_I = 0$  to  $2.5$ . The test matrix is described in Section 3.2.1 and the test conditions are documented

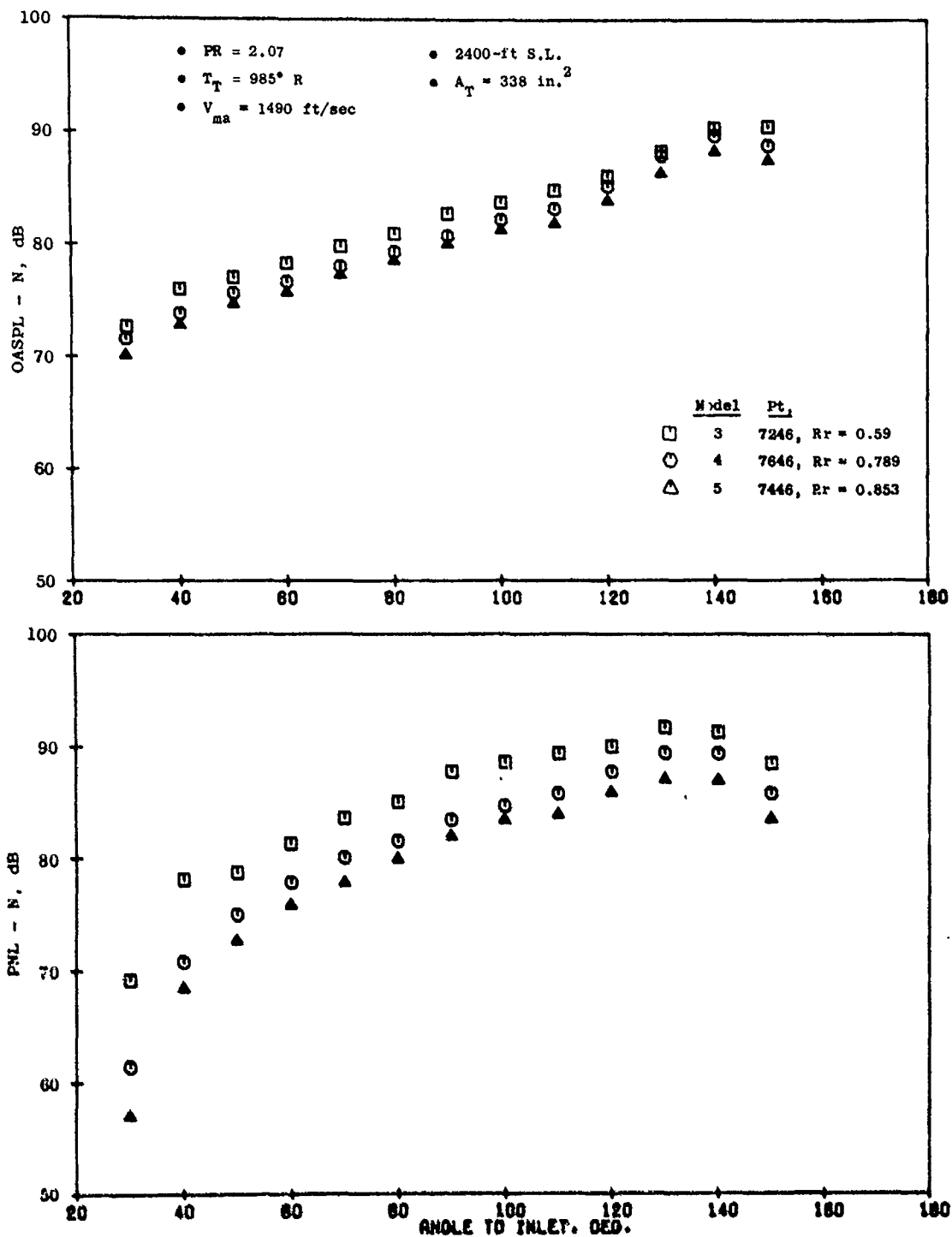


Figure 3-50. Impact of Plug Radius Ratio on OASPL and PNL Directivity,  $V_{ma} = 1490 \text{ ft/sec}$ .



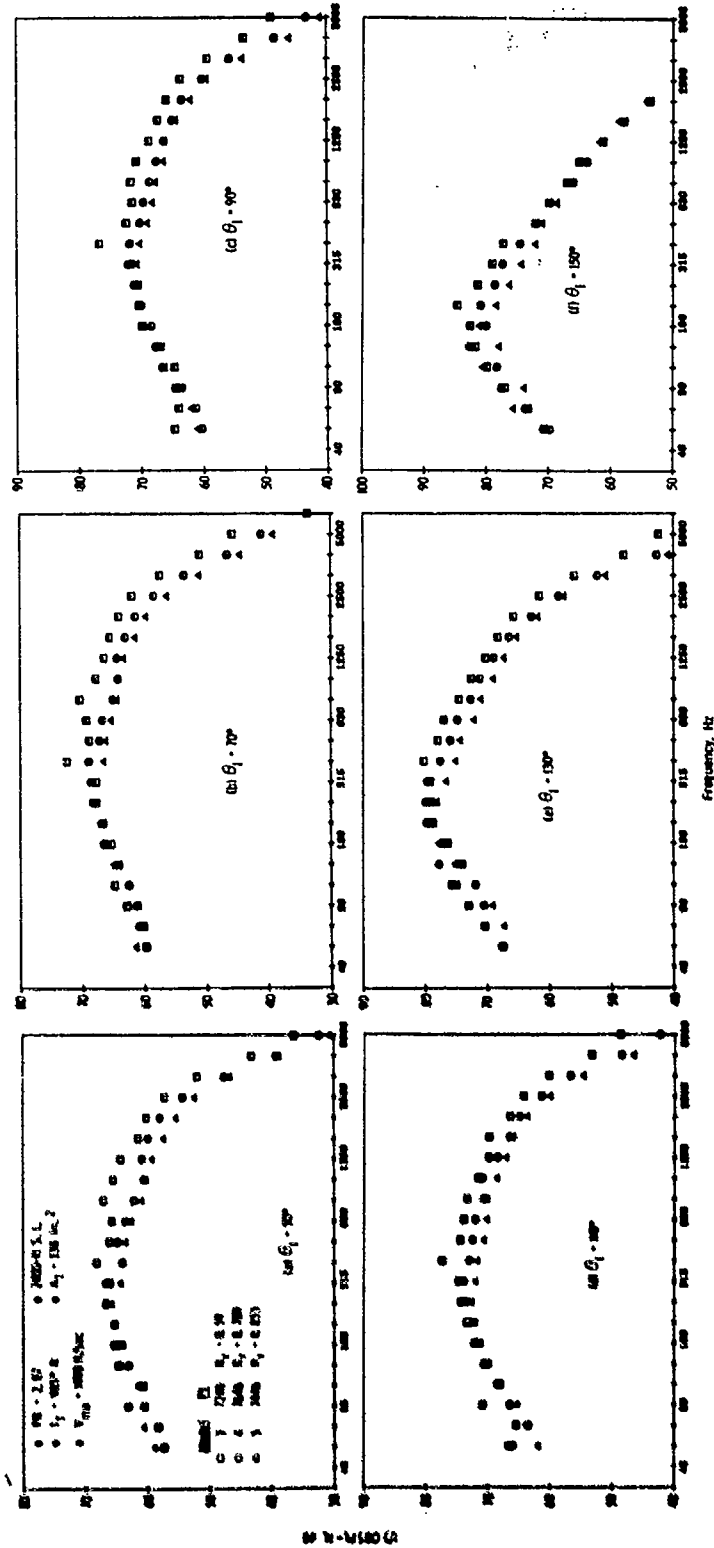


Figure 3-51. Impact of Plug Radius Ratio on OASPL and PNL Directivity,  $V_{ma} = 1490$  ft/sec.

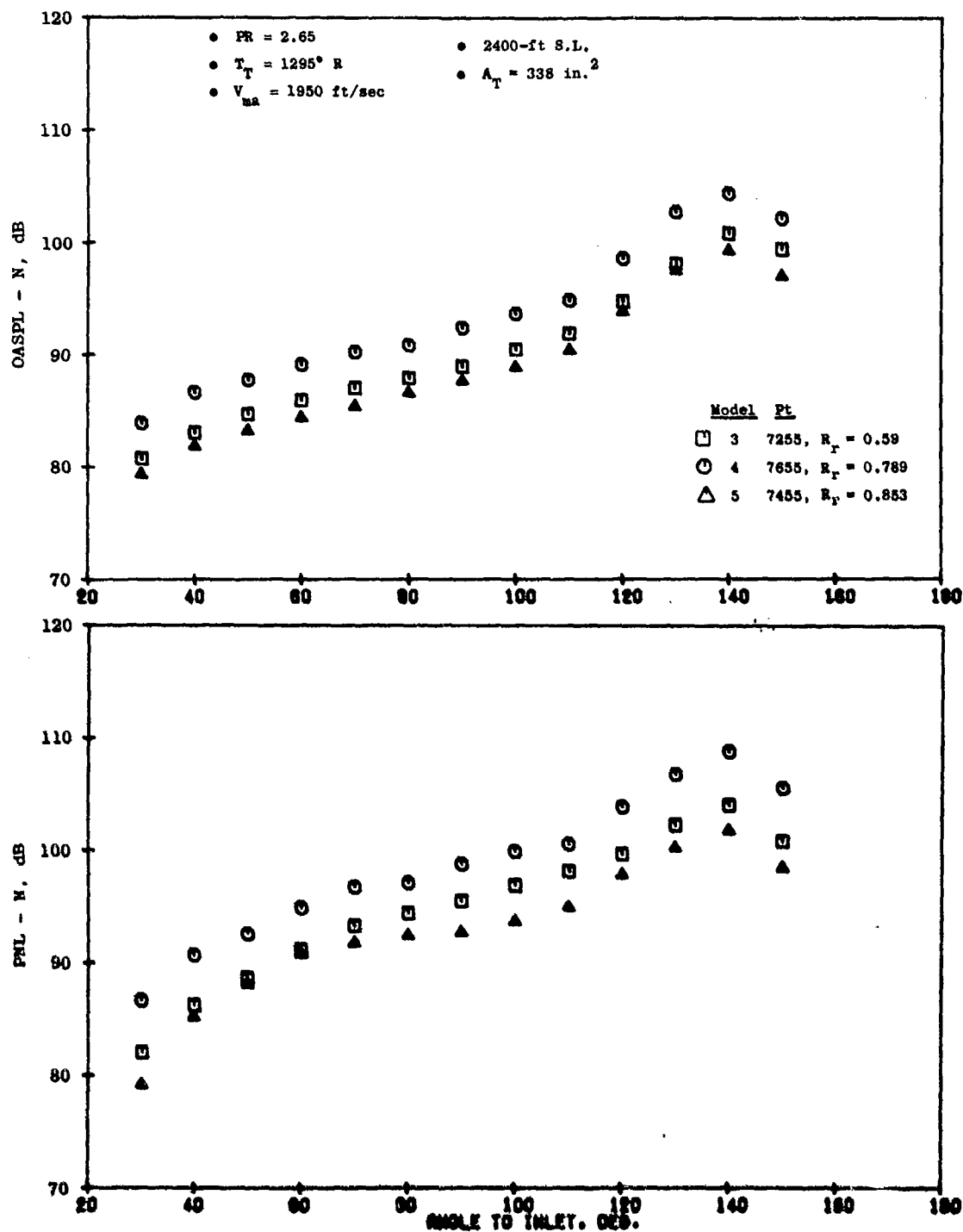


Figure 3-52. - Impact of Plug Radius Ratio on OASPL and PNL Directivity,  $V_{ma} = 1950 \text{ ft/sec.}$

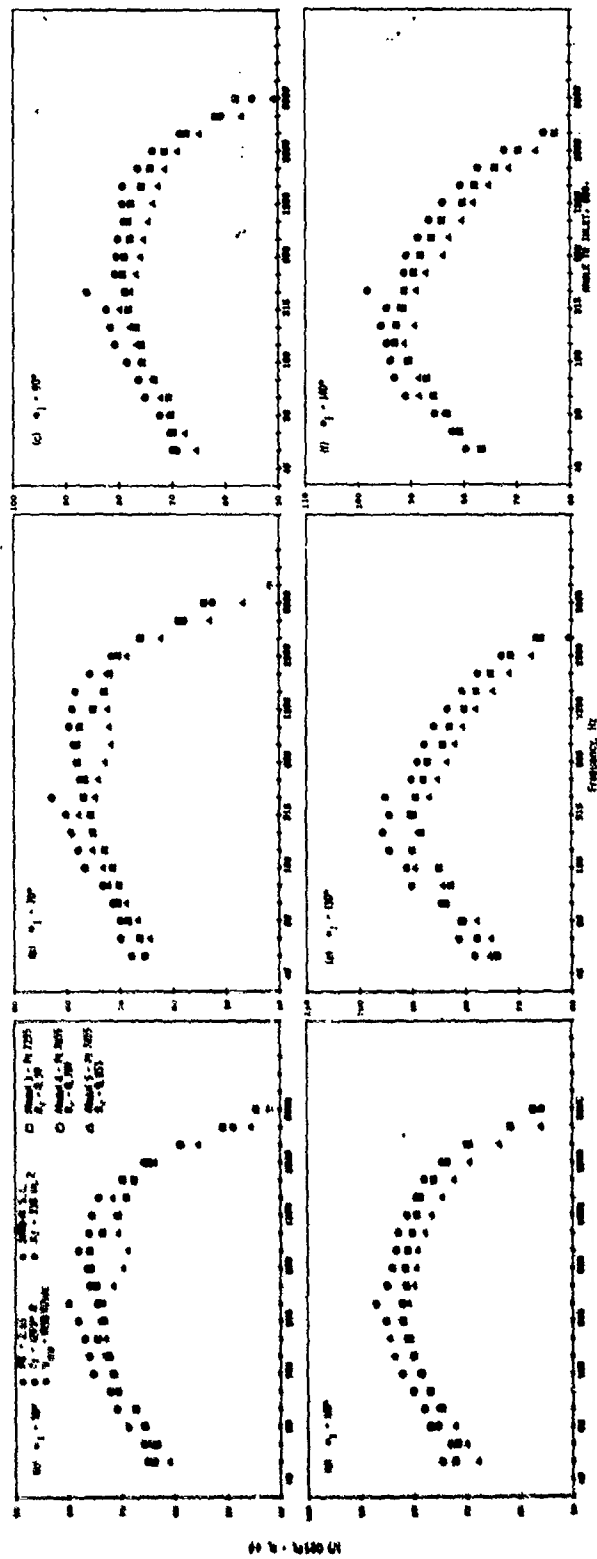


Figure 3-53. Impact of Plug Radius Ratio on Spectra ,  $V_{ma} = 1950$  ft/sec.

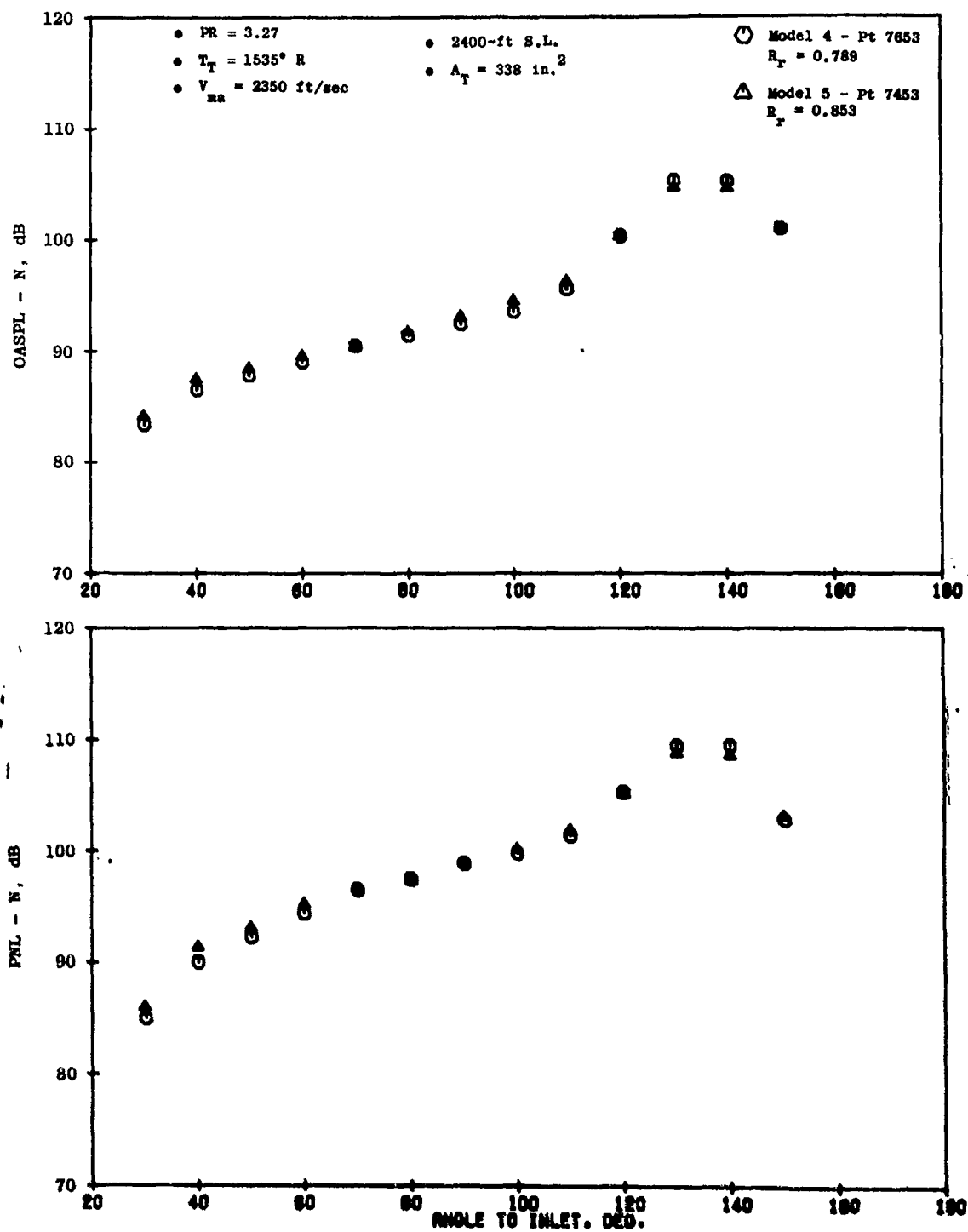


Figure 3-54. Impact of Plug Radius Ratio on OASPL and PNL Directivity,  $V_{na} = 2350 \text{ ft/sec.}$



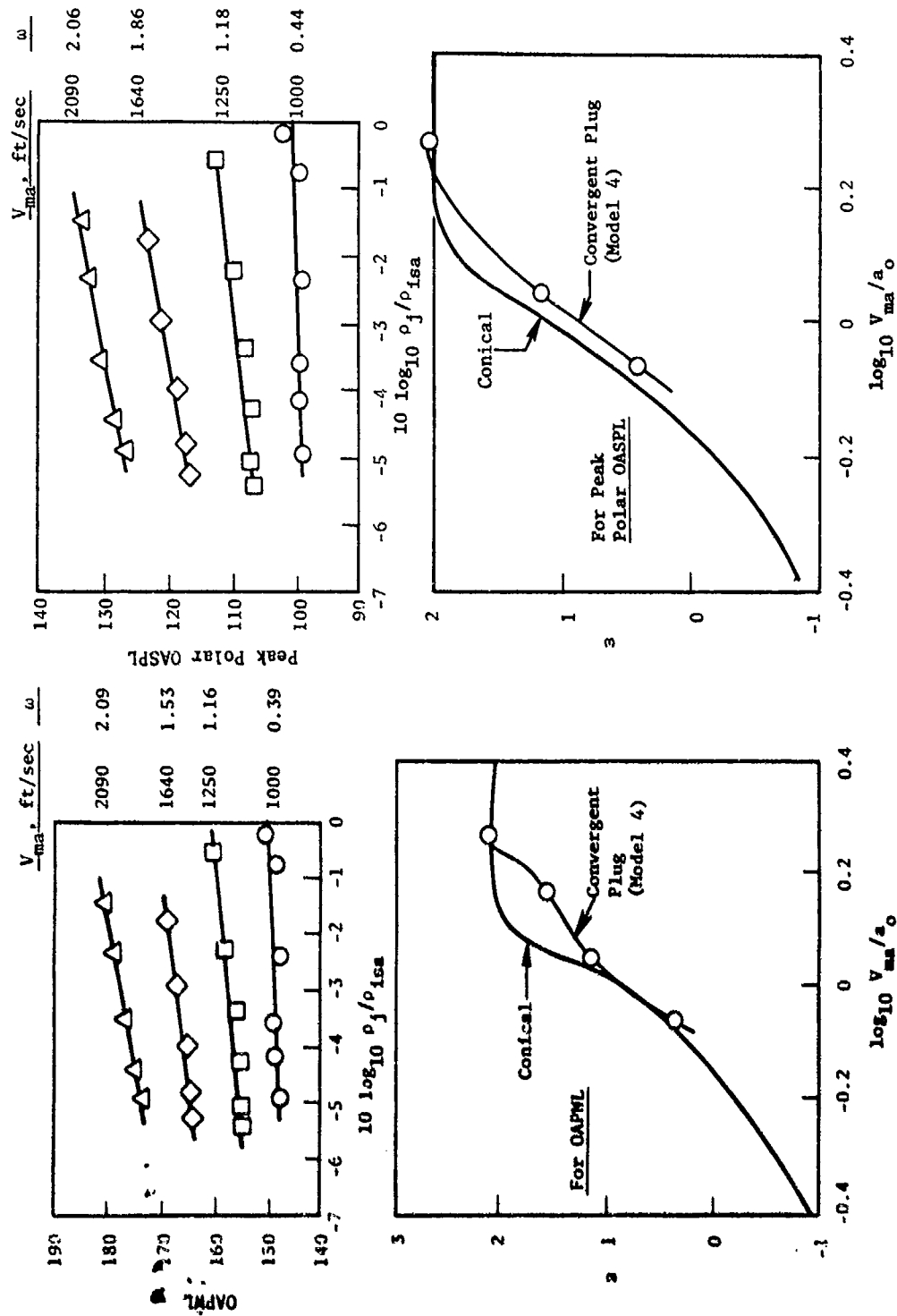


Figure 3-56. Jet Density Exponent Correlation.

on Table 6 of Appendix B. Conventional bypass as well as inverted flow cycle conditions were evaluated. A conventional bypass cycle is defined as when  $V_0/V_1 < 1.0$ . An inverted flow cycle is when  $V_0/V_1 > 1.0$ .

These data were used to support the theory/data comparisons presented in Section 4.7.8 of the Task 2 final report, Reference 7 and in Section 4.3.4 of Volume I of this report.

The PNL and OASPL directivity characteristics for velocity ratios ( $V_0/V_1$ ) ranging from 0.17 to 1.27 are presented on Figure 3-57. The inner stream velocity was held constant at 1000 ft/sec. The data have been normalized as discussed in Section 3.3.1.7. The minimum noise level is observed to occur at a velocity ratio of 0.5 to 0.6. This is similar to the results presented in References 26, 27, and 28. Typical spectra comparisons at angles of 50°, 90° and 140° are presented on Figure 3-58. The spectra comparisons indicate that the level of noise reduction at a velocity ratio of 0.5 is relatively frequency independent in the aft quadrant and frequency dependent in the forward quadrant. The apparent deviation of the  $V_0/V_1 = 1.27$  data in the forward quadrant is due to the presence of shock noise, as demonstrated by the shape of the 60° spectra.

A similar data set was obtained holding the outer velocity,  $V_0$ , constant at 1000 ft/sec and varying the inner velocity,  $V_1$ , resulting in  $0.63 < V_0/V_1 < 2.66$ . Also, the stagnation temperature of the inner stream was maintained at 1290° R. In contrast to the previous case, the minimum noise did not occur in the velocity ratio region of 0.5 to 0.6, but was observed to decrease as velocity ratio increased. Normalized PNL and OASPL directivity characteristics are presented on Figure 3-59 to support this observation. A 17 dB reduction in OASPL in the aft quadrant is observed as  $V_0/V_1$  increases from 0.63 to 2.86. Spectra are presented on Figure 3-60 to illustrate that the noise reduction with increasing velocity ratio primarily occurs in the low to midfrequency range.

The data are examined further by normalizing and comparing the data points for both sets on the basis of mixed flow velocity as defined in Section 3.3.1.7. This parameter was not effective in collapsing these two data sets into a unified line in the low velocity regime.

The nozzle was also evaluated at several conditions where both mass average velocity and velocity ratio were held constant. Typical directivity examples are presented for inverted flow cycles of  $V_0/V_1 = 1.25$  and 2.0 on Figures 3-61 and 3-62, respectively. The normalization parameter generally causes the collapse of the directivity pattern at a given mass average velocity while velocity ratio is held constant. This observation is also correct for the velocity ratio of 2.0 as illustrated by Figure 3-62. Typical spectra comparisons are presented on Figures 3-63(a) and (b) to verify the observations based on the directivity characteristics. In general, the spectra at the various angles indicate that this normalization parameter is effective in correlating the test data.

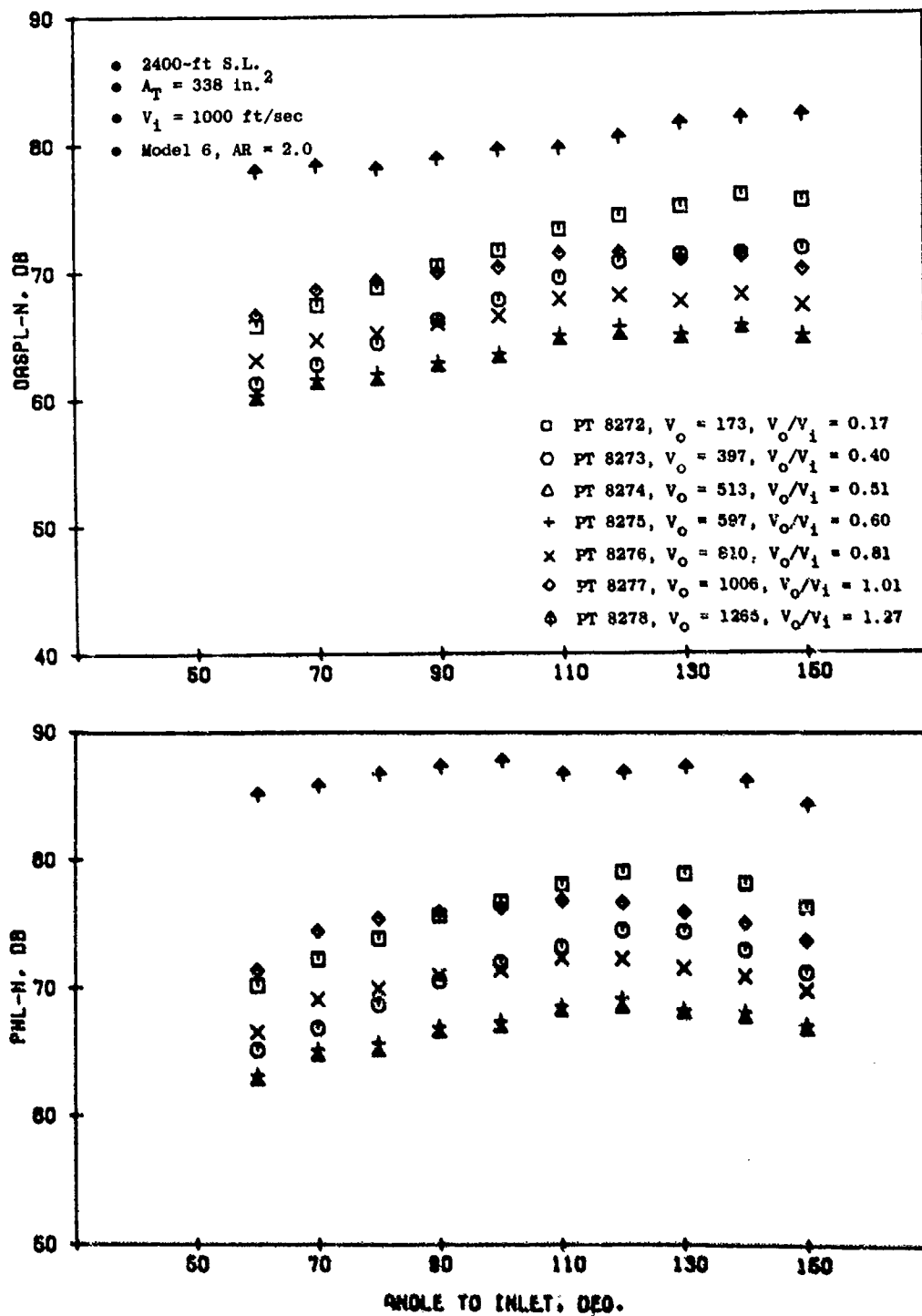


Figure 3-57. Impact of Velocity Ratio on OASPL and PNL Directivity, AR = 2.0 Coplanar-Coannular Nozzle (Model 6).



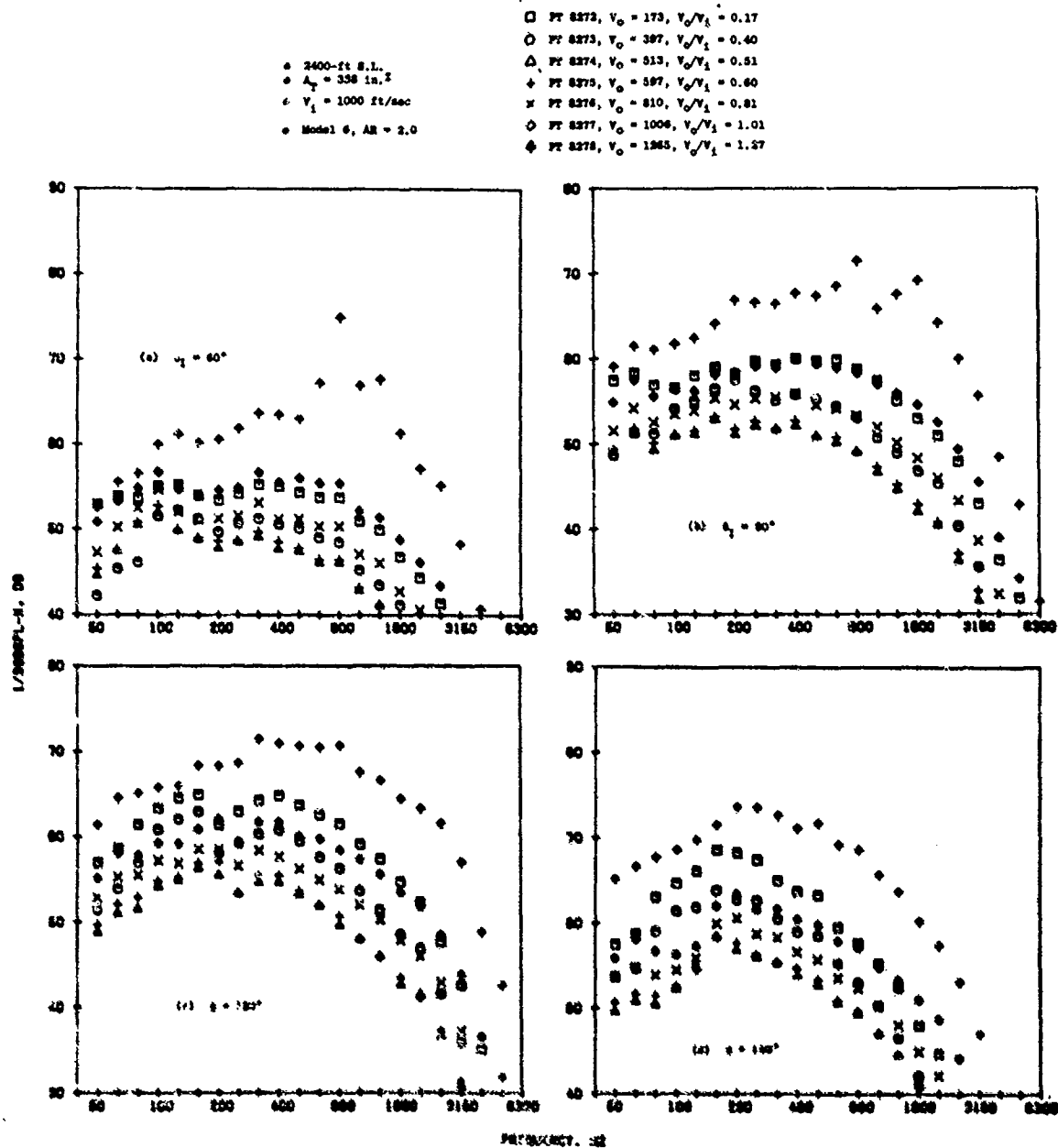


Figure 3-58. Impact of Velocity Ratio on Spectra, AR = 2.0 Coplanar-Coannular Nozzle (Model 6).

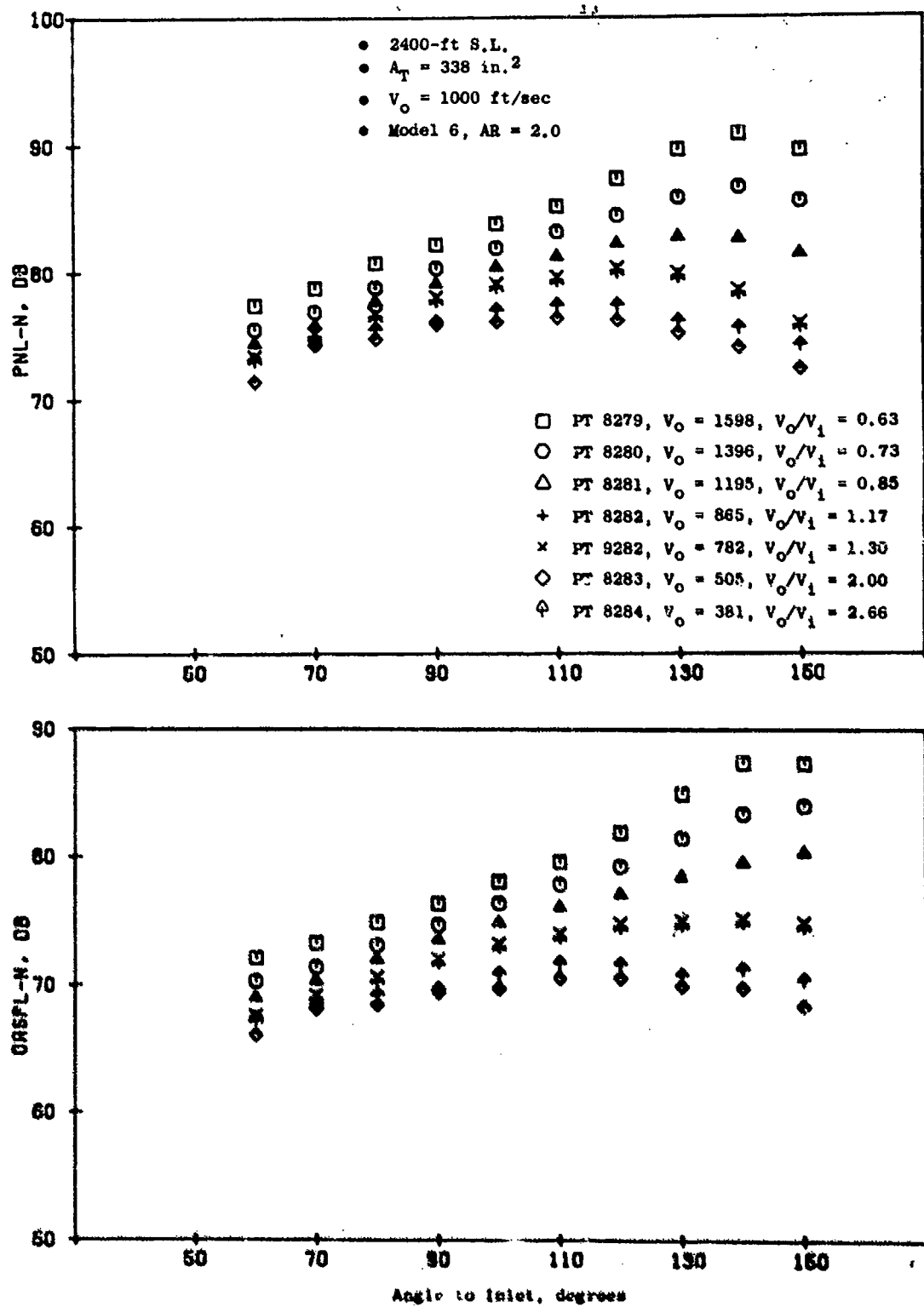


Figure 3-59. Impact of Velocity Ratio on GASPL and PNL Directivity.

- 2400-ft S.L.<sub>2</sub>
- $A_T = 338 \text{ in.}^2$
- $V_0 = 1000 \text{ ft/sec}$
- Model 6,  $Ah = 2.0$

- PT 8279,  $V_0 = 1596$ ,  $V_0/V_1 = 0.63$
- PT 8280,  $V_0 = 1396$ ,  $V_0/V_1 = 0.73$
- △ PT 8281,  $V_0 = 1195$ ,  $V_0/V_1 = 0.85$
- + PT 8282,  $V_0 = 965$ ,  $V_0/V_1 = 1.17$
- × PT 8283,  $V_0 = 782$ ,  $V_0/V_1 = 1.30$
- ◇ PT 8284,  $V_0 = 505$ ,  $V_0/V_1 = 2.00$
- ◊ PT 8284,  $V_0 = 381$ ,  $V_0/V_1 = 2.66$

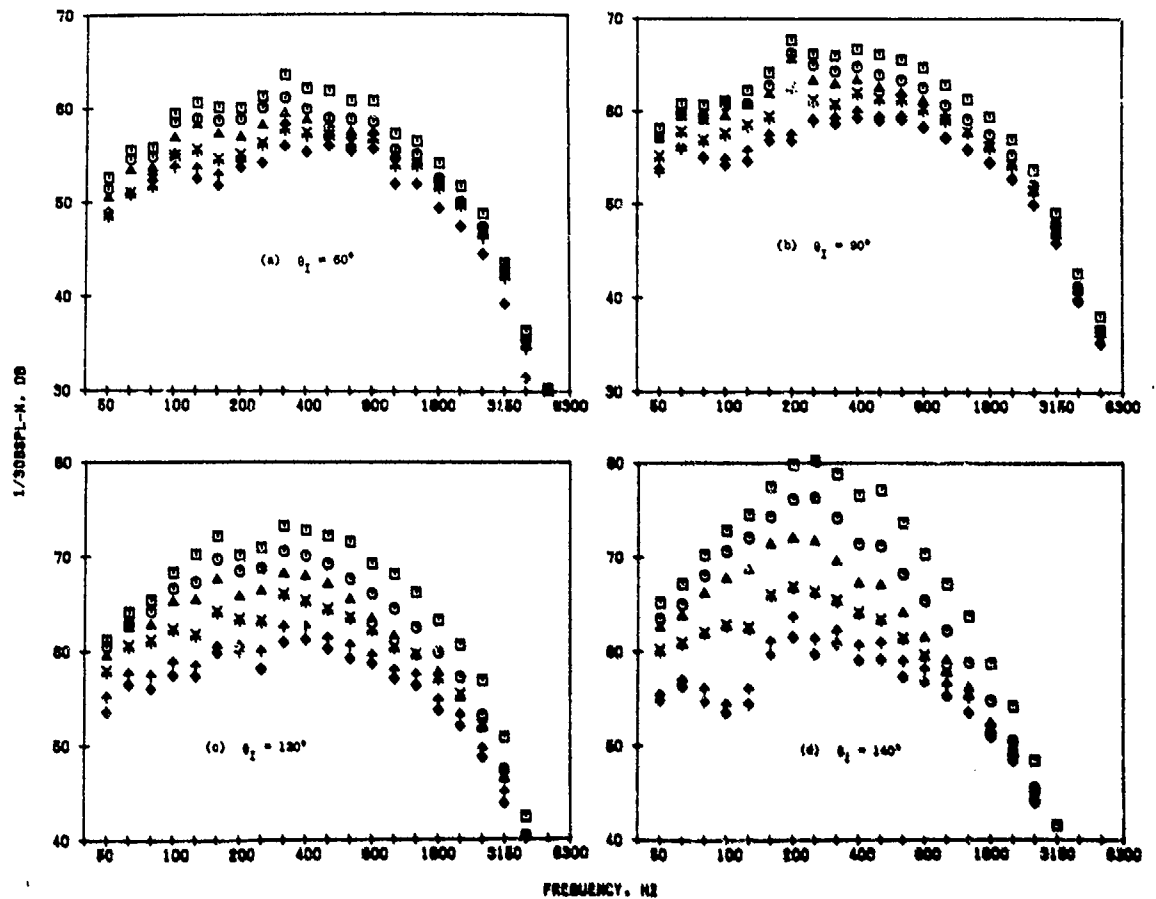


Figure 3-60. Impact of Velocity Ratio on Spectra.

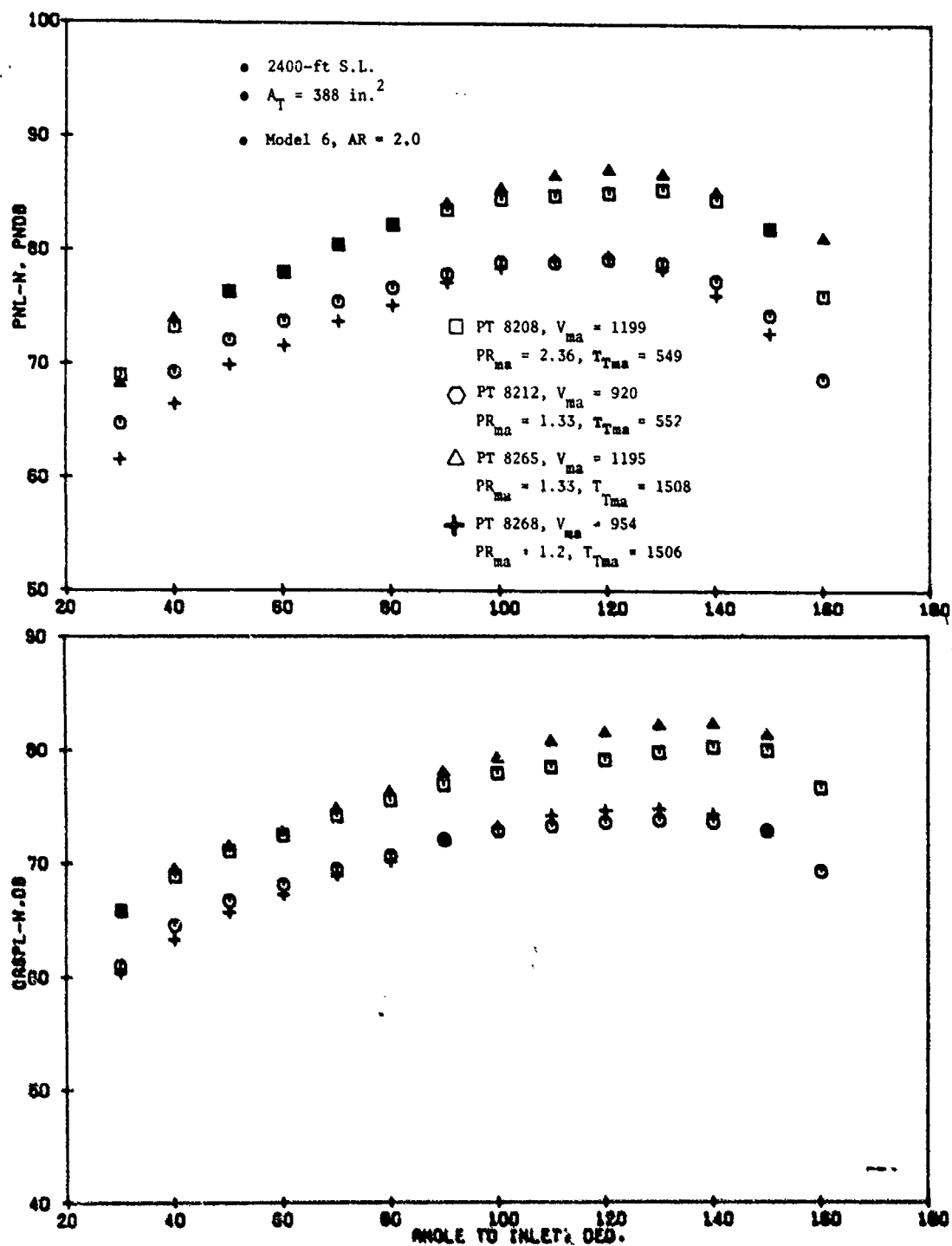


Figure 3-61. Comparison of OASPL and PNL Directivity at  $V_0/V_1 = 1.25$ , AR = 2.0 Coplanar-Coannular Nozzle (Model 6).

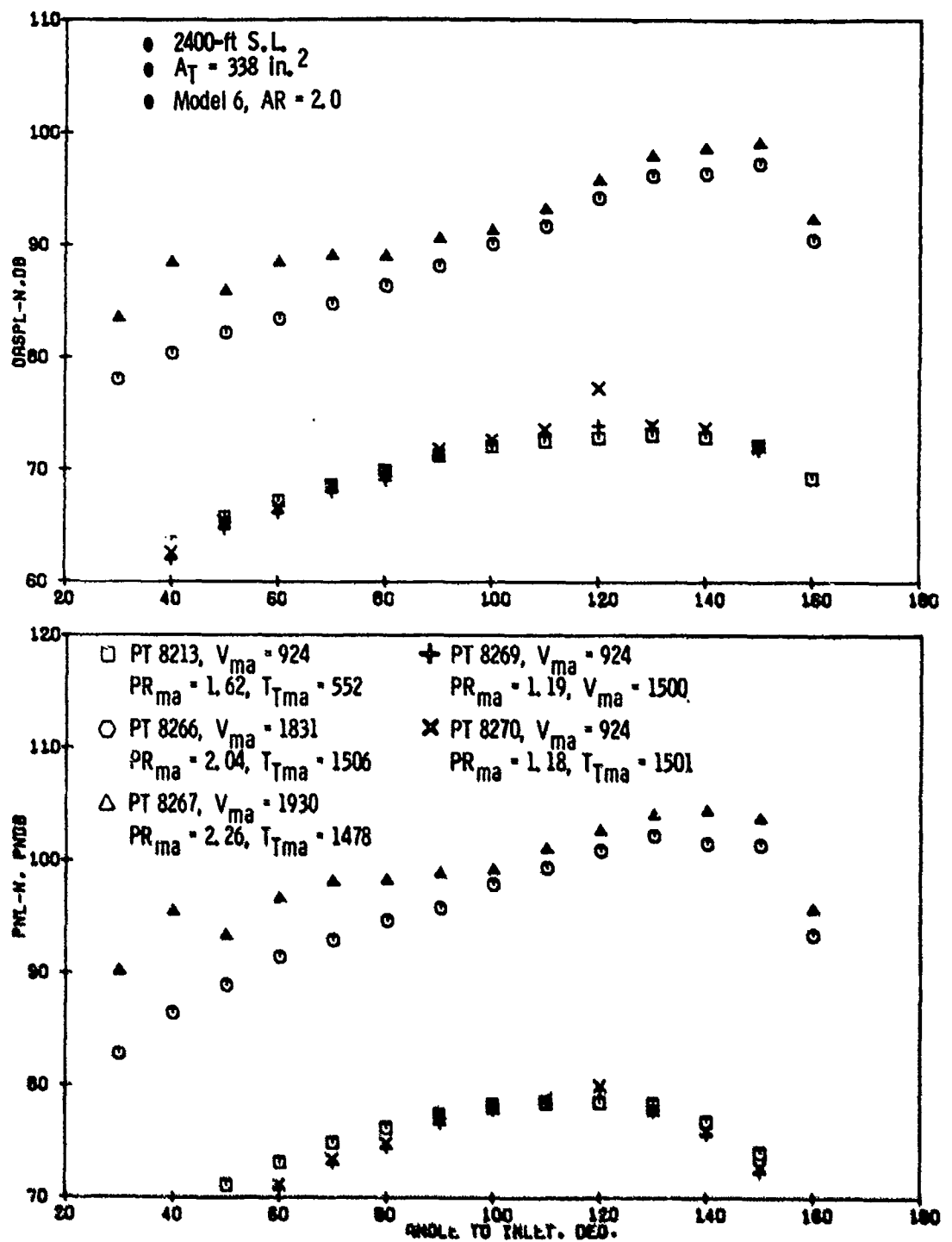


Figure 3-62. Comparison of OASPL and PNL Directivity,  $V_o/V_i = 2.0$ , AR = 2.0 Coplanar-Coannular Nozzle (Model 6).

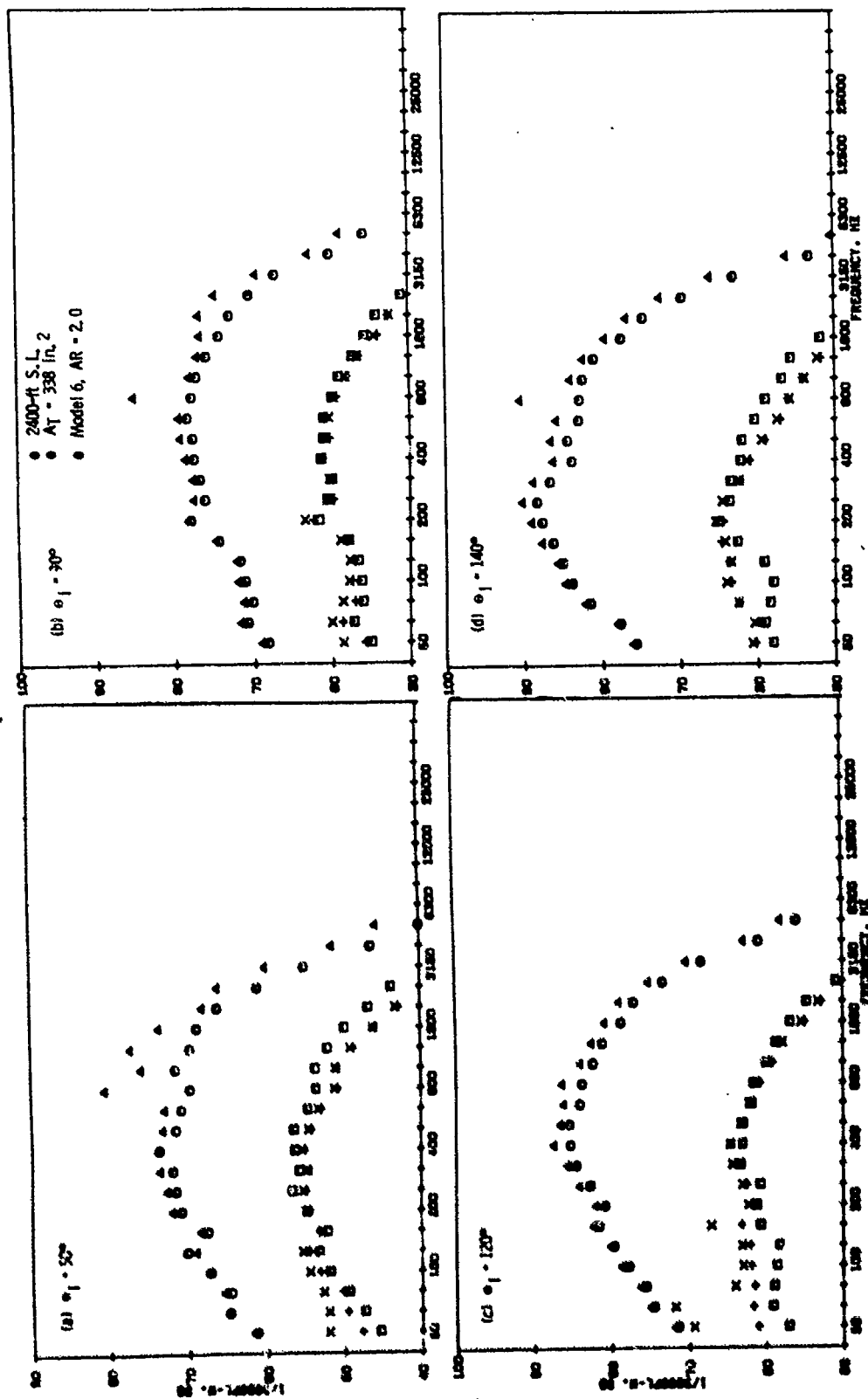


Figure 3-63(a). Normalized Spectra,  $V_0/V_1 = 1.25$ ,  $AR = 2.0$  Coplanar-Coannular Nozzle (Model 6).

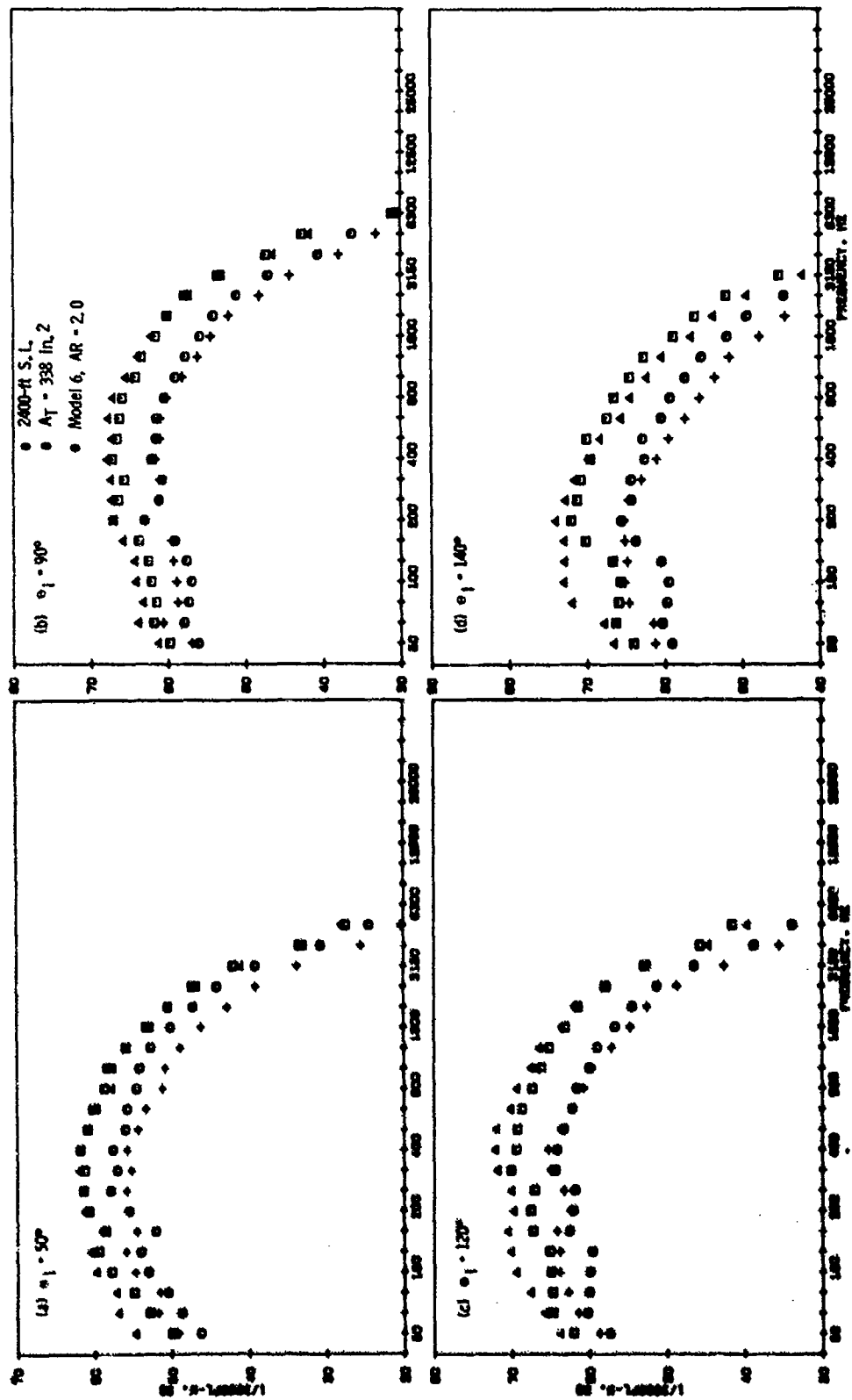


Figure 3-63(b). Normalized Spectra,  $V_0/V_1 = 2.0$ , Coplanar-Coannular Nozzle (Model 6).

#### 3.4.1.5 Dual-Flow Parametric Study (Models 6, 7, and 8)

Test data similar to that described in the previous section were obtained on AR = 0.65 (Model 7) and 0.4 (Model 8) coplanar-coannular nozzles. In conjunction with the previous results, they will be used to evaluate the impact of nozzle area ratio on suppression characteristics for inverted-flow cycles.

The geometric characteristics of these nozzles are defined on Figures A-7 and A-8 in Appendix A. The thermodynamic conditions are summarized on Tables 7 and 8 in Appendix B.

Normalized PNL levels for the three nozzles are on Figure 3-64, along with conical nozzle data; presented as a reference for establishing suppression level. No consistent trend of suppression with area ratio is observed. The maximum suppression level obtained is 4 dB and occurs at both velocity ratios of 1.5 and 2.0. Peak OASPL comparisons on Figure 3-65 exhibit similar trends, however, suppression levels up to 5 dB are observed. Normalized OASPL and PNL characteristics at 90° are summarized on Figure 3-66. Trends are similar to those observed at the peak noise angle with the exception that the absolute level of suppression has decreased. Comparisons at 50° are presented on Figure 3-67 and show suppression level to increase as velocity ratio decreases. The variation of noise level with nozzle area ratio is a function of velocity ratio.

Directivity and spectra comparisons are presented on Figures 3-68 through 3-73. PNL and OASPL directivity characteristics are evaluated for velocity ratios of 1.0, 1.5 and 2.0. The inner velocity, is held constant at 1000 ft/sec and the data are normalized for thrust and temperature. Comparisons at a velocity ratio of 1.0, on Figure 3-68, show no significant change in PNL or OASPL characteristics as area ratio varies. Similarly at velocity ratios of 1.5 and 2.0, on Figures 3-69 and 3-70, a reduction of 3 to 9 dB occurs as area ratio decreases from 2.0 to 0.4. The variation in noise level is a function of area ratio, velocity ratio, and acoustic angle; the maximum variation occurring at a velocity ratio of 2.0. Noise level variation with area ratio is significant when holding inner stream cycle conditions constant and normalizing for thrust and temperature. On the basis of constant mass average velocity,  $V_{ma}$ , this variation is reduced and demonstrates that noise may be correlated using this parameter. Spectra variations at 50°, 90°, 120° and 140° are summarized on Figure 3-71 for a velocity ratio of 1.0. With the exception of frequencies below 160 Hz, where the data are strongly influenced by ground reflection, the spectrum shapes and levels are equivalent. Similar comparisons for velocity ratios of 1.5 and 2.0 are summarized on Figures 3-72 and 3-73. The difference between the three configurations is frequency dependent. Comparison of the 50° spectra for velocity ratios of 1.5 and 2.0 illustrates a change in spectrum shape as the outer stream pressure ratio increases. Also the variation in level due to nozzle area ratio is found to increase significantly compared to the 1.5 velocity ratio comparisons. This is attributed to shock noise occurring in the forward quadrant. The comparisons also suggest that reduction of the outer stream annulus height is an effective way to reduce shock noise as discussed in Section 4.6.7, Reference 7.



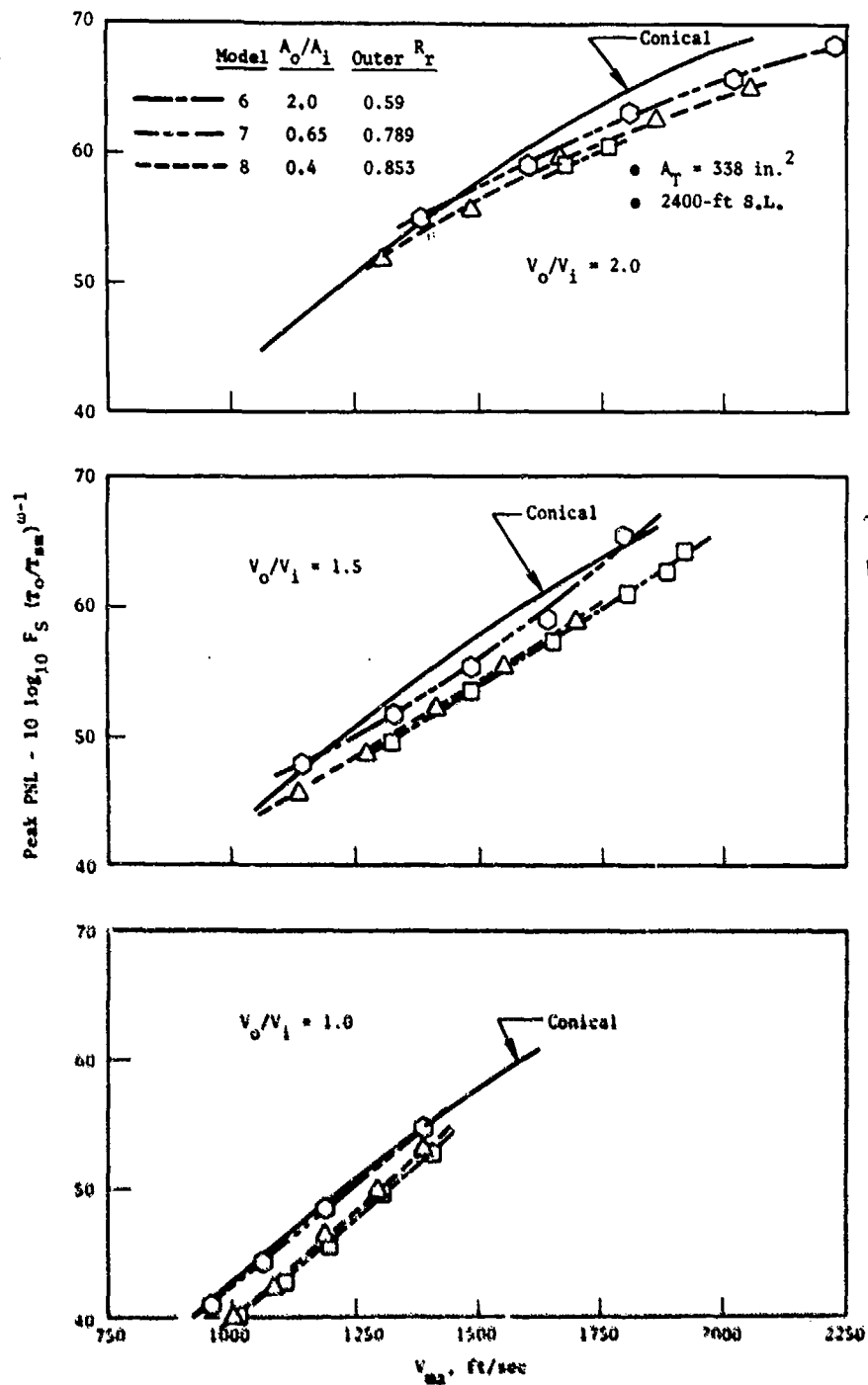


Figure 3-64. Peak PNL Coplanar-Coannular Nozzle Area Ratio Variation.

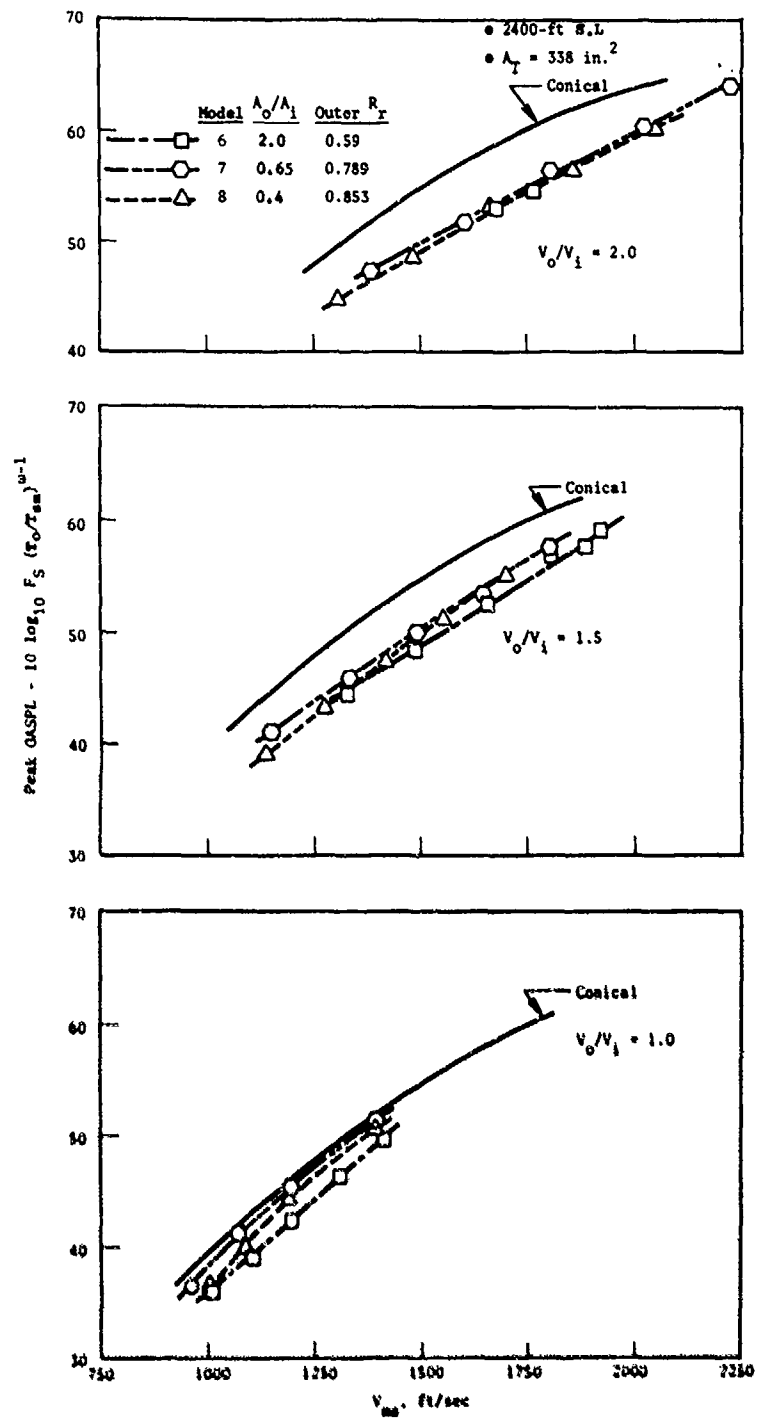


Figure 3-65. Peak OASPL Coplanar-Coannular Nozzle Area Ratio Variation.

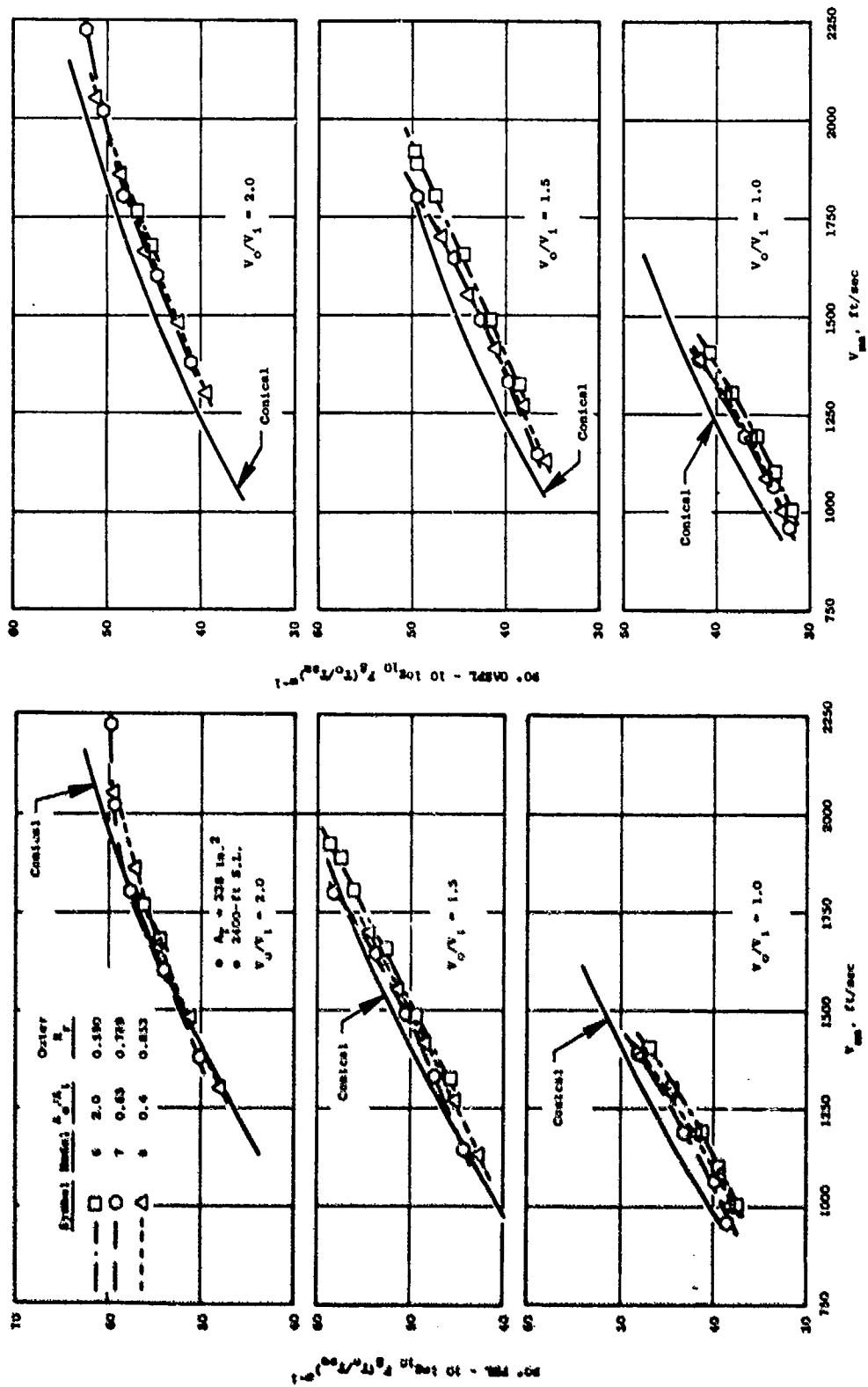


Figure 3-66. 90° FFL and QASPL Coplanar-Coannular Nozzle Area Ratio Variation.

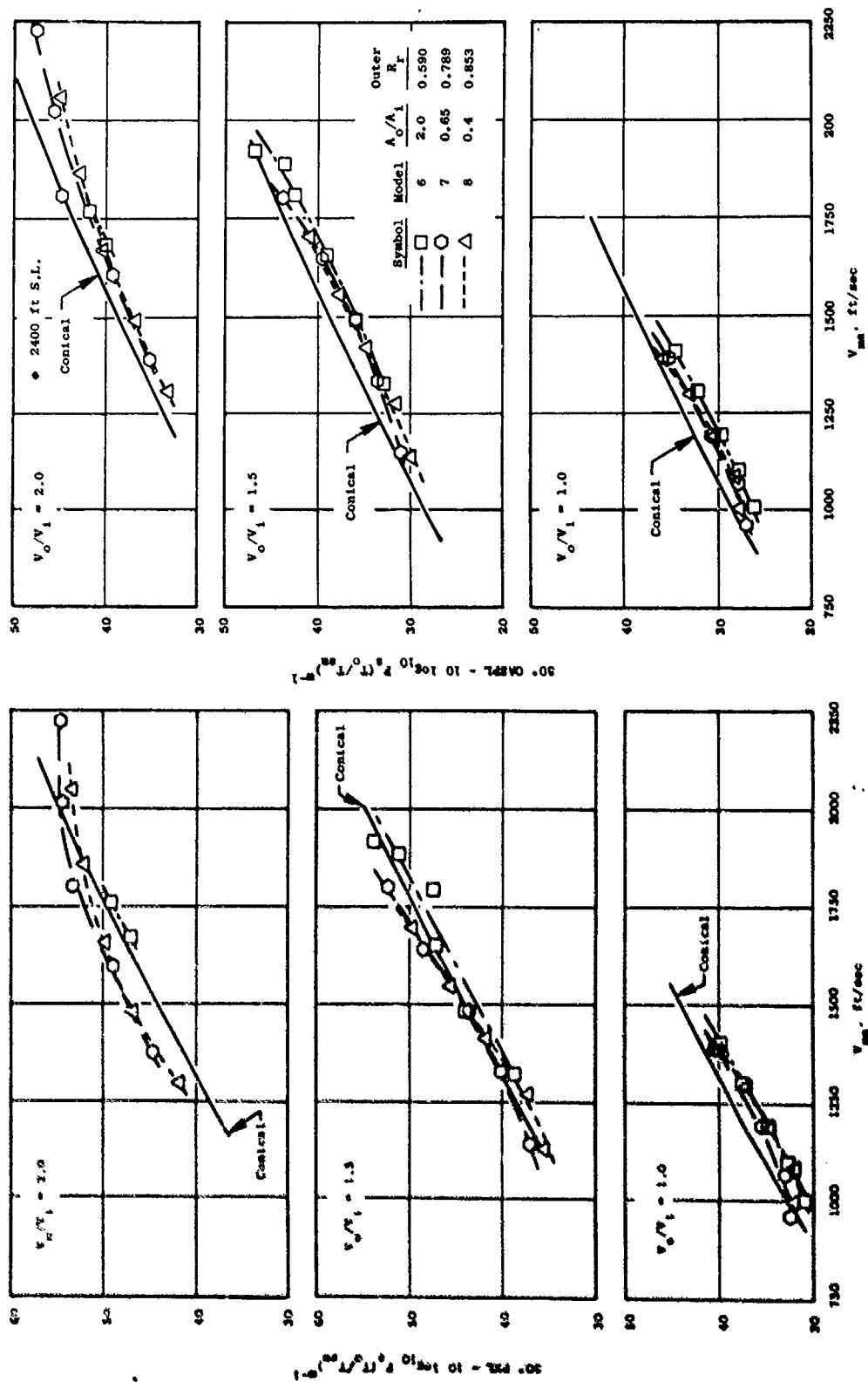


Figure 3-67. 50° FNL and OASPL Coplanar-Coannular Nozzle Area Ratio Variation.

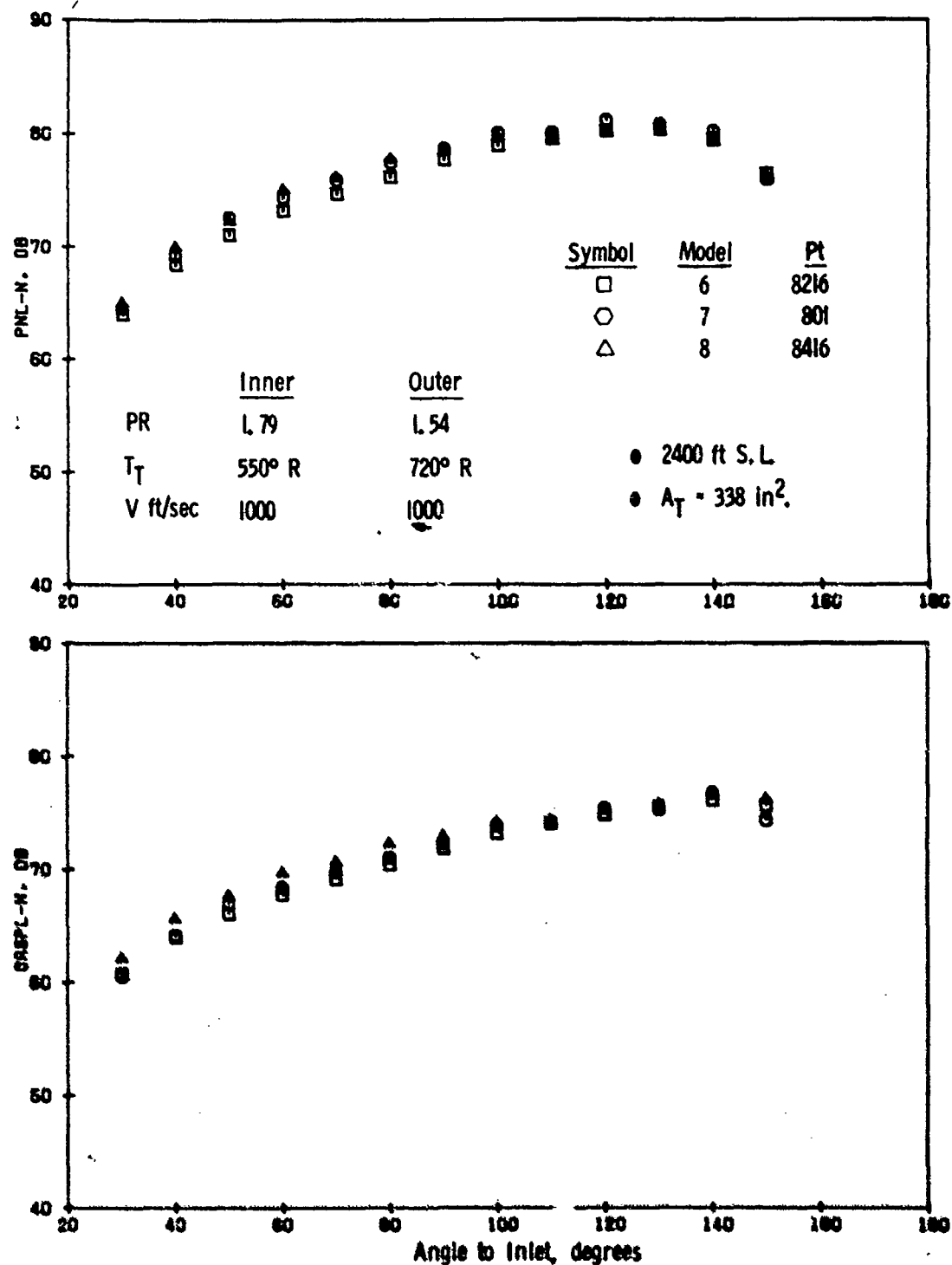


Figure 3-68. OASPL and PNL Directivity Variation with Area Ratio,  $V_0/V_1 = 1.0$ .

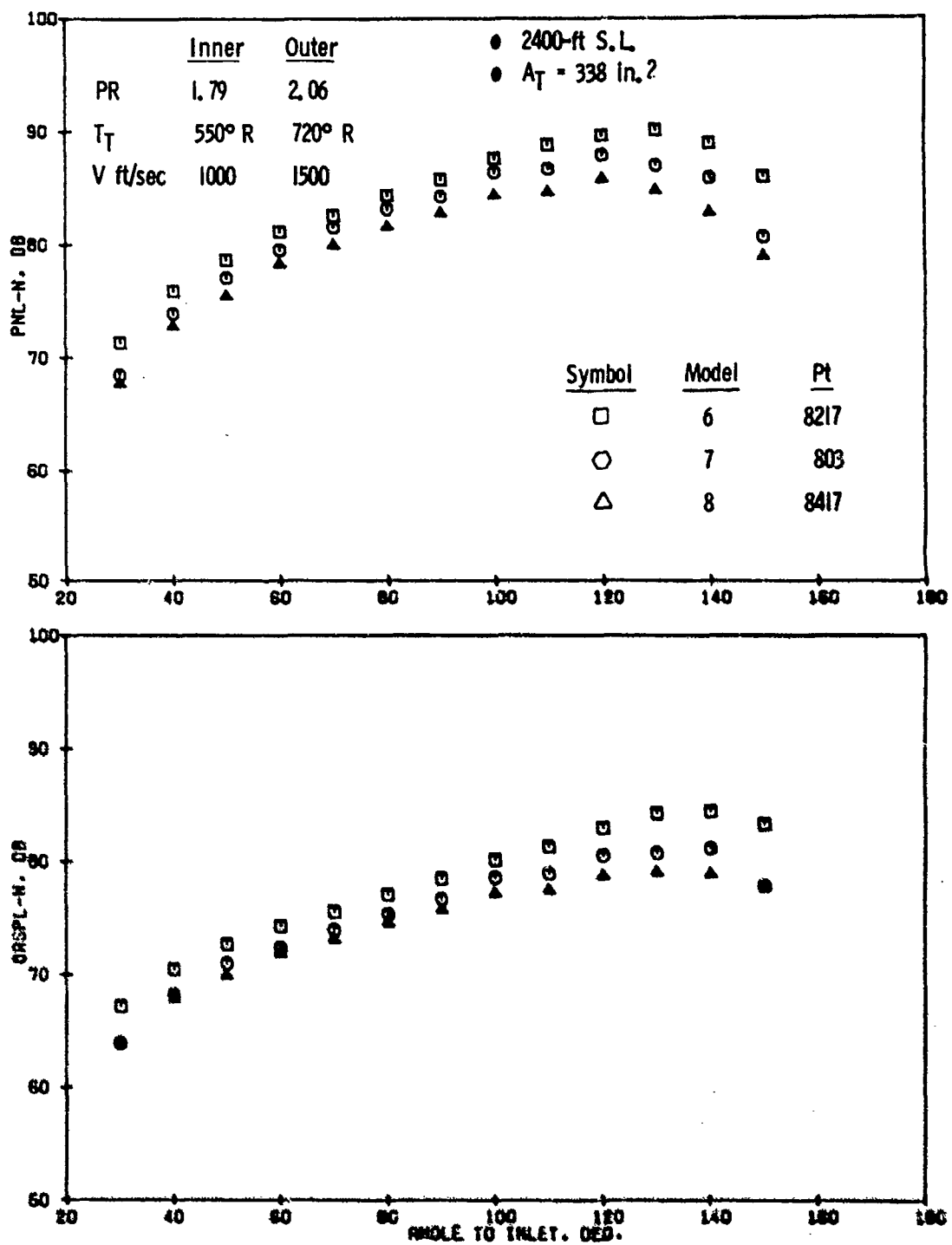


Figure 3-69. OASPL and PNL Directivity Variation with Area Ratio,  $V_0/V_1 = 1.5$ .

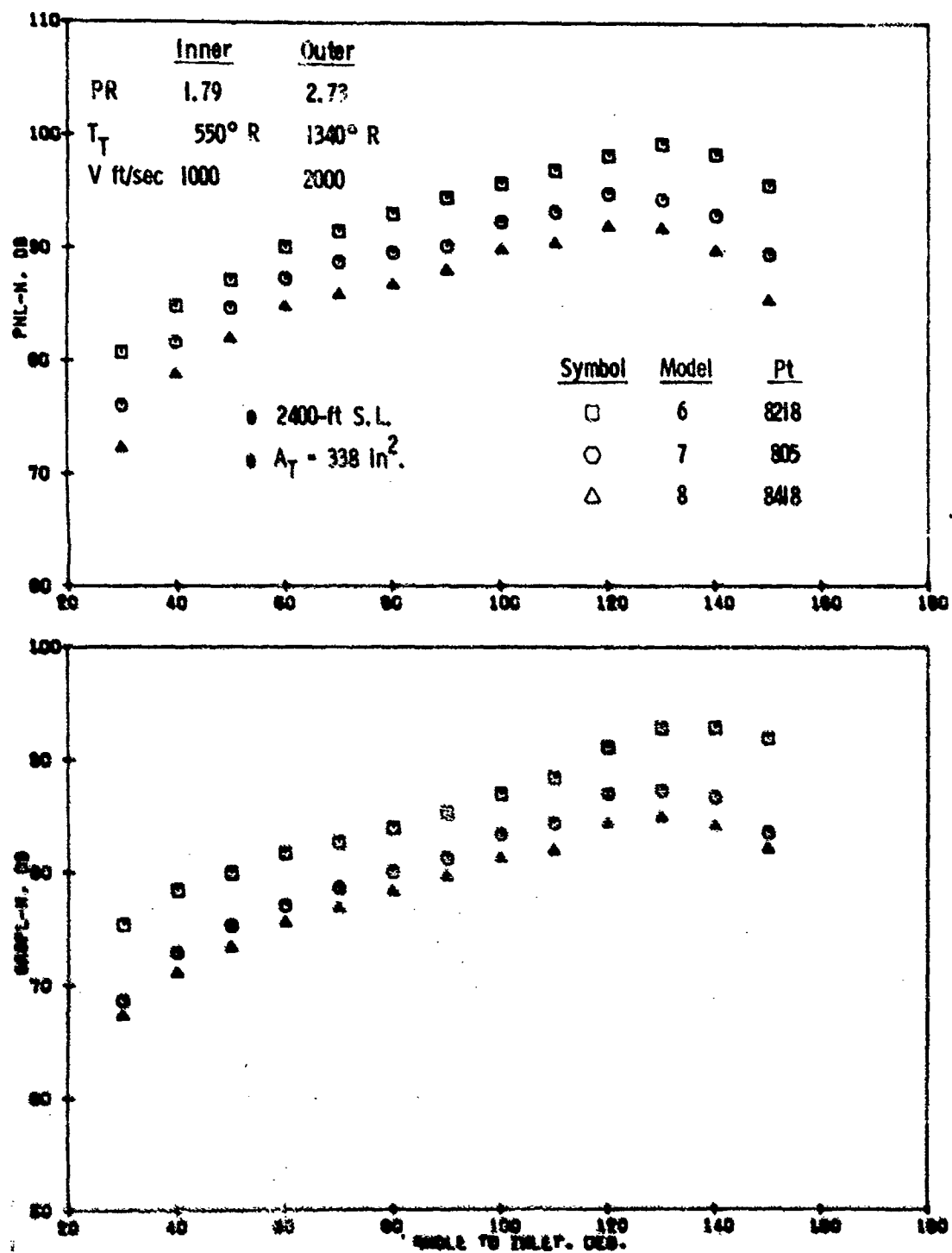


Figure 3-70. CASPL and PNL Directivity Variation with Area Ratio,  
 $V_0/V_1 = 2.0$ .





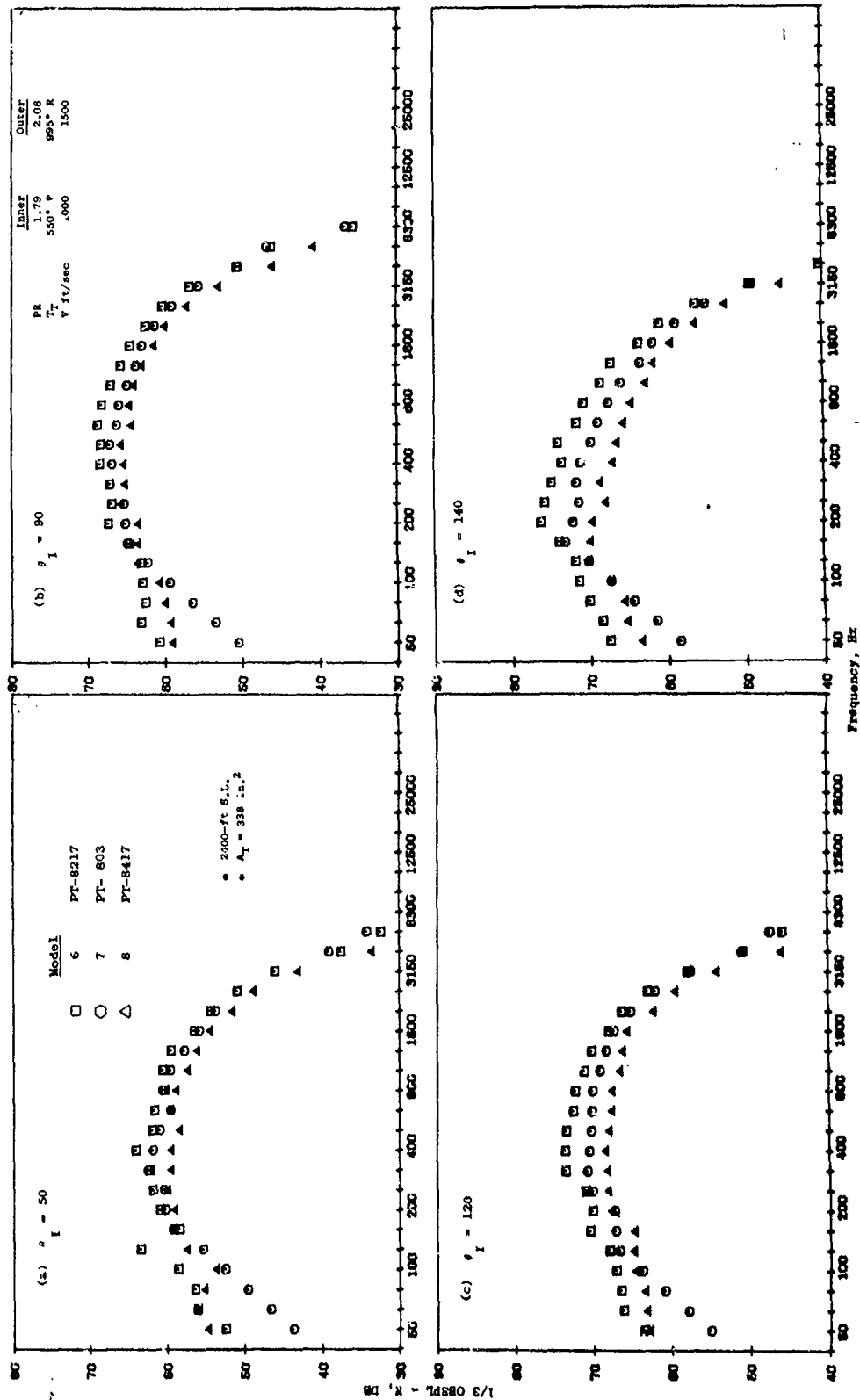


Figure 3-72. Spectra Variation with Area Ratio,  $V_o/V_i = 1.5$ .

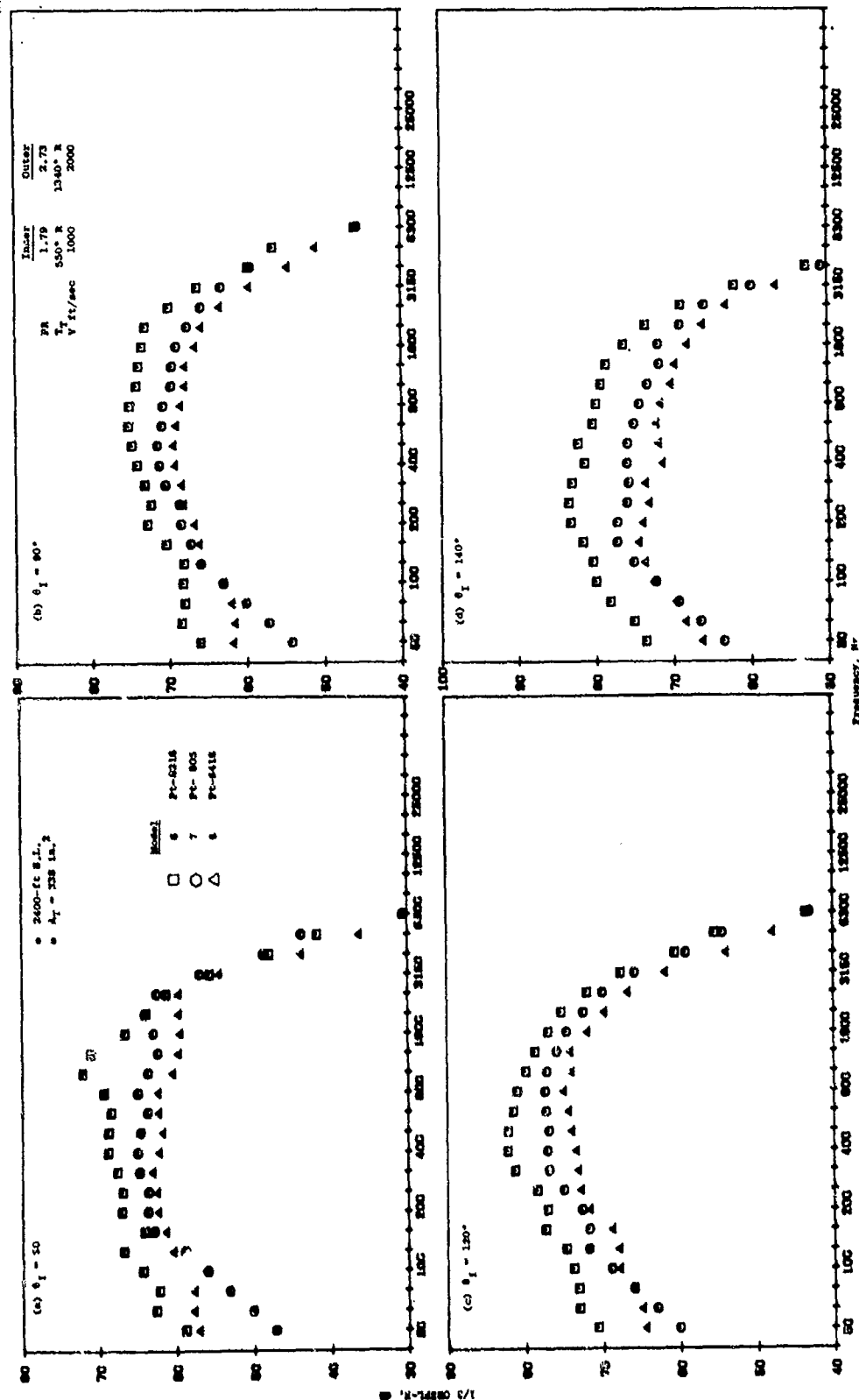


Figure 3-73. Spectra Variation with Area Ratio,  $V_0/V_1 = 2.0$ .

### 3.4.1.6 Unsuppressed Annular Jet Study

In addition to conventional and inverted flow cycles, coplanar coannular nozzles were also tested at cycle conditions where (a) the inner stream flow was reduced to zero and (b) it was held to be less than 10% of the outer stream: termed testing with "low inner flow."

The low inner flow configurations were nozzles 9, 10, and 12 having  $A_o/A_i = 2.0, 0.65$  and  $0.4$ , respectively. The zero inner flow nozzles were configurations 11 and 13 have  $A_o/A_i = 0.65$  and  $0.4$ , respectively.

The detailed geometric parameters of these exhaust nozzles are summarized on Figures A-9 through A-13 in Appendix A. The thermodynamic conditions are summarized on Tables 9 thru 13 in Appendix B.

Normalized peak and  $90^\circ$  suppression levels as a function of velocity are summarized for the low inner flow test series on Figure 3-74(a). Suppression levels increase as area ratio decreases;  $>8$  peak PNdB being measured for the  $A_i/A_o = 0.4$  nozzle (Model 12) in contrast to only 4 peak PNdB for  $A_i/A_o = 2.0$  (Model 9). This trend is significantly different than discussed in the previous section for inverted-flow cycles, where suppression level was only a weak function of area ratio.

The influence of zero inner flow for the  $A_o/A_i = 0.4$  coplanar-coannular nozzle (Model 13) is summarized on Figure 3-75. The reduction of inner flow to zero is found to decrease the average suppression at the peak noise angle by 3 to 7 PNdB. Significant changes in the noise levels at  $90^\circ$  are also observed.

A similar comparison for the  $A_o/A_i = 0.65$  configuration (Model 11) is presented on Figure 3-76. Suppression is also observed to decrease with reduction of the inner flow to zero, however, the decrease in suppression is from 1 to 3 dB. The absolute level of suppression also decreases when compared with the  $A_o/A_i = 0.4$  configuration (Model 13).

Normalized PNL and OASPL directivity patterns are presented on Figures 3-77 and 3-78 for outer stream velocities of 2350 ft/sec and 1800 ft/sec. Peak noise level is decreased as area ratio decreases. The noise levels of the three nozzles are within 1 dB at  $90^\circ$ . Selected spectra comparisons at these conditions are on Figures 3-79 and 3-80, along with conical data at comparable conditions. The  $50^\circ$  spectra at 2350 ft/sec illustrates the classical shock noise spectrum shape. The peak frequency of shock noise increases as area ratio decreases and suppression relative to the conical nozzle in the aft quadrant occurs in the mid to high frequency regime.

Similar directivity and spectra comparisons for  $A_o/A_i = 0.4$  and  $0.65$  coplanar-coannular nozzles, having no inner flow or low inner flow conditions, are summarized on Figures 3-82 thru 3-87. The reduction of the inner flow to zero causes an increase in noise level, particularly in the aft quadrant. The PNL change in the forward quadrant is not as significant as OASPL, indicating a low frequency variance. This observation is supported by the spectra comparisons presented. The trends are similar for the  $A_o/A_i = 0.4$

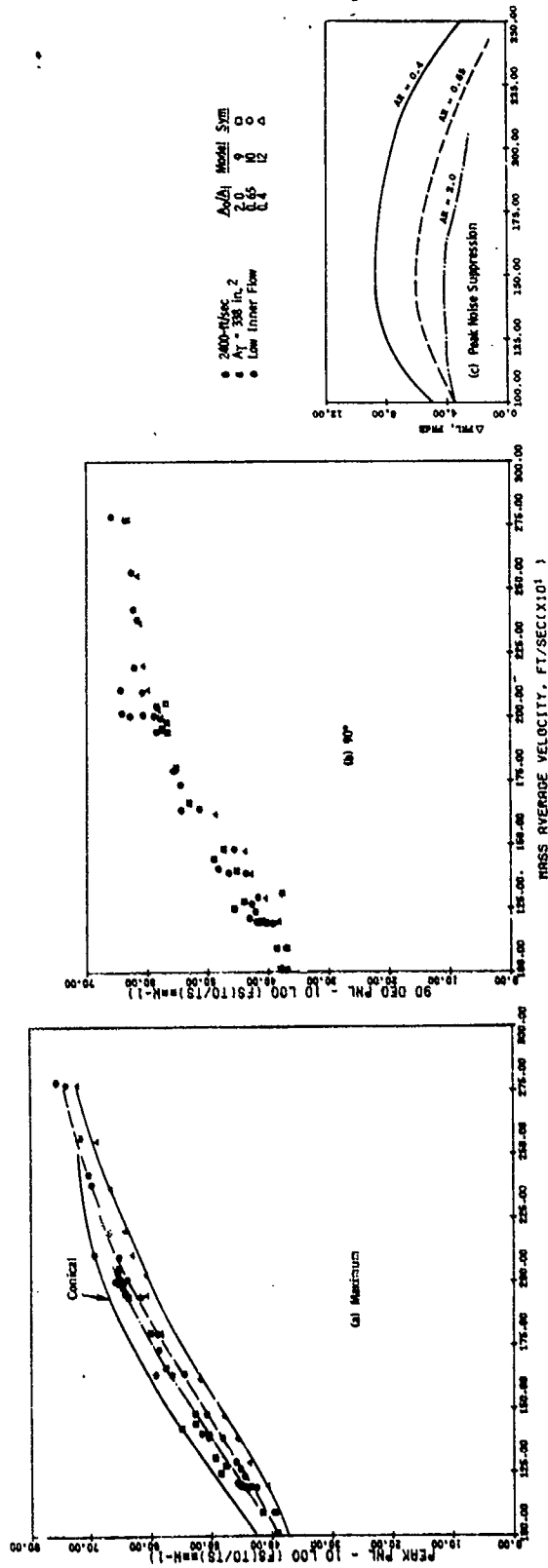


Figure 3-74. Coannular-Coplanar Nozzle Suppression Characteristics with Varying Nozzle Area Ratio.

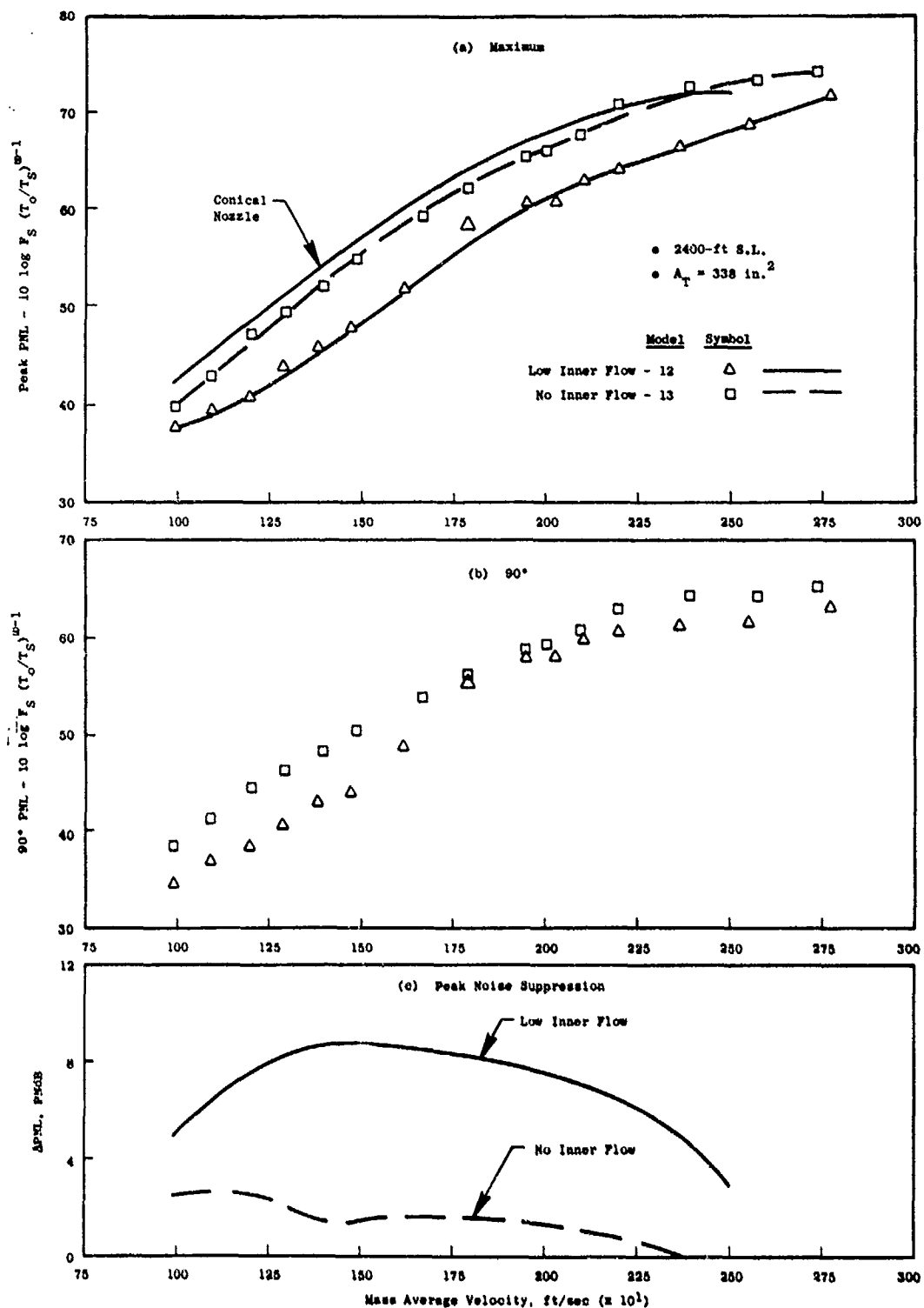


Figure 3-75. Impact of Cycle Variation on Suppression Characteristics of  $A_0/A_1 = 0.4$  Coplanar-Coannular Nozzle (Models 12 and 13).

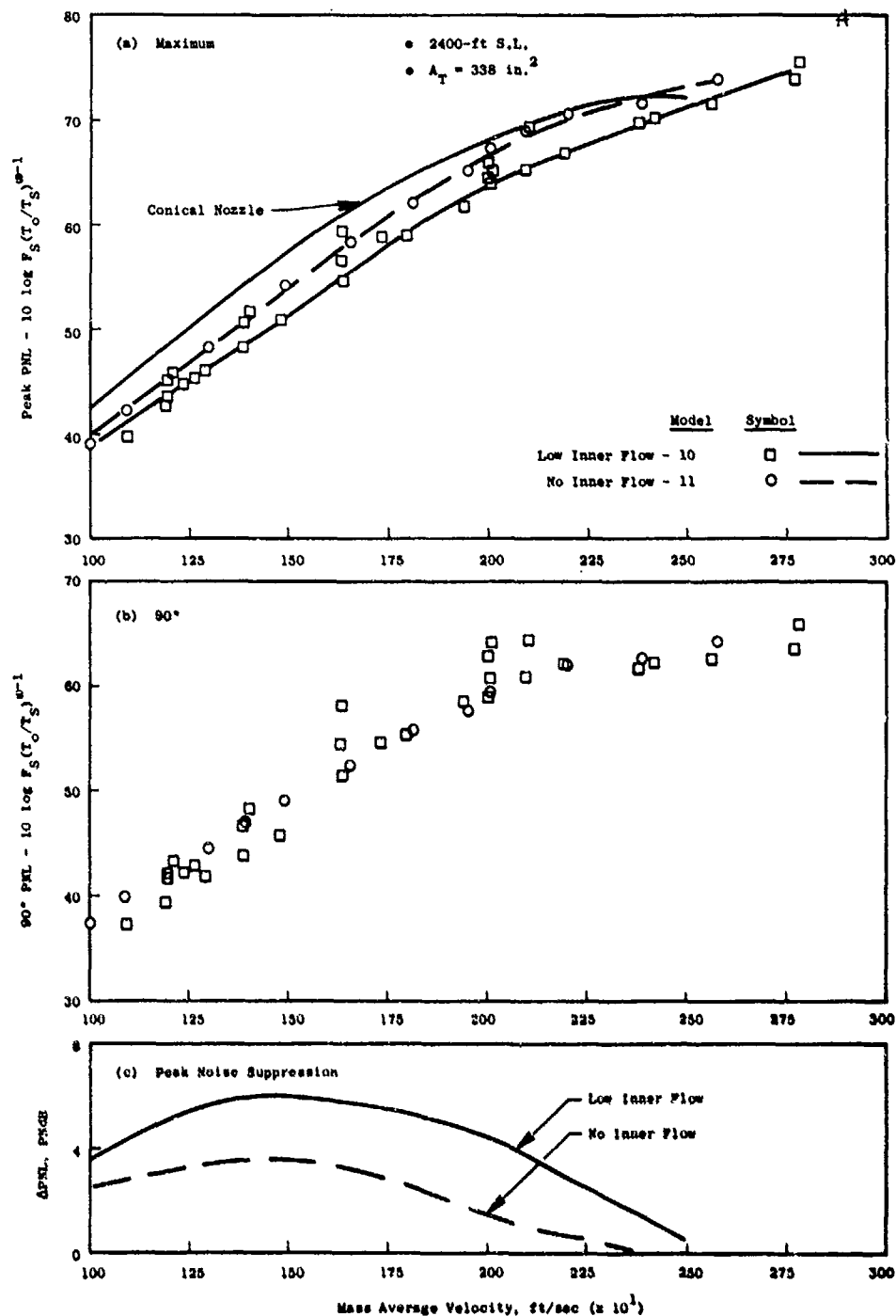


Figure 3-76. Impact of Cycle Variation on Suppression Characteristics of  $A_O/A_1 = 0.65$  Coplanar-Coannular Nozzle (Models 10 and 11).

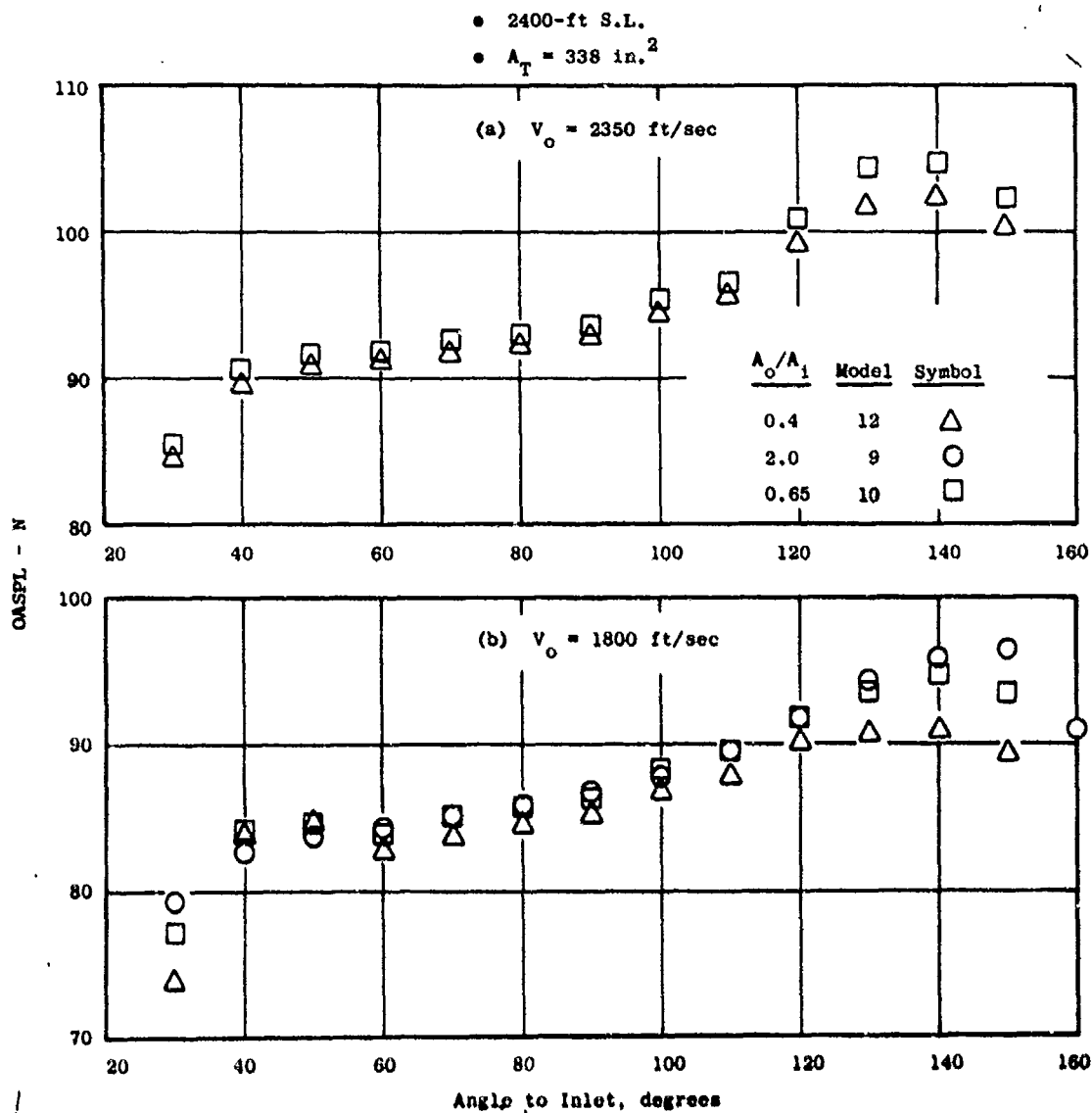


Figure 3-77. OASPL Directivity Variation with Area Ratio,  $w_1/w_o < 0.1$ .

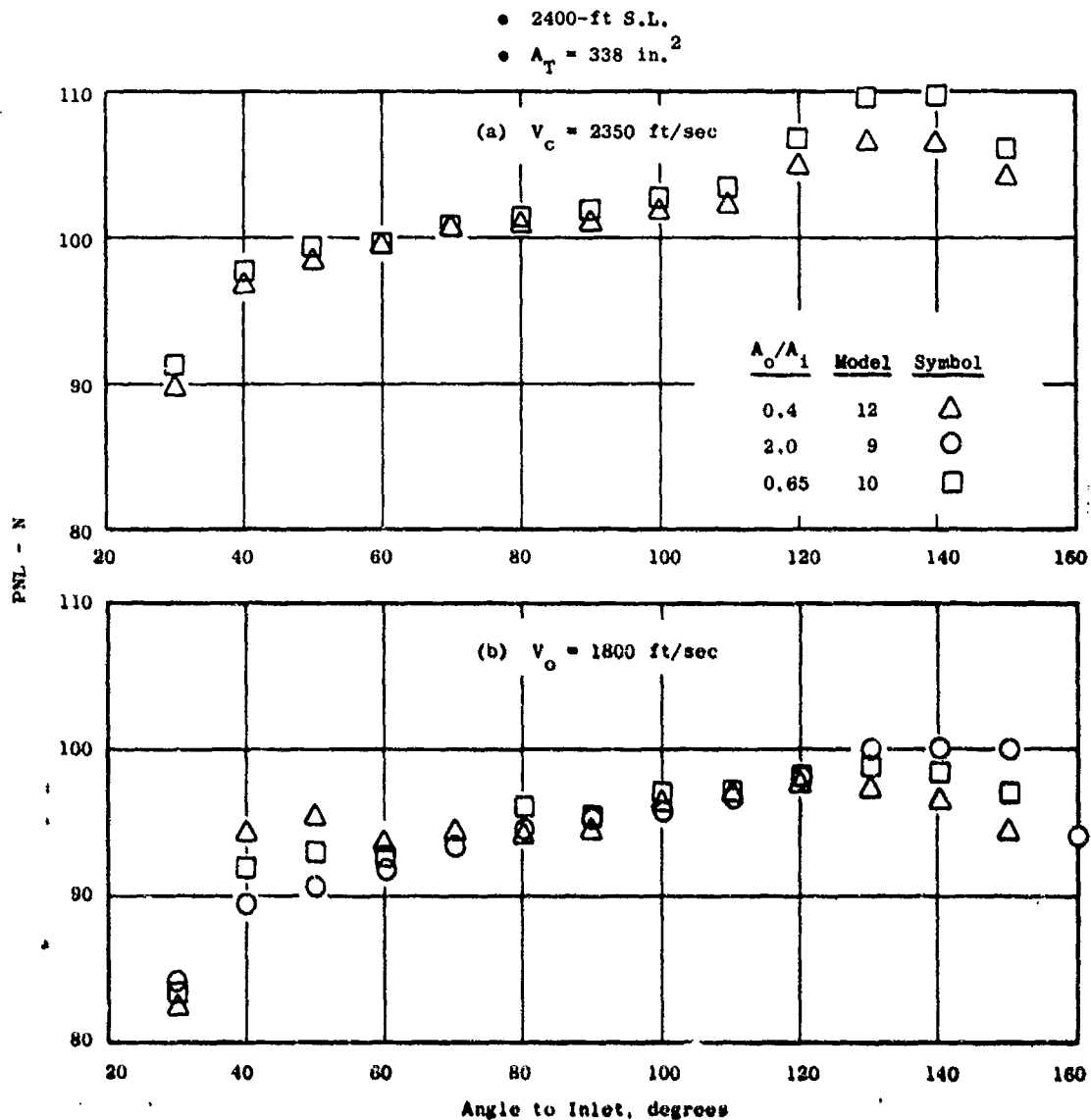


Figure 3-78. PNL Directivity Variation with Area Ratio,  $w_1/w_o < 0.1$ .



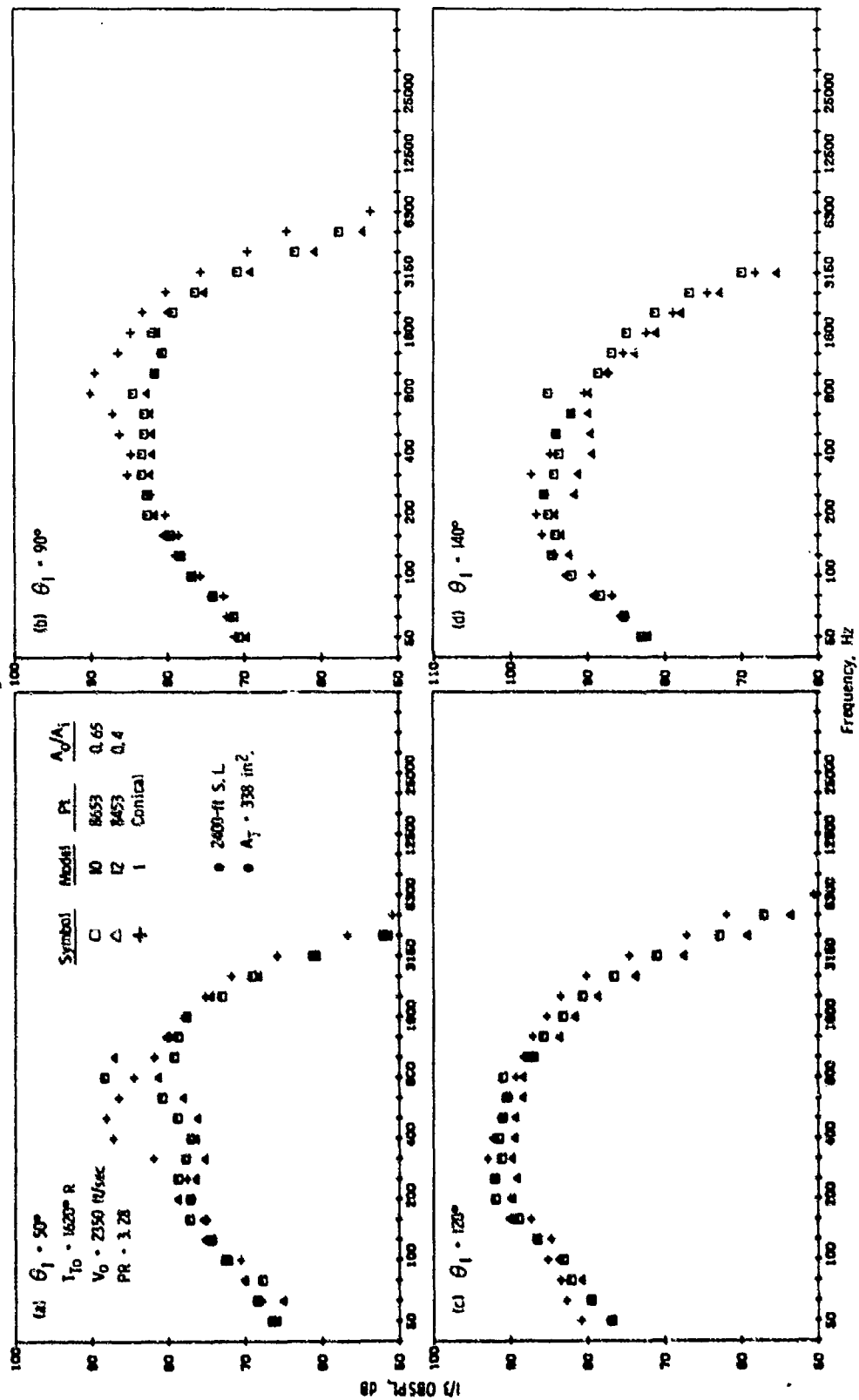


Figure 3-79. Spectra Variation with Area Ratio,  $V_{ma} = 2350 \text{ ft/sec}$ .

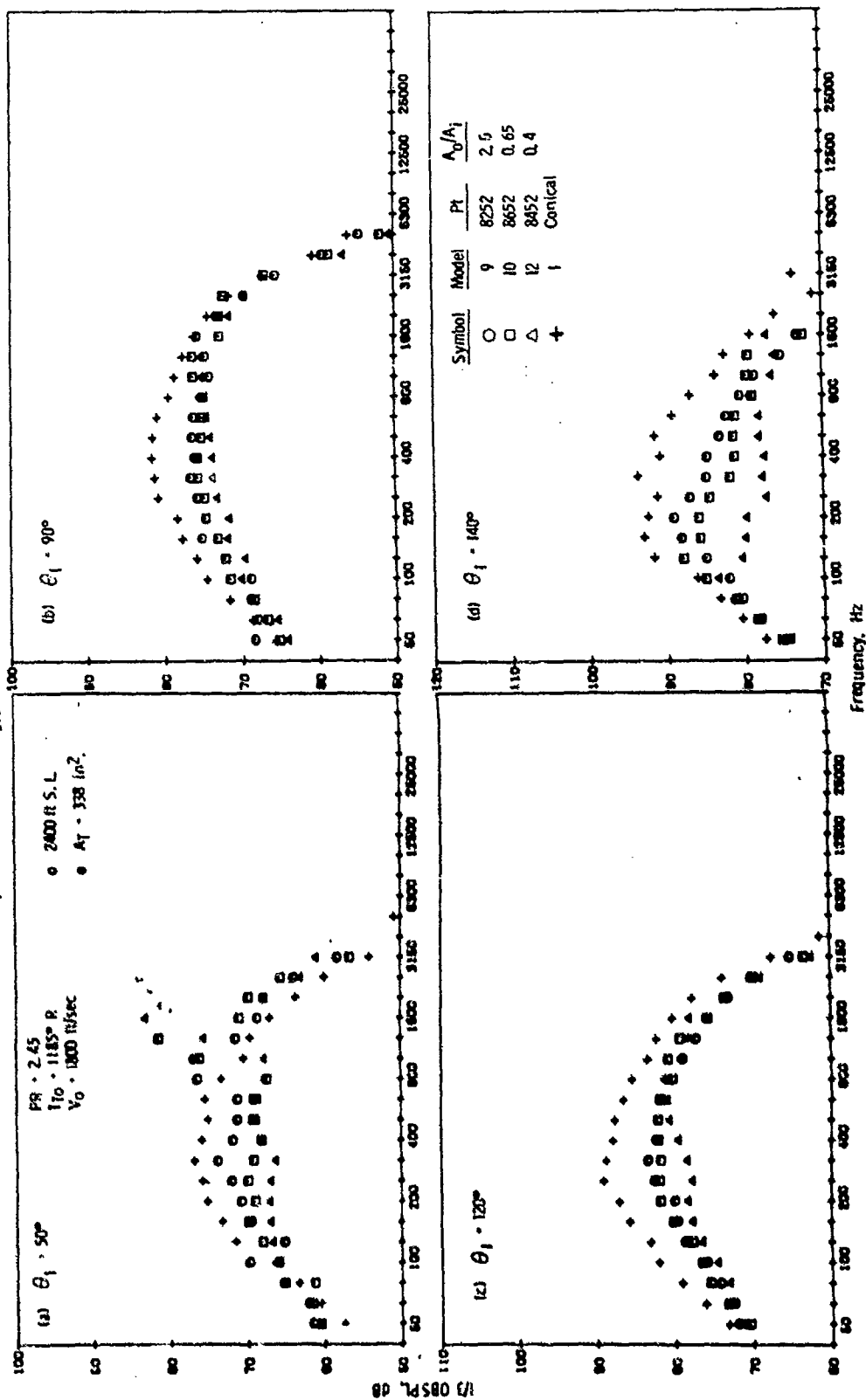


Figure 3-80. Spectra Variation with Area Ratio,  $V_{ma} = 1800$  ft/sec.

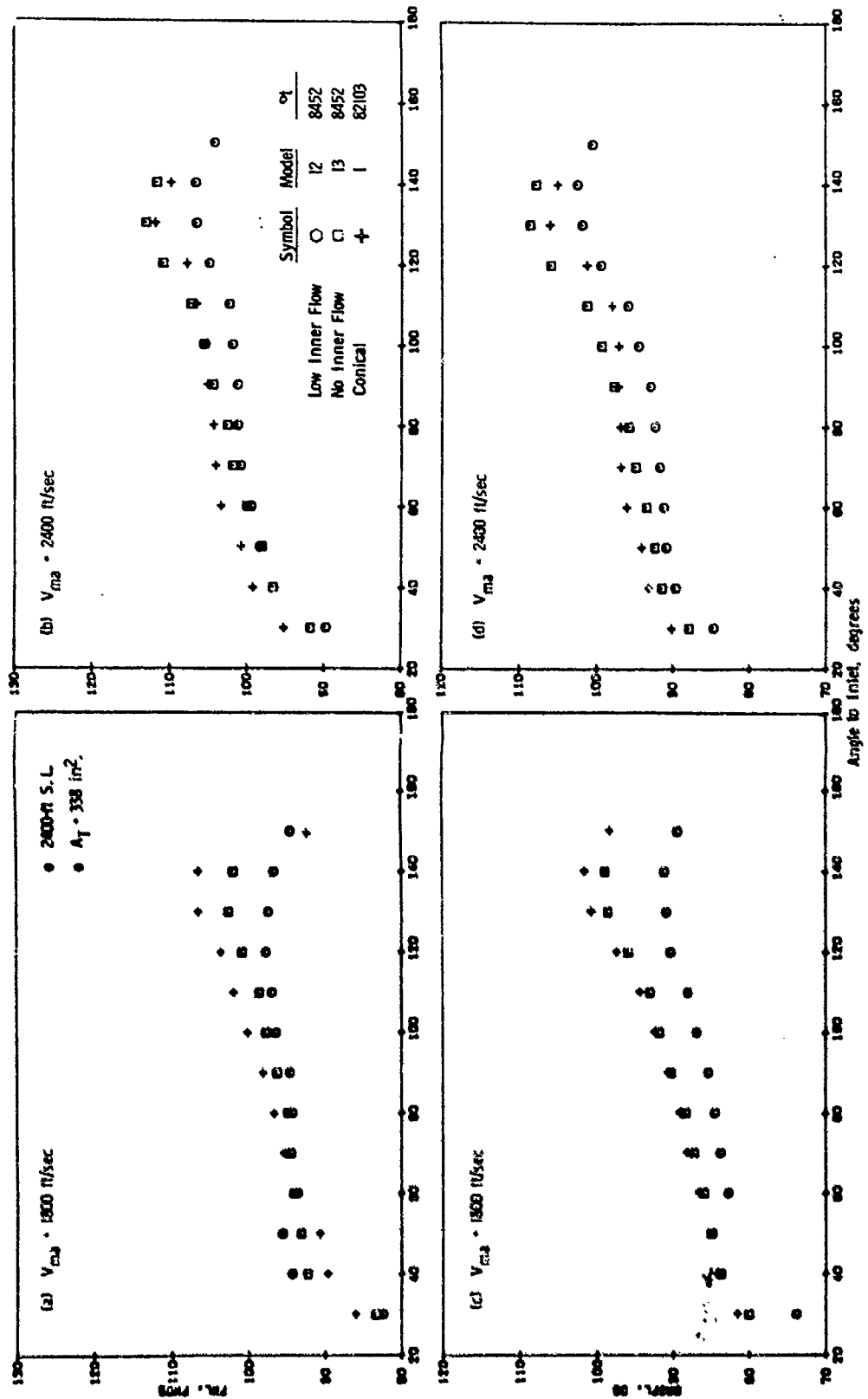


Figure 3-81. Impact of Inner Flow Variation,  $A_0/A_1 = 0.4$ , PNL and OASPL Directivity.

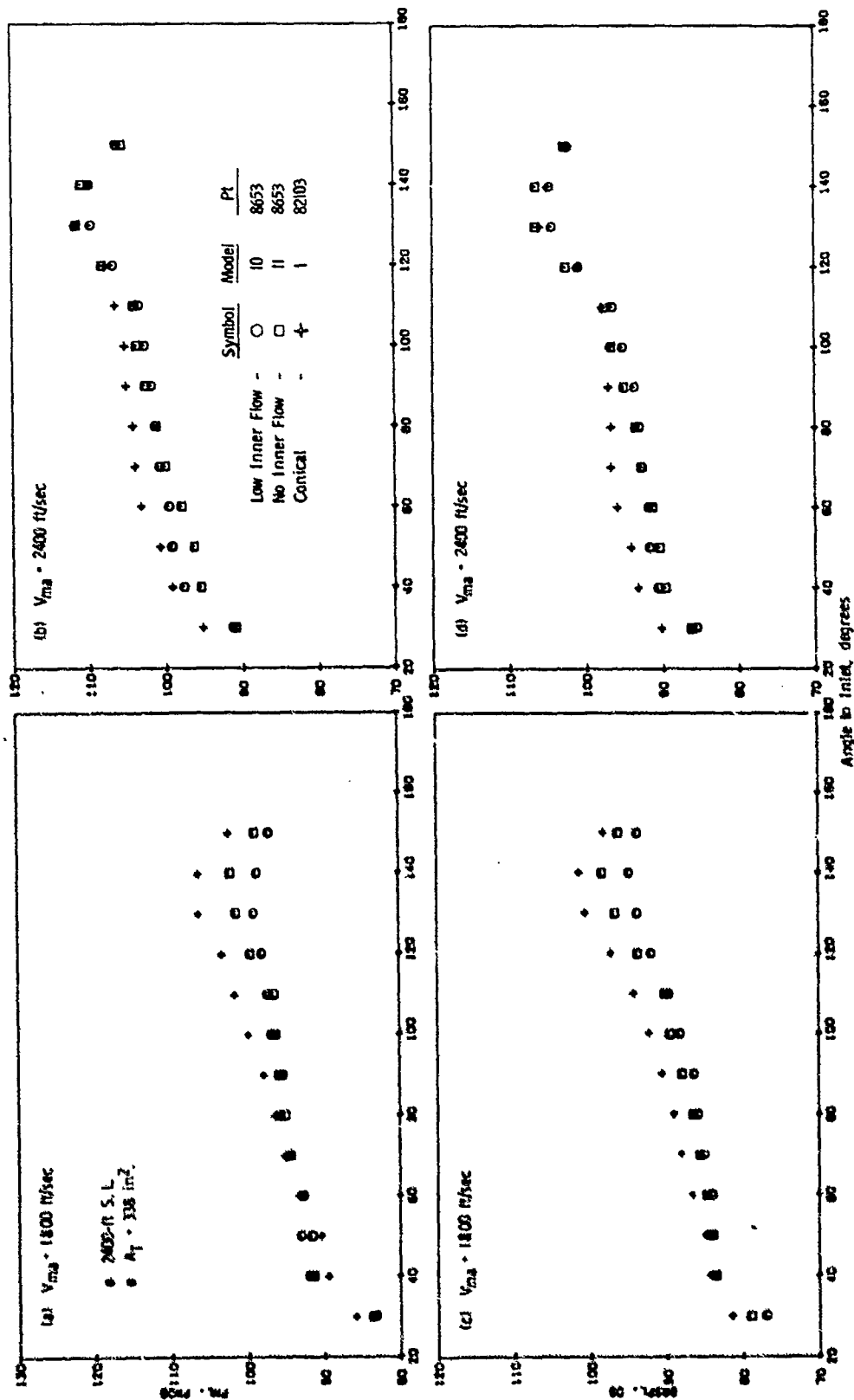


Figure 3-82. Impact of Inner Flow Variation,  $A/A_1 = 0.65$ , PNL and OASPL Directivity.

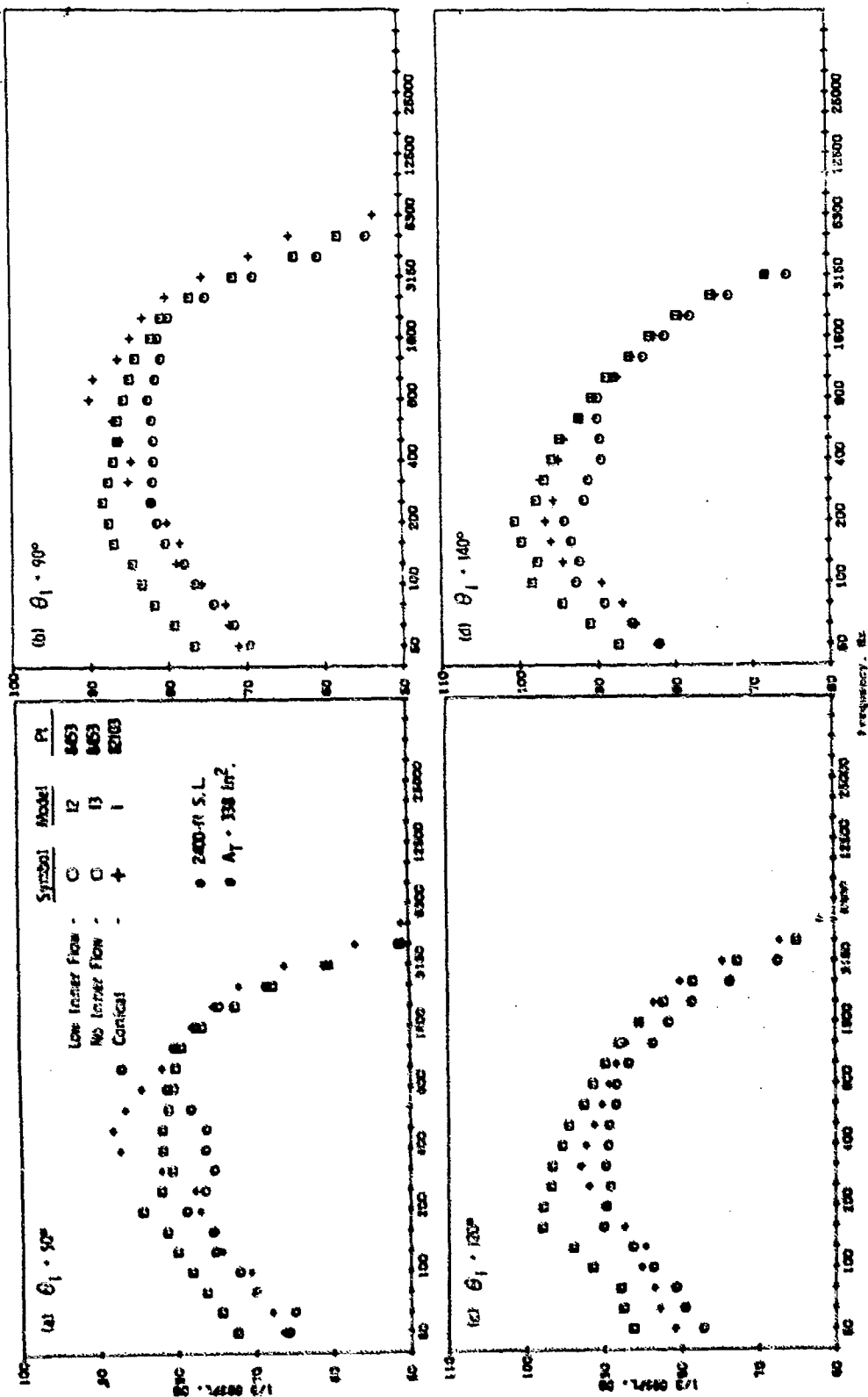


Figure 3-83. Impact of Inner Flow Variation on Spectra,  $A_0/A_1 = 0.4$ ,  $V_{na} = 2400 \text{ ft/sec}$ .

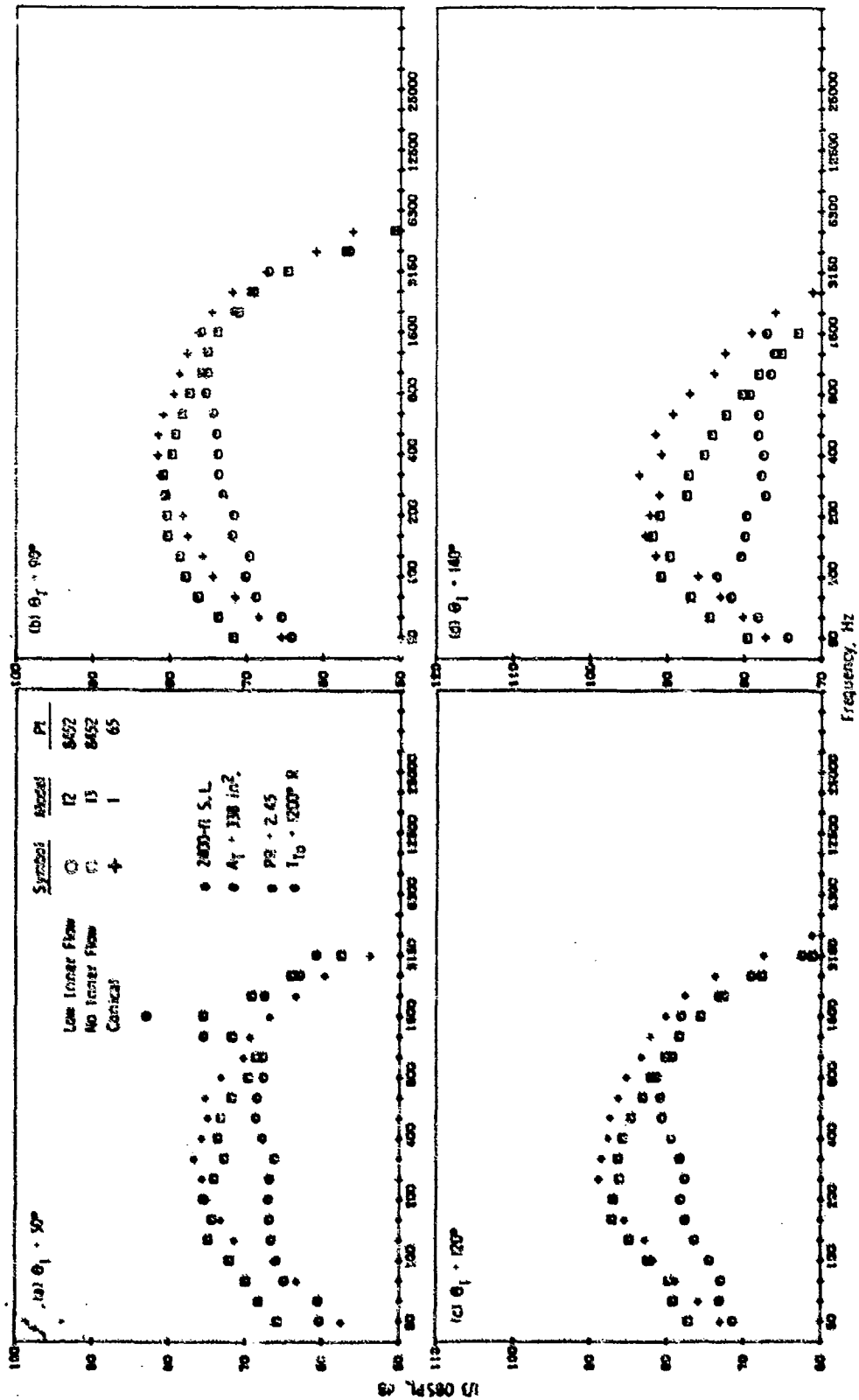


Figure 3-84. Impact of Inner Flow Variation on Spectra.  $A_0/A_1 = 0.4$ ,  $V_{ma} = 1800 \text{ ft/sec}$ .

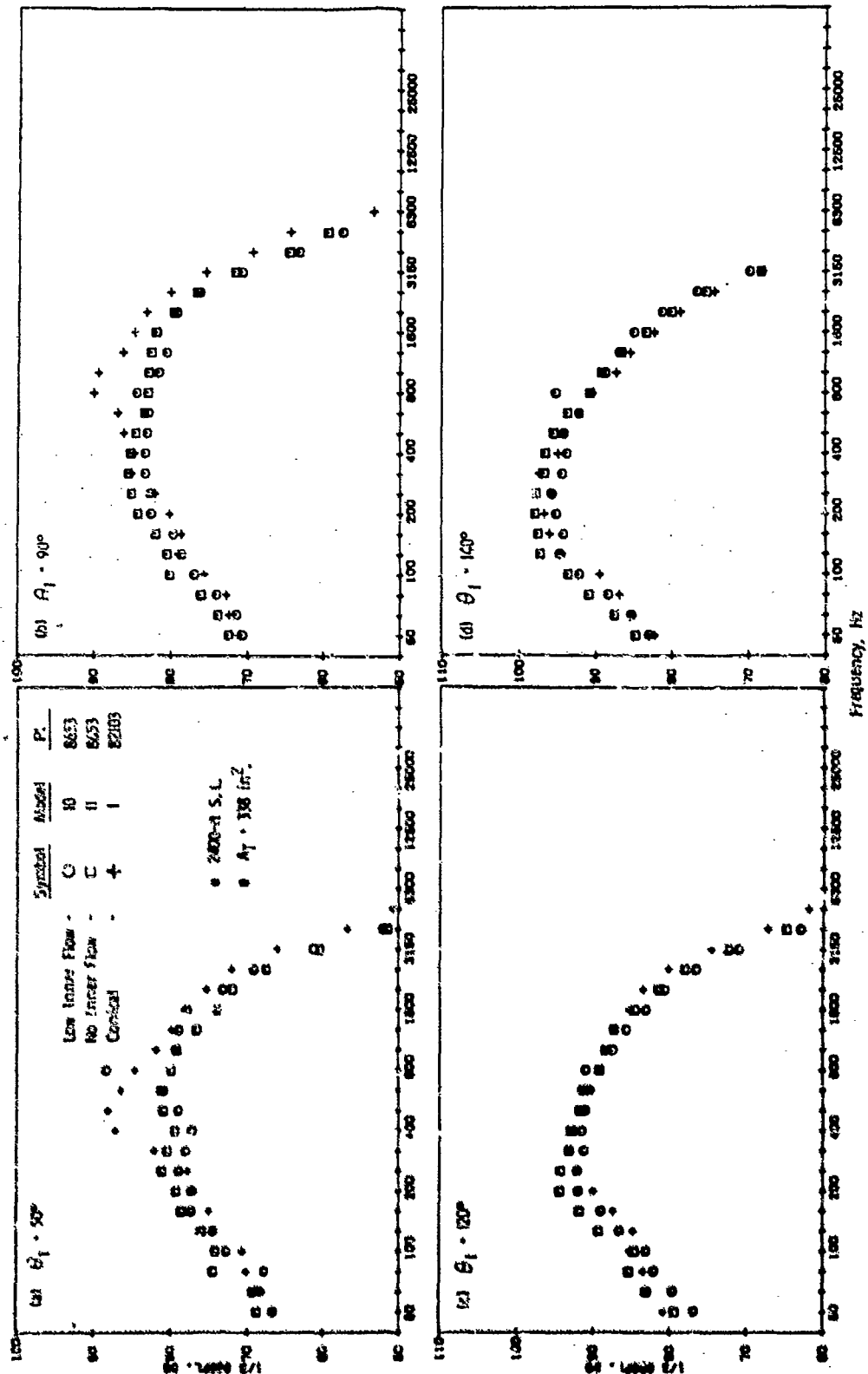


Figure 3-85. Impact of Inner Flow Variation on Spectra,  $A_0/A_1 = 0.65$ ,  $V_{ma} = 2400 \text{ ft/sec}$ .

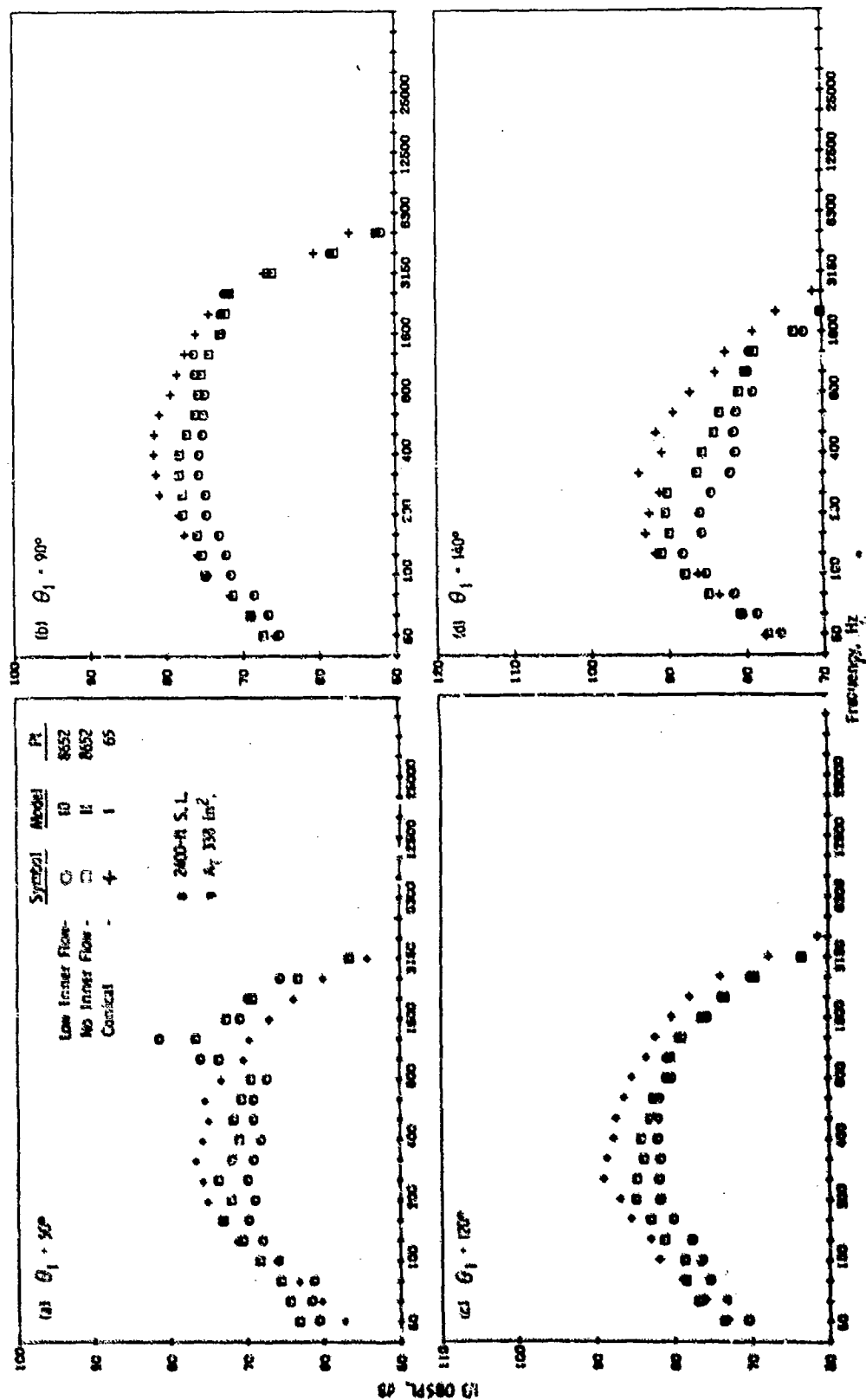


Figure 3-86. Impact of Inner Flow Variation on Spectra,  $A_0/A_1 = 0.65$ ,  $V = 1800$  ft/sec.



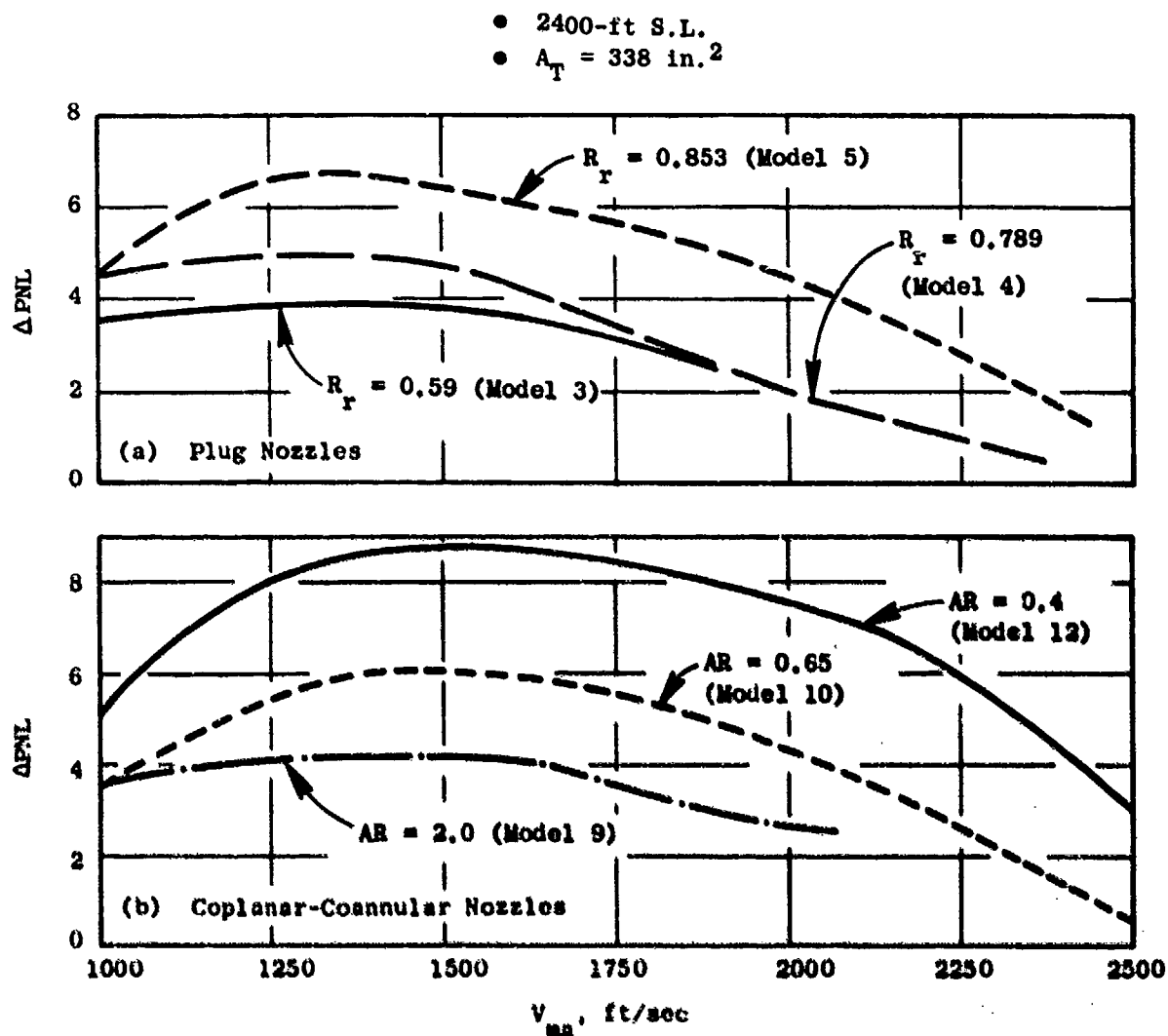


Figure 3-87. Summary of Plug Nozzle and Coplanar-Coannular Nozzle Peak PNL Suppression Levels.

(Models 12 and 13) and 0.65 (Models 10 and 11) nozzles, however, sensitivity of directivity and spectra characteristics to inner stream conditions increases as flow area ratio decreases.

#### 3.4.1.7 Summary

Conical nozzle reference noise levels have been established on the basis of PNL and OASPL variation with velocity, PNL and OASPL directivity, and spectra. These levels will be used as a reference for establishing suppression levels. Measured conical noise levels correlated well with those predicted using existing methods.

Parametric variation of plug nozzle radius ratio showed that the suppression increased with radius ratio as illustrated on Figure 3-87. Parametric studies utilizing coplanar-coannular nozzles having  $A_0/A_1 = 0.4, 0.6$  and 2.0 indicated that for inverted flow cycles, only slight variation of suppression level occurred with change in area ratio. However, a similar study utilizing these configurations showed that if inner-to-outer flow ratio was held to less than 10%, a significant variation of suppression level with area ratio occurred as illustrated on Figure 3-87. Reduction of the inner flow to zero caused a significant loss of suppression.

#### 3.4.2 Tests Related to Suppressors Influenced by Geometric and Cycle Variations, Single- and Dual-Flow Nozzles

This section presents the results of a series of acoustic studies to establish suppression depending on geometric and cycle variations. Both single and dual flow exhaust nozzles were considered. A suppressor design implemented on a single flow nozzle was termed a full span suppressor. The implementation of a suppressor on a dual flow nozzle is termed a half span suppressor, as it extends only across the outer flow stream.

Section 3.4.2.1 presents the results of studies performed to determine the influence of suppressor area ratio and radius ratio on a series of 36-chute nozzles implemented as both half span and full span suppressors. Flow management and inner stream geometry variations are discussed in Section 3.4.2.2. Flow management principles include variation of outer to inner stream parameters of velocity ratio,  $V_0/V_1$ , weight flow ratio,  $\beta = W_0/W_1$ , and area ratio,  $A_0/A_1$ . Flow segmentation studies discussed in Section 3.4.2.3 utilized half span suppressors having 20, 30 and 40 shallow-chutes implemented on a common flowpath geometry. The element type studies in Section 3.4.2.4 utilized 36-spoke and 36-chute nozzles, as both half span and full span suppressors, to establish suppression trends. Studies to evaluate treated ejectors are discussed in Section 3.4.2.5.

In each section the peak noise suppression level was established as a function of jet velocity; referenced to the conical nozzle data of Section 3.4.1.1. The suppression level was found to vary significantly with jet velocity and with several of the geometric parameters evaluated.

### 3.4.2.1 Chute Area and Radius Ratio Studies

#### Area Ratio and Radius Ratio Variable, Turbojet (Models 15, 16 and 17)

This study investigated the influence of changing suppressor nozzle area ratio and radius ratio on a turbojet exhaust nozzle system (see Figure 4.3-1 for description of parameters). Models 15, 16 and 17 of Figure 3-88 were used. Detailed schematics of the test configurations are in Appendix A, Figures 9, 10 and 11. The aft plug geometry ( $15^\circ$  half-angle and plug length) was maintained, as well as the flow area of  $23.76 \text{ in.}^2$  and segmentation with 36 elements. For consistency of design, the chute depth to width ratio,  $D_c/W_c$ , was maintained at 2.54 at the shroud and at 1.53 at the hub.

The following values applied to the model set:

Model No.	Area Ratio	$A_{\text{Blocked}}$ , $\text{in.}^2$	$R_p$ , in.	$R_s$ , in.	$R_r$	$\theta_{\text{plug}}$ , deg.
15	2.5	35.64	3.739	5.738	0.653	7.42
16	2.0	23.76	4.00	5.571	0.716	11.61
17	1.5	11.88	4.22	5.399	0.782	15.86

The acoustic test matrix was defined in Section 3.2.1, Figure 3-8 and utilized both the conventional turbojet cycle line and the high  $T_T$  cycle line.

Acoustic results are presented as peak OASPL and PNL levels along with curve-fitted-data suppression trends relative to the conical baseline in Figures 3-89 and 3-90. Each figure has data separated into the conventional turbojet and high  $T_T$  cycle lines. OASPL and PNL at  $90^\circ$  are presented in Figure 3-91,  $50^\circ$  OASPL and PNL in Figure 3-92 and overall power levels in Figure 3-93. In reviewing the figures it is seen that:

- On a peak OASPL basis, Figure 3-89:
  - Maximum suppression levels of 16 and 15 dB are seen for the the  $AR = 2.5/R_r = 0.653$  suppressor (Model 15) on the high  $T_T$  and conventional turbojet cycle lines, respectively.
  - As area ratio increases from 1.5, Model 17, to 2.5, Model 15, (and radius ratio subsequently decreases from 0.782 to 0.653) the peak OASPL suppression is substantially improved at all mid-to-high  $V_{ma}$  values; an increase in suppression of 6 to 8  $\Delta$ dB is seen at 2250 ft/sec, as an example.
  - At very low  $V_{ma}$  each suppressor performs equivalently, yet all maintain a suppression level near 8 to 9  $\Delta$ OASPL.

● 36 CAUTE

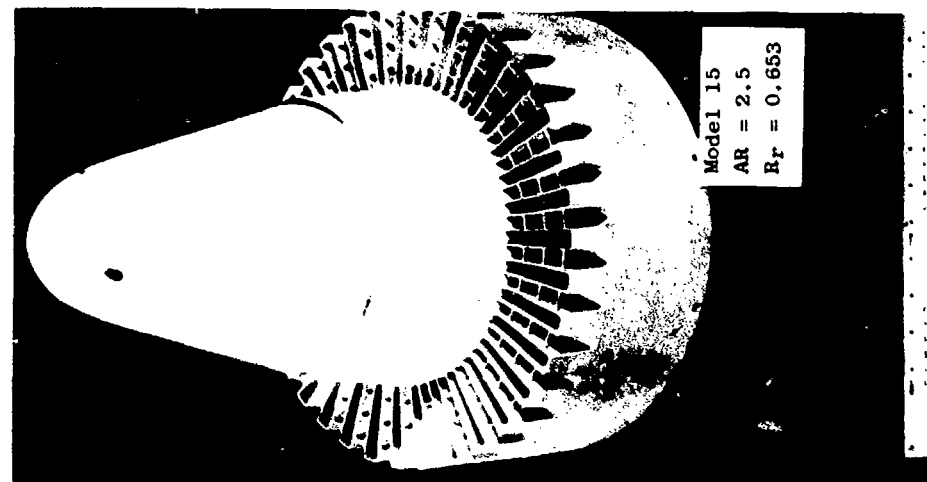
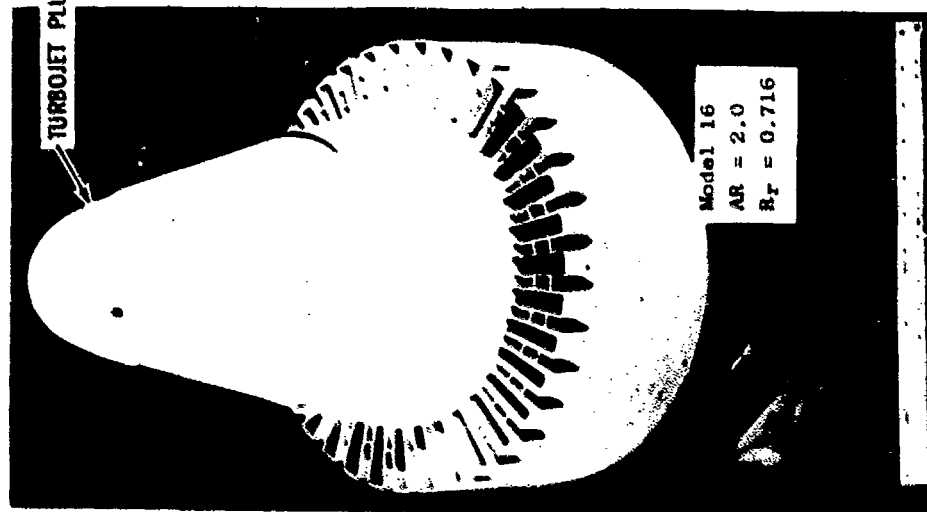
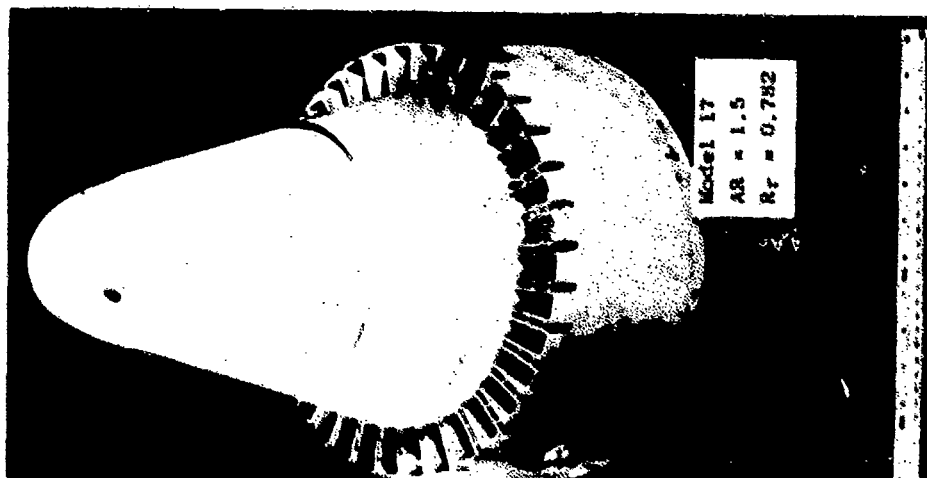


Figure 3-88. Annular Suppressor Area Ratio and Radius Ratio Variation on Turbojet.

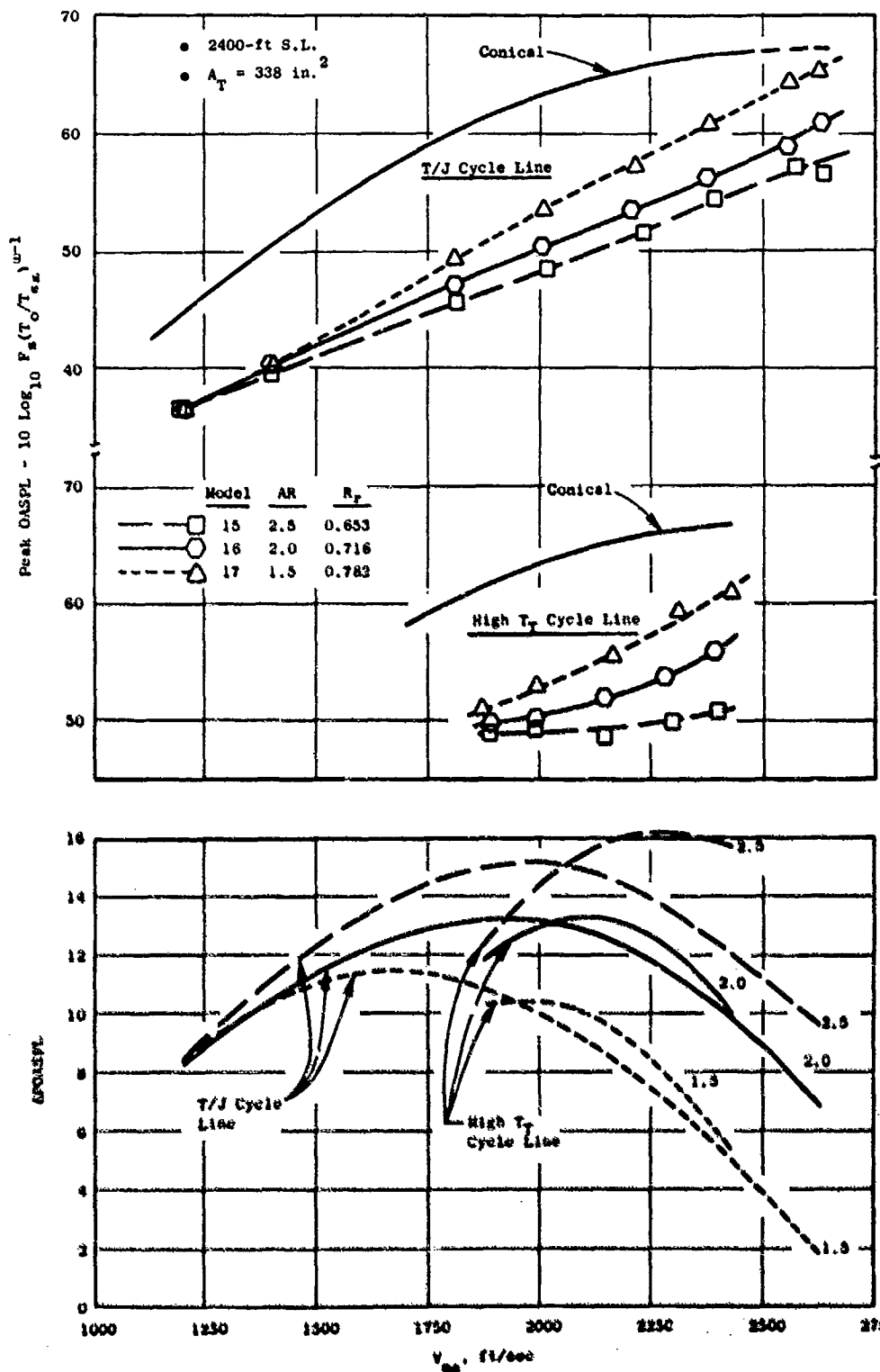


Figure 3-89. Impact of Area Ratio and Radius Ratio on Peak OASPL.

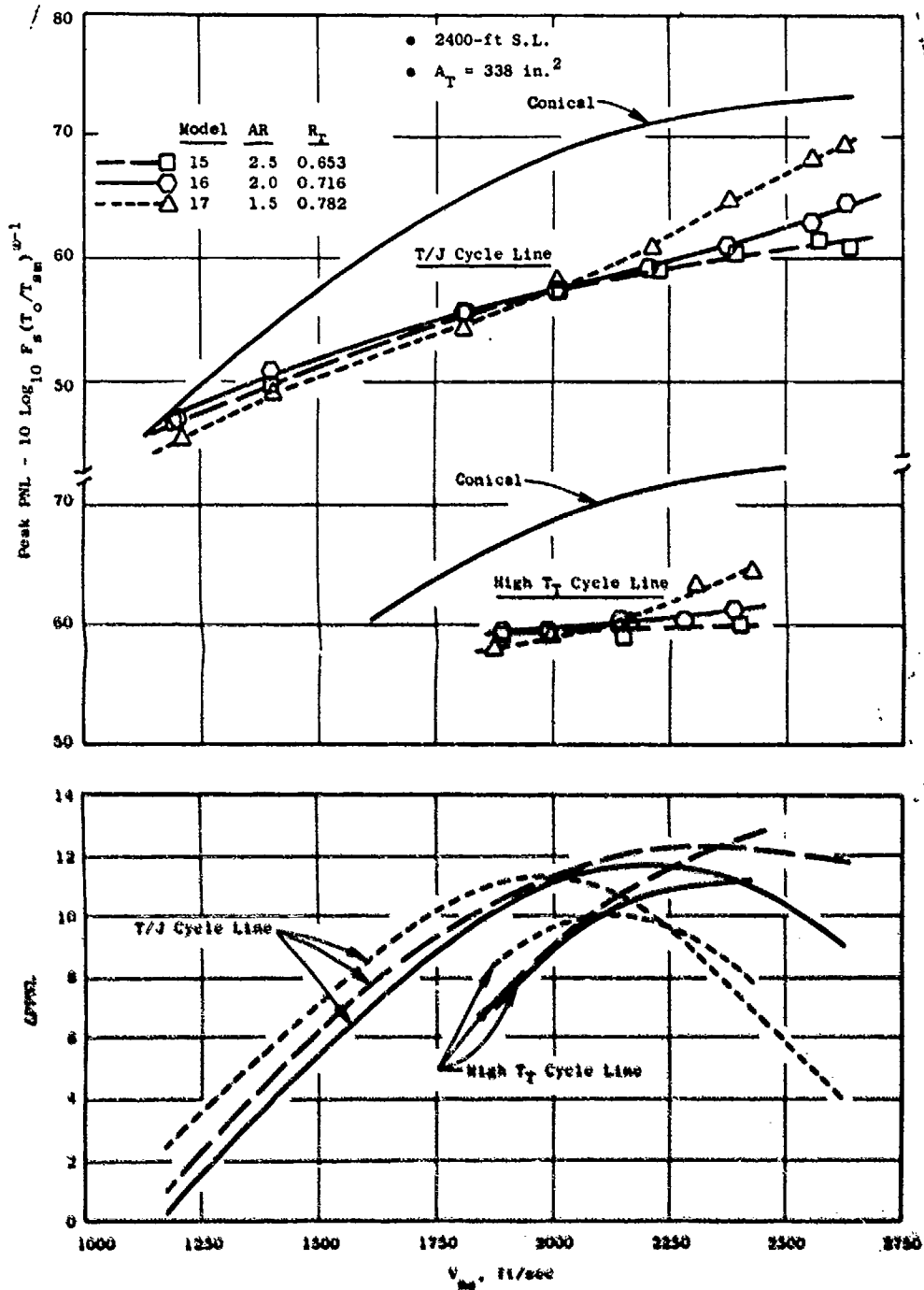


Figure 3-90. Impact of Area Ratio and Radius Ratio on Peak PNL.

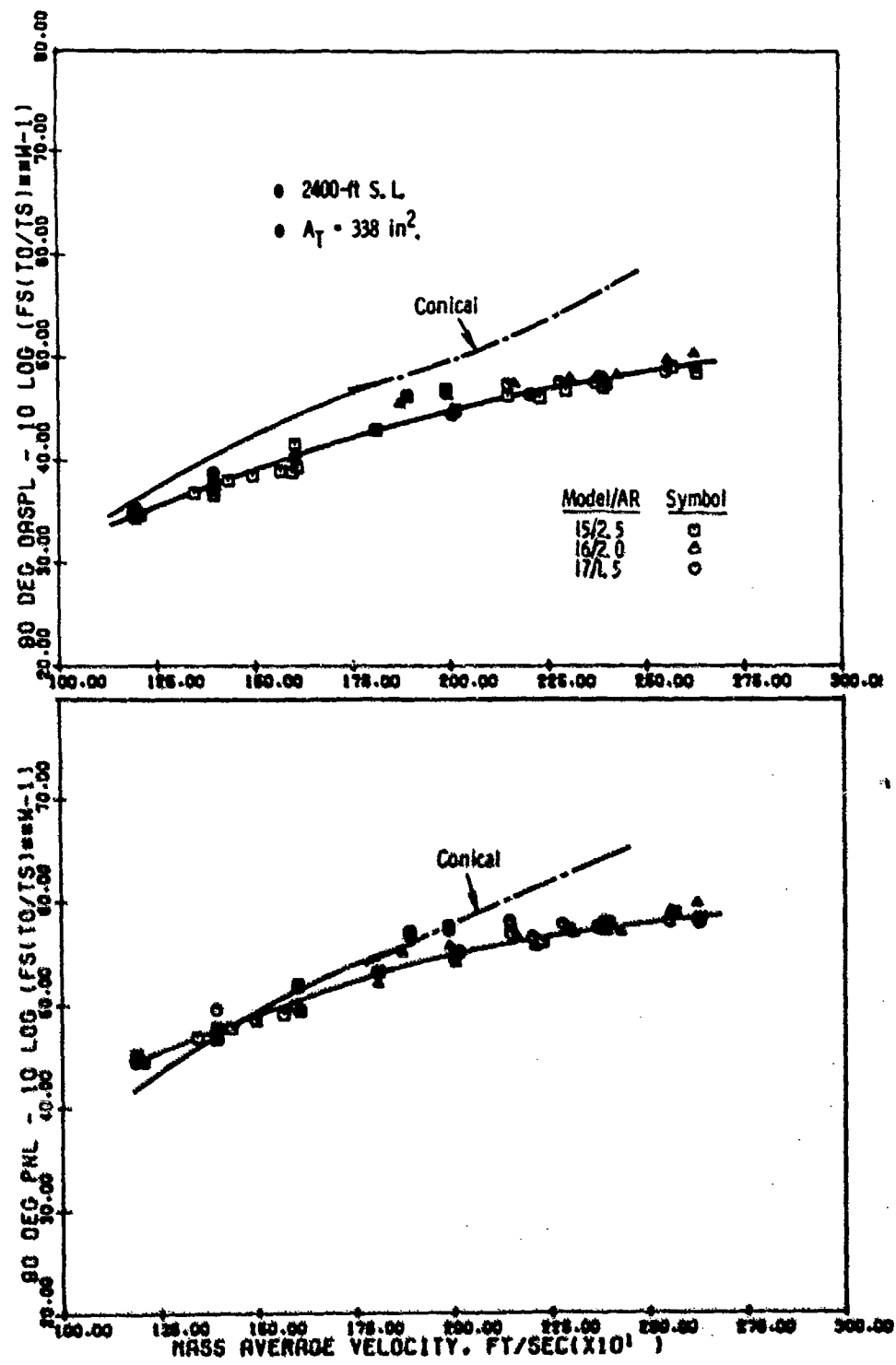


Figure 3-91. Impact of Area Ratio and Radius Ratio on 90° PNL and QASPL.

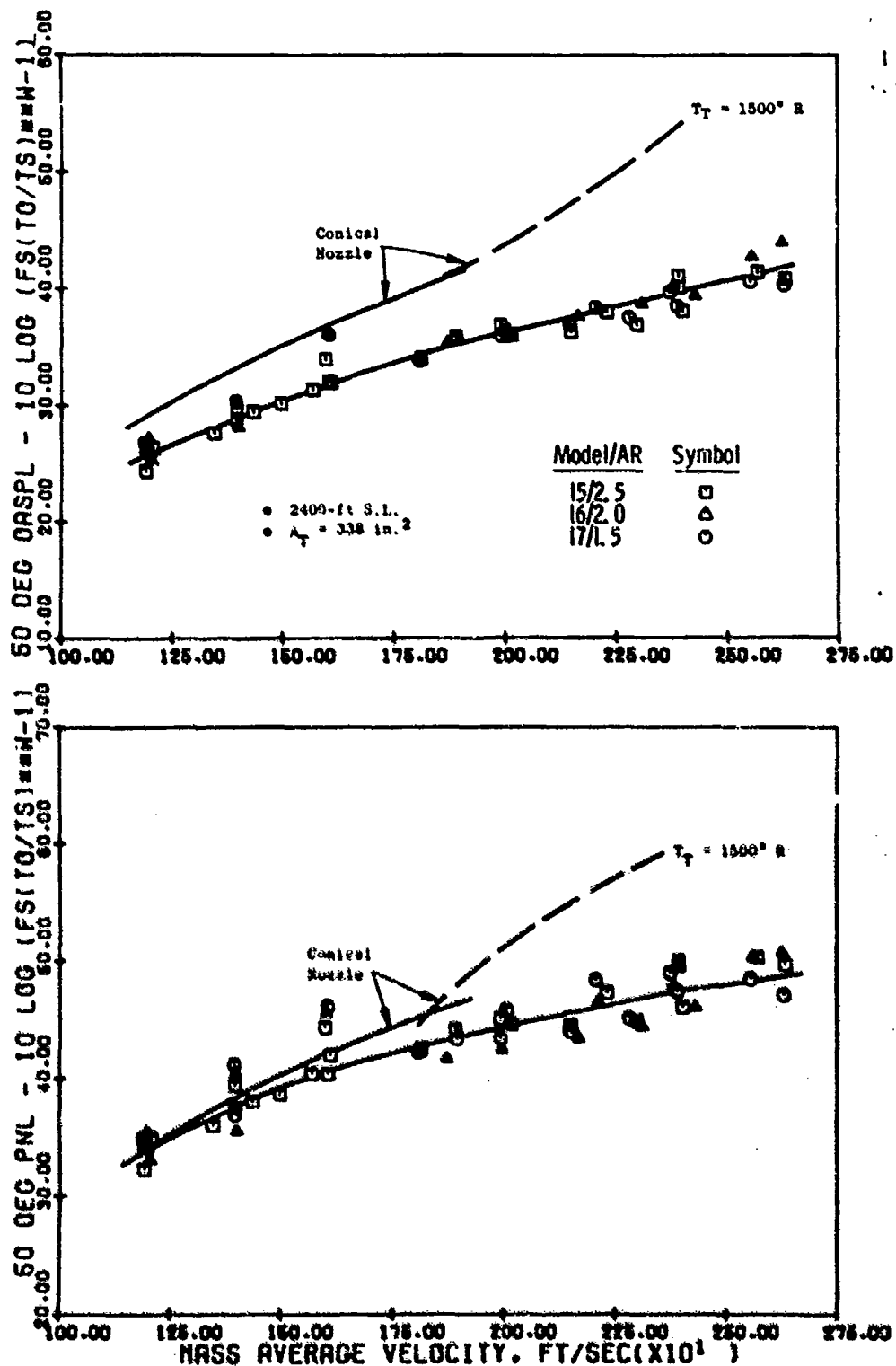


Figure 3-92. Impact of Area Ratio and Radius Ratio on 50° PNL and OASPL.



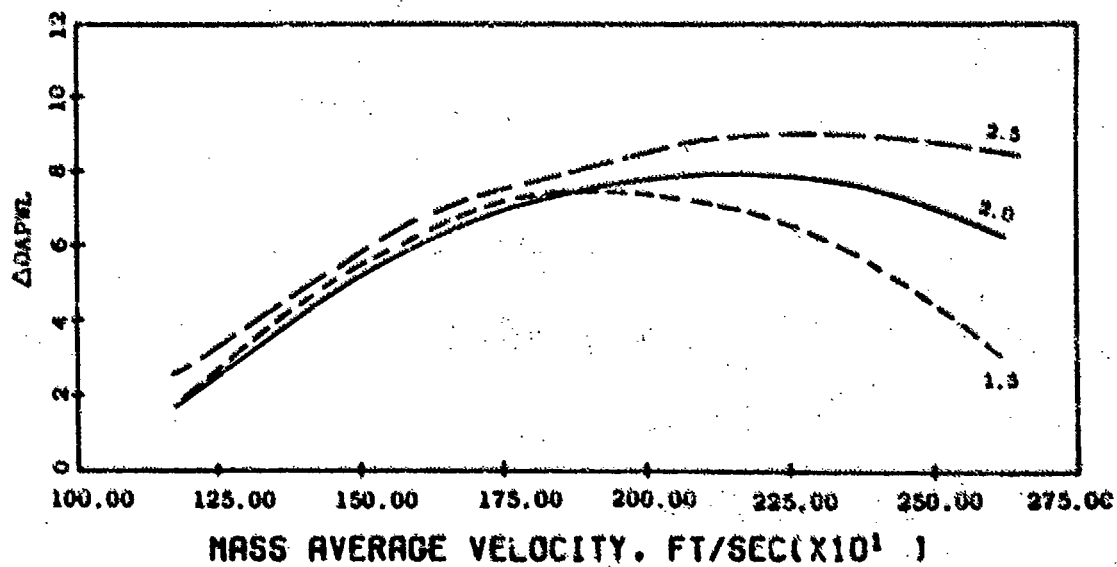
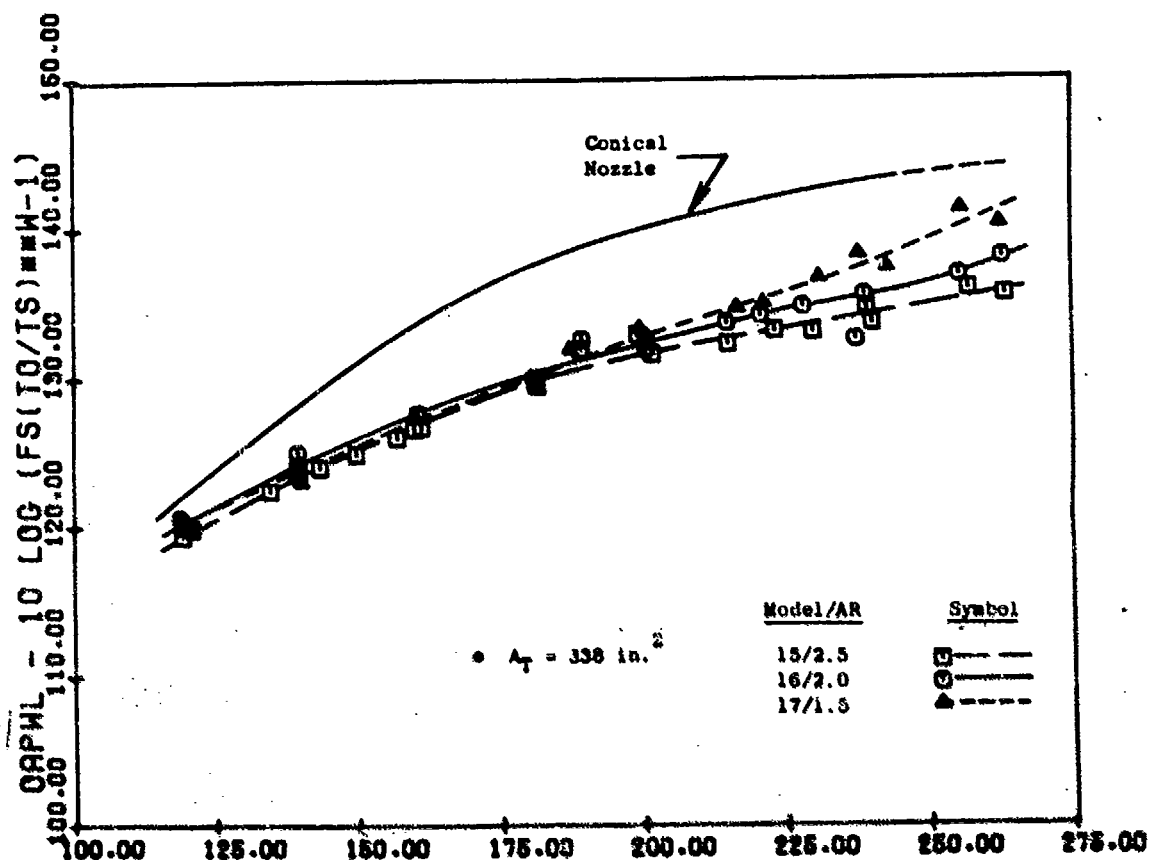


Figure 3-93. Impact of Area Ratio and Radius Ratio on OAPWL.

- On a peak PNL basis, Figure 3-90:
  - A maximum suppression level of near 12 to 12.5 dB is seen for the  $AR = 2.5/R_T = 0.653$  suppressor (Model 15) for both the conventional turbojet and high  $T_T$  cycle lines of test.
  - Suppression variance with area ratio/radius ratio is very predominant, particularly at high  $V_{ma}$ . The trend with area ratio reverses at low  $V_{ma}$ ; the magnitude in span of suppression was lower than in the high velocity region. At high  $V_{ma}$ , the change in AR from 1.5, Model 17, to 2.5, Model 15, (and in radius ratio from 0.782 to 0.653 is seen to enhance suppression by 4.5 to 5 dB at  $V_{ma} = 2400$  ft/sec, as an example. At low  $V_{ma}$ , the lower area ratio (1.5)/higher radius ratio (0.782), Model 17, performs most effectively, showing approximately a 2 dB suppression gain relative to the  $AR = 2.5$  suppressor (Model 15).
- At  $90^\circ$ , Figure 3-91, on both an OASPL and PNL basis, minimal distinction is seen among the three area ratio models, and between the conventional turbojet and high  $T_T$  cycle lines. A significant level of suppression relative to the conical nozzle is retained, both on a PNL and OASPL basis but not of the magnitude measured at peak noise angles in the aft quadrant.
- At  $50^\circ$ , Figure 3-92, distinction between the three area ratio/radius ratio models and between the two cycle lines is a little more predominant than at  $90^\circ$ . Suppression relative to the conical nozzle is also somewhat higher due to reduction in the shock-cell noise contribution which normally adds to the conical nozzle noise signature in the forward quadrant at supercritical operating conditions.
- On an OAPWL basis, Figure 3-93, the data trends are similar to those of the peak OASPL and Peak PNL plots, showing suppression improvement with area ratio increase at high  $V_{ma}$  and a near equivalency at low  $V_{ma}$ . Maximum suppression of 9 dB is seen for the area ratio = 2.5 at 2250 ft/sec.

To illustrate the more detailed changes in noise characteristics associated with changing area ratio and radius ratio, sets of PNL and OASPL directivity plus spectra plots are included as follows:

- Figures 3-94 and 3-95 Data Point 7,  $V_{ma} = 3625$  ft/sec, TJ Cycle Line
- Figures 3-96 and 3-97 Data Point 13,  $V_{ma} = 2150$  ft/sec, High  $T_T$  Cycle Line
- Figures 3-98 and 3-99 Data Point 6,  $V_{ma} = 1400$  ft/sec, TJ Cycle Line.

Examination of the first data set shows that at the highest measured test point: a) The aft quadrant directivity patterns are distinctly sharper for the lower area ratio/higher radius ratio, b) at broadside the levels are nearly identical, and c) in the inlet quadrant, distinct differences in

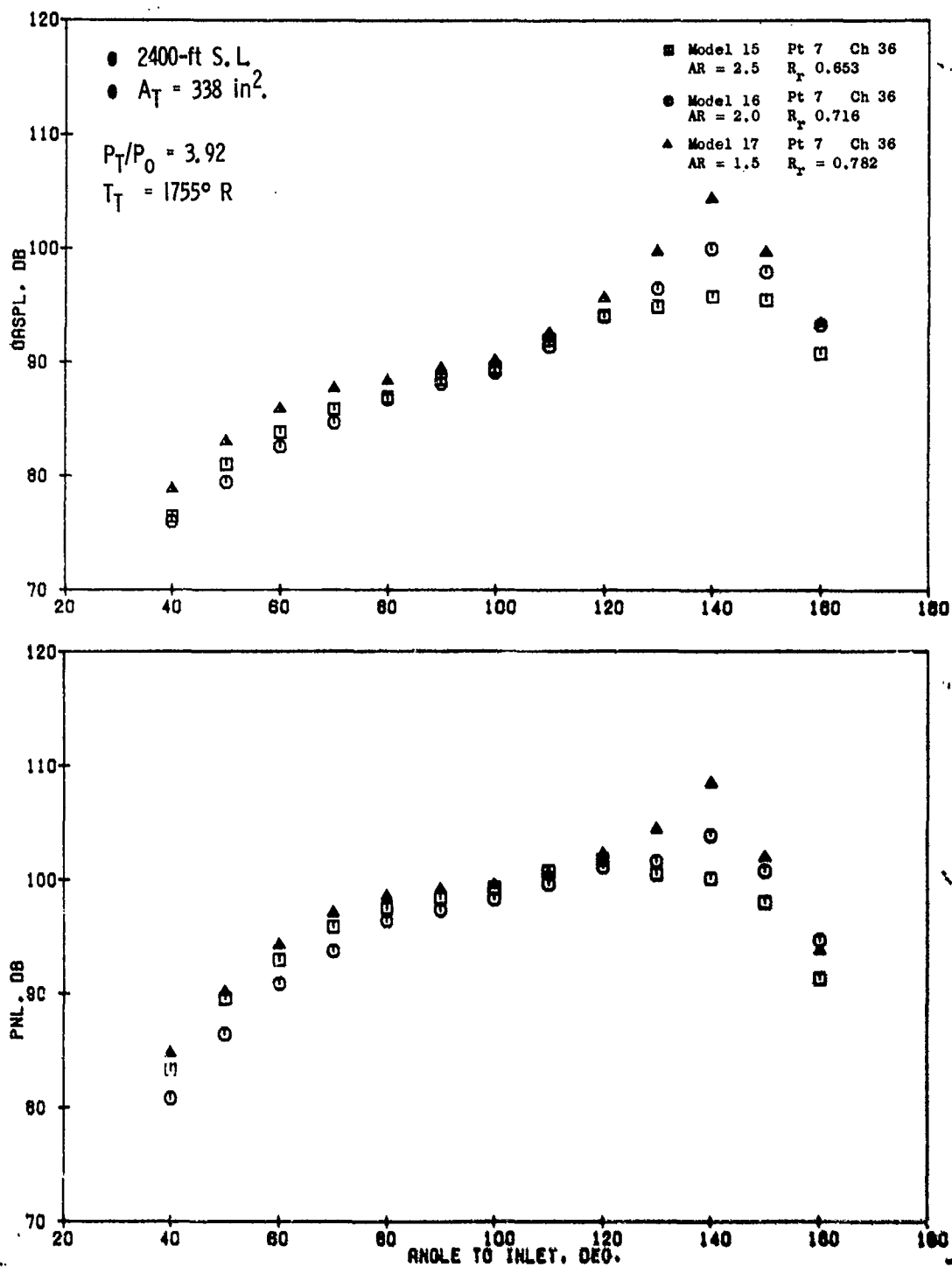


Figure 3-94. Impact of Area Ratio and Radius Ratio on PNL and OASPL Directivity,  $V_{ms} = 2625 \text{ ft/sec.}$

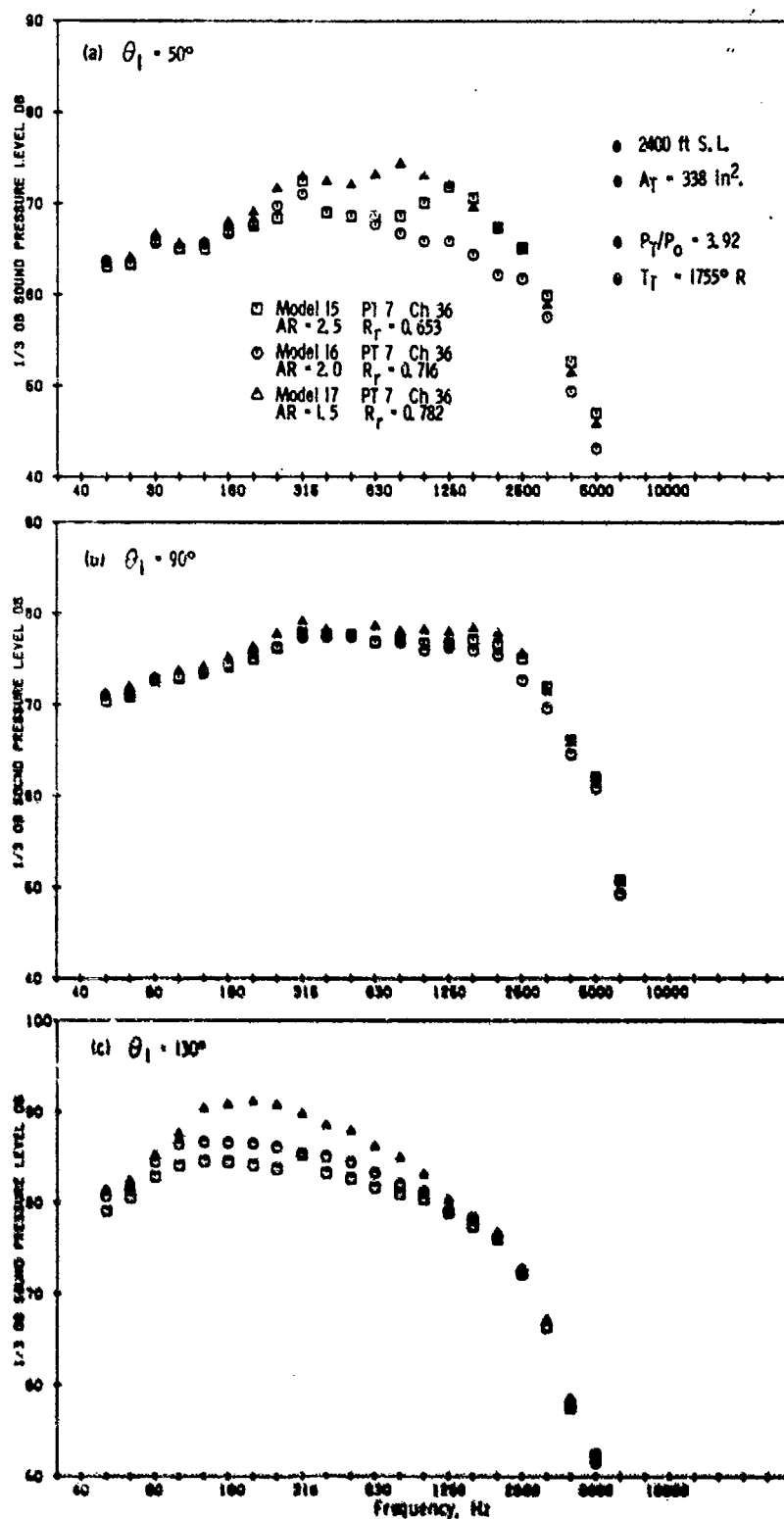


Figure 3-95. Impact of Area Ratio and Radius Ratio on Spectra,  $V_{\text{max}} = 2625 \text{ ft/sec.}$

levels are seen but not of the magnitude observed at peak noise angles. The highest area ratio/lowest radius ratio is always the best suppressor in the aft quadrant but then show equivalency to, or slightly poorer performance than, the area ratio = 2.0 nozzle (Model 16) within the forward quadrant. The lowest area ratio/highest radius ratio is the poorest suppressor at all angles.

An increase in area ratio will generally decrease noise at a supercritical operating point as the effect is to produce more rapid plume decay. This is observed in the aft angle 130° spectra, Figure 3-95, where post merged low-to-intermediate frequency noise is significantly lower for the higher area ratio. For this reason the normal double-humped spectra characteristics of multi-element suppressors are not seen.

At 90° the spectra shapes are all nearly similar as were the PNL and OASPL levels.

Within the inlet quadrant, changes in spectra are primarily in the mid to high frequency range and bear out changes seen in the OASPL/PNL directivity patterns.

Looking at the second data set, Figures 3-96 and 3-97 at  $V_{ma} = 2150$  ft/sec, where peak PNL's are nearly the same for the three area ratio models but peak OASPL's show a spread of about 7 dB, the following are observed:

- Peak PNL's occur at 120°, 110° and 140° for AR = 2.5, 2.0 and 1.5, respectively. OASPL directivity shifts to be peaked at the further aft angles.
- PNL directivity is fairly flat broadside and in the near aft quadrant (90° to 140°) with peaks occurring at 120°, 110° and 140° for AR = 2.5 (Model 15), 2.0 (Model 16) and 1.5 (Model 17), respectively, whereas OASPL directivity peaks further aft.
- The very sharp aft quadrant and near level forward quadrant directivity patterns of the conical nozzle are not present for the suppressors. Shock-cell noise is the primary suppressor mechanism responsible for the forward quadrant suppression, the forward quadrant angles showing about 6APNL below the conical at 80° and approximately 19 APNL at 40°, with even greater A's for OASPL.
- Looking more closely at 50°, OASPL's are identical but PNL varies about 3 dB; the spectra showing a crossover of high and low frequency influence with area ratio variation. This indicates a delicate balance between the high frequency premerged and low frequency postmerged jet noise characteristics.
- Broadside, at 90°, the same spectral crossover with area ratio is maintained.
- In the aft quadrant (12° to 150°) spectra suppression relative to the conical is primarily in the mid-to-high frequency range with

- |   |           |                              |                                |                                |
|---|-----------|------------------------------|--------------------------------|--------------------------------|
| □ | Model 15  | PT 13                        | CH 36                          |                                |
|   | AR = 2.5  | $R_T = 0.653$                |                                |                                |
| ○ | Model 16  | PT 13                        | CH 36                          | • 2400-ft S.L.                 |
|   | AR = 2.0  | $R_T = 0.716$                |                                | • $A_T = 338 \text{ in.}^2$    |
| △ | Model 17  | PT 13                        | CH 36                          | • $P_T/P_0 = 2.38$             |
|   | AR = 1.5  | $R_T = 0.782$                |                                | • $T_T = 1732^\circ \text{ R}$ |
| + | Model 14  | PT 24 Conical                |                                |                                |
|   | PR = 2.92 | $T_T = 1512^\circ \text{ R}$ | $V_{ma} = 2200 \text{ ft/sec}$ |                                |

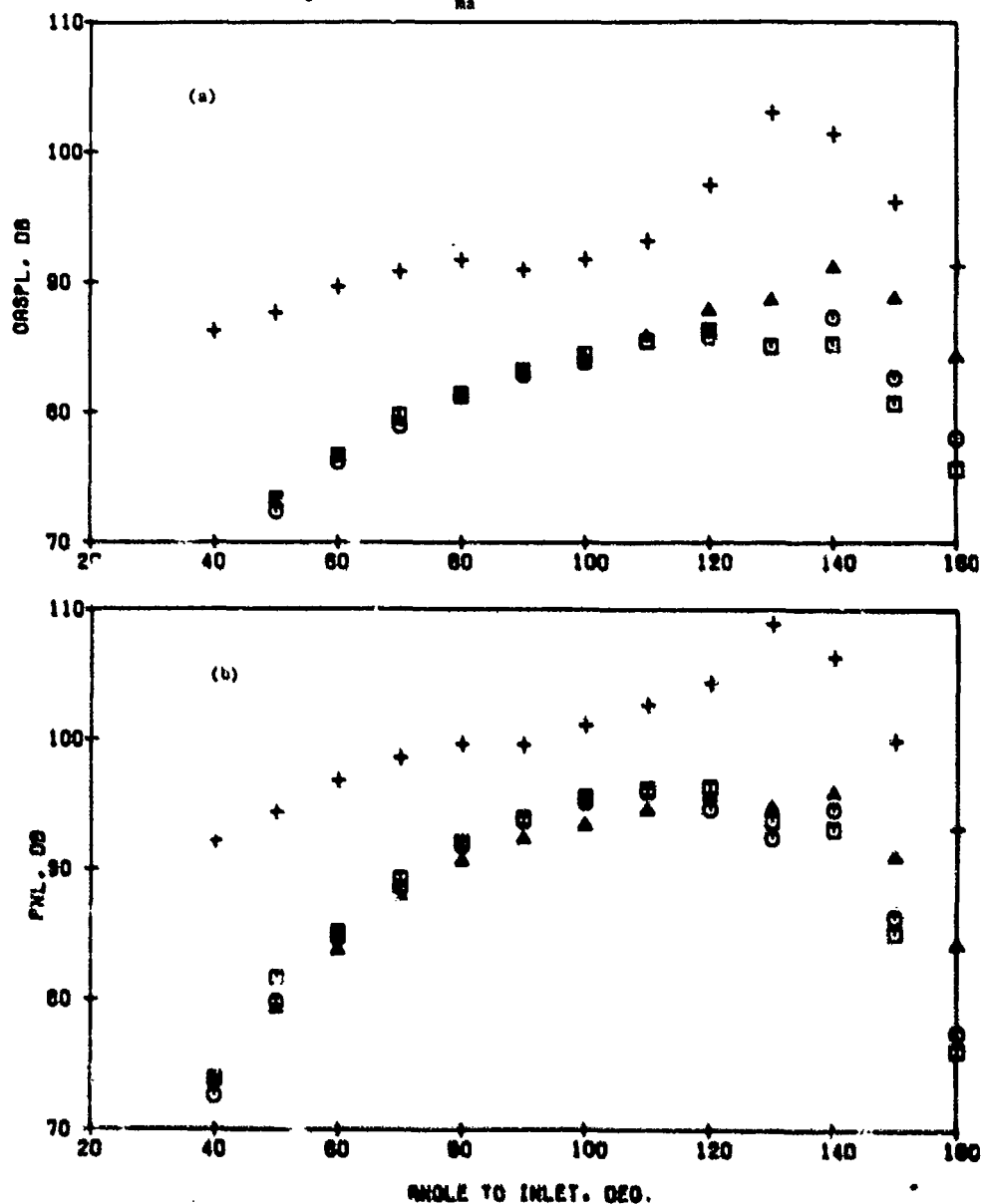


Figure 3-96. Impact of Area Ratio and Radius Ratio on PNL and OASPL Directivity,  $V_{ma} = 2150 \text{ ft/sec}$ .

Model 15 PT 13 CH 36  
 AS - 2.5  $R_T$  - 0.65  
 Model 16 PT 13 CH 36  
 AS - 2.0  $R_T$  - 0.76  
 Model 17 PT 13 CH 36  
 AS - 1.5  $R_T$  - 0.72  
 Model 14 PT 24 Conical  
 PM - 2.92  $T$  - 152° R  $V_{10}$  - 220 ft/sec  
 2400-ft S.L.  
 $A_T$  - 338 in. 2  
 $T_f$  - 173° R  
 $P_f/P_0$  - 2.38

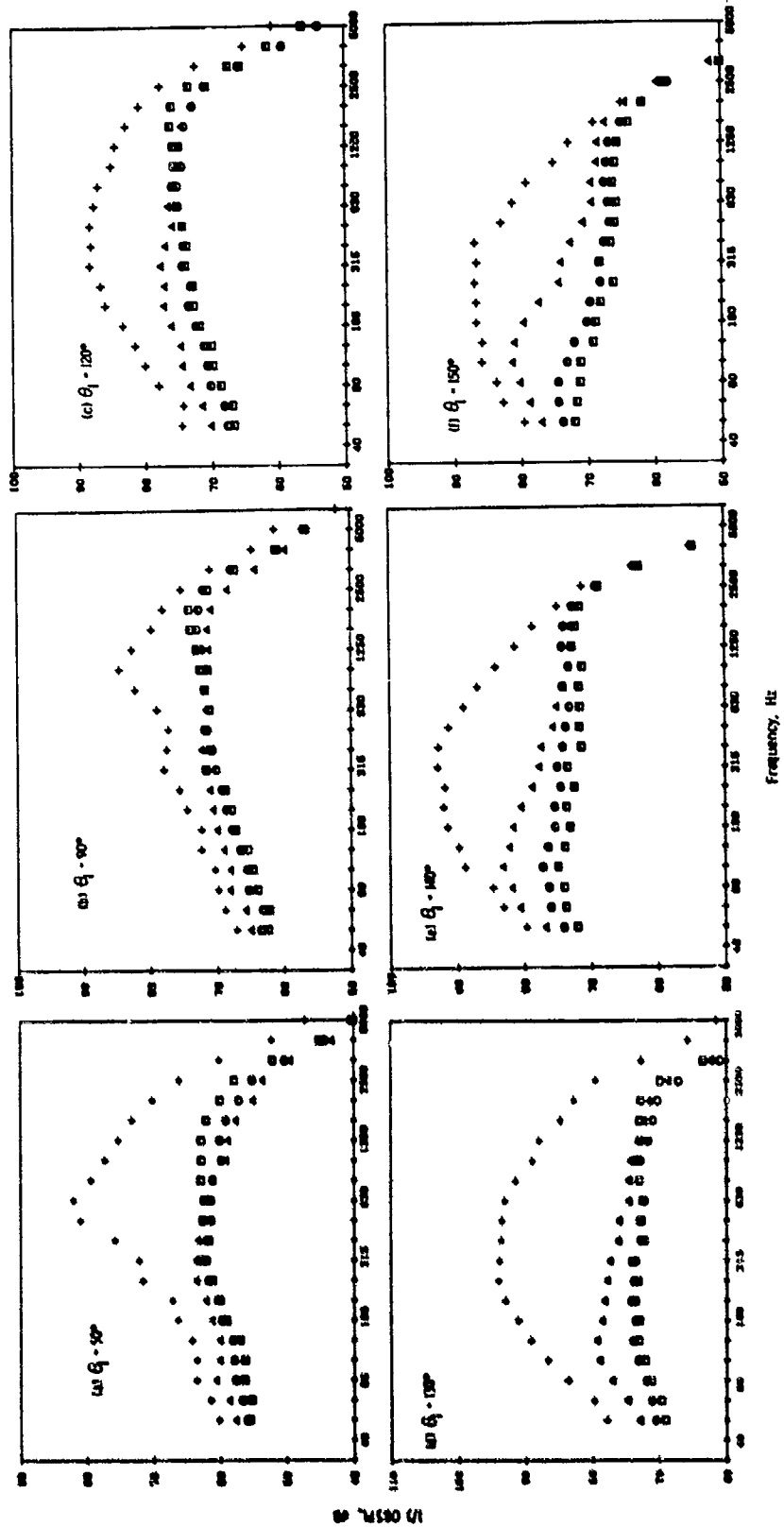


Figure 3-97. Impact of Area Ratio and Radius Ratio on Spectra,  $V_{ma} = 2150$  ft/sec.

lower area ratio indicating quicker merging of individual jets and, therefore, generating a higher content of low frequency noise. Very high frequency premerged noise at far aft angles (e.g., 150°) still shows significantly different levels for the three models, reversed from the pattern at inlet angles (e.g., 50°) but they no longer control OASPL or PNL.

For the third data set, Figures 3-98 and 3-99 at  $V_{ma} = 1400$  ft/sec, where the three models still maintain approximately 10  $\Delta$ POASPL and 4 to 5.5  $\Delta$ PPNL suppression, the following observations are noted:

- Noise variance with area ratio/radius ratio is minor as PNL and OASPL directivity patterns show, except in the very aft quadrant where higher area ratio still maintains best PNL and OASPL suppression and shows variance relative to the lowest area ratio of 3  $\Delta$ PNL to 5  $\Delta$ OASPL at 160°.
- The crossover of noise directivity patterns with changing area ratio still exists as it did at mid and high-velocity. The higher area ratio is noisier at inlet angles and quieter in the aft quadrant, crossover normally occurring in the 100° to 140° region.

#### Area Ratio and Radius Ratio Variable, Dual Flow (Models 22, 24 and 27)

This study extended the previous investigation to a dual flow exhaust nozzle system. Models 22, 24, and 27 of Figure 3-100 were used, each maintaining the 36-chute suppressors of Models 15, 16 and 17, respectively, with area ratios and radius ratios of 2.5/0.653, 2.0/0.716 and 1.5/0.782. In place of the full plug turbojet geometry, an inner plug of 0.7" annulus step height was used in the retracted position. This set the outer to inner area ratio,  $A_0/A_1$ , at 1.92. Inner plug radius ratio was 0.779. Figures 16, 18 and 21 of Appendix A detail the model geometries. The inner stream geometry does not utilize a mechanical suppressor. The suppressor is applied only to the outer stream and is termed a half span suppressor.

Farfield acoustic testing in the Cell 41 Anechoic Facility followed the matrix described in Section 3.2.1, Figure 3-10 and Table 3-3. Each model used the following cycle series:

- $W_1 = 15\% W_0$
- $W_1 = 30\% W_0$
- DBTF/Inverted Dual Flow cycle with  $1.0 \leq V_0/V_1 \leq 2.0$
- AST/V:E

Additionally, Model 24 was tested with no inner flow while maintaining normal outer stream cycle conditions.



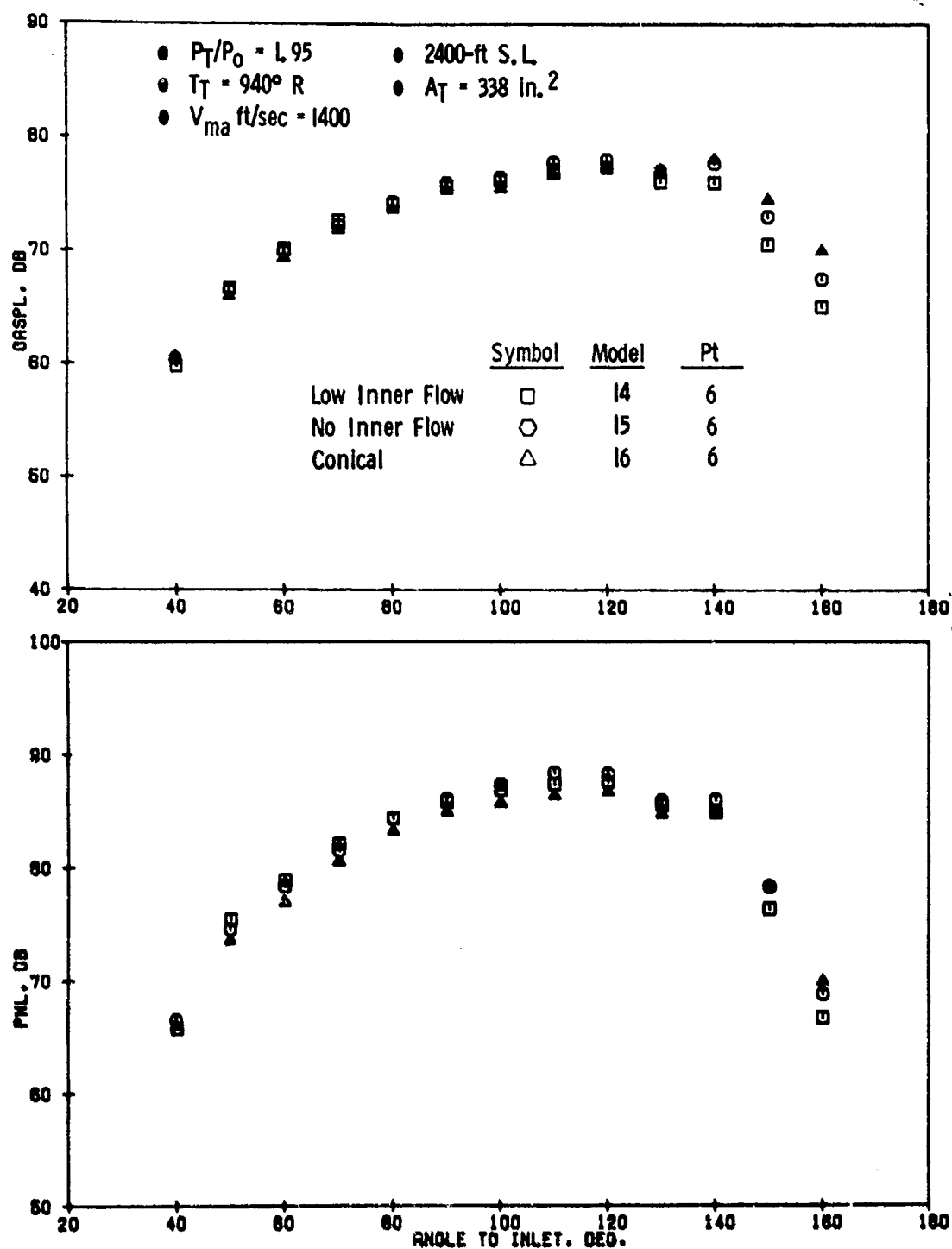


Figure 3-98. Impact of Area Ratio and Radius Ratio on PNL and QASPL Directivity,  $V_{ma} = 1400 \text{ ft/sec}$ .

• 2ND-R.S.L.  
 •  $A_T = 338 \text{ in.}^2$   
 •  $P_T/P_0 = 1.95$   
 •  $T_T = 940^\circ \text{R}$   
 Model 15 PT 6 CH 36  
 AR - 2.5  $R_T = 0.653$   
 Model 16 PT 6 CH 36  
 AR - 2.0  $R_T = 0.716$   
 Model 17 PT 6 CH 36  
 AR - 1.5  $R_T = 0.782$

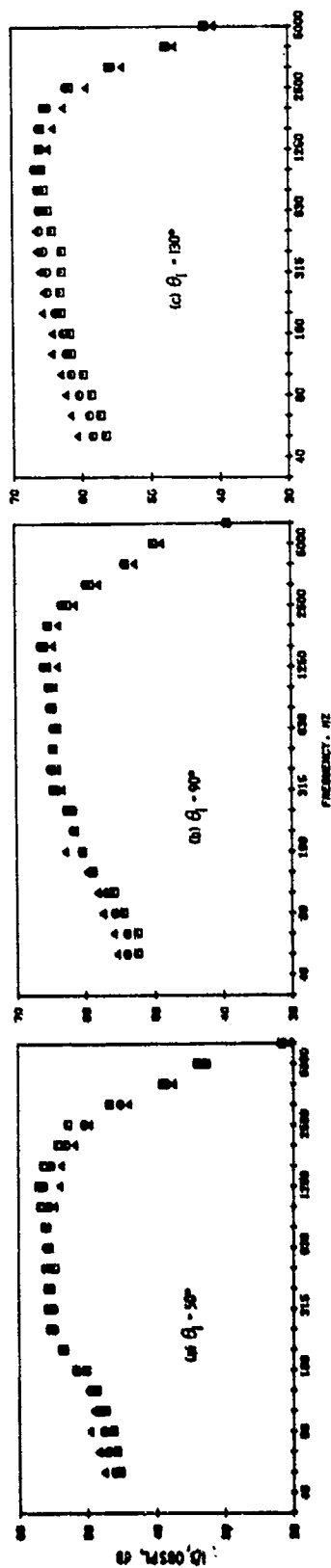


Figure 3-99. Impact of Area Ratio and Radius Ratio on Spectra,  $V_{ma} = 1400 \text{ ft/sec.}$

• 36 CHUTE

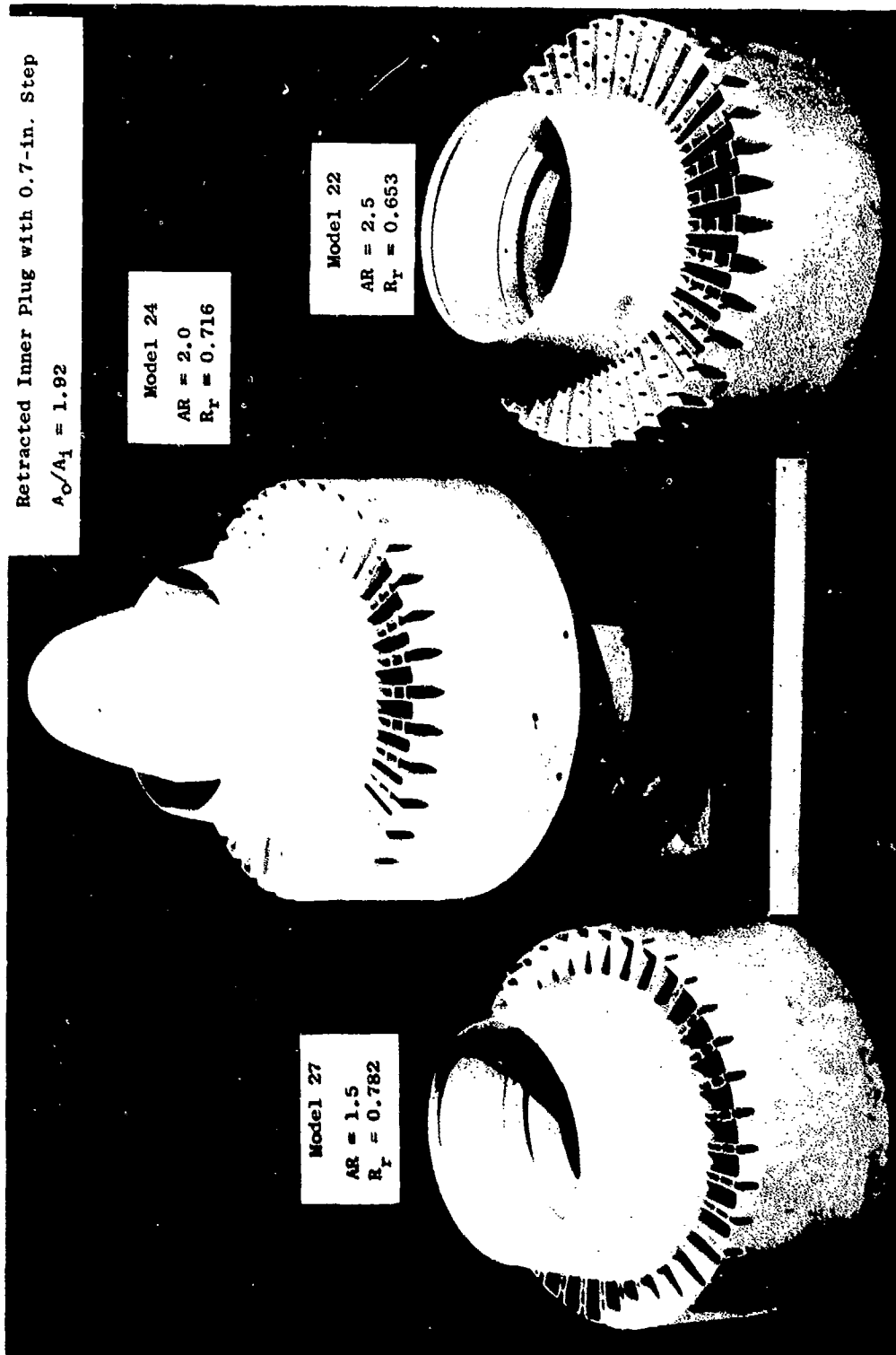


Figure 3-100. Half-Span Suppressor Area Ratio and Radius Ratio Variation on Dual Flow.

Acoustic results on a peak PNL basis, Figure 3-101, are shown for three data sets, i.e., (a) for all data points, (b) for the  $W_1 = 30\% W_0$  cycle, and (c) for the DBTF/Inverted Dual Flow cycle. The results shown are selected as representative of all the data cycle sets. For area ratio = 1.5 (Model 27) the three data-fitted curves are nearly duplicates, except that the DBTF cycle peaks at 11  $\Delta$ PPNL suppression instead of at 10 as did the other two. For the AR = 2.0, the three curves behave similarly within approximately  $\pm 0.3$   $\Delta$ PPNL, peak suppressions being at 9 to 9.5  $\Delta$ PPNL. The three data curves for the area ratio 2.5 nozzle, Model 22 are generally the same with  $\pm 0.3$  dB at high  $V_{ma}$  but show a spread of nearly 2  $\Delta$ PPNL at low  $V_{ma}$ . The above observations indicate that outer to inner stream cycle variations, within the range tested, do not significantly alter suppressor performance; if the measurements are normalized with respect to thrust, mixed flow density, and correlated as a function of  $V_{ma}$ . In general:

- The area ratio and radius ratio excursions within the test range show a noise variance of 1.5  $\Delta$ PPNL min. to 3.5 max.; magnitude of variance dependent on cycle  $V_{ma}$ .
- The low area ratio/high radius ratio is consistently better at low-to-intermediate  $V_{ma}$ , just as it was for the full span turbojet nozzle application.
- Peak suppression levels of 11, 9.5 and 10.4 for area ratios for 1.5 (Model 27), 2.0 (Model 24) and 2.5 (Model 22), respectively, are somewhat below those of the same applications to the turbojet which were 11.5, 12.0 and 12.5; indicating that a full span turbojet suppressor is slightly more efficient than a half span suppressor application to a dual flow system.
- The AR = 2.5/ $R_r = 0.653$  suppressor (Model 22) is consistently poorer at low  $V_{ma}$  and potentially better at high  $V_{ma}$ . On the turbojet system the same was true at high  $V_{ma}$ , but, at low  $V_{ma}$  little distinction was seen between the AR = 2.0 and 2.5 (Models 24 and 22 respectively).
- The maximum PPNL suppression level for the AR = 2.5 nozzle, Model 22, occurs at a higher velocity than for the 1.5 (Model 27) and 2.0 (Model 24) and in some instances the maximum value may not have been achieved within the test range.
- Peak PNL suppression curves for each area ratio model show a trend crossover occurring in the 2000 to 2350 ft/sec  $V_{ma}$  range, generally consistent with the 2000 to 2100 ft/sec range of the single flow system.

Peak OASPL data are presented in the same manner in Figure 3-102 as were peak PNL data, namely, (a) for all data points, (b) for  $W_1 = 30\% W_0$  and (c) for DBTF/Inverted Dual Flow. The following are noted:

- Consistency of data for the three cycle sets is very good, particularly when comparing equivalent curve-fitted trends of  $\Delta$ POASPL where variance for each model is within  $\pm 0.5$  dB.

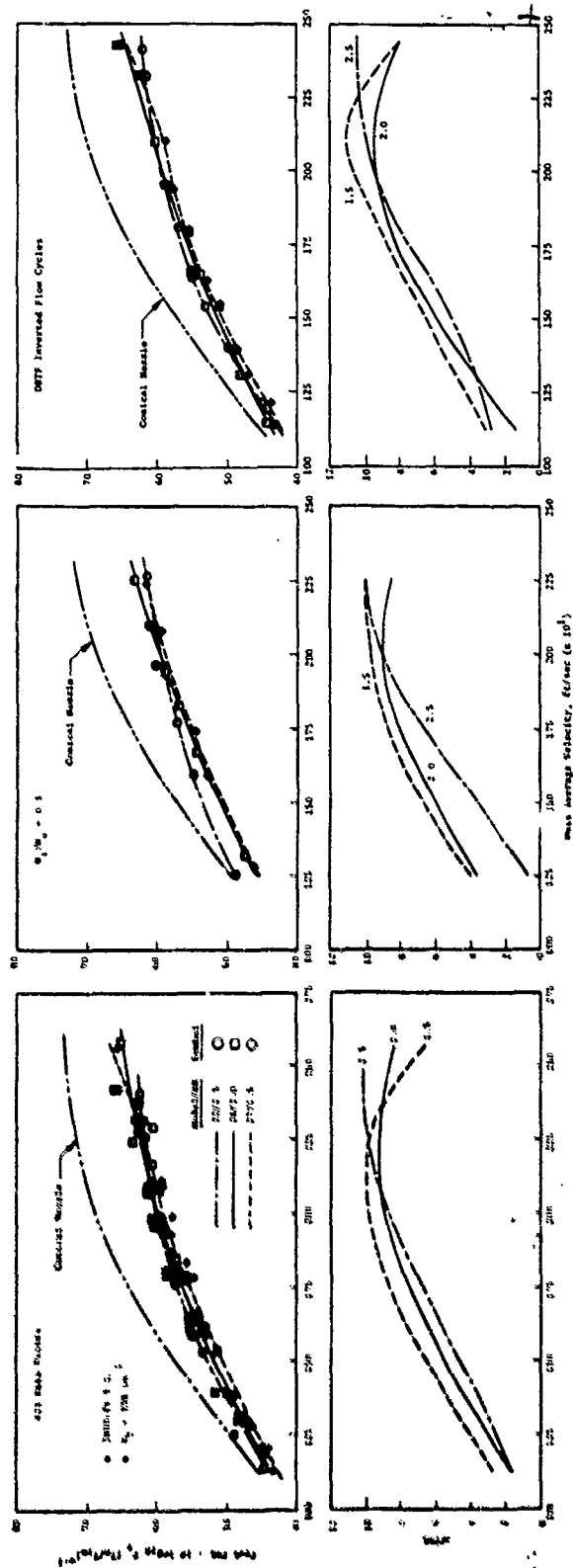


Figure 3-101. Impact of Area Ratio and Radius Ratio on Peak PNL, Dual Flow.

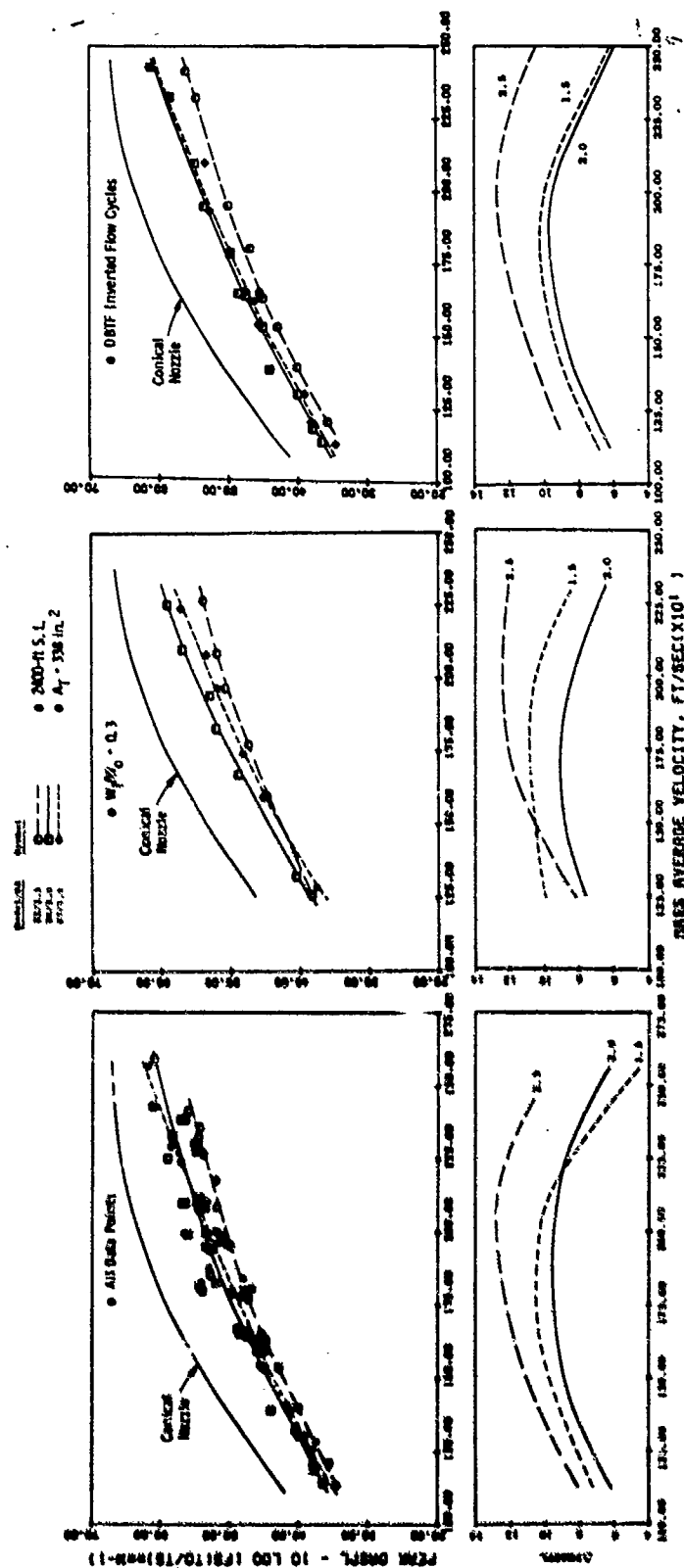


Figure 3-102. Impact of Area Ratio and Radius Ratio on Peak OASPL, Dual Flow.

- Variance in area ratio/radius ratio over the design range yielded a min. to max.  $\Delta$ POASPL of 2 to 5 dB, greater than the 1.5 to 3.5  $\Delta$ dB span experienced on PPNL.
- Maximum levels of peak OASPL suppression are also lower than those of the previous turbojet full span suppressors, i.e., 11, 9.5 and 12.5  $\Delta$ POASPL for dual flow area ratios = 1.5, 2.0 and 2.5, respectively, compared to 11, 13 and 15.5 for equivalent turbojet models. This again implies that suppression of the full stream is somewhat more effective than suppressor application to the outer annulus alone.
- The relationship for sequence of models in improving suppression from 1.5 to 2.0 to 2.5 seems to hold up on the peak OASPL basis.
- Crossover of  $\Delta$ POASPL trend curves in the mid-to-high  $V_{ma}$  range is not seen for the area ratio = 2.5 nozzle, Model 22, as it was on the  $\Delta$ PPNL basis. Area ratio of 2.5 is consistently the best suppressor, even at low  $V_{ma}$ . Maximum POASPL suppression levels are higher than they were for PPNL at about 12.5 to 13  $\Delta$ POASPL versus 10 to 10.5  $\Delta$ PPNL.
- The AR = 2.0 nozzle, Model 24, is almost always the poorest POASPL suppressor; however, AR = 1.5 exhibits near the same noise levels, within 0.5 to 2 dB across the  $V_{ma}$  range.

Data at 90°, Figure 3-103 for PNL and Figure 3-104 for OASPL, indicate that some suppression is retained broadside (primarily on the OASPL basis), particularly at mid-to-high  $V_{ma}$  where shock-cell noise is prevalent in the conical nozzle but negligible, if at all present, in the segmented suppressors. Suppression levels relative to the conical nozzle are of similar magnitude to those of the previous section's full span turbojet suppressors.

On both a PNL and OASPL basis, a maximum variation of 3 dB is seen among the three models on the  $W_1 = 30\% W_0$  cycle data. No consistent trend of PNL with area ratio is evident, but OASPL progressively increases as AR changes from 2.0 to 1.5 to 2.5.

Similar 50° data, Figure 3-105 for PNL and Figure 3-106 for OASPL show substantial forward quadrant suppression, even at low  $V_{ma}$ , much higher levels than at broadside. At high  $V_{ma}$ , with supercritical pressure ratio, levels are very significantly below those of the conical nozzle due to absence of shock-cell noise.

OASPL levels for the three models are fairly near the same level and no distinction between area ratio is made, except for the  $W_1 = 30\% W_0$  cycle where a spread of 2 dB is seen.

On the PNL basis, variation of AR/ $R_r$  shows the AR = 2.5 (Model 22) to now be highest in level and the AR = 1.5 (Model 27) to consistently maintain the highest suppression in the forward quadrant.

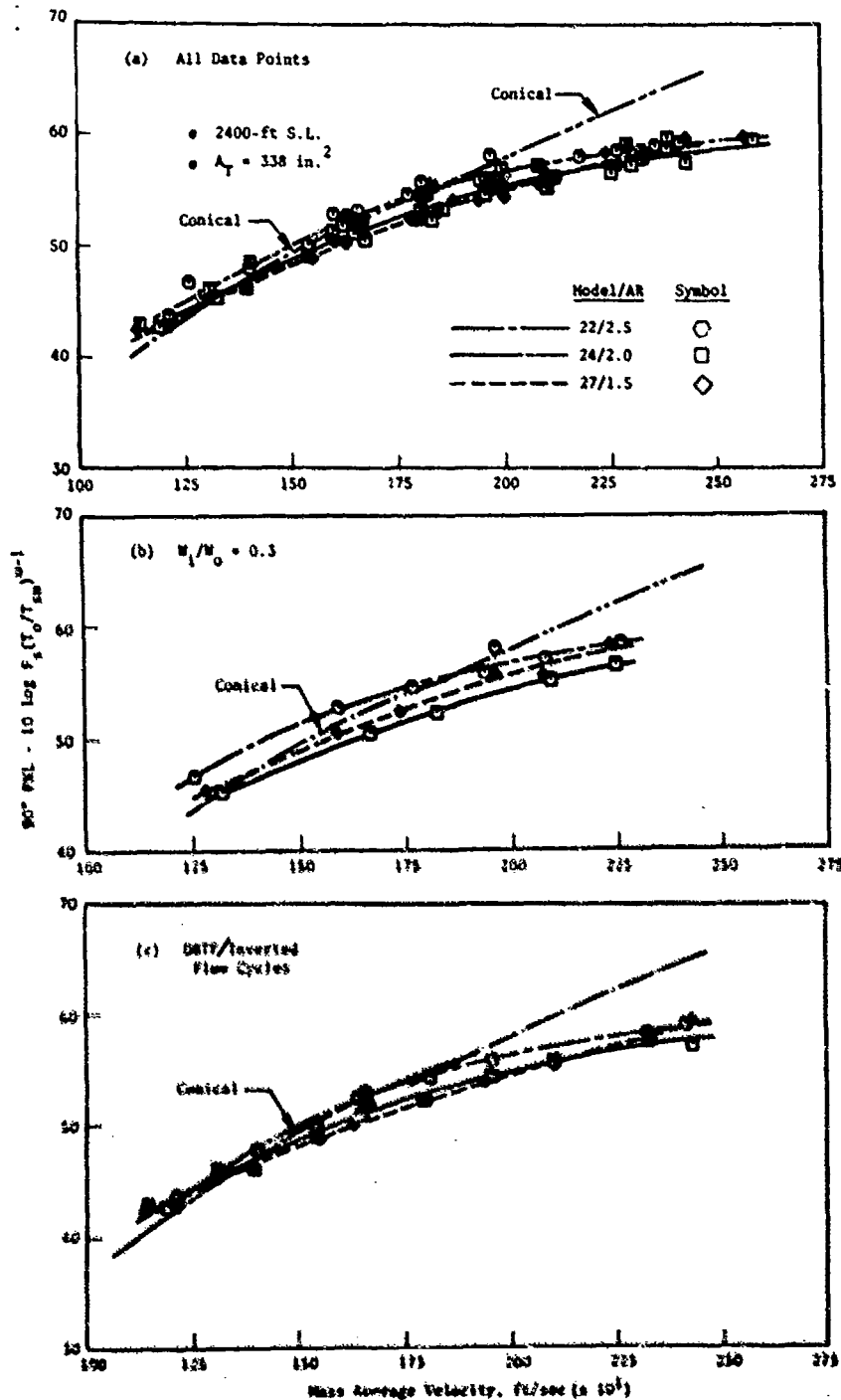


Figure 3-103. Impact of Area Ratio and Radius Ratio on 90° FNL, Dual Flow.



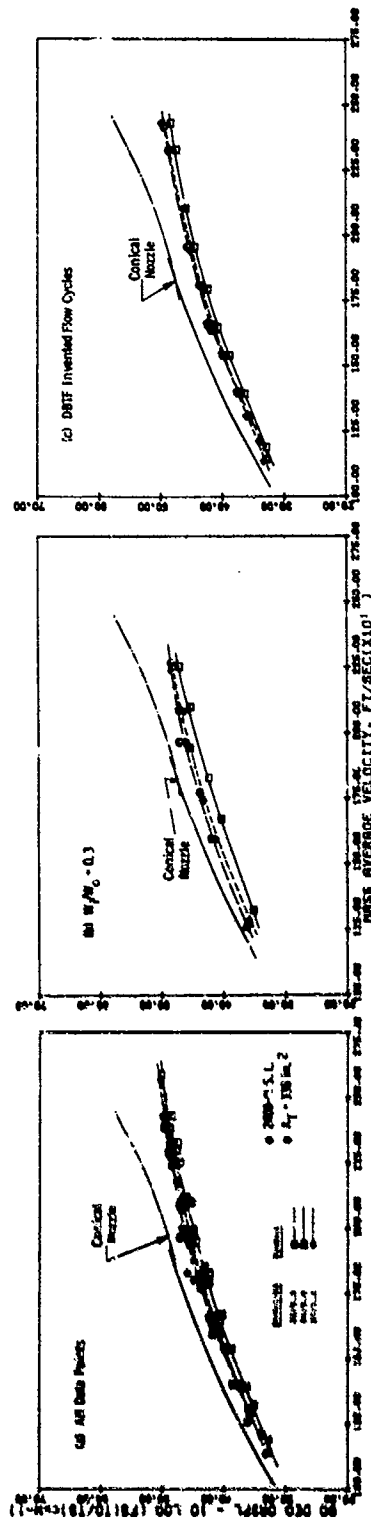


Figure 3-104. Impact of Area Ratio and Radius Ratio on 90° OASPL, Dual Flow.

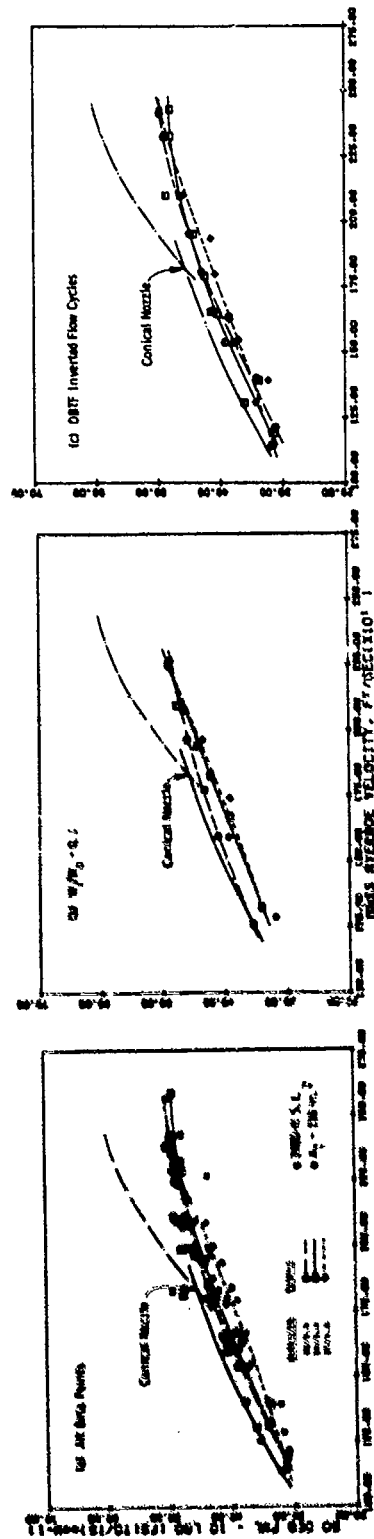


Figure 3-105. Impact of Area Ratio and Radius Ratio on 50° PNL, Dual Flow.

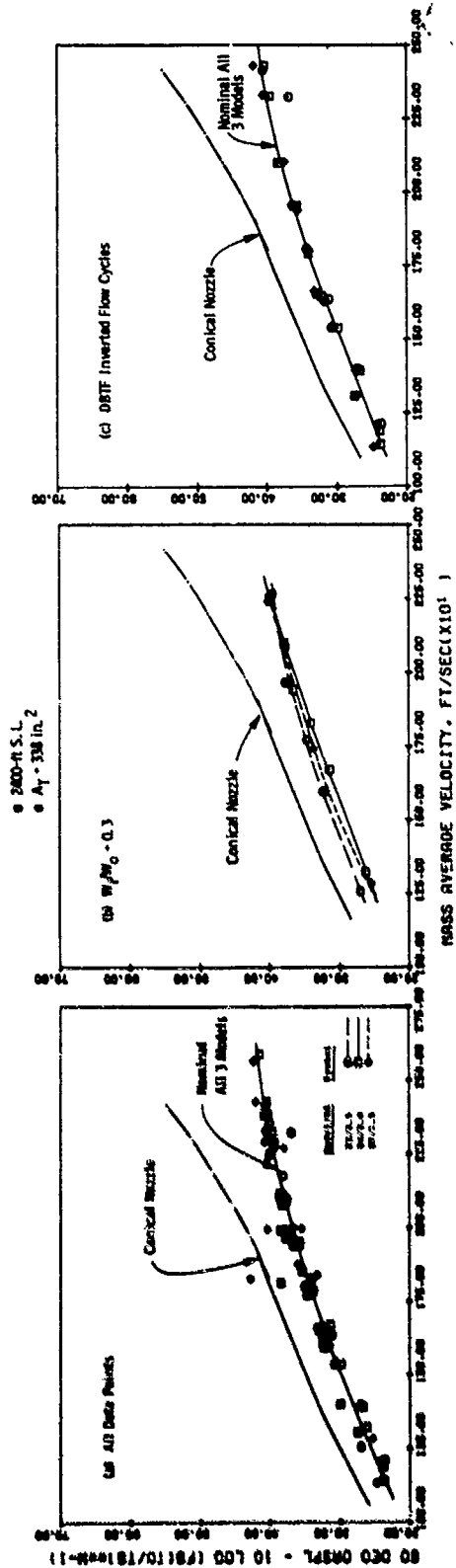


Figure 3-106. Impact of Area Ratio and Radius Ratio on 50° OASPL, Dual Flow.

OAWPL data are included as Figure 3-107 to show that no significant variation with cycle or area ratio/radius ratio is present.

For more detailed variations in noise characteristics of PNL & OASPL directivity plus spectra, the following data sets from the DBTF cycle matrix were selected for inclusion:

Figures 3-108 and 3-109 Data Point 37,  $V_{ma} = 2425$  ft/sec,  
Figures 3-110 and 3-111 Data Point 24,  $V_{ma} = 1200$  ft/sec,  
Figures 3-112 and 3-113 Data Point 36,  $V_{ma} = 1945$  ft/sec,

The following observations are made from the first data set at high  $V_{ma}$ :

- OASPL and PNL directivity bear out the trends of noise at peak,  $90^\circ$  and  $50^\circ$  versus  $V_{ma}$  in that significant suppression is seen at peak, minimum at broadside and then somewhat higher levels in the forward quadrant.
- Noise directivity of the suppressor nozzles has shifted from the conventional conical nozzle pattern to now peak somewhat further aft. At mid-to-low  $V_{ma}$  the suppressor's directivity patterns more closely match those of the conical or tend to shift peak noise more toward the broadside locations. Directivity patterns are not uniform among the three area ratios in that the 1.5 (Model 27) and 2.0 (Model 24) are more peaked than the smooth distribution of the 2.5 (Model 22). Maximum variation in suppressor noise levels is seen in the peak aft quadrant; however, levels are more uniform and within a maximum spread of about 3 dB in the forward quadrant.
- Spectra at this high  $V_{ma}$  point, for inlet to broadside angles, have the characteristic flat to somewhat double-humped distribution with suppression primarily in the midfrequency range where conical nozzle shock-cell tone and broadband noise are normally dominant. At further aft and peak angles, the spectra lose the high frequency second hump associated with the premerged jets and they more closely resemble the conical nozzle. Suppression is still primarily maintained in a broad band of frequencies, primarily centered in midrange. At all angles, the very low-frequency noise levels associated with the postmerged jets are similar in level to the conical.

Best suppression on a flight transformed basis would be from the AR = 2.5 nozzle, Model 22, (see  $\theta = 130^\circ$  and  $140^\circ$ ) where high frequency noise is somewhat below that of the 2.0 (Model 24) and 1.5 (Model 27), in addition to the greatly reduced midfrequency levels.

At the low  $V_{ma}$  point (1200 ft/sec and both streams operating subcritically):

- OASPL and PNL directivities are consistent with plots of peak noise versus  $V_{ma}$ , showing 3-4  $\Delta$ PNL and 7-9  $\Delta$ OASPL. At  $90^\circ$ , PNL levels

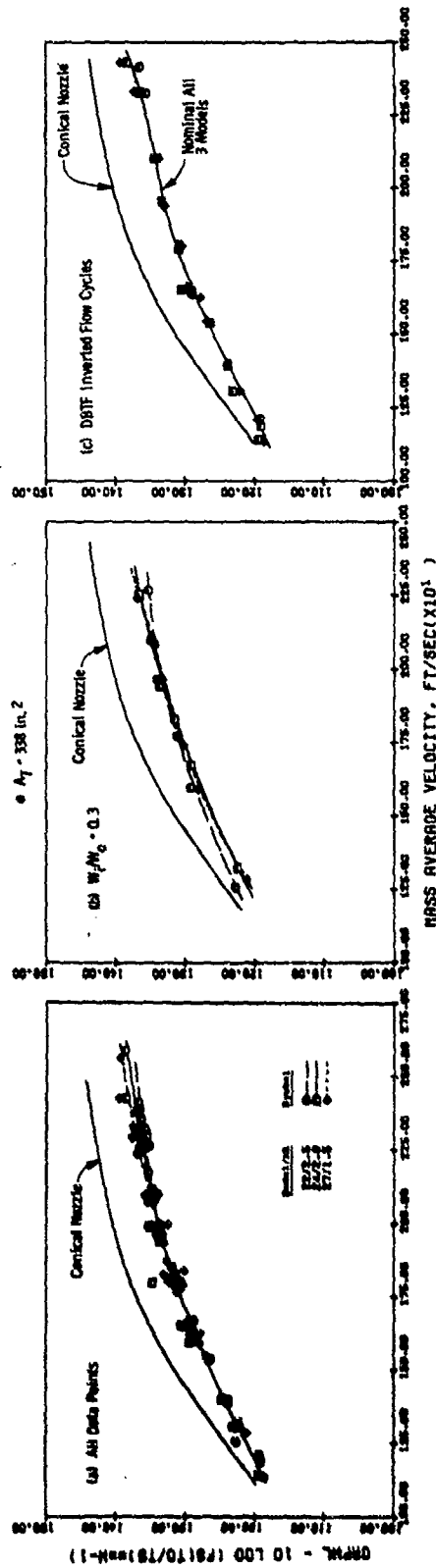


Figure 3-107. Impact of Area Ratio and Radius Ratio on OAPWL, Dual Flow.

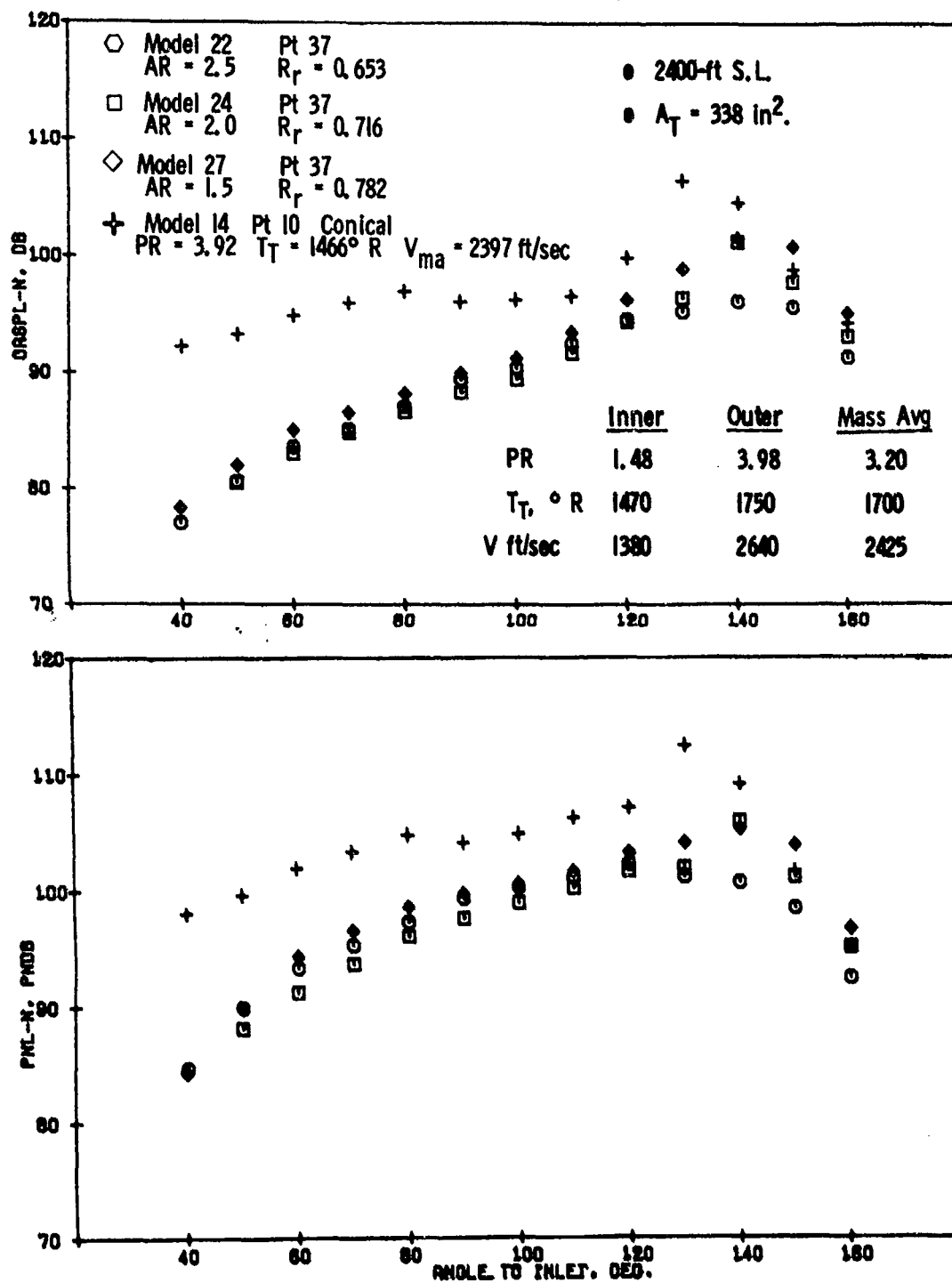


Figure 3-108. Impact of Area Ratio and Radius Ratio on OASPL and PNL Directivity,  $V_{ma} = 2425 \text{ ft/sec}$ , Dual Flow.

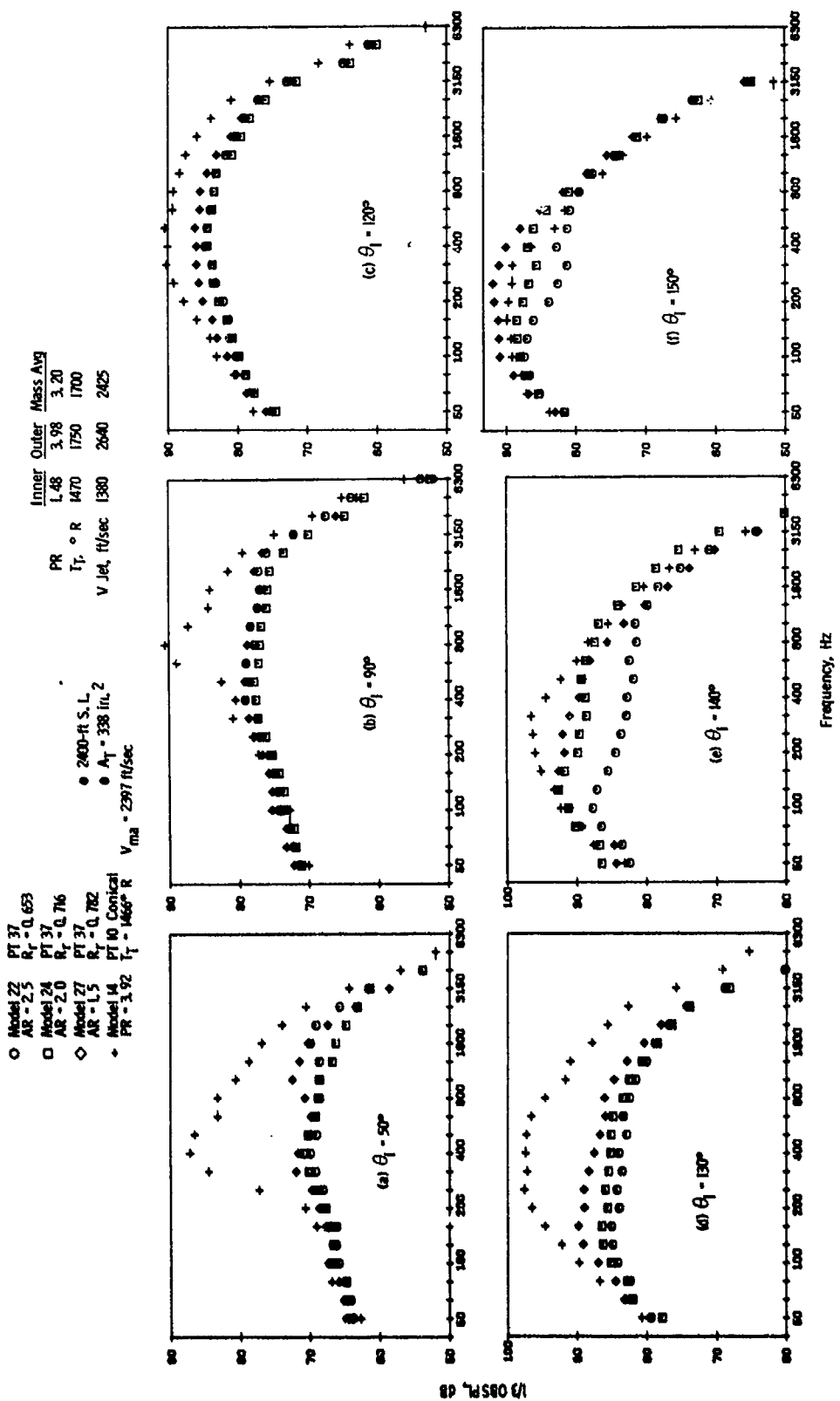


Figure 3-109. Impact of Area Ratio and Radius Ratio on Spectra,  $V_{ma} = 2425 \text{ ft/sec}$ , Dual Flow.

- 2400-ft S.L.
- $A_T = 338 \text{ in.}^2$

	Inner	Outer	Mass Avg.
PR	1.55	1.73	1.67
$T_T, ^\circ \text{R}$	1000	840	885
V Jet ft/sec	1190	1210	1200

- Model 22 PT 24  
AR = 2.5  $R_T = 0.653$
- Model 24 PT 24  
AR = 2.0  $R_T = 0.716$
- ◇ Model 27 PT 24  
AR = 1.5  $R_T = 0.782$
- + Mod 14 PT 18 Cone  
PR = 1.56  $T_T = 990^\circ \text{R}$

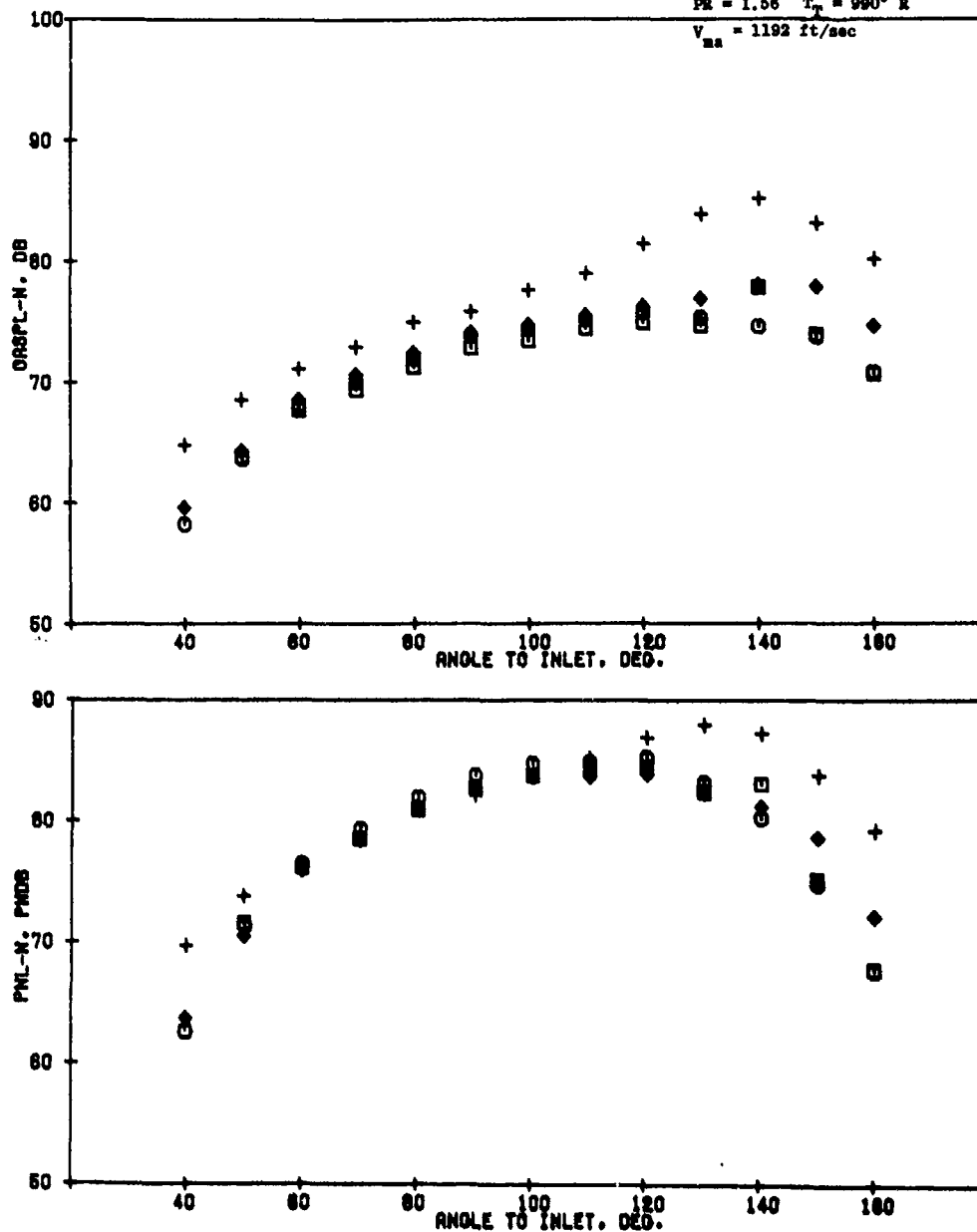


Figure 3-110. Impact of Area Ratio and Radius Ratio on OASPL and PNL Directivity,  $V_{ms} = 1200 \text{ ft/sec}$ , Dual Flow.



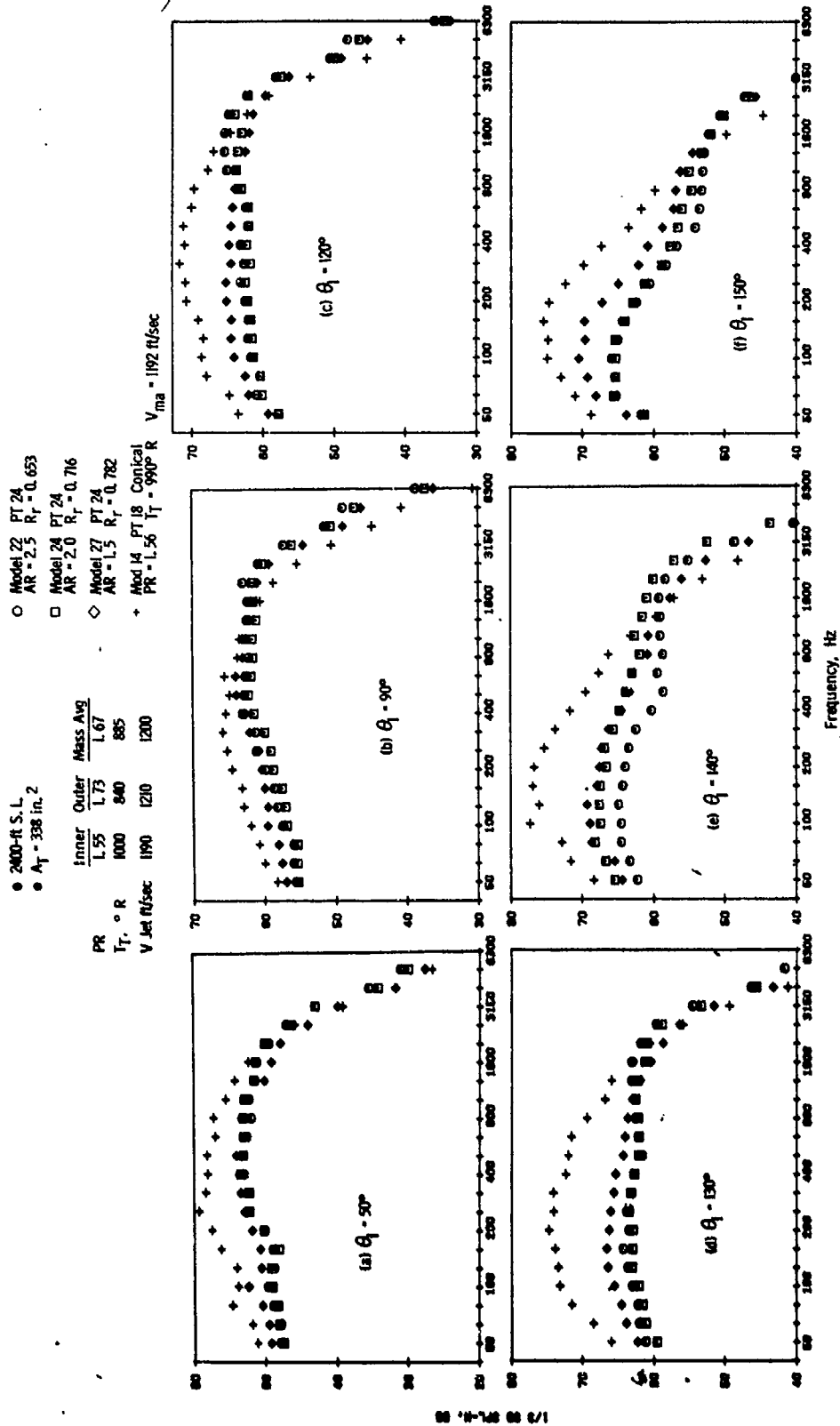


Figure 3-111. Impact of Area Ratio and Radius Ratio on Spectra,  $V_{ma} = 1200 \text{ ft/sec}$ , Dual Flow.

- 2400-ft S. L.
- $A_T = 338 \text{ in.}^2$

	Inner	Outer	Mass Avg
PR	1.48	2.83	2.38
$T_T, ^\circ R$	1460	1425	1425
V Jet ft/sec	1370	2100	1945

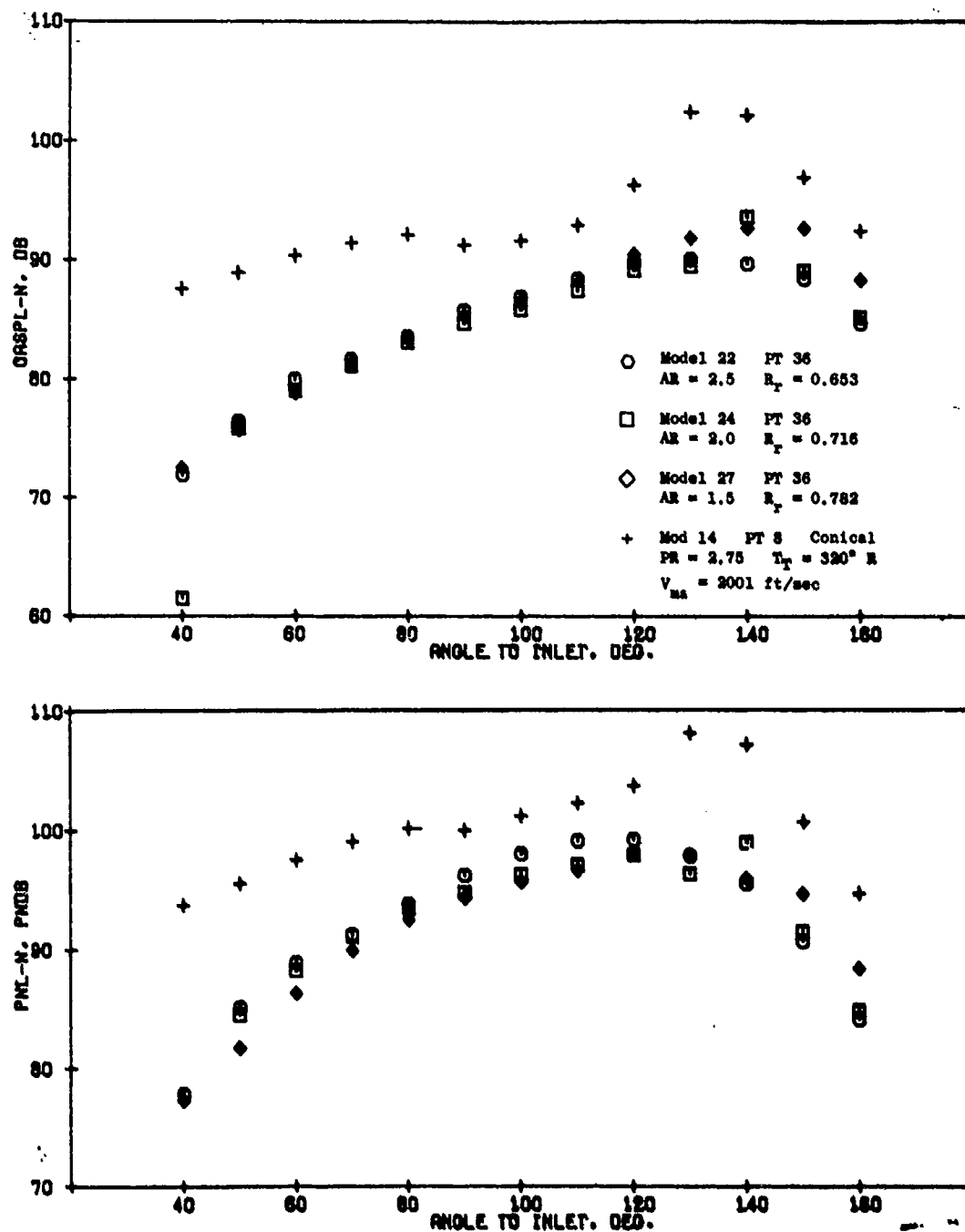


Figure 3-112. Impact of Area Ratio and Radius Ratio on PNL and OASPL Directivity,  $V_{ma} = 1945 \text{ ft/sec}$ , Dual Flow.

• 2400-ft S. L.  
 •  $A_T = 338 \text{ in.}^2$   
 • Model 22 PT 36  
 AR = 2.5  $R_T = 0.653$   
 • Model 24 PT 36  
 AR = 2.0  $R_T = 0.716$   
 • Model 27 PT 36  
 AR = 1.5  $R_T = 0.782$   
 • Model 14 PT 8 Conical  
 PR = 2.75  $T_T = 1520^\circ \text{R}$   
 V Jet ft/sec  
 Inner Outer Mass Avg  
 L 48 2.83 2.38  
 1460 1425 1425  
 1370 2100 1945  
 PR = 8  
 $T_T = 1520^\circ \text{R}$   
 V Jet ft/sec

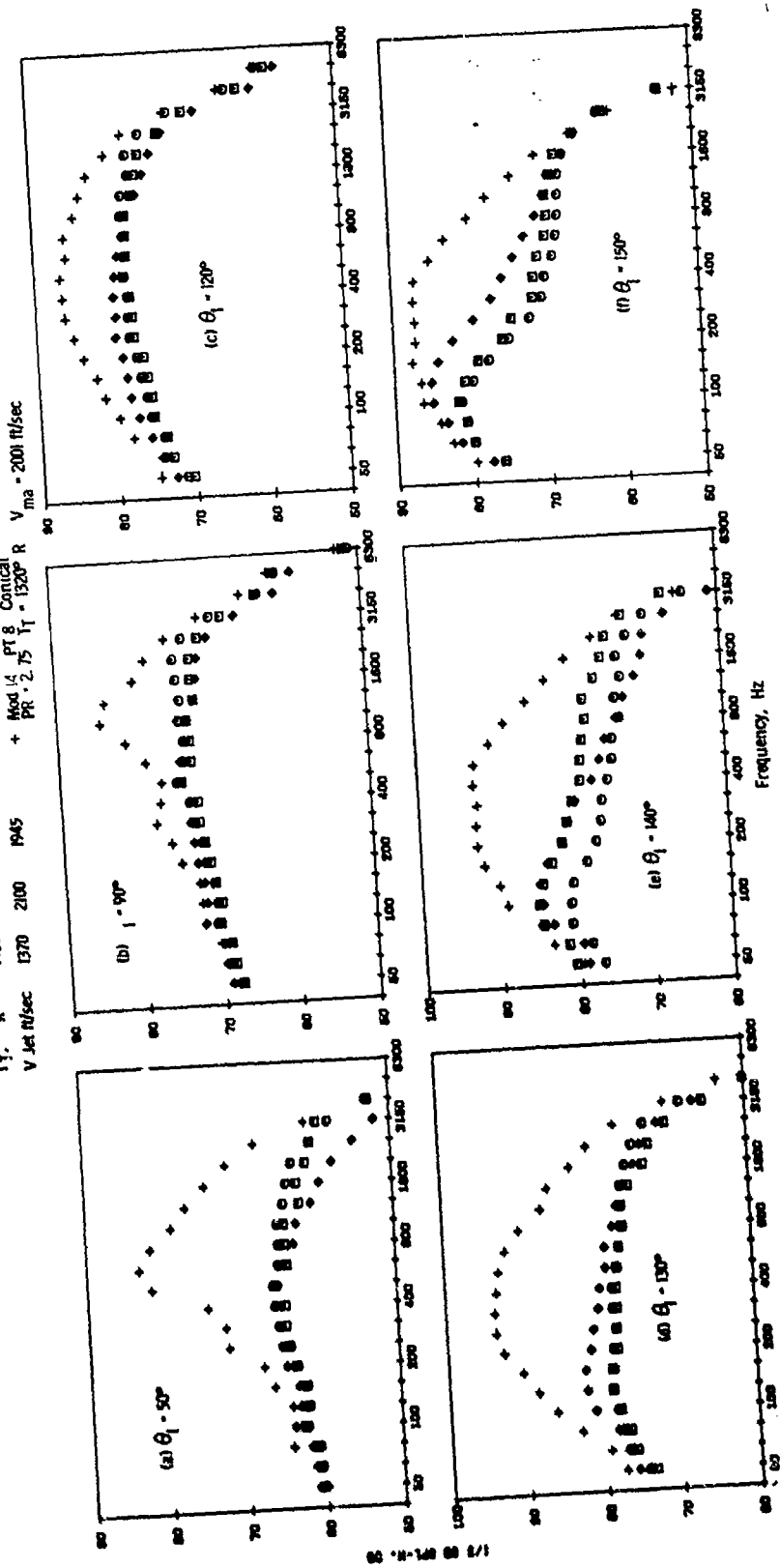


Figure 3-113. Impact of Area Ratio and Radius Ratio on Spectra,  $V_{ma} = 1945 \text{ ft/sec}$ , Dual Flow.

are slightly above the conical nozzle (as the conical nozzle was also operated subcritically and had no shock-cell noise) and OASPL levels show 2-3 dB suppression. At 50°,  $\Delta$ PNL and  $\Delta$ OASPL are somewhat greater than at broadside.

- In general the variance in noise level with changing area ratio is primarily seen only in the aft quadrant and with maximum variance of about 4 PNL and OASPL at 150°. The AR = 2.5 (Model 22) is seen to generally be the best suppressor on a directivity basis.
- Plots at 50°, 90° and 120° to 150° show slightly greater predominance of the premerged high frequency spectra at aft quadrant and peak angles. Suppression relative to the conical nozzle is still primarily maintained in the midfrequency range but with high-frequency noise levels approaching those of the baseline much sooner than at high  $V_{ma}$  and with some low frequency noise suppression observed, dissimilar to that observed at high  $V_{ma}$  for comparable angles.

For consistency of data presentation in comparison to similar data on the full span turbojet suppressor models of the previous section, Figures 3-112 and 3-113 are included for a midvelocity point at  $V_{ma} = 1945$  ft/sec.

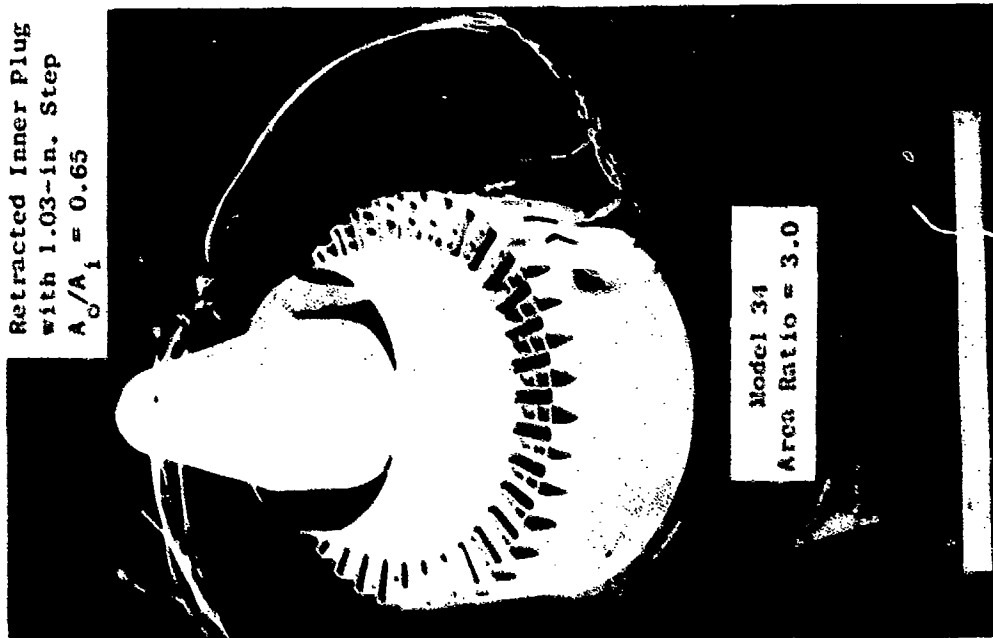
#### Area Ratio Variable, Radius Ratio Constant, Dual Flow (Models 33 and 34)

The purpose of this study was to isolate acoustic performance as a function of area ratio alone, maintaining constant suppressor radius ratio. Models 33 and 34 were utilized per Figure 3-114, each with a nominal value of 0.78 suppressor radius ratio and with a suppressor area ratio of 2.5 and 3.0, respectively. Schematics of the detailed system geometries are per Appendix A, Figures A-27 and A-28. Model 33 of AR = 2.5, from the NASA-Lewis/GE Duct Burning Turbofan program NAS3-18008 (Reference 10), was adapted to the Cell 41 Anechoic Facility. Model 34 adds a new AR = 3.0 annular chute suppressor to the same inner stream geometry. Pertinent parameters for the models are:

Model No.	Outer				Inner				System
	Flow Area, in. <sup>2</sup>	No. of Chutes	Area Ratio	Radius Ratio	Flow Area, in. <sup>2</sup>	Step Height, in.	Plug Location	Radius Ratio	Area Ratio
33	17.21	38	2.5	0.783	11.13	1.034	Retracted	0.674	0.66
34	17.21	38	3.0	0.783	11.13	1.034	Retracted	0.674	0.66

- 36 Chute
- Radius Ratio = 0.78

Retracted Inner Plug  
with 1.03-in. Step  
 $A_o/A_i = 0.65$



Retracted Inner Plug  
with 1.03-in. Step  
 $A_o/A_i = 0.65$

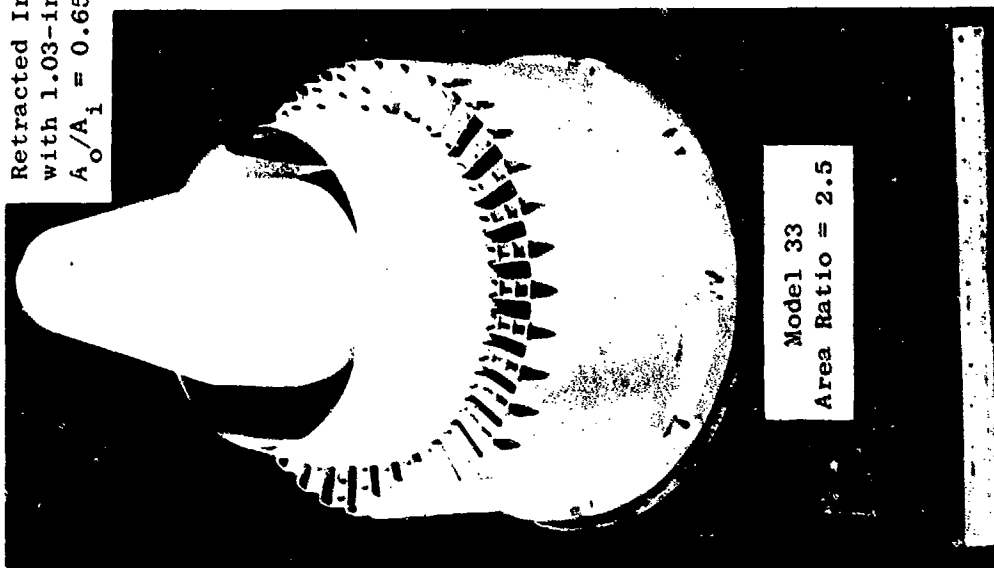


Figure 3-114. Annular Suppressor Area Ratio Variation at Constant Radius Ratio, Dual Flow.

As shown in the tabulation, Models 33 and 34 maintained the same inner flowpath geometry and flow area ratio of 0.65 and thus formed a true variation of suppressor area ratio at constant suppressor radius ratio.

Far-field acoustic testing was performed in the Cell 41 Anechoic Facility following a matrix similar to Section 3.2.1, Figure 3-10 and Table 3-3, but expanded to be more consistent with the test matrix of the DBTF Program (Reference 10). The following cycle series was used.

- $W_1 = 0, 15, \text{ and } 30\% W_0$
- DBTF/Inverted Dual Flow Cycle
- AST/VCE

Comparative acoustic data plots for the two models are included in the following format for the  $W_1 = 0, 15, \text{ and } 30\% W_0$  cycles, each normalized and versus  $V_{ma}$ .

- Figures 3-115 and 3-116 peak OASPL and PNL
- Figures 3-117 and 3-118  $90^\circ$  OASPL and PNL
- Figures 3-119 and 3-120  $50^\circ$  OASPL and PNL
- Figure 3-121 OAPWL

Acoustic data for Models 33 and 34 were presented and discussed in Section 3.4.2.2 (System Velocity Ratio Variation at Fixed  $A_0/A_1$  and Duct Suppressor Geometry). It was shown that noise levels for low system area ratio,  $A_0/A_1 = 0.65$ , vary widely with cycle  $V_0/V_1$ , particularly studied within the dBTF/Inverted Dual Flow cycle matrix for  $0.6 \leq V_0/V_1 \leq \infty$ . Within this section, for isolation of suppressor area ratio impact on acoustic performance, comparisons between the two models at fixed values of  $V_0/V_1 = 0.6, 0.8, 1.0, 1.25, 1.5, 2.0, \text{ and } \infty$  (no inner flow) are included in Figures 3-122 and 3-123 for peak OASPL and peak PNL.

Supporting OASPL and PNL directivity data plus  $1/3$  OASPL spectra, selected as representative of the wide data matrix, are included in the following graphs:

- Figures 3-124 and 3-125  $W_1 = 30\% W_0, V_{ma} = 2075 \text{ ft/sec}$
- Figures 3-126 and 3-127  $W_1 = 30\% W_0, V_{ma} = 1340 \text{ ft/sec}$

Review of the data elicits the following general observations:

- Levels of peak OASPL/PNL suppression vary considerably with the particular cycle under consideration. Maximum  $\Delta$  peak PNL values are seen to be approximately 19/13.5, 16.3/11.5, and 13.5/9.7 for  $W_1 = 0, 15, \text{ and } 30\% W_0$  cycles for the  $AR = 2.5$  suppressor (Model 33) and 18.5/13, 16.7/12, and 15.5/10.7 for the  $AR = 3.0$  nozzle (Model 34). This results in a spread of 5.5/3.7 and 3.1/2.3 peak OASPL/PNL. A greater spread is seen in the DBTF cycle where  $0.6 \leq V_0/V_1 \leq \infty$ , as per data of Section 3.4.2.2.

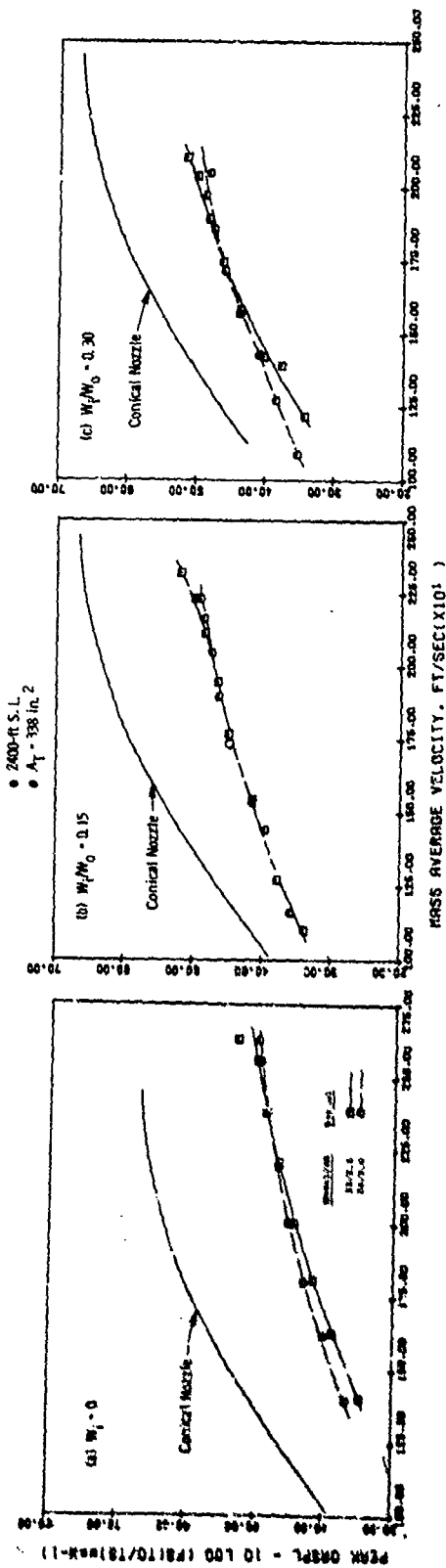


Figure 3-115. Area Ratio Variation at Constant Radius Ratio, Peak QASPL.

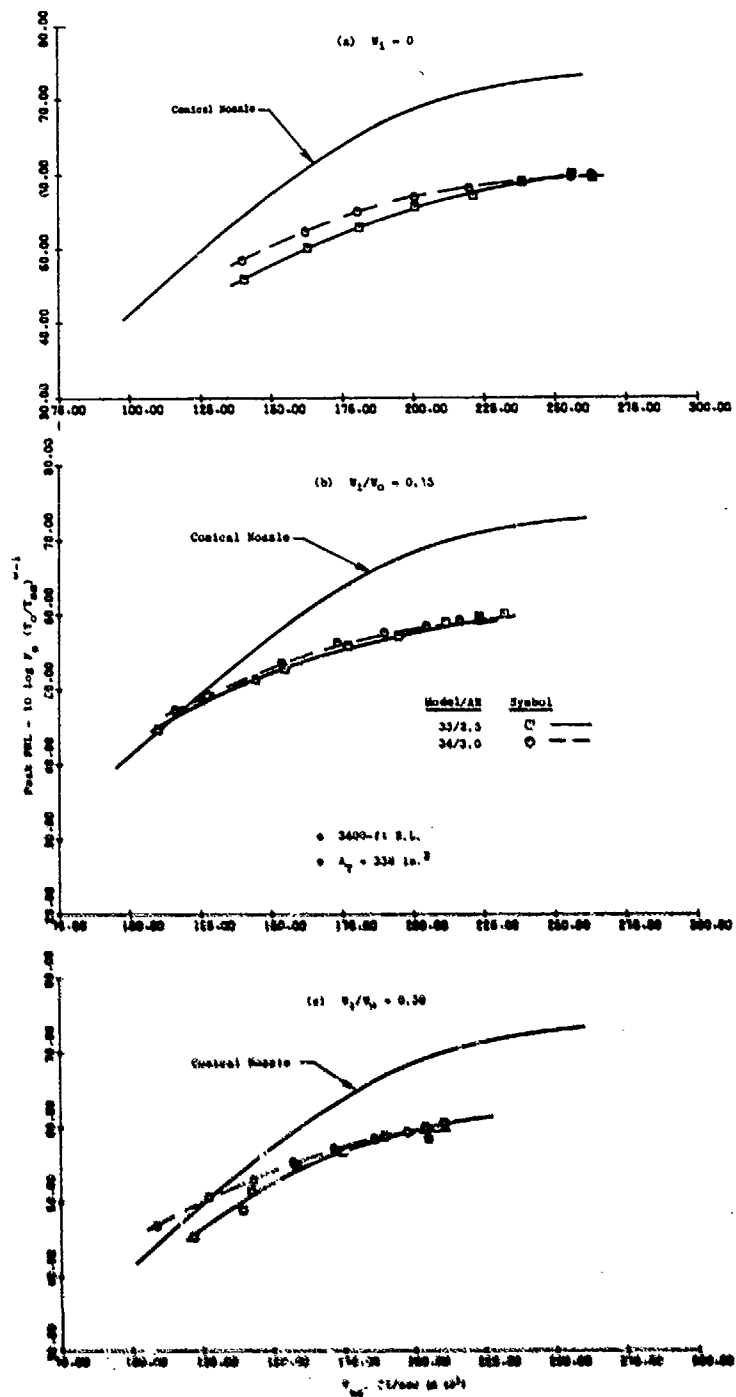


Figure 3-116. Area Ratio Variation at Constant Radius Ratio, Peak PHL.



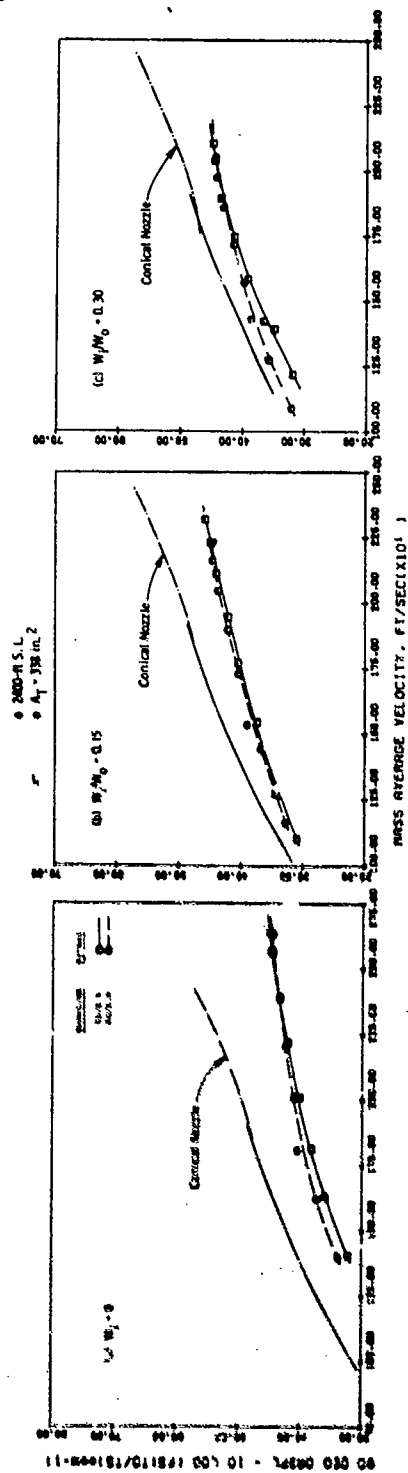


Figure 3-117. Area Ratio Variation at Constant Radius Ratio, 90° OASPL.

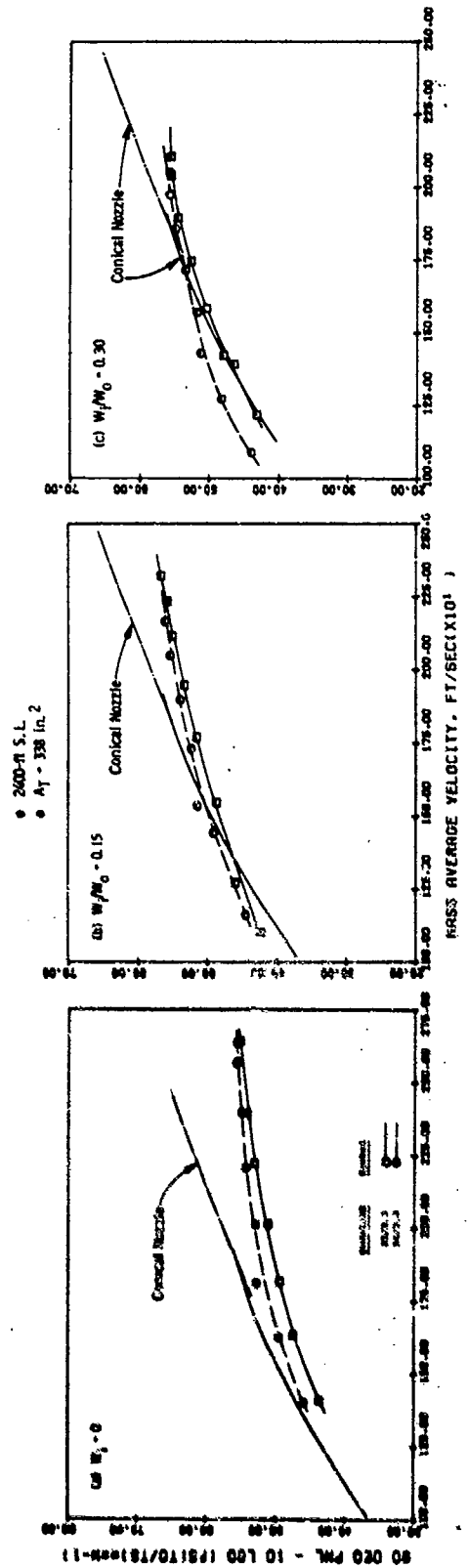


Figure 3-118. Area Ratio Variation at Constant Radius Ratio, 90° PNL.

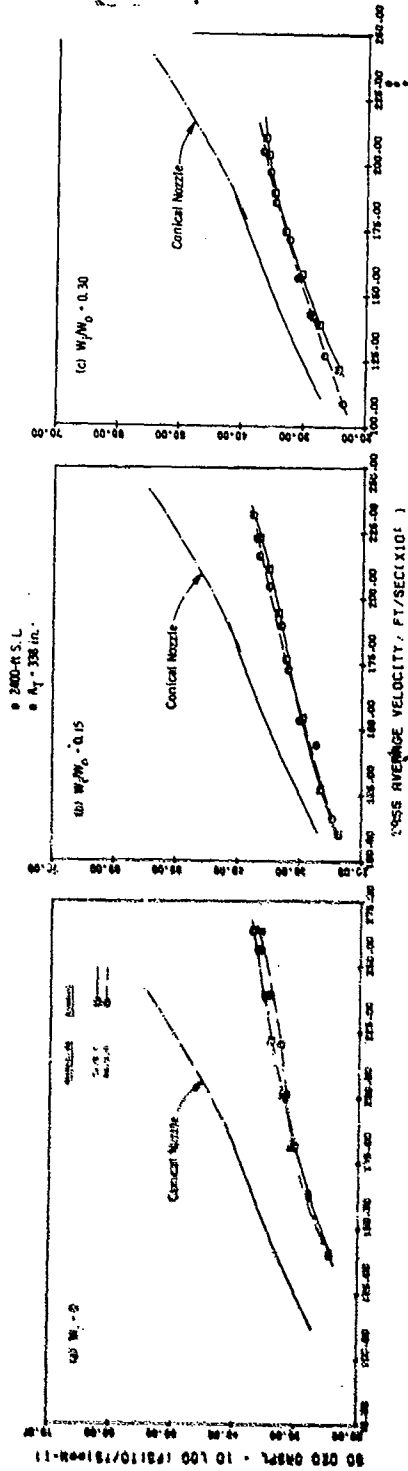


Figure 3-119. Area Ratio Variation at Constant Radius Ratio, 50° OASPL.

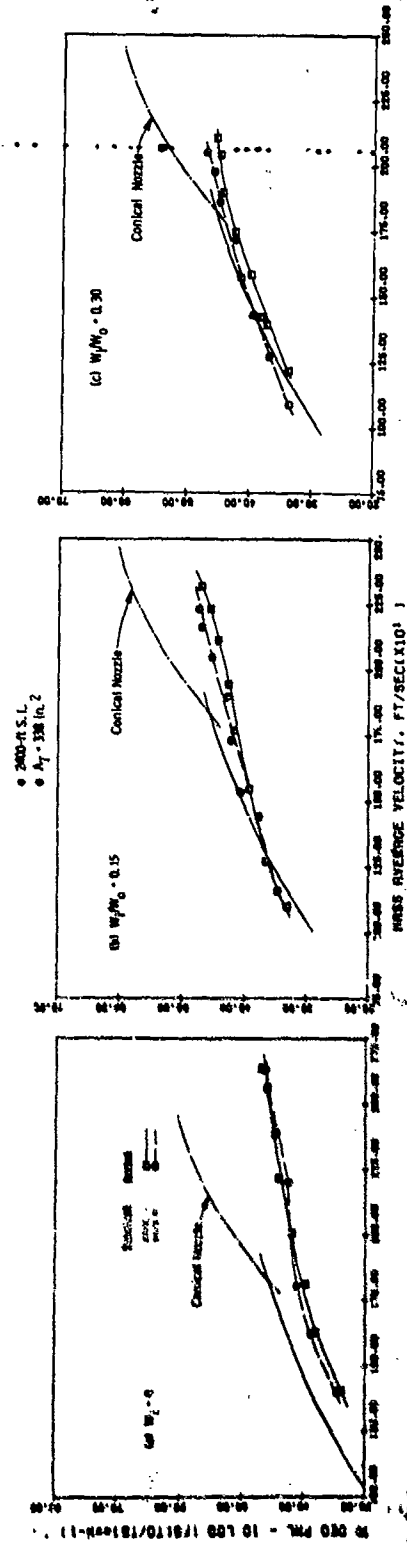


Figure 3-120. Area Ratio Variation at Constant Radius Ratio, 50° PNL.

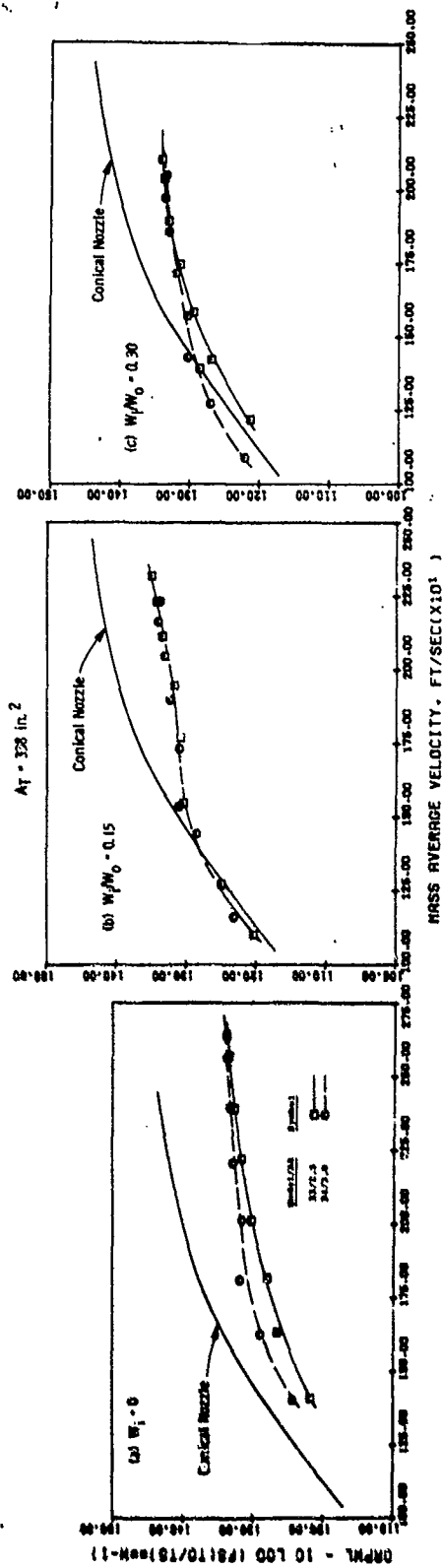


Figure 3-121. Area Ratio Variation at Constant Radius Ratio, OAPWL.

- 2400-ft S.L.
- $A_T = 338 \text{ in.}^2$

- Model 33, AR = 2.5
- - -○- - Model 34, AR = 3.0

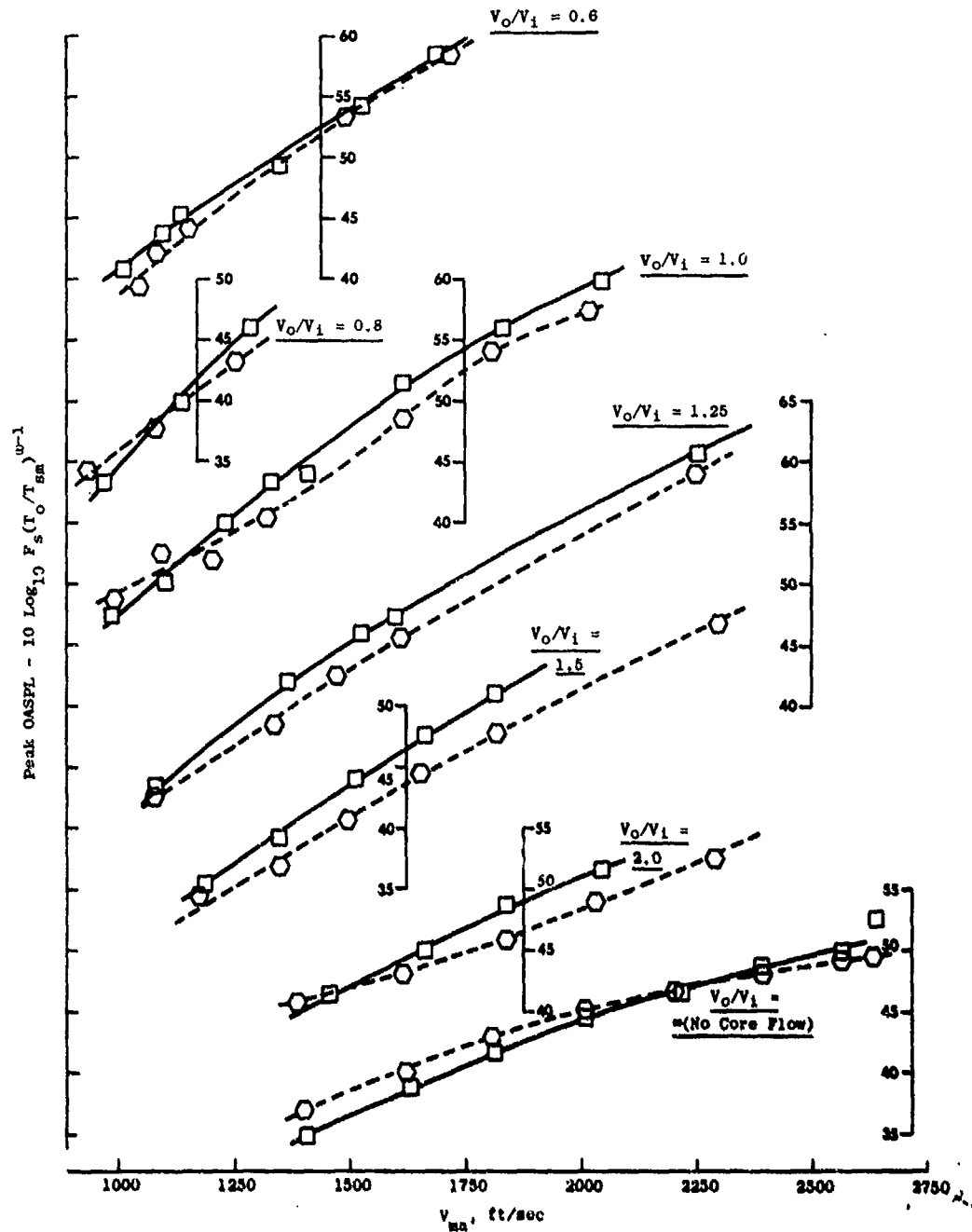


Figure 3-122. Area Ratio Variation at Constant Velocity Ratio, Peak OASPL.

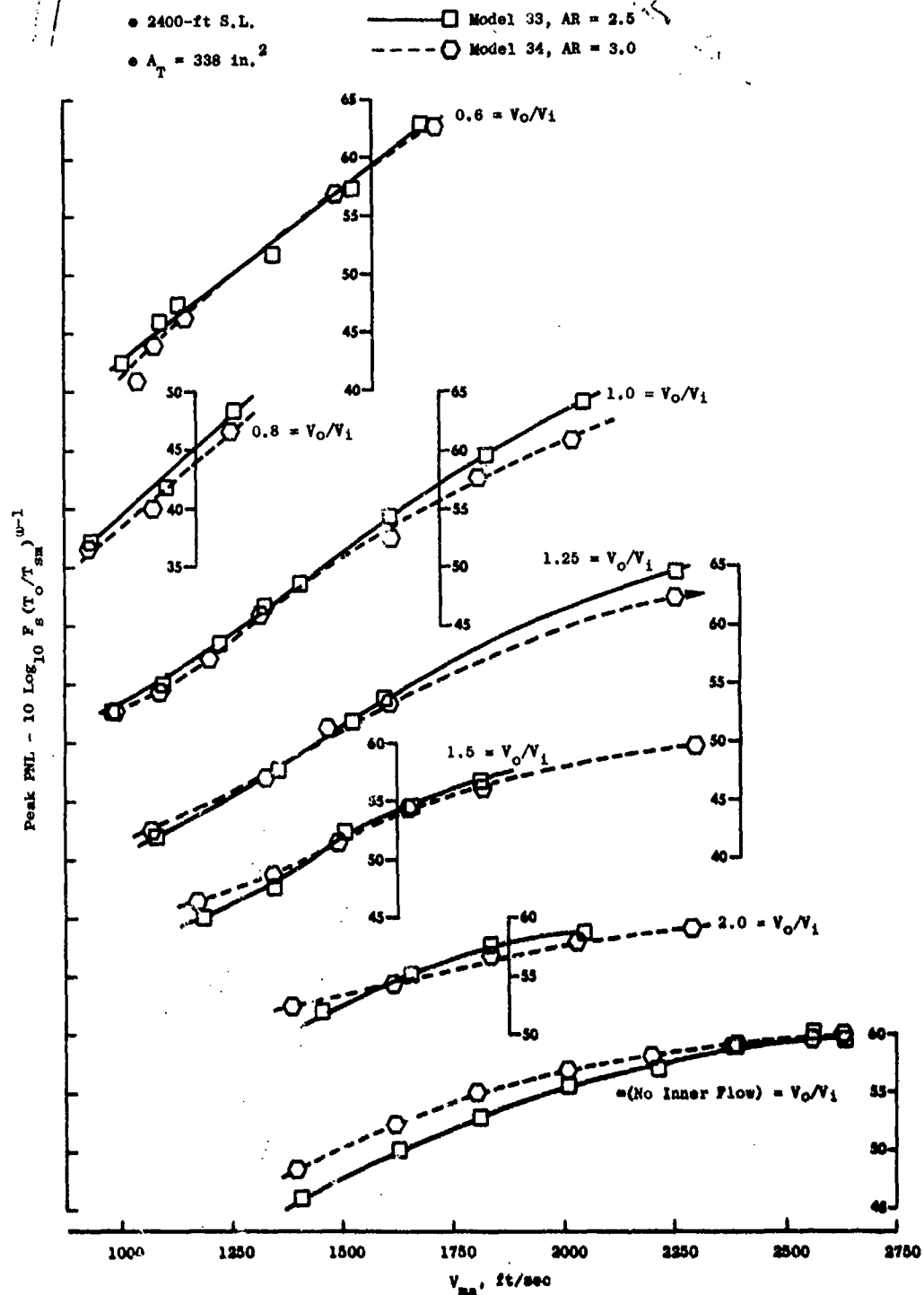


Figure 3-123. Area Ratio Variation at Constant Velocity Ratio, Peak PNL.

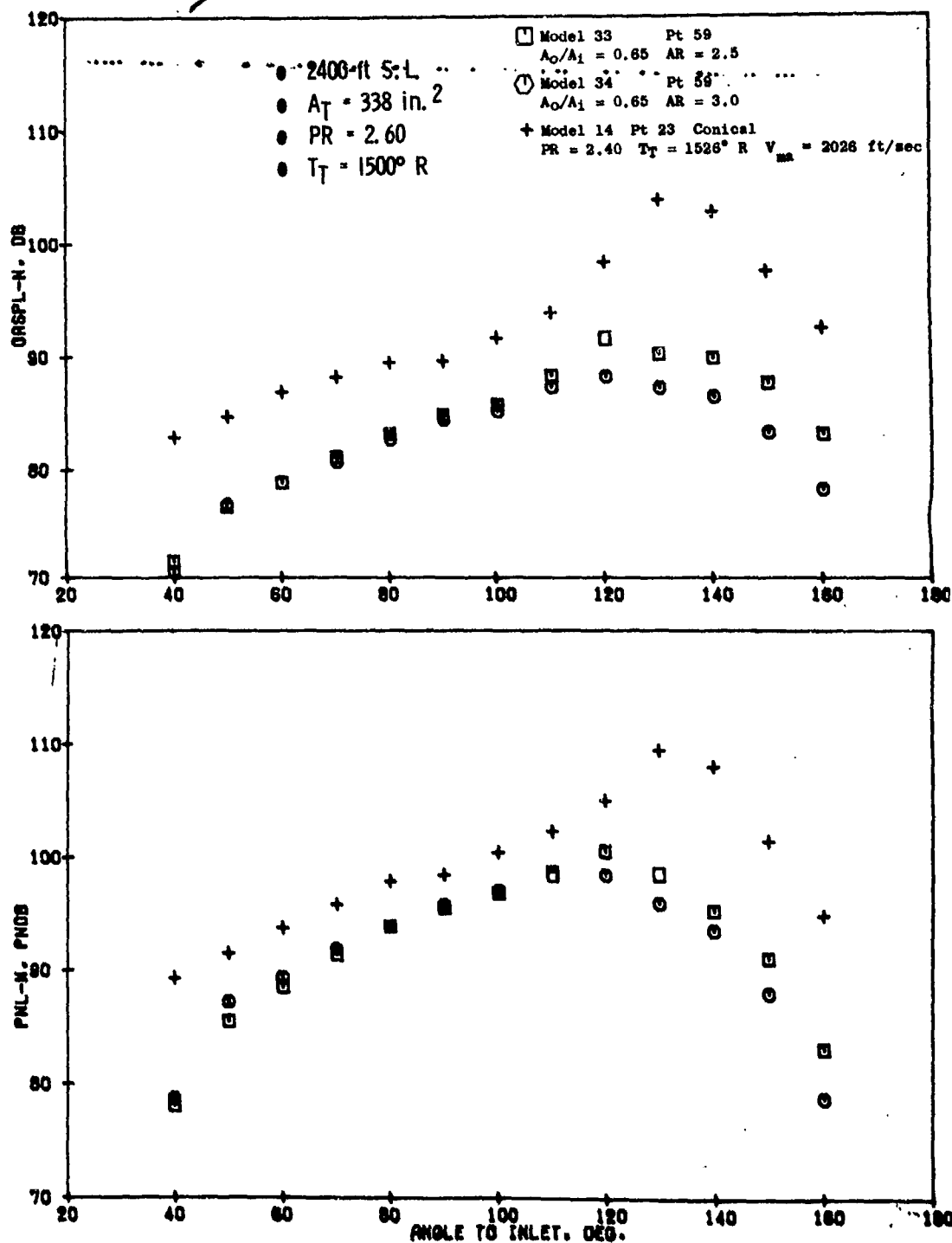


Figure 3-124. Area Ratio Variation at Constant Radius Ratio, OASPL, and PNL Directivity,  $V_{ma} = 2075 \text{ ft/sec}$ .

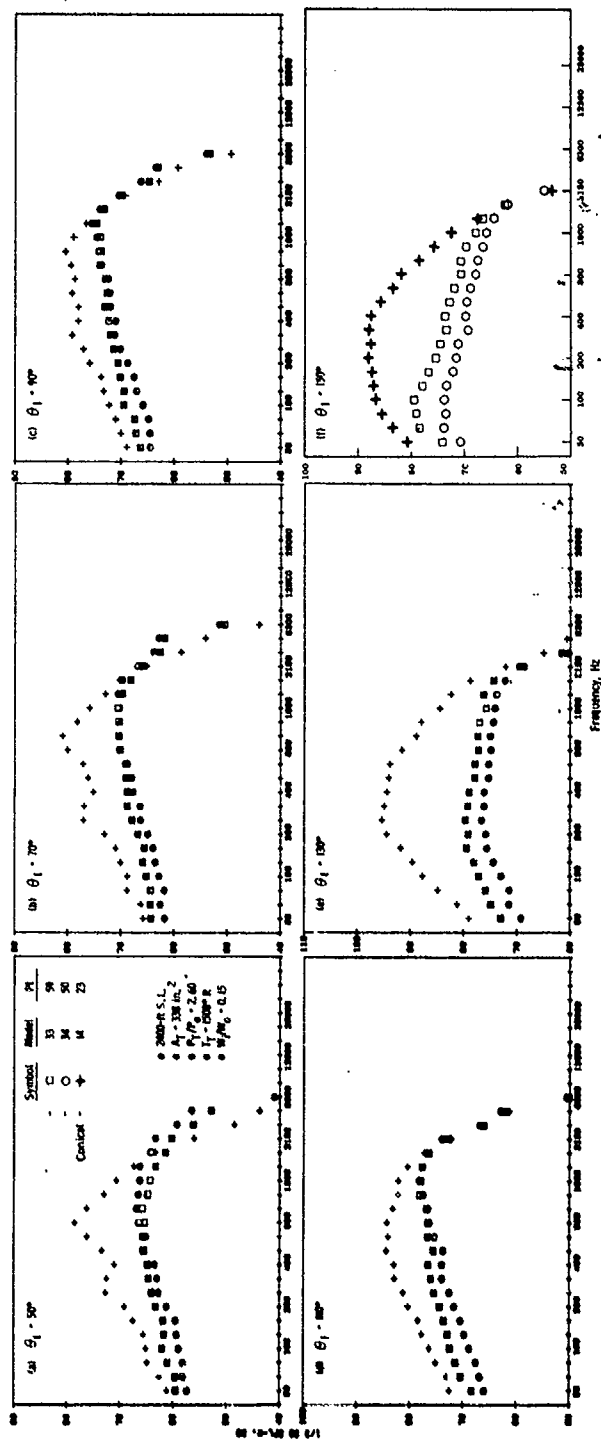


Figure 3-125. Area Ratio Variation at Constant Radius Ratio, Spectra,  $V_{ma} = 2075$  ft/sec.

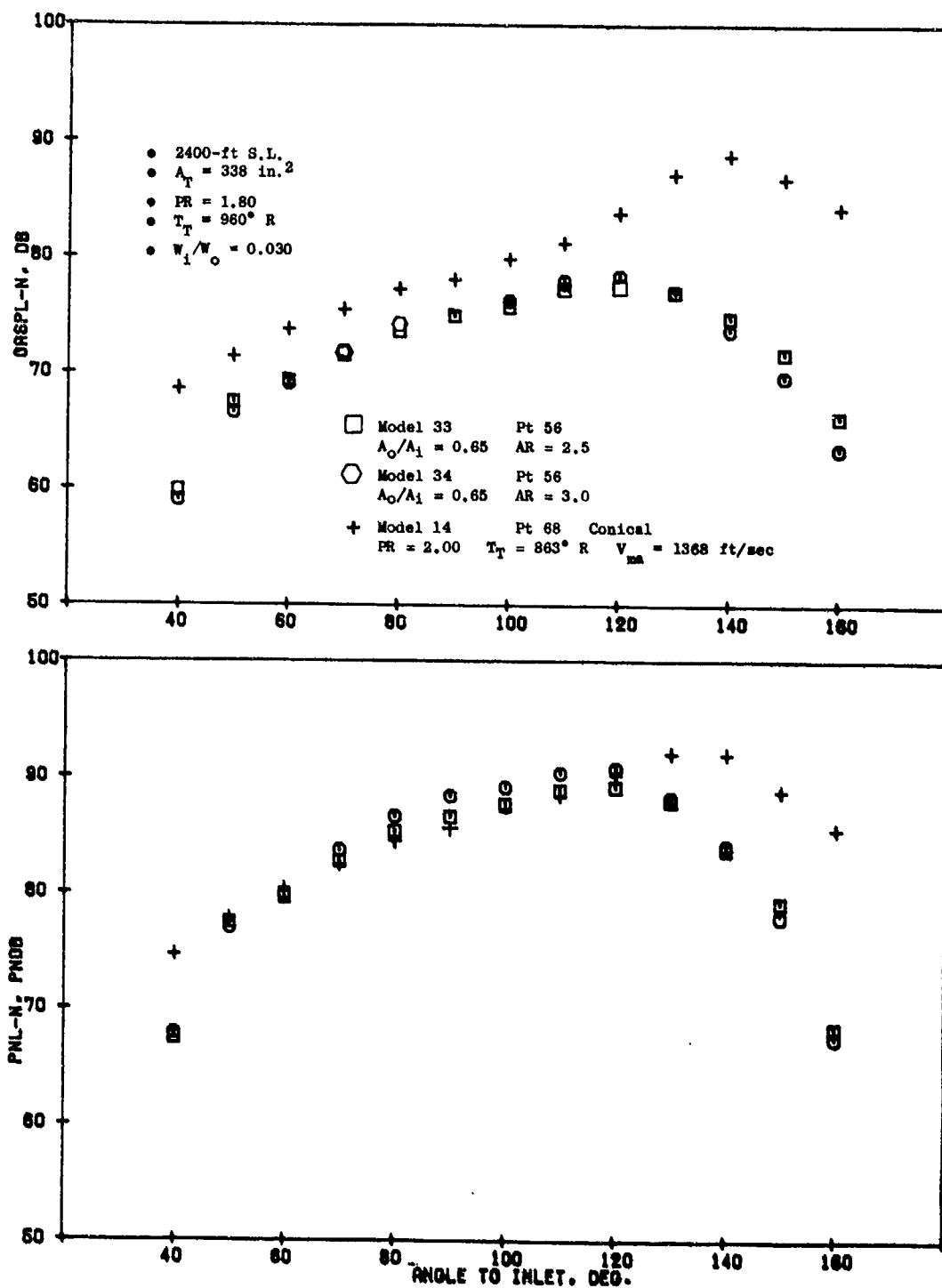


Figure 3-126. Area Ratio Variation at Constant Radius Ratio, OASPL and PNL Directivity,  $V_{na} = 1340 \text{ ft/sec}$ .



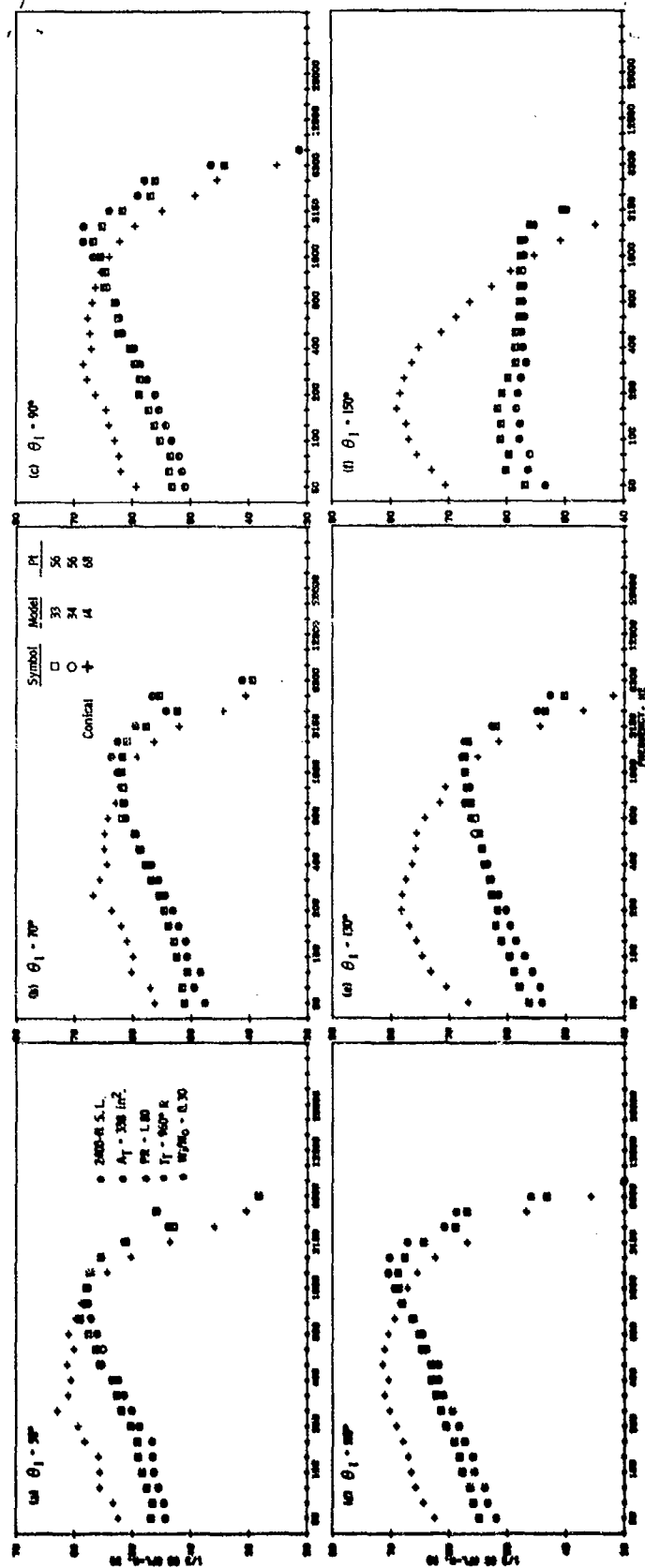


Figure 3-127. Area Ratio Variation at Constant Radius Ratio, Spectra,  $V_{ma} = 1340 \text{ ft/sec.}$

- On a peak OASPL/PNL basis for the  $W_1 = 0, 15, \text{ and } 30\% W_0$  cycle, Figures 3-115 and 3-116 show suppression trends with area ratio are similar to those of the previous section's trends of area ratio/radius ratio variation on a dual flow system in that; (a) at low  $V_{ma}$ , the lower AR = 2.5 (Model 33) shows consistently better suppression from 0 to 3 on peak OASPL and from 1 to 4 on peak PNL, (b) at high  $V_{ma}$  the higher AR = 3.0 (Model 34) consistently shows a potential for better suppression with improvements of 1 to 2 seen on peak OASPL and 0 to 1 on peak PNL, and (c) the crossover in trend occurs in the  $V_{ma}$  range of 2000-2250 ft/sec. This occurs for both peak PNL and peak OASPL whereas in the previous section for area ratio and radius ratio variation on a dual flow system, it was not a consistent trend on peak OASPL.
- At  $90^\circ$ , Figures 3-117 and 3-118, some suppression is retained broadside for most cycles, particularly for OASPL and most noticeably at mid-to-high  $V_{ma}$  where shock-cell noise is not predominant in the segmented jets flow field. For all cycles and for both PNL and OASPL, the lower AR = 2.5 (Model 33) is consistently the better suppressor, indicating levels of 1 to 4 lower PNL noise and from 0 to 2 lower OASPL noise than the AR = 3.0 (Model 34).
- Similarly at  $50^\circ$ , Figures 3-119 and 3-120, substantial forward quadrant suppression is seen relative to the conical nozzle; greater than at broadside. Basic differences between the two area ratios are not obvious as differences in levels are mostly nominal, and where they do occur, they form no consistent trend for the various data sets. This is consistent with the previous section's variation of area ratio and radius ratio on the OASPL basis where  $50^\circ$  data showed no distinguishable preference with area ratio variation. On the PNL basis, the previous data showed lower area ratio to maintain better suppression by several  $\Delta$ PNL.
- OAPWL data for the three chosen cycles, Figure 3-121, indicate similarity of levels to better suppression by the lower AR = 2.5 nozzle, Model 33, from 0 to 4  $\Delta$ OAPWL looking from high to low  $V_{ma}$ . Previous data showed no significant variation with area ratio and radius ratio.
- Reviewing Figures 3-122 and 3-123, peak OASPL and peak PNL comparisons for the DBTF cycle at constant  $V_0/V_1 = 0.6, 0.8, 1.0, 1.25, 1.5, 2.0, \text{ and } \infty$  (no inner flow) shows: (a) consistent trends of improved OASPL suppression with higher AR = 3.0 (Model 34) for all velocity ratios and  $V_{ma}$  values, except when inner flow was completely shut off ( $V_0/V_1 = \infty$ ); and (b) peak PNL trends are similar to those of Figure 3-116 for  $W_1 = 0, 15, \text{ and } 30\% W_0$ , in that at low  $V_{ma}$  the low AR (Model 33) is the better suppressor and at high  $V_{ma}$  the higher AR = 3.0 (Model 34) shows potential for greater suppression.
- The OASPL and PNL directivity data of Figures 3-124 and 3-126 indicate (a) differences in OASPL level are primarily observed in the

aft quadrant for both high  $V_{ma} = 2075$  ft/sec and the low  $V_{ma} = 1340$  ft/sec, maximum variance of 5  $\Delta$ OASPL being seen at  $160^\circ$  for the high  $V_{ma}$  point, and (b) for PNL, low  $V_{ma}$  variance is broadside where high  $V_{ma}$  variance is in the aft quadrant with a maximum  $\Delta$ PNL of 4 seen at  $160^\circ$  for the high  $V_{ma}$  point. Thus, no exceptionally large differences are seen in the  $AR = 2.5$  to  $3.0$  range. The data are consistent with previous observations on the peak basis in that at low  $V_{ma}$  the  $AR = 2.5$  (Model 33) has lower noise level and at high  $V_{ma}$  the  $AR = 3.0$  (Model 34) is the better suppressor.

- Supporting spectra (Figures 3-125 and 3-127) indicate that major differences in noise content are in the low frequency range associated with the postmerged jets and in all cases indicate lower levels associated with the  $AR = 3.0$  (Model 34). This would suggest more rapid decay of the premerged individual jet plumes prior to coalescence into a common jet, thereby resulting in a lower merged velocity. Spectra comparisons at high frequency show dominance of the  $AR = 3.0$  (Model 34) at low  $V_{ma}$ , thus, showing better suppression for the  $AR = 2.5$  (Model 33) as the high frequency levels are controlling both OASPL and PNL. At  $V_{ma} = 2075$  ft/sec the high frequency spectra for the  $AR = 3.0$  (Model 34) are normally lower level than the  $AR = 2.5$  (Model 33), thus effecting the previously observed improved performance.

#### 3.4.2.2 Flow Management and Inner Stream Geometry Studies

System overall parameters of area ratio ( $A_0/A_1$ ), velocity ratio ( $V_0/V_1$ ), and by-pass ratio ( $\beta = W_0/W_1$ ) are developed in detail to establish the basic propulsion nozzle for each dual flow system considered for application of an annular half span suppressor. Detailed individual stream aerodynamic cycle composition in terms of  $P_{T1,0}/P_0$ ,  $T_{1,0}$  and  $V_{1,0}$  are selected consistent with state-of-the-art component and cycle designs to provide system efficiency. These variables were also found to sharply influence the acoustic effectiveness of a system which incorporates an annular mechanical suppressor. Three studies were performed to develop qualitative and quantitative suppressor design directions. These are:

##### (a) System Velocity Ratio Variation With Fixed $A_0/A_1$ and Fixed Outer Stream Suppressor Geometry.

Outer to inner stream velocity ratio variance over a range of  $0.6 \leq V_0/V_1 \leq \infty$  has been considered for various annular suppressors. Detailed results are presented for six representative chute, spoke and shallow-chute models; three at  $A_0/A_1 = 0.65$ , two at 1.92 and one at 3.61. The results indicate that  $V_0/V_1$  influence is most predominant on low area ratio systems, due to the more controlling influence of the inner stream.

(b) System  $\beta$  Variation With Fixed  $A_0/A_1$  and Fixed Outer Stream Geometry.

Outer to inner stream weight flow ratio,  $\beta$ , at fixed values of  $\infty$ , 6.7, and 3.3 (corresponding to  $W_1 = 0, 15$  and  $30\%$  of  $W_0$ ) have been considered in application to seven models. Detailed results from four of these models are discussed and consistently indicate increased acoustic efficiency of the annular suppressor with increase in  $\beta$ .

(c) System Area Ratio and Inner Stream Plug Geometry Variation - Fixed Outer Stream Suppressor Geometry

A controlled study was considered utilizing six models to isolate the impact on suppression potential due to system area ratio changes, within the practical range for a variable cycle engine (VCE) system ( $A_0/A_1 = 1.92$  and  $3.61$ ). Changes in inner stream plug geometry were evaluated, duplicating practical engine designs to induce low amounts of flow into the inner stream. Results indicate that higher system area ratio (effectively forcing a greater portion of the flow through the suppressed annulus) yields higher suppression. Inner flow geometry variance has minor impact on suppression for the high  $A_0/A_1$  system and mixed results for the low  $A_0/A_1$  system.

System Velocity Ratio Variation at Fixed  $A_0/A_1$  and Outer Stream Suppressor Geometry

This study attempted to isolate the influence of velocity ratio ( $V_0/V_1$ ) for a dual flow system. Systematic variation of velocity ratio was accomplished with fixed system area ratios ( $A_0/A_1$ ) and utilizing select multi-element annular suppressors, independent of any attempt to maintain consistent values of by-pass ratio ( $\beta = W_0/W_1$ ). This was accomplished on Models 22 to 32 and 36, of  $A_0/A_1 = 1.92$  and  $3.61$ , utilizing the DBTF/Inverted Dual Flow test matrix of Section 3.2.1, which set values of  $V_0/V_1$  at 1.0, 1.25, 1.5 and 2.0 and on Models 33, 34 and 35 utilizing an expanded DBTF/Inverted Dual Flow test matrix with  $V_0/V_1$ 's = 0.6, 0.8, 1.0, 1.25, 1.5, 2.0 and  $\infty$  (no inner flow). Of these various models, six were selected for presentation of results herein, as follows:

Model No.	System $A_0/A_1$	Outer Stream				Inner Stream				Appendix A Figure Reference
		Element Description	AR	$\beta$	Flow Area, in. <sup>2</sup>	Step Height, in.	Plug Location	$U_1$	Flow Area, in. <sup>2</sup>	
33	0.65	36 Chute	2.5	0.783	17.21	1.034	Retracted	0.674	11.12	27
34	0.65	36 Chute	3.0	0.783	17.21	1.034	Retracted	0.674	11.12	28
35	0.65	36 Spoke	2.5	0.783	17.21	1.034	Retracted	0.674	11.12	29
31	1.92	30 Shallow Chute	1.75	0.717	23.76	0.70	Retracted	0.779	12.39	25
27	1.92	36 Chute	1.5	0.782	23.76	0.70	Retracted	0.779	12.39	21
26	3.61	36 Chute	2.0	0.716	23.76	0.33	Retracted	0.89	8.58	20

The last column of the above chart refers to the detailed geometric definitions for each model in Appendix A. The first three suppressors, Models 33, 34 and 35 of Figure 3-128, are of  $A_0/A_1 = 0.65$ , the next two, Models 31 and 27 of Figure 3-129, are of  $A_0/A_1 = 1.92$ , and the last, Model 26 of Figure 3-130, is of  $A_0/A_1 = 3.61$ . Results are discussed as an aggregate for each  $A_0/A_1$  value. The three basic varieties of the spoke/chute family of segmented suppressors are represented, i.e., deep-chutes, spokes and shallow-chutes. All models are of relatively high suppressor radius ratio,  $R_T^0 = 0.716$  to  $0.783$ , consistent with advanced technology suppressor systems. Suppressor area ratio range of 1.5 to 2.5 is also represented.

Results of peak,  $90^\circ$  and  $50^\circ$  PNL and OASPL are presented in the following Figures for the three models of  $A_0/A_1 = 0.65$ , each data set normalized as per Section 3.3.1.7 and plotted versus  $V_{ma}$ .

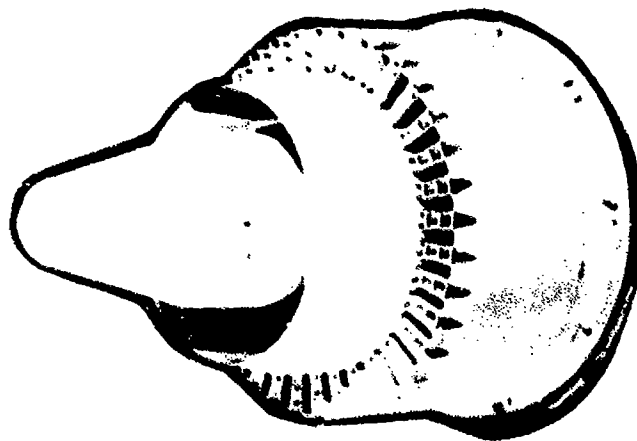
Model No.	Peak	$90^\circ$	$50^\circ$
33	3-131	3-132	3-133
34	3-134	3-135	3-136
35	3-137	3-138	3-139

Partial acoustic results from the three models are discussed in other sections of this report (Section 3.4.2.1 "Area Ratio Variable, Radius Ratio Constant - Dual Flow" compares Model 33 and 34's Area Ratio = 2.5 and 3.0 results, and Section 3.4.2.4 "Element Type Study-Dual Flow of Low System Area Ratio" compares Model 33 and 35 chute versus spoke results).

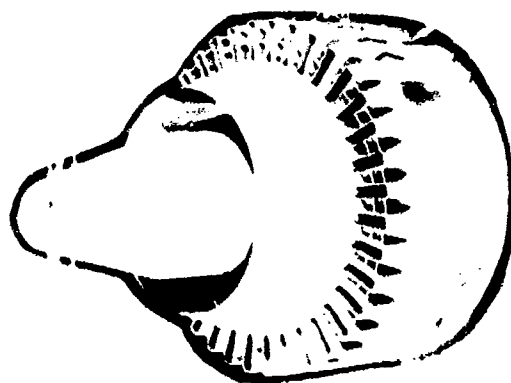
Observations of results from the above curves in relation to the goal of isolating the impact of system velocity ratio are as follows:

- When isolated on data-fitted curves at constant  $V_0/V_1$  values, peak OASPL and PNL acoustic results form progressive and consistent trends of noise level. Trends on a peak OASPL basis are consistently progressive from  $V_0/V_1 = 0.6$  to  $\infty$  for all three models, at any  $V_{ma}$ . The noise levels are consistent with or slightly in excess of, the conical baseline at  $V_0/V_1 = 0.6$ , and they vary progressively until  $\Delta OASPL$  suppression levels approach 19 dB in the  $2000 \leq V_{ma}$ , ft/sec,  $\leq 2500$  range for  $V_0/V_1 = \infty$ , for each model.  $V_0/V_1 = \infty$  is attained when the inner flow is curtailed completely (by use of a positive shutoff mechanism placed about one diameter upstream of the inner exit plane). A blunt base region remains at the inner exit annulus, over which the outer stream flow expands.
- At mid-to-high  $V_{ma}$ , maximum PNL suppression levels of 13.5 to 16 PNdB are observed for the three models. The peak PNL levels decrease uniformly as  $V_0/V_1$  increases, but do not display the same magnitude of change as on peak OASPL. At lower  $V_{ma}$ , a reversing of noise level trends is seen at the higher  $V_0/V_1$  ratios and levels of suppression are substantially reduced.

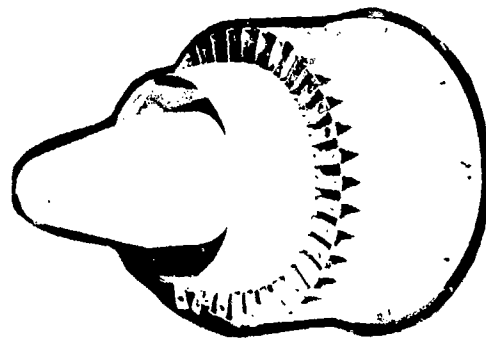
- $A_o/A_1 = 0.65$
- 1.03-in. Core Annulus Height
- Plug Retracted



Model 33  
36-Chute, AR = 2.5

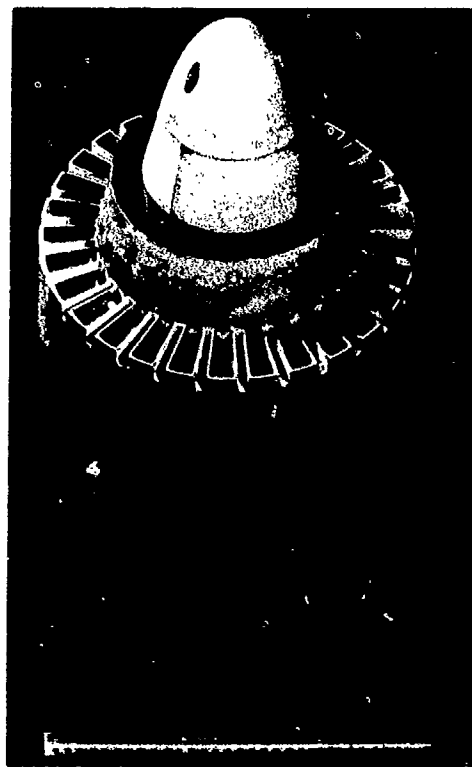


Model 34  
36-Chute, AR = 3.0

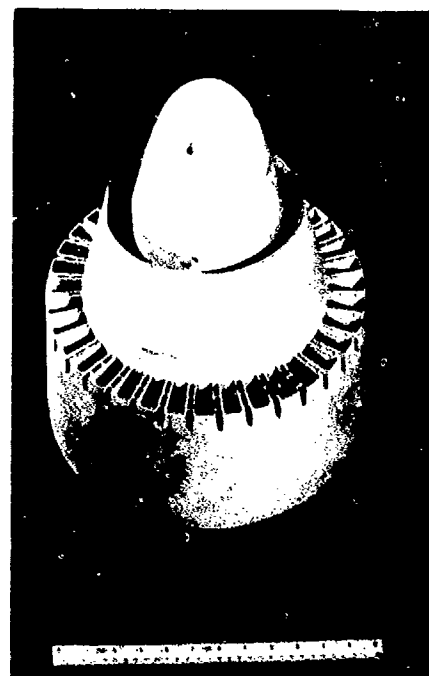


Model 35  
36-Spoke, AR = 2.3

Figure 3-128. Dual-Flow Models for Velocity Ratio Investigation at  $A_o/A_1 = 0.65$ .

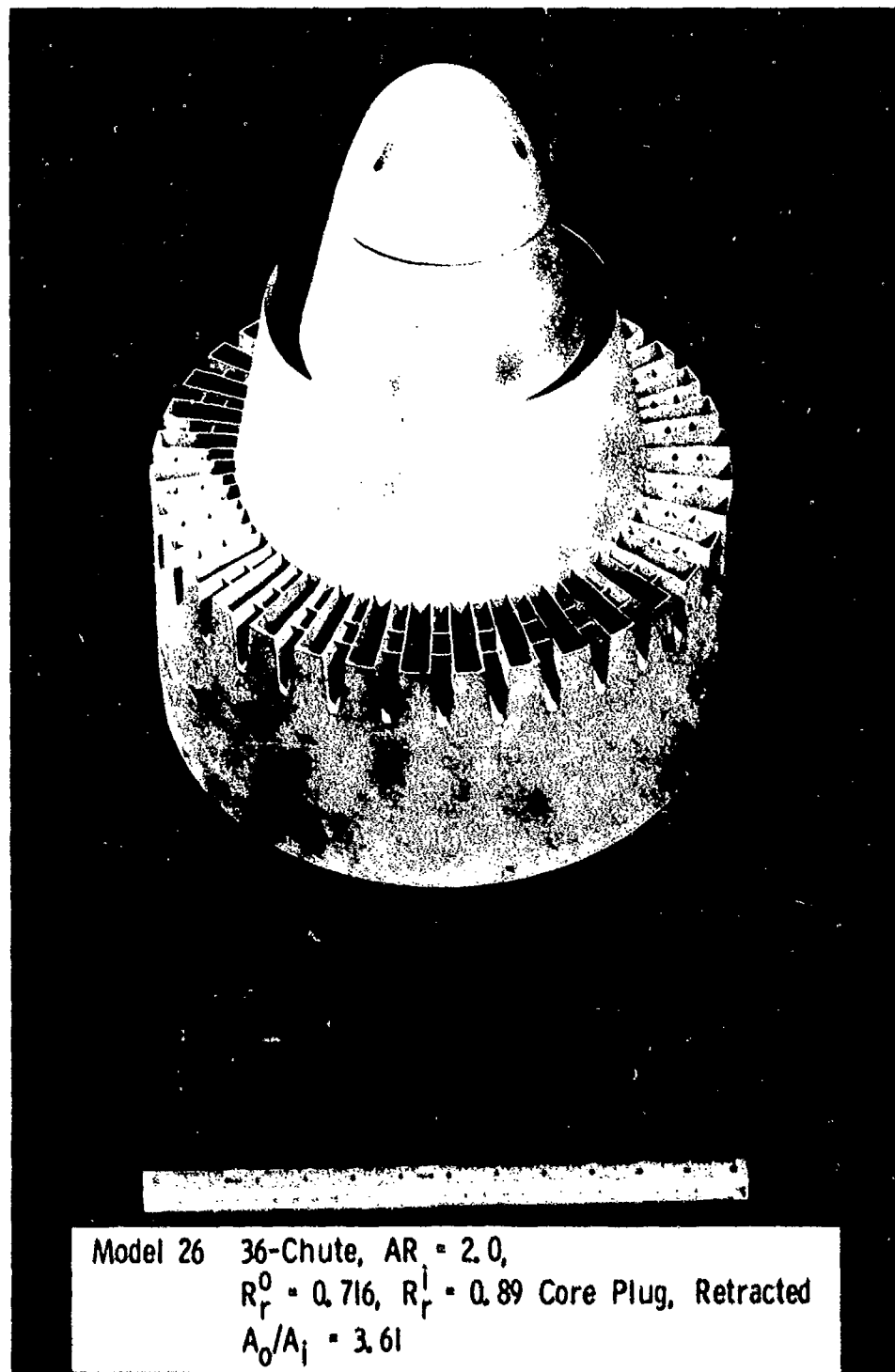


Model 31 30-Shallow Chute, AR = 1.75  
 $R_p^0 = 0.717$ ,  $R_p^1 = 0.779$  Core Plug, Retracted  
 $A_0/A_1 = 1.92$



Model 27 36-Chute, AR = 1.5  
 $R_p^0 = 0.782$ ,  $R_p^1 = 0.779$  Core Plug, Retracted  
 $A_0/A_1 = 1.92$

Figure 3-129. Dual-Flow Models for Velocity Ratio Investigation at  $A_0/A_1 = 1.92$ .



Model 26 36-Chute,  $AR = 2.0$ ,  
 $R_r^0 = 0.716$ ,  $R_r^1 = 0.89$  Core Plug, Retracted  
 $A_0/A_1 = 3.61$

Figure 3-130. Dual-Flow Models for Velocity Ratio Investigation at  $A_0/A_1 = 3.61$ .



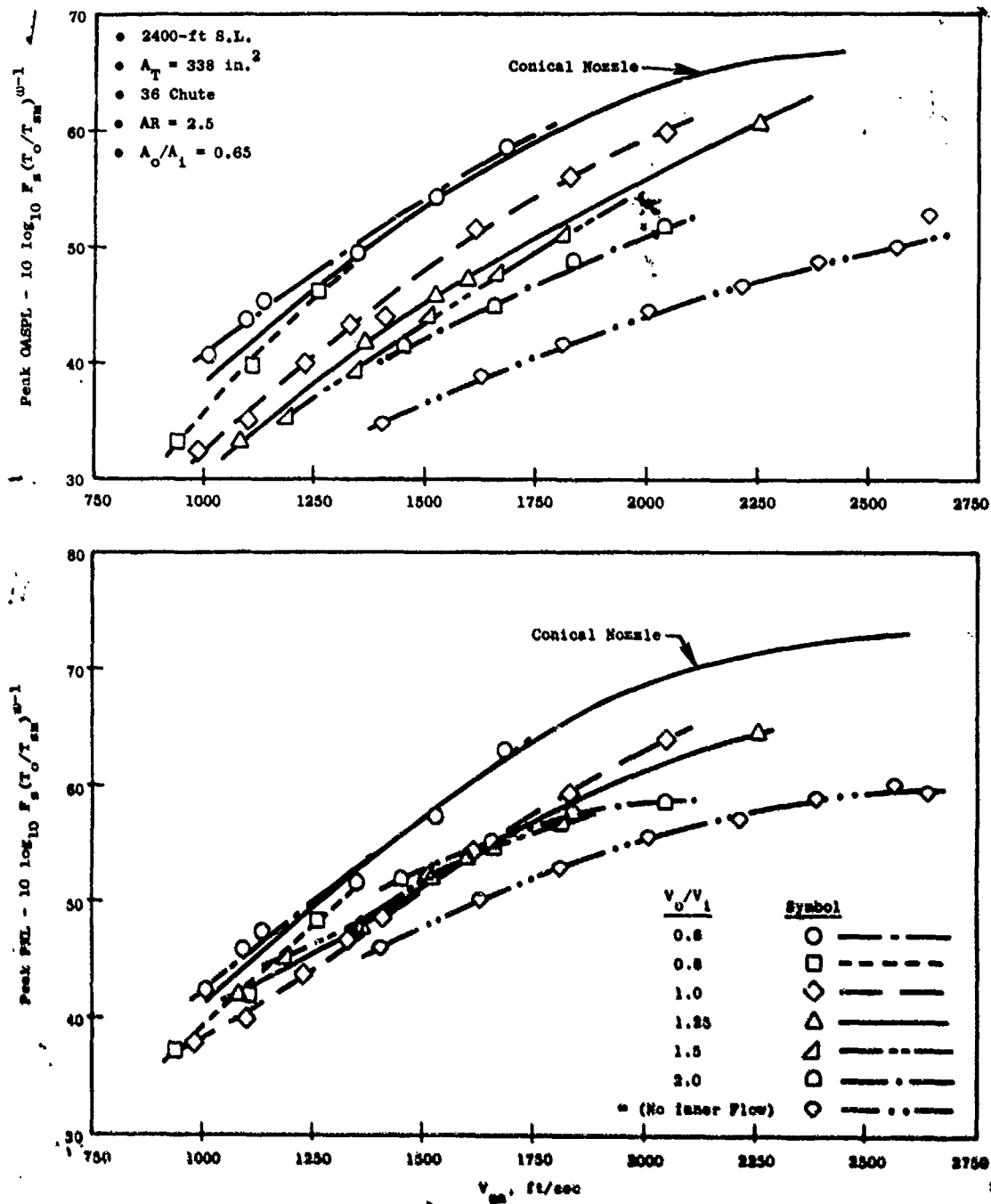


Figure 3-131. Peak PNL and OASPL Variation with  $V_o/V_1$ , Model 33.

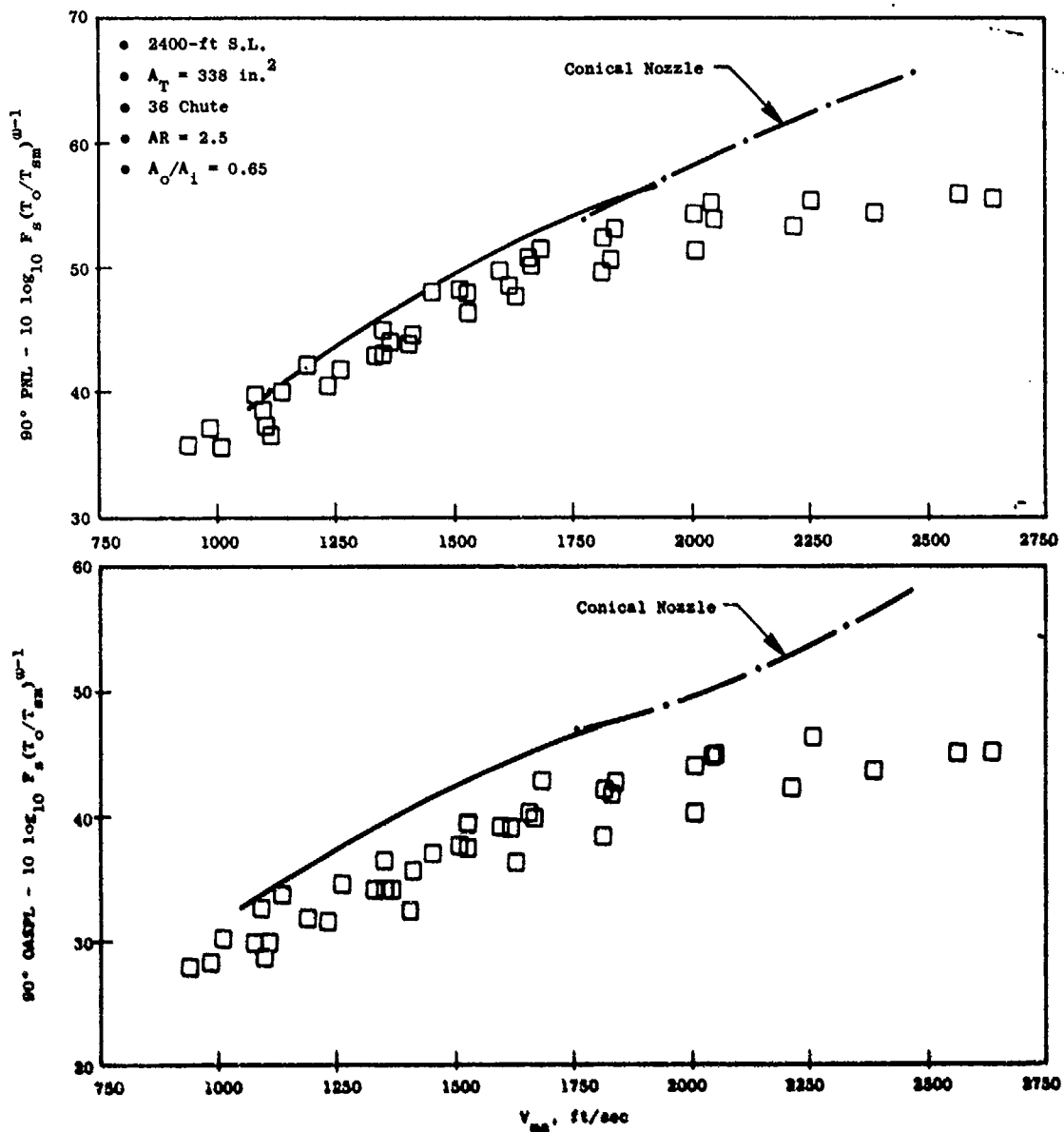


Figure 3-132. 90° PNL and QASPL Variation with  $V_o/V_1$ , Model 33.

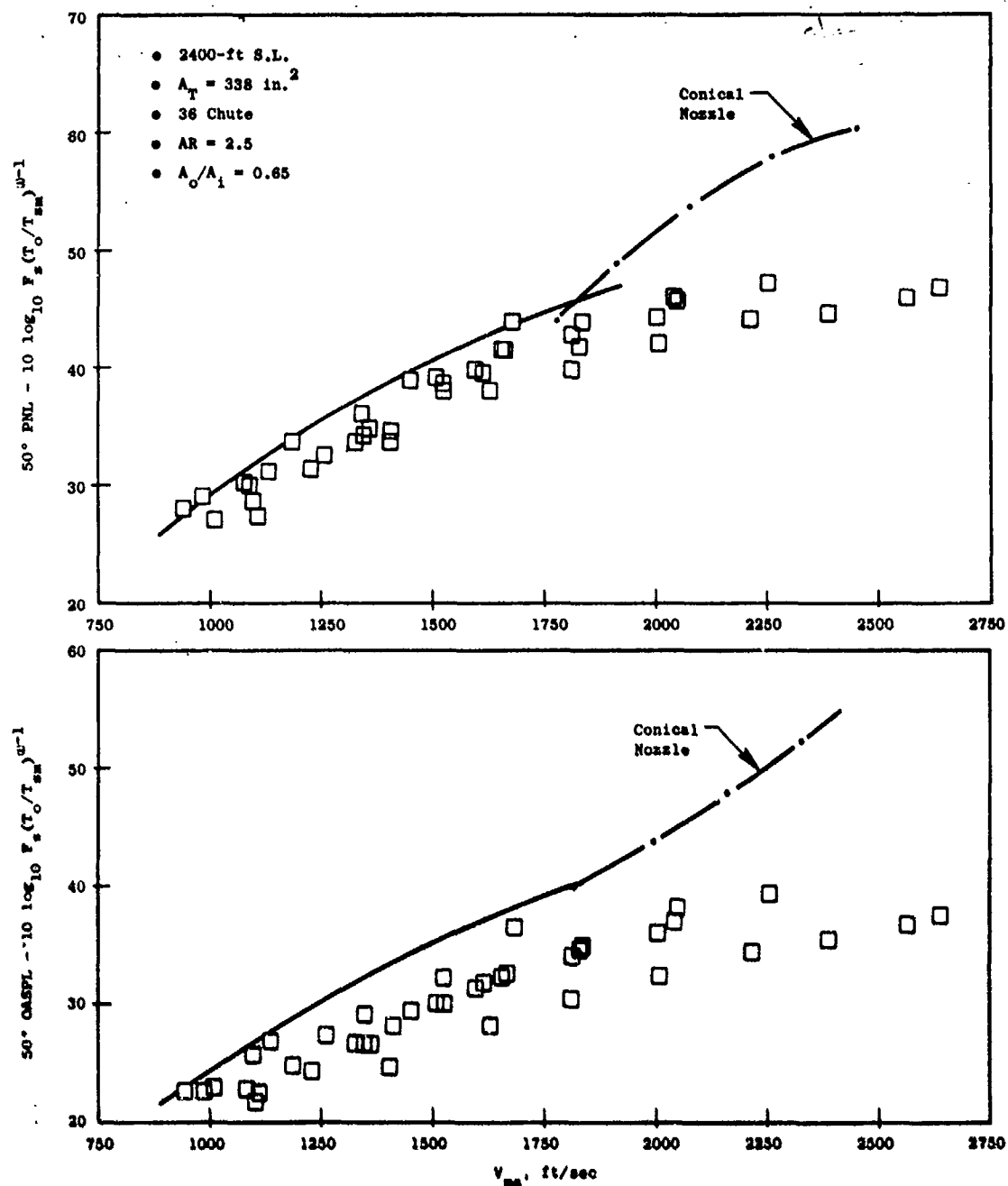


Figure 3-133. 50° PNL and OASPL Variation with  $V_O/V_I$ , Model 33.

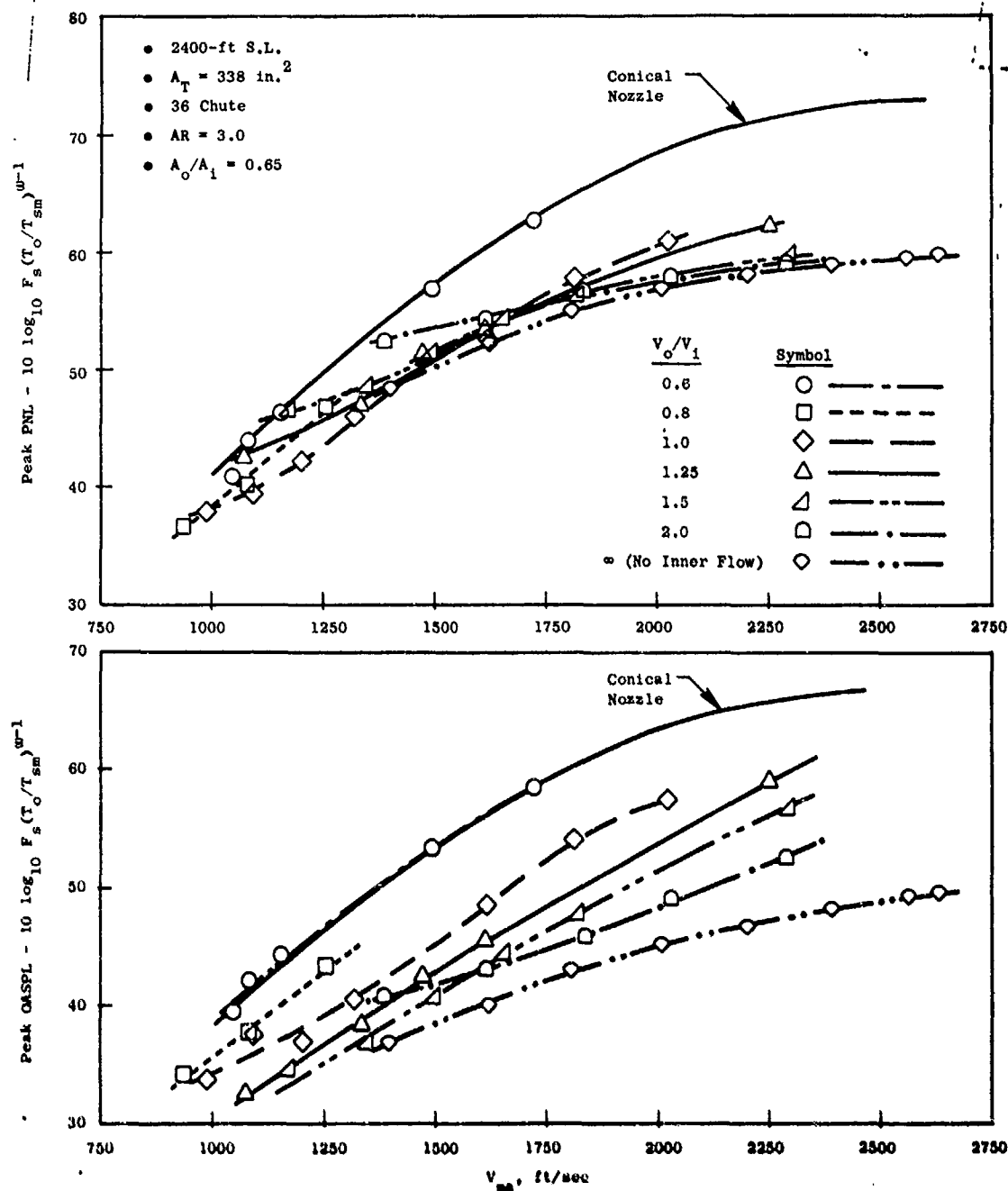


Figure 3-134. Peak PNL and OASPL Variation with  $V_O/V_I$ , Model 34.

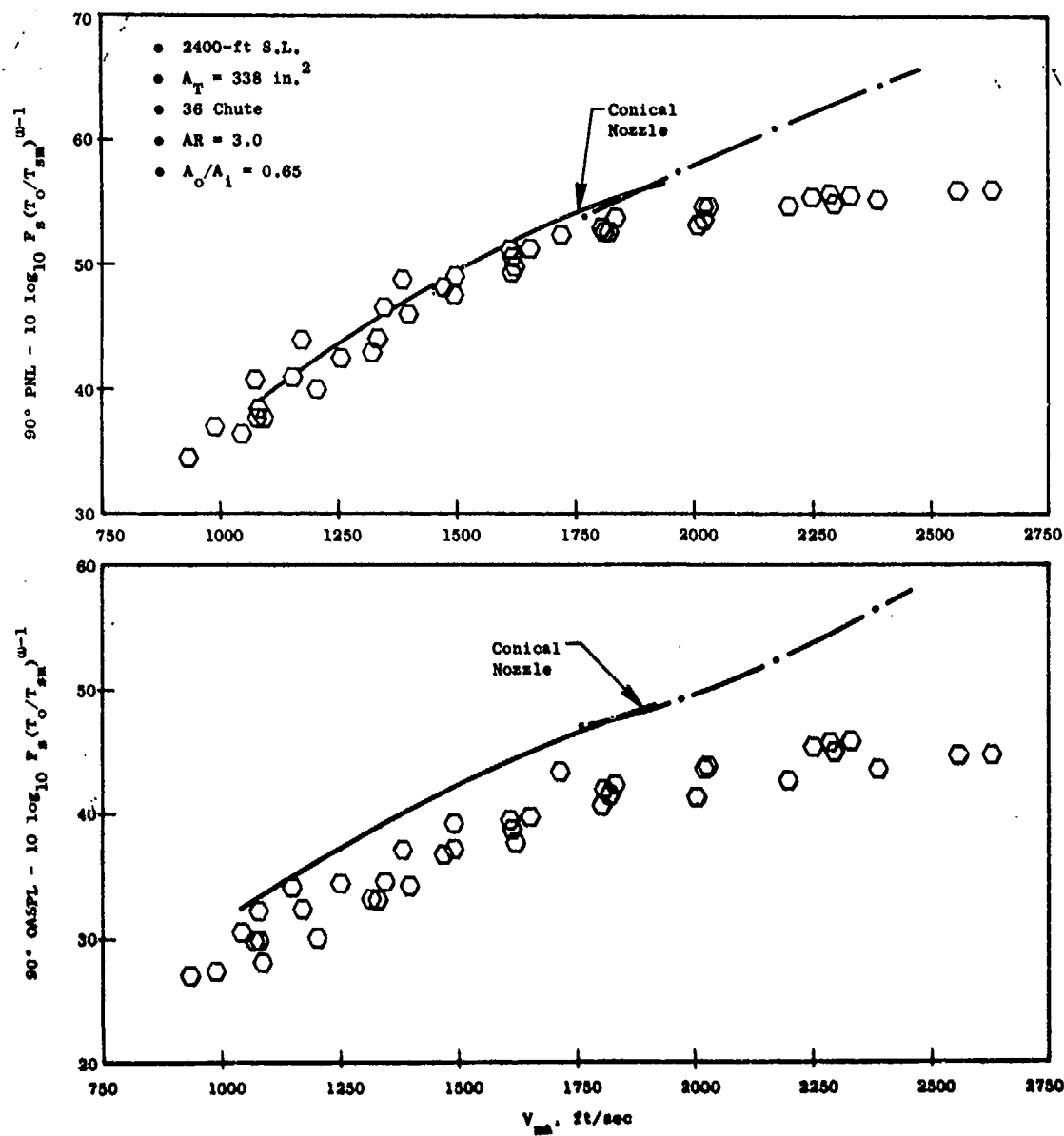


Figure 3-135. 90° PNL and OASPL Variation with  $V_o/V_1$ , Model 34.

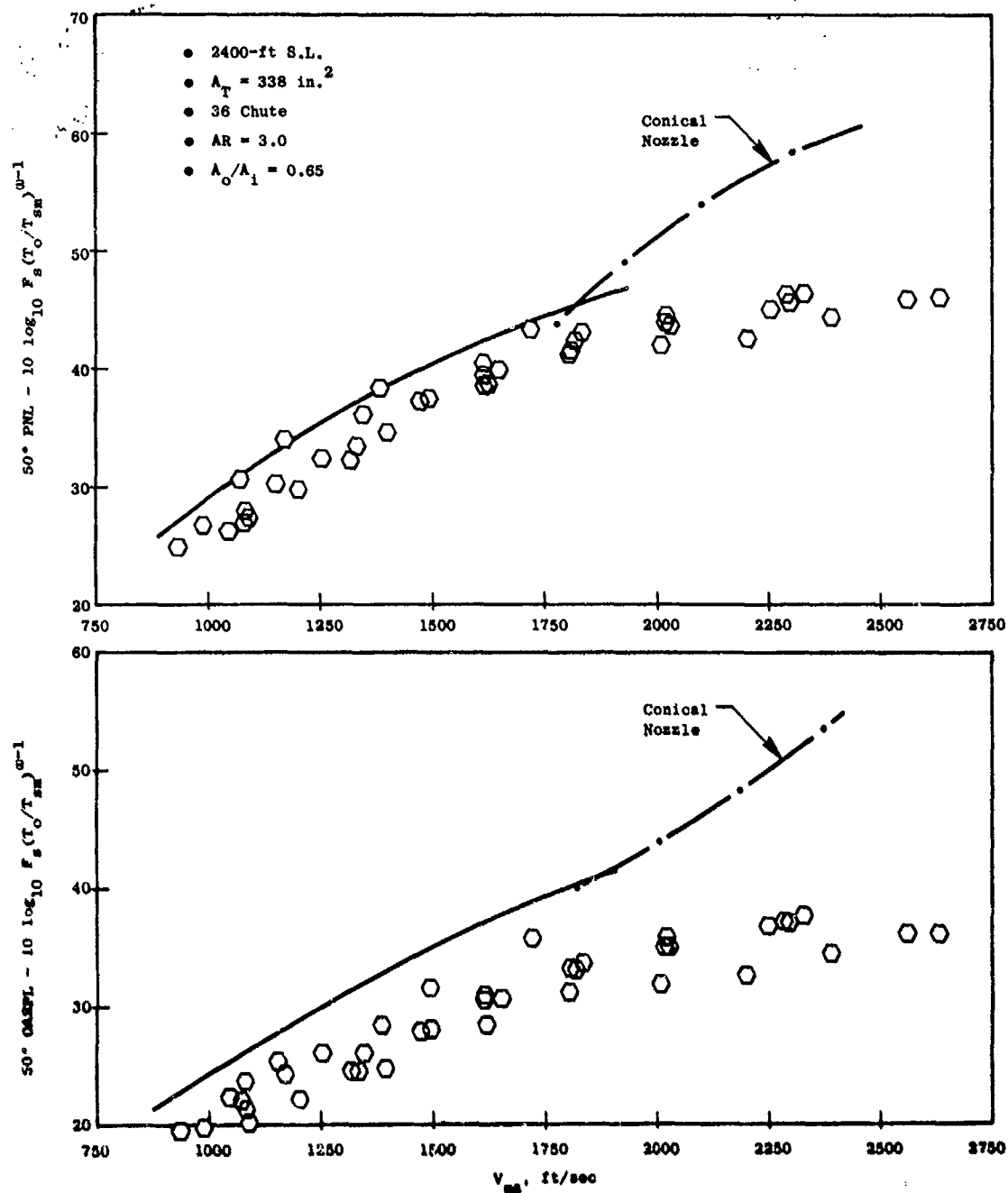


Figure 3-136. 50° PNL and OASPL Variation with  $V_o/V_1$ , Model 34.

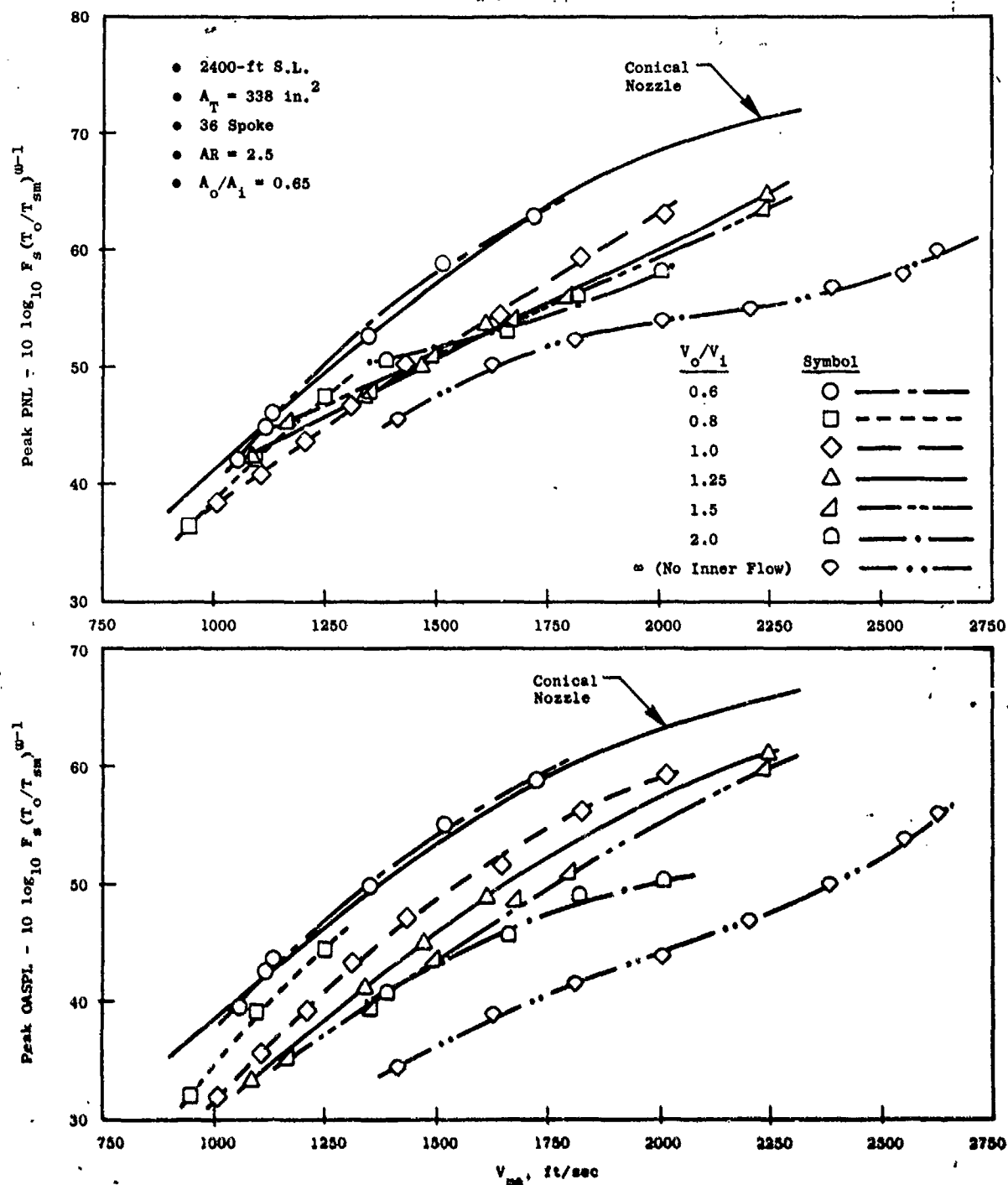


Figure 3-137. Peak PNL and QASPL Variation with  $V_o/V_i$ , Model 35.

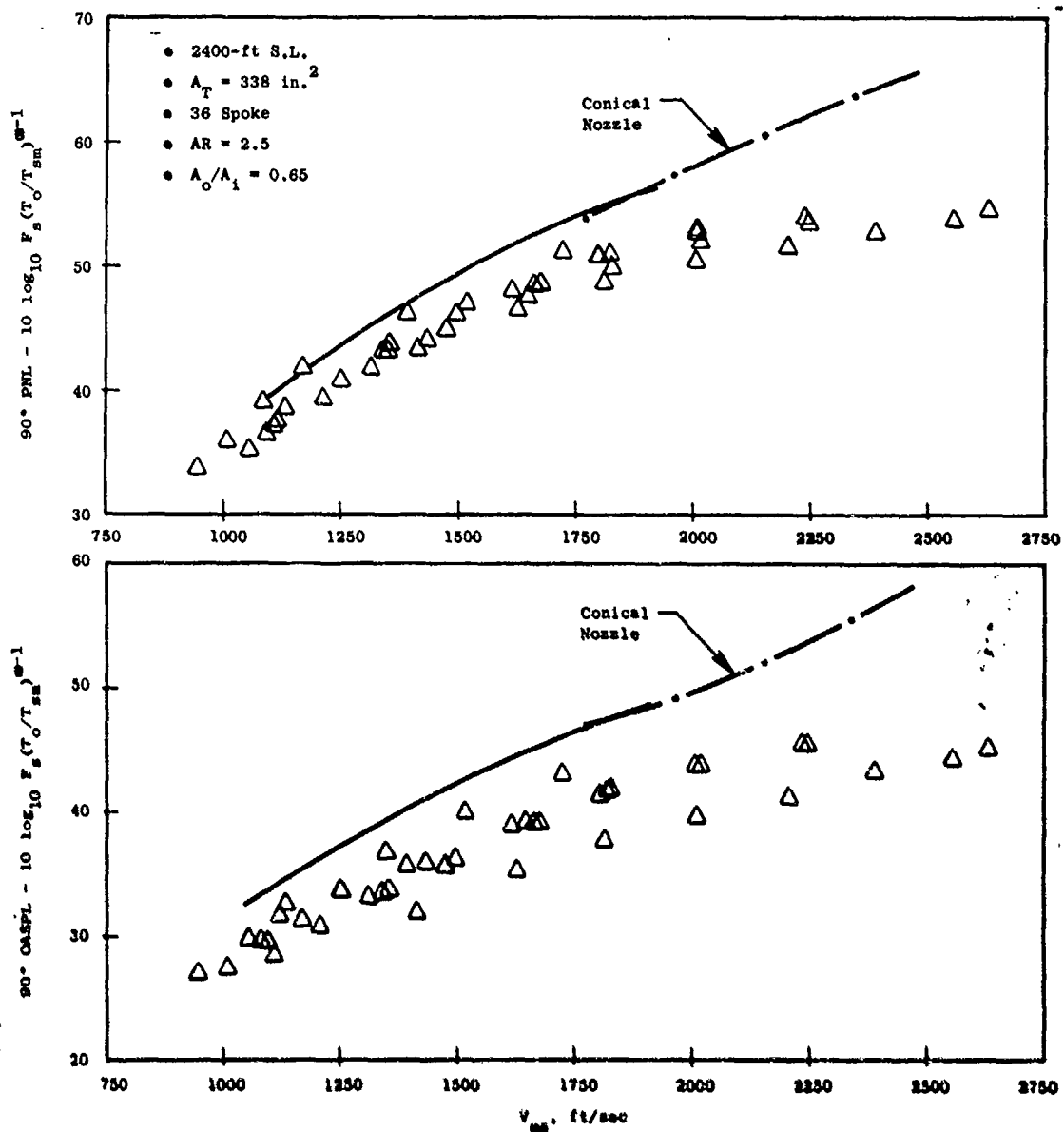


Figure 3-138.  $90^\circ$  PNL and OASPL Variation with  $V_0/V_1$ , Model 35.



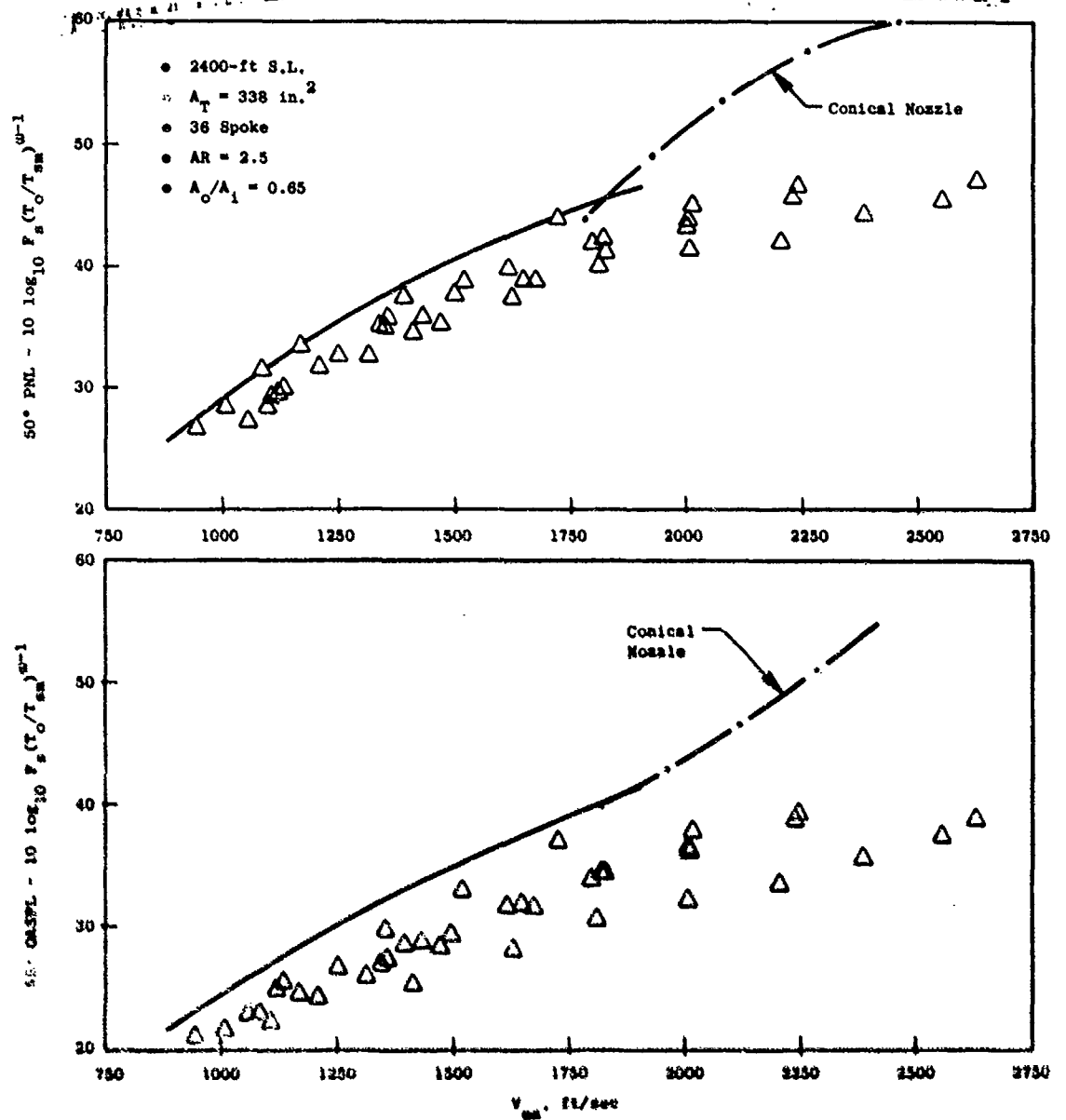


Figure 3-139. 50° PNL and QASPL Variation with  $V_0/V_1$ , Model 35.

- 8 excursions for the individual  $V_0/V_1$  cycle lines are:

$V_0/V_1$	$\beta$
0.6	0.6 - 0.9
0.8	0.4 - 1.0
1.0	0.5 - 1.0
1.25	0.5 - 1.2
1.5	0.6 - 1.3
2.0	0.6 - 1.3
$\infty$	$\infty$

Normally at a fixed  $V_{ma}$ , the inner and outer stream cycle conditions selected for the test will result in increased  $\beta$  as  $V_0/V_1$  is increased. Therefore, in addition to gradual dominance of the noise caused by the outer stream velocity increase, the outer stream weight flow increase also increases the noise. For the  $V_0/V_1 = 0.6$  line, where  $V_0$  is 40% less than  $V_1$ , and  $W_0$  is 10 to 40% less than  $W_1$ , total predominance of the inner stream would be expected. Suppression normally attributed to the annular plug effect ( $R_1^1 = 0.674$ ) is not apparent. For the  $V_{ma}$  range tested, as  $V_0/V_1$  increases and the outer stream dominates both velocity and mass flow, the effectiveness of the segmented suppressor becomes more paramount and levels of suppression gradually increase.

- The greater the loss of peak PNL suppression as opposed to peak OASPL suppression at low  $V_{ma}$ , and the much higher level of peak OASPL suppression than peak PNL suppression at high  $V_{ma}$  indicates that a complex and changing interaction exists in the spectral composition for dominance of high or low frequency. This is related to relative noise levels of the inner and outer streams and depends on the individual stream cycle composition in addition to any possible inner/outer flow interactions affecting noise generation.
- Figures 3-132, 3-135 and 3-138 show substantially less suppression for the 90° PNL and OASPL data compared to the aft quadrant, however, significant level of suppression are still attained. A primary observation, in relation to this study's goal, is that discrete trends with system velocity ratio variation are not nearly as discernible as they were at the peak noise angle. Data are therefore presented without individual curve fits for fixed  $V_0/V_1$  values. In assembling the data, however, a fairly distinct data trend was observed for the  $V_0/V_1 = \infty$  case. Appendix B contains the specific acoustic and aerodynamic cycle information.

- At 50°, Figures 3-133, 3-136 and 3-139, the PNL and OASPL data are similar to the 90° data. Again, trends are not as discernible with set velocity ratio and information is plotted without data-fitted curves.

To illustrate the more detailed changes in noise characteristics associated with system velocity ratio influence at fixed system  $A_0/A_1$  and fixed annular suppressor geometry, the following representative sets of PNL and OASPL directivities plus spectra plots are included; selected from Model 33 and 34's data banks:

Figures 3-140 and 3-141	Model 33, $V_{ma} = 2010 - 2050$ ft/sec
Figures 3-142 and 3-143	Model 33, $V_{ma} = 1685 - 1840$ ft/sec
Figures 3-144 and 3-145	Model 34, $V_{ma} = 2250 - 2390$ ft/sec
Figures 3-146 and 3-147	Model 34, $V_{ma} = 1720 - 1830$ ft/sec

The following general observations are made:

- PNL and OASPL directivity for the first data set on Model 33, where  $V_0/V_1 = 1.0, 2.0$  and  $\infty$  are compared, show major and systematic changes for 120° and aft. Significant, yet not as systematic, reductions occur broadside and in the forward quadrant, the largest change occurring between  $V_0/V_1$  of 2.0 and  $\infty$ .
- Spectra for the same data set show very broad changes in composition, particularly in the aft quadrant at 140°, for  $V_0/V_1 = 1.0$  ( $V_0 \approx V_1 \approx 2050$  ft/sec,  $\beta = 0.7$ ). The inner stream low frequency noise dominates, and high frequency associated with the segmented suppressor is very low. As velocity ratio increases to 2.0 ( $V_0 \approx 2600$  ft/sec,  $V_1 \approx 1300$  ft/sec,  $\beta = 1.3$ ), the low frequency contribution to the spectra is extremely reduced. When inner flow is cut completely, only a fairly flat spectra remains at 140°, where normally an annular suppressor spectra would be more low frequency dominated.

Changes with  $V_0/V_1$  at 120° are similar to 140°, but not of the same magnitude. In general both OASPL and PNL are low-to-mid frequency dominated for the aft quadrant, therefore, changes at low frequencies control both, and substantiate the large variances seen at higher  $V_{ma}$  in Figure 3-131.

- At 90° and 50°, the low  $V_0/V_1$  spectra are more equally balanced for low and high frequency composition. Changes again are primarily observed in the low-to-mid frequencies. Low frequency no longer fully controls OASPL and PNL, therefore, the changes in these values are minor compared to those in the aft quadrant.
- The second data comparison for Model 33 at  $V_{ma}$  from 1685 to 1840 ft/sec for values of  $V_0/V_1$  of 0.6, 1.0, 1.5, 2.0 and  $\infty$ , indicates both PNL and OASPL trends similar to the previous comparison. Aft

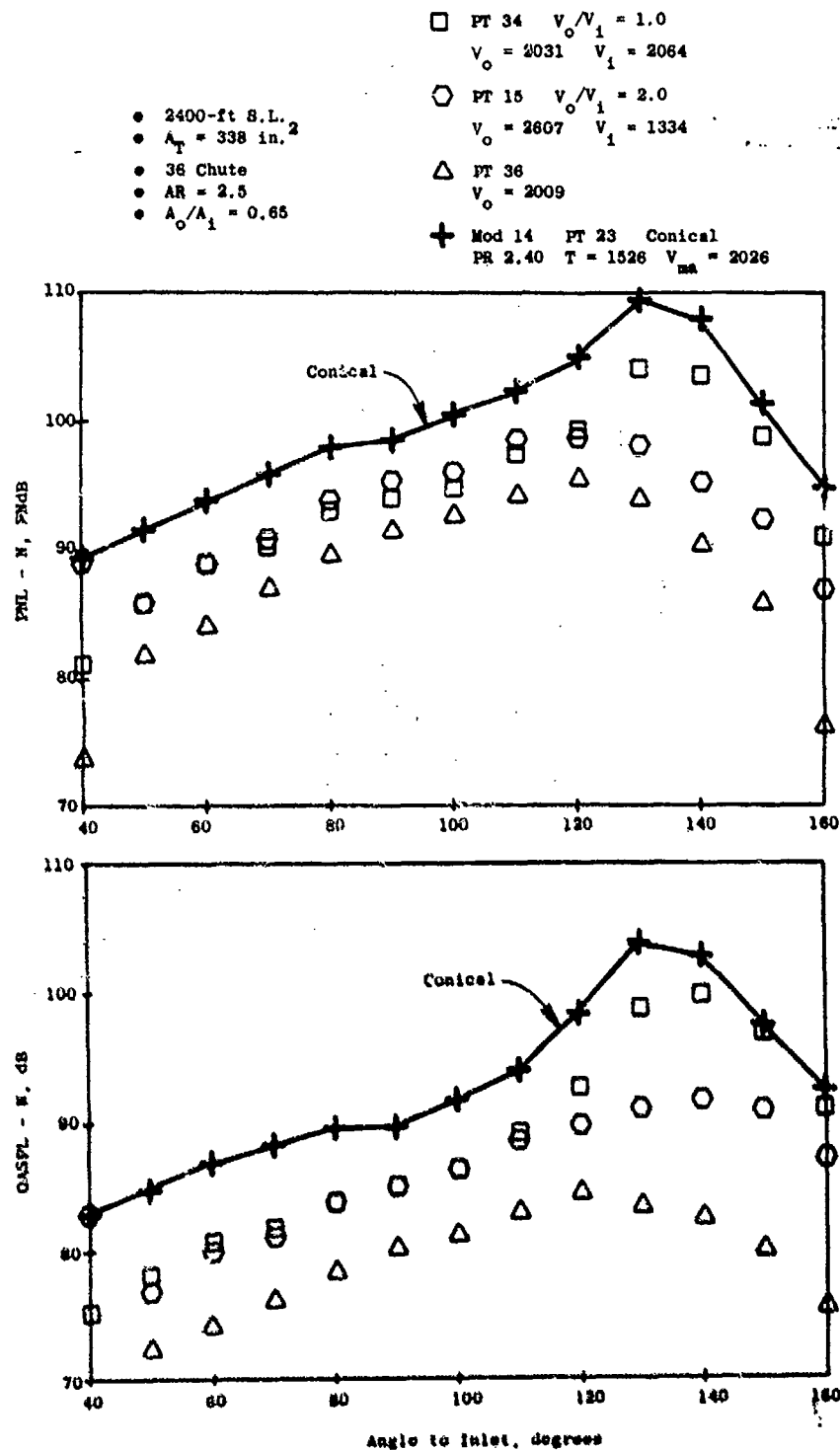


Figure 3-140. Impact of  $V_0/V_1$  on PNL and OASPL. Directivity, Model 33,  $V_{ma} = 2010$  to  $2050 \text{ ft/sec.}$

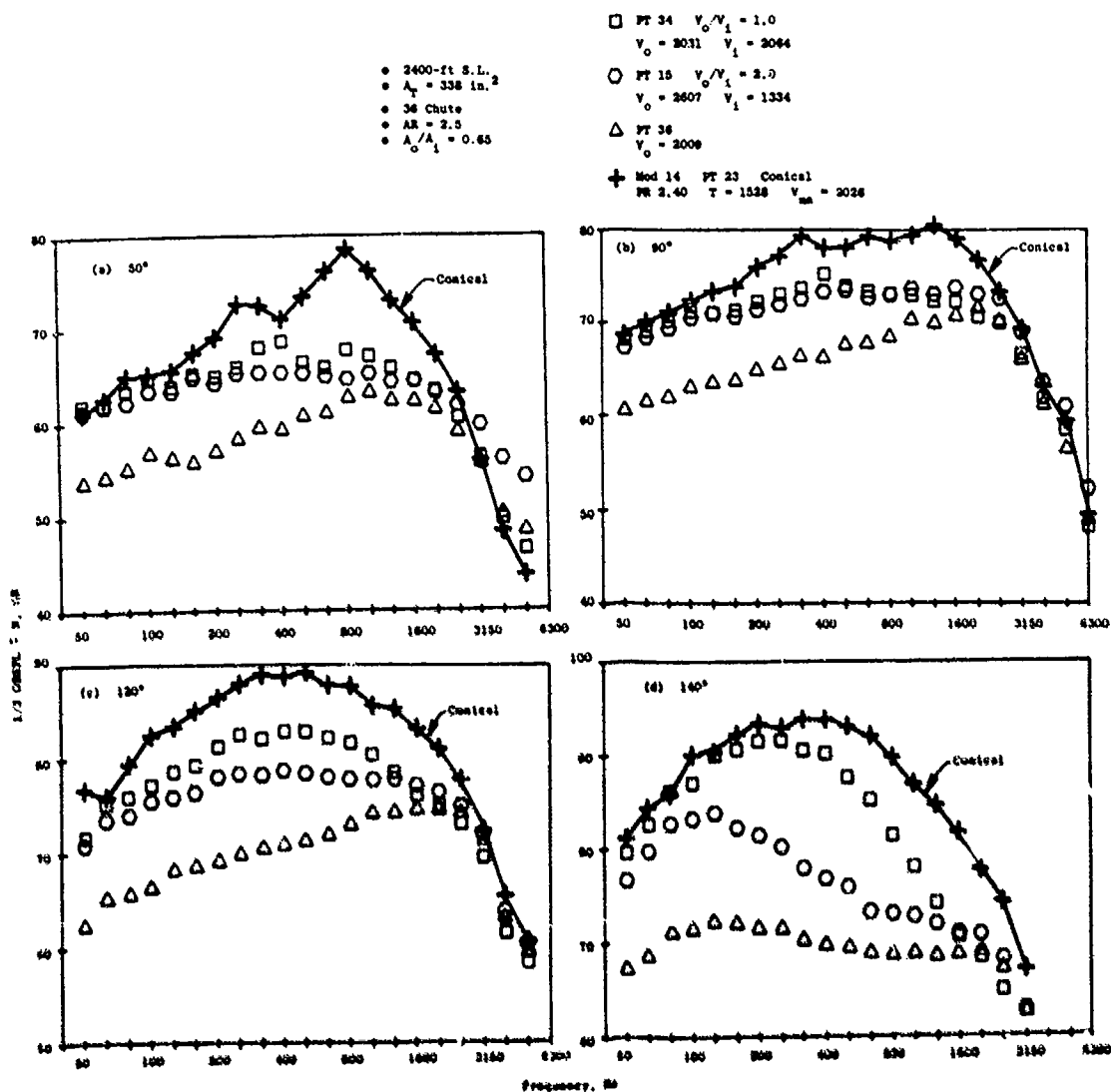


Figure 3-141. Impact of  $V/V_1$  on Spectra, Model 33,  $V_{max} = 2010$  to  $2050 \text{ ft/sec.}$

- $\square$  PT 35  $V_0/V_1 = 0.6$   
 $V_0 = 1186$   $V_1 = 1986$   
 $\circ$  PT 31  $V_0/V_1 = 1.0$   
 $V_0 = 1841$   $V_1 = 1827$   
 $\triangle$  PT 18  $V_0/V_1 = 1.5$   
 $V_0 = 2123$   $V_1 = 1422$   
 $+$  PT 11  $V_0/V_1 = 2.0$   
 $V_0 = 2393$   $V_1 = 1254$

$\times$  PT 38  
 $V_0 = 1813$

$\diamond$  Mod 14 PT 7 Conical  
 PR 2.29  $T_1 = 1266^\circ \text{R}$   $V_{\text{ma}} = 1796 \text{ ft/sec}$

- 2400-ft S.L.
- $A_T = 338 \text{ in.}^2$
- 36 Chute
- $AR = 2.5$
- $A_0/A_1 = 0.65$

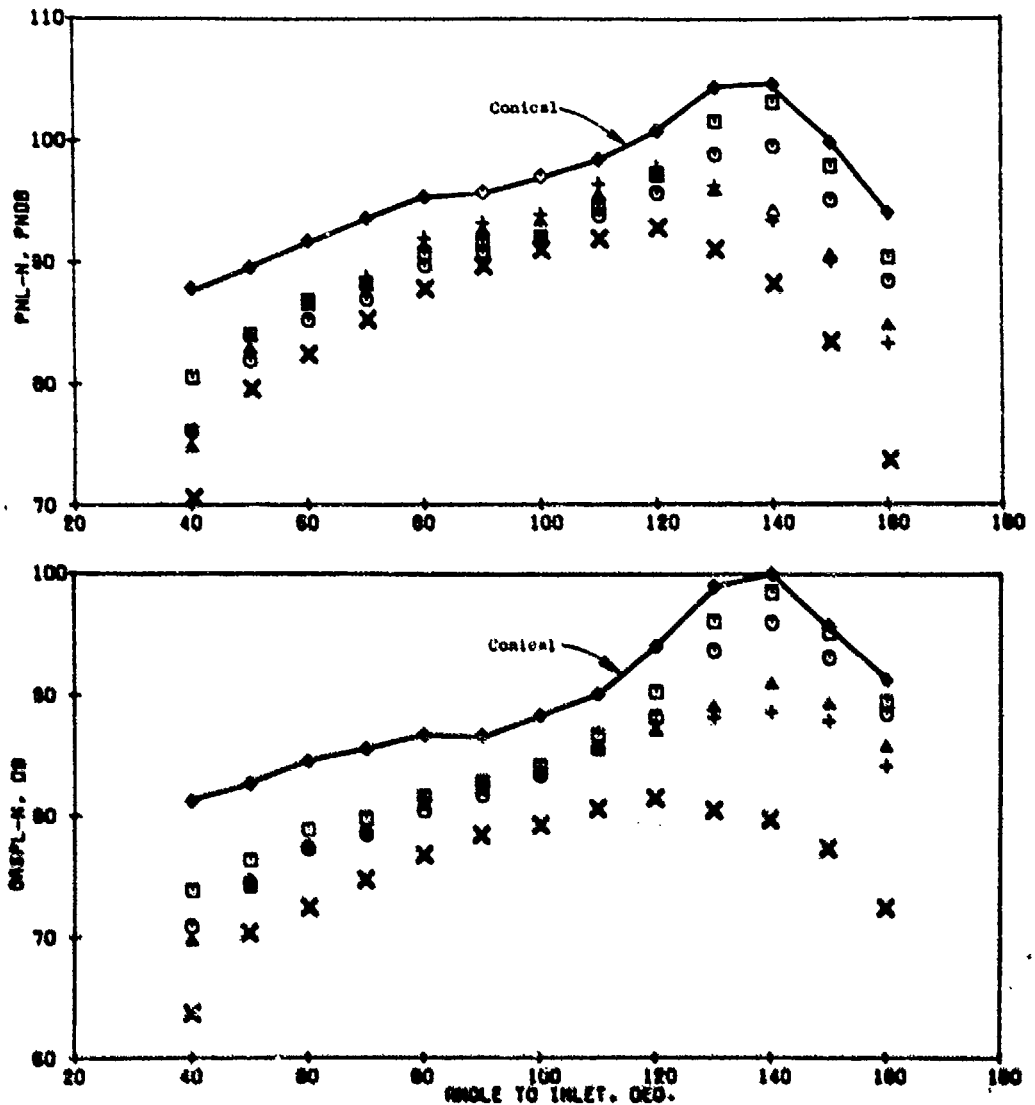


Figure 3-142. Impact of  $V_0/V_1$  on PNL and OASPL Directivity, Model 33,  $V_{\text{ma}} = 1685-1840 \text{ ft/sec}$ .

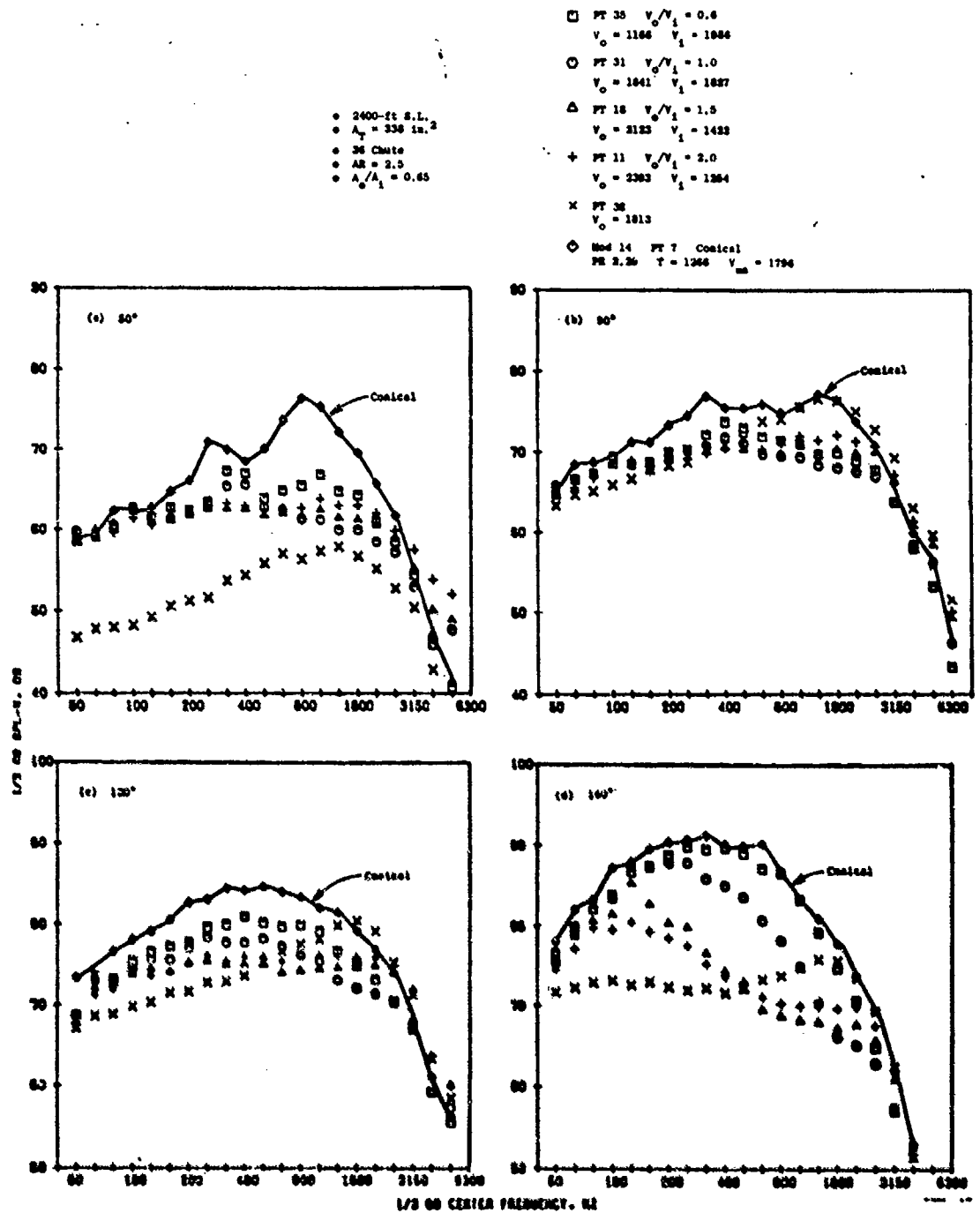


Figure 3-143. Impact of  $V_0/V_1$  on Spectra - Model 33 -  $V_{m1} = 1685-1840 \text{ ft/sec.}$

- 2400-ft S.L.
- $A_T = 338 \text{ in.}^2$
- 36 Chute
- $AR = 3.0$
- $A_0/A_1 = 0.65$

- PT 33  $V_0/V_1 = 1.25$   
 $V_0 = 2518 \quad V_1 = 2028$
- PT 30  $V_0/V_1 = 1.5$   
 $V_0 = 2692 \quad V_1 = 1783$
- △ PT 20  $V_0/V_1 = 2.0$   
 $V_0 = 2766 \quad V_1 = 1410$
- + PT 39  
 $V_0 = 2392$
- × Mod 14 PT 64 Conical  
PR 2.65  $T_T = 1752^\circ \text{ R}$   $V_{\text{max}} = 2279 \text{ ft/sec}$

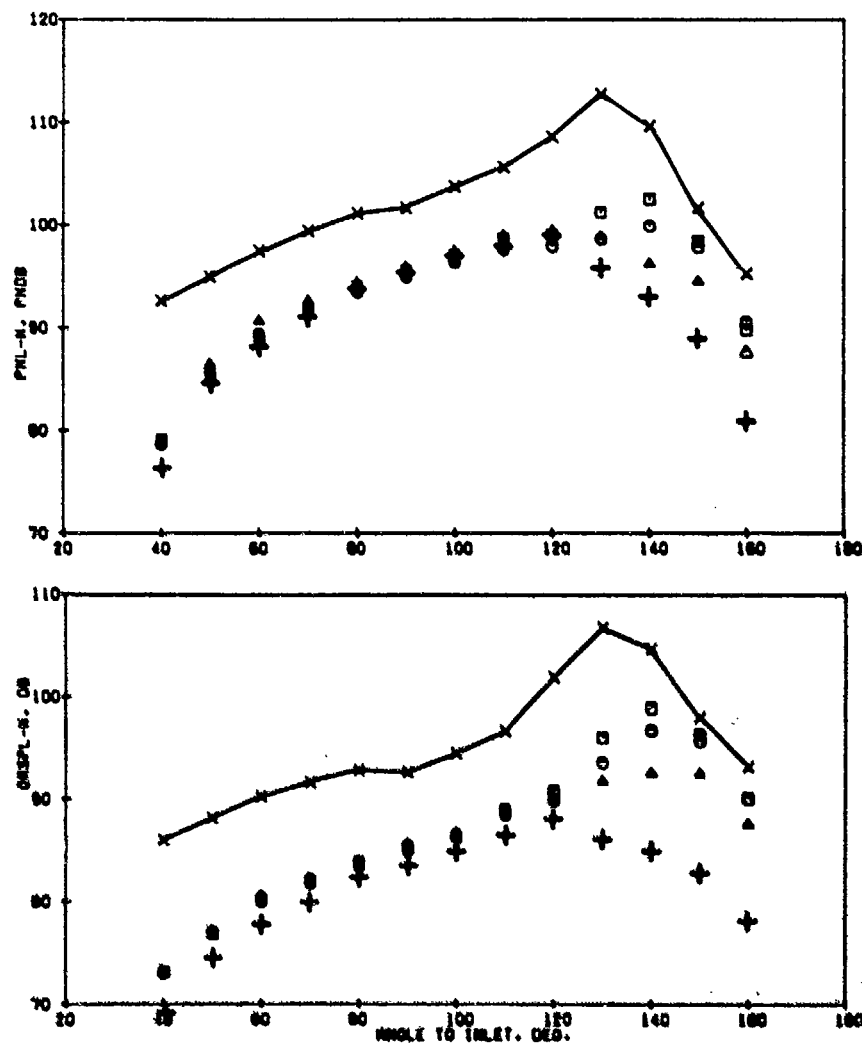


Figure 3-144. Impact of  $V_0/V_1$  on PNL and OASPL Directivity, Model 34,  $V_{\text{max}} = 2250\text{-}2390 \text{ ft/sec}$ .



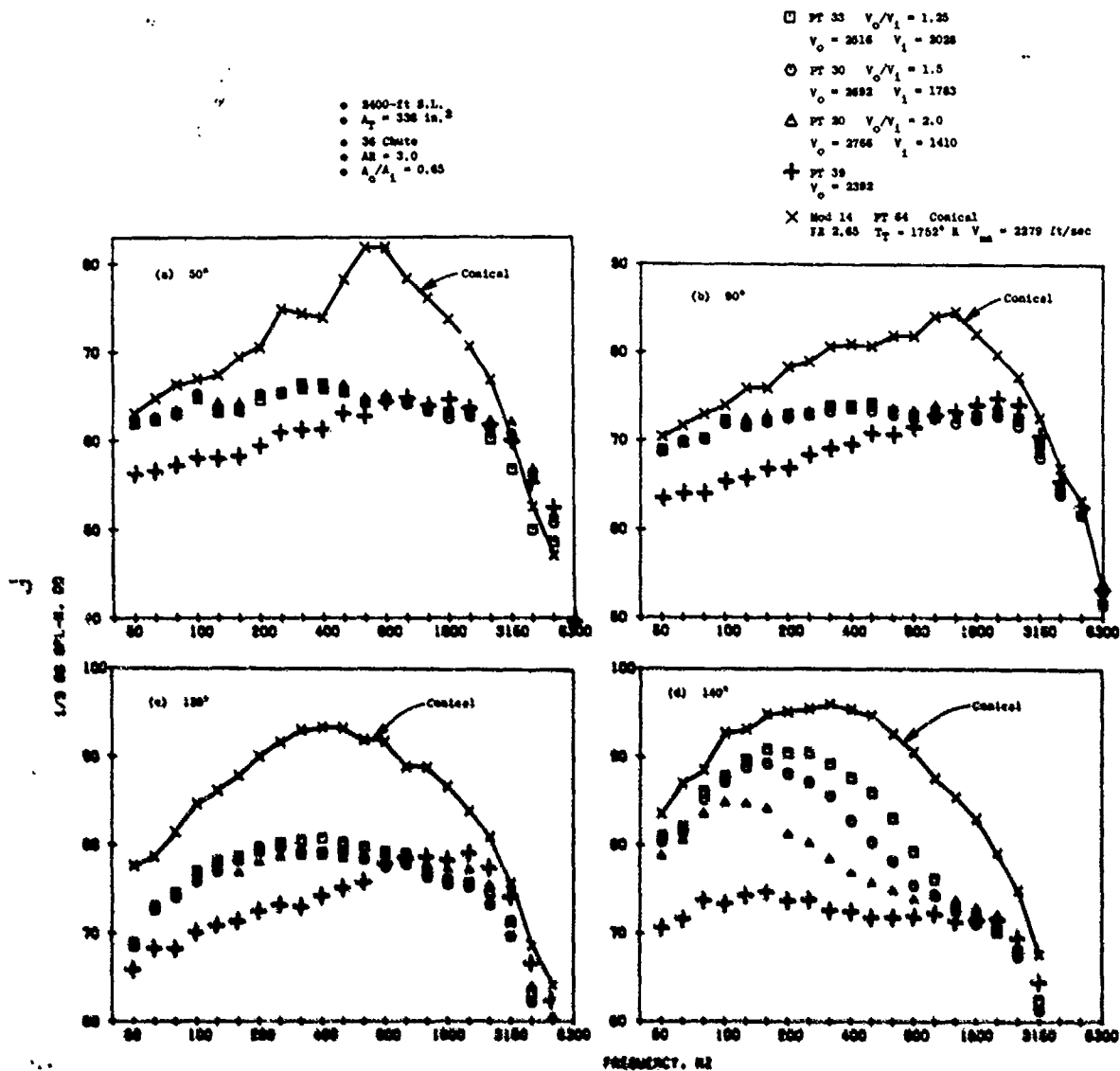


Figure 3-145. Impact of  $V_0/V_1$  on Spectra, Model 34,  $V_m = 2250-2390 \text{ ft/sec}$ .

- 2400-ft S.L.
- $A_T = 338 \text{ in.}^2$
- 36 Chute
- $AR = 3.0$
- $A_O/A_I = 0.65$

- PT 35  $V_O/V_I = 0.6$   
 $V_O = 1218 \quad V_I = 2034$
- PT 31  $V_O/V_I = 1.0$   
 $V_O = 1819 \quad V_I = 1802$
- △ PT 18  $V_O/V_I = 1.5$   
 $V_O = 2125 \quad V_I = 1410$
- + PT 11  $V_O/V_I = 2.0$   
 $V_O = 2407 \quad V_I = 1217$
- × PT 38  
 $V_O = 1806$
- ◇ Mod 14 PT 7 Conical  
PR 2.29  $T_T = 1266^\circ \text{ R}$   $V_{\infty} = 1796 \text{ ft/sec}$

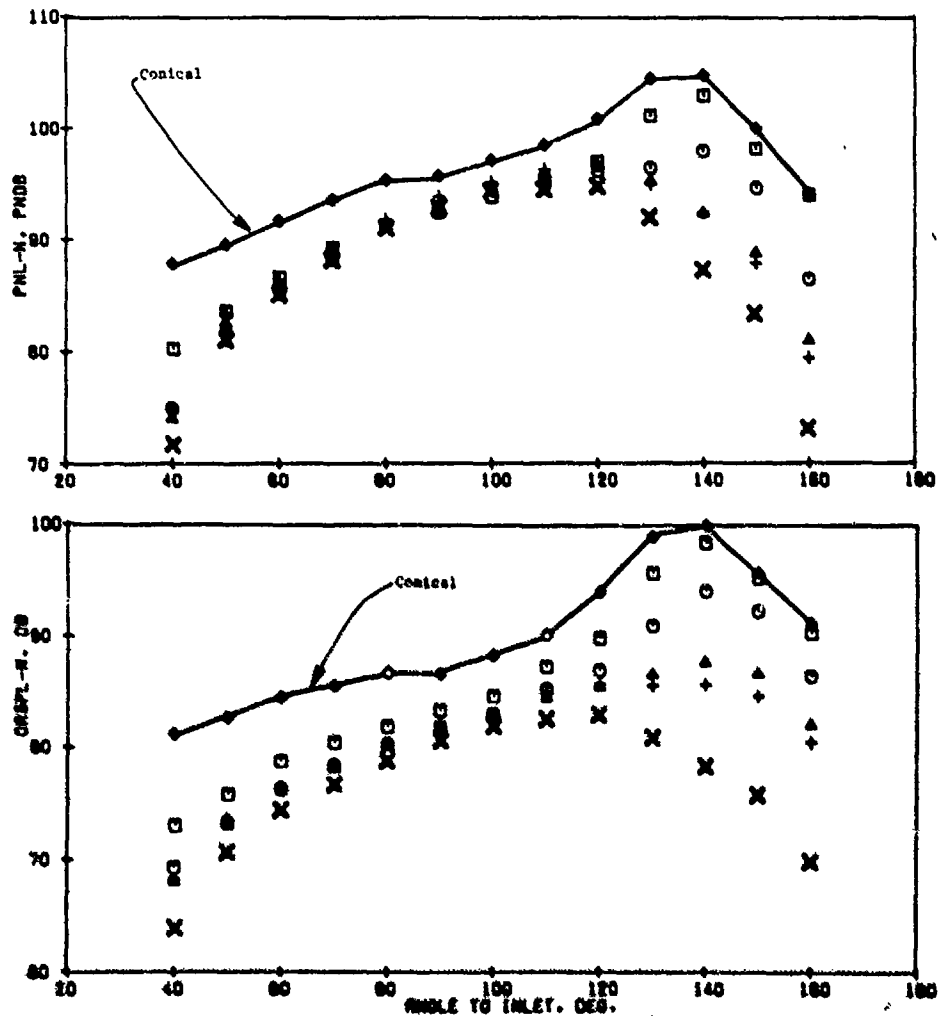


Figure 3-146. Impact of  $V_O/V_I$  on PNL and QASPL Directivity, Model 34,  $V_{\infty} = 1720-1830 \text{ ft/sec}$ .

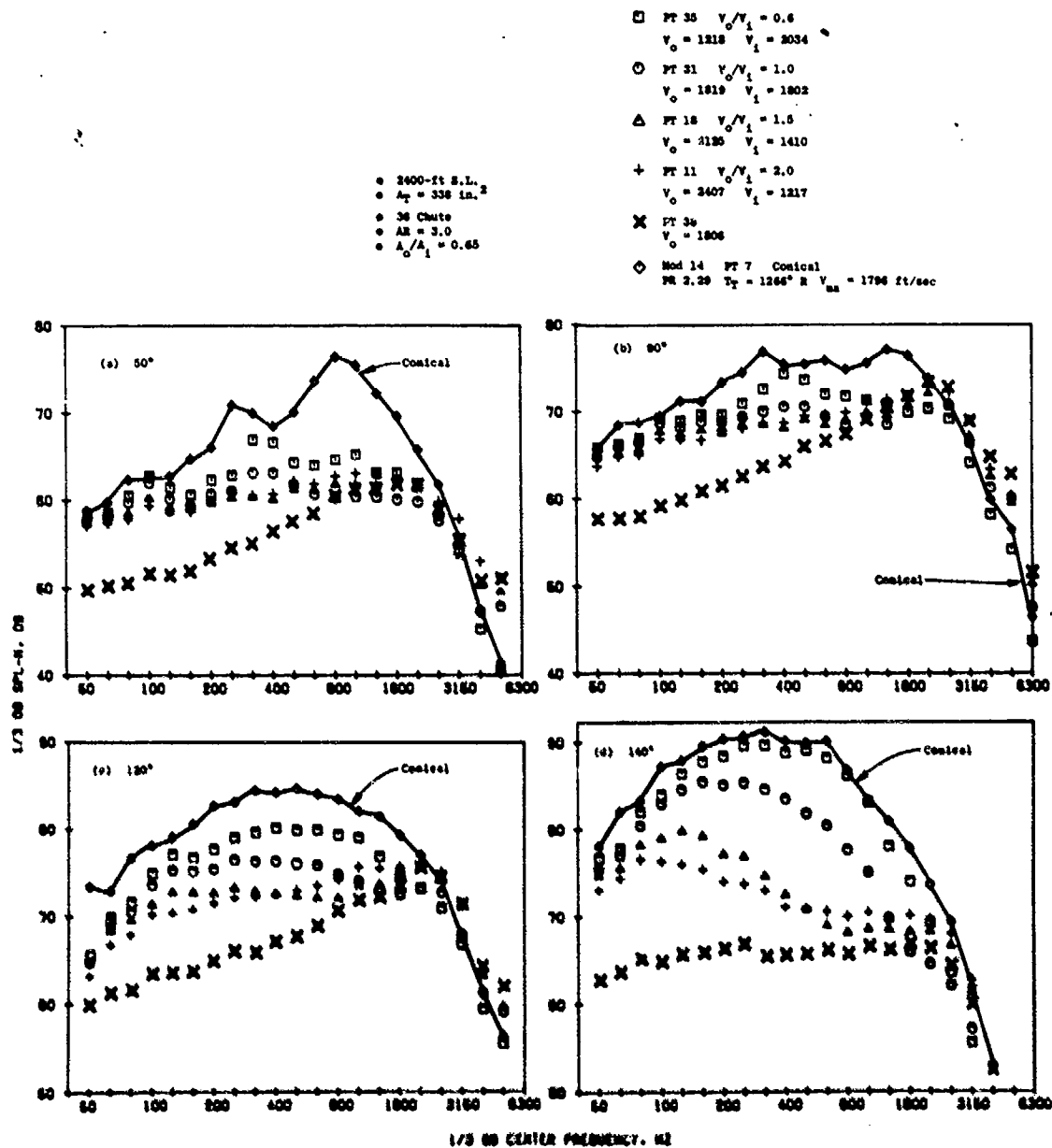


Figure 3-147. Impact of  $V_0/V_1$  on Spectra, Model 34,  $V_{ms} = 1720$ -1830 ft/sec.

quadrant changes are very systematic and progress with system velocity ratio change as shown in Figure 3-131. Broadside and forward quadrant changes, as mentioned previously, are not as distinguishable, except for  $V_0/V_1 = \infty$ .

- Spectra comparisons at aft angles for this data set show low  $V_0/V_1 = 0.8$  spectra shapes approaching the conical nozzle. Suppression starts primarily in mid-frequency at  $V_0/V_1 = 1.0$  and is then more broadband from low-to-mid frequency for  $V_0/V_1 = 1.5$  to 2.0. Terminating inner flow again results in near flat spectra. In general the broadside and forward quadrant spectra changes are mainly at mid-to-high frequency for  $V_0/V_1 = 0.8$  to 2.0. When inner flow is terminated, the low frequency levels are also substantially reduced. Again, the mid-to-high frequencies control PNL and OASPL and therefore the low-to-mid frequency reductions do not significantly reduce either.
- Model 34 data comparisons, Figures 3-144 thru 3-147, exhibit trends similar to those of Model 33.

Results of peak, 90°, and 50° PNL and OASPL are included in the following figures for Models 31 and 27 at  $A_0/A_1 = 1.92$ .

Model No.	Peak	90°	50°
31	3-148	3-149	3-150
27	3-151	3-152	3-153

For this model set the DBTF/Inverted Dual Flow cycle matrix consisted of 12 data points at select values of  $V_0/V_1 = 1.0, 1.25, 1.5$  and 2.0. Therefore, it did not cover the expanded range of the previous  $A_0/A_1 = 0.65$  models and broad results are not as conclusive. Data for these two models are partially presented elsewhere in this report (Section 3.4.2.3 "Flow Segmentation Study" for Model 31, comparing 20, 30 and 40 elements and Section 3.4.2.1 "Area Ratio and Radius Ratio Variable - Dual Flow" for Model 27, comparing area ratios/radius ratios of 1.5/0.782, 2.0/0.716, and 2.5/0.653). The results are presented in those sections as data fitted curves through the aggregate of test points. They normally show that the variance from the mean line is small enough to consider no distinguishable noise trend with  $V_0/V_1$ .

The last model of the six selected for data presentation is Model 26 (36-chute of  $A_0/A_1 = 3.61$ ). Peak, 90° and 50° PNL/OASPL data are presented in Figures 3-154, 3-155 and 3-156, respectively for this model. The parameter  $\beta$  ranges from 2.8 to 8.8, therefore the outer stream dominates in noise generation. Little variance is distinguishable for the four  $V_0/V_1$  settings, and what little exists is less than the variance seen in the  $A_0/A_1 = 1.92$  system. No inner/outer flow interaction mechanism seems to be present to enhance the suppression above that of a basic suppressed annulus.

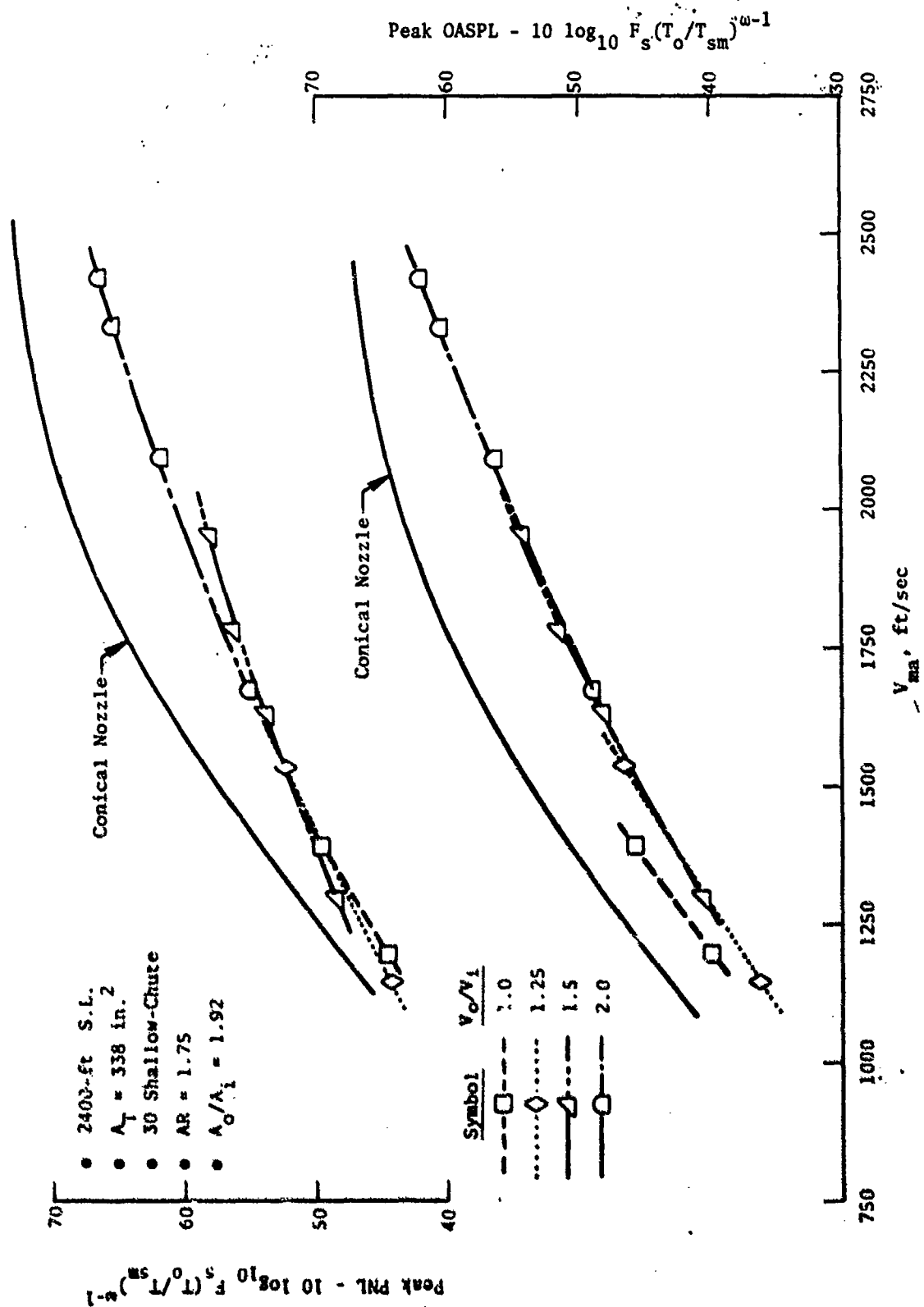


Figure 3-148. Peak PNL and OASPL Variation with  $V_0/V_1$ , Model 31.

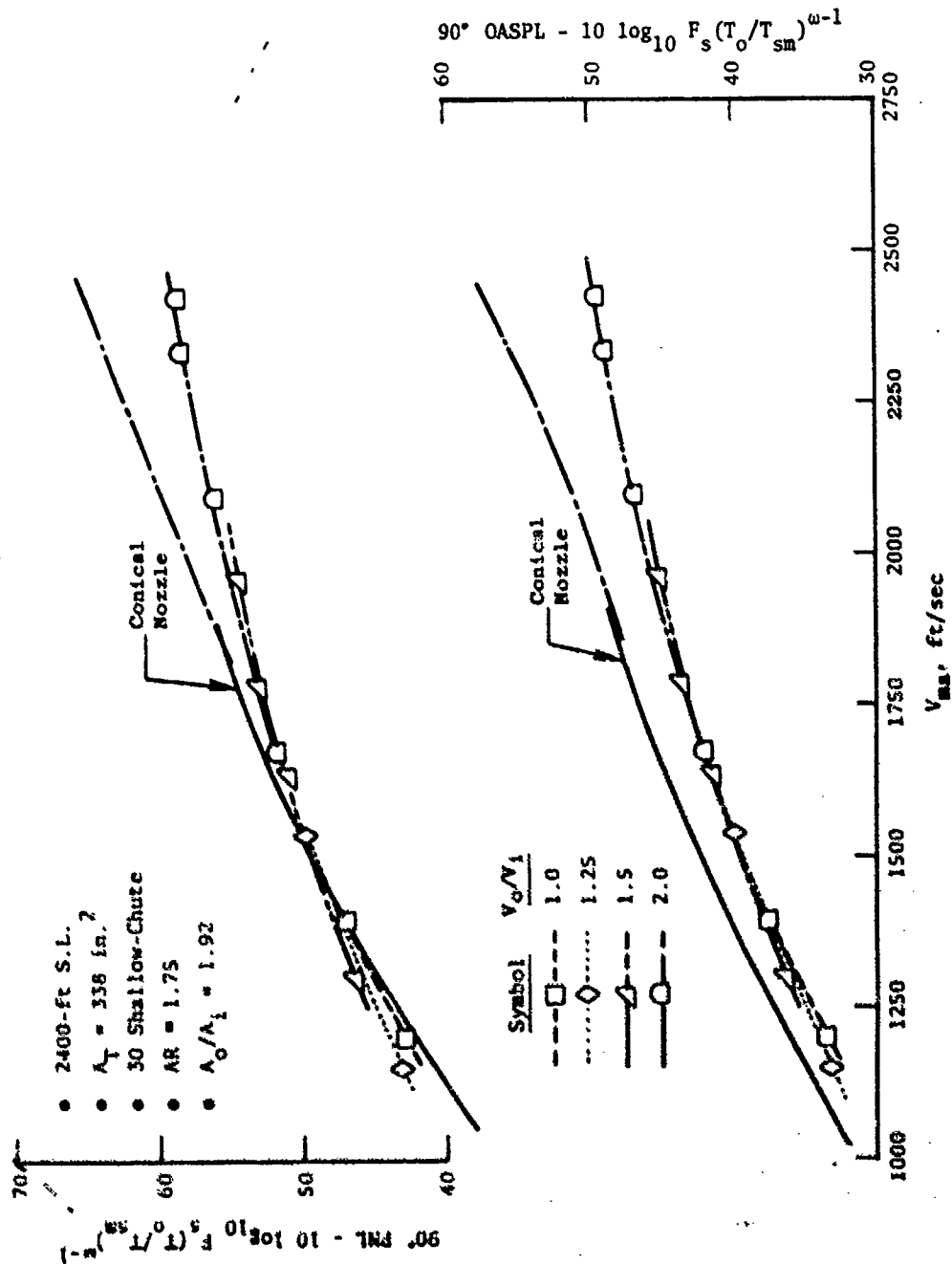


Figure 3-149. 90° FNL and OASPL Variation with  $V_0/V_1$ , Model 31.

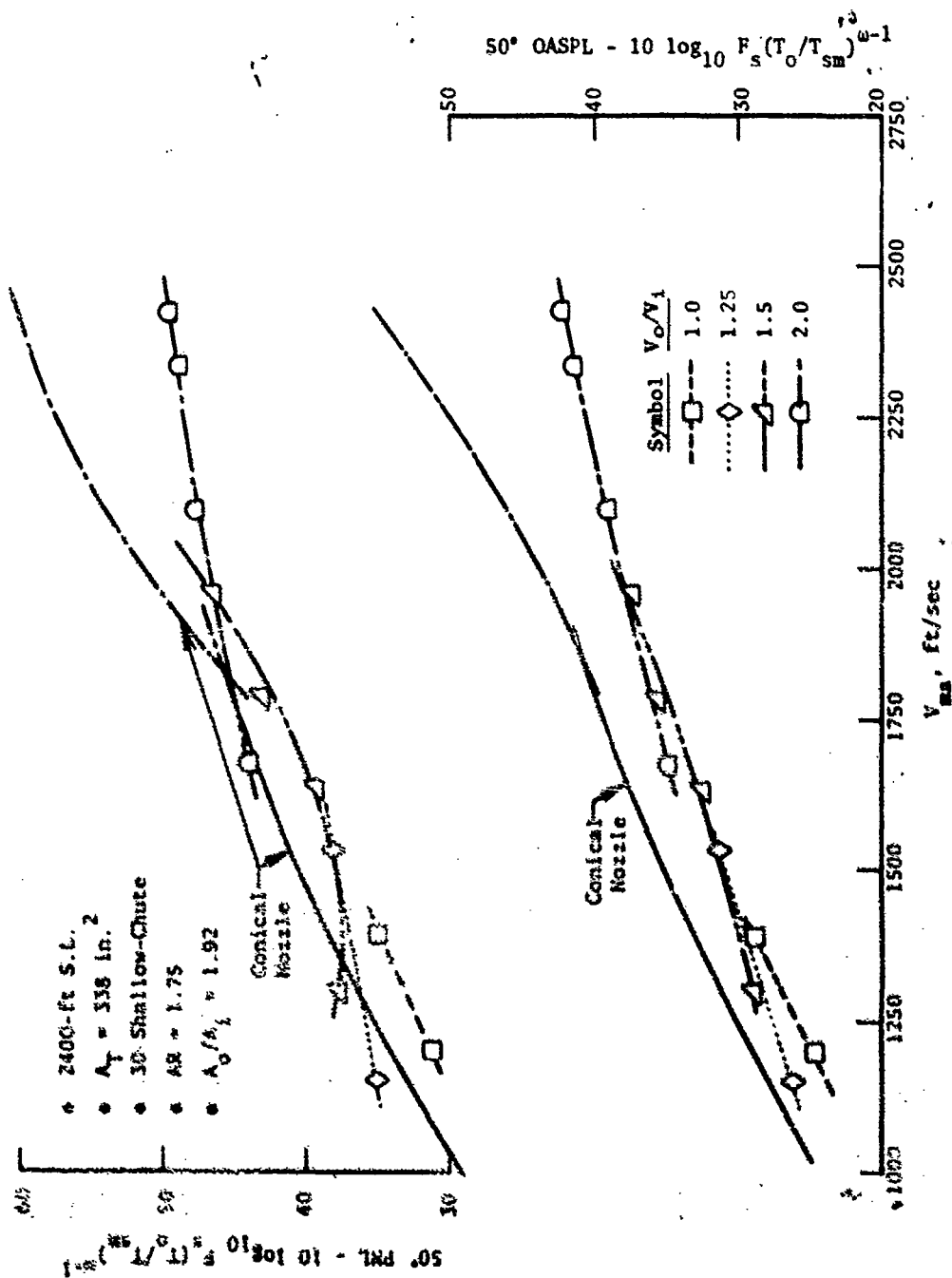


Figure 3-150. 50° PNL and OASPL Variation with  $V_0/V_1$ , Model 31.

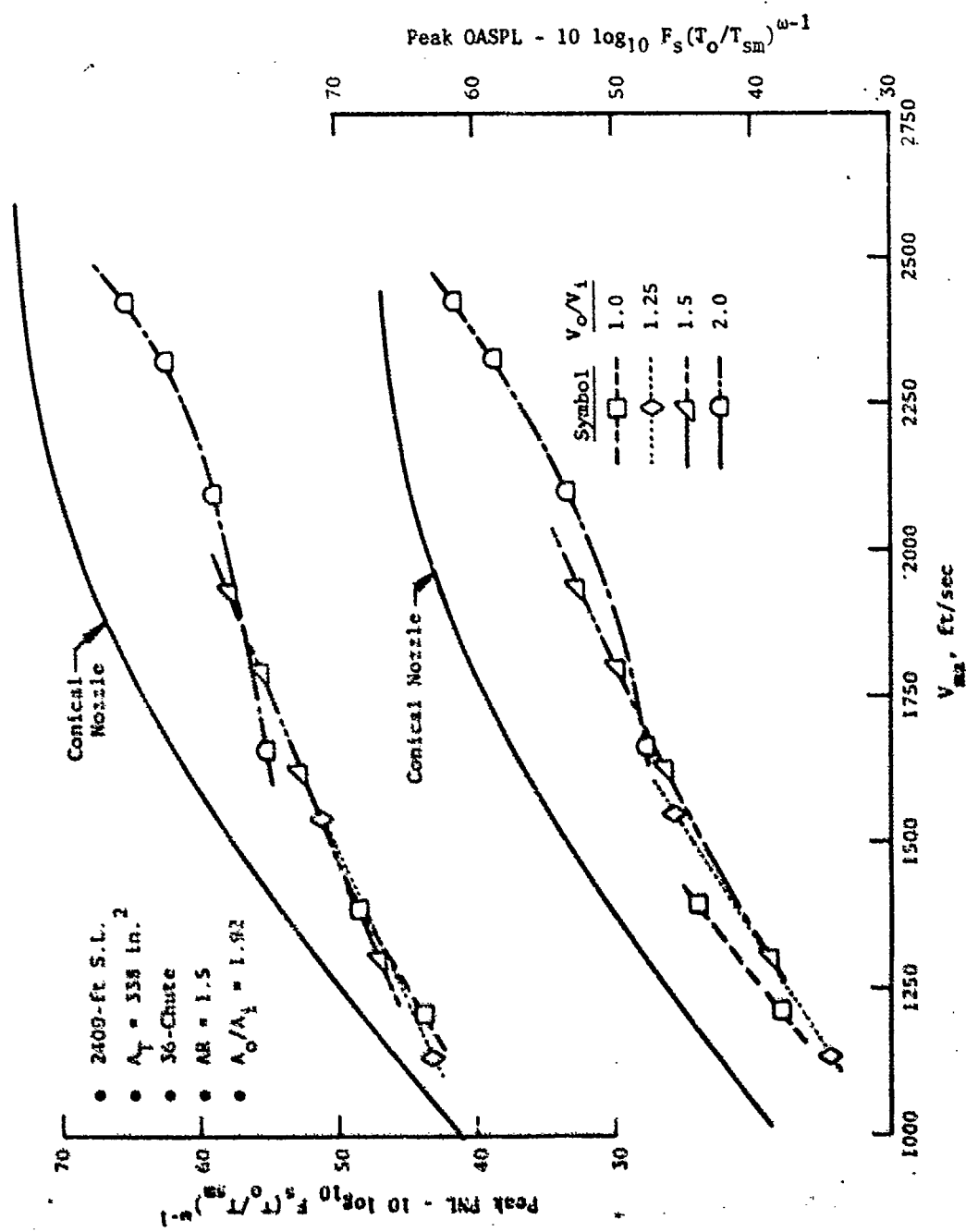


Figure 3-151. Peak FNL and OASPL variation with  $V_0/V_1$ , Model 27.



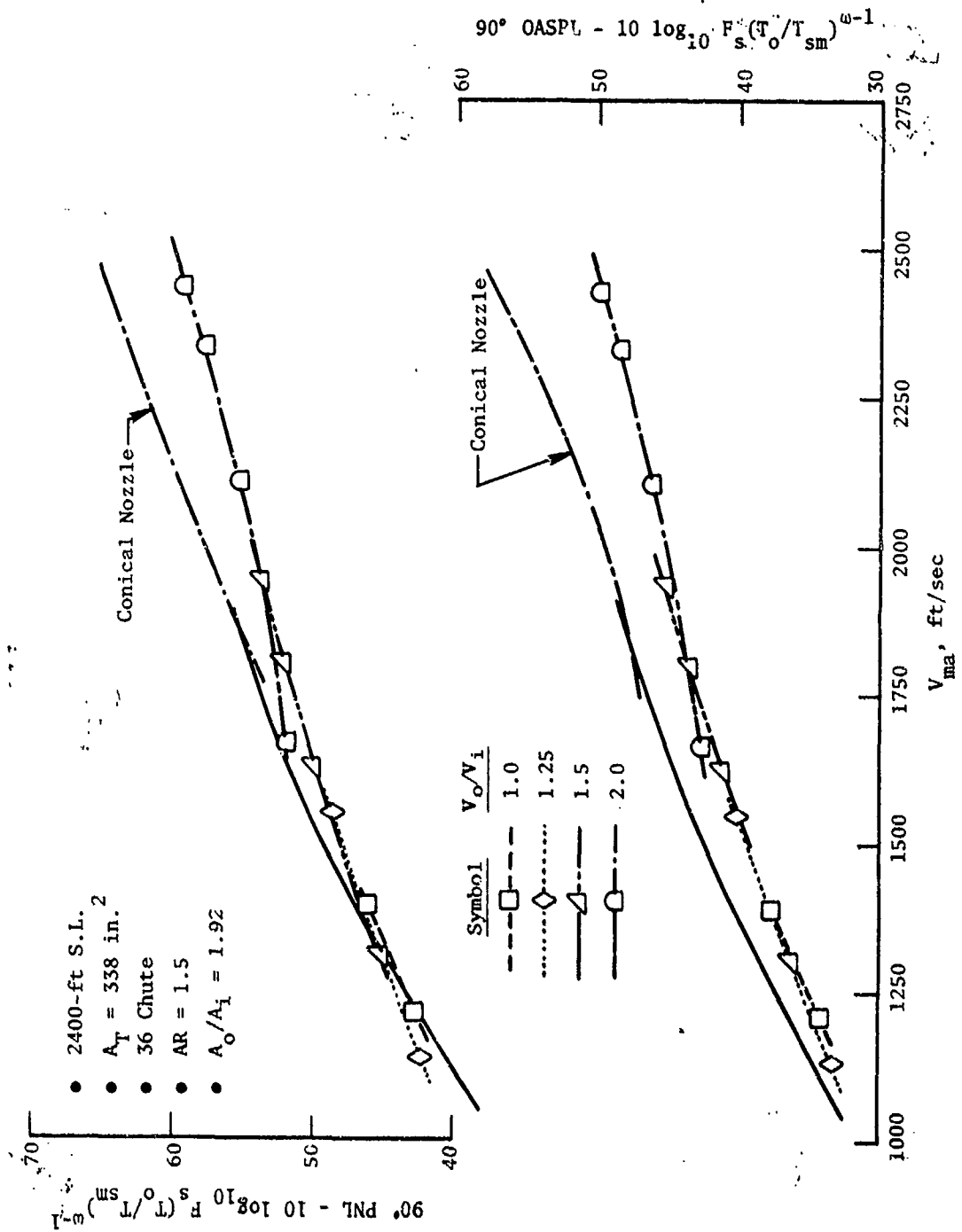


Figure 3-152. 90° PNL and QASPL Variation with  $V_o/V_i$ , Model 27.

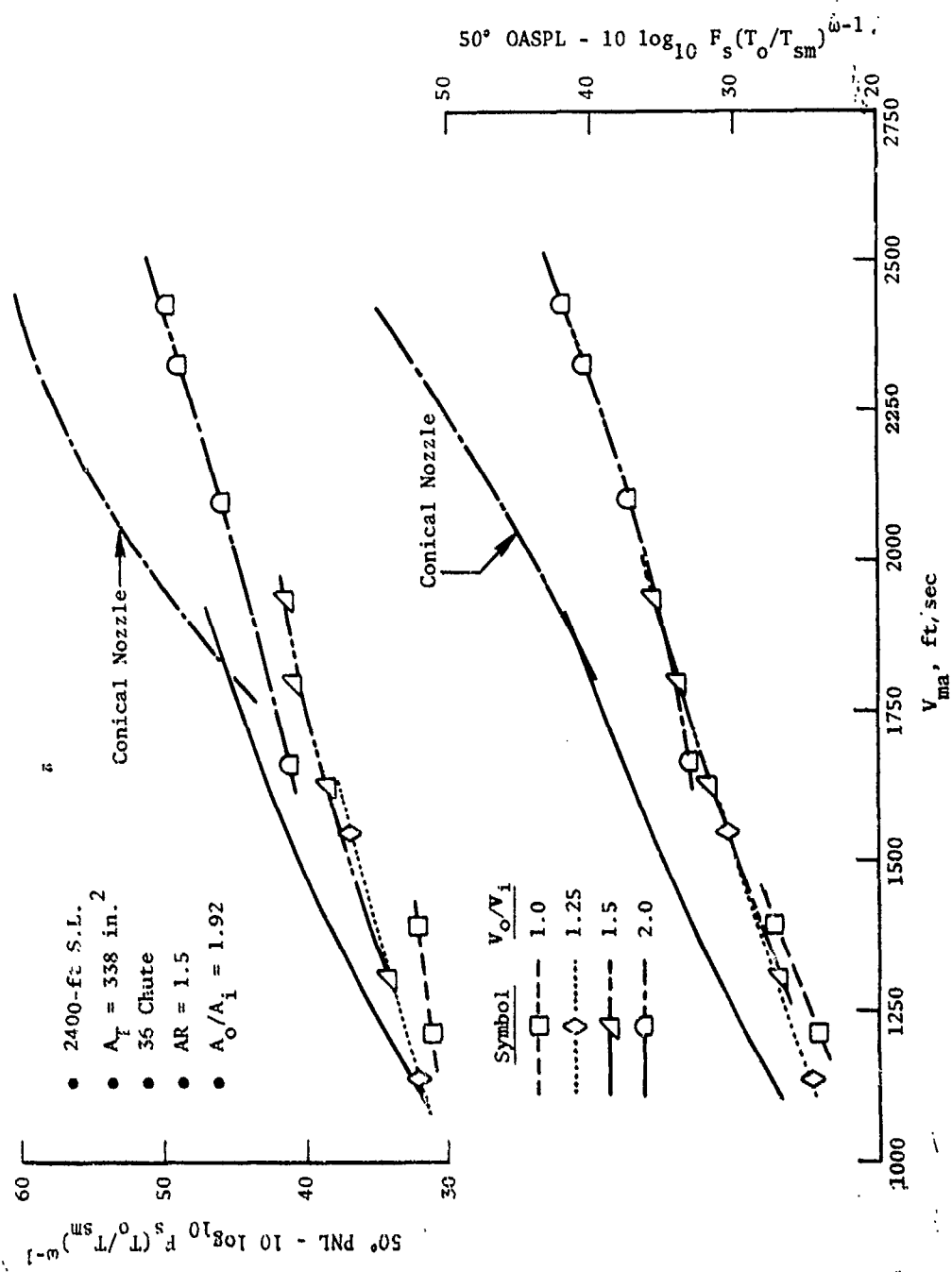


Figure 3-153. 50° PNL and OASPL Variation with  $V_o/V_i$ , Model 27.

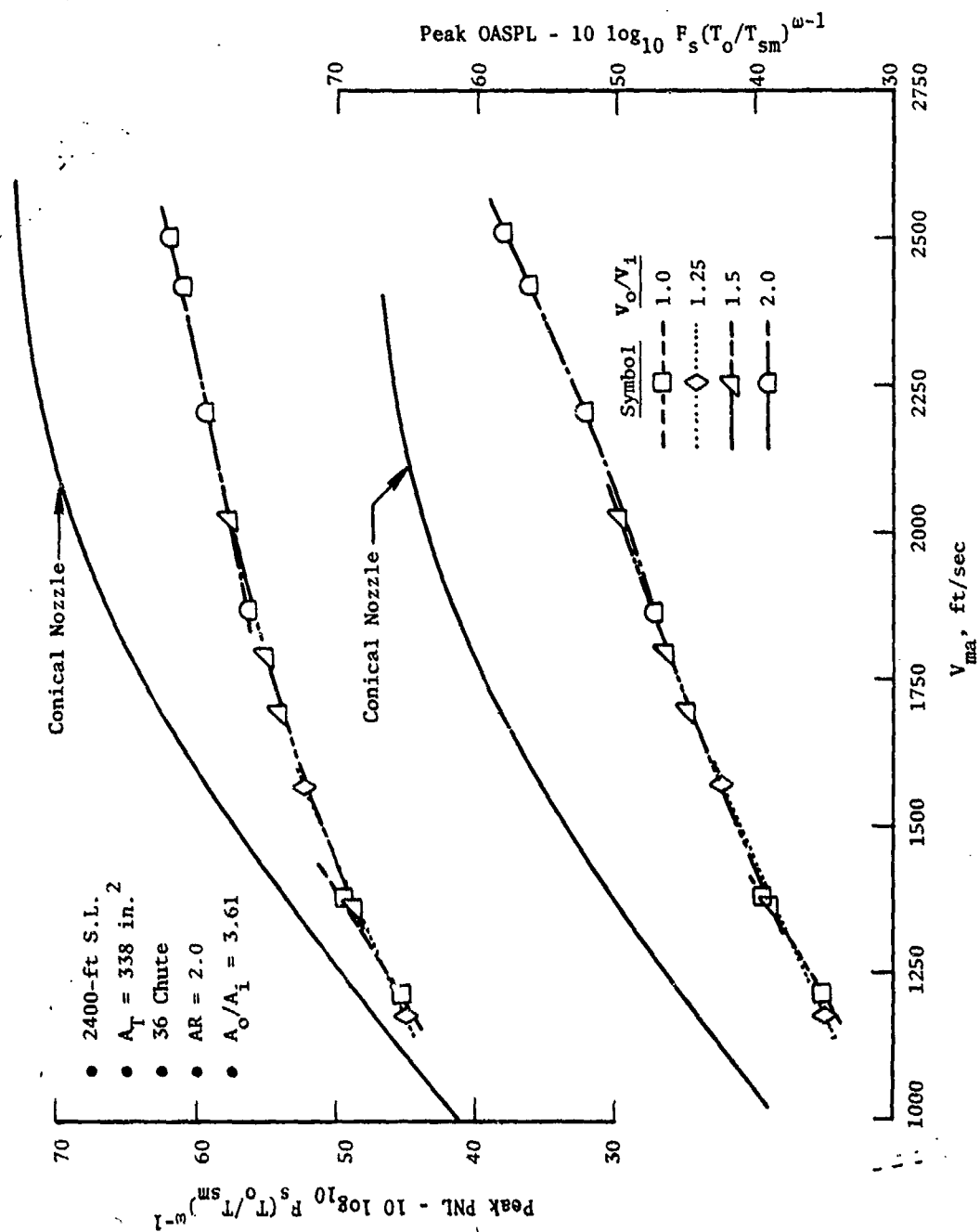


Figure 3-154. Peak PNL and OASPL Variation with  $V_o/V_i$ , Model 26.

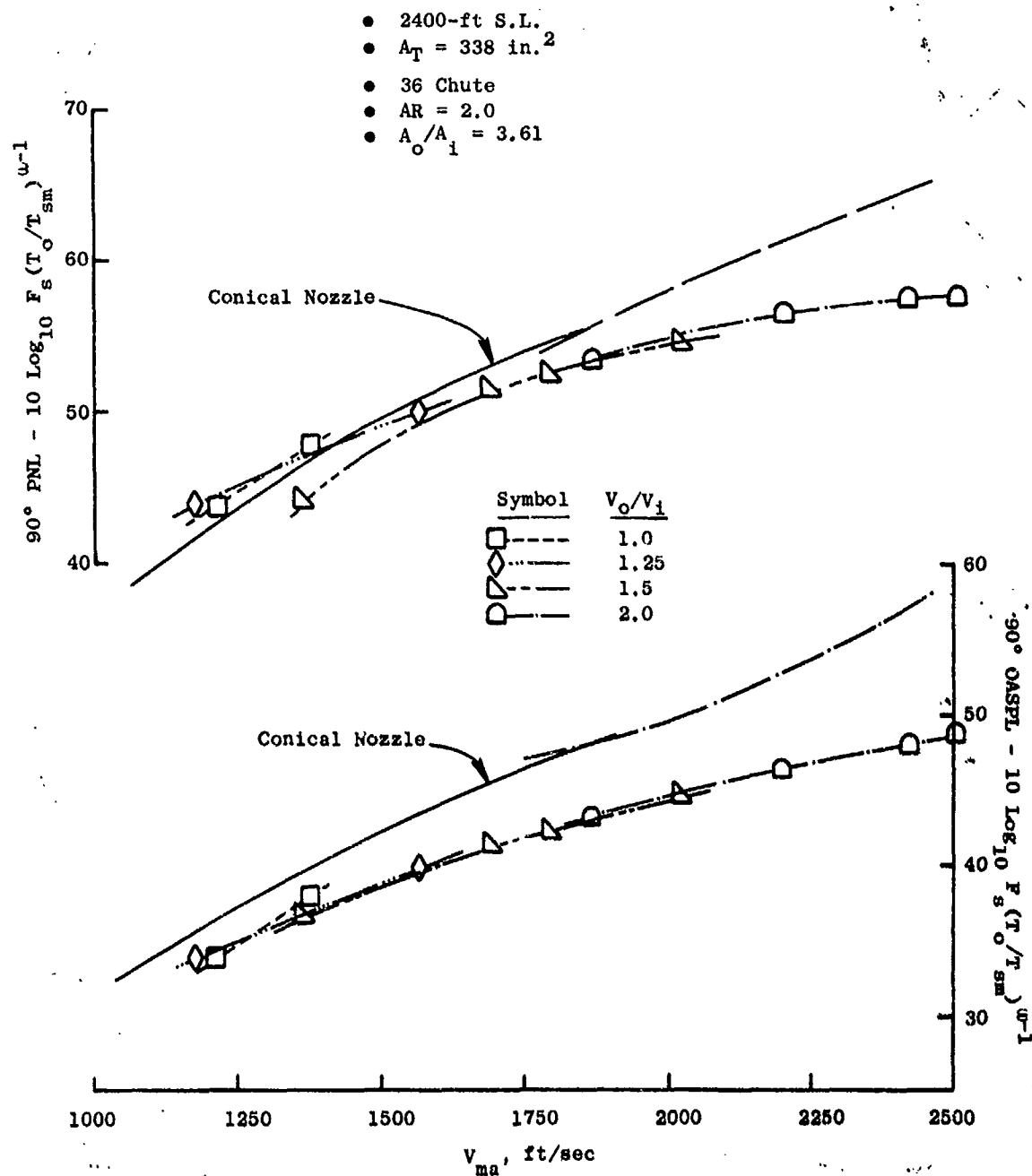


Figure 3-155. 90° PNL and OASPL Variation with  $V_o/V_1$ , Model 26.

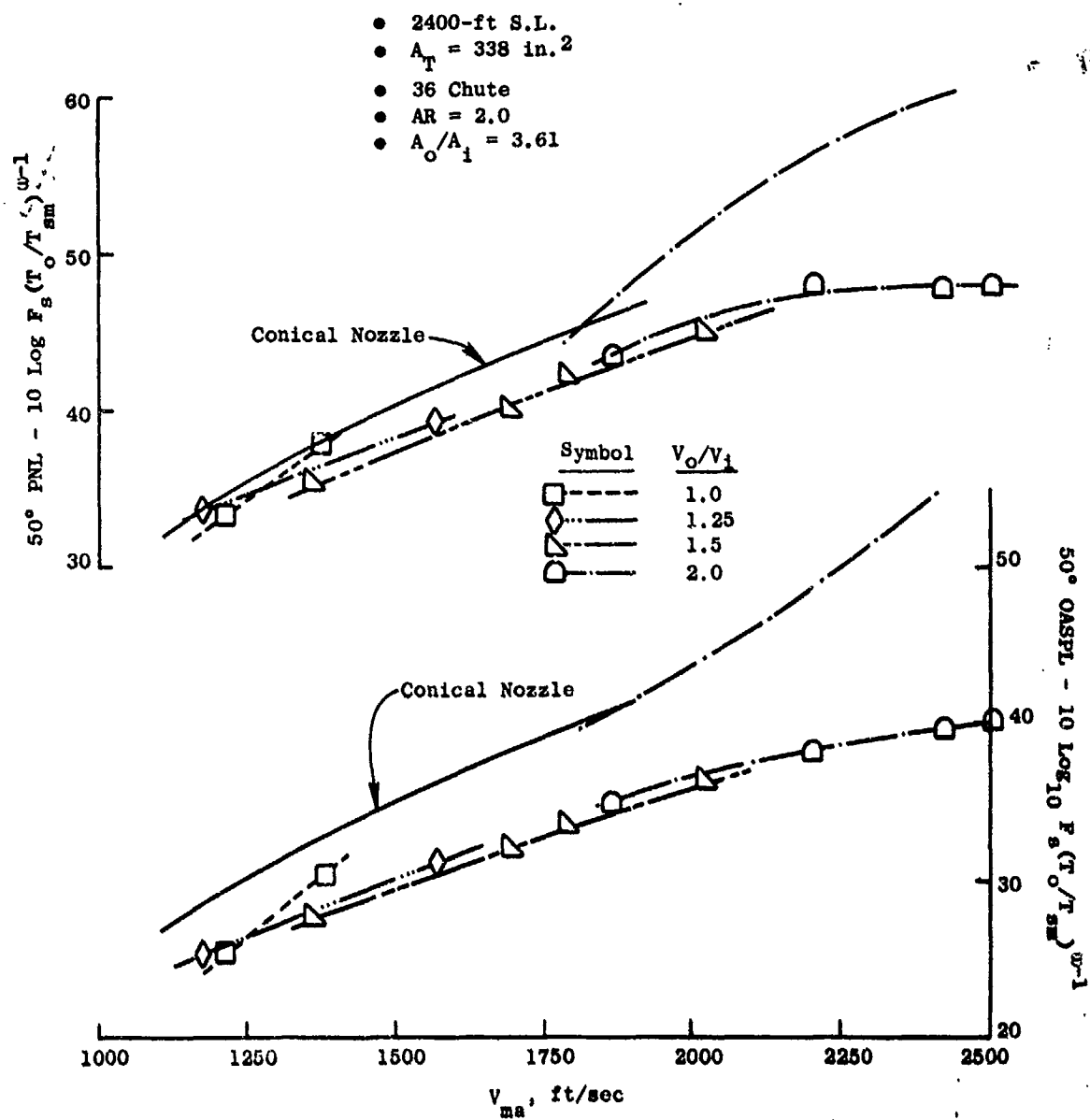


Figure 3-156. 50° PNL and OASPL Variation with  $V_o/V_1$ , Model 26.

### System $\beta$ Variation at Fixed $A_0/A_1$ and Duct Suppressor Geometry

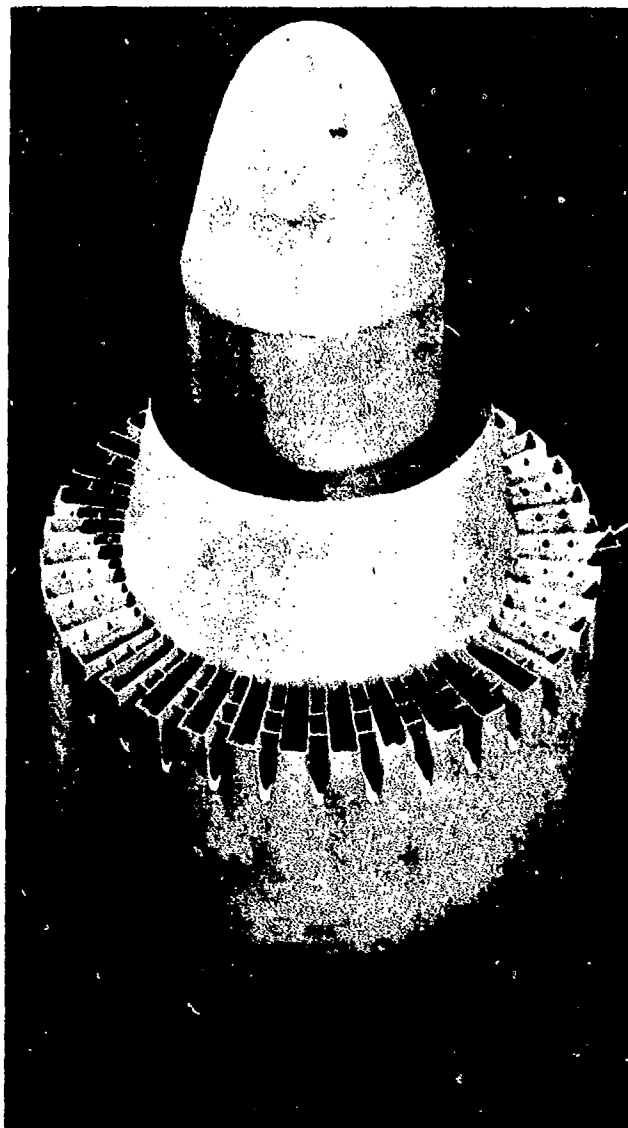
This study continues the theme of system variation investigations. The previous section isolated the influence of system velocity ratio and this section isolates the impact of system weight flow ratio,  $\beta$ . Primary emphasis is placed on systems which utilize low amounts of inner flow, in an effort to extend preliminary results of the NASA-Lewis/GE Duct-Burning Turbofan Program (Reference 10). These results indicate that unsuppressed coannular and suppressed annular systems show enhanced suppression with low amounts of inner stream flow.

Seven test configurations were utilized, varying system area ratio and annular suppressor geometry, and the following four were selected for presentation of results herein:

Model No.	System $A_0/A_1$	Outer Stream				Inner Stream				Appendix A Figure Reference
		Element Description	AR	$R_F$	Flow Area, in. <sup>2</sup>	Step Height in.	Plug Location	$R_F$	Flow Area, in. <sup>2</sup>	
33	0.65	36-Chute	2.5	0.783	17.21	1.03	Retracted	0.674	11.12	27
34	0.65	36-Chute	3.0	0.783	17.21	1.03	Retracted	0.674	11.12	28
31	1.92	30-Shallow Chute	1.75	0.717	23.76	0.70	Retracted	0.779	12.39	25
23	1.92	36-Chute	2.0	0.716	23.76	0.70	In-Line	0.779	12.39	17

The first three models are the same as in the previous section (shown in Figures 3-129 and 3-130). A photo of Model 23 is included as Figure 3-157. The last column of the above chart references the detailed geometry sketches for each model as shown in Appendix A. Three of the configurations have annular deep-chute suppressors and Model 31 has an annular shallow-chute suppressor. The first two models have  $A_0/A_1$  of 0.65 and the remaining two have  $A_0/A_1$  of 1.92. The suppressor area ratio range is 1.75 to 3.0 and the radius ratio range is 0.716 to 0.783. Each model is representative of an advanced technology dual flow system with half-span suppressor application.

Systematic variation of weight flow ratio was accomplished using pre-selected  $\beta$  values of 3.3, 6.7 and  $\infty$ . This corresponded to metering inner stream flow rates at 30, 15 and 0% of the outer stream. The  $\beta = \infty$  case is attained when the inner flow is curtailed completely by use of a positive shut-off mechanism placed about one diameter upstream of the inner flow exit plane. Through this  $\beta$  variation, for the two  $A_0/A_1$  systems selected, the system velocity ratio varied as follows:



Model 23

- 36 Chute,  $AR = 2.0$
- $R_r^0 = 0.716$ ,  $R_r^1 = 0.779$  In-Line Inner Plug
- $A_0/A_1 = 1.92$

Figure 3-157. Dual Flow Model for  $\beta$  Investigation  
at  $A_0/A_1 = 1.92$ .

$A_0/A_1$	$\beta$	$\approx V_0/V_1$
0.65	6.7	6 - 14
	3.3	6 - 11
1.92	6.7	2.5 - 8
	3.3	1 - 3

Acoustic results in terms of peak, 90° and 50° PNL and OASPL are presented individually for each model in the following figures. Each data set is normalized per Section 3.3.1.7 and plotted versus  $V_{ma}$ . The peak PNL and OASPL data sets have  $\Delta$  plots showing suppression relative to the baseline convergent nozzle.

Model No.	Peak PNL	Peak OASPL	90° PNL & OASPL	50° PNL & OASPL
33	3-158	3-159	3-160	3-161
34	3-162	3-163	3-164	3-165
31	3-166	3-167	3-168	3-169
23	3-170	3-171	3-172	3-173

The following are observed:

- System weight flow ratio,  $\beta$ , is a strong parameter which influences peak PNL and peak OASPL significantly. The magnitude of influence is somewhat greater for low system  $A_0/A_1$  of 0.65 than for 1.92. The influence is fairly systematic, progressively decreasing suppression capability as  $\beta$  is lowered from  $\infty$ , to 6.7, to 3.3. Influence of  $\beta$  on the  $A_0/A_1 = 0.65$  system is fairly consistent over the  $V_{ma}$  test range, whereas, on the  $A_0/A_1 = 1.92$  systems, it's influence is primarily at mid-to-high  $V_{ma}$ ; suppression variance decreasing on both PNL and OASPL basis.
- At  $A_0/A_1 = 0.65$  (Models 33 and 34), peak PNL changes up to 5 dB at low  $V_{ma}$  (between  $\beta = 3.3$  and  $\infty$ ) and up to 3 dB at high  $V_{ma}$ . The corresponding peak OASPL variances are about 5 and 6 dB, respectively.
- In the previous study, system velocity ratio varied over the  $0.6 \leq V_0/V_1 \leq \infty$  range, with small incremental and systematic variations exercised within the 0.6 to 2.0 range. Accompanying  $\beta$  ranged from 0.4 to 1.3. Variations in noise level appear to be primarily controlled by whichever stream's noise dominated the spectral composition. At preselected values of  $\beta$  of 3.3 and 6.7,  $V_0/V_1$  vari-



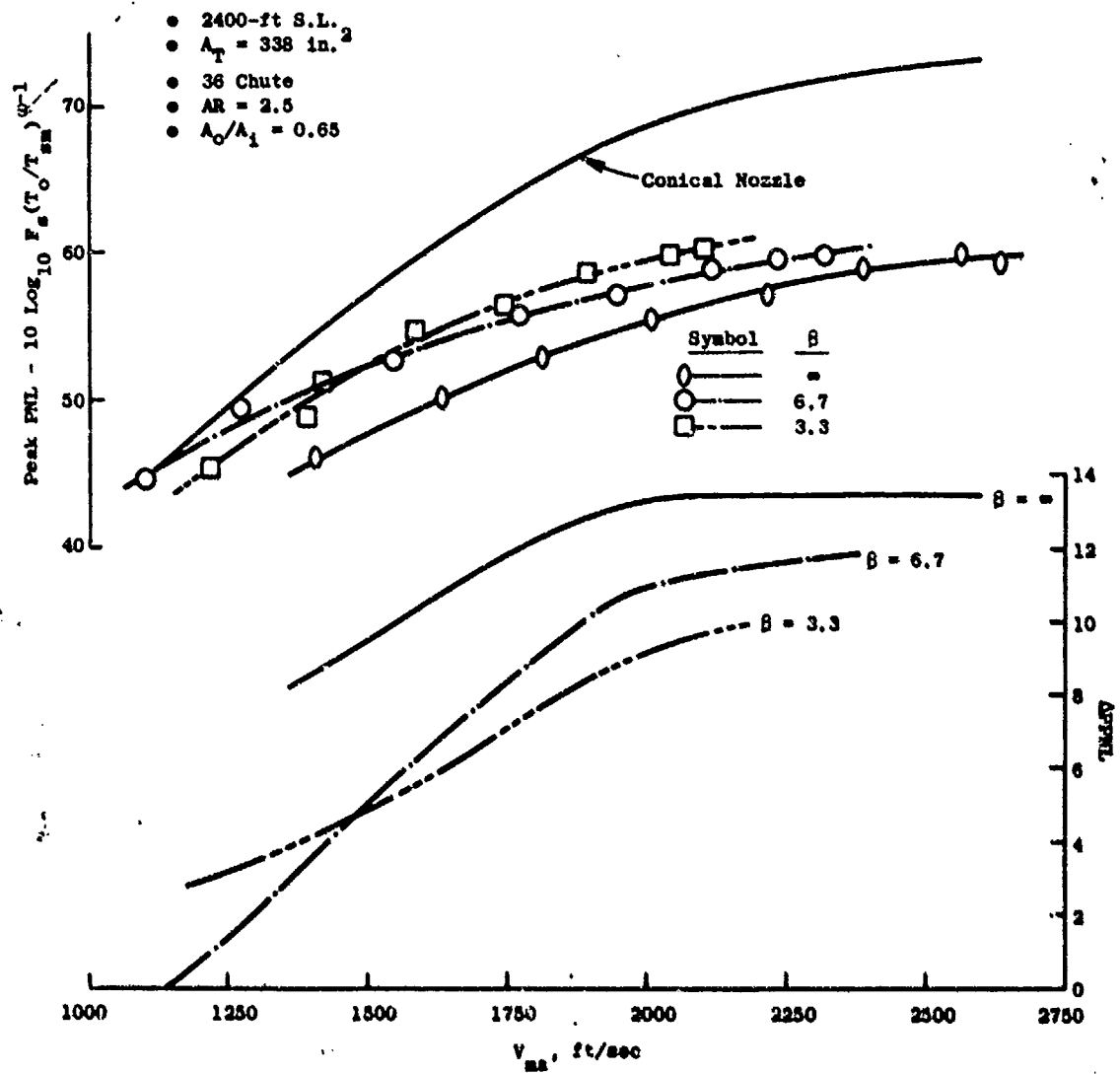


Figure 3-158. Peak PNL Variation with  $\beta$ , Model 33.

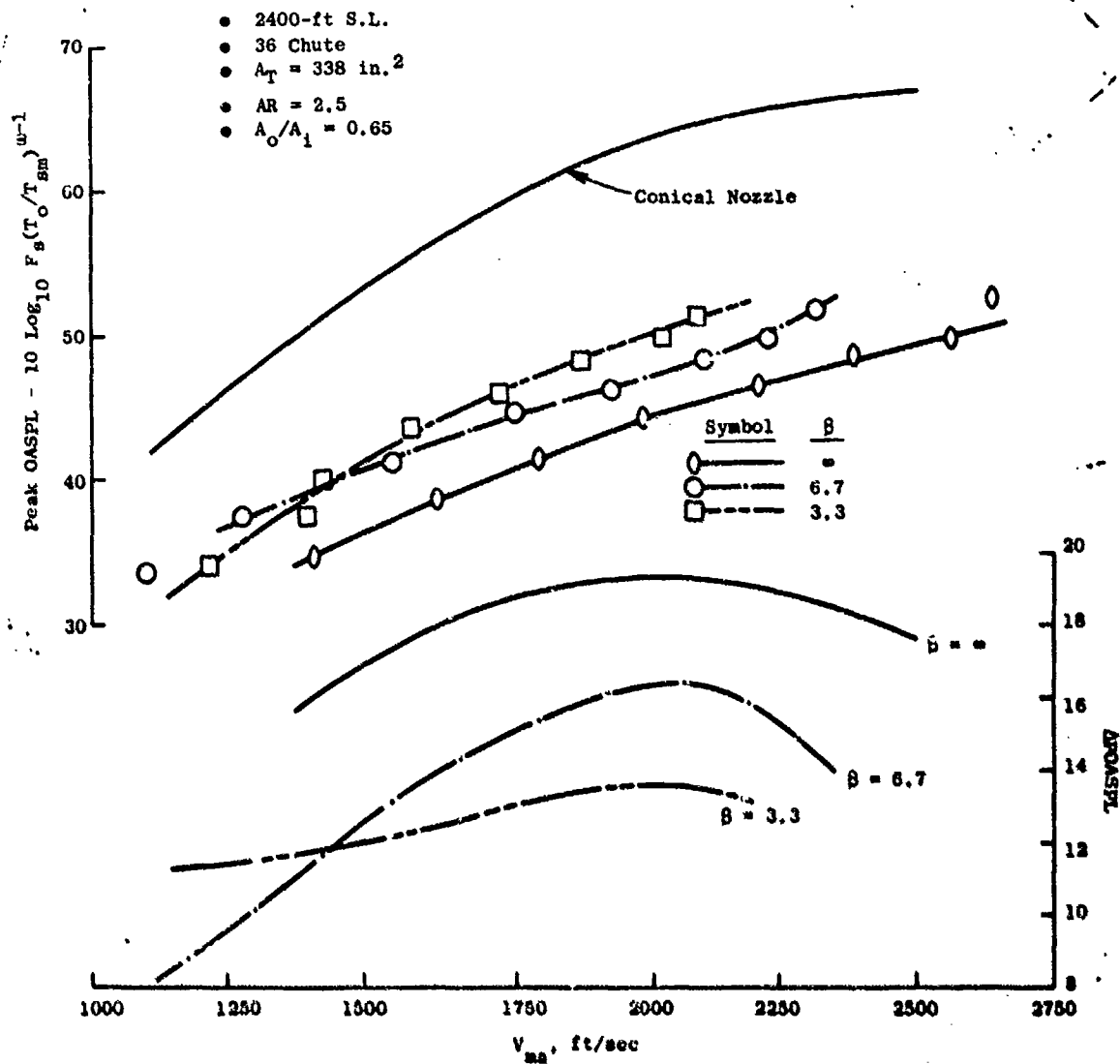


Figure 3-159. Peak OASPL Variation with  $\beta$ , Model 33.

- 2400-ft S.L. 2
- $A_T = 338$  in. 2
- 36 Chute
- $A_2 = 2.5$
- $A_0/A_1 = 0.65$

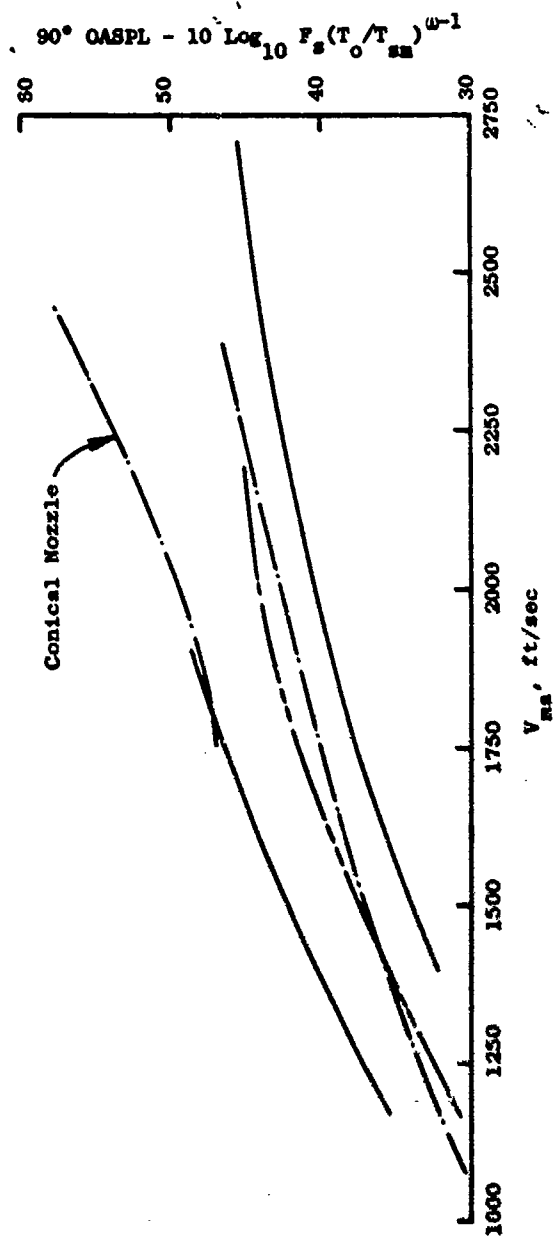
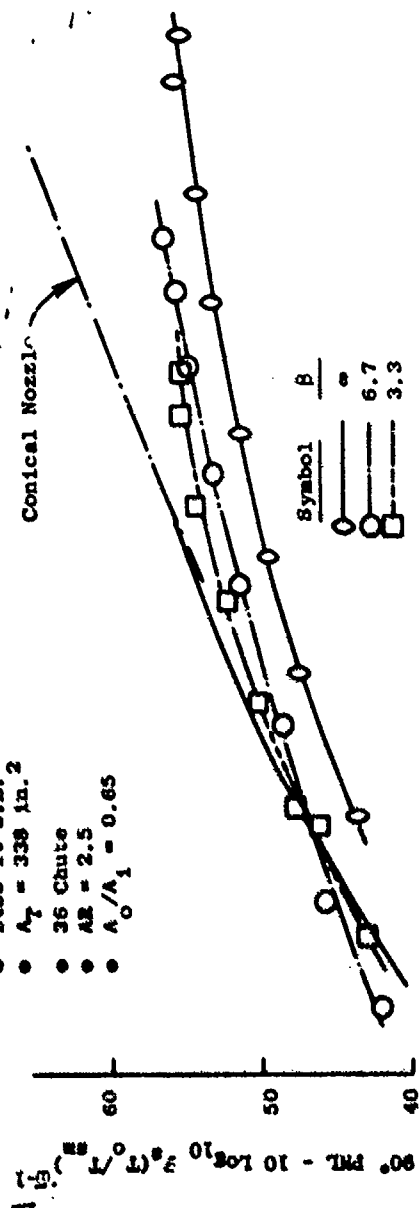


Figure 3-160. 90° PML and OASPL Variation with  $\beta$ , Model 33.

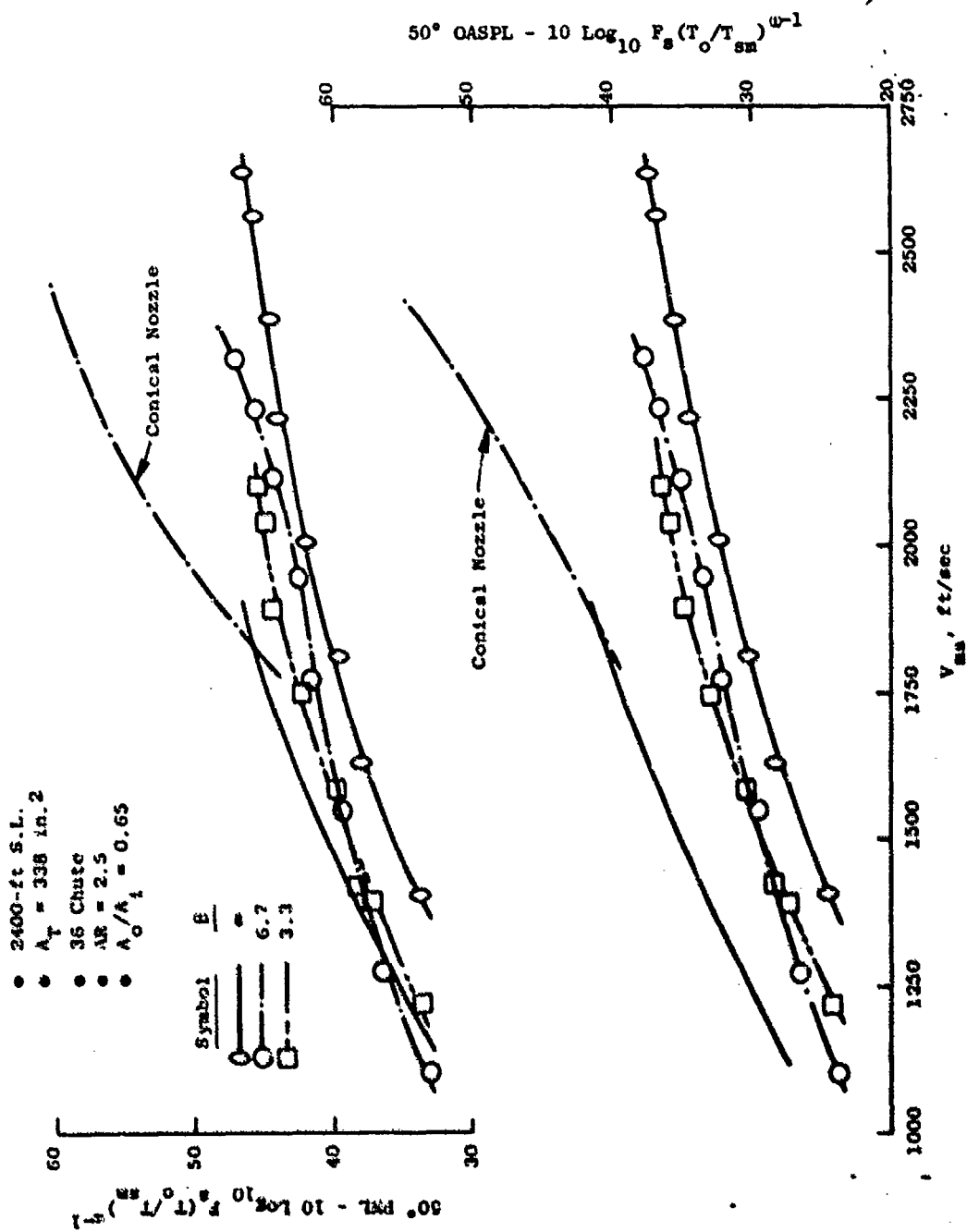


Figure 3-161. 60° FWL and QASPL Variation with  $\beta$ , Model 33.

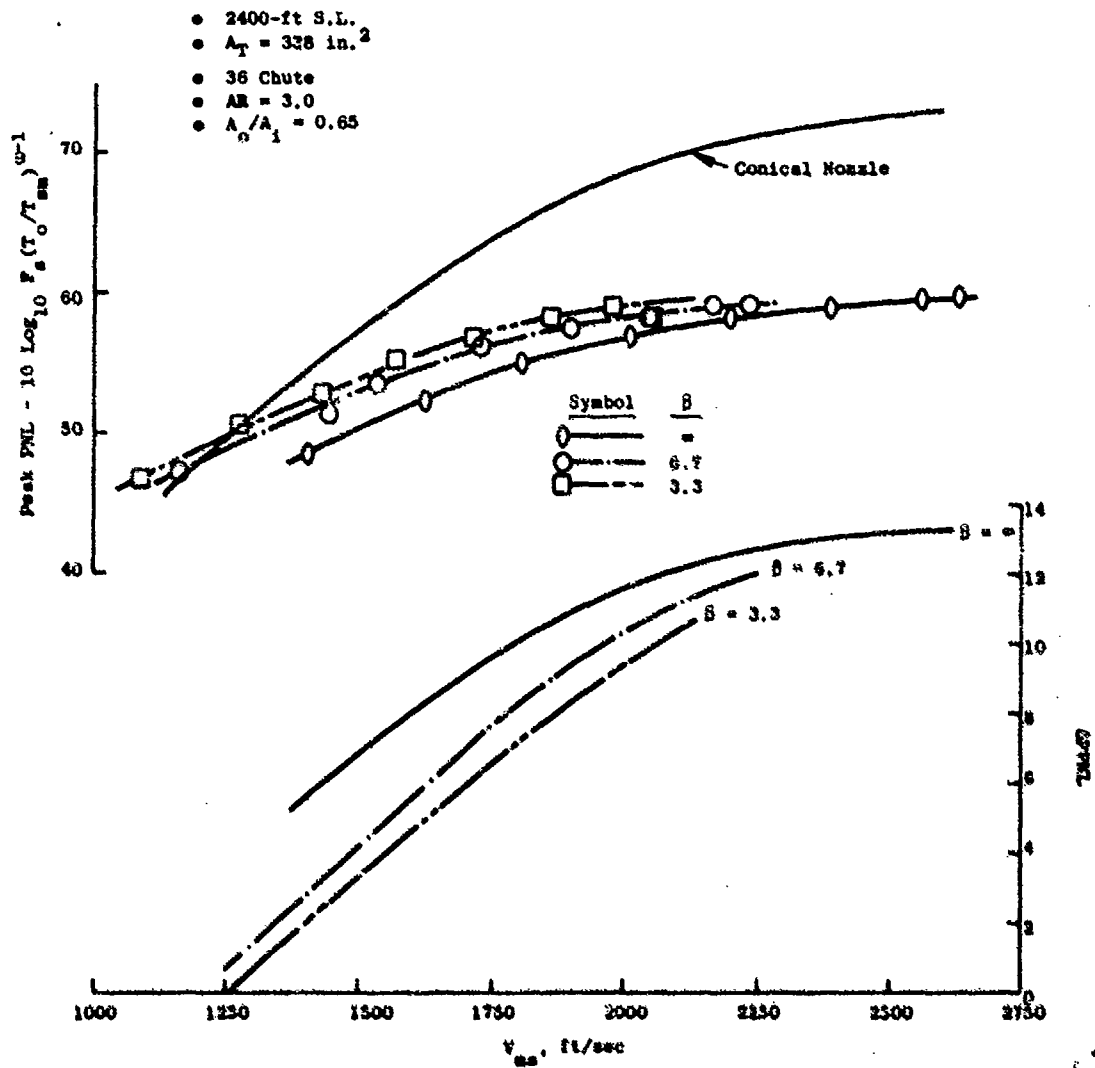


Figure 3-162. Peak PNL Variation with B, Model 34.

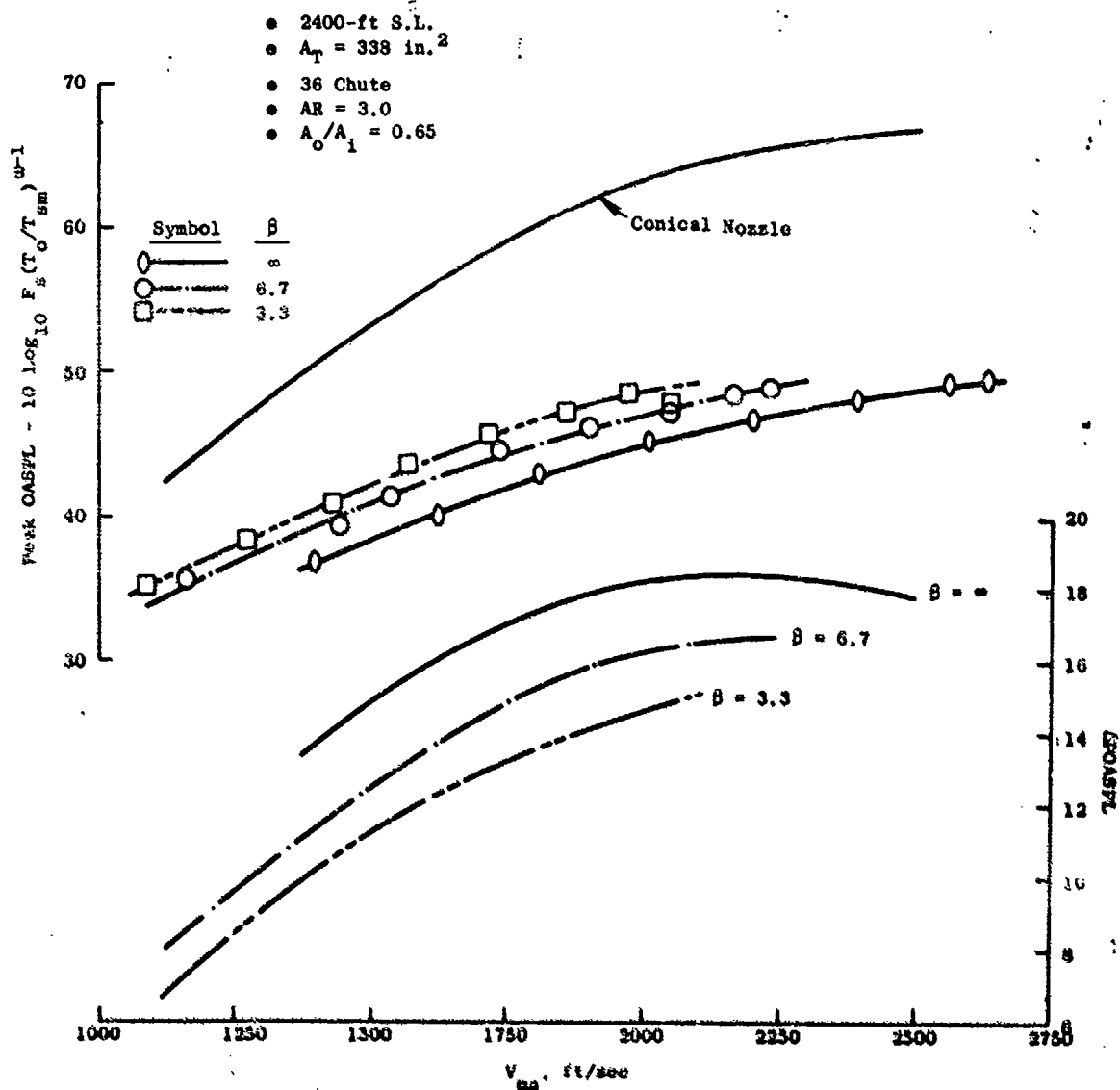


Figure 3-163. Peak OASPL Variation with  $\beta$ , Model 34.

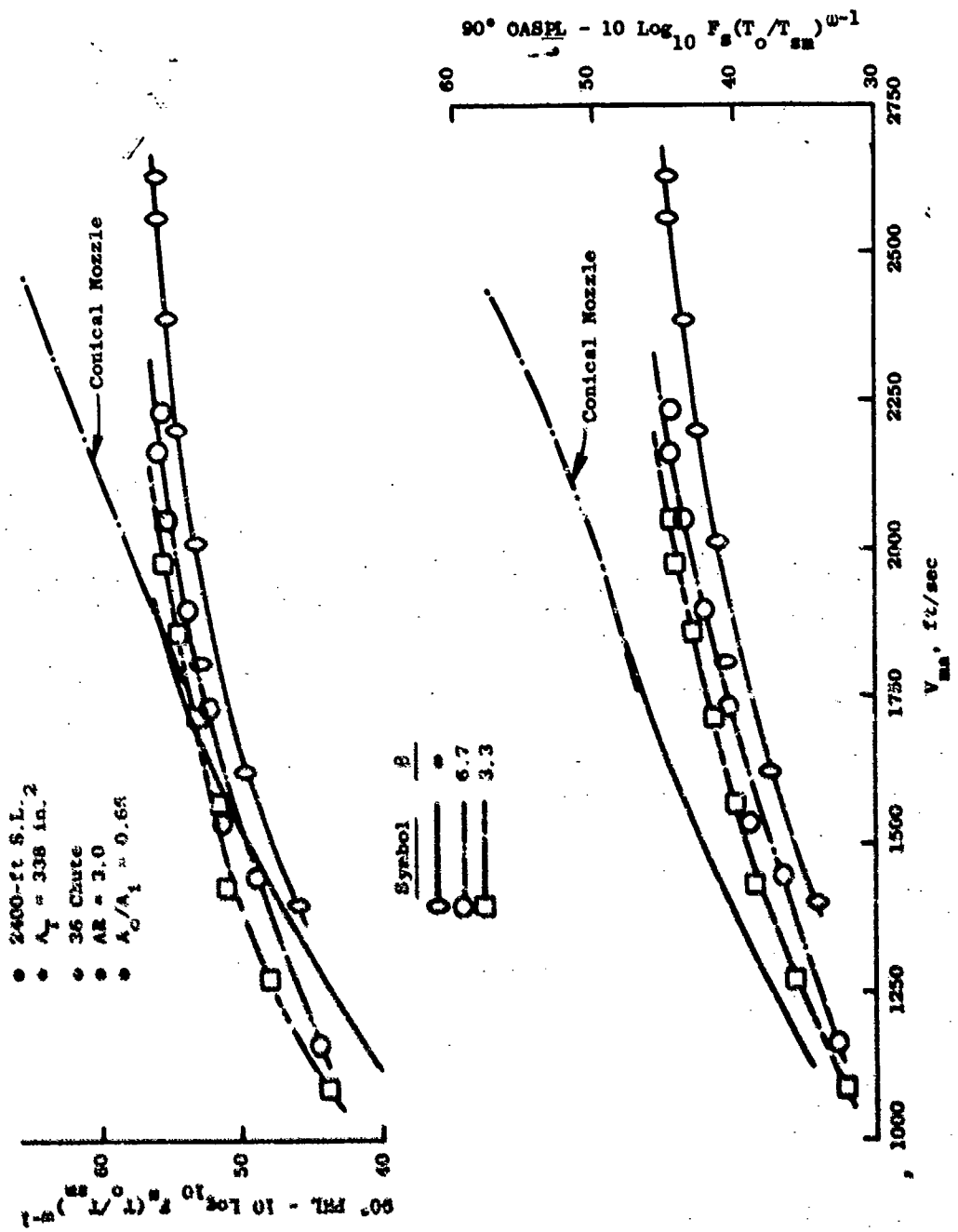


Figure 3-164. 90° FFL and OASPL Variation with  $\beta$ , Model 34.

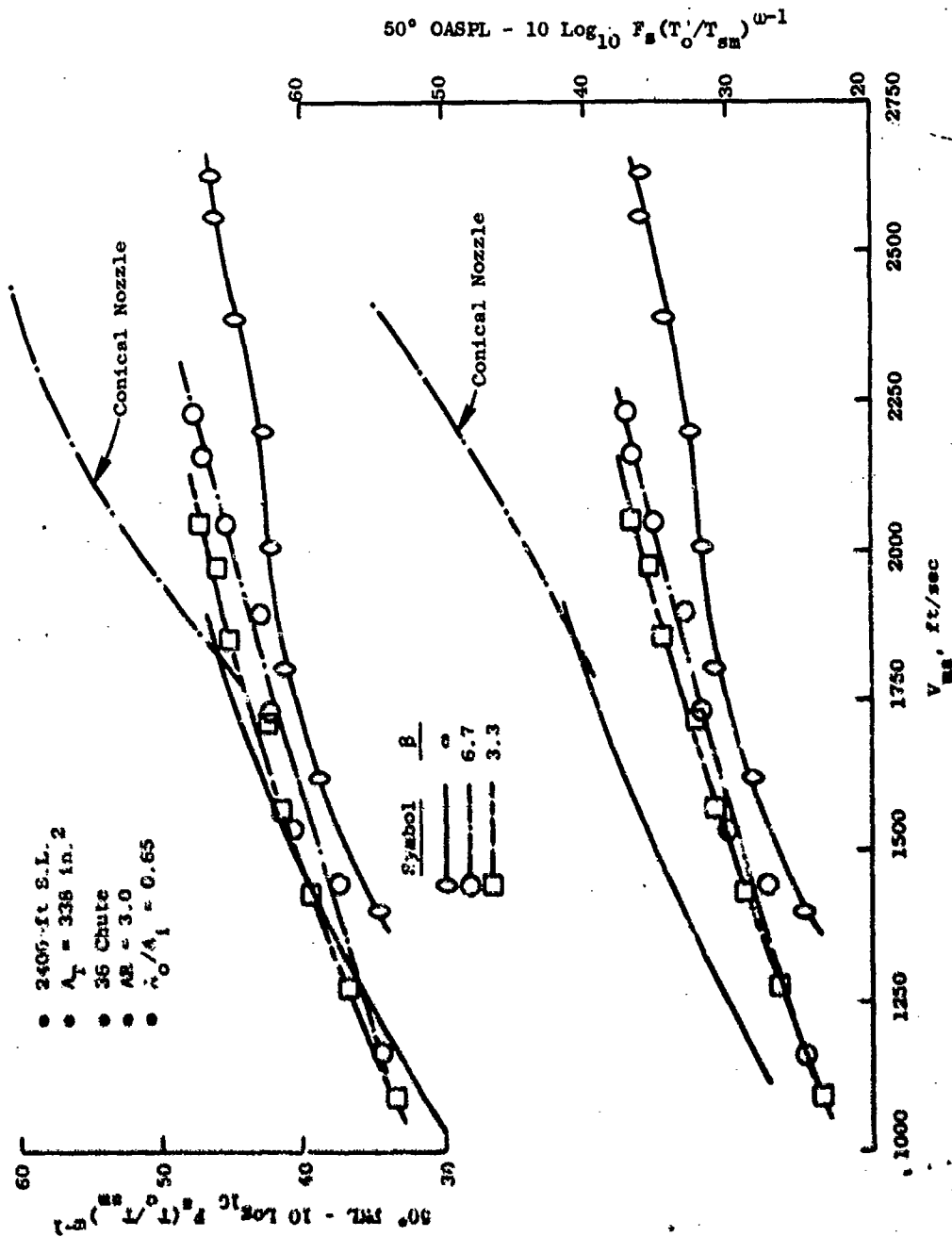


Figure 3-165.  $50^\circ \text{ PN}$ , and OASPL Variation with  $\beta$ , Model 34.



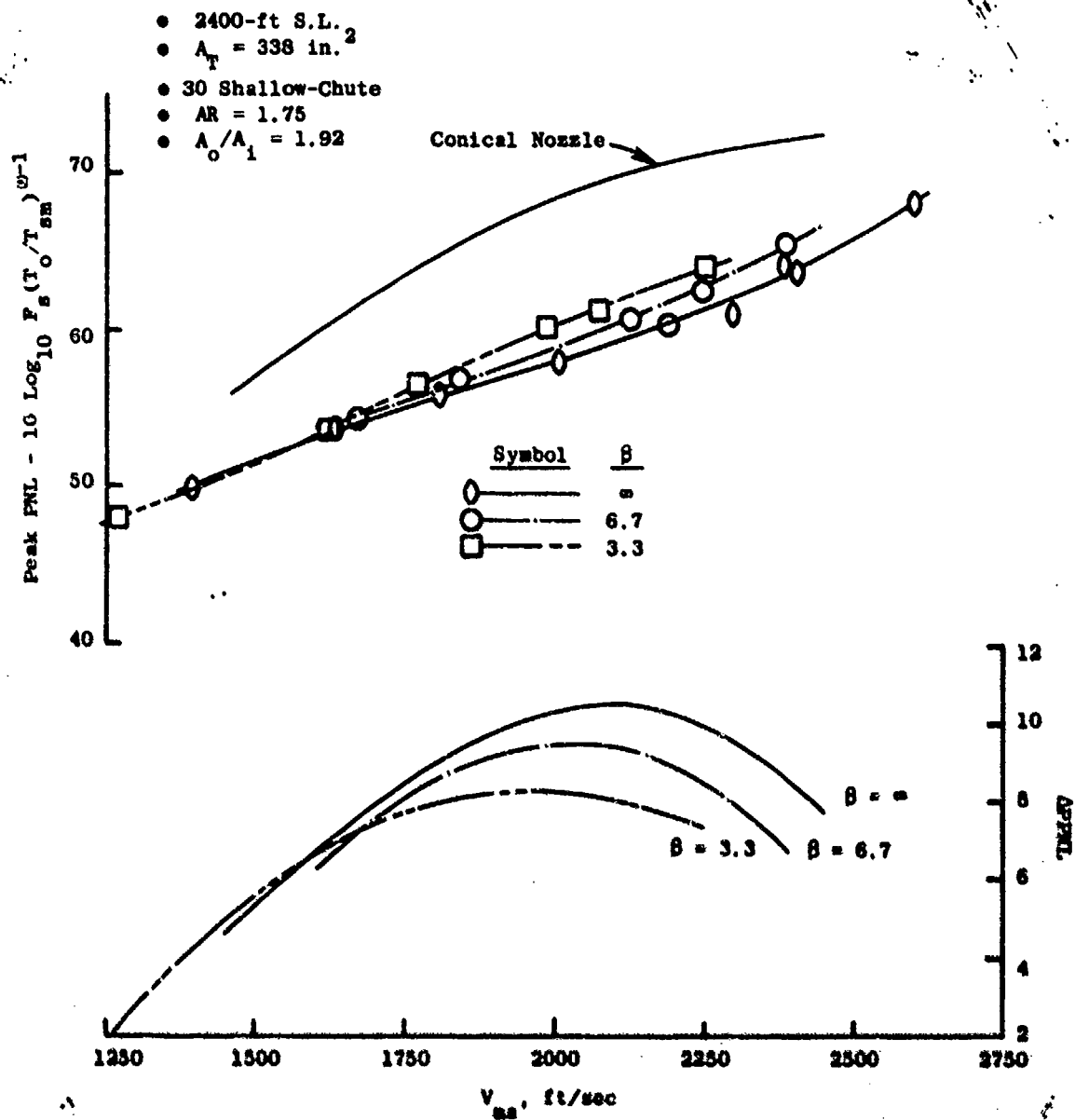


Figure 3-166. Peak PNL Variation with  $\beta$ , Model 31.

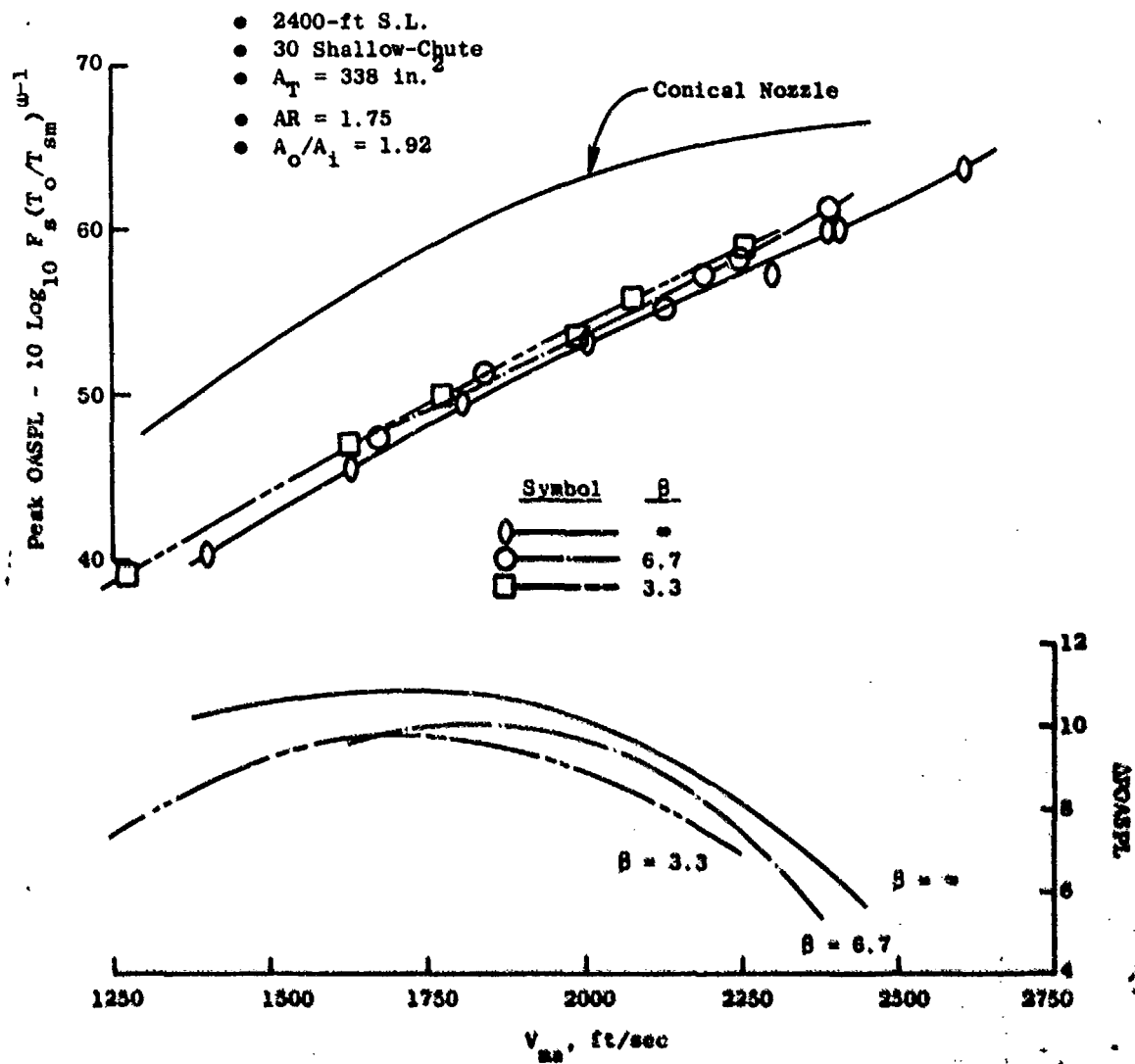


Figure 3-167. Peak OASPL Variation with  $\beta$ , Model 31.

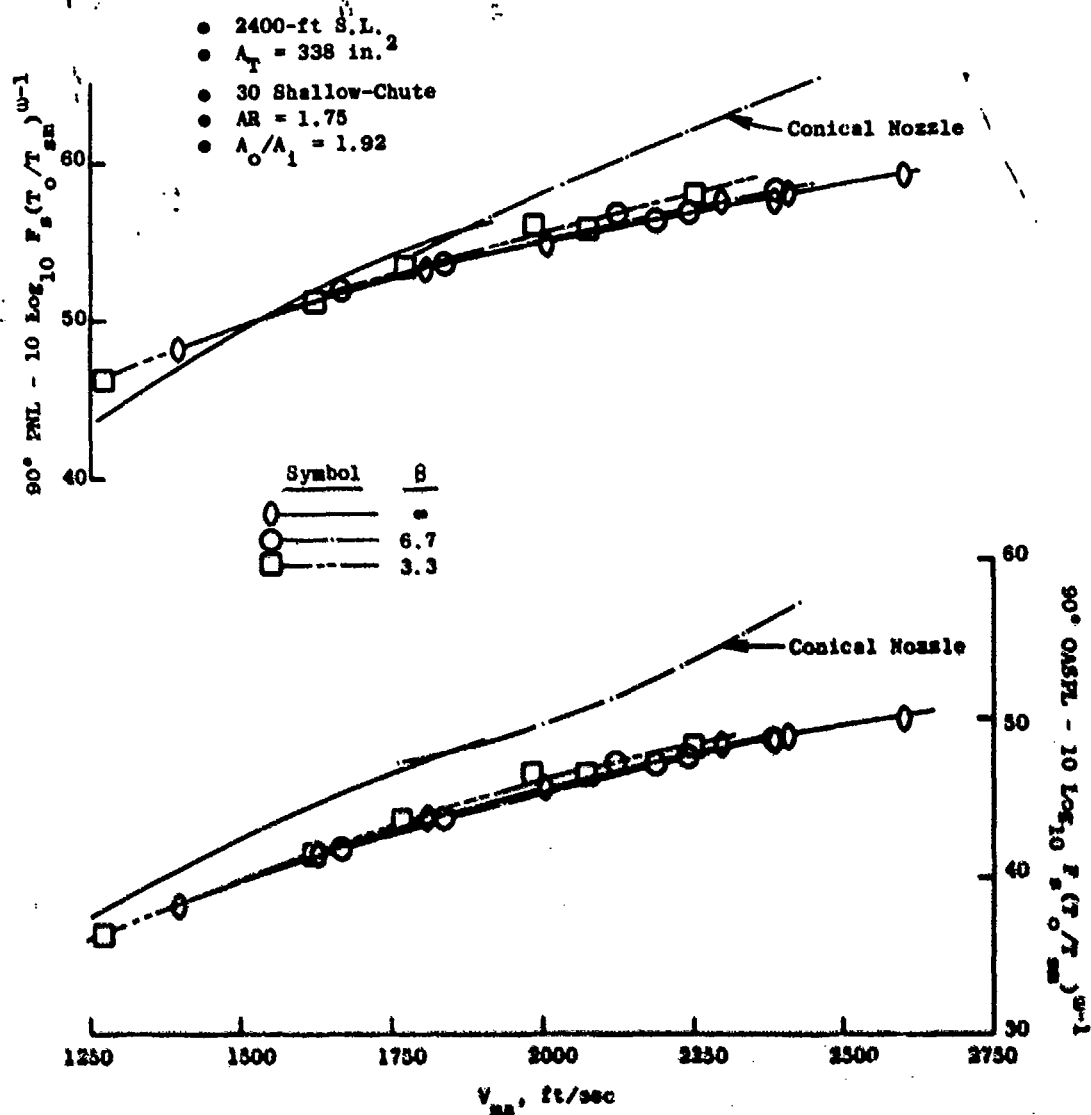


Figure 3-168. 90° PNL and OASPL Variation with  $\beta$ , Model 31.

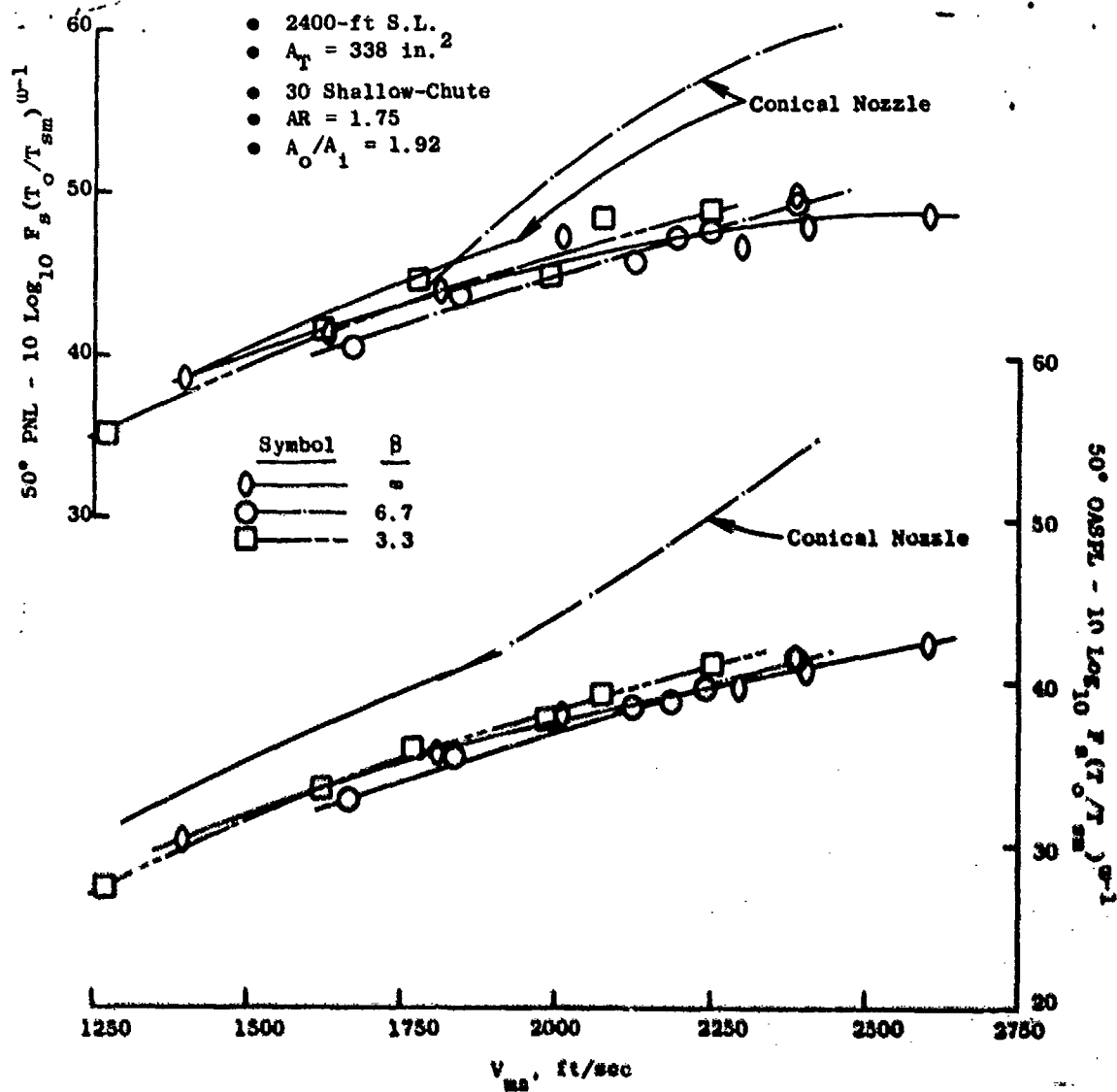


Figure 3-169. 50° PNL and OASPL Variation with  $\beta$ , Model 31.

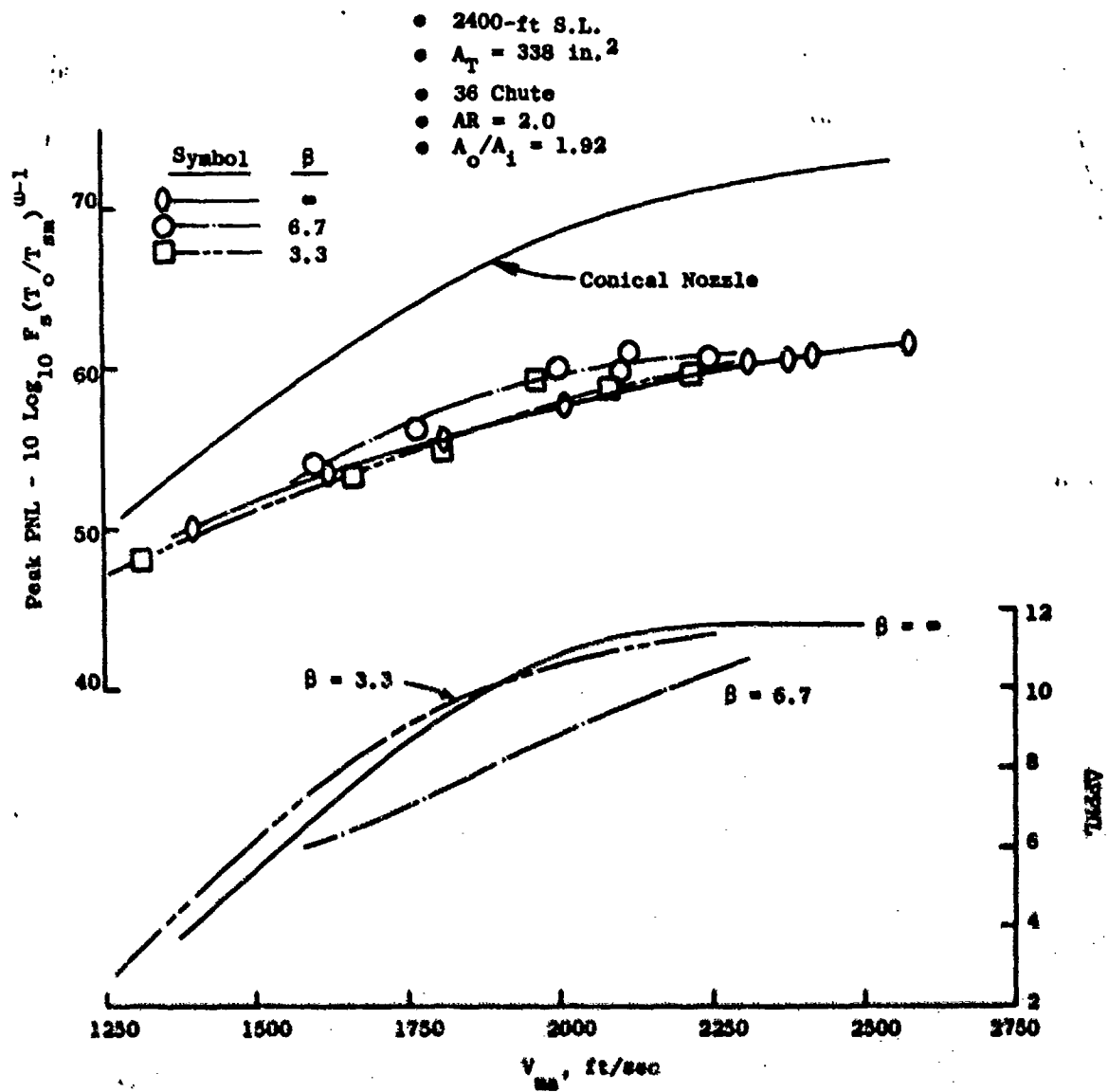


Figure 3-170. Peak PNL Variation with  $\beta$ , Model 23.

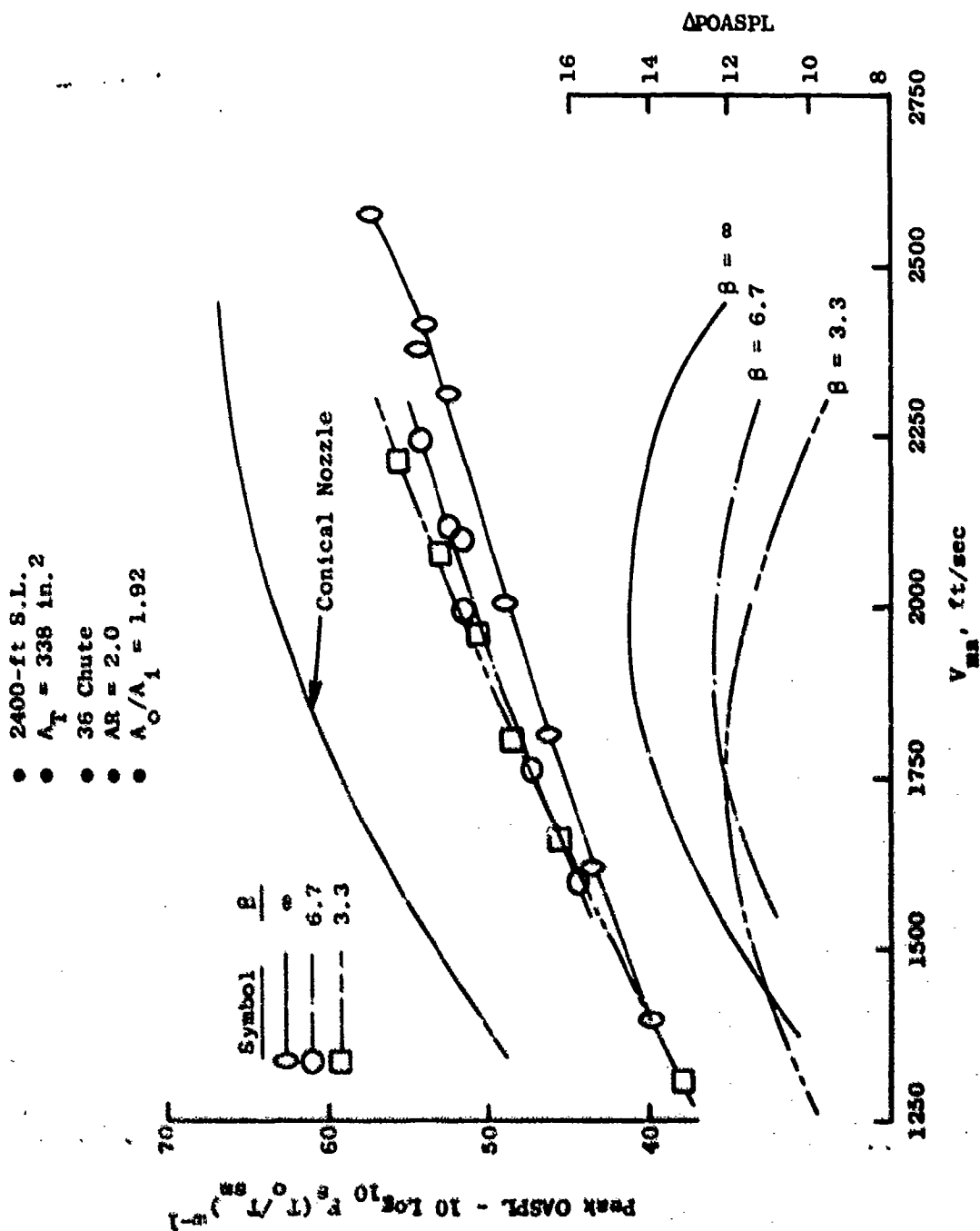


Figure 3-171. Peak OASPL Variation with  $\beta$  - Model 23.

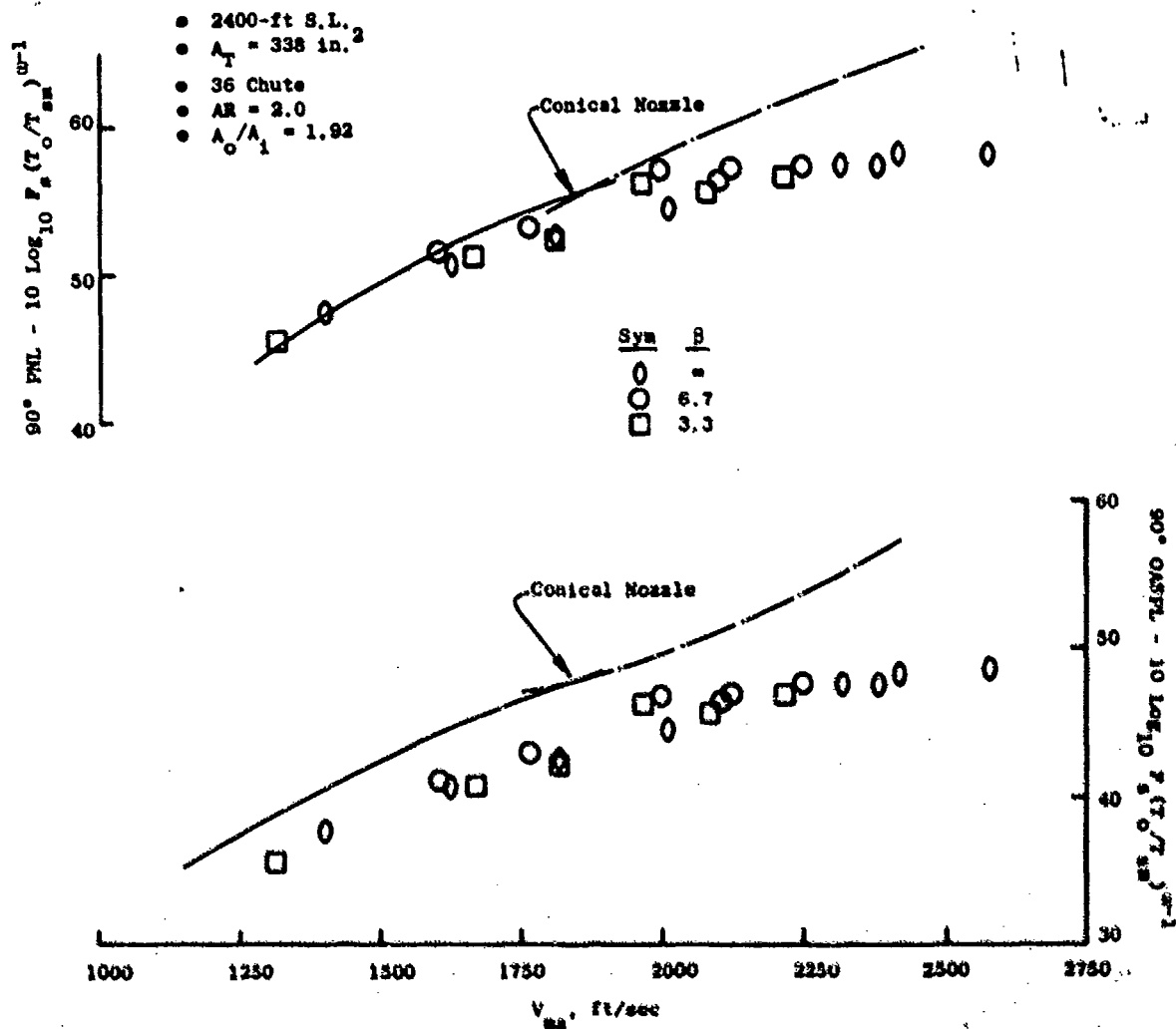


Figure 3-172.  $90^\circ$  PNL and OASPL Variation with  $\beta$ , Model 23.

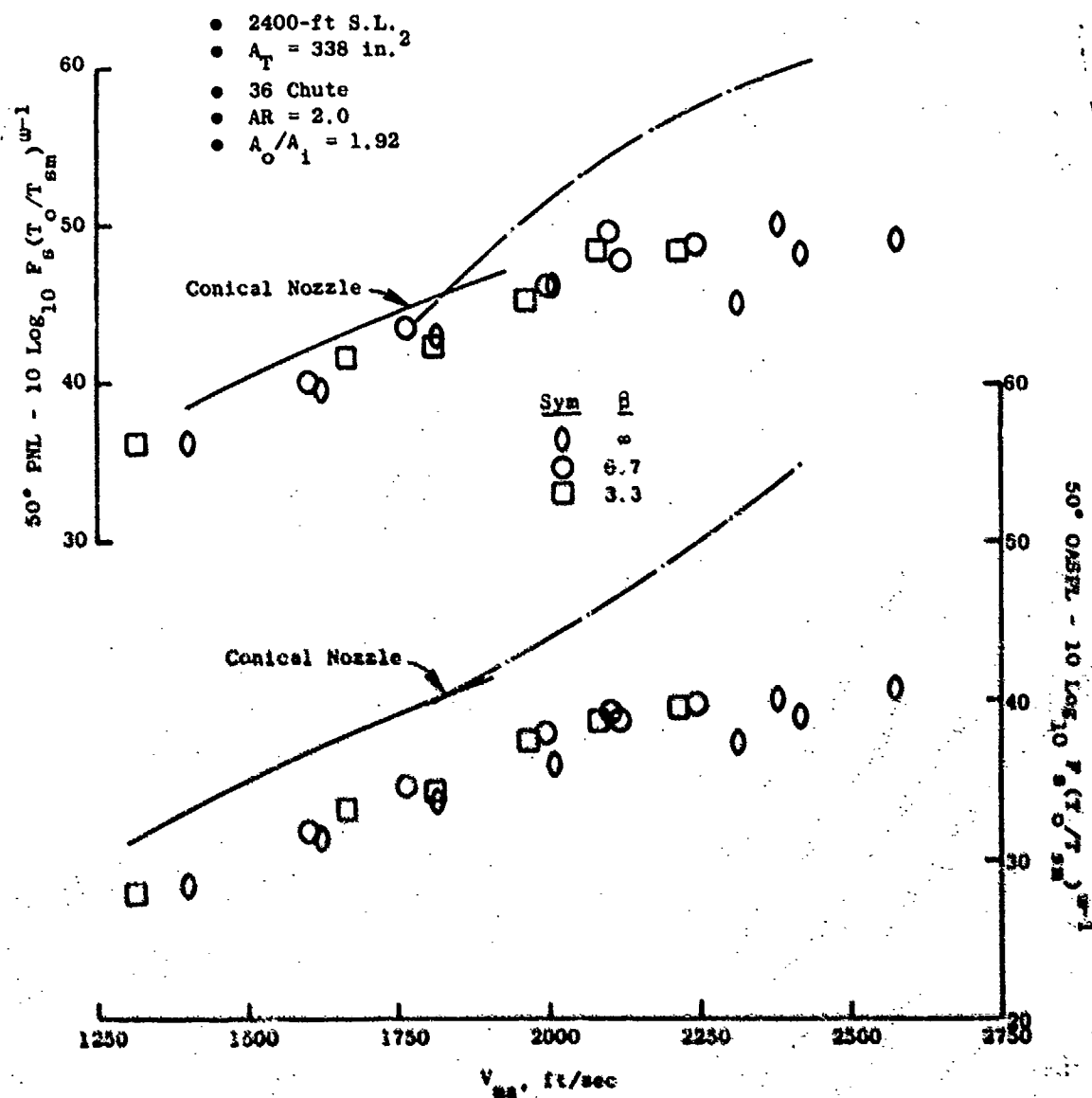


Figure 3-173.  $50^\circ$  PNL and OASPL Variation with  $\beta$ , Model 23.



ations range from 1 to 14. Therefore, flow and velocity dominance is always in the outer suppressed stream and inner stream flow and velocity are always minor on a thrust contribution basis. The resultant systematic changes in noise as  $\beta$  progress from 3.3 to 6.7 to  $\infty$  are judged to be attributable to flow interaction mechanisms rather than pure inner/outer flow dominance.

- At  $90^\circ$  the  $\beta$  influence on PNL and OASPL is almost as strong and consistent as at peak angle for the  $A_0/A_1 = 0.65$  systems, but is configuration dependent for the  $A_0/A_1 = 1.92$  systems. Little variance is seen for Model 31, whereas the  $90^\circ$  data for Model 23 still shows considerable variance, but it is not progressively systematic.
- $50^\circ$  data trends are quite similar to those at  $90^\circ$  and are configuration dependent. The  $A_0/A_1 = 0.65$  systems still exhibit distinct and progressive variance with  $\beta$  changes and the  $A_0/A_1 = 1.92$  Model 23 data again shows non-systematic variance. The Model 31 data however, show some magnitude of systematic variance, similar to that of the peak noise levels.
- Examination of the model definition table above and the detailed schematics of Appendix A shows that for Models 31 and 23, the area ratios were equivalent. However, Model 31 had a retracted inner geometry, similar to that of the  $A_0/A_1 = 0.65$  systems, and Model 23 had an in-line inner flow plug geometry. This difference may explain the variations in data seen between Models 31 and 23 and the closer match of Model 31's trends to those of the  $A_0/A_1 = 0.65$  systems.

#### System Area Ratio and Inner Stream Plug Geometry Variation - Fixed Outer Stream Suppressor Geometry

The last of the three studies supporting the impact of Flow Management/ Core Geometry considerations on noise was a controlled effort to isolate the effects of system area ratio and inner stream plug geometry. Each of these parameters was varied within the practical range for a variable cycle engine system. Six models were used, per the following chart:

Model No.	System $A_0/A_1$	Outer Stream				Inner Stream				Appendix A Figure Reference
		Element Description	AR	$\beta$	Flow Area, In. <sup>2</sup>	Step Height, In.	Plug Location	$A_1/A_2$	Flow Area, In. <sup>2</sup>	
23	1.92	36-Chute	2.0	0.716	23.76	0.70	In-Line	0.779	12.39	17
24	1.92	36-Chute	2.0	0.716	23.76	0.70	Retracted	0.779	12.39	18
25	1.61	36-Chute	2.0	0.716	23.76	0.25	In-Line	0.69	6.58	19
26	1.61	36-Chute	2.0	0.716	23.76	0.25	Retracted	0.69	6.58	20
28	1.92	36-Spoke	2.0	0.716	23.76	0.70	Retracted	0.779	12.39	22
29	1.92	36-Spoke	2.0	0.716	23.76	0.70	In-Line	0.779	12.39	23

Photos of Models 23 through 26 are included in Figure 3-174. Figure 3-175 shows Models 28 and 29. The last column of the above chart refers to the detailed sketches of each model shown in Appendix A.

Variations of system area ratio and inner stream plug geometry were accomplished by using interchangeable modular inner stream hardware, schematically shown in Figure 3-176. An inner stream plug, allowing 0.70" annulus height (schematics a and b), resulted in an inner flow area of 12.39 in.<sup>2</sup>. This, combined with the outer flow area of 23.76 in.<sup>2</sup>, effected an  $A_0/A_1$  of 1.92. Using the 0.35" annulus height inner stream plug changed the inner flow area to 6.58 in.<sup>2</sup> and the  $A_0/A_1$  to 3.61 (schematics c and d). In-Line inner stream plug geometry (schematics a and c) was altered to retracted, (schematics b and d) through removal of a support spacer.

As shown in the above table, two basic annular suppressors were used (36-chute and 36-spoke), each of  $AR = 2.0$  and  $R_0 = 0.716$ . Within model sets 23/25 and 24/26, system area ratio,  $A_0/A_1$ , varied from 1.92 to 3.61. The first set utilized an in-line plug, and the second set utilized a retracted plug geometry. Comparisons for inner stream geometry variations were made using model sets 23/24, 25/26 and 28/29 (the first and second sets with the 36-chute suppressor at  $A_0/A_1 = 1.92$  and 3.61, respectively, and the third set with the 36-spoke suppressor of  $A_0/A_1 = 1.92$ ).

The six models were tested in the Cell 41 Anechoic Facility per the matrix of Section 3.2.1, Figure 3-10 and Table 3-3, utilizing the cycle lines of:

- $W_1 = 15$  and 30%  $W_0$
- DBTF/Inverted Dual Flow
- AST/VCE

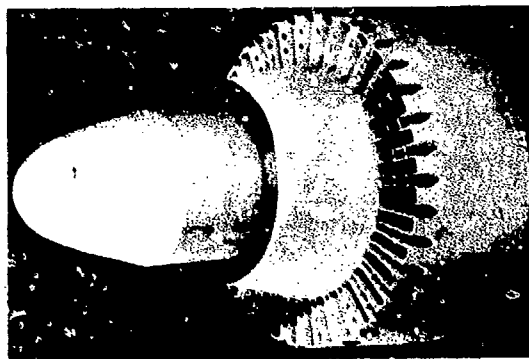
Data in terms of peak, 90° and 50° (PNL and OASPL) are presented in the following figures, normalized per Section 3.3.1.7 and plotted versus  $V_{max}$ :

Model	$W_1 = 15\% W_0$	$W_1 = 30\% W_0$	DBTF/Inv. Dual Flow
23, 24, 25 & 26	3-177 to 3-180	3-181 to 3-184	3-185 to 3-188
28 and 29			3-189 to 3-191

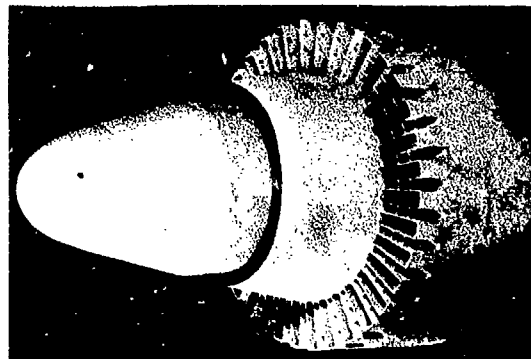
Comparing the model sets for system area ratio variation (Models 23/25 and 24/26), the following observations are noted:

- Peak PNL for all three data cycle sets indicate that  $A_0/A_1 = 3.61$  is universally the better suppressor system, because a greater proportion of flow is passed through the segmented annular suppressor. Differences between Models 24 and 26, with retracted

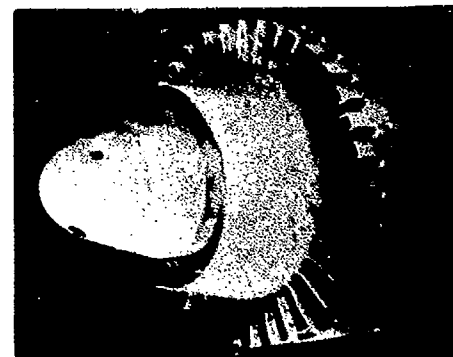
- 36 Chute
- Area Ratio = 2.0
- Radius Ratio = 0.716



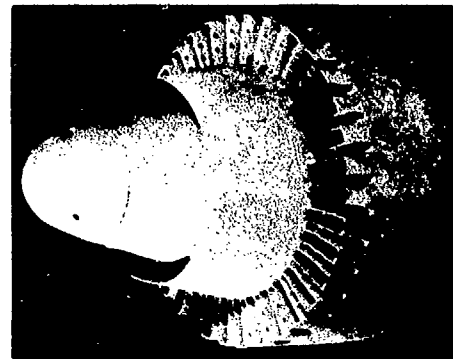
Model 23  
In-Line Inner Plug  
with 0.7-in. Step  
 $A_o/A_i = 1.92$



Model 25  
In-Line Inner Plug  
with 0.35-in. Step  
 $A_o/A_i = 3.61$



Model 24  
Retracted Inner Plug  
with 0.7-in. Step  
 $A_o/A_i = 1.92$



Model 26  
Retracted Inner Plug  
with 0.35-in. Step  
 $A_o/A_i = 3.61$

Figure 3-174. Dual Flow Models 23, 24, 25, and 26 for  $A_o/A_i$  and Inner Plug Geometry Variation.

- 36 Spoke
- Area Ratio = 2.0
- Radius Ratio = 0.716
- $A_0/A_1 = 1.92$

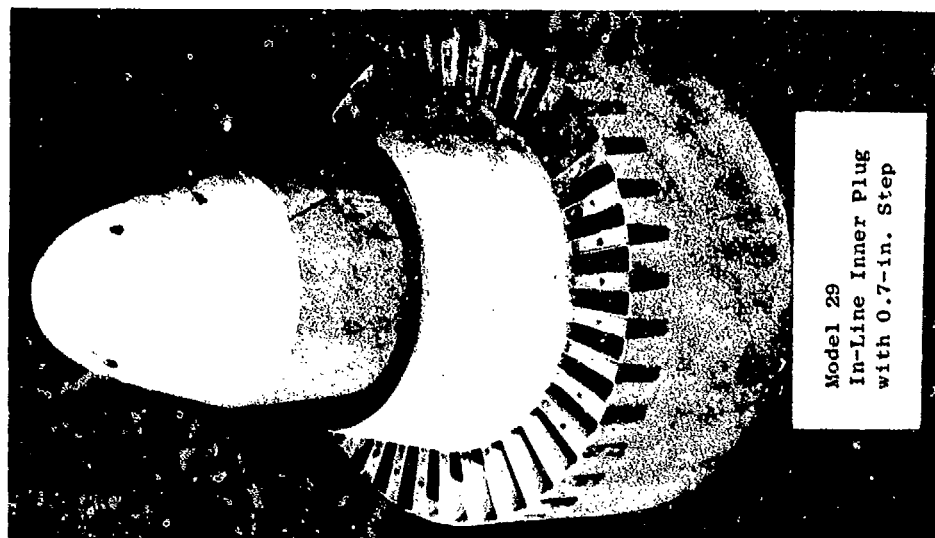
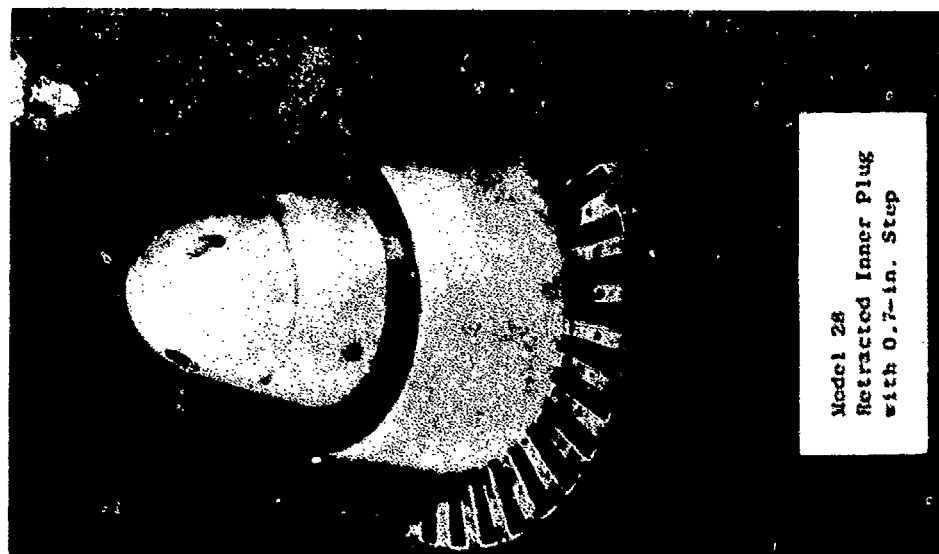


Figure 3-175. Dual Flow Models 28 and 29 for  $A_0/A_1$  and Inner Plug Geometry Variation.

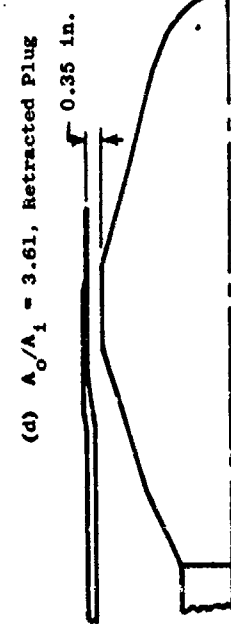
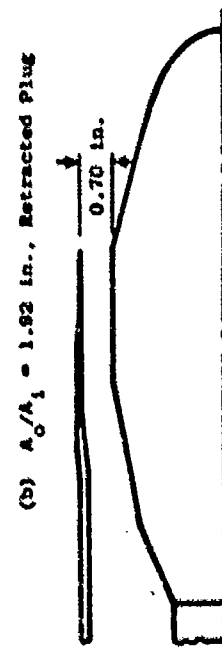
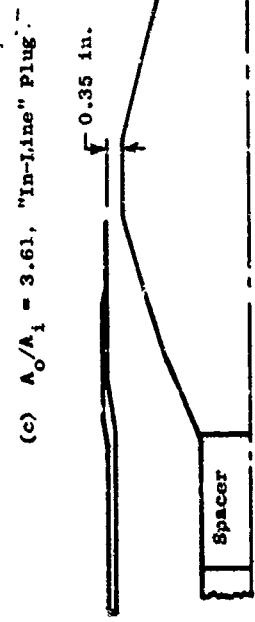
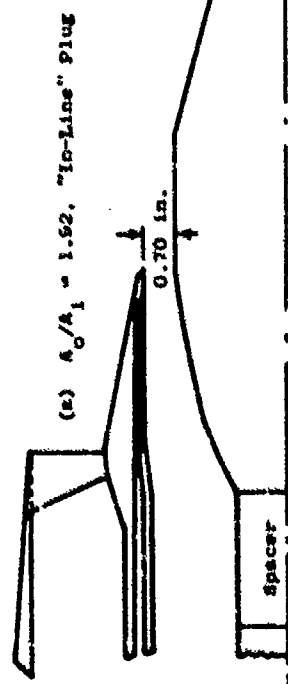


Figure 3-176. Schematic of Inner Plug Geometry Variations.

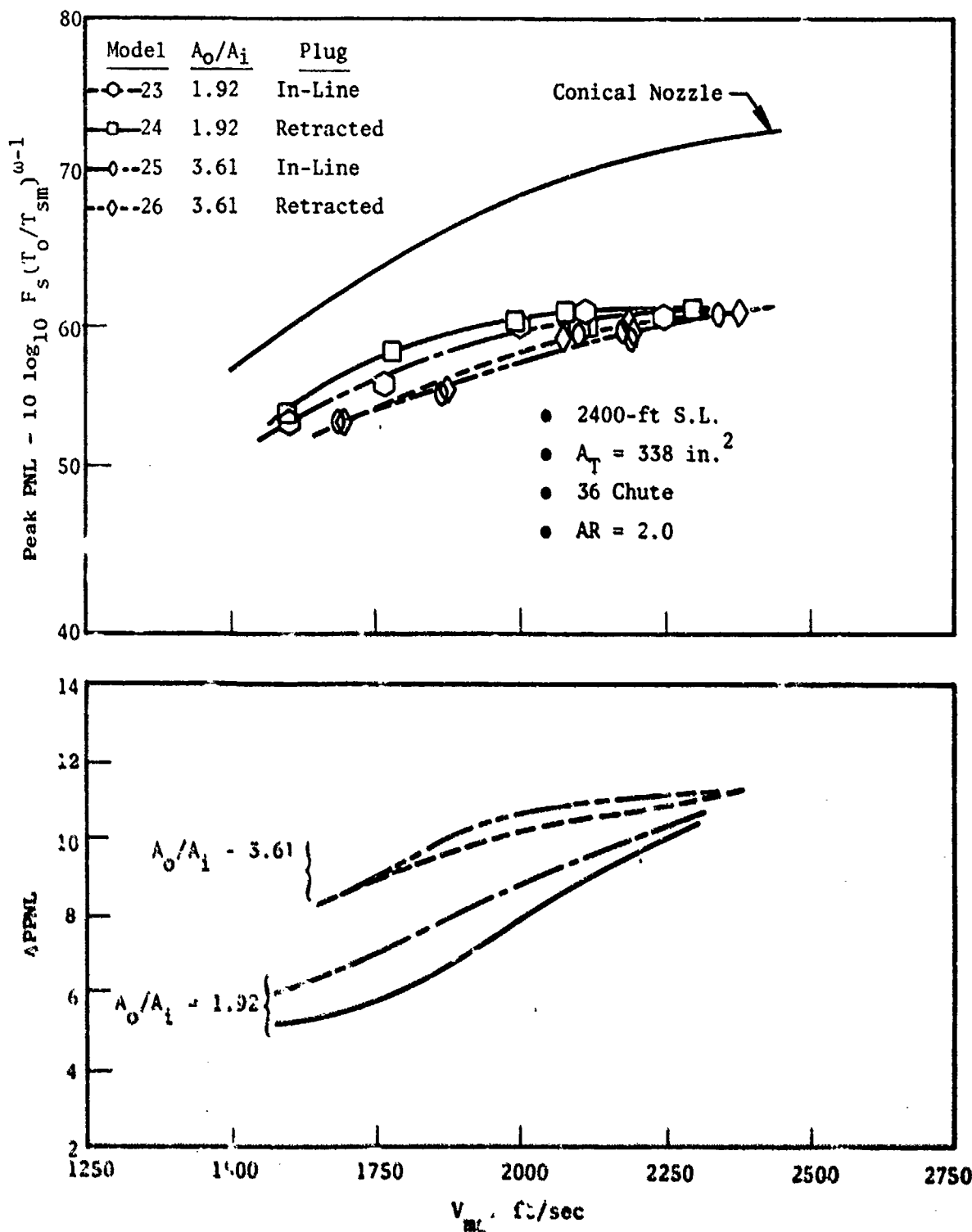


Figure 3-177. Peak PNL Variation with  $A_o/A_i$  and Inner Plug Geometry, Models 23 - 26,  $W_{Inner} = 15\% W_{Outer}$  Cycle.

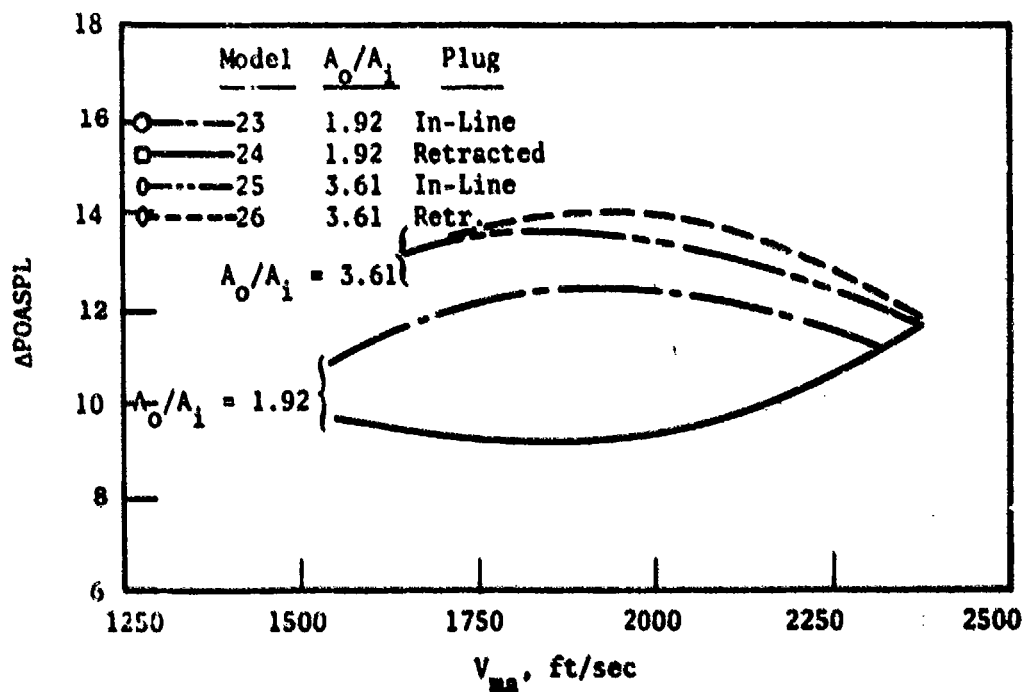
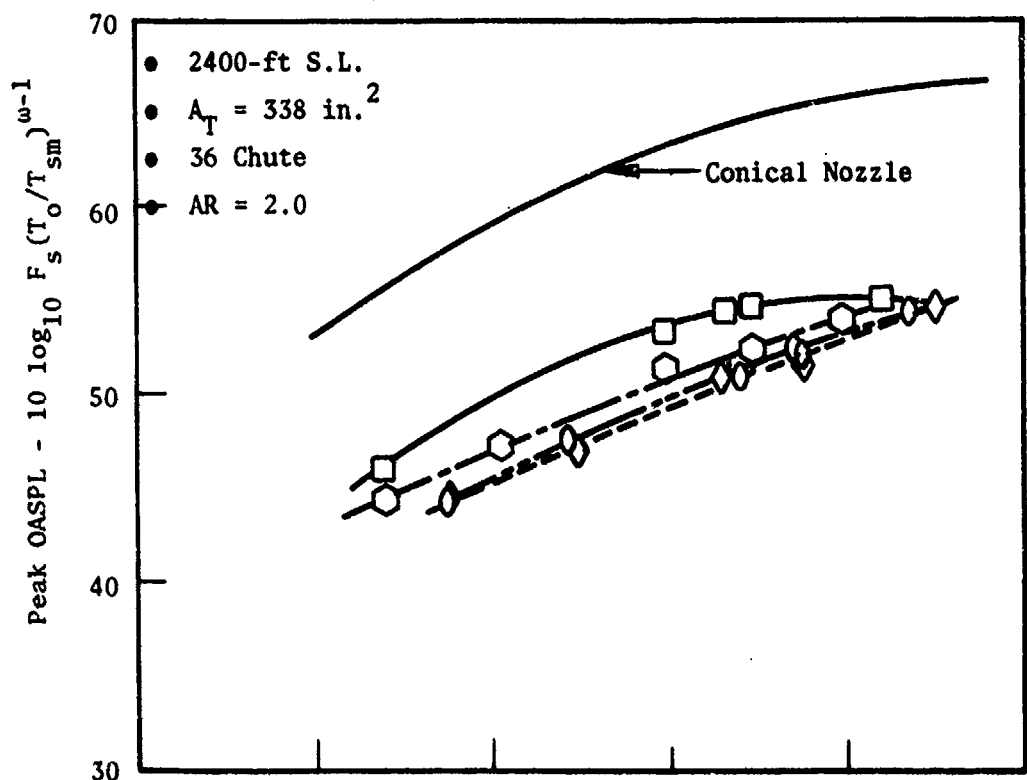


Figure 3-178. Peak OASPL Variation with  $A_o/A_i$  and Inner Plug Geometry, Models 23 - 26,  $W_{Inner} = 15\% W_{Outer}$  Cycle.

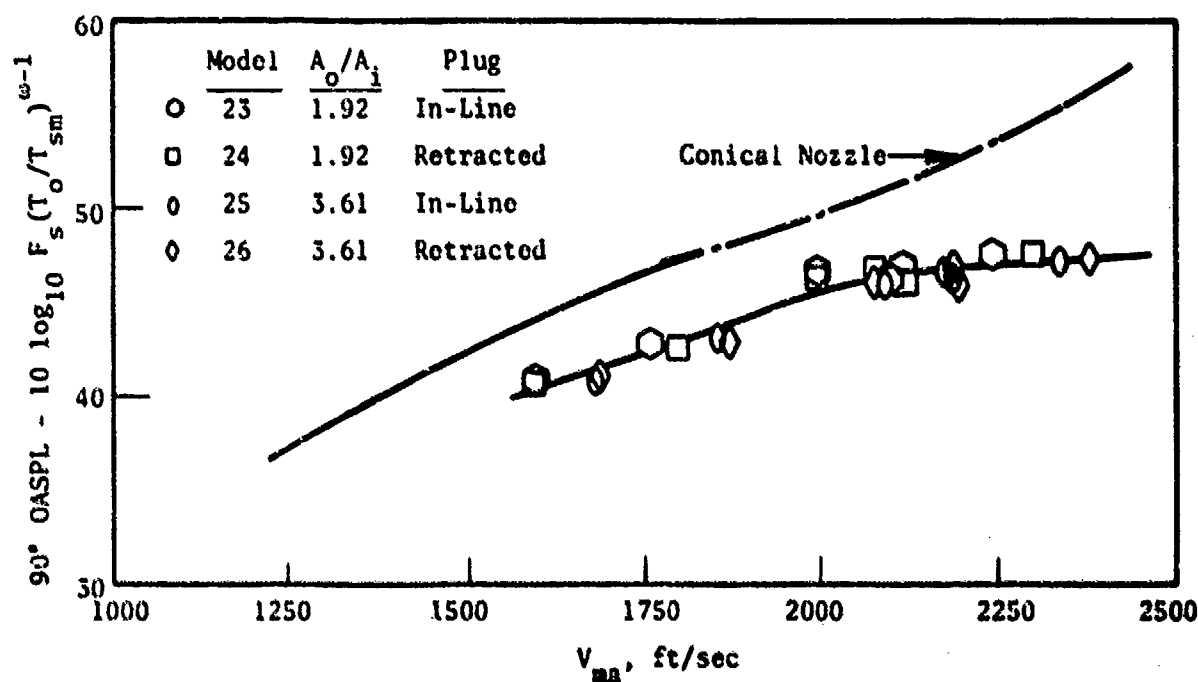
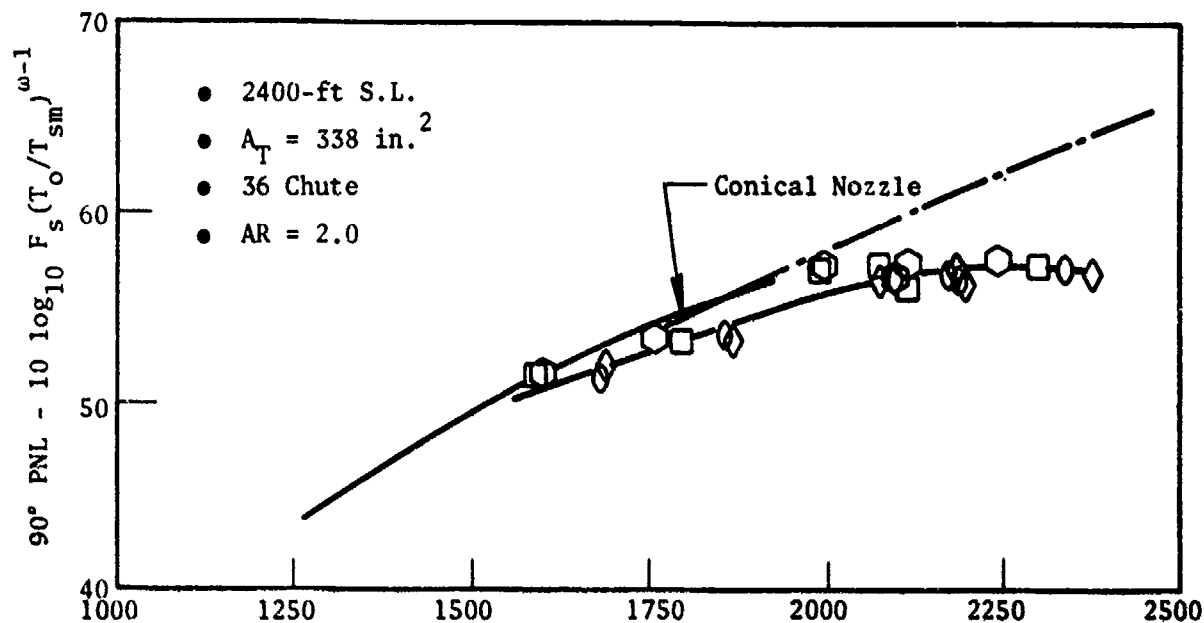


Figure 3-179. 90° PNL and OASPL Variation with  $A_o/A_i$  and Inner Plug Geometry, Models 23 - 26,  $N_{Inner} = 16\% N_{Outer}$  Cycle.



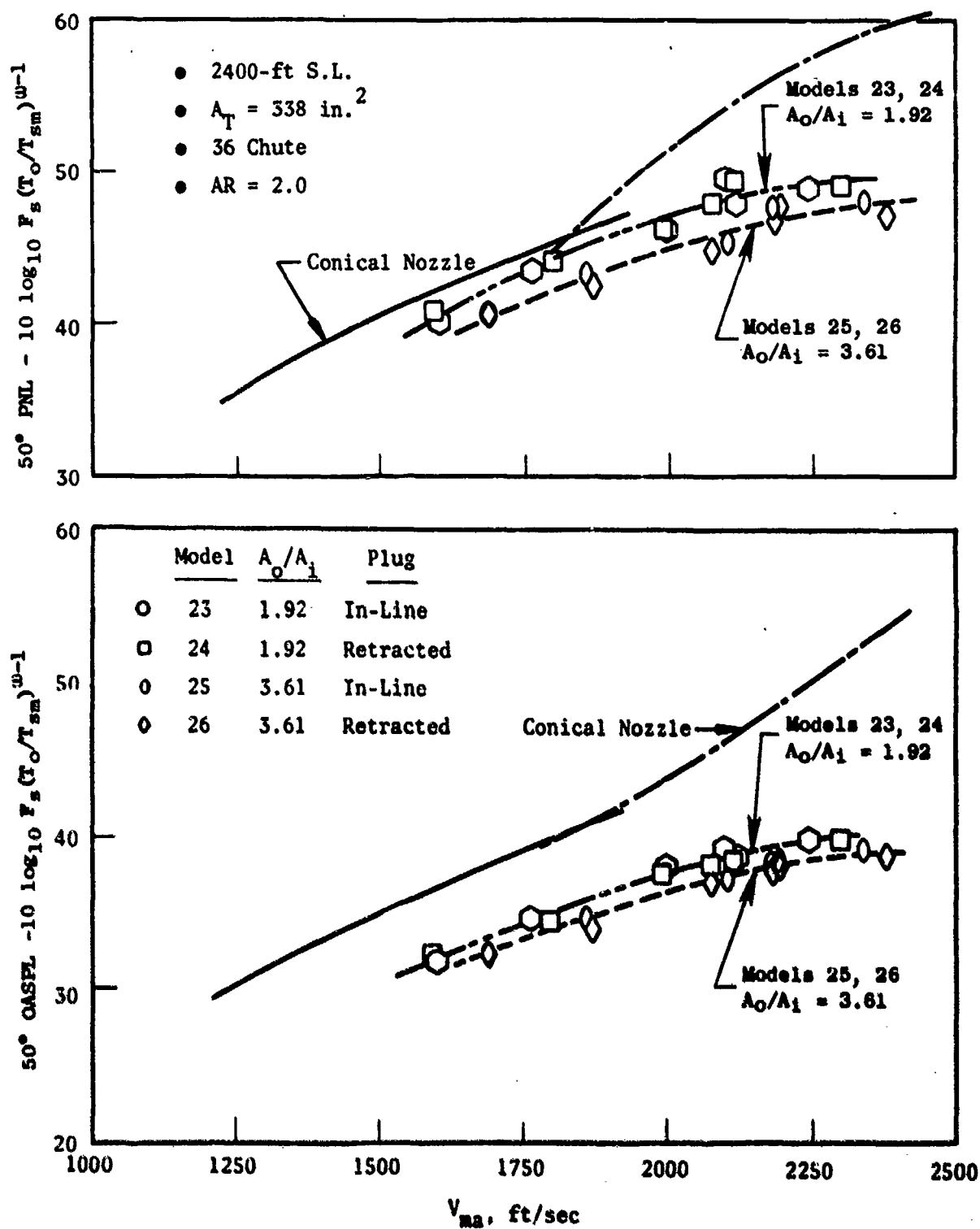


Figure 3-180.  $50^\circ$  PNL and OASPL Variation with  $A_0/A_1$  and Inner Plug Geometry, Models 23 - 26,  $W_{\text{Inner}} = 15\% W_{\text{Outer}}$  Cycle.

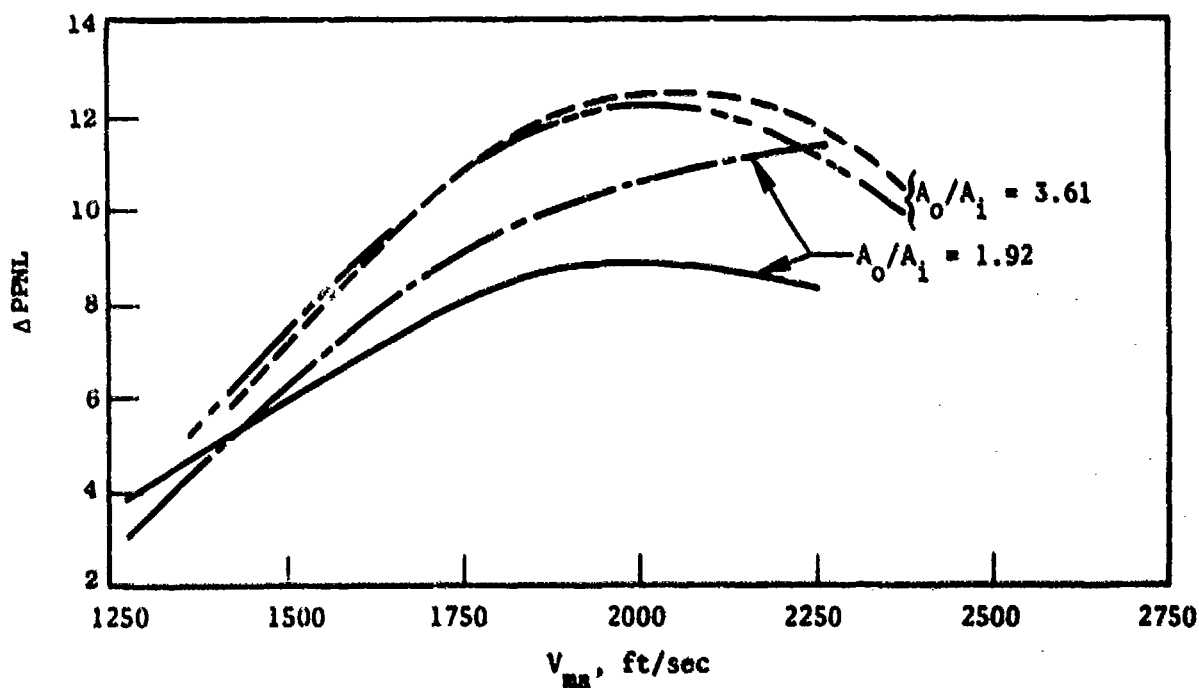
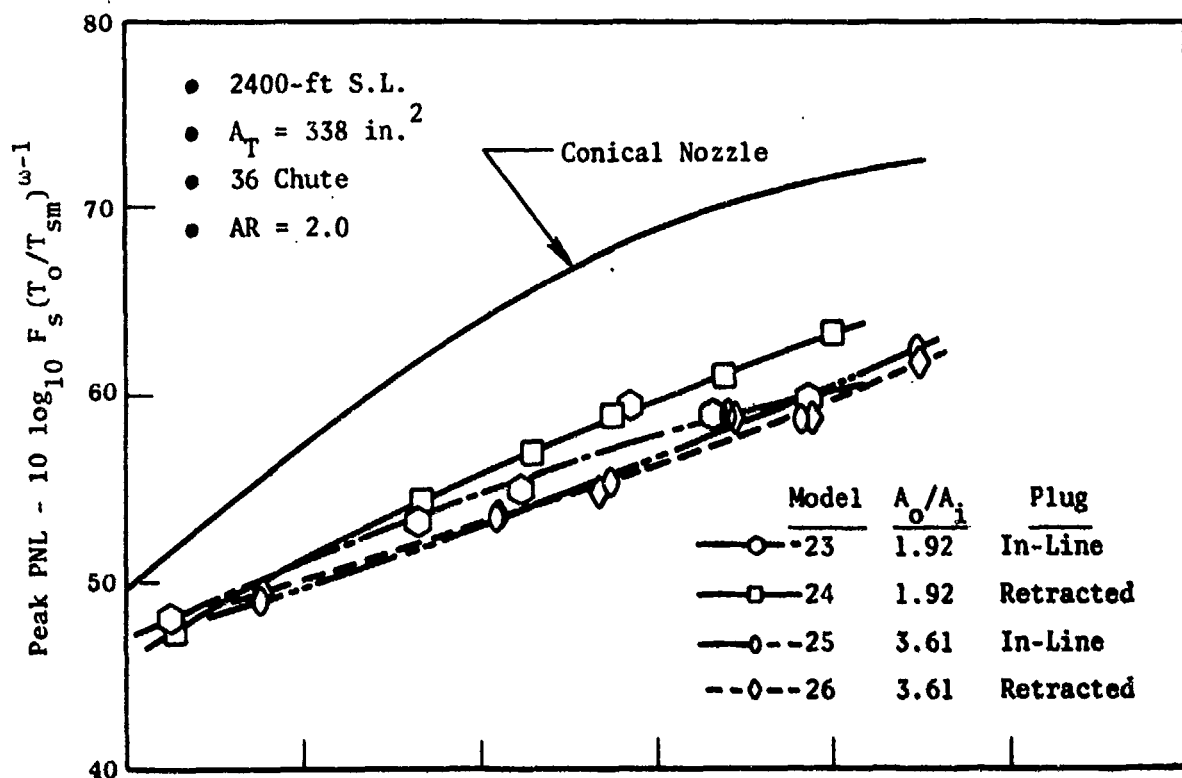


Figure 3-181. Peak PNL Variation with  $A_o/A_i$  and Inner Plug Geometry, Models 23 - 26,  $W_{\text{Inner}} = 30\% W_{\text{Outer}}$  Cycle.

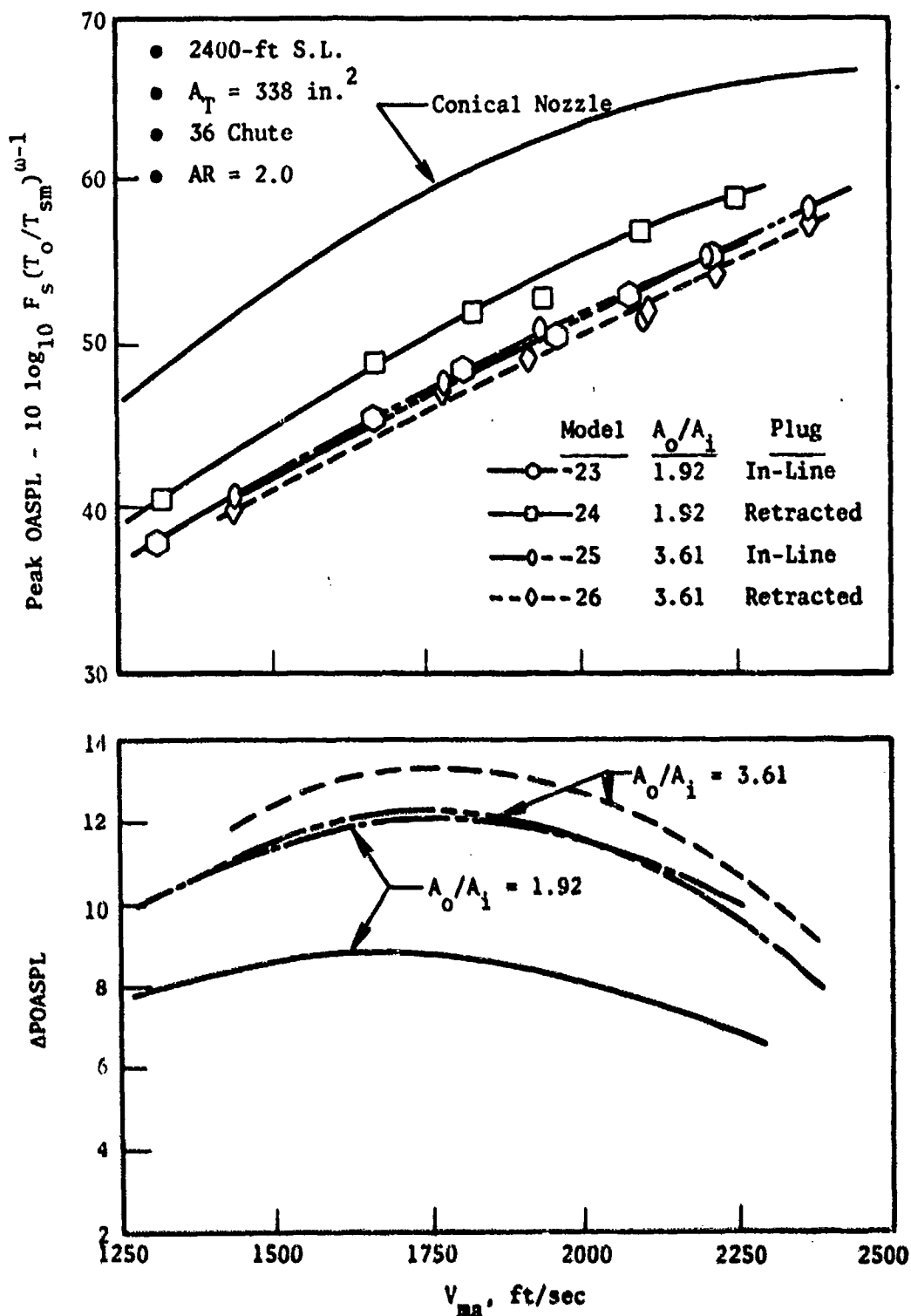


Figure 3-182. Peak OASPL Variation with  $A_o/A_i$  and Inner Plug Geometry, Models 23 - 26, Winner = 30% Wouter Cycle.

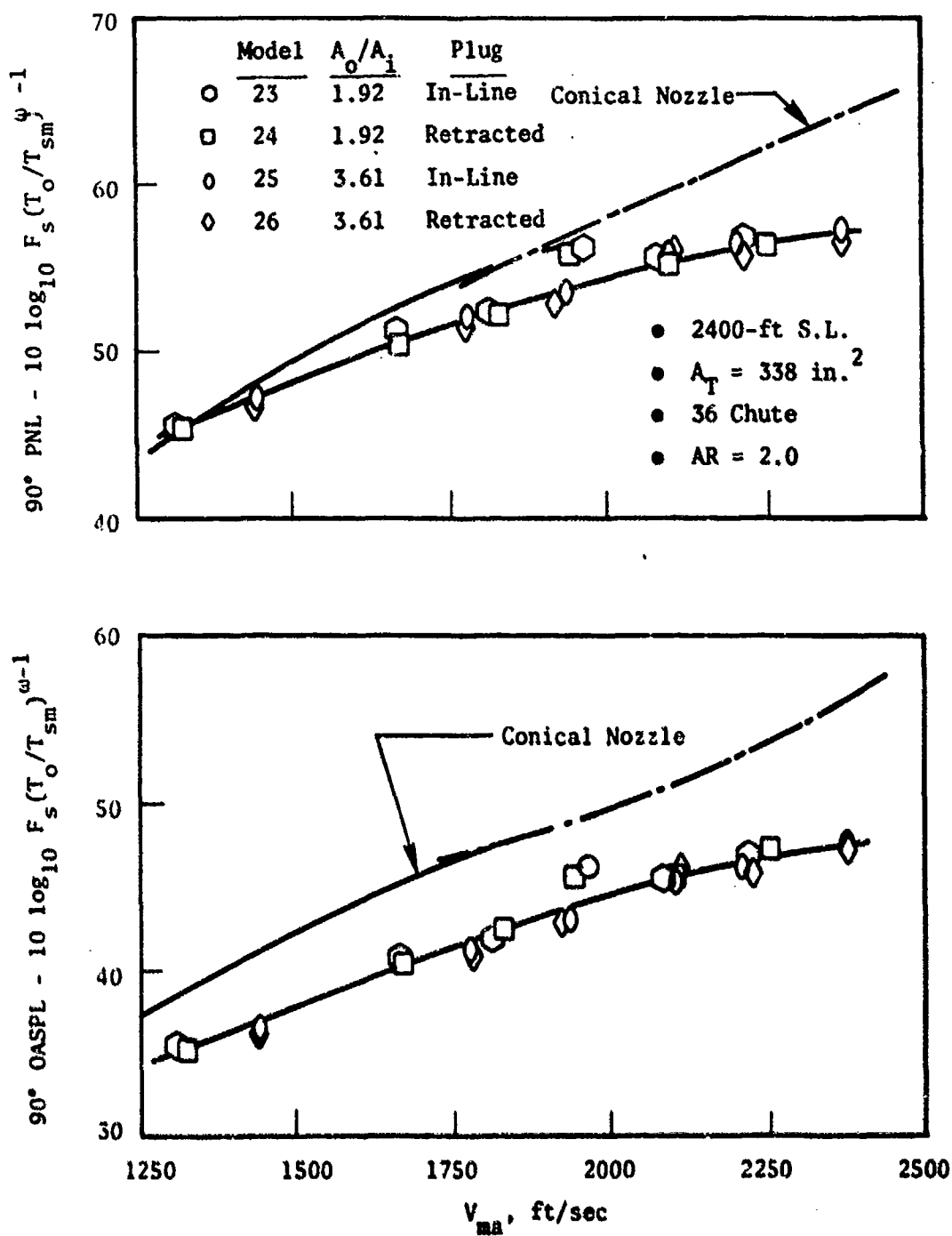


Figure 3-183. 90° PNL and QASPL Variation with  $A_o/A_i$  and Inner Plug Geometry, Models 23 - 26,  $W_{Inner} = 30\% W_{Outer}$  Cycle.

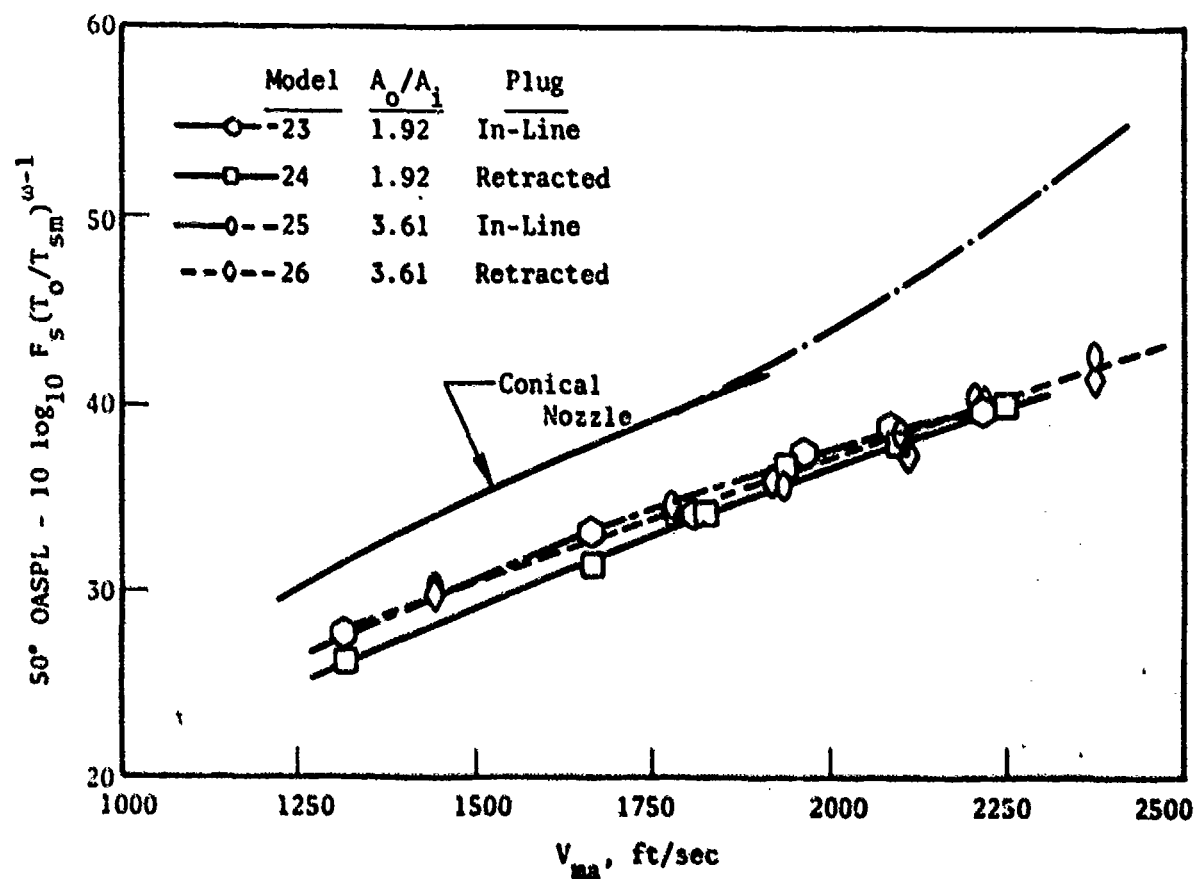
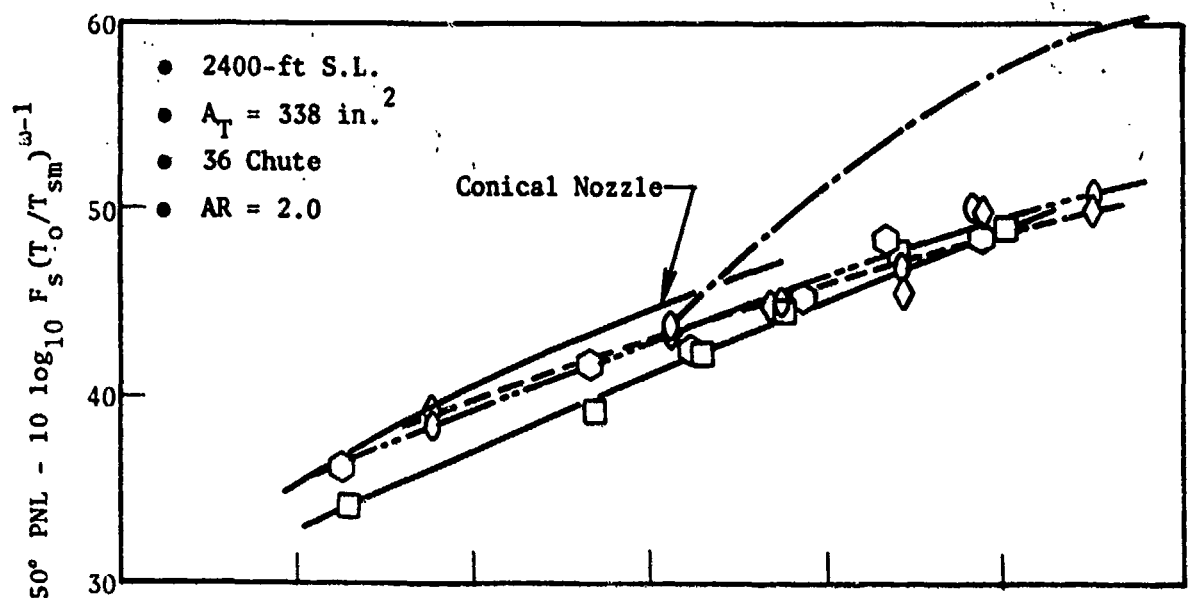


Figure 3-184.  $50^\circ$  PNL and OASPL Variation with  $A_o/A_i$  and Inner Plug Geometry, Models 23 - 26,  $W_{Inner} = 0.30 W_{Outer}$  Cycle.

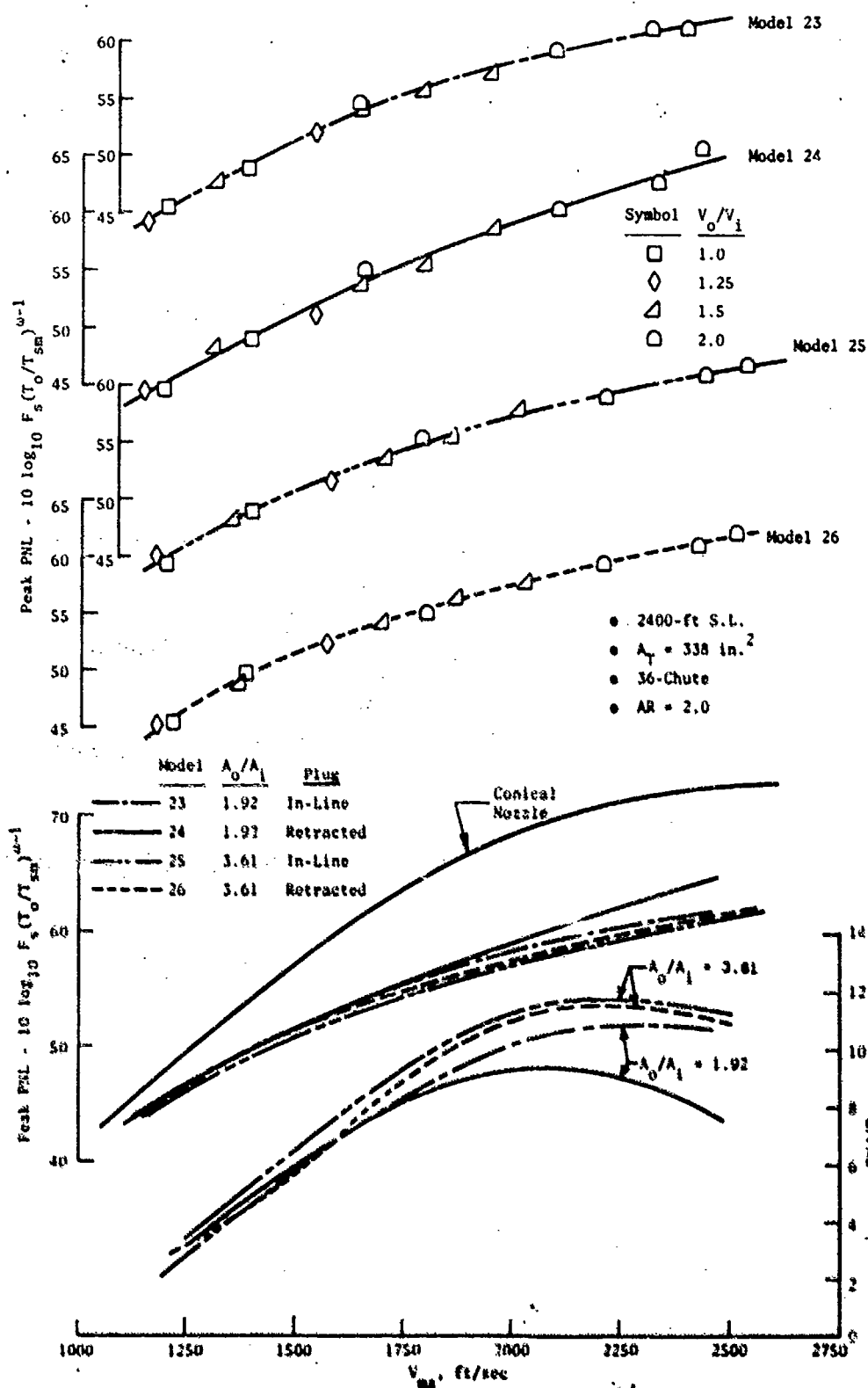


Figure 3-185. Peak PNL Variation with  $A_0/A_1$  and Inner Plug Geometry, Models 23-26, DBT/Inverted Dual Flow Cycle.

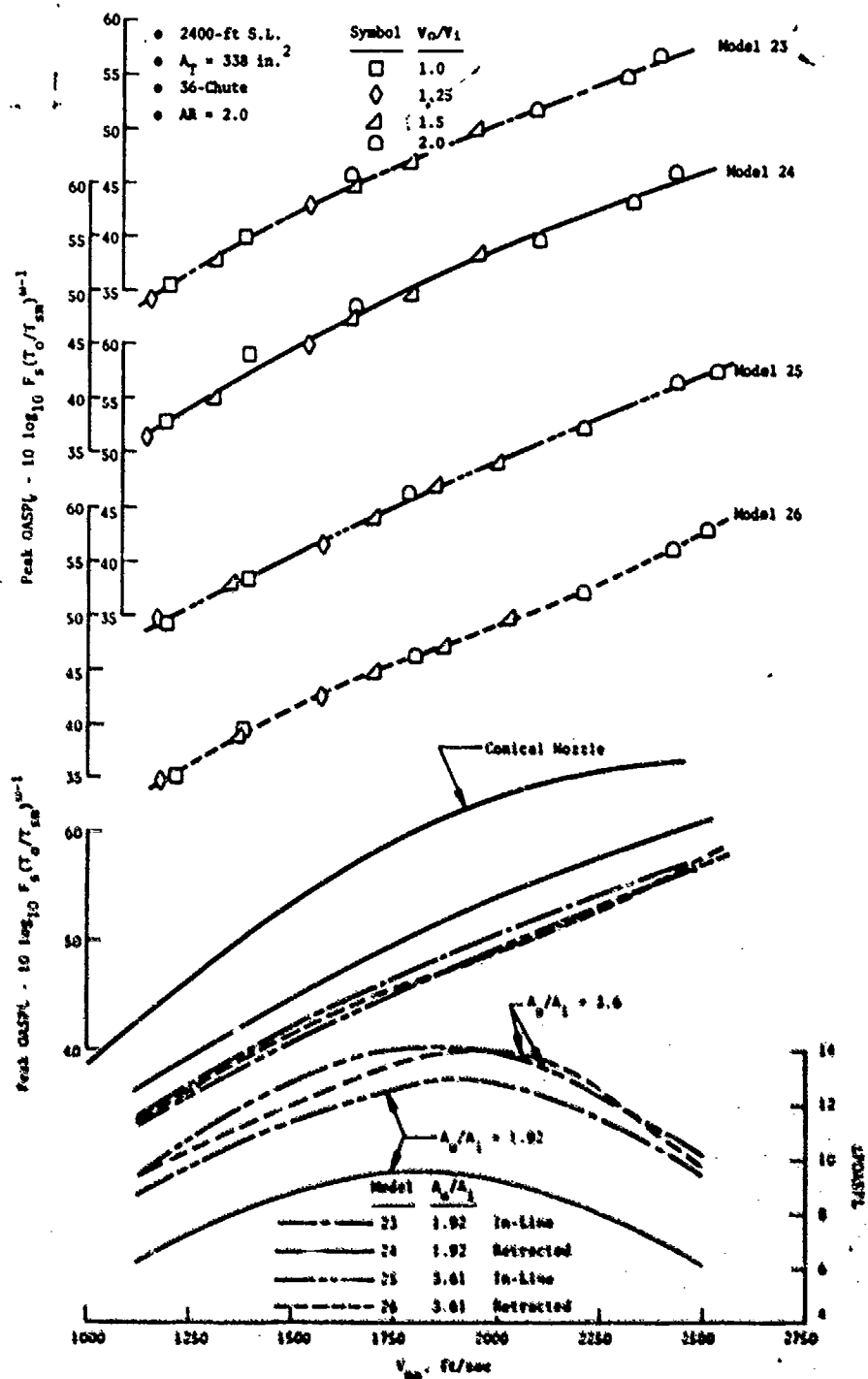


Figure 3-186. Peak OASPL Variation with  $A_0/A_1$  and Inner Plug Geometry, Models 23-26, DBF/Inverted Dual Flow Cycle.

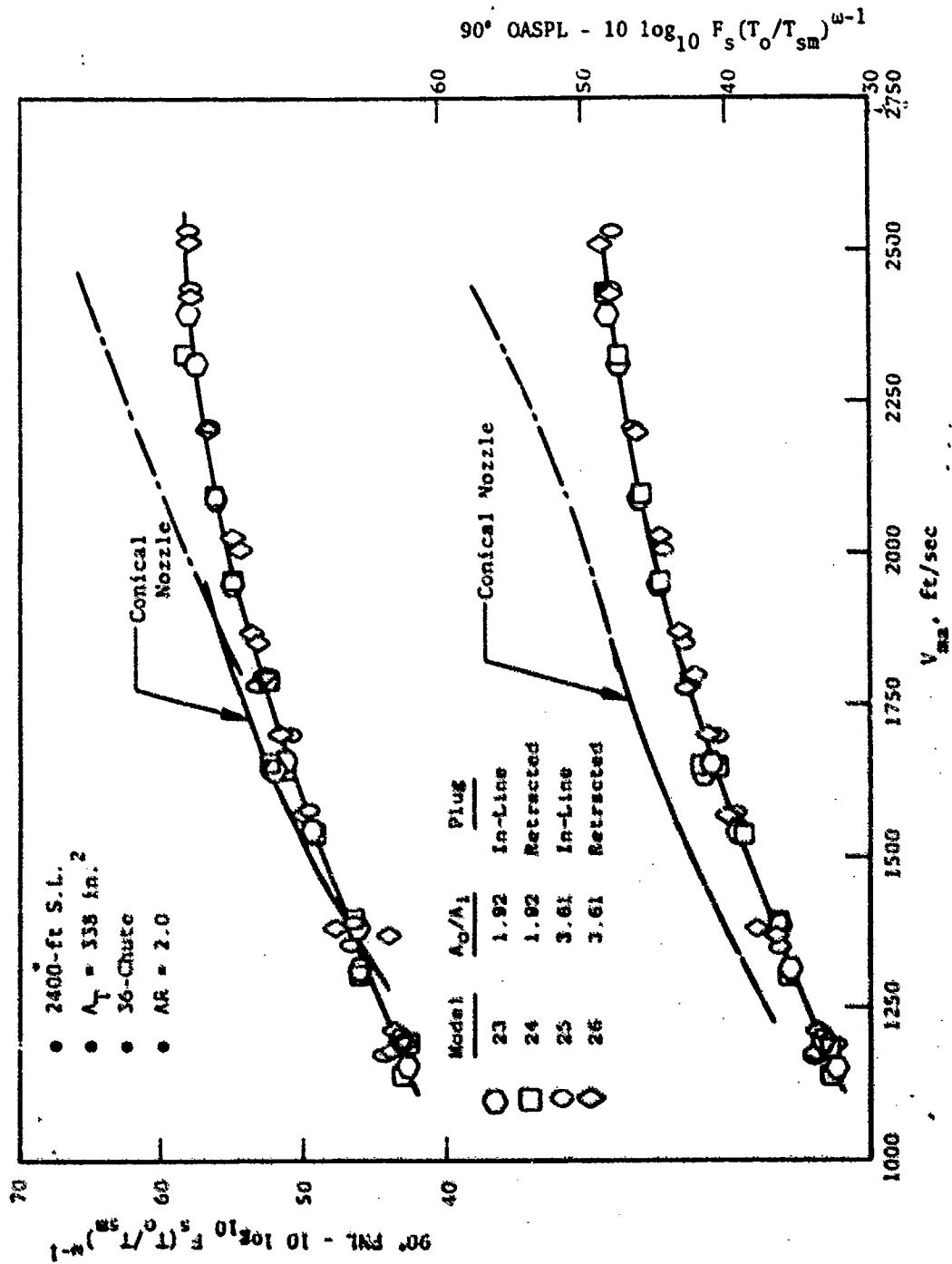


Figure 3-187. 90° FNL and OASPL Variation with  $A_0/A_1$  and Inner Plug Geometry, Models 23-26, DBFF/Inverted Dual Flow Cycle.



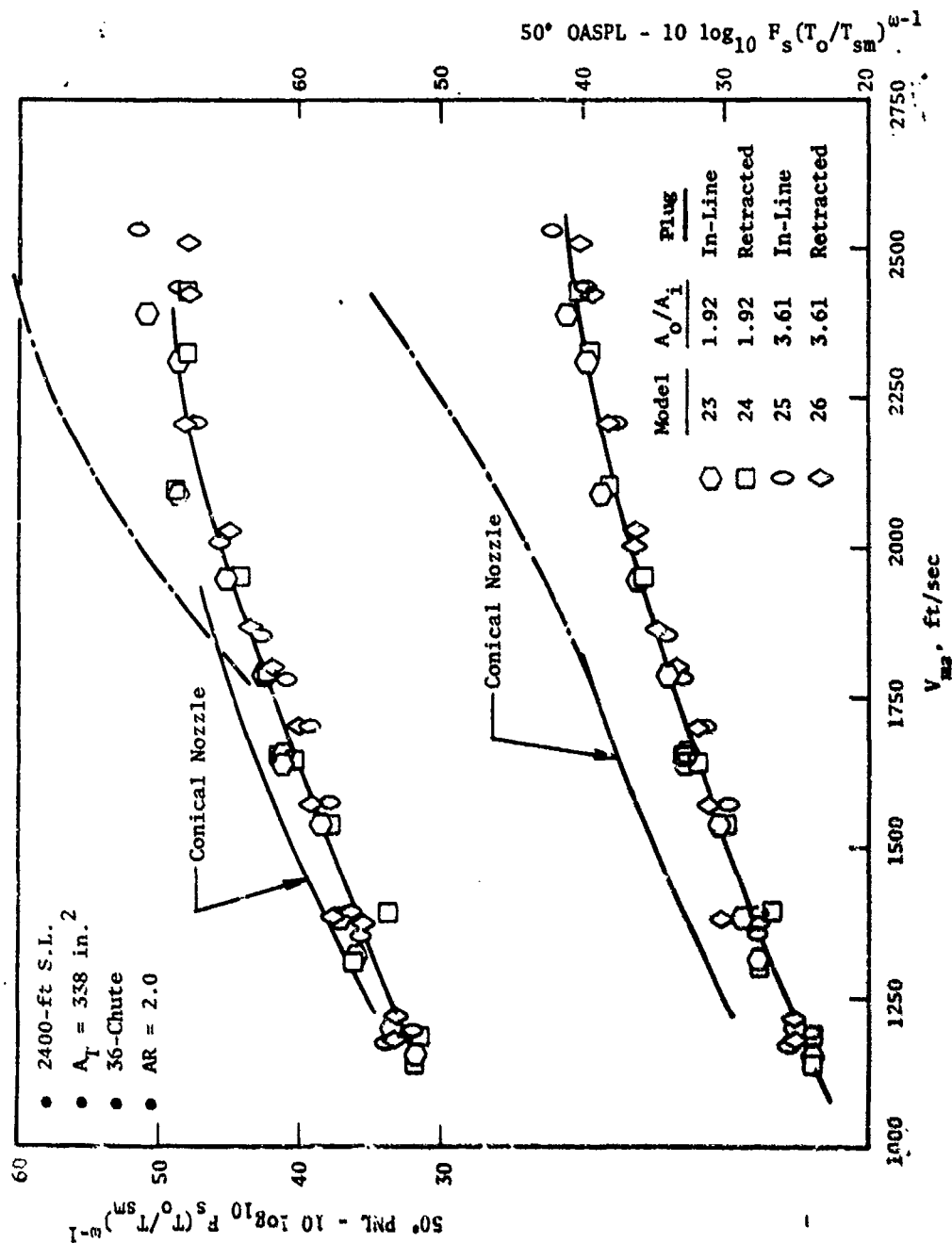


Figure 3-188. 50° PNL and OASPL Variation with  $A_o/A_i$  and Inner Plug Geometry, Models 23-26, DBTF/Inverted Dual Flow Cycle.

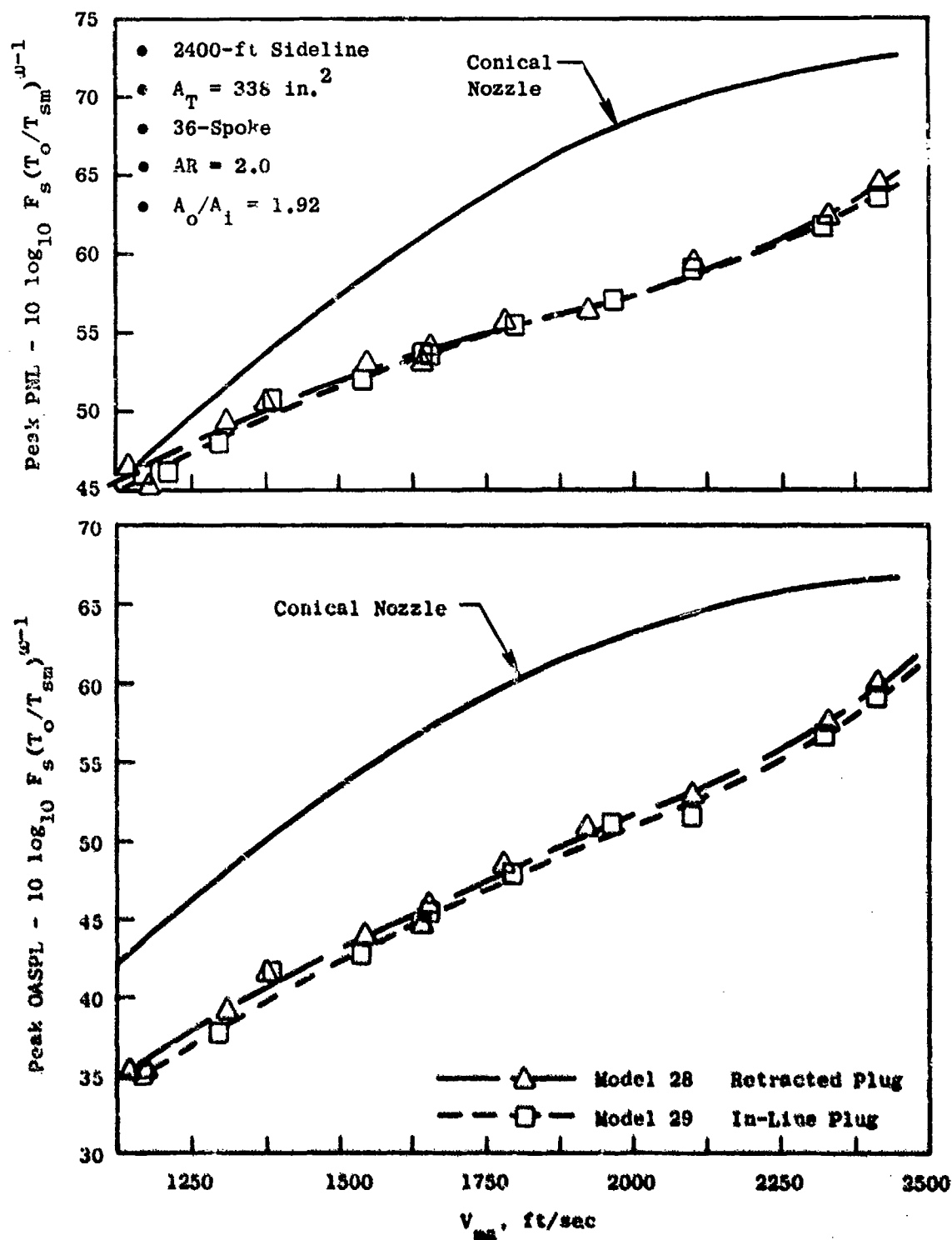


Figure 3-189. Peak PNL and OASPL Variation with Inner Plug Geometry, Models 28 and 29, DBTF/Inverted Dual Flow Nozzle.

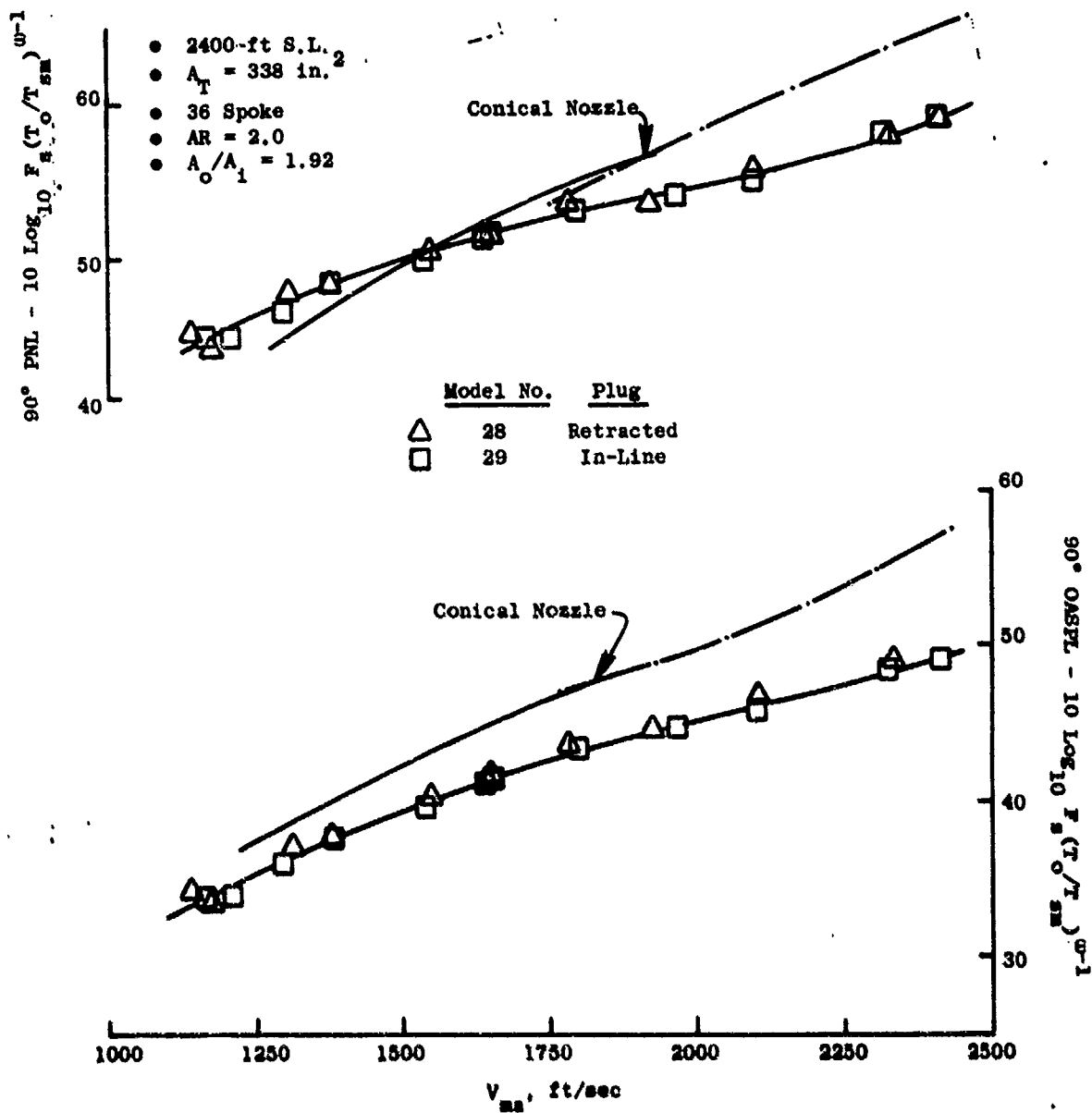


Figure 3-190. 90° FNL and OASPL Variation with Inner Plug Geometry, Models 28 and 29, DBTF/Inverted Dual Flow Cycle.

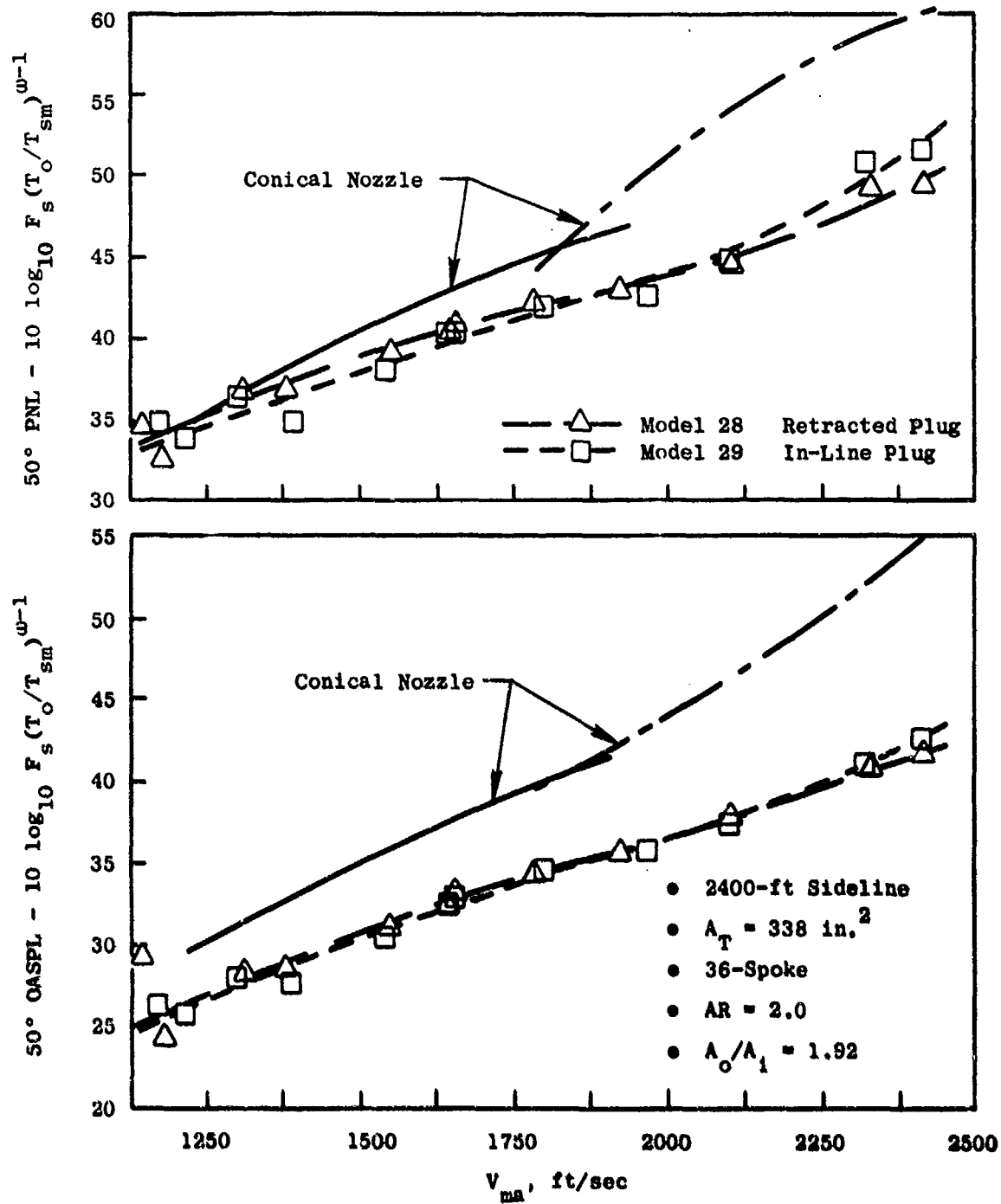


Figure 3-191. 50° PNL and QASPL Variation with Inner Plug Geometry, Models 28 and 29, DBTF/Inverted Dual Flow Cycle.

inner stream geometry, represent up to 3.5 dB greater suppression for higher area ratio at  $\approx 2000$  ft/sec  $V_{ma}$ . Differences between Models 23 to 25, with in-line plug geometry, however, are not as uniform in trend or magnitude.

- On the peak OASPL basis, trends similar to the peak PNL data are observed, with the higher  $A_0/A_1 = 3.61$  (Models 25 and 26) consistently exhibiting greater suppression than the  $A_0/A_1 = 1.92$  (Models 23 and 24). Model 26 shows up to  $\approx 5$   $\Delta$ dB greater suppression than Model 24 at mid- $V_{ma}$  range, but again, Models 23 and 25 show much less variance.
- At  $90^\circ$ , on all three cycle lines, all four models have similar noise levels (no distinction observable for system area ratio change on either a PNL or OASPL basis).
- Results at  $50^\circ$  are generally similar to the  $90^\circ$  data, with no predominant distinction between models. The  $W_1 = 15\% W_0$  cycle data is an exception, where separate data-fitted-curves can be drawn through the aggregate of  $A_0/A_1 = 1.92$  and  $3.61$  data sets. This indicates  $\approx 1$   $\Delta$ OASPL and  $\approx 2$   $\Delta$ PNL greater suppression for the higher area ratio.

In comparing model sets for change in core geometry from in-line to retracted at fixed  $A_0/A_1$  (Model sets 23/24, 25/26 and 28/29) the following observations are noted:

- Model set 25/26 on all three cycle lines (Figures 3-177, 3-181 and 3-185), and Model set 28/29 on the DBTF/Inverted Dual Flow cycle line (Figure 3-189), show no significant difference in peak PNL noise levels with change in inner stream geometry, at any  $V_{ma}$  tested. These model sets are of  $A_0/A_1 = 3.61$  and  $1.92$ , respectively. Model set 23/24, of in-line and retracted geometries, respectively, do show some variance, particularly at higher  $V_{ma}$ ; the in-line geometry indicates somewhat greater suppression potential.
- Models 28 and 29 (Figure 3-189) show no pronounced difference in levels on a peak OASPL basis. Models 25 and 26 (Figures 3-178, 3-182 and 3-186) are basically equivalent except for  $\approx 0.5$  to  $0.8$   $\Delta$ dB greater suppression for the retracted position on the  $W_1 = 30\% W_0$  cycle line. Models 23 and 24 (Figures 3-178, 3-182 and 3-186) again show variance favoring the in-line geometry on each of the cycle lines tested.
- For  $90^\circ$  data, (Figures 3-179, 3-183, 3-187 and 3-190) for all model comparisons on all cycle lines, no distinction is seen between in-line and retracted core geometries.
- $50^\circ$  PNL and OASPL (Figures 3-180, 3-184, 3-188 and 3-191) show no inner flow geometry preference except for the  $W_1 = 30\% W_0$  cycle

line where the Model 24 retracted inner stream plug shows  $\approx 1$   $\Delta$ OASPL and up to  $\approx 2$   $\Delta$ PNL greater suppression at low  $V_{ma}$  than the Model 23 in-line plug.

For the impact of system area ratio and inner stream geometry changes on PNL/OASPL directivity and spectra, the following representative data are included for Models 23, 24, 25 and 26, from the  $W_i = 30\% W_o$  cycle line:

- Figures 3-192 and 3-193,  $V_{ma} = 2300$  ft/sec
- Figures 3-194 and 3-195,  $V_{ma} = 1875$  ft/sec
- Figures 3-196 and 3-197,  $V_{ma} = 1380$  ft/sec

#### Summary-Flow Management and Inner Stream Geometry Studies

Flow Management and Inner Stream Geometry Studies for a dual-flow nozzle system incorporating an outer stream half-span mechanical suppressor have investigated the aerodynamic cycle and geometric nozzle variations which would most significantly impact noise suppression capability. Consideration has been given to: a) system velocity ratio ( $V_o/V_i$ ); b) system weight flow ratio ( $B = W_o/W_i$ ); c) system area ratio ( $A_o/A_i$ ) and d) inner stream plug geometry. Primary design considerations evolved from a series of three distinct studies are as follows:

- Velocity ratio influence is most predominant in systems of low area ratio where the inner stream exerts more of a controlling influence. Progressive and systematic increases in peak OASPL suppression occur as  $V_o/V_i$  changes from 0.6 to  $\infty$ . Fairly systematic changes in peak PNL are also observed, but not of the magnitude or as progressively uniform as on peak OASPL. At broadside, and in the forward quadrant, systematic variation of noise levels with  $V_o/V_i$  variation is not evident.
- Highest suppression levels are attained when inner flow is completely terminated and the outer stream effectively discharges over an abrupt-step formed by the inner stream annulus. Peak PNL suppression levels of up to 13.5 dB were seen on the 2400 ft. sideline for Model 33, the 36 chute  $AR = 2.5$ ,  $R_r^o = 0.783$  system of  $A_o/A_i = 0.65$ . Figure 3-198 compares this closed inner stream system's suppression to levels attained by three full plug turbojet configurations; namely, Models 15 & 17, of  $AR$ ,  $R_r = 2.5/0.653$  and  $1.5/0.782$  discussed in Section 3.4.2.1 and Model 41 of  $AR$ ,  $R_r = 2.5/0.78$  presented in Section 3.4.3.1. In all cases the abrupt-step system showed greater suppression potential. It is recognized that this system may be unacceptable from an aero performance consideration. However, it does provide an upper limit in noise reduction which could conceivably be achieved by judiciously bleeding the inner flow.

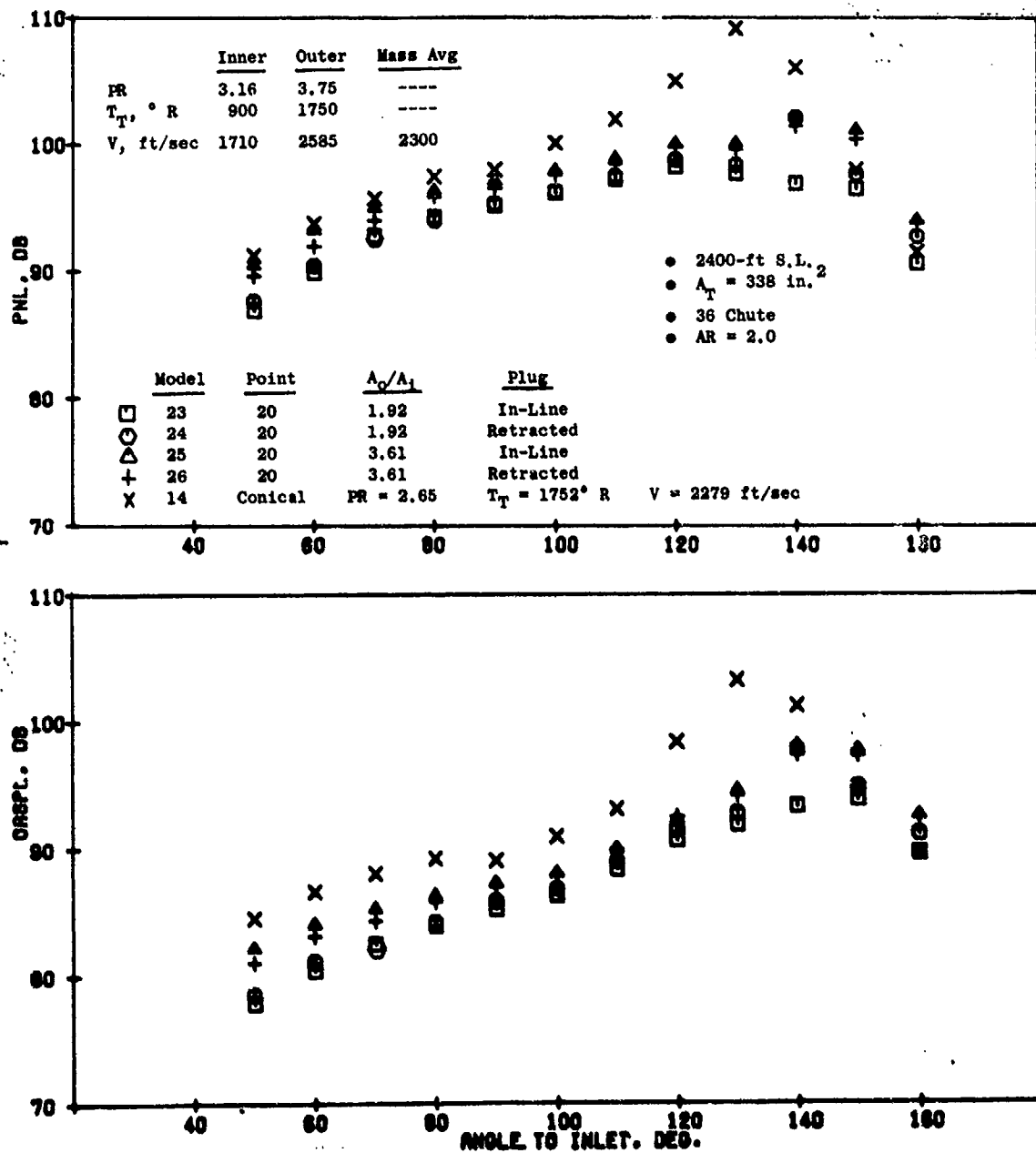


Figure 3-192. Impact of  $A_0/A_1$  and Inner Plug Geometry on PNL and OASPL Directivity, Models 23-26, Winner = 30%  $W_{\text{Outer Cycle}}$ ,  $V_{\text{ma}} = 2300 \text{ ft/sec}$ .

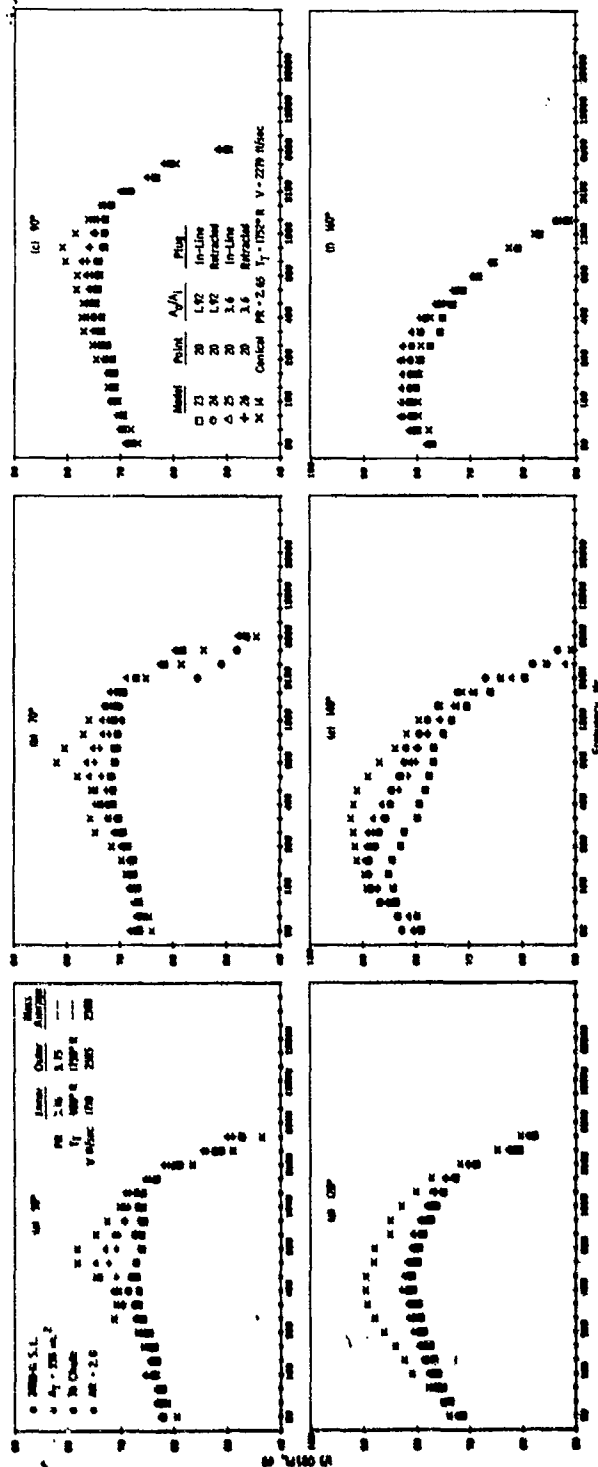


Figure 3-193. Impact of  $A/A_i$  and Inner Plug Geometry on Spectra, Models 23 - 26,  
 $V_{Inner} = 302 \text{ ft/sec}$ ,  $V_{Outer} = 2300 \text{ ft/sec}$ .



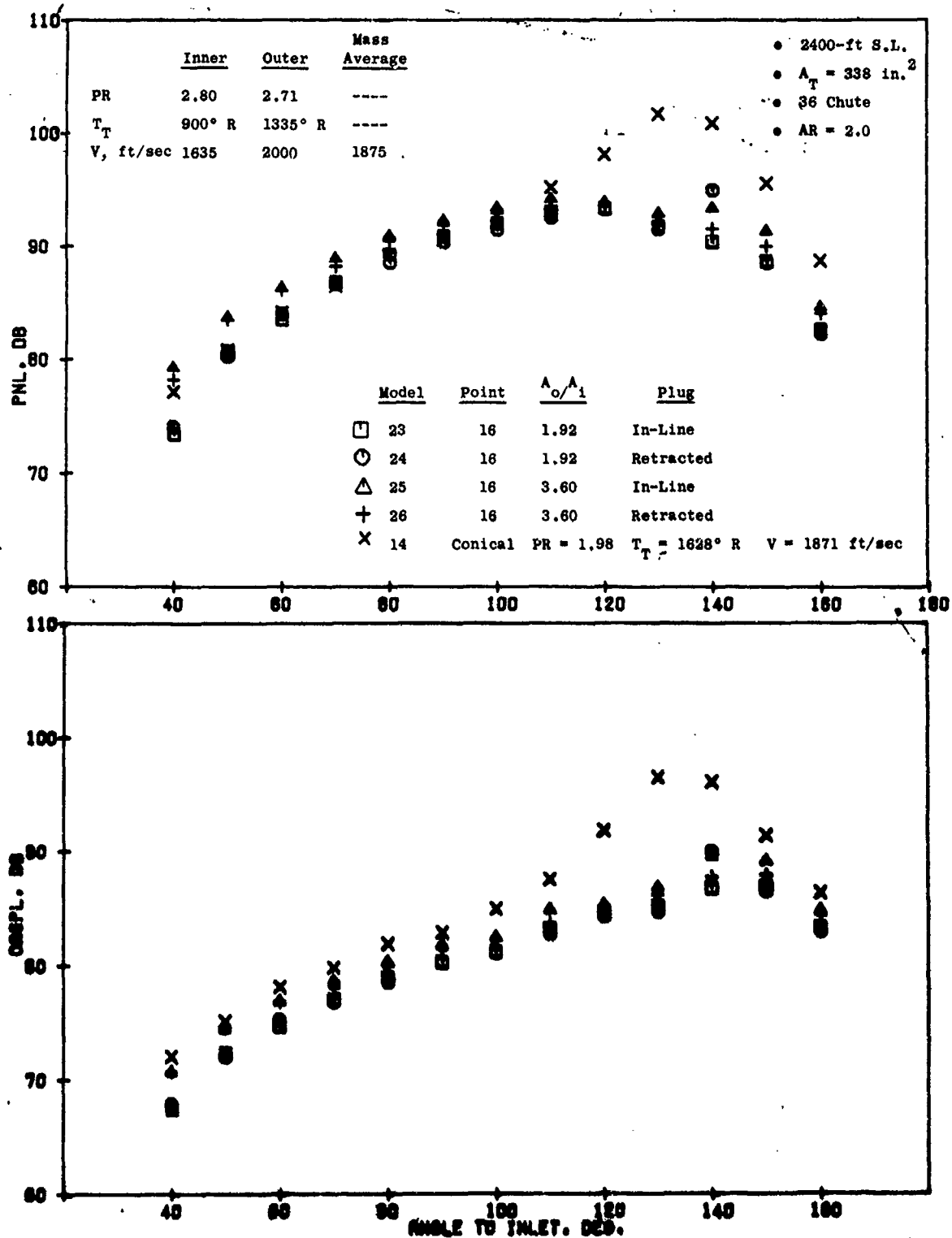


Figure 3-194. Impact of  $A_0/A_1$  and Inner Plug Geometry on PNL and QASPL Directivity, Models 23-26,  $W_{\text{Inner}} = 30\% W_{\text{Outer}}$  Cycle,  $V_{\text{in}} = 1875 \text{ ft/sec}$ .

Inner Outer Mass Avg  
 PR 2.80 2.71 —  
 $T_r$  R 900 1335 —  
 V, R/sec 1635 2000 1875

• 2400-ft S. L.  
 •  $A_r = 338$  in. 2  
 • 36 Chute  
 • AR - 2.0

Model Point  $A_0/A_1$  Plug  
 □ 23 16 In-Line  
 ○ 25 16 Retracted  
 △ 26 16 In-Line  
 × 14 16 Retracted

Conical PR = 1.98  $T_r = 1628^\circ$  R V = 1871 ft/sec

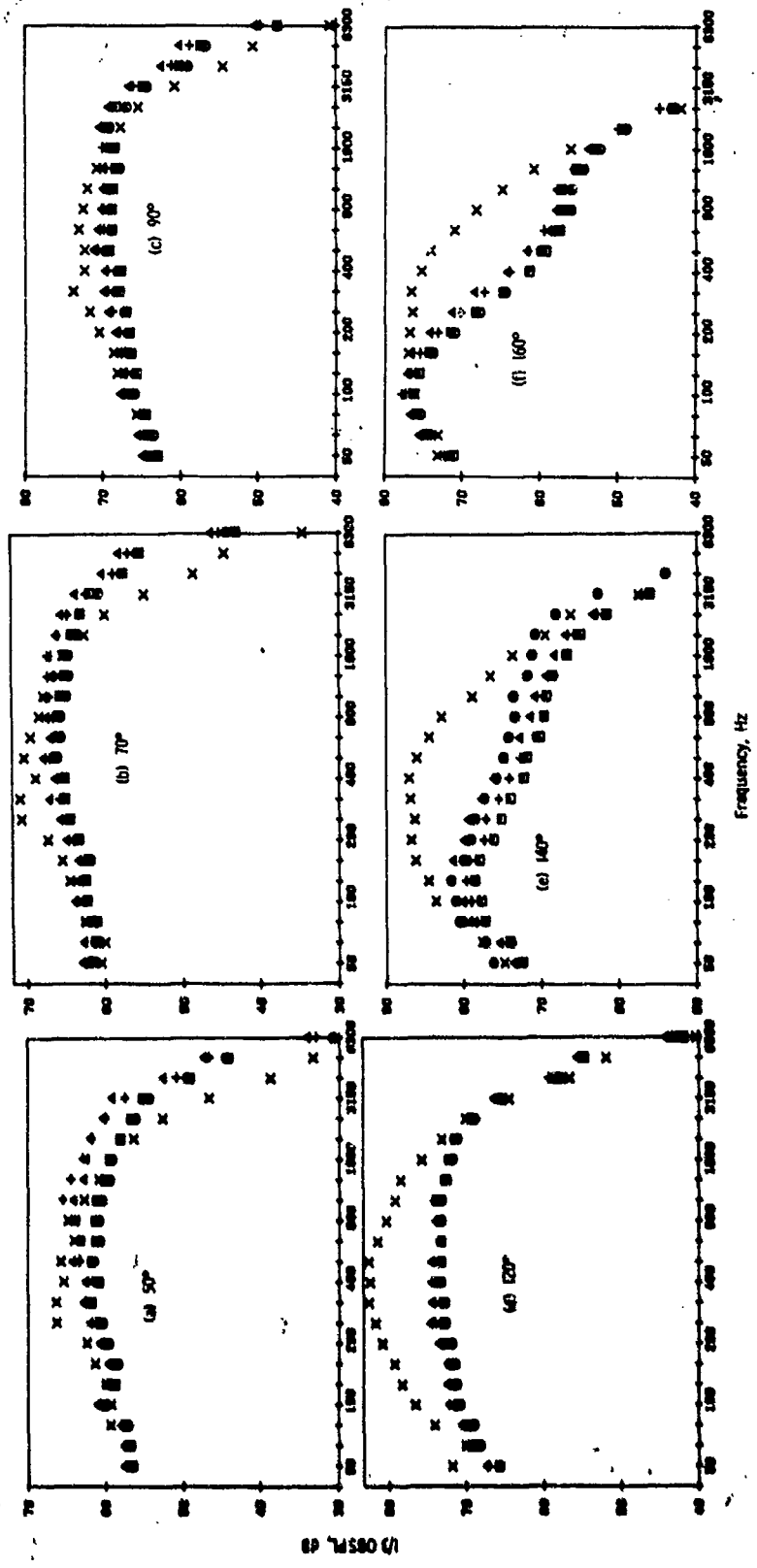


Figure 3-195. Impact of  $A_0/A_1$  and Inner Plug Geometry on Spectra, Models 23-26, Winner = 30% WOuter Cycle,  $V_{na} = 1875$  ft/sec.

- 2400-ft S.L.
- $A_T = 338 \text{ in.}^2$
- 36 Chute
- $AR = 2.0$

Model	Point	$A_0/A_1$	Plug	PR	Inner	Outer	Mass Avg
□	23	15	1.92 In-Line	$T_T = 707^\circ \text{ R}$	2.02	1.94	-----
○	24	15	1.92 Retracted		900	930	-----
△	25	15	3.6 In-Line	V, ft/sec	1370	1390	1380
+	26	15	3.6 Retracted				
×	14	Conical	PR = 2.49 $T_T = 707^\circ \text{ R}$	V = 1397 ft/sec			

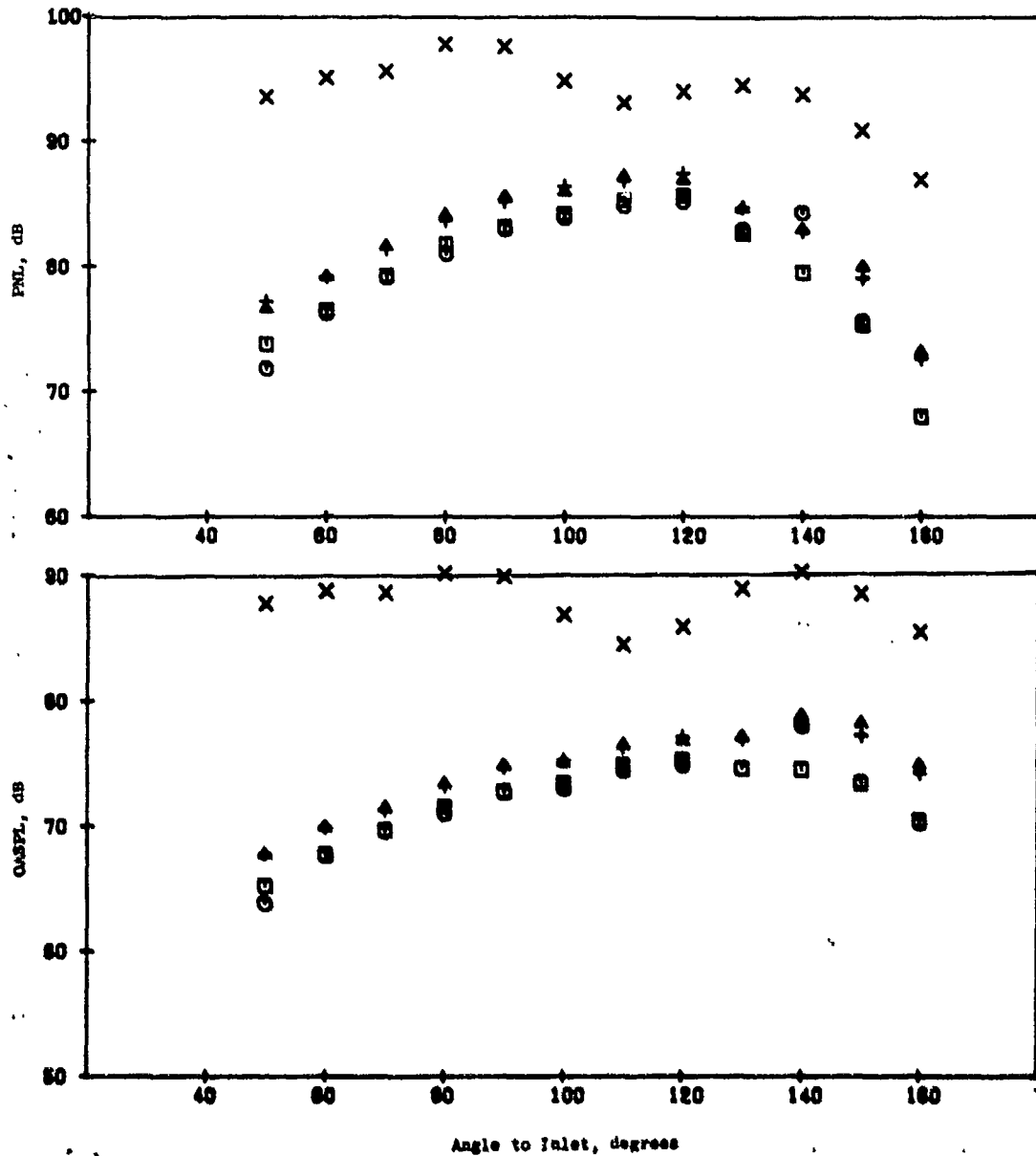


Figure 3-196. Impact of  $A_0/A_1$  and Inner Plug Geometry on PNL and OASPL Directivity, Models 23-26,  $W_{\text{Inner}} = 30\% W_{\text{Outer}}$  Cycle,  $V_{\text{ma}} = 1380 \text{ ft/sec}$ .

Model Point  $A/A_1$  Plug  
 23 15 1.92 In-Line  
 24 15 1.92 Retracted  
 25 15 1.6 In-Line  
 26 15 1.6 Retracted  
 27 14 Conical  $P_R = 2.49$   $T_P = 70^\circ R$   $V = 1397$  ft/sec

2400-ft S.L.  
 $A_T = 338$  in.<sup>2</sup>  
 36 Chute  
 AR = 2.0

PR 2.02 Inner Outer Mass Avg  
 $T_P = R$  900 930 ---  
 $V$ , ft/sec 1370 1390 1380

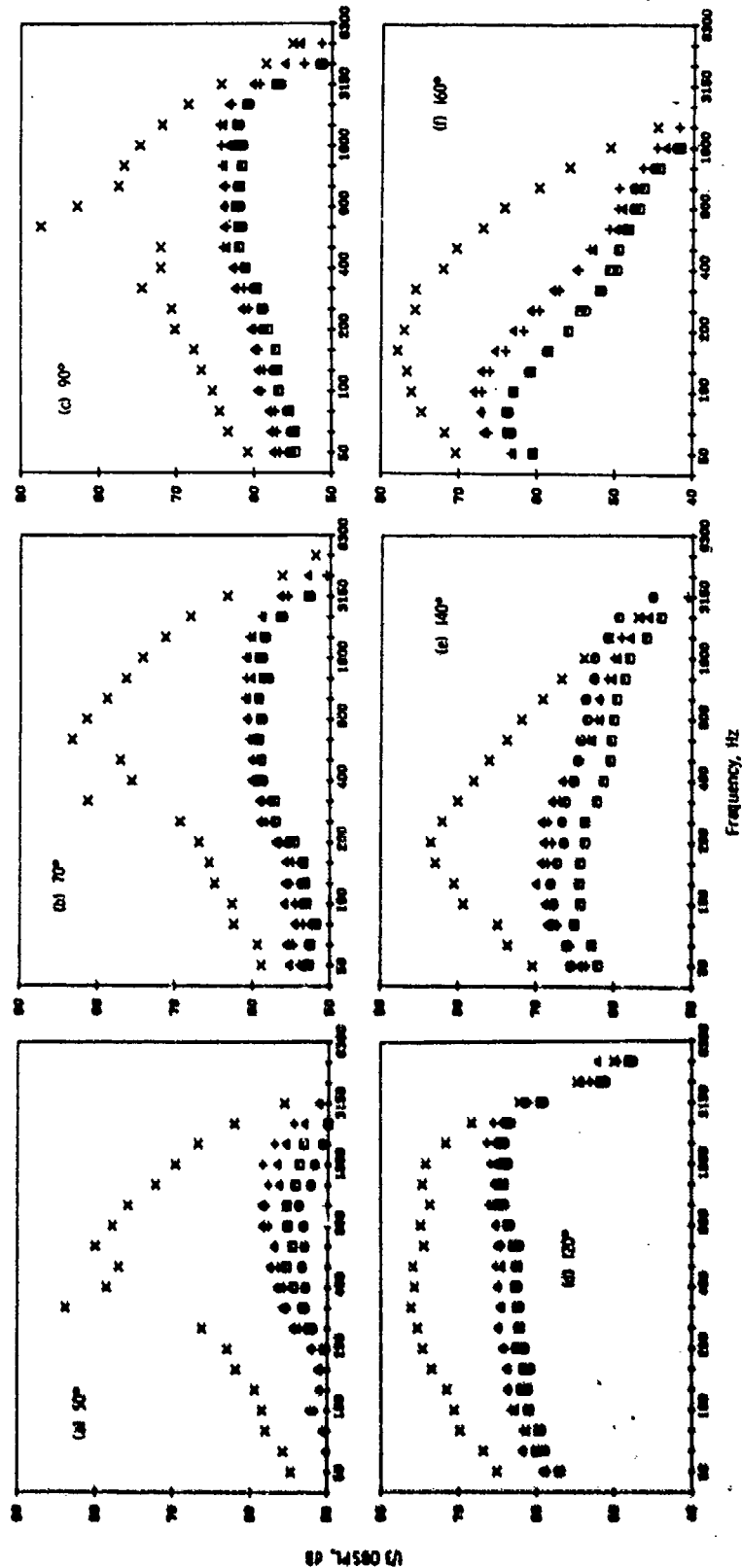


Figure 3-197. Impact of  $A_0/A_1$  and Inner Plug Geometry on Spectra, Models 23-26, Winner = 30% Wouter Cycle,  $V_{ma} = 1380$  ft/sec.

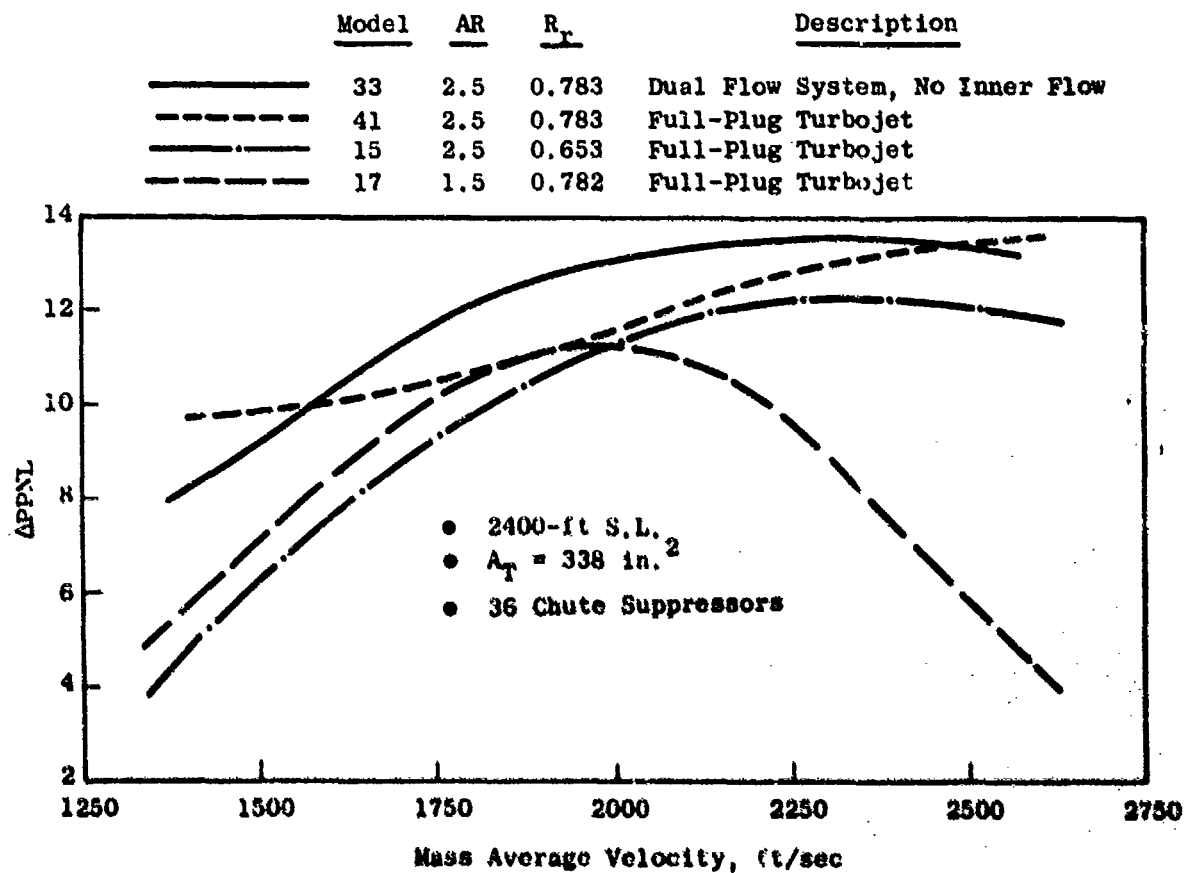


Figure 3-198. Summary Comparison of Suppressed Dual Flow with No Inner Flow to Full-Plug Turbojets.

- For systems of  $A_0/A_1 = 1.92$  the magnitude of noise variance with  $V_0/V_1$  is not present as it is for the low area ratio system, as the outer stream now controls the major portion of the system flow. Individual data sets, however, do show some distinct variance with velocity ratio within the range of 1.5 to 2.0.
- For  $A_0/A_1 = 3.61$ , with  $\beta$  from 2.8 to 8.8, the outer stream dominates noise generation and little variance is discernible for  $1.0 \leq V_0/V_1 \leq 2.0$
- Injecting low amounts of inner flow to effect  $\beta$  values of 3.3, 6.7, and  $\infty$  shows  $\beta$  to be a strong system parameter influencing suppression. The influence is greater for low system area ratio and changes are fairly systematic, decreasing suppression as  $\beta$  is lowered from  $\infty$  to 3.3. Changes in peak PNL range from 5 to 3  $\Delta$ dB at low to high  $V_{ma}$  over the  $\beta$  range tested.
- System area ratio variation impacts suppression performance significantly. The high  $A_0/A_1$  value of 3.61 indicates peak PNL and peak OASPL suppression gains up to 3.5 and 5  $\Delta$ dB, respectively over the lower  $A_0/A_1$  counterparts. Impact is primarily in the aft quadrant with  $90^\circ$  showing no systematic trends and  $50^\circ$  only indicating higher  $A_0/A_1$  is still favorable.
- Inner stream geometry variation from the in-line to the retracted configurations has negligible impact on suppression. Variance within the model sets is not strong or consistent enough to substantiate any preference of geometry.

#### 3.4.2.3 Flow Segmentation Study

The intention of this study was to investigate the impact of degree of segmentation of an annular duct suppressor within a dual flow exhaust nozzle system. Models 30, 31, and 32 (Figure 3-199) of 20, 30 and 40 shallow chute element, respectively, were utilized. Detailed schematics of the models are in Appendix A, Figures 24, 25 and 26. Inner stream flowpath geometry was held constant using the 0.7-in. annulus height plug in the retracted position. Parameters of the outer flowpath held constant were:

- Flow area = 21.76 in.<sup>2</sup>
- Blocked area = 17.82 in.<sup>2</sup>
- Suppressor area ratio = 1.75
- Suppressor radius ratio = 0.717
- Shroud I.D. = 10.44 in.
- Plug O.D. = 7.48 in.
- Upstream flow geometry
- System area ratio,  $A_0/A_1$ , = 1.92

- Retracted Inner Plug with 0.7-in. Step
- Area Ratio = 1.75
- Radius Ratio = 0.717
- $A_o/A_i = 1.92$

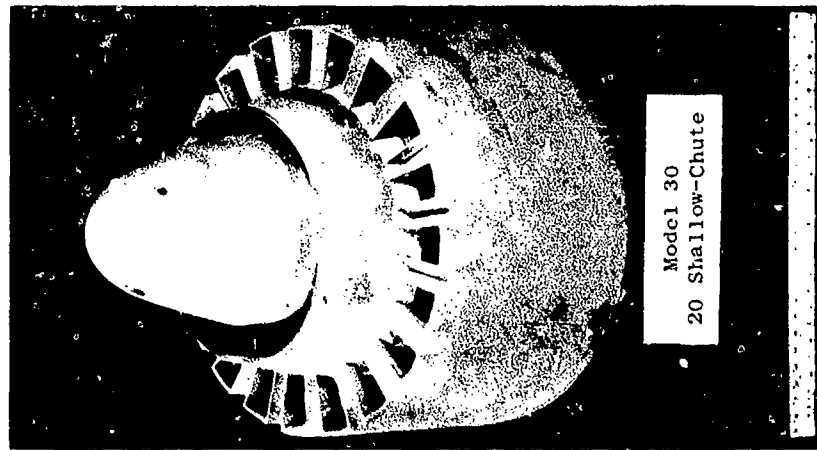
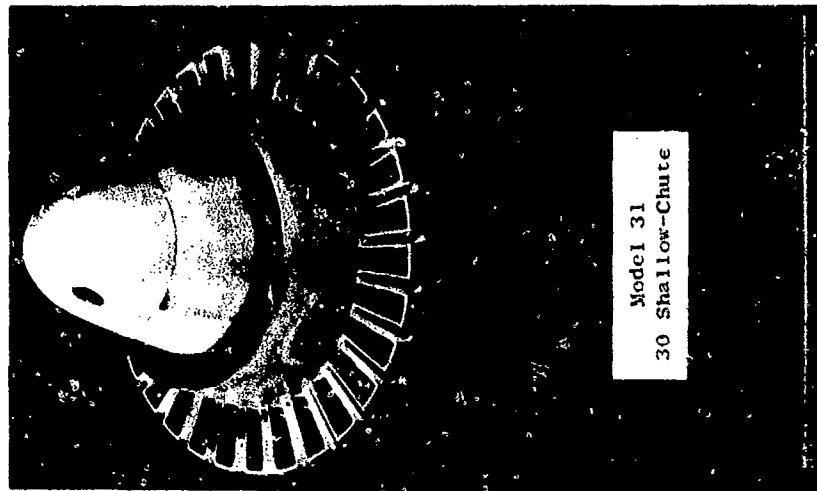
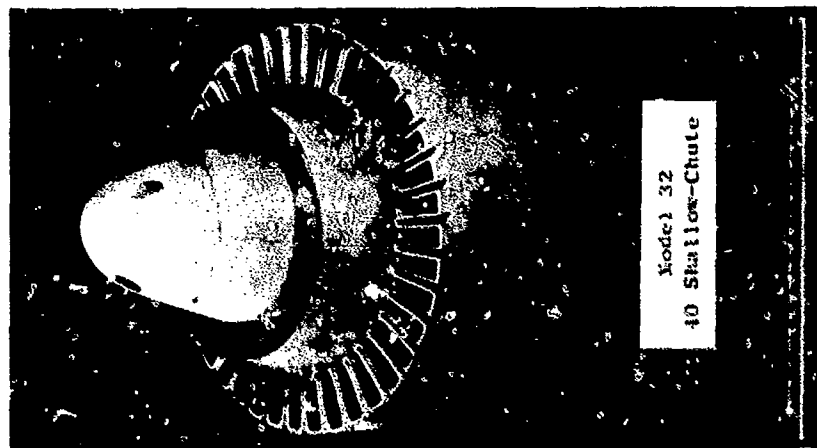


Figure 3-199. Half-Span Suppressor Element Number Variation on Dual Flow.

The only geometric variable was element number, more finely segmenting both flow and blocked areas as element number increased.

Acoustic test matrices were as described in Section 3.2.1, Figure 3-10 and Table 3-3, testing each model for the following cycle series:

- $W_1 = 15\% W_0$
- $W_1 = 30\% W_0$
- DBTF/Inverted Dual Flow with  $1.0 \leq V_0/V_1 \leq 2.0$
- AST/VCE

Model 31 was additionally tested with no inner flow while maintaining a normal outer flow cycle.

Acoustic results, if presented as an aggregate of all test data on the basis of peak noise levels, show (as in Figure 3-200) that:

- Maximum suppression levels of 10  $\Delta$ PPNL and 11.5  $\Delta$ POASPL were attained.
- At low and intermediate  $V_{ma}$ , finer segmentation is more effective on a peak PNL basis; however, a switch to lower element number is more effective at  $V_{ma} > 2250$  ft/sec.
- On the peak OASPL basis the coarser segmentation of 20 elements (Model 30) is significantly more effective and no significant distinction is seen between the finer segmentation of 30 or 40 shallow-chutes (Models 31 and 32).

Closer evaluations of the data, as applicable to the individual cycles of a)  $W_1 = 15\% W_0$  b)  $W_1 = 30\% W_0$ , and c) DBTF/Inverted Dual Flow, are presented in the following:

Figures 3-201 and 3-202 Peak PNL & OASPL  
Figures 3-203 and 3-204 90° PNL & OASPL  
Figures 3-205 and 3-206 50° PNL & OASPL  
Figure 3-207 OAPWL

Peak PNL data in Figure 3-201 for all three cycle lines show that finer segmentation yields more effective suppression at low and intermediate  $V_{ma}$ , and a maximum level of near 10  $\Delta$ PPNL is experienced. Degree of segmentation is relatively unimportant at  $2000 < V_{ma} < 2250$  ft/sec, then coarser segmentation becomes more effective at  $V_{ma} > 2250$  ft/sec. Variance of up to 5  $\Delta$ PPNL is seen for the study excursion range of 20 to 40 elements, magnitude depending on cycle line and  $V_{ma}$  selected.

Figure 3-202, peak OASPL data for the three cycle curves, shows lower element number segmentation to be consistently more effective. A variance of 1 to 4  $\Delta$ POASPL is seen from 20 to 40 elements, magnitude of variance always



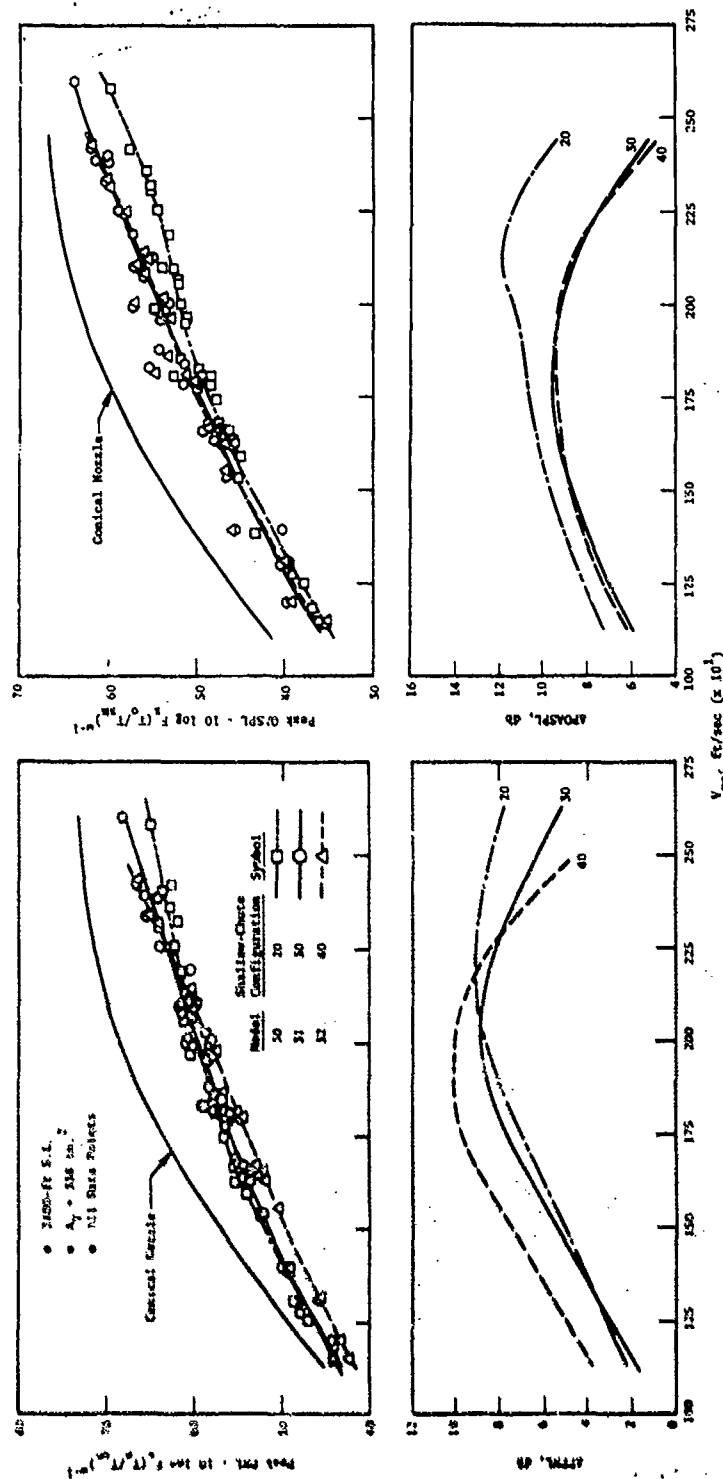


Figure 3-200. Suppressor Element Number Variation, Peak Noise and Suppression Levels.

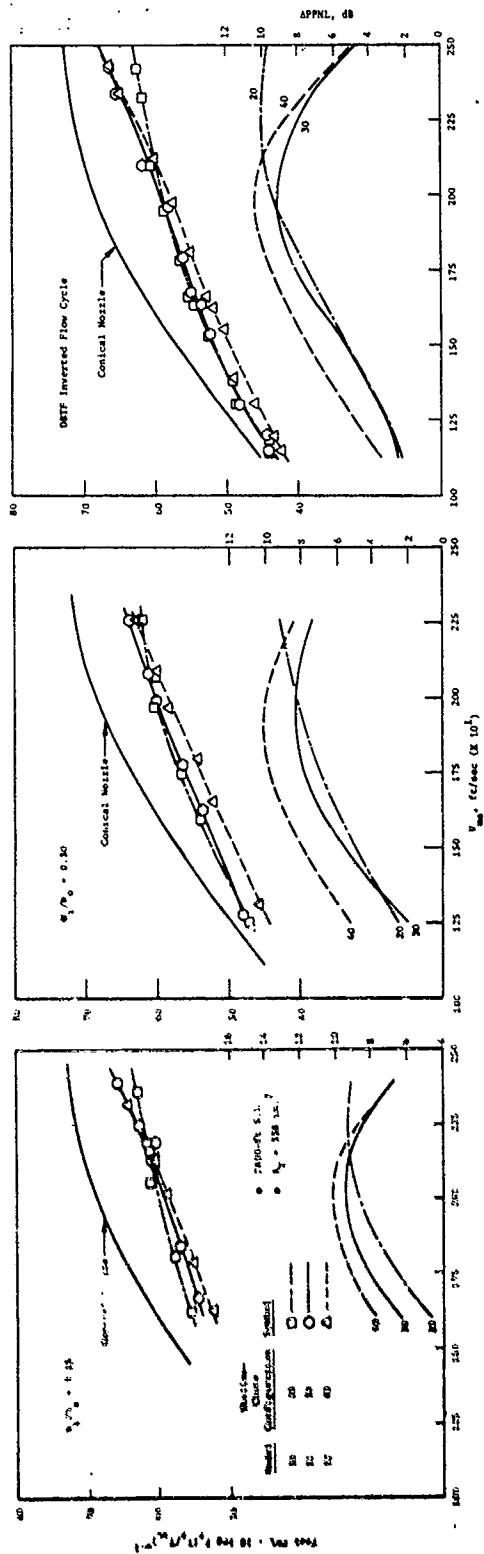


Figure 3-201. Suppressor Element Number Variation, Peak PNL and Suppression Levels.

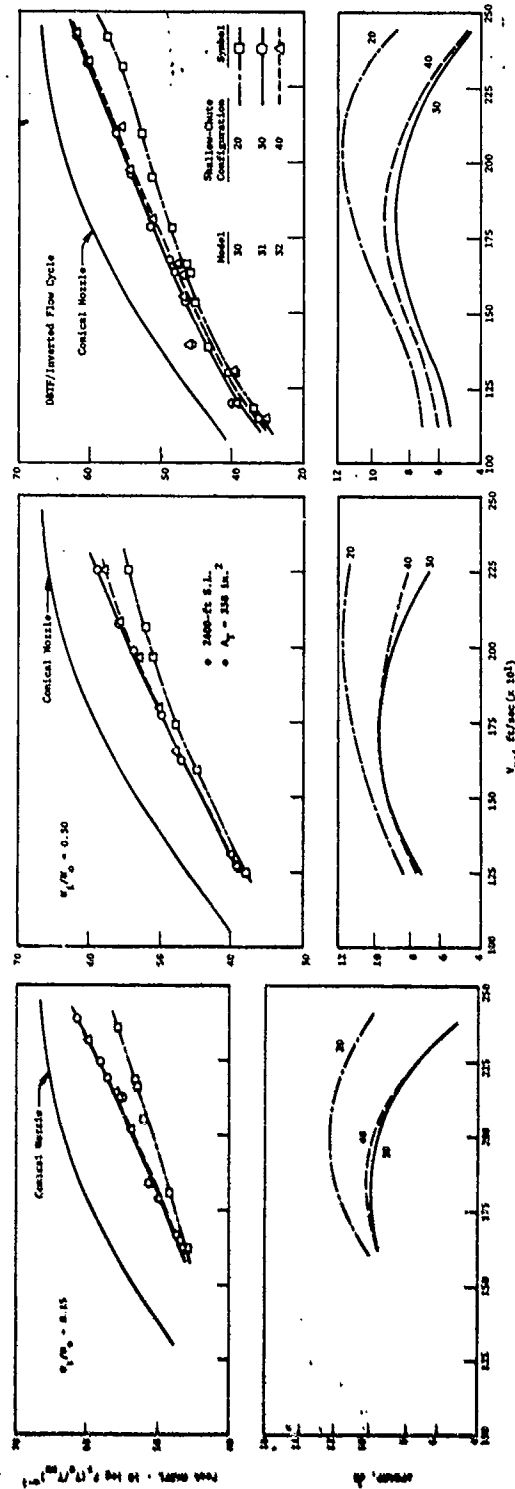


Figure 3-202. Suppressor Element Number Variation, Peak OASPL and Suppression Levels.

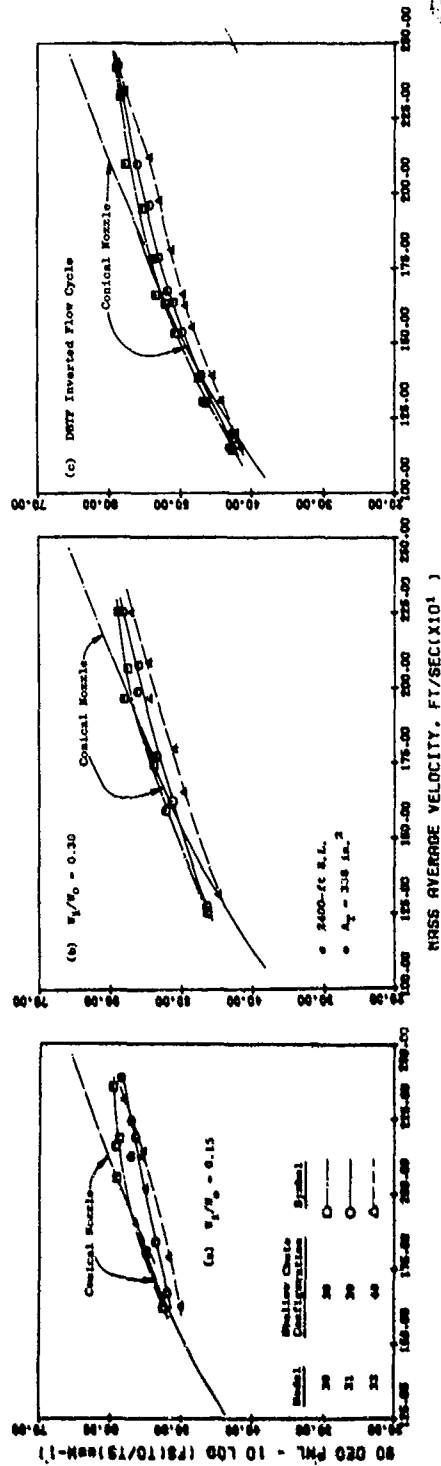


Figure 3-203. Suppressor Element Number Variation, 90° PNL.

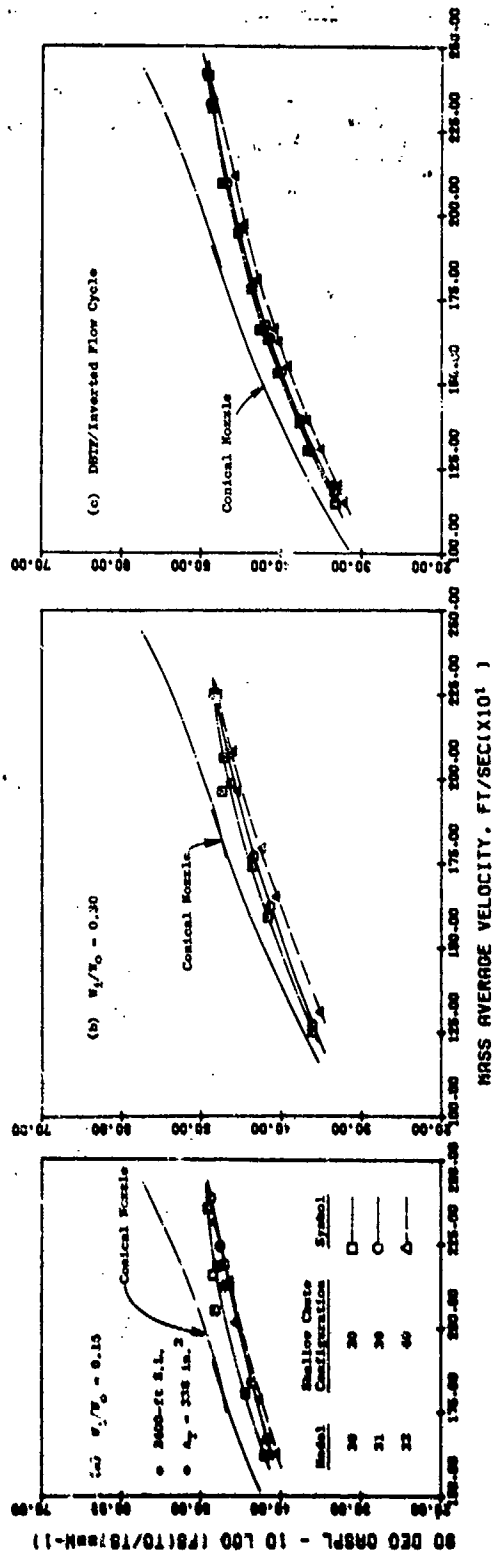


Figure 3-204. Suppressor Element Number Variation, 90° OASPL.

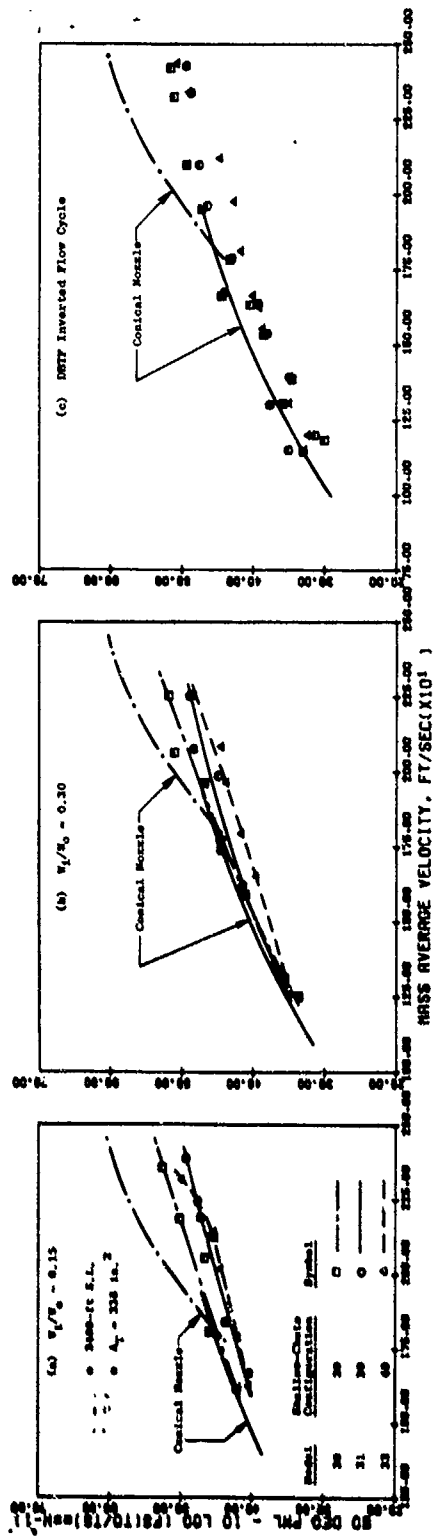


Figure 3-205. Suppressor Element Number Variation, 50° PNL.

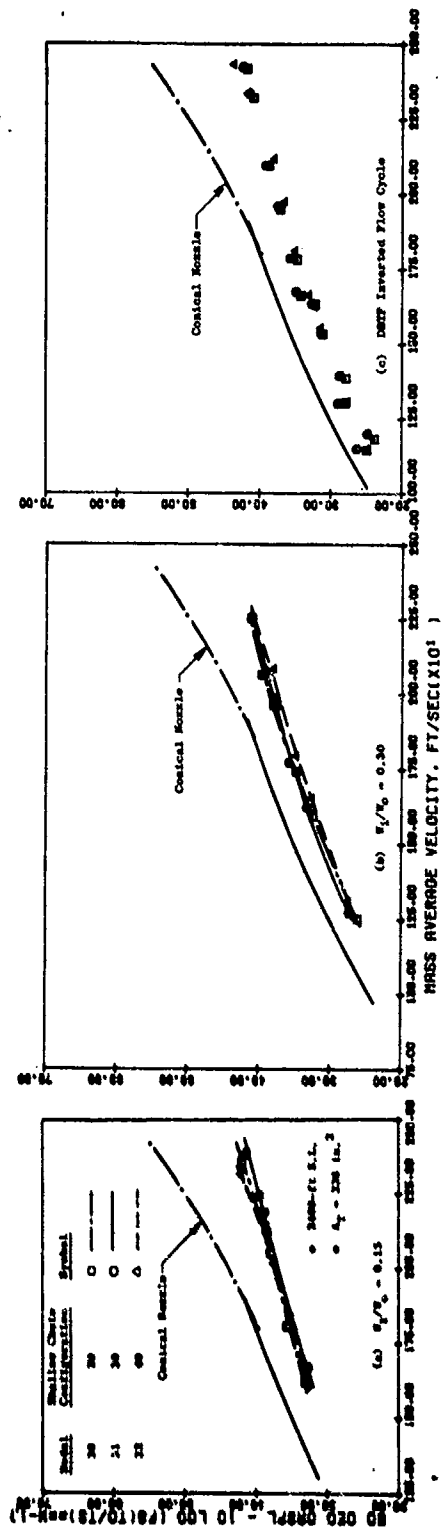


Figure 3-206. Suppressor Element Number Variation, 50° OASPL.

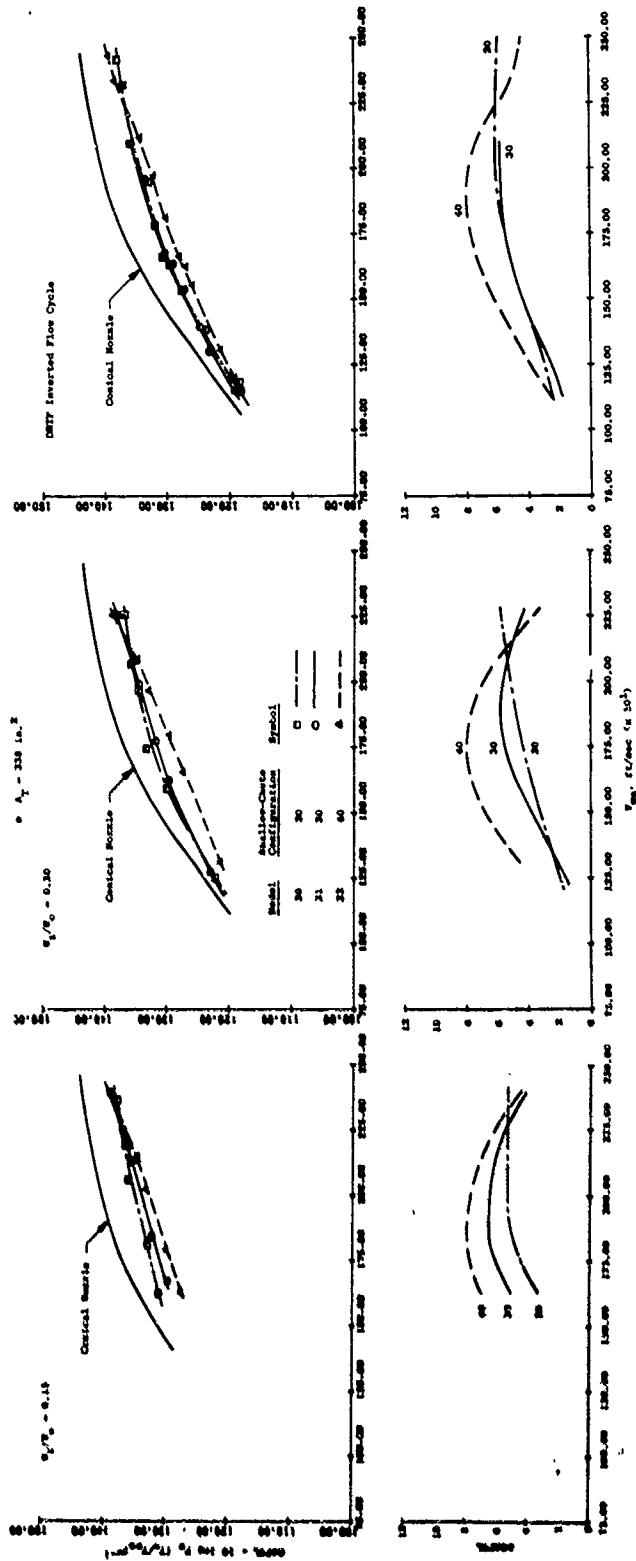


Figure 3-207. Suppressor Element Number Variation, OAPWL.



greater at higher  $V_{ma}$ . Distinction between 30 and 40 shallow-chute performance is nil. For the DBTF/Inverted Dual Flow cycle data, both for peak PNL and OASPL, minimal distinction is seen for  $V_0/V_1$  variance from 1.0 to 2.0; the data adhering well to smooth singular trend curves.

Figures 3-203 and 3-204, for 90° PNL and OASPL, show that PNL suppression is still attained at intermediate and high  $V_{ma}$  settings, but at low  $V_{ma}$  the self noise of the shallow-chutes raises the PNL levels slightly above the baseline. Moderate levels of OASPL suppression are maintained at all  $V_{ma}$  values. Finer segmentation is more effective at all cycles, at all velocity values and for both PNL and OASPL, a nominal 3 to 4  $\Delta$ PNL greater suppression afforded by 40 (Model 32) relative to 20 elements (Model 30).

Figures 3-205 and 3-206, for 50° PNL and OASPL, show that substantial PNL and OASPL suppression is maintained in the forward quadrant, both at low  $V_{ma}$  where turbulent mixing noise is prevalent and at higher  $V_{ma}$  (supercritical pressure ratio) where the suppressor very significantly lowers noise levels relative to the conical noise levels. On an OASPL basis, little distinction is seen in fineness of segmentation, whereas higher element number still offers significant improvement on a PNL basis.

OAPWL trends with  $V_{ma}$ , Figure 3-207, are consistent with those of PPNL in that (a) finer segmentation is more effective at low and intermediate  $V_{ma}$ , (b) degree of segmentation is relatively unimportant for  $2000 < V_{ma} < 2250$ , and (c) trend is for more effective suppression with fewer element at  $V_{ma} > 2250$  ft/sec.

For a more detailed evaluation of suppressor segmentation influence on PNL and OASPL directivity plus spectra characteristics, the following data sets from the DBTF cycle are included as representative of the overall test results.

Figures 3-208 and 3-209 Data Point 37,  $V_{ma} = 2425$  ft/sec,  $V_0/V_1 = 1.9$

Figures 3-210 and 3-211 Data Point 26,  $V_{ma} = 2100$  ft/sec,  $V_0/V_1 = 2.0$

Figures 3-212 and 3-213 Data Point 24,  $V_{ma} = 1200$  ft/sec,  $V_0/V_1 = 1.0$

A general review of the above data suggests:

- The PNL angular variation of these multielement suppressors hint at the classical migration of maximum noise angles at lower inlet angles relative to the conical nozzle.
- At high  $V_{ma}$  (supercritical pressure ratio in the outer stream), large amounts of inlet angle suppression are seen. The primary suppression mechanism is reduction of the strong puretone and broadband shock-cell noise, prevalent in the conical nozzle noise signature.

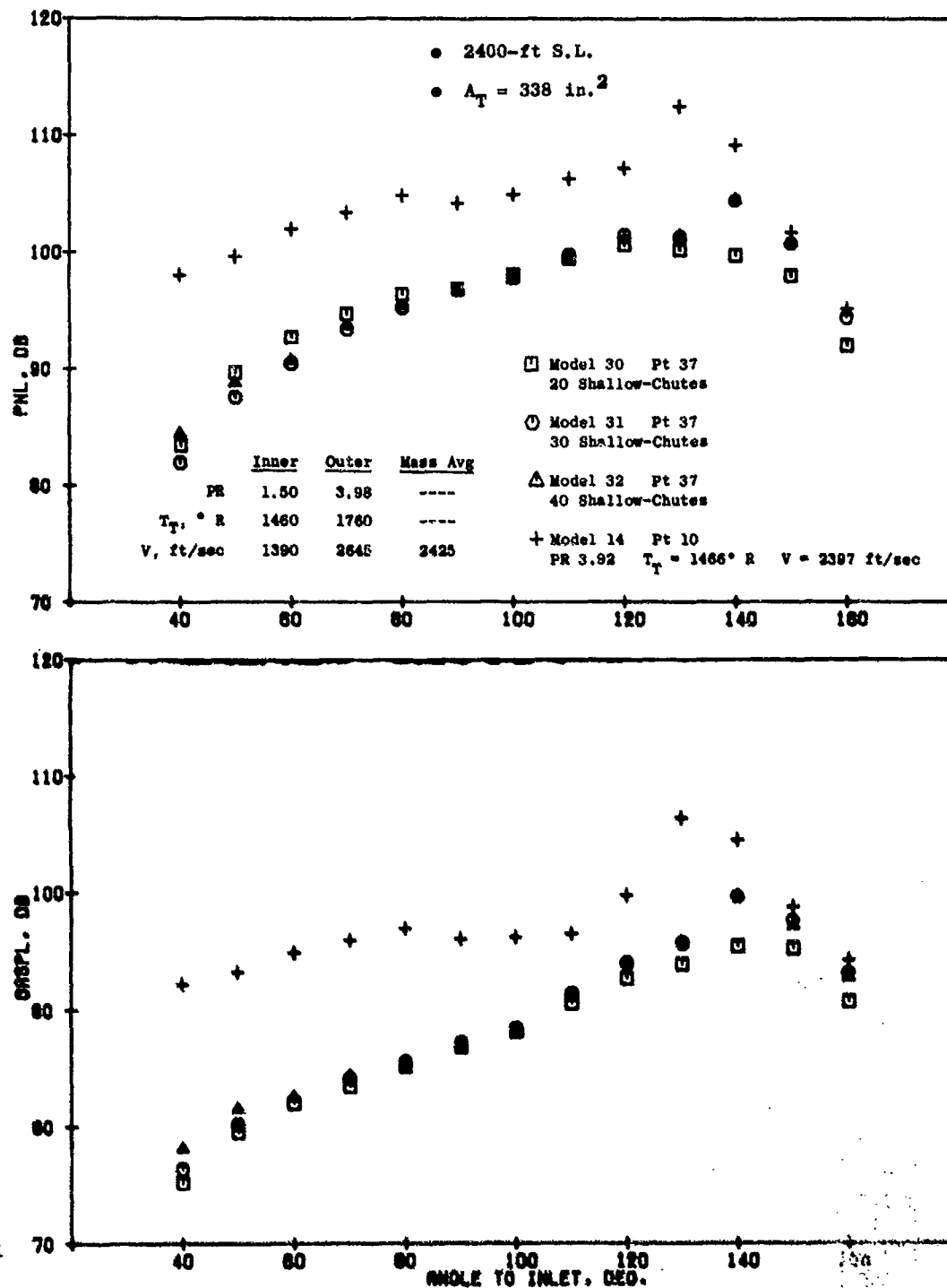


Figure 3-208. Suppressor Element Number Variation, OASPL and PNL Directivity,  $V_{ms} = 2425 \text{ ft/sec}$ .

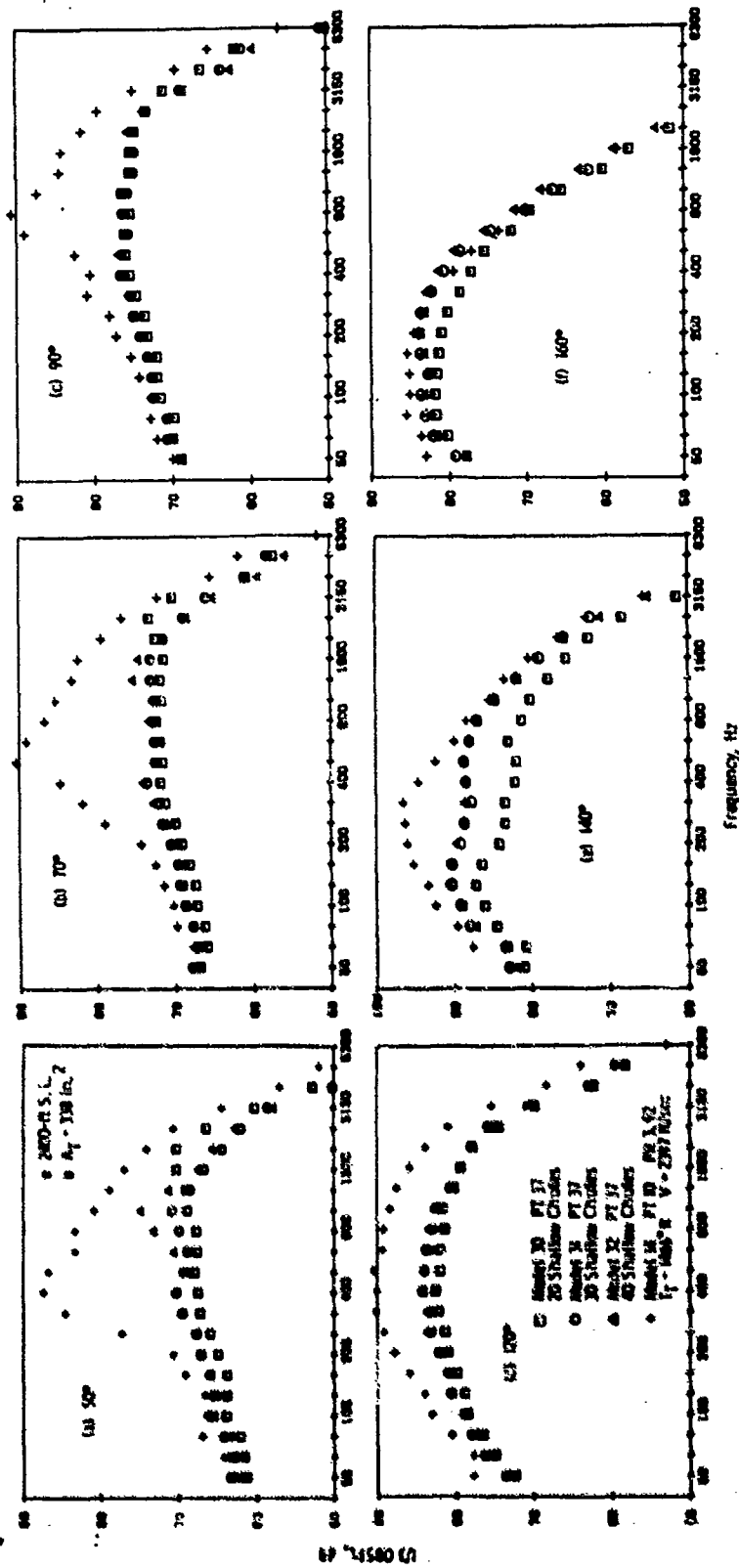


Figure 3-209. Suppressor Element Number Variation, Spectra,  $V_{ma} = 2425$  ft/sec.

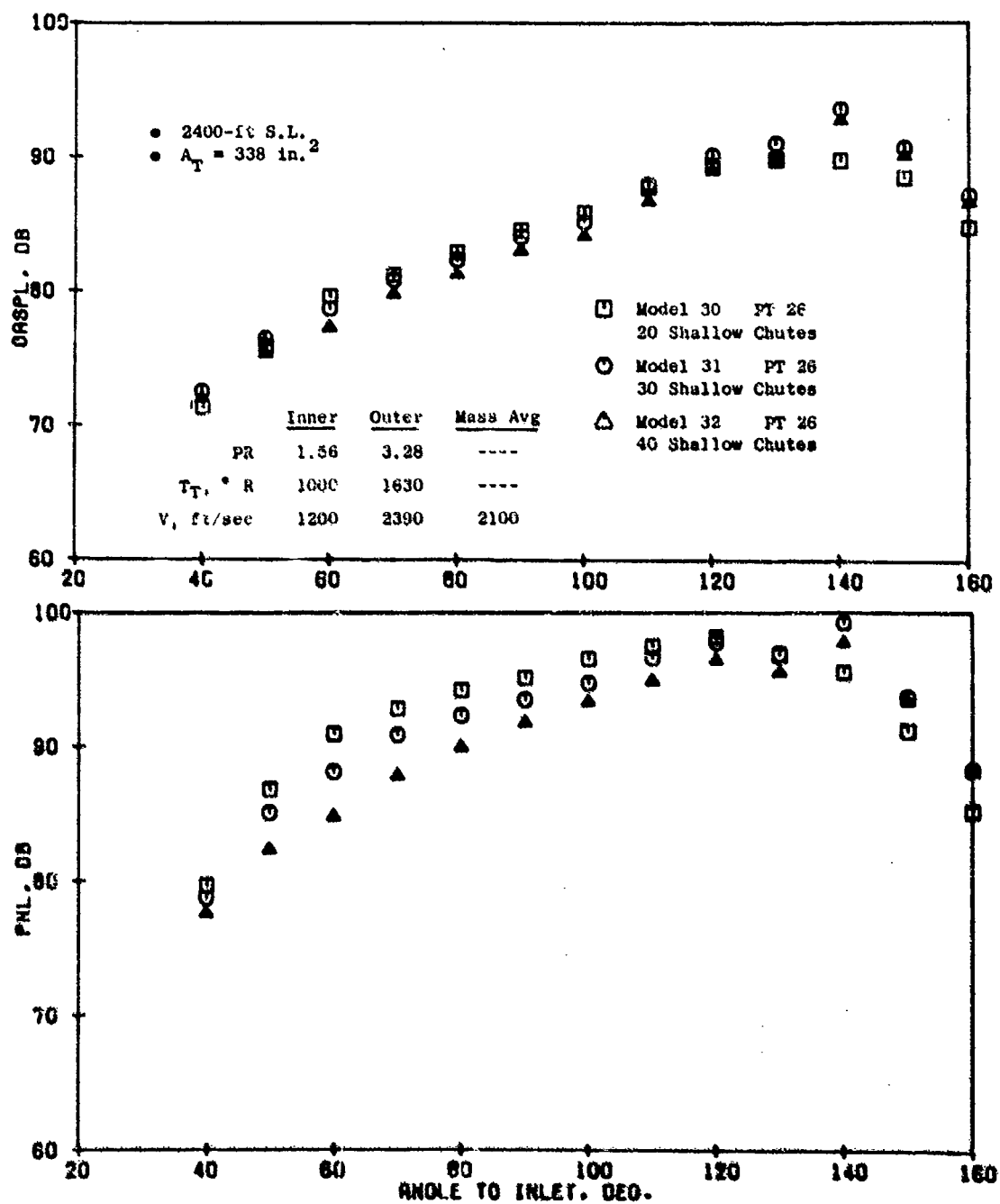


Figure 3-210. Suppressor Element Number Variation, CASPL and PNL Directivity,  $V_{ma} = 2100 \text{ ft/sec}$ .

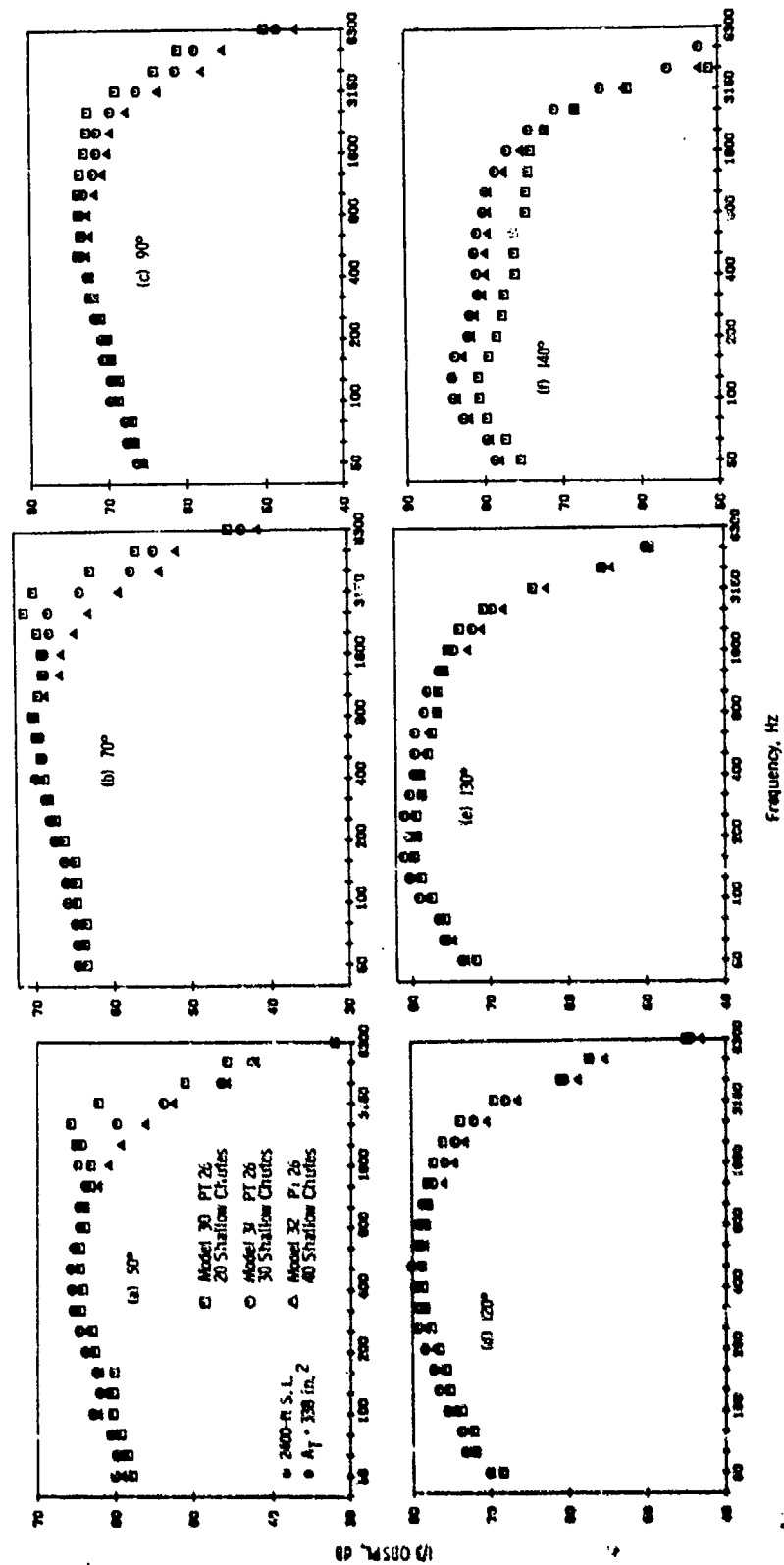


Figure 3-211. Suppressor Element Number Variation, Spectra,  $V_{ma} = 2100 \text{ ft/sec.}$

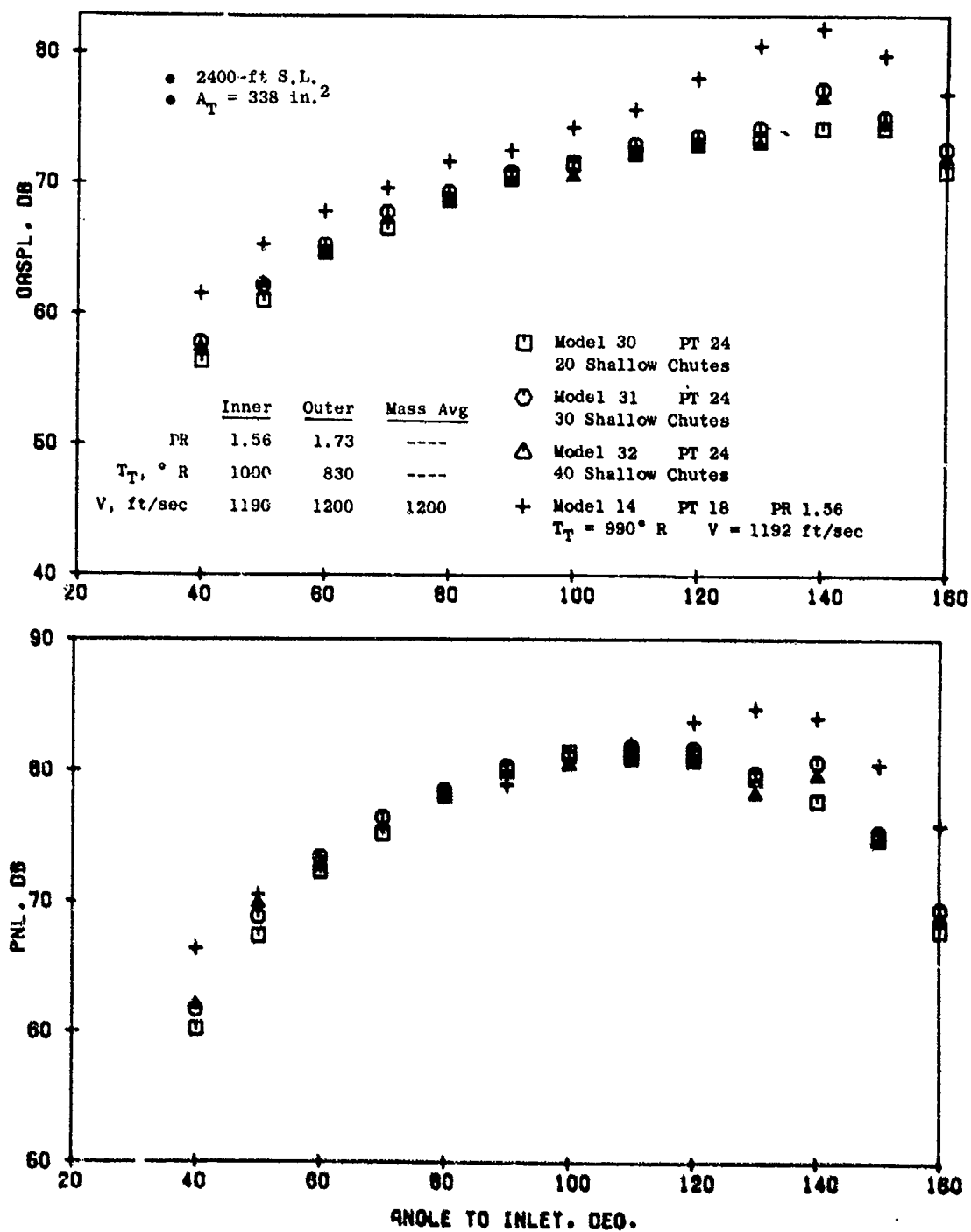


Figure 3-212. Suppressor Element Number Variation, OASPL and PNL Directivity,  $V_{ma} = 1200 \text{ ft/sec}$ .

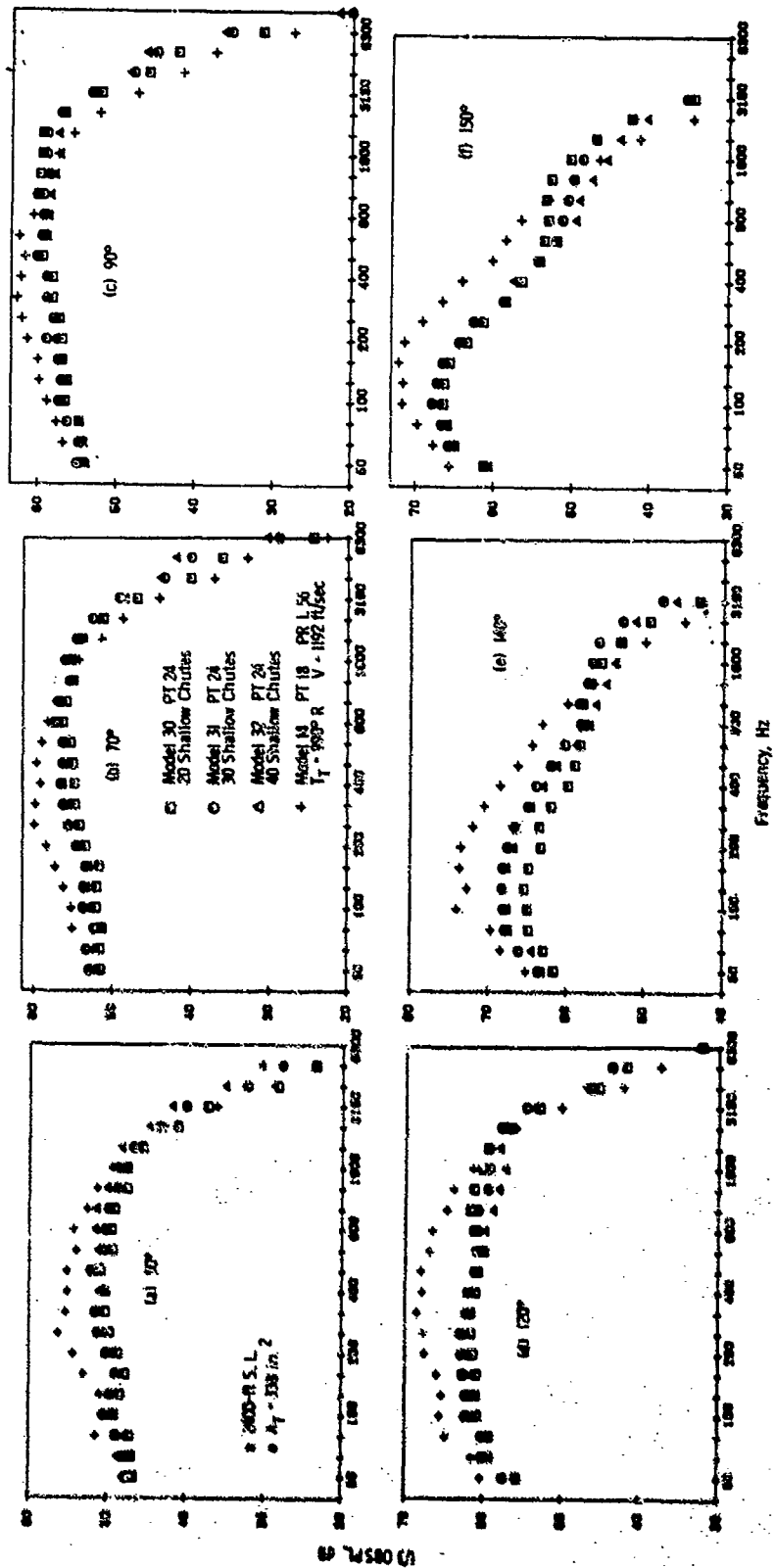


Figure 3-213. Suppressor Element Number Variation, Spectra,  $V_{ma} = 1200 \text{ ft/sec}$ .

- The multielement suppressor's noise signature is observed to be a fair balance of pre and postmerged jet noise sources. At forward quadrant angles, the double humped spectra distribution, and in cases dominance of the premerged or high frequency noise, is normally seen. As expected at aft quadrant peak noise angles, the low frequency noise portion of the spectra tends to contribute more to the total noise with increasing velocity. This result implies greater importance of the merged-flow region in ultimately defining the velocity range of noise suppression.

In depth examination of the first data set, Figures 3-208 and 3-209 at  $V_{ma} = 2425$  ft/sec, suggests the following:

- At peak noise angles, significant suppression relative to the conical nozzle is realized by the shallow chute models, particularly for 20 element segmentation (Model 30). Aft quadrant suppression is low to nil. Forward quadrant suppression is extremely high, up to 12  $\Delta$ PNL and 13  $\Delta$ OASPL at 50° due to reduced shock noise. The conical nozzle and outer stream cycle pressure ratios were at 3.92 and 3.98, respectively, for this data set. Slight amounts of shock noise influence can still be detected in the suppressed nozzle spectra at 50 and 70°.
- In the aft quadrant, suppressor spectra shape closely approximates that of the conical nozzle; at 120° fairly broadband suppression is observed, at 140° midfrequency levels are best reduced and at 150°, little-to-no suppression is present.

For the intermediate  $V_{ma} = 2100$  ft/sec data set, Figures 3-210 and 3-211, the following are observed:

- Little variance is seen in peak PNL level but peaks shift from 120° for the 20 element to 140° for the 30 and 40 element suppressors. At the 140° location, spectra are similar for the 30 and 40 shallow-chute, Models 31 and 32, and suppression for the 20 element, Model 30 is quite broadband.
- The 20 shallow-chute, Model 30 noise is highest at inlet and broadside angles then lowest at aft angles on both PNL and OASPL bases, a full reversal of trends.
- Variation in PNL at forward angles is more pronounced than for OASPL. This is because low and intermediate frequency spectra are near to the same levels for the three models, and essentially control OASPL. In contrast, larger variance in PNL is controlled by high frequency spectra, still somewhat influenced by tone and broadband shock noise for the 20 and 30 element models. The larger characteristic flow dimensions and wider spacing between individual jets of the more coarsely segmented streams allow for development of shock structure and for radiation of associated tone and broadband noise before shock structure has decayed or has been destroyed



by merging of the individual jets. The duct stream was operating at a supercritical pressure ratio of 3.28 for this test point.

The third data set, Figures 3-212 and 3-213, is at  $V_0 = V_1 = V_{ma} = 1200$  ft/sec. Significant PNL suppression occurs only in the peak and aft quadrant angles and is fairly broadband in frequency range. Low element number is slightly more effective at most angles. This is attributable to suppression of the controlling low and midfrequency spectra, even though high frequency noise levels are normally above those of the 30 and 40 element models.

#### 3.4.2.4 Element Type Studies

Previous technology on multielement suppressors had indicated that ventilation capability of the segmenting element is an important parameter in the overall suppressor selection and system design. From an installed performance viewpoint, well ventilated chutes had substantially less thrust loss than low or nonventilated spokes, due primarily to the differences in base drag associated with the chute/spoke blockage area. Spokes, however, are mechanically far easier to implement within a nozzle system than chutes. They can be stowed on the plug surface and deployed simply for suppressor activation. Deeply ventilated chutes, due to their large size, must be stowed within the plug itself and are significantly more complex to deploy.

Data previously available for comparing chute to spoke performance was on a turbojet annular suppressor of low duct radius ratio. The current studies extend this data base to systems of high duct radius ratio for applications of full span suppressors to turbojets and of half-span suppressors on dual flow systems of moderate and low system area ratio, i.e.,  $A_0/A_1 = 1.92$  and 0.65.

#### Element Type Study, Turbojet

The impact of varying element design from a fully ventilated chute to a nonventilated spoke was investigated on a full plug turbojet system within this study. Models 16 and 18 were used per Figure 3-214 photo and Figures 10 and 12 of Appendix A. The base model was a 36-chute suppressor of area ratio = 2.0 and radius ratio = 0.716. Removable filler inserts were used to convert from a well-ventilated chute to a nonventilated spoke designed to be flush with the shroud outer flowpath and with the chute exit plane. The acoustic test matrix for these turbojet configurations followed the matrix Section 3.2.1, Figure 3-8, using conventional turbojet and high TT cycle lines.

Review of the acoustic results in terms of peak OASPL in Figure 3-215 and peak PNL in Figure 3-216, (each showing the two cycle line results separately) indicates:

- A maximum suppression level of 13.5 dB is achieved relative to the conical nozzle by the spoke, on both a peak OASPL and a peak PNL basis.

- 36 ELEMENTS
- AREA RATIO = 2.0
- RADIUS RATIO = .716

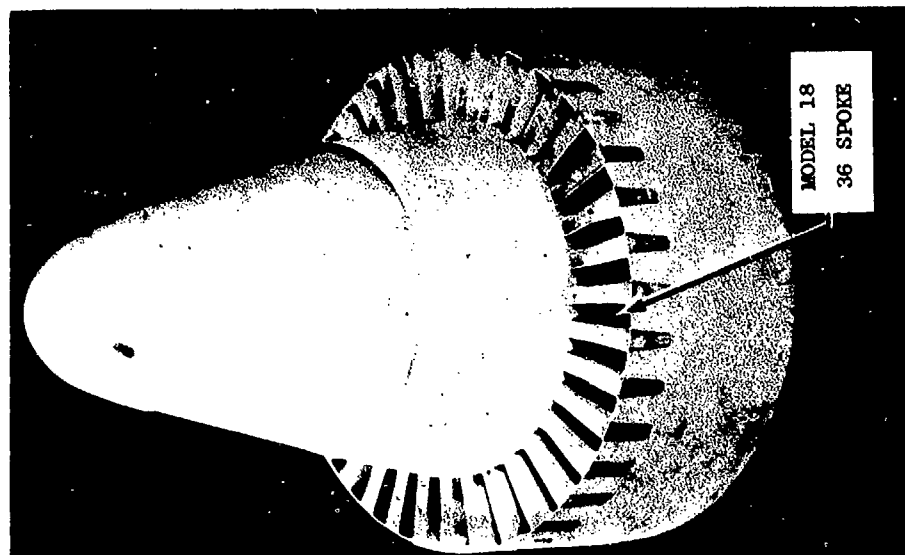
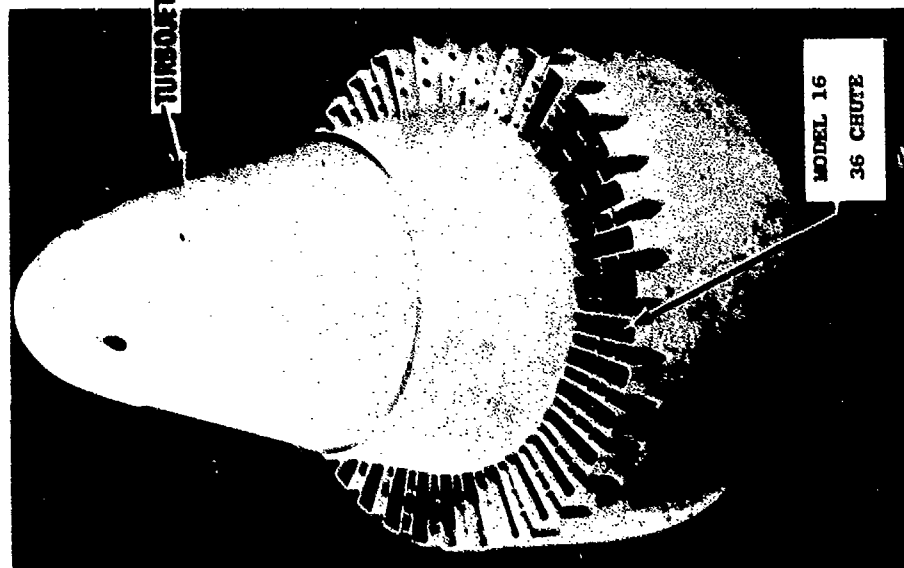


Figure 3-214. Element Type Variation on Turbojet.

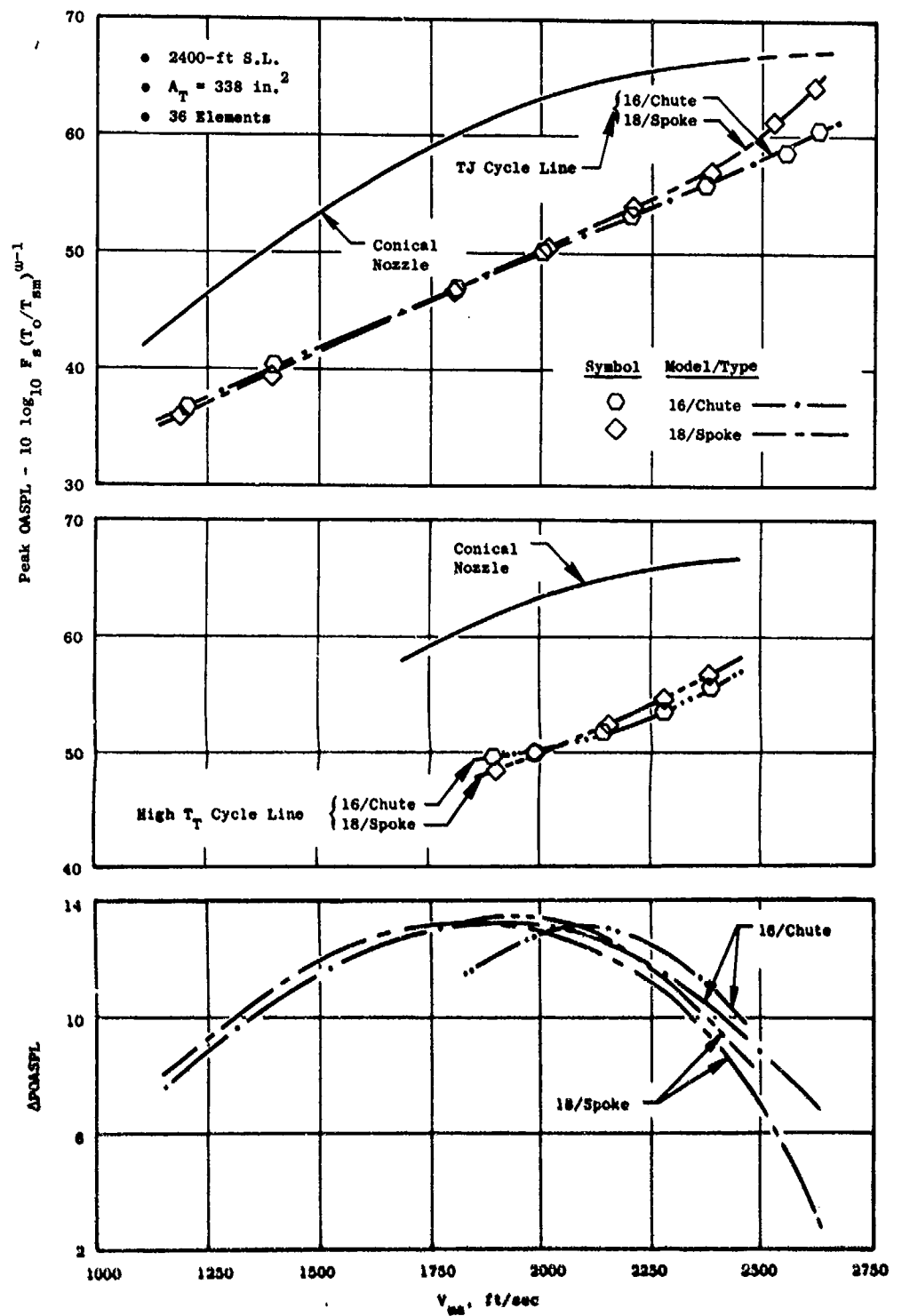


Figure 3-215. Variation of Element Type, Turbojet, Peak OASPL and Suppression Levels.

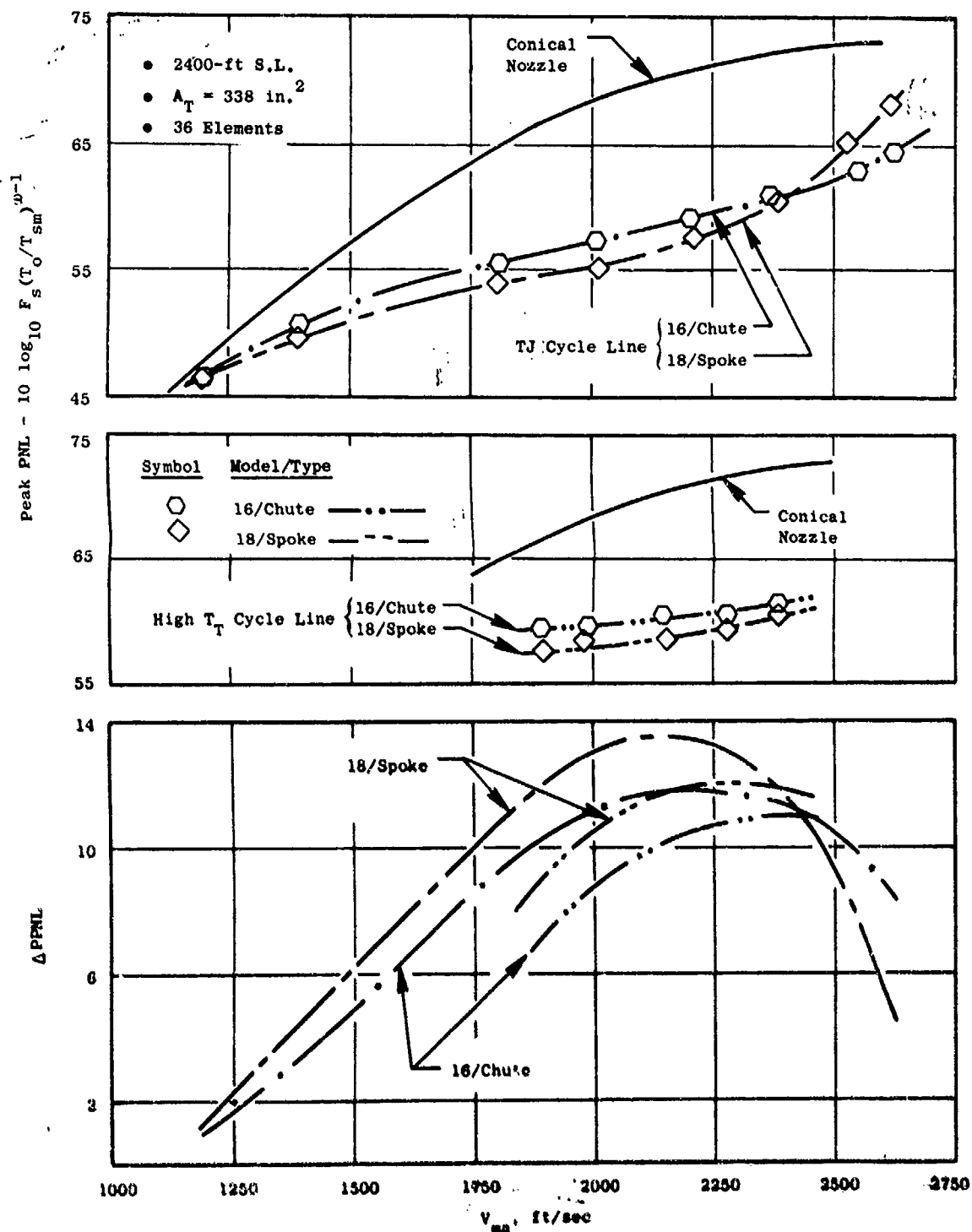


Figure 3-216. Variation of Element Type, Turbojet, Peak PNL and Suppression Levels.

- On the peak OASPL basis, the spokes and chutes are equivalent except at high velocity where the spokes become less effective than the chutes.
- In the high  $V_{ma}$  range, the spokes become substantially noisier than the chutes.

At 90°, Figure 3-217, spokes are more effective than chutes, from 1 to 2.5  $\Delta PNL$  in the mid- $V_{ma}$  range, and become equivalent to chutes at the highest  $V_{ma}$  tested.

At 50°, Figure 3-218, results show that effectiveness of element type is more dependent on cycle line, the high  $T_T$  cycle line showing equivalence of spoke/chute and the conventional turbojet cycle line showing the spokes significantly more effective on a PNL basis.

On an overall power level basis, Figure 3-219, trends are the same as for peak PNL, showing spokes superior at mid- $V_{ma}$ , then equivalent to or poorer than chutes at high  $V_{ma}$ .

Primary areas of interest on a PNL and OASPL directivity and spectral distribution basis are presented in:

Figure 3-220 OASPL and PNL vs  $\theta$  at  $V_{ma} = 2380$  ft/sec

Figure 3-221 Spectra at 50, 90 and 130° at  $V_{ma} = 2380$  ft/sec

Figure 3-222 OASPL and PNL vs  $\theta$  at  $V_{ma} = 2620$  ft/sec

Figure 3-223 Spectra at 50, 90 and 130° at  $V_{ma} = 2620$  ft/sec

The above two data sets exemplify the distinct difference in suppression characteristics at mid and high velocity points.

For the first set at 2380 ft/sec, the OASPL distributions are similar at all angles, particularly broadside and in the aft quadrant, while PNL is similar at peak and aft, but much lower for the spoke in the forward quadrant. The 130° spectra bear out similar frequency distribution; but at 90° and 50°, the high frequency levels of the chute are much more predominant. Distribution and level suggest a broadband shock cell noise influence at this highly supercritical pressure ratio of 3.28.

At the higher  $V_{ma} = 2620$  ft/sec data point, PNL and OASPL distributions are similar for the spoke and chute except near peak angle and in the far forward quadrant, where the spoke is now noisier than the chute. At 130° the spectra suggest this is a low frequency jet mixing noise phenomena; and at 50°, the difference is primarily in higher frequency bands, again associated with shock-cell noise at this high pressure ratio of 3.92.

As in the previous spectra at lower  $V_{ma}$ , shock-noise was present for only one of the designs (not the same one), suggesting a phenomena associated

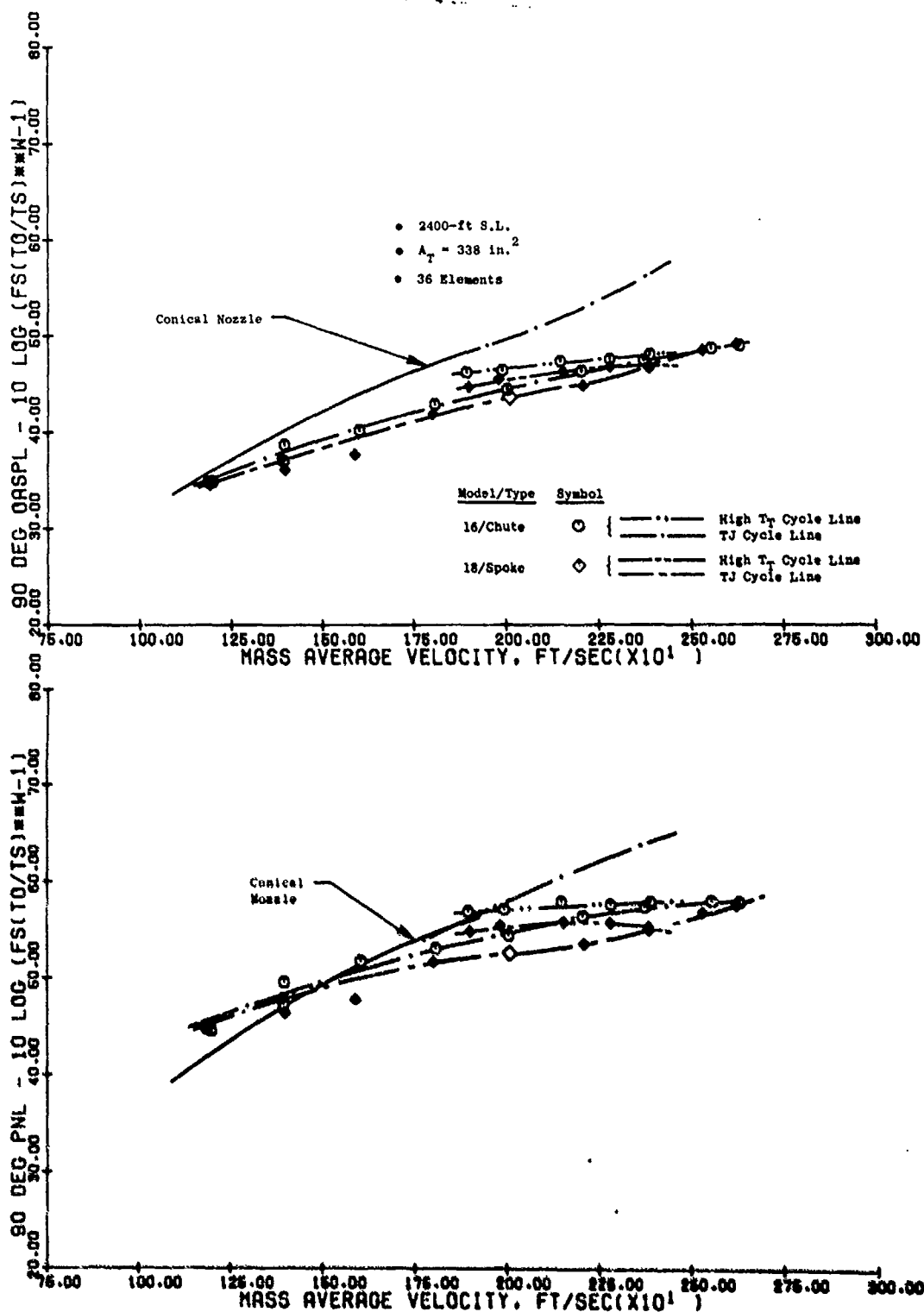


Figure 3-217. Variation of Element Type, Turbojet, 90° OASPL and PNL.

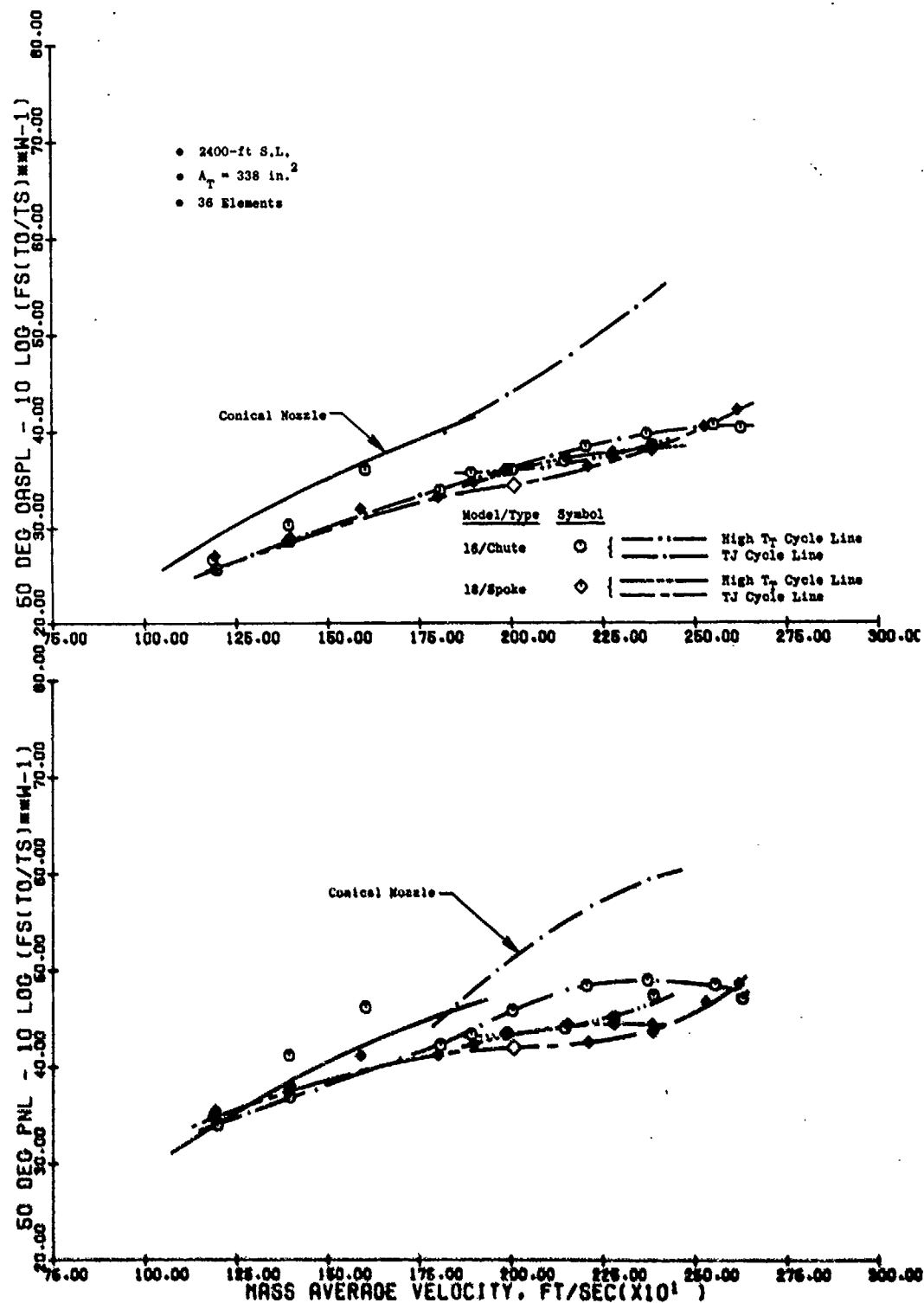


Figure 3-218. Variation of Element Type, Turbojet, 50° OASPL and PNL.

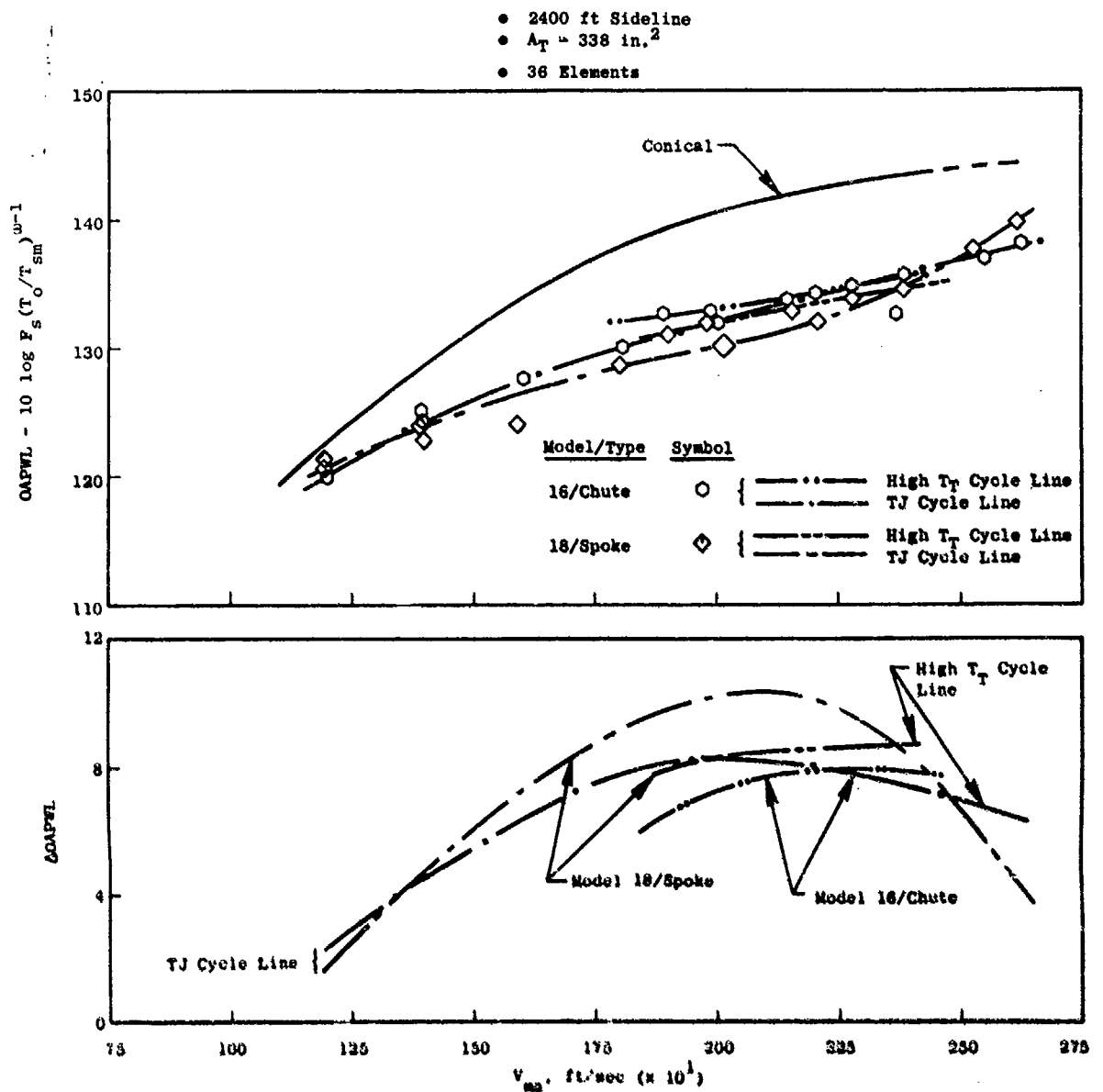


Figure 3-219. Variation of Element Type, Turbojet, OAPWL and Suppression Levels.



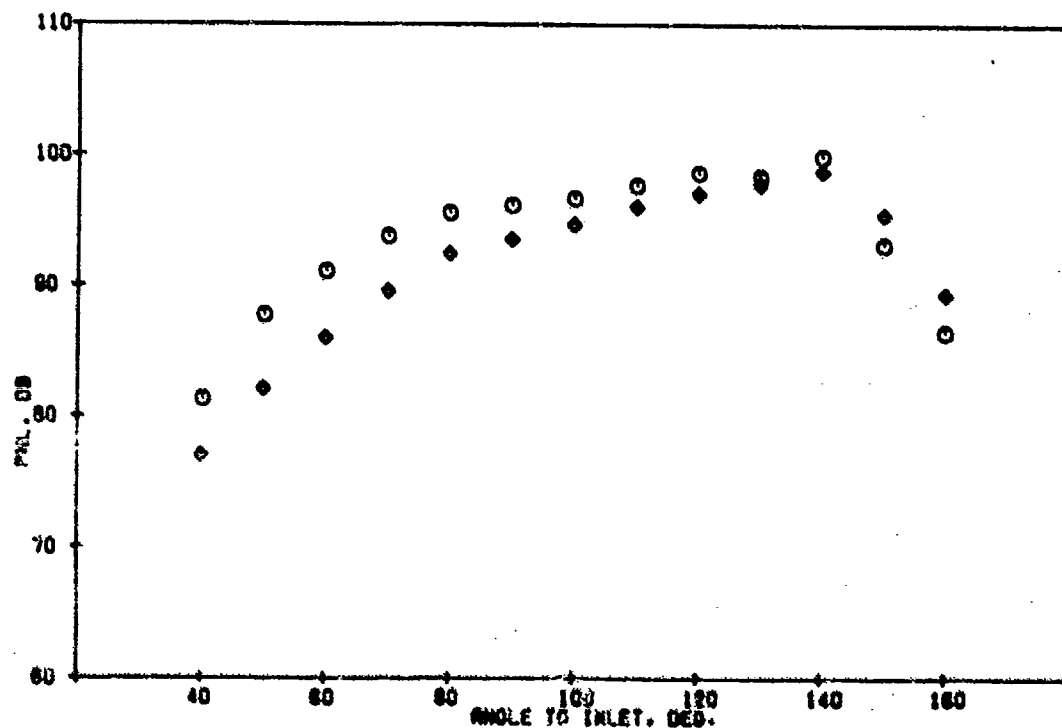
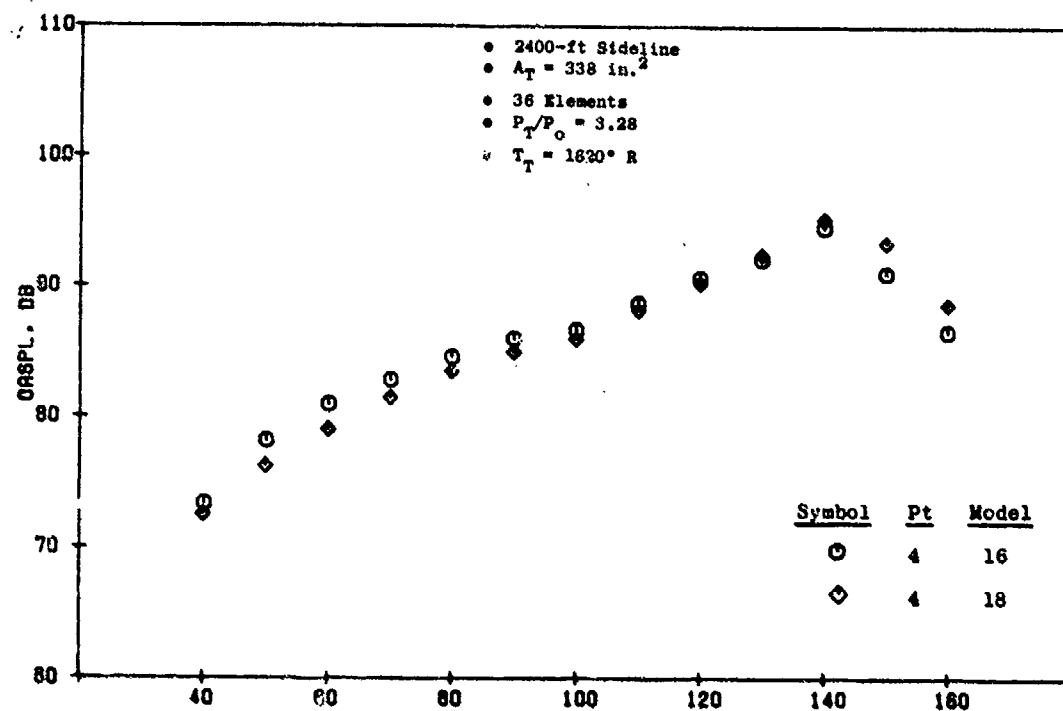


Figure 3-220. Variation of Element Type, Turbojet, CASPL and PNL Directivity,  $V_{in} = 2380 \text{ ft/sec.}$

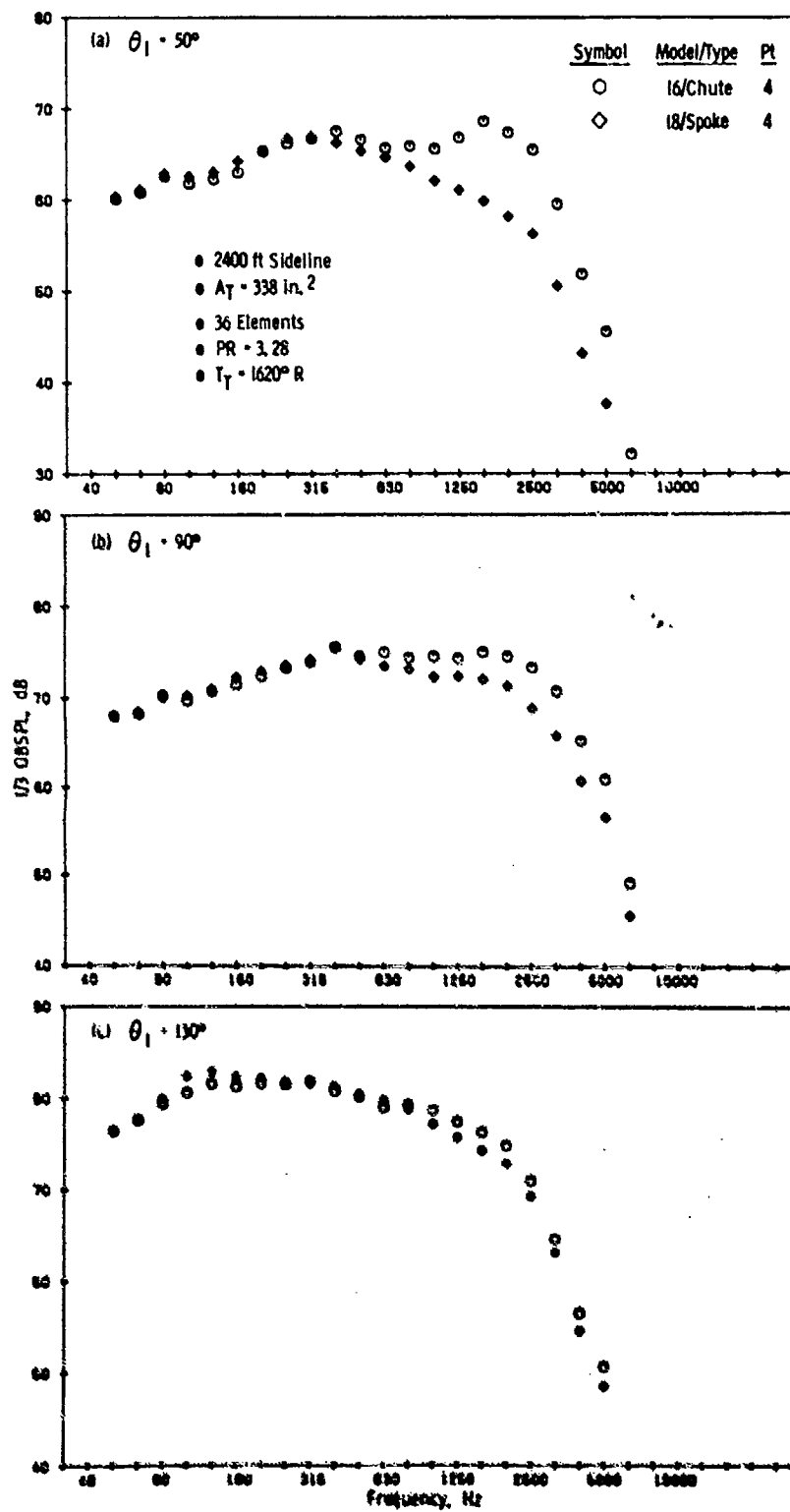


Figure 3-221. Variation of Element Type, Turbo-jet, Spectra,  $V_{max} = 2380 \text{ ft/sec.}$

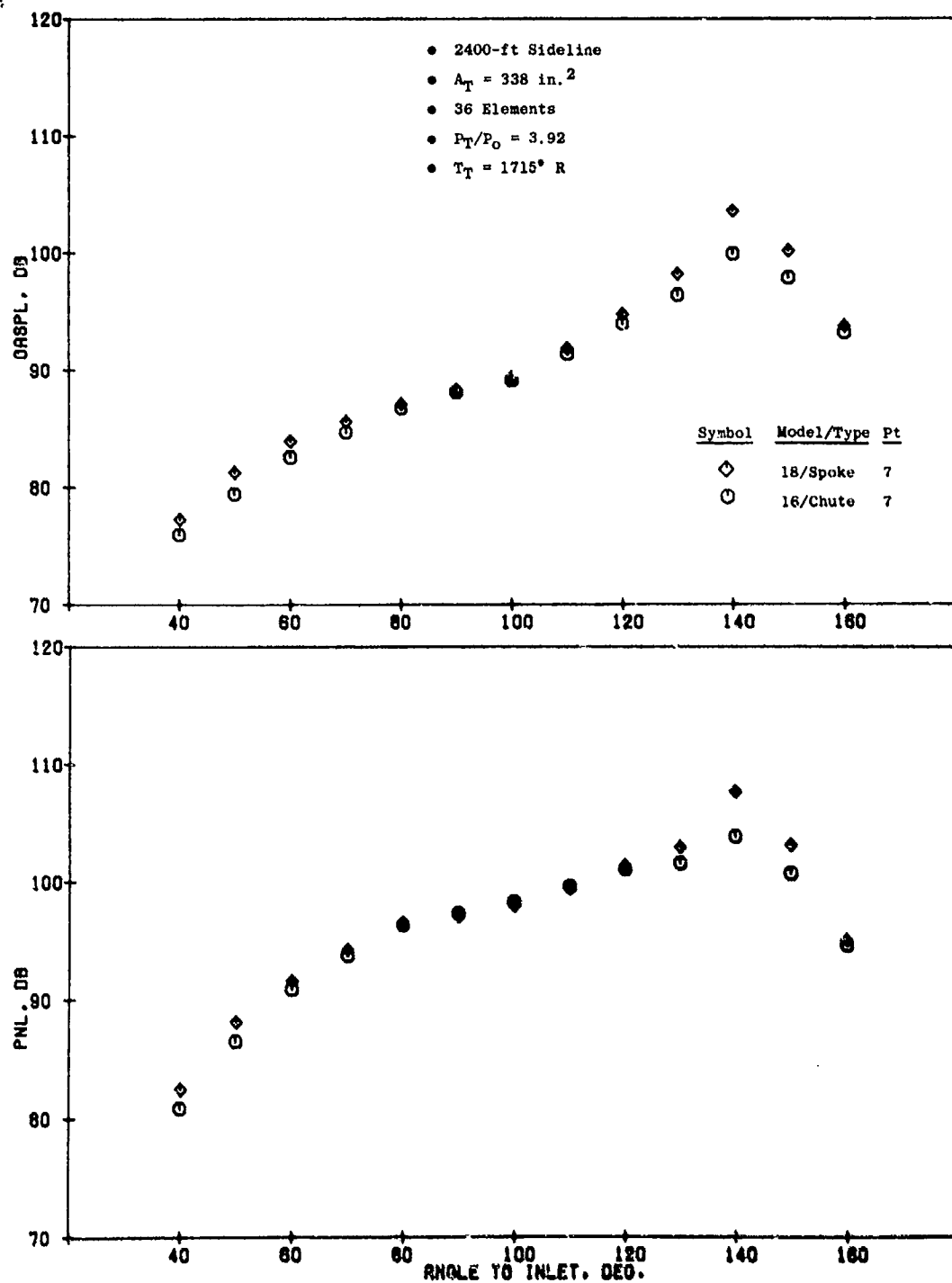


Figure 3-222. Variation of Element Type, Turbojet, QASPL and PNL Directivity,  $V_{ma} = 2620 \text{ ft/sec.}$

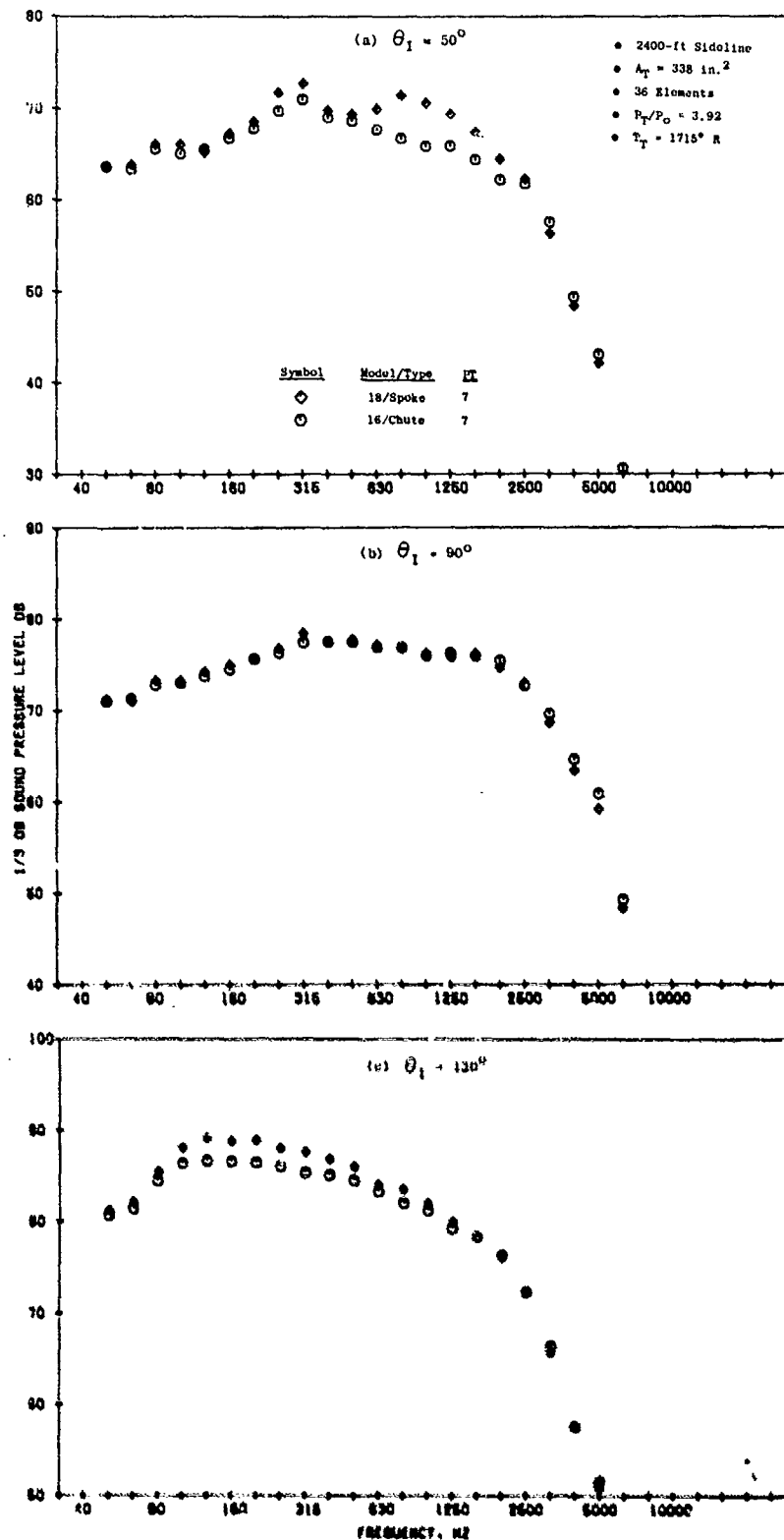


Figure 3-223. Variation of Element Type, Turbojet, Spectra,  $V_{ms} = 2620 \text{ ft/sec.}$

with the large variance in ventilation capability and its resultant impact on mixing potential and base pressurization, effecting the potential to generate strong shock-cell noise.

#### Element Type Study - Dual Flow of High System Area Ratio

This study extended investigation of varying element type from the deeply ventilated chutes to nonventilated spokes, but now on a dual flow nozzle with system area ratio of 1.92. Models 24 and 28 were used, Figure 3-224 photo and details in Appendix A, Figures 18 and 22. Model 24 was similar to Model 16 of the previous study in that the annular suppressor has 36 elements,  $AR = 2.0$  and  $RQ = 0.716$ . Model 24 has a core plug of 0.7" annulus height located in the retracted position. Model 28 used the same filler inserts as Model 18 to convert the base chute model to the spoke configuration.

The acoustic test matrix for these dual flow models was per Section 3.2.1, Figure 3-10 and Table 3-3, using the following cycle lines:

- $W_1 = 0, 15$  and  $30\% W_0$
- DBTF/Inverted Dual Flow
- AST/VCE

The following study results are included, selected from the DBTF/Inverted Dual Flow and  $W_1 = 30\% W_0$  cycle lines and are representative of overall cycle trends:

- Figure 3-225 Peak PNL
- Figure 3-226 Peak OASPL
- Figure 3-227  $90^\circ$  OASPL and PNL
- Figure 3-228  $50^\circ$  OASPL and PNL

Review of the data indicates:

- On the basis of peak OASPL, Figure 3-226, spokes attain a maximum suppression level slightly greater than 12 dB; approximately 3 dB higher suppression than the chutes. This maximum suppression level is slightly under the 3.5  $\Delta$ POSPL attained on Model 18 spoke/turbojet system; however, peak suppression levels on both turbojet and dual flow systems are attained by spokes.
- A significant margin of better performance by the spokes is observed for the dual-flow system over the test velocity range. This is contrary to the results of the turbojet application, where spokes and chutes were essentially equivalent except at high  $V_{ma}$  where spokes became somewhat less effective than chutes.

- Area Ratio = 2.0
- Radius Ratio = 0.716

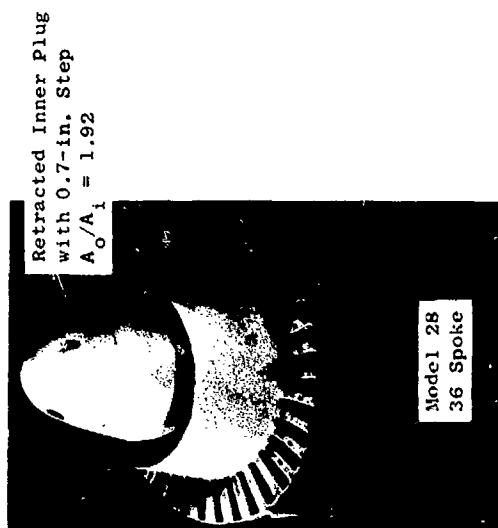
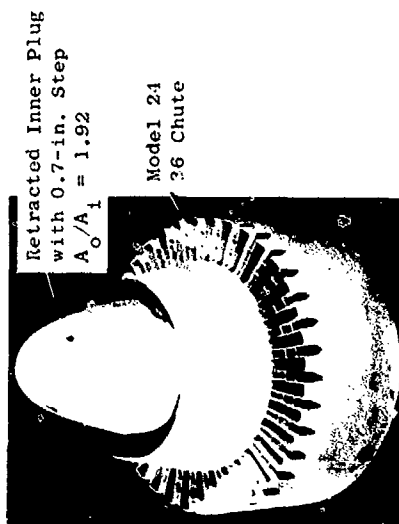
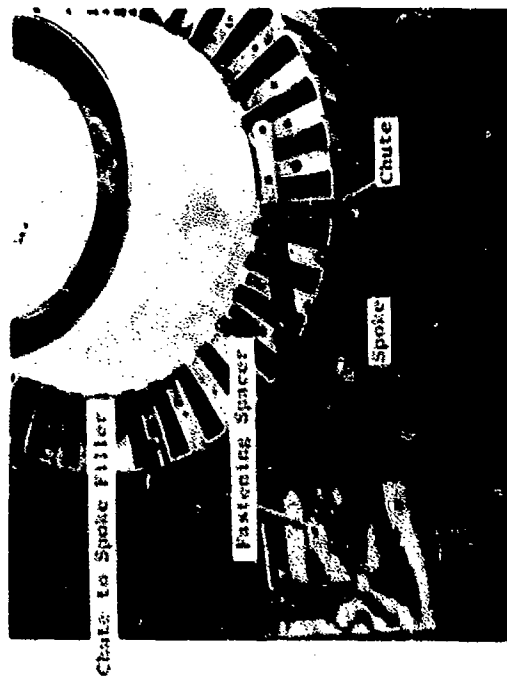


Figure 3-224. Conversion of Half-Span Suppressor from Chutes to Spokes.

- 2400-ft Sideline
- $A_T = 338 \text{ in.}^2$
- 36 Elements

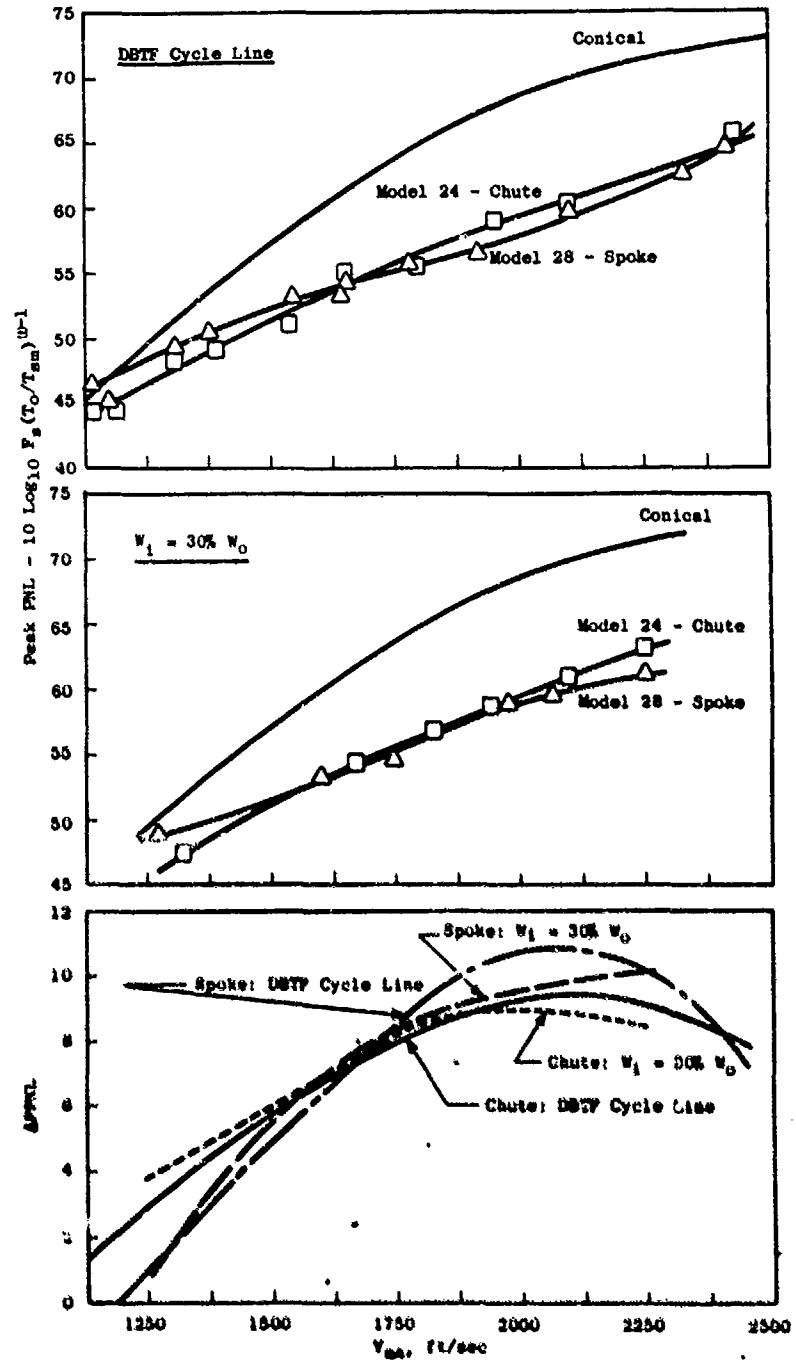


Figure 3-225. Element Type Variation, Dual Flow, Peak PNL and Suppression Levels.

- 2400-ft Sideline
- $A_T = 338 \text{ in.}^2$
- 36 Elements

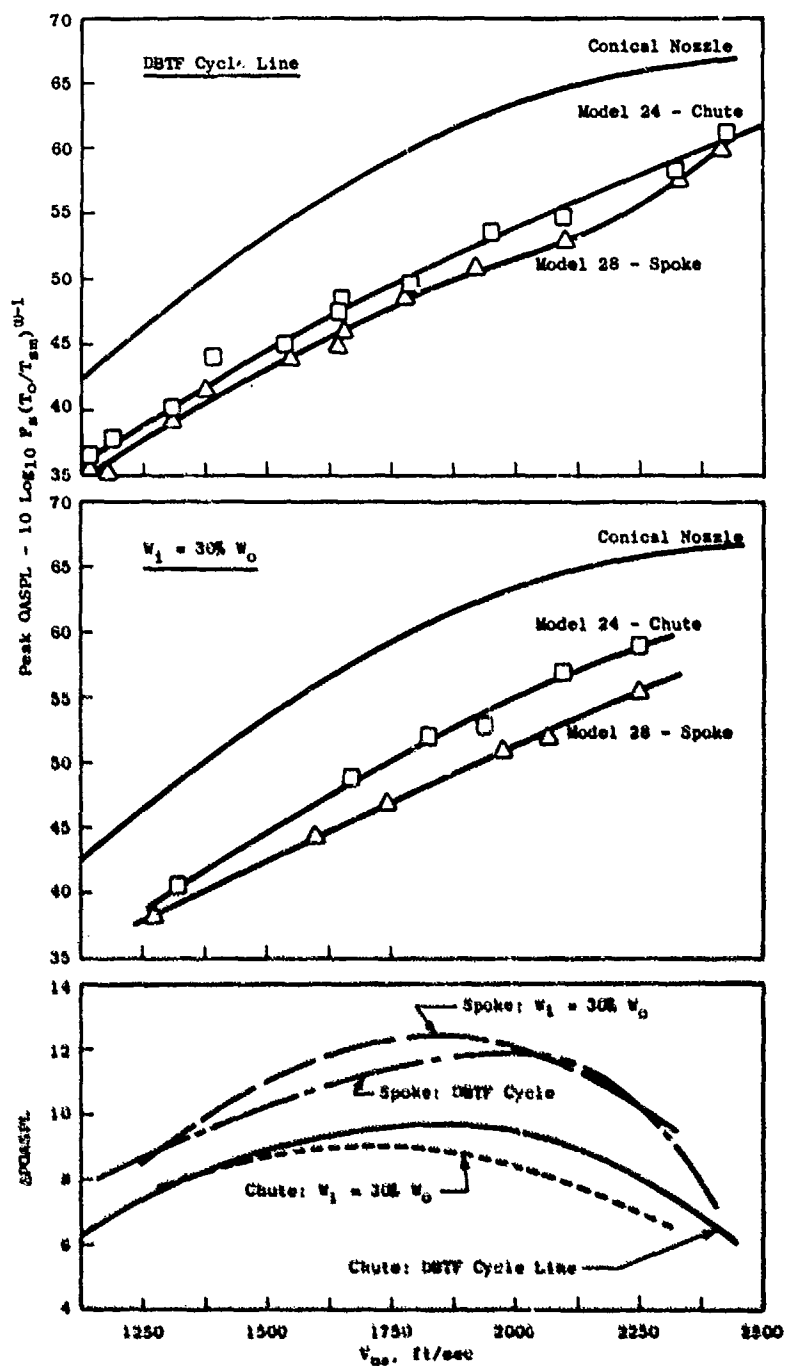


Figure 3-226. Element Type Variations, Dual Flow, Peak PNL and Suppression Levels.



- 2400-ft Sideline
- $A_T = 338 \text{ in.}^2$
- 36 Elements

- Model 24 - Chute
- △ Model 28 - Spoke

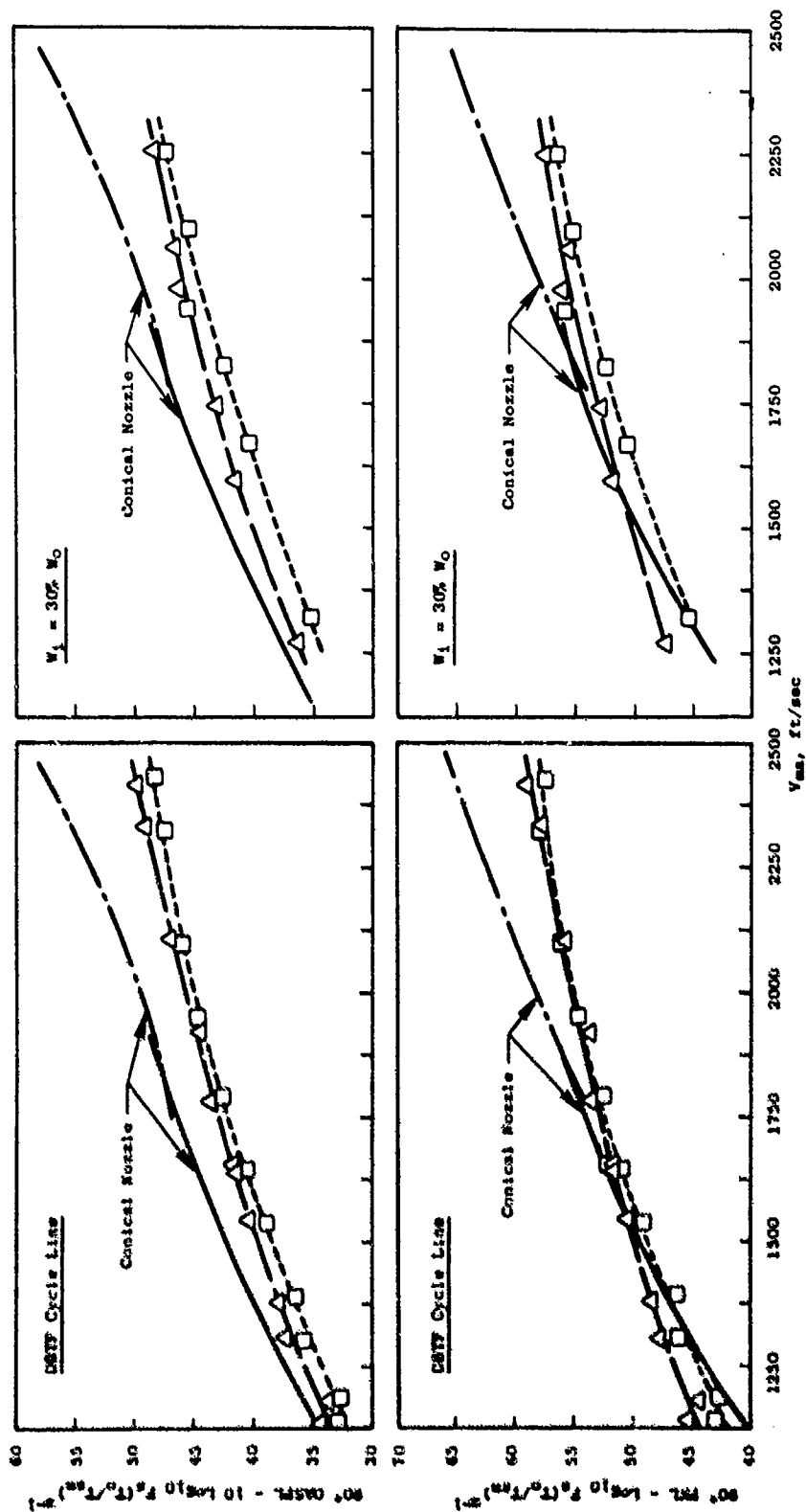


Figure 3-227. Element Type Variation, Dual Flow, 90° OASPL and PNL.

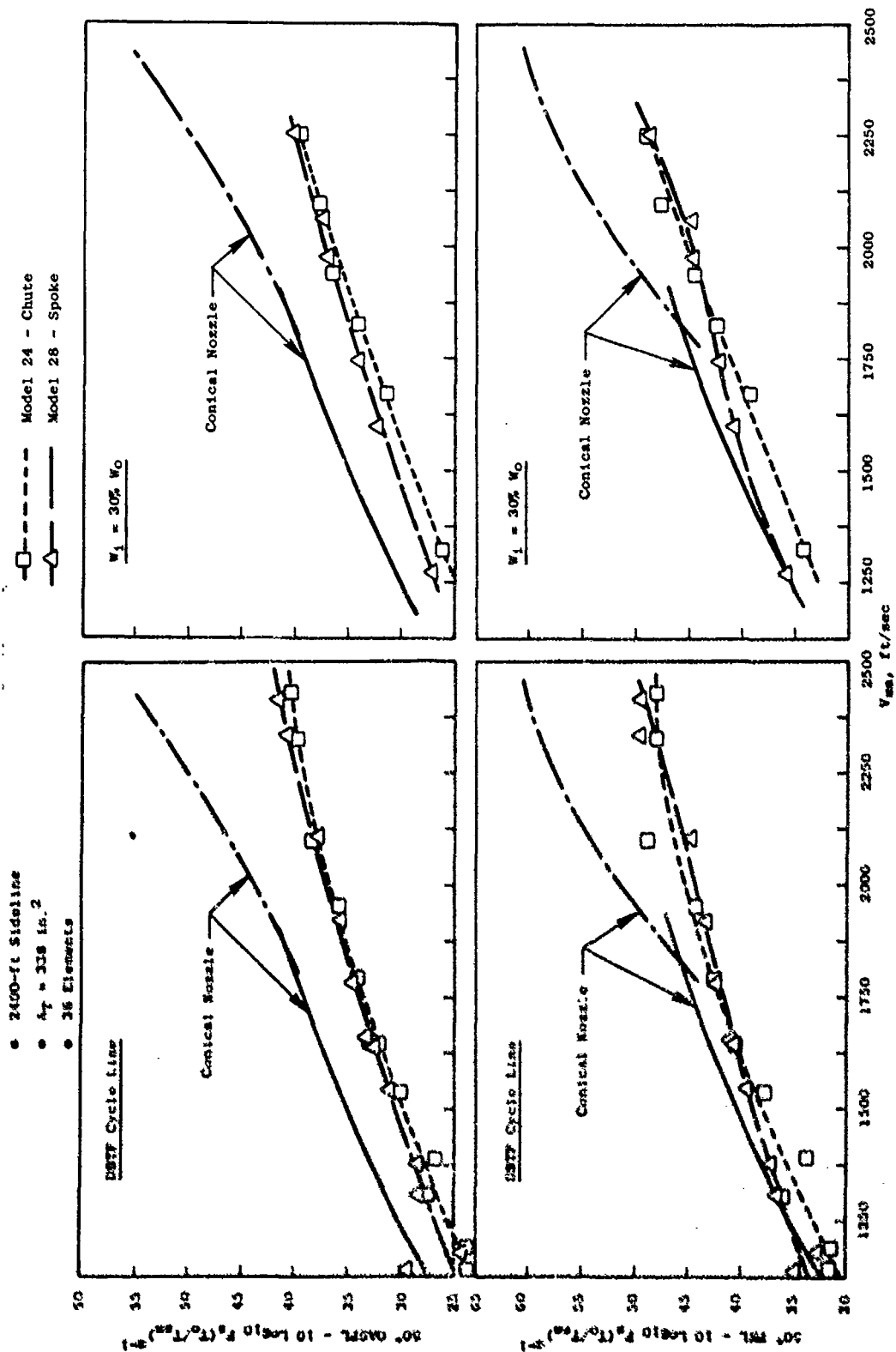


Figure 3-228. Element Type Variation, Dual Flow, 50° OASPL and PNL.

- On the basis of peak PNL, Figure 3-225, a maximum suppression level of about 10.5 dB is observed, which is significantly less than the 13.5 APPNL attained by turbojet spokes. In the mid-to-high velocity range, the spokes are from 0.5 to 1.5 dB more effective than chutes for either cycle line presented. The span of increased effectiveness of the spokes is not observed, as it was for the spoke/chute-turbojet systems. At lower velocity and chutes (Model 24) are slightly more effective than the spokes (Model 28).
- Review of the 90 and 50° data, Figures 3-227 and 3-228, shows in most instances that the spoke loses its performance edge and is either equivalent to or somewhat noisier than the chutes. This again is somewhat dissimilar to the turbojet application where spokes retained significant suppression advantage at broadside and forward quadrant angles.

#### Element Type Study - Dual Flow of Low System Area Ratio

This third study of element type variation compares deeply-ventilated chutes to nonventilated spokes, on a dual flow system of  $A_0/A_1 = 0.65$ . Models 33 and 35 were used (Figure 3-229) and detailed schematics of Appendix A Figures 27 and 29 show chute and spoke nozzles, respectively. Model 33 of suppressor area ratio = 2.5, from the NASA-Lewis/GE Duct Burning Turbofan Program, NAS3-18008, (Reference 10) was adapted to the Cell 41 Anechoic Facility. Model 35 converted Model 33 to nonventilated spokes through application of filler inserts, maintaining the same inner flowpath geometry. Pertinent parameters for the models are:

Model No.	El. No & Type	Outer			Inner				
		Flow Area, in. <sup>2</sup>	Area Ratio	Radius Ratio	Flow Area, in. <sup>2</sup>	Step Height, in.	Plug Location	Radius Ratio	System Area Ratio
33	36 Chute	17.21	2.5	0.783	11.12	1.034	Retracted	0.674	0.65
35	36 Spoke	17.21	2.5	0.783	11.12	1.034	Retracted	0.674	0.65

Far-field acoustic testing was performed in the Cell 41 Anechoic Facility following a matrix similar to Section 3.2.1, Figure 3-10 and Table 3-3, but expanded to be more consistent with the matrix of the Reference 10 DBTF program. The following cycle series was used:

- $W_1 = 0, 15 \text{ and } 30\% W_0$
- DBTF/Inverted Dual Flow Cycle
- AST/VCE

- 36 Elements
- Area Ratio = 2.5
- Radius Ratio = 0.783

Retracted Inner Plug  
with 1.03-in. Step  
 $A_0/A_1 = 0.65$

Model 33  
36 Chute

Model 35  
36 Spoke

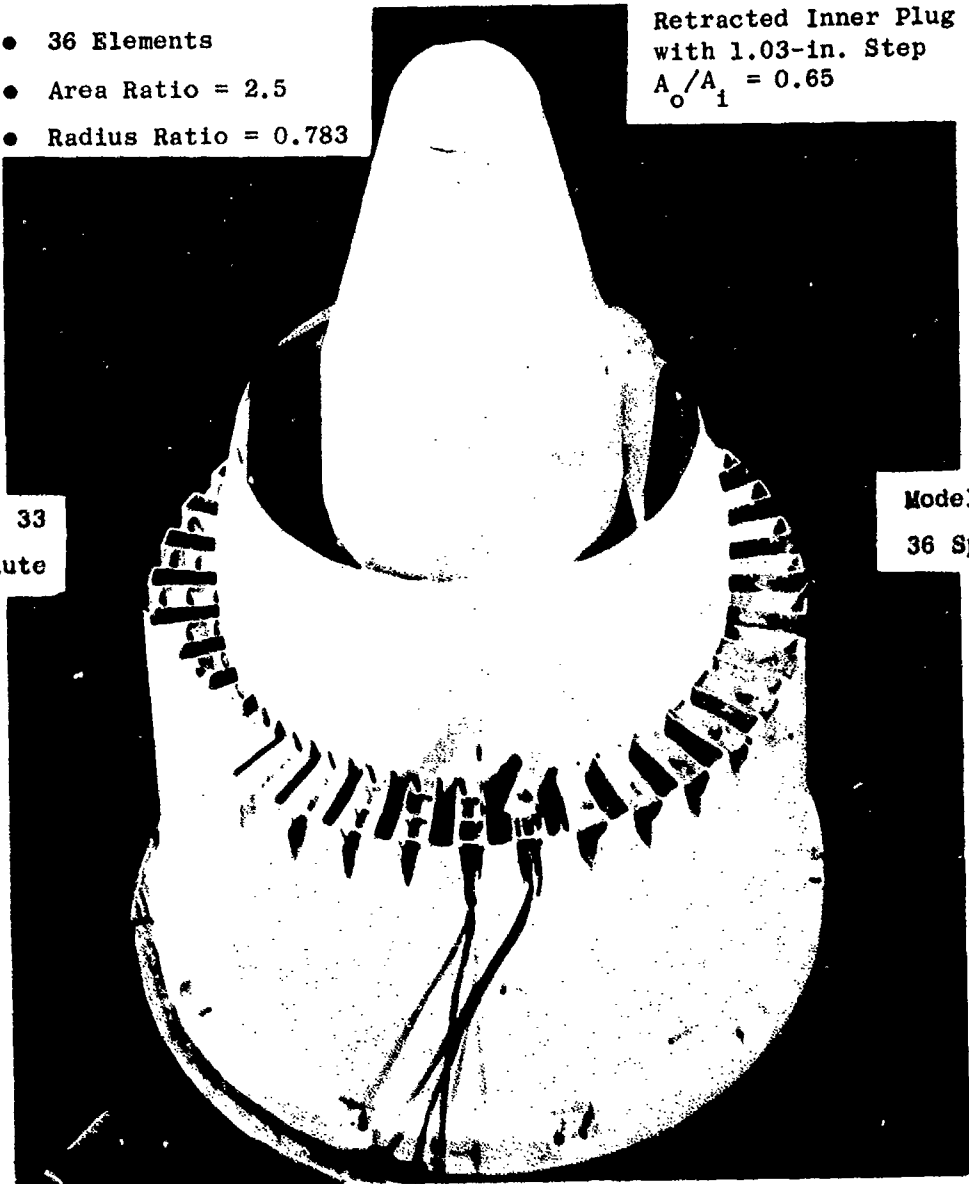


Figure 3-229. Element Type Variation, Dual Flow, Low System Area Ratio.

Primary acoustic data for the two models, tested within the DBTF/Inverted Dual Flow cycle matrix are presented and discussed in Section 3.4.2.2 (System Velocity Ratio Variation at Fixed  $A_0/A_1$  and Duct Suppressor Geometry). It is shown that noise levels for systems of low area ratio, e.g.  $A_0/A_1 = 0.65$ , vary widely with cycle velocity ratio,  $V_0/V_1$  the inner flow more strongly governs the overall system. Within this section, for isolation of suppressor element type impact on acoustic performance, comparisons between the two models at fixed values of  $V_0/V_1 = 0.6, 0.8, 1.0, 1.25, 1.5, 2.0$  and  $\infty$  (no inner flow) are included in Figure 3-230 for peak PNL and in Figure 3-231 for peak OASPL, selected to be representative of all test data.

For the peak PNL data, again, only minor variances are seen, particularly at low  $V_0/V_1$ . For  $V_0/V_1 \geq 1.5$ , a slight margin of better performance by 1 to 2.5  $\Delta$ PNL is seen for the spokes. On the previous study's spoke/chute application to a dual flow system of  $A_0/A_1 = 1.92$ , from mid-to-high  $V_{ma}$ , the spokes were also slightly better by 0.5 to 1.5  $\Delta$ PNL than the chutes. For the turbojet system at low-to-mid  $V_{ma}$ , the spokes were better than the chutes by approximately 2  $\Delta$ PNL at 2000 to 2200 ft/sec, but at high  $V_{ma}$ , the spokes become substantially noisier than their counterparts.

On the basis of peak OASPL, very little difference is seen between spokes and chutes for any  $V_0/V_1$  ratio; the small variance that exists shows no significant trend. If any distinctions had to be extracted from the data they would be: a) At low  $V_0/V_1$  the chute (Model 33) is slightly noisier than the spoke (Model 35), b) at intermediate values of  $V_0/V_1$  the two are near comparable with only a slight margin of better chute performance at high  $V_{ma}$ , and c) at the very high  $V_0/V_1$  the chute is normally about 1  $\Delta$ OASPL quieter. These results are compatible with those of the two previous studies where turbojet application showed spokes and chutes almost the same except for the small advantage by chutes at high  $V_{ma}$ , and dual flow application showed the spokes somewhat better at any  $V_{ma}$ .

With the small variance observed in suppression potential between deeply-ventilated chutes and nonventilated spokes, acoustic performance may not be the principle design consideration. Aerodynamic performance differences and mechanical implementation considerations will have a strong influence in the ultimate selection process. These aspects are discussed in Volume III.

#### 3.4.2.5 Treated Ejector Applications

##### Treated Ejector Application, Turbojet

The potential for additional noise reduction of annular suppressed jets was evaluated through application of an acoustically treated ejector to a basic turbojet propulsion nozzle. Models 16 and 19, as shown in Figure 3-232 and in the detailed schematics of Appendix A, Figures A-10 and A-19, were used. The basic Model 16 as described in Section 3.4.2.1 "Area Ratio and Radius Ratio Variable, Turbojet" consists of a 36-chute,  $AR = 2.0$ ,  $R_0^2 = 0.716$

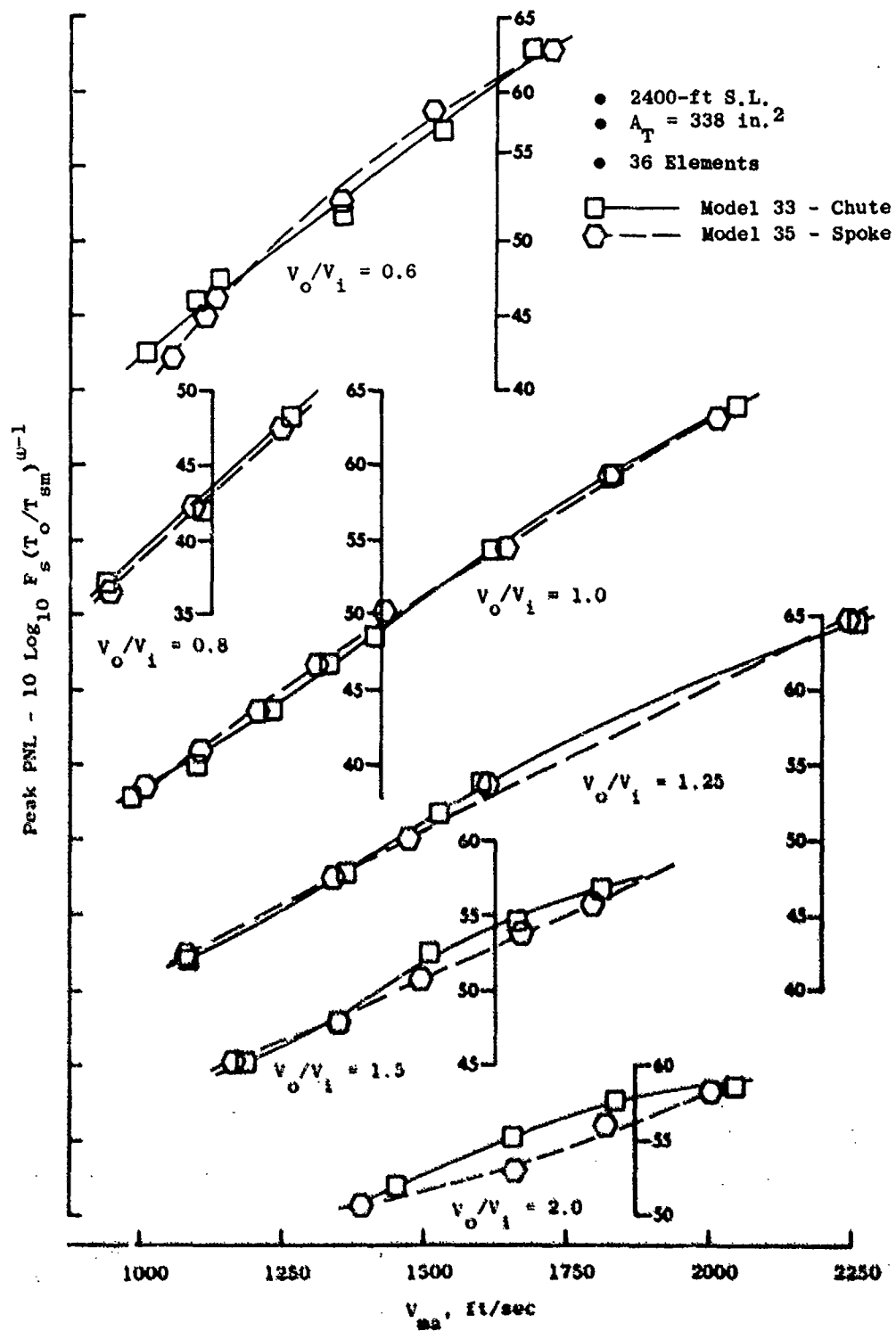


Figure 3-230. Element Type Study, Dual Flow, Low System Area Ratio, Peak PNL.

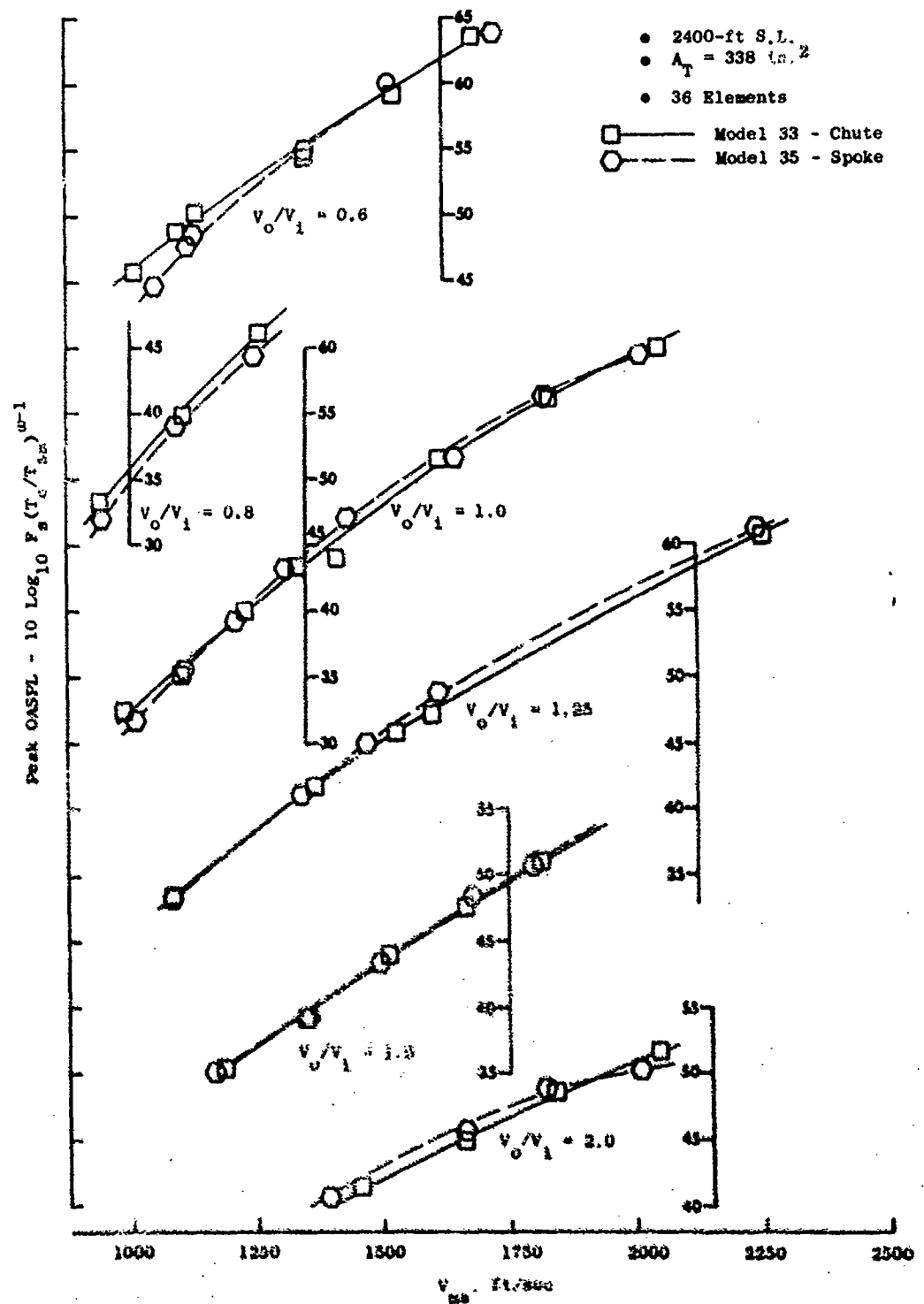


Figure 3-231. Element Type Study, Dual Flow, Low System Area Ratio, Peak QASPL.

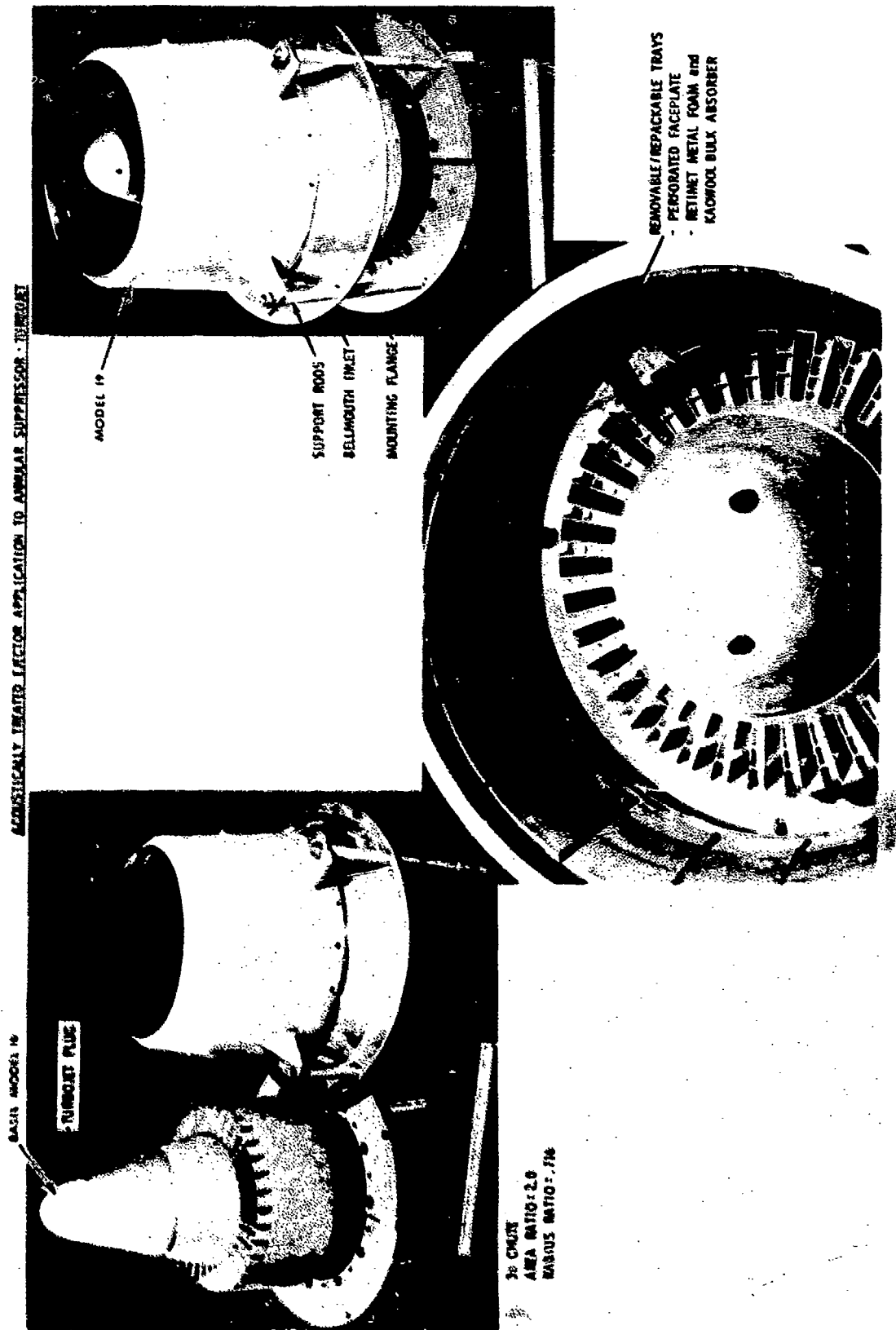


Figure 3-232. Acoustically treated ejector application to Annular Suppressor, Turbojet.



annular suppressor on a full-plug turbojet. The acoustic performance of the basic segmented suppressor was expected to be enhanced, partially due to physical shielding of the ejector shroud, but primarily due to energy absorption by the acoustic treatment within the wall. Highly segmented annular suppressors redistribute acoustic energy to the higher frequency range where it is more effectively absorbed by a broadband bulk absorbing material. The basic design of the high-radius-ratio annular plug nozzle positions the suppressor elements, and their accompanying segmented jet noise sources, within close proximity of the ejector treatment. Previous suppressed annular plug/treated ejector systems, Reference 4, were of low radius ratio design and possibly did not benefit from this feature.

The ejector's internal flow lines were designed for good aerodynamic performance, using Figure 3-1 and the guidelines of Reference 10 as follows:

- Ejector inlet diameter to suppressor shroud diameter ratio ( $D_{E1}/D_S$ ) of 1.11 was set, a fairly tight fitting ejector design.
- Ejector axial positioning was set by the ratio of offset spacing to suppressor shroud radius ( $X_S/R_S$ ) = 0.27; therefore,  $X_S$  = 1.5 in.
- Ejector length was established from practical system considerations and limitations, with ratio of ejector length to ejector inlet diameter ( $L_E/D_{E1}$ ) set at 0.75 therefore,  $L_E$  = 9.28 in.) This terminates the ejector near the center plug's tip.
- Ejector exit diameter ( $D_{Ee}$ ) was set by equating exit flow area to inlet flow area for proper flow filling within the ejector to prevent flow separation and base pressure loss. The inlet area considers ejector offset spacing and chute ventilation.

The acoustic treatment system design and material selections were based on a combination of approximate theoretical considerations and available experimental results. The bulk absorber material was selected to withstand high temperature in the nozzle exhaust environment and to have good acoustic absorption properties over a reasonably wide frequency range. Details of construction and packing of the ejector system are shown in Figure 3-233. Removable/repackable trays were used so that the bulk absorber material could be refurbished if degradation occurred due to exposure to the highly turbulent environment. Construction details are as follows:

- Cavity depth was approximately 0.43 in, faced with 37% porous perforated sheet metal using 0.045-in.-diameter holes on a straight line pattern with 0.067 in. spacing between centers, 225 holes/in.<sup>2</sup>, 24 gage material.
- The cavity was lined with approximately 0.1-in. thick 95% porous RETIMET NiCr Metal Foam, 60-70 cgs Rayls, to protect the ceramic fiber absorber from degradation. The remaining cavity depth was packed with KAOWOOL, a ceramic refractory fiber bulk absorber,

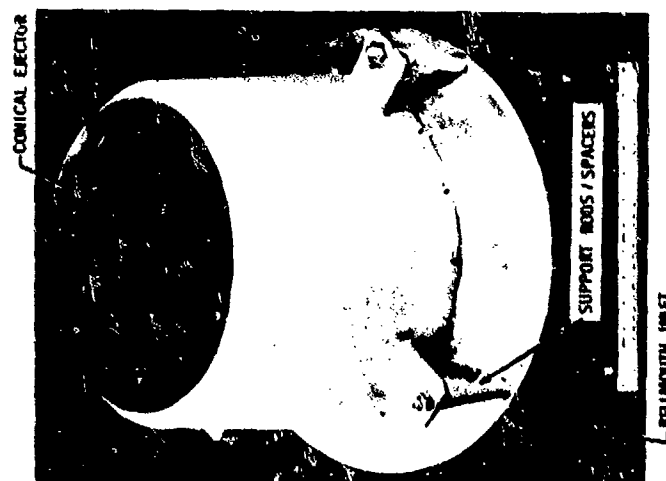
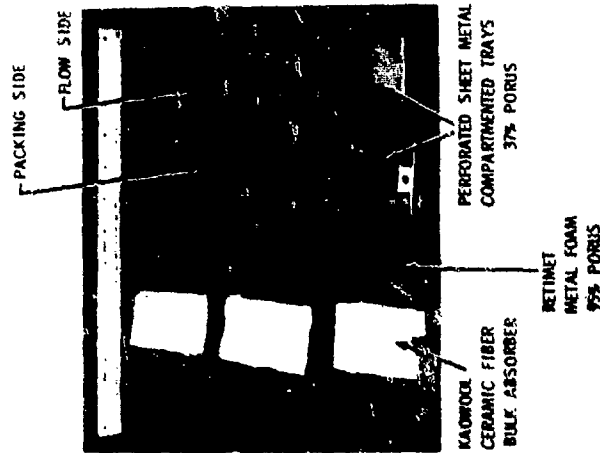
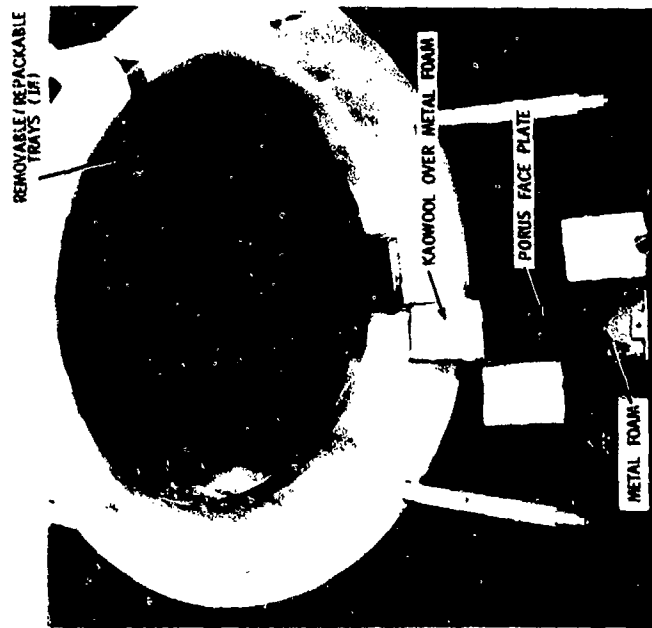


Figure 3-233. Details of the Acoustically Treated Ejector.

compressed to 3 lb/ft<sup>3</sup> density. The material has good absorption and insulation characteristics and is capable of sustained use at 2300° R without devitrifying.

A contoured bellmouth inlet was used for the static acoustic tests to provide idealized flow to the ejector, thus eliminating the possibility of an extraneous noise source from flow separation around a sharp lip.

Acoustic tests were performed in the Cell 41 Anechoic Facility and followed the matrix of Section 3.2.1, Figure 3-8, using conventional and high  $T_T$  cycle lines.

Peak PNL acoustic results, Figure 3-234, are shown separately as applicable to the conventional turbojet and high  $T_T$  cycle lines, each relative to the conical baseline. The lower part of the graph shows the suppression level ( $\Delta$ PPNL) of Model 19 referenced first to the conical nozzle for overall system suppression level, then referenced to Model 16 for gaging the effectiveness of the treated ejector application. Similar data plots for peak OASPL are shown in Figure 3-235. It is observed that maximum suppression levels of 15.5  $\Delta$ PPNL and 11.5  $\Delta$ POASPL are achieved at  $V_{ma}$  ~2100 to 2200 ft/sec. Peak PNL suppression drops drastically above and below the maximum value, to 5  $\Delta$ PPNL at high  $V_{ma}$ , and 7 at low  $V_{ma}$ . On a peak noise basis, the ejector is very effective, accounting for 5.5  $\Delta$ PPNL and approximately 4  $\Delta$ POASPL at low  $V_{ma}$  and about 4  $\Delta$ PPNL and 2  $\Delta$ POASPL at mid- $V_{ma}$ . At highest  $V_{ma}$ , however, the suppression trend is actually reversed and the ejector application appears to generate greater noise than the nonejector system.

Comparing the turbojet cycle line to the high  $T_T$  cycle line, basic overall suppression levels relative to conical vary somewhat, particularly for  $\Delta$ PPNL at 1800 to 2100 ft/sec. However, suppression levels attributable to the ejector alone are reasonably consistent.

At 90°, Figure 3-236, the Model 19 system yields suppression at all velocity values. This system has a distinct advantage over the basic nonejector Model 16, particularly in the low and midvelocity region where the system exhibits noise levels comparable to, or higher than, the baseline. Suppression attributable to the ejector alone (plotted as Model 19 relative to Model 16) shows levels and trends of  $\Delta$ OASPL and  $\Delta$ PNL closely matching those at peak angle.

Figure 3-237, 50° OASPL and PNL data, shows significant levels of suppression with the ejector relative to the conical baseline at all jet velocities. Suppression attributable to the ejector is fairly well maintained even within the forward quadrant, particularly on a  $\Delta$ PNL basis in the low and midvelocity range. At high  $V_{ma}$  the loss of suppression and/or some noise enhancement is seen, similar to what occurred at the peak noise angles.

The overall power level data of Figure 3-238 show trends and ejector levels of effectiveness paralleling those of the PPNL data. Low and mid-velocities show significant noise reduction relative to the basic system; high-velocity suppression is negated and/or shows noise enhancement.

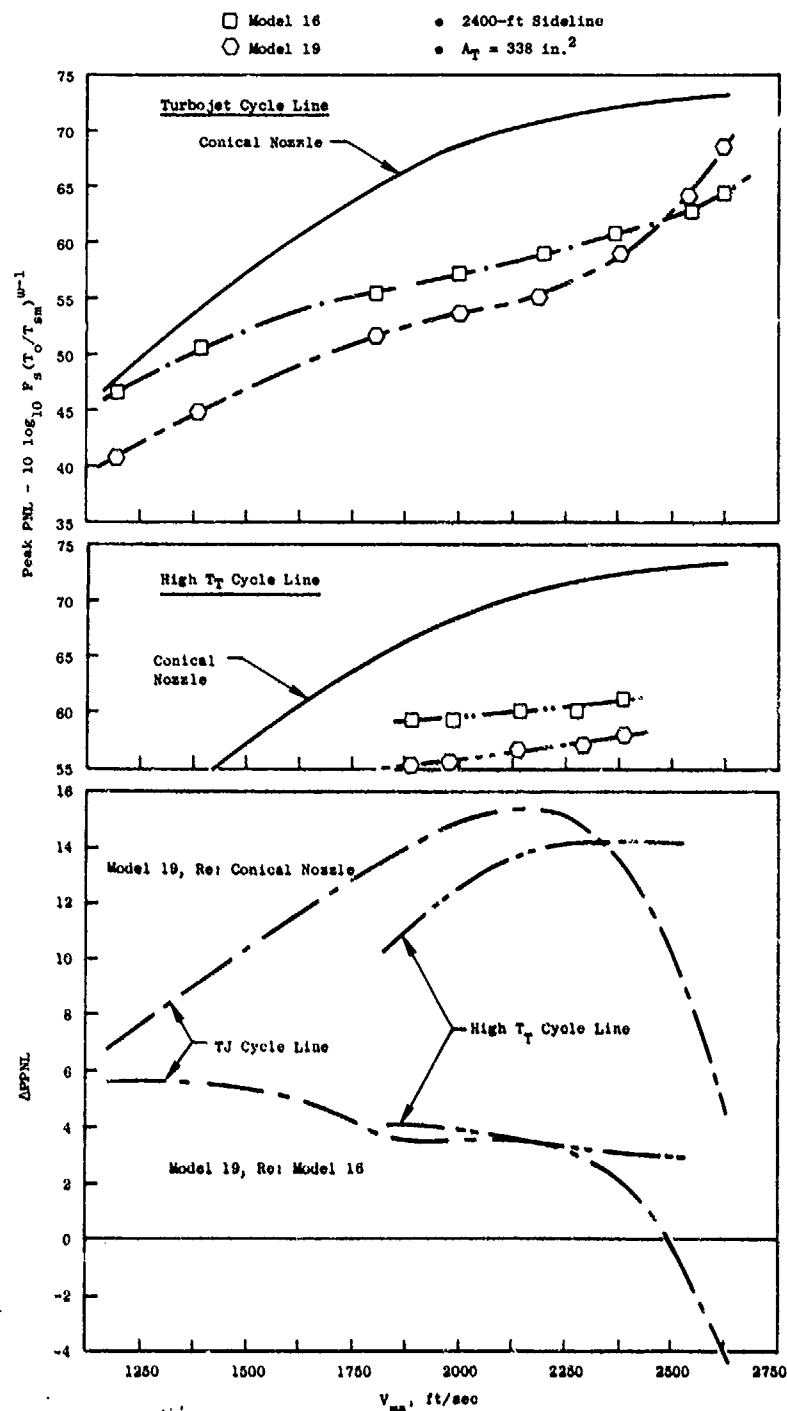


Figure 3-234. Impact of Acoustically Treated Ejector, Turbojet, Peak PNL.

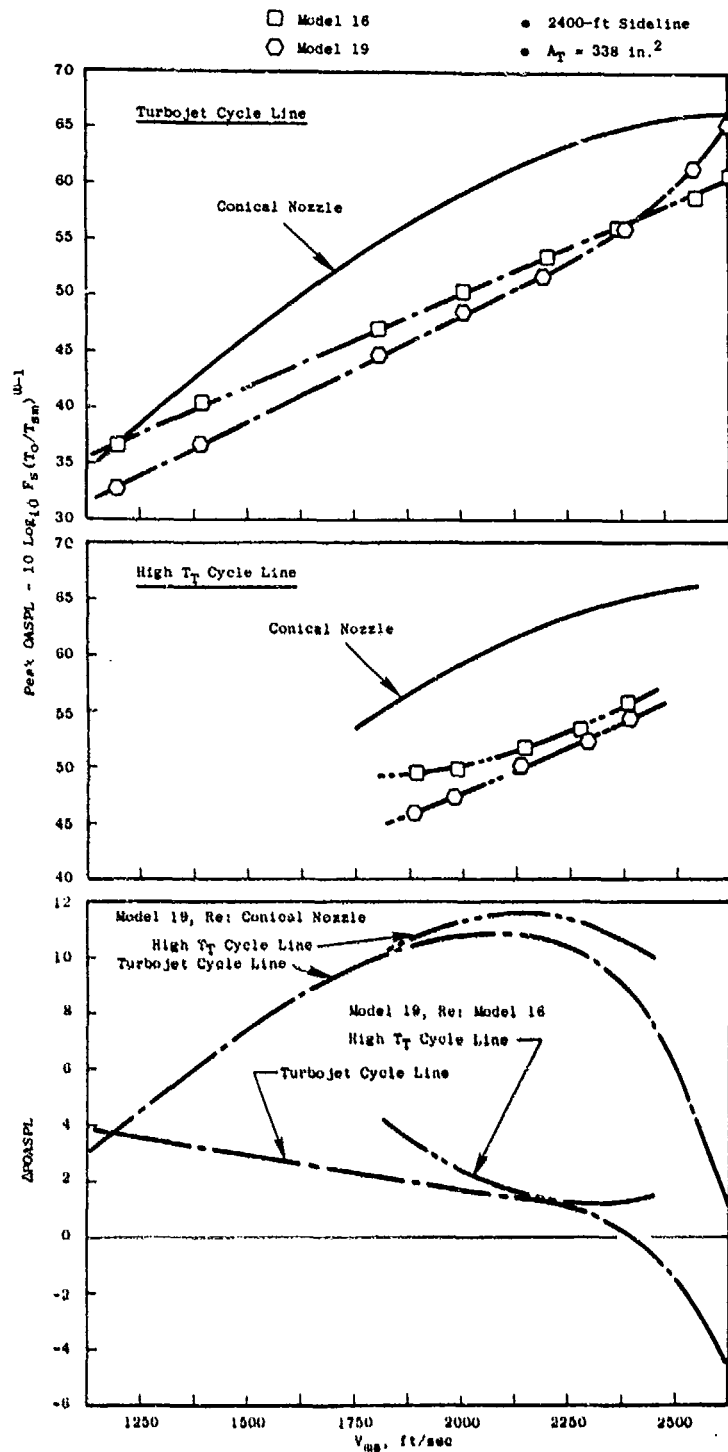


Figure 3-235. Impact of Acoustically Treated Ejector, Turbojet, Peak QASPL.

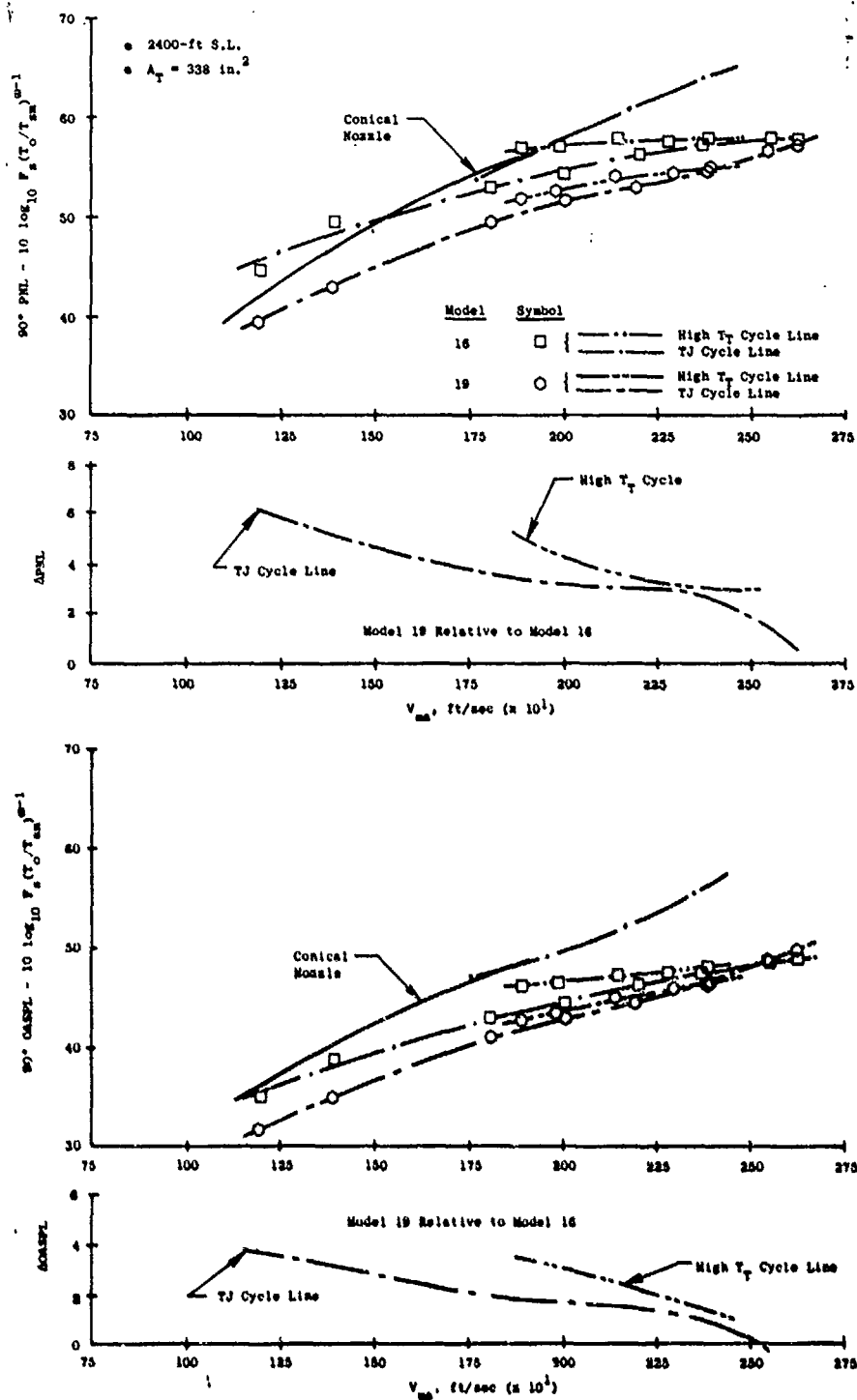


Figure 3-236. Impact of Acoustically Treated Ejector, Turbojet, 90° OASPL, PNL, and Suppression Levels.

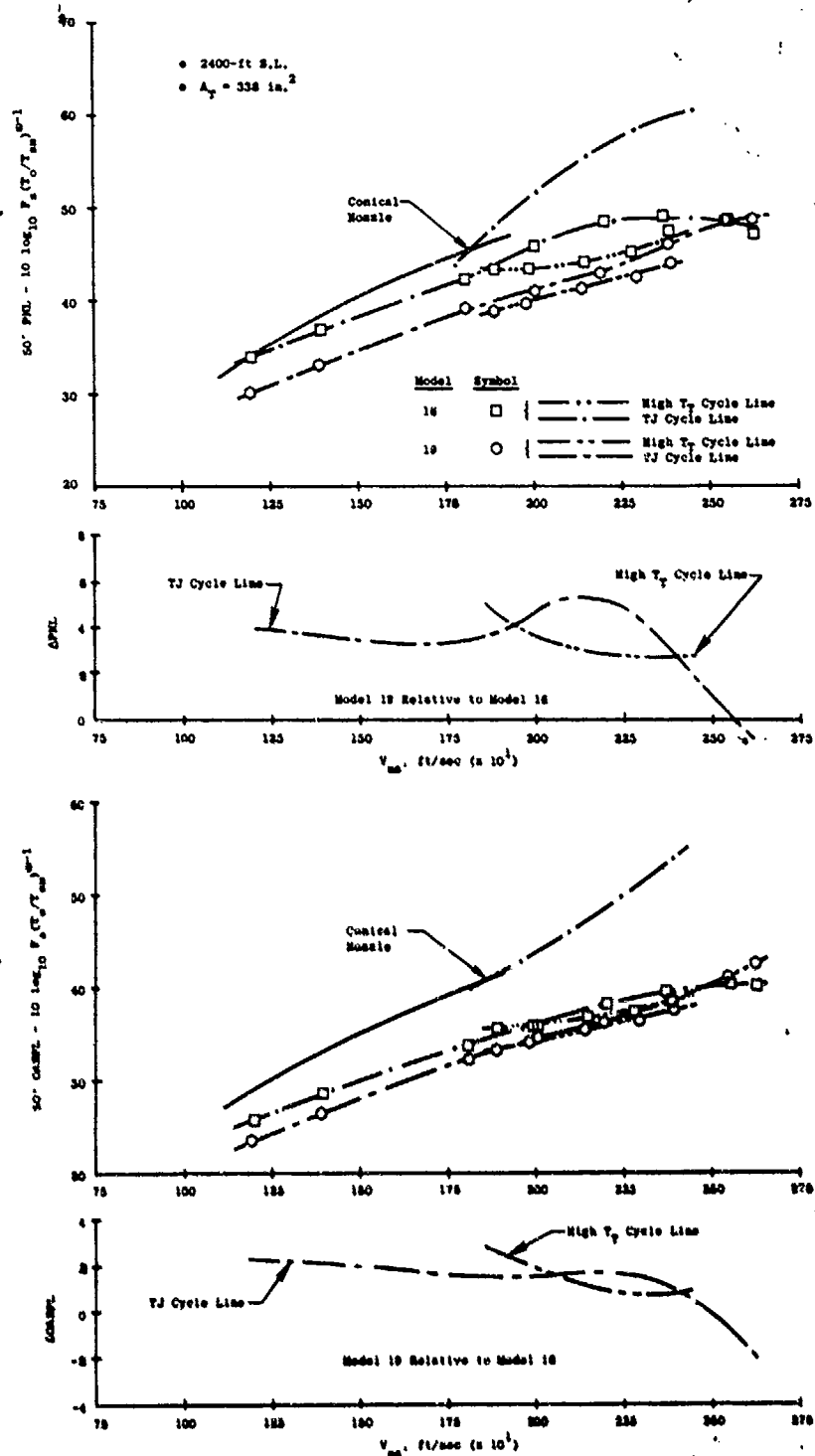


Figure 3-237. Impact of Acoustically Treated Ejector, Turbojet, 50° OASPL, PNL, and Suppression Levels.

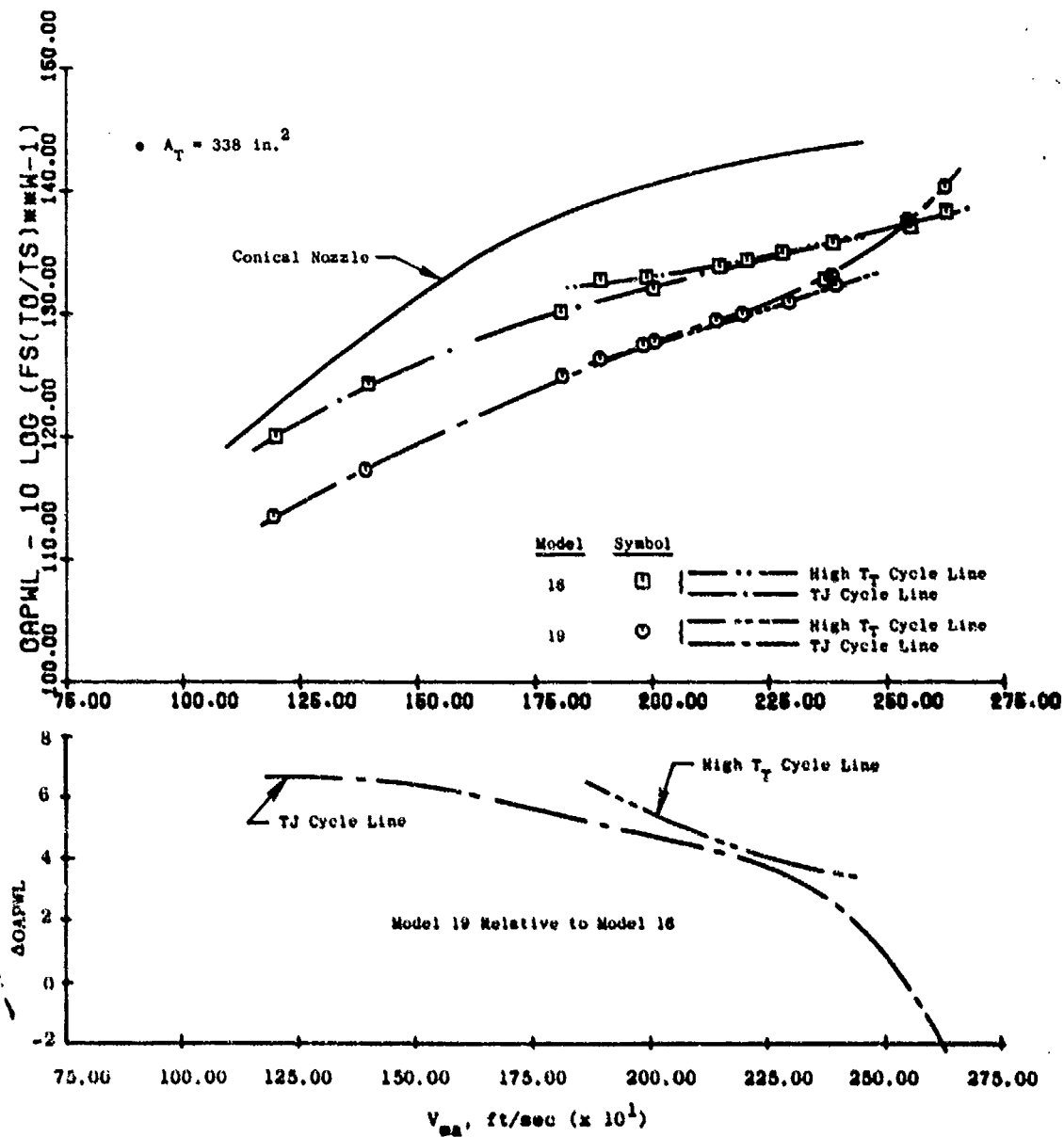


Figure 3-238. Impact of Acoustically Treated Ejector, Turbojet, OAPWL and Suppression Levels.



The following are included for a closer look at noise distribution with angle and at spectral composition.

- Figure 3-239 OASPL and PNL distributions at  $V_{ma} \approx 2000$  ft/sec
- Figure 3-240 Spectra at select angles at  $V_{ma} \approx 2000$  ft/sec
- Figure 3-241 OASPL and PNL distribution at  $V_{ma} \approx 2625$  ft/sec
- Figure 3-242 Spectra at selected angles at  $V_{ma} \approx 2625$  ft/sec

The first set of data at 2000 ft/sec reinforce the previous plots at peak,  $90^\circ$ , and  $50^\circ$ . Suppression of the total system is significant at all angles and suppression enhancement by application of the ejector is considerable in magnitude and fairly uniform for all angles. The spectra, Figure 3-240 illustrates that the significant change is in the high-frequency range, as anticipated.

Figure 3-241 and 3-242, at the high  $V_{ma} = 2625$  ft/sec point, also reinforce the trends seen in peak,  $90^\circ$ , and  $50^\circ$  plots; the noise levels are generally greater with the ejector applied. This is correct to some extent for all angles, but principally in the forward and aft quadrants. On a spectral basis, the higher levels exist primarily over the low and midfrequency ranges with a slight amount of high-frequency suppression still achieved by the acoustic treatment.

#### Treated Ejector Application, Dual flow

This study extends the previous section's investigation to a dual flow application. Model 24 is the base configuration (Figure 3-243 and Figure A-18 in Appendix A) and the same 36-chute,  $AR = 2.0$ ,  $R_f^0 = 0.716$  annular suppressor as the base turbojet Model 16, modified with a retracted inner plug in lieu of the full turbojet plug. The inner stream is an annulus with a step height of 0.7 in. and the system area ratio ( $A_0/A_1$ ) is 1.92. The same treated ejector as described in the previous section was applied (Figure 3-243 and Figure A-30 in Appendix A), maintaining axial spacing and ejector diameter to suppressor shroud diameter ratio (Model 36).

Acoustic testing in the Cell 41 Anechoic Facility followed the matrix of Section 3.2.1, Figure 3-10 and Table 3-3, using the cycle lines of:

- $W_1 = 15\% W_0$
- $W_1 = 30\% W_0$
- DBTF/Inverted Dual Flow
- AST/VCE

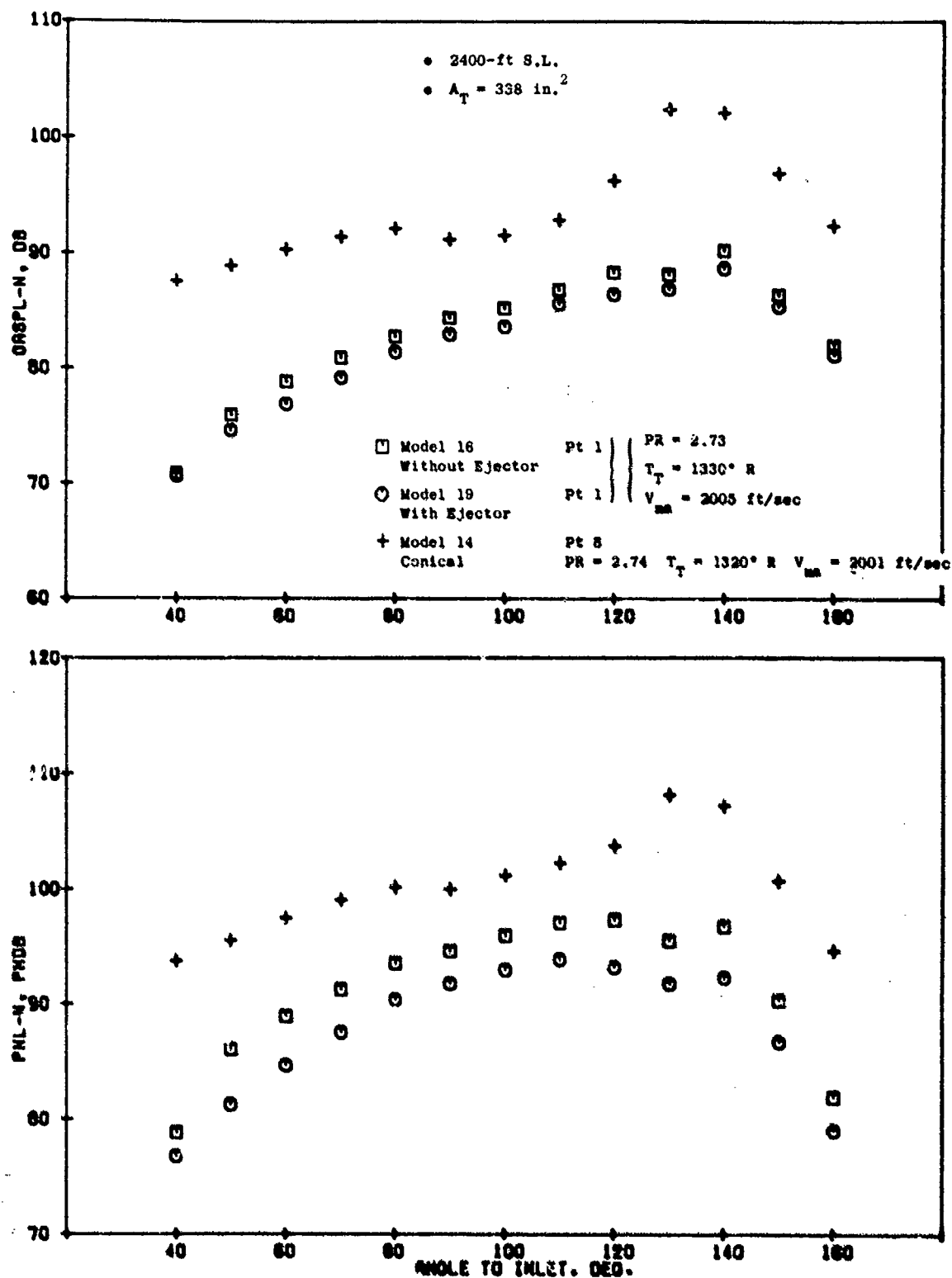


Figure 3-239. Impact of Acoustically Treated Ejector, Turbojet, OASPL and PNL Directivity,  $V_{m1} = 2005 \text{ ft/sec}$ .

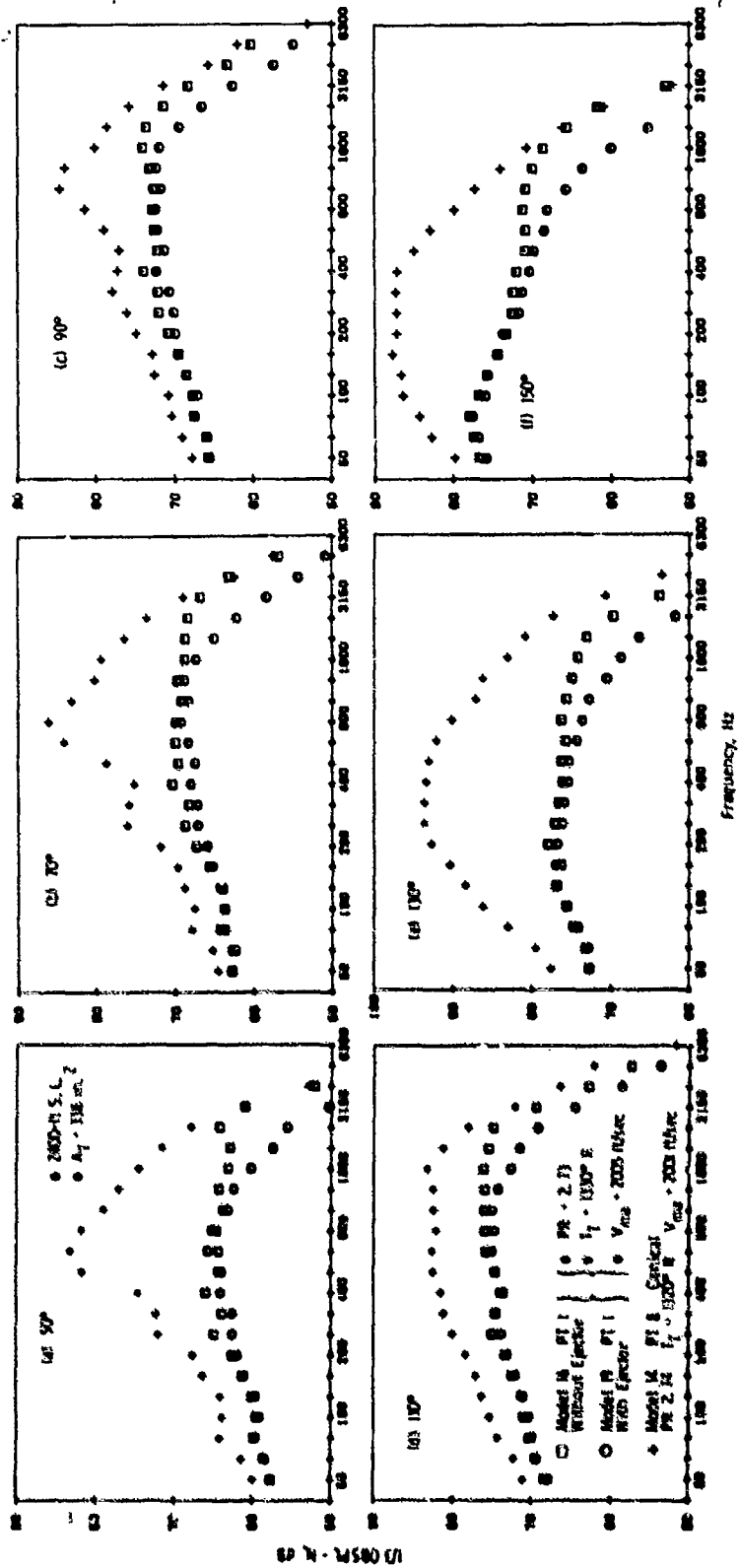


Figure 3-240. Impact of Acoustically Treated Ejector, Turbojet, Spectra,  $V_{ma} = 2005$  ft/sec.

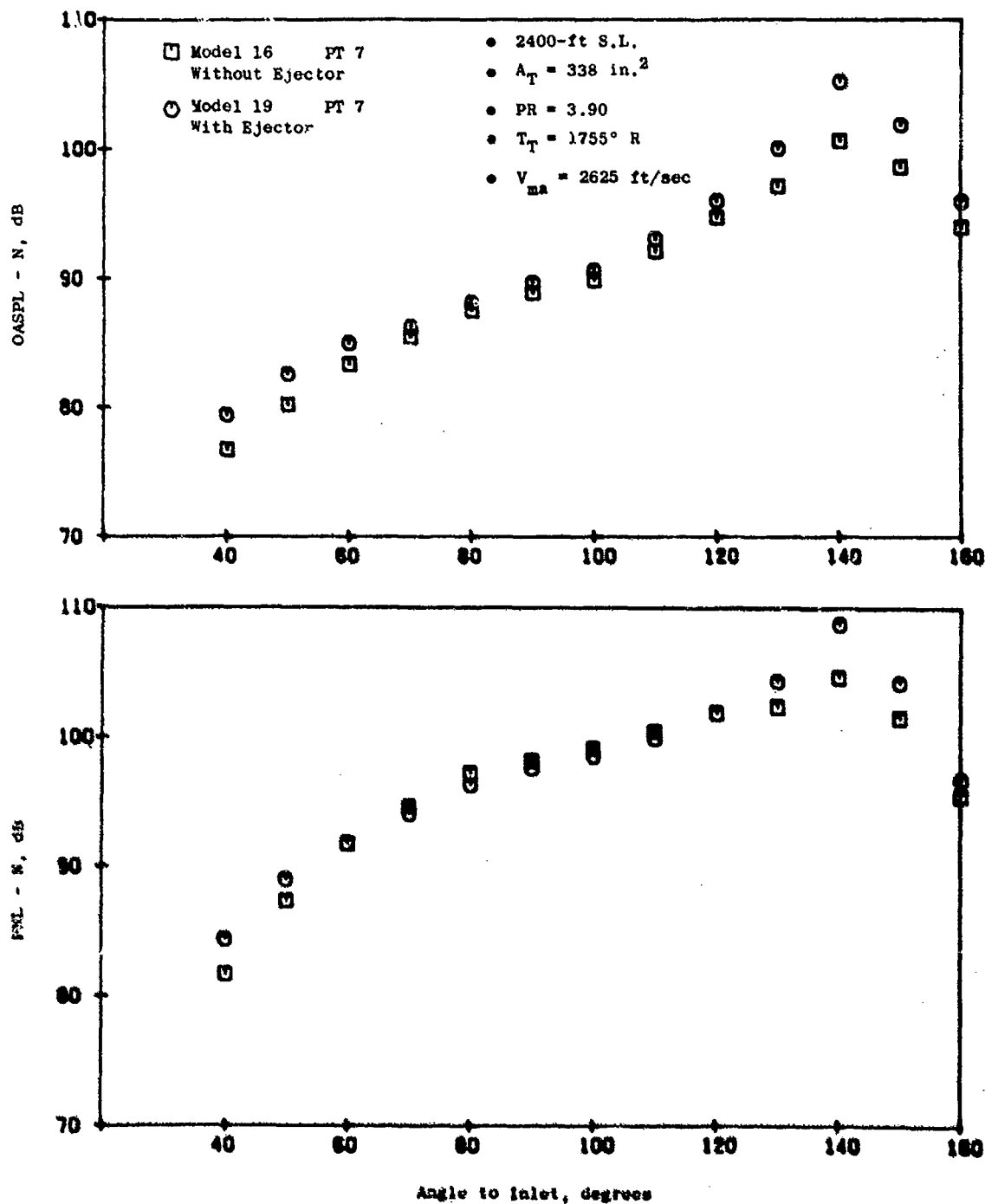


Figure 3-241. Impact of Acoustically Treated Ejector, Turbojet, OASPL, and PNL Directivity,  $V_{ma} = 2625 \text{ ft/sec}$ .



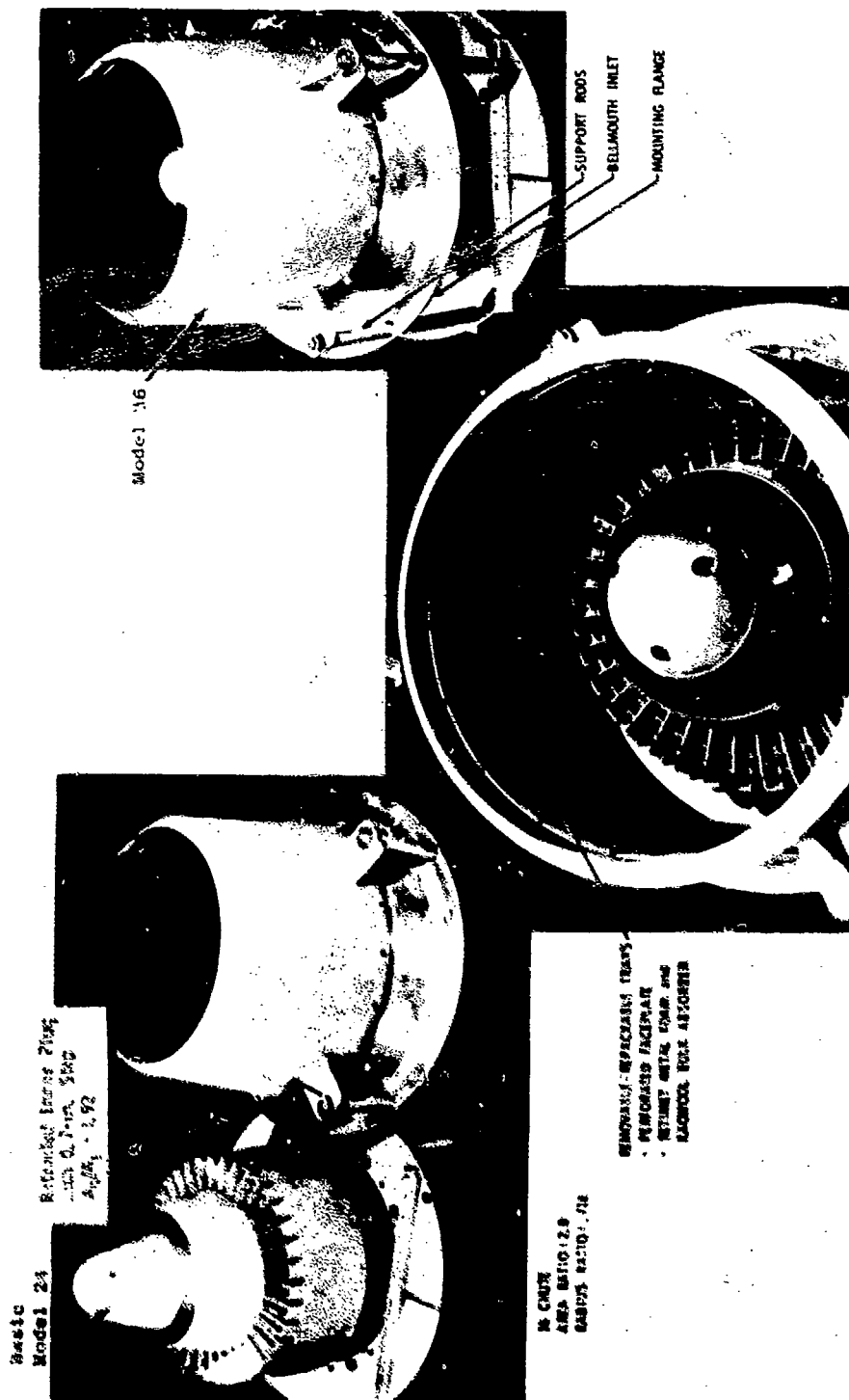


Figure 3-243. Acoustically Treated Ejector Application to Annular Suppressor, Dual Flow.

A summary of PPNL and POASPL levels for the 15%, 30%, and AST/VCE cycle lines is shown in Figures 3-244 and 3-245 along with suppression plots of the ejector Model 36 relative to the conical and relative to the non-ejector Model 24. The data indicate maximum system suppression levels of near 13  $\Delta$ PNL and 14  $\Delta$ OASPL in comparison to the previous 15.5 and 11.5 of the turbojet system. System overall suppression levels do not seem to drop off as rapidly at higher  $V_{ma}$  as is the case with the turbojet/ejector application.

Suppression attributable to the ejector alone averages 4  $\Delta$ PNL and 4.5  $\Delta$ OASPL over a wide  $V_{ma}$  range. This is dramatically different than the ejector application to the suppressed turbojet where maximum suppression values of 4  $\Delta$ PNL/5.5  $\Delta$ OASPL at low  $V_{ma}$  dissipated to noise enhancement at high  $V_{ma}$ .

PNL and OASPL data obtained from testing along the DBTF/Inverted Dual Flow cycle line are shown in Figures 3-246, 3-247, and 3-248 for peak, 90°, and 50°, respectively. Each of these figures also displays the suppression curves attributable only to application of the ejector, i.e., Model 36 relative to Model 24.

At 90°, noise reduction due to ejector application is still present, but at a reduced level from that at peak noise angle, maintaining 2-4  $\Delta$ PNL and 1-2  $\Delta$ OASPL across the test velocity range. This is also reduced from that achieved in the previous turbojet/ejector study. Additionally, the overall system suppression at 90° is somewhat less than the turbojet/ejector system.

At 50°, significant overall system suppression is regained relative to the conical nozzle, both on OASPL and PNL. This is observed primarily at high  $V_{ma}$  relative to the shock-cell infested conical nozzle, and to a lesser degree at low  $V_{ma}$ . Suppression levels attributable to the ejector alone are from 2-4  $\Delta$ PNL and up to 2  $\Delta$ OASPL. These levels are in concert with those achieved on the turbojet/ejector system. Again, as at 90° and peak angle, the additional suppression attributable to the ejector does not as readily dissipate with increasing  $V_{ma}$ , as was seen with the turbojet/ejector system.

An overall power level data plot is also included as Figure 3-249, and its trends fairly well parallel those of the PPNL/POASPL curves.

Figures 3-250 and 3-251 are included as typical examples of PNL and OASPL directivity and of spectral distributions. The data shown are from the AST/VCE cycle line at  $V_{ma} = 2095$  ft/sec and were selected as representative of trends for most of the test points. Observations show, as in the case of turbojet/ejector data at low to moderate velocities, suppression attributable to the ejector persists at all angles, except the most aft, particularly on a PNL basis. The suppression is again attributable to acoustic absorption in the high-frequency regime.

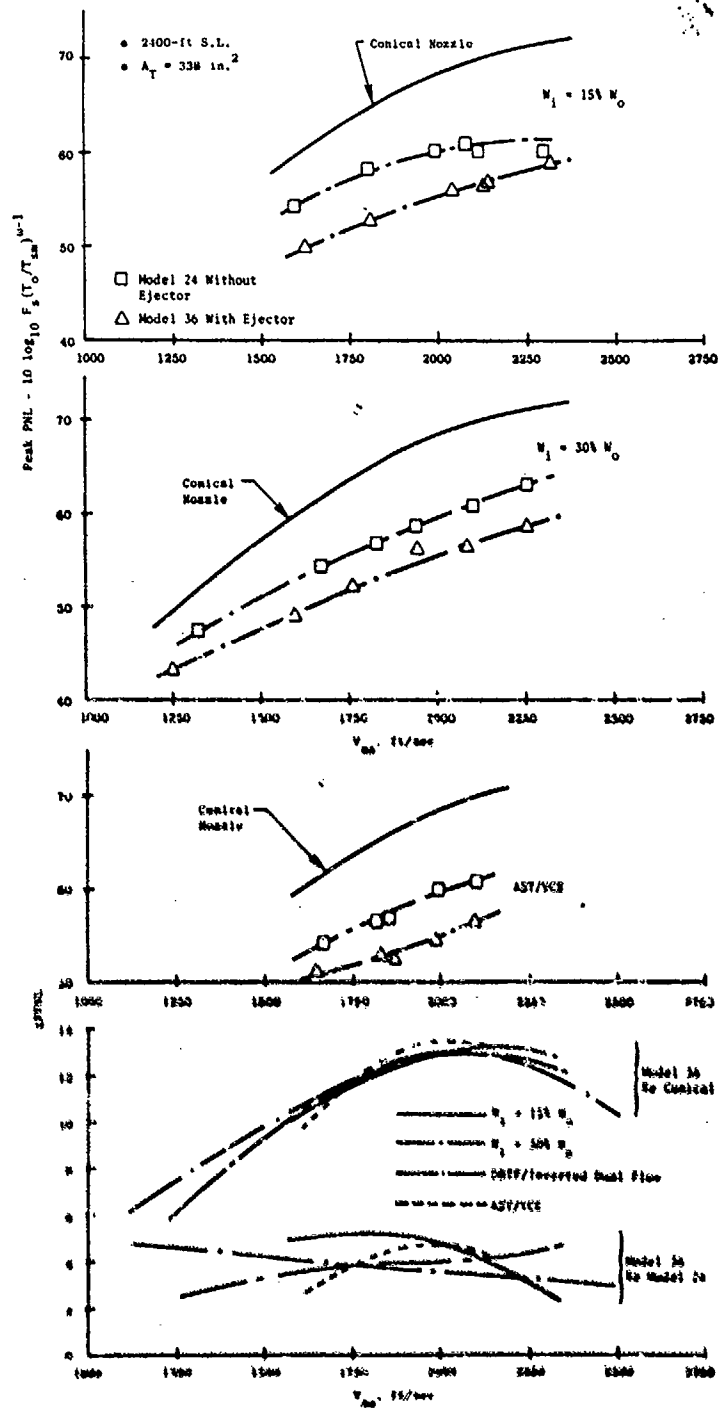


Figure 3-244. Treated Ejector Application to Dual Flow, Peak PNL and Suppression Levels.



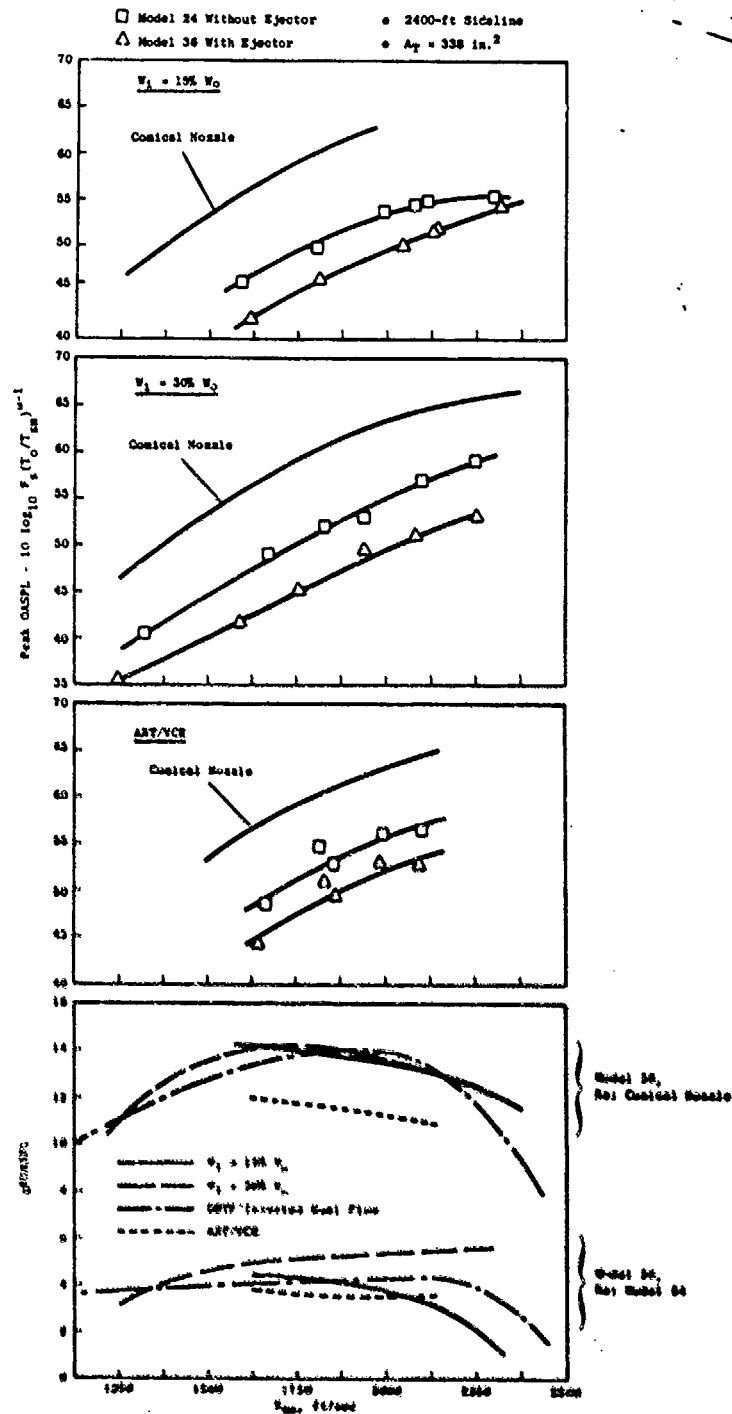


Figure 3-245. Treated Ejector Application to Dual Flow, Peak OASPL and Suppression Levels.

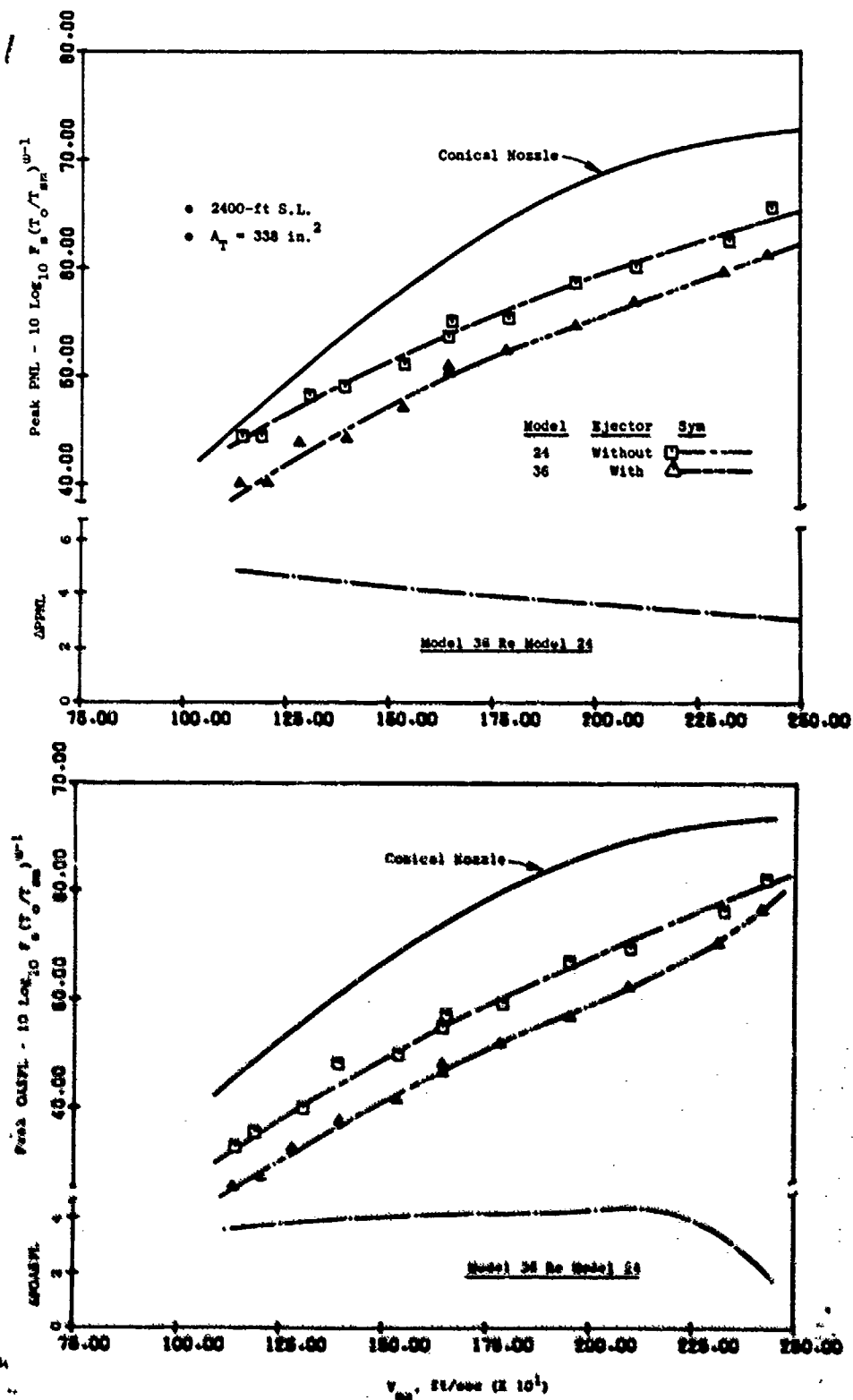


Figure 3-246. "Treated Ejector Application to Dual Flow, DBTP Cycle, Peak OASFL, PNL, and Suppression Levels.

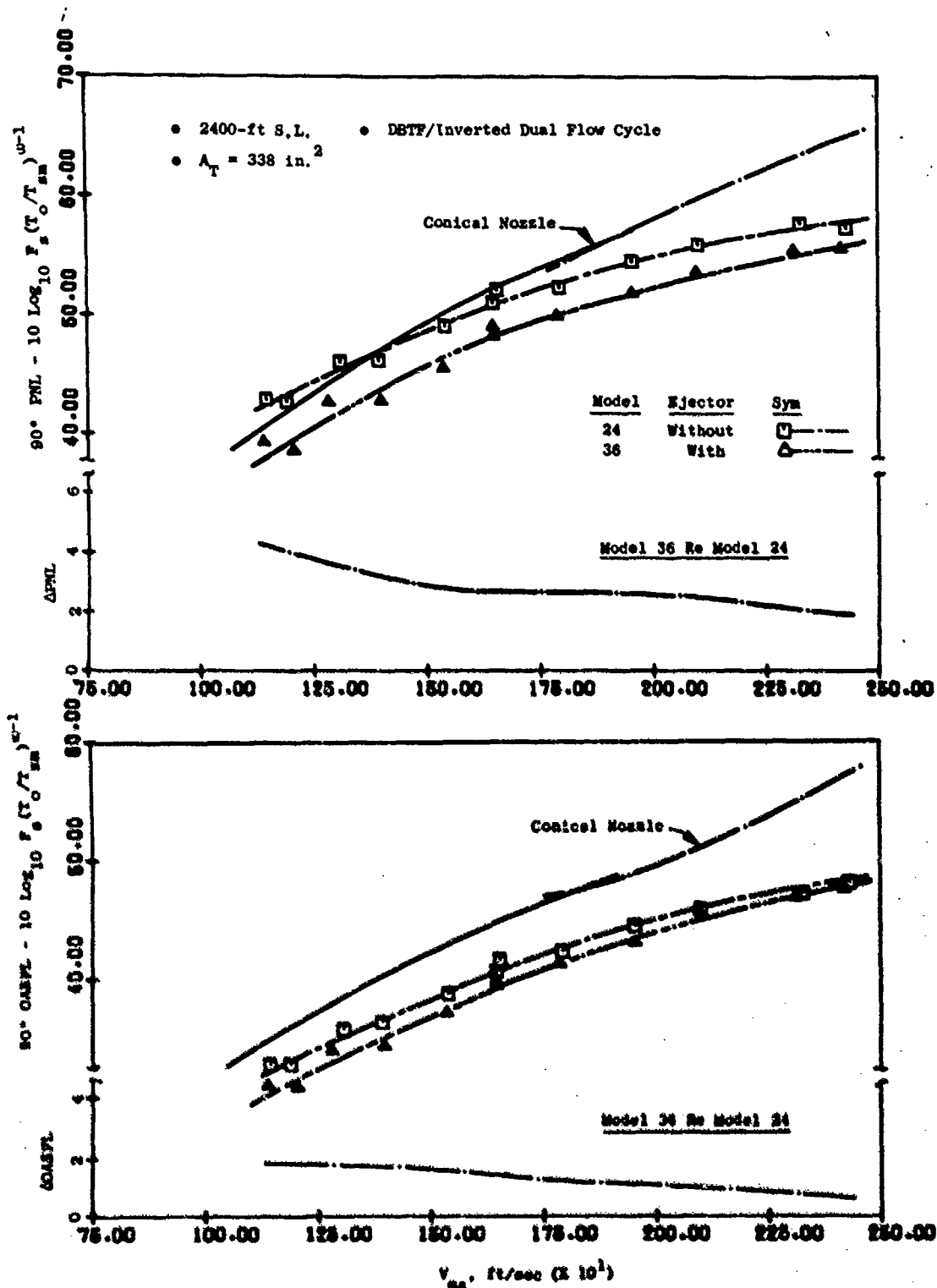


Figure 3-247. Treated Ejector Application to Dual Flow,  $90^\circ$  QASPL, PNL, and Suppression Levels.

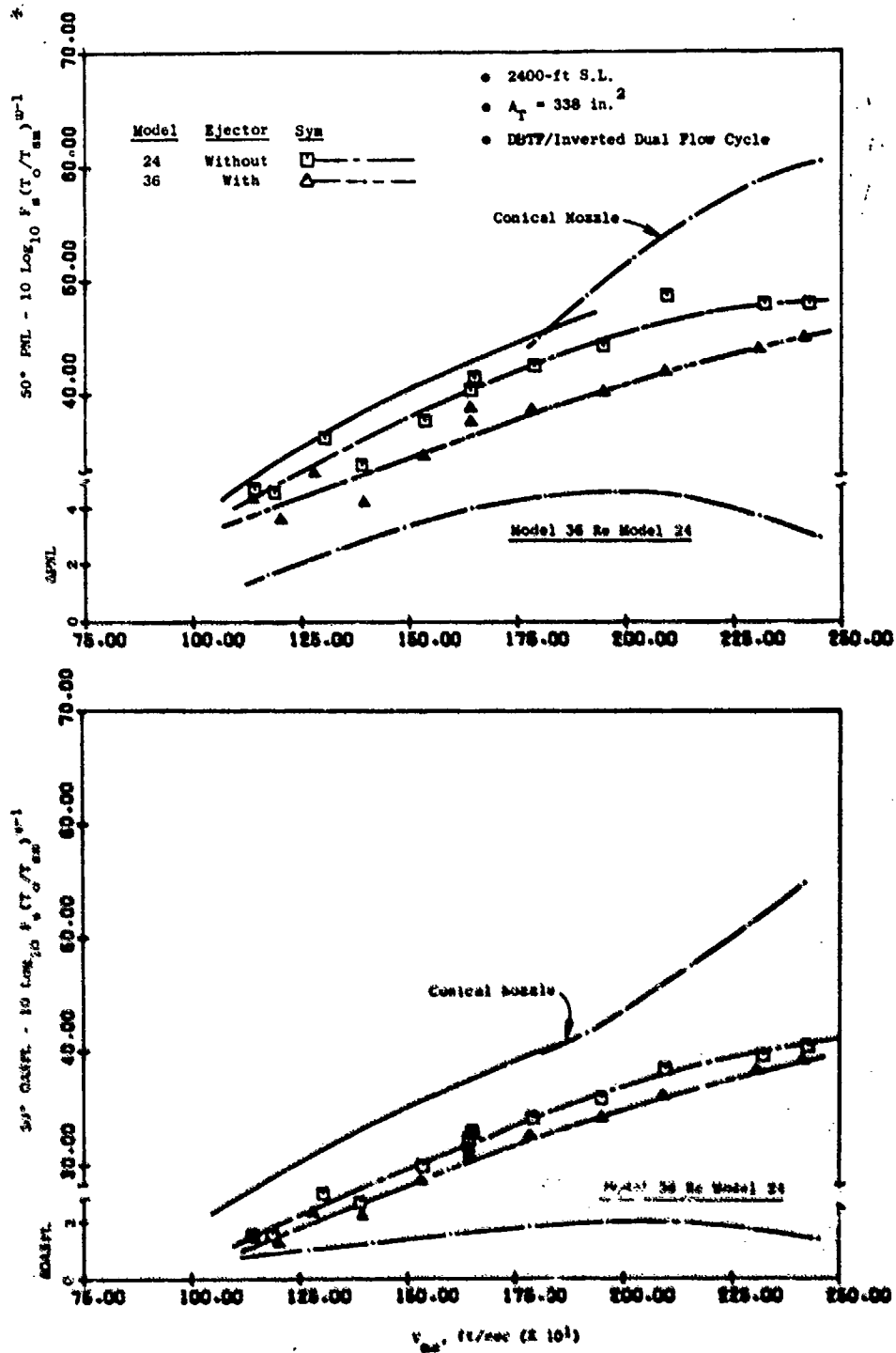


Figure 3-248. Treated Ejector Application to Dual Flow, 50° OASPL, PNL, and Suppression Levels..

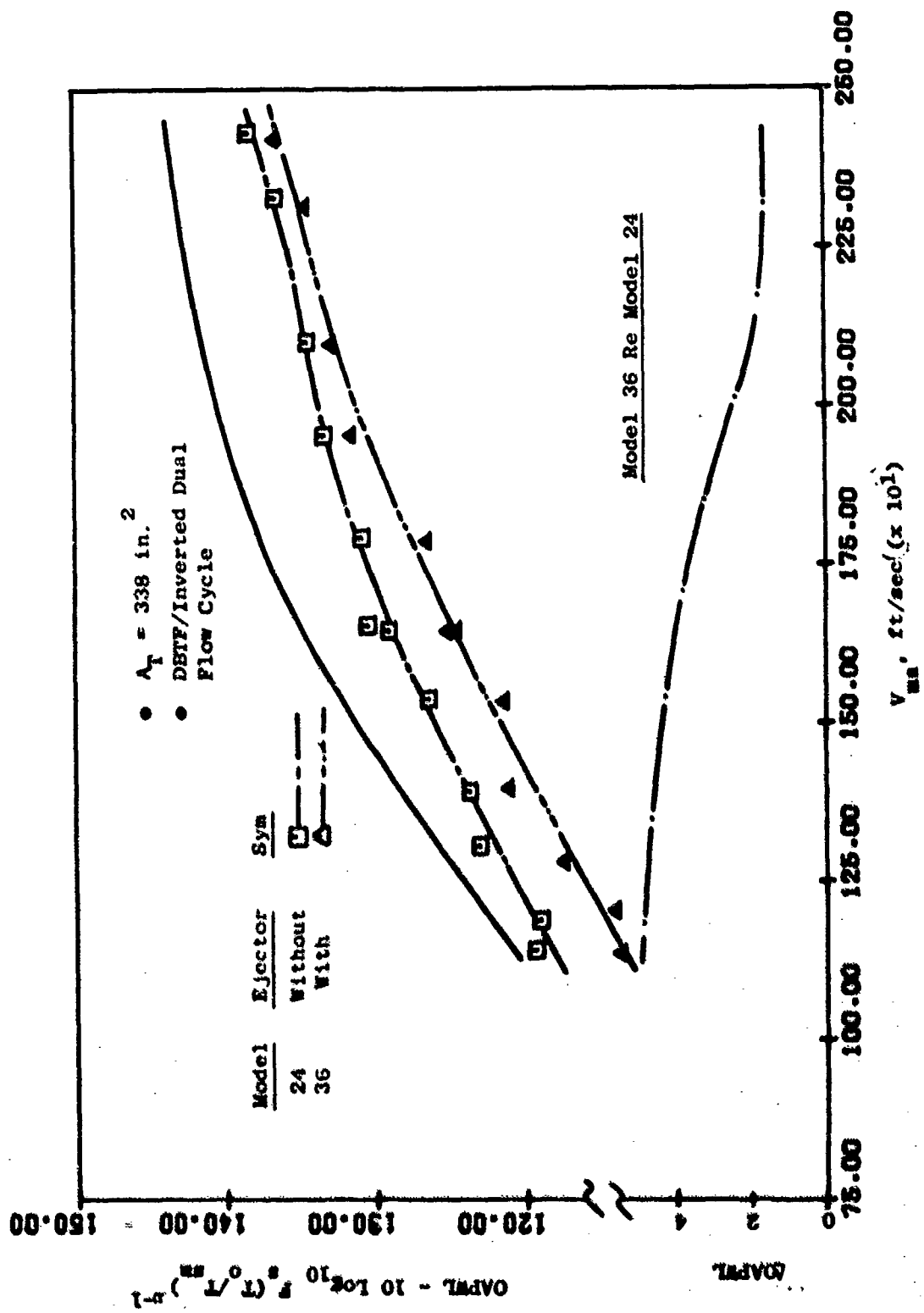


Figure 3-249. Treated Ejector Application to Dual Flow - OAPWL and Suppression Levels.

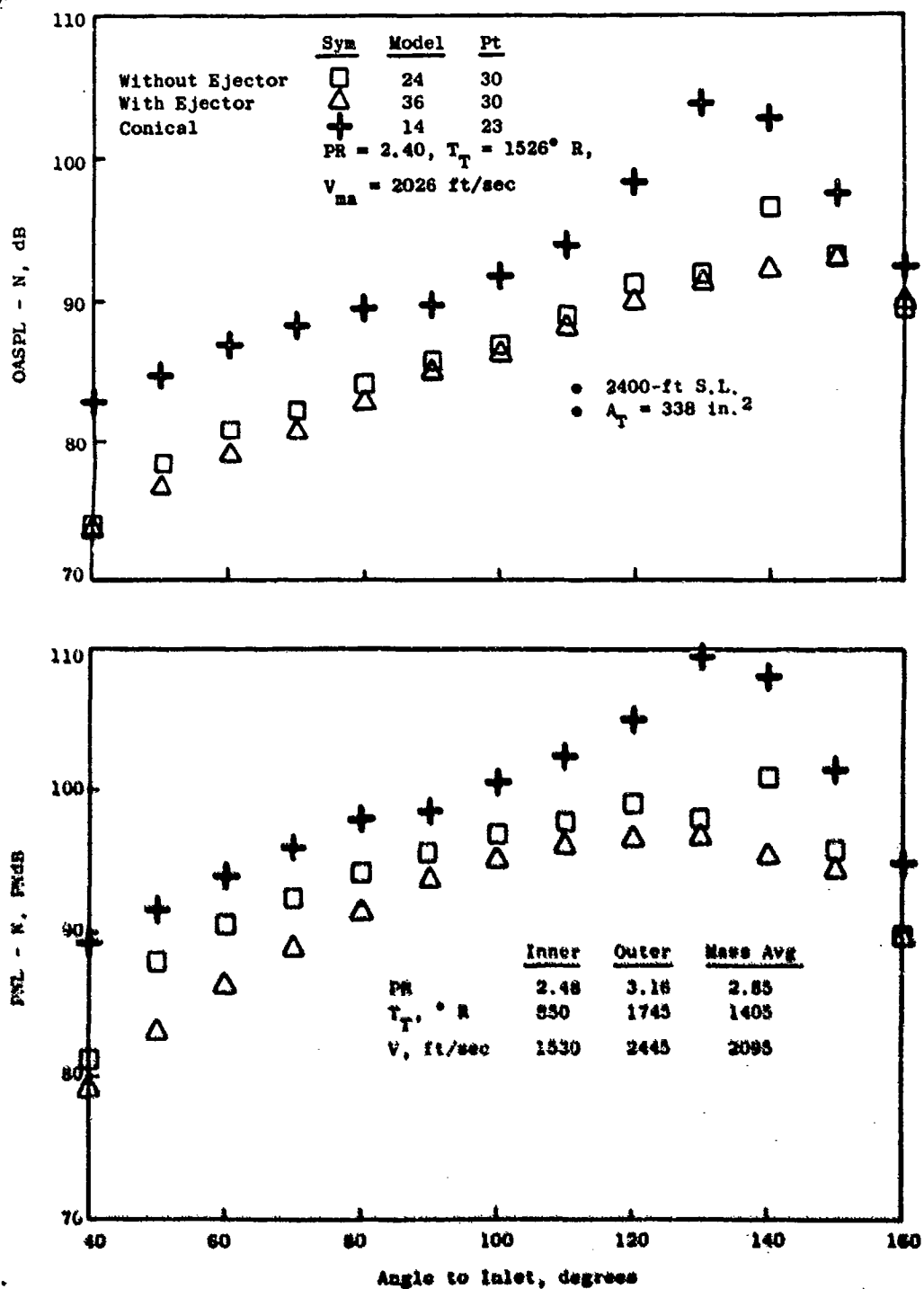


Figure 3-250. Treated Ejector Application to Dual Flow, OASPL and PNL Directivity,  $V_{ma} = 2095 \text{ ft/sec}$ .

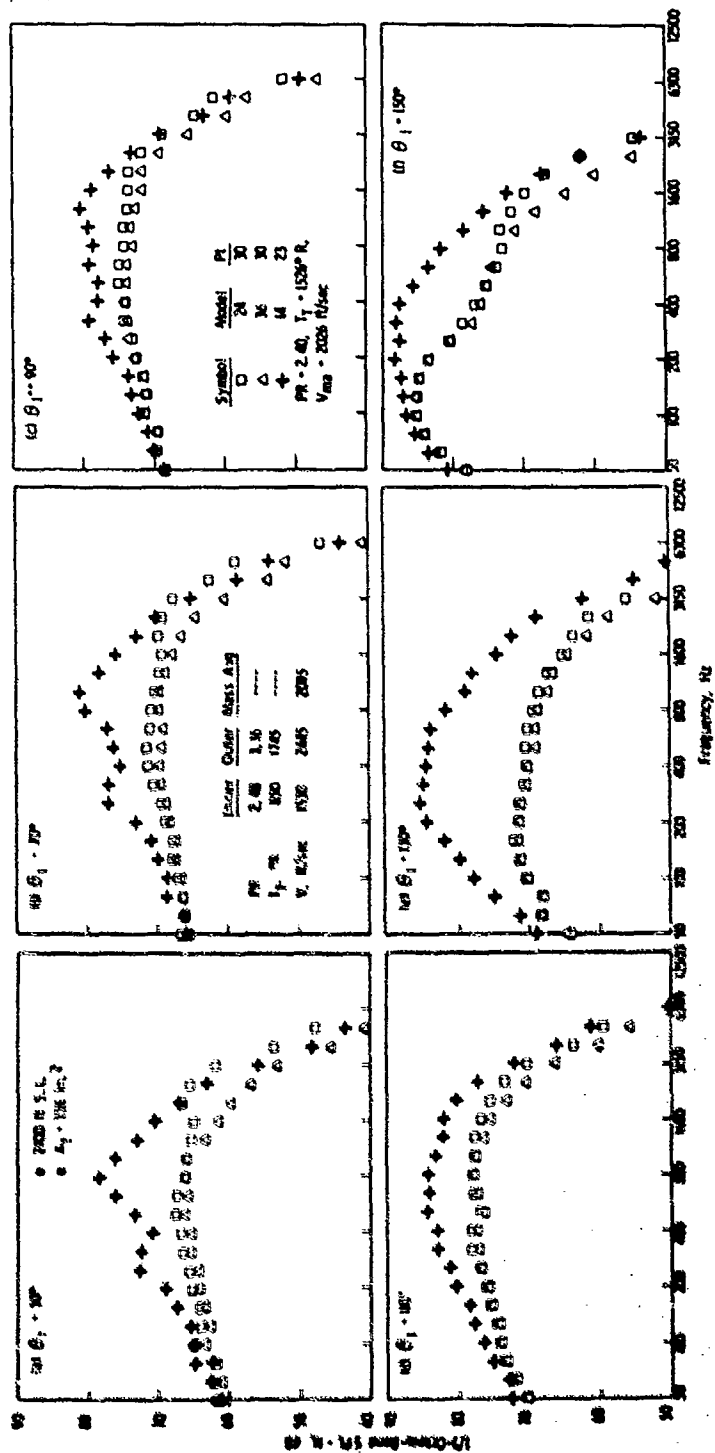


Figure 3-251. Treated Ejector Application to Dual Flow, Spectra,  $V_{in} = 2095 \text{ ft/sec}$ .

### Treated Ejector Application, Unsuppressed Coannular Nozzles

The two previous sections evaluated application of an acoustically treated ejector to systems whose mid-to-high-frequency noise generation region was in close proximity to the nozzle exit plane which is inherent in the mechanics of highly segmented annular suppressors. The suppressor systems in themselves are mechanically more complex, heavier, and aerodynamically poorer than unsuppressed coannular-noncoplanar dual plug propulsion nozzles of equivalent thrust rating. The unsuppressed coannular nozzle on its own, due to the nature of its high duct radius ratio, normally affords suppression relative to the conical nozzle. It, too, may have mid-to-high frequency noise sources in near proximity of the nozzle exit plane. Location, frequency distribution, and noise levels are dependent on the physical geometry of the system and aerodynamic cycle. The small annulus heights associated with duct nozzles approach the characteristic dimensions (chute/flow widths and heights) associated with segmented suppressors. Therefore, application of a treated ejector to an unsuppressed coannular system was expected to possibly enhance acoustic performance sufficient to make the system favorably competitive to the more mechanically complex and heavier suppressor systems without ejectors.

For the study, Models 37 and 38 were used. Details are presented in Appendix A, Figures A-31 and A-32 and in Figure 3-252. Pertinent system parameters were as follows:

Model No.	Outer		Inner		System	Ejector				
	$R_o^i$	$A_{flow}$ , in. <sup>2</sup>	$D_s$ , in.	$R_i^i$		$A_o/A_i$	$D_{ei}$ , in.	$D_{ei}/D_s$	$X_s/R_s$	$L_g/D_{ei}$
37	0.852	18.05	9.19	.800	11.35	1.59	11.0	1.20	0.29	0.76
38	0.926	8.61	8.46	.800	11.35	0.71	11.0	1.30	0.32	0.76

The basic coannular nozzles were from the NASA-Lewis contract NAS3-19777, (Reference 11) and the acoustic ejector was from the NASA-Lewis contract NAS3-18008 (Reference 10). The ejector design and packing were similar to that discussed in Section 3.4.2.5.

The acoustic test matrix within the Cell 41 Anechoic Facility followed an abbreviated form of Section 3.2.1 Figure 3-10 and Table 3-3 and basically uses parts of the DBTF/Inverted Dual Flow and the AST/VCE cycle matrices.

Acoustic results are presented as peak PNL/OASPL levels plus curves of suppression relative to the conical baseline in Figure 3-253, 90° OASPL/PNL in Figure 3-254, 50° OASPL/PNL in Figure 3-255, and overall power levels in Figure 3-256. Figure 3-253 shows that maximum suppression levels on a peak OASPL basis approach 5 and 4, and on a peak PNL basis approach 6.5 and 5 for Models 38 and 37, respectively. At 90° and 50°, noise levels approach those of the conical baseline.



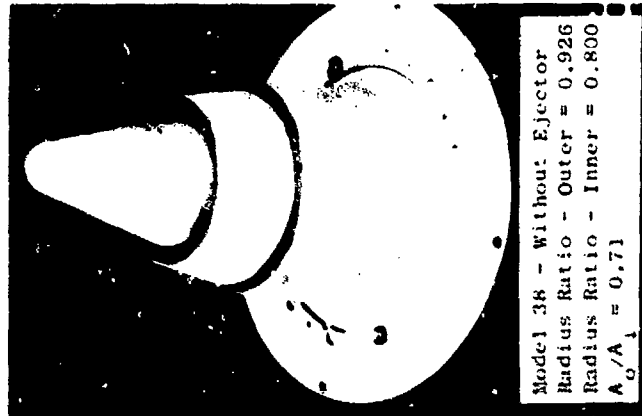
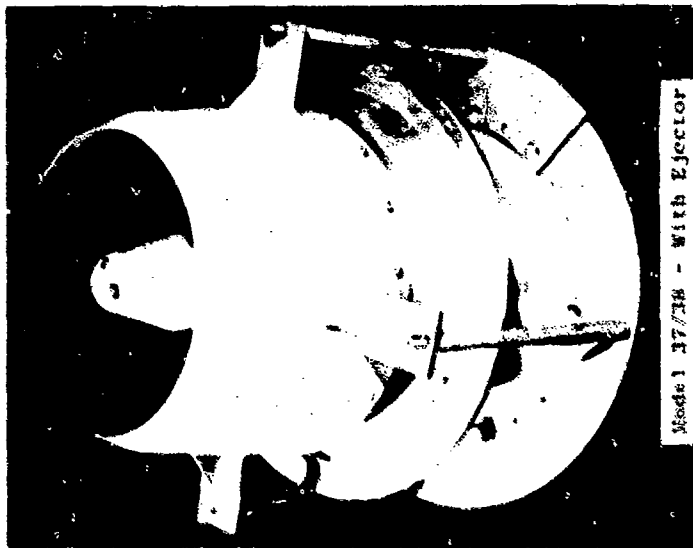
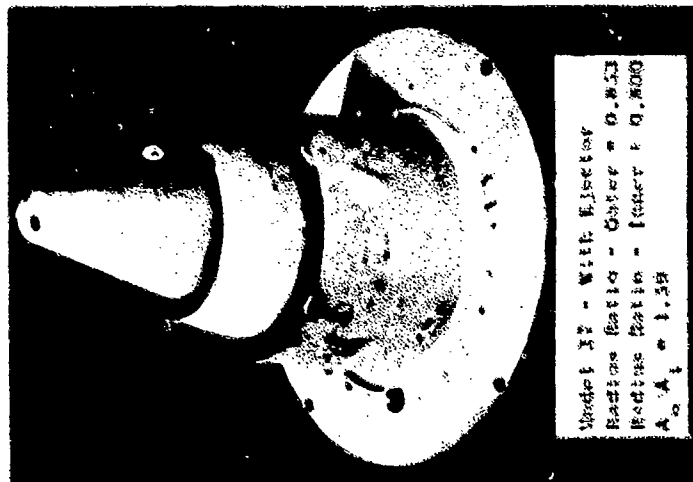


Figure 3-252. Unsuppressed Cosmular Nozzles with Acoustically Treated Ejector.

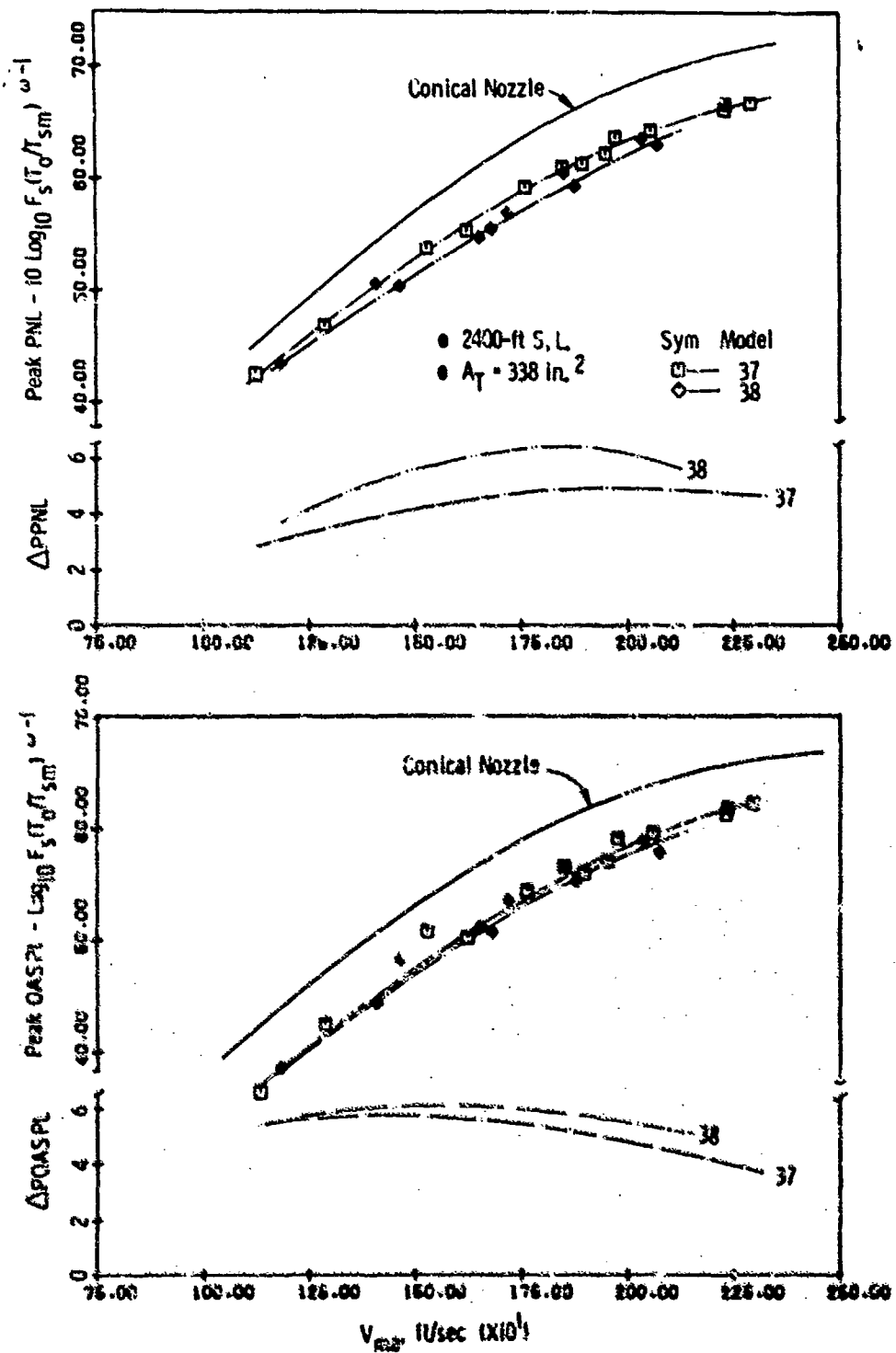


Figure 3-253. Unsuppressed Conical Nozzles with Treated Ejectors, Peak QASPL, PNL, and Suppression Levels.

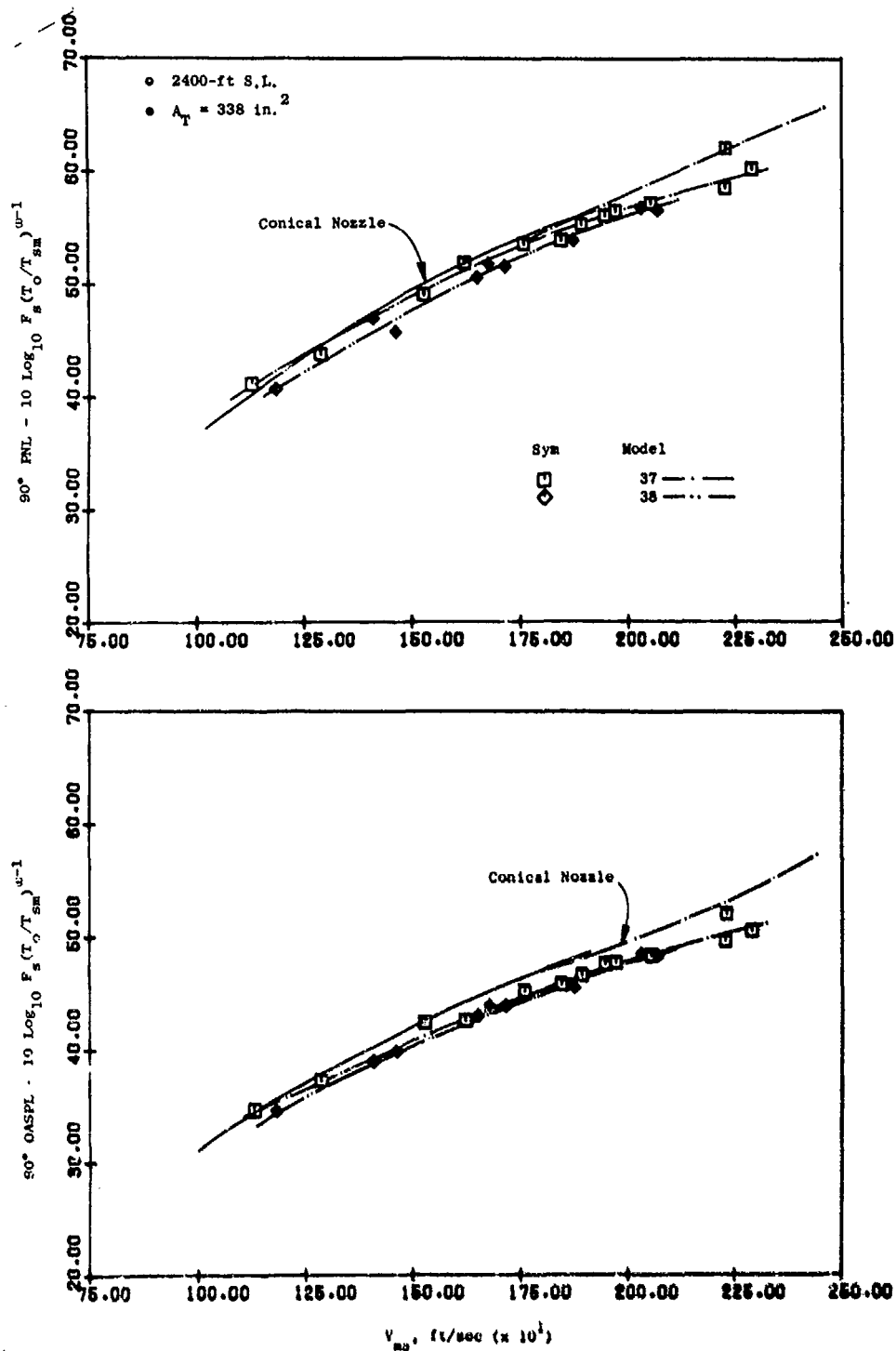


Figure 3-254. Unsuppressed Coannular Nozzles with Treated Ejectors, 90° OASPL and PNL.

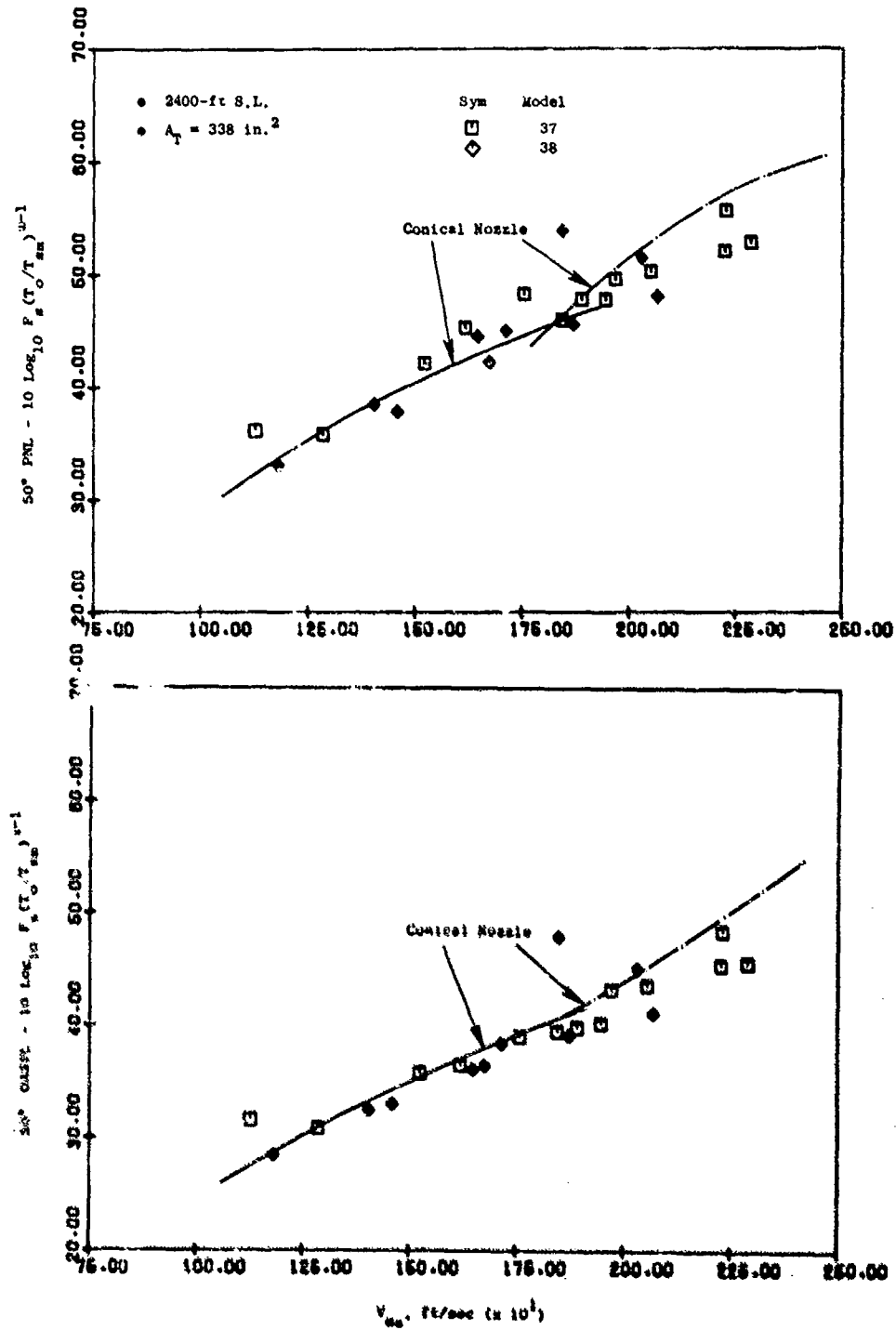


Figure 3-255. Unsuppressed Conical Nozzles with Treated Ejectors, 50° OASPL and PNL.

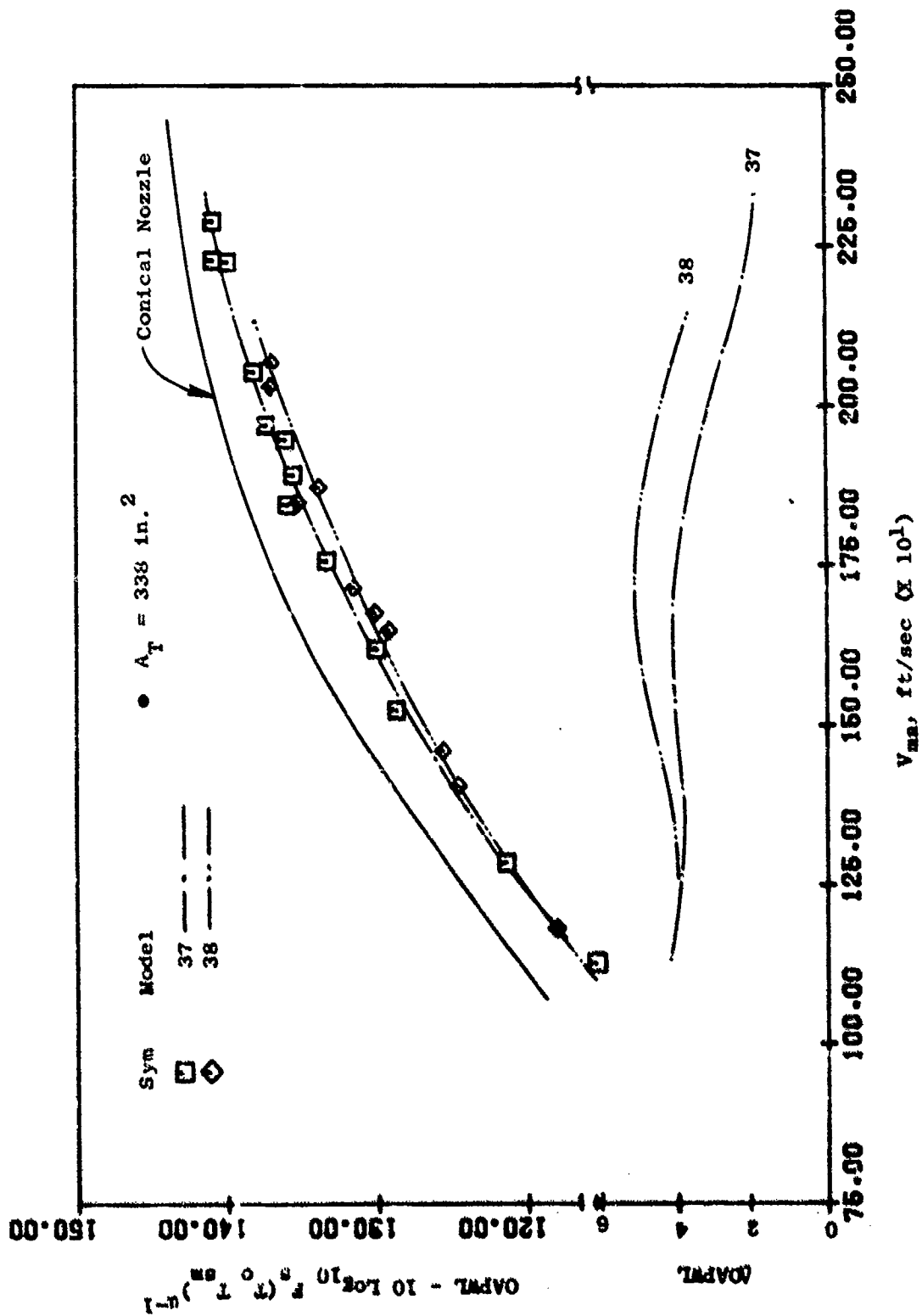


Figure 3-256. Unsuppressed Coannular Nozzle with Treated Ejectors, OAPWL and Suppression Levels.

To establish treated ejector effectiveness on its own, Figure 3-257 compares the peak PNL suppression trends of Models 37 and 38 (from Figure 3-253) to the levels established in Reference 11 for the basic nonejector coannular noncoplanar systems (Configurations 5 and 6, respectively, from Reference 11 for Models 37 and 38). This comparison points out that application of the treated ejector to the system of higher duct radius ratio (Configuration 6 and Model 38) increased peak PNL suppression levels to 6.5 dB, the ejector effecting near 2 PNL suppression on its own in the midvelocity range. This level is considerably less than the basic 4  $\Delta$ PNL obtained with the treated ejector applied to a suppressed turbojet or suppressed dual flow system (Model 19 relative to Model 16 in Section 3.4.2.5 and Model 37 relative to Model 24 in Section 3.4.2.5). This is perhaps partially attributable to the ejector's looser fit to the base nozzle system ( $D_{e1}/D_8 = 1.3$  for Model 38 compared to 1.11 for Models 19 and 36). On the Model 37 system of lower duct radius ratio, the ejector performs well at high velocity and then loses all suppression potential at low  $V_{ma}$ , to the point of increasing system noise levels.

As an evaluation of the overall study goal (i.e., to determine whether an unsuppressed coannular plug system, through application of a treated ejector, can achieve suppression levels similar to a suppressed annular turbojet or dual flow system without ejector), Figure 3-257 also includes peak PNL suppression curves of Models 16 and 24 of the previous two sections. These were 36-chute, AR = 2.0 turbojet and dual flow suppressors, respectively. It is readily seen that, in the mid-to-high-velocity region associated with engine cycles at takeoff and community power settings, the performance of the ejected unsuppressed coannular systems is well below that of the more mechanically complex multielement systems. In fact, little or no suppression enhancement through ejector application is available at high velocity for either system studied.

To exemplify the more detailed noise characteristics of this type of system, a set of PNL and OASPL directivity and spectra plots is included. Figures 3-258 and 3-259 are at  $V_{ma} = 2060$  ft/sec and show (a) PNL and OASPL distributions in concert with the previous peak,  $90^\circ$ , and  $50^\circ$  plots, (b) suppression is slightly greater for the higher duct radius ratio model at peak angle and toward the inlet but at  $90^\circ$  suppression for both models is nil, and (c) spectra distributions show suppression relative to the conical nozzle is primarily in the midfrequency range.

#### 3.4.2.6 Summary of Suppression Levels

The preceding sections have described parametric test data which were used to establish the suppression levels for several types of nozzle configurations. Suppressor and system aerodynamic and geometric parameters evaluated experimentally included the following: suppressor area ratio, radius ratio, flow management (system velocity ratio, weight flow ratio, and area ratio), inner stream geometry, element number, element type, and treated ejectors on multielement and unsuppressed inverted-coannular-flow nozzles.

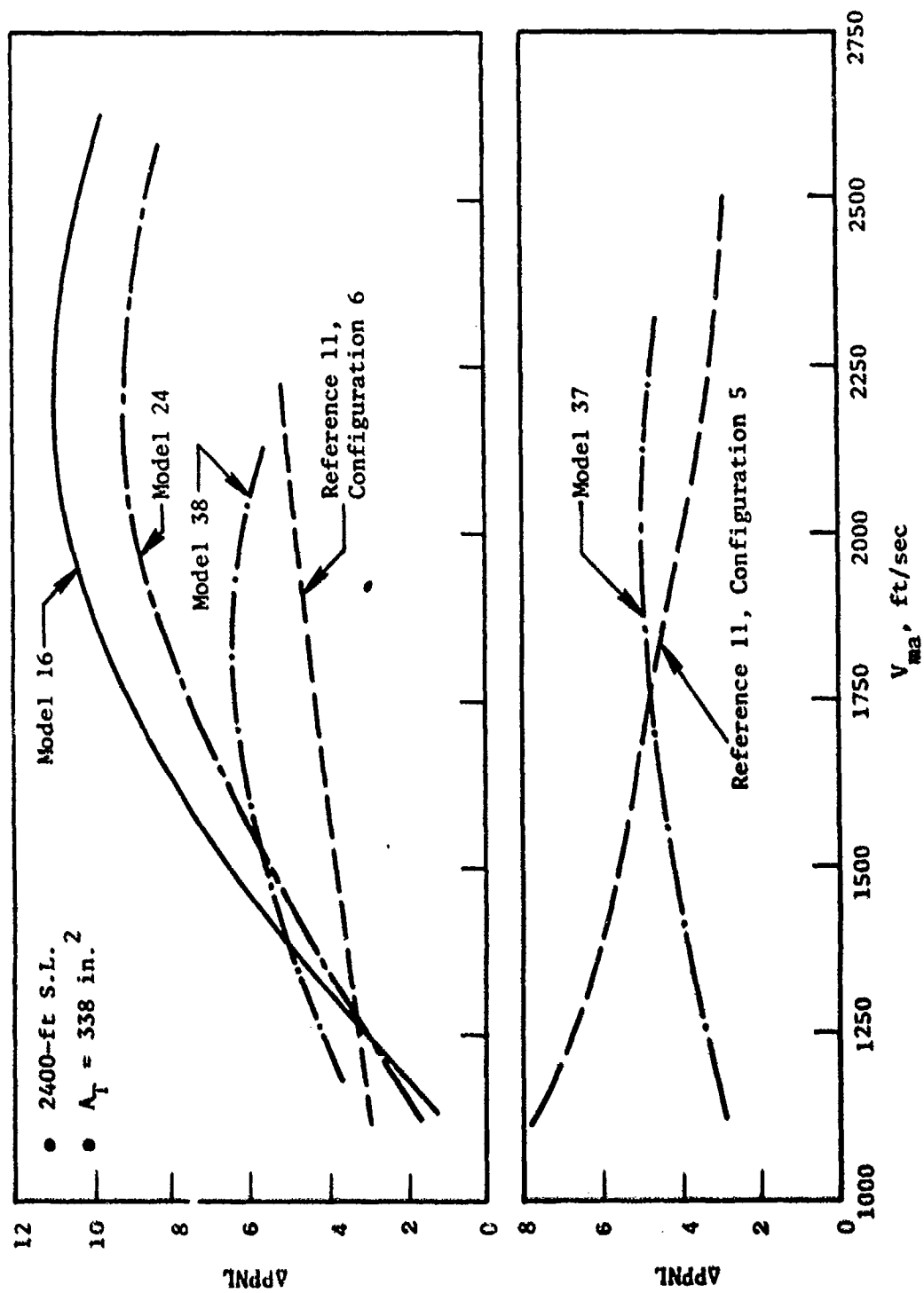


Figure 3-257. Summary of Results for Treated Ejector Application to Unsuppressed Coannular Systems.

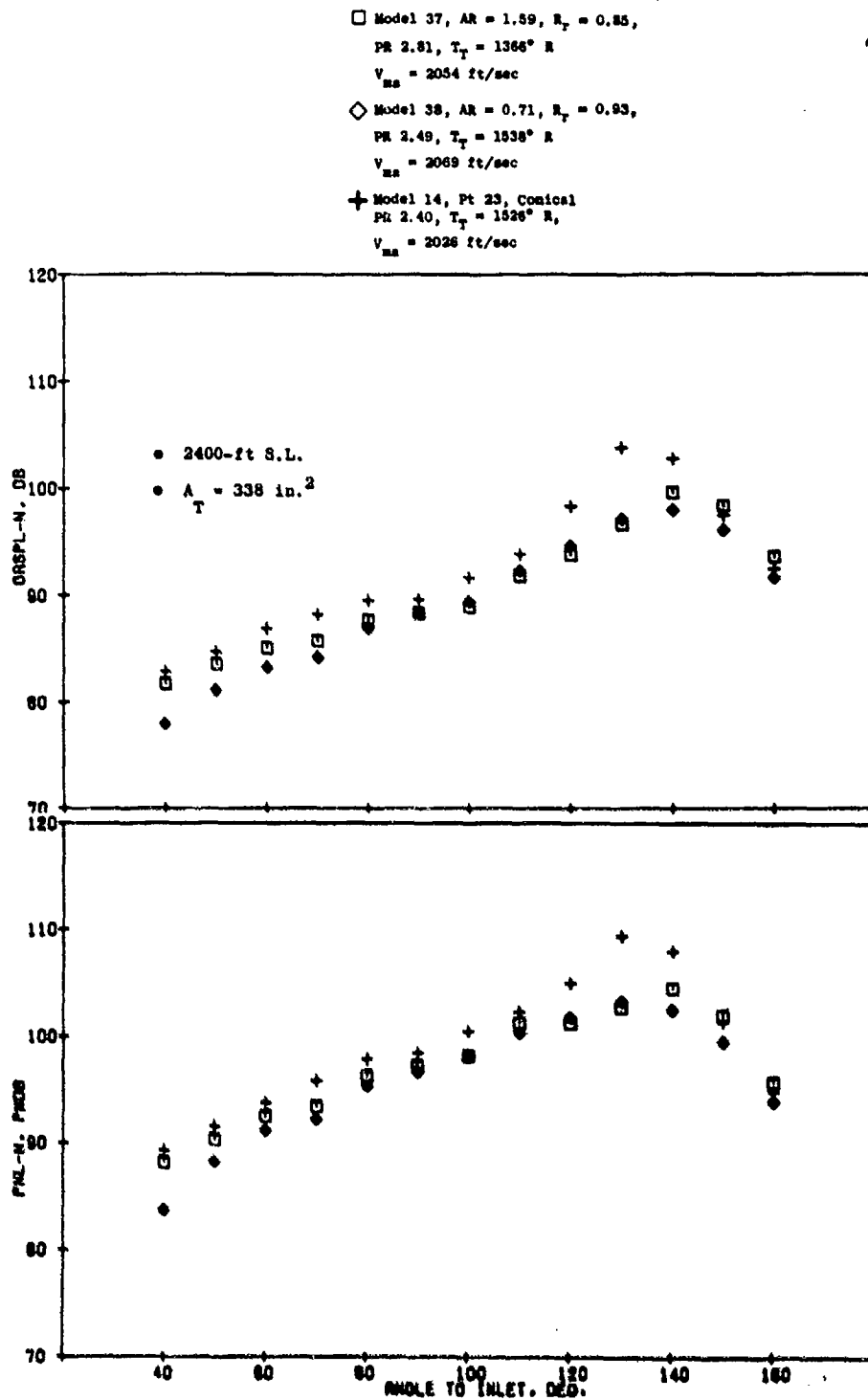


Figure 3-258. Unsuppressed Coannular Nozzles with Treated Ejectors, OASPL and PNL Directivity.



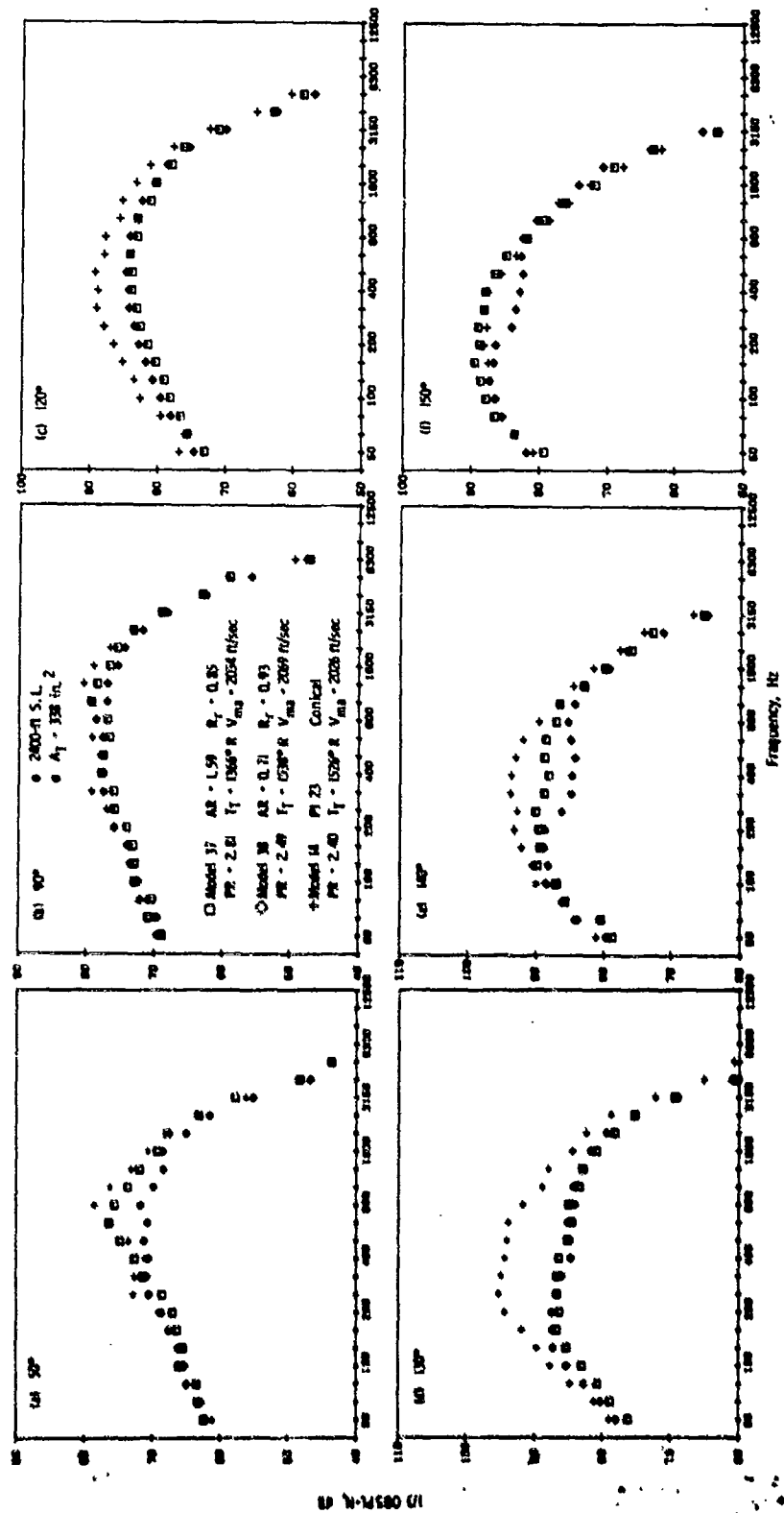


Figure 3-259. Unsuppressed Coannular Nozzles with Treated Ejectors, Spectra.

Figure 3-260 summarizes the typical suppression levels measured while testing half-span and full-span suppressors. Suppression levels are quoted relative to the conical reference nozzle. The configurations chosen in general are those which attained the highest suppression levels in their respective nozzle families.

Full-span suppressor designs which have static suppression levels in excess of 14 PNdB have been demonstrated. The 36-chute nozzle with acoustically treated ejector and 36-spoke configurations attained the highest suppression levels. Half-span suppressors implemented on the outer stream of dual flow nozzles resulted in measured peak suppression levels of 10 to 13 PNdB. The AR = 2.0 36-chute nozzle incorporating an acoustically treated ejector attained the highest suppression. In general, suppression levels attained with half-span suppressors were slightly less than similar full-span suppressor designs. These slight acoustic differences dictate that aerodynamic performance and suppressor weight must also be considered in any ranking procedure for determining the best suppressor design. This procedure is discussed in Volume III of this report.

### 3.4.3 Tests to Evaluate the Influence of Simulated Flight

This section will present the results of a series of free-jet scale model tests on baseline and suppressor nozzles. All free-jet data have been transformed using the method presented in Reference 12. The transformation is accomplished by extracting the static directivity of the noise after correcting for refraction, turbulent scattering, and absorption effects and then employing a suitable multipole source decomposition to evaluate the proper dynamic effect.

#### 3.4.3.1 Simulated Flight Investigation for Several Configurations

Eight nozzles, ranging from simple to complex geometry, were tested to determine their static and simulated flight acoustic characteristics. These nozzles were tested on the JENOTS free-jet facility (Reference 12). The model descriptions and test matrices are discussed in Sections 3.1 and 3.2.1, respectively. Photographs of the suppressor nozzle families evaluated are summarized on Figure 3-261. The ensuing discussions focus on answering four key questions, i.e.:

- Do suppressor nozzles provide a reduction in peak PNL level in flight relative to a conical nozzle? If so, is the magnitude of suppression equivalent to, greater than, or less than what is observed statically?
- Are the velocity indices of suppressor nozzles similar to those of a conical nozzle?

•  $A_{\text{Total}} = 338 \text{ in.}^2$

• 2400 ft Sideline

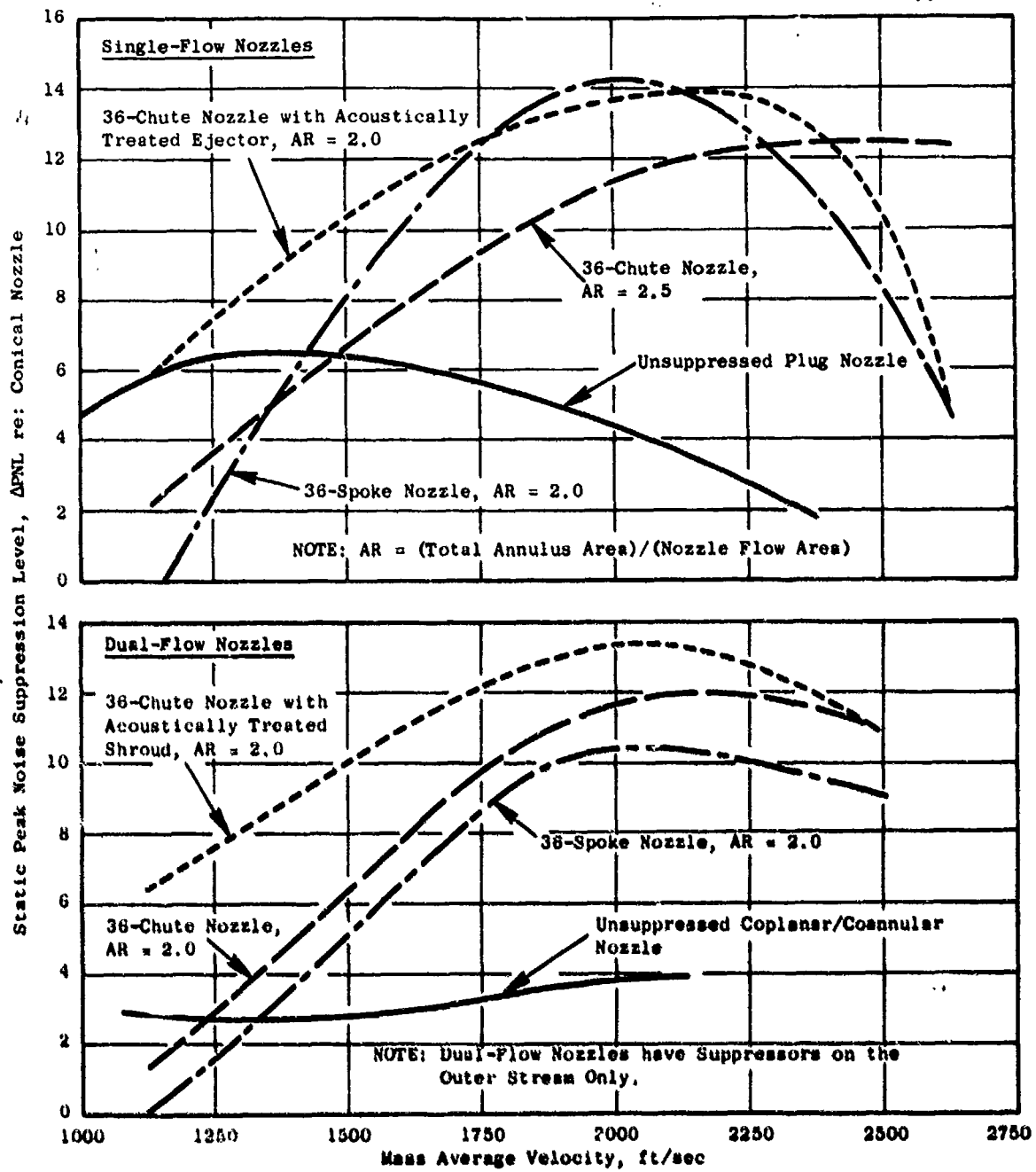


Figure 3-280. Typical Peak Static Noise Suppression Characteristics.

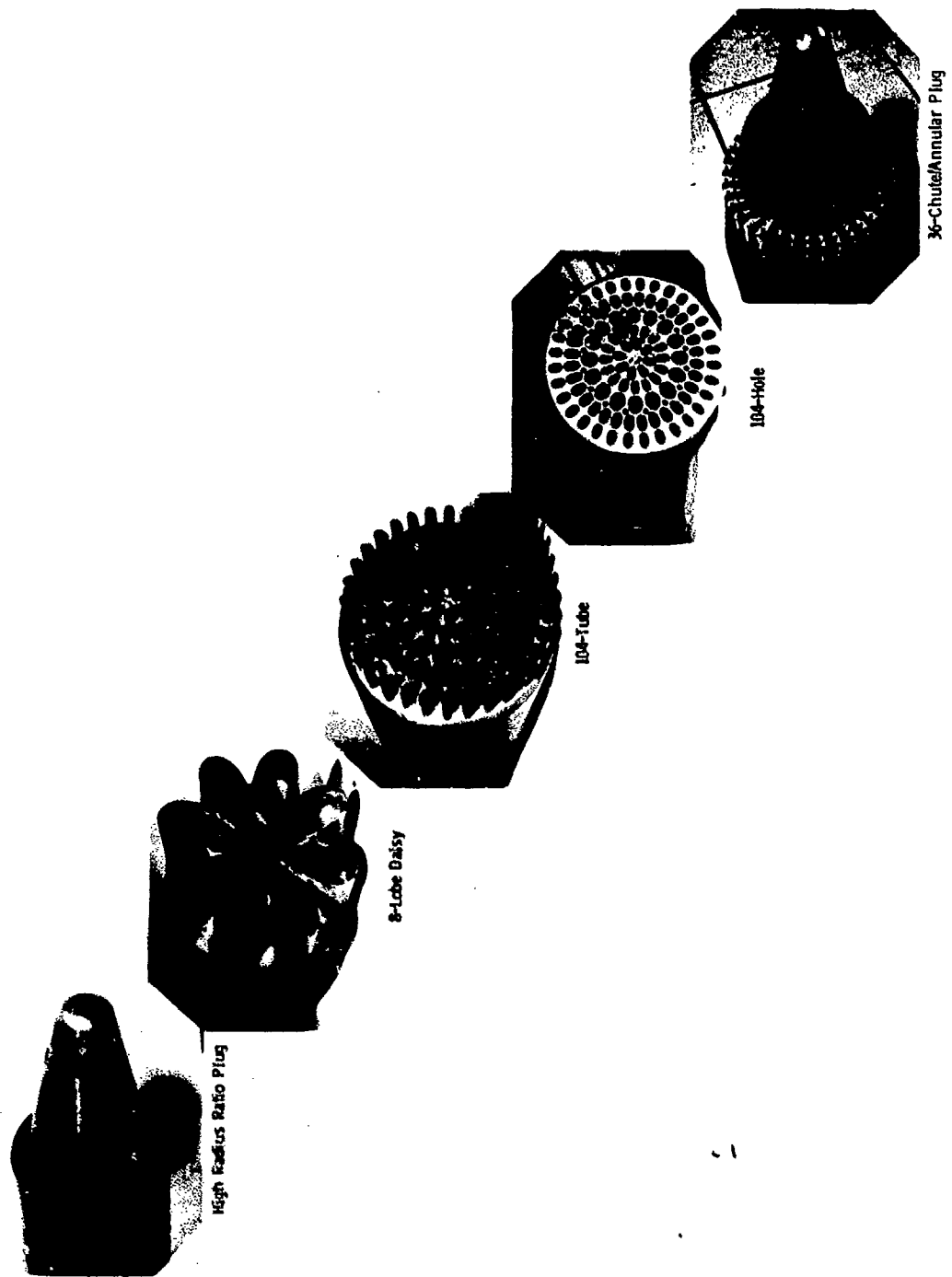


Figure 3-261. Tests to Evaluate the Influence of Simulated Flow, Summary of Suppressor Nozzle Families.

- What are the effects of flight on the spectral shapes of a suppressor nozzle?
- Is there a noise reduction at the 90° acoustic angle?

The level of peak PNL suppression as a function of velocity was established for both static and flight conditions by subtracting the normalized PNL levels presented on Figure 3-262 for select suppressor nozzles from those of the conical nozzle. The resulting suppression levels are summarized on Figure 3-263. The flight peak noise suppression of the 0.85-radius ratio plug nozzle is equivalent to the static suppression. An improvement of 1.5 to 2.0 ΔPNdB during flight occurs for the 0.789 radius ratio plug nozzle. The static suppression of each of the three chute nozzles was equivalent, whereas in flight a decrease occurs. Similar comparisons for 104-tube and 104-hole nozzles over a limited test matrix show flight and static suppression levels to be equivalent.

Table 3-6 summarizes typical static and flight peak noise suppression levels at a jet velocity of 2500 ft/sec. For baseline systems such as plug nozzles, the flight levels of suppression are near equivalent to the static levels and for the tube nozzle they are equivalent. The chute nozzles exhibit an approximate 3 PNdB loss of suppression in flight.

Peak OASPL and 90° PNL levels as a function of velocity are summarized on Figures 3-264 and 3-265, respectively. The peak OASPL reduction from static to flight is greater than on a PNL basis. The differences are configuration dependent. For example, chute nozzles exhibited a zero to 1-PNdB increase and a zero to 1-dB decrease on the basis of OASPL. Differences between peak PNL and OASPL noise trends are attributed to frequency-dependent spectra changes from static to flight. A greater reduction in OASPL indicates that low frequencies realize more reduction in flight than high frequencies; 90° PNL static and flight levels are within ±1 PNdB for the conical, 0.789 plug and 104-hole nozzles. The 0.85 radius ratio plug nozzle PNL levels increase from zero to 2 dB depending on the condition being compared. This increase is attributed to shock-cell noise dominance and is discussed in Section 3.4.3.2. The 36-chute nozzles show an increase in noise level of 3 to 4 dB, a trend which differs significantly from the other nozzle families.

PNL directivity characteristics for each of the nozzles are summarized in terms of velocity indices ( $N_0$ ) calculated by using the following equation:

$$N_0 = \left[ \frac{\text{OASPL}_{\text{static}} - \text{OASPL}_{\text{flight}} - 10 \log (1 - M_{a/c} \cos \theta)}{\log \frac{V_J}{V_J - V_{a/c}}} \right]$$

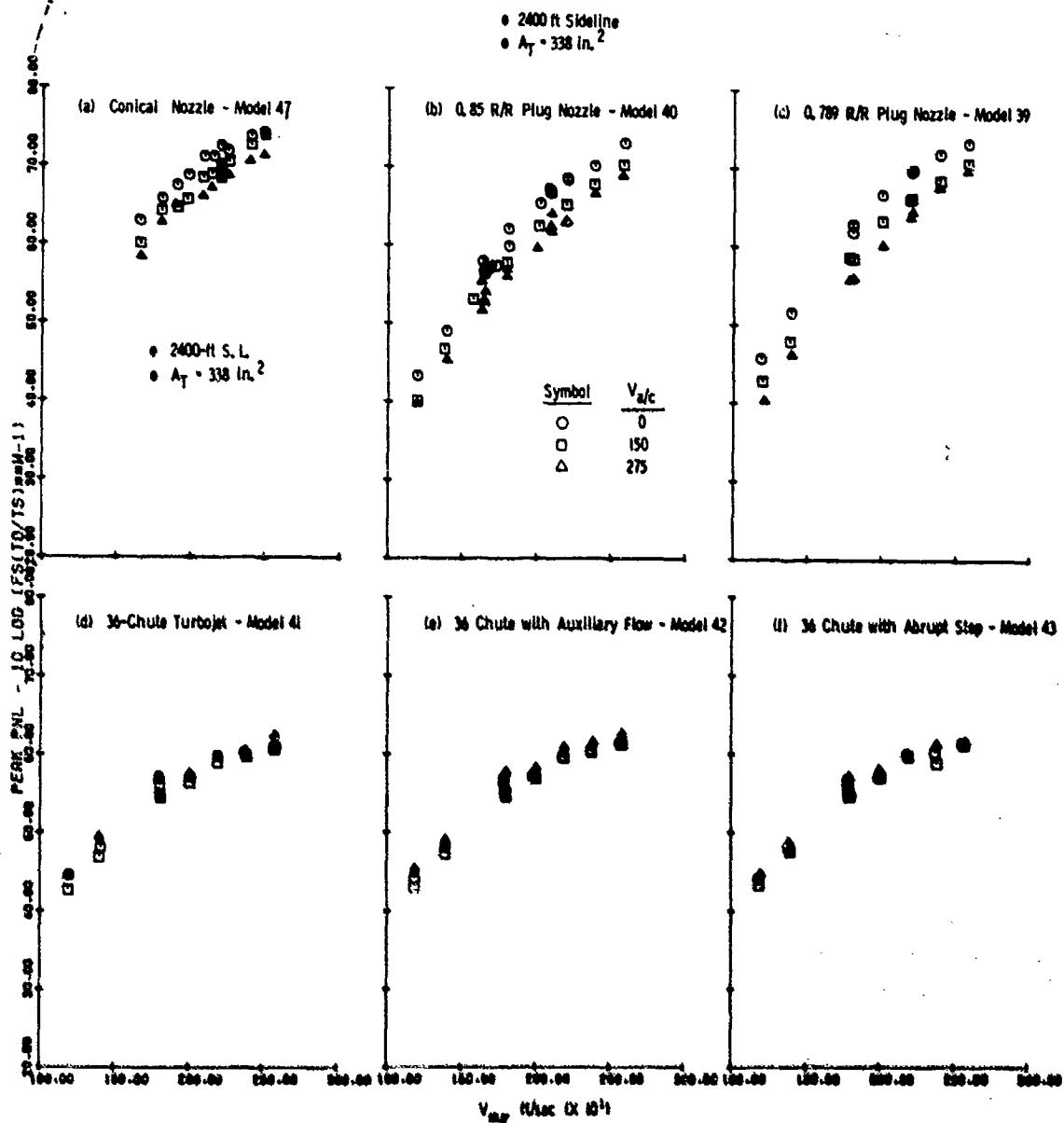


Figure 3-262. Static and Flight Peak PNL Levels.

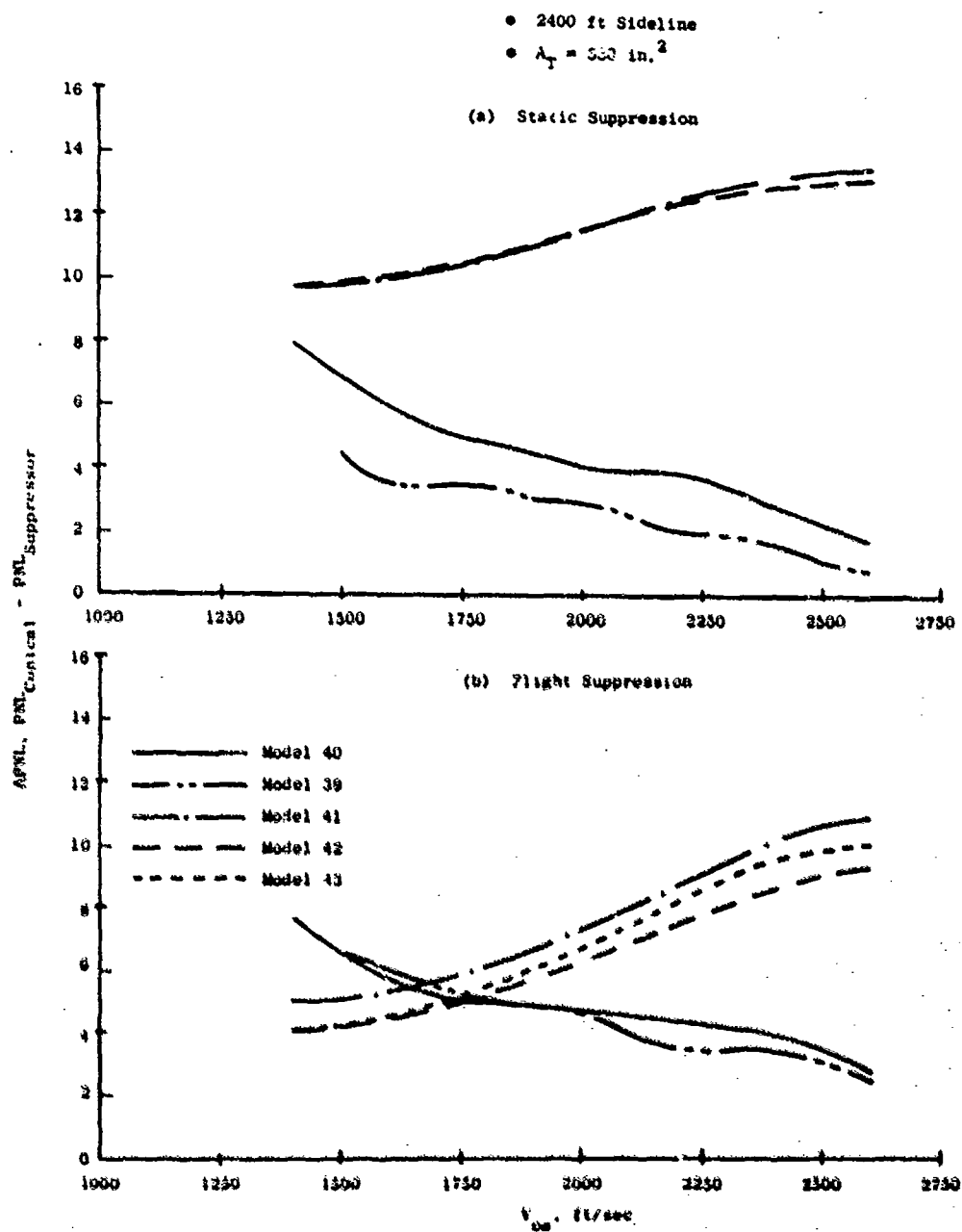


Figure 3-263. Static and Flight PNL Suppression Levels.

Table 3-6. Summary of Nozzle Static and Projected Flight Peak PNL Suppression Characteristics.

- Suppression Levels are Relative to a Conical Nozzle
- 2400-ft Sideline
- $V_j = 2500$  ft/sec
- $A_T = 338$  in.<sup>2</sup>

<u>Model No.</u>	<u>Configuration</u>	<u>Suppression Level, dB</u>	
		<u>Static</u>	<u>Flight</u>
39	Plug Nozzle - 0.789 Radius Ratio	1.3	3.0
40	Plug Nozzle - 0.85 Radius Ratio	2.3	3.7
46	8-Lobe Nozzle	5.6	5.6
41	AR = 2.5 36-Chute Nozzle	13.5	10.9
42	AR = 2.5 36-Chute Nozzle with Auxiliary Flow	12.5	9.4
44	104-Tube Nozzle	12.0	12.0



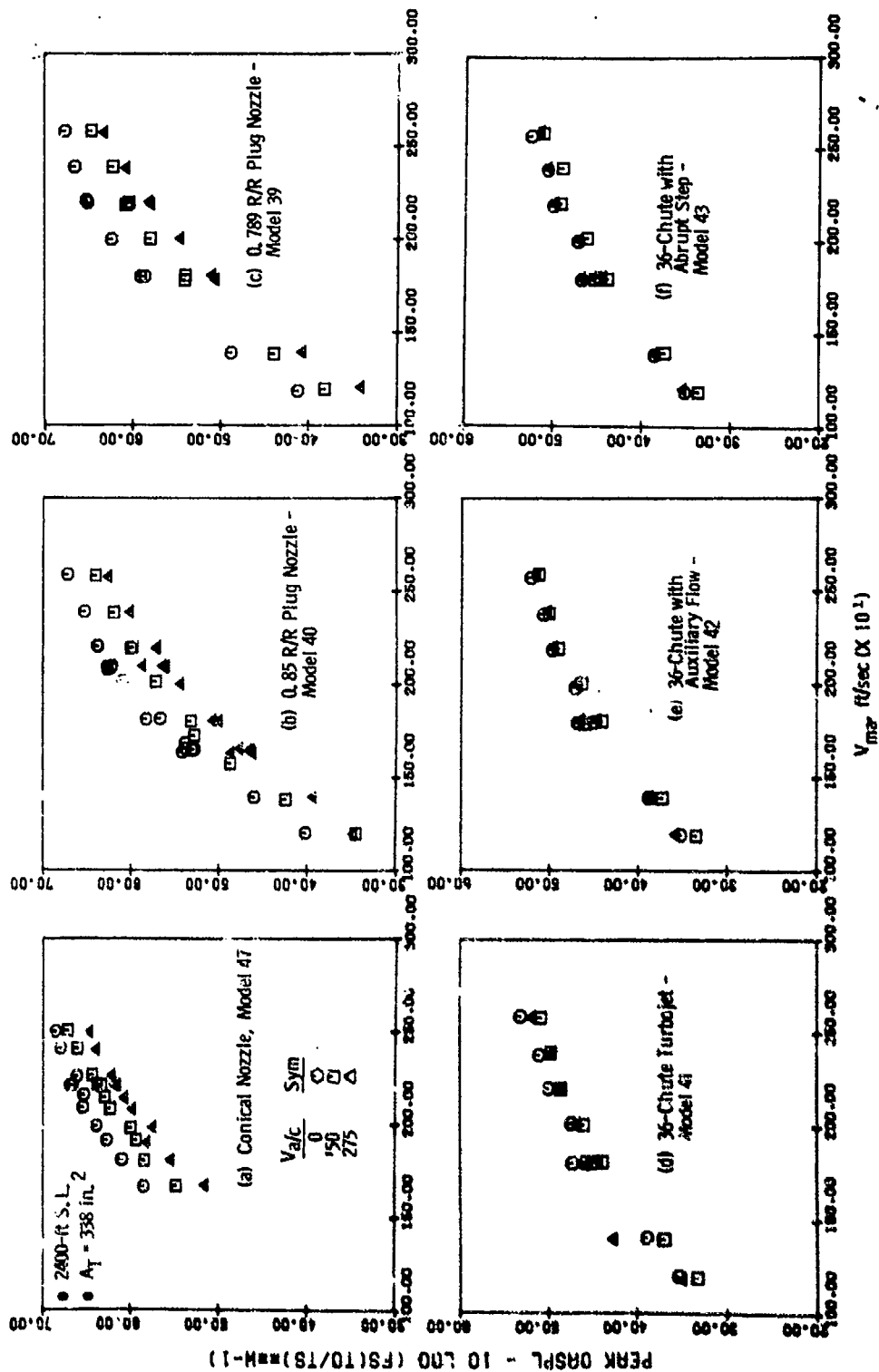


Figure 3-264. Static and Flight Peak QASPL Levels.

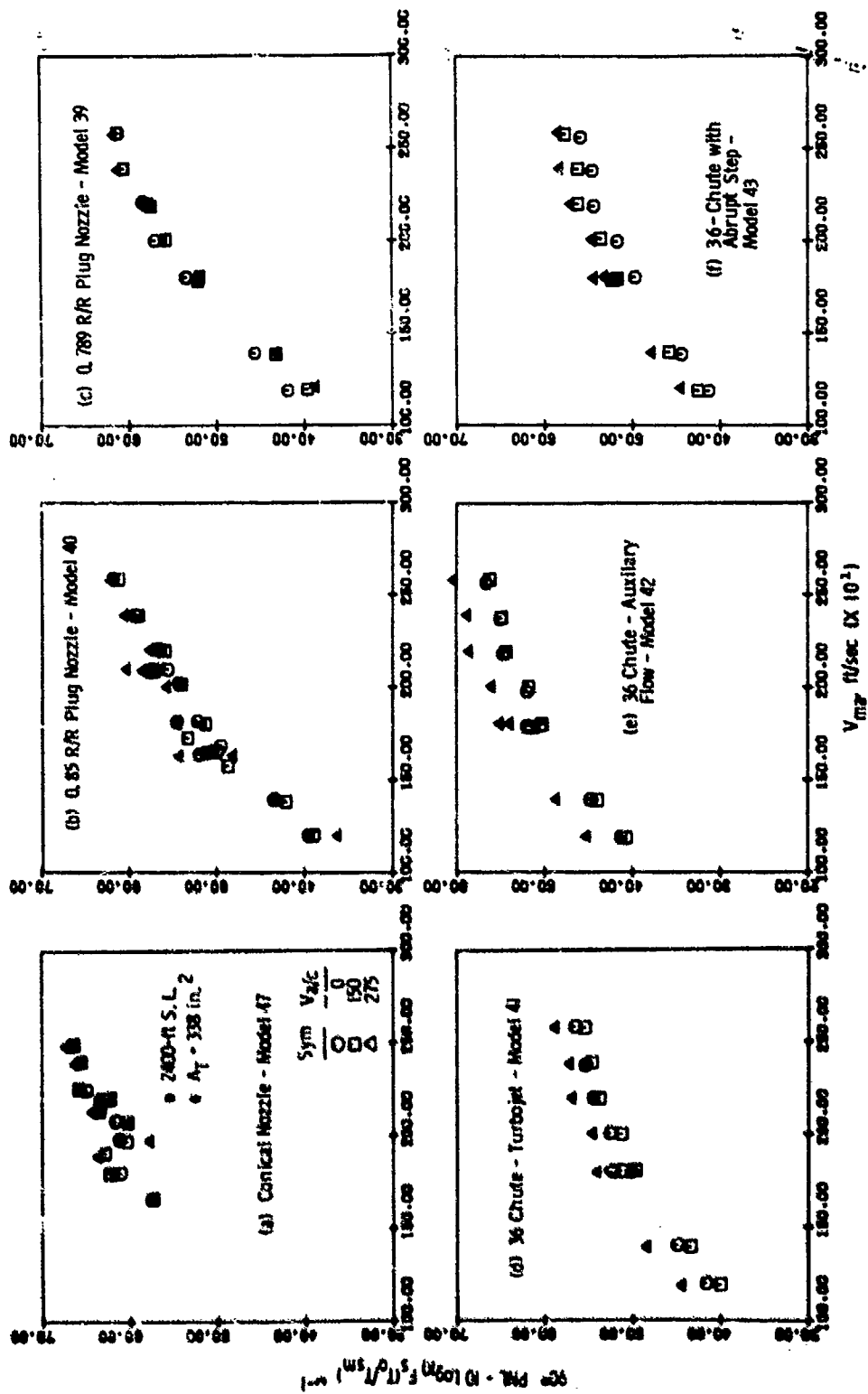


Figure 3-265. Static and Flight 90° PNL Levels.

Velocity indices were calculated for jet velocities ranging from 1800 ft/sec through 2600 ft/sec, as summarized on Figures 3-266 through 3-269. Data at free-jet velocities of 150 and 275 ft/sec were utilized. The velocity index parameter was not sufficient to collapse the data into one set of indices which is correct for all configurations. Plug nozzles and conical nozzles have similar indices in the aft quadrant. In the forward quadrant the effect of shock-cell noise is apparent. In general, for the conical nozzle (Figure 3-266) as pressure ratio increases, forward quadrant indices become negative which indicates a noise increase in flight. The suppressor nozzles exhibit a velocity pattern which is distinctly different from the conical nozzle and varies with nozzle type. Chute nozzles in particular show a sharp decrease in velocity index beginning at an acoustic angle of  $130^\circ$ .

The velocity indices are compared on Figure 3-270 for several configurations. The tube nozzle and plug nozzles have velocity index patterns of similar shape and level. The conical nozzle deviates from these configurations, particularly in the forward quadrant, due to the presence of shock noise. Velocity indices of the chute nozzle configurations are significantly less than that of the other configurations at  $130^\circ$ . Examination of the spectra should provide some insight into the cause of this variation.

The spectra presented on Figures 3-271(a) and 3-271(b) are at  $130^\circ$  for both the chute (Model 41) and tube (Model 44) nozzles. Three spectra are presented for each configuration: static spectra and wind-on spectra before and after transformation. The reduction in the low frequency portion of the spectra is within 1 dB for both the chute and tube nozzle configurations. In the high frequency portion of the spectra, dominated by the premerged noise, both nozzles have a slight increase in level. However, the absolute level relative to the low frequency portion of the spectra is extremely different. The transformed spectra of the chute and tube nozzles are compared on Figure 3-272. There is a 10 dB difference in the high frequency portion of the spectra. The dominance of the high frequency noise is the reason for the lack of flight effect on these chute nozzles.

In addition to being analyzed on a velocity index basis, the directivity patterns were also analyzed on the basis of PNL suppression level as a function of angle for several jet velocities. Jet velocities of 2200 ft/sec and 2600 ft/sec are discussed in detail.

The acoustic suppression levels in terms of APNL versus angle are summarized on Figures 3-273 through 3-275. Static and flight suppression levels, Figure 3-273, are equivalent for the plug nozzle. The chute nozzles, Figure 3-274, exhibit a loss of suppression in the aft quadrant and generally maintain suppression in the forward quadrant. The 104-tube (Model 44) and 104-hold (Model 45) nozzles, Figure 3-275, show essentially no change in suppression level relative to a conical nozzle (Model 47) in flight.

A summary of PNL, OASPL, and spectra comparisons for each of the configurations is presented in Figures 3-276 through 3-301 for jet velocities of 150 and 2000 ft/sec. Four acoustic angles of  $50^\circ$ ,  $90^\circ$ ,  $110^\circ$ , and  $130^\circ$  were

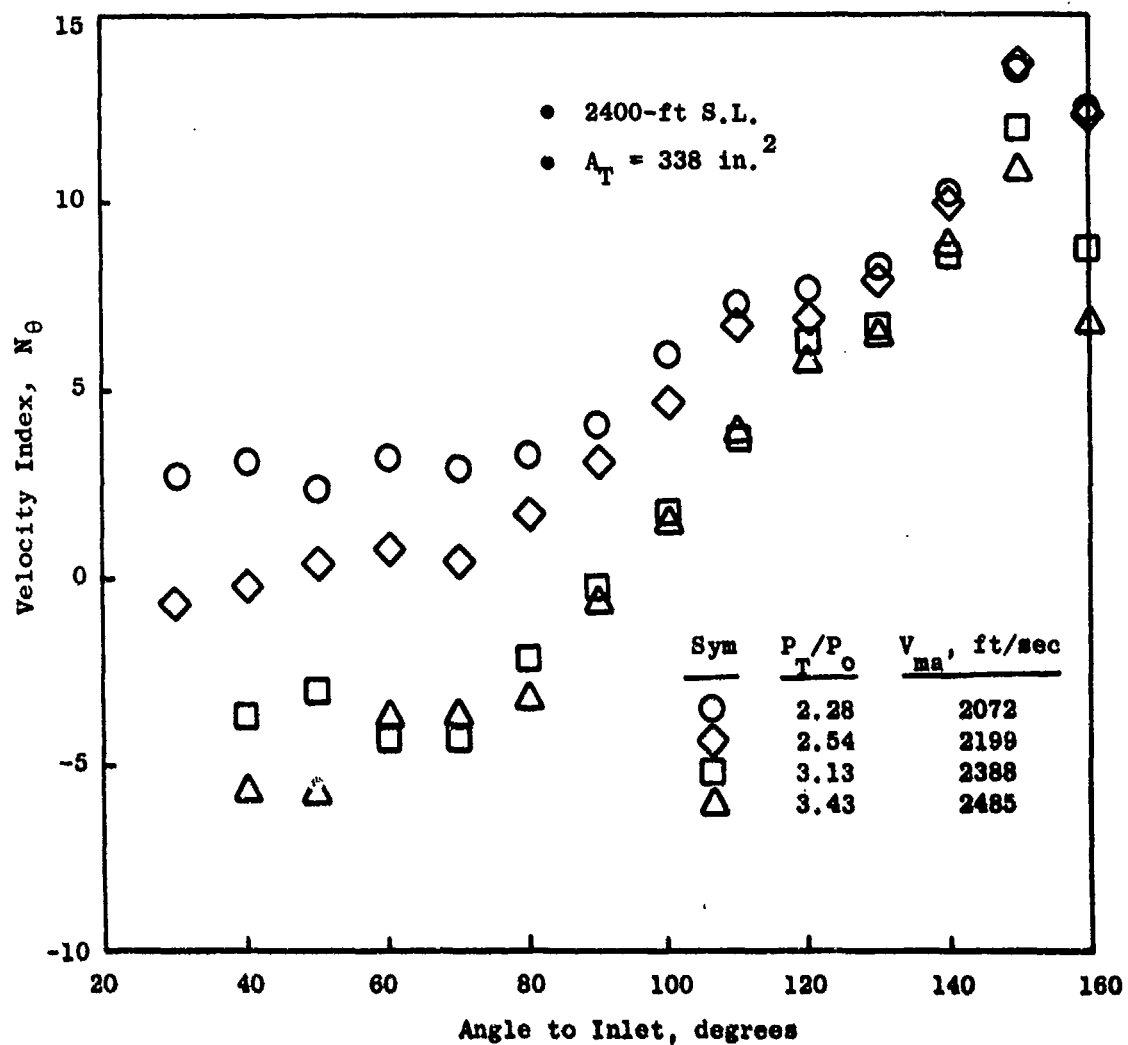


Figure 3-266. Conical Nozzle (Model 47) Velocity Indices.

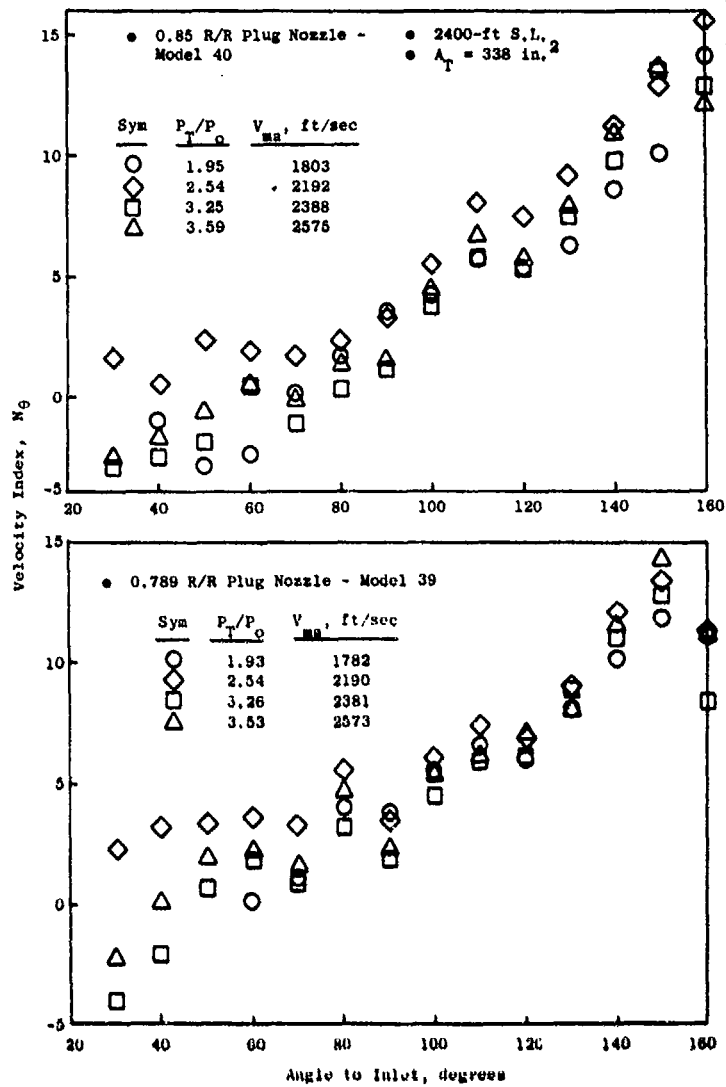


Figure 3-267. Plug Nozzle (Models 39 and 40) Velocity Indices.

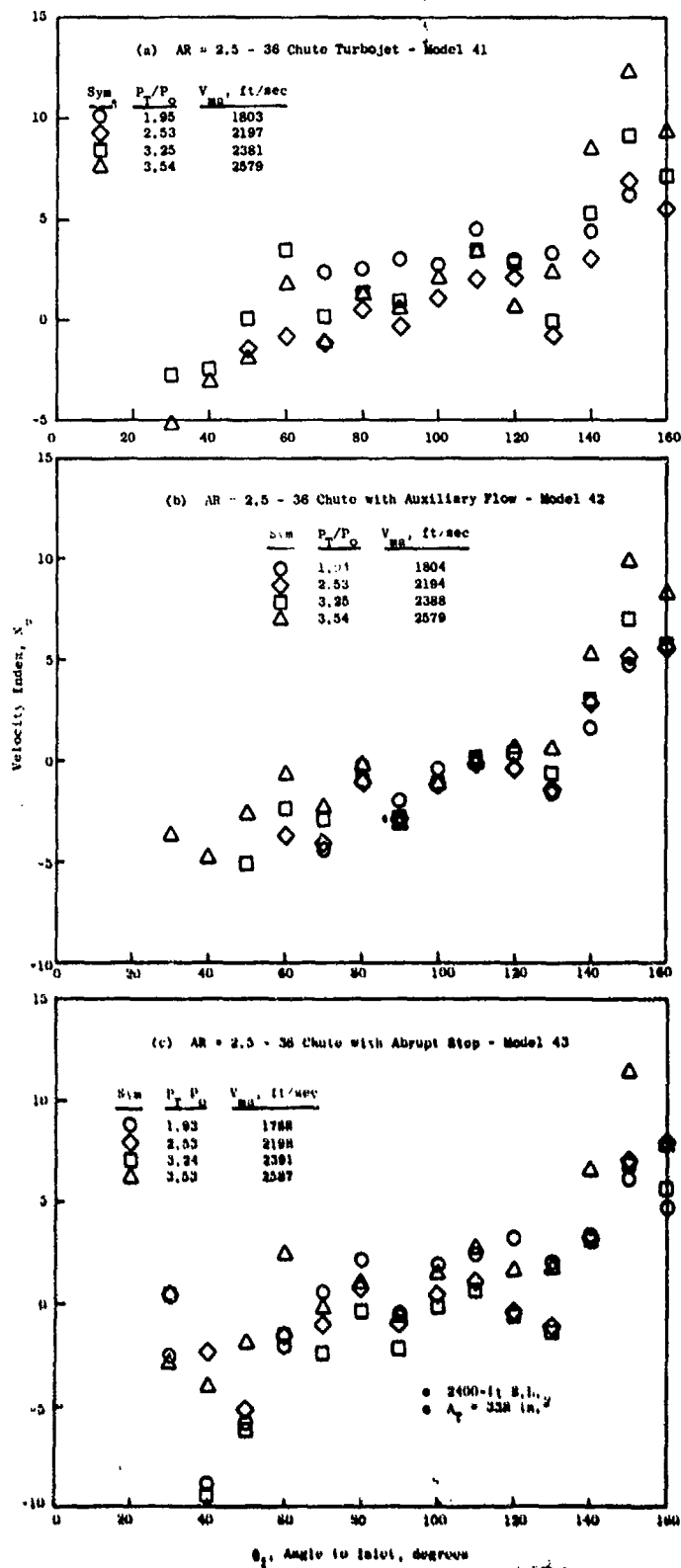


Figure 3-268. Chute Nozzle (Models 41, 42, and 43) Velocity Indices.

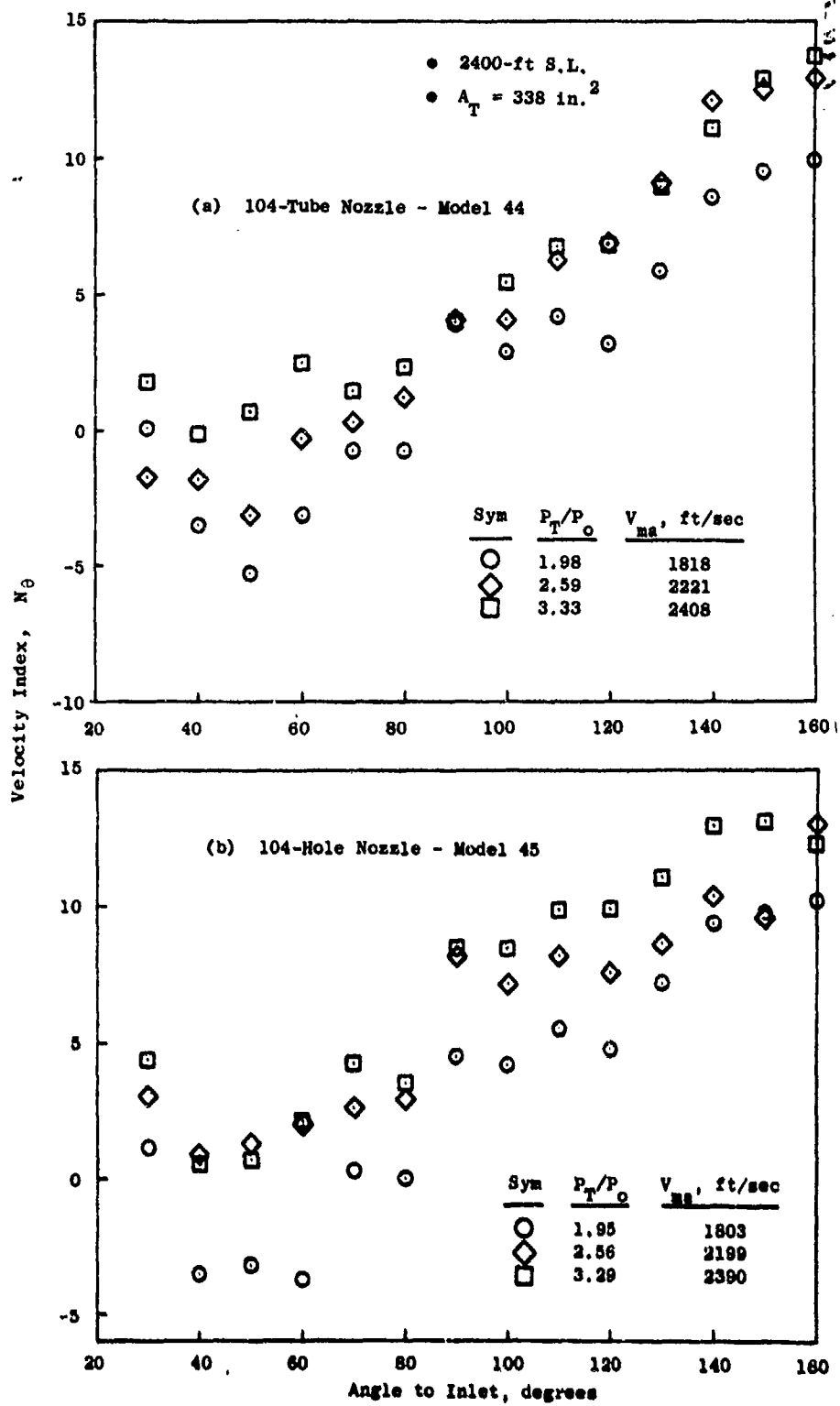


Figure 3-269. 104-Tube (Model 44) 104-Hole (Model 45) Nozzle Velocity Indices.

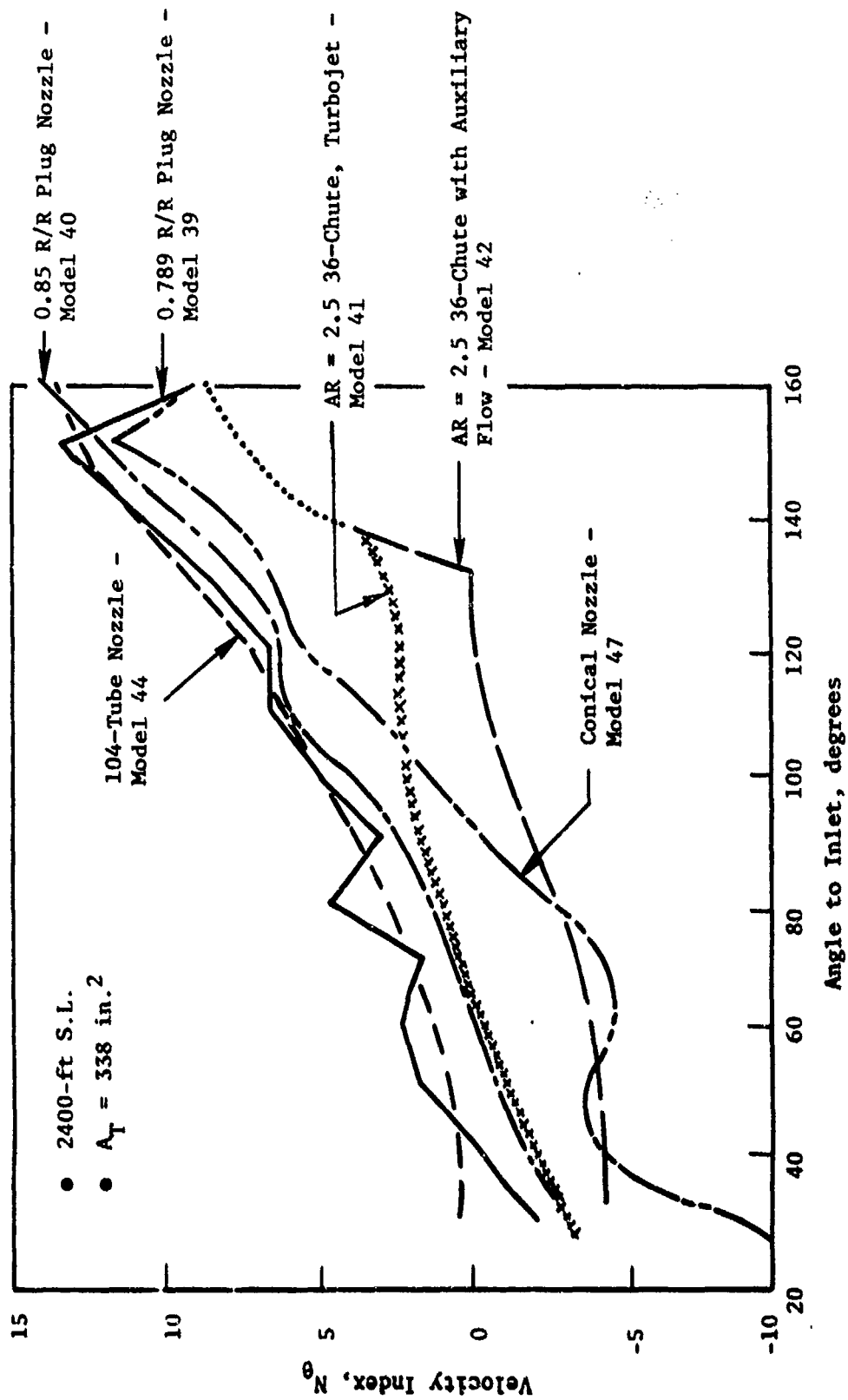
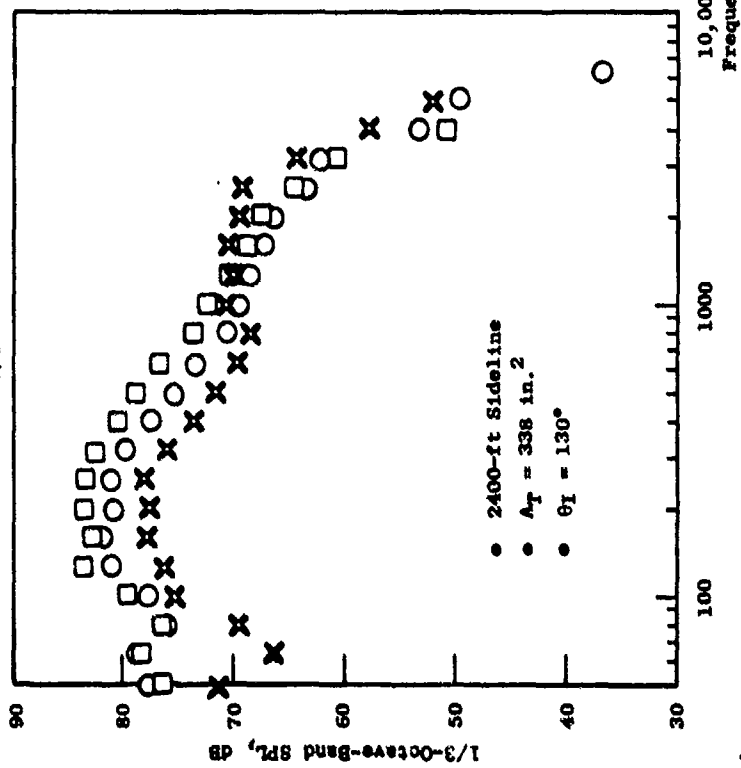


Figure 3-270. Velocity Indices for Several Nozzles.



a. 104-Tube Nozzle - Model 44  
 $V_{ma} = 2408$  ft/sec;  $V_a/c = 287$  ft/sec



b. AR = 2.5, 36-Chute Nozzle - Model 41  
 $V_{ma} = 2381$  ft/sec;  $V_a/c = 287$  ft/sec

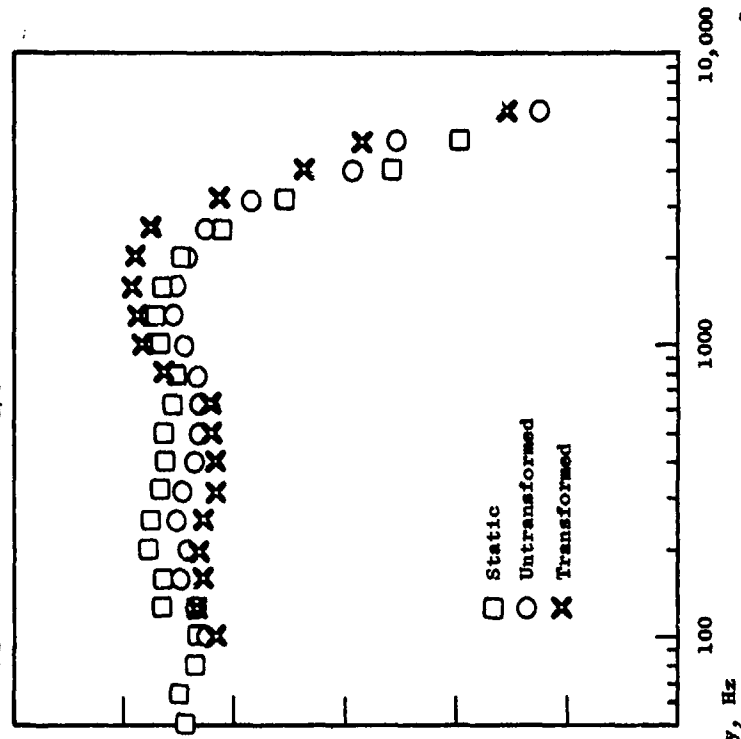


Figure 3-271. Comparison of Static and Flight Spectra, 104-Tube and 36-Chute Nozzles (Models 44 and 41).

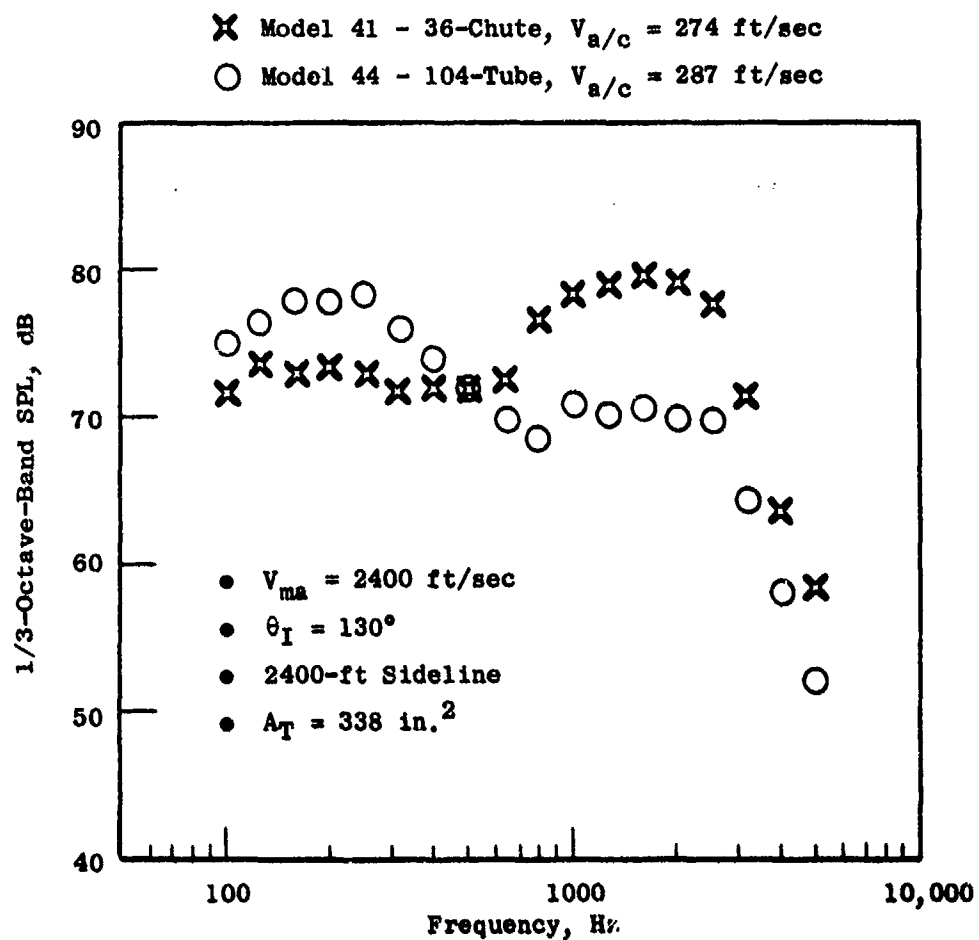


Figure 3-272. A Comparison of the Flight Spectra for 104-Tube (Model 44) and 36-Chute (Model 42) Nozzles.

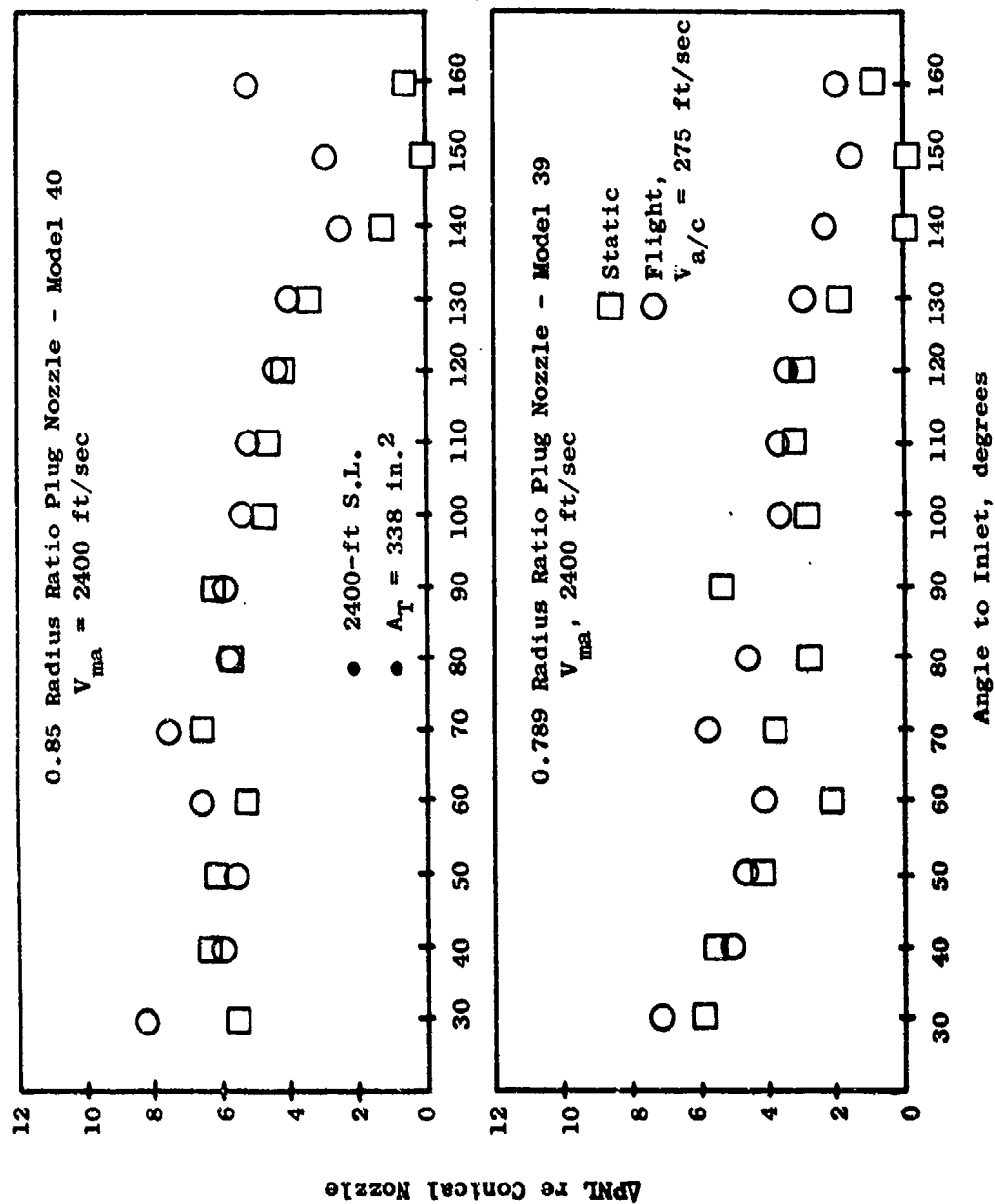


Figure 3-273. Summary of Static and Flight PNL Suppression Characteristics (Models 39 and 40).

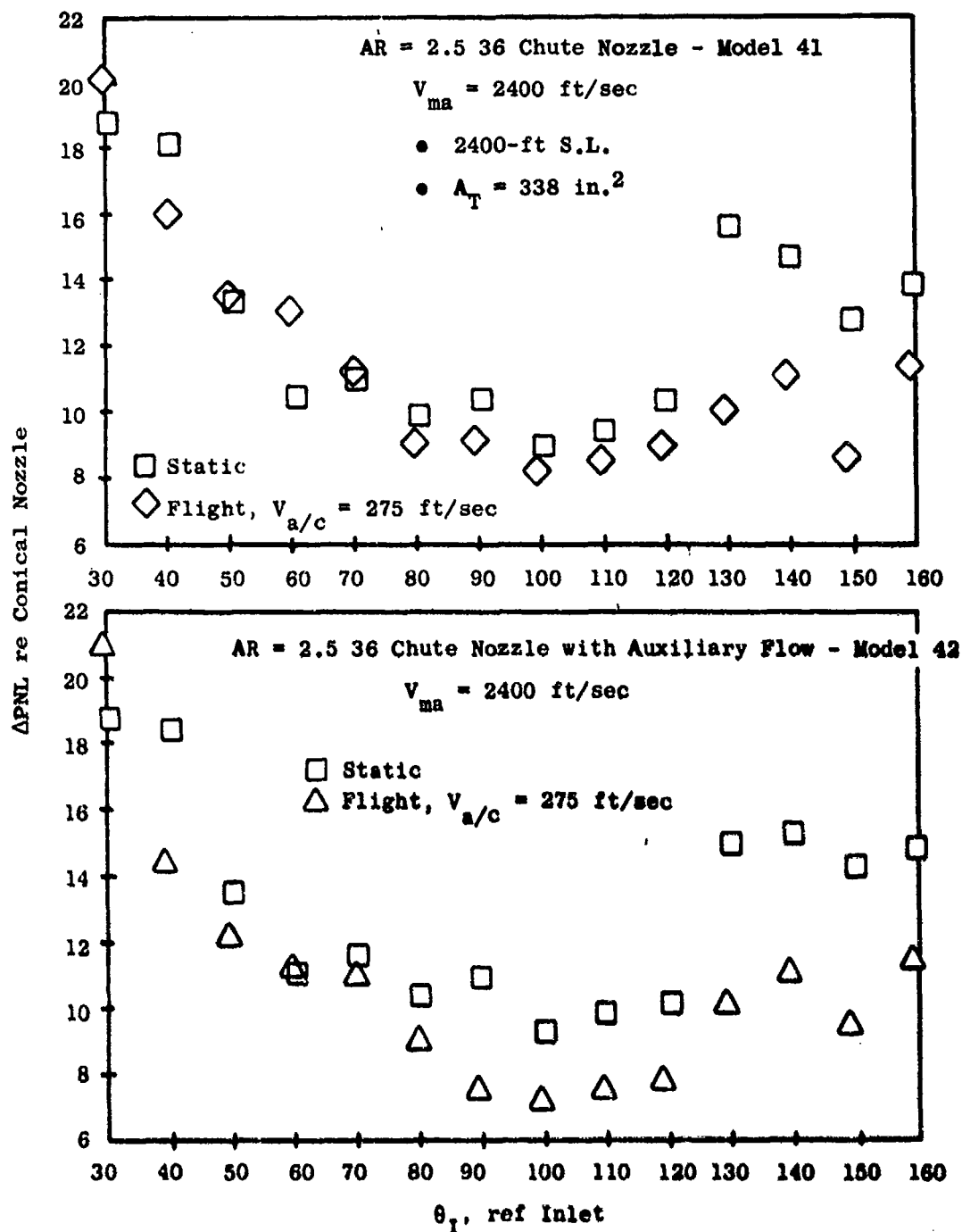


Figure 3-274. Summary of Static and Flight Suppression Characteristics (Models 41 and 42).

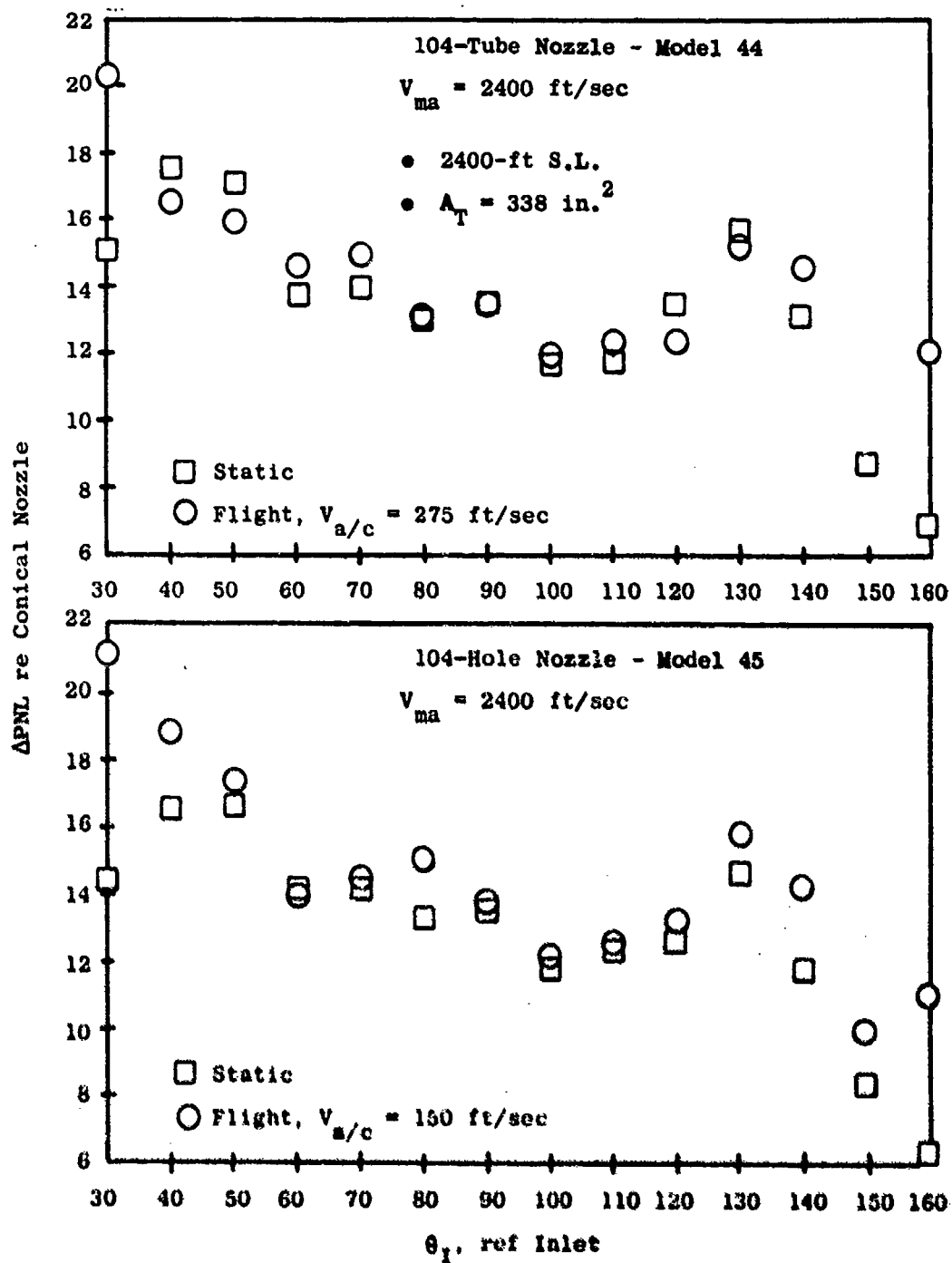


Figure 3-275. Summary of Static and Flight Suppression Characteristics (Models 44 and 45).

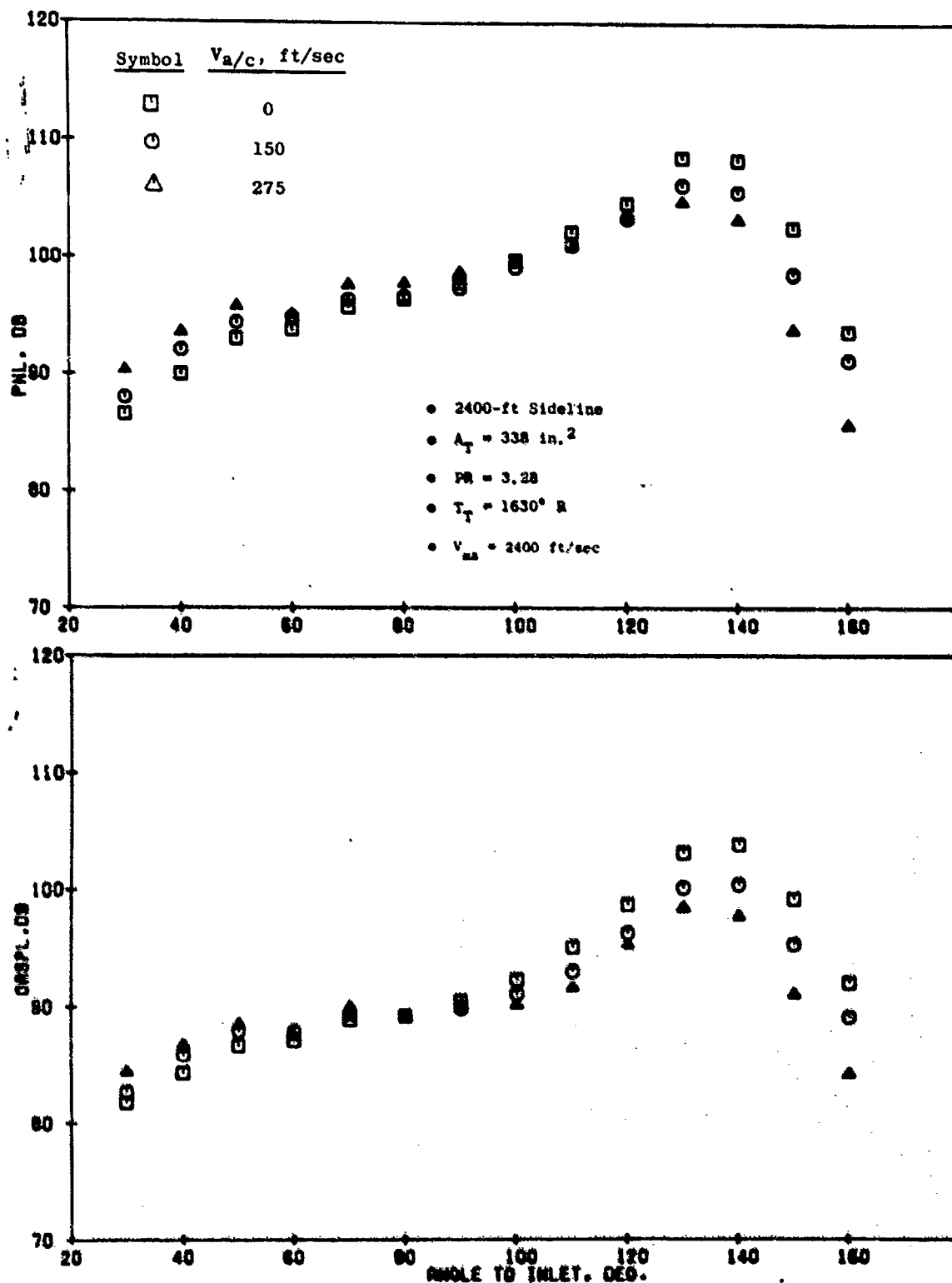


Figure 3-276. 0.85 R/R Plug Nozzle (Model 40) PNL and OASPL Directivity,  $V_{ma} = 2400 \text{ ft/sec}$ .

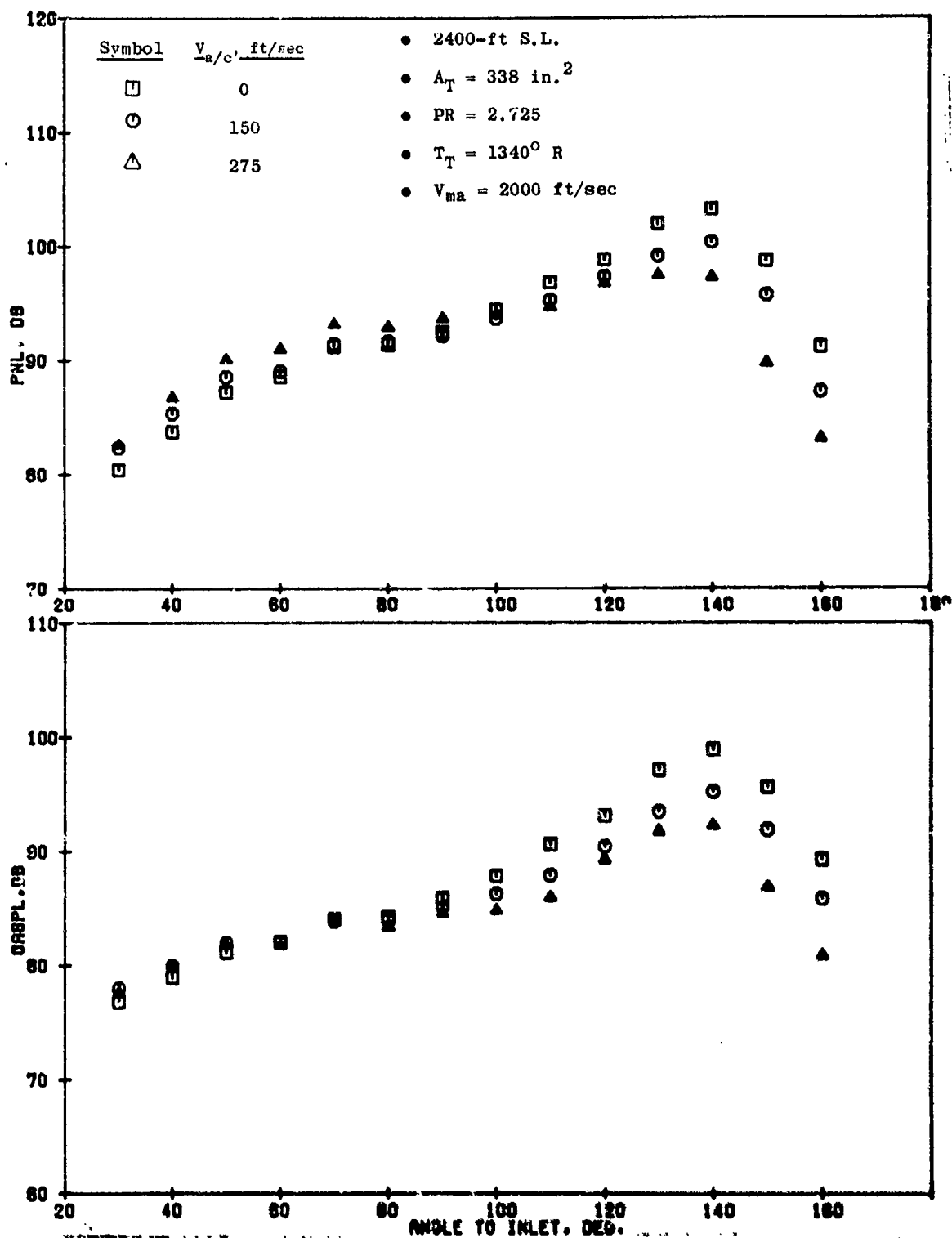


Figure 3-277. 0.85 R/R Plug Nozzle (Model 40) PNL and OASPL Directivity,  $V_{ma} = 2000 \text{ ft/sec}$ .

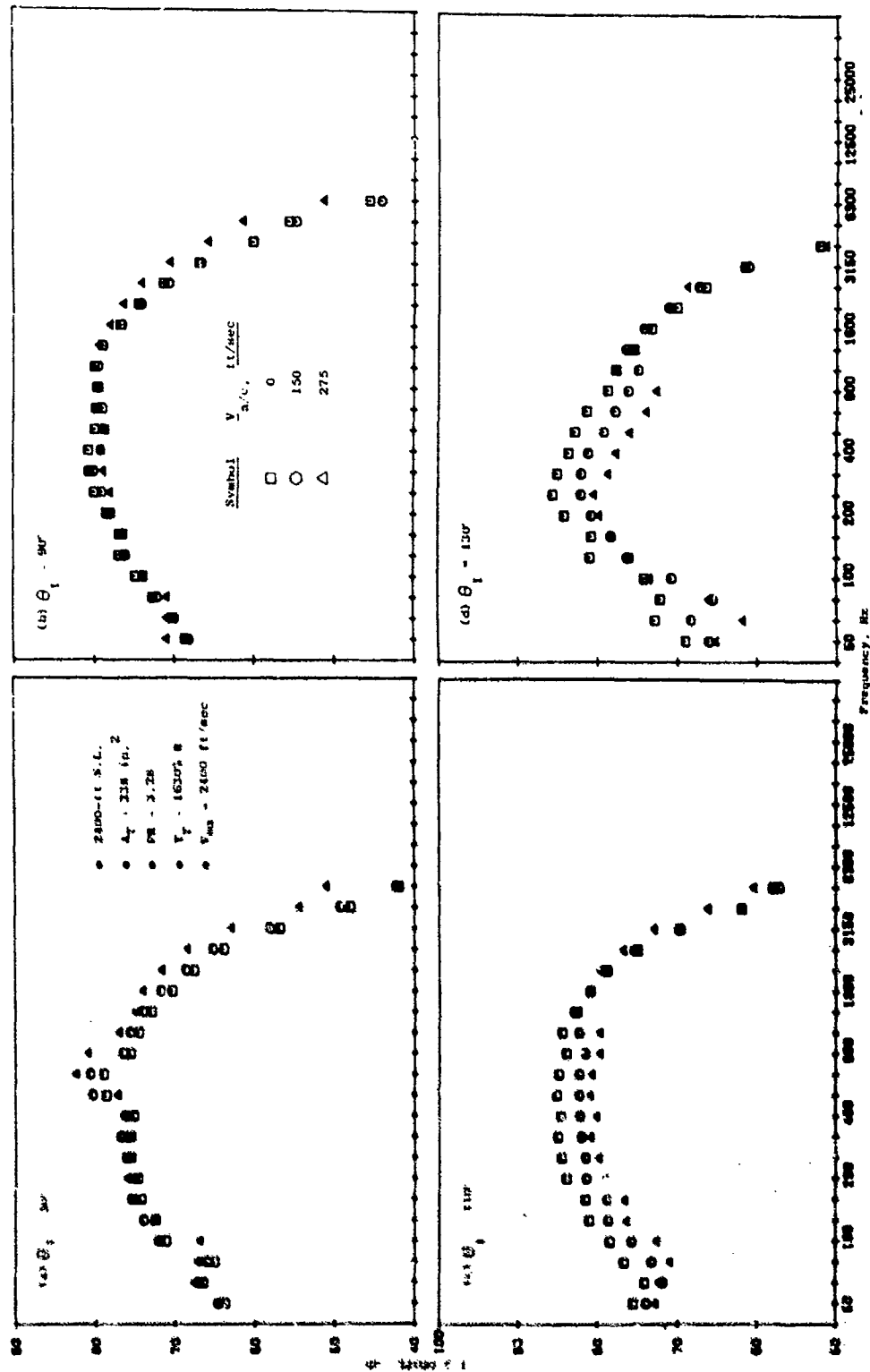


Figure 3-278. 0.85 Radius Ratio Plug Nozzle (Model 40) Spectra,  $V_{ma} = 2400$  ft/sec.



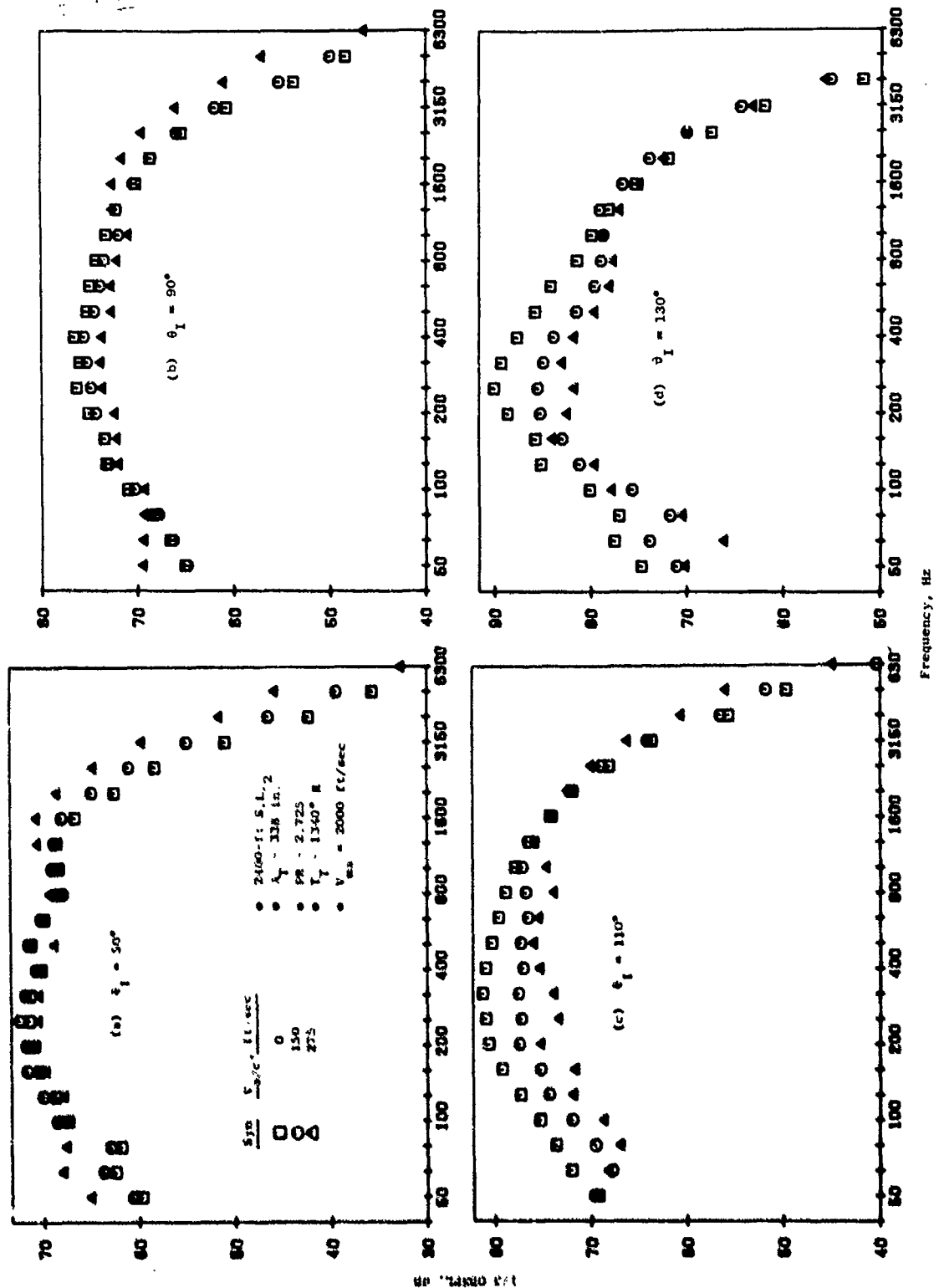


Figure 3-279. 0.85 Radius Ratio Plug Nozzle (Model 40) Spectra,  $V_{ma} = 2000$  ft./sec.

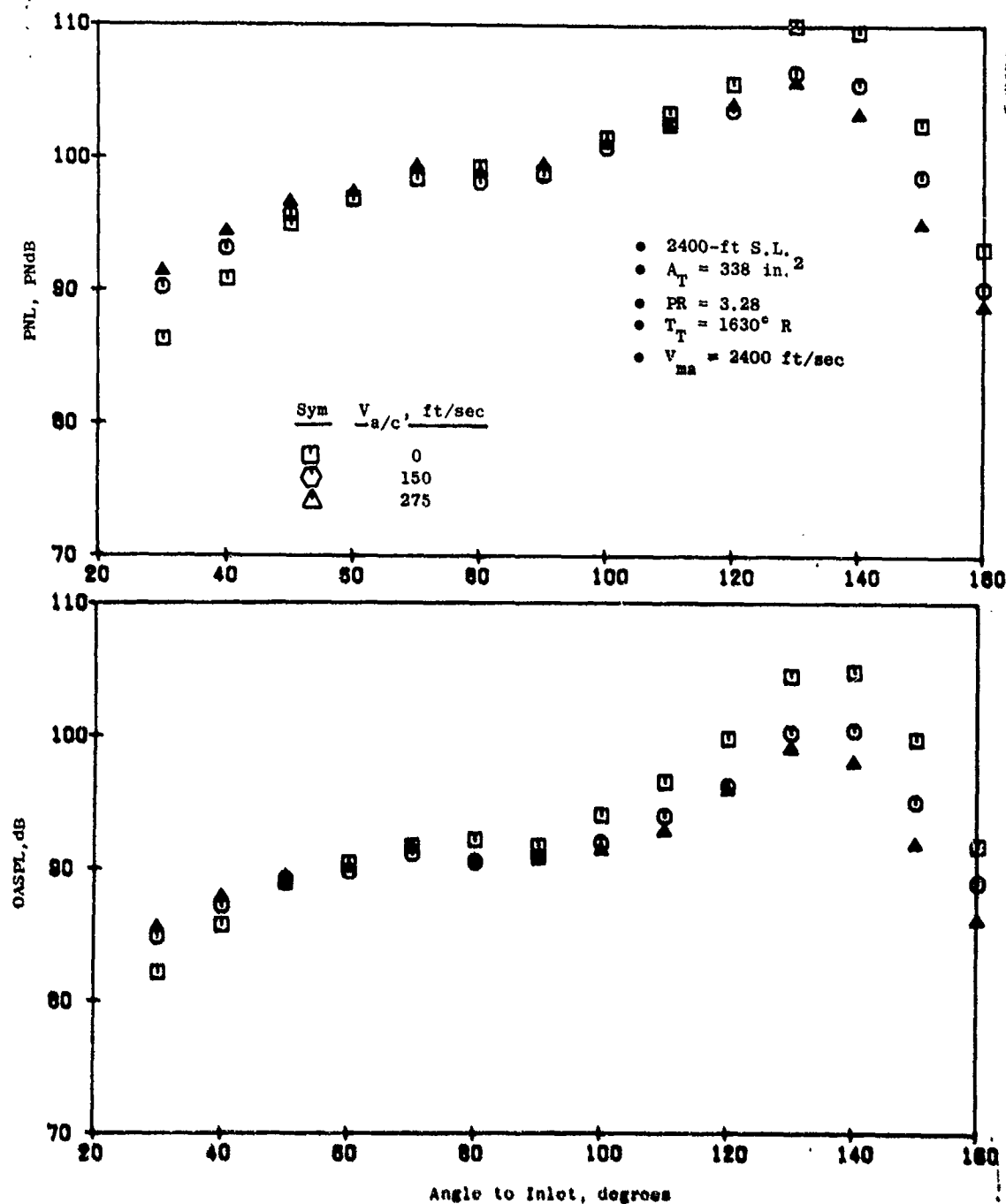


Figure 3-280. 0.789 Radius Ratio Plug Nozzle (Model 39) PNL and OASPL Directivity,  $V_{na} = 2400 \text{ ft/sec}$ .

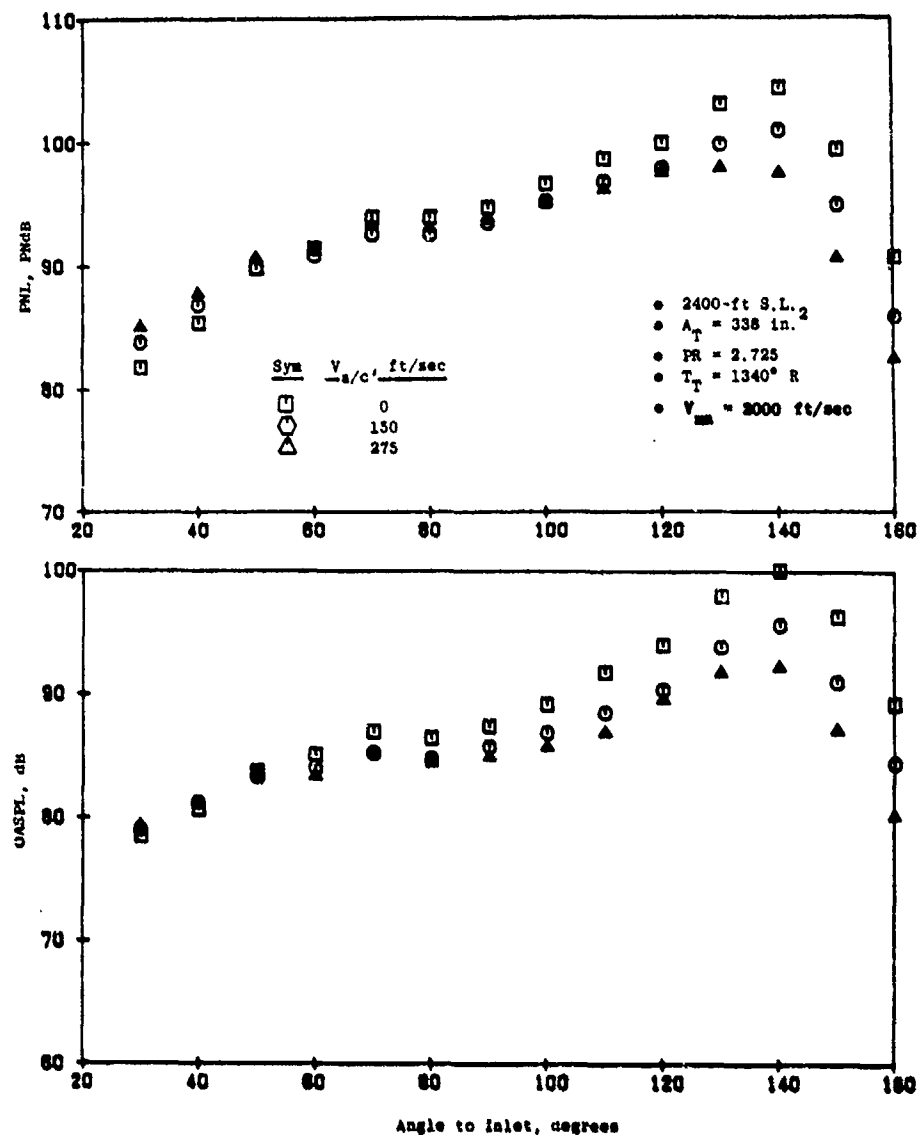


Figure 3-281. 0.789 Radius Ratio Plug Nozzle (Model 39)  
PNL and OASPL Directivity,  $V_{ma} = 2000$   
ft/sec.

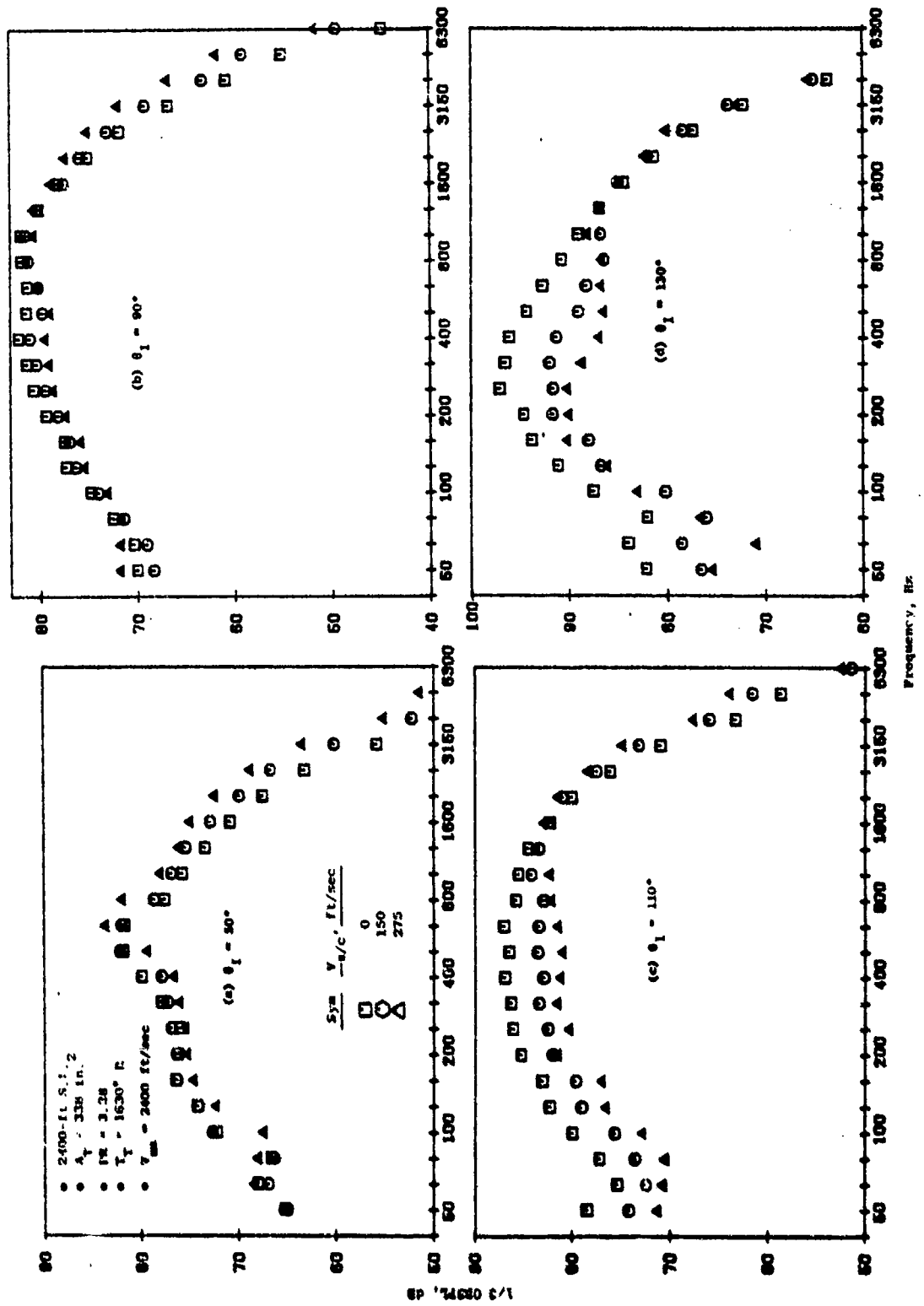


Figure 3-282. 0.789 Radius Ratio Plug Nozzle (Model 39) Spectra,  $V_{ma} = 2400 \text{ ft/sec}$ .

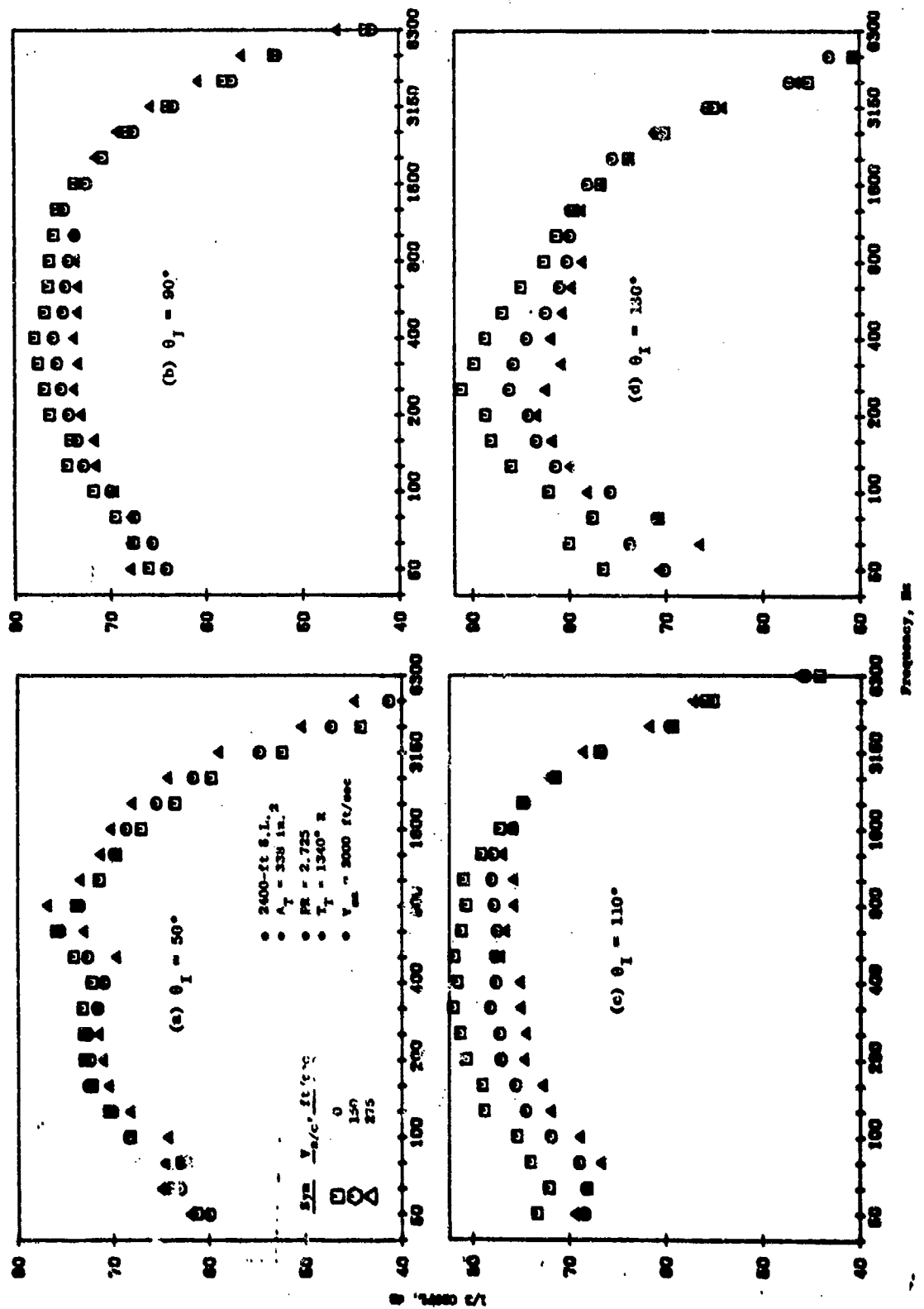


Figure 3-283. 0.789 Radius Ratio Plug Nozzle (Model 39) Spectra,  $V_{ma} = 2400 \text{ ft/sec}$ .

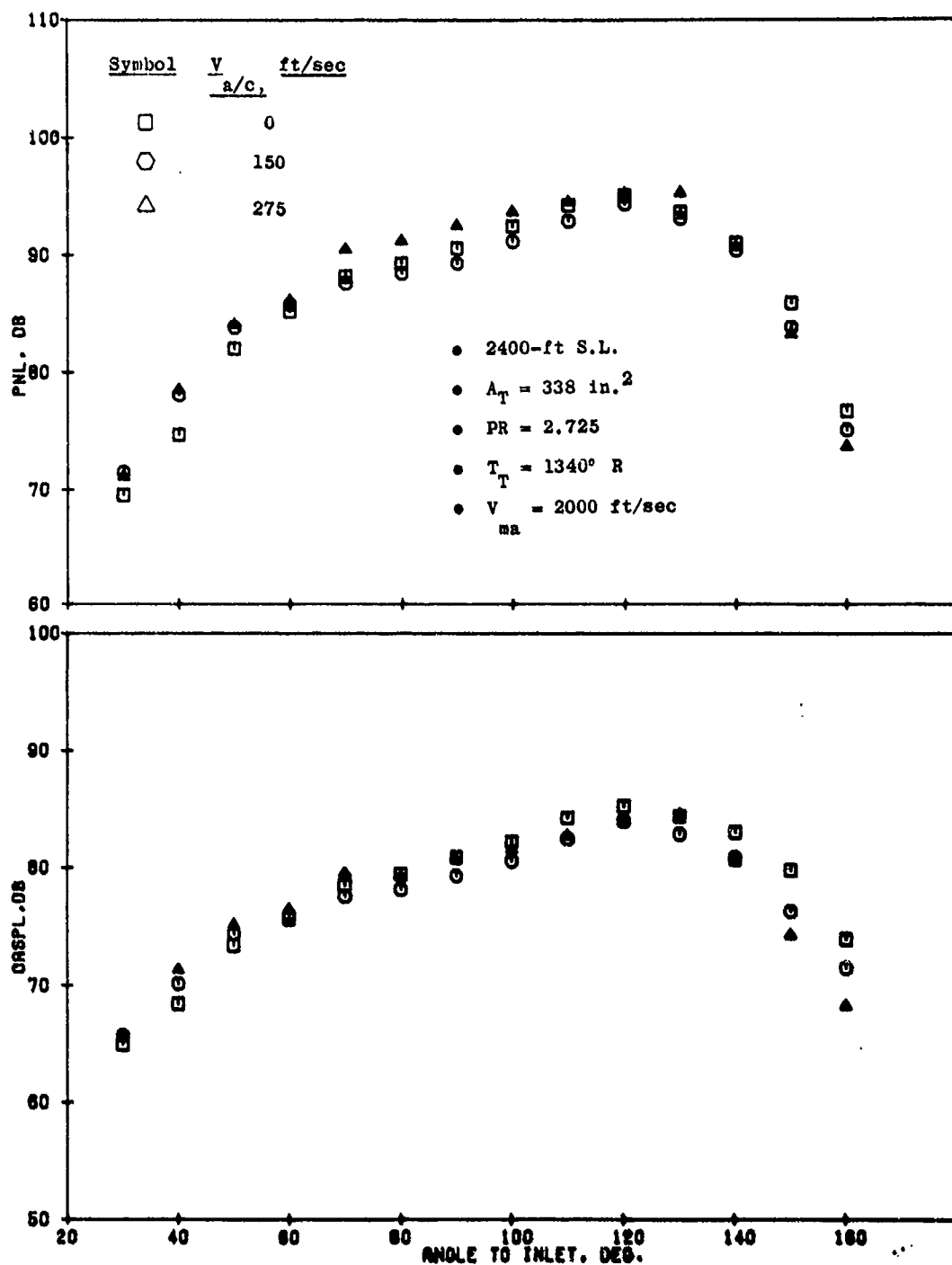


Figure 3-284. AR = 2.5 35-Chute, Turbojet (Model 41), PNL and OASPL Directivity,  $V_{ma} = 2000 \text{ ft/sec.}$

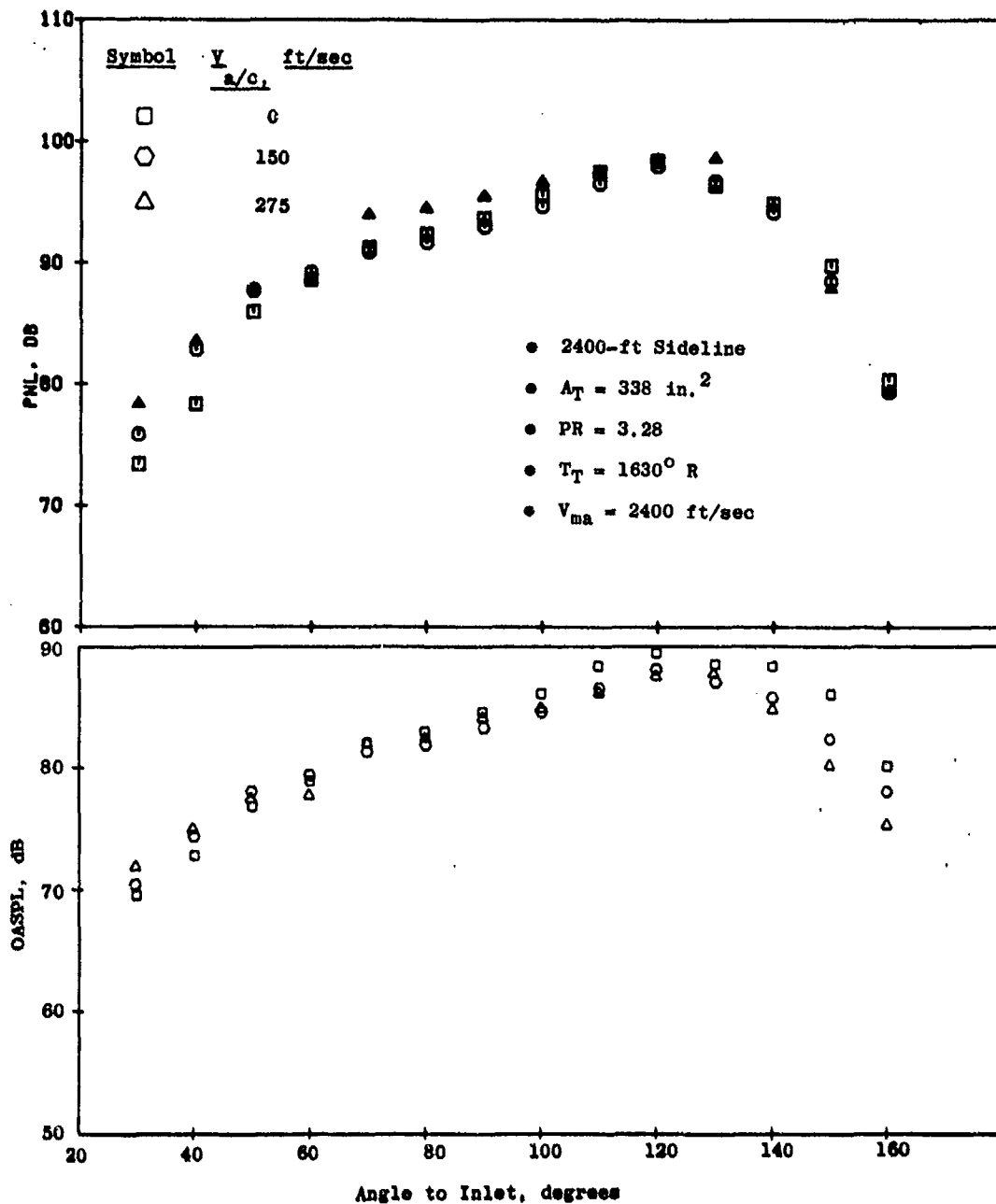


Figure 3-285. AR = 2.5 36-Chute (Model 41), Turbojet, PNL and OASPL Directivity,  $V_{ma} = 2400 \text{ ft/sec}$ .

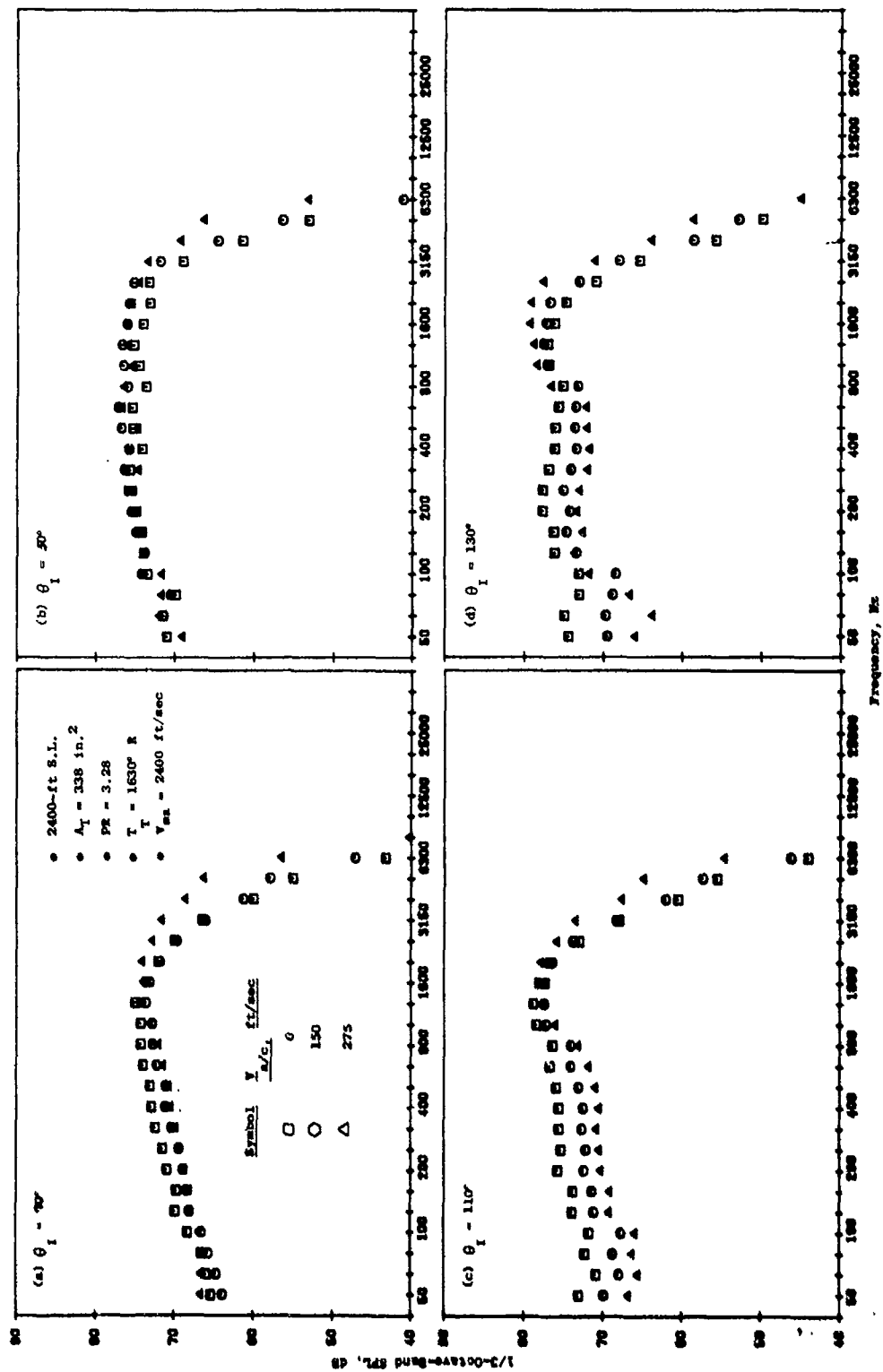


Figure 3-286. AR = 2.5 36-Chute (Model 41), Turbojet, Spectra,  $V_{ma} = 2400 \text{ ft/sec}$ .



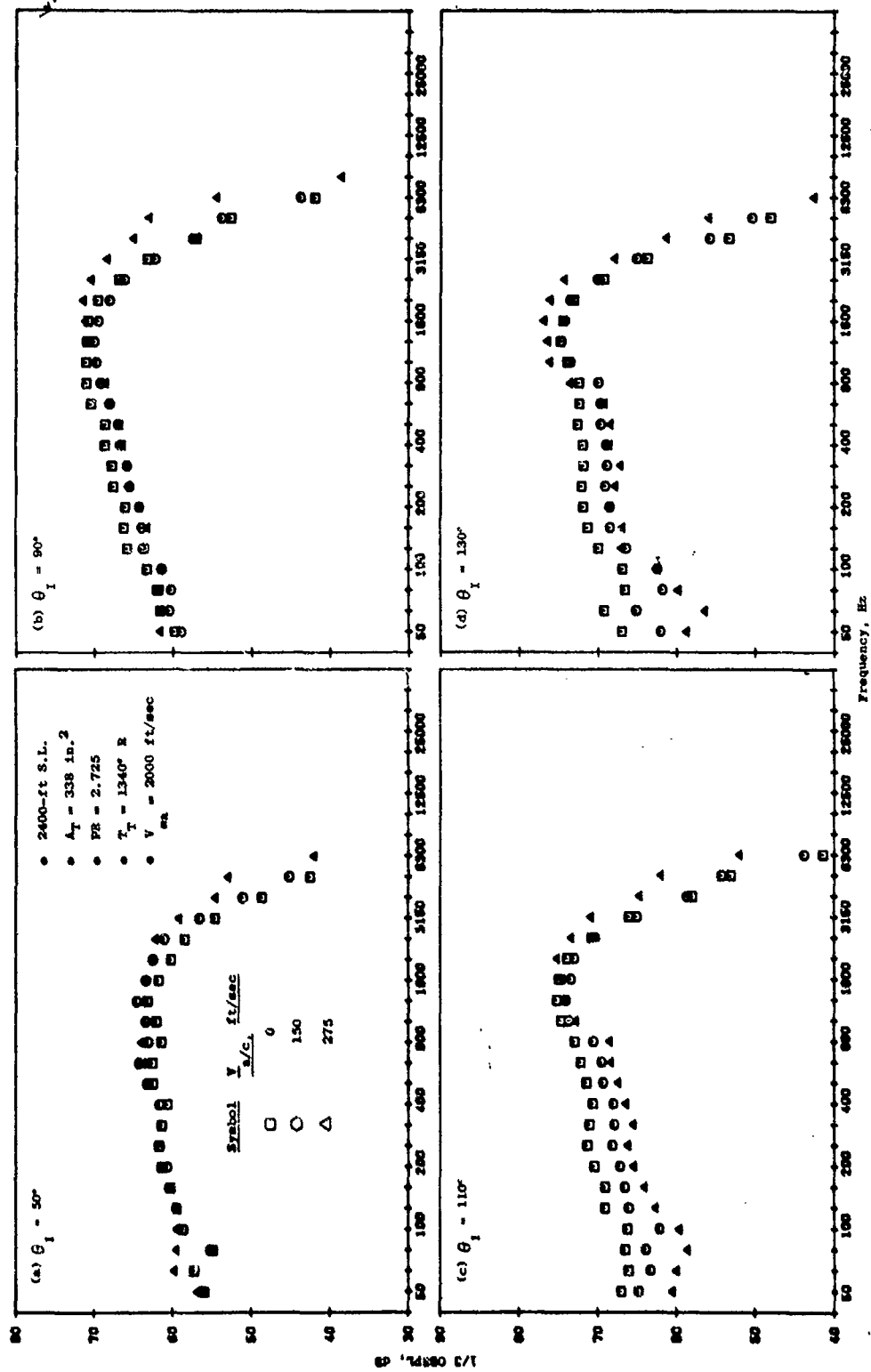


Figure 3-287. AR = 2.5 36-Chute, Turbojet (Model 41) Spectra,  $V_{ma} = 2000$  ft/sec.

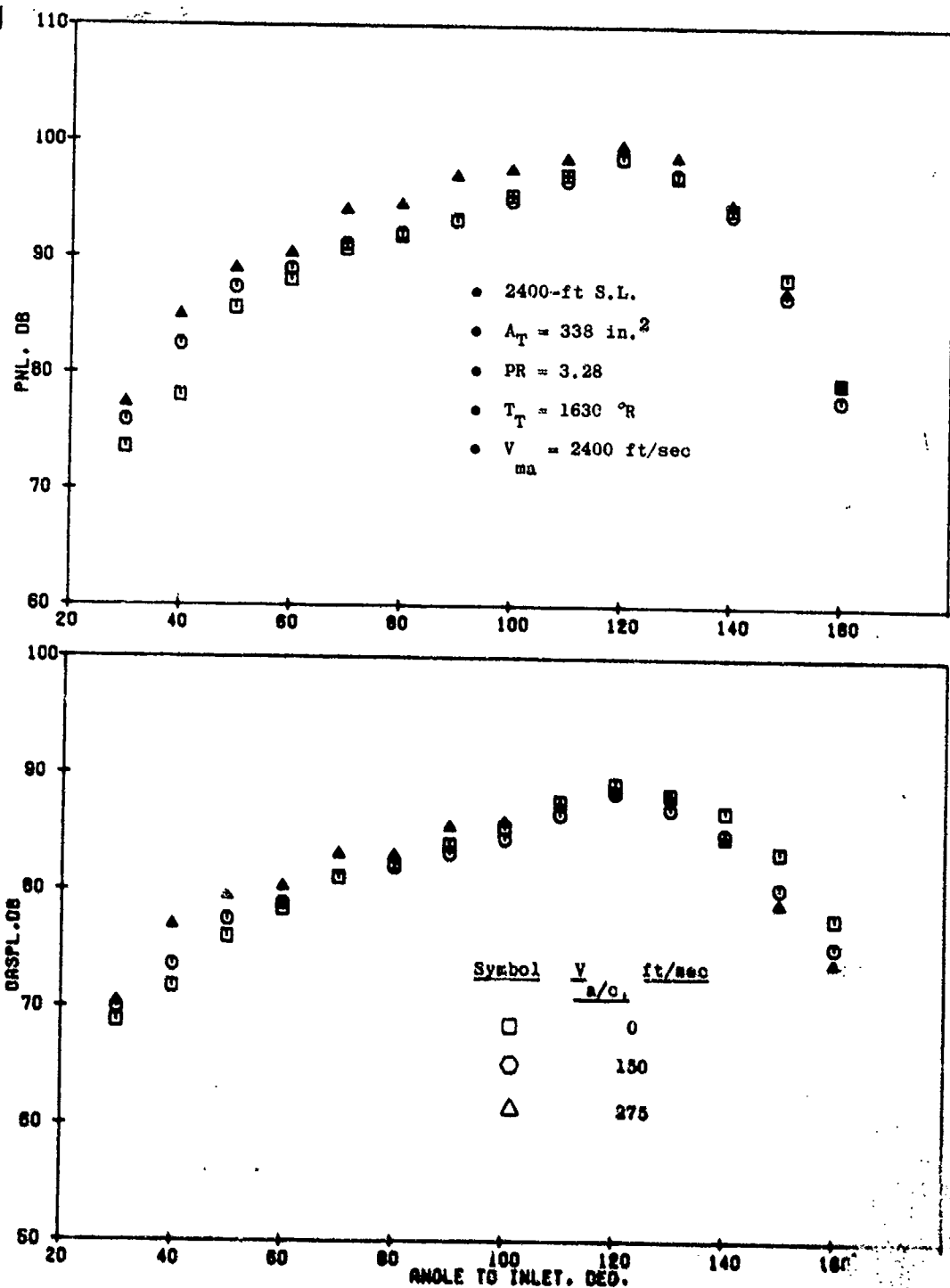


Figure 3-288. AR = 2.5 36-Chute with Auxiliary Flow (Model 42), PNL and QASPL Directivity,  $V_{ma} = 2400 \text{ ft/sec}$ .

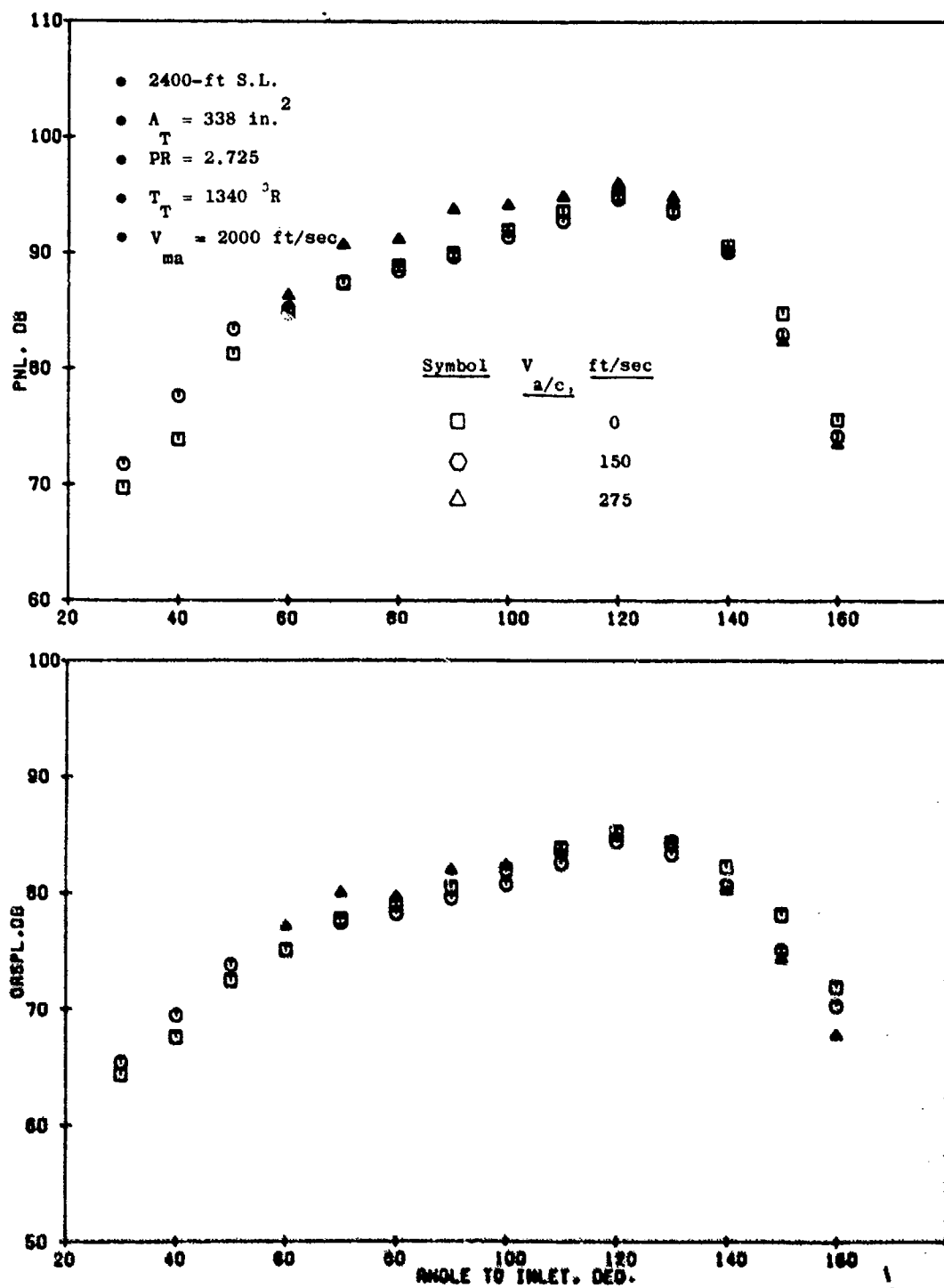


Figure 3-289. AR = 2.6 36-Chute with Auxiliary Flow (Model 42), PNL and GASPL Directivity,  $V_{ma} = 2000 \text{ ft/sec}$ .

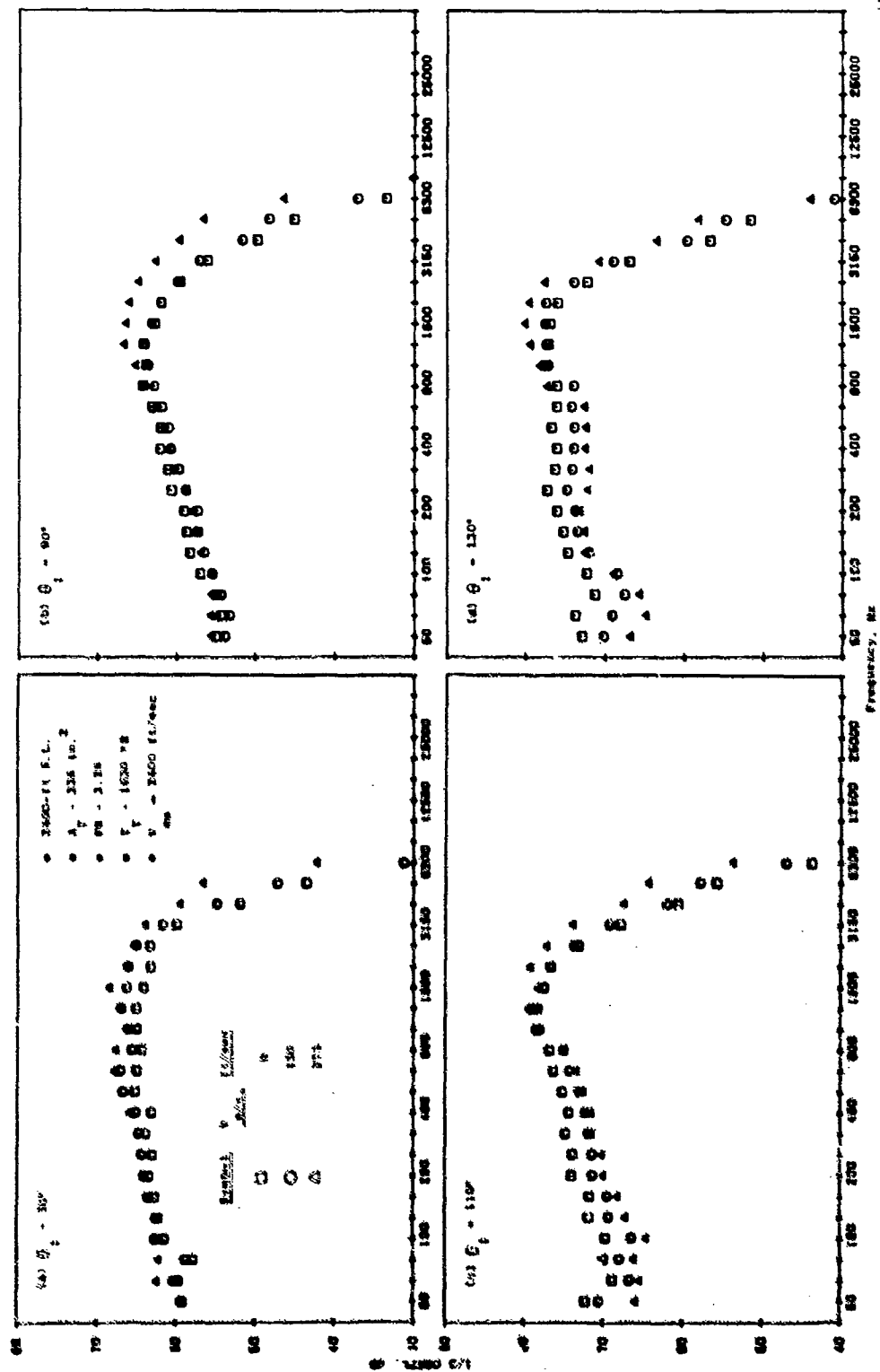


Figure 3-290.  $A = 2.5$  38-Chute with Auxiliary Flow (Model 42), Spectra,  $V = 2400 \text{ ft/sec}$ .

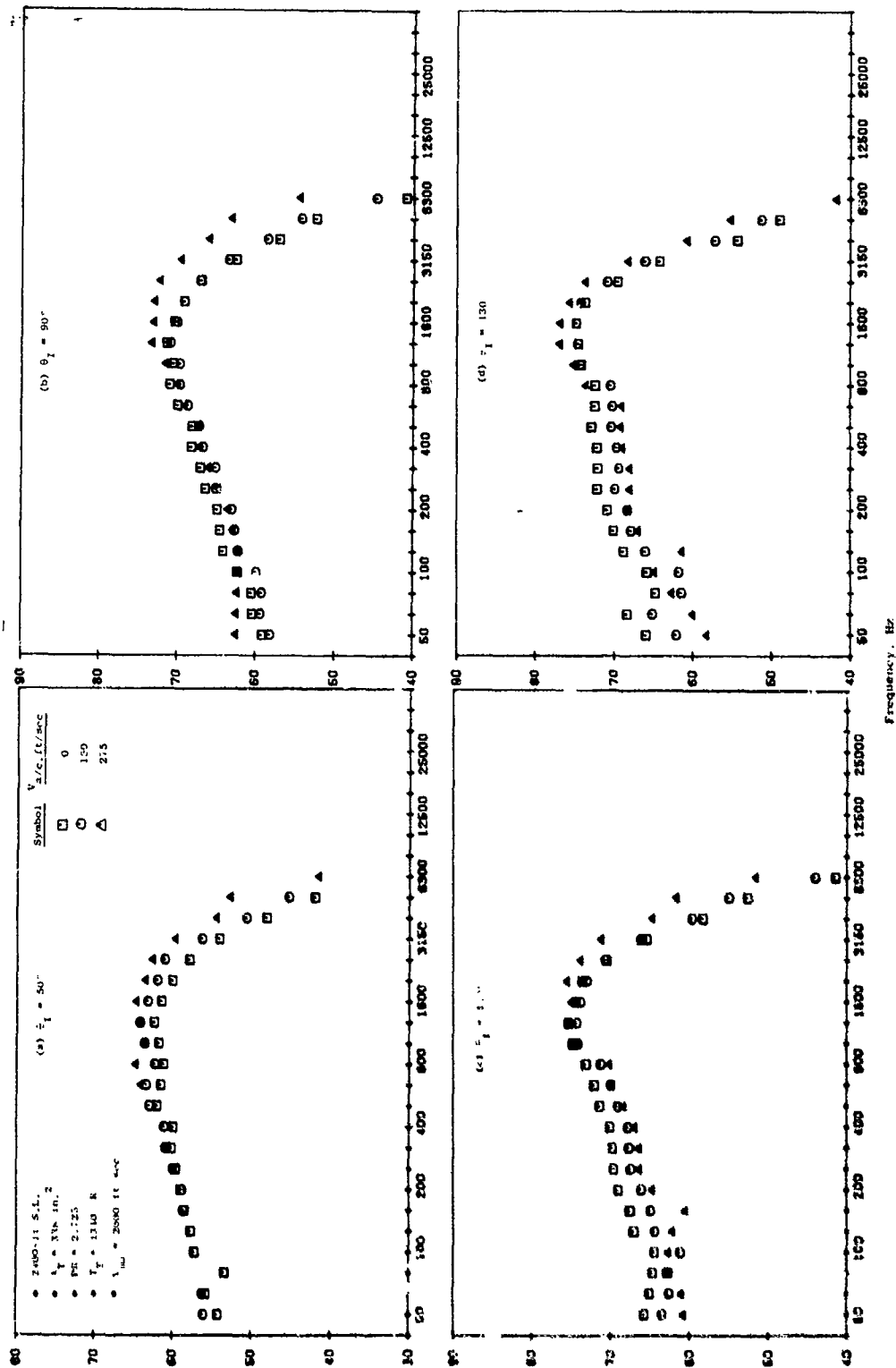


Figure 3-291. AR = 2.5 36-Chute with Auxiliary Flow (Model 42), Spectra,  $V_{ma} = 2000 \text{ ft/sec}$ .

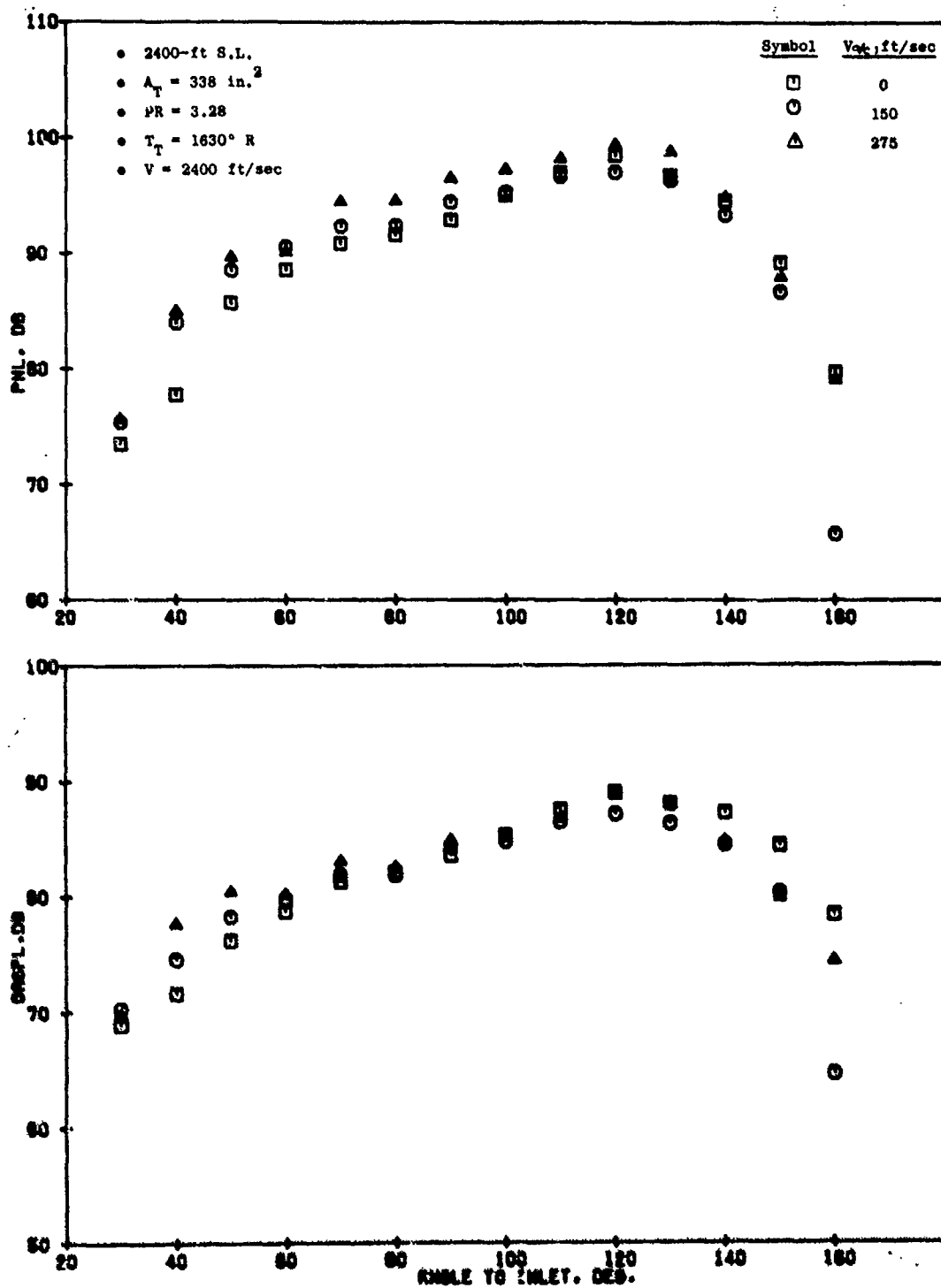


Figure 3-292. AR = 2.5 36-Chute with Abrupt Step (Model 43), PNL and OASPL Directivity,  $V_{\text{ex}} = 2400 \text{ ft/sec}$ .

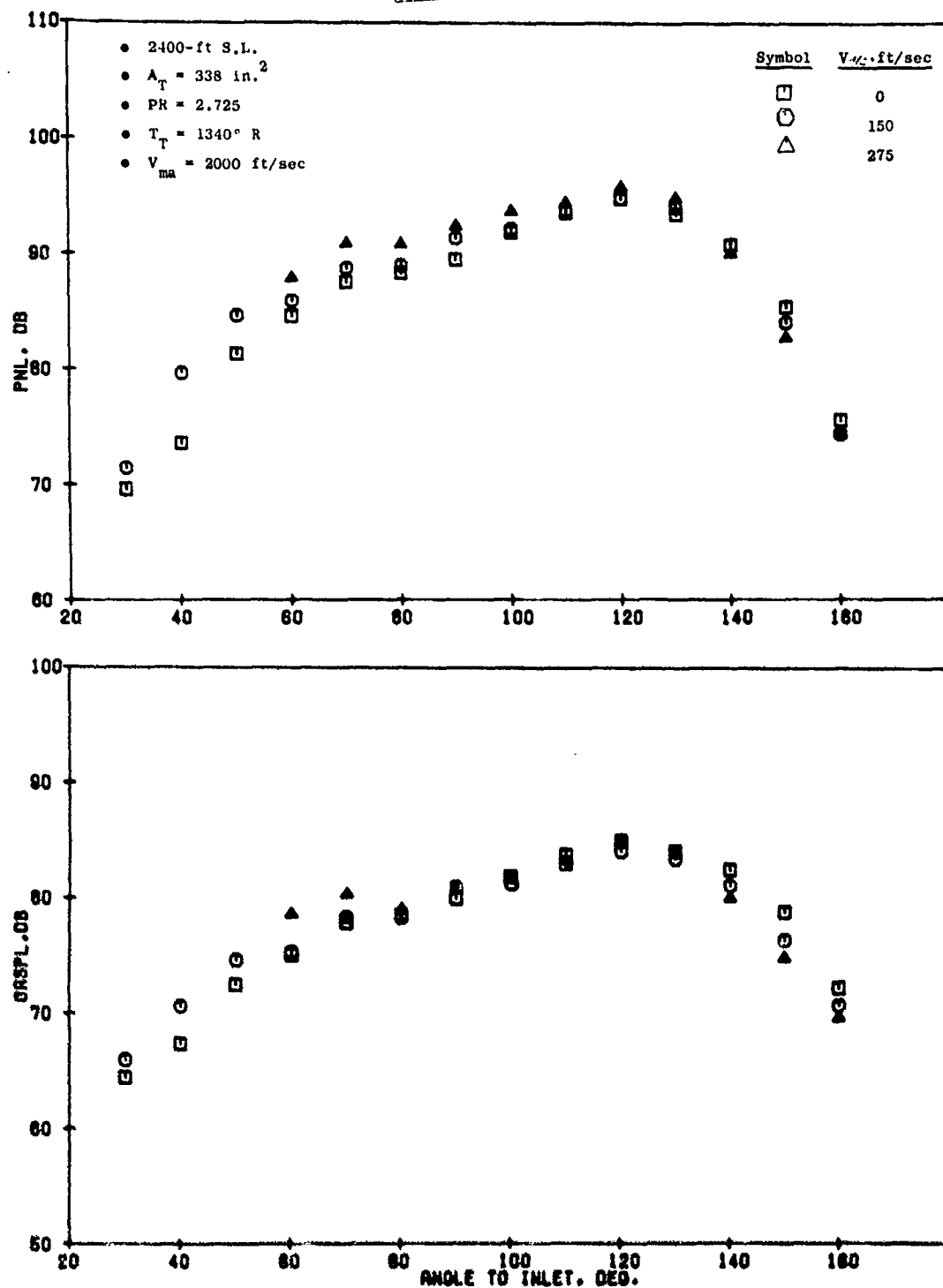


Figure 3-293. AR = 2.5 36-Chute with Abrupt Step (Model 43), PNL and OASPL Directivity,  $V_{ma} = 2000 \text{ ft/sec}$ .

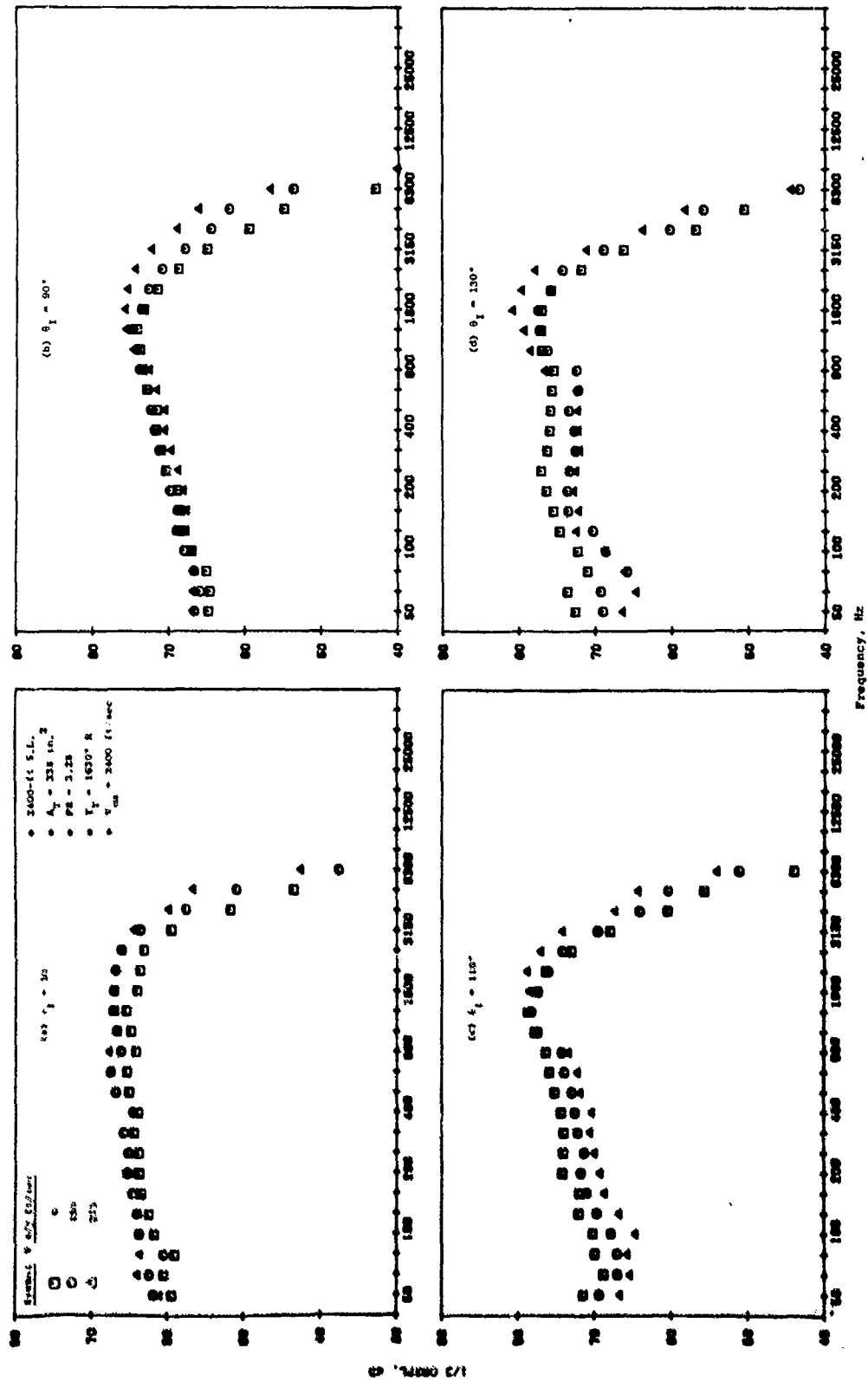


Figure 3-294. AR = 2.5 36-Chute with Abrupt Step (Model 43), Spectra,  $V_{ma} = 2400 \text{ ft/sec}$ .



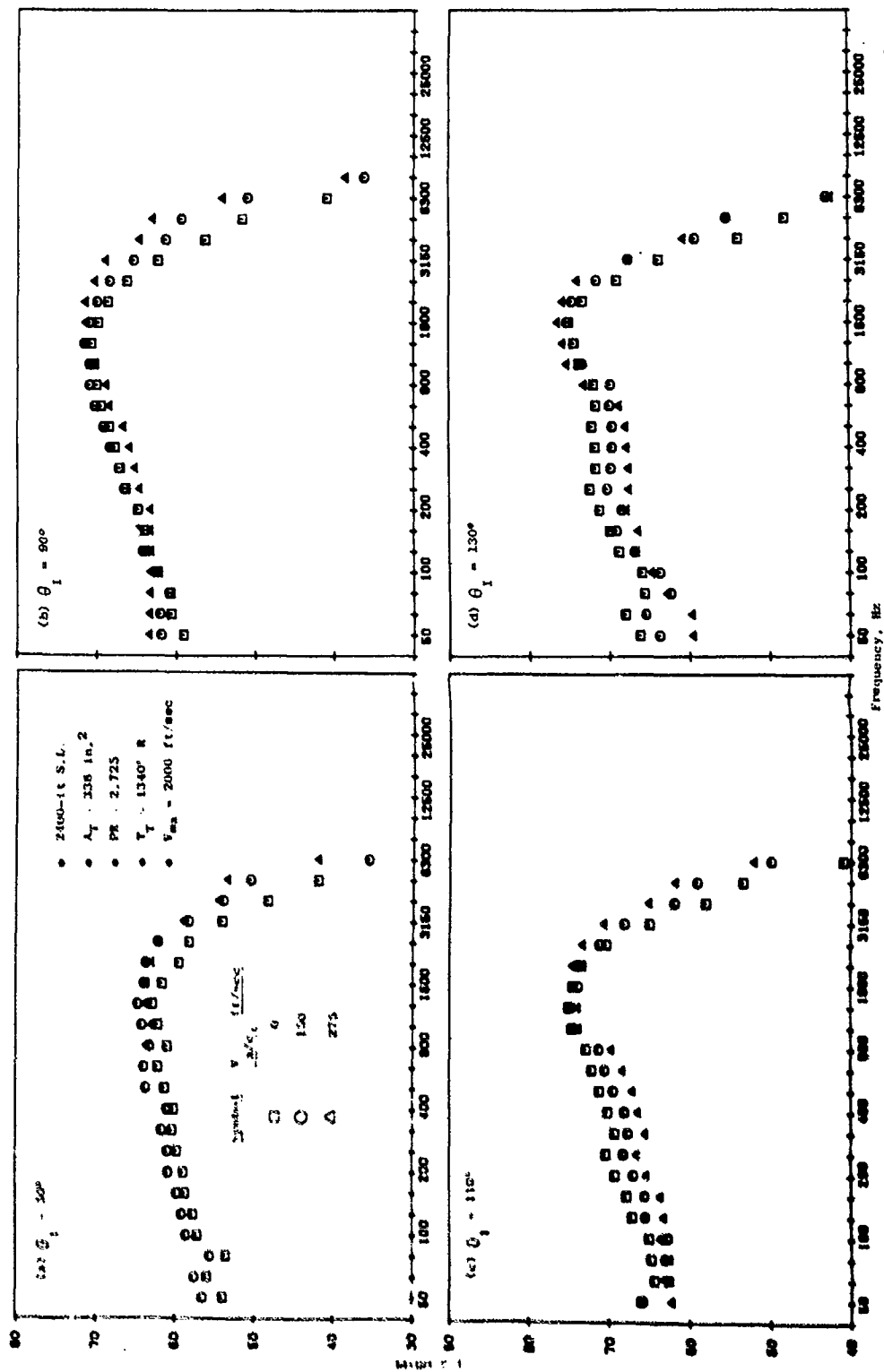


Figure 3-295. AR = 2.5 36-Chute with Abrupt Step (Model 43), Spectra,  $V_{ma} = 2000 \text{ ft/sec}$ .

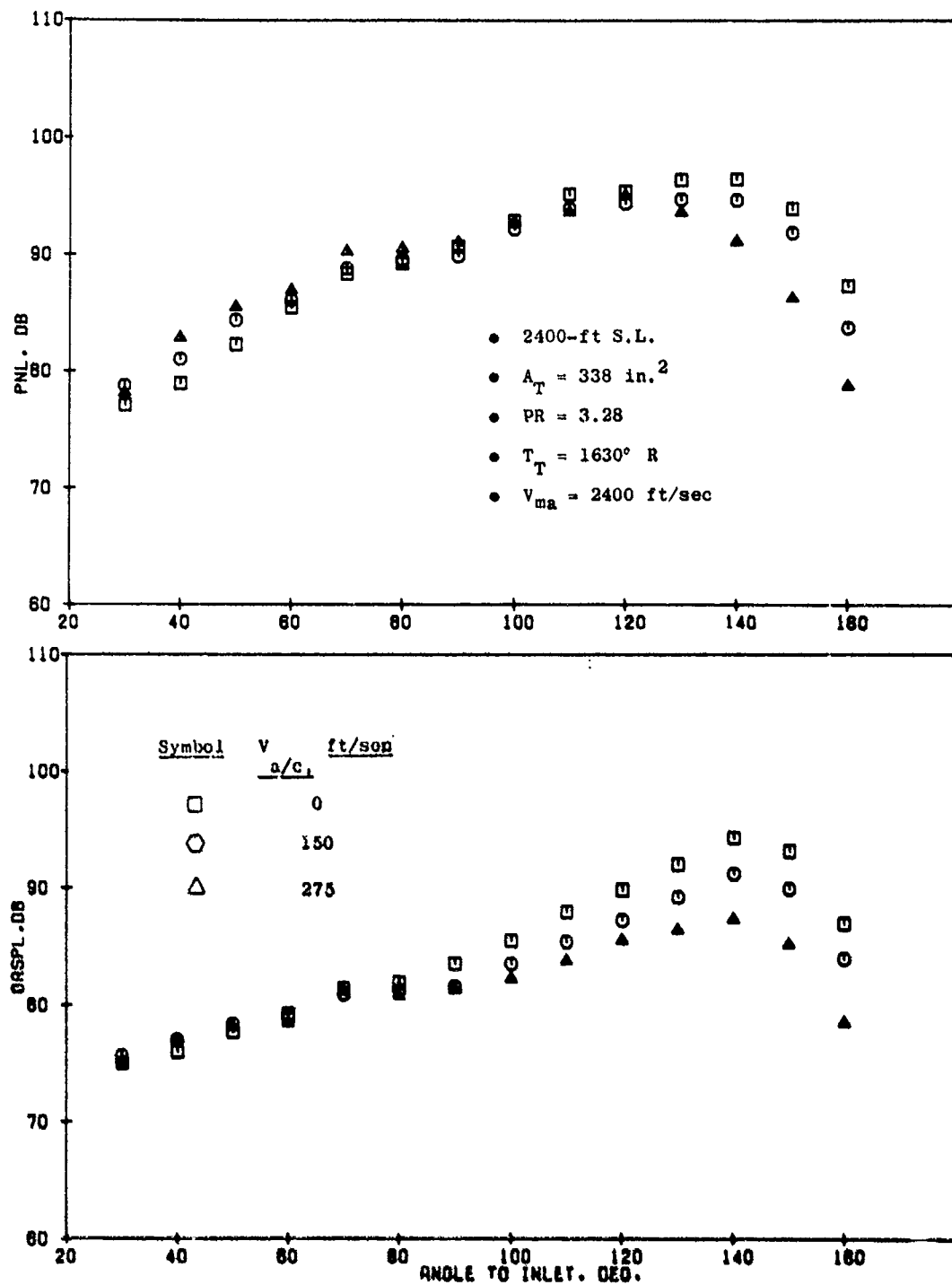


Figure 3-296. 104-Tube Nozzle (Model 44), PNL and OASPL Directivity,  $V_{ma} = 2400 \text{ ft/sec}$ .

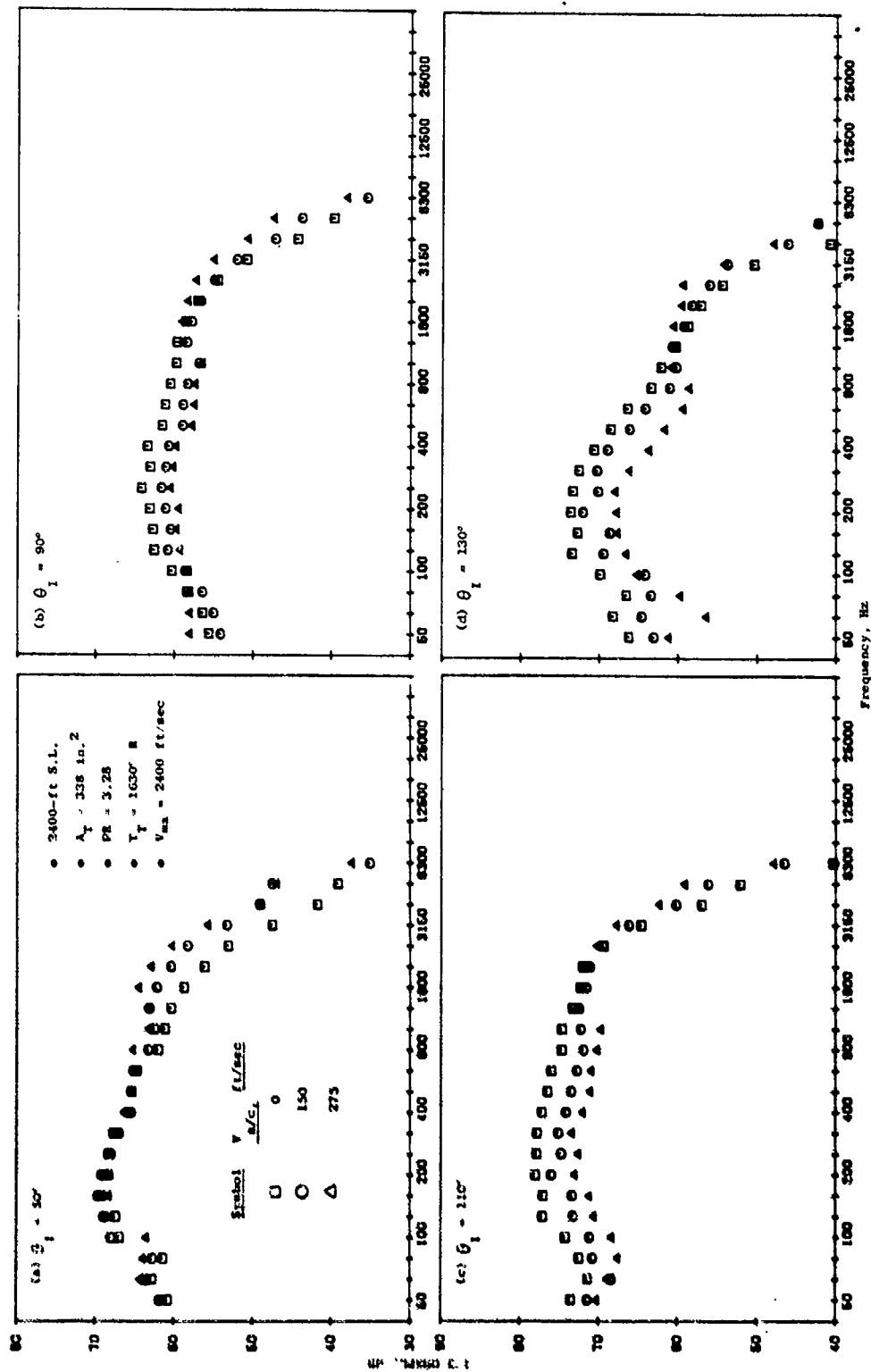


Figure 3-297. 104-Tube Nozzle (Model 44), Spectra,  $V_{ma} = 2400 \text{ ft/sec}$ .

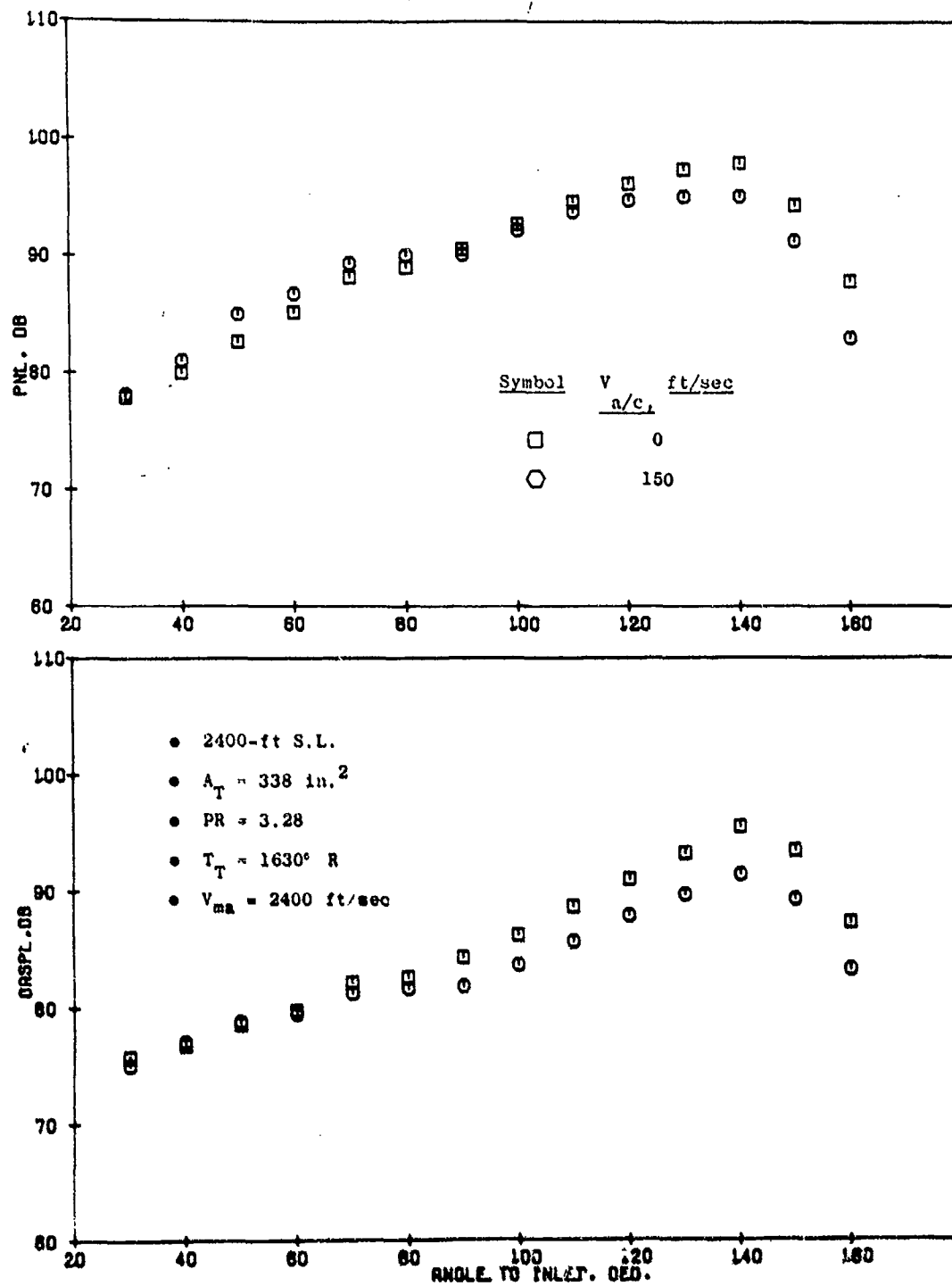


Figure 3-298. 104-Hole Nozzle (Model 45), PNL and GASPL Directivity.  
 $V_{ma} = 2400 \text{ ft/sec.}$

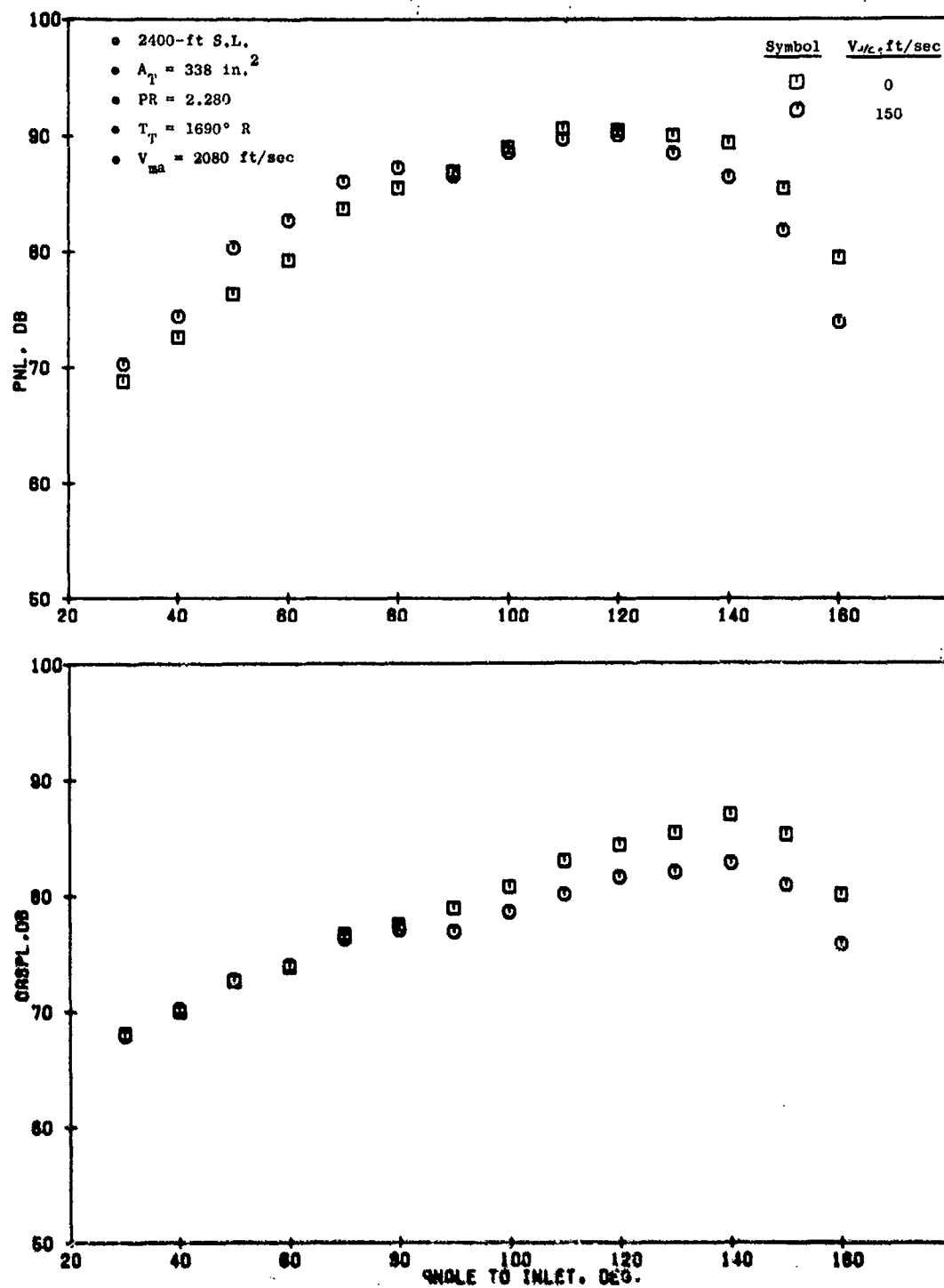


Figure 3-299. 104-Hole Nozzle (Model 45), PNL and OASPL Directivity,  $V_{ma} = 2080 \text{ ft/sec}$ .

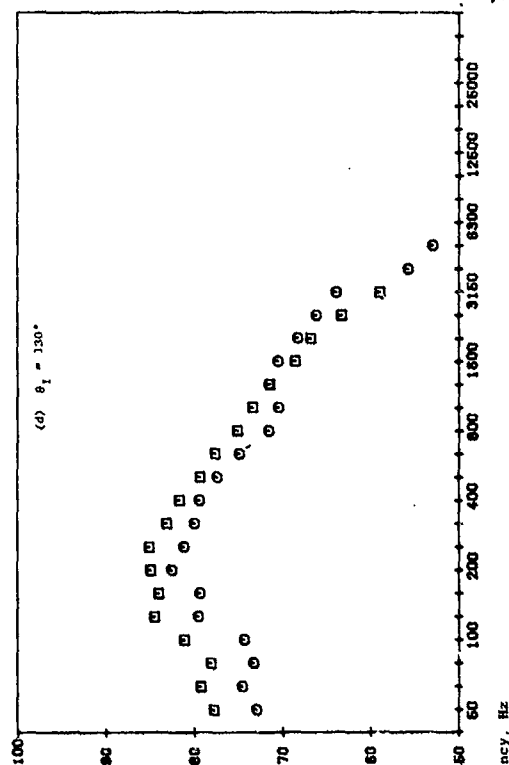
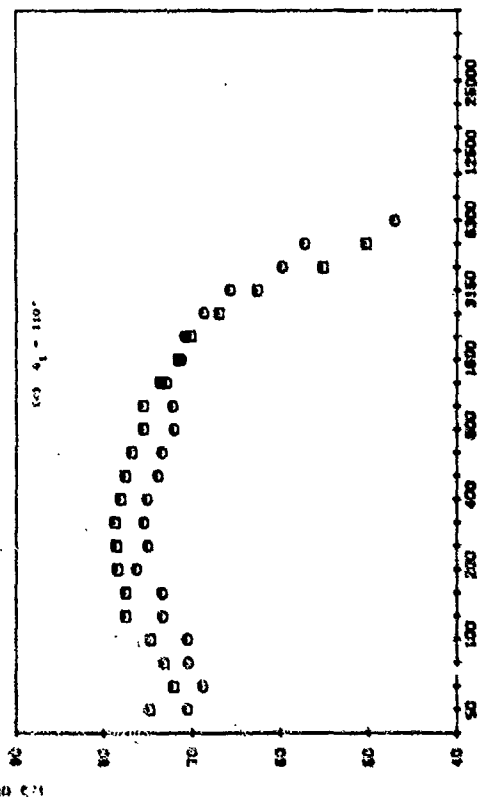
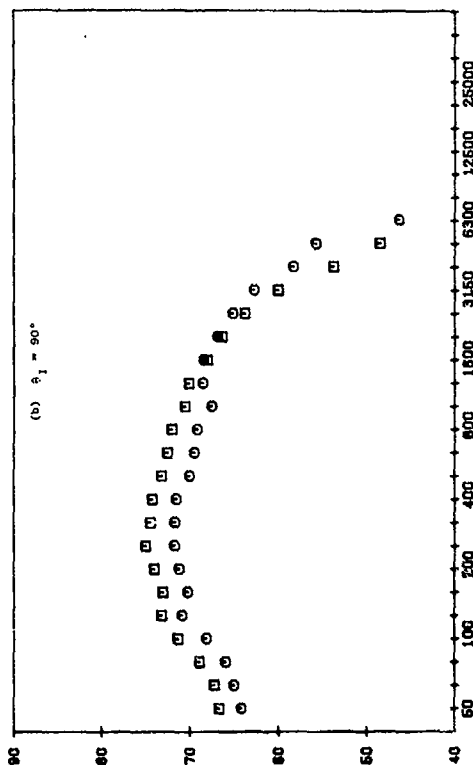
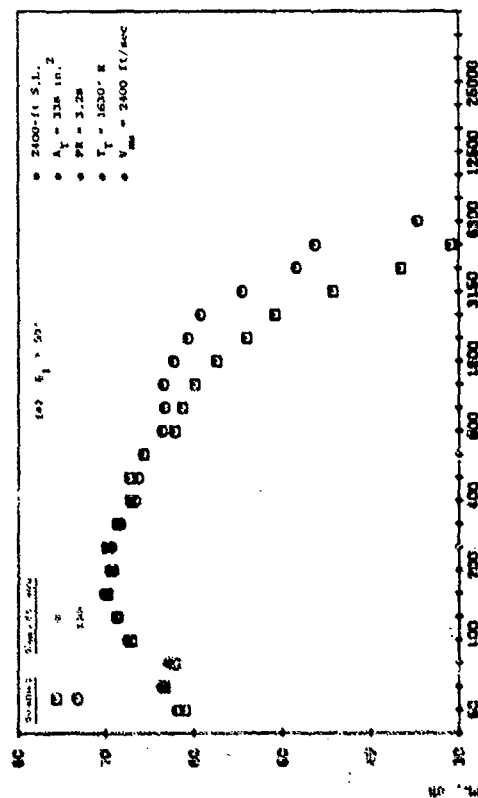


Figure 3-300. 104-Hole Nozzle (Model 45), Spectra,  $V_{\text{ma}} = 2400 \text{ ft/sec}$ .

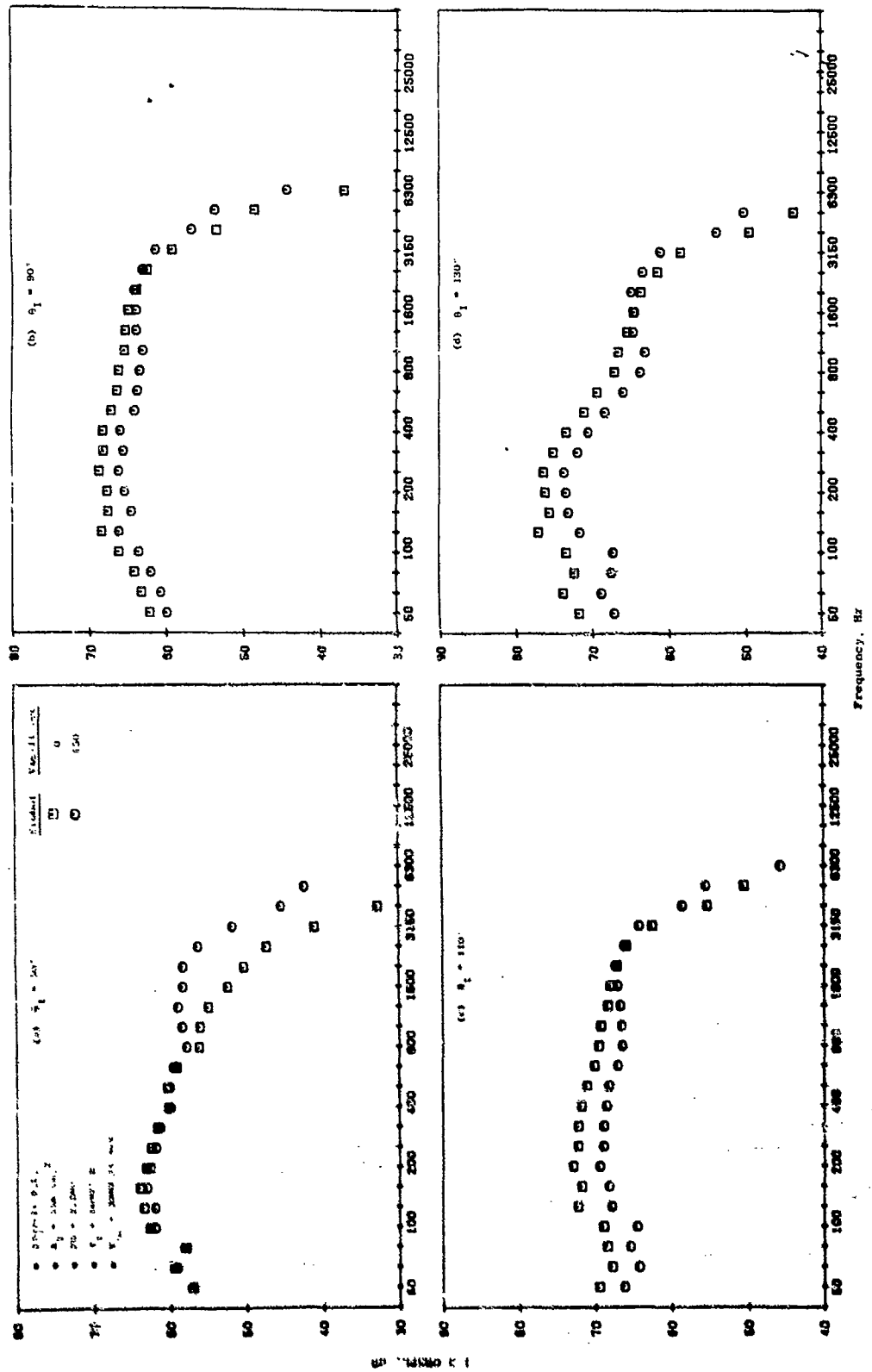


Figure 3-301. 104-Hole Nozzle (Model 45), Spectra,  $V_{ma} = 2080$  ft/sec.

chosen for presentation. The following comments are pertinent for each of the suppressor families. The plug nozzles (Models 39 and 40), Figures 3-276 through 3-281, have very similar directivity patterns. The general simulated-flight trend is a significant noise reduction in the aft quadrant, no change at  $90^\circ$ , and a slight increase (on the order of 1 PNdB) at select angles in the forward quadrant. At  $50^\circ$ , the spectrum shape (Figures 3-278, 3-279, 3-282, and 3-283) is dominated by shock-cell noise; an increase of the peak spectrum level of 3 dB is observed. This corresponds exactly to the level which would be predicted by using  $40 \log [1/1 - M \cos \theta_I]$ .

The  $90^\circ$  spectra, Figures 3-278 and 3-279, show no change for the 0.85 radius ratio configuration, Model 40. The 0.789 radius ratio plug nozzle (Model 39)  $90^\circ$  spectra, Figures 3-282 and 3-283, has a modest low-frequency reduction with an increase occurring in the high frequency portion of the spectra. The spectra have a significant low and midfrequency reduction with no change in the high frequency portion of the spectrum.

The PNL, OASPL and spectra characteristics of the three chute configurations (Models 41, 42, and 43) are summarized on Figures 3-284 through 3-295. The patterns are distinctly different than those of the plug nozzle configurations. In general, aft angle suppression is observed for  $\theta_I > 130^\circ$  with level varying anywhere from 1 to 4 PNdB depending on the chute configuration. However, for  $\theta_I \leq 130^\circ$ , the static and flight levels are generally within 2 dB. These trends are supported by the spectra comparisons presented in Figure 3-286. At  $90^\circ$  there is a low-frequency reduction but it is negated by an increase in the high-frequency noise. The trend at  $130^\circ$  is significantly different, as previously discussed. Low-frequency reduction on the order of 5 dB occurs; however, this again is negated by the increase in high-frequency noise. The relative levels of the high-frequency and low-frequency noise is the reason for a lack of flight effect.

The directivity and spectra characteristics of the 104-tube (Model 44) and 104-hole (Model 45) nozzles are presented on Figures 3-296 through 3-301. The changes in directivity pattern from static to flight are similar to those for the plug nozzle configuration. There is a significant reduction at the angle of maximum noise. At  $90^\circ$ , a modest reduction of 1 dB occurs with equivalent static and flight levels in the forward quadrant. Spectra comparison at  $50^\circ$  shows static and flight levels to be equivalent in the low frequency portion of the spectra with an increase in the high frequency portion of the spectra. At  $90^\circ$ , significant low-frequency suppression and a slight increase in the high-frequency portion of the spectra is observed.

Studies to evaluate the influence of simulated flight (using the free-jet technique) have established that a common set of velocity indices may not be established for both baseline and suppressor nozzles. The chute nozzles evaluated have shown a 3-PNdB loss in in-flight peak noise suppression due to dominance of the high frequency portion of the spectra (which realizes only a minimal flight effect). The minimization of high-frequency noise is considered to be a critical design parameter for a suppressor nozzle to realize a reduction of noise in flight.



### 3.4.3.2 Shock Noise Studies

The effect of shock noise, both statically and in simulated flight, was explored for five nozzles: a conical nozzle (Model 47), a 0.85 radius ratio plug nozzle (Model 40), an AR = 2.5 36-chute nozzle (Model 41), a 104-tube nozzle (Model 44), and a 104-hole nozzle (Model 45). The shock noise characteristics of the 8-lobe nozzle (Model 46) are discussed in detail in Reference 7.

According to the Harper-Bourne Fisher (HBF) theory (Reference 24) the OASPL, if dominated by shock-cell noise, should be only a function of the pressure ratio parameter  $\beta$ , given by the following equation:

$$\beta = \sqrt{M^2 - 1}$$

OASPL's at angles of 40° through 90° are presented as a function of  $\beta$  on Figure 3-302 for the conical nozzle (Model 47). At angles such as 40°, the shock noise appears to be dominant; this is reflected in the collapse of the data, for all temperatures, close to a line which varies as  $\beta^4$ . Transformed free-jet data are also presented on Figure 3-302. In general, the transformed results show an increase in noise due to the dynamic effect. The increase in level is a function of angle and  $\beta$ . However at negative values of  $\beta$  this noise increase in flight is not as apparent. The approximate level of increase is predicted by  $40 \log [1/1 - M_a/c \cos \theta_1]$  in the  $\beta$  range where shock noise is clearly dominant.

Similar static OASPL comparisons were made at 50° for the 0.85 radius ratio plug nozzle (Model 40), AR = 2.5 36-chute nozzle (Model 41), 104-tube nozzle (Model 44), and 104-hole nozzle (Model 45). The plug nozzle did follow the classical  $\beta^4$  line, but the other suppressors did not show a significant trend. Spectra comparisons for the four nozzles are shown on Figure 3-303. The conical and 0.85  $R_r$  plug nozzles exhibit the spectrum shapes indicative of shock noise whereas the multielement suppressors do not.

Spectra comparisons for the 0.85  $R_r$  plug nozzle (Model 40) at pressure ratios of 2.5, 3.0, and 3.5 are presented in Figure 3-304. The spectra for the three velocity conditions at a pressure ratio of 2.5 collapse in the frequency range of  $400 \leq f \leq 5000$  Hz. Spectrum levels below 400 Hz increase as jet velocity increases. However, the frequency dependent trend is not repeated at pressure ratios of 3.0 and 3.5. The spectrum shapes are observed to be equivalent and suggest the spectrum is dominated by shock noise rather than jet noise. OASPL directivity comparisons were also made in a similar manner and are presented on Figure 3-305.

Shock noise dominates at a pressure ratio of 2.5 up to 70°, at a pressure ratio of 3.0 up to 90°, and at a pressure ratio of 3.5 up to 100°. In general, as nozzle pressure ratio is increased and total temperature is held constant, the region of shock noise dominance will extend into the aft quadrant.

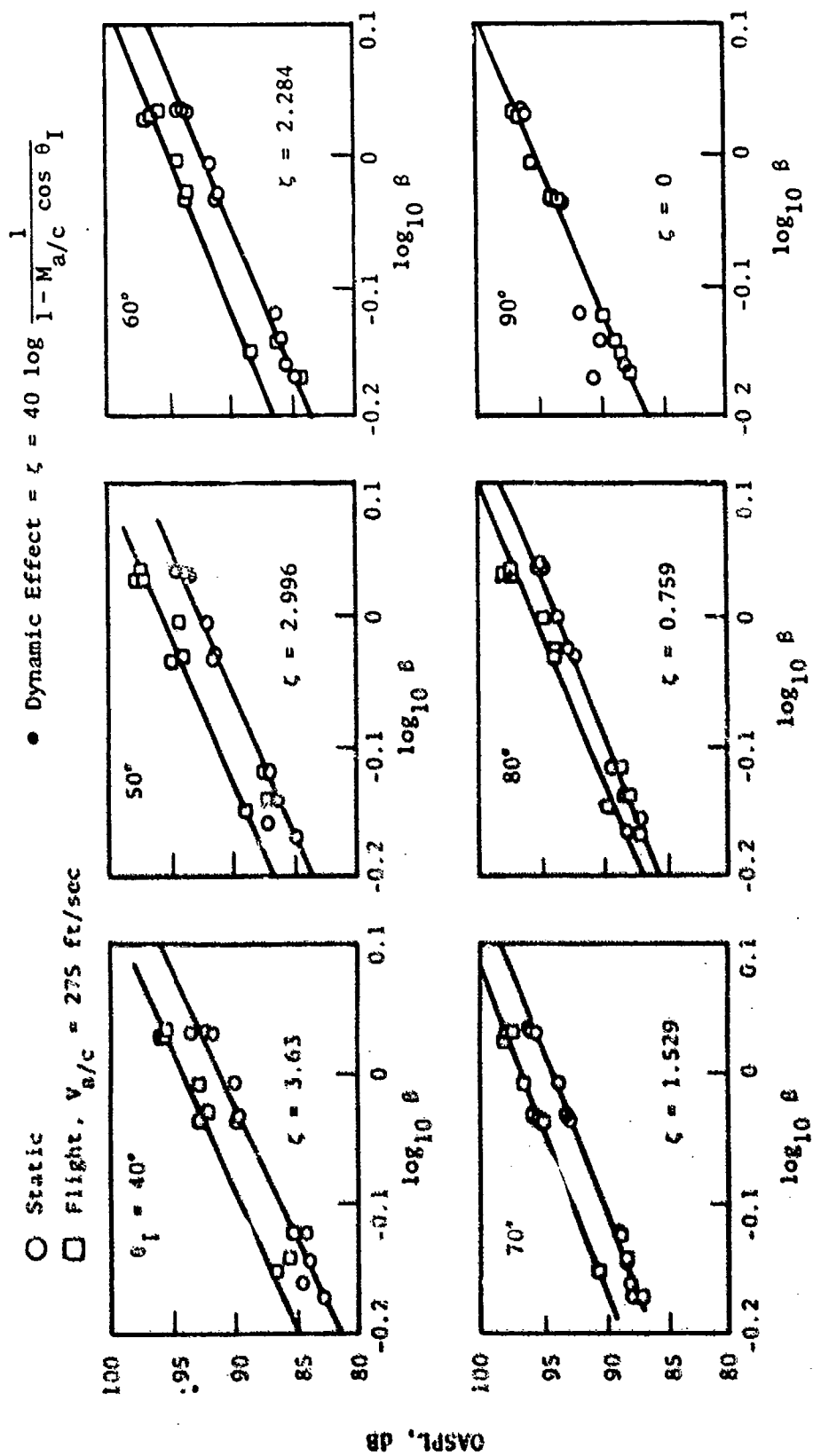


Figure 3-302. Summary of Conical Nozzle (Model 47) Forward Quadrant Noise Trends.

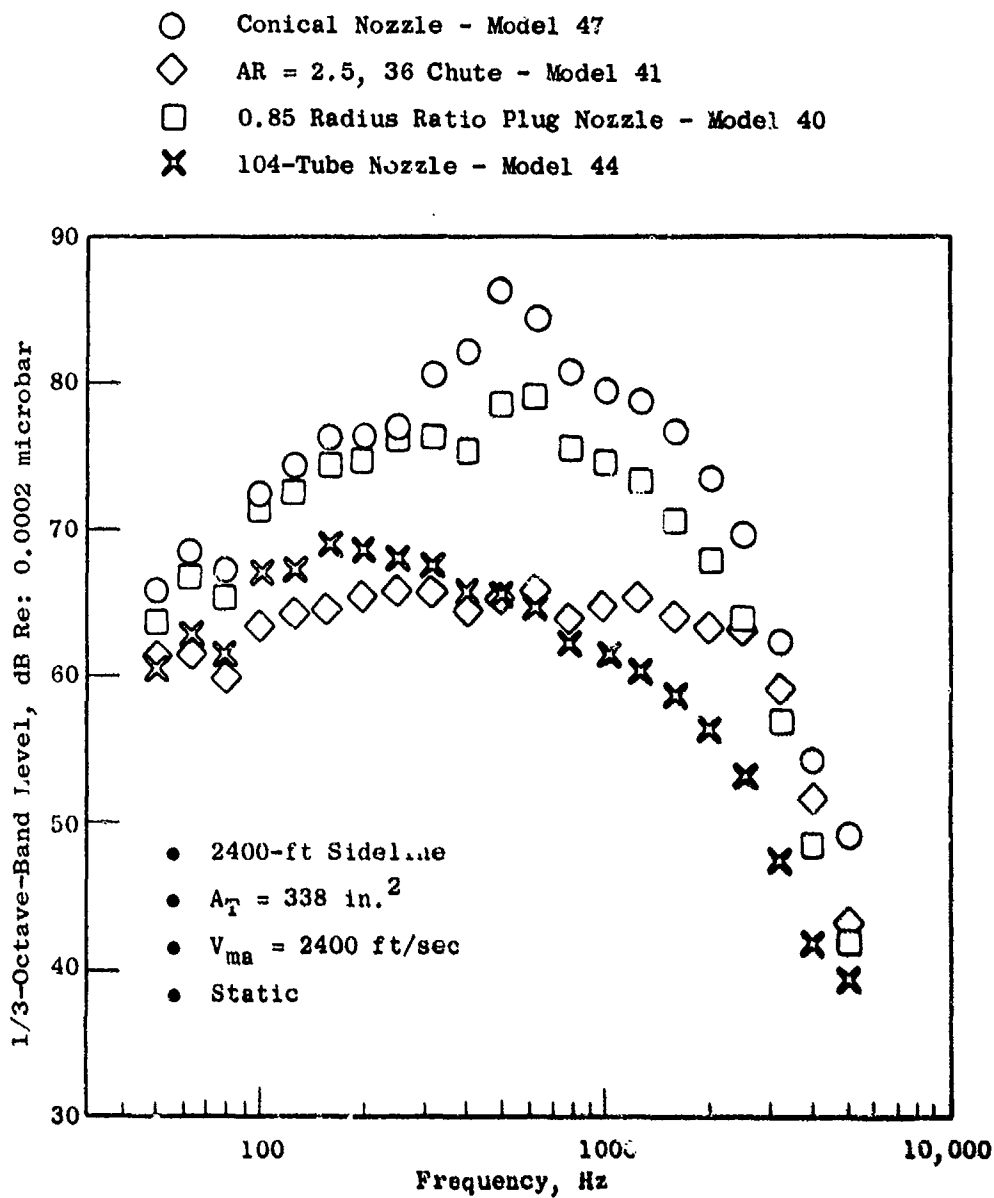


Figure 3-303. Summary of 50° Spectra Characteristics.

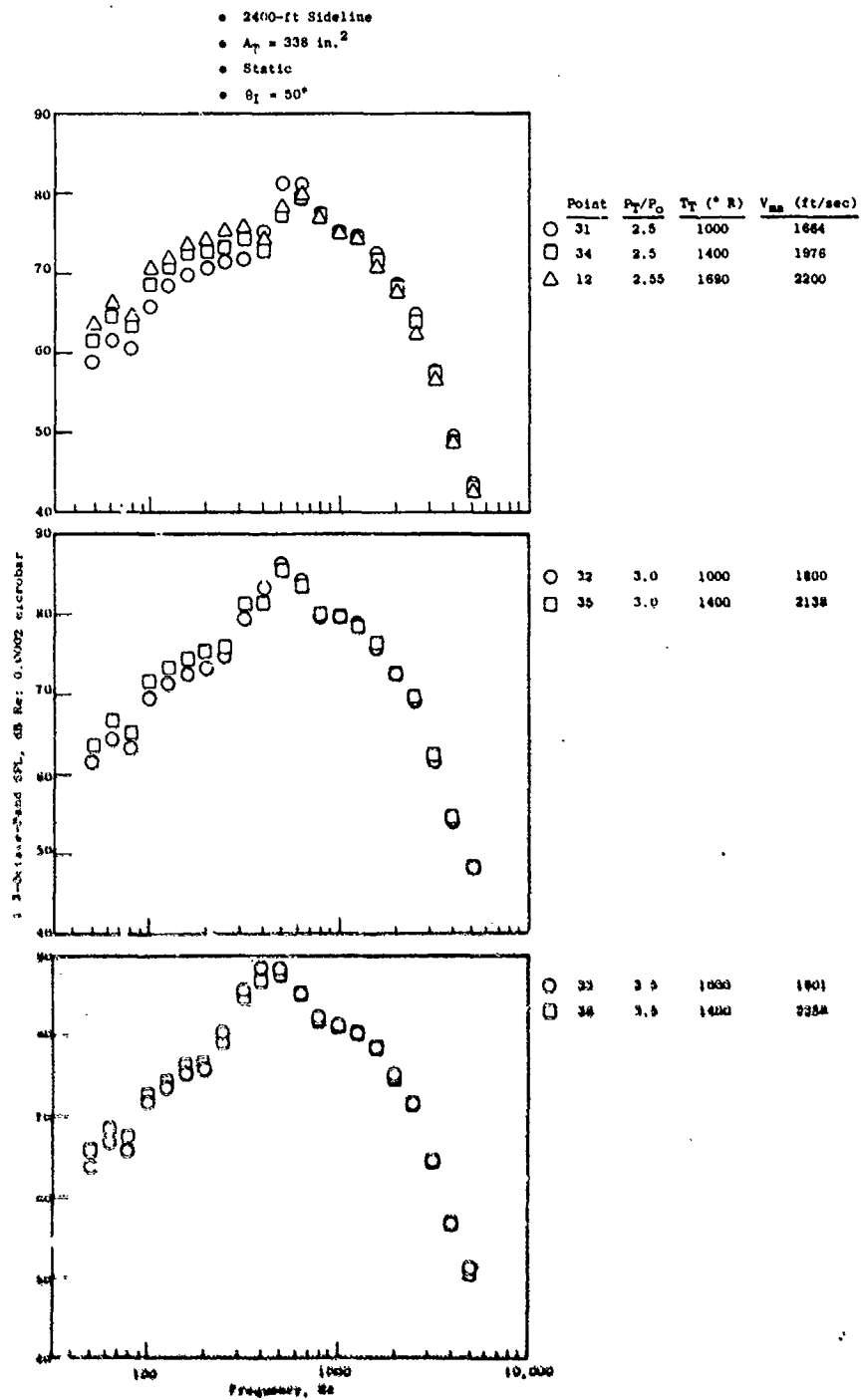


Figure 3-304. 0.85 Radius Ratio Plug Nozzle (Model 40)  
50° Spectra at Constant Pressure Ratio.

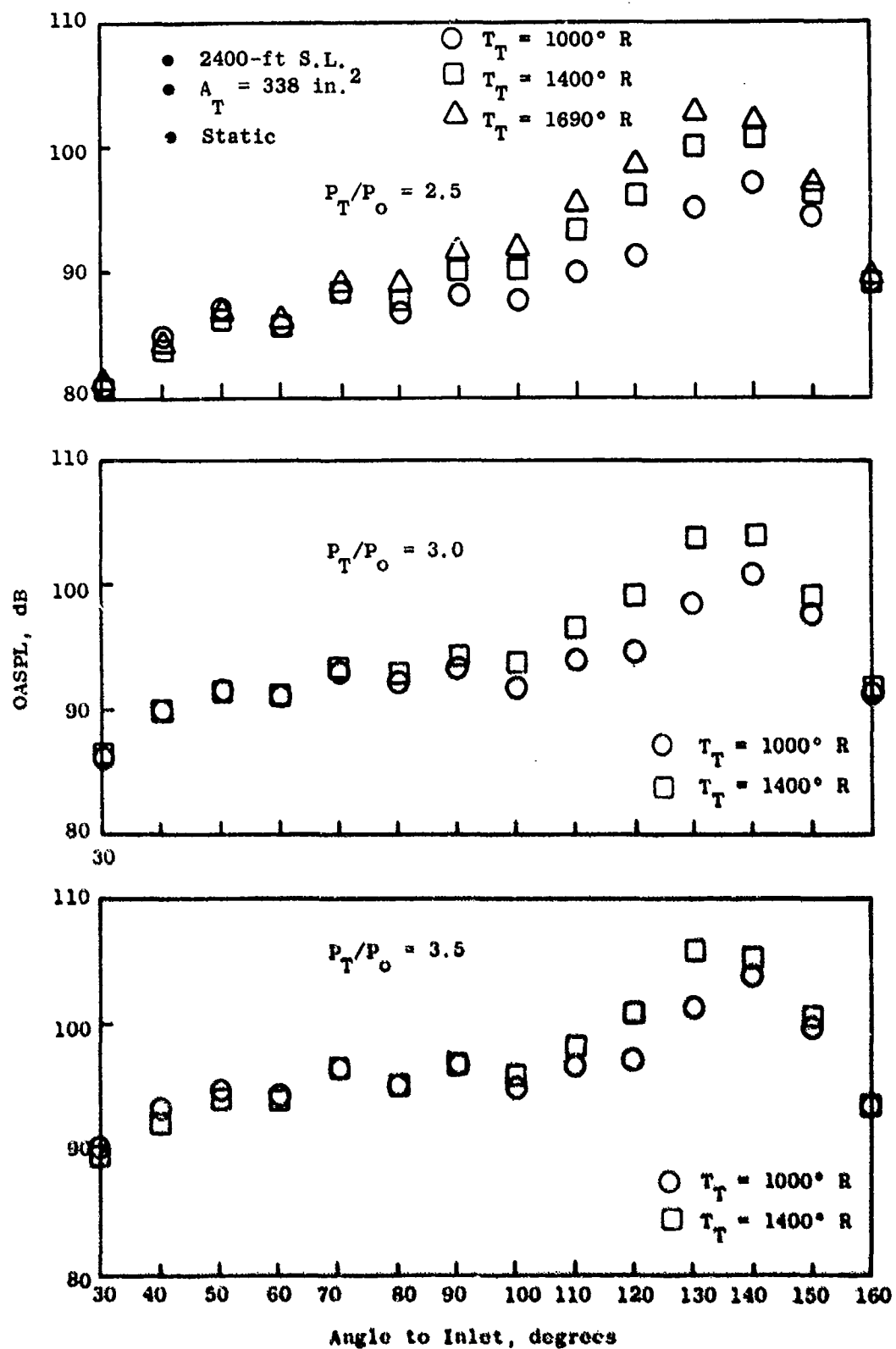


Figure 3-305. 0.85 Radius Ratio Plug Nozzle (Model 40) Directivity at Constant Pressure Ratio.

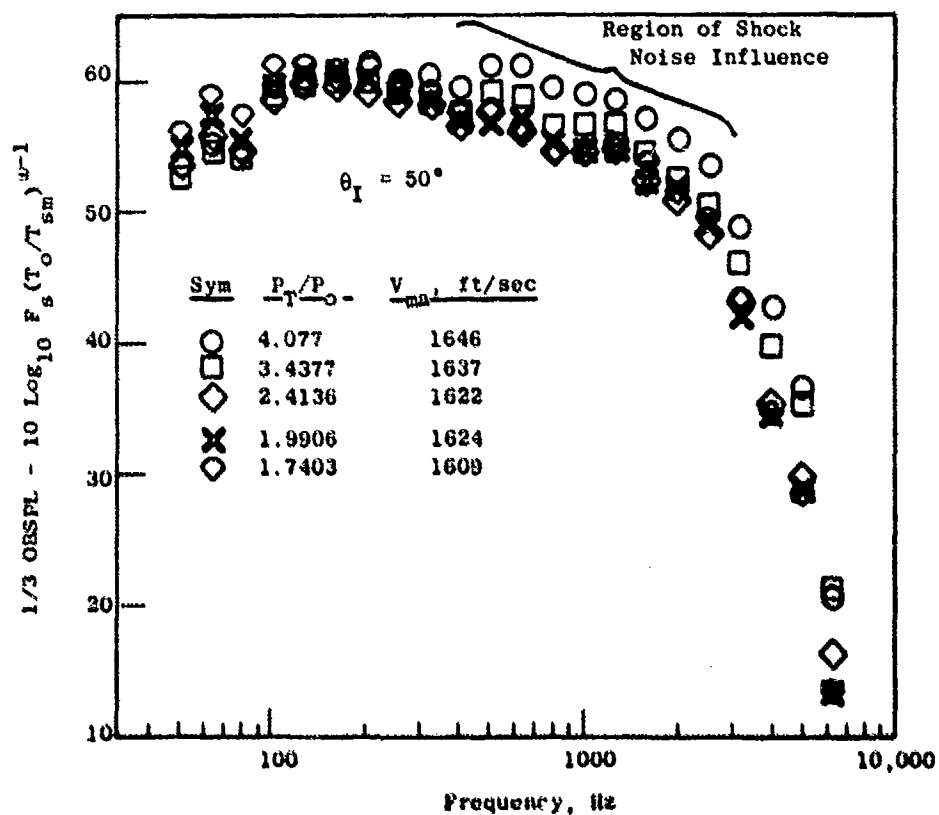
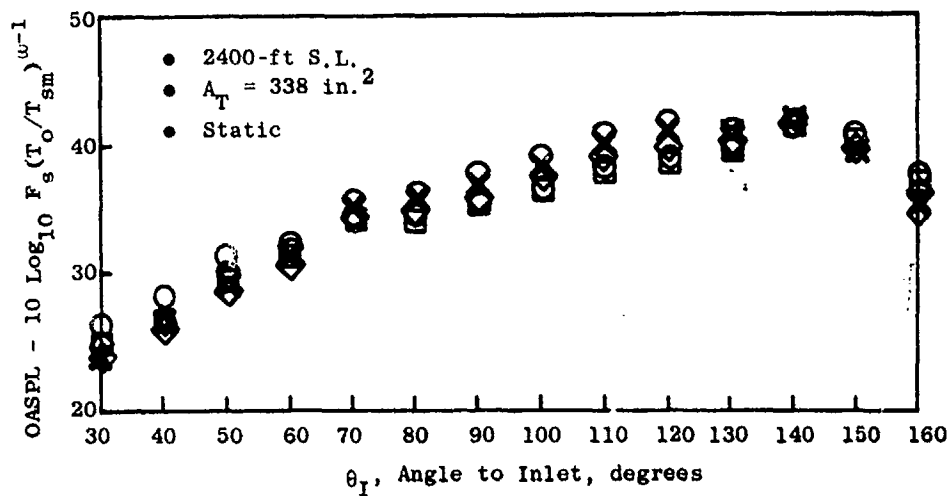


Figure 3-306. The Effect of Pressure Ratio Variation on the Directivity and Spectra Characteristics of a 104-Hole Nozzle (Model 45).

The 104-hole nozzle (Model 45) was chosen to illustrate the influence of shock noise on multielement suppressor nozzles. The results of this study were distinctly different than those observed for the conical (Model 47) and plug (Model 40) nozzles. Directivity and spectra comparisons are presented on Figure 3-306.

The directivity comparisons were made for five conditions where jet velocity varied from 1609 ft/sec to 1646 ft/sec. However, nozzle pressure ratio varied from 1.74 through 4.07. If the 104-hole nozzle was dominated by shock noise, the data would not collapse when normalized by the  $10 \log F_8 (T_0/T_{8m})^{\omega-1}$  factor. However, the levels for all five points do collapse within a  $\pm 1$  dB band. This implies that the directivity pattern of this nozzle is not dominated by shock noise. Spectrum wise ( $\theta_1 = 50^\circ$ ), a variation with pressure ratio is observed in the frequency range of  $400 < f < 6300$  Hz for the 3.43 and 4.0 pressure ratio conditions, suggesting a slight influence due to shock noise in spite of the apparent collapse of the OASPL data. However, at low pressure ratios the data collapse when normalized by this parameter.

The major results of this exploratory study show that shock noise dominates the forward quadrant noise levels at supercritical pressure ratios, that the region of shock noise influence increases at pressure ratio is increased and temperature is decreased, and that the shock noise levels follow a  $\beta^4$  slope and are amplified in flight according the  $40 \log [1/1 - M_{a/c} \cos \theta_1]$  based on transformed free-jet data.

Plug nozzles also have significant shock noise; however, on an absolute level it is less than for a conical nozzle. Complex suppressor nozzles, such as the 104-hole nozzle, do not have a significant shock-noise component.

#### 3.4.4 Laser Velocimeter Results

Laser velocimeter (LV) measurements were conducted on baseline and several suppressor nozzles to determine if the mean velocity decay characteristics were similar for baseline and suppressor nozzles, and to determine if suppressor turbulence intensity levels were equivalent to a conical nozzle. The effects of geometric changes on the mixing characteristics of exhaust nozzles were also examined. These geometric studies included variation of element type, single versus dual flow, suppressor area ratio variation and the influence of a treated ejector. The baseline nozzles were tested on the JENOTS facility and the suppressor nozzles were tested in the anechoic chamber.

Laser velocimeter measurements were also taken on several baseline and suppressor configurations in a freejet on the JENOTS facility to establish the change in mixing characteristics with the addition of external flow.

The baseline nozzles evaluated include a conical nozzle (from Task 4, Reference 12), a 0.67 radius ratio convergent-divergent plug nozzle (Model 2), and an  $A_0/A_1 = 1.0$  planar-coannular nozzle (Model 6). Mean velocity and turbulence intensity profiles for the first two configurations were compared extensively with the analytical predictions in Section 4.5.8 of Reference 7 and

will not be repeated here except for selected comparisons. The results of this study are presented as mean-velocity decay characteristics and turbulence intensity levels for several baseline and multi-element-suppressor nozzles. The test matrix and data reduction/acquisition were discussed in Sections 3.2.2 and 3.3.2, respectively.

Figure 3-307 summarizes mean-velocity decay characteristics for the conical (Reference 12) and two inverted-flow, coplanar-coannular nozzles (Models 6 and 7). The coannular data are normalized with respect to the area and the calculated isentropic velocity of the outer flow. The peak velocity decay is enhanced by the inverted-flow cycle in the  $3.0 < X/D_{eq} < 11.0$  region reduced at  $X/D_{eq} < 11$  for the range investigated. Turbulence intensity levels at the location of maximum mean velocity are summarized on Figure 3-308. Turbulence levels are approximately 3 to 4% in the region where the measured velocity is equivalent to the isentropic velocity. The maximum turbulence levels produced by the coplanar-coannular nozzles are observed to occur closer to the nozzle exit plane than was the case with the conical nozzle. Peak turbulence levels, which in general do not occur at the same location as the peak mean velocity, are summarized on Figure 3-309 for the conical nozzle and also for the 0.65  $A_0/A_1$  coplanar-coannular nozzle (Model 7). The peak turbulence level of the coplanar-coannular nozzle is approximately 2% lower than for the conical nozzle and occurs nearer to the nozzle exit plane.

The AR = 2.0 coplanar-coannular nozzle (Model 6) was also tested to determine the influence of velocity ratio on the centerline mean-velocity decay characteristics. The studies were conducted with the inner and outer streams both operating at stagnation temperatures of ambient and 1500° R. The results are summarized on Figures 3-310 and 3-311. As velocity ratio ( $V_0/V_1$ ) increases, the decay rate of the mean velocity is substantially reduced. The increase in stagnation temperature also enhances the velocity decay rate, when compared to ambient conditions.

Mean velocity and turbulence intensity levels were established for several single and dual flow suppressor nozzles. In general, the segmentations of the exhaust plume caused a more rapid decay of the mean velocity when compared to the unsuppressed case. The downstream, postmerged, mean velocity characteristics of the suppressor nozzles are very similar to the baseline configurations.

The mixing characteristics of two typical turbojet suppressor nozzles (AR = 2.0 36-chute (Model 16) and AR = 2.0 36-spoke (Model 18)) are summarized on Figures 3-312 and 3-313. The data were obtained by radial traverses on a chute or spoke centerline. Measured data for the 3.56 conical nozzle (Reference 12) is presented at locations where it is available. The spoke and chute nozzles both have very similar mean velocity profiles at axial locations in the  $X/D$  range from 0.4 to 24. The turbulence intensity levels are very similar, with the maximum variance occurring at  $X/D \leq 1.0$ . When compared to the conical nozzle, both configurations display a significant reduction in mean velocity up to an  $X/D$  of 8.0. At  $X/D = 16$ , the peak velocity level of the conical



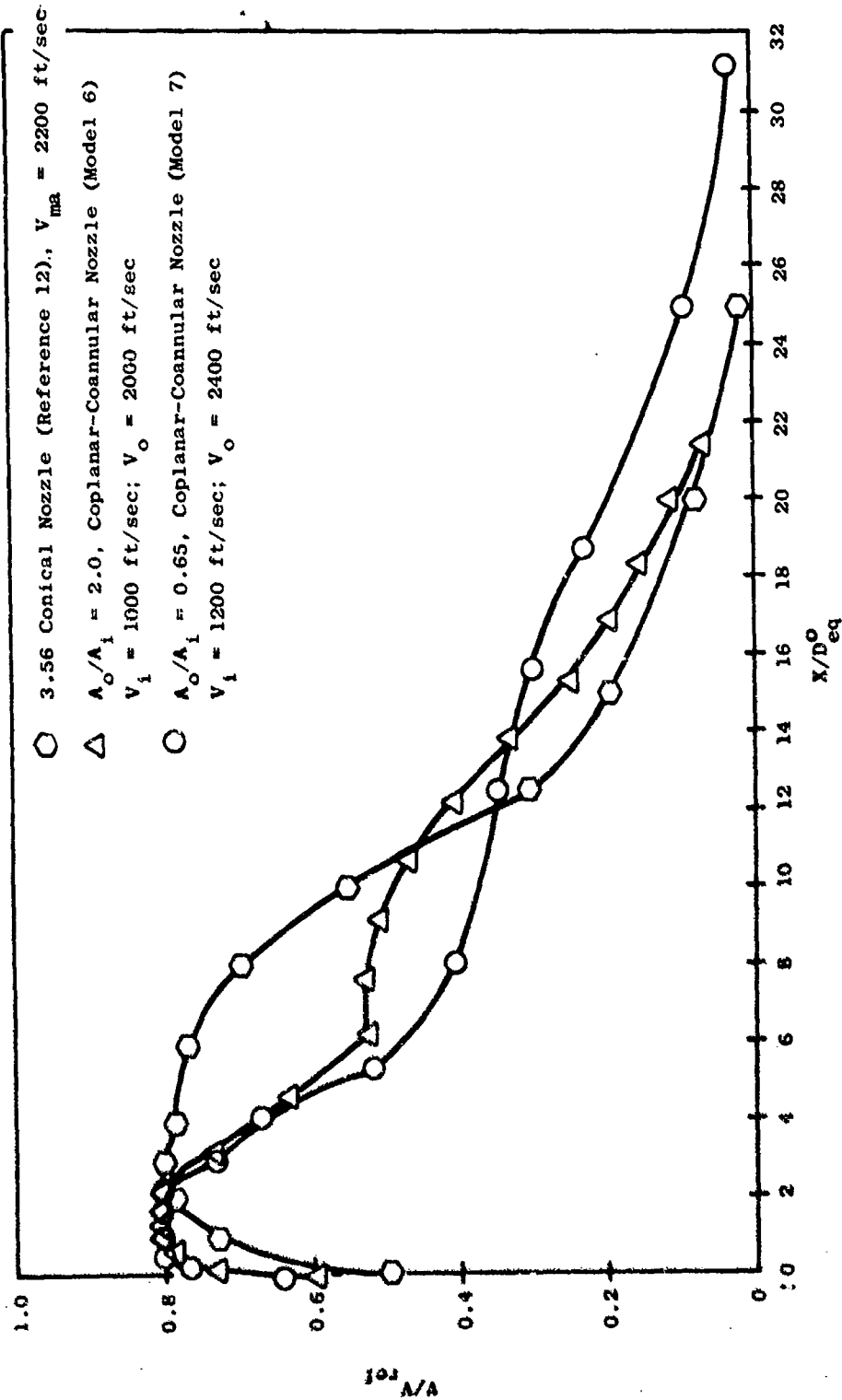


Figure 3-307. Summary of Peak Mean Velocity Decay Characteristics.

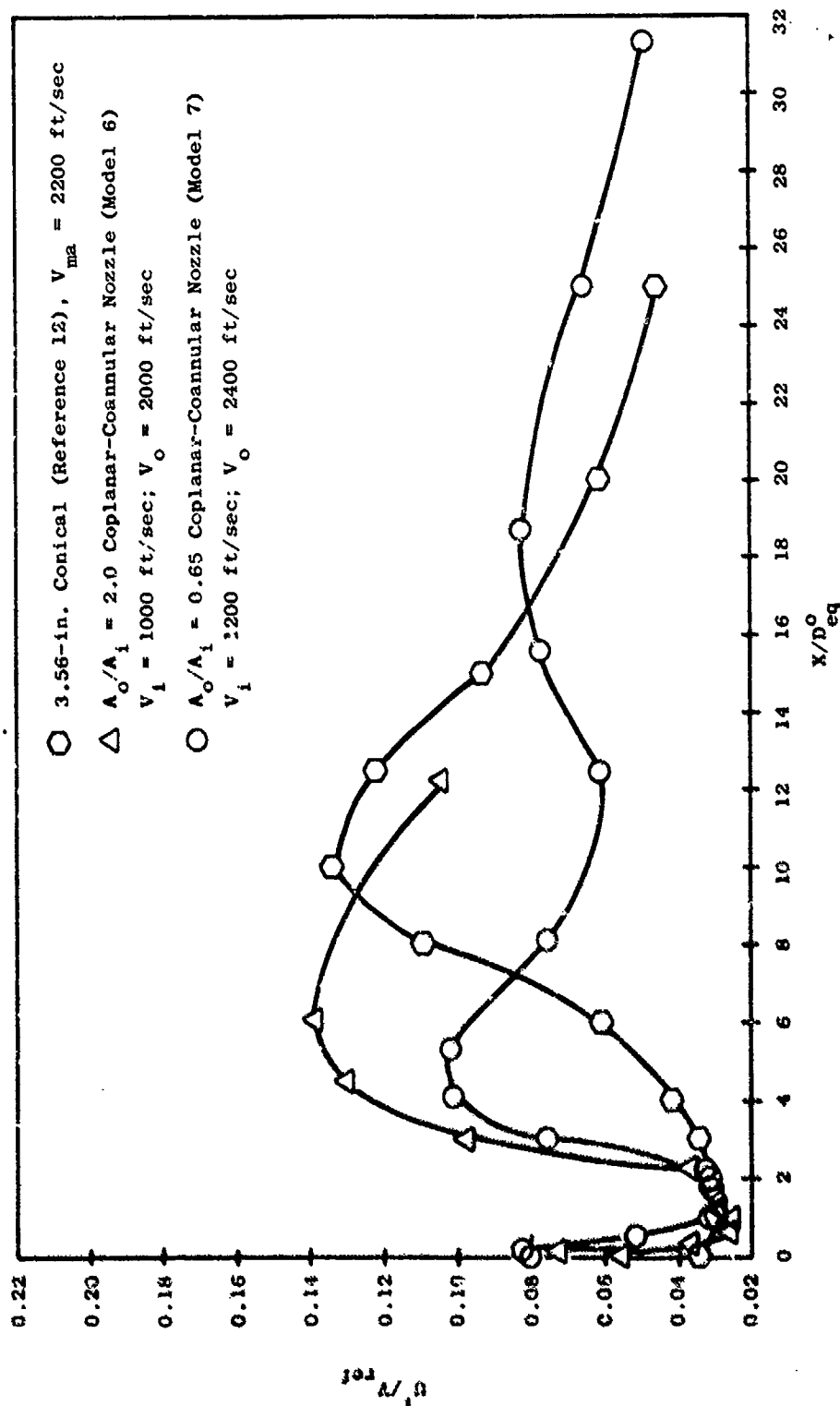


Figure 3-308. Turbulence Intensity Levels at Location of Peak Mean Velocity.

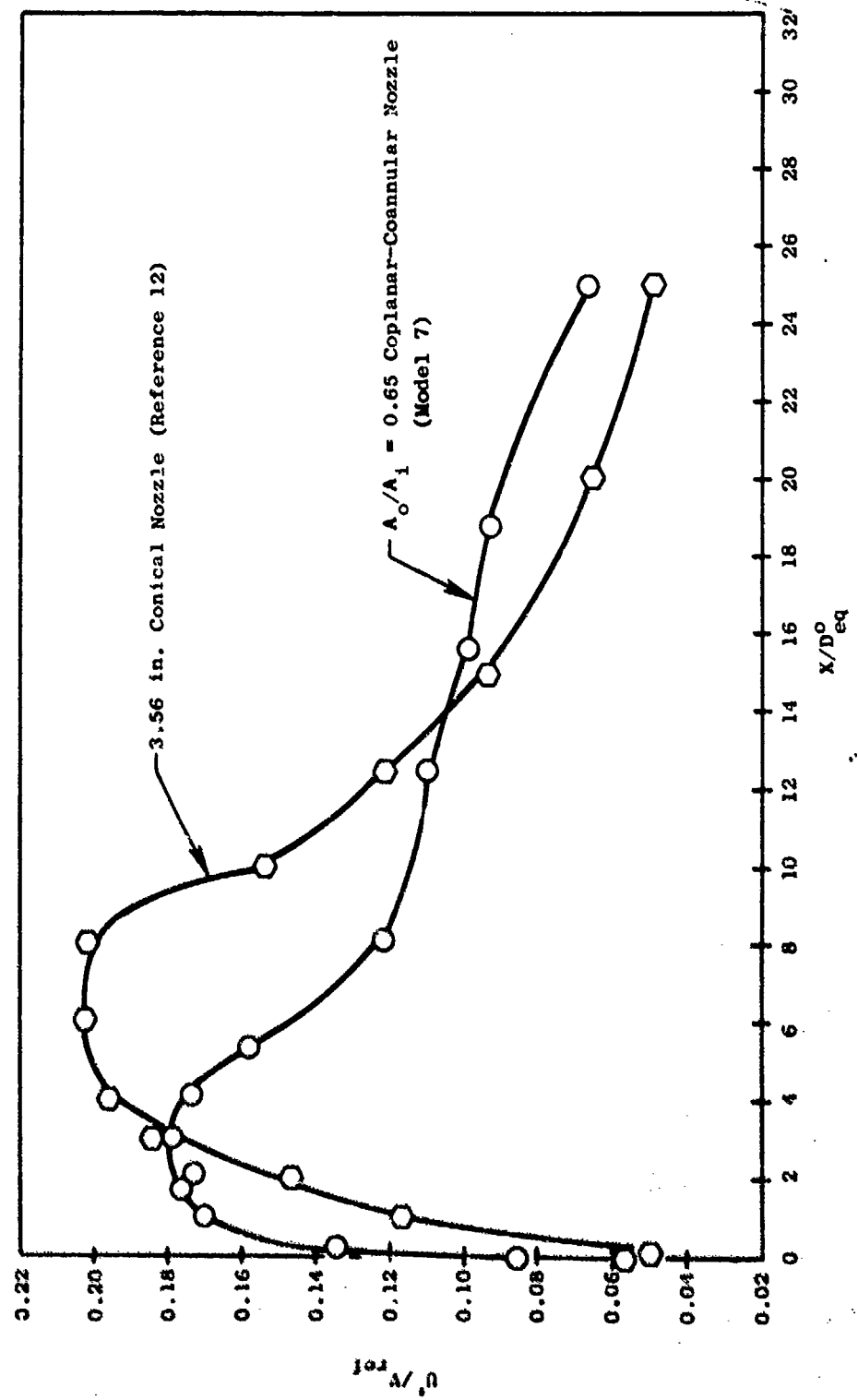


Figure 3-309. Peak Turbulence Intensity Levels.

• Model 6

- A-1  $V_1 = 1000$  ft/sec;  $V_0 = 0$
- A-2  $V_1 = 1000$  ft/sec;  $V_0 = 200$  ft/sec
- A-3  $V_1 = 1000$  ft/sec;  $V_0 = 400$  ft/sec
- A-4  $V_1 = 1000$  ft/sec;  $V_0 = 600$  ft/sec
- A-5  $V_1 = 1000$  ft/sec;  $V_0 = 800$  ft/sec
- A-6  $V_1 = 1000$  ft/sec;  $V_0 = 1010$  ft/sec
- A-7  $V_1 = 1000$  ft/sec;  $V_0 = 1250$  ft/sec
- A-8  $V_1 = 500$  ft/sec;  $V_0 = 1000$  ft/sec

- $AR = 2.0$
- $A_0/A_1 = 2.0$ , Coplanar-Coannular Nozzle
- $T_{T_0} = T_{T_1} = \text{Ambient}$

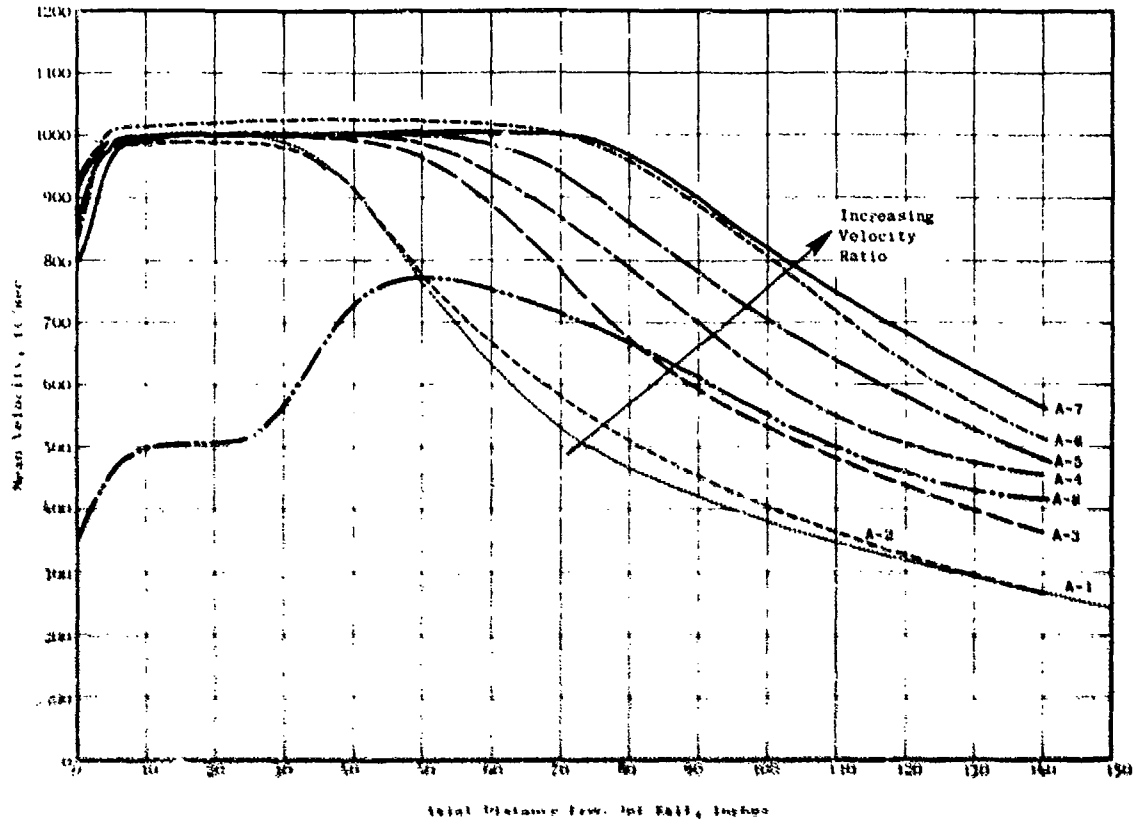


Figure 3-310. Centerline Velocity Decay Characteristics.

• Model 6

- D-1  $V_1 = 1000$  ft/sec;  $V_0 = 400$  ft/sec  
D-2  $V_1 = 1000$  ft/sec;  $V_0 = 600$  ft/sec  
D-3  $V_1 = 1000$  ft/sec;  $V_0 = 1000$  ft/sec  
D-4  $V_1 = 1000$  ft/sec;  $V_0 = 2000$  ft/sec  
D-5  $V_1 = 1027$  ft/sec;  $V_0 = 0$

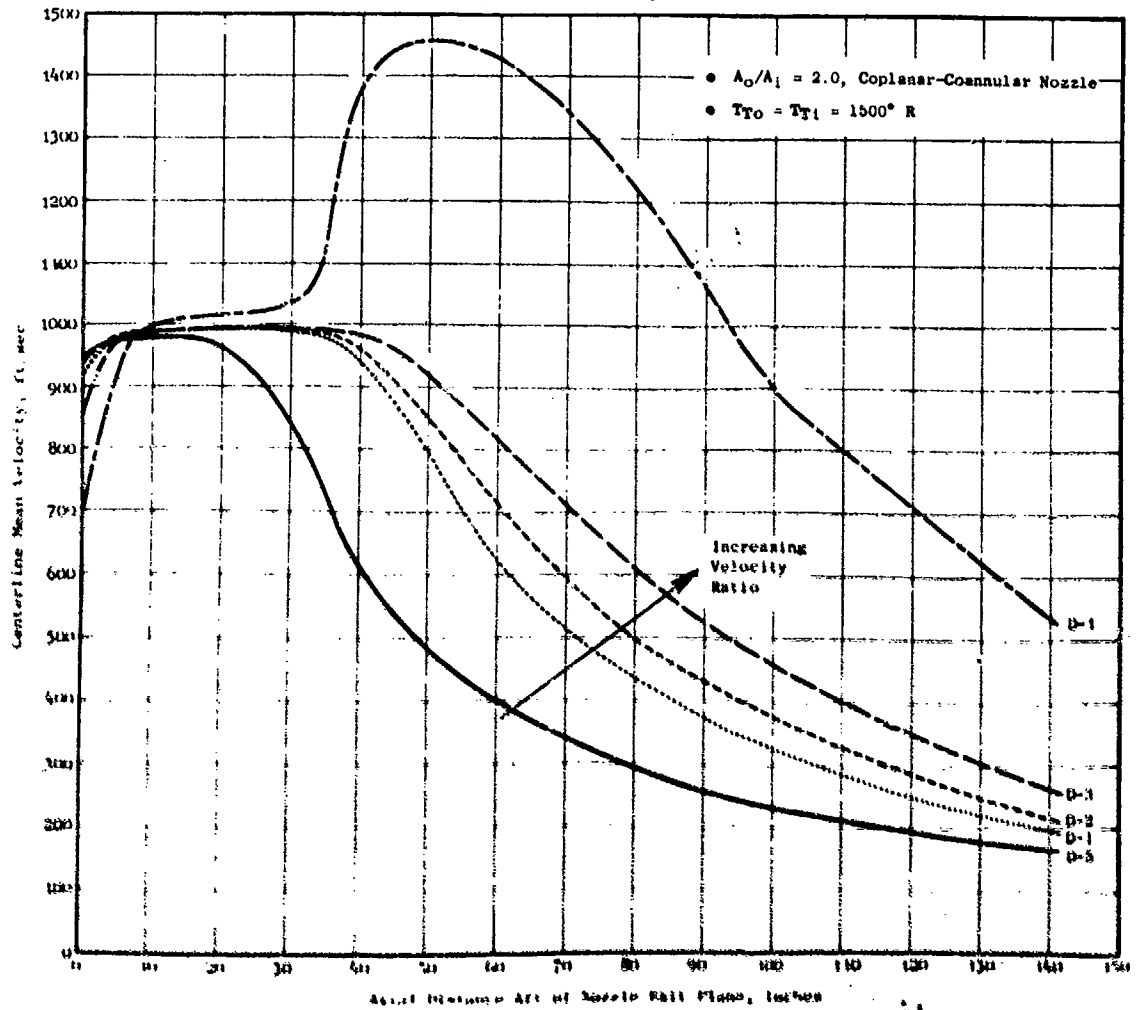


Figure 3-311. Centerline Velocity Decay Characteristics.

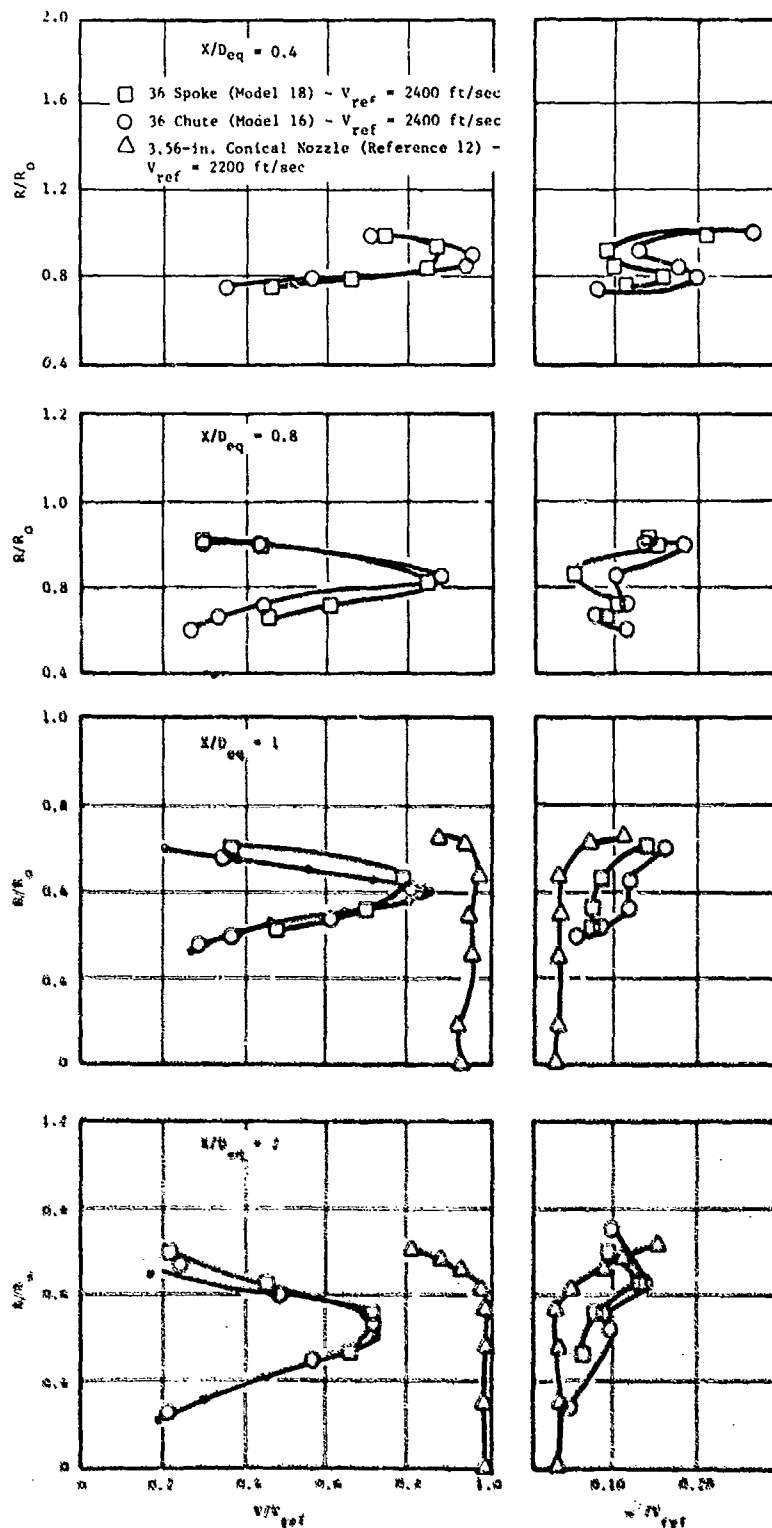


Figure 3-312. AR = 2.0 36-Chute (Model 16) and 36-Spoke (Model 18) Nozzles - Mean Velocity and Turbulence Profiles.

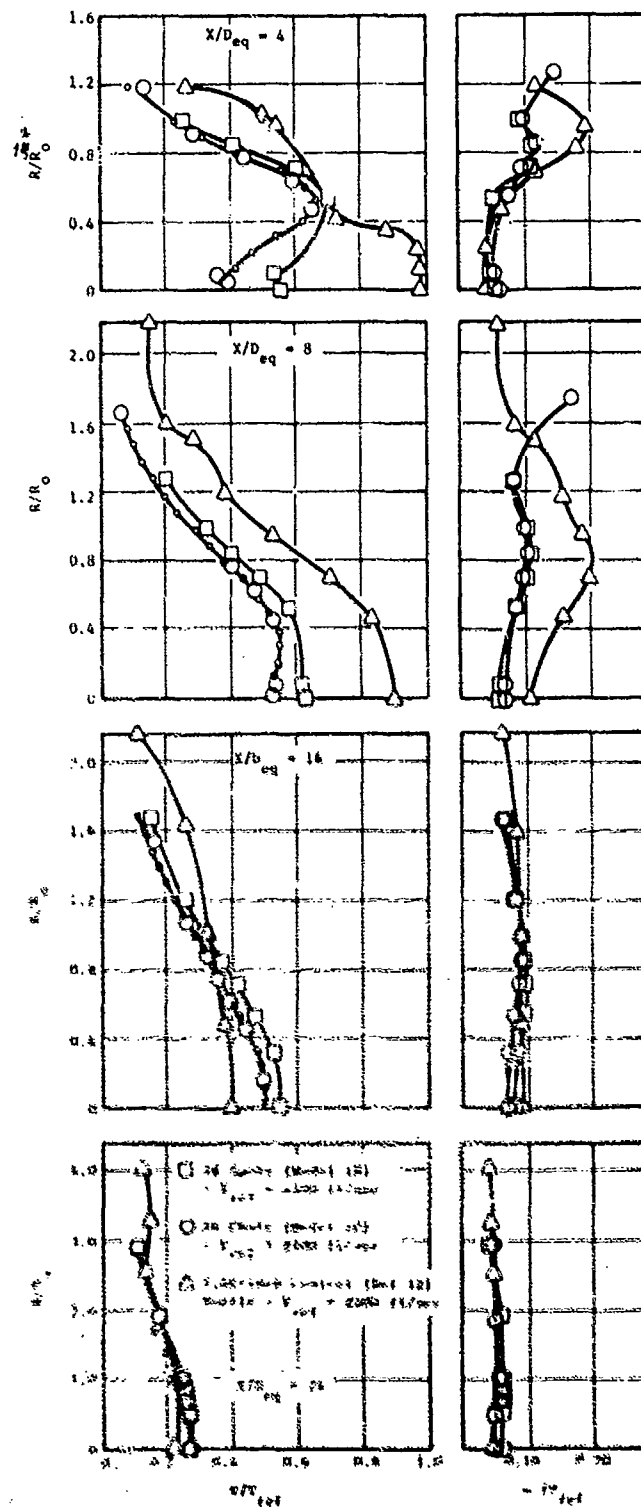


Figure 3-313. AR = 2.0 36 Chute and 36 Spoke Nozzles - Mean Velocity and Turbulence Profiles.

nozzle is actually less than the suppressor nozzles. The baseline and suppressor nozzles are equivalent at an  $X/D = 24$ .

Comparison of the spoke (Model 18) and chute (Model 16) mean velocity and turbulence profiles indicate only small differences between the configurations. The comparison of acoustic data for these configurations was presented in Section 3.4.2.4. The peak noise levels at the comparable cycle conditions for the plume are found to be essentially equivalent (which is supported by the similarity of the mean velocity and turbulence intensity comparisons).

Mean velocity and turbulence intensity measurements were made to determine the influence of suppressor area ratio variation. Models 22, 24 and 27 were utilized to perform this study. They were dual flow nozzles incorporating half-span suppressors having 36 elements. The acoustic data comparisons for these configurations are presented in Section 3.4.2.1. The outer stream velocity was 2400 ft/sec and the inner stream velocity was 1200 ft/sec. Figure 3-314 summarizes the decay characteristics of the peak velocity at whatever radial location it occurs. The  $AR = 2.5$  nozzle configuration (Model 22) causes the most rapid decay in mean velocity. It is interesting to note that noise reduction potential was generally enhanced with excessive suppressor area ratio which in turn exhibited the more rapid velocity decay rates.

Detailed mean velocity and turbulence profiles are summarized on Figures 3-315 and 3-316, for several axial locations. The trend of noise with suppressor area ratio variation is best illustrated by the comparisons at  $X/D = 2.0$  and  $X/D = 4.0$ . Minor differences in the turbulence intensity profiles are also apparent, however, they cannot be related to the noise generation process on a quantitative basis.

A study was conducted with Model 24 as the base configuration and with Model 36 to determine the effect that adding a treated ejector has on the mean velocity and turbulence intensity profiles. These comparisons are summarized on Figure 3-317. The comparisons at  $X/D = 2.0$  are at the exit plane of the ejector. The addition of the treated ejector resulted in only a minor change in the shape and level of the mean velocity and turbulence intensity profiles at the nozzle exit plane. A similar conclusion is drawn from the measurements made at the other axial locations. The acoustic comparisons presented in Section 3.4.2.7 showed a suppression improvement of 3-4 PNdB at the maximum noise angle. Since mean velocity and turbulence intensity profiles were shown to be similar, the beneficial effect of the ejector can probably be attributed to physical shielding and acoustic treatment effectiveness.

Measurements were also made on the JENOTS free-jet facility to determine the change in the mean velocity and turbulence intensity profiles in simulated flight. The characteristics are discussed below for a conical nozzle (Reference 12), plug nozzle (Model 40), chute nozzle (Model 41), and a 104-tube nozzle (Model 44).

The peak mean velocity decay characteristics for the conical nozzle (Reference 12) are summarized on Figure 3-318. The measurements show a slowing down of the mean velocity decay rate with increasing simulated aircraft velocity ( $V_{a/c}$ ) as discussed in Reference 29. A similar type of comparison



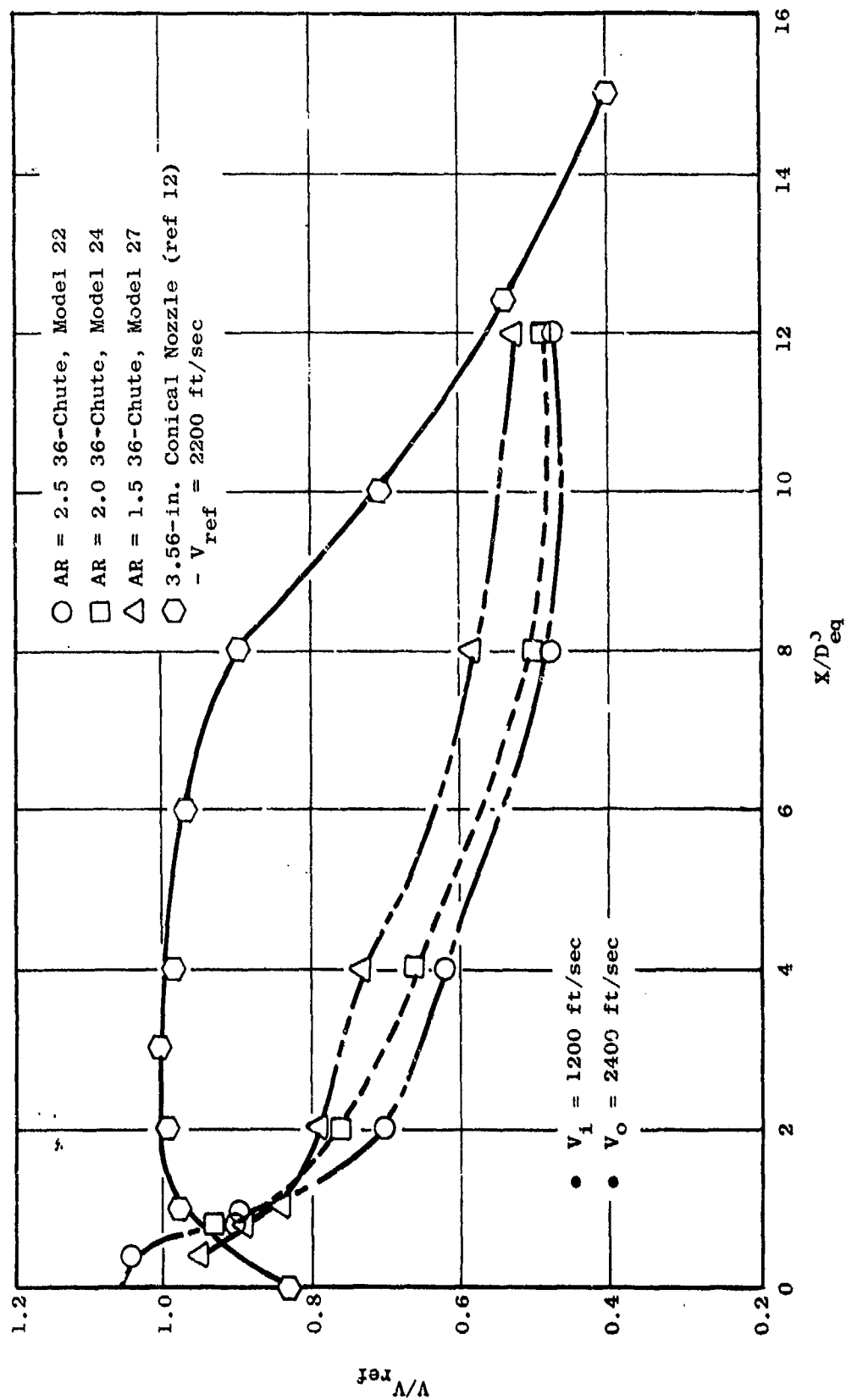


Figure 3-314. Effect of Area Ratio on Peak Axial Velocity Decay Characteristics.

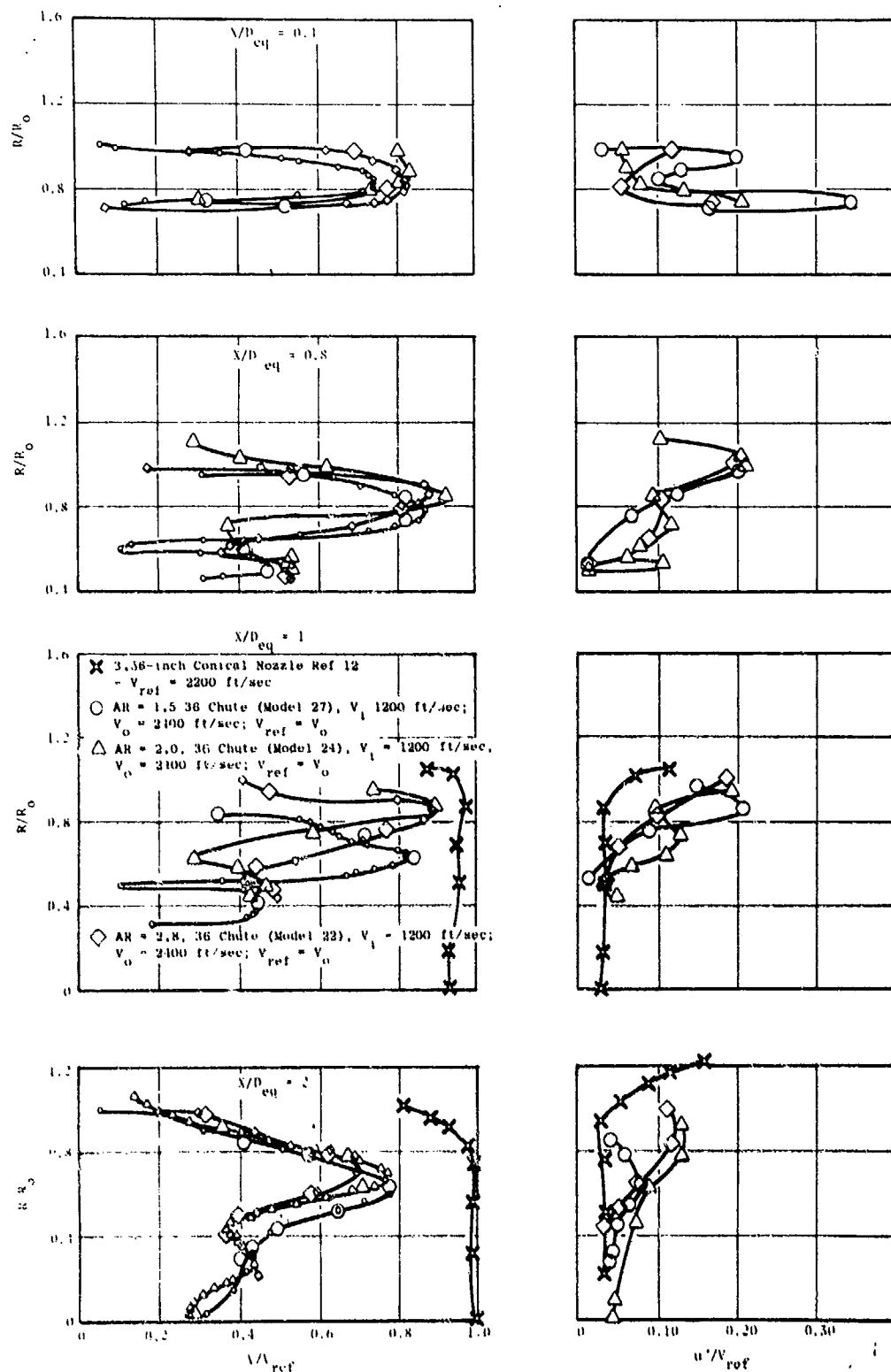


Figure 3-315. Impact of Suppressor Area Ratio on Radial Mean Velocity and Turbulence Intensity Profiles.

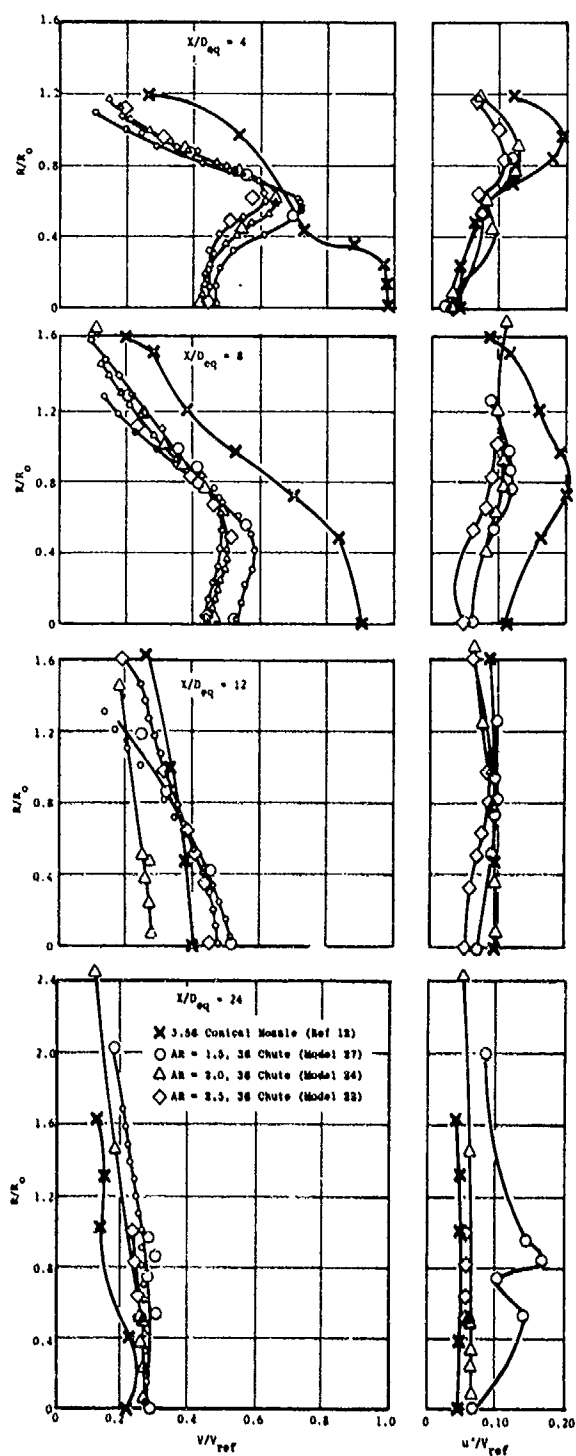


Figure 3-316. Impact of Suppressor Area Ratio on Mean Velocity and Turbulence Intensity Profiles.

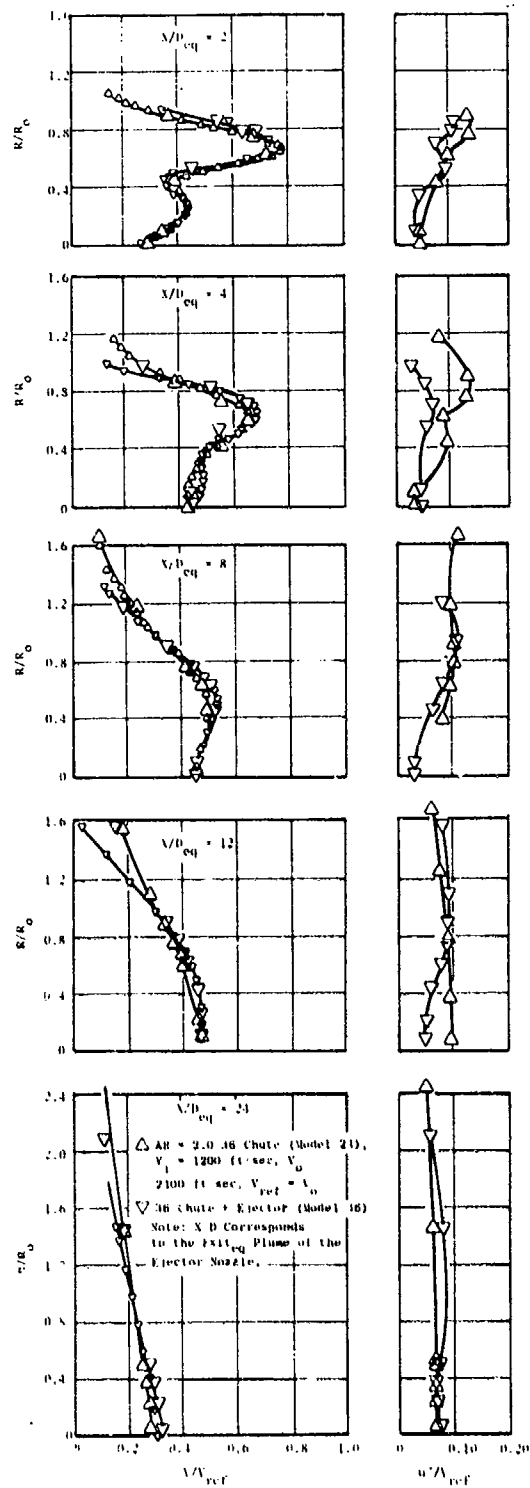


Figure 3-317. Impact of a Treated Ejector on the Mean Velocity and Turbulence Profiles of a 36 Chute Nozzle.

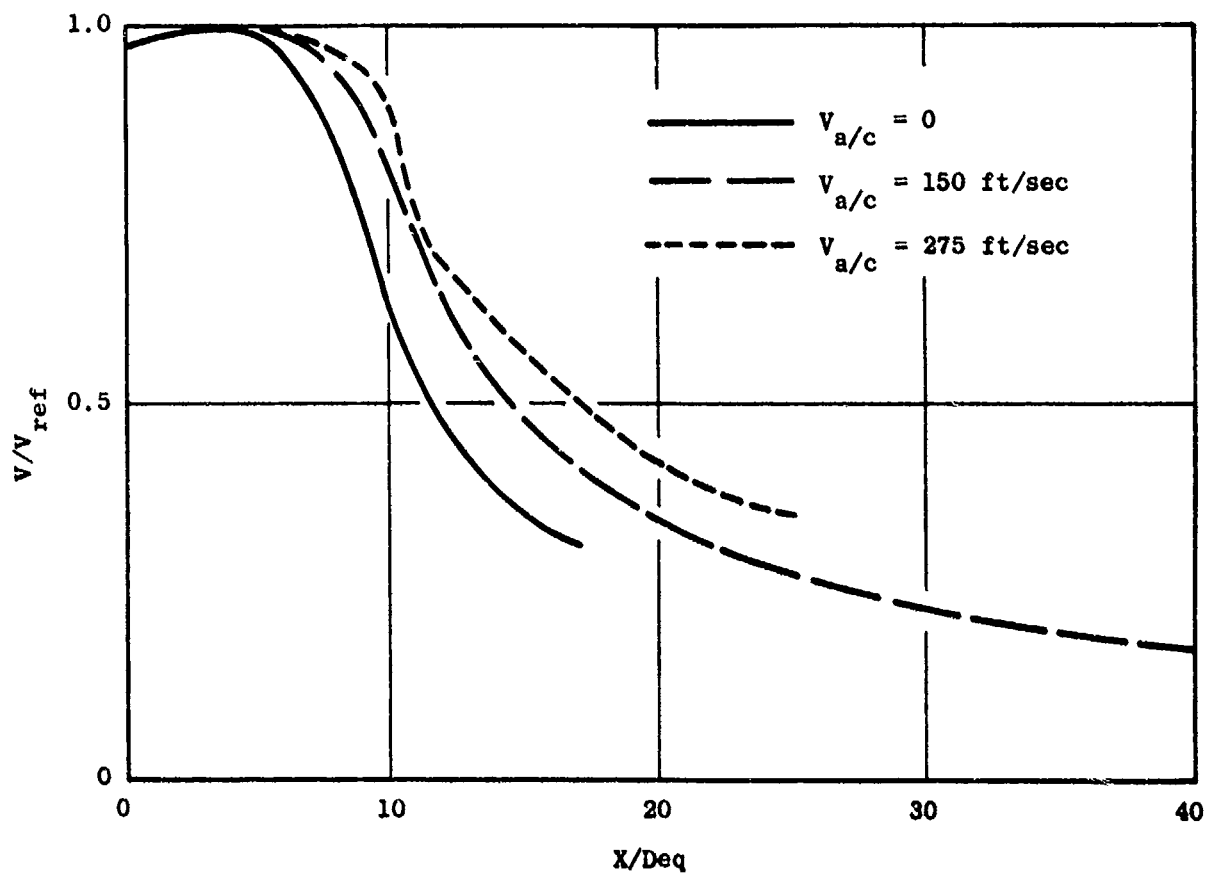


Figure 3-318. Centerline Velocity Decay for 3.56-inch Conical Nozzle (Reference 12),  $V_{ref} = 2200 \text{ ft/sec}$ .

for the 0.85 R/R plug nozzle, Model 40, is presented on Figure 3-319. These data were obtained by performing a series of axial traverses at the nozzle centerline and at normalized radial locations. The trends are similar to the conical nozzle.

The 8-lobe nozzle (Model 46) static and flight mean velocity decay characteristics are summarized on Figure 3-320. The rate of velocity decay has increased significantly relative to the conical nozzle at  $X/D < 14$ . The region of maximum mean velocity gradient ( $0 < X/D < 4.0$ ) appears to be only slightly sensitive to forward flight. In the axial region of  $4.0 < X/D < 15$  the velocity decay rate of this configuration is enhanced rather than decreased as was the case for the conical nozzle. The static and flight peak turbulence intensity levels for this configuration are also summarized on Figure 3-320. The turbulence level near the nozzle exit plane is slightly increased in flight very near the nozzle exit plane ( $X/D < 2.0$ ) and slightly reduced at other axial locations. The peak turbulence intensity levels also occur very near the nozzle exit plane.

Select measurements were made on the AR = 2.5 36-chute nozzle (Model 41). The mean velocity decay characteristics for this configuration, based on a series of axial traverses directly behind a flowing chute centerline at two radial locations, are summarized on Figure 3-321. The decay of the peak velocity near the nozzle exit plane is insensitive to flight. However at  $X/D > 12$  where the segmentized jets have lost their individual identity (or coalesced), the characteristics exhibited are the same characteristics observed for the conical nozzle. Mean velocity and turbulence intensity levels for a 104-tube nozzle Model 44 are summarized on Figures 3-322 and 3-323. The measurements were made along the centerline of the nozzle and at the centerlines of inner, middle, and outer tubes. The centerline static and flight mean velocity comparisons show a trend identical to that exhibited by the AR = 2.5 36-chute nozzle (e.g., influence of free-stream velocity is observed up to  $X/D = 7$ , while beyond this point the velocity decay rate is slowed down). The mean velocity levels of inner and middle tubes are essentially identical up to  $X/D$  of 3 with a slight divergence of 2% to 5% between  $X/D$  of 2 and 6. The decay characteristics of the outer tube are more sensitive to free-stream velocity. Turbulence intensity levels are compared on Figure 3-223. The maximum turbulence intensity levels occur in the jet plume of the outer tube in the region of maximum mean velocity gradient. The levels are similar to those of the conical nozzle. In flight, minimal change in turbulence intensity levels occurs near the nozzle exit plane; in the region of the coalesced jet, the levels are reduced.

The prior data comparisons support the following conclusions. Suppressors generally cause the increase in mean velocity decay until the velocity reaches 60% or less of the fully expanded isentropic velocity. This point generally occurs within 10 to 15 equivalent nozzle diameters and is a function of the suppressor design. The axial location of peak turbulence intensity is a function of nozzle type, and generally occurs in the region where the mean velocity gradient is a maximum. For example, the peak turbulence intensity levels for the conical nozzle occurred at  $6 < X/D < 8$  whereas the peak turbulence intensity level for the chute nozzles occurred at  $X/D < 0.4$ .

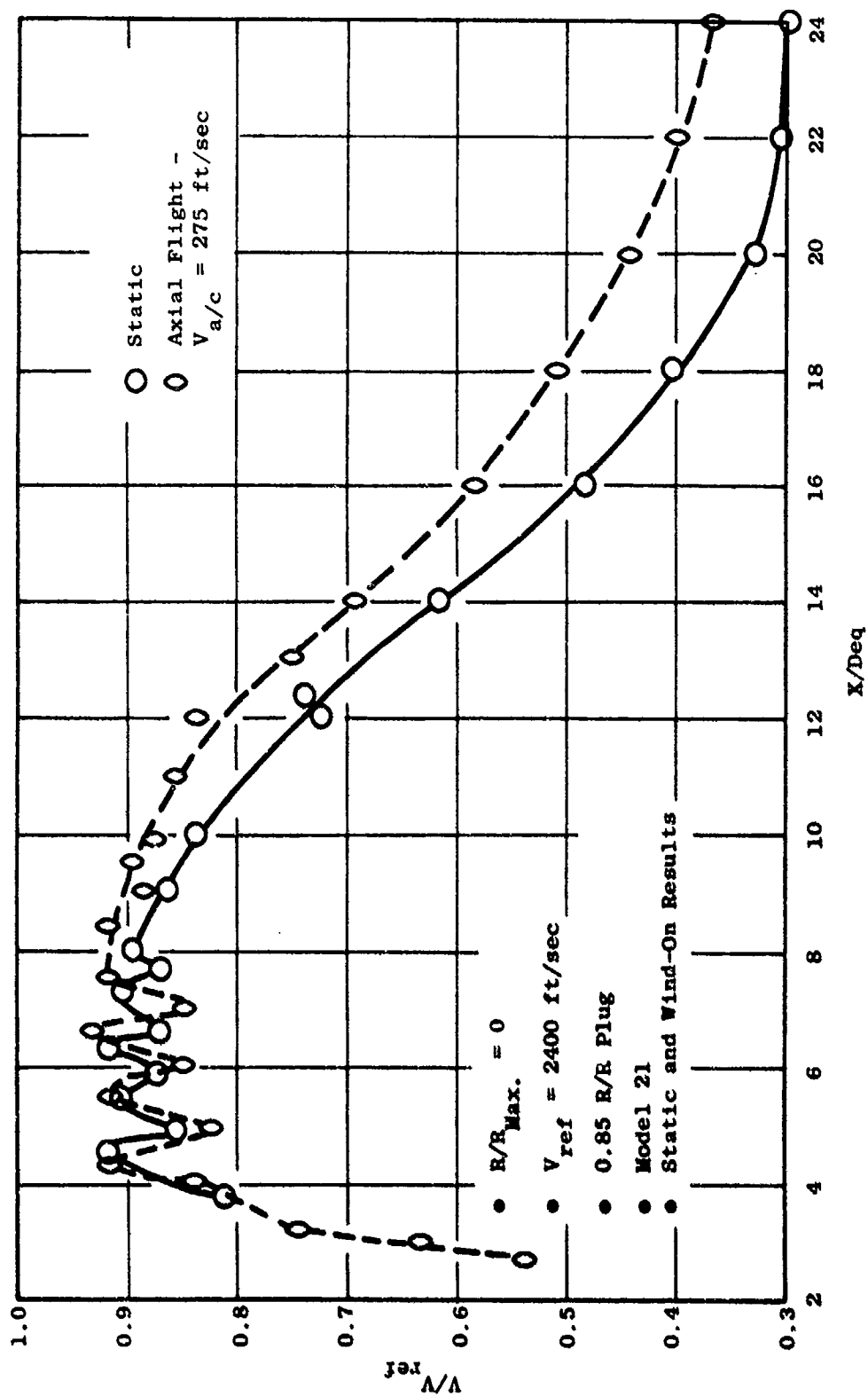


Figure 3-319. 0.85 Radius Ratio Plug Nozzle (Model 40) Centerline Mean Velocity Decay Characteristics.

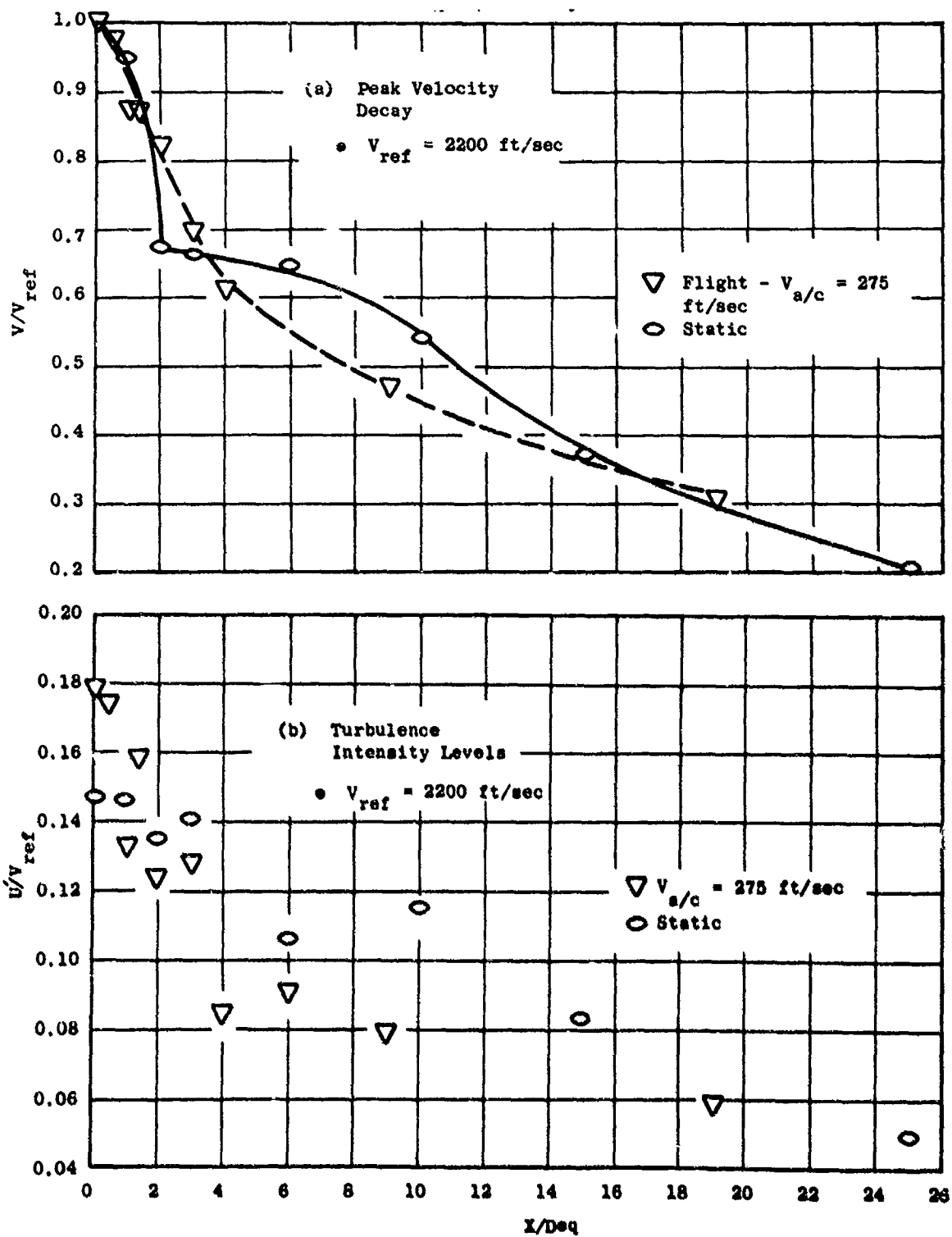


Figure 3-320. 8-Lobe Nozzle (Model 46), Static and Flight.



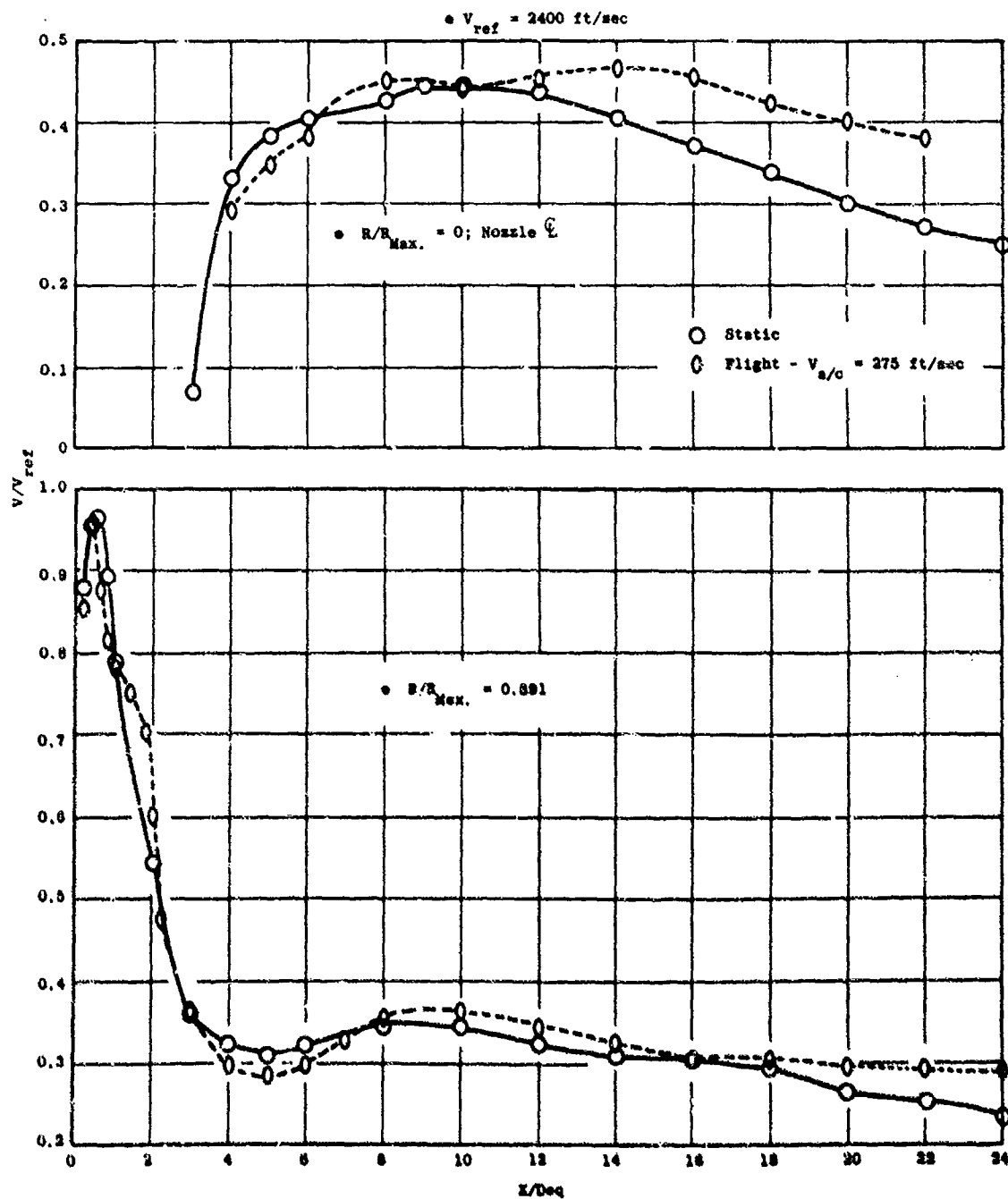


Figure 3-321. 36-Chute Nozzle (Model 41) Mean Velocity Decay Characteristics Static and Flight.

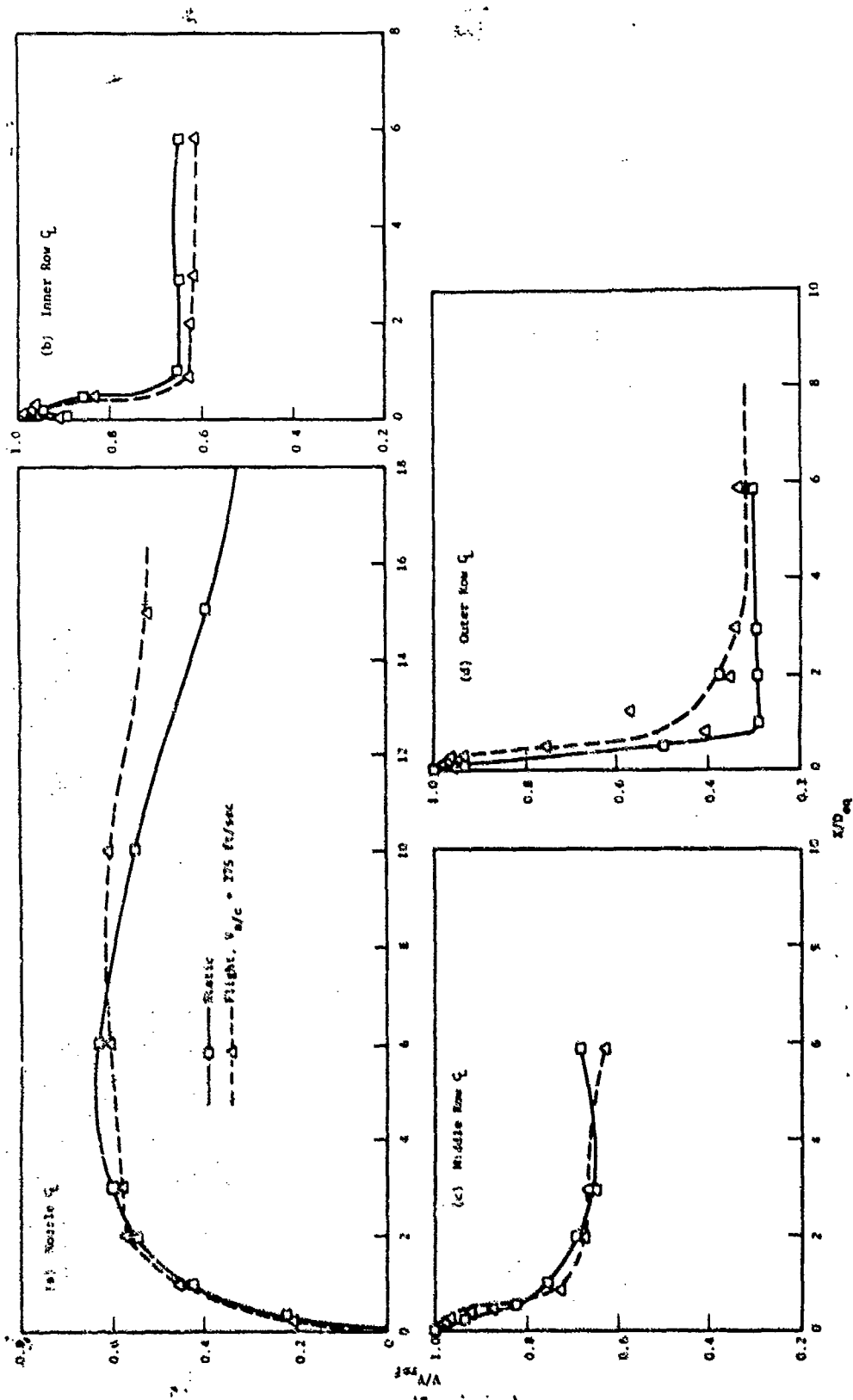


Figure 3-322. 104-Tube Nozzle (Model 44) Mean Velocity Characteristics, Static and Flight.

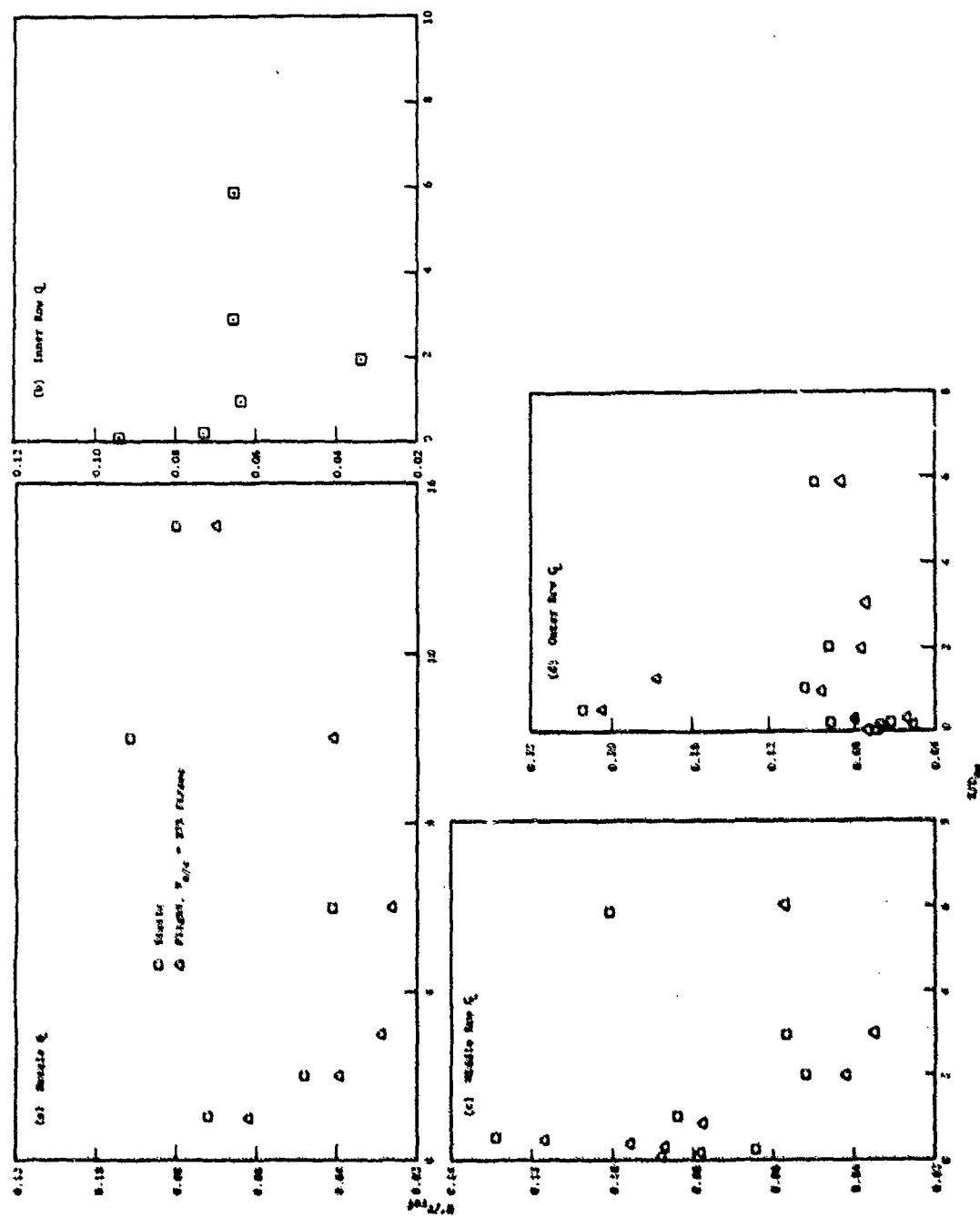


Figure 3-323. 104-Tube Nozzle (Model 44) Turbulence Intensity Characteristics, Static and Flight.

In general, for a complex multielement suppressor nozzle the region of peak turbulence intensity was found to occur within one equivalent nozzle diameter for the configurations evaluated. Although axial locations of peak turbulence intensity levels are a function of nozzle type, the absolute level ranges from 18 to 22% and does not correlate with exhaust nozzle type.

In simulated flight, the velocity decay rate for the conical nozzle was retarded (e.g., decayed at a much lower rate). The suppressor showed very little sensitivity to forward velocity with the exception of the downstream coalesced jet. Turbulence intensity levels were found to decrease in the coalesced jet in-flight compared to static. The levels near the exit plane were found to be generally comparable.

Overall, the laser velocimeter was demonstrated to be extremely useful in determining the differences in aerodynamic mixing characteristics of baseline and complex multielement suppressor nozzles. The aerodynamic data, in conjunction with the acoustic data bank, may be utilized to aid in the validation of current and future jet noise analytical prediction models.

#### 3.4.5 Ellipsoidal Mirror (EM) Testing

This section presents the results of ellipsoidal mirror (EM) source location measurements made on several scale model suppressor nozzles during the Task 3 test program. EM testing was conducted on a total of twenty-two different nozzle configurations. Of these, fourteen configurations were tested at the jet noise anechoic facility using the 34.654-inch diameter deep-dish mirror, and eight were tested at the JENOTS free-jet facility, using the 18-inch-diameter shallow-dish mirror. Test setup and data acquisition were described in Section 3.3.3, and Appendices D and E describe the EM developments.

##### 3.4.5.1 Data Analysis

The EM test matrix was planned to allow evaluation of several geometric and operating parameters by comparison of measured source distributions for specific data points. The results of these comparisons are presented in this section. The source distributions are expressed as Strouhal Number ( $f D_{eq}/V_o$ ) versus normalized axial distance ( $X_{peak}/D_{eq}$ ), where  $D_{eq}$  is the equivalent circular diameter based on nozzle area,  $V_o$  is the ideally expanded jet velocity and  $X_{peak}$  is the peak source location for a given frequency,  $f$ . For dual flow configurations,  $D_{eq}$  is calculated from total area (inner plus outer) and  $V_o$  is based on the higher velocity (outer) stream.

Integral closure checks were made for all EM data points in the test program. Typical results are shown in Figures 3-324 through 3-328 for measurements made in the anechoic facility with the deep-dish mirror. Note that the data obtained with 2-sec integration time yielded the best results, even at lower frequencies, and was subsequently used to completely define the majority of the source distributions.

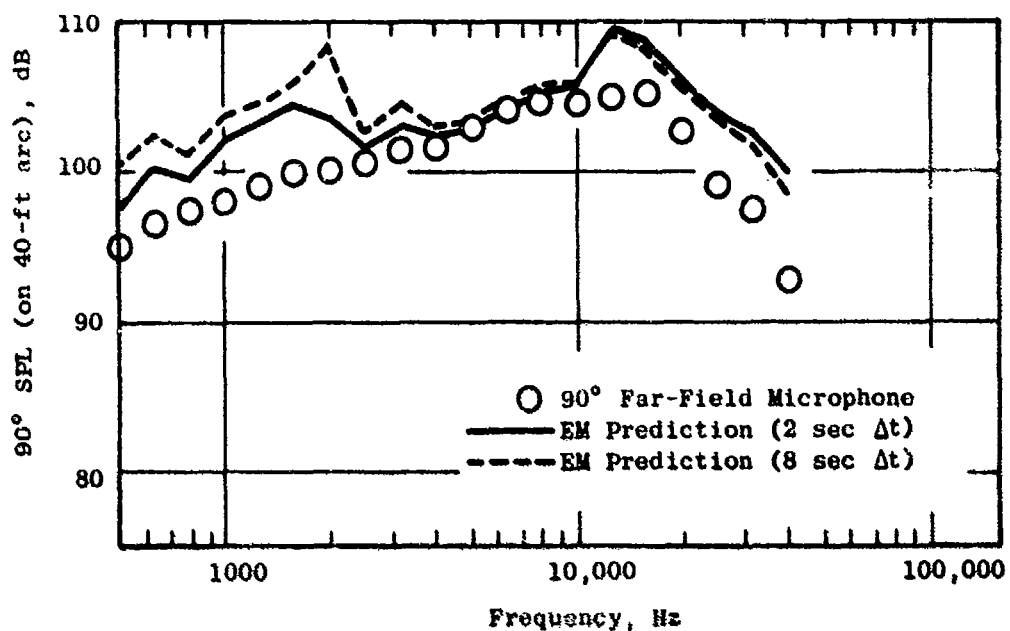


Figure 3-324. Integral Closure Check for AR = 2.0 36-Chute Nozzle,  $V_0 = 2384$  ft/sec,  $V_1 = 1187$  ft/sec.

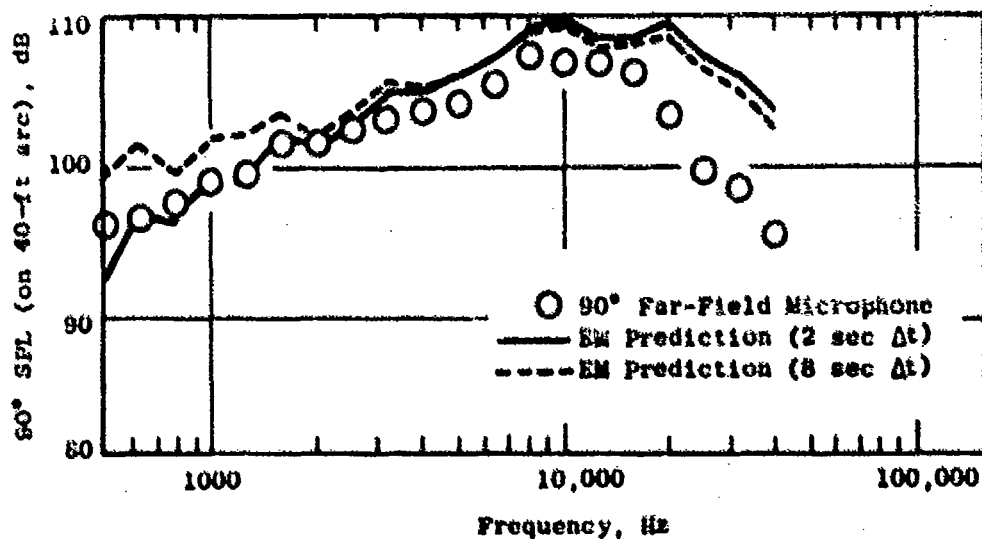


Figure 3-325. Integral Closure Check for AR = 1.75 20-Shallow-Chute Nozzle,  $V_0 = 2375$  ft/sec,  $V_1 = 1167$  ft/sec.

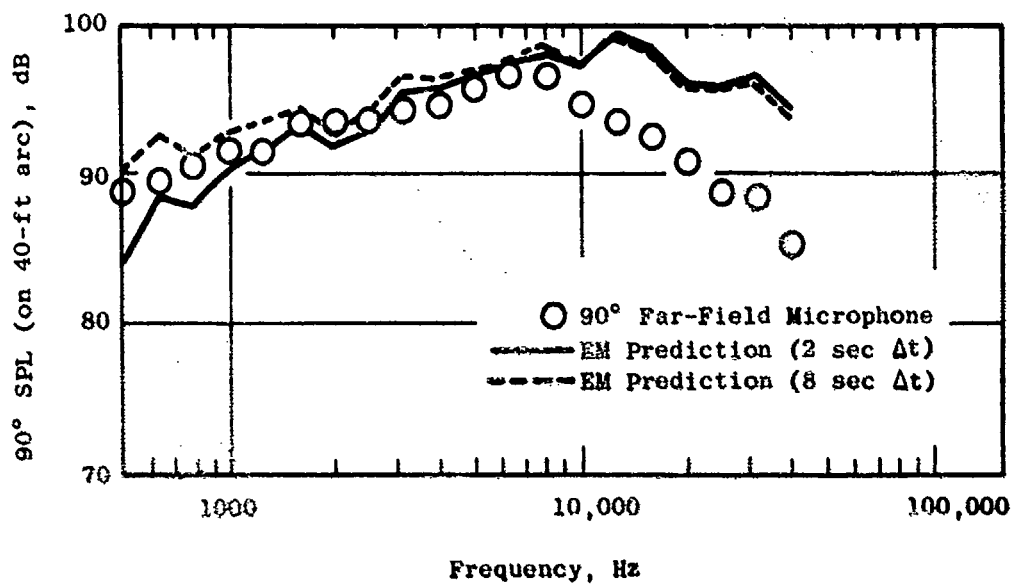


Figure 3-326. Integral Closure Check for AR = 2.0 36-Chute Nozzle with Treated Ejector,  $V_0 = 1803$  ft/sec,  $V_1 = 1173$  ft/sec.

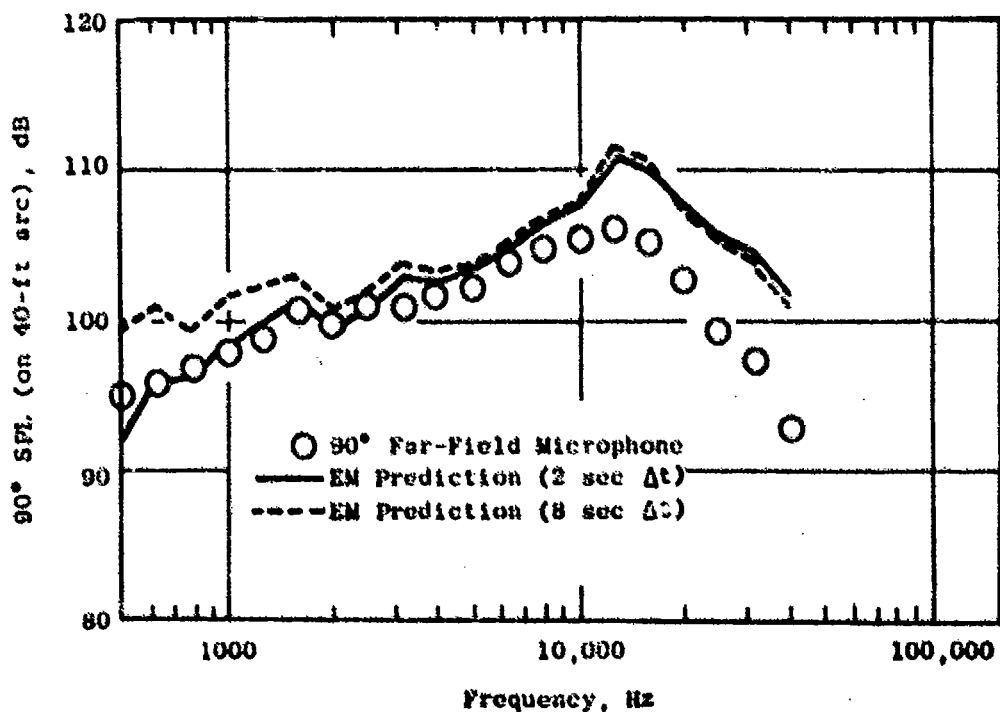


Figure 3-327. Integral Closure Check for AR = 2.0 36-Chute Nozzle,  $V_1 = 2375$  ft/sec.

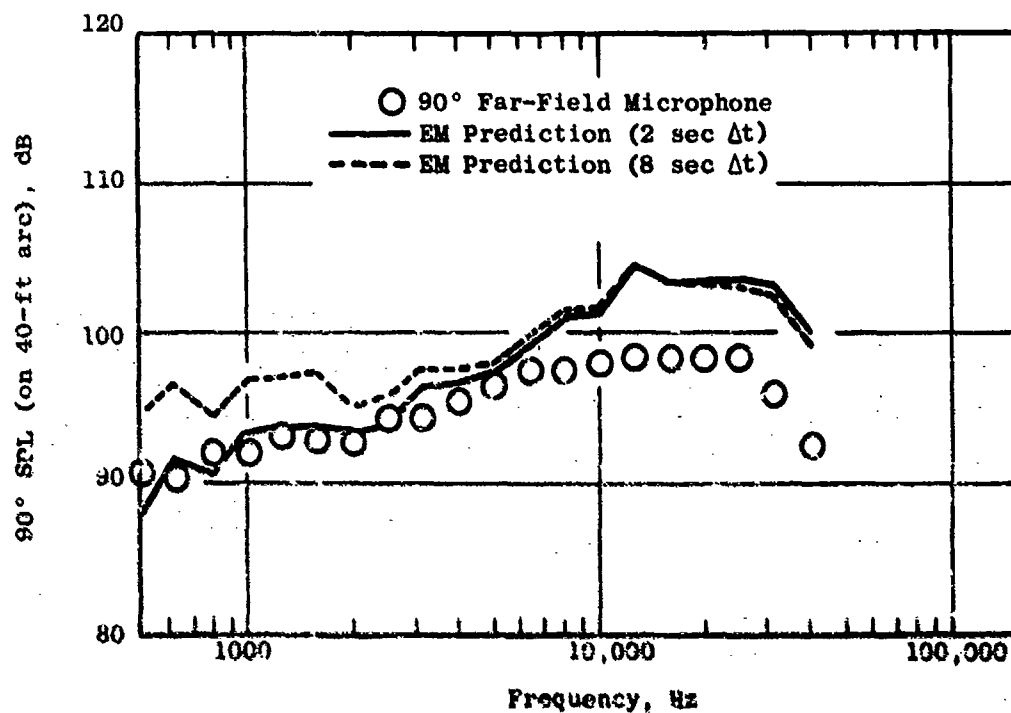


Figure 3-328. Integral Closure Check for AR = 2.5 36-Spoke Nozzle,  $V_o = 2382$  ft/sec,  $V_i = 1269$  ft/sec.

Figure 3-329 shows a comparison of peak source distributions for 20-, 30-, and 40-shallow-chute, dual-flow suppressors (Models 30, 31, and 32). While there is no significant difference between the 30- and 40-element data, high-frequency sources for the 20-element configuration peak farther downstream of the nozzle exit.

A comparison of peak source distributions for 36-chute, dual-flow suppressors with area ratios 2.5 and 3.0 (Models 33 and 34) is shown in Figure 3-330. The source distribution for area ratio 3.0 is seen to peak farther downstream at all frequencies.

Figure 3-331 shows a comparison of 36-chute and 36-spoke suppressors (Models 33 and 35). The source distribution for the chute nozzle peaks slightly closer to the nozzle exit for higher frequencies.

Figure 3-332 compares 36-chute dual-flow and turbojet suppressors (Models 24 and 16), while Figure 3-333 shows the same comparison with ejectors (Models 36 and 19). In both cases, the turbojet distributions peak farther downstream in the high and midfrequency ranges.

Figures 3-334 and 3-335 show the effect of ejectors on 36-chute nozzles for dual-flow (Models 24 and 36) and turbojet (Models 16 and 19) configurations, respectively. In each case, the peak high-frequency source distributions occur farther downstream with the ejector. There is no significant effect on low-frequency source distributions which normally peak downstream of the ejector exit.

Typical axial distributions of sound source intensity for a suppressor (Model 32) are shown in Figure 3-336. These 40-shallow-chute, dual-flow suppressor results confirm the expectation that source distributions become broader and flatter with decreasing frequency.



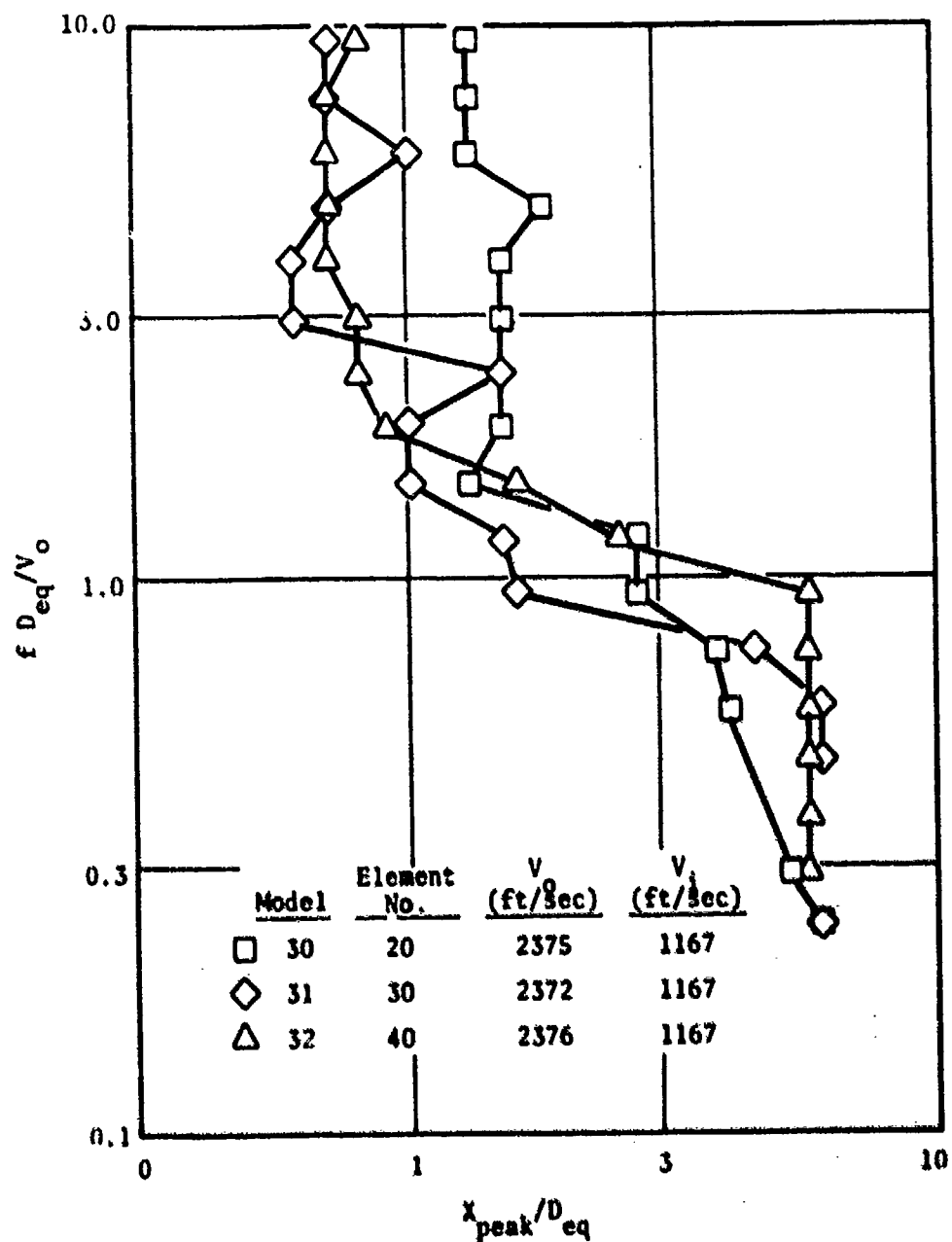


Figure 3-329. Effect of Element Number on Multispoke (Shallow Chute) Dual-Flow Suppressor Noise Source Distributions.

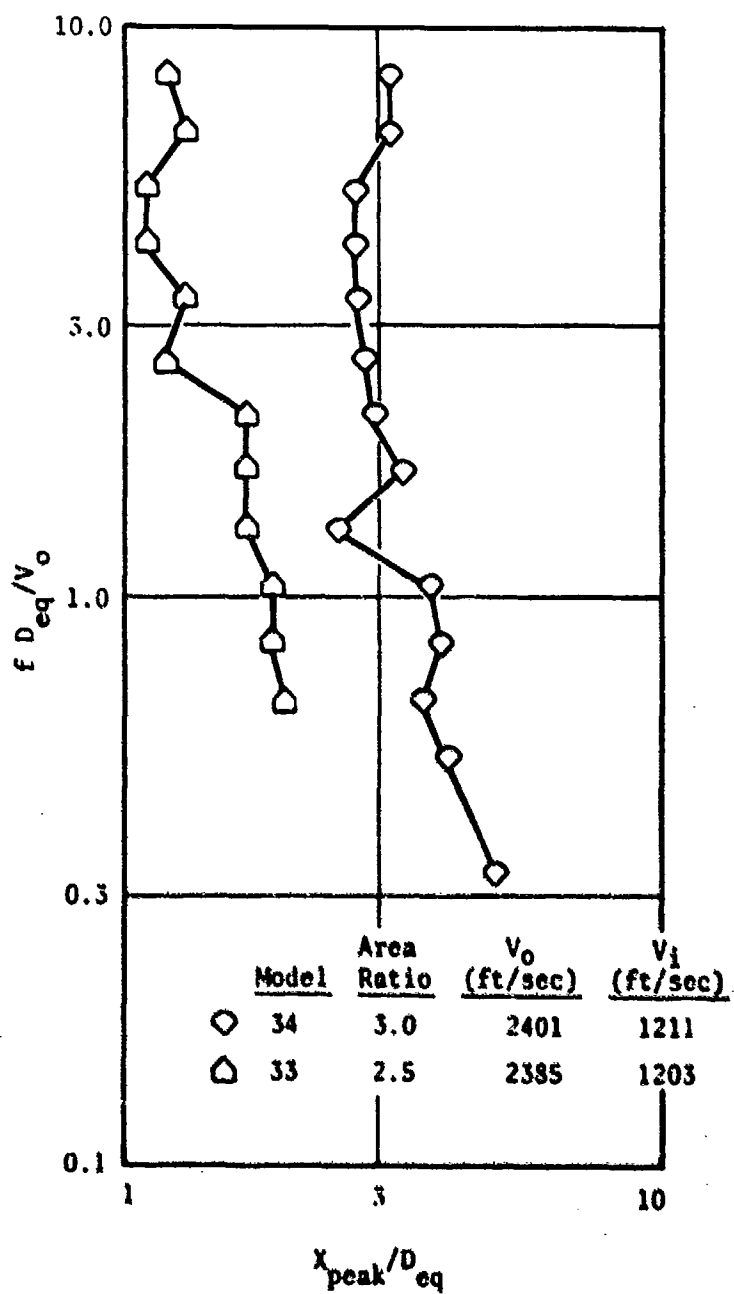


Figure 3-330. Effect of Chute Area Ratio on Multi-chute Dual-Flow Suppressor Noise Source Distributions.

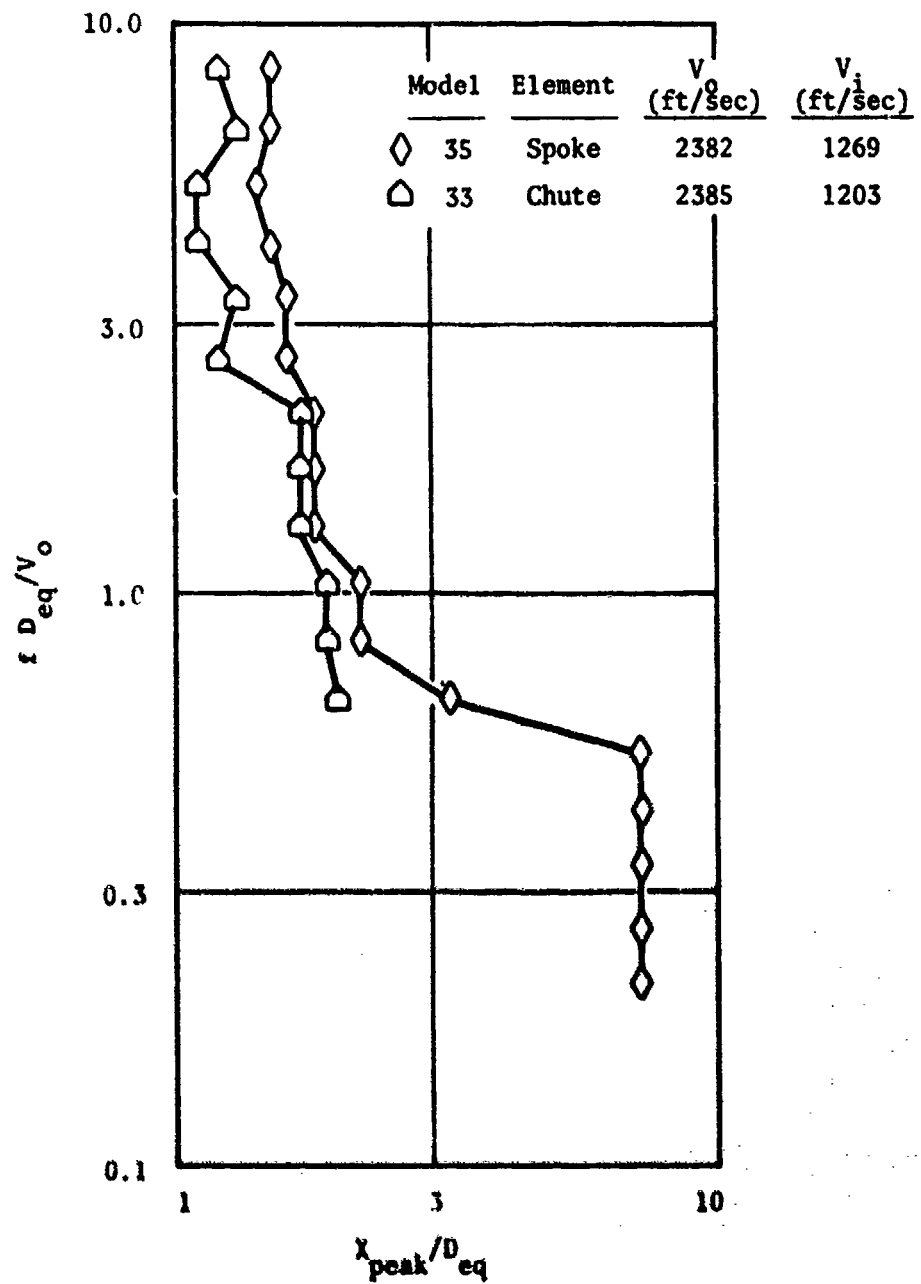


Figure 3-331. Comparison of Noise Source Distributions for Multichute and Multispoke Dual-Flow Suppressors.

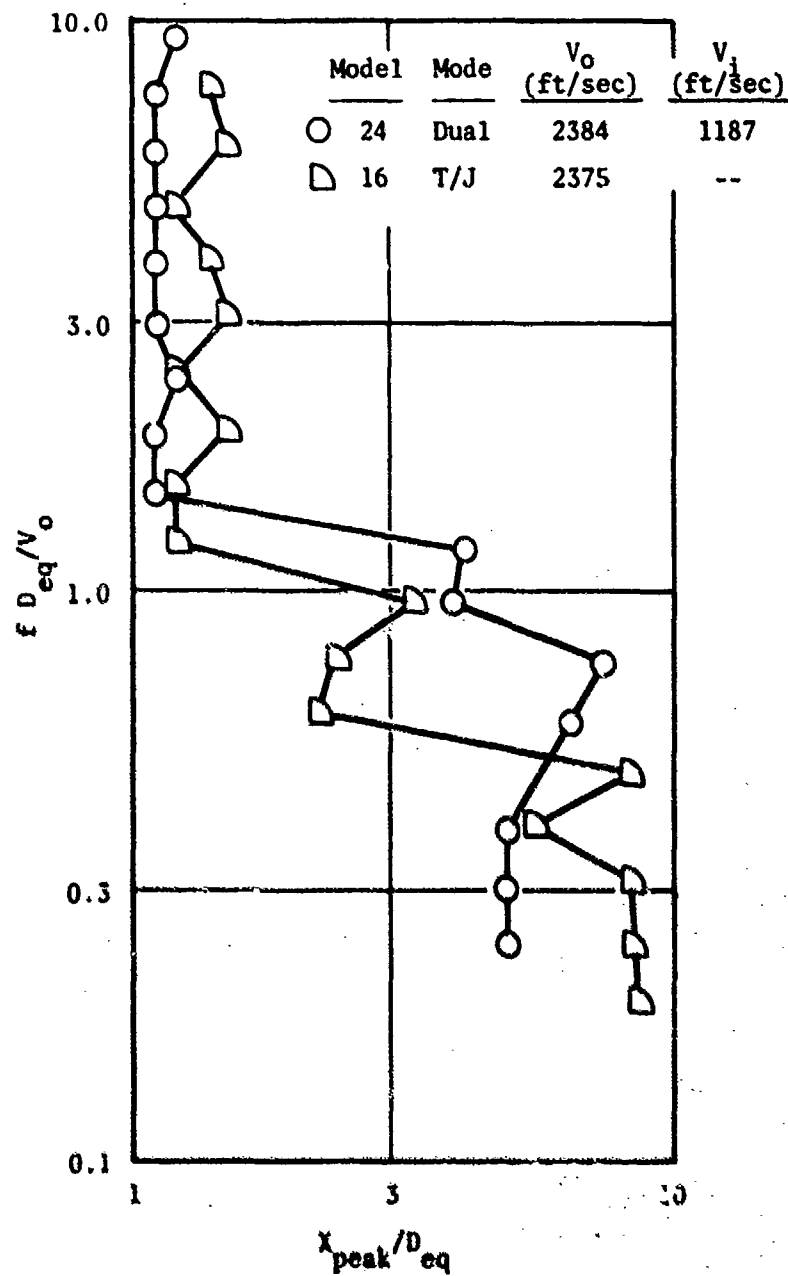


Figure 3-332. Comparison of Noise Source Distributions for Multichute Dual-Flow and Turbojet Suppressors.

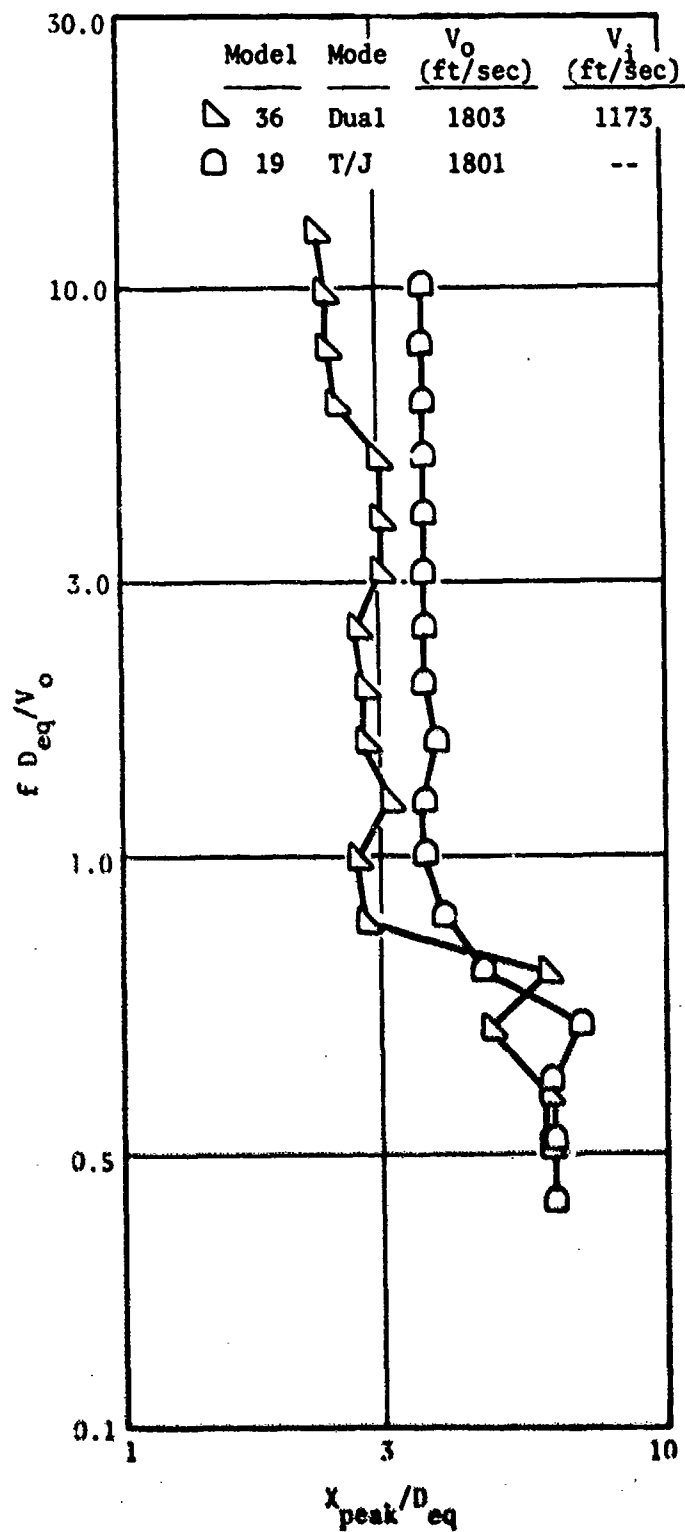


Figure 3-333. Comparison of Noise Source Distributions for Multichute Dual-Flow and Turbojet Suppressors with Ejectors.

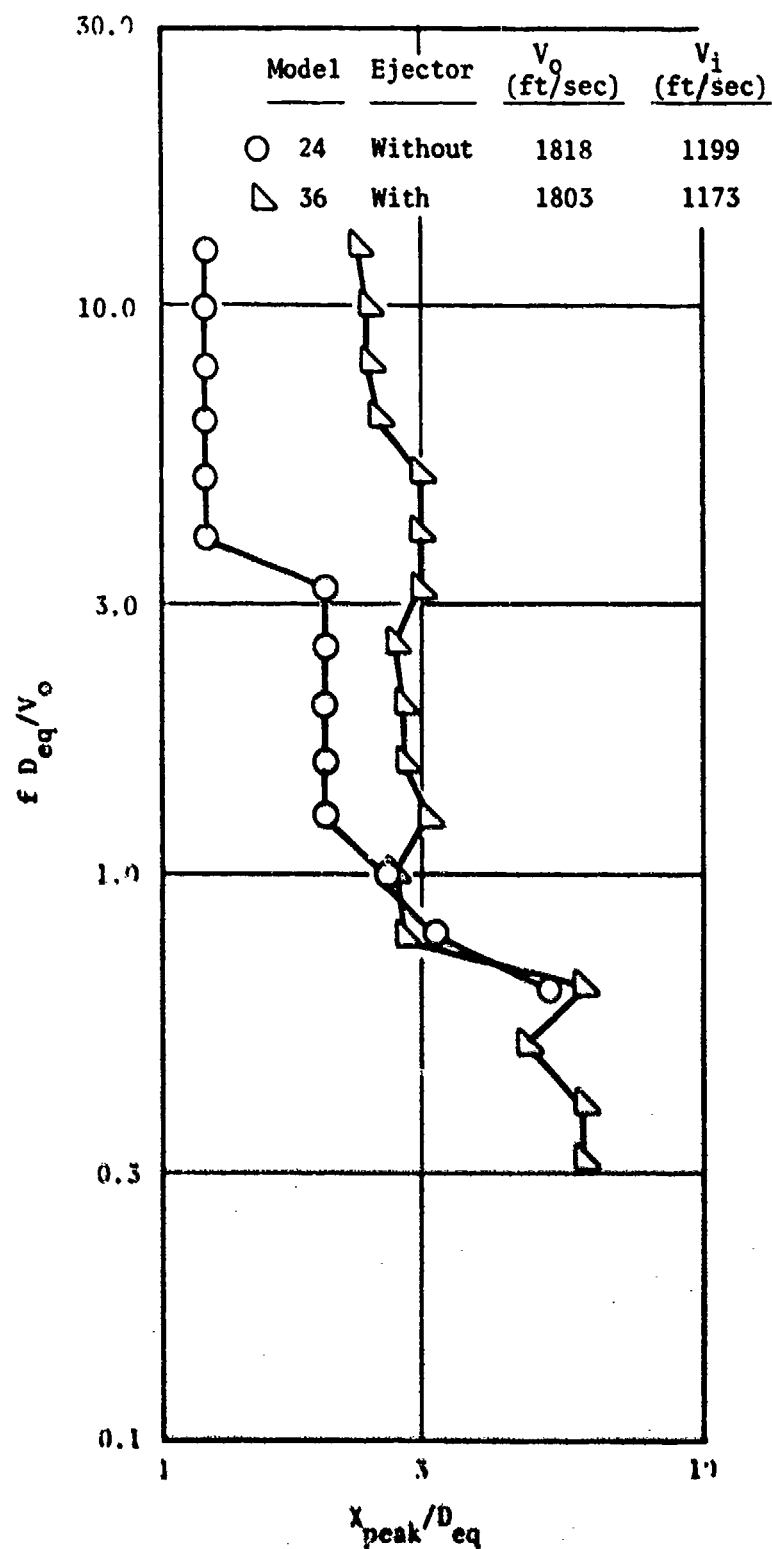


Figure 3-334. Effect of an Ejector on Multichute Dual-Flow Suppressor Noise Source Distributions.

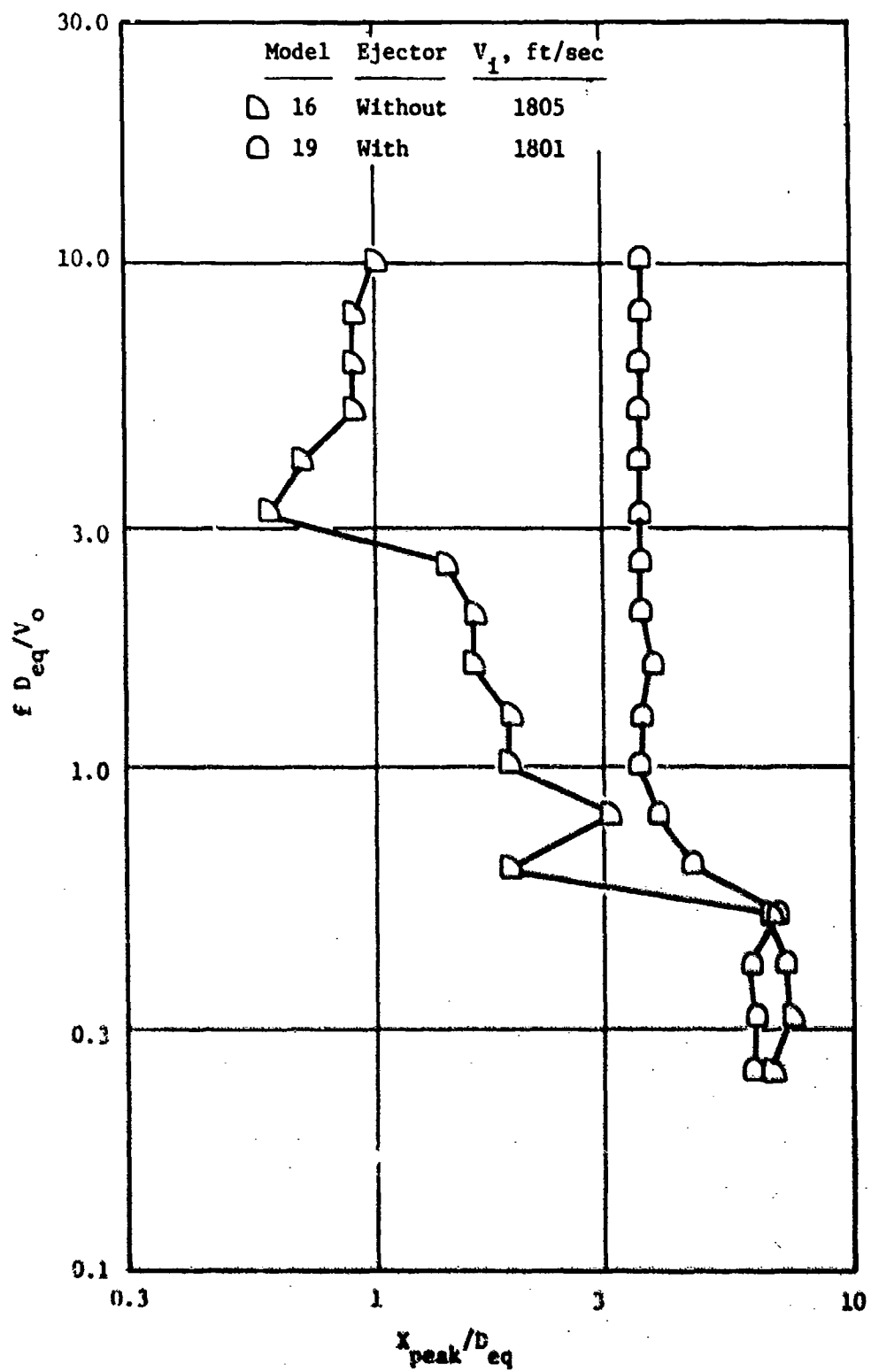


Figure 3-335 Effect of an Ejector on Multichute Turbojet Suppressor Noise Source Distributions.

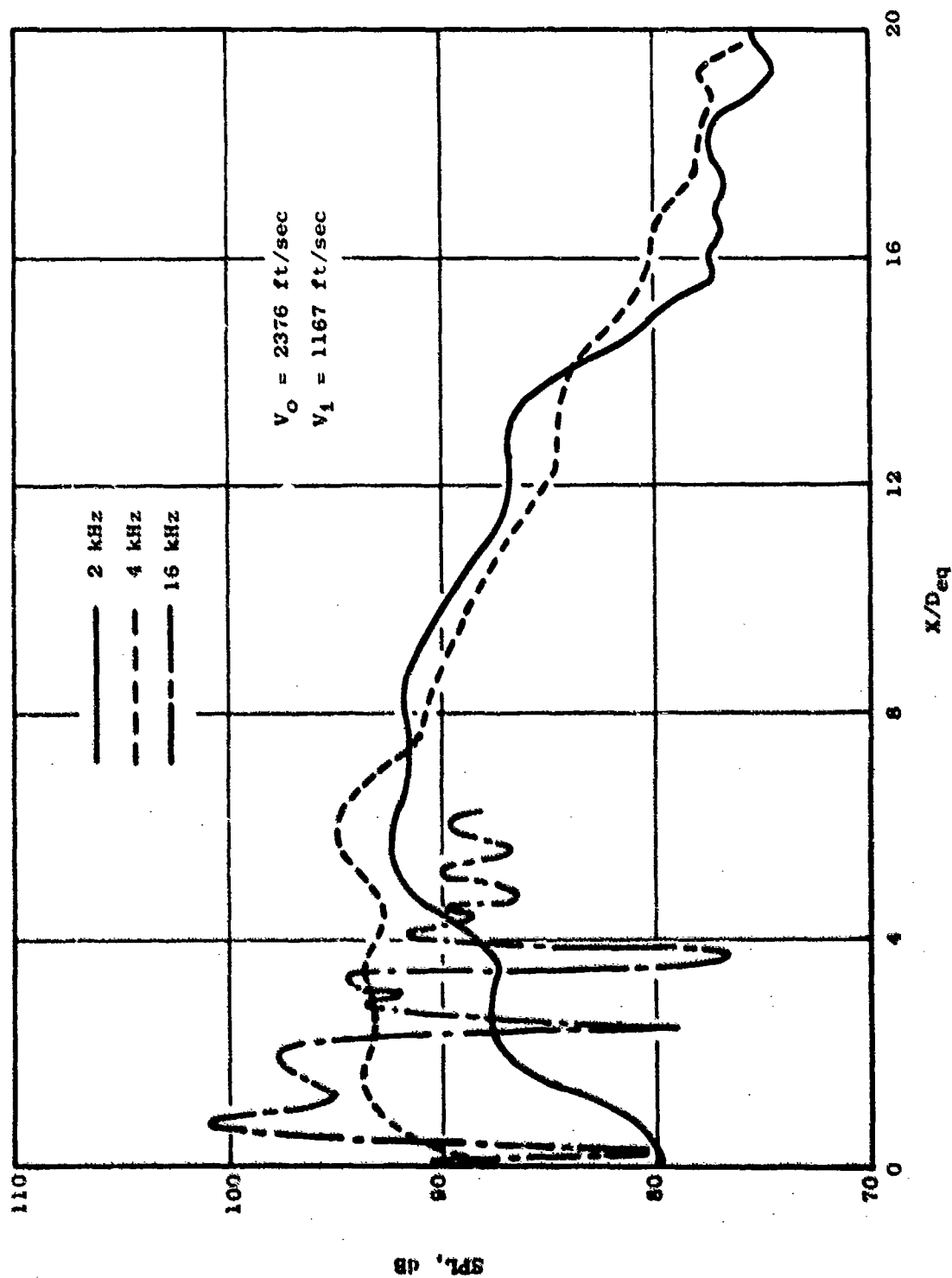


Figure 3-336. Axial Distributions of Sound Source Intensity for a 40-Shallow-Chute Dual-Flow Suppressor (Model 32).



#### 4.0 AERODYNAMIC PERFORMANCE TEST PROGRAM

Historically, the introduction of mechanical jet noise suppression devices into the exhaust gases of turbine engines has resulted in significant losses in thrust, usually in proportion to the amount of suppression achieved. In addition, the base areas associated with suppressor elements introduce a performance (thrust loss) sensitivity to external flow conditions not normally encountered with nonsuppressing exhaust nozzles. The task of designing a viable jet noise suppressing exhaust system therefore depends heavily on an understanding of the effect of nozzle geometric parameters on in-flight suppression and performance. With this understanding, the designer can conduct trade studies leading to a low-noise exhaust system with good aerodynamic performance.

Past programs, such as the DOT Supersonic Transport Noise Reduction Technology Program, identified the annular (plug) nozzle with exit plane suppressor elements as a promising high velocity jet noise suppression system. A significant parametric data base on the effect of nozzle geometric variations, such as element number and area ratio, was, however, not available. More importantly, recent advances in engine technology (variable cycle engines) and acoustic work on the benefits of inverted flow nozzles with high radius ratios resulted in even greater voids in the available performance prediction technology base. Unknowns included the effect of inner nozzle geometry, location, and area on overall nozzle performance. In addition, high radius ratio, parametric jet noise suppressor performance data were unavailable. The current program provided the vehicle for filling these technology voids.

##### 4.1 GENERAL PROGRAM OBJECTIVES AND SCOPE

The overall objective of the wind tunnel test program was to generate a comprehensive parametric data base on the aerodynamic performance of both dual- and single-flow annular nozzle/chute-type suppressor systems. These data would augment existing data from previous programs (such as the SST Phase II Program) and provide information necessary to conduct the trade studies and aircraft integration studies reported in Volume III, and provide design data for the noise abatement nozzle design guide (Task 6 of this program).

Specifically, the objectives of the aerodynamic performance test program were to obtain performance data under simulated flight conditions on the effects of suppressor area ratio, suppressor element number, and suppressor ventilation area. In the case of the dual flow nozzles, data were required on the effects of inner nozzle geometry. Suppressor element base pressure data were required as an integral part of the basic performance data. Previous programs had identified element base drag as the major contributor to exhaust system thrust loss. Parametric base pressure information would provide a basis for correlation of these data resulting in a performance

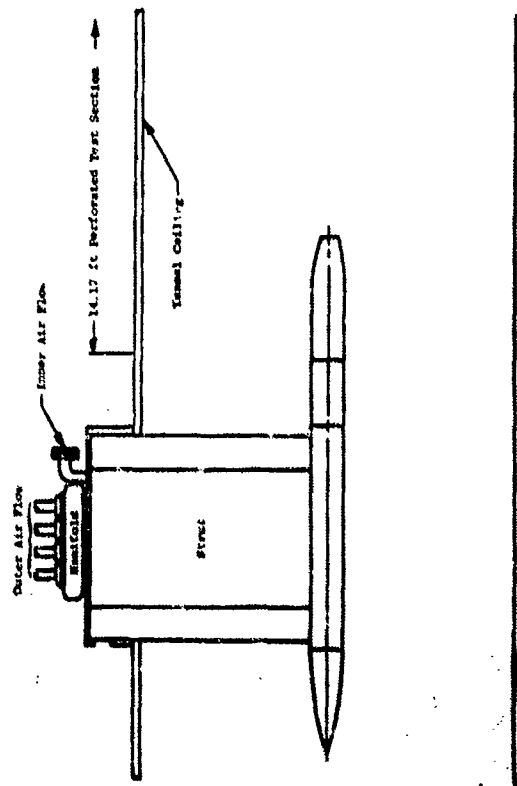
prediction tool for future design studies. The program involved the design and fabrication of model hardware, geometrically duplicating acoustic models described in Section 3.1, and testing in the Lewis Research Center 8- by 6-foot Wind Tunnel. Data obtained in the test program included nozzle thrust coefficients and model surface static pressures. Data were taken over a range of inner to outer stream pressure ratios representative of takeoff conditions with tunnel Mach numbers of 0.0, 0.36, and 0.45.

#### 4.2 TEST FACILITY DESCRIPTION

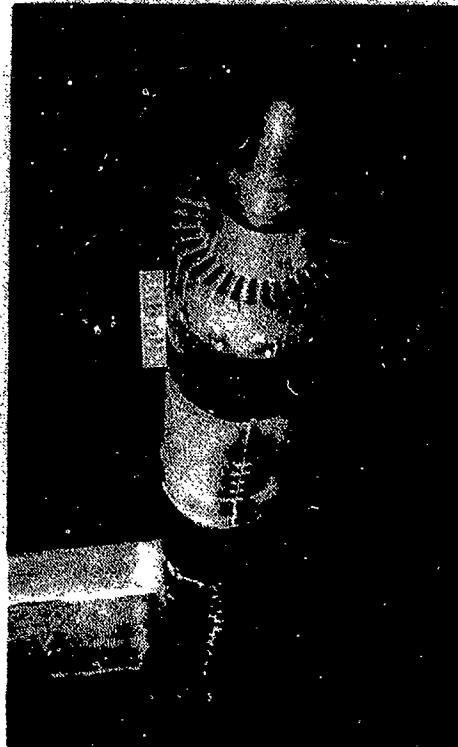
The test program was conducted in the NASA-Lewis 8- by 6-foot supersonic wind tunnel. The test nozzles were mounted to a 8.5-inch diameter cylindrical sting which was supported in the test section by a perpendicular strut connected to the tunnel ceiling. A schematic and photograph illustrating this mounting system is shown in Figure 4-1. Air was supplied to the model through tubes running down the strut and emptying into coannular air passages leading aft to the model. The air source was a continuous supply of 450 psig compressor air which passed through a system of control valves, flowmeters, and into the strut. A schematic of the air supply system is shown in Figure 4-2. The outer nozzle air was metered through a 1.248 inch diameter choked venturi. The inner nozzle air supply was metered through either a 1.1598-inch or 0.3985-inch diameter choked venturi, depending on the flow rate required.

The nozzle thrust was measured with a load cell mounted in the forward portion of the sting as shown schematically in Figure 4-3. The coannular air passages in the sting were mounted to the load cell and were metric; i.e., forces on the coannular air passages were measured by the load cell. The air supply tubes internal to the strut were fixed to the tunnel ceiling and thus formed flexure columns bridging the nonmetric and metric portions of the test rig. Interactions resulting from the bridging are accounted for in the balance calibration. Airflow from the tubes entered the sting perpendicular to the sting axis and thus created no entering momentum force on the load cell. The air passages themselves were suspended inside the sting with bearings which supported the concentric passages and allowed the axial forces to be transmitted to the load cell. Static pressure instrumentation was located on the forward-facing portions of the internal metric hardware so that the tare force could be accounted for in cases where internal static pressures were different from ambient.

The load cell was calibrated by mounting the Supersonic Tunnel Association (STA) model on the sting and applying a known axial force along the centerline of the model and the load cell. This known force was generated by a hydraulic cylinder connected to a circular pad which applied force to the nozzle in an axial direction. The correlation of the known applied force and the millivolt output of the load cell comprised the desired calibration. The calibration was made from 0 to 1000 pounds, the maximum allowable balance load.



● Model Installed in 8 x 6 foot Supersonic Wind Tunnel



● Schematic of Model Mount System

Figure 4-1. Typical Model Installation.

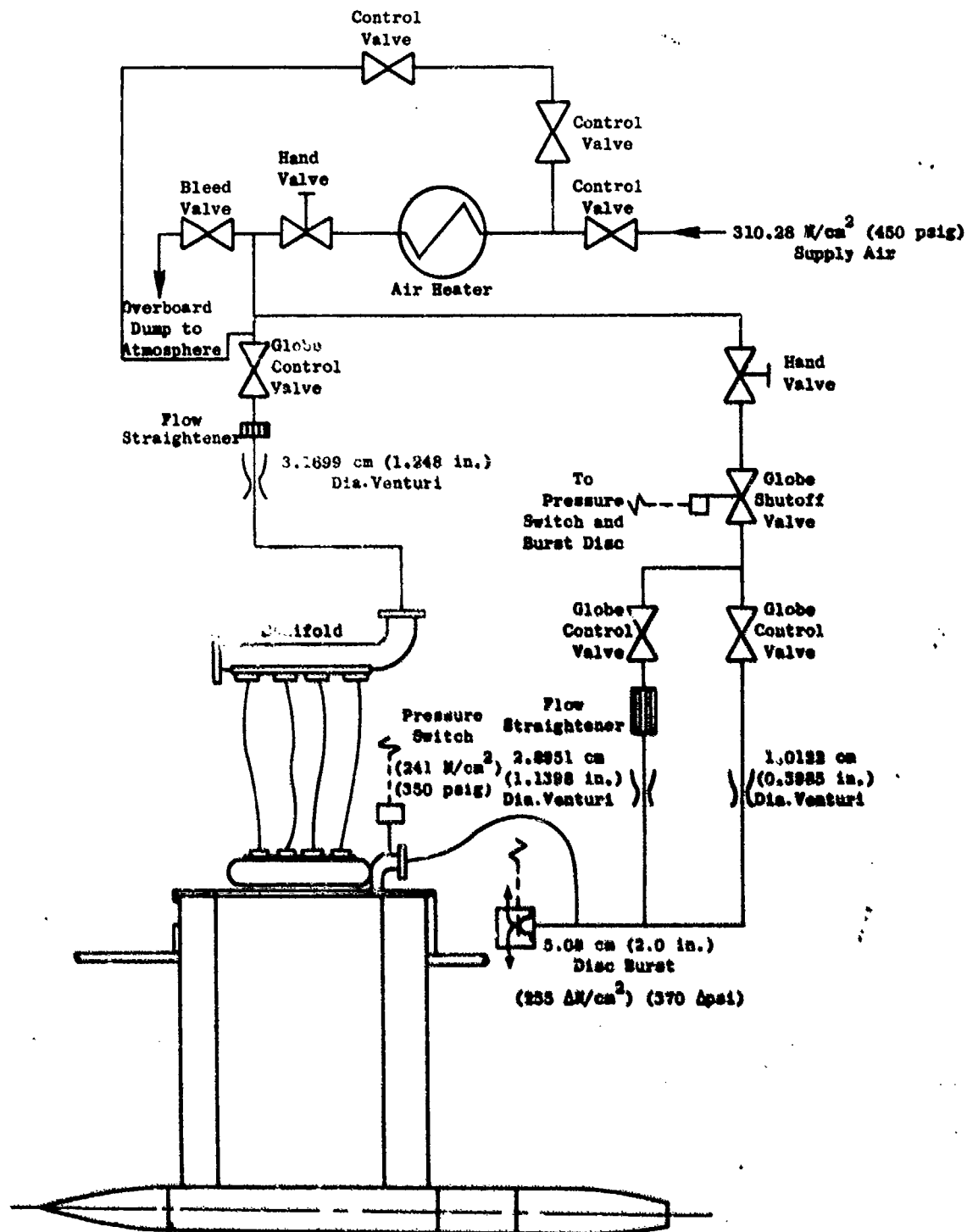


Figure 4-2. Schematic of Model Air Supply.

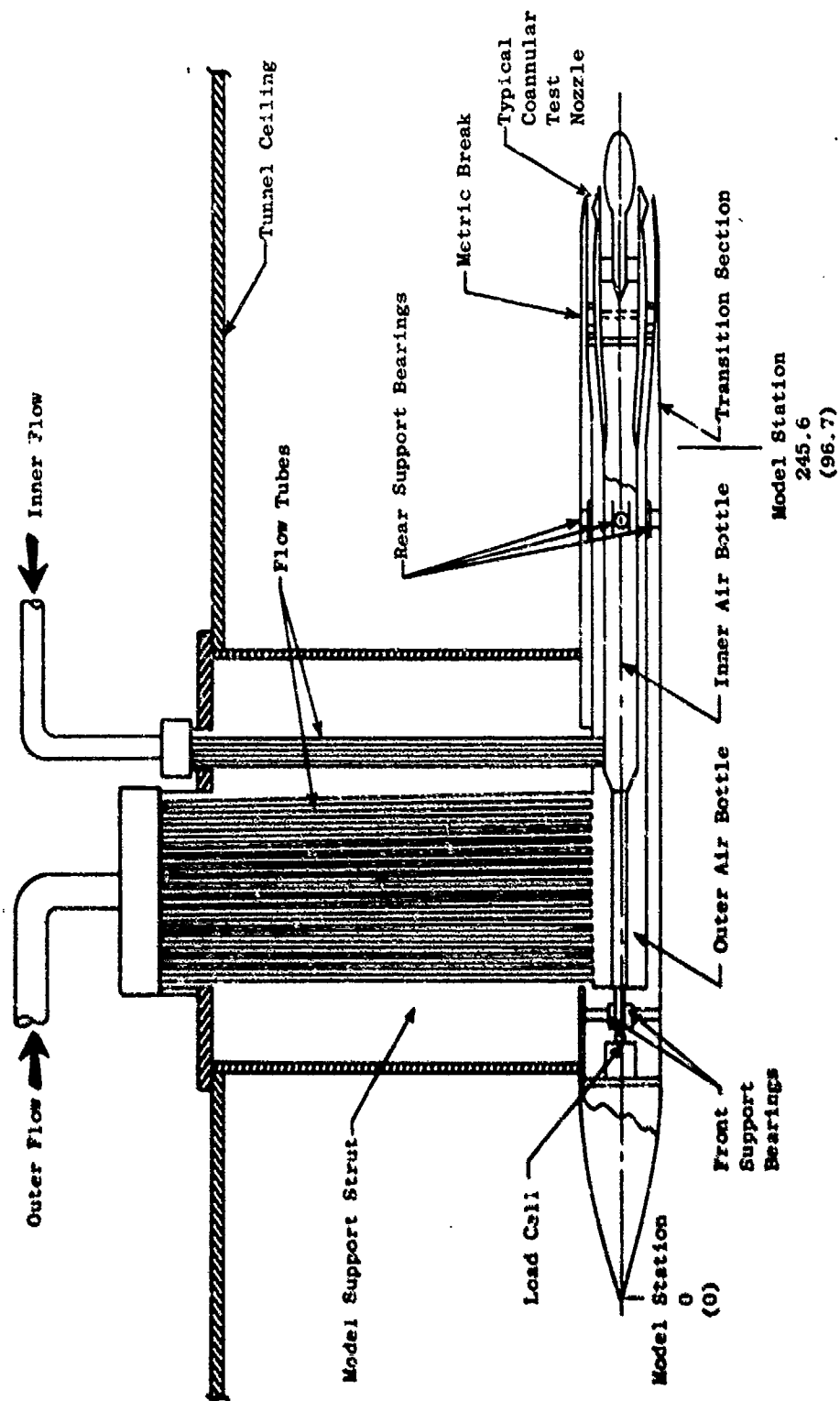


Figure 4-3. Schematic of Model Thrust-Measuring System.

#### 4.3 MOLEL DESCRIPTION

The suppressor models tested in the NASA Lewis 8- by 6-foot supersonic wind tunnel included 15 annular suppressed nozzle configurations, a 104-tube nozzle, and an eight-lobe nozzle. The annular nozzles simulated both turbojet installations (single flow) and advanced, inverted-flow variable cycle engine installations (dual flow). In addition to the suppressor models, a reference nozzle, the Supersonic Tunnel Association (STA) model, was also tested. A description of these models is presented below. Details of the model geometries and instrumentation are presented in Appendix F.

##### 4.3.1 Annular Suppressed Models

A schematic of a typical annular suppressed nozzle configuration is shown in Figure 4-4 to illustrate the variables investigated. Principle variables evaluated included: element number,  $N$ , for a given suppressor area ratio; suppressor area ratio,  $AR$ , for a given element number; inner nozzle area (or radius ratio); axial location of the inner plug,  $X$ ; and chute ventilation area, or depth,  $d$ . Table 4-1 lists the configurations tested and key geometric variables. Figure 4-5 presents a pictorial summary of the models tested.

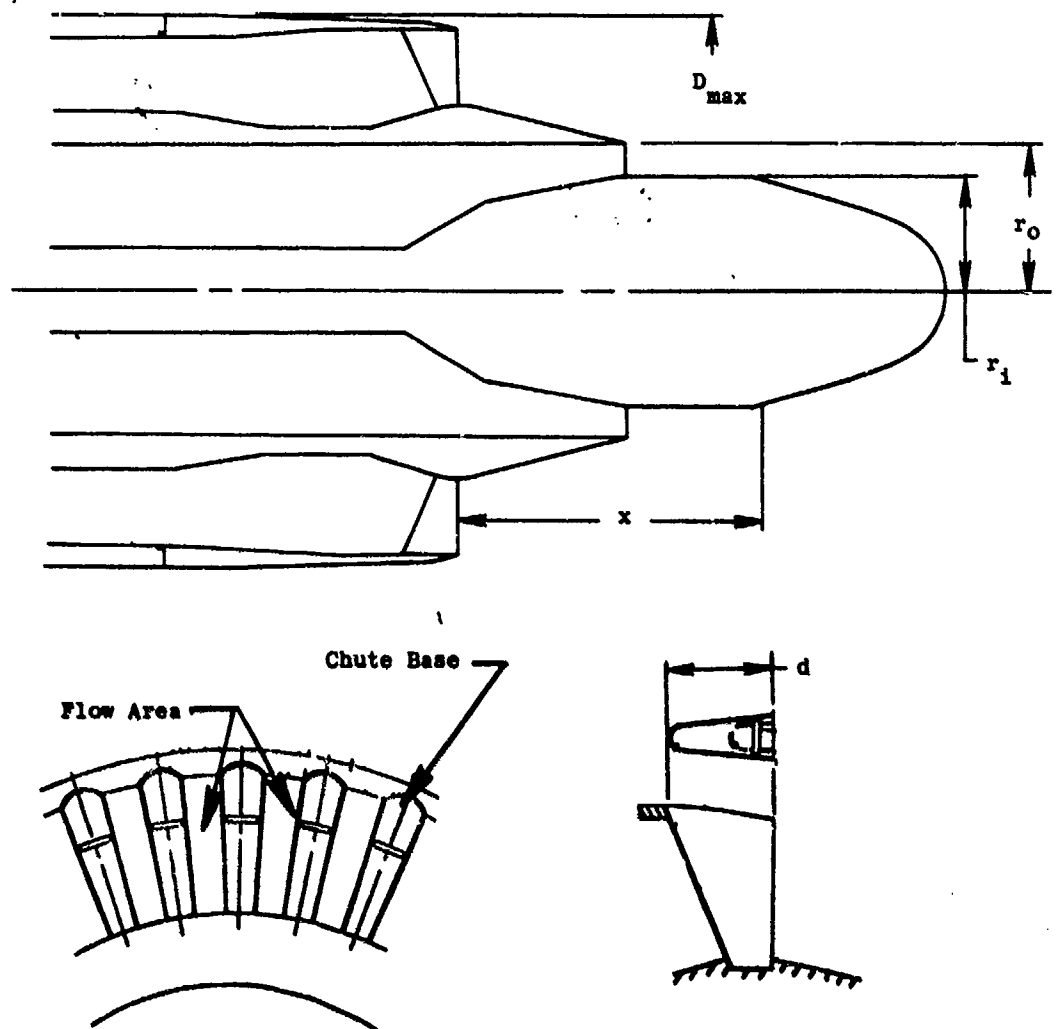
Basically the annular nozzles are representative of current concepts for supersonic transport exhaust systems. The two inner plug ( $15^\circ$  half angle) axial locations represent either an expandable flap and seal design for inner area control ( $X/D_{max} = 0.412$ ) or a similar system with a translating plug ( $X/D_{max} = 0.161$ ).

The inner plug radius ratios tested represent a variation in engine cycle, i.e., the variation on the amount of fan flow relative to core flow for given pressure/temperature conditions in each stream. The  $(R_r)_1 = 0$  configurations are representative of a turbojet or mixed-flow turbofan design.

The shallow-chute suppressor designs, with a suppressor area ratio ( $AR$ ) of 1.75, represent a potentially light, easily stowable system. Element number,  $N$ , was varied between 20 and 40, representing a practical range for this variable. Based on previous test experience, 20 represents a lower limit for reasonable suppression while 40 represents an upper limit for reasonable performance.

The deep-chute suppressor designs, with 36 elements, represent a system with good performance; i.e., the chute depth implies good ventilation for maintaining low base drag. The area ratio was varied between 1.5 and 2.5, again representing practical limits. In this case, 1.5 represents the lower limit for acoustic reasons and 2.5 an upper limit for mechanical design reasons.

In addition to the shallow-chute and deep-chute designs, a "spoke" suppressor was tested. The spoke suppressor has historically been an



- Suppressor Area Ratio =  $(A_o + A_{ch})/A_o$   
 where:  $A_o$  = Total Outer Flow Area  
 $A_{ch}$  = Total Chute Base Area
- Element Number = N, Total Number of Suppressor Elements
- Chute Ventilation Depth = d
- Inner Nozzle Radius Ratio =  $(R_r)_i = r_i/r_o$   
 ( $r_o$  was Constant for all Dual Flow Configurations)
- Inner Plug Axial Spacing Ratio =  $x/D_{max}$

Figure 4-4. Schematic of Annular Suppressed Nozzle Showing Key Geometric Variables.

Table 4-1. Nozzle Configuration Description.

Nozzle Configuration	Suppressor Type	N	AR	Inner Plug Description	X/D <sub>max.</sub>	(R <sub>r</sub> ) <sub>i</sub>
SC1	Shallow Chute	20	1.75	Baseline	0.412	0.78
SC2	Shallow Chute	30	1.75	Baseline	0.412	0.78
SC3	Shallow Chute	30	1.75	Reduced Area	0.412	0.89
SC4	Shallow Chute	30	1.75	Full	---	---
SC5	Shallow Chute	30	1.75	Forward	0.181	0.78
SC6	Shallow Chute	40	1.75	Baseline	0.412	0.78
DC1	Deep Chute	36	1.5	Baseline	0.412	0.78
DC2	Deep Chute	36	1.5	Full	---	---
DC3	Deep Chute	36	2.0	Baseline	0.412	0.78
DC4	Deep Chute	36	2.0	Reduced Area	0.412	0.89
DC5	Deep Chute	36	2.0	Full	---	---
DC6	Deep Chute	36	2.0	Forward	0.181	0.78
DC7	Deep Chute	36	2.5	Baseline	0.412	0.78
DC8	Deep Chute	36	2.5	Full	---	---
DC3 (Spoke)	Spoke	36	2.0	Baseline	0.412	0.78



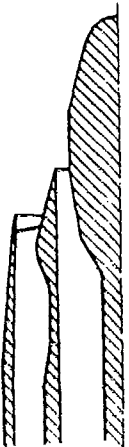

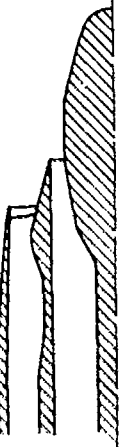



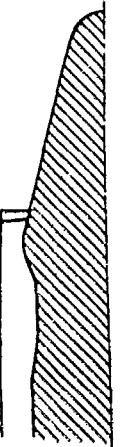

Model	Suppressor Type	Number of Elements	Area Ratio	Flowpath	Photograph	Model Details in Figure No. (Appendix F)
SC-1	Shallow Chute	20	1.75			F-1
SC-2	Shallow Chute	30	1.75			F-2
SC-3	Shallow Chute	30	1.75			F-3
SC-4	Shallow Chute	30	1.75			F-4

Figure 4-5. Summary of Annular Suppressor Models Tested.

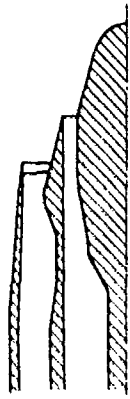

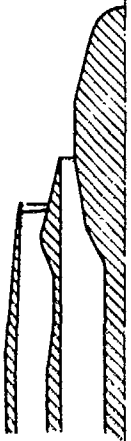

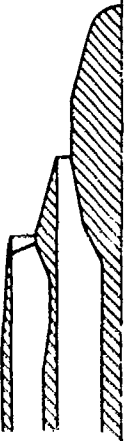

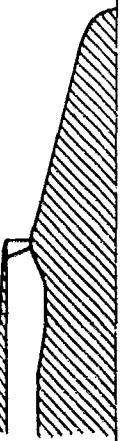

Model	Suppressor Type	Number of Elements	Area Ratio	Flowpath	Photograph	Model Details in Figure No. (Appendix F)
SC-5	Shallow Chute	30	1.75			P-5
SC-6	Shallow Chute	40	1.75			P-6
DC-1	Deep Chute	36	1.5			P-7
DC-2	Deep Chute	36	1.5			P-8

Figure 4-5. Summary of Annular Suppressor Models Tested (Continued).

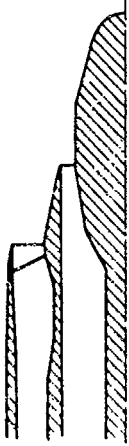

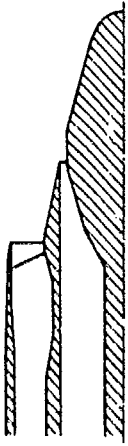

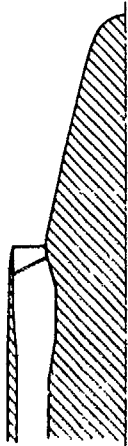

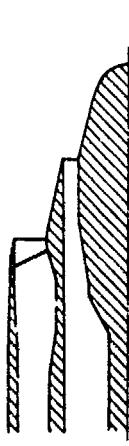

Model	Suppressor Type	Number of Elements	Area Ratio	Flowpath	Photograph	Model Details in Figure No. (Appendix F)
DC-3	Deep Chute	36	2.0			P-9
DC-4	Deep Chute	36	2.0			P-10
DC-5	Deep Chute	36	2.0			P-11
DC-6	Deep Chute	36	2.0			P-12

Figure 4-5. Summary of Annular Suppressor Models Tested (Continued).

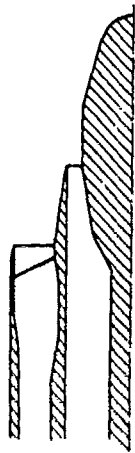

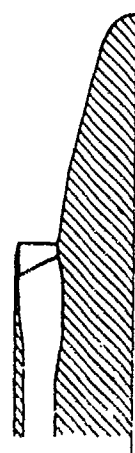

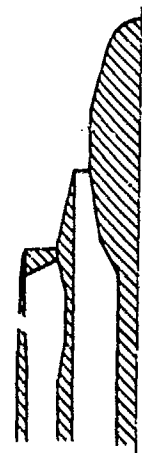

Model	Suppressor Type	Number of Elements	Area Ratio	Floppath	Photograph	Model Details in Figure No. (Appendix F)
DC-7	Deep Chute	36	2.5			F-13
DC-8	Deep Chute	36	2.5			F-14
DC-3 (Spoke)	Spoke	36	2.0			F-15

Figure 4-5. Summary of Annular Suppressor Models Tested (Concluded).

attractive concept due to its potential for low weight and ease of storage in the unsuppressed mode. The spoke configuration [model DC-3 (spoke)] was derived by filling the ventilation area of configuration DC-3 with inserts, as shown in Figure 4-5 and Figure F-15, Appendix F.

A schematic of a typical annular suppressed nozzle installed on the model support string is shown in Figure 4-6. Adapters connected the model flowpaths to the inner and outer air supply passages. The nozzle total pressure and temperature measurements were made with instrumentation rakes downstream of flow conditioners (choked plates and screens) to assure flat flow profiles. The outer diameter of the models was 8.0 inches, which required a reduction from the 8.5-inch diameter sting. This reduction was made via a nonmetric transition fairing. The metric break (the separation between the metric and nonmetric portion of the system) was provided by a 0.05-inch gap between the fairing and model shroud, as shown in Figure 4-6.

#### 4.3.2 104-Tube Model

The 104-tube suppressor model was the same as that tested in the JENOTS free jet facility as described in Reference 12. A photograph of the model is shown in Figure 4-7. The model outer diameter is 7.245 inches and the physical throat area is 12.56 in.<sup>2</sup>. The suppressor area ratio is 2.8. Key geometric parameters are shown in Figure 4-8.

#### 4.3.3 Eight-Lobe Suppressor Model

The eight-lobe suppressor was also the same hardware tested in the JENOTS free jet under Task 4. A photograph of the model installed in the 8-by 6-foot wind tunnel is shown in Figure 4-9. The model outer diameter is 6.625 inches and the throat area is 13.121 in.<sup>2</sup>. The model simulated a full-scale turbojet exhaust system which would utilize secondary air from the inlet to purge and cool the cavity between the nacelle and engine. The cooling air would exit at the trailing edge of the lobes. This secondary air gap can be seen in the closeup of the nozzle exit, Figure 4-9. For the wind tunnel test, the secondary airflow was not simulated.

#### 4.3.4 Reference Nozzle

The SuperSonic Tunnel Association (STA) nozzle was used as a reference and calibration device for the wind tunnel test series. This nozzle, shown in Figure 4-10, is basically a modified ASME nozzle with a circular-arc boattail. The use of the STA nozzle as a reference is described in detail in Section 4.5.1.

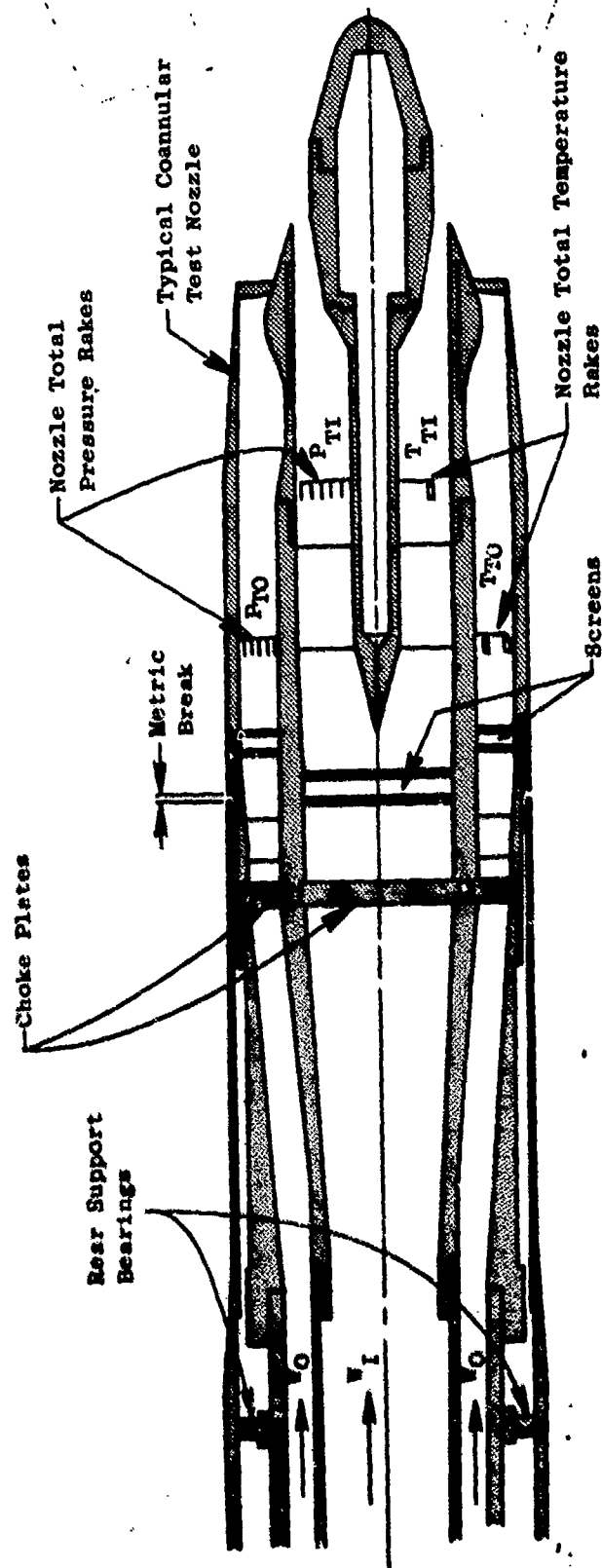


Figure 4-6. Schematic of Dual Flow Suppressor Installation.

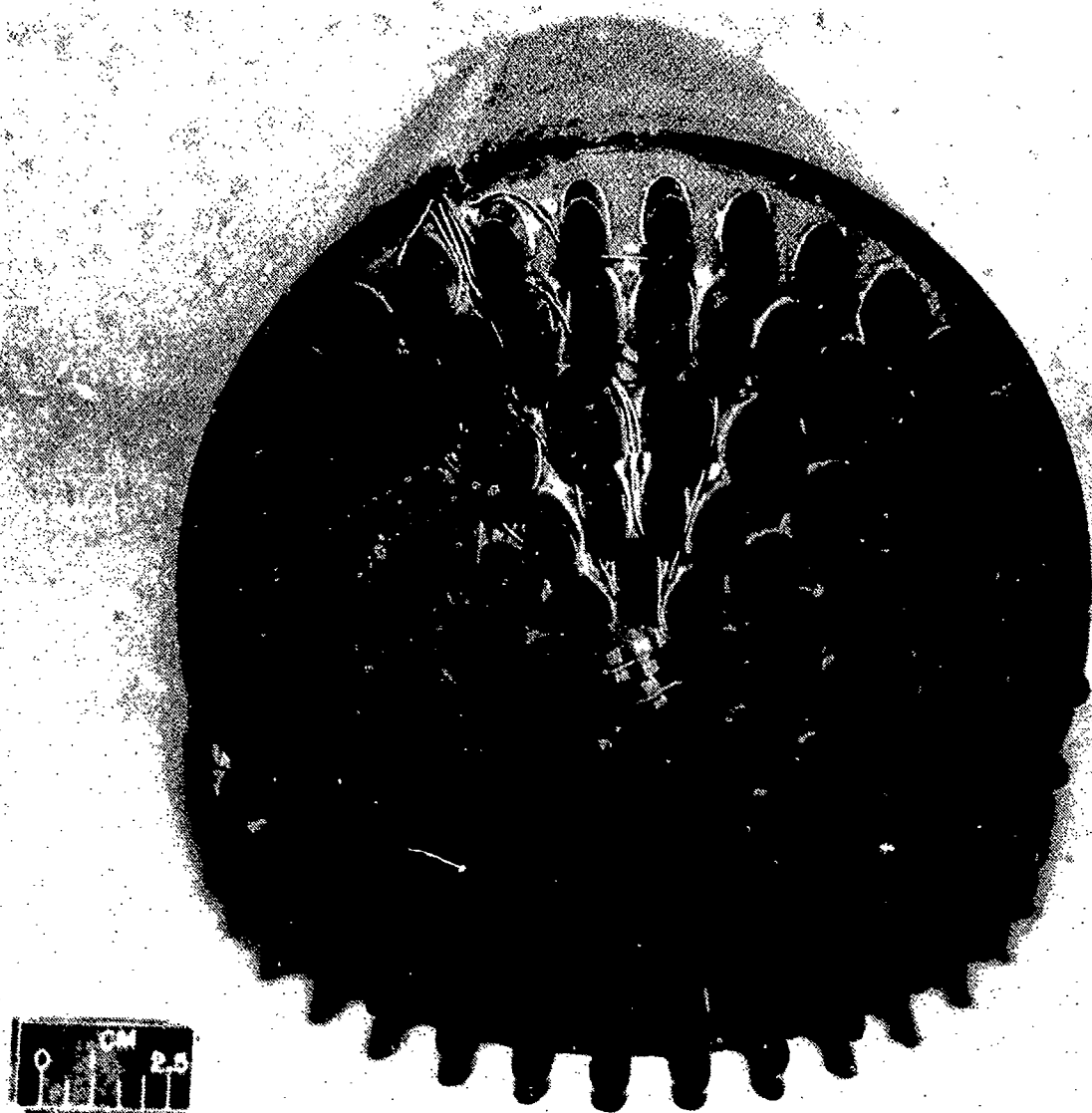
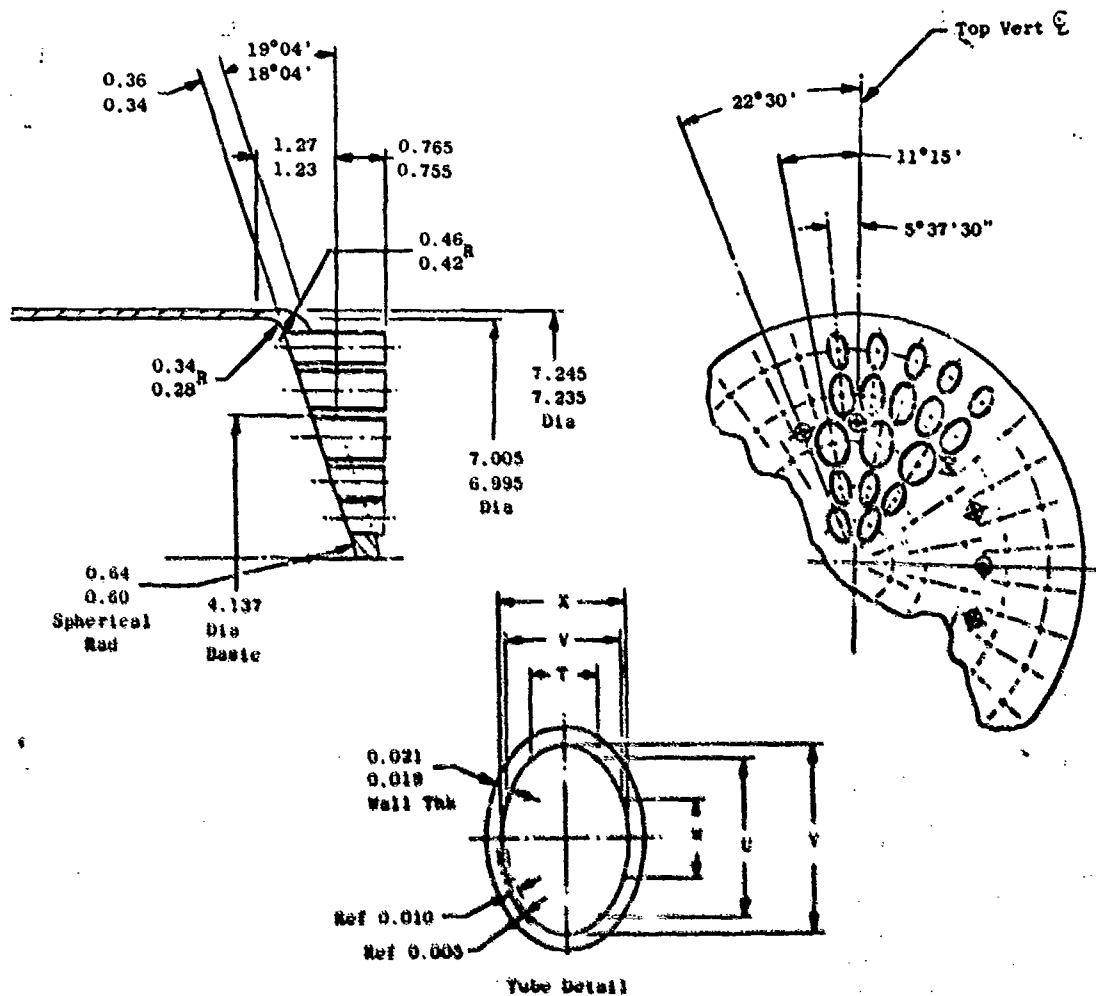


Figure 4-7. 104 Tube Nozzle.



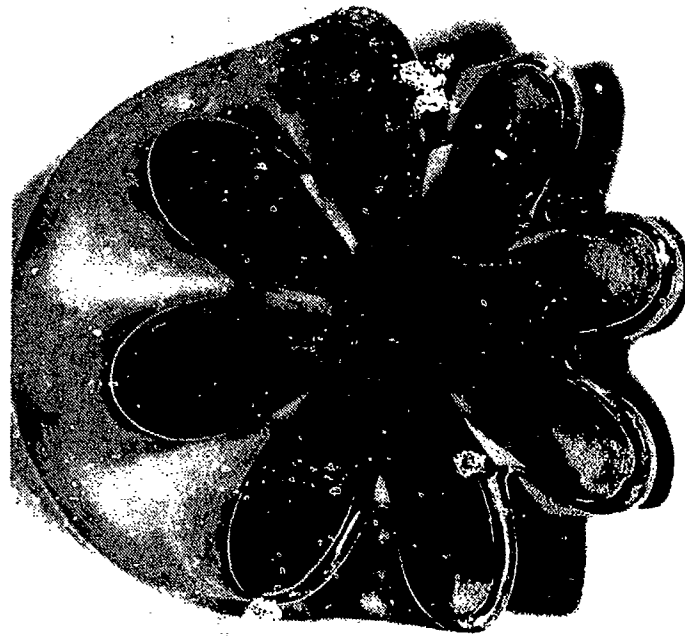
Tube	Y Dia	U Dia	V Dia	W Dia	X Dia	Y Dia
A	0.112	0.420	0.227	0.227	0.360	0.465
B	0.130	0.444	0.273	0.273	0.317	0.535
C	0.149	0.558	0.365	0.365	0.468	0.589
D	0.112	0.420	0.227	0.227	0.360	0.465
E	0.112	0.420	0.227	0.227	0.360	0.465

Figure 4-8. 104 Tube Nozzle Geometric Details...



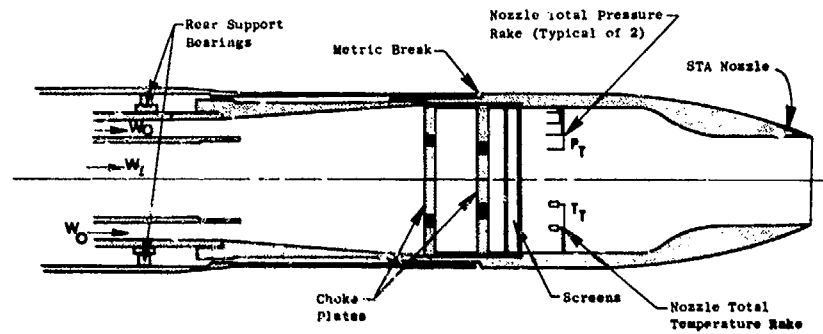


● 8-Lobe Nozzle Installation

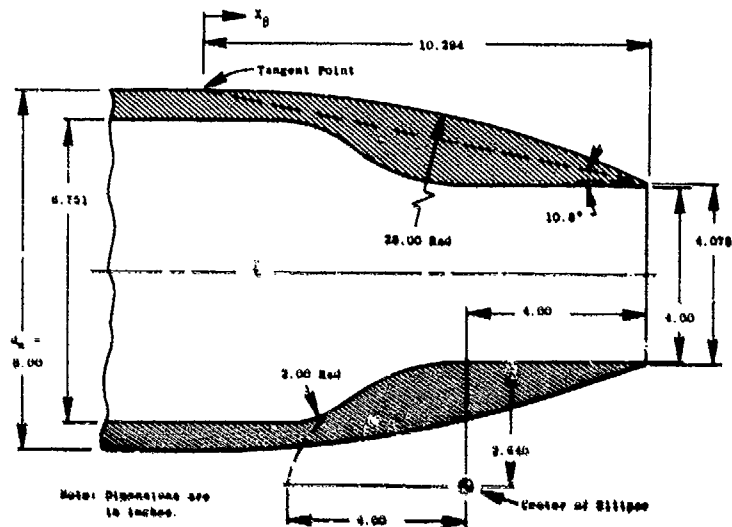


● Close-Up of 8-Lobe Nozzle Exit

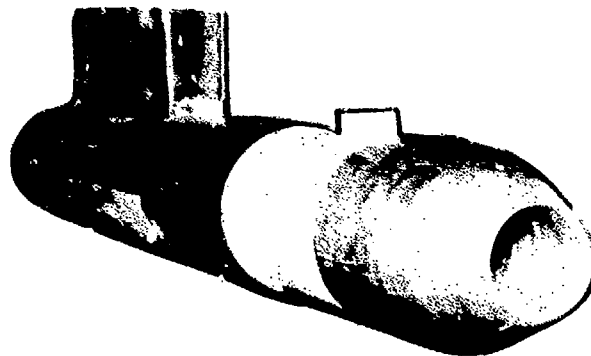
Figure 4-9. 8-Lobe Nozzle.



(a) Test Nozzle Internal Geometry and Instrumentation



(b) Definition of Internal and External Flowpath



(c) Photograph of Nozzle

Figure 4-10. Supersonic Tunnel Association (STA) nozzle.

#### 4.4 DATA REDUCTION PROCEDURES

General descriptions of the methods used to determine model flow rates and nozzle thrust are contained in the following subsections. A more extensive detailing of the data reduction procedures is included in Appendix F.

##### 4.4.1 Flow Rates

The mass flow through the outer nozzle was measured with a 1.248-inch throat diameter choked venturi meter, located as shown in Figure 4-2. The flow rate was calculated using the measured gas total temperature and pressure,  $TTV_o$  and  $PTV_o$ , respectively, and the equation:

$$W_o = C_{DV_o} \frac{K_{V_o} P_{TV_o} A_{V_o}}{\sqrt{TTV_o}} \quad (1)$$

where  $C_{DV_o}$  is the venturi flow coefficient. The critical flow factor,  $K_{V_o}$ , was calculated as a function of total pressure and temperature to account for real gas effects as given in Reference 36.

The mass flow through the inner nozzle was measured with either of two choked venturi meters located as shown in Figure 4-2. The flow for high inner flow rates was measured using the 1.1398-inch-throat-diameter venturi. The flow for the low inner flow rate testing was measured with the 0.3985-inch-throat-diameter venturi. For both meters, the flow rate was computed from a calibration of the meters made by the manufacturer utilizing the measured venturi pressure and total temperature.

##### 4.4.2 Flow Coefficients

The flow coefficient of a nozzle is defined as the ratio of actual mass flow rate through the nozzle to the ideal isentropic flow rate at the temperature and pressure of the flow:

$$C_D = \frac{\text{measured flow}}{\text{ideal flow}} \quad (2)$$

The ideal weight flow for the outer nozzle was calculated from the relation:

$$W_{I_o} = \frac{K_o A_o P_{T_o}}{\sqrt{TT_o}} \frac{A^*}{A_o} \quad (3)$$

where  $A_0$ ,  $P_{T0}$ , and  $T_{T0}$  are the outer nozzle physical throat area, total pressure, and total temperature, respectively. The critical flow factor,  $K_0$ , was corrected for real gas effects;  $A^*/A_0$  is the ratio of the flow area at sonic conditions to the outer nozzle throat area ( $A^*/A_0 = 1.0$  for values of nozzle pressure ratios greater than 1.8929).

The inner nozzle ideal weight flow was calculated in a similar fashion using the inner nozzle throat area and the inner flow pressure and temperature. For the low inner flow testing, the inner nozzle total pressures required to supply the low flow rates were generally lower than ambient pressure due to the pumping effect of the outer flow. In these cases, the ideal flow rate and flow coefficients are meaningless and were not calculated.

#### 4.4.3 Thrust Measurements

The thrust of the exhaust nozzles is defined as the axial exit momentum of the exhaust flow, plus the excess of exit pressure over ambient pressure times the exit area normal to the axis, minus the axial drag on the nozzle external surface, i.e.,

$$F = \int_{A_{\text{exit}}} d(wv)_{\text{axial}} + \int_{A_{\text{exit}}} (P - P_a) dA - D_{\text{external}} \quad (4)$$

The external drag consists of both the pressure drag on the boattail surface and the and suppressor element bases, and the axial component of skin friction. Figure 4-11 shows a control volume applied to the test nozzles. The momentum equation in the axial direction for this control volume is:

$$F = F_{LC} + F_{AS} + A_1(P_1 - P_a) + A_2(P_2 - P_a) + A_3(P_3 - P_a) + A_4(P_4 - P_a) \quad (5)$$

where  $F_{LC}$  is the axial force applied to the load cell and  $F_{AS}$  is the axial force applied at the boundary of the control volume by the air supply tubes. The static pressures  $P_1$ ,  $P_2$ ,  $P_3$ , and  $P_4$  were measured with static taps at each of the four areas (Figure 4-11). The force measuring system was calibrated by applying known forces and correlating this force against the load cell output, as previously described in Section 4.2.

An adjustment was made to the measured thrust to account for external friction drag on the cylindrical section upstream of the nozzle shroud. The axial force on this 8.0-inch diameter section, which extended from the metric-break to the attach-point of the nozzle shrouds, was not included in the nozzle net thrust. The friction drag was calculated by the equation:

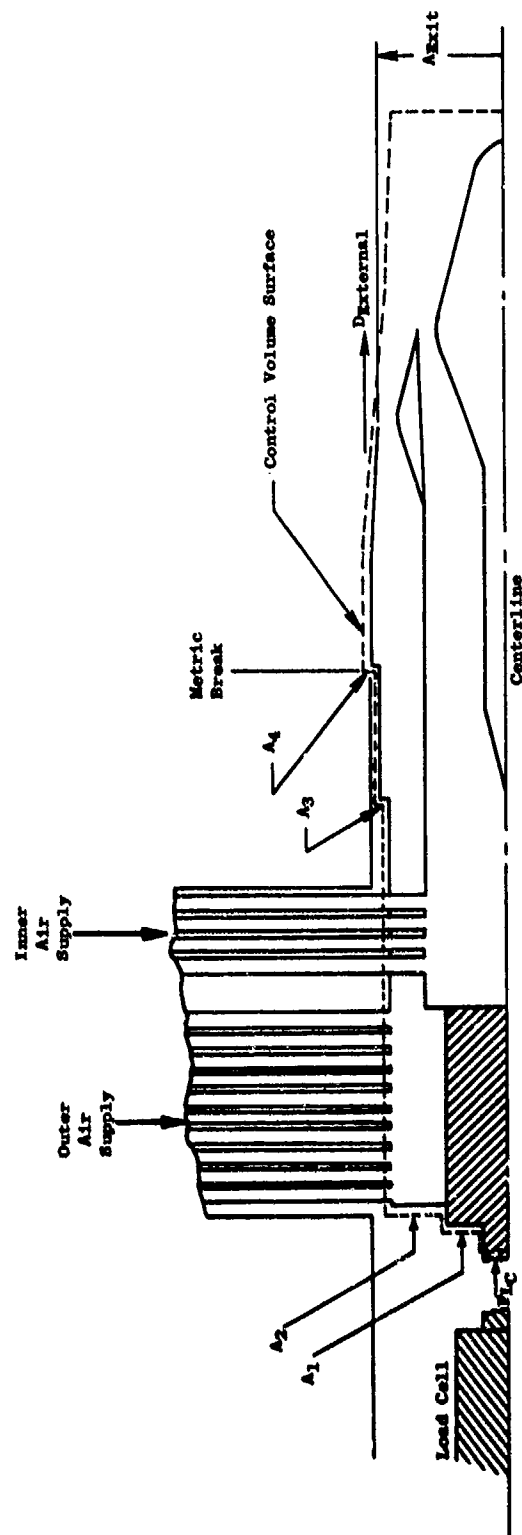


Figure 4-11. Control Volume Applied to Model Test Setup.

$$D_f = \frac{\gamma}{2} P_a M_a^2 A_c C_f \quad (6)$$

where  $A_c$  is the wetted surface area of the cylindrical section and  $C_f$  is the skin friction drag coefficient.

The thrust of the nozzles for this test was therefore given by:

$$F = F_{LC} + F_{AS} + A_1(P_1 - P_a) + A_2(P_2 - P_a) + A_3(P_3 - P_a) + A_4(P_4 - P_a) + D_f. \quad (7)$$

#### 4.4.4 Thrust Coefficient

The thrust coefficient is the ratio of the measured nozzle thrust to the ideal thrust of the inner duct flow plus the ideal thrust of the outer duct flow. The ideal thrust for each stream equals the actual mass flow rate times the ideal velocity, i.e., the velocity of the stream expanded isentropically from the total pressure to the ambient pressure. The equation for the thrust coefficient is thus:

$$C_T = \frac{F}{W_o V_{I_o} + W_i V_{I_i}} \quad (8)$$

The ideal thrust for the nozzles was calculated using the dimensionless ideal-thrust function which is a function of only the nozzle pressure ratio.

During much of the low inner flow rate testing, the total pressure of the inner nozzle flow was lower than ambient. In these cases, the ideal thrust of the inner nozzle was set equal to zero.

For the static tests of the STA model, a dimensionless stream-thrust parameter was also calculated as:

$$f_g = \frac{F + P_a A_g}{P T A_g} \quad (9)$$

where  $A_g$  is the STA nozzle exit area.

#### 4.4.5 Pressure Data

Total pressures in the models and static pressures on the model surfaces were measured with scanning valve/transducer arrangements. The individual static pressure readings were also nondimensionalized by the ambient pressure. Axial pressure forces on the aft-facing portions of the shroud, outer

plug, inner plug, and suppressor element bases were calculated by multiplying the difference between the static pressure at each tap and ambient by an incremental projected area represented by the particular tap and summing the products, i.e.,

$$F_p = \Sigma(P-P_a)\Delta A \quad (10)$$

These pressure forces were also nondimensionalized by the total ideal thrust of the nozzle:

$$\frac{F_p}{W_i V_{I_i} + W_o V_{I_o}} \quad (11)$$

Specific tap locations are presented in Appendix F.

#### 4.5 TEST RESULTS AND DISCUSSION

##### 4.5.1 Data Quality

Prior to testing the plug nozzle models in the 8- by 6-foot tunnel, a Supersonic Tunnel Association (STA) model was tested as a means of investigating the force and weight-flow measurement accuracy of the test equipment. The STA model assembly is shown in Figure 4-10. The model has a 4.0-inch diameter throat and an 8.0-inch maximum outside diameter, corresponding to the 8.0-inch maximum outside diameter of the annular nozzle models. Air could be supplied to the STA model using either the outer or inner flowpath as shown in the schematic of Figure 4-10. The tests were conducted with air supplied through either the 1.248-inch-diameter meter for the outer nozzle air supply or with air supplied by the larger of the two inner flowmeters, which was 1.1398 inch in diameter. The smaller of the two inner flowmeters was not tested with the STA model because flow sufficient to choke the STA model could not be supplied due to pressure limitations. This did not compromise the the facility checkout because the small meter was used only to meter flow for the low inner flow test points, where the flow rates ranged from one to six percent of the outer flow. Small errors in this measurement could not affect overall results.

The criteria against which the STA measurements were compared to determine the facility thrust and flow measurement accuracies were calculated values of STA thrust coefficient, flow coefficient, and dimensionless stream-thrust parameter for the static tests and previous measured values for wind-on testing. The calculated static values are derived from semi-empirical methods of calculating standard ASME long radius nozzle performance, as described in Reference 37. These ASME equations are modified to include the effect of a small difference in length of the internal flowpaths between the ASME and STA nozzles. The resulting equations, for nozzle pressure ratios equal to or greater than 1.89, are as follows:

$$C_D = 1 - 0.241 RN^{-0.2}$$

$$C_V = 1 - 0.143 RN^{-0.2}$$

$$F_g = G(1 + 1.4 C_D C_V) (0.52828)$$

where

$$G = 1.00012 + 9,9112 \times 10^{-6} \times P_T$$

and  $C_V$  is the peak thrust coefficient.

These equations are based on a large data base and provide an accurate method for calculating the static STA nozzle performance parameters. For the wind-on tests, the data are compared to previous results on the same STA model in the NASA Lewis 8- by 6-foot tunnel using different flowmetering and force measuring hardware. These previous tests are reported in Reference 38.

Comparisons of the measured static thrust and flow coefficients and stream-thrust parameter with the calculated values are shown in Figures 4-12 and 4-13 for the 1.248-inch and 1.1398-inch-diameter meters, respectively. Figure 4-14 compares the measured thrust coefficient to previous test results at Mach numbers of 0.36, 0.40, and 0.45. Agreement between the measured values and the calculated or previously determined data is good, as is the repeatability of the data (five to eight static points and two wind-on points were taken at most nozzle pressure ratios). Repeatability of the wind-on data was better than the static data, possibly due to the increased tunnel vibration which would reduce hysteresis in the support bearings.

The number of repeat points taken at static conditions allowed a statistical evaluation of the data. Standard deviations and the bias of the mean value of the data from the "known" (or calculated) value were calculated by the following equations:

$$\text{Standard Deviation} = \sqrt{\frac{\sum (X_i - \bar{X})^2}{n - 1}} \quad (12)$$

$$\text{Bias} = \bar{X} - m$$

where

$X_i$  = individual measured value of the parameter (e.g., thrust coefficient or flow coefficient)

$\bar{X}$  = mean of measured values of the parameter

$m$  = known value of parameter

$n$  = number of samples taken of the given parameter



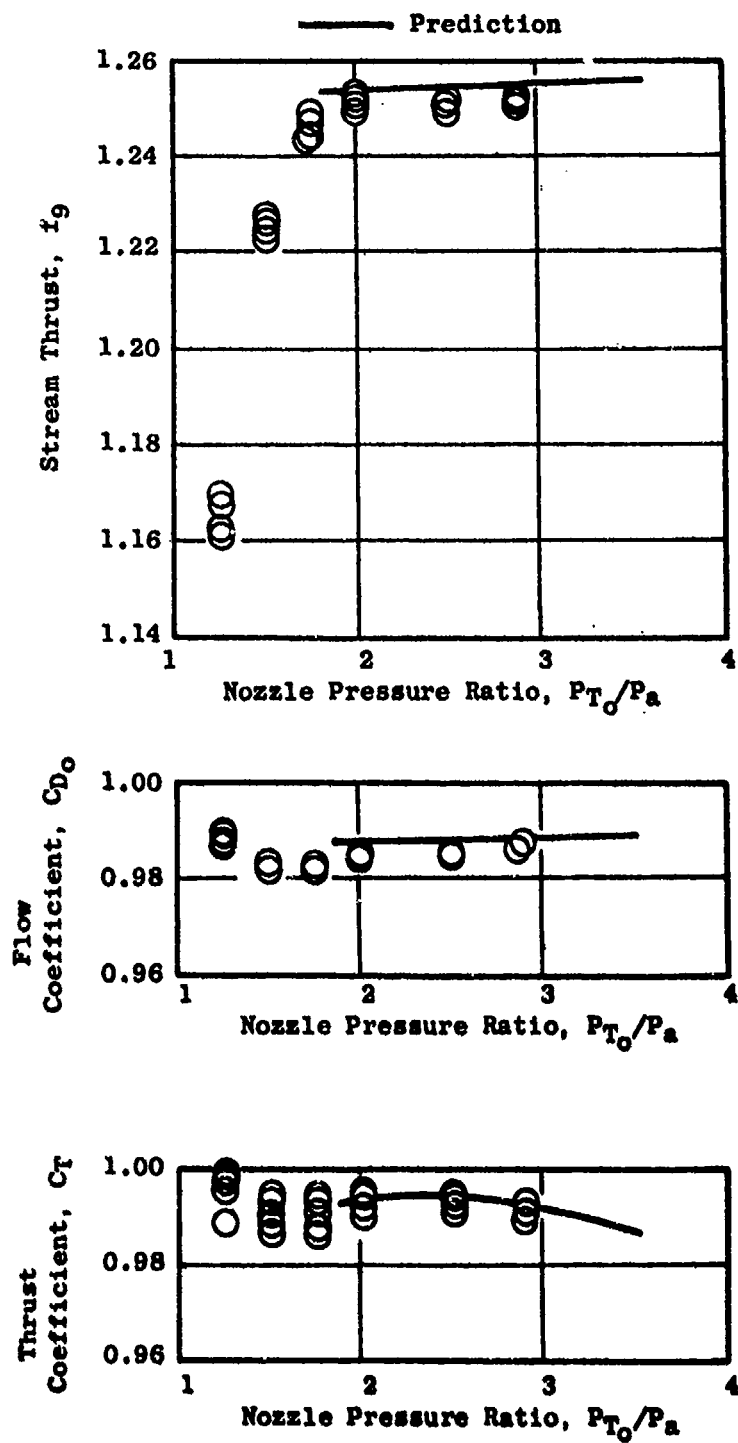


Figure 4-12. STA Static Performance with the 1.248-in.-Diameter Outer Flowmeter.

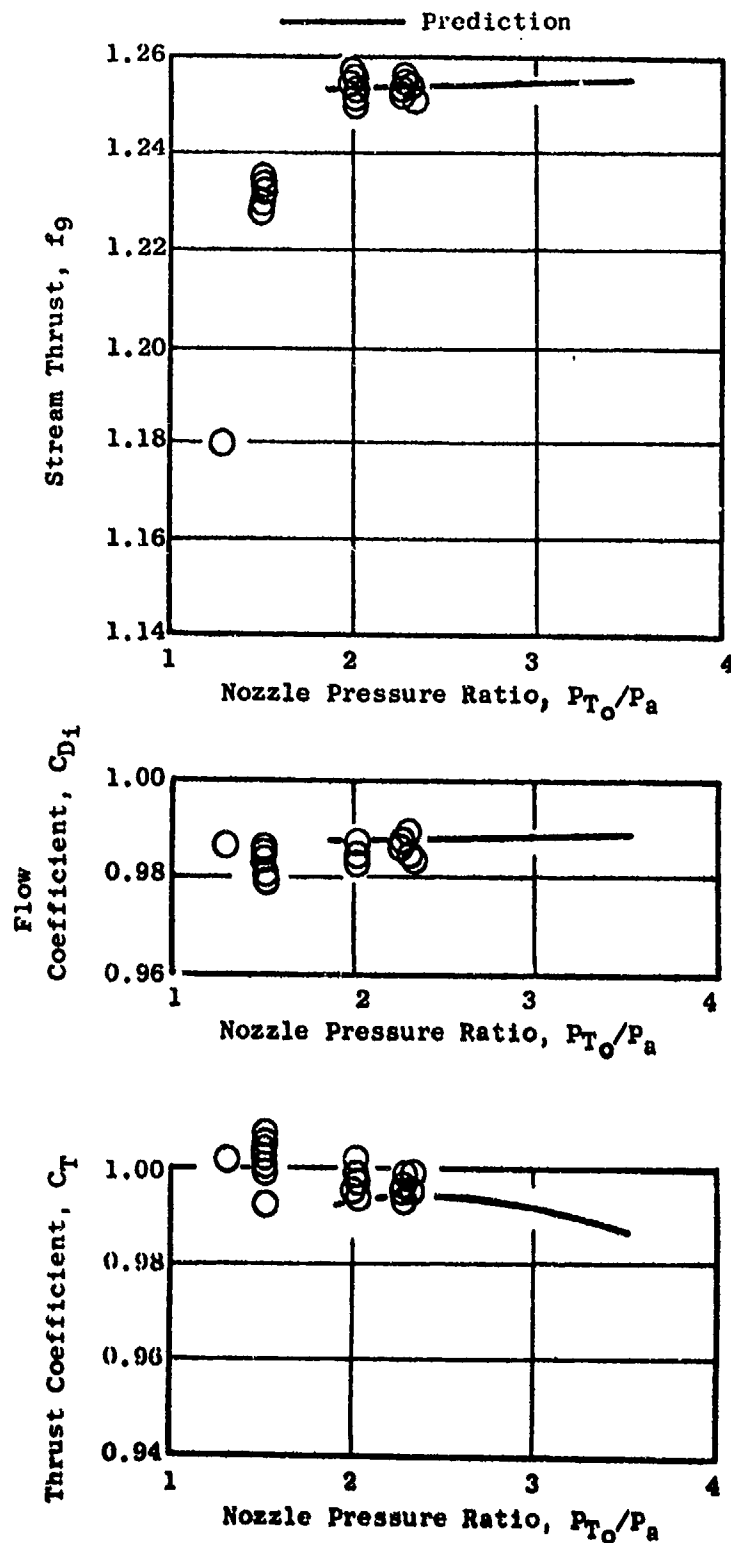


Figure 4-13. STA Static Performance with the 1.1398-in.-Diameter Inner Flow-meter.

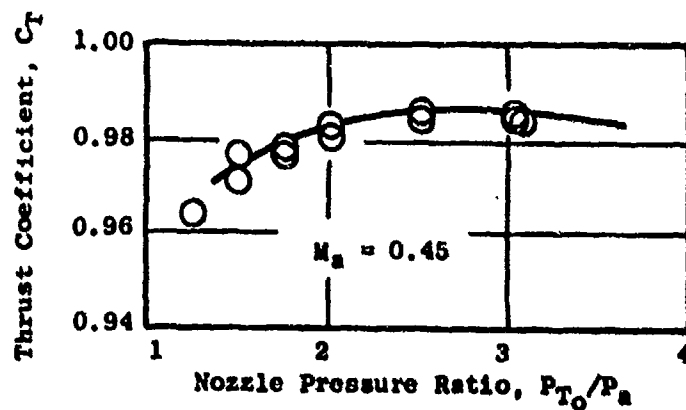
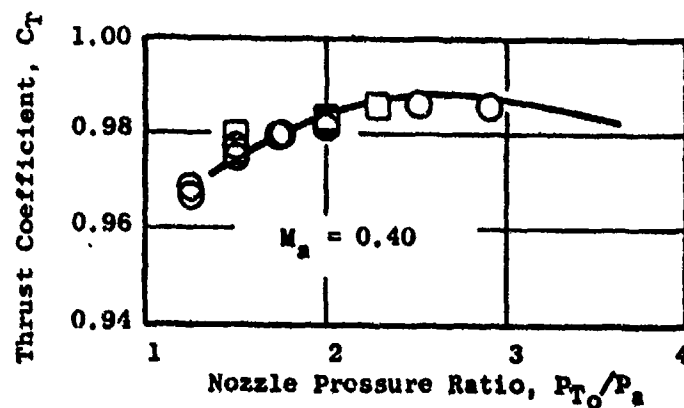
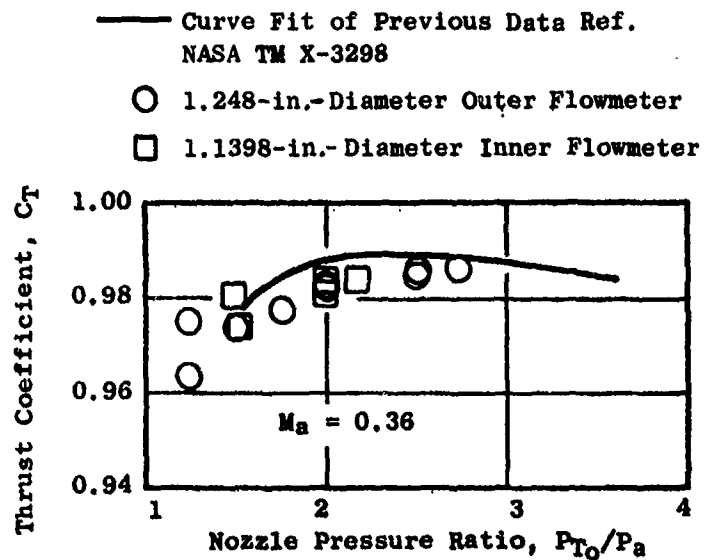


Figure 4-14. Wind-On STA Nozzle Thrust Coefficients.

Standard deviation calculations were made at each pressure ratio for which repeat points were taken. Bias calculations were made at each pressure ratio above 1.89 for which repeat points were taken, as the calculation procedure for the known values does not apply below this pressure ratio. The procedure used for taking repeat points was to set each data point once in the order of increasing nozzle pressure ratio and then repeat each point going down in pressure ratio, until a zero flow condition was reached; then the process was repeated. In some instances either wind-on test points or tests utilizing the other flowmeter were conducted between repeating cycles.

The results of the statistical analysis are shown in Figures 4-15 and 4-16 for the thrust coefficient and flow coefficient, respectively. The thrust coefficient deviation and bias were dependent on the magnitude of the nozzle thrust and are, therefore, plotted as a function of balance load in Figure 4-15. The flow coefficient parameters are shown as a function of the flowmeter total pressure over the range for which STA data were taken. The upper limit to the STA model airflow and force balance loading was the maximum supply pressure at the venturis, approximately 400 to 420 psia. These results indicate an accuracy and repeatability of greater than  $\pm 0.5\%$  which are well within acceptable limits for the test program. Additional information can be found in Reference 38.

#### 4.5.2 Annular Nozzle Thrust Coefficients

A total of 15 suppressed annular nozzle configurations was tested. All configurations were tested at tunnel Mach numbers of 0, 0.36, and 0.45. The outer nozzle pressure ratio was varied from 1.5 to 3.3. Two separate regimes of inner nozzle flow conditions were investigated; a "low" or bleed flow regime where the inner nozzle flow rate was varied from zero to six percent of the outer nozzle flow, and a "high" flow regime in which the inner stream pressure ratio was varied from 1.5 to 3.5.

Performance in terms of nozzle thrust coefficient,  $C_{fg}$ , is summarized for the 15 annular suppressed configurations in Table 4-II. The thrust coefficients presented in the table were selected at a nominal inner and outer nozzle pressure ratio,  $P_{T1}/P_a$  and  $P_{T0}/P_a$ , of 2.5. Both static ( $M_a = 0$ ) and Mach 0.36 performance are listed. Table 4-2 illustrates the "spread" in performance obtained between the various configurations and also illustrates differences between static and wind-on performance. The detailed performance of each nozzle as affected by inner and outer nozzle pressure ratios and external flow conditions is included in Appendix F. Also contained in Appendix F are the summary off-line data printouts containing all key measured parameters.

#### 4.5.3 Effect of Suppressor Element Number

The effect of the number of suppressor elements on performance, for a given suppressor area ratio, can be investigated by comparing model SC-1, SC-2, and SC-6 test results. Thrust coefficients are presented in Figure 4-17 as a function of suppressor element number and inner nozzle pressure

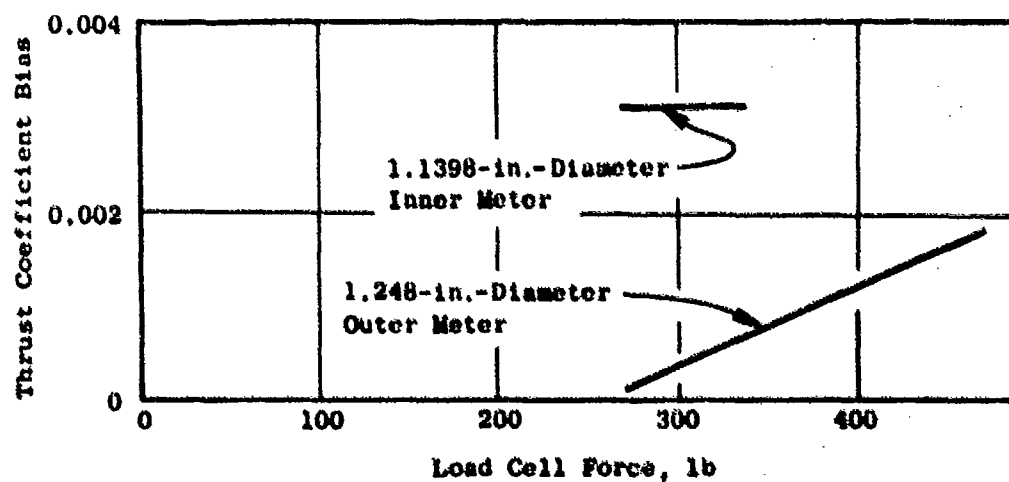
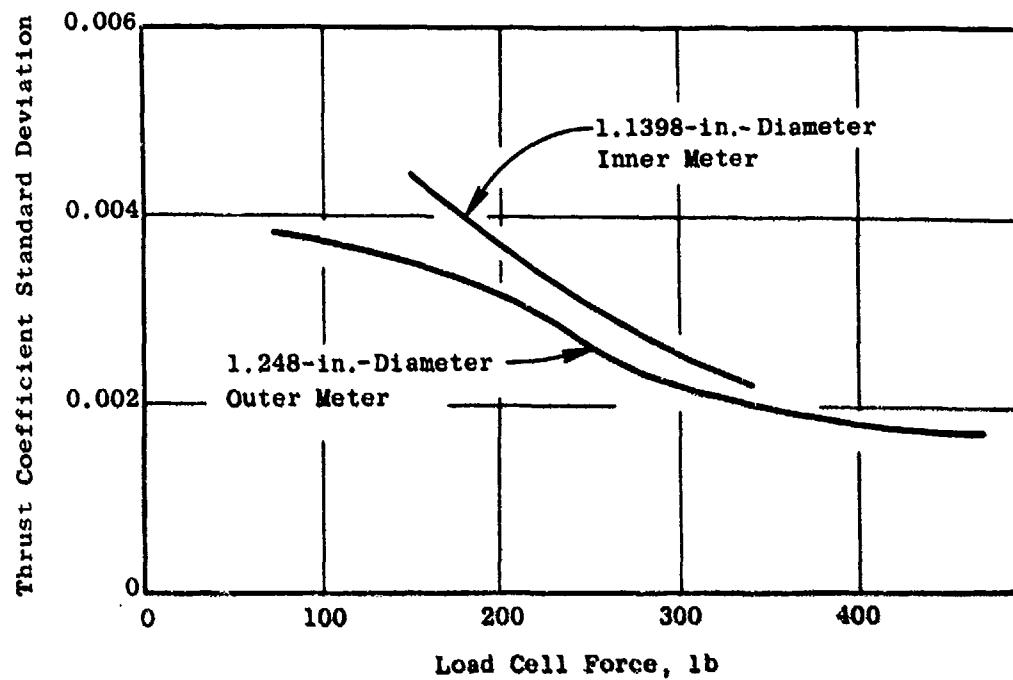


Figure 4-15. STA Nozzle Bias and Standard Deviation on Static Thrust Coefficient.

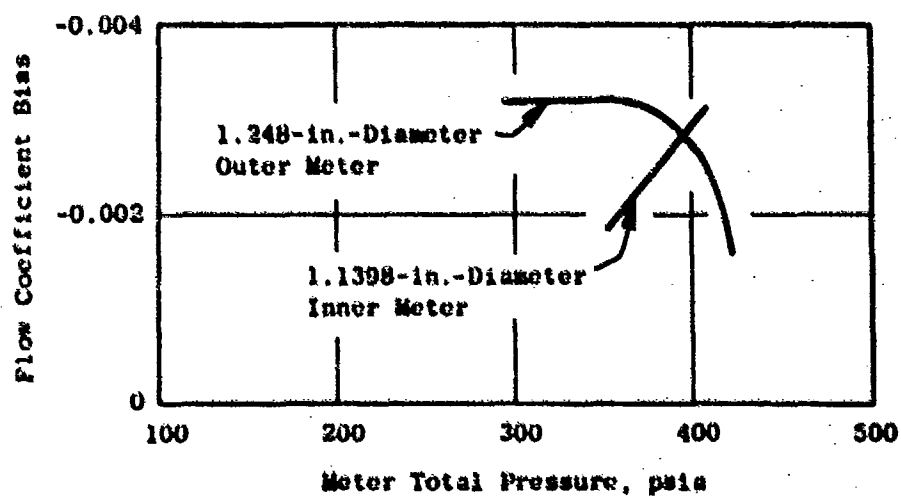
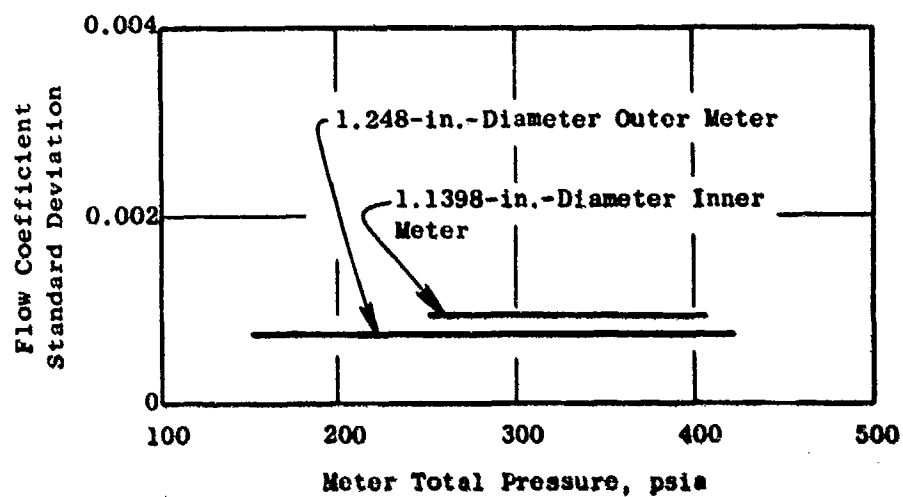


Figure 4-16. STA Nozzle Bias and Standard Deviation on Flow Coefficient.

Table 4-2. Annular Nozzle Performance Summary.

Area in.²	No. Elements	Description	Inner Plug Geometry			
			Full ( $R_I$ ) <sub>i</sub> = 0	Baseline ( $R_I$ ) <sub>c</sub> = 0.78	Reduced Area ( $R_I$ ) = 0.89	Forward Plug
1.75	20	Shallow Chutes		0.929*(0.955)		
"	30	"	0.895(0.927)	0.914(0.934)	0.907(0.934)	0.918(0.941)
"	40	"		0.906(0.923)		
1.5	36	Deep Chutes	0.895(0.920)	0.920(0.933)		
2.0	"	"	0.877(0.910)	0.910(0.941)	0.894(0.936)	0.907(0.944)
2.0	"	Spokes		0.863(0.884)		
2.5	"	Deep Chutes	0.890*0.957	0.913(0.958)		

\*  $C_{f8}$  Overall at  $P_{T0}/P_a - P_{T1}/P_a = 2.5$ ,  $M_a = 0.36(0)$

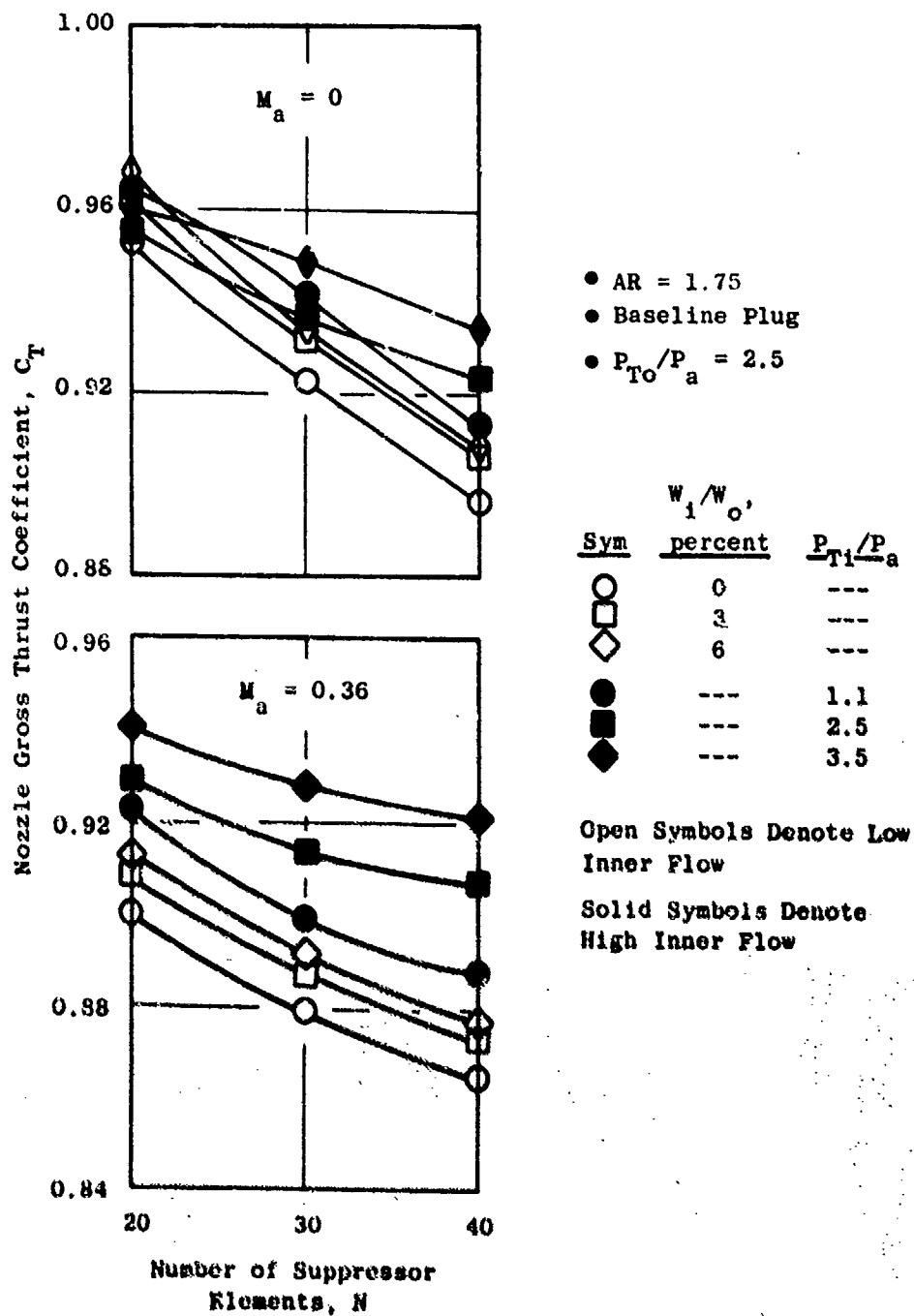


Figure 4-17. Effect of Suppressor Element Number and Inner Flow on Nozzle Gross Thrust Coefficients of Shallow-Chute Nozzles.



ratio for an outer pressure ratio of 2.5 at static and Mach 0.36 conditions. In all cases, performance decreases as element number increases. For an inner nozzle pressure ratio of 2.5, the thrust coefficient decreased from 0.929 for 20 elements to 0.907 for 40 elements. This decrease in nozzle performance with element number reflects the increase in element base drag as illustrated in Figure 4-18 where both performance and element base drag, in terms of ideal thrust, are shown as a function of element number and external Mach number for an inner and outer nozzle pressure ratio of 2.5.

Figure 4-19 presents trends in performance as a function of element number and outer pressure ratio for an inner pressure ratio of 2.5. Note that performance sensitivity to element number increases as outer pressure ratio increases. In summary, performance is adversely affected by an increase in the number of elements for a given suppressor area ratio at outer nozzle pressure ratios greater than 1.5.

#### 4.5.4 Effect of Suppressor Area Ratio

The effect of suppressor area ratio on performance can be investigated by comparing test results for models DC-1, DC-3, and DC-7. Thrust coefficients as a function of suppressor area ratio and inner nozzle flow condition for a constant outer nozzle pressure ratio of 2.5 are presented in Figure 4-20. At static conditions, performance increases as area ratio increases for all inner flow conditions. At Mach 0.36, performance first decreases, then increases with area ratio for "low" flow conditions and remains relatively constant for "high" inner flow conditions. These trends appear to contradict element base pressure drag trends shown in Figure 4-21. Figure 4-21 illustrates the loss in gross thrust due to element base pressures as a function of suppressor area ratio for inner and outer nozzle pressure ratio of 2.5. Statically, the base drag loss does not vary with area ratio, while at Mach 0.36 and 0.45, drag increases with area ratio. The reason for this apparent anomaly is that, in conjunction with increasing area ratio, the plug half angle immediately downstream of the suppression was decreased. The angle was  $15.8^\circ$  for the area ratio 1.5 suppressor,  $11.7^\circ$  for the area ratio 2.0, suppressor, and only  $7.4^\circ$  for the area ratio 2.5 suppressor (see Appendix F). In addition, as area ratio was increased, the external shroud boattail angle and projected area were decreased. As a result, shroud and plug drag decreases tended to compensate for the increased element drag at Mach 0.36 and 0.45 as area ratio was increased. Based on previous experience with increasing area ratio, Reference 3, it could be expected that if the plug angle downstream of the suppressor were held constant as area ratio was increased, the performance trend at Mach 0.36 and 0.45 would follow the same trend as the element base pressure losses, i.e., lower performance with higher area ratios.

#### 4.5.5 Effect of Inner Nozzle Area (Inner Radius Ratio)

Trends in performance as the inner nozzle area is varied can be investigated by comparing model SC-2, SC-3, and SC-4 (AR 1.75, 30 shallow

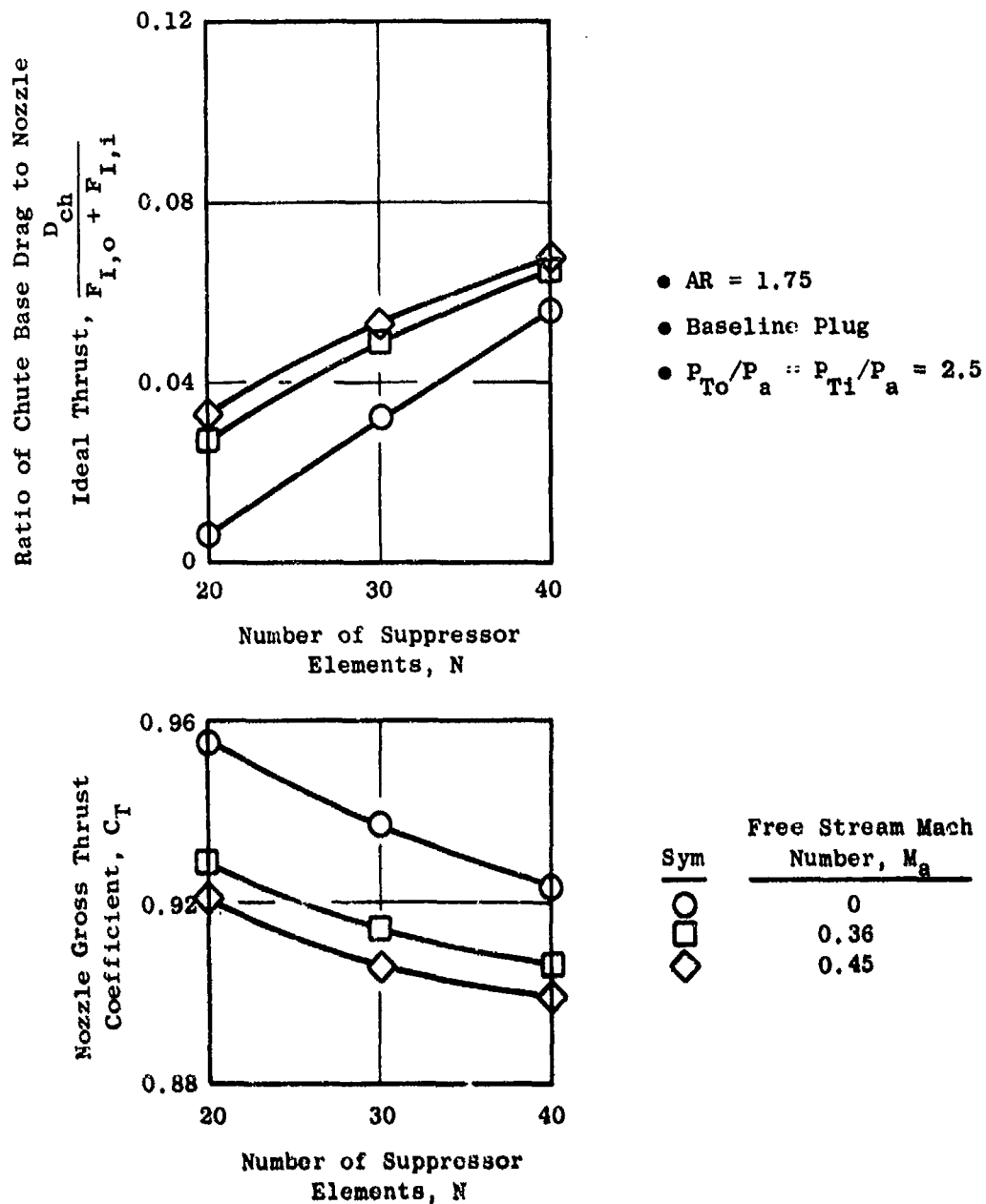


Figure 4-18. Effect of Suppressor Element Number and Free-Stream Mach Number on Nozzle Performance of Shallow-Chute Nozzles.

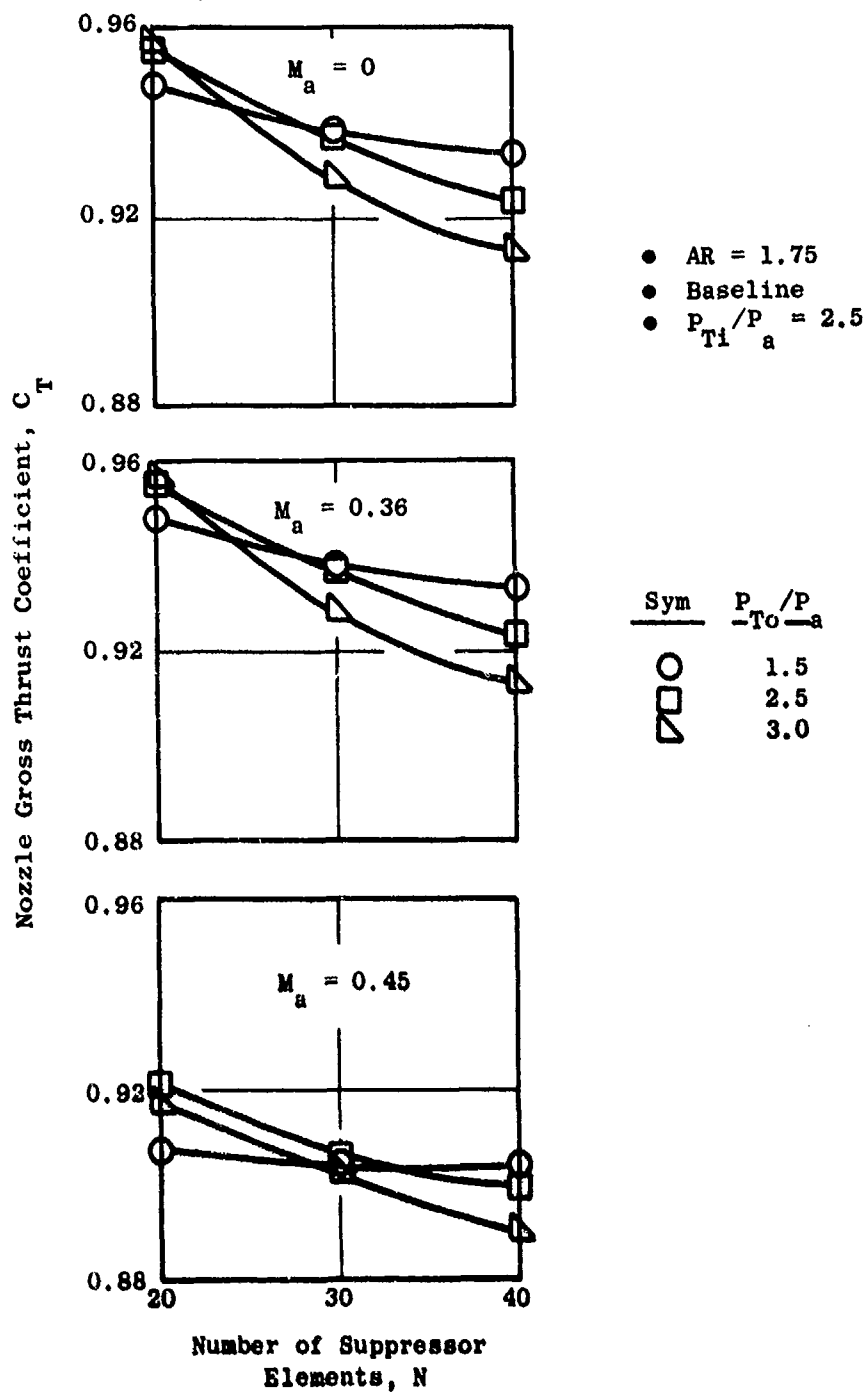


Figure 4-19. Effect of Suppressor Element Number and Outer Flow on Nozzle Gross Thrust Coefficients of Shallow-Chute Nozzles.

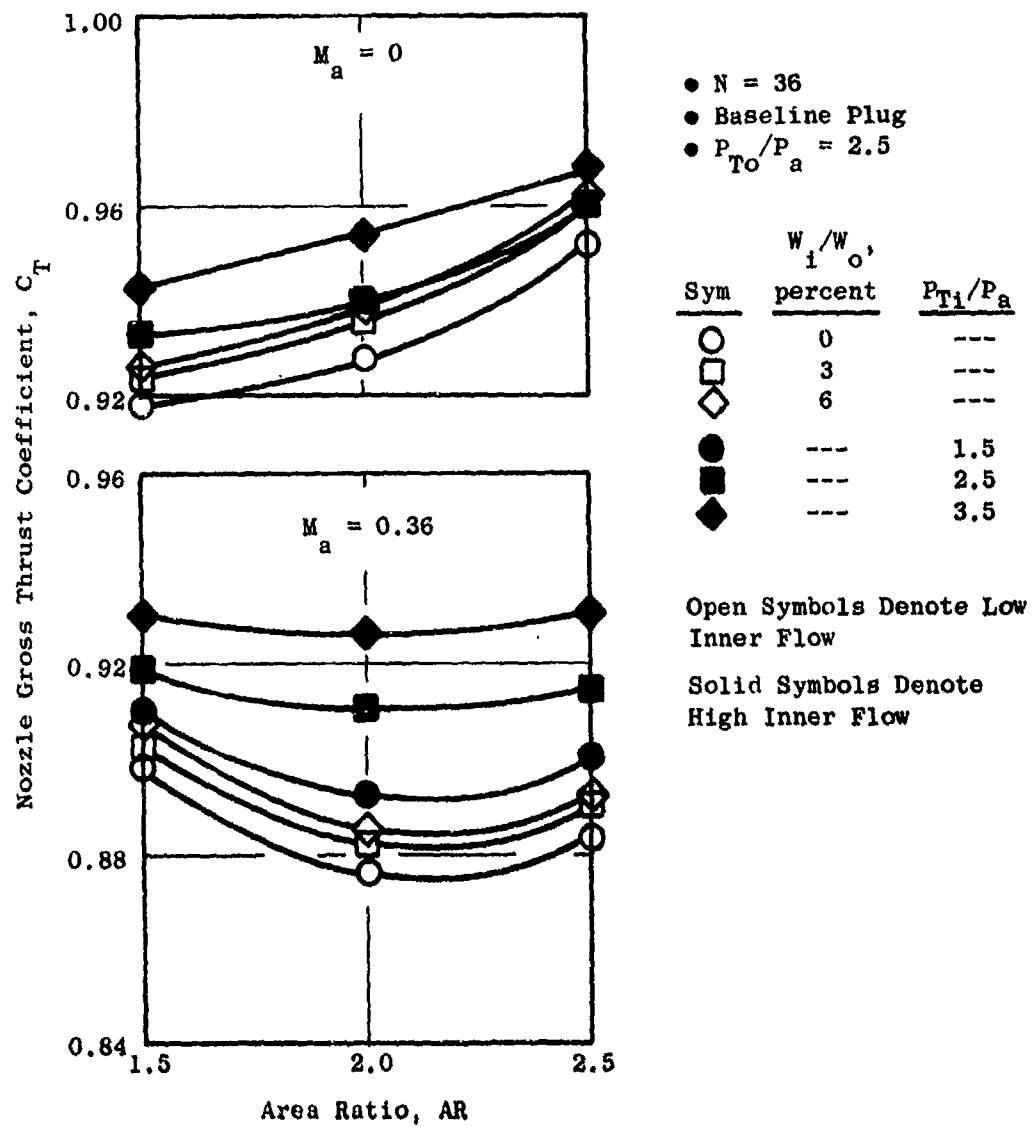


Figure 4-20. Effect of Suppressor Area Ratio and Inner Flow on Nozzle Gross Thrust Coefficients of Deep-Chute Nozzles.

Sym	Free Stream Mach Number, $M_a$	
○	0	• $N = 36$
□	0.36	• Baseline
◇	0.45	• $P_{To}/P_a = P_{Ti}/P_a = 2.5$

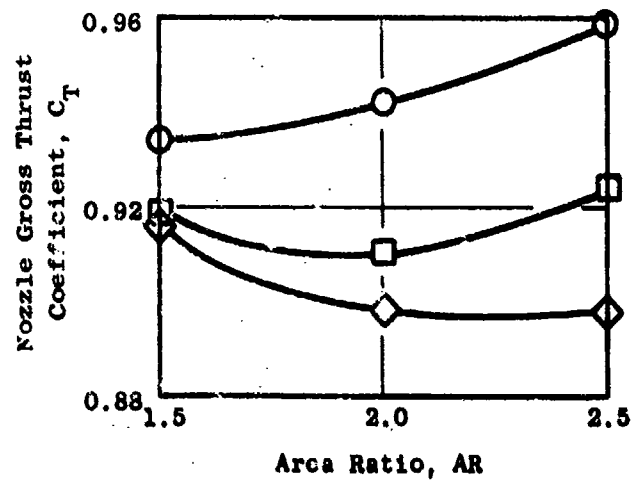
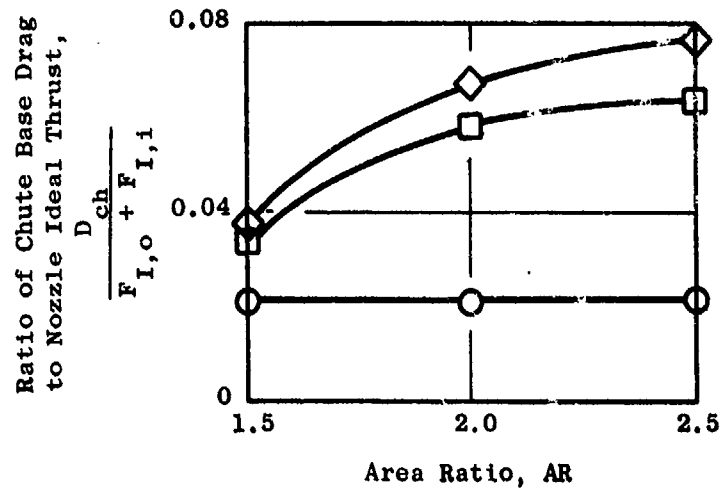


Figure 4-21. Effect of Suppressor Area Ratio and Free-Stream Mach Number on Nozzle Performance of Deep-Chute Nozzles.

chutes) and models DC-3, DC-4, and DC-5 (AR 2.0, 36 deep chutes). The effect of reducing the inner nozzle flow area (increasing radius ratio) on the performance of the area-ratio-1.75, 30-shallow-chute suppressor is presented in Figure 4-22 for a typical outer nozzle and inner nozzle pressure ratio of 2.5 and Mach numbers of 0, 0.36 and 0.45. As the inner nozzle area is decreased, performance is reduced. Figure 4-22 also shows the effect of inner nozzle area on the suppressor base drag. Note that the drag is referenced to the sum of the ideal thrusts of both inner and outer streams. If it were possible to measure the performance of the inner and outer nozzles independently, it could be expected that the outer flow losses would be high relative to the inner flow losses due to the influence of the suppressor. Therefore, as the ratio of unsuppressed to suppressed flow decreased, the total nozzle performance could be expected to decrease, as illustrated by the test results.

Trends for the 36-deep-chute, area-ratio-2.0 nozzle are presented in Figure 4-23. These trends are the same as those described above for the shallow-chute models.

#### 4.5.6 Effect of Inner Plug Axial Location

The effect of inner plug axial location can be investigated by comparing the performance of models SC-2 and SC-5, 30-shallow-chute, area-ratio-1.75 suppressor, and models DC-3 and DC-6, 36-deep-chute, area-ratio-2.0 suppressor. The shallow-chute comparison is shown in Figure 4-24. Performance is compared as a function of outer nozzle pressure ratio for an inner nozzle pressure ratio of 2.5 at Mach 0, 0.36, and 0.45. At outer nozzle pressure ratios of 2.5 and less, axial position of the inner plug had very little effect on nozzle performance. At pressure ratios greater than 2.5, the forward plug location gave the higher level of performance.

Comparisons for the 36-deep-chute suppressor are shown in Figure 4-25. For this model, the effect of axial inner plug location is minimal except at Mach 0.45 where the forward position gives slightly better performance above pressure ratios of 2.5.

#### 4.5.7 Effect of Inner Nozzle Area (Radius Ratio) and Plug Location on Element Base Pressure

The effect of inner nozzle geometry on suppressor element base pressure is shown in Figure 4-26 for Mach 0.36 and an inner nozzle pressure ratio of 2.5 for both the shallow-chute and deep-chute suppressors. The key here is that changes in inner plug area and axial location did not significantly influence the element base pressure. This could be expected based on the fact that the inner nozzle is downstream of the suppressor exit plane. The influence of inner nozzle changes should not feed upstream, especially in cases where the outer, or suppressed, stream pressure ratio is above choked.

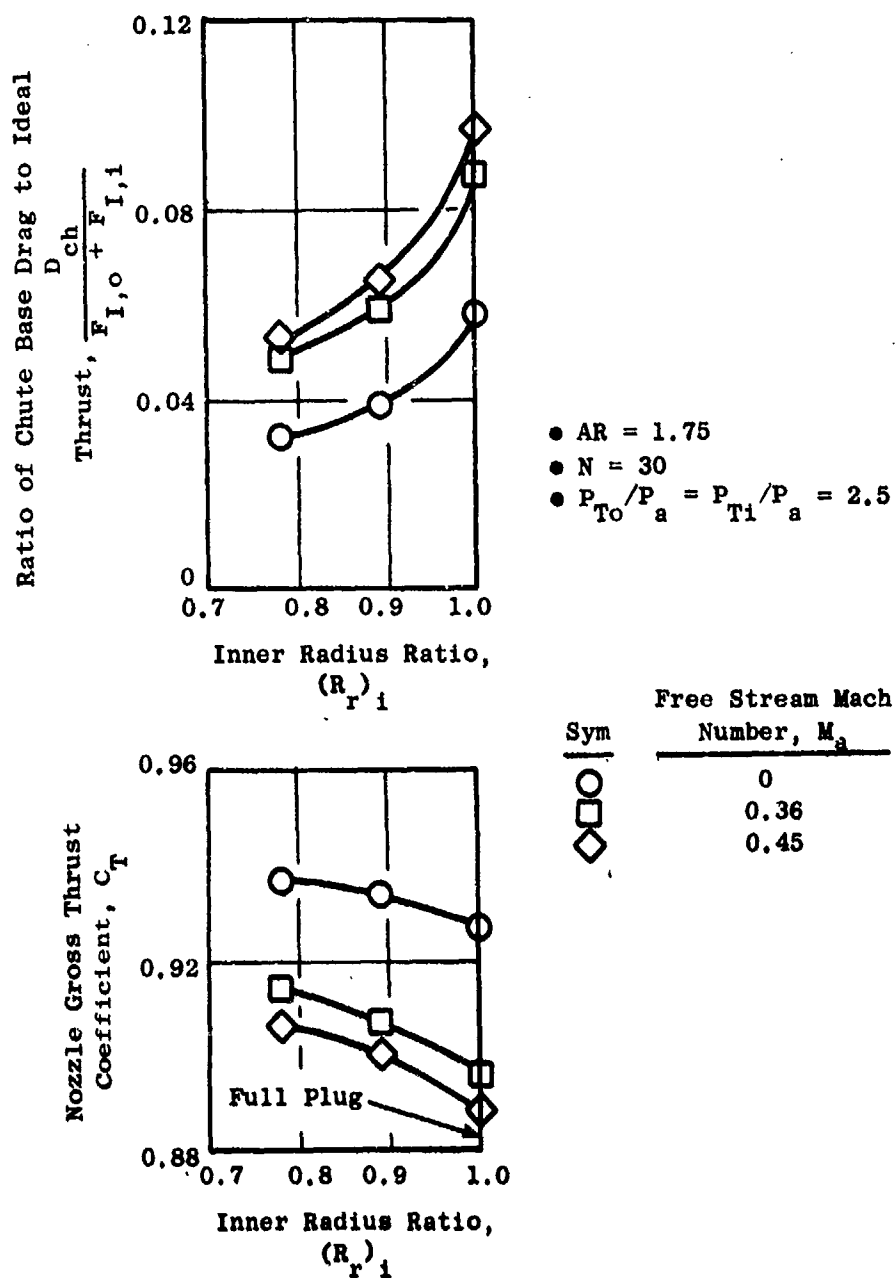
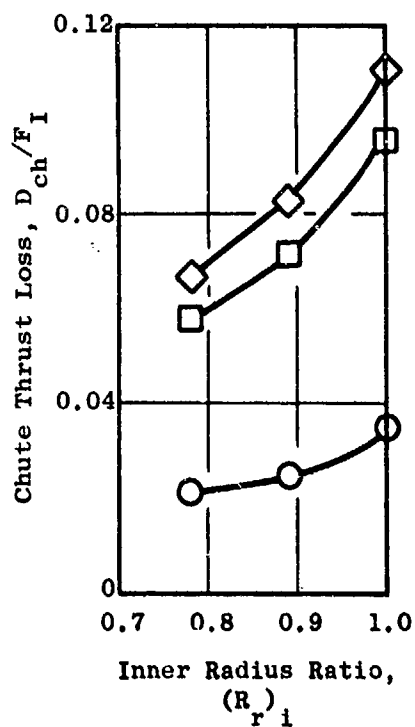


Figure 4-22. Effect of Inner Radius Ratio and Free-Stream Mach Number on Nozzle Performance of Shallow-Chute Nozzles.



- AR = 2.0
- N = 36
- $P_{To}/P_a = P_{Ti}/P_a = 2.5$

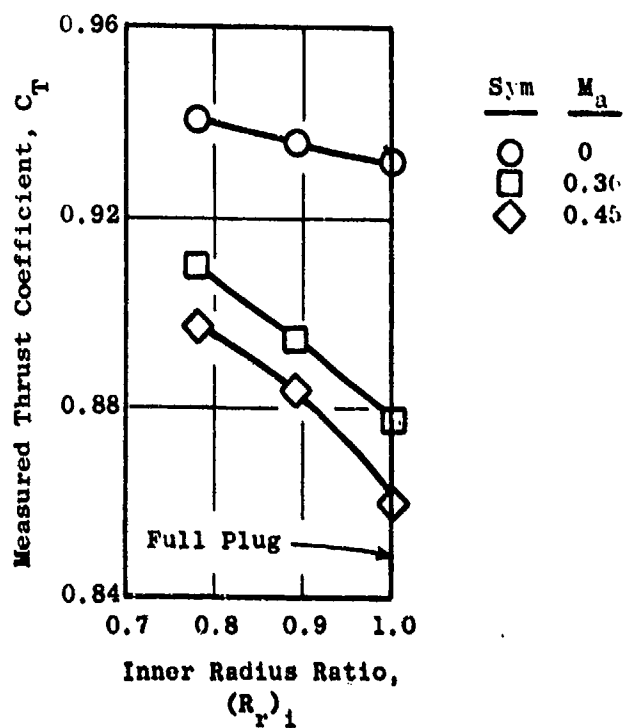


Figure 4-23. Inner Radius Ratio Performance Trends, Deep-Chute Models.



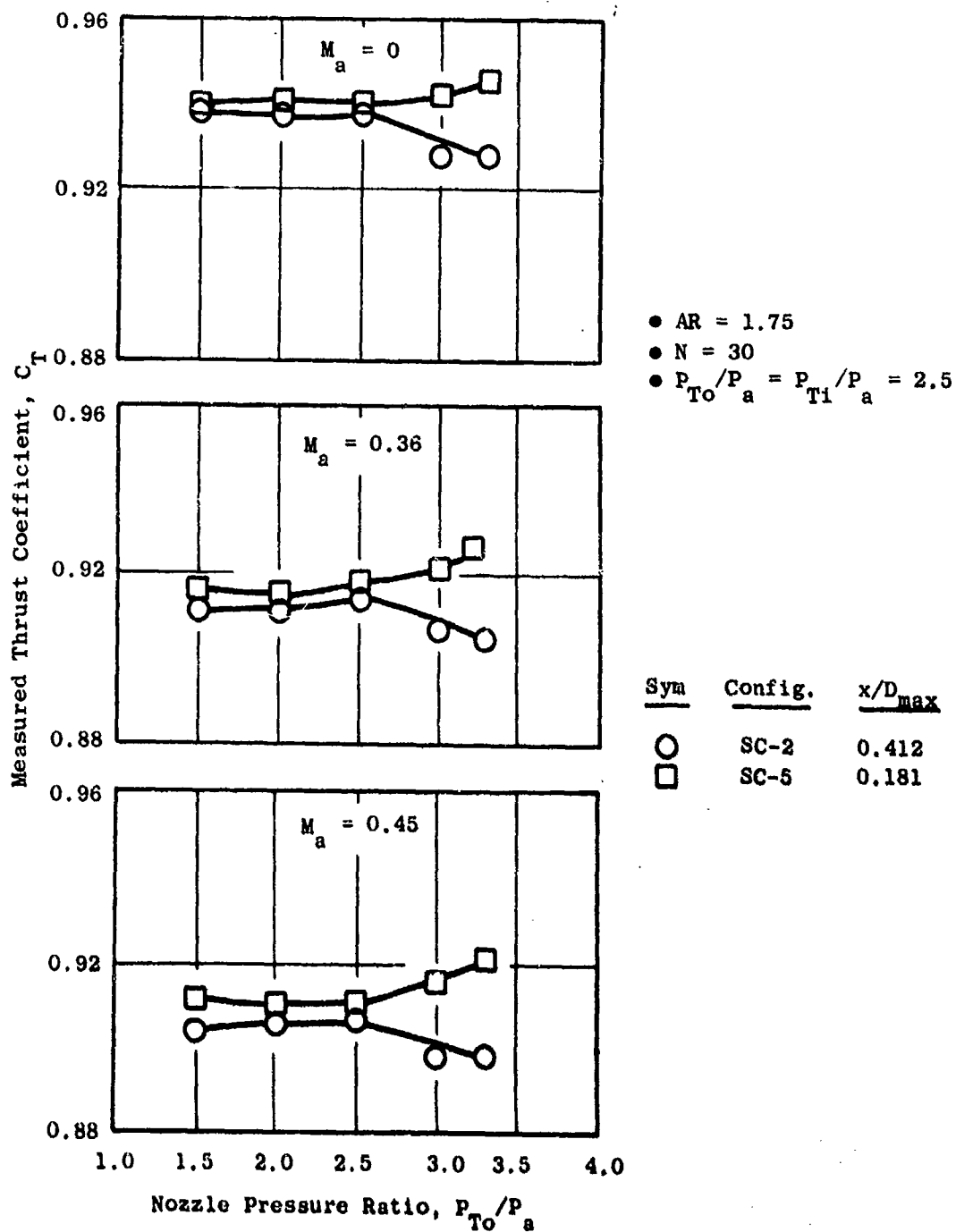


Figure 4-24. Inner Plug Axial Position Performance Trends, Shallow-Chute Models.

Sym	Config.	$x/D_{max}$	• AR = 2.0
○	DC-3	0.418	• N = 36
□	DC-6	0.181	• $P_{To}/P_a = P_{Ti}/P_a = 2.5$

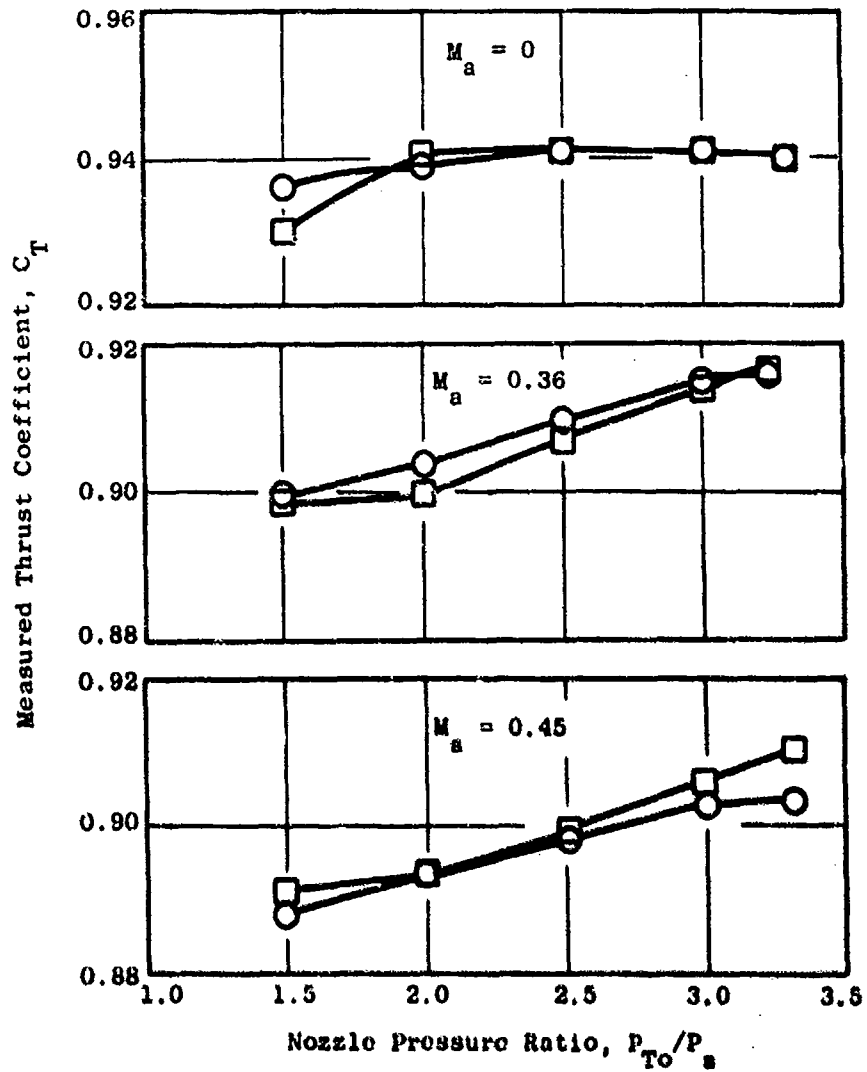


Figure 4-25. Inner Plug Axial Location Performance Trends, Deep-Chute Models.

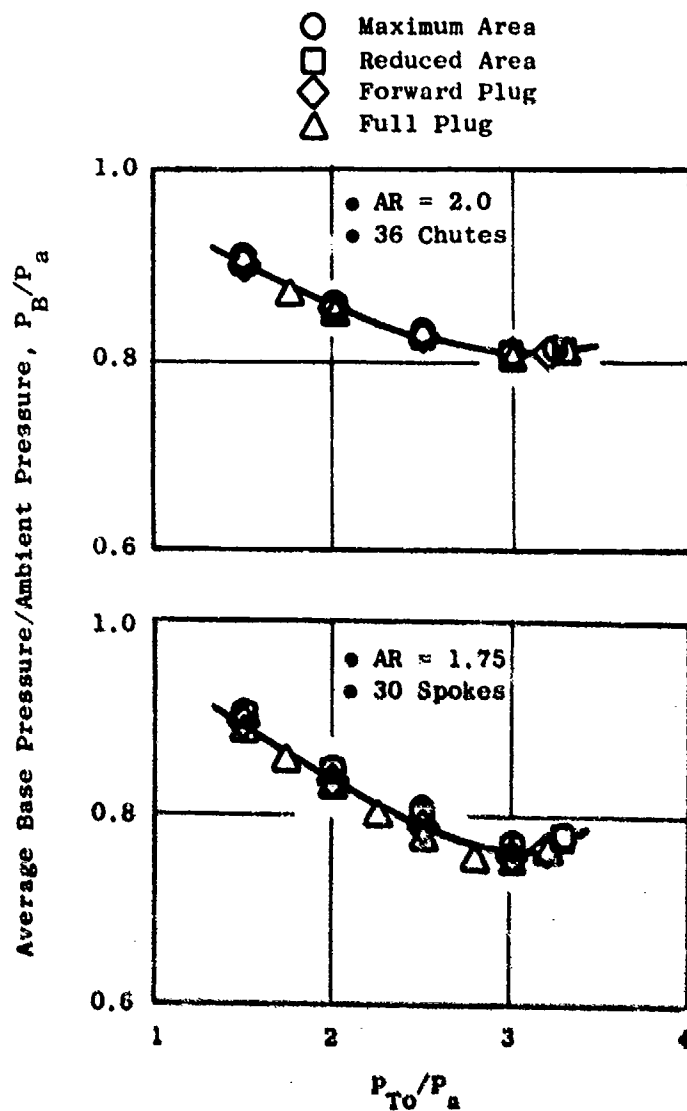


Figure 4-26. Inner Plug Effects on  
 Suppressor Base Pressures,  
 $M_o = 0.36$ ,  $P_{T1}/P_a = 2.5$ .

#### 4.5.8 Effect of Suppressor Ventilation on Performance

The importance of suppressor ventilation on performance is shown in Figure 4-27 where model DC-3, the 36-chute, area-ratio-2.0 suppressor is compared to model DC-3 (spoke). As was described in Section 4.3.1, inserts were placed in the suppressor to effectively eliminate base ventilation from the perimeter of the elements. As can be seen in Figure 4-27, elimination of the ventilation area significantly impacted nozzle performance, resulting in a loss of from three percent at low outer nozzle pressure ratios to seven percent at a pressure ratio of 3.0. It can be concluded from this test that good aerodynamic performance is highly dependent on the amount of available ventilation area.

#### 4.5.9 Effect of External Mach Number

In all cases, increasing external Mach number had a detrimental effect on nozzle performance. Figure 4-28 shows trends in thrust coefficient as a function of tunnel Mach number for the shallow-chute models. The loss in thrust coefficient between Mach 0.45 and static conditions varied between 1.5% and 4%, depending on the configuration. The largest loss occurred for the full plug design, model SC-4.

Similar trends are shown in Figure 4-29 for the deep-chute models. The loss in thrust coefficient between static conditions and Mach 0.45 varied from 1.6% for the area-ratio-1.5 suppressor to 8.8% for the area-ratio-2.5 suppressor with full plug.

#### 4.5.10 104-Tube Nozzle Test Results

Thrust coefficients for the 104-tube nozzle are shown in Figure 4-30. The peak static performance obtained was 0.887 at a nozzle pressure ratio of 3.1. At Mach 0.36, a thrust coefficient of 0.864 was obtained at a pressure ratio of 3.0. The suppressor base plate pressure drag is a major loss component for the 104-tube nozzle, as illustrated in Figure 4-31. In this Figure, both the overall thrust loss as measured by the force balance, and the base drag loss calculated by integrating static pressures, are compared. At a nozzle pressure ratio of 3.0 at Mach 0.36, the overall loss is 13.6%, of which 7.4% is base drag. Remaining losses include tube internal friction and tube entrance losses. As in the case of spoke and chute suppressors, external flow has a significant detrimental effect on performance, about 2.1% in thrust coefficient between static conditions and Mach 0.36.

#### 4.5.11 Fight-Lobe Nozzle Test Results

Thrust coefficients for the 6-lobe nozzle are presented in Figure 4-32. Again, external Mach number has a significant adverse effect on performance.

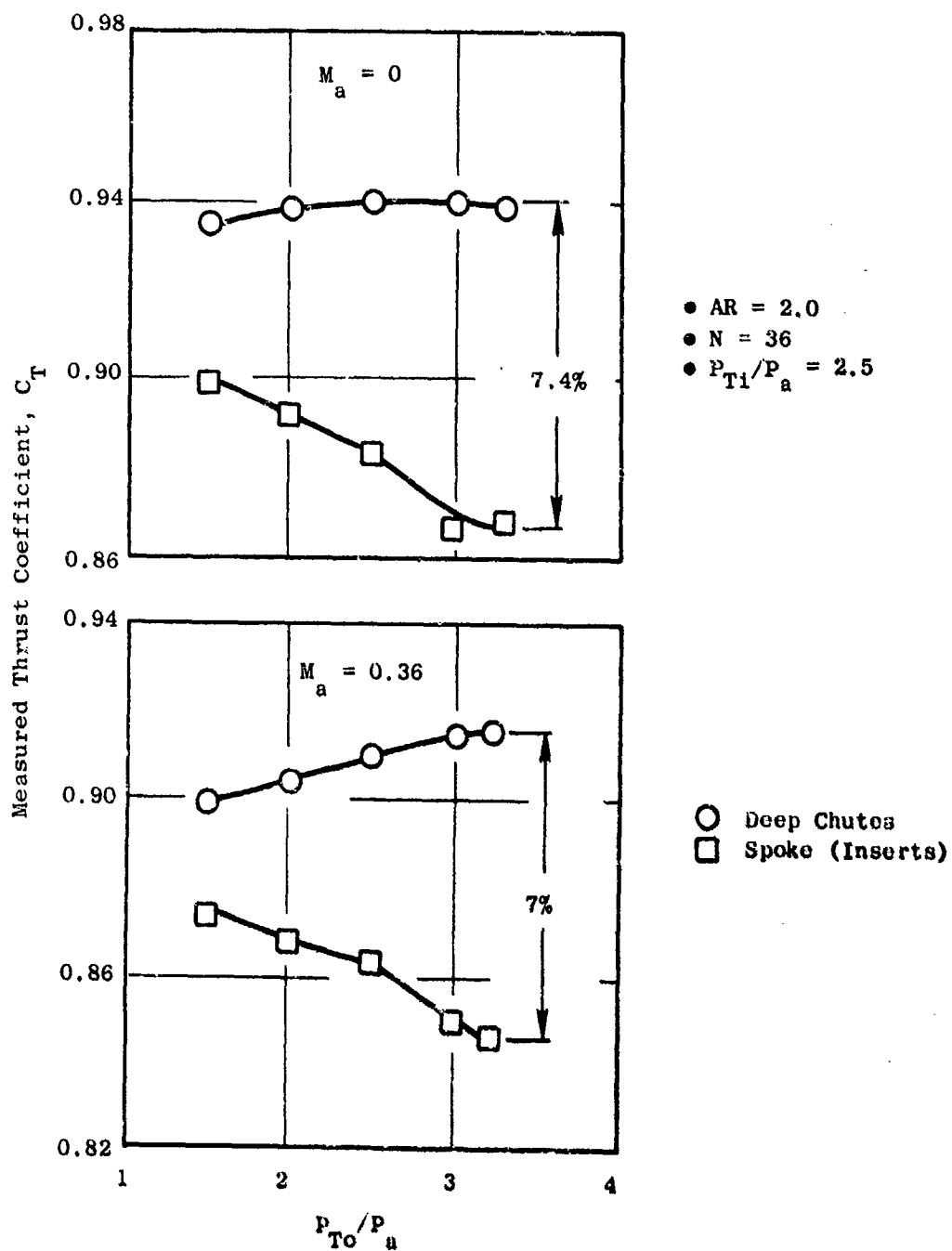


Figure 4-27. Comparison of Chute and Spoke Model Performance.

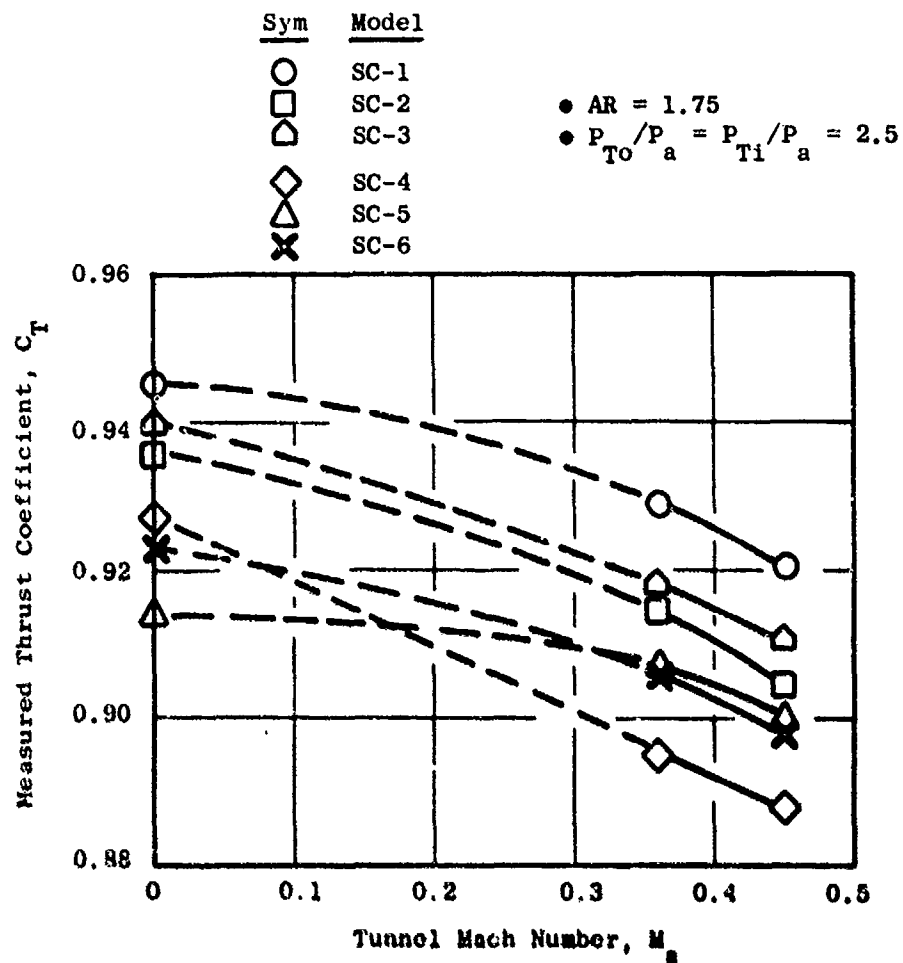


Figure 4-28. Performance Trends with External Mach Number Shallow-Chute Models.

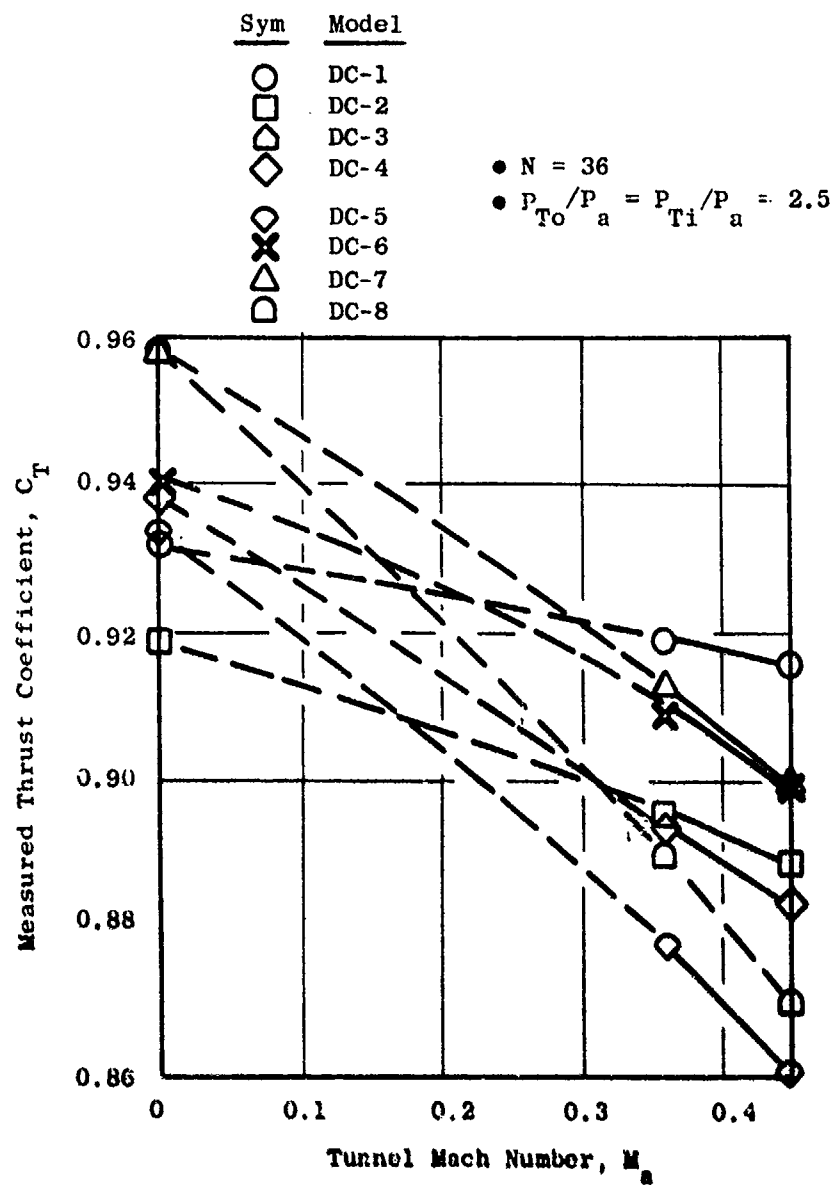


Figure 4-29. Performance Trends with External Mach Number, Deep Chutes

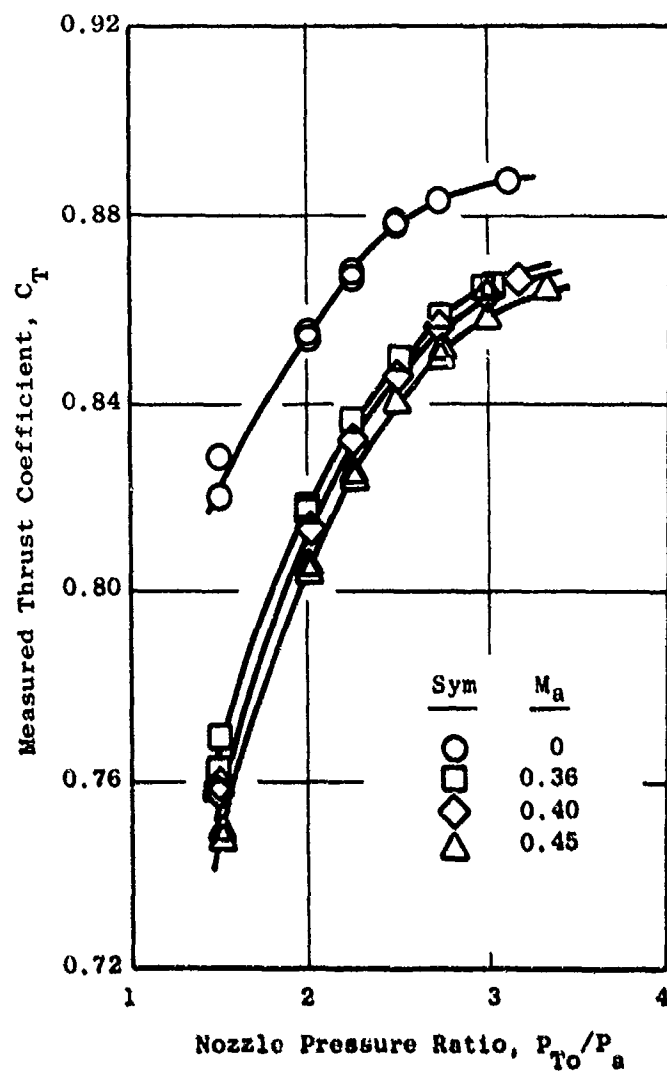


Figure 4-30. 104-Tube Nozzle Performance Trends.



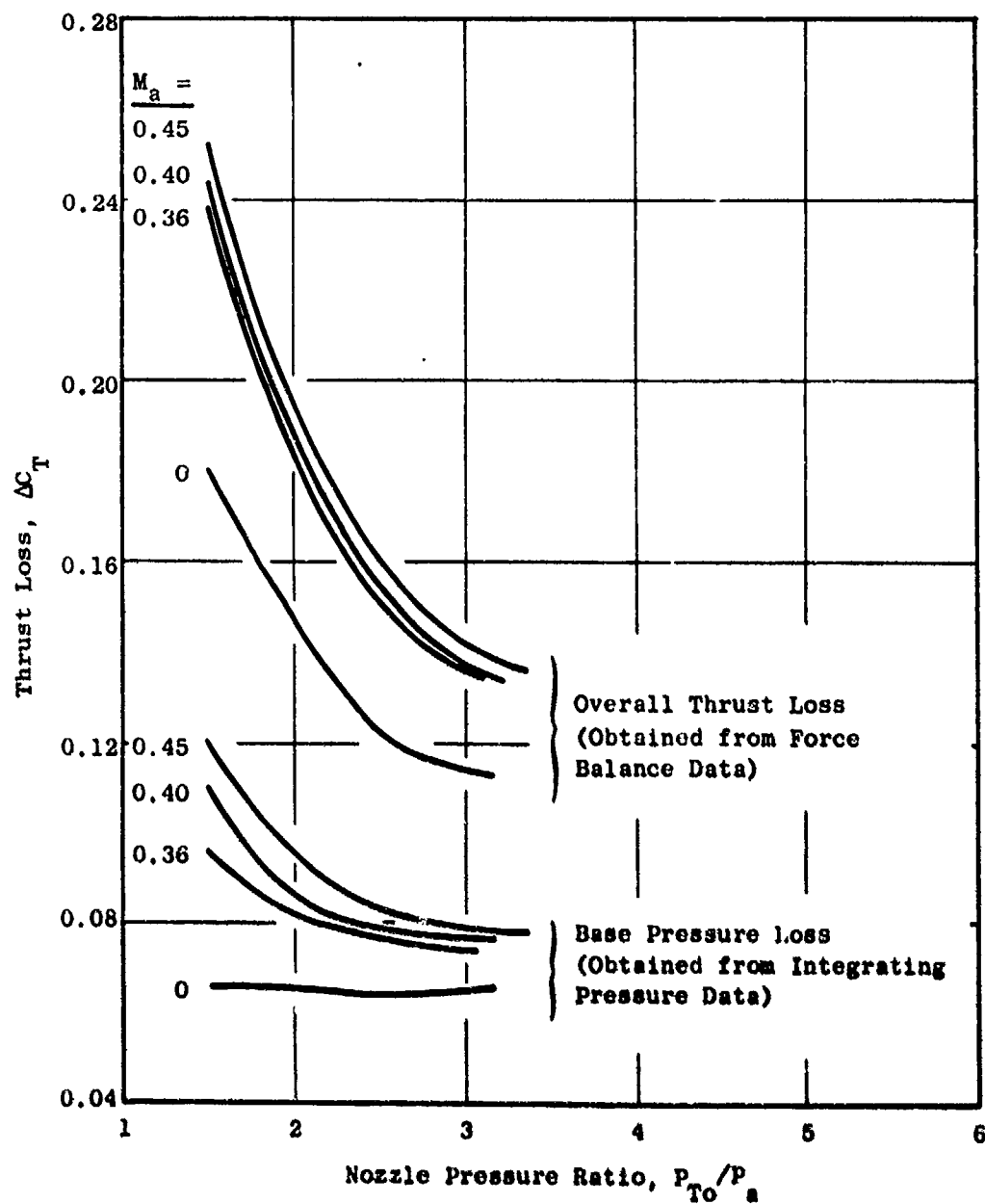


Figure 4-31. 104-Tube Nozzle Base Drag Losses.

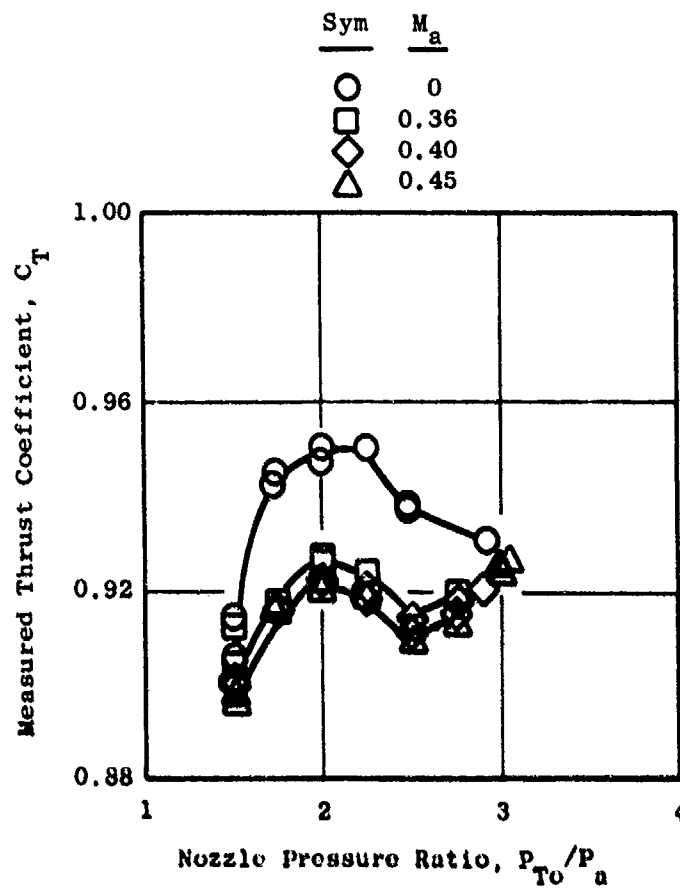


Figure 4-32. Eight-Lobe Performance Characteristics.

Statically, a thrust coefficient of 0.950 at a pressure ratio of 2.0 was measured, while at Mach 0.36, the thrust coefficient was 0.926. The performance of this nozzle would be significantly improved if secondary air were available to fill the gap between the primary nozzle and the outer shroud, as explained in Section 4.4.3. Because the model did not provide a passage for secondary air, the gap area would be "pumped" to less than ambient pressure by the primary jet, resulting in abnormally high base drag losses. In addition, secondary air would reduce the nozzle performance sensitivity to external flow.

#### 4.5.12 Suppressor Flow Coefficients

Suppressor flow coefficients are functions only of suppressor geometry above choked pressure ratios. Flow coefficients are useful in the design of full scale exhaust systems for setting the nozzle physical throat area required to match engine cycle conditions. For scale model tests, they are also useful as a diagnostic tool. For example, a changing flow coefficient above choked conditions could be indicative of either a leak in the model system or a deflection in the suppressor elements with increased pressure (throat area changes). Nothing of this nature was encountered in this test. Flow coefficients are tabulated below for each suppressor configuration.

<u>Suppressor Type</u>	<u>AR</u>	<u>N</u>	<u>CD<sub>0</sub></u>
Shallow Chute	1.75	30	0.971
Shallow Chute	1.75	40	0.966
Deep Chute	1.5	36	0.968
Deep Chute	2.0	36	0.948
Deep Chute	2.5	36	0.978

Flow coefficients for each data point taken can be found in Appendix F in the off-line data summary tabulations.

#### 4.6 CONCLUSIONS

The results of the aerodynamic performance test program again illustrate that exhaust nozzles which incorporate element base areas as an integral part of the jet noise suppression mechanism are sensitive to external Mach number. Static testing is an inadequate means of estimating the in-flight performance of a full scale system since not only performance levels, but trends with geometric variables may be different in flight than statically. This was demonstrated in the area ratio variation experiment where results indicated that, statically, performance increased with increasing area ratio. At Mach 0.45, however, performance decreased with increasing area ratio.

In general, the highest exhaust nozzle loss mechanism is suppressor element base drag. The so-called "base ventilation area" has a dramatic impact on element base drag as was demonstrated by the deep-chute versus

"spoke" experiment, which resulted in a greater than seven percent loss in thrust coefficient when the chute ventilation area was blocked.

The test results also illustrate that the number of elements, for a given suppressor area ratio, is an important variable as far as performance is concerned. Increasing the number of elements had a detrimental effect on performance. For a typical outer and inner nozzle pressure ratio of 2.5, at Mach 0.36, a 2.2% loss was recorded when the element number was increased from 20 to 30.

Increasing the area of the inner nozzle, for a given suppressor geometry, improved the overall performance of the exhaust system, as might be expected since the inner nozzle is "unsuppressed" and only small losses are incurred relative to the outer suppressed stream. Increasing the inner nozzle area while keeping the outer nozzle area constant resulted in increased total nozzle flow rate. Nozzles with no inner flow, i.e., simulated turbojet nozzles, exhibited the lowest performance since all engine flow passes through the mechanical suppressor.

Inner nozzle flow or geometric conditions had little or no effect on suppressor element base pressures. This allows some freedom in the design of the inner nozzle without fear of increasing suppressor base drag. However, care should be exercised in the design of the inner nozzle to prevent excessive inner flow performance losses. Although all inner plugs in this test program had essentially the same contours, test results reported in Reference 39 have shown that the shape of the inner plug can have a significant effect on performance.

In summary, the data taken in the NASA-Lewis Research Center 8- by 6-foot wind tunnel was of high quality, with accuracy and repeatability generally better than  $\pm 0.5\%$  over the range of interest. The results of the test program significantly add to the data base already available for the design of advanced, high velocity jet noise suppressor systems. Specifically, these data were utilized in performing trade studies of performance versus suppression, and aircraft integration studies reported in Volume III. Also, correlation of these data was a key element in formulating performance prediction procedures for the Task 6 Design Guide.

## 5.0 RESULTS AND CONCLUSIONS

Task 3 of the High Velocity Jet Noise Program involved a series of parametric acoustic, aerodynamic and source measurement tests on baseline and suppressed nozzles. This report (Volume II of IV) has documented the model configurations, test efforts, and results.

Baseline conical nozzle acoustic data have been shown to agree well with present SAE prediction methods for jet mixing noise, especially with respect to peak noise level and to shock cell noise when correlated with  $\sqrt{M^2-1}$ . Plug nozzle studies have shown that suppression increases with radius ratio. Suppression levels up to 6  $\Delta$ PNdB have been achieved at high radius ratio. Coplanar-coannular nozzles with outer to inner flow area ratios of 0.4 to 2.0 have demonstrated inner to outer flow ratio to be an important design variable. Maximum suppression was achieved when  $W_o/W_i$  was less than 0.1. The variation with area ratio was minimal above this ratio. Complete blockage of the inner flow caused a significant loss in suppression.

Suppressor and system aerodynamic and geometric parameters evaluated experimentally included the following: suppressor area ratio, radius ratio, flow management (system velocity ratio, weight flow ratio and area ratio), inner stream geometry, element number, element type, and treated ejectors on multi-element and unsuppressed inverted coannular flow nozzles. Suppressor area ratio variation for single-flow nozzles has established that peak noise suppression increases with increasing area ratio at high jet velocity and decreases with increasing area ratio at low jet velocities. For example, a 5 PNdB difference existed between a 1.5 and a 2.5 area ratio nozzle at 2400 ft/sec. Minimal distinction was seen at 90°. The area ratio study conducted on dual-flow nozzles (with only the outer stream suppressed) shows a maximum of 3.5 peak PNdB variance between the configurations, with the suppression level dependent on jet velocity. Low-area-ratio, high-radius-ratio designs were consistently better at low to intermediate jet velocities, as they were for the full span turbojet nozzles. Peak noise suppression levels of 11, 9.5 and 10.4 for area ratios of 1.5, 2.0 and 2.5, respectively, were below those of the same suppressor applied to a single-flow turbojet (i.e.,  $\Delta$ PNL = 11.5, 12.0 and 12.5), suggesting that a full-span turbojet suppressor is slightly more efficient than a half-span suppressor applied to a dual-flow system.

Flow management and inner stream geometry studies were conducted utilizing a dual-flow nozzle system incorporating an outer stream half-span mechanical suppressor. These studies established that velocity ratio is an important design consideration with systems of low area ratio, e.g.,  $A_o/A_i = 0.65$ . Highest suppression levels were attained when inner flow was completely eliminated. For systems of  $A_o/A_i = 1.92$  and 3.6, variance due to velocity ratio was not as distinct and decreased as area ratio increased. Injecting low amounts of inner flow to effect bypass ratios of 3.3 and 6.7 showed bypass ratio to be a strong parameter influencing suppression. The influence was

greater for low system area ratio, with suppression decreasing as  $W_0/W_i$  was lowered from  $\infty$  to 3.3. Increasing flow area ratio caused an increase in suppression of between 3.5 and 5 PNdB over its lower  $A_0/A_i$  counterparts. Inner stream plug geometry variation showed only minor change in suppression.

Flow segmentation studies showed that maximum suppression levels of 10 PNdB were attainable. Increasing element number was more effective at mass average velocity less than 2250 ft/sec. Reduction of element number was more effective above this velocity.

Spoke/chute element type studies on a full-span suppressor achieved a maximum suppression of 13.5  $\Delta$ PNdB. Spoke and chutes were found in general to exhibit equivalent peak noise suppression levels. At high mass average velocities, spoke suppressor effectiveness was diminished. A similar spoke/chute study on a half span suppressor showed a peak PNL suppression level of 10.5 PNdB, significantly less than the 13.5 peak PNL attained by the full-span application. The spoke nozzles were from 0.5 to 1.5 PNdB more effective than chutes.

Application of acoustically treated ejectors to half and full span 36-element suppressors was found to effect a significant increase in suppression. Similar application to an unsuppressed inverted-flow coannular plug nozzle was not as effective.

Studies to assess the influence of simulated flight using the freejet technique established that a common set of velocity indices may not be established for both baseline and suppressor nozzles. Chute nozzles in general have shown a 3 PNdB loss of suppression in flight due to dominance of the high frequency portion of the spectra, which realizes only a minimal flight effect. The minimization of high frequency noise has been demonstrated to be a critical design criterion for a suppressor if it is to realize a beneficial flight effect.

Laser velocimeter measurements established that suppressors enhance mean velocity decay until the velocity approached 60% or less of the fully expanded isentropic velocity. The axial location of peak turbulence intensity is a function of nozzle type and may be related to the region of maximum mean velocity gradient. Axial location of peak turbulence intensity was found to be a function of nozzle type; however, the absolute turbulence level range of 18 to 22% could not be correlated with exhaust nozzle type. Conical nozzle velocity decay rate was reduced in simulated flight. Complex suppressor nozzles showed very little sensitivity to forward velocity, until the downstream region of the coalesced jet. The turbulence intensity levels near the exit plane were found to be generally comparable. Overall, the laser velocimeter has been demonstrated to be extremely useful in determining the aerodynamic mixing characteristics for complex multi-element suppressor nozzles.

A wind tunnel test program illustrated that the aerodynamic performance of suppressed nozzles which incorporate elemental base areas as an integral

part of the design are sensitive to external Mach number. Static testing was shown to be an inadequate means of estimating in-flight performance of a potential full-scale suppressor. In-flight performance levels, as well as trends with geometric variables, may be different than static. The area ratio variation study demonstrated this result when static performance improved with increasing suppressor area ratio, and Mach 0.45 performance decreased with the same area ratio increase.

In general, suppressor element base drag is the most important loss mechanism. The so-called base ventilation area has a dramatic impact on element based drag as demonstrated by the seven percent loss in thrust coefficient incurred when a deep-chute ventilation area was blocked as a spoke.

Tests results also illustrate that suppressor segmentation is an important performance variable. Increasing element number decreased performance. For a typical outer and inner nozzle pressure ratio of 2.5, at flight Mach 0.36, a 2.2% loss was associated with element number increase from 20 to 30.

Decreasing system area ratio ( $A_0/A_i$ ) for a fixed half-span suppressor improved the overall system performance. This was anticipated, since the inner nozzle is unsuppressed and only small losses are incurred relative to the outer suppressed stream. Systems with no inner flow, i.e., turbojet nozzles, exhibited the highest performance loss, since all flow passes through the suppressor.

Inner nozzle flow rate and plug geometry variation had little or no effect on suppressor element base pressure. This allows some flexibility for inner nozzle design by eliminating concern of increasing base drag. Although inner plug geometries in this study maintained similar contours, results from previous studies have shown that inner plug shape can impact performance significantly.

The NASA-Lewis Research Center's 8-by-6-foot wind tunnel data was of high quality, with accuracy and repeatability generally better than  $\pm 0.5\%$  over the range of interest. Study results significantly add to the aerodynamic performance data base available for the design of advanced, high velocity jet noise suppressor systems.

• All Dimensions in Inches

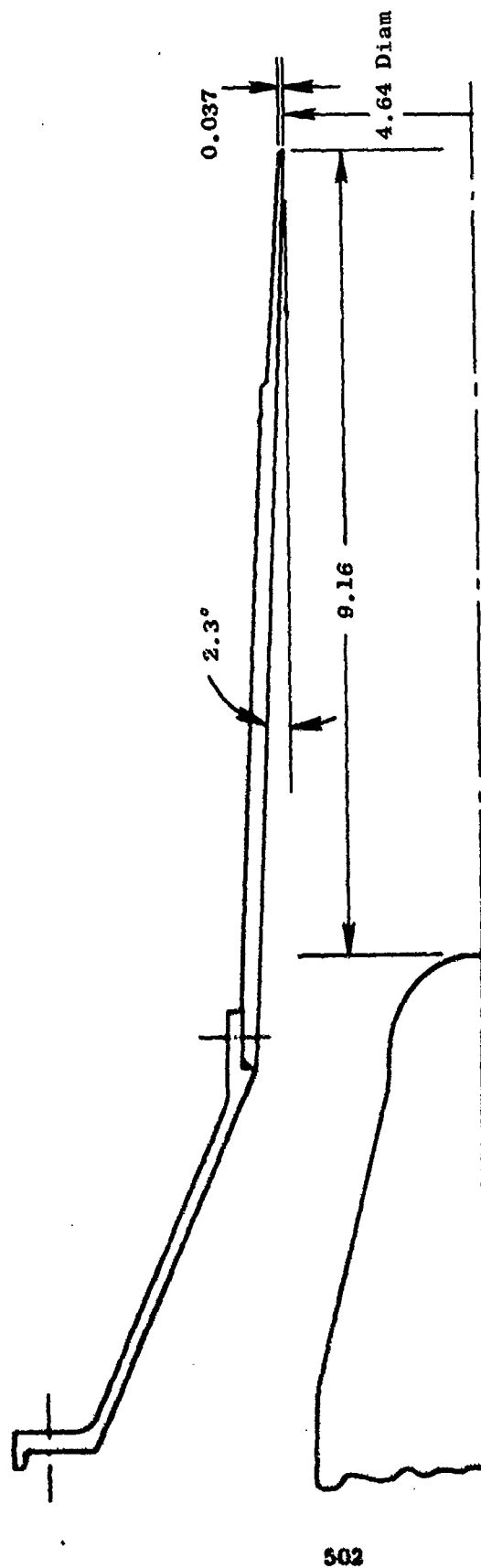


Figure A-1. Model 1 - 4.64-in.-Diameter Conical Nozzle Adapted to JEFOTS. Model 14 - 4.64-in.-Diameter Conical Nozzle Adapted to Cell 41, Anechoic.



## APPENDIX A

Figures A-1 through A-41 are dimensioned, schematic illustrations of the test models discussed in Section 4.3 of this document.

• All Dimensions in Inches

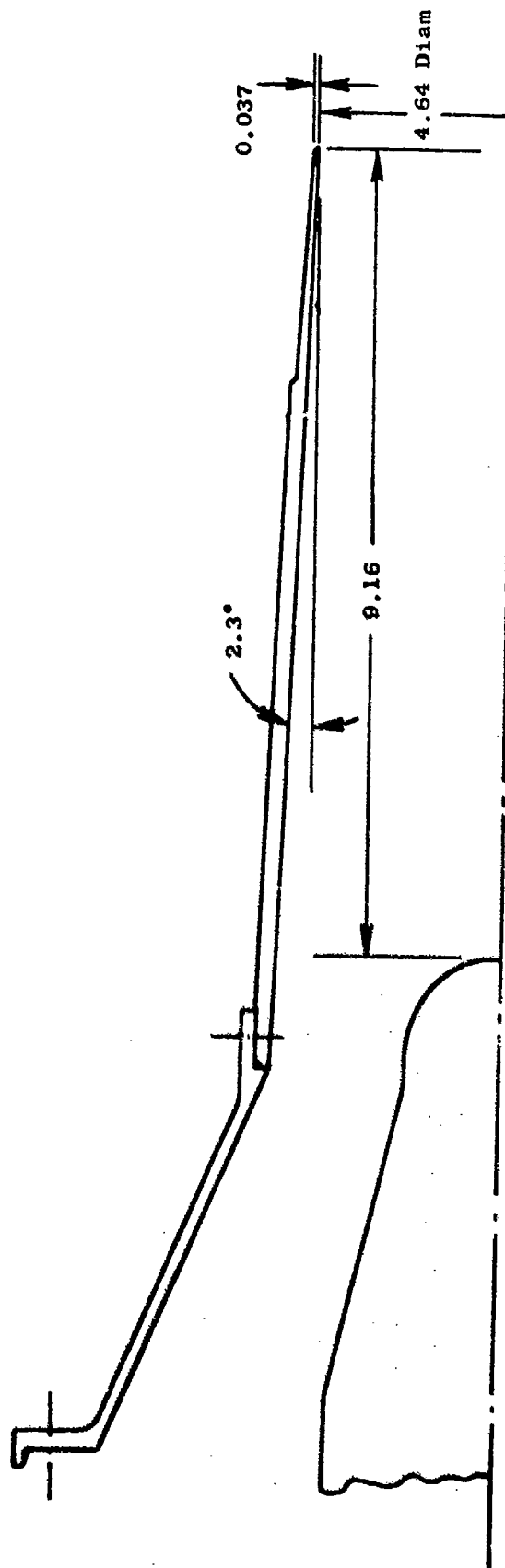


Figure A-1. Model 1 - 4.64-in.-Diameter Conical Nozzle Adapted to JENOTS. Model 14 - 4.64-in.-Diameter Conical Nozzle Adapted to Cell 41, Anechoic.

- $A_9/A_8 = 1.22$
- $D_9 \text{ eq}/D_8 \text{ eq} = 1.10$
- All Dimensions in Inches

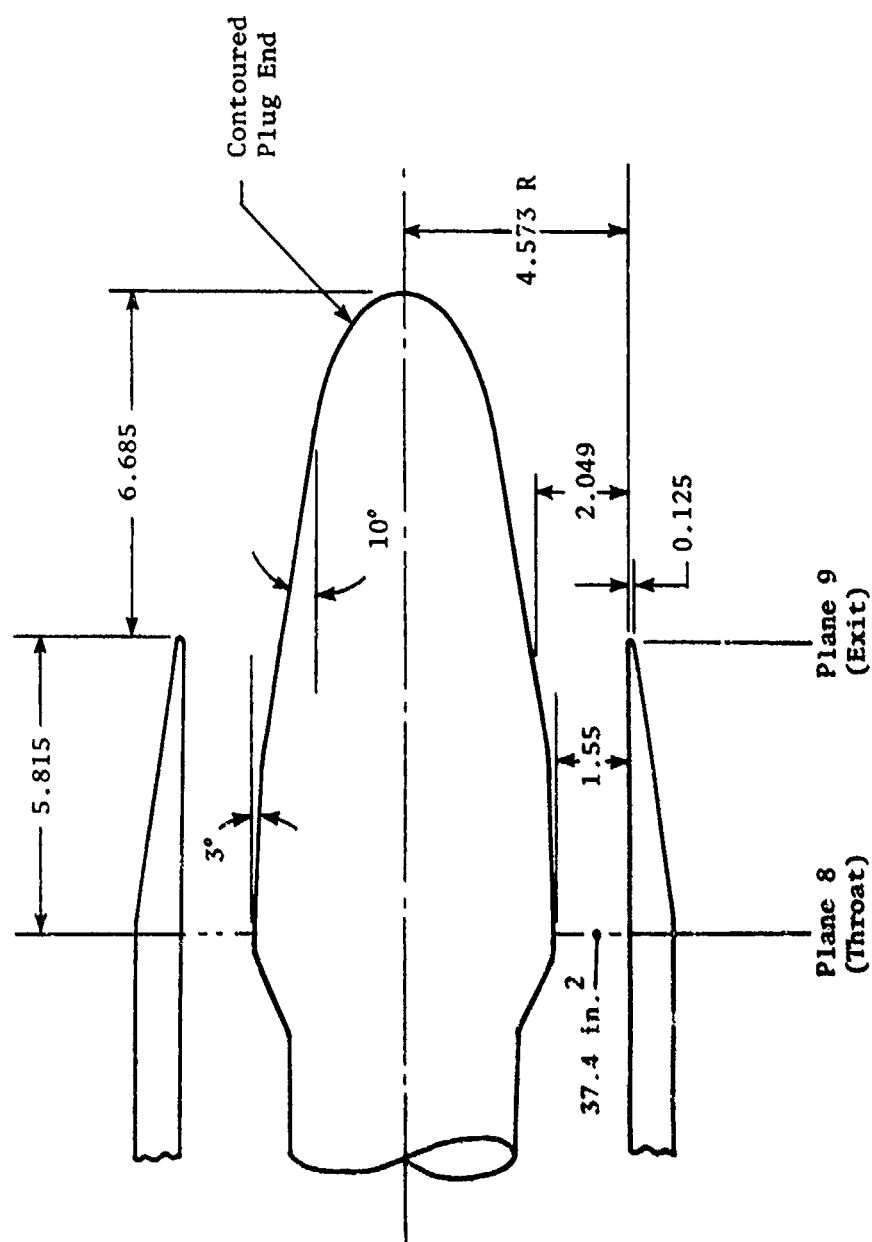


Figure A-2. Model 2 - Convergent-Divergent Plug, Single Flow.

• All Dimensions in Inches

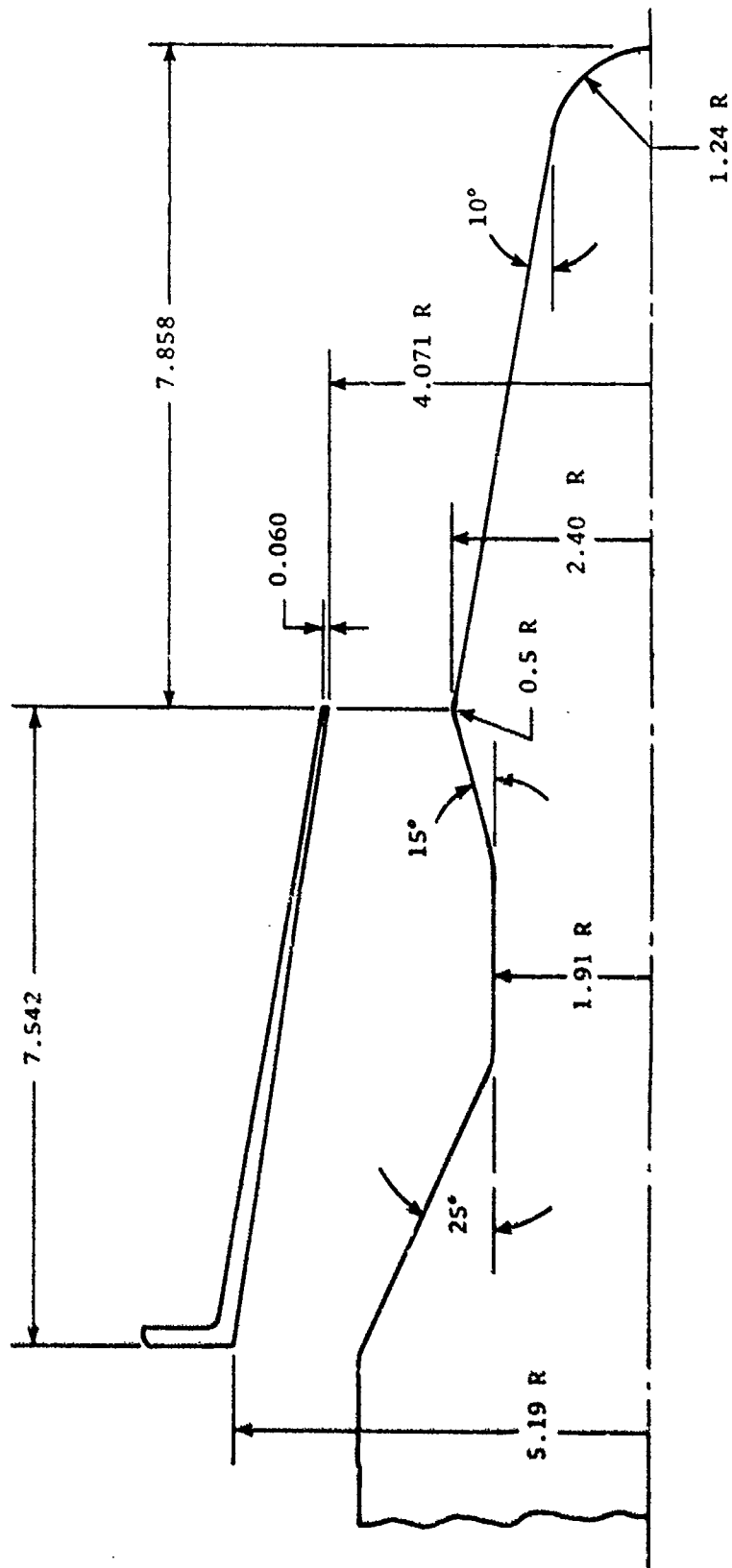


Figure A-3. Model 3 - Converging Plug,  $R_r = 0.59$ , Single Flow.

- All Dimensions in Inches

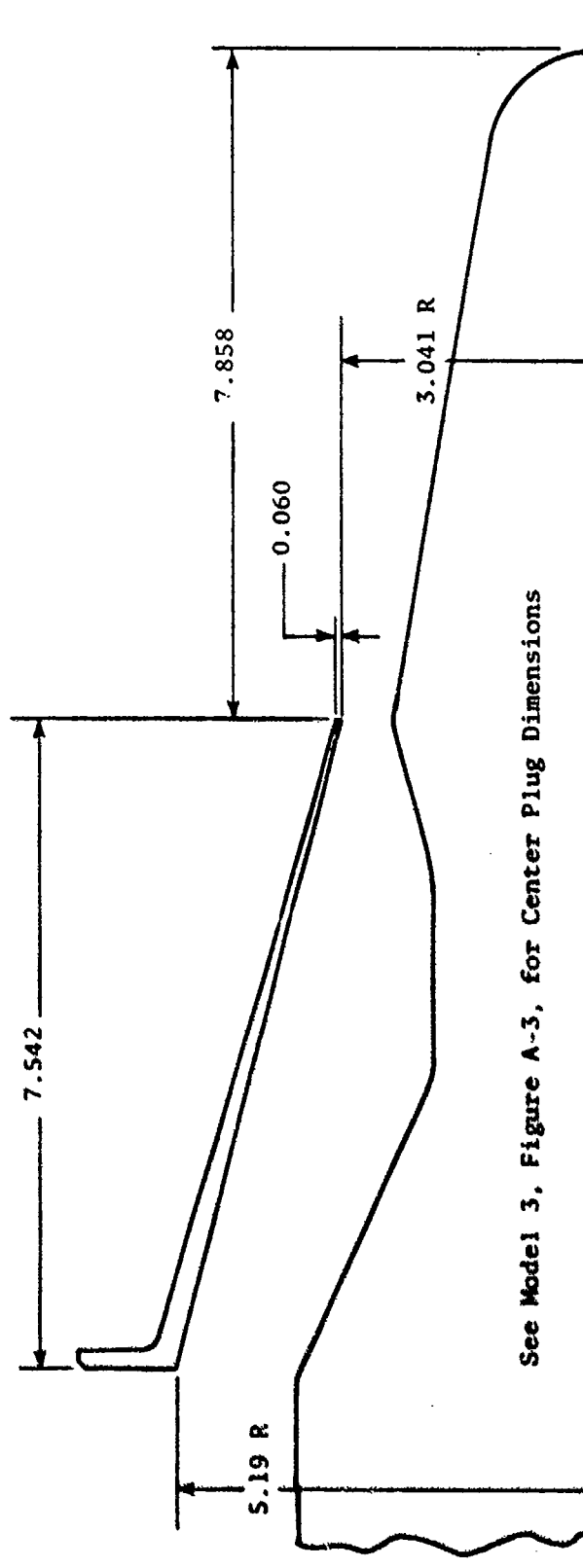


Figure A-4. Model 4 - Converging Plug,  $R_T = 0.789$ , Single Flow.

• All Dimensions in Inches

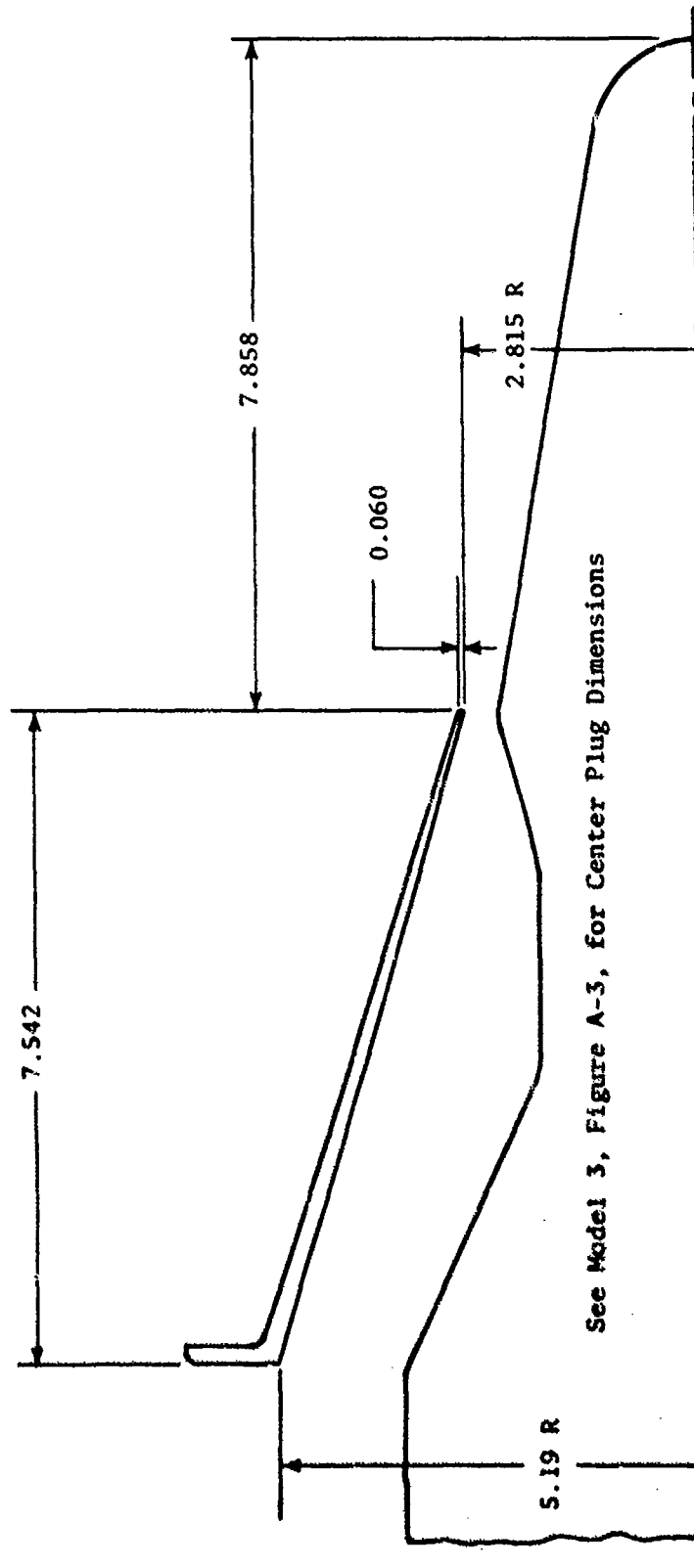


Figure A-5. Model 5 - Converging Plug,  $R_r = 0.853$ , Single Flow.

• All Dimensions in Inches

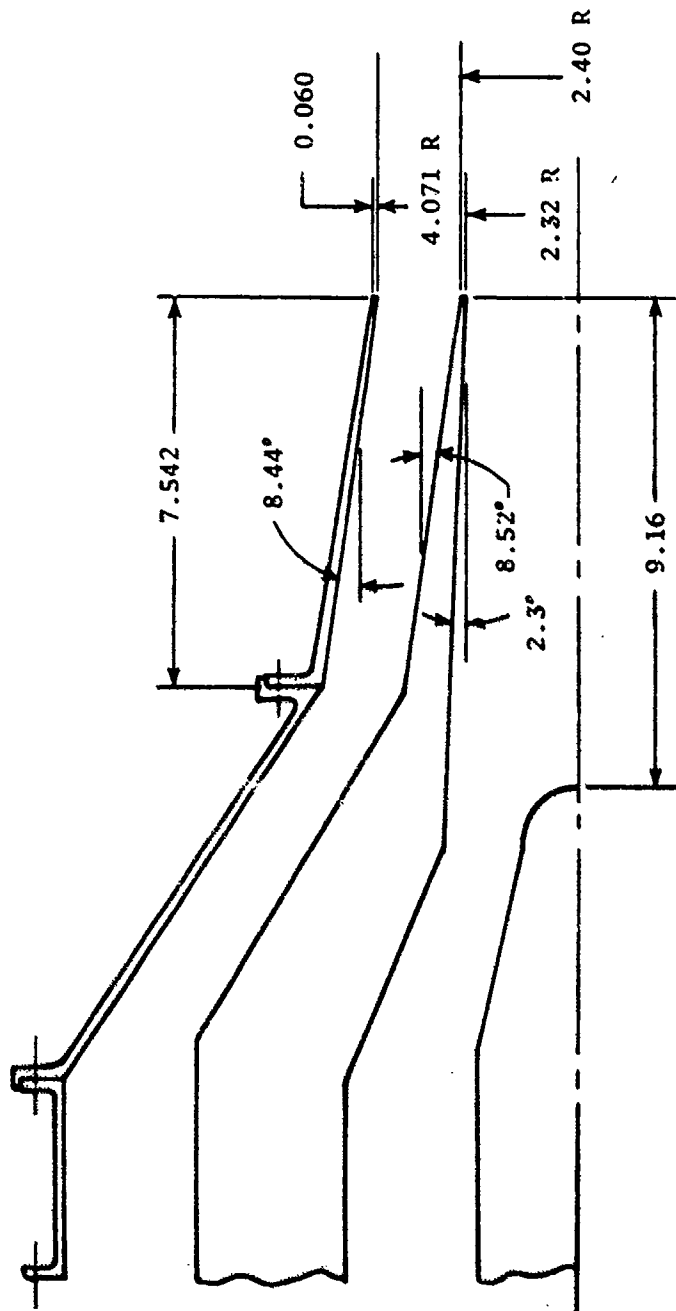


Figure A-6. Model 6 - Dual-Flow Coannular Coplanar,  $A_o/A_i = 2.0$ . Model 9 - Coannular Coplanar,  $A_o/A_i = 2.0$ , Low Inner Flow.

• All Dimensions in Inches

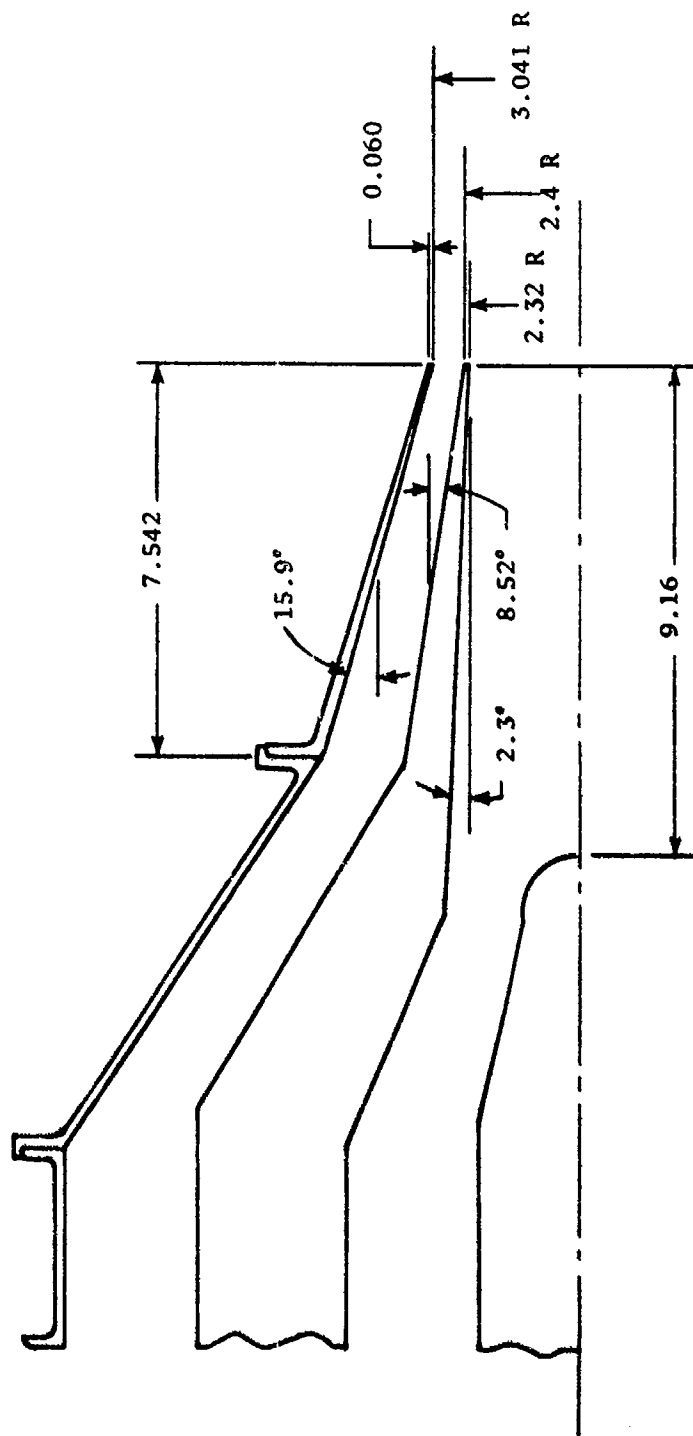


Figure A-7. Model 7 - Dual-Flow Coannular-Coplanar,  $A_0/A_1 = 0.65$ .  
 Models 10 and 11 - Coannular-Coplanar,  $A_0/A_1 = 0.65$ ,  
 Low Inner Flow and No Inner Flow, Respectively.



• All Dimensions in Inches

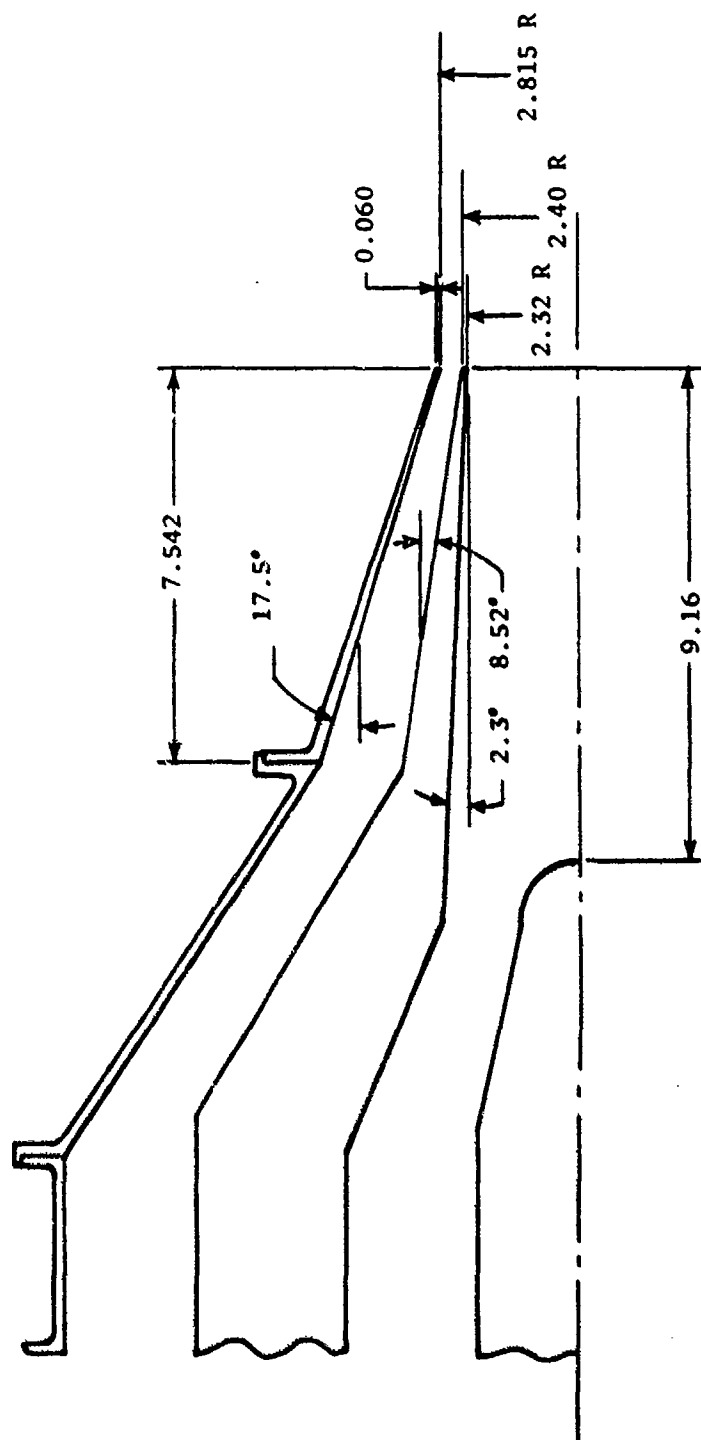


Figure A-8. Model 8 - Dual-Flow Coannular Coplanar,  $A_0/A_i = 0.4$ . Models 12 and 13 - Coannular Coplanar,  $A_0/A_i = 0.4$ , Low Inner Flow and No Inner Flow, Respectively.

• All Dimensions in Inches

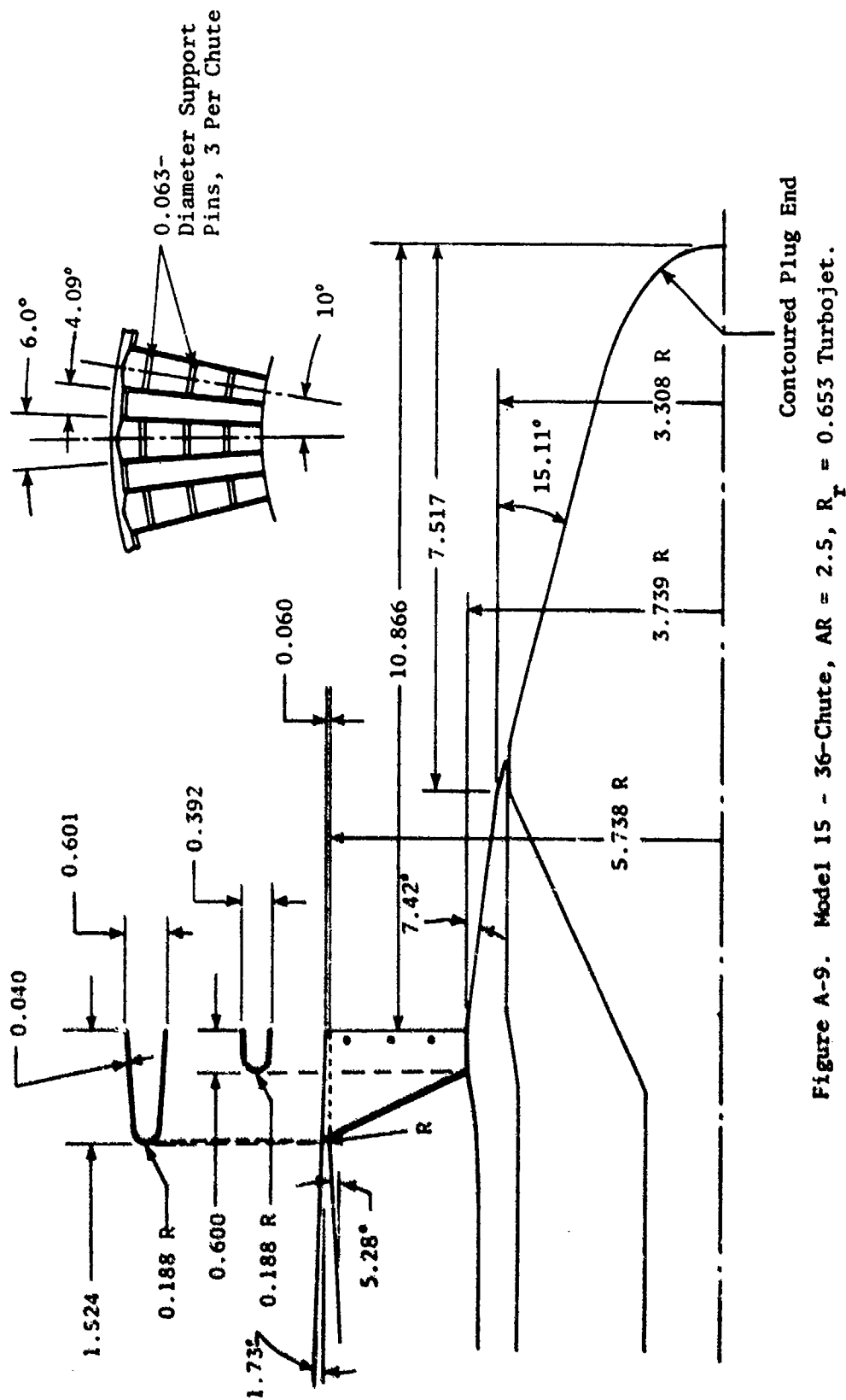


Figure A-9. Model 15 - 36-Chute, AR = 2.5,  $R_T = 0.653$  Turbojet.

• All Dimensions in Inches

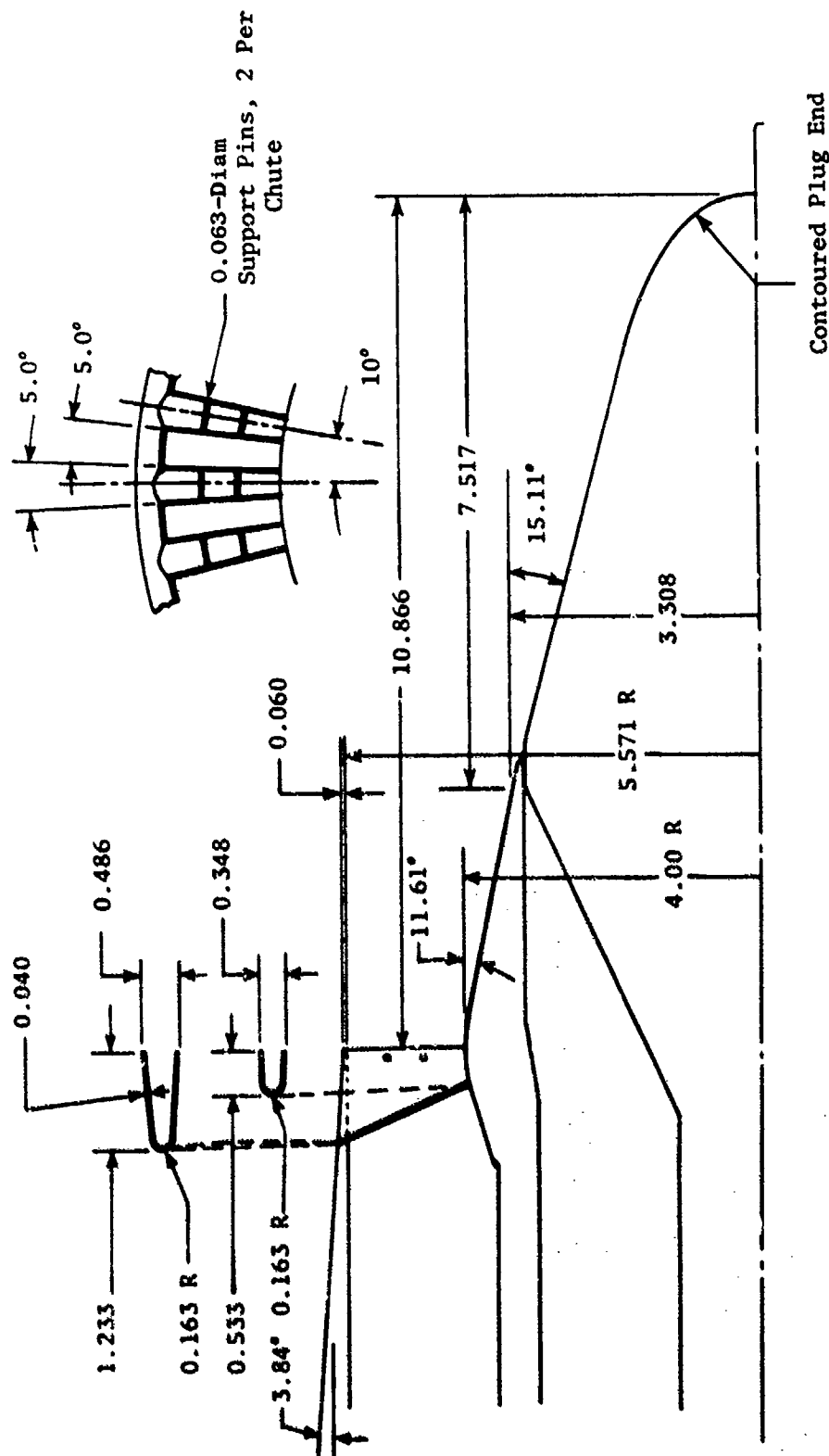


Figure A-10. Model 16 - 36-Chute, AR = 2.0,  $R_r = 0.716$  Turbojet.

• All Dimensions in Inches

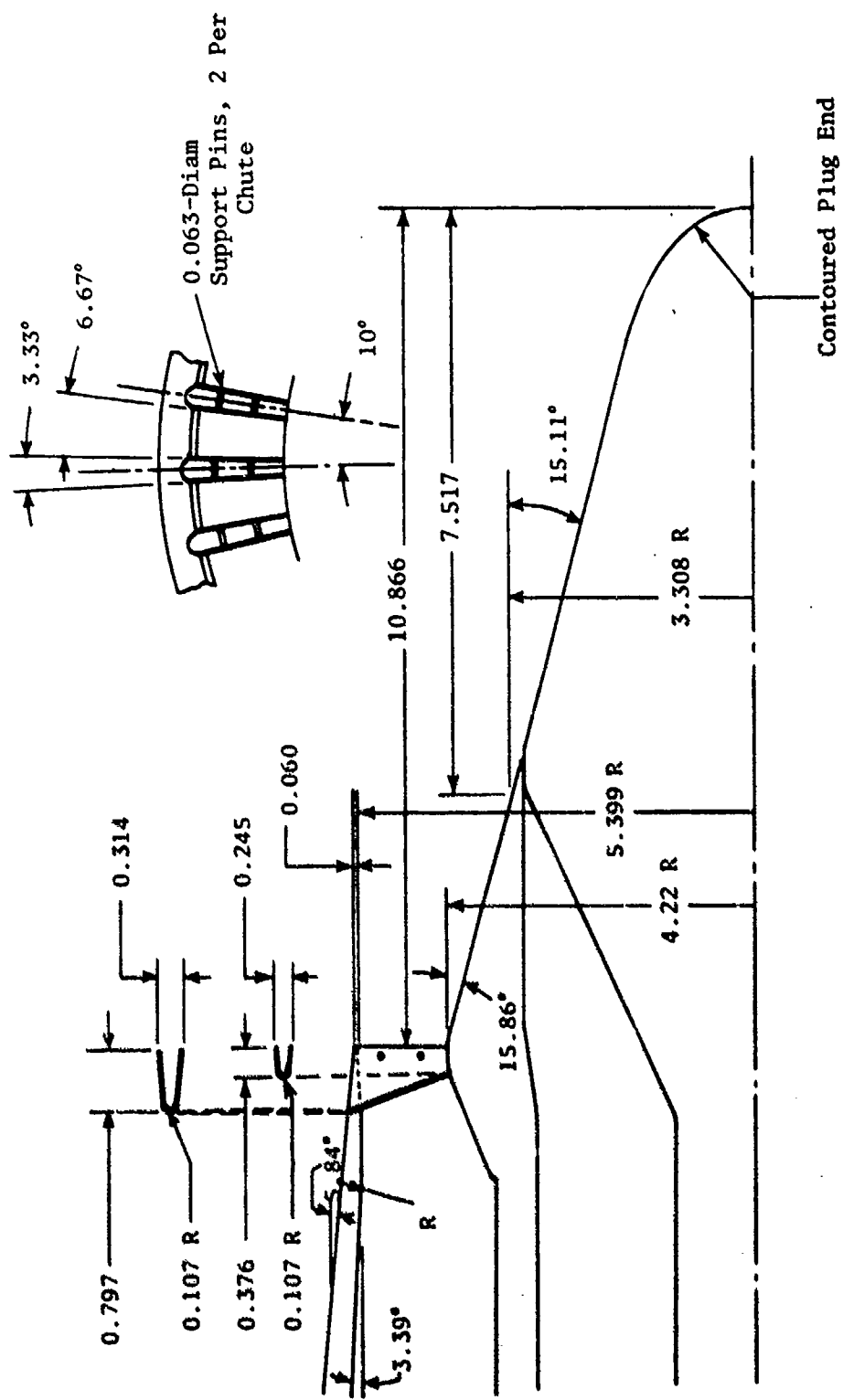


Figure A-11. Model 17 - 36-Chute, AR = 1.5,  $R_T = 0.782$  Turbojet.

• All Dimensions in Inches

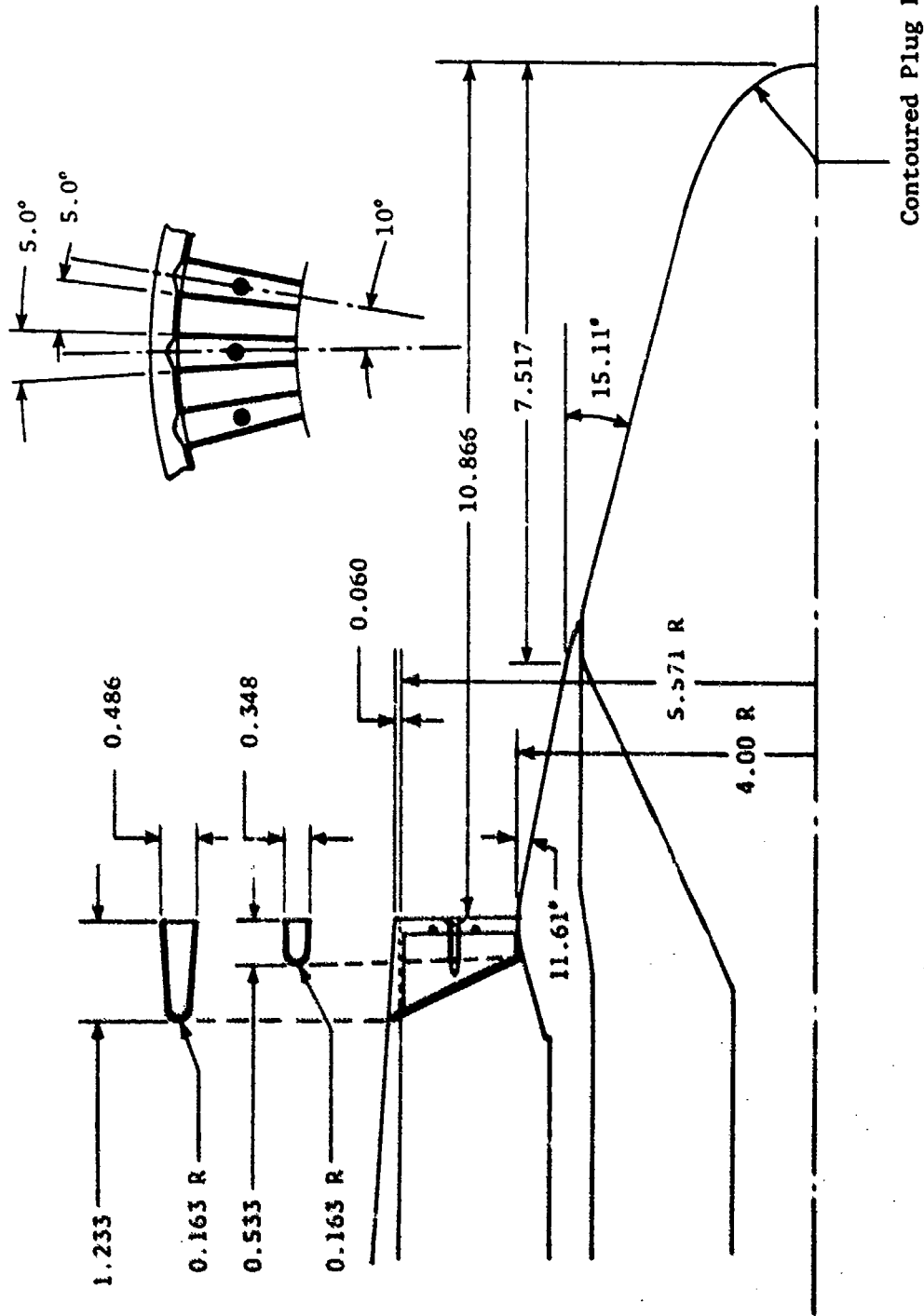


Figure A-12. Model 18 - 36-Spoke, AR = 2.0,  $R_T = 0.716$  Turbojet.

• All Dimensions in Inches

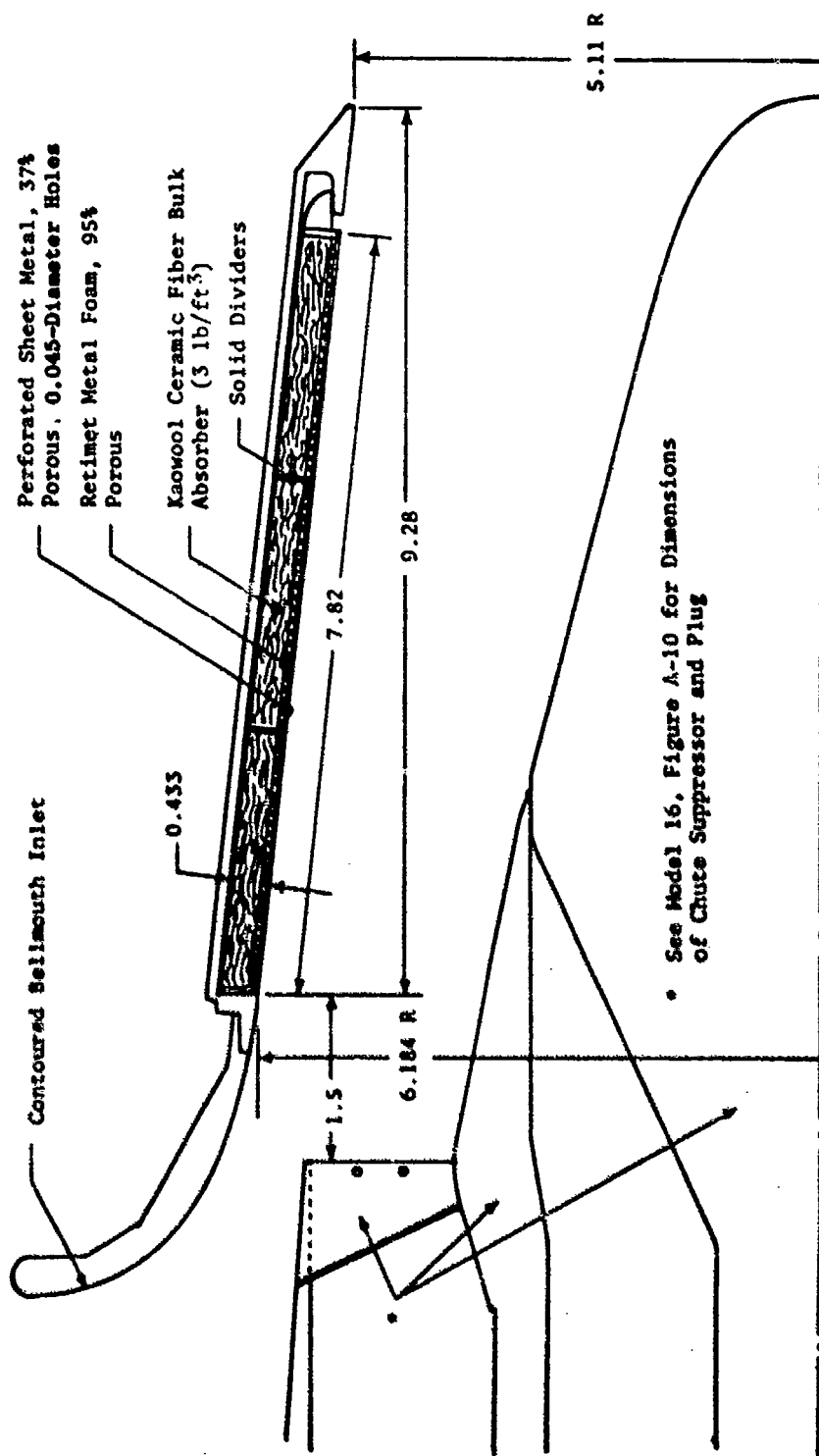


Figure A-13. Model 19 - 36-Chute, AR = 2.0,  $R_r = 0.716$  Turbojet with Acoustically Treated Secondary Ejector.

- All Dimensions in Inches
- Exit Plane ID = 0.743
- All Tubes

Base Radius	No. of Tubes
$r_1 = 3.374$	18
$r_2 = 4.330$	6
$r_3 = 4.480$	18
$r_4 = 4.252$	12
$r_5 = 5.491$	18

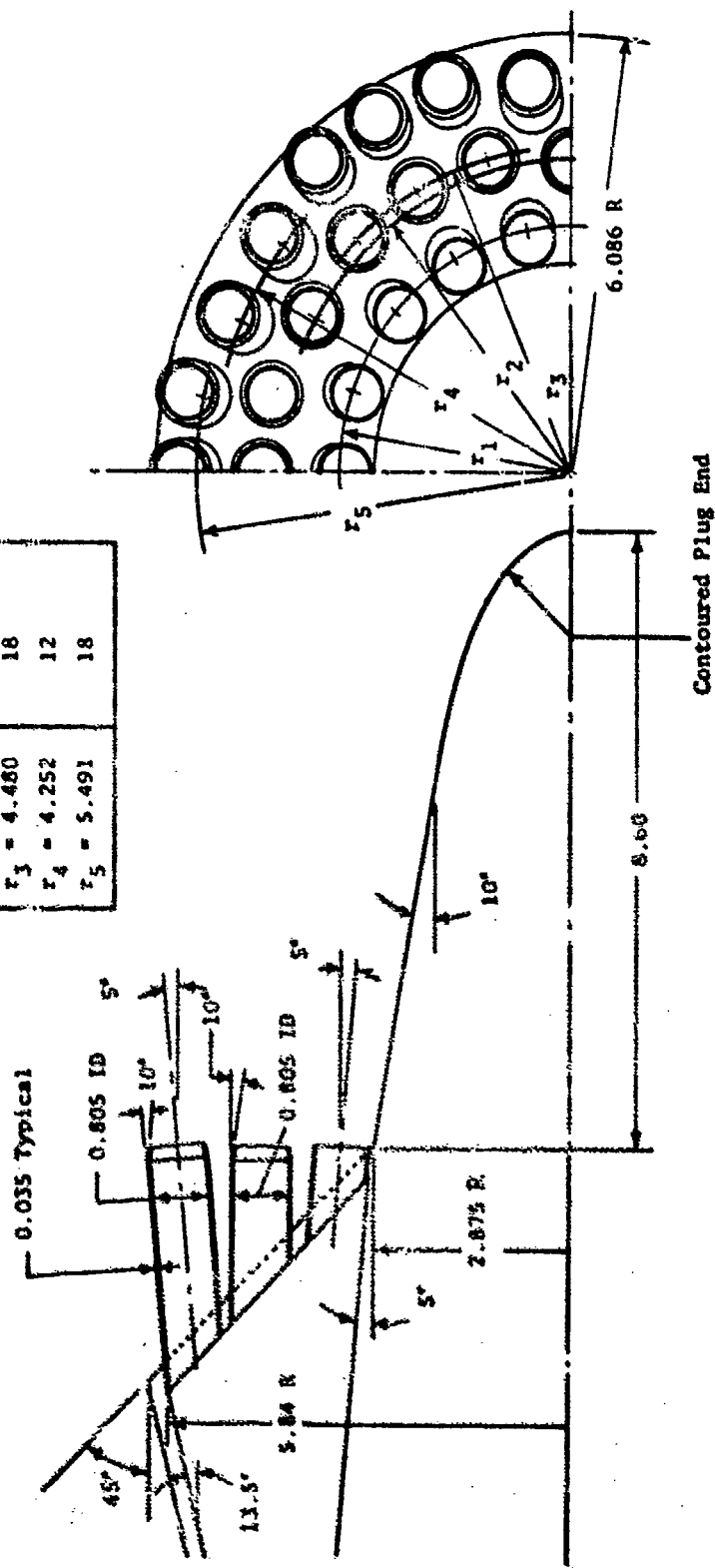


Figure A-14. Model 20 - 72-Tube/Plug, AR = 2.95 Turbojet.

• All Dimensions in inches

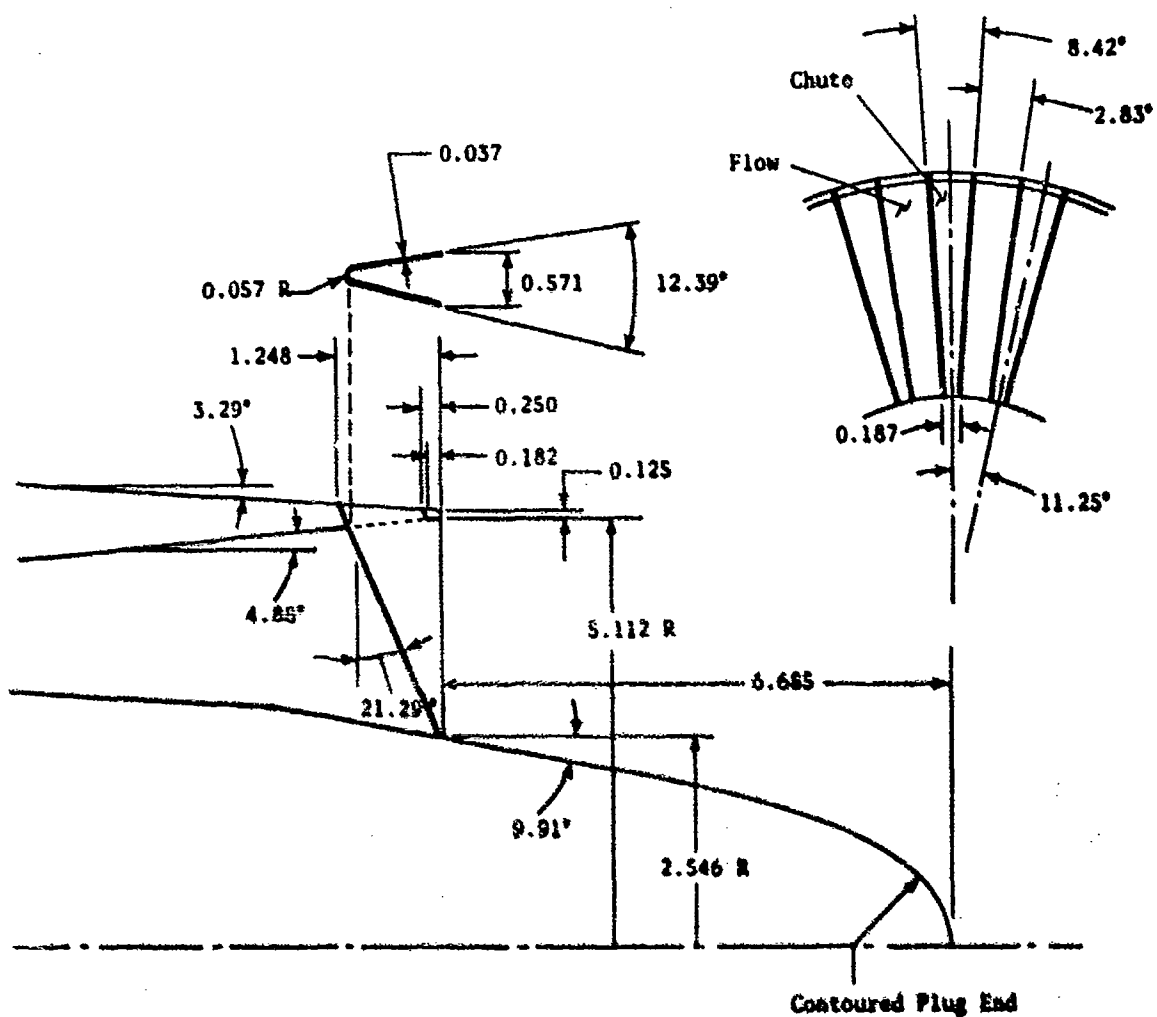


Figure A-15. Model 21 - 32-Chute,  $AR = 2.0$ ,  $R_T = 0.498$  Turbojet.



• All Dimensions in Inches

\* See Model 15, Figure A-9 for Dimensions of Chute Suppressor

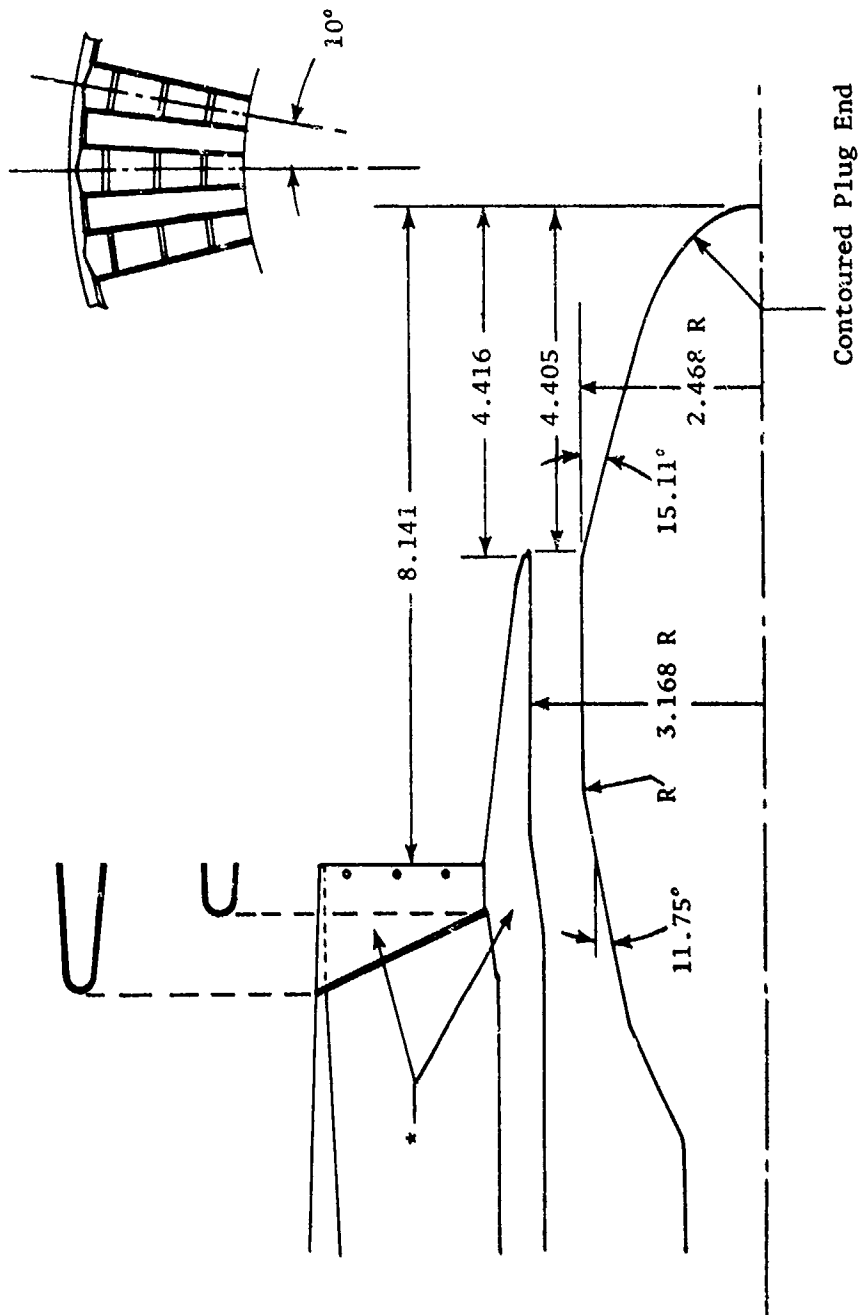


Figure A-16. Model 22 - 36-Chute,  $AR = 2.5$ ,  $R_T^0 = 0.653$  Outer Suppressor;  $A_0/A_i = 1.92$ ,  $R_i^1 = 0.779$  Inner Plug, Retracted.

\* See Model 16, Figure A-10 for Dimensions of Chute Suppressor

• All Dimensions in Inches

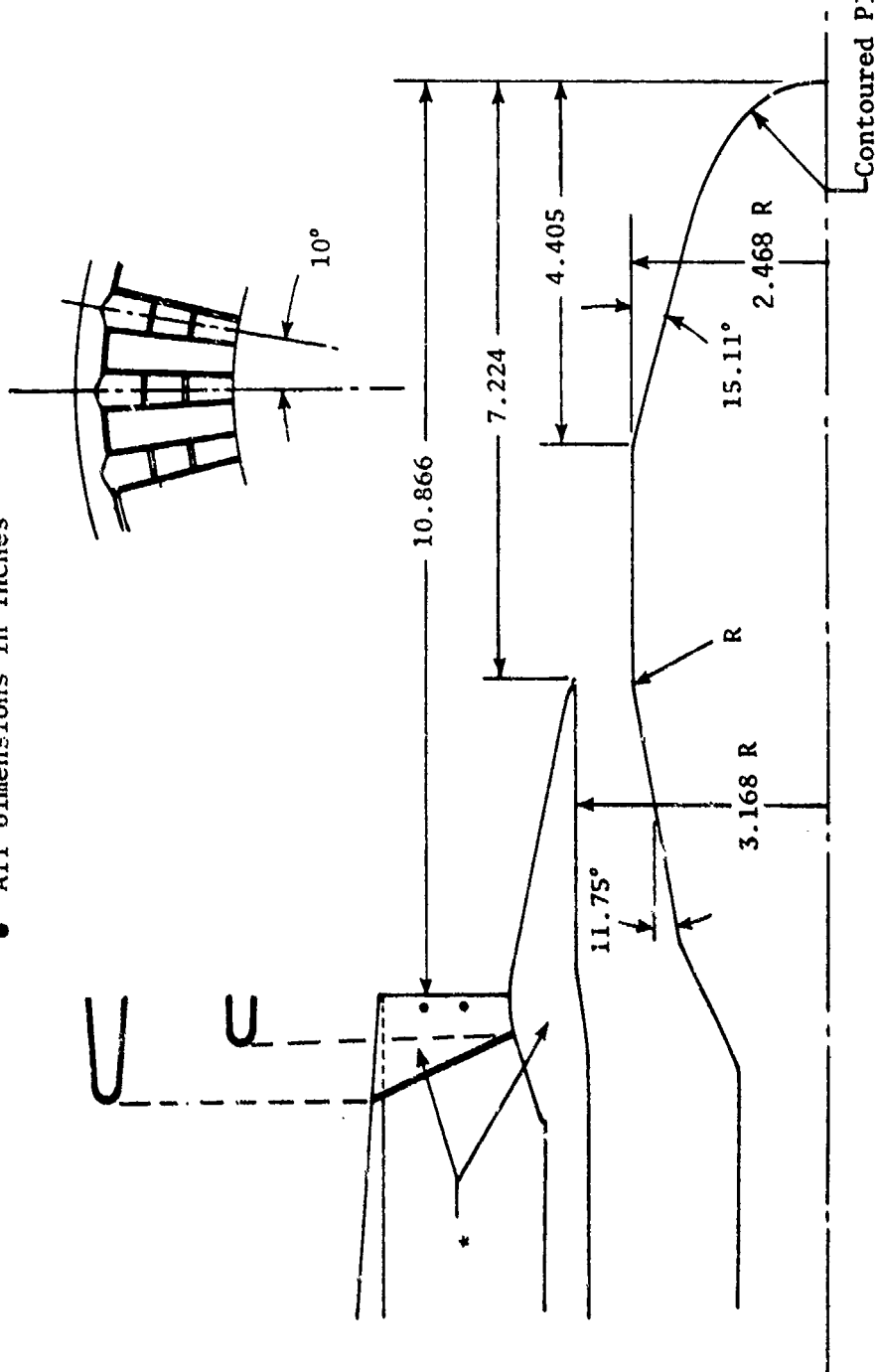


Figure A-17. Model 23 - 36-Chute,  $AR = 2.0$ ,  $R^O = 0.716$  Outer Suppressor;  $A_0/A_1 = 1.92$ ,  $R^I = 0.779$  Inner Plug, In-Line.

• All Dimensions in Inches

\* See Model 16, Figure A-10, for Dimensions of Chute Suppressor

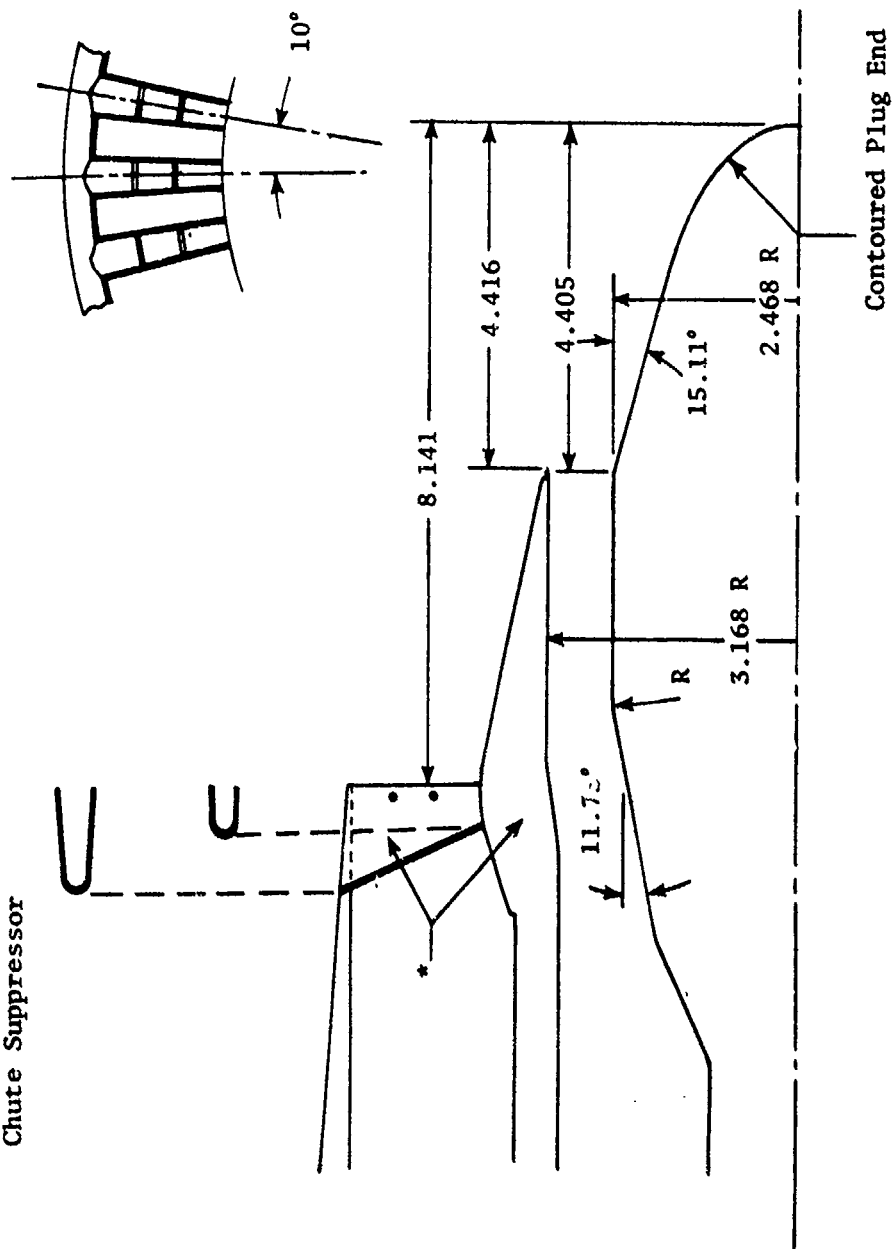


Figure A-18. Model 24 - 36-Chute, AR = 2.0,  $R_o^o = 0.716$  Outer Suppressor;  $A_o/A_i = 1.92$ ,  $R_i^1 = 0.779$  Inner Plug, Retracted.

- All Dimensions in Inches

\* See Model 16, Figure A-10, for Dimensions of Chute Suppressor

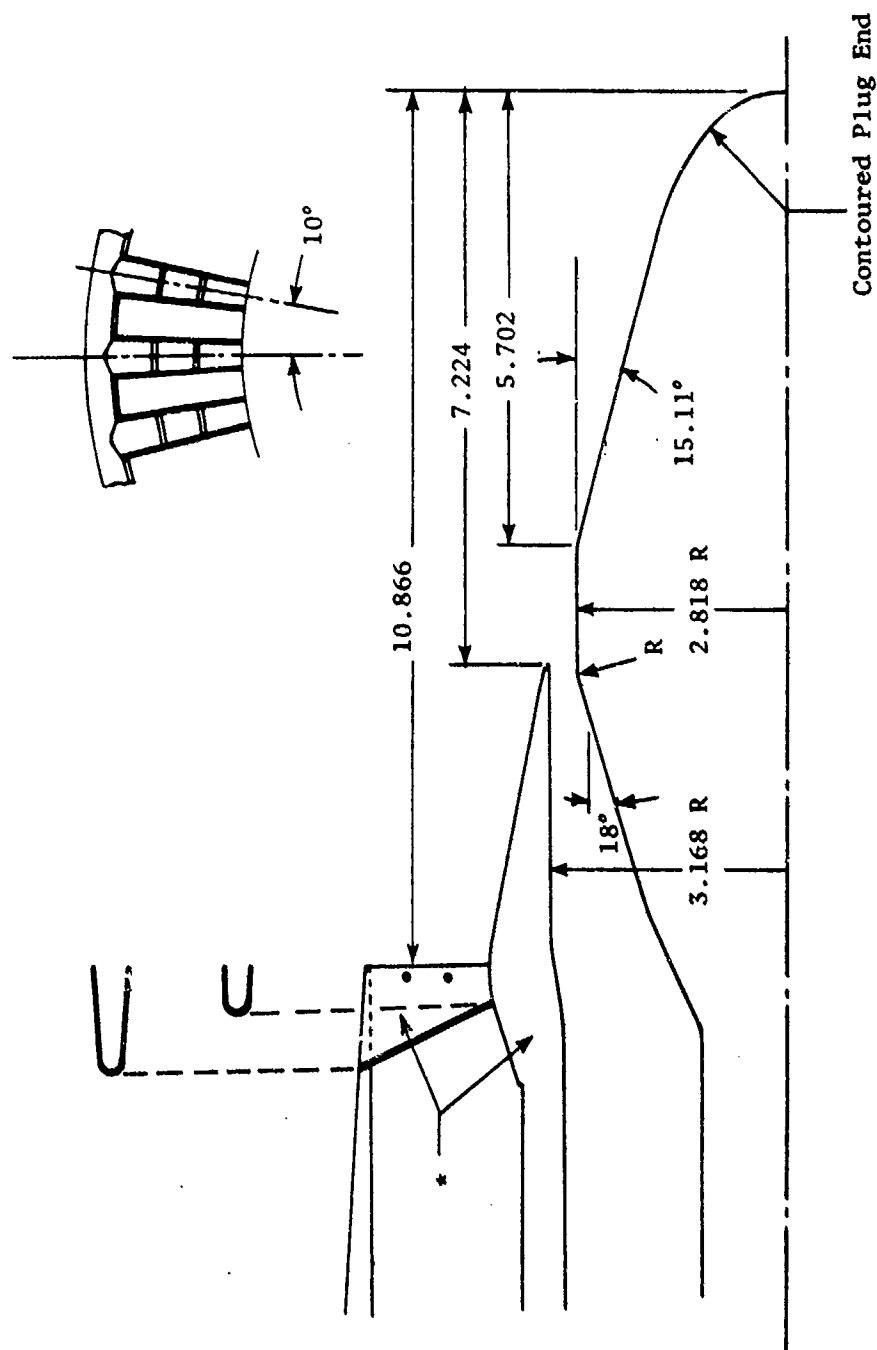


Figure A-19. Model 25 - 36-Chute,  $AR = 2.0$ ,  $R_o^o = 0.716$  Outer Suppressor;  
 $A_o/A_i = 3.61$ ,  $R_i^i = 0.89$  Inner Plug, In-Line.

• All Dimensions in Inches

\* See Model 16, Figure A-10, for Dimensions of Chute Suppressor

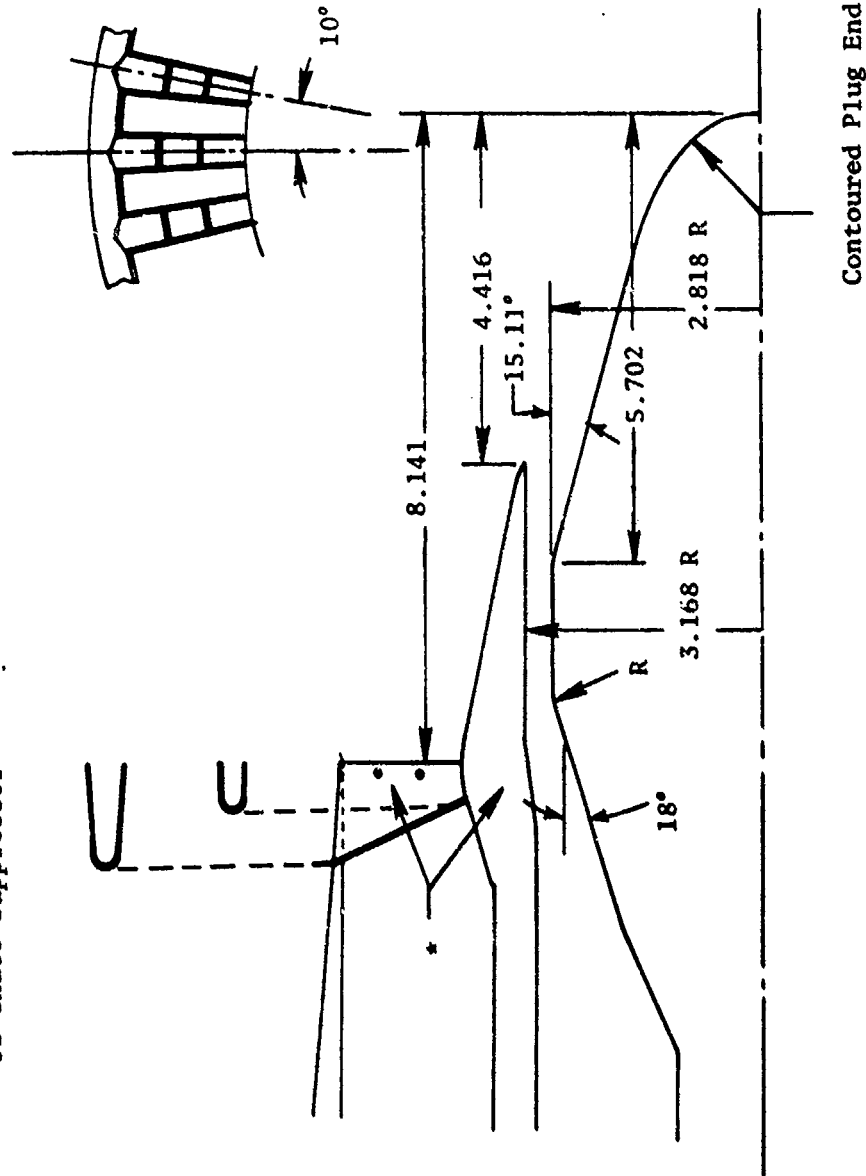


Figure A-20. Model 26 - 36-Chute,  $AR = 2.0$ ,  $R^0 = 0.716$  Outer Suppressor;  
 $A_0/A_1 = 3.61$ ,  $R_1^0 = 0.89$  Inner Plug, Retracted.

• All Dimensions in Inches

• See Model 17, Figure A-11, for Dimensions of Chute Suppressor

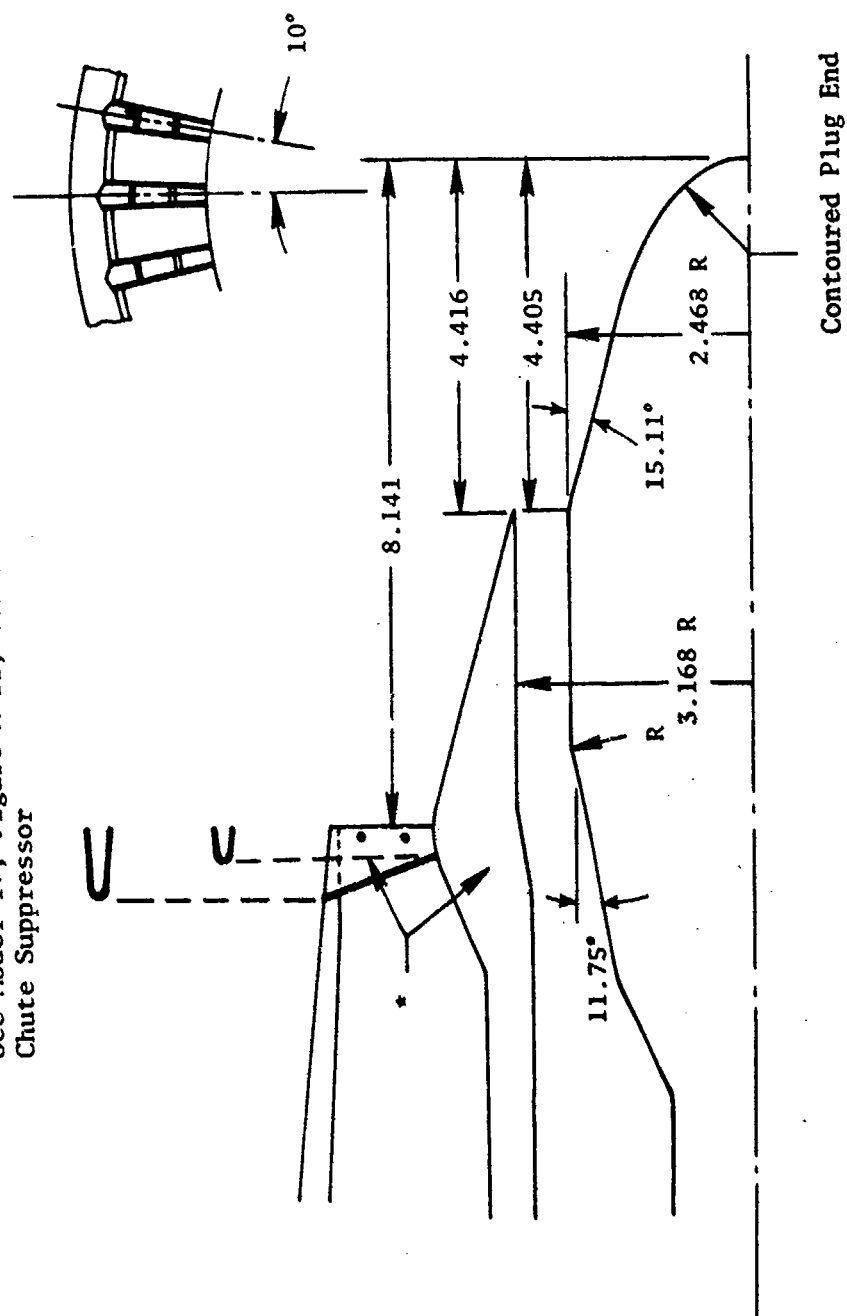


Figure A-21. Model 27 - 36-Chute,  $AR = 1.5$ ,  $R^O = 0.782$  Outer Suppressor;  
 $A_o/A_i = 1.92$ ,  $R_i^i = 0.779$  Inner Plug, Retracted.

• All Dimensions in Inches

\* See Model 18, Figure A-12, for Dimensions of Spoke Suppressor

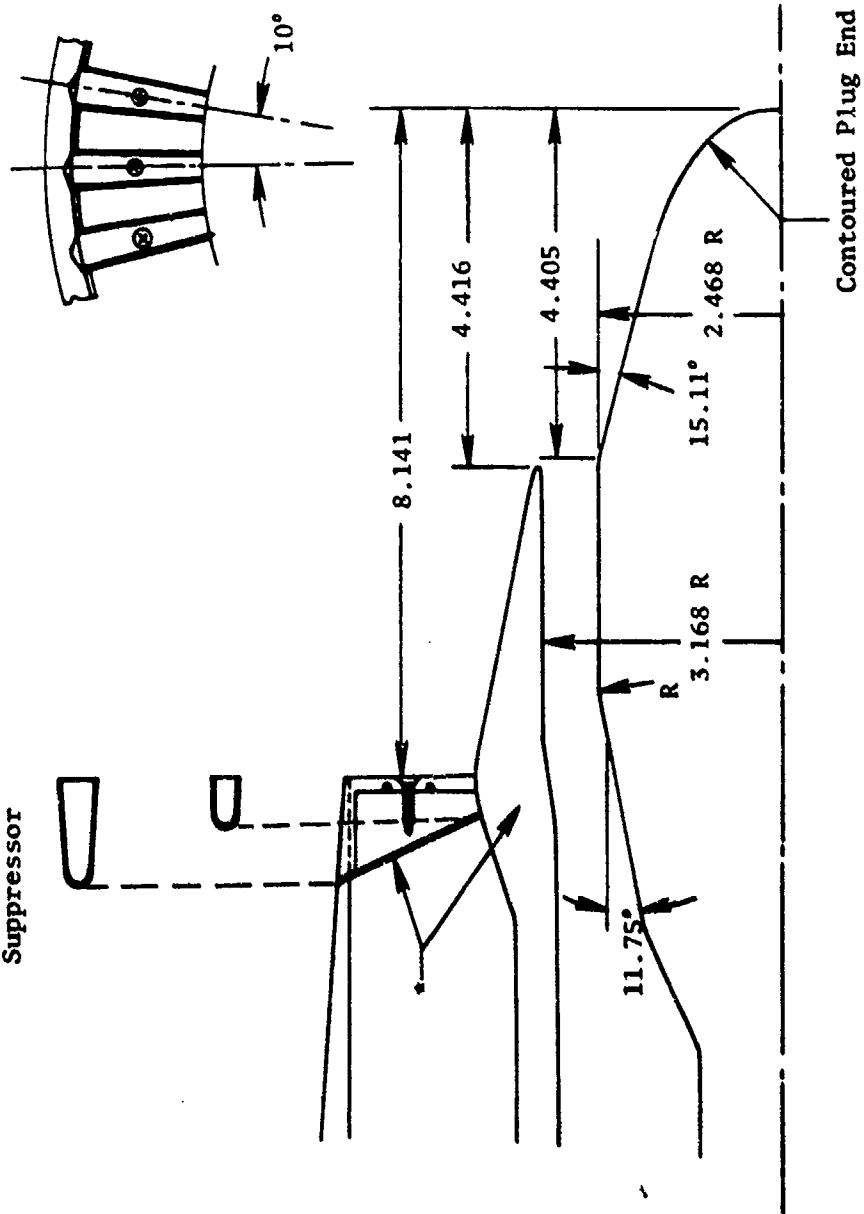


Figure A-22. Model 28 - 36-Spoke,  $AR = 2.0$ ,  $R_o^0 = 0.716$  Outer Suppressor;  $A_o/A_i = 1.92$ ,  $R_i^1 = 0.779$  Inner Plug, Retracted.

• All Dimensions in Inches

\* See Model 18, Figure A-12, for Dimensions of Spoke Suppressor

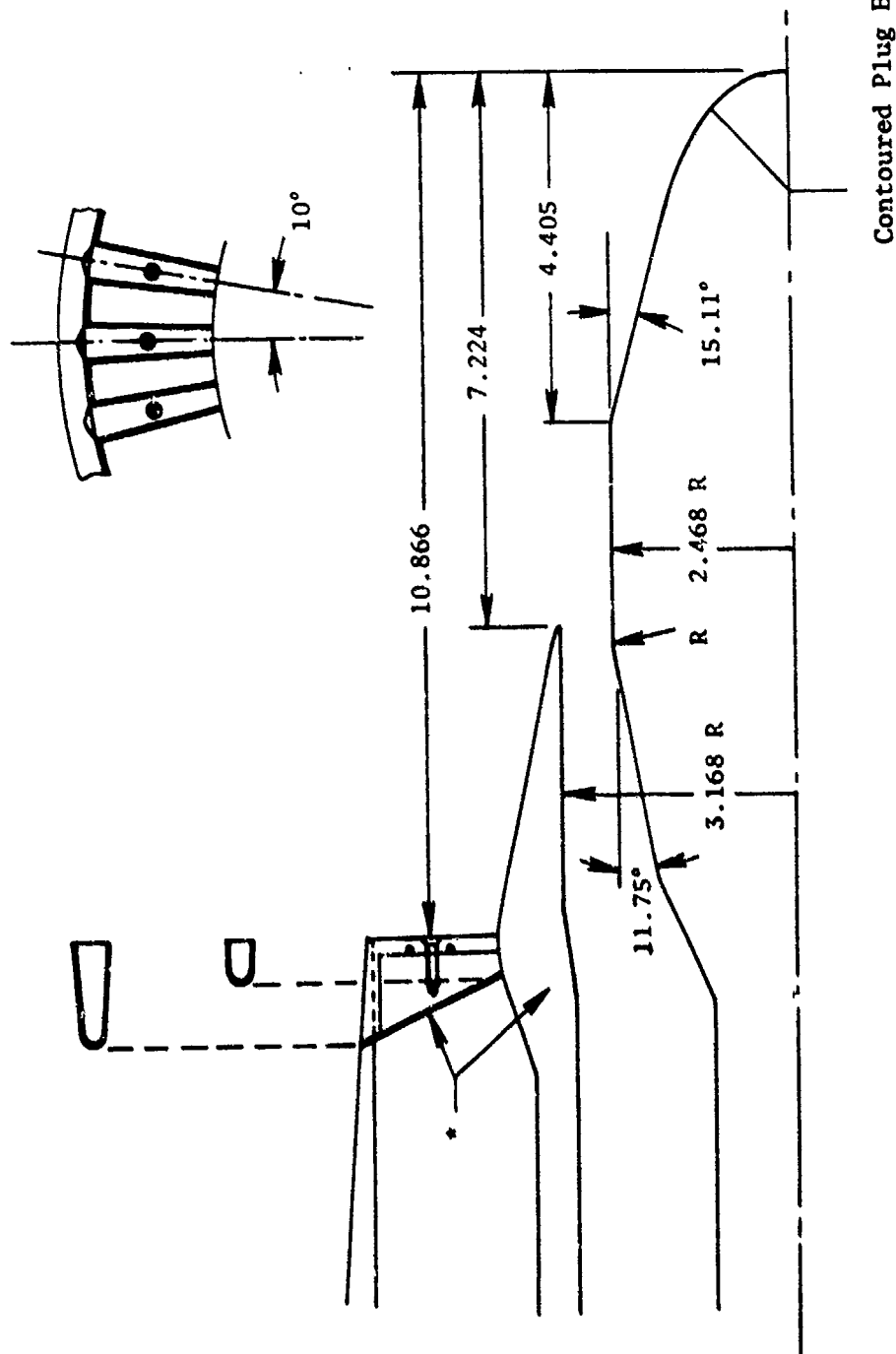
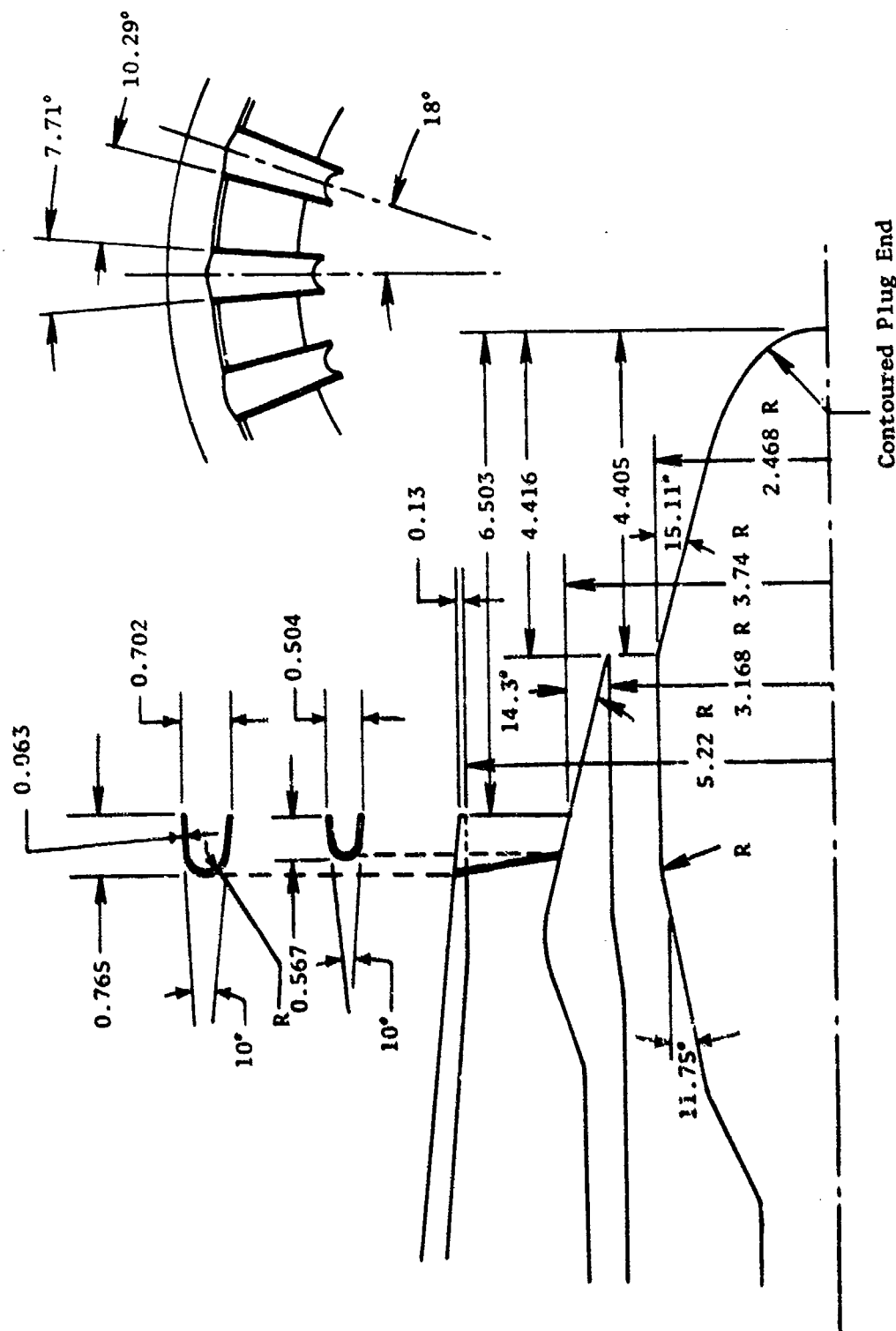


Figure A-23. Model 29 - 36-Spoke,  $AR = 2.0$ ,  $R_T^O = 0.716$  Outer Suppressor;  
 $A_O/A_i = 1.92$ ,  $R_T^I = 0.779$  Inner Plug, In-Line.



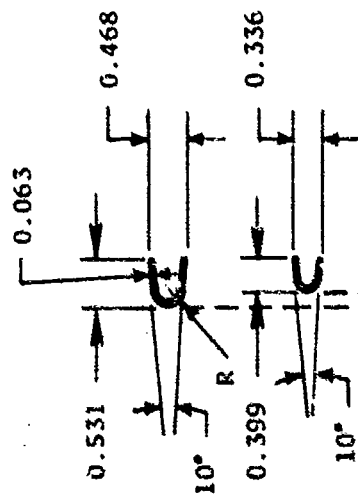
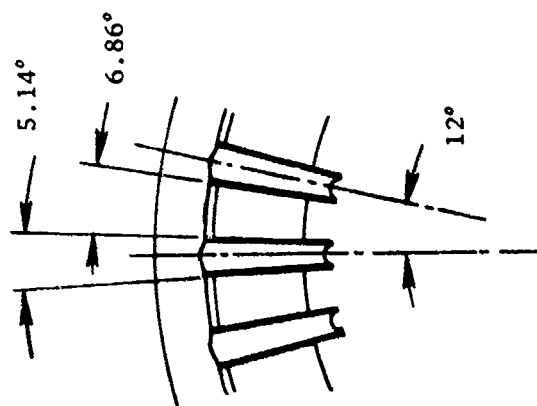
• All Dimensions in Inches



Contoured Plug End

Figure A-24. Model 30 - 20-Shallow-Chute;  $AR = 1.75$ ,  $R_o^o = 0.717$  Outer Suppressor;  $A_o/A_i = 1.92$ ,  $R_i = 0.779$  Inner Plug, Retracted.

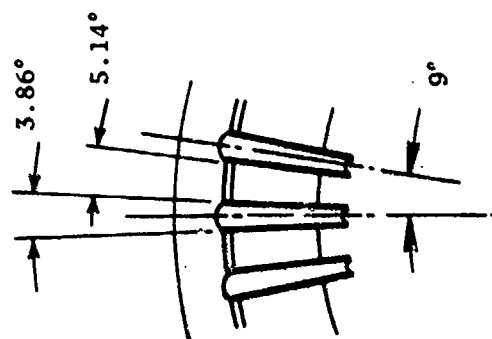
• All Dimensions in Inches



See Model 30, Figure A-24,  
for Dimensions

Figure A-25. Model 31 - 30-Shallow-Chute,  $AR = 1.75$ ,  $R_o^0 = 0.717$  Outer Suppressor;  
 $A_o/A_i = 1.92$ ,  $R_i^1 = 0.779$  Inner Plug, Retracted.

• All Dimensions in Inches



See Model 30, Figure A-24,  
for Dimensions

Figure A-26. Model 32 - 40-Shallow-Chute, AR = 1.75,  $R^0 = 0.717$  Outer Suppressor;  
 $A_0/A_i = 1.92$ ,  $R_i = 0.779$  Inner Plug, Retracted.

• All Dimensions in Inches

• Model From NASA-Lewis/GE DBTF Program.  
Contract NAS3-18008

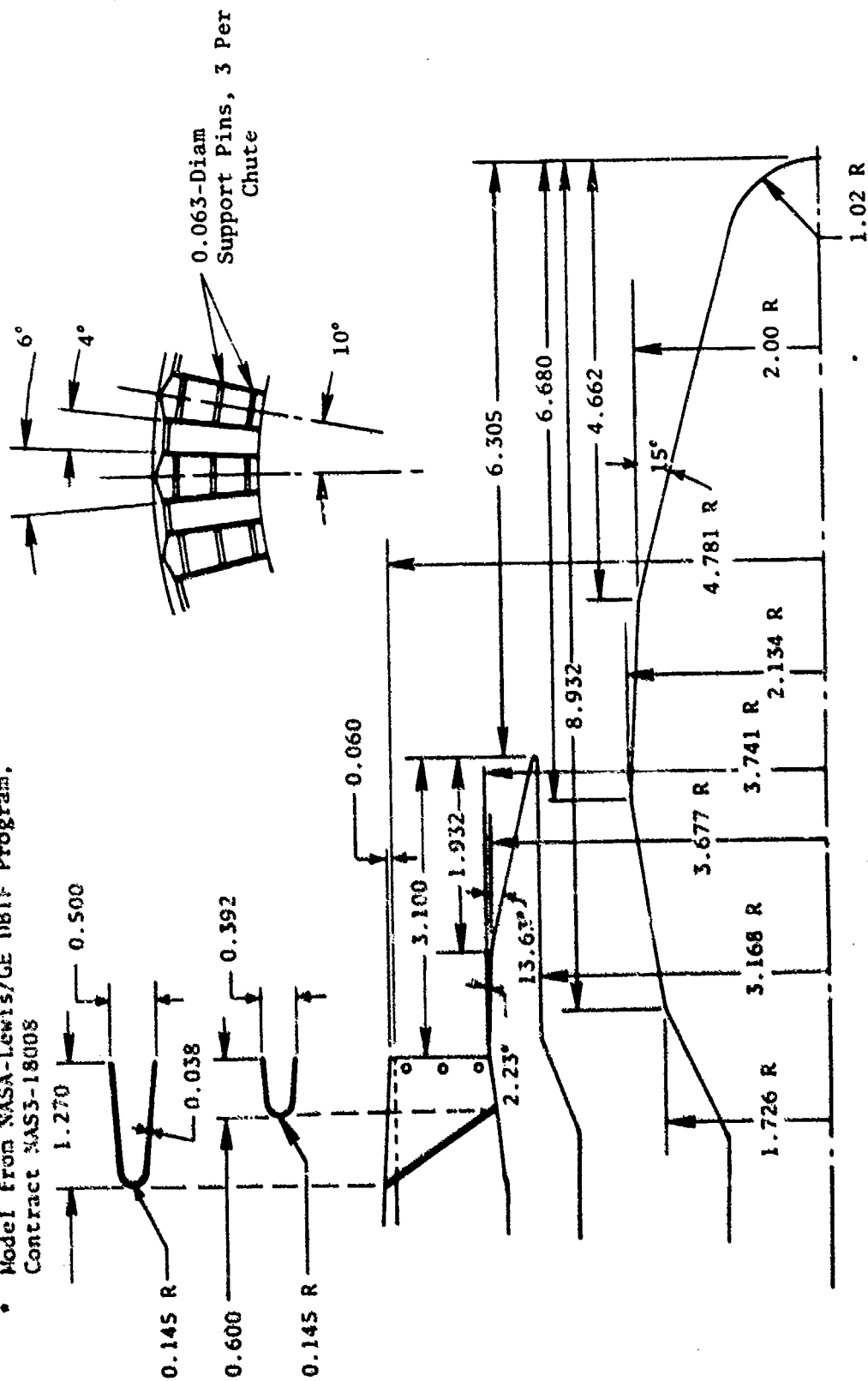


Figure A-27. • Model 33 - 36-Chute, AR = 2.5,  $R_o^o = 0.783$  Outer Suppressor;  
 $A_o/A_i = 0.65$ ,  $R_i^i = 0.674$  Inner Plug, Retracted.

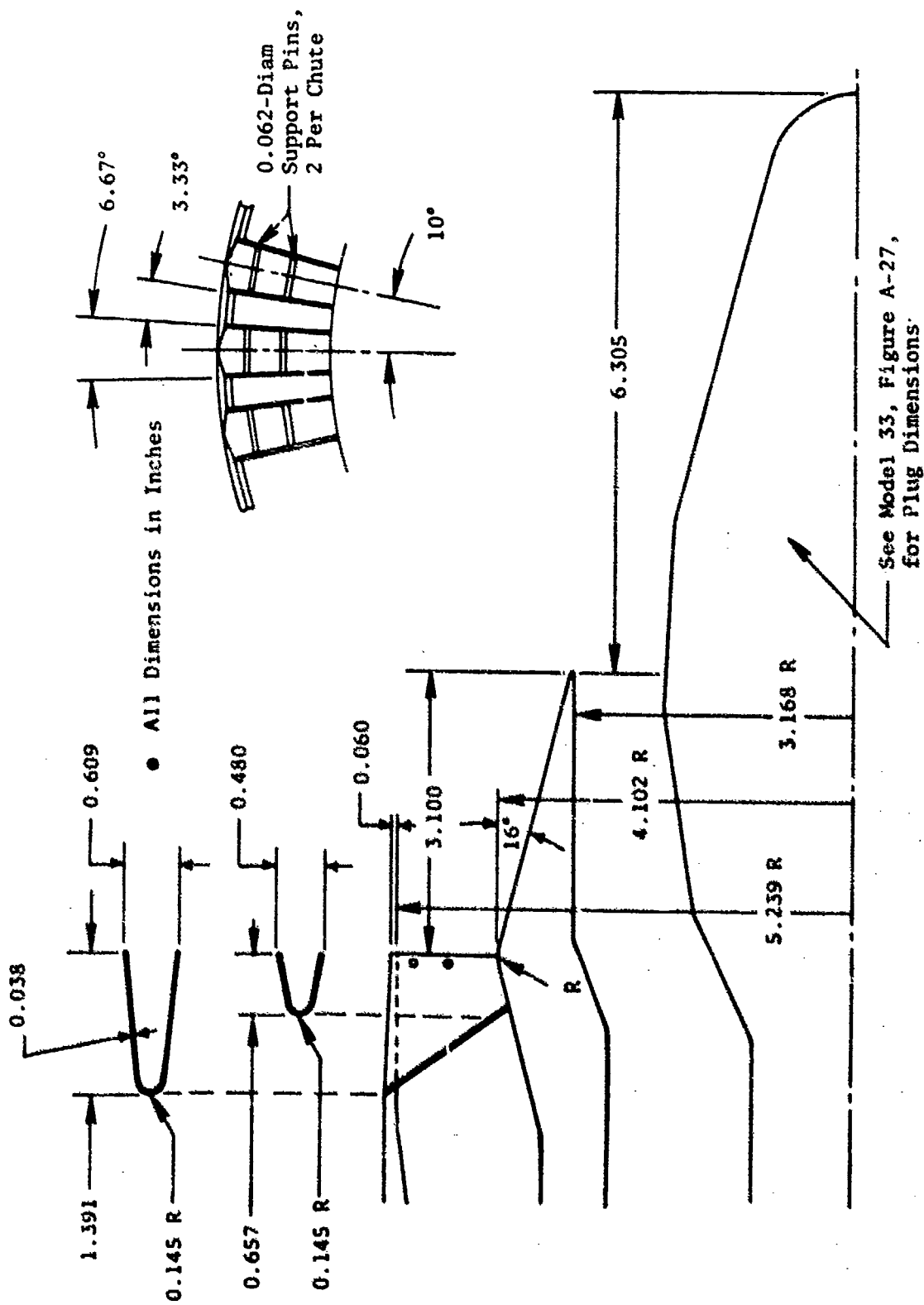
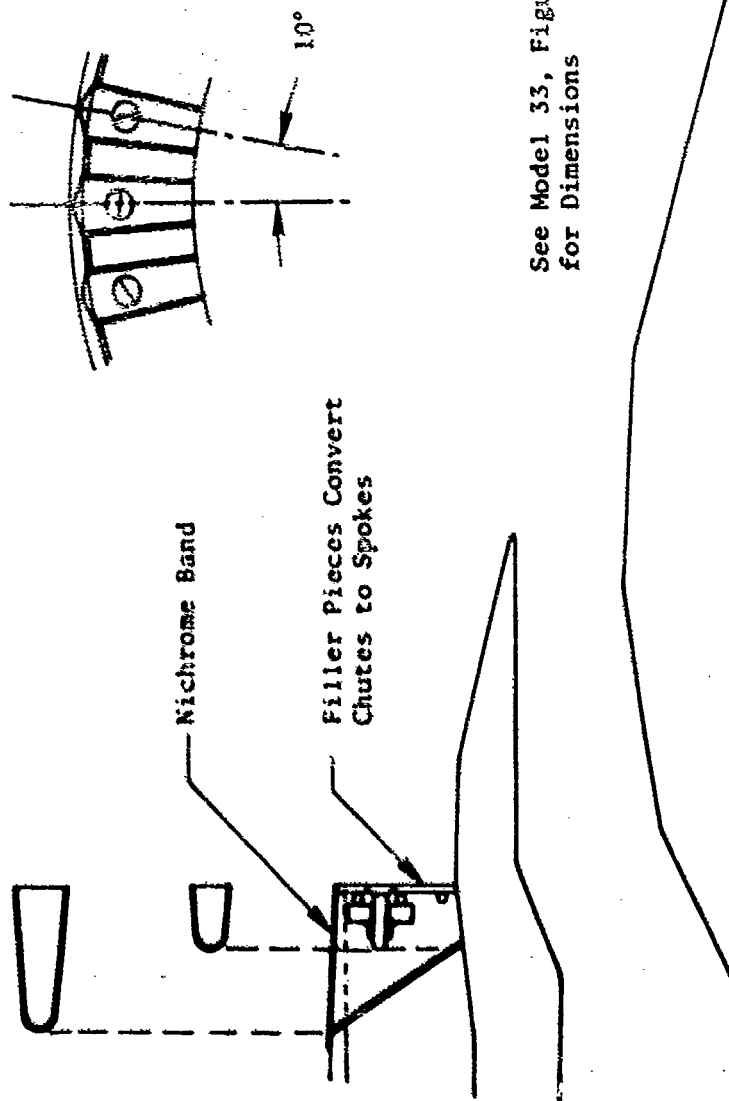


Figure A-28. Model 34 - 36-Chute,  $AR = 3.0$ ,  $R_0^0 = 0.783$  Outer Suppressor;  $A_0/A_1 = 0.65$ ,  $R_1^1 = 0.674$  Inner Plug, Retracted.



See Model 33, Figure A-27,  
for Dimensions

Figure A-29. Model 35 - 36-Spoke, AR = 2.5,  $R^O = 0.783$  Outer Suppressor;  
 $A_O/A_i = 0.65$ ,  $R_i^I = 0.674$  Inner Plug, Retracted.

• All Dimensions in Inches

• See Model 16, Figure A-10, for Dimensions of Chute Suppressor

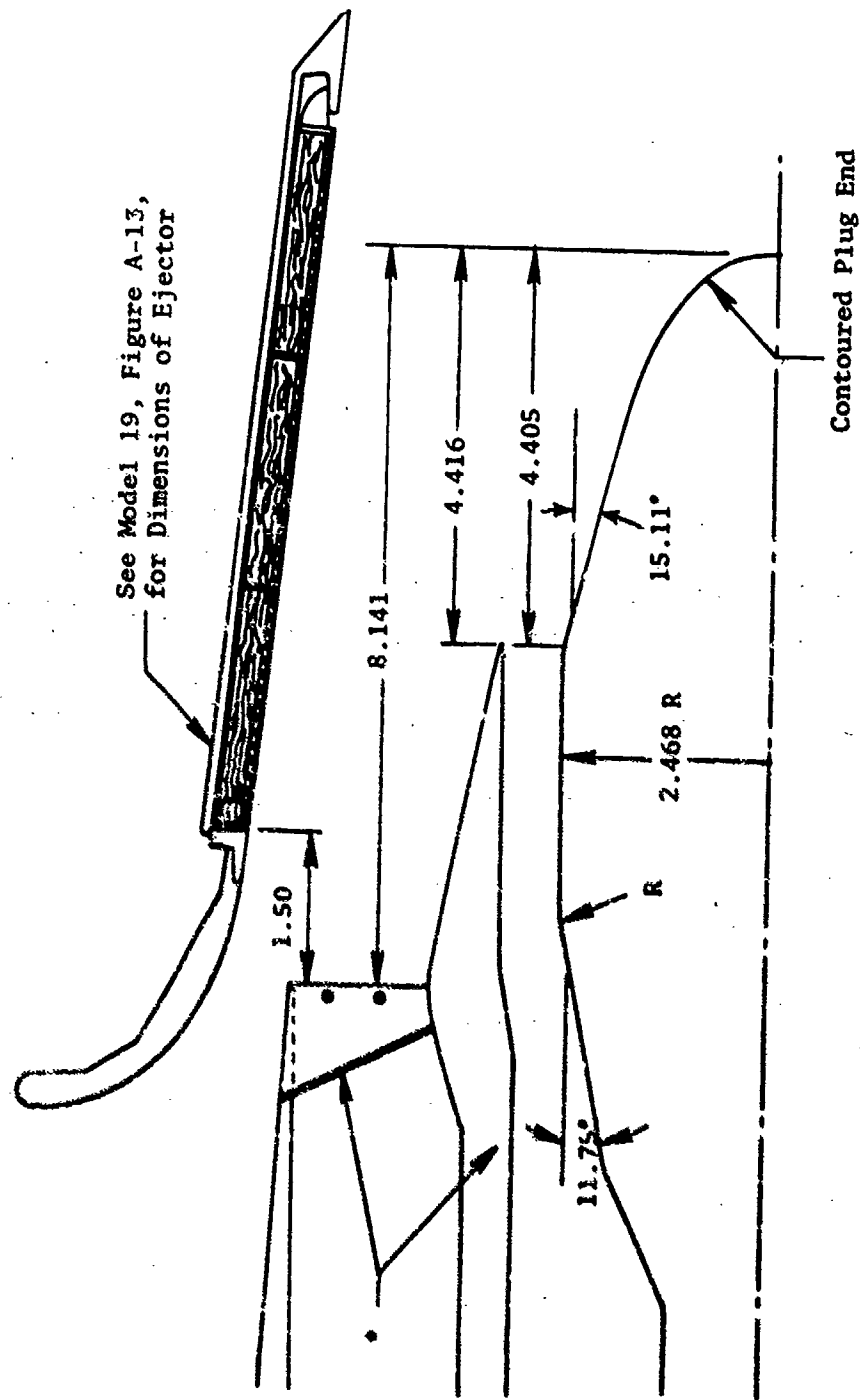


Figure A-30. Model 36 - 36-Chute,  $AR = 2.0$ ,  $R^0 = 0.716$  Outer Suppressor;  
 $A/A_1 = 1.92$ ,  $R_1 = 0.779$  Inner Plug, Retracted with  
Acoustically Treated Ejector.

• All Dimensions in Inches

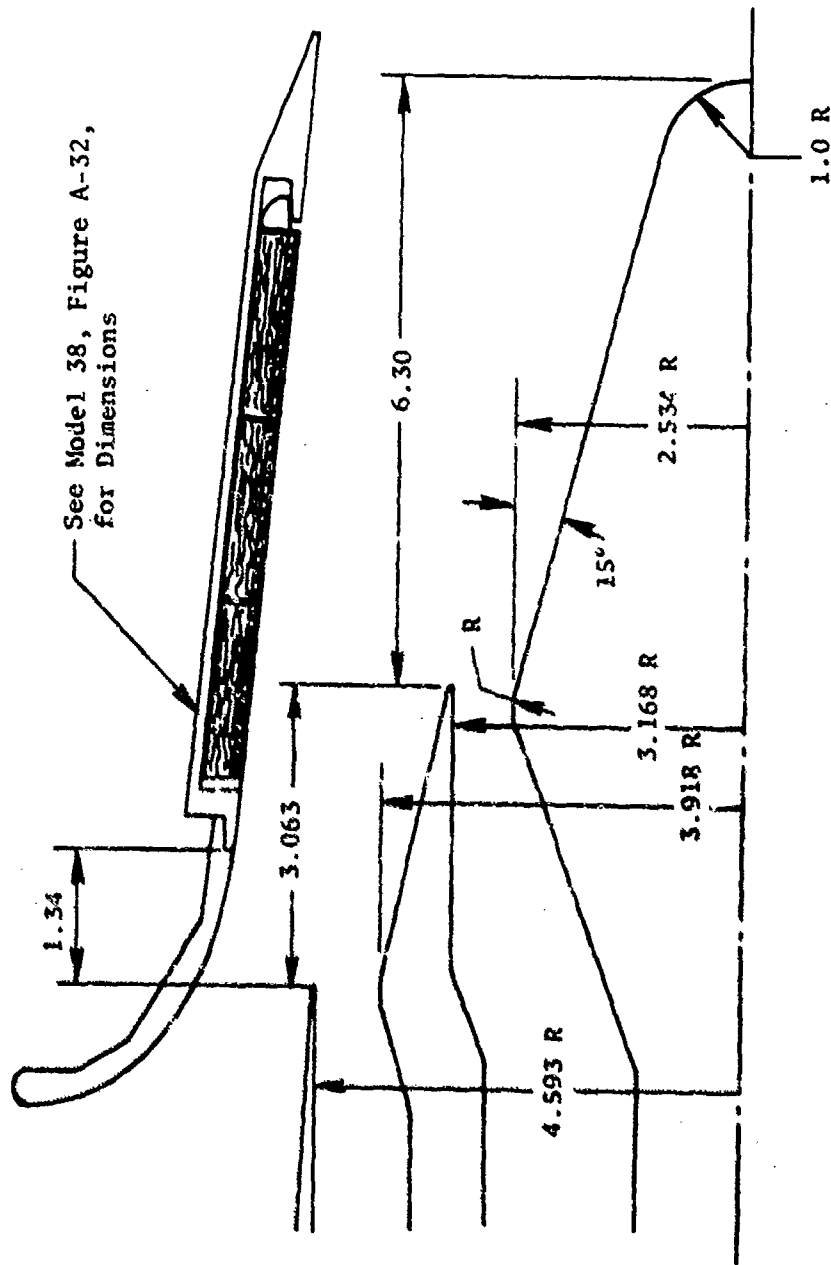


Figure A-31. Model 37 - Conmular-Noncoplanar Dual-Plug Nozzle,  
 $RO = 0.853$ ,  $A/A_i = 1.59$ ,  $R_i = 0.800$  with Acoustically  
 Treated Secondary Ejector.



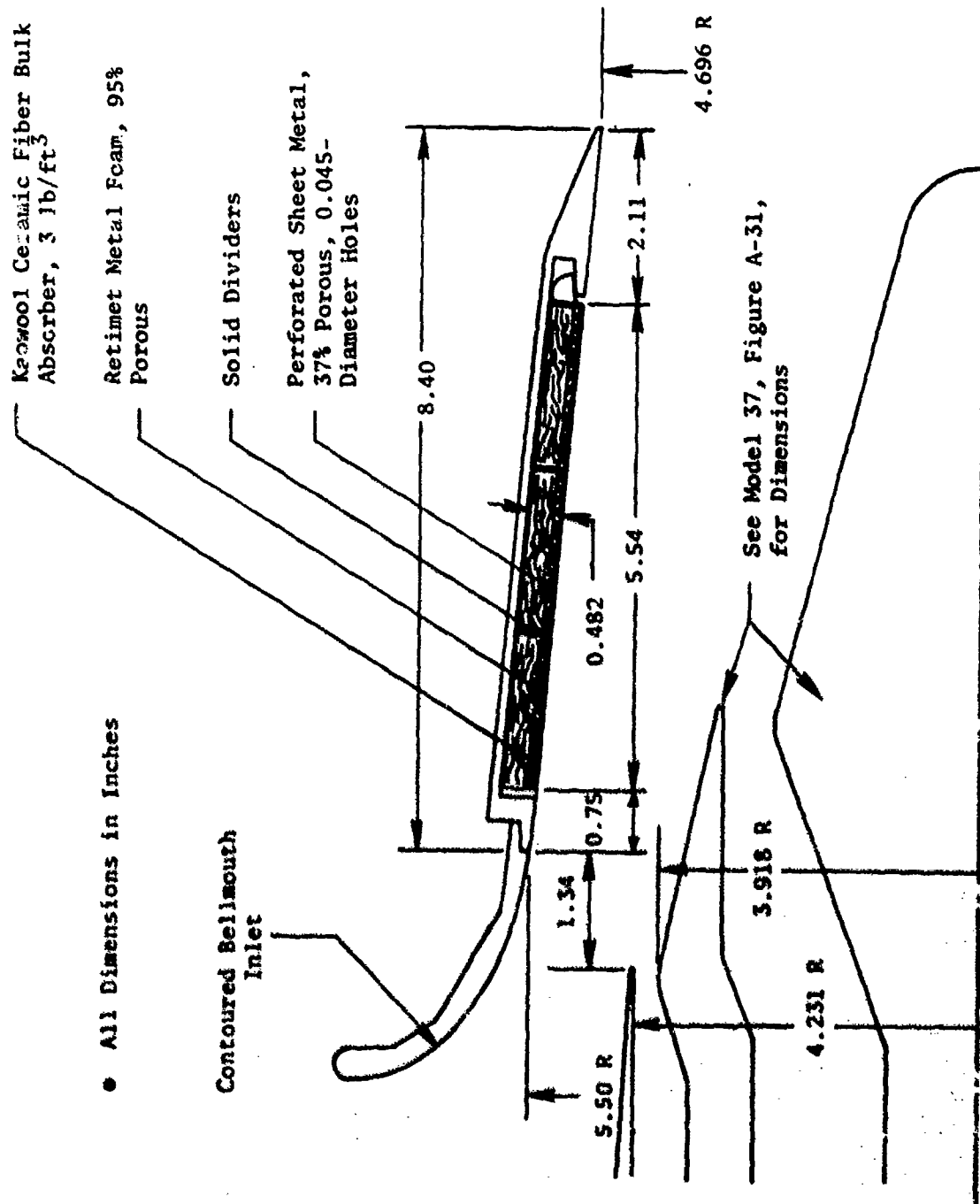


Figure A-52. Model 38 - Coannular-Noncoplanar Dual-Plug Nozzle,  $R_n^0 = 0.926$ ,  $A_0/A_i = 0.71$ ,  $R_i^0 = 0.800$  with Acoustically Treated Secondary Ejector.

• All Dimensions in Inches

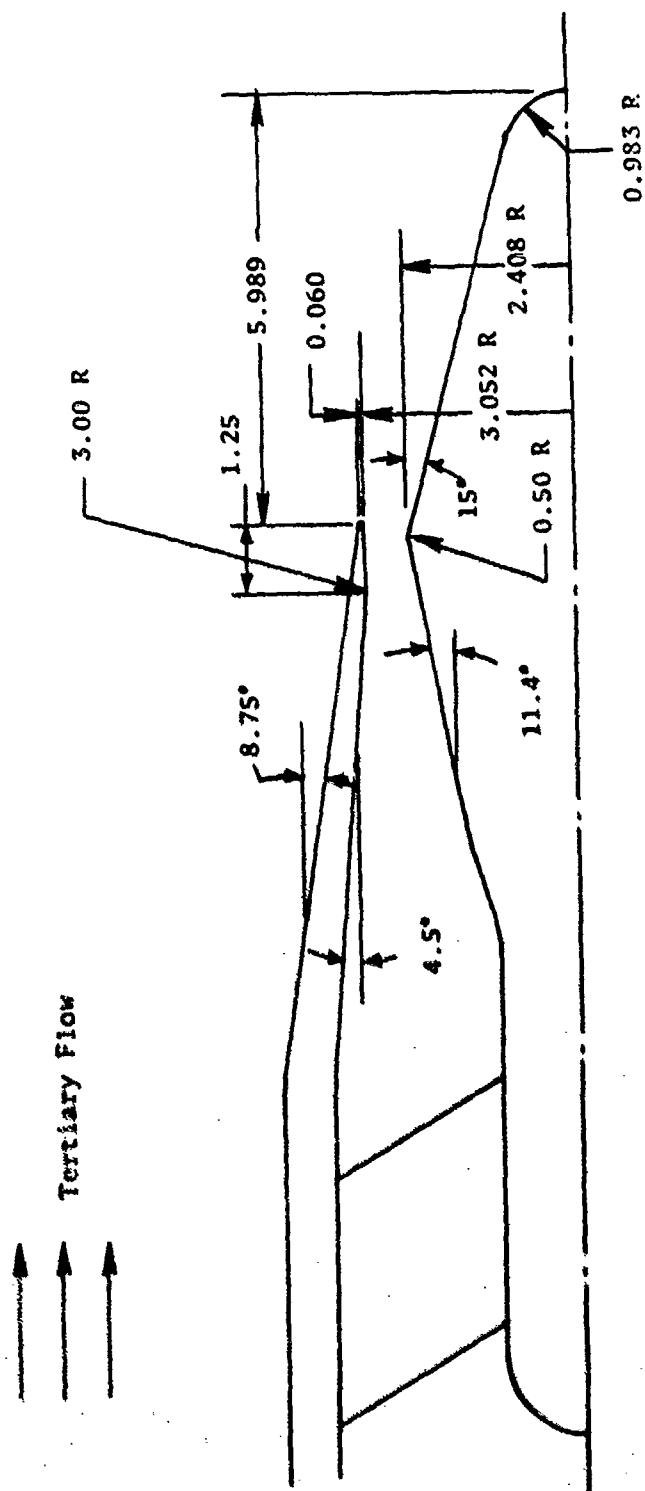


Figure A-33. Model 39 - Converging Plug, Single-Flow,  $R_r = 0.789$ .

• All Dimensions in Inches

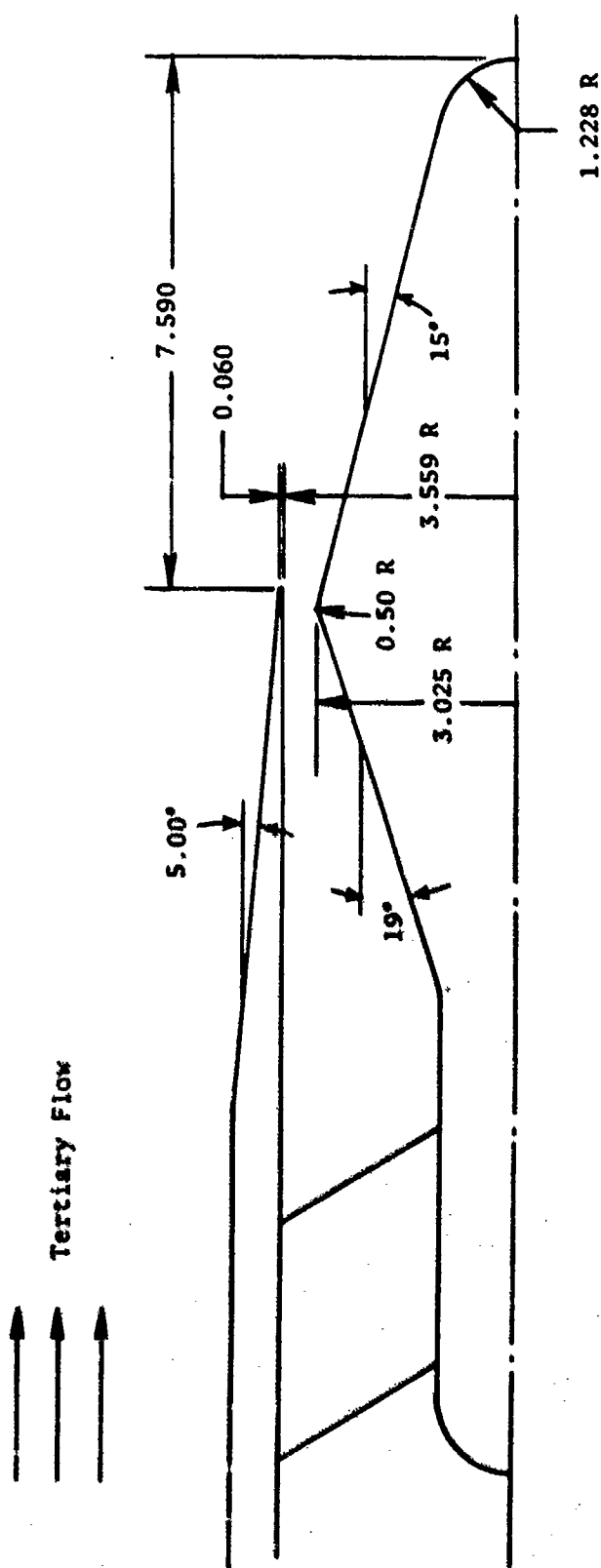


Figure A-34. Model 40 - Converging Plug, Single-Flow,  $R_r = 0.85$ .

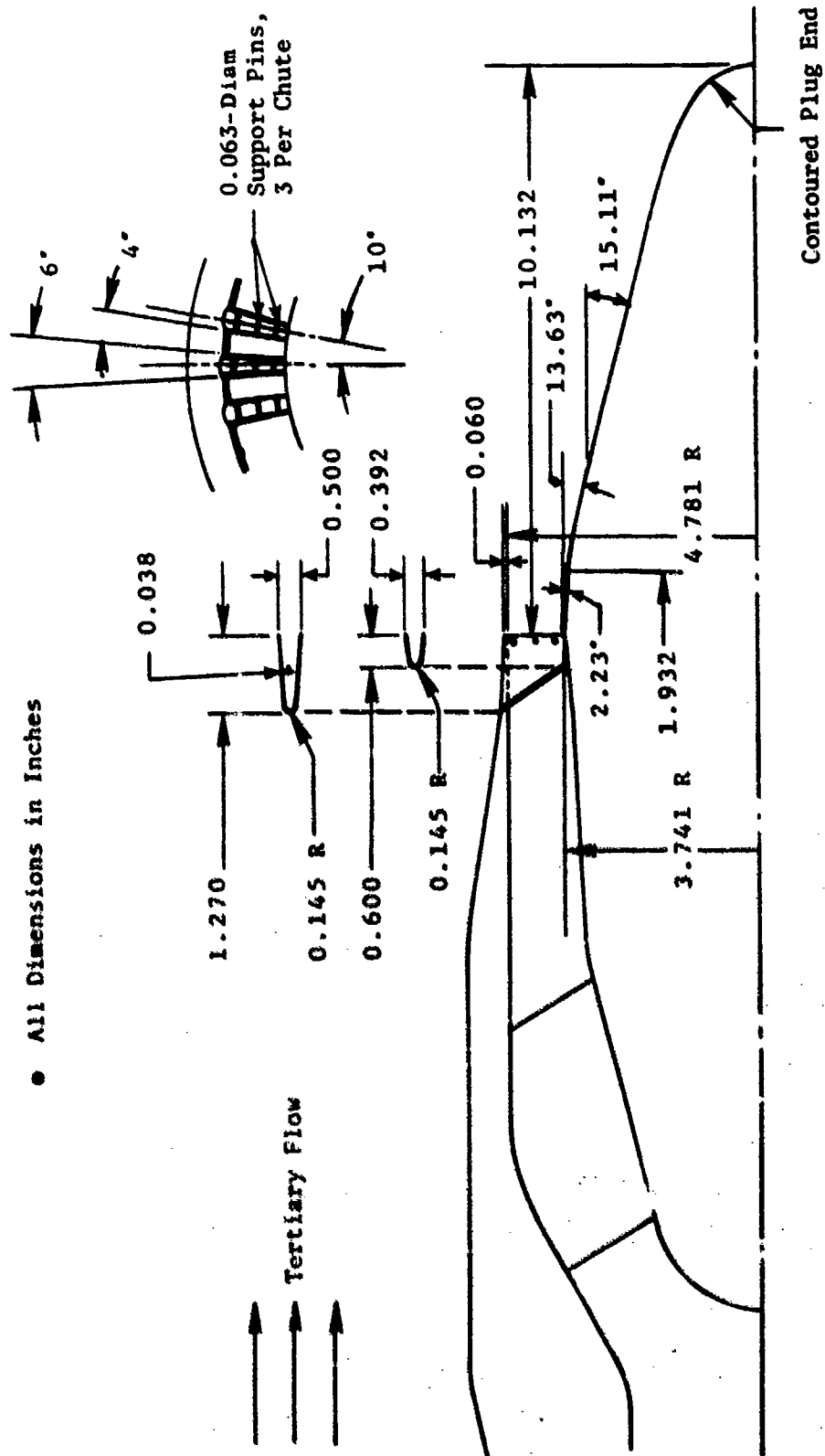


Figure A-35. Model 41 - 36-Chute,  $AR = 2.5$ ,  $R_T = 0.78$  Turbojet.

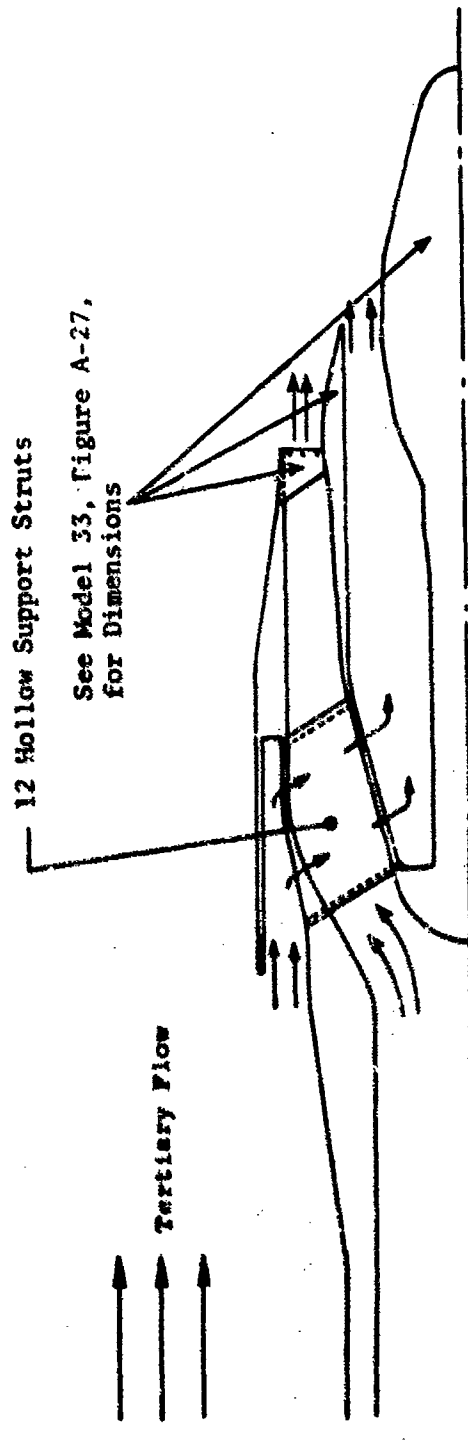


Figure A-36. Model 42 - 36-Chute,  $AR = 2.5$ ,  $R_o^0 = 0.78$  Outer Suppressor with Induced Flow Through  $A_o/A_i = 0.65$ ,  $R_i^1 = 0.674$  Inner Plug, Retracted.

See Model 33, Figure A-27,  
for Dimensions

↑  
↑  
↑  
Tertiary Flow

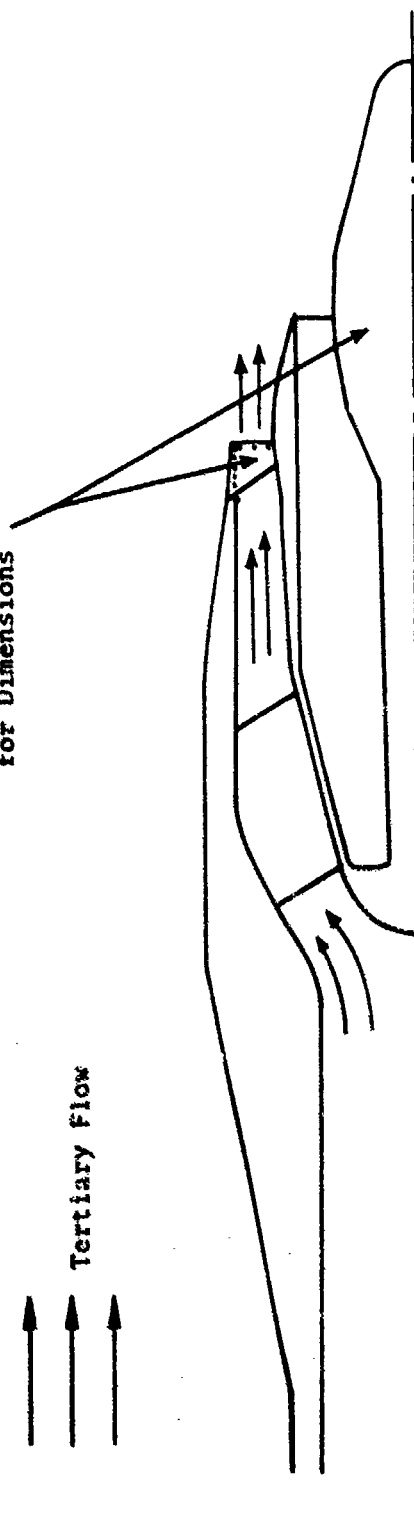


Figure A-37. Model 43 - 36-Chute,  $AR = 2.5$ ,  $R^0 = 0.78$  Outer Suppressor with Abrupt Step Over  $A_0/A_i = 0.65$ ,  $R_I^1 = 0.674$  Inner Plug, Retracted.

• All Dimensions in Inches

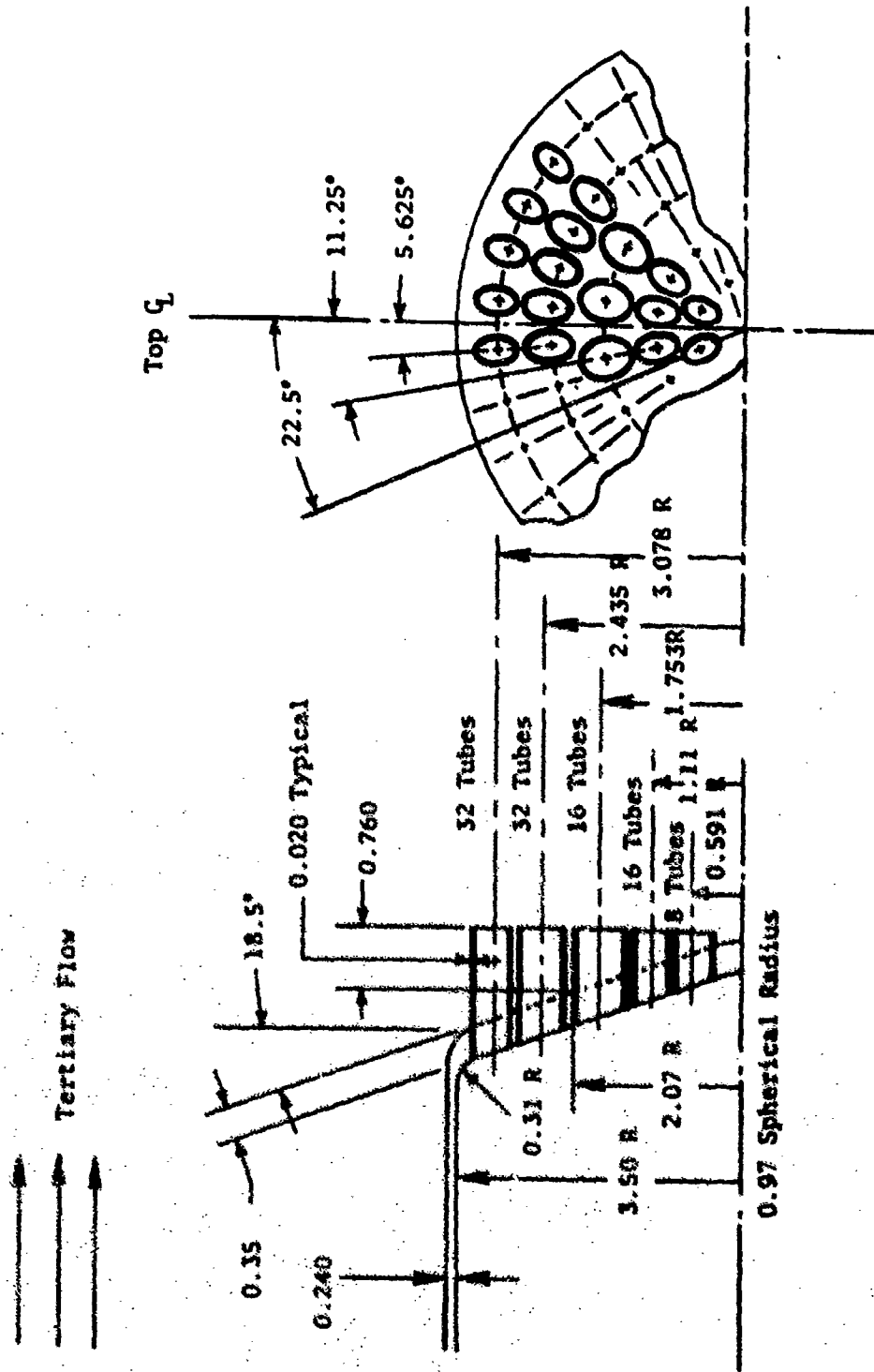


Figure A-38. Model 44 - 104 Elliptical Tubes, AR = 2.8.

• All Dimensions in Inches

Filler Plate Added to Model 44;  
See Model 44 for Basic Dimensions

→ Tertiary Flow

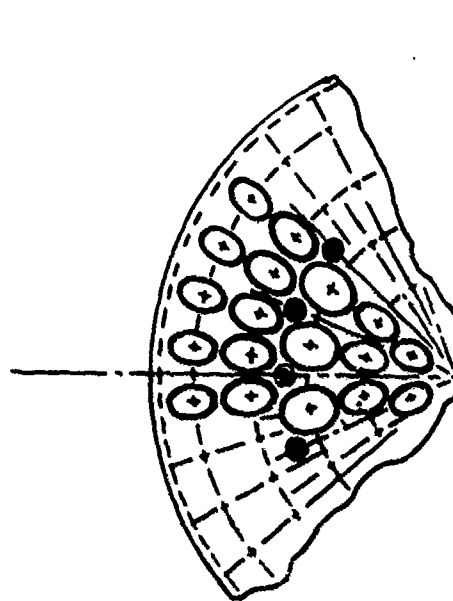
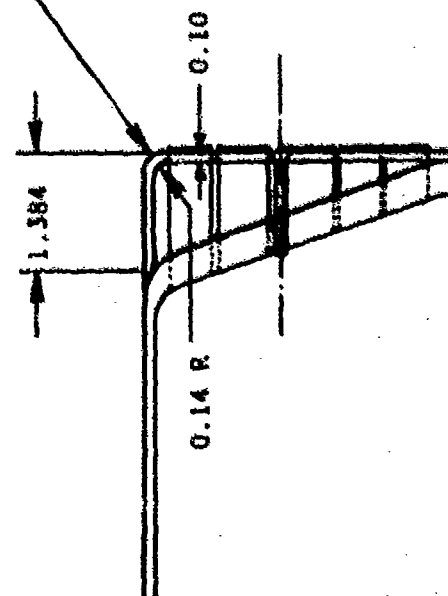


Figure A-39. Model 45 - 104 Elliptical Holes, AR = 2.8.



Tertiary Flow

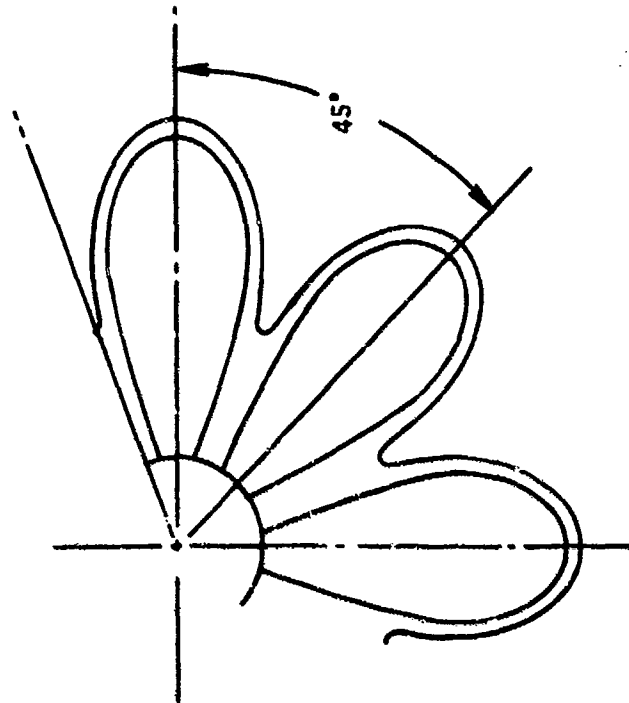
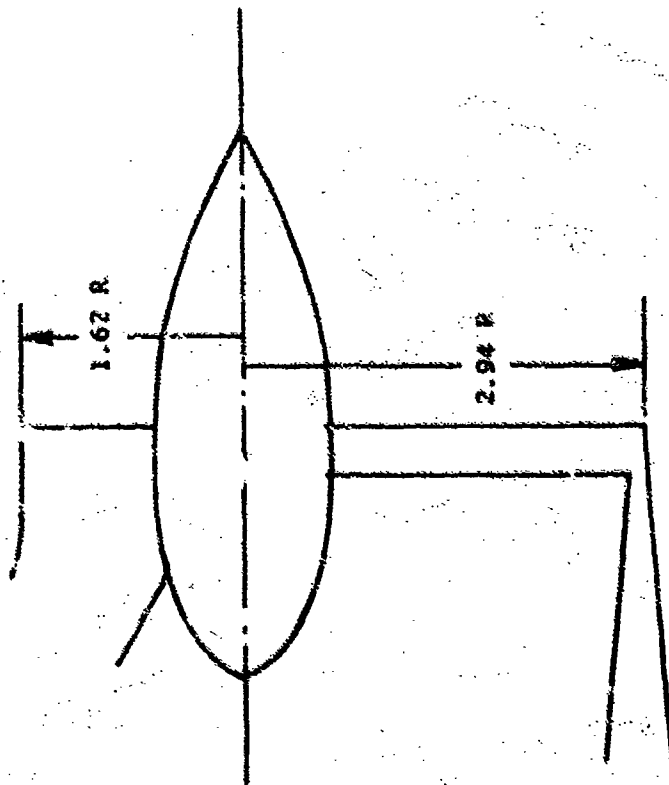


Figure A-40. Model 46 - 8-Lobe Daisy, AR = 2.1.

• All Dimensions in Inches

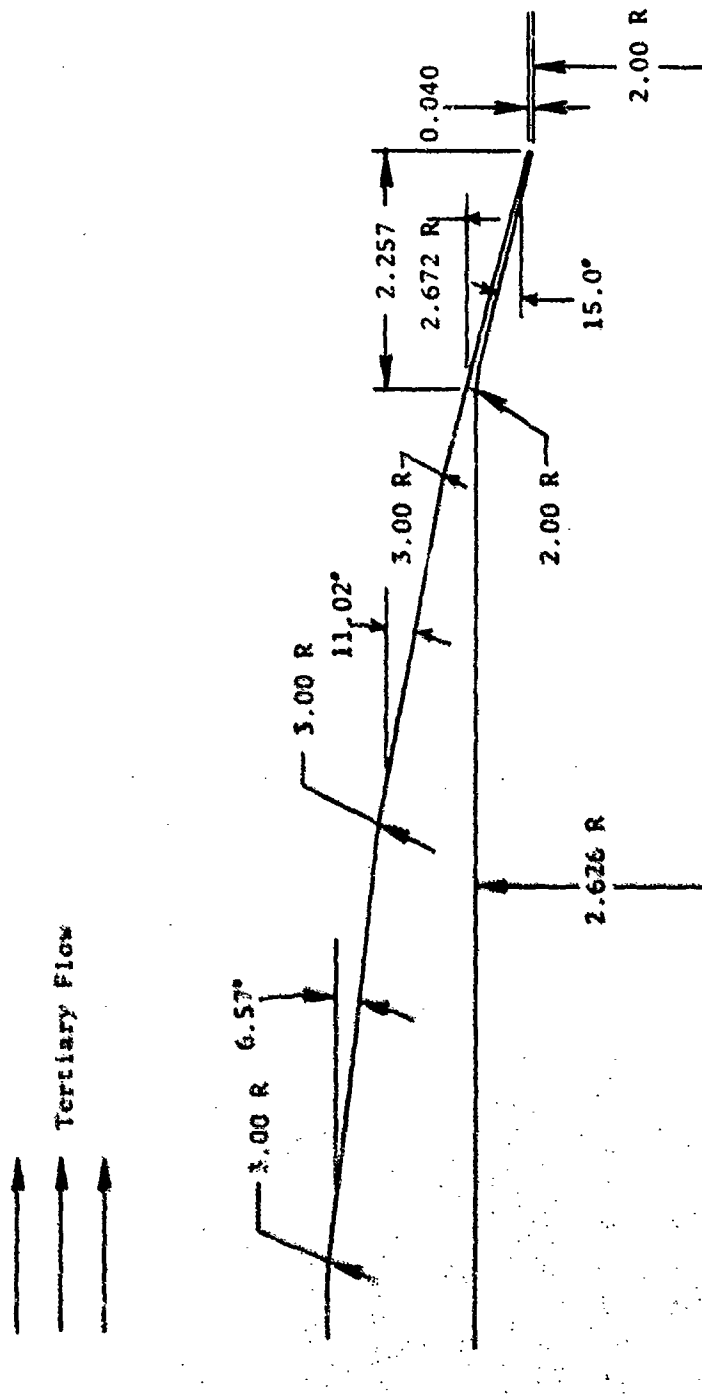


Figure A-41. Model 47 - 4.0-in.-Diameter Conical.

## APPENDIX B

### ACOUSTIC TEST MATRICES, AERODYNAMIC TEST CONDITIONS

The following tables summarize the aerodynamic cycle parameters, meteorological conditions, normalization parameters, and pertinent 2400-ft sideline acoustic data (scaled to a total flow area of 338 in.<sup>2</sup>) associated with the far-field acoustic tests in support of Task 3, "Experimental Investigation of Suppression Principles." Table numbers B-1 through B-45 correspond to the model numbers defined in Section 4.3 and Appendix A (e.g., Model 1 through model 45); Table B-46 represents Model 47.

Table B-i. Model No. 1: 4.64-inch-Diameter Conical, Adapted to JENOTS.

$A_1 = 16.82 \text{ in.}^2$  Linear Scale Factor to 335 in.  $2 = 4.48$

Data Point No.	Inner		Meteorological Conditions		Normal Parameters		2400-ft S.L. Data					
	$(P_1/P_0)_1$ ( $^{\circ}\text{K}$ )	$\frac{V_1}{V_0}$ (ft/sec)	$T_{DB}$ ( $^{\circ}\text{F}$ )	$T_{Wet}$ ( $^{\circ}\text{F}$ )	$10 \log_{10} \frac{10}{V_0}$	$10 \log_{10} \frac{410}{F_0(T_0/T_{sm})^{0.1}}$	OASPL	PNL	50°	90°	PPNL	POASPL
8201	1.798	548	1085	65	-4.38	37.8	66.3	71.4	71.7	77.5	79.2	74.8
8271	1.266	1298	1010	62	-4.29	35.5	63.6	67.2	69.9	75.1	77.6	75.1
8189	1.816	541	1452	68	1.146	43.8	91.3	96.6	93.2	100.4	100.4	93.2
8290	1.842	1290	1580	70	1.510	35.8	76.0	80.8	81.4	87.9	94.8	90.0
8231	1.592	1297	1356	79	0.972	35.5	72.0	76.5	78.3	84.5	89.4	86.3
8292	1.407	1295	1205	70	0.333	35.5	68.1	72.2	74.2	80.0	83.6	80.6
8293	1.155	1287	791	70	-1.495	35.3	58.3	60.8	64.1	67.7	69.4	66.8
8294	1.060	1288	505	70	-1.435	34.6	49.9	47.8	53.1	51.5	54.6	55.8
8295	1.752	545	1416	60	1.098	41.4	90.9	96.2	93.2	100.3	100.3	93.2
8296	1.448	1467	1333	77	0.775	34.7	70.4	74.8	76.6	82.5	87.1	83.2
8287	1.826	765	1092	70	-0.090	37.4	66.8	71.1	72.2	78.2	81.2	77.9
8298	1.523	1224	1293	77	0.649	35.8	70.0	74.4	76.4	82.4	86.8	83.6
8299	1.348	1496	1991	70	2.516	36.3	83.1	89.3	87.6	95.6	104.0	99.3
82100	2.451	1453	2099	89	2.746	37.2	86.8	93.6	90.3	98.6	105.8	100.6
82101	2.952	1497	2199	89	2.948	38.0	89.8	96.7	92.8	100.9	108.2	102.6
82102	3.322	1500	2299	89	3.139	38.8	92.0	98.5	94.9	103.0	109.8	104.1
82103	3.757	1500	2393	89	3.315	39.7	93.9	100.3	96.8	104.7	111.4	105.7
4	1.1	499	402	77	-4.43	29.2	40.0	42.9	44.9	50.0	50.9	45.6
5	1.15	501	485		-3.62	30.9	45.0	48.5	50.3	55.6	56.4	51.2
6	1.231	502	590		-2.77	32.6	50.4	54.2	56.2	61.0	62.0	57.2
7	1.346	503	703		-1.84	34.6	56.0	60.2	61.6	66.9	67.9	63.2
8	1.444	503	790		-1.50	35.4	59.8	64.2	65.8	71.6	72.5	67.1
9	1.632	504	890		-1.0	36.6	63.7	68.5	69.7	76.0	76.9	71.7
10	1.853	506	991		-0.5	37.7	69.6	72.8	73.1	79.6	81.0	76.3
11	2.516	507	1187		0.27	40.2	84.6	90.3	85.9	93.5	93.5	87.8
12	2.959	510	1278		0.59	4.5	90.9	96.3	93.3	100.9	100.9	93.8
13	1.046	993	390		-4.5	32.0	40.6	38.7	45.7	46.5	47.0	46.8
14	1.074	1001	494		-3.5	33.4	46.0	46.5	51.8	54.9	55.6	53.2
15	1.283	999	909		-0.9	35.8	61.3	65.5	68.2	73.7	75.9	72.7
16	1.355	1001	1001		-0.47	36.1	64.0	68.3	70.9	76.6	80.1	76.6
17	1.829	999	1386		0.94	37.3	73.3	78.1	79.8	86.7	92.6	89.4
18	1.011	1577	470		-3.76	34.9	46.1	43.5	50.7	48.8	50.7	53.7
19	1.044	1488	467		-3.78	34.6	47.0	46.6	51.5	53.7	54.4	52.9
20	1.068	1492	578		-2.86	35.0	51.6	52.8	56.8	60.1	61.2	58.5
21	1.101	1495	700		-2.03	35.2	56.0	58.7	61.8	66.0	67.3	64.1

Table B-1. Model No. 1: 4.64-Inch-Diameter Conical, Adapted to JENOTS (Concluded).

$k_1 = 16.62$  in. 2 Linear Scale Factor to 138 in. 2 = 4.48

Data Point No.	Inner		Normalization Parameters			2400-ft S.I. Data					
	$(P_1/P_0)_1$	$T_{12}$ ( $^{\circ}$ R)	$V_1$ (ft/sec)	$10 \log_{10} V/\omega_0$	$10 \log_{10} \frac{10 \log_{10} P_0(T_0/T_{12})}{P_1}$	50°	90°	PNL	PPNL	$\theta$	POASPL $\theta$
26	1.134	1493	796	-1.47	35.3	58.6	61.7	69.4	71.0	110	67.3
27	1.168	1500	887	-.997	35.3	61.2	64.9	72.5	74.3	120	70.7
28	1.219	1496	997	-.490	35.2	64.0	67.8	70.3	78.1	120	74.9
29	1.349	1494	1316	-.373	34.8	68.0	72.2	74.8	84.3	130	81.5
30	1.495	1496	1401	.988	34.5	73.1	77.5	79.4	91.0	130	88.0
31	2.362	1499	1990	2.51	36.3	84.8	91.1	97.6	105.9	140	100.8
62	1.577	997	1210	.351	36.8	68.6	73.4	82.3	87.0	130	83.8
63	1.518	1453	1485	1.000	34.7	72.5	77.5	79.0	90.8	130	87.3
64	1.806	1448	1651	1.701	34.9	76.7	82.0	82.8	97.1	130	92.4
65	2.047	1452	1804	2.086	35.4	80.4	86.0	86.2	101.9	140	97.0
66	2.48	1450	2004	2.542	36.8	85.6	92.3	89.9	106.5	130	100.7
67	1.519	714	983	-.551	36.8	64.3	69.7	70.9	80.2	130	75.9
117	1.058	896	414	-4.307	32.0	41.2	40.5	46.3	48.9	110	47.8
122	1.239	1255	982	-.556	85.6	63.4	67.5	75.4	78.3	110	74.6

Table B-2. Model No. 2: Convergent-Divergent Plug, Single Flow.

$A_1 = 37.40 \text{ in.}^2$ , Linear Scale Factor to 338 in. 2 = 3.00

Data Point No.	Inlet		Normalization Parameters			2128-ft S.L. Data					
	$(P_1/P_0)_1$	$T_{r1}$ ( $^{\circ}\text{R}$ )	$V_1$ (ft/sec)	$10 \log_{10} V/a_0$	$10 \log_{10} P_1/T_{r1}$	$50^{\circ}$	$90^{\circ}$	PNL	PPNL	$\theta$	POASPL $\theta$
1	1.116	1493	744	-1.756	35.3	65.7	71.4	74.9	78	120	75.7
2	1.226	1516	1016	-0.406	35.1	70.6	77.8	82.7	86.6	120	83.5
3	1.375	1497	1253	0.303	34.7	73.6	81.2	86.3	91	110	87.8
4	1.585	1485	1487	0.125	34.5	75.7	80.4	88.9	93.5	130	90.7
5	1.736	1485	1618	0.161	34.6	77.1	82.2	90.3	96.8	130	93.4
6	1.928	1501	1757	1.973	34.8	73.7	84.2	92.1	100.3	130	95.7
7	2.374	1501	1995	2.524	36.3	84	89.7	96.4	107.5	140	103
8	2.461	1515	2048	2.637	36.3	85.1	90.6	97.9	108.2	140	103.7
9	3.047	1556	2239	3.082	38.9	89.9	96.5	102.3	113.3	130	107.6
11	3.176	1511	2582	3.644	37.2	89.9	96	103.5	115.8	130	110.4
12	2.005	1939	2062	2.666	33.7	82.9	88.6	96.2	106.4	130	101.8
13	1.495	2006	1624	1.530	31.9	78.7	83.1	91.9	97.5	110	93.6
14	1.161	2018	1007	-0.442	34.4	71	73.2	81.5	86.3	110	82.5
15	1.192	1763	1019	-0.391	34.7	71	73.7	82.3	87.7	110	83.1
16	1.607	1757	1647	1.678	33.0	78.1	82.6	91.4	97.4	110	93.4
17	2.119	1734	2071	2.686	35.1	84.2	89.8	96.6	107.8	130	103.1
18	3.253	1285	2106	2.759	39.3	89.3	95.6	100.7	111	140	106.3
19	1.978	1249	1633	1.655	36.2	77.2	82.4	90.3	97.2	140	94.2
20	1.274	1266	1009	-0.435	32.0	70.5	73.3	81.2	86.5	110	82.7
21	1.369	1009	1020	-0.389	36.2	68.7	72.2	79.4	84.7	120	80
22	2.411	1019	1649	1.698	38.5	81.3	87.5	92.2	109	130	104.1
23	3.912	1177	2071	2.687	41.3	94.1	100.4	103.9	112.8	140	108.1
26	1.888	509	1007	-0.444	37.9	69	74.9	81.8	84.1	110	76.8
27	1.482	857	1046	-0.280	36.7	67.6	72.8	79.5	82.9	120	78.9
28	1.835	2259	2093	2.732	32.3	82.7	88	96.4	104.8	130	99.9
29	1.712	2511	2087	2.719	31.2	83.1	88.2	96.4	103.7	130	99.2
30	1.184	1507	924	-0.817	35.2	69.3	71.3	78.6	89.4	110	80.9
31	1.289	1111	1129	0.051	34.9	71.6	74.7	83.9	90.3	110	84.5
32	1.447	1506	1349	0.826	34.5	74.9	79	87.4	93.6	110	89.3
33	1.482	1560	1327	0.755	34.5	75.4	79.9	88	94	110	89.5
34	2.779	505	1239	0.456	41.0	86.1	92.6	94.3	94.5	100	90
36	1.632	1006	1257	0.517	34.8	71.1	75.9	83.7	87.4	120	83.6
37	1.469	1255	1254	0.509	35.6	72.7	77.2	85.5	90.5	110	85.9
38	1.321	1760	1274	0.578	33.8	73.9	77.6	87	94.5	110	87.3
39	1.374	2003	1271	0.588	33.1	79.3	77.3	86.3	92.8	110	87
40	1.444	2261	1667	1.744	30.8	78.9	83.2	85.5	91.7	120	99.3
41	1.395	2492	1687	1.731	29.9	78.7	82.6	85.2	91.1	120	94.2
42	1.234	2245	1257	0.518	32.6	74.6	77.4	80.9	90.7	110	87.3

Table B-3. Model No. 3. Convergent Plug,  $R_r = 0.59$ , Single Flow.

$A_1 = 33.43 \text{ in.}^2$  Linear Scale Factor to 338 in. $^2 = 3.17$

Data Point No.	Inner			Meteorological Conditions		Normalization Parameters		50°	2400-ft S.L. Data			
	$(P/P_0)_i$	$T_{ri}$ ( $^{\circ}\text{F}$ )	$V_i$ (ft/sec)	$T_{dry}$ ( $^{\circ}\text{F}$ )	$T_{wet}$ ( $^{\circ}\text{F}$ )	$10 \log_{10} V/a_0$	$10 \log_{10} F_0(T_0/T_{sm})^{-1}$		QASPL	PNL	PPNL	FOASPL
7245	1.535	701	986	86	73	-538	37.0	64.0	68.9	74.3	75.8	71.8
7246	2.072	986	1493	88	73	1.264	38.0	75.0	81.3	88.2	91.9	88.5
7248	1.627	759	1088	86	73	-110	37.4	66.3	71.2	76.8	79.4	75.8
7249	2.238	1085	1651	88	73	1.701	37.9	77.9	84.8	90.0	96.0	92.2
7251	1.737	812	1194	86	73	0.293	37.8	68.4	73.7	79.9	83.3	79.6
7252	2.452	1192	1804	88	73	2.086	37.7	79.9	85.9	92.2	99.5	95.6
7254	1.85	871	1299	86	73	0.659	37.9	70.8	76.2	82.3	86.1	82.7
7255	2.557	1288	1948	88	73	2.419	37.9	82.6	88.9	94.7	103.1	98.7
7257	1.963	927	1397	88	73	0.975	38.0	75.6	82.4	86.5	89.6	85.9

Table B-4. Model No. 4: Convergent Plug,  $R_r = 0.789$ , Single Flow.

$A_1 = 10.85 \text{ in.}^2$  Linear Scale Factor to 318  $\text{in.}^2 = 5.58$

Data No.	Inner			Meteorological Conditions		Normalization Parameters			2400-ft S.L. Data					
	$(P_0/P_1)_i$	$T_{r_i}$ (° R)	$V_i$ (ft/sec)	$T_{dry}$ (° F)	$T_{wet}$ (° F)	$10 \log_{10} V/a_0$	$10 \log_{10} F_a(T_0/T_{ref})^{0.1}$		50°		90°		PPNL	$\theta$
									OASPL	PNL	OASPL	PNL	PPNL	$\theta$
7601	1.719	572	993	85	75	-597	37.5		65.3	70.7	69.1	74.8	75.7	120
7602	1.513	684	958	85	75	-663	36.8		63.2	67.8	66.6	72.3	73.4	130
7603	1.351	962	976	90	75	-582	36.2		62.0	65.6	66.4	71.3	73.4	130
7604	1.263	1244	984	90	75	-547	35.6		62.2	65.5	67.0	71.6	73.7	120
7605	1.213	1492	983	89	73	-551	35.2		62.0	65.1	66.9	71.7	73.5	120
7606	1.184	1658	971	87	73	-600	35.0		61.1	64.3	66.4	70.8	72.9	120
7607	1.177	1851	1008	87	73	-642	34.7		62.8	66.3	67.3	73.7	75.7	120
7608	2.382	580	1238	85	75	-451	40.0		72.3	79.0	77.0	83.9	85.2	140
7609	1.628	982	1239	90	75	-454	37.0		70.2	76.2	74.6	80.8	85.5	120
7610	1.469	1236	1246	90	75	-479	35.8		67.0	71.4	72.5	78.0	81.7	130
7611	1.369	1486	1241	90	75	-461	34.8		66.5	70.6	72.0	77.2	80.7	130
7612	1.308	1743	1247	87	73	-482	34.0		66.7	70.7	72.1	77.3	80.7	130
7613	1.276	1895	1341	87	73	-461	33.6		65.7	69.2	72.2	77.3	80.3	120
7614	2.928	985	1628	90	75	-1.640	38.8		78.8	86.8	82.3	90.1	95.6	140
7615	2.055	1227	1660	88	74	-1.720	36.6		75.8	80.8	81.0	87.1	94.6	140
7616	1.749	1484	1628	90	75	-1.640	34.6		73.3	77.9	79.2	85.1	91.5	140
7617	1.660	1734	1625	87	73	-1.632	33.2		73.6	78.8	78.9	84.8	90.8	130
7618	1.541	1907	1639	87	73	-1.669	32.4		72.6	77.1	78.6	84.3	90.5	130
7619	4.059	1061	2051	89	73	-2.643	41.8		91.9	98.3	93.9	101.5	107.9	140
7620	3.301	1223	2065	89	73	-2.673	39.7		87.5	94.0	90.4	98.3	108.0	140
7621	2.618	1487	2083	90	75	-2.710	37.1		82.7	89.1	87.9	95.2	106.8	140
7622	2.236	1765	2101	89	73	-2.748	35.1		80.8	86.8	86.3	93.2	103.7	140
7623	2.07	1901	2084	87	73	-2.712	34.2		79.0	84.6	85.0	91.7	101.7	140
7645	1.534	715	995	88	73	-498	37.0		64.6	69.0	68.5	74.4	76.0	130
7646	2.061	989	1491	99	74	-1.258	37.9		73.6	78.9	78.7	84.9	90.6	140
7647	2.723	1333	2004	90	75	-2.542	37.9		83.2	89.9	87.4	94.9	104.8	140
7648	1.622	762	1088	88	73	-1.110	37.4		66.8	72.4	70.7	76.6	78.9	130
7649	2.282	1083	1647	88	74	-1.680	37.9		77.1	84.5	81.7	88.1	95.2	140
7650	3.007	1468	2193	90	75	-2.934	38.2		84.5	90.4	89.5	96.6	107.8	140
7651	1.734	821	1199	88	74	-0.312	37.7		70.7	76.5	74.3	80.8	83.4	120
7652	2.45	1191	1802	88	74	-2.081	37.7		81.0	88.4	85.5	93.0	101.4	140
7653	3.294	1557	2337	89	73	-2.210	38.6		86.4	92.6	91.0	98.6	109.0	140
7654	1.841	880	1301	88	74	-0.666	37.9		69.2	73.9	74.7	80.5	85.0	130
7655	2.635	1296	1947	90	75	-2.417	35.0		82.7	87.4	87.4	94.8	109.7	140
7656	3.548	1764	2561	89	73	-3.607	38.6		87.0	93.0	92.3	100.0	110.7	130
7657	1.95	934	1397	88	74	-0.975	37.9		71.7	76.4	76.8	82.7	88.0	140
7658	2.861	1293	2053	90	75	-2.731	38.1		83.8	90.2	88.2	96.0	105.5	140
7659	3.893	1950	2772	89	73	-3.951	38.7		90.5	97.0	95.1	102.8	113.0	130



Table B-5. Model No. 5: Convergent Plug,  $R_f = 0.853$ , Single Flow.

$A_1 = 6.73 \text{ in.}^2$  linear scale factor to 338 in. 2 = 7.09

Data Point No.	Inner		Meteorological Conditions		Normalization Parameters		2400-ft. S.L. Data								
	$(P/P_0)_1$	$T_1$ ( $^{\circ}$ R)	$V_1$ (ft/sec)	$T_{dry}$ ( $^{\circ}$ F)	$T_{wet}$ ( $^{\circ}$ F)	$IC \log_{10} V/a$	$10 \log_{10} P_a(T_0/T_{wet})^{0.1}$	QASPL	PNL	QASPL	PNL	QASPL	PNL	QASPL	PNL
7445	1.543	718	1003	81	71	-0.464	37.1	64.1	68.9	68.5	73.8	75.3	130	71.4	140
7446	2.057	979	1481	82	72	0.123	38.1	72.8	77.7	78.2	84.0	89.2	140	86.5	140
7447	2.719	1310	1985	84	73	2.501	38.1	81.7	86.9	86.1	93.0	102.4	140	98.0	140
7448	1.632	764	1095	81	71	-0.008	37.6	65.7	70.5	70.5	75.9	77.8	130	74.4	140
7449	2.259	1096	1656	82	72	1.716	37.9	75.9	81.8	81.1	87.2	93.5	140	90.4	140
7450	2.99	1480	2197	84	73	2.942	38.3	84.2	91.2	88.5	95.7	105.8	140	100.9	140
7451	1.732	819	1197	81	71	0.301	37.9	67.5	72.1	72.5	78.0	80.6	140	77.9	140
7452	2.447	1200	1808	82	72	2.095	37.8	79.2	86.5	83.5	90.1	97.5	140	93.9	140
7453	3.26	1638	2382	84	73	3.293	38.4	86.8	93.1	91.5	98.4	108.1	130	103.1	130
7454	1.841	875	1298	81	71	0.656	38.0	69.2	74.0	74.5	80.2	83.4	140	80.7	140
7455	2.645	1297	1951	82	72	2.426	38.0	81.2	88.5	85.7	92.5	101.4	140	97.3	140
7456	3.545	1791	2572	85	73	3.631	38.6	88.5	95.3	93.7	101.0	113.9	130	107.2	130
7457	1.978	934	1396	81	71	0.972	38.0	70.9	75.6	76.0	81.7	86.2	140	83.4	140
7458	2.854	1398	2095	84	73	2.735	38.2	83.4	90.6	87.6	94.5	103.6	140	99.4	140
7459	3.861	1950	2765	85	73	3.940	38.8	88.5	94.5	94.3	101.6	111.7	130	106.7	130

Table B-6. Model No. 6: Dual-Flow Coannular-Coplanar,  $A/A_1 = 2.0$ .

Data Point No.	Inlet $(P_0/P_1)_0$ ( $\frac{P_0}{P_1}$ ) $T_0$ (°F)	Outlet $(P_0/P_1)_e$ ( $\frac{P_0}{P_1}$ ) $T_e$ (°F)	Refrac. $\tau_{01}/\tau_1$ $\mu_0/\mu_1$ $\rho_0/\rho_1$	Mass Averages $(P_0/P_1)_m$ ( $\frac{P_0}{P_1}$ ) $T_m$ (°F)	Metastable Conditions $T_{01}$ (°F)	Normalization Parameters $10 \log_{10} \frac{10 \log_{10} \frac{P_0}{P_1}}{P_0/P_1}$	2400-ft S.L. Data			
							50°	90°	PHL	POAFL
0102	1.001	1.001	1.001	1.001	1.001	1.001	59.4	64.8	71.1	71.1
0103	1.002	1.002	1.002	1.002	1.002	1.002	58.4	62.9	69.4	71.1
0104	1.003	1.003	1.003	1.003	1.003	1.003	57.4	61.8	68.4	71.1
0105	1.004	1.004	1.004	1.004	1.004	1.004	56.4	60.7	67.4	71.1
0106	1.005	1.005	1.005	1.005	1.005	1.005	55.4	59.6	66.4	71.1
0107	1.006	1.006	1.006	1.006	1.006	1.006	54.4	58.5	65.4	71.1
0108	1.007	1.007	1.007	1.007	1.007	1.007	53.4	57.4	64.4	71.1
0109	1.008	1.008	1.008	1.008	1.008	1.008	52.4	56.3	63.4	71.1
0110	1.009	1.009	1.009	1.009	1.009	1.009	51.4	55.2	62.4	71.1
0111	1.010	1.010	1.010	1.010	1.010	1.010	50.4	54.1	61.4	71.1
0112	1.011	1.011	1.011	1.011	1.011	1.011	49.4	53.0	60.4	71.1
0113	1.012	1.012	1.012	1.012	1.012	1.012	48.4	51.9	59.4	71.1
0114	1.013	1.013	1.013	1.013	1.013	1.013	47.4	50.8	58.4	71.1
0115	1.014	1.014	1.014	1.014	1.014	1.014	46.4	49.7	57.4	71.1
0116	1.015	1.015	1.015	1.015	1.015	1.015	45.4	48.6	56.4	71.1
0117	1.016	1.016	1.016	1.016	1.016	1.016	44.4	47.5	55.4	71.1
0118	1.017	1.017	1.017	1.017	1.017	1.017	43.4	46.4	54.4	71.1
0119	1.018	1.018	1.018	1.018	1.018	1.018	42.4	45.3	53.4	71.1
0120	1.019	1.019	1.019	1.019	1.019	1.019	41.4	44.2	52.4	71.1
0121	1.020	1.020	1.020	1.020	1.020	1.020	40.4	43.1	51.4	71.1
0122	1.021	1.021	1.021	1.021	1.021	1.021	39.4	42.0	50.4	71.1
0123	1.022	1.022	1.022	1.022	1.022	1.022	38.4	40.9	49.4	71.1
0124	1.023	1.023	1.023	1.023	1.023	1.023	37.4	39.8	48.4	71.1
0125	1.024	1.024	1.024	1.024	1.024	1.024	36.4	38.7	47.4	71.1
0126	1.025	1.025	1.025	1.025	1.025	1.025	35.4	37.6	46.4	71.1
0127	1.026	1.026	1.026	1.026	1.026	1.026	34.4	36.5	45.4	71.1
0128	1.027	1.027	1.027	1.027	1.027	1.027	33.4	35.4	44.4	71.1
0129	1.028	1.028	1.028	1.028	1.028	1.028	32.4	34.3	43.4	71.1
0130	1.029	1.029	1.029	1.029	1.029	1.029	31.4	33.2	42.4	71.1
0131	1.030	1.030	1.030	1.030	1.030	1.030	30.4	32.1	41.4	71.1
0132	1.031	1.031	1.031	1.031	1.031	1.031	29.4	31.0	40.4	71.1
0133	1.032	1.032	1.032	1.032	1.032	1.032	28.4	29.9	39.4	71.1
0134	1.033	1.033	1.033	1.033	1.033	1.033	27.4	28.8	38.4	71.1
0135	1.034	1.034	1.034	1.034	1.034	1.034	26.4	27.7	37.4	71.1
0136	1.035	1.035	1.035	1.035	1.035	1.035	25.4	26.6	36.4	71.1
0137	1.036	1.036	1.036	1.036	1.036	1.036	24.4	25.5	35.4	71.1
0138	1.037	1.037	1.037	1.037	1.037	1.037	23.4	24.4	34.4	71.1
0139	1.038	1.038	1.038	1.038	1.038	1.038	22.4	23.3	33.4	71.1
0140	1.039	1.039	1.039	1.039	1.039	1.039	21.4	22.2	32.4	71.1
0141	1.040	1.040	1.040	1.040	1.040	1.040	20.4	21.1	31.4	71.1
0142	1.041	1.041	1.041	1.041	1.041	1.041	19.4	20.0	30.4	71.1
0143	1.042	1.042	1.042	1.042	1.042	1.042	18.4	18.9	29.4	71.1
0144	1.043	1.043	1.043	1.043	1.043	1.043	17.4	17.8	28.4	71.1
0145	1.044	1.044	1.044	1.044	1.044	1.044	16.4	16.7	27.4	71.1
0146	1.045	1.045	1.045	1.045	1.045	1.045	15.4	15.6	26.4	71.1
0147	1.046	1.046	1.046	1.046	1.046	1.046	14.4	14.5	25.4	71.1
0148	1.047	1.047	1.047	1.047	1.047	1.047	13.4	13.4	24.4	71.1
0149	1.048	1.048	1.048	1.048	1.048	1.048	12.4	12.4	23.4	71.1
0150	1.049	1.049	1.049	1.049	1.049	1.049	11.4	11.4	22.4	71.1
0151	1.050	1.050	1.050	1.050	1.050	1.050	10.4	10.4	21.4	71.1
0152	1.051	1.051	1.051	1.051	1.051	1.051	9.4	9.4	20.4	71.1
0153	1.052	1.052	1.052	1.052	1.052	1.052	8.4	8.4	19.4	71.1
0154	1.053	1.053	1.053	1.053	1.053	1.053	7.4	7.4	18.4	71.1
0155	1.054	1.054	1.054	1.054	1.054	1.054	6.4	6.4	17.4	71.1
0156	1.055	1.055	1.055	1.055	1.055	1.055	5.4	5.4	16.4	71.1
0157	1.056	1.056	1.056	1.056	1.056	1.056	4.4	4.4	15.4	71.1
0158	1.057	1.057	1.057	1.057	1.057	1.057	3.4	3.4	14.4	71.1
0159	1.058	1.058	1.058	1.058	1.058	1.058	2.4	2.4	13.4	71.1
0160	1.059	1.059	1.059	1.059	1.059	1.059	1.4	1.4	12.4	71.1
0161	1.060	1.060	1.060	1.060	1.060	1.060	0.4	0.4	11.4	71.1

Table B-6. Model No. 6: Dual-Flow Coannular-Coplanar,  $A/A_1 = 2.0$  (Concluded).

Data Point No.	Inlet		Outlet		Section		Mass Averages		Metamorphological Conditions		Normalization Parameters		2400-ft S.L. Data			
	$(P_1/P_0)_1$	$T_1$ (°F)	$(P_2/P_0)_2$	$T_2$ (°F)	$T_0/T_1$	$\rho_0/\rho_1$	$(P_1/P_0)_m$	$T_m$ (°F)	$T_m/T_1$	$T_m/T_2$	$10 \log_{10} (P_1/P_0)$	$10 \log_{10} (T_2/T_1)$	50° QASTL	90° QASTL	PDEL	°
6163	1.222	1499	1.159	1519	2.1	5.5	2.283	1478	1.000	1.000	2.380	35.7	81.5	86.1	94.3	99.9
6164	1.233	1505	1.169	1524	1.7	5.5	2.197	1506	1.000	1.000	-0.482	35.2	80.8	87.3	94.3	99.9
6165	1.244	1511	1.179	1530	1.4	5.5	2.111	1536	1.000	1.000	-0.821	34.9	59.4	84.1	91.3	97.4
6270	1.255	1517	1.189	1536	1.1	5.5	2.025	1566	1.000	1.000	-0.821	34.8	60.2	84.1	91.3	97.4
6271	1.266	1523	1.199	1542	0.8	5.5	1.939	1596	1.000	1.000	-2.287	33.0	57.6	80.9	88.2	94.3
6272	1.276	1529	1.209	1548	0.5	5.5	1.853	1626	1.000	1.000	-2.402	33.4	63.2	87.0	94.3	99.9
6273	1.287	1535	1.219	1554	0.2	5.5	1.767	1656	1.000	1.000	-2.281	34.4	70.7	88.9	94.3	99.9
6274	1.298	1541	1.229	1560	0.1	5.5	1.681	1686	1.000	1.000	-1.992	34.8	74.4	92.7	97.4	100.0
6275	1.309	1547	1.239	1566	0.0	5.5	1.595	1716	1.000	1.000	-1.185	35.9	78.0	96.5	100.0	100.0
6276	1.320	1553	1.249	1572	0.0	5.5	1.509	1746	1.000	1.000	-0.458	37.1	75.6	96.2	100.0	100.0
6277	1.331	1559	1.259	1578	0.0	5.5	1.423	1776	1.000	1.000	-0.434	39.2	73.0	98.0	100.0	100.0
6278	1.342	1565	1.269	1584	0.0	5.5	1.337	1806	1.000	1.000	-0.170	40.0	68.7	94.4	100.0	100.0
6279	1.353	1571	1.279	1590	0.0	5.5	1.251	1836	1.000	1.000	-0.083	37.8	66.5	91.1	97.4	100.0
6280	1.364	1577	1.289	1596	0.0	5.5	1.165	1866	1.000	1.000	-0.352	37.5	65.1	90.1	96.4	100.0
6281	1.375	1583	1.299	1602	0.0	5.5	1.079	1896	1.000	1.000	-0.511	37.0	63.0	88.1	94.4	100.0
6282	1.386	1589	1.309	1608	0.0	5.5	0.993	1926	1.000	1.000	-0.615	36.4	61.5	86.6	92.0	100.0
6283	1.397	1595	1.319	1614	0.0	5.5	0.907	1956	1.000	1.000	-0.792	36.3	61.2	86.1	91.5	100.0
6284	1.408	1601	1.329	1620	0.0	5.5	0.821	1986	1.000	1.000	-0.982	36.3	61.2	86.1	91.5	100.0
6285	1.419	1607	1.339	1626	0.0	5.5	0.735	2016	1.000	1.000	-1.185	36.2	61.2	86.1	91.5	100.0
6286	1.430	1613	1.349	1632	0.0	5.5	0.649	2046	1.000	1.000	-1.388	36.2	61.2	86.1	91.5	100.0
6287	1.441	1619	1.359	1638	0.0	5.5	0.563	2076	1.000	1.000	-1.591	36.6	61.2	86.1	91.5	100.0
6288	1.452	1625	1.369	1644	0.0	5.5	0.477	2106	1.000	1.000	-1.794	36.6	61.2	86.1	91.5	100.0
6289	1.463	1631	1.379	1650	0.0	5.5	0.391	2136	1.000	1.000	-1.997	36.6	61.2	86.1	91.5	100.0
6290	1.474	1637	1.389	1656	0.0	5.5	0.305	2166	1.000	1.000	-2.199	36.6	61.2	86.1	91.5	100.0
6291	1.485	1643	1.399	1662	0.0	5.5	0.219	2196	1.000	1.000	-2.402	36.6	61.2	86.1	91.5	100.0
6292	1.496	1649	1.409	1668	0.0	5.5	0.133	2226	1.000	1.000	-2.605	36.6	61.2	86.1	91.5	100.0
6293	1.507	1655	1.419	1674	0.0	5.5	0.047	2256	1.000	1.000	-2.808	36.6	61.2	86.1	91.5	100.0
6294	1.518	1661	1.429	1680	0.0	5.5	0.000	2286	1.000	1.000	-3.011	36.6	61.2	86.1	91.5	100.0
6295	1.529	1667	1.439	1686	0.0	5.5	0.000	2316	1.000	1.000	-3.214	36.6	61.2	86.1	91.5	100.0
6296	1.540	1673	1.449	1692	0.0	5.5	0.000	2346	1.000	1.000	-3.417	36.6	61.2	86.1	91.5	100.0
6297	1.551	1679	1.459	1698	0.0	5.5	0.000	2376	1.000	1.000	-3.620	36.6	61.2	86.1	91.5	100.0
6298	1.562	1685	1.469	1704	0.0	5.5	0.000	2406	1.000	1.000	-3.823	36.6	61.2	86.1	91.5	100.0
6299	1.573	1691	1.479	1710	0.0	5.5	0.000	2436	1.000	1.000	-4.026	36.6	61.2	86.1	91.5	100.0
6300	1.584	1697	1.489	1716	0.0	5.5	0.000	2466	1.000	1.000	-4.229	36.6	61.2	86.1	91.5	100.0
6301	1.595	1703	1.499	1722	0.0	5.5	0.000	2496	1.000	1.000	-4.432	36.6	61.2	86.1	91.5	100.0
6302	1.606	1709	1.509	1728	0.0	5.5	0.000	2526	1.000	1.000	-4.635	36.6	61.2	86.1	91.5	100.0
6303	1.617	1715	1.519	1734	0.0	5.5	0.000	2556	1.000	1.000	-4.838	36.6	61.2	86.1	91.5	100.0
6304	1.628	1721	1.529	1740	0.0	5.5	0.000	2586	1.000	1.000	-5.041	36.6	61.2	86.1	91.5	100.0
6305	1.639	1727	1.539	1746	0.0	5.5	0.000	2616	1.000	1.000	-5.244	36.6	61.2	86.1	91.5	100.0
6306	1.650	1733	1.549	1752	0.0	5.5	0.000	2646	1.000	1.000	-5.447	36.6	61.2	86.1	91.5	100.0
6307	1.661	1739	1.559	1758	0.0	5.5	0.000	2676	1.000	1.000	-5.650	36.6	61.2	86.1	91.5	100.0
6308	1.672	1745	1.569	1764	0.0	5.5	0.000	2706	1.000	1.000	-5.853	36.6	61.2	86.1	91.5	100.0
6309	1.683	1751	1.579	1770	0.0	5.5	0.000	2736	1.000	1.000	-6.056	36.6	61.2	86.1	91.5	100.0
6310	1.694	1757	1.589	1776	0.0	5.5	0.000	2766	1.000	1.000	-6.259	36.6	61.2	86.1	91.5	100.0
6311	1.705	1763	1.599	1782	0.0	5.5	0.000	2796	1.000	1.000	-6.462	36.6	61.2	86.1	91.5	100.0
6312	1.716	1769	1.609	1788	0.0	5.5	0.000	2826	1.000	1.000	-6.665	36.6	61.2	86.1	91.5	100.0
6313	1.727	1775	1.619	1794	0.0	5.5	0.000	2856	1.000	1.000	-6.868	36.6	61.2	86.1	91.5	100.0
6314	1.738	1781	1.629	1800	0.0	5.5	0.000	2886	1.000	1.000	-7.071	36.6	61.2	86.1	91.5	100.0
6315	1.749	1787	1.639	1806	0.0	5.5	0.000	2916	1.000	1.000	-7.274	36.6	61.2	86.1	91.5	100.0
6316	1.760	1793	1.649	1812	0.0	5.5	0.000	2946	1.000	1.000	-7.477	36.6	61.2	86.1	91.5	100.0
6317	1.771	1799	1.659	1818	0.0	5.5	0.000	2976	1.000	1.000	-7.680	36.6	61.2	86.1	91.5	100.0
6318	1.782	1805	1.669	1824	0.0	5.5	0.000	3006	1.000	1.000	-7.883	36.6	61.2	86.1	91.5	100.0
6319	1.793	1811	1.679	1830	0.0	5.5	0.000	3036	1.000	1.000	-8.086	36.6	61.2	86.1	91.5	100.0
6320	1.804	1817	1.689	1836	0.0	5.5	0.000	3066	1.000	1.000	-8.289	36.6	61.2	86.1	91.5	100.0
6321	1.815	1823	1.699	1842	0.0	5.5	0.000	3096	1.000	1.000	-8.492	36.6	61.2	86.1	91.5	100.0
6322	1.826	1829	1.709	1848	0.0	5.5	0.000	3126	1.000	1.000	-8.695	36.6	61.2	86.1	91.5	100.0
6323	1.837	1835	1.719	1854	0.0	5.5	0.000	3156	1.000	1.000	-8.898	36.6	61.2	86.1	91.5	100.0
6324	1.848	1841	1.729	1860	0.0	5.5	0.000	3186	1.000	1.000	-9.101	36.6	61.2	86.1	91.5	100.0
6325	1.859	1847	1.739	1866	0.0	5.5	0.000	3216	1.000	1.000	-9.304	36.6	61.2	86.1	91.5	100.0
6326	1.870	1853	1.749	1872	0.0	5.5	0.000	3246	1.000	1.000	-9.507	36.6	61.2	86.1	91.5	100.0
6327	1.881	1859	1.759	1878	0.0	5.5	0.000	3276	1.000	1.000	-9.710	36.6	61.2	86.1	91.5	100.0
6328	1.892	1865	1.769	1884	0.0	5.5	0.000	3306	1.000	1.000	-9.913	36.6	61.2	86.1	91.5	100.0
6329	1.903	1871	1.779	1890	0.0	5.5	0.000	3336	1.000	1.000	-10.116	36.6	61.2	86.1	91.5	100.0
6330	1.914	1877	1.789	1896	0.0	5.5	0.000	3366	1.000	1.000	-10.319	36.6	61.2	86.1	91.5	100.0
6331	1.925	1883	1.799	1902	0.0	5.5	0.000	3396	1.000	1.000	-10.522	36.6	61.2	86.1	91.5	100.0
6332	1.936	1889	1.809	1908	0.0	5.5	0.000	3426	1.000	1.000	-10.725	36.6	61.2	86.1	91.5	100.0
6333	1.947	1895	1.819	1914	0.0	5.5	0.000	3456	1.000	1.000	-10.928	36.6	61.2	86.1	91.5	100.0
6334	1.958	1901	1.829	1920	0.0	5.5	0.000	3486	1.000	1.000	-11.131	36.6	61.2	86.1	91.5	100.0
6335	1.969	1907	1.839	1926	0.0	5.5	0.000	3516	1.000	1.000	-11.334	36.6	61.2	86.1	91.5	100.0
6336	1.980	1913	1.849	1932	0.0	5.5	0.000	3546	1.000	1.000	-11.537	36.6	61.2	86.1	91.5	100.0
6337	1.991	1919	1.859	1938	0.0	5.5	0.000	3576	1.000	1.000	-11.740	36.6	61.2	86.1	91.5	100.0
6338	2.002	1925	1.869	1944	0.0	5.5	0.000	3606	1.000	1.000	-11.943	36.6	61.2	86.1	91.5	100.0
6339	2.013	1931	1.879	1950												

Table B-7. Model No. 7: Dual-Flow Countercurrent-Coplanar,  $A_0/A_1 = 0.65$ .

$A_0 = 28.43 \text{ cm}^2$ ,  $A_1 = 16.82 \text{ cm}^2$ ,  $\text{Linear Velocity Factor} = 118 \text{ cm}^2 \text{ hr}^{-1} = 1.50$

Date	Time	Inlet		Outlet		Method	Mass Average		Meteorological Conditions		Normalization Parameters		2400-16 S.L. Data			
		$(P/P_0)_{in}$	$(T/T_0)_{in}$	$(P/P_0)_{out}$	$(T/T_0)_{out}$		$(P/P_0)_{in}$	$(T/T_0)_{out}$	$T_{air}$	$T_{wet}$	$10 \log_{10} (P/P_0)$	$10 \log_{10} (T/T_0)$	50° PHL	50° PFL	QASPL PHL	QASPL PFL
803	1:25	1.203	1.203	1.203	1.203	1.0	1.203	1.203	31	34	-0.445	37.2	64.1	69.5	69.5	78.2
804	1:30	1.204	1.204	1.204	1.204	1.0	1.204	1.204	32	35	-0.445	37.2	64.1	69.5	69.5	78.2
805	1:35	1.205	1.205	1.205	1.205	1.0	1.205	1.205	33	36	-0.445	37.2	64.1	69.5	69.5	78.2
806	1:40	1.206	1.206	1.206	1.206	1.0	1.206	1.206	34	37	-0.445	37.2	64.1	69.5	69.5	78.2
807	1:45	1.207	1.207	1.207	1.207	1.0	1.207	1.207	35	38	-0.445	37.2	64.1	69.5	69.5	78.2
808	1:50	1.208	1.208	1.208	1.208	1.0	1.208	1.208	36	39	-0.445	37.2	64.1	69.5	69.5	78.2
809	1:55	1.209	1.209	1.209	1.209	1.0	1.209	1.209	37	40	-0.445	37.2	64.1	69.5	69.5	78.2
810	2:00	1.210	1.210	1.210	1.210	1.0	1.210	1.210	38	41	-0.445	37.2	64.1	69.5	69.5	78.2
811	2:05	1.211	1.211	1.211	1.211	1.0	1.211	1.211	39	42	-0.445	37.2	64.1	69.5	69.5	78.2
812	2:10	1.212	1.212	1.212	1.212	1.0	1.212	1.212	40	43	-0.445	37.2	64.1	69.5	69.5	78.2
813	2:15	1.213	1.213	1.213	1.213	1.0	1.213	1.213	41	44	-0.445	37.2	64.1	69.5	69.5	78.2
814	2:20	1.214	1.214	1.214	1.214	1.0	1.214	1.214	42	45	-0.445	37.2	64.1	69.5	69.5	78.2
815	2:25	1.215	1.215	1.215	1.215	1.0	1.215	1.215	43	46	-0.445	37.2	64.1	69.5	69.5	78.2
816	2:30	1.216	1.216	1.216	1.216	1.0	1.216	1.216	44	47	-0.445	37.2	64.1	69.5	69.5	78.2
817	2:35	1.217	1.217	1.217	1.217	1.0	1.217	1.217	45	48	-0.445	37.2	64.1	69.5	69.5	78.2
818	2:40	1.218	1.218	1.218	1.218	1.0	1.218	1.218	46	49	-0.445	37.2	64.1	69.5	69.5	78.2
819	2:45	1.219	1.219	1.219	1.219	1.0	1.219	1.219	47	50	-0.445	37.2	64.1	69.5	69.5	78.2
820	2:50	1.220	1.220	1.220	1.220	1.0	1.220	1.220	48	51	-0.445	37.2	64.1	69.5	69.5	78.2
821	2:55	1.221	1.221	1.221	1.221	1.0	1.221	1.221	49	52	-0.445	37.2	64.1	69.5	69.5	78.2
822	3:00	1.222	1.222	1.222	1.222	1.0	1.222	1.222	50	53	-0.445	37.2	64.1	69.5	69.5	78.2
823	3:05	1.223	1.223	1.223	1.223	1.0	1.223	1.223	51	54	-0.445	37.2	64.1	69.5	69.5	78.2
824	3:10	1.224	1.224	1.224	1.224	1.0	1.224	1.224	52	55	-0.445	37.2	64.1	69.5	69.5	78.2
825	3:15	1.225	1.225	1.225	1.225	1.0	1.225	1.225	53	56	-0.445	37.2	64.1	69.5	69.5	78.2
826	3:20	1.226	1.226	1.226	1.226	1.0	1.226	1.226	54	57	-0.445	37.2	64.1	69.5	69.5	78.2
827	3:25	1.227	1.227	1.227	1.227	1.0	1.227	1.227	55	58	-0.445	37.2	64.1	69.5	69.5	78.2
828	3:30	1.228	1.228	1.228	1.228	1.0	1.228	1.228	56	59	-0.445	37.2	64.1	69.5	69.5	78.2
829	3:35	1.229	1.229	1.229	1.229	1.0	1.229	1.229	57	60	-0.445	37.2	64.1	69.5	69.5	78.2
830	3:40	1.230	1.230	1.230	1.230	1.0	1.230	1.230	58	61	-0.445	37.2	64.1	69.5	69.5	78.2
831	3:45	1.231	1.231	1.231	1.231	1.0	1.231	1.231	59	62	-0.445	37.2	64.1	69.5	69.5	78.2
832	3:50	1.232	1.232	1.232	1.232	1.0	1.232	1.232	60	63	-0.445	37.2	64.1	69.5	69.5	78.2
833	3:55	1.233	1.233	1.233	1.233	1.0	1.233	1.233	61	64	-0.445	37.2	64.1	69.5	69.5	78.2
834	4:00	1.234	1.234	1.234	1.234	1.0	1.234	1.234	62	65	-0.445	37.2	64.1	69.5	69.5	78.2
835	4:05	1.235	1.235	1.235	1.235	1.0	1.235	1.235	63	66	-0.445	37.2	64.1	69.5	69.5	78.2
836	4:10	1.236	1.236	1.236	1.236	1.0	1.236	1.236	64	67	-0.445	37.2	64.1	69.5	69.5	78.2
837	4:15	1.237	1.237	1.237	1.237	1.0	1.237	1.237	65	68	-0.445	37.2	64.1	69.5	69.5	78.2
838	4:20	1.238	1.238	1.238	1.238	1.0	1.238	1.238	66	69	-0.445	37.2	64.1	69.5	69.5	78.2
839	4:25	1.239	1.239	1.239	1.239	1.0	1.239	1.239	67	70	-0.445	37.2	64.1	69.5	69.5	78.2
840	4:30	1.240	1.240	1.240	1.240	1.0	1.240	1.240	68	71	-0.445	37.2	64.1	69.5	69.5	78.2
841	4:35	1.241	1.241	1.241	1.241	1.0	1.241	1.241	69	72	-0.445	37.2	64.1	69.5	69.5	78.2
842	4:40	1.242	1.242	1.242	1.242	1.0	1.242	1.242	70	73	-0.445	37.2	64.1	69.5	69.5	78.2
843	4:45	1.243	1.243	1.243	1.243	1.0	1.243	1.243	71	74	-0.445	37.2	64.1	69.5	69.5	78.2
844	4:50	1.244	1.244	1.244	1.244	1.0	1.244	1.244	72	75	-0.445	37.2	64.1	69.5	69.5	78.2
845	4:55	1.245	1.245	1.245	1.245	1.0	1.245	1.245	73	76	-0.445	37.2	64.1	69.5	69.5	78.2
846	5:00	1.246	1.246	1.246	1.246	1.0	1.246	1.246	74	77	-0.445	37.2	64.1	69.5	69.5	78.2
847	5:05	1.247	1.247	1.247	1.247	1.0	1.247	1.247	75	78	-0.445	37.2	64.1	69.5	69.5	78.2
848	5:10	1.248	1.248	1.248	1.248	1.0	1.248	1.248	76	79	-0.445	37.2	64.1	69.5	69.5	78.2
849	5:15	1.249	1.249	1.249	1.249	1.0	1.249	1.249	77	80	-0.445	37.2	64.1	69.5	69.5	78.2
850	5:20	1.250	1.250	1.250	1.250	1.0	1.250	1.250	78	81	-0.445	37.2	64.1	69.5	69.5	78.2
851	5:25	1.251	1.251	1.251	1.251	1.0	1.251	1.251	79	82	-0.445	37.2	64.1	69.5	69.5	78.2
852	5:30	1.252	1.252	1.252	1.252	1.0	1.252	1.252	80	83	-0.445	37.2	64.1	69.5	69.5	78.2
853	5:35	1.253	1.253	1.253	1.253	1.0	1.253	1.253	81	84	-0.445	37.2	64.1	69.5	69.5	78.2
854	5:40	1.254	1.254	1.254	1.254	1.0	1.254	1.254	82	85	-0.445	37.2	64.1	69.5	69.5	78.2
855	5:45	1.255	1.255	1.255	1.255	1.0	1.255	1.255	83	86	-0.445	37.2	64.1	69.5	69.5	78.2
856	5:50	1.256	1.256	1.256	1.256	1.0	1.256	1.256	84	87	-0.445	37.2	64.1	69.5	69.5	78.2
857	5:55	1.257	1.257	1.257	1.257	1.0	1.257	1.257	85	88	-0.445	37.2	64.1	69.5	69.5	78.2
858	6:00	1.258	1.258	1.258	1.258	1.0	1.258	1.258	86	89	-0.445	37.2	64.1	69.5	69.5	78.2
859	6:05	1.259	1.259	1.259	1.259	1.0	1.259	1.259	87	90	-0.445	37.2	64.1	69.5	69.5	78.2
860	6:10	1.260	1.260	1.260	1.260	1.0	1.260	1.260	88	91	-0.445	37.2	64.1	69.5	69.5	78.2

Table B-8. Model No. 8: Dual-Flow Coannular-Coplanar,  $A_o/A_i = 0.4$ .

[illegible]

Table B-9. Model No. 9: Coannular-Coplanar,  $A/A_0 = 2.0$ , Low Inner Flow.

Linear Scale Factor on 1A to 2 = 3.17 (Outer Only)

Data Point No.	Isotry $T_1$ (°C)	$\frac{V_1}{V_2}$ (cc/mole)	Oxide		Ratios	Meteorological Conditions	Normalization Parameters		2.0- $\mu$ S. L. Data									
			$T_0$ (°C)	$T_0$ (cc/mole)			$\frac{V_1}{V_2}$	$\frac{V_1}{V_2}$	$\frac{10 \log_{10} F_0(T_0/T_{ref})}{V_1/V_2}$	$\frac{10 \log_{10} F_0(T_0/T_{ref})}{V_1/V_2}$	50° QASPL PNL	90° QASPL PNL	PPNL	POASPL				
8231	1.032	153	203	1.160	34.7	323	2.8	5.4	78	49	48.6	45.4	57.6	51.7	52.4	110	53.6	110
8232	1.075	152	218	1.225	35.0	405	2.8	5.9	78	49	48.0	49.7	53.7	56.4	57.4	110	54.7	110
8233	1.075	153	218	1.225	35.0	405	2.8	5.9	78	49	48.0	49.7	53.7	56.4	57.4	110	54.7	110
8234	1.075	153	218	1.225	35.0	405	2.8	5.9	78	49	48.0	49.7	53.7	56.4	57.4	110	54.7	110
8235	1.075	153	218	1.225	35.0	405	2.8	5.9	78	49	48.0	49.7	53.7	56.4	57.4	110	54.7	110
8236	1.075	153	218	1.225	35.0	405	2.8	5.9	78	49	48.0	49.7	53.7	56.4	57.4	110	54.7	110
8237	1.075	153	218	1.225	35.0	405	2.8	5.9	78	49	48.0	49.7	53.7	56.4	57.4	110	54.7	110
8238	1.075	153	218	1.225	35.0	405	2.8	5.9	78	49	48.0	49.7	53.7	56.4	57.4	110	54.7	110
8239	1.075	153	218	1.225	35.0	405	2.8	5.9	78	49	48.0	49.7	53.7	56.4	57.4	110	54.7	110
8240	1.075	153	218	1.225	35.0	405	2.8	5.9	78	49	48.0	49.7	53.7	56.4	57.4	110	54.7	110
8241	1.075	153	218	1.225	35.0	405	2.8	5.9	78	49	48.0	49.7	53.7	56.4	57.4	110	54.7	110
8242	1.075	153	218	1.225	35.0	405	2.8	5.9	78	49	48.0	49.7	53.7	56.4	57.4	110	54.7	110
8243	1.075	153	218	1.225	35.0	405	2.8	5.9	78	49	48.0	49.7	53.7	56.4	57.4	110	54.7	110
8244	1.075	153	218	1.225	35.0	405	2.8	5.9	78	49	48.0	49.7	53.7	56.4	57.4	110	54.7	110
8245	1.075	153	218	1.225	35.0	405	2.8	5.9	78	49	48.0	49.7	53.7	56.4	57.4	110	54.7	110
8246	1.075	153	218	1.225	35.0	405	2.8	5.9	78	49	48.0	49.7	53.7	56.4	57.4	110	54.7	110
8247	1.075	153	218	1.225	35.0	405	2.8	5.9	78	49	48.0	49.7	53.7	56.4	57.4	110	54.7	110
8248	1.075	153	218	1.225	35.0	405	2.8	5.9	78	49	48.0	49.7	53.7	56.4	57.4	110	54.7	110
8249	1.075	153	218	1.225	35.0	405	2.8	5.9	78	49	48.0	49.7	53.7	56.4	57.4	110	54.7	110
8250	1.075	153	218	1.225	35.0	405	2.8	5.9	78	49	48.0	49.7	53.7	56.4	57.4	110	54.7	110
8251	1.075	153	218	1.225	35.0	405	2.8	5.9	78	49	48.0	49.7	53.7	56.4	57.4	110	54.7	110
8252	1.075	153	218	1.225	35.0	405	2.8	5.9	78	49	48.0	49.7	53.7	56.4	57.4	110	54.7	110
8253	1.075	153	218	1.225</														

Table B-10. Model No. 10: Dual-Flow Coannular-Coplanar,  $A_o/A_i = 0.65$  Low Inner Flow.

$A_o = 12.67$  in.<sup>2</sup>,  $A_i = 19.67$  in.<sup>2</sup> Annular-Kinetic Factor to 518 in.<sup>2</sup> = 5.56 (Outer Only)

Data Point No.	Inlet $T_{01}$ °F	Inlet $P_{01}$ psia	Inlet $T_{02}$ °F	Inlet $P_{02}$ psia	Outlet $T_{03}$ °F	Outlet $P_{03}$ psia	Exit $T_{04}$ °F	Exit $P_{04}$ psia	Thermodynamic Conditions	Normalization Parameters	2400-ft S.L. Data					
											50° OASPL	50° PRL	90° OASPL	90° PRL	PFNL	POASPL
1	1000	100	1000	100	1000	100	1000	100	1000	1000	60.8	64.6	66.1	71.6	73.3	69.3
2	1000	100	1000	100	1000	100	1000	100	1000	1000	71.5	76.4	77.6	83.6	88.7	130
3	1000	100	1000	100	1000	100	1000	100	1000	1000	88.0	95.6	89.1	98.5	101.7	130
4	1000	100	1000	100	1000	100	1000	100	1000	1000	63.3	67.2	69.1	74.5	77.0	130
5	1000	100	1000	100	1000	100	1000	100	1000	1000	77.7	87.2	81.0	89.2	92.3	130
6	1000	100	1000	100	1000	100	1000	100	1000	1000	91.2	98.5	91.6	100.2	104.9	140
7	1000	100	1000	100	1000	100	1000	100	1000	1000	66.5	70.1	71.6	77.0	80.3	140
8	1000	100	1000	100	1000	100	1000	100	1000	1000	82.2	90.5	84.1	91.9	96.6	140
9	1000	100	1000	100	1000	100	1000	100	1000	1000	90.0	97.4	91.7	99.9	108.0	140
10	1000	100	1000	100	1000	100	1000	100	1000	1000	67.5	71.9	73.7	79.6	83.8	140
11	1000	100	1000	100	1000	100	1000	100	1000	1000	85.0	92.6	87.1	96.3	99.5	140
12	1000	100	1000	100	1000	100	1000	100	1000	1000	89.0	95.5	93.0	101.0	110.0	140
13	1000	100	1000	100	1000	100	1000	100	1000	1000	69.8	74.2	75.9	81.7	86.1	140
14	1000	100	1000	100	1000	100	1000	100	1000	1000	83.6	95.4	89.8	98.8	103.2	140
15	1000	100	1000	100	1000	100	1000	100	1000	1000	90.0	96.0	94.6	102.1	112.5	140
16	1000	100	1000	100	1000	100	1000	100	1000	1000	38.9	38.1	43.7	45.8	45.3	100
17	1000	100	1000	100	1000	100	1000	100	1000	1000	42.4	43.5	47.1	51.1	51.8	110
18	1000	100	1000	100	1000	100	1000	100	1000	1000	46.9	49.3	51.9	57.2	56.0	110
19	1000	100	1000	100	1000	100	1000	100	1000	1000	57.0	56.1	57.6	63.8	64.7	110
20	1000	100	1000	100	1000	100	1000	100	1000	1000	56.3	61.0	62.2	68.5	69.4	110
21	1000	100	1000	100	1000	100	1000	100	1000	1000	61.0	65.8	66.0	73.0	74.5	110
22	1000	100	1000	100	1000	100	1000	100	1000	1000	64.9	69.8	70.5	76.7	78.0	110
23	1000	100	1000	100	1000	100	1000	100	1000	1000	78.6	85.8	81.6	91.5	91.7	100
24	1000	100	1000	100	1000	100	1000	100	1000	1000	88.8	95.9	93.0	100.7	101.8	100
25	1000	100	1000	100	1000	100	1000	100	1000	1000	60.8	40.7	45.2	47.6	48.0	100
26	1000	100	1000	100	1000	100	1000	100	1000	1000	53.6	56.5	58.5	63.1	63.9	110
27	1000	100	1000	100	1000	100	1000	100	1000	1000	64.8	69.4	71.9	78.7	87.0	110
28	1000	100	1000	100	1000	100	1000	100	1000	1000	69.8	76.7	77.0	83.9	87.8	130
29	1000	100	1000	100	1000	100	1000	100	1000	1000	57.0	56.1	57.6	63.8	64.7	110
30	1000	100	1000	100	1000	100	1000	100	1000	1000	56.3	61.0	62.2	68.5	69.4	110
31	1000	100	1000	100	1000	100	1000	100	1000	1000	61.0	65.8	66.0	73.0	74.5	110
32	1000	100	1000	100	1000	100	1000	100	1000	1000	64.9	69.8	70.5	76.7	78.0	110
33	1000	100	1000	100	1000	100	1000	100	1000	1000	78.6	85.8	81.6	91.5	91.7	100
34	1000	100	1000	100	1000	100	1000	100	1000	1000	88.8	95.9	93.0	100.7	101.8	100
35	1000	100	1000	100	1000	100	1000	100	1000	1000	60.8	40.7	45.2	47.6	48.0	100
36	1000	100	1000	100	1000	100	1000	100	1000	1000	53.6	56.5	58.5	63.1	63.9	110
37	1000	100	1000	100	1000	100	1000	100	1000	1000	64.8	69.4	71.9	78.7	87.0	110
38	1000	100	1000	100	1000	100	1000	100	1000	1000	69.8	76.7	77.0	83.9	87.8	130
39	1000	100	1000	100	1000	100	1000	100	1000	1000	57.0	56.1	57.6	63.8	64.7	110
40	1000	100	1000	100	1000	100	1000	100	1000	1000	56.3	61.0	62.2	68.5	69.4	110
41	1000	100	1000	100	1000	100	1000	100	1000	1000	61.0	65.8	66.0	73.0	74.5	110
42	1000	100	1000	100	1000	100	1000	100	1000	1000	64.9	69.8	70.5	76.7	78.0	110
43	1000	100	1000	100	1000	100	1000	100	1000	1000	78.6	85.8	81.6	91.5	91.7	100
44	1000	100	1000	100	1000	100	1000	100	1000	1000	88.8	95.9	93.0	100.7	101.8	100
45	1000	100	1000	100	1000	100	1000	100	1000	1000	60.8	40.7	45.2	47.6	48.0	100
46	1000	100	1000	100	1000	100	1000	100	1000	1000	53.6	56.5	58.5	63.1	63.9	110
47	1000	100	1000	100	1000	100	1000	100	1000	1000	64.8	69.4	71.9	78.7	87.0	110
48	1000	100	1000	100	1000	100	1000	100	1000	1000	69.8	76.7	77.0	83.9	87.8	130
49	1000	100	1000	100	1000	100	1000	100	1000	1000	57.0	56.1	57.6	63.8	64.7	110
50	1000	100	1000	100	1000	100	1000	100	1000	1000	56.3	61.0	62.2	68.5	69.4	110
51	1000	100	1000	100	1000	100	1000	100	1000	1000	61.0	65.8	66.0	73.0	74.5	110
52	1000	100	1000	100	1000	100	1000	100	1000	1000	64.9	69.8	70.5	76.7	78.0	110
53	1000	100	1000	100	1000	100	1000	100	1000	1000	78.6	85.8	81.6	91.5	91.7	100
54	1000	100	1000	100	1000	100	1000	100	1000	1000	88.8	95.9	93.0	100.7	101.8	100
55	1000	100	1000	100	1000	100	1000	100	1000	1000	60.8	40.7	45.2	47.6	48.0	100
56	1000	100	1000	100	1000	100	1000	100	1000	1000	53.6	56.5	58.5	63.1	63.9	110
57	1000	100	1000	100	1000	100	1000	100	1000	1000	64.8	69.4	71.9	78.7	87.0	110
58	1000	100	1000	100	1000	100	1000	100	1000	1000	69.8	76.7	77.0	83.9	87.8	130
59	1000	100	1000	100	1000	100	1000	100	1000	1000	57.0	56.1	57.6	63.8	64.7	110
60	1000	100	1000	100	1000	100	1000	100	1000	1000	56.3	61.0	62.2	68.5	69.4	110
61	1000	100	1000	100	1000	100	1000	100	1000	1000	61.0	65.8	66.0	73.0	74.5	110
62	1000	100	1000	100	1000	100	1000	100	1000	1000	64.9	69.8	70.5	76.7	78.0	110
63	1000	100	1000	100	1000	100	1000	100	1000	1000	78.6	85.8	81.6	91.5	91.7	100
64	1000	100	1000	100	1000	100	1000	100	1000	1000	88.8	95.9	93.0	100.7	101.8	100
65	1000	100	1000	100	1000	100	1000	100	1000	1000	60.8	40.7	45.2	47.6	48.0	100
66	1000	100	1000	100	1000	100	1000	100	1000	1000	53.6	56.5	58.5	63.1	63.9	110
67	1000	100	1000	100	1000	100	1000	100	1000	1000	64.8	69.4	71.9	78.7	87.0	110
68	1000	100	1000	100	1000	100	1000	100	1000	1000	69.8	76.7	77.0	83.9	87.8	130
69	1000	100	1000	100	1000	100	1000	100	1000	1000	57.0	56.1	57.6	63.8	64.7	110
70	1000	100	1000	100	1000	100	1000	100	1000	1000	56.3	61.0	62.2	68.5	69.4	110
71	1000	100	1000	100	1000	100	1000	100	1000	1000	61.0	65.8	66.0	73.0	74.5	110
72	1000	100	1000	100	1000	100	1000	100	1000	1000	64.9	69.8	70.5	76.7	78.0	110
73	1000	100	1000	100	1000	100	1000	100	1000	1000	78.6	85.8	81.6	91.5	91.7	100
74	1000	100	1000	100	1000	100	1000	100	1000	1000	88.8	95.9	93.0	100.7	101.8	100
75	1000	100	1000	100	1000	100	1000	100	1000	1000	60.8	40.7	45.2	47.6	48.0	100
76	1000	100	1000	100	1000	100	1000	100	1000	1000	53.6	56.5	58.5	63.1	63.9	110
77	1000	100	1000	100	1000	100	1000	100	1000	1000	64.8	69.4	71.9	78.7	87.0	

Table B-11. Model No. 11: Coannular-Coplanar,  $A_0/A_1 = 0.65$ , No Inner Flow.

$A_0 = 10.95 \text{ in.}^2$ ,  $A_1 = 16.82 \text{ in.}^2$  Linear Scale Factor to 318 in.  $2 = 5.58$  (Outer Only)

Date Point No.	Outer		Meteorological Conditions		Normalization Parameters		2400-ft. S.L. Data								
	$(P_0/P_{00})_0$	$T_0$ (°R)	$V_0$ (ft/sec)	$T_{00}$ (°F)	$T_{00}$ (°F)	$10 \log_{10} V_0/a_0$	$10 \log_{10} T_0/(T_{00})^{0.7}$	QASPL	PWL	QASPL	PWL	PPHL	8	POASPL	0
8645	1.539	737	1000	13	75	-0.474	37.0	63	67	69.4	74.4	76	130	73.3	140
8646	2.053	995	1451	82	75	-0.126	37.8	74.8	79.7	81.1	86.8	91.9	140	89.5	140
8647	2.724	1314	2005	84	76	2.545	37.9	85.3	91.5	90.2	97.3	105.1	140	101.3	140
8648	1.62	746	1049	82	75	-0.104	37.4	65.6	69.7	71.9	77.2	79.5	130	77	140
8649	2.738	1095	1655	84	76	1.712	37.7	78.4	85.9	83.8	90	95.9	140	93.2	140
8650	2.977	1481	2203	84	76	2.949	38.1	88.5	94.2	93.2	100.1	108.6	130	104.5	140
8651	1.728	820	1145	82	75	-0.297	37.7	68	72.1	74.5	79.8	83.3	130	90.7	140
8652	2.65	1204	1812	84	76	2.106	37.6	81.6	89	85.6	93.3	99.6	140	96	140
8653	3.263	1631	3385	85	76	3.200	38.3	88.7	94.5	93.3	100.8	109.8	130	104.9	130
8654	1.837	880	1399	82	75	0.660	37.8	70.4	74.6	76.7	82.2	85.9	130	83.4	140
8655	2.032	1303	1950	84	76	2.425	37.7	83.4	90.6	87.8	95.3	102.7	140	99	140
8656	3.945	1793	2577	85	76	3.635	38.4	90.5	96.4	95.2	102.5	112.7	130	107.1	130
8657	1.955	978	1394	82	75	0.968	37.9	73	77.6	79.3	84.8	82.9	130	87	140
8658	2.253	1399	2095	84	76	2.735	38.0	86.9	92.6	91.6	98.6	106.9	140	103	140
8659	3.878	1970	2783	84	76	3.969	38.6	93.2	97	95.7	104.2	113.8	140	108.7	130

Table B-12. Model No. 12: Coannular-Coplanar,  $A_0/A_1 = 0.4$ , Low Inner Flow.

$A_0 = 6.33 \text{ in.}^2$ ,  $A_1 = 16.82 \text{ in.}^2$  Linear Scale Factor to 318 in.  $2 = 1.09$  (Outer Only)

Data Point No.	Inner		Outer		Barometric Conditions	Normalization Parameters		2400-ft S.L. Data					
	$(P_0/P_{00})_0$	$T_0$ ( $^{\circ}\text{R}$ )	$V_0$ (ft/sec)	$T_0$ ( $^{\circ}\text{F}$ )		$10 \log_{10} V_0/a_0$	$10 \log_{10} T_0/(T_{00})^{0.7}$	QASPL	PWL	QASPL	PWL	QASPL	PWL
8665	1.053	186	101	989	6.1	2.3	39.9	60.5	64.3	65.3	65.8	71.4	74.4
8666	1.004	248	121	1272	14.1	3.3	37.9	69.7	74.4	74.4	76.4	81.8	85.8
8667	1.009	104	103	2028	13.8	3.8	37.8	87.1	95.8	86.6	95.8	98.6	105.8
8668	1.017	401	186	1093	5.9	2.1	37.3	62.6	67.1	68.2	74.1	76.6	81.8
8669	1.001	195	92	1817	32.9	11.6	38.0	75.4	85.6	79.0	86.7	89.9	93.0
8670	1.002	220	70	2098	37.3	8.3	38.1	89.1	96.8	89.9	98.7	102.3	105.8
8671	1.017	610	186	1298	6.4	2.2	37.7	64.3	68.5	70.8	76.0	78.4	81.8
8672	1.005	222	113	1789	16.1	5.1	38.2	82.5	93.0	83.0	92.1	95.1	98.6
8673	1.005	965	127	2062	18.8	6.0	38.4	89.3	96.6	91.3	99.5	104.9	109.8
8674	1.005	636	104	1896	12.4	4.3	37.8	66.6	70.8	72.7	78.3	81.6	85.0
8675				1947	37	63	38.5	91.1	95.5	86.5	95.7	98.5	102.7
8676	1.009	946	172	2369	14.8	4.6	38.6	89.8	96.7	92.2	100.0	107.3	110.5
8677	1.003	228	104	1864	13.7	4.5	38.0	68.7	72.8	76.8	80.9	83.8	86.8
8678	1.003	724	84	2409	19.4	6.7	38.0	88.9	96.5	88.9	97.8	101.0	104.0
8679	1.017	983	216	2770	14.8	3.3	38.4	90.5	97.3	94.2	101.6	110.5	113.0

Table B-13. Model No. 13: Coannular-Coplanar,  $A/A_1 = 0.4$ , No Inner Flow.

Data Point No.	Outer		Matemovological Conditions		Normalization Parameters		Linear Scale Factor to 13E (in. $\pm$ 7.59 (Outer Only)					
	$(T/T_0)_0$	$(T/T_0)_0$	$T_0$	$T_0$	$10 \log 10$	$10 \log 10$	$50^\circ$	$50^\circ$	$2400\text{-ft S.L. Data}$	$50^\circ$	$50^\circ$	$50^\circ$
	$(T/T_0)_0$	$(T/T_0)_0$	$(T/T_0)_0$	$(T/T_0)_0$	$(T/T_0)_0$	$(T/T_0)_0$	$(T/T_0)_0$	$(T/T_0)_0$	$(T/T_0)_0$	$(T/T_0)_0$	$(T/T_0)_0$	$(T/T_0)_0$
8445	1.528	713	997	89	76	89	68.5	70.9	75.3	76.7	120	74.5
8446	2.047	994	1638	90	77	90	81.1	83.1	88.2	92.8	130	90.1
8447	2.718	1334	2803	92	77	92	85.6	88.6	92.6	97.1	130	100.5
8448	1.62	770	1592	89	76	89	67.9	71.9	78.6	80.3	130	78.3
8449	2.383	1106	1666	90	77	90	80.2	86	91.5	97.1	130	94.3
8450	2.999	1474	2155	95	77	95	94.4	96.6	100.9	109.1	130	105
8451	1.716	823	1302	89	76	89	70.8	76.7	81.5	84.3	130	82.3
8452	2.416	1189	1748	90	77	90	82.6	88	93.7	100	130	96.6
8453	2.786	1434	2188	90	77	90	90.6	96	102.5	111.1	130	106.9
8454	1.834	875	1394	89	76	89	77.1	79	84	87.3	130	84.6
8455	2.44	1292	1945	90	77	90	84.9	90.5	96.5	103.4	130	99.8
8456	2.549	1342	2371	90	77	90	90.6	95.7	102.5	111.9	130	107.5
8457	1.942	980	1397	90	77	90	74.7	81.1	86	90	130	87.5
8458	2.855	1399	2095	90	77	90	86.8	93.5	98.8	105.9	130	100.8
8459	2.894	1494	2734	90	77	90	91.5	96.7	103.9	113.1	130	108.5



Table B-14. Model No. 14: 4.64-inch-Diameter Conical, Adapted to Cell 41, Anechoic.

$A_1 = 16.82$  in. 2 Linear Scale Factor to 333 in. 2 = 4.48

Data Point No.	Inner		Meteorological Conditions		Normalization Parameters		2400-ft S.L. Data							
	$(P/P_0)_i$	$V_i$ (ft/sec)	Tdry (° F)	Twet (° F)	$10 \log_{10} V/a_0$	$10 \log_{10} F_g(T_0/T_{\text{melt}})^{0.5-1}$	OASPL	PNL	90°	PPNL	$\theta$	POASPL	$\theta$	
1	1.099	1017	52	54	-2.9	34.1	17.6	48.0	53.9	55.5	58.0	120	57.2	130
2	1.215	1309	52	44	-1.3	35.5	55.3	58.6	62.1	66.4	69.7	120	67.3	130
3	1.037	1084	51	44	-0.6	35.9	60.1	64.4	67.3	72.6	76.7	130	73.9	140
4	1.474	1109	50	42	0.3	36.2	64.8	69.8	72.3	78.3	83.8	130	81.1	140
5	1.723	1173	49	42	1.1	36.3	69.8	75.2	77.0	83.9	91.5	130	88.2	140
6	1.971	1203	49	42	1.6	36.5	72.8	78.3	80.1	87.5	96.6	130	92.7	140
7	2.251	1266	48	41	2.1	36.9	79.6	86.3	83.5	92.4	101.4	140	96.1	140
8	2.745	1320	48	41	2.5	38.0	86.9	93.4	89.2	97.9	106.0	130	101.6	130
9	3.246	1380	40	41	2.9	39.0	90.9	97.3	93.6	101.4	109.1	130	103.4	130
10	3.924	1466	43	42	3.3	40.0	93.2	99.5	96.0	104.0	112.3	130	106.5	130
11	1.319	1625	51	43	0.4	34.3	65.4	70.0	72.5	78.0	83.4	130	81.0	140
12	1.601	1697	50	43	1.6	33.4	71.2	76.2	78.5	85.2	94.0	140	90.9	140
13	2.059	1739	49	41	2.5	34.5	76.1	81.6	83.8	91.5	103.5	130	98.1	130
14	1.329	1737	49	42	1.3	35.7	55.6	59.9	62.7	67.6	70.8	130	68.0	140
15	1.947	1764	49	42	0.4	38.6	67.8	74.1	73.8	80.8	86.1	130	82.7	140
16	2.493	1707	49	42	1.0	40.2	87.8	93.4	90.1	97.5	97.7	80	90.4	140
17	3.491	1705	48	41	1.6	42.5	91.1	97.1	92.6	100.4	100.8	120	95.5	140
18	1.559	990	49	42	0.3	36.8	65.3	70.4	72.6	78.9	84.7	130	81.9	140
19	2.296	1607	48	41	1.6	38.3	80.7	87.2	82.3	91.2	98.2	140	94.2	140
20	3.962	1981	49	43	2.5	41.9	93.8	99.9	96.0	104.0	108.0	140	103.3	140
21	1.148	1501	52	45	1.3	35.3	51.6	60.8	64.3	68.2	71.4	120	69.9	130
22	1.797	1501	50	42	1.6	34.4	71.9	77.1	79.0	86.0	94.7	140	91.2	140
23	2.404	1526	47	41	2.6	36.3	81.0	87.7	85.9	94.6	105.6	130	100.1	130
24	2.915	1512	48	41	2.9	37.8	87.6	94.3	91.0	99.5	108.8	130	103.0	130
25	3.674	1504	48	42	3.3	39.5	92.9	99.1	95.5	103.5	111.9	130	106.2	130
26	1.162	842	57	45	-2.3	34.3	49.8	52.2	56.6	60.2	62.9	120	61.0	130
27	1.251	1018	52	44	-1.1	35.7	56.1	59.7	62.9	67.5	70.9	120	66.9	120
28	2.958	1069	48	42	2.1	39.9	89.8	96.2	91.2	99.0	104.4	140	99.7	140
29	1.381	1493	50	43	0.5	34.7	66.0	70.9	73.2	79.0	85.2	130	82.3	140
30	2.012	1497	49	42	2.1	35.1	74.7	80.3	82.3	89.7	100.1	130	95.5	140
64	2.480	1712	48	41	3.1	36.4	84.6	91.1	89.0	97.8	108.9	130	103.1	130
65	1.979	1626	49	42	2.2	34.4	75.1	80.7	82.9	90.4	101.5	130	96.5	130
66	1.197	1712	52	44	-1.1	35.5	57.6	61.2	64.3	68.7	72.3	120	70.1	140
67	1.787	862	48	41	0.5	37.8	67.0	72.7	73.8	79.8	86.9	130	83.9	140
68	2.024	863	48	41	0.9	38.3	69.7	75.9	76.3	83.4	90.2	130	87.1	140
69	2.196	849	47	40	1.1	38.9	79.7	86.4	80.9	89.5	92.9	140	89.6	140
70	2.380	815	47	41	1.3	39.3	82.6	89.3	84.2	92.0	97.3	150	92.8	140
71	2.648	850	48	41	1.4	40.1	86.7	92.4	89.3	97.1	99.1	140	95.3	140
72	2.809	854	49	42	1.6	40.3	88.1	94.0	91.8	99.7	100.8	140	96.6	147

Table B-15. Model No. 15: 36 Chute, AR = 2.5,  $R_r = 0.653$ , Turbojet.

$A_1 = 11.76$  in. 2 Atmos. Scale Factor to 135 in. 2 = 1.62

Data Point No.	Inlet $P_0$ (psi) $P_0$ (psi)	Inlet $T_0$ (°R) $T_0$ (°F)	Inlet $V_0$ (ft/sec) $V_0$ (ft/sec)	Metastable Conditions $T_0$ (°R) $T_0$ (°F)	Normalization Parameters		2400-ft S.L. Data					
					$10 \log 10$ $V_0$	$10 \log 10$ $F_0 (T_0/T_{SM})^{0.1}$	50°		90°		FOASPL	
							QASPL	PNL	QASPL	PNL	QASPL	PNL
1	2.028	1148	2019	80	2.462	37.9	72.9	82.6	82.7	93.0	95.2	120
2	2.076	1141	2129	81	2.404	38.3	76.2	85.7	84.3	94.1	97.3	110
3	2.124	1134	2239	82	2.346	37.7	71.7	80.3	80.6	90.9	93.1	120
4	2.172	1127	2349	83	2.288	38.1	78.3	88.2	85.9	96.0	98.5	140
5	2.220	1120	2459	84	2.230	38.6	79.9	89.0	87.6	97.5	100.0	140
6	2.268	1113	2569	85	2.172	37.9	66.7	75.4	75.8	85.7	87.5	120
7	2.316	1106	2679	86	2.114	39.2	79.9	89.0	87.6	97.6	100.1	140
8	2.364	1099	2789	87	2.056	39.0	65.5	73.9	73.4	83.5	83.7	110
9	2.412	1092	2899	88	2.000	40.6	70.3	80.0	77.2	87.4	88.6	120
10	2.460	1085	3009	89	1.944	42.1	76.0	86.5	80.9	91.9	92.4	140
11	2.508	1078	3119	90	1.888	37.3	75.3	83.5	84.7	95.2	97.3	120
12	2.556	1071	3229	91	1.832	36.5	73.1	81.5	83.2	93.8	96.2	120
13	2.604	1064	3339	92	1.776	35.6	71.8	80.2	81.8	92.5	94.5	110
14	2.652	1057	3449	93	1.720	34.6	70.4	78.8	80.7	91.4	93.7	120
15	2.700	1050	3559	94	1.664	35.0	71.8	80.2	81.8	92.5	94.5	120
16	2.748	1043	3669	95	1.608	37.6	63.6	72.0	72.9	82.8	83.9	120
17	2.796	1036	3779	96	1.552	36.2	60.5	68.4	71.4	80.8	82.2	120
18	2.844	1029	3889	97	1.496	36.5	68.5	76.9	78.0	88.4	90.7	120
19	2.892	1022	3999	98	1.440	40.2	81.2	90.3	87.2	97.5	100.5	140
20	2.940	1015	4109	99	1.384	35.4	53.7	60.5	63.6	71.7	72.2	100
21	2.988	1008	4219	100	1.328	37.6	64.9	73.5	73.3	81.1	83.8	110
22	3.036	1001	4329	101	1.272	38.3	65.9	74.3	75.1	86.7	86.7	120
23	3.084	994	4439	102	1.216	38.9	68.3	76.9	76.9	86.7	88.5	120
24	3.132	987	4549	103	1.160	39.3	69.4	78.0	77.8	87.8	89.8	120
25	3.180	980	4659	104	1.104	39.9	71.2	80.3	78.8	89.0	90.7	120
26	3.228	973	4769	105	1.048	40.3	78.2	87.3	79.6	89.7	91.7	120
27	3.276	966	4879	106	1.000	40.3	78.2	87.3	79.6	89.7	91.7	120

Table B-16. Model No. 16: 36 Chute, AR = 2.0,  $R_T = 0.716$ , Turbojet.

$A_1 = 23.76$  in. 2 Linear Scale Factor to 338 in. 2 = 3.77

Data Point No.	Inner		Meteorological Conditions	Normalization Parameters		2400-ft S.L. Data					
	$(P_T/P_{O_2})_1$ ( $^{\circ}$ R)	$T_{T_1}$ ( $^{\circ}$ R)		$10 \log_{10} V/a_0$	$10 \log_{10} F_g(T_{O_2}/T_{T_1})^{0.1}$	50°		90°		POASPL	
		$V_1$ (ft/sec)	$T_{Dry}$ ( $^{\circ}$ F)	$T_{Wet}$ ( $^{\circ}$ F)		OASPL	PWL	OASPL	PWL	$\theta$	$\theta$
1	2.745	1324	2004	75	66	73.9	83.9	82.4	92.5	95.2	120
2	3.002	1434	2204	71	64	76.4	86.6	84.4	94.6	97.2	120
3	2.416	1204	1807	71	64	71.4	79.9	80.5	90.7	93.1	120
4	3.264	1611	2371	76	67	78.2	87.7	86.0	96.1	99.5	140
5	3.566	1753	2552	78	68	79.1	87.2	87.2	96.7	101.5	140
6	1.928	947	1396	65	61	66.4	74.7	82.5	88.4	88.4	120
7	3.902	1756	2627	77	67	79.4	86.4	88.1	97.2	103.7	140
8	2.026	634	1188	70	62	65.6	73.7	73.7	83.6	84.5	120
9	2.565	655	1194	66	60	70.7	81.6	77.4	87.7	88.6	120
10	3.302	739	1603	66	62	77.9	88.1	82.1	93.7	94.5	140
11	2.953	1756	2387	76	67	75.7	84.8	85.3	95.3	98.6	140
12	2.665	1745	2279	76	67	73.9	81.7	84.0	94.2	96.8	120
13	2.368	1733	2146	78	69	72.4	79.7	82.9	93.6	95.9	110
14	2.009	1632	1892	77	68	70.2	78.0	80.8	91.6	93.9	110
15	2.124	1673	1990	77	68	70.9	78.5	81.4	92.2	94.4	110
16	1.734	820	1199	66	61	63.4	71.7	72.6	82.3	84.3	120

Table B-17. Model No. 17: 36 Chute, AR = 1.5,  $R_T = 0.782$ , Turbojet.

$A_1 = 23.76$  in. 2 Linear Scale Factor to 338 in. 2 = 3.77

Data Point No.	Inner		Meteorological Conditions	Normalization Parameters		2400-ft S.L. Data					
	$(P_T/P_{O_2})_1$ ( $^{\circ}$ R)	$T_{T_1}$ ( $^{\circ}$ R)		$10 \log_{10} V/a_0$	$10 \log_{10} F_g(T_{O_2}/T_{T_1})^{0.1}$	50°		90°		POASPL	
		$V_1$ (ft/sec)	$T_{Dry}$ ( $^{\circ}$ F)	$T_{Wet}$ ( $^{\circ}$ F)		OASPL	PWL	OASPL	PWL	$\theta$	$\theta$
1	2.699	1347	2007	62	64	74.2	82.5	82.7	91.8	95.8	140
2	3.001	1493	2210	62	64	76.2	84.7	84.5	93.7	98.8	140
3	2.463	1194	1809	62	64	71.7	79.9	80.4	89.7	91.8	140
4	3.266	1620	2378	62	64	78.3	86.2	86.4	95.7	102.9	140
5	3.567	1758	2556	65	67	81.1	88.9	88.2	97.6	106.5	140
6	1.951	939	1401	63	65	66.0	73.4	75.4	84.8	86.6	120
7	3.924	1744	2623	64	66	83.0	90.0	89.5	99.0	108.4	140
8	2.077	634	1199	62	64	66.1	74.4	73.7	83.3	83.5	110
9	2.599	650	1397	62	64	70.6	80.9	77.3	87.0	87.0	140
10	3.316	734	1600	62	64	78.1	87.6	82.1	93.4	93.4	140
11	3.064	1766	2428	63	65	76.7	83.6	85.6	94.5	101.8	140
12	2.700	1782	2308	63	65	75.1	81.0	84.4	93.4	99.7	140
13	2.405	1735	2165	63	65	73.2	79.2	83.0	92.2	95.8	140
14	1.987	1618	1871	62	64	69.8	76.2	79.9	89.5	92.2	120
15	2.151	1665	1994	62	64	71.3	77.5	81.2	90.6	93.8	120
16	1.744	819	1204	63	65	63.0	70.7	72.9	82.1	82.9	120

Table B-18. Model No. 18: 36 Spoke, AR = 2.0,  $R_T = 0.716$ , Turbojet.

$A_1 = 23.76$  in. 2 Linear Scale Factor to 338 in. 2 = 3.77

Data Point No.	Intr-Er		Meteorological Conditions		Normalization Parameters		2400-ft S.L. Data								
	$(P_T/P_0)_1$	$V_1$ (ft/sec)	$T_{Dry}$ (° F)	$T_{Wet}$ (° F)	$10 \log_{10} V/A_0$	$10 \log_{10} F_g(T_0/T_{em})^{\omega-1}$	50°		90°		PPNL	$\theta$	POASPL	$\theta$	
1	2.723	1344	2012	67	67	2.560	37.9	72.2	79.7	81.3	90.7	93.0	120	88.4	140
2	3.000	1491	2209	80	68	2.965	38.1	74.3	80.7	82.9	91.7	95.7	140	92.1	140
3	2.440	1194	1801	79	67	2.078	37.7	70.8	79.0	79.6	89.4	91.5	110	84.4	140
4	3.288	1622	2385	80	68	3.258	39.3	76.2	82.0	84.9	93.4	98.7	140	95.3	140
5	3.560	1723	2528	80	68	3.551	38.6	78.9	85.4	87.0	95.5	103.8	140	100.0	140
6	1.926	939	1389	80	68	0.950	37.8	66.4	75.2	75.1	85.7	97.3	110	77.0	140
7	3.924	1718	2618	80	68	3.703	39.3	81.3	88.0	88.3	97.0	107.5	140	103.6	140
8	2.041	644	1194	79	67	0.293	38.9	66.0	74.4	73.7	84.1	84.9	110	74.5	110
9	2.611	673	1398	79	67	0.978	40.6	69.6	78.7	76.7	87.1	87.4	110	77.3	110
10	3.308	726	1590	79	68	1.537	42.0	73.9	83.2	79.7	89.8	89.8	90	85.1	140
11	2.948	1175	2384	80	68	3.330	37.2	75.6	81.7	84.0	92.6	97.4	140	93.9	140
12	2.664	1746	2280	80	68	3.103	36.5	74.2	81.0	83.2	92.3	95.7	140	91.2	140
13	2.398	1723	2154	80	68	2.856	35.7	72.8	80.2	81.9	91.6	94.1	120	88.1	140
14	2.030	1621	1899	80	68	2.309	34.7	69.3	77.1	79.4	89.6	92.2	110	82.9	140
15	2.132	1661	1982	80	68	2.494	35.0	70.8	78.4	80.5	90.5	93.3	110	84.9	140
16	1.718	823	1191	79	68	0.282	37.7	63.4	72.3	72.2	82.9	84.1	110	73.5	110

Table B-19. Model No. 19: 36 Chute, AR = 2.0,  $R_T = 0.716$ , Turbojet with Acoustically Treated Secondary Ejector.

$A_1 = 23.76$  in. 2 Linear Scale Factor to 338 in. 2 = 3.77

Data Point No.	Inner		Meteorological Conditions		Normalization Parameters			2400-ft S.L. Data						
	$\tau_{r_1}$ ( $^{\circ}$ R)	$V$ (ft/sec)	$T_{Dry}$ ( $^{\circ}$ F)	$T_{Wet}$ ( $^{\circ}$ F)	$10 \log_{10} V/a_0$	$10 \log_{10} F_0(T_0/T_{ref})^{0.1}$	50°		90°		PPNL	$\theta$	POASPL	$\theta$
1	2.727	1336	66	61	2.549	37.9	72.5	79.0	80.8	89.6	91.6	110	86.5	140
2	3.013	1465	66	62	2.934	38.2	74.5	81.2	82.7	91.3	93.4	110	89.9	140
3	2.444	1202	66	61	2.098	37.6	69.9	76.8	78.6	87.2	89.3	110	82.3	140
4	3.300	1620	65	61	3.298	38.4	77.0	84.5	34.7	83.1	97.5	140	94.5	140
5	3.553	1748	65	61	3.580	38.5	79.6	87.2	87.2	95.3	102.7	140	99.9	140
6	1.935	935	68	62	0.954	37.9	64.3	71.0	72.7	80.9	82.8	120	74.6	120
7	3.897	1754	65	62	3.713	39.2	81.8	88.0	88.9	96.7	107.8	140	104.5	140
8	0.042	658	73	65	0.344	38.9	64.2	70.7	71.8	79.5	80.1	110	72.4	110
9	2.578	683	67	62	0.969	40.5	69.2	76.2	76.5	84.8	85.2	110	78.3	140
10	3.303	742	69	64	1.584	41.9	76.6	85.9	81.3	91.6	92.1	80	85.9	140
11	2.984	1745	65	61	3.311	37.3	74.9	81.3	83.8	92.4	95.4	140	91.8	140
12	2.683	1756	66	62	3.127	36.5	73.0	79.1	82.4	91.1	93.7	110	88.9	140
13	2.367	1722	66	62	2.825	35.6	71.1	76.9	80.6	89.8	92.4	110	85.9	140
14	2.016	1621	68	63	2.289	34.6	67.9	73.5	77.3	86.5	89.9	110	80.6	140
15	2.135	1659	67	62	2.494	35.0	69.1	74.7	78.4	87.6	90.6	110	82.4	140
16	1.723	823	71	65	0.293	37.7	61.2	87.8	69.3	77.2	78.5	120	70.5	120

Table B-20. Model No. 20: 72 Tube/Plug, AR = 2.95, Turbojet.

 $A_1 = 30.87$  in. 2 Linear Scale Factor to 338 in. 2 = 3.31

Data Point No.	Inner		Meteorological Conditions		Normalization Parameters		2400-ft S.L. Data					
	$(P_T/P_0)_1$ ("R)	$T_{T1}$ ("R)	$T_{Dry}$ ("F)	$T_{Wet}$ ("F)	$10 \log_{10} V/a_0$	$10 \log_{10} F_s(T_0/T_{sm})^{\omega-1}$	50° OASPL	50° PNL	90° OASPL	90° PNL	PPNL	POASPL
1	2.772	1309	2001	37	2.5	38.1	72.8	82.5	80.1	91.5	93.9	84.3
2	3.001	1240	2009	46	2.6	38.9	73.4	83.3	80.6	91.6	93.6	85.2
3	2.471	1180	1806	40	2.1	37.8	71.0	80.8	71.0	89.8	92.2	81.4
4	3.244	1171	2008	45	2.6	39.8	74.1	84.6	81.1	92.2	94.3	86.7
5	2.232	1081	1634	37	1.7	37.6	69.3	79.2	76.8	88.5	90.4	79.5
6	3.566	1116	2022	45	2.6	40.7	74.9	85.6	81.6	92.4	94.9	88.3
7	1.931	937	1390	37	1.0	37.8	66.1	76.0	73.7	85.3	86.8	75.6
8	3.880	1057	2020	54	2.6	41.5	75.8	86.7	82.0	92.7	95.2	83.0
9	2.986	1262	2024	46	2.6	38.8	73.5	83.4	80.6	91.6	93.9	85.5
10	2.378	1411	1936	55	2.4	36.6	71.4	81.2	78.8	90.3	92.4	81.7
11	1.780	1398	1603	41	1.6	35.1	67.4	77.4	74.6	86.4	88.8	77.8
12	1.490	1135	1214	39	0.4	36.1	62.1	71.7	69.2	80.2	82.5	71.7
13	2.061	646	1204	34	0.3	38.9	65.9	75.7	72.7	84.3	84.9	73.6
14	2.591	675	1390	35	1.0	40.5	69.6	79.6	75.8	87.4	88.3	77.4
15	3.305	764	1630	43	1.6	41.8	73.1	84.5	78.6	90.1	91.0	81.9
16	1.691	1163	1398	38	1.0	36.3	65.2	74.9	72.5	84.0	86.0	75.0

Table B-21. Model No. 21: 32 Chute, AR = 2.0,  $R_T = 0.498$ , Turbojet. $A_1 = 30.83$  in. 2 Linear Scale Factor to 338 in. 2 = 3.31

Data Point No.	Inner		Meteorological Conditions		Normalization Parameters		2400-ft S.L. Data					
	$(P_T/P_0)_1$ ("R)	$T_{T1}$ ("R)	$T_{Dry}$ ("F)	$T_{Wet}$ ("F)	$10 \log_{10} V/a_0$	$10 \log_{10} F_s(T_0/T_{sm})^{\omega-1}$	50° OASPL	50° PNL	90° OASPL	90° PNL	PPNL	POASPL
1	2.727	1326	2001	60	2.536	37.9	71.7	79.9	75.6	89.9	92.7	89.6
2	3.013	1257	2026	68	2.590	38.9	73.3	81.9	80.6	89.8	95.1	92.1
3	2.453	1183	1797	59	2.069	37.7	69.6	78.1	77.5	87.6	90.2	85.0
4	3.289	1206	2049	66	2.639	39.7	75.6	85.5	81.9	90.9	97.2	94.2
5	2.220	1072	1622	61	1.624	37.8	67.4	76.3	75.1	85.7	88.1	80.5
6	3.595	1124	2034	61	2.607	40.7	78.0	87.0	83.3	92.6	98.7	95.7
7	1.941	942	1398	61	0.978	37.8	64.0	73.4	71.8	83.1	85.1	75.4
8	3.925	1046	2016	68	2.568	41.6	81.9	89.1	85.4	94.9	100.6	97.4
9	3.017	1308	2067	66	2.677	38.7	73.4	81.8	80.8	89.8	95.4	92.2
10	2.388	1458	1973	66	2.475	36.5	70.7	79.0	78.9	89.0	91.6	87.3
11	1.811	1355	1599	59	1.562	35.4	65.6	74.6	73.8	84.9	87.1	78.3
12	1.497	1133	1219	59	0.383	36.1	63.0	72.7	67.6	79.0	80.6	70.2
13	2.077	636	1200	64	0.315	39.0	63.0	72.8	69.8	81.4	81.9	71.5
14	2.596	678	1395	58	0.909	40.5	67.2	76.8	73.7	84.6	85.5	77.9
15	3.368	741	1616	64	1.608	42.1	64.0	74.3	68.7	78.8	79.5	76.2
16	1.711	1107	1416	64	1.034	36.3	62.9	72.2	71.1	82.5	84.3	74.4

Table B-22. Model No. 22: 36 Chute, AR = 2.5,  $R_I^0 = 0.653$  Outer Suppressor;  $A_0/A_1 = 1.92$ ,  $R_I^1 = 0.779$  Inner Plug, Retracted.

$A_0 = 11.76 \text{ in.}^2$ ,  $A_1 = 1.59 \text{ in.}^2$  Linear Scale Factor to 138 in.<sup>2</sup> = 3.06

Data Factor No.	Inner		Outer		Ratio		Mass Averages		Meteorological Conditions		Normalization Parameters		3400-ft S.L. Data			
	$(P_0/P_{01})_i$	$(T_0/T_{01})_i$	$(P_0/P_{0o})_o$	$(T_0/T_{0o})_o$	$V_i/V_o$	$W_i/W_o$	$(P_0/P_{01})_{ma}$	$(T_0/T_{01})_{ma}$	$V_{ma}$ (ft/sec)	$T_{01}$ (°F)	$10 \log_{10}$ $(V/A_0)$	$10 \log_{10}$ $(P_0/T_{01})$	QASPL	FWL	QASPL	FWL
9	1.063	808	520	1546	1.8	6.5	2.273	1286	1802	58	2.082	36.1	71.1	80.0	81.0	91.8
10	1.082	818	530	1582	1.8	6.7	2.104	1148	1628	58	2.039	36.4	71.3	77.9	78.3	89.1
11	1.095	822	537	1606	1.8	7.5	2.219	1260	1776	58	2.000	36.5	71.6	83.4	86.0	95.5
12	1.098	831	544	1656	1.8	7.8	2.062	1067	1556	60	2.264	37.0	71.0	86.4	85.8	95.5
13	1.214	896	599	1791	1.8	8.2	1.729	908	1253	59	0.516	37.1	64.1	72.7	73.4	83.8
14	1.189	896	603	1862	2.1	3.2	2.258	1251	1771	59	2.004	36.7	71.4	80.0	80.6	91.3
15	1.204	913	613	1867	2.7	3.4	2.206	1272	1864	58	2.654	35.3	73.0	81.3	82.4	93.4
16	1.15	896	605	1851	2.3	3.3	2.079	1122	1625	58	2.711	37.9	69.2	83.0	84.1	94.1
17	1.15	896	605	1851	2.3	3.3	2.079	1122	1625	58	2.711	37.9	69.2	83.0	84.1	94.1
20	1.16	907	625	1909	2.5	3.6	2.844	1581	2265	58	3.073	37.6	71.1	86.2	86.0	96.1
23	1.278	926	625	1992	1.9	1.6	2.309	1068	1653	60	1.706	38.1	71.1	79.5	80.5	91.2
24	1.313	1009	1182	2251	1.0	2.4	1.461	904	1211	59	0.354	37.2	60.9	68.4	71.1	80.9
25	1.316	992	1174	2254	1.5	2.7	2.099	1161	1635	59	1.657	36.9	68.1	75.5	76.8	89.5
27	1.326	1129	1312	2413	1.2	1.3	2.099	1161	1635	59	1.657	36.9	68.1	75.5	76.8	89.5
28	1.330	1127	1305	2407	1.2	1.3	2.099	1161	1635	59	1.657	36.9	68.1	75.5	76.8	89.5
30	1.330	1127	1305	2407	1.2	1.3	2.099	1161	1635	59	1.657	36.9	68.1	75.5	76.8	89.5
33	1.487	1444	1343	2666	1.0	3.2	1.769	1081	1399	59	0.982	36.7	63.5	71.0	74.3	84.6
36	1.673	1659	1559	2812	1.6	3.7	2.366	1446	1954	59	2.433	36.3	72.7	81.2	81.2	92.3
37	1.675	1657	1567	2829	1.6	4.8	1.188	1696	2413	59	3.348	37.7	78.3	87.4	87.1	96.9

Table B-23. Model No. 23: 36 Chute, AR = 2.0,  $R_I^0 = 0.716$  Outer Suppressor:  $A_0/A_1 = 1.92$ ,  $R_I^1 = 0.779$   
Inner Plug, In-Line.

$A_0 = 21.26 \text{ in.}^2$ ,  $A_1 = 12.39 \text{ in.}^2$   
No. 1-27 at 1.87 Chute Plane

Linear Scale Factor to 338 in.<sup>2</sup>, No. 1-8 at 3.37 (Outer Only):

Data Point No.	Lower		Outer		Ratios		Mass Averages		Meteorological Conditions		Normalization Parameters		2400-ft S.L. Data			
	$(V_1/V_0)_1$	$(V_1/V_0)_2$	$(V_1/V_0)_3$	$(V_1/V_0)_4$	$V_1/V_0$	$V_0/V_1$	$(V_1/V_0)_m$	$(V_1/V_0)_m$	$T_{avg}$	$T_{avg}$	$10 \log_{10} (V_1/V_0)$	$10 \log_{10} (V_0/V_1)$	QASFL	90°	90°	POASFL
1	0	0	0	0	0	0	0	0	75	70	2.6	37.9	74.0	84.1	82.3	95.7
2	0	0	0	0	0	0	0	0	74	70	3.4	37.2	76.1	85.4	85.4	96.2
3	0	0	0	0	0	0	0	0	76	70	2.1	37.8	71.6	80.8	80.3	93.5
4	0	0	0	0	0	0	0	0	75	70	3.3	38.3	78.4	88.4	85.8	98.9
5	0	0	0	0	0	0	0	0	76	70	1.6	37.8	69.2	77.5	78.3	91.4
6	0	0	0	0	0	0	0	0	76	71	3.6	38.5	79.2	87.6	87.1	100.2
7	0	0	0	0	0	0	0	0	76	70	1.0	37.9	66.3	74.2	75.5	85.3
8	0	0	0	0	0	0	0	0	73	69	3.2	36.5	73.9	81.6	84.0	97.1
9	0	0	0	0	0	0	0	0	71	65	2.0	36.5	71.1	80.0	79.5	92.7
10	0	0	0	0	0	0	0	0	70	65	2.9	35.7	74.4	83.5	82.5	96.7
11	0	0	0	0	0	0	0	0	70	65	2.5	35.1	73.1	81.2	81.8	95.1
12	0	0	0	0	0	0	0	0	71	65	1.6	36.7	68.5	76.8	77.6	90.6
13	0	0	0	0	0	0	0	0	69	65	2.7	36.8	76.0	86.3	83.0	96.6
14	0	0	0	0	0	0	0	0	70	65	3.0	37.0	76.7	85.8	84.5	97.7
15	0	0	0	0	0	0	0	0	70	64	0.7	37.5	65.3	73.7	72.9	85.6
16	0	0	0	0	0	0	0	0	72	65	2.1	38.3	72.4	80.6	80.3	93.2
17	0	0	0	0	0	0	0	0	71	65	2.5	36.0	73.4	81.2	82.1	92.2
18	0	0	0	0	0	0	0	0	66	64	2.5	36.0	70.9	79.4	78.4	91.0
19	0	0	0	0	0	0	0	0	72	61	1.7	37.8	76.9	86.5	83.6	93.8
20	0	0	0	0	0	0	0	0	72	66	3.0	38.4	77.9	86.8	85.2	95.1
21	0	0	0	0	0	0	0	0	71	66	0.1	38.0	61.9	69.8	70.3	82.3
22	0	0	0	0	0	0	0	0	76	66	0.7	38.4	66.1	74.4	74.0	84.3
23	0	0	0	0	0	0	0	0	78	67	1.7	38.0	70.9	79.2	79.5	89.8
24	0	0	0	0	0	0	0	0	74	71	0.3	37.3	62.4	70.6	70.6	82.8
25	0	0	0	0	0	0	0	0	74	70	1.7	37.1	70.0	78.3	78.0	88.3
26	0	0	0	0	0	0	0	0	76	69	2.7	37.2	76.0	85.8	83.1	96.1
27	0	0	0	0	0	0	0	0	74	66	1.4	37.1	67.6	75.5	76.2	86.6
28	0	0	0	0	0	0	0	0	77	67	2.0	36.7	70.9	79.1	79.1	89.1
29	0	0	0	0	0	0	0	0	76	68	3.2	37.2	77.0	85.7	84.7	94.4
30	0	0	0	0	0	0	0	0	76	65	2.6	37.8	76.6	86.0	83.4	92.7
31	0	0	0	0	0	0	0	0	73	64	2.5	38.0	77.0	86.3	83.0	93.8
32	0	0	0	0	0	0	0	0	72	64	2.2	36.9	74.0	83.0	80.9	91.9
33	0	0	0	0	0	0	0	0	69	63	1.7	36.1	69.9	78.0	78.0	89.2
34	0	0	0	0	0	0	0	0	70	63	2.1	37.4	75.6	85.2	81.0	92.2
35	0	0	0	0	0	0	0	0	77	67	0.9	36.9	65.7	73.0	73.0	83.0
36	0	0	0	0	0	0	0	0	77	67	2.4	36.5	72.7	81.7	81.1	91.1
37	0	0	0	0	0	0	0	0	75	66	3.3	37.6	78.9	88.4	85.8	95.4

Table B-24. Model No. 24: 36 Chute, AR = 2.0,  $R_r^0 = 0.716$  Outer Suppressor;  $A_0/A_i = 1.92$ ,  $R_r^i = 0.779$   
Inner Plug, Retracted.

$A_0 = 21.76 \text{ in.}^2$ ,  $A_i = 12.99 \text{ in.}^2$  Linear Scale Factor to 11B (a. 2 Sec. 1-8 at 3.77 (Outer Only); No. 9-37 at 3.07 (Dual Flow))

Data Point No.	Inner		Outer		Ratio	Mass Averages		Micrological Conditions		Normalization Parameters		2400-ft S.L. Data			
	$(P_r/P_0)_i$	$\frac{V_i}{V_0}$	$(P_r/P_0)_o$	$\frac{V_o}{V_0}$		$(P_r/P_0)_m$	$\frac{V_m}{V_0}$	$T_{DTP}$	$T_{Wet}$	$\frac{10 \log_{10} (V/V_0)}{(V/V_0)}$	$\frac{10 \log_{10} F_r(T_r/T_m)^{0.5}}{(V/V_0)}$	50°	90°	PPPL	POASPL
1	0	0	2.479	1.732	1.989	2.443	1.332	61	59	2.5	37.8	75.4	83.4	96.9	140
2	0	0	2.958	1.751	2.385	2.962	1.351	63	61	3.3	37.2	77.4	86.8	99.5	140
3	0	0	2.43	1.290	1.802	2.433	1.200	60	59	2.1	37.6	72.4	81.1	94.9	140
4	0	0	1.261	1.630	2.384	1.265	1.630	62	60	3.3	38.3	79.0	88.7	100.5	140
5	0	0	2.185	1.984	1.611	2.188	1.084	62	60	1.6	37.6	70.0	78.1	92.7	140
6	0	0	3.738	1.749	2.588	3.745	1.749	62	60	3.7	38.9	80.3	88.2	103.8	140
7	0	0	1.943	1.646	1.602	1.946	1.602	62	60	1.0	37.8	67.8	75.8	89.3	140
8	0	0	2.681	1.767	2.287	2.686	1.767	63	61	3.1	36.5	75.8	84.3	98.9	140
9	0.148	0.12	2.732	1.823	1.999	2.737	1.823	79	73	2.0	36.5	71.0	80.4	92.7	140
10	0.15	0.16	2.962	1.712	2.359	2.967	1.712	73	71	2.7	35.8	74.0	83.5	96.9	140
11	0.147	0.11	2.481	1.753	2.291	2.486	1.600	74	72	2.5	35.0	72.6	81.1	95.4	140
12	0.144	0.04	2.398	1.526	1.794	2.401	1.152	80	73	1.6	36.4	68.6	77.2	90.8	140
13	0.182	0.02	3.271	1.625	2.383	3.276	1.512	79	74	2.8	36.7	75.2	85.9	98.9	140
14	0.182	0.18	3.779	1.736	2.578	3.784	1.613	73	71	3.1	37.3	77.2	86.2	94.5	140
15	0.1604	0.07	3.941	1.930	1.389	3.946	1.824	81	74	0.7	37.6	63.8	71.8	82.9	140
16	0.239	0.02	2.715	1.365	2.031	2.720	1.187	80	74	2.1	37.9	72.0	80.2	90.2	140
17	0.499	0.02	2.627	1.737	2.278	2.632	1.667	77	73	2.4	36.2	72.8	80.6	91.7	140
18	0.499	0.04	2.436	1.203	1.804	2.441	1.094	80	74	1.8	37.8	69.2	77.0	88.3	140
19	0.431	0.02	3.286	1.634	2.393	3.291	1.375	78	73	2.7	38.3	76.1	85.9	93.7	140
20	0.43	0.07	3.748	1.749	2.590	3.753	1.675	72	70	3.0	38.7	78.6	87.6	95.2	140
21	0.39	0.02	3.177	1.319	1.232	3.182	1.187	74	72	0.1	37.9	61.7	69.6	70.7	140
22	0.383	0.02	2.056	0.942	1.439	2.061	0.842	74	72	0.6	37.9	63.8	74.5	74.2	140
23	0.383	0.02	2.698	1.526	1.990	2.703	1.086	73	71	1.7	38.1	71.0	79.6	79.8	140
24	0.364	0.03	3.721	1.721	2.194	3.726	1.659	81	75	0.2	37.3	61.2	68.7	70.1	140
25	0.358	0.07	2.443	1.508	1.812	2.448	1.151	75	71	1.6	37.0	69.2	77.4	77.7	140
26	0.464	0.02	3.284	1.629	2.389	3.289	1.616	82	75	2.7	37.2	75.6	85.9	92.2	140
27	0.373	0.02	2.298	1.420	1.402	2.303	1.116	85	75	2.3	36.9	70.7	79.1	79.0	140
28	0.373	0.02	2.298	1.420	1.402	2.303	1.116	85	75	2.3	36.9	70.7	79.1	79.0	140
29	0.373	0.02	3.729	1.723	2.587	3.734	1.656	82	74	3.2	38.0	77.2	85.6	95.4	140
30	0.468	0.04	3.127	1.744	2.146	3.132	1.606	82	75	2.7	38.1	76.3	86.0	93.8	140
31	0.419	0.04	2.703	1.790	2.283	2.708	1.317	75	73	2.5	38.1	76.5	85.7	93.1	140
32	0.312	0.02	2.321	1.711	2.122	2.326	1.287	82	74	2.2	36.8	72.2	80.6	90.1	140
33	0.307	0.04	2.017	1.603	1.894	2.022	1.184	81	73	2.7	36.8	70.7	79.1	79.0	140
34	0.307	0.04	2.017	1.603	1.894	2.022	1.184	81	73	2.7	36.8	70.7	79.1	79.0	140
35	0.307	0.04	2.017	1.603	1.894	2.022	1.184	81	73	2.7	36.8	70.7	79.1	79.0	140
36	0.497	0.02	2.833	1.638	2.106	2.838	1.627	81	74	2.4	36.4	72.2	80.7	91.0	140
37	0.499	0.02	2.833	1.638	2.106	2.838	1.627	81	74	2.4	36.4	72.2	80.7	91.0	140



Table B-25. Model No. 25: 36 Chute, AR = 2.0,  $R_I^0 = 0.716$  Outer Suppressor;  $A/A_1 = 3.61$ ,  $R_I^1 = 0.89$  Inner Plug, In-Line.

$A_0 = 21.16 \text{ in.}^2$ ,  $A_1 = 6.58 \text{ in.}^2$  Linear Scale Factor to 100 in.  $2 = 1.38$

Data Point No.	Inlet		Outlet		Ratio		Mass Averages		Meteorological Conditions		Normalization Parameters		2400-ft S.L. Data			
	$(P_0/P_1)_1$	$T_0/T_1$	$(P_0/P_1)_2$	$T_0/T_1$	$v_0/v_1$	$v_0/v_1$	$\dot{m}_0/\dot{m}_1$	$(T_0/T_1)_m$	$T_0/T_1$	$T_0/T_1$	$10 \log_{10} (v_0/v_1)$	$10 \log_{10} (T_0/T_1)$	QASPL	PRL	QASPL	PRL
9	1.72	897	1264	1264	1.1	4.5	2.479	1251	1857	63	2.2	37.5	72.2	80.8	80.7	91.0
10	1.709	899	1265	1265	1.1	4.5	2.479	1251	1857	63	2.2	37.5	72.2	80.8	80.7	91.0
11	1.696	907	1266	1266	1.1	4.5	2.479	1251	1857	63	2.2	37.5	72.2	80.8	80.7	91.0
12	1.678	903	1222	1222	1.1	4.2	2.477	1250	1857	63	2.2	37.5	72.2	80.8	80.7	91.0
13	1.708	901	1260	1260	1.1	4.5	2.479	1251	1857	63	2.2	37.5	72.2	80.8	80.7	91.0
14	1.712	915	1276	1276	1.1	4.5	2.479	1251	1857	63	2.2	37.5	72.2	80.8	80.7	91.0
15	1.709	897	1265	1265	1.1	4.5	2.479	1251	1857	63	2.2	37.5	72.2	80.8	80.7	91.0
16	1.711	900	1271	1271	1.1	4.5	2.479	1251	1857	63	2.2	37.5	72.2	80.8	80.7	91.0
17	1.701	898	1268	1268	1.1	4.5	2.479	1251	1857	63	2.2	37.5	72.2	80.8	80.7	91.0
18	1.711	898	1268	1268	1.1	4.5	2.479	1251	1857	63	2.2	37.5	72.2	80.8	80.7	91.0
19	1.716	898	1272	1272	1.1	4.5	2.479	1251	1857	63	2.2	37.5	72.2	80.8	80.7	91.0
20	1.709	899	1265	1265	1.1	4.5	2.479	1251	1857	63	2.2	37.5	72.2	80.8	80.7	91.0
21	1.707	897	1264	1264	1.1	4.5	2.479	1251	1857	63	2.2	37.5	72.2	80.8	80.7	91.0
22	1.701	898	1268	1268	1.1	4.5	2.479	1251	1857	63	2.2	37.5	72.2	80.8	80.7	91.0
23	1.704	898	1267	1267	1.1	4.5	2.479	1251	1857	63	2.2	37.5	72.2	80.8	80.7	91.0
24	1.702	897	1266	1266	1.1	4.5	2.479	1251	1857	63	2.2	37.5	72.2	80.8	80.7	91.0
25	1.704	897	1266	1266	1.1	4.5	2.479	1251	1857	63	2.2	37.5	72.2	80.8	80.7	91.0
26	1.702	897	1266	1266	1.1	4.5	2.479	1251	1857	63	2.2	37.5	72.2	80.8	80.7	91.0
27	1.704	897	1266	1266	1.1	4.5	2.479	1251	1857	63	2.2	37.5	72.2	80.8	80.7	91.0
28	1.704	897	1266	1266	1.1	4.5	2.479	1251	1857	63	2.2	37.5	72.2	80.8	80.7	91.0
29	1.704	897	1266	1266	1.1	4.5	2.479	1251	1857	63	2.2	37.5	72.2	80.8	80.7	91.0
30	1.704	897	1266	1266	1.1	4.5	2.479	1251	1857	63	2.2	37.5	72.2	80.8	80.7	91.0
31	1.704	897	1266	1266	1.1	4.5	2.479	1251	1857	63	2.2	37.5	72.2	80.8	80.7	91.0
32	1.704	897	1266	1266	1.1	4.5	2.479	1251	1857	63	2.2	37.5	72.2	80.8	80.7	91.0
33	1.704	897	1266	1266	1.1	4.5	2.479	1251	1857	63	2.2	37.5	72.2	80.8	80.7	91.0
34	1.704	897	1266	1266	1.1	4.5	2.479	1251	1857	63	2.2	37.5	72.2	80.8	80.7	91.0
35	1.704	897	1266	1266	1.1	4.5	2.479	1251	1857	63	2.2	37.5	72.2	80.8	80.7	91.0
36	1.704	897	1266	1266	1.1	4.5	2.479	1251	1857	63	2.2	37.5	72.2	80.8	80.7	91.0
37	1.704	897	1266	1266	1.1	4.5	2.479	1251	1857	63	2.2	37.5	72.2	80.8	80.7	91.0

Table B-26. Model No. 26: 36 Chute, AR = 2.0,  $R_I^O = 0.716$  Outer Suppressor;  $A_O/A_I = 3.61$ ,  $R_I^I = 0.89$  Inner Plug, Retracted.

Linear Scale Factor to 338 in. = 3.38

Data Point No.	Inlet		Outlet		Ratio	Mean Averages		Meteorological Conditions		Normalization Parameters		2400-ft S.L. Data			
	$(P_1/P_2)_0$	$T_1$ (°F)	$(P_1/P_2)_0$	$T_2$ (°F)	$\eta_0/\eta_1$	$(P_1/P_2)_m$	$T_m$ (°F)	$T_{avg}$ (°F)	$T_{diff}$ (°F)	$10 \log_{10} (V/\eta_0)$	$10 \log_{10} P_0(T_0/T_m)^{0.1}$	QASPL	50° FPL	90° FPL	POASPL
9	1.676	904	1221	2.72	1343	2010	1365	1870	68	66	2.2	71.4	79.4	80.4	93.3
10	1.542	902	1123	3.005	1751	2399	1685	2185	68	67	2.9	76.9	83.6	83.8	97.2
11	1.413	904	1178	2.689	1745	2288	1583	2075	67	65	2.7	73.4	81.1	82.4	95.7
12	1.433	905	1187	2.403	1215	1803	1157	1690	67	65	1.8	69.7	77.9	78.5	91.3
13	1.608	911	1311	3.253	1636	2384	1514	2192	67	65	2.9	75.8	85.4	83.9	94.0
14	1.798	909	1299	3.712	1751	2508	1615	2378	70	68	3.3	77.2	85.5	85.7	95.3
15	1.496	895	1573	1.948	930	1393	921	1442	67	65	1.1	67.8	77.1	74.7	85.1
16	1.352	899	1376	2.701	1314	1942	1168	1920	67	65	2.4	74.5	83.4	81.5	91.7
17	1.794	899	1458	2.705	1749	2397	1498	2108	68	66	2.8	74.6	82.8	81.1	93.3
18	1.16	896	1371	2.435	1191	1796	1102	1777	68	66	2.0	72.8	81.9	79.5	90.0
19	1.042	896	1836	3.283	1632	2391	1404	2220	75	72	3.0	79.2	88.8	85.0	95.0
20	1.925	901	1872	3.77	1750	2587	1696	2373	79	74	3.3	81.1	89.5	87.0	96.4
21	1.793	941	1052	1.778	840	1237	767	1179	75	72	0.2	63.2	71.3	71.5	81.7
22	1.782	943	1037	2.065	985	1440	866	1371	75	73	0.9	65.8	73.6	74.8	85.3
23	1.799	903	1058	2.727	1335	2007	1174	1798	74	72	2.1	71.5	80.1	80.2	90.6
24	1.591	908	1184	1.77	826	1222	854	1215	67	65	0.3	62.9	70.8	71.3	81.3
25	1.348	904	1185	2.429	1200	1801	1151	1700	67	66	1.8	69.4	77.4	78.6	88.9
26	1.557	1013	1206	3.237	1629	2377	1539	2205	75	69	3.0	75.9	85.7	83.9	94.1
27	1.52	1216	1287	2.232	1073	1419	1095	1569	67	66	1.5	68.5	76.5	77.1	87.4
28	1.323	1291	1291	2.664	1300	1961	1289	1867	67	66	2.2	72.1	80.5	80.3	90.6
29	1.318	1293	1293	3.703	1747	2579	1683	2422	71	69	3.4	77.6	85.8	86.0	95.6
30	1.318	871	1546	3.163	1743	2435	1320	2211	67	65	3.0	76.2	85.4	84.3	94.1
31	1.618	850	1663	2.708	1756	2383	1468	2100	66	65	2.7	75.3	81.5	83.0	93.4
32	1.493	831	1533	2.373	1727	2148	1362	1878	66	65	2.3	72.3	80.1	81.4	92.0
33	1.098	846	1366	2.016	1628	1994	1412	1745	67	66	1.9	69.8	78.0	78.9	89.9
34	1.021	845	1655	2.154	1675	2002	1373	1876	66	65	2.3	72.8	81.5	80.5	91.5
35	1.498	1431	1374	1.826	930	1382	1003	1381	68	67	0.9	67.7	75.0	75.2	85.1
36	1.496	1456	1381	2.982	1410	2118	1616	2028	68	66	2.6	73.5	81.8	81.8	92.0
37	1.493	1461	1383	3.997	1741	2634	1713	2508	71	69	3.5	78.7	86.4	87.1	96.3

Table B-27. Model No. 27: 36 Chute, AR = 1.5,  $R_o^0 = 0.782$  Outer Suppressor;  $A_o/A_i = 1.92$ ,  $R_T^i = 0.779$   
Inner Plug, Retracted.

$A_o = 13.36 \text{ in.}^2$ ,  $A_i = 11.38 \text{ in.}^2$  Linear Scale Factor to 338 in.<sup>2</sup> No. 9-37 at 3.07 (Qual Flow); No. 38-41 at 3.77 (Outer Only)

Data Point No.	Inner		Outer		Exit		Mass Averages		Meteorological Conditions		Normalization Parameters		2400-ft S.L. Data			
	$(T_o/T_o^0)_i$	$T_o^0$ (°K)	$(T_o/T_o^0)_o$	$T_o^0$ (°K)	$\rho_o/\rho_i$	$u_o/u_i$	$(\rho_o/\rho_o^0)$	$T_o^0$ (°K)	$T_o^0$ (°K)	$T_{wet}$ (°F)	$10 \log_{10}$ $(V/A_o)$	$10 \log_{10}$ $T_o(T_o/T_o^0)^{-1}$	QASPL PHL	QASPL PHL	PFHL	FOASPL
9	1.124	898	2.657	1354	3.2	5.4	2.233	1274	1777	60	2.0	36.2	70	77.2	88.6	120
10	1.126	895	2.81	1367	3.9	5.1	2.407	1624	2093	66	2.7	35.6	71.1	77.6	91.8	130
11	1.128	894	2.665	1361	3.8	5.9	2.227	1613	2000	67	2.5	35.0	71.6	81.8	92.2	130
12	1.127	894	2.631	1375	3.0	5.6	2.071	1129	1599	71	1.6	36.6	74.9	75.4	89.8	120
13	1.132	819	3.254	1627	3.5	5.5	2.661	1519	2120	73	2.9	36.7	74.9	84.2	95.7	140
14	1.178	889	3.12	1251	3.7	5.6	2.958	1621	2291	64	3.1	37.2	77.9	86.7	99.5	140
15	1.290	854	3.85	1427	3.4	5.3	2.754	927	1285	69	0.6	37.3	77.9	86.7	99.5	140
16	1.364	884	3.64	1399	2.0	3.1	2.22	1231	1741	74	1.9	36.8	70.5	80.1	91.3	120
17	1.431	884	2.706	1263	2.4	3.4	2.232	1552	1984	66	2.5	35.5	72.4	81.7	91.3	120
18	1.377	895	2.423	1187	1.8	3.2	2.077	1117	1592	70	1.5	37.1	69	76.5	87.6	120
19	1.443	894	2.385	1437	2.2	3.2	2.669	1650	2080	74	2.7	37.3	75	83.8	92.9	140
20	1.507	892	2.48	1455	2.2	3.1	2.918	1557	2232	64	3.0	37.7	77.8	86.2	96	140
21	1.552	944	2.747	1455	1.2	1.5	1.739	733	1134	72	0.1	37.9	62.7	70.2	71.2	120
22	1.773	911	2.707	1407	1.5	1.6	1.924	834	1307	61	0.6	38.3	65.4	72.7	74.5	120
23	1.772	911	2.701	1360	2.0	1.9	2.318	1075	1662	55	1.7	38.2	71.5	79.4	80.8	130
24	1.562	1021	1.763	818	1.0	2.4	1.495	871	1210	73	0.4	37.4	61.7	67.7	71.5	120
25	1.565	960	2.62	1186	1.5	2.7	2.124	1113	1626	74	1.8	37.2	69.1	75.7	78.4	120
26	1.559	1005	3.207	1411	2.0	3.2	2.124	1468	2101	74	2.7	37.4	74.9	83.3	93.0	140
27	1.512	1206	2.207	1085	1.4	1.7	1.495	1127	1544	75	1.4	36.9	67.6	74	77	120
28	1.516	1206	2.433	1382	1.3	1.6	2.264	1287	1799	72	2.1	36.7	70.7	77.5	80.2	120
29	1.525	1213	3.731	1756	2.0	3.9	3.02	1647	2329	74	3.2	37.6	78.2	86.6	96.1	140
30	2.488	844	3.136	1787	1.6	1.6	2.826	1415	2097	60	2.5	38.1	76.7	83.9	85	140
31	2.896	663	2.662	1755	1.4	1.7	2.696	1316	1877	60	2.5	38.0	78.3	85.2	84.3	140
32	2.477	838	2.396	1765	1.4	1.2	2.157	1241	1867	57	2.3	36.9	72.9	79.9	81.9	120
33	2.003	660	2.022	1838	1.4	1.4	1.984	1254	1867	75	1.7	36.1	68.6	74	78.3	120
34	3.023	832	2.181	1640	1.2	1.0	2.42	1240	1828	74	2.1	37.5	80.3	87	93.5	120
35	3.023	1559	1.807	964	1.0	3.2	1.755	1083	1392	62	1.0	37.5	64.2	68.1	74.4	120
36	1.486	1463	2.833	1772	3.5	3.9	2.39	1606	2396	74	2.4	37.7	72.2	78	83.7	140
37	1.481	1481	3.959	1764	1.9	4.8	3.196	1715	2428	52	3.6	38.9	81.2	89	98.1	140
38	1.465		3.723	1723	2.565		3.731	1723	2345	53	3.6	38.9	81.2	89	98.1	140
39			2.631	1739	2270		2.46	1739	2270	49	2.1	34.5	74.5	80.3	84.7	140
40			2.718	1327	1998		2.723	1327	1998	55	2.5	37.9	70.6	77.6	82.9	140
41			2.438	1317	1861		2.443	1317	1861	53	2.2	37.4	70.6	77.6	82.9	140

Table B-28. Model No. 28: 36 Spoke, AR = 2.0,  $R_o^o = 0.716$  Outer Suppressor;  $A_o/A_i = 1.92$ ,  $R_i^i = 0.779$  Inner Plug, Retracted.

$A_o = 71.14 \text{ in.}^2$ ,  $A_i = 12.19 \text{ in.}^2$  Inner Scale Factor to 318 in. 2 No. 1-8 at 3.77 (Outer Only); No 9-37 at 3.09 (Dual Flow)

Data Point No.	Inlet		Outlet		Ratio	Mass Average		Metamorphological Conditions		Normalization Parameters		2400-ft S.L. Data							
	$(P/P_o)_i$	$T_i$	$(P/P_o)_o$	$T_o$		$(P/P_o)_m$	$T_m$	$T_{avg}$	$T_{het}$	$10 \log_{10} (V/V_o)$	$10 \log_{10} (T_o/T_m)^{-1}$	50° QASPL	50° PHL	90° QASPL	90° PHL	POASPL			
1	1.123	688	2.726	1335	2.007	2.726	1334	2007	65	63	2.549	37.9	75.2	83.4	92.5	95.1	130	89.4	140
2	1.123	688	2.726	1335	2.007	2.726	1334	2007	65	63	2.549	37.9	75.2	83.4	92.5	95.1	130	89.4	140
3	1.123	688	2.726	1335	2.007	2.726	1334	2007	65	63	2.549	37.9	75.2	83.4	92.5	95.1	130	89.4	140
4	1.123	688	2.726	1335	2.007	2.726	1334	2007	65	63	2.549	37.9	75.2	83.4	92.5	95.1	130	89.4	140
5	1.123	688	2.726	1335	2.007	2.726	1334	2007	65	63	2.549	37.9	75.2	83.4	92.5	95.1	130	89.4	140
6	1.123	688	2.726	1335	2.007	2.726	1334	2007	65	63	2.549	37.9	75.2	83.4	92.5	95.1	130	89.4	140
7	1.123	688	2.726	1335	2.007	2.726	1334	2007	65	63	2.549	37.9	75.2	83.4	92.5	95.1	130	89.4	140
8	1.123	688	2.726	1335	2.007	2.726	1334	2007	65	63	2.549	37.9	75.2	83.4	92.5	95.1	130	89.4	140
9	1.123	688	2.726	1335	2.007	2.726	1334	2007	65	63	2.549	37.9	75.2	83.4	92.5	95.1	130	89.4	140
10	1.123	688	2.726	1335	2.007	2.726	1334	2007	65	63	2.549	37.9	75.2	83.4	92.5	95.1	130	89.4	140
11	1.123	688	2.726	1335	2.007	2.726	1334	2007	65	63	2.549	37.9	75.2	83.4	92.5	95.1	130	89.4	140
12	1.123	688	2.726	1335	2.007	2.726	1334	2007	65	63	2.549	37.9	75.2	83.4	92.5	95.1	130	89.4	140
13	1.123	688	2.726	1335	2.007	2.726	1334	2007	65	63	2.549	37.9	75.2	83.4	92.5	95.1	130	89.4	140
14	1.123	688	2.726	1335	2.007	2.726	1334	2007	65	63	2.549	37.9	75.2	83.4	92.5	95.1	130	89.4	140
15	1.123	688	2.726	1335	2.007	2.726	1334	2007	65	63	2.549	37.9	75.2	83.4	92.5	95.1	130	89.4	140
16	1.123	688	2.726	1335	2.007	2.726	1334	2007	65	63	2.549	37.9	75.2	83.4	92.5	95.1	130	89.4	140
17	1.123	688	2.726	1335	2.007	2.726	1334	2007	65	63	2.549	37.9	75.2	83.4	92.5	95.1	130	89.4	140
18	1.123	688	2.726	1335	2.007	2.726	1334	2007	65	63	2.549	37.9	75.2	83.4	92.5	95.1	130	89.4	140
19	1.123	688	2.726	1335	2.007	2.726	1334	2007	65	63	2.549	37.9	75.2	83.4	92.5	95.1	130	89.4	140
20	1.123	688	2.726	1335	2.007	2.726	1334	2007	65	63	2.549	37.9	75.2	83.4	92.5	95.1	130	89.4	140
21	1.123	688	2.726	1335	2.007	2.726	1334	2007	65	63	2.549	37.9	75.2	83.4	92.5	95.1	130	89.4	140
22	1.123	688	2.726	1335	2.007	2.726	1334	2007	65	63	2.549	37.9	75.2	83.4	92.5	95.1	130	89.4	140
23	1.123	688	2.726	1335	2.007	2.726	1334	2007	65	63	2.549	37.9	75.2	83.4	92.5	95.1	130	89.4	140
24	1.123	688	2.726	1335	2.007	2.726	1334	2007	65	63	2.549	37.9	75.2	83.4	92.5	95.1	130	89.4	140
25	1.123	688	2.726	1335	2.007	2.726	1334	2007	65	63	2.549	37.9	75.2	83.4	92.5	95.1	130	89.4	140
26	1.123	688	2.726	1335	2.007	2.726	1334	2007	65	63	2.549	37.9	75.2	83.4	92.5	95.1	130	89.4	140
27	1.123	688	2.726	1335	2.007	2.726	1334	2007	65	63	2.549	37.9	75.2	83.4	92.5	95.1	130	89.4	140
28	1.123	688	2.726	1335	2.007	2.726	1334	2007	65	63	2.549	37.9	75.2	83.4	92.5	95.1	130	89.4	140
29	1.123	688	2.726	1335	2.007	2.726	1334	2007	65	63	2.549	37.9	75.2	83.4	92.5	95.1	130	89.4	140
30	1.123	688	2.726	1335	2.007	2.726	1334	2007	65	63	2.549	37.9	75.2	83.4	92.5	95.1	130	89.4	140
31	1.123	688	2.726	1335	2.007	2.726	1334	2007	65	63	2.549	37.9	75.2	83.4	92.5	95.1	130	89.4	140
32	1.123	688	2.726	1335	2.007	2.726	1334	2007	65	63	2.549	37.9	75.2	83.4	92.5	95.1	130	89.4	140
33	1.123	688	2.726	1335	2.007	2.726	1334	2007	65	63	2.549	37.9	75.2	83.4	92.5	95.1	130	89.4	140
34	1.123	688	2.726	1335	2.007	2.726	1334	2007	65	63	2.549	37.9	75.2	83.4	92.5	95.1	130	89.4	140
35	1.123	688	2.726	1335	2.007	2.726	1334	2007	65	63	2.549	37.9	75.2	83.4	92.5	95.1	130	89.4	140
36	1.123	688	2.726	1335	2.007	2.726	1334	2007	65	63	2.549	37.9	75.2	83.4	92.5	95.1	130	89.4	140
37	1.123	688	2.726	1335	2.007	2.726	1334	2007	65	63	2.549	37.9	75.2	83.4	92.5	95.1	130	89.4	140

Table B-29. Model No. 29: 36 Spoke, AR = 2.0,  $R_r^0 = 0.716$  Outer Suppressor;  $A_0/A_1 = 1.92$ ,  $R_r^1 = 0.779$   
Inner Plug, In-Line.

$A_0 = 2.5 \times 10^{-3}$  in.<sup>2</sup>,  $A_1 = 1.2 \times 10^{-3}$  in.<sup>2</sup> Used Scale Factors to 100 for  $\beta$ , 4-12 at 1.09 (Dial Film); No. 18-41 at 1.77 (Outer Only)

Data Point No.	Energy $(\text{MeV})$	Angle $(^\circ)$	Mass Averages $(\text{MeV})$	Series $(\text{MeV})$	Micrological Conditions $(\text{MeV})$	Normalization Parameters $(\text{MeV})$	2400-ft S.L. Data			
							50°	90°	PPPL	POASPL
1	0.10	0.10	0.10	0.10	0.10	0.10	0.10	0.10	0.10	0.10
2	0.15	0.15	0.15	0.15	0.15	0.15	0.15	0.15	0.15	0.15
3	0.20	0.20	0.20	0.20	0.20	0.20	0.20	0.20	0.20	0.20
4	0.25	0.25	0.25	0.25	0.25	0.25	0.25	0.25	0.25	0.25
5	0.30	0.30	0.30	0.30	0.30	0.30	0.30	0.30	0.30	0.30
6	0.35	0.35	0.35	0.35	0.35	0.35	0.35	0.35	0.35	0.35
7	0.40	0.40	0.40	0.40	0.40	0.40	0.40	0.40	0.40	0.40
8	0.45	0.45	0.45	0.45	0.45	0.45	0.45	0.45	0.45	0.45
9	0.50	0.50	0.50	0.50	0.50	0.50	0.50	0.50	0.50	0.50
10	0.55	0.55	0.55	0.55	0.55	0.55	0.55	0.55	0.55	0.55
11	0.60	0.60	0.60	0.60	0.60	0.60	0.60	0.60	0.60	0.60
12	0.65	0.65	0.65	0.65	0.65	0.65	0.65	0.65	0.65	0.65
13	0.70	0.70	0.70	0.70	0.70	0.70	0.70	0.70	0.70	0.70
14	0.75	0.75	0.75	0.75	0.75	0.75	0.75	0.75	0.75	0.75
15	0.80	0.80	0.80	0.80	0.80	0.80	0.80	0.80	0.80	0.80
16	0.85	0.85	0.85	0.85	0.85	0.85	0.85	0.85	0.85	0.85
17	0.90	0.90	0.90	0.90	0.90	0.90	0.90	0.90	0.90	0.90
18	0.95	0.95	0.95	0.95	0.95	0.95	0.95	0.95	0.95	0.95
19	1.00	1.00	1.00	1.00	1.00	1.00	1.00	1.00	1.00	1.00
20	1.05	1.05	1.05	1.05	1.05	1.05	1.05	1.05	1.05	1.05
21	1.10	1.10	1.10	1.10	1.10	1.10	1.10	1.10	1.10	1.10
22	1.15	1.15	1.15	1.15	1.15	1.15	1.15	1.15	1.15	1.15
23	1.20	1.20	1.20	1.20	1.20	1.20	1.20	1.20	1.20	1.20
24	1.25	1.25	1.25	1.25	1.25	1.25	1.25	1.25	1.25	1.25
25	1.30	1.30	1.30	1.30	1.30	1.30	1.30	1.30	1.30	1.30
26	1.35	1.35	1.35	1.35	1.35	1.35	1.35	1.35	1.35	1.35
27	1.40	1.40	1.40	1.40	1.40	1.40	1.40	1.40	1.40	1.40
28	1.45	1.45	1.45	1.45	1.45	1.45	1.45	1.45	1.45	1.45
29	1.50	1.50	1.50	1.50	1.50	1.50	1.50	1.50	1.50	1.50
30	1.55	1.55	1.55	1.55	1.55	1.55	1.55	1.55	1.55	1.55
31	1.60	1.60	1.60	1.60	1.60	1.60	1.60	1.60	1.60	1.60
32	1.65	1.65	1.65	1.65	1.65	1.65	1.65	1.65	1.65	1.65
33	1.70	1.70	1.70	1.70	1.70	1.70	1.70	1.70	1.70	1.70
34	1.75	1.75	1.75	1.75	1.75	1.75	1.75	1.75	1.75	1.75
35	1.80	1.80	1.80	1.80	1.80	1.80	1.80	1.80	1.80	1.80
36	1.85	1.85	1.85	1.85	1.85	1.85	1.85	1.85	1.85	1.85
37	1.90	1.90	1.90	1.90	1.90	1.90	1.90	1.90	1.90	1.90
38	1.95	1.95	1.95	1.95	1.95	1.95	1.95	1.95	1.95	1.95
39	2.00	2.00	2.00	2.00	2.00	2.00	2.00	2.00	2.00	2.00
40	2.05	2.05	2.05	2.05	2.05	2.05	2.05	2.05	2.05	2.05
41	2.10	2.10	2.10	2.10	2.10	2.10	2.10	2.10	2.10	2.10



Table B-31. Model No. 31: 30 Shallow Chute, AR = 1.75,  $R^0 = 0.717$  Outer Suppressor;  $A_0/A_1 = 1.92$ ,  $R^1 = 0.779$  Inner Plug, Retracted.

Linear Scale Factor to 338 in. No. 1-8 at 3.77 (Outer Only); No. 9-37 at 3.08 (Dual Flow)

Data Point No.	Inlet	Orifice	Ratio	Mass Averages	Meteorological Conditions	Normalization Parameters				2400-ft S.L. Data			
	$T_{in}$ (°F)	$T_{or}$ (°F)	$V_0/V_1$	$(P_0/P_{atm})$	$T_{in}$ (°F)	$T_{or}$ (°F)	$V_0/V_1$	$(P_0/P_{atm})$	$T_{in}$ (°F)	$T_{or}$ (°F)	$V_0/V_1$	$(P_0/P_{atm})$	$T_{in}$ (°F)
1	1.014	1.014	1.014	1.014	1.014	1.014	1.014	1.014	1.014	1.014	1.014	1.014	1.014
2	1.014	1.014	1.014	1.014	1.014	1.014	1.014	1.014	1.014	1.014	1.014	1.014	1.014
3	1.014	1.014	1.014	1.014	1.014	1.014	1.014	1.014	1.014	1.014	1.014	1.014	1.014
4	1.014	1.014	1.014	1.014	1.014	1.014	1.014	1.014	1.014	1.014	1.014	1.014	1.014
5	1.014	1.014	1.014	1.014	1.014	1.014	1.014	1.014	1.014	1.014	1.014	1.014	1.014
6	1.014	1.014	1.014	1.014	1.014	1.014	1.014	1.014	1.014	1.014	1.014	1.014	1.014
7	1.014	1.014	1.014	1.014	1.014	1.014	1.014	1.014	1.014	1.014	1.014	1.014	1.014
8	1.014	1.014	1.014	1.014	1.014	1.014	1.014	1.014	1.014	1.014	1.014	1.014	1.014
9	1.014	1.014	1.014	1.014	1.014	1.014	1.014	1.014	1.014	1.014	1.014	1.014	1.014
10	1.014	1.014	1.014	1.014	1.014	1.014	1.014	1.014	1.014	1.014	1.014	1.014	1.014
11	1.014	1.014	1.014	1.014	1.014	1.014	1.014	1.014	1.014	1.014	1.014	1.014	1.014
12	1.014	1.014	1.014	1.014	1.014	1.014	1.014	1.014	1.014	1.014	1.014	1.014	1.014
13	1.014	1.014	1.014	1.014	1.014	1.014	1.014	1.014	1.014	1.014	1.014	1.014	1.014
14	1.014	1.014	1.014	1.014	1.014	1.014	1.014	1.014	1.014	1.014	1.014	1.014	1.014
15	1.014	1.014	1.014	1.014	1.014	1.014	1.014	1.014	1.014	1.014	1.014	1.014	1.014
16	1.014	1.014	1.014	1.014	1.014	1.014	1.014	1.014	1.014	1.014	1.014	1.014	1.014
17	1.014	1.014	1.014	1.014	1.014	1.014	1.014	1.014	1.014	1.014	1.014	1.014	1.014
18	1.014	1.014	1.014	1.014	1.014	1.014	1.014	1.014	1.014	1.014	1.014	1.014	1.014
19	1.014	1.014	1.014	1.014	1.014	1.014	1.014	1.014	1.014	1.014	1.014	1.014	1.014
20	1.014	1.014	1.014	1.014	1.014	1.014	1.014	1.014	1.014	1.014	1.014	1.014	1.014
21	1.014	1.014	1.014	1.014	1.014	1.014	1.014	1.014	1.014	1.014	1.014	1.014	1.014
22	1.014	1.014	1.014	1.014	1.014	1.014	1.014	1.014	1.014	1.014	1.014	1.014	1.014
23	1.014	1.014	1.014	1.014	1.014	1.014	1.014	1.014	1.014	1.014	1.014	1.014	1.014
24	1.014	1.014	1.014	1.014	1.014	1.014	1.014	1.014	1.014	1.014	1.014	1.014	1.014
25	1.014	1.014	1.014	1.014	1.014	1.014	1.014	1.014	1.014	1.014	1.014	1.014	1.014
26	1.014	1.014	1.014	1.014	1.014	1.014	1.014	1.014	1.014	1.014	1.014	1.014	1.014
27	1.014	1.014	1.014	1.014	1.014	1.014	1.014	1.014	1.014	1.014	1.014	1.014	1.014
28	1.014	1.014	1.014	1.014	1.014	1.014	1.014	1.014	1.014	1.014	1.014	1.014	1.014
29	1.014	1.014	1.014	1.014	1.014	1.014	1.014	1.014	1.014	1.014	1.014	1.014	1.014
30	1.014	1.014	1.014	1.014	1.014	1.014	1.014	1.014	1.014	1.014	1.014	1.014	1.014
31	1.014	1.014	1.014	1.014	1.014	1.014	1.014	1.014	1.014	1.014	1.014	1.014	1.014
32	1.014	1.014	1.014	1.014	1.014	1.014	1.014	1.014	1.014	1.014	1.014	1.014	1.014
33	1.014	1.014	1.014	1.014	1.014	1.014	1.014	1.014	1.014	1.014	1.014	1.014	1.014
34	1.014	1.014	1.014	1.014	1.014	1.014	1.014	1.014	1.014	1.014	1.014	1.014	1.014
35	1.014	1.014	1.014	1.014	1.014	1.014	1.014	1.014	1.014	1.014	1.014	1.014	1.014
36	1.014	1.014	1.014	1.014	1.014	1.014	1.014	1.014	1.014	1.014	1.014	1.014	1.014
37	1.014	1.014	1.014	1.014	1.014	1.014	1.014	1.014	1.014	1.014	1.014	1.014	1.014

Table B-32. Model No. 32: 40 Shallow Chute, AR = 1.75,  $R_1^0 = 0.717$  Outer Suppressor;  $A_0/A_1 = 1.92$ ,  $R_1^1 = 0.779$  Inner Plug, Retracted.

$A_0 = 51.56$ ,  $A_1 = 26.84$ ,  $A_2 = 21.25$  in.<sup>2</sup> Distance Between Particles 44.358 in.,  $S = 0.04$

Data No.	Date	Time	Temp °F	Wind mi/hr	Dir	Rel Hum %	Pres in	Wet Bulb °F	Wet Bulb °C	Wet Bulb °F	Wet Bulb °C	Wet Bulb °F	Wet Bulb °C	Wet Bulb °F	Wet Bulb °C	Wet Bulb °F	Wet Bulb °C	Wet Bulb °F	Wet Bulb °C	Wet Bulb °F	Wet Bulb °C	Wet Bulb °F	Wet Bulb °C	Wet Bulb °F	Wet Bulb °C	Wet Bulb °F	Wet Bulb °C	Wet Bulb °F	Wet Bulb °C	Wet Bulb °F	Wet Bulb °C	Wet Bulb °F	Wet Bulb °C	Wet Bulb °F	Wet Bulb °C	Wet Bulb °F	Wet Bulb °C	Wet Bulb °F	Wet Bulb °C	Wet Bulb °F	Wet Bulb °C	Wet Bulb °F	Wet Bulb °C	Wet Bulb °F	Wet Bulb °C	Wet Bulb °F	Wet Bulb °C	Wet Bulb °F	Wet Bulb °C	Wet Bulb °F	Wet Bulb °C	Wet Bulb °F	Wet Bulb °C	Wet Bulb °F	Wet Bulb °C	Wet Bulb °F	Wet Bulb °C	Wet Bulb °F	Wet Bulb °C	Wet Bulb °F	Wet Bulb °C	Wet Bulb °F	Wet Bulb °C	Wet Bulb °F	Wet Bulb °C	Wet Bulb °F	Wet Bulb °C	Wet Bulb °F	Wet Bulb °C	Wet Bulb °F	Wet Bulb °C	Wet Bulb °F	Wet Bulb °C	Wet Bulb °F	Wet Bulb °C	Wet Bulb °F	Wet Bulb °C	Wet Bulb °F	Wet Bulb °C	Wet Bulb °F	Wet Bulb °C	Wet Bulb °F	Wet Bulb °C	Wet Bulb °F	Wet Bulb °C	Wet Bulb °F	Wet Bulb °C	Wet Bulb °F	Wet Bulb °C	Wet Bulb °F	Wet Bulb °C	Wet Bulb °F	Wet Bulb °C	Wet Bulb °F	Wet Bulb °C	Wet Bulb °F	Wet Bulb °C	Wet Bulb °F	Wet Bulb °C	Wet Bulb °F	Wet Bulb °C	Wet Bulb °F	Wet Bulb °C	Wet Bulb °F	Wet Bulb °C	Wet Bulb °F	Wet Bulb °C	Wet Bulb °F	Wet Bulb °C	Wet Bulb °F	Wet Bulb °C	Wet Bulb °F	Wet Bulb °C	Wet Bulb °F	Wet Bulb °C	Wet Bulb °F	Wet Bulb °C	Wet Bulb °F	Wet Bulb °C	Wet Bulb °F	Wet Bulb °C	Wet Bulb °F	Wet Bulb °C	Wet Bulb °F	Wet Bulb °C	Wet Bulb °F	Wet Bulb °C	Wet Bulb °F	Wet Bulb °C	Wet Bulb °F	Wet Bulb °C	Wet Bulb °F	Wet Bulb °C	Wet Bulb °F	Wet Bulb °C	Wet Bulb °F	Wet Bulb °C	Wet Bulb °F	Wet Bulb °C	Wet Bulb °F	Wet Bulb °C	Wet Bulb °F	Wet Bulb °C	Wet Bulb °F	Wet Bulb °C	Wet Bulb °F	Wet Bulb °C	Wet Bulb °F	Wet Bulb °C	Wet Bulb °F	Wet Bulb °C	Wet Bulb °F	Wet Bulb °C	Wet Bulb °F	Wet Bulb °C	Wet Bulb °F	Wet Bulb °C	Wet Bulb °F	Wet Bulb °C	Wet Bulb °F	Wet Bulb °C	Wet Bulb °F	Wet Bulb °C	Wet Bulb °F	Wet Bulb °C	Wet Bulb °F	Wet Bulb °C	Wet Bulb °F	Wet Bulb °C	Wet Bulb °F	Wet Bulb °C	Wet Bulb °F	Wet Bulb °C	Wet Bulb °F	Wet Bulb °C	Wet Bulb °F	Wet Bulb °C	Wet Bulb °F	Wet Bulb °C	Wet Bulb °F	Wet Bulb °C	Wet Bulb °F	Wet Bulb °C	Wet Bulb °F	Wet Bulb °C	Wet Bulb °F	Wet Bulb °C	Wet Bulb °F	Wet Bulb °C	Wet Bulb °F	Wet Bulb °C	Wet Bulb °F	Wet Bulb °C	Wet Bulb °F	Wet Bulb °C	Wet Bulb °F	Wet Bulb °C	Wet Bulb °F	Wet Bulb °C	Wet Bulb °F	Wet Bulb °C	Wet Bulb °F	Wet Bulb °C	Wet Bulb °F	Wet Bulb °C	Wet Bulb °F	Wet Bulb °C	Wet Bulb °F	Wet Bulb °C	Wet Bulb °F	Wet Bulb °C	Wet Bulb °F	Wet Bulb °C	Wet Bulb °F	Wet Bulb °C	Wet Bulb °F	Wet Bulb °C	Wet Bulb °F	Wet Bulb °C	Wet Bulb °F	Wet Bulb °C	Wet Bulb °F	Wet Bulb °C	Wet Bulb °F	Wet Bulb °C	Wet Bulb °F	Wet Bulb °C	Wet Bulb °F	Wet Bulb °C	Wet Bulb °F	Wet Bulb °C	Wet Bulb °F	Wet Bulb °C	Wet Bulb °F	Wet Bulb °C	Wet Bulb °F	Wet Bulb °C	Wet Bulb °F	Wet Bulb °C	Wet Bulb °F	Wet Bulb °C	Wet Bulb °F	Wet Bulb °C	Wet Bulb °F	Wet Bulb °C	Wet Bulb °F	Wet Bulb °C	Wet Bulb °F	Wet Bulb °C	Wet Bulb °F	Wet Bulb °C	Wet Bulb °F	Wet Bulb °C	Wet Bulb °F	Wet Bulb °C	Wet Bulb °F	Wet Bulb °C	Wet Bulb °F	Wet Bulb °C	Wet Bulb °F	Wet Bulb °C	Wet Bulb °F	Wet Bulb °C	Wet Bulb °F	Wet Bulb °C	Wet Bulb °F	Wet Bulb °C	Wet Bulb °F	Wet Bulb °C	Wet Bulb °F	Wet Bulb °C	Wet Bulb °F	Wet Bulb °C	Wet Bulb °F	Wet Bulb °C	Wet Bulb °F	Wet Bulb °C	Wet Bulb °F	Wet Bulb °C	Wet Bulb °F	Wet Bulb °C	Wet Bulb °F	Wet Bulb °C	Wet Bulb °F	Wet Bulb °C	Wet Bulb °F	Wet Bulb °C	Wet Bulb °F	Wet Bulb °C	Wet Bulb °F	Wet Bulb °C	Wet Bulb °F	Wet Bulb °C	Wet Bulb °F	Wet Bulb °C	Wet Bulb °F	Wet Bulb °C	Wet Bulb °F	Wet Bulb °C	Wet Bulb °F	Wet Bulb °C	Wet Bulb °F	Wet Bulb °C	Wet Bulb °F	Wet Bulb °C	Wet Bulb °F	Wet Bulb °C	Wet Bulb °F	Wet Bulb °C	Wet Bulb °F	Wet Bulb °C	Wet Bulb °F	Wet Bulb °C	Wet Bulb °F	Wet Bulb °C	Wet Bulb °F	Wet Bulb °C	Wet Bulb °F	Wet Bulb °C	Wet Bulb °F	Wet Bulb °C	Wet Bulb °F	Wet Bulb °C	Wet Bulb °F	Wet Bulb °C	Wet Bulb °F	Wet Bulb °C	Wet Bulb °F	Wet Bulb °C	Wet Bulb °F	Wet Bulb °C	Wet Bulb °F	Wet Bulb °C	Wet Bulb °F	Wet Bulb °C	Wet Bulb °F	Wet Bulb °C	Wet Bulb °F	Wet Bulb °C	Wet Bulb °F	Wet Bulb °C	Wet Bulb °
-------------	------	------	------------	---------------	-----	--------------	------------	----------------	----------------	----------------	----------------	----------------	----------------	----------------	----------------	----------------	----------------	----------------	----------------	----------------	----------------	----------------	----------------	----------------	----------------	----------------	----------------	----------------	----------------	----------------	----------------	----------------	----------------	----------------	----------------	----------------	----------------	----------------	----------------	----------------	----------------	----------------	----------------	----------------	----------------	----------------	----------------	----------------	----------------	----------------	----------------	----------------	----------------	----------------	----------------	----------------	----------------	----------------	----------------	----------------	----------------	----------------	----------------	----------------	----------------	----------------	----------------	----------------	----------------	----------------	----------------	----------------	----------------	----------------	----------------	----------------	----------------	----------------	----------------	----------------	----------------	----------------	----------------	----------------	----------------	----------------	----------------	----------------	----------------	----------------	----------------	----------------	----------------	----------------	----------------	----------------	----------------	----------------	----------------	----------------	----------------	----------------	----------------	----------------	----------------	----------------	----------------	----------------	----------------	----------------	----------------	----------------	----------------	----------------	----------------	----------------	----------------	----------------	----------------	----------------	----------------	----------------	----------------	----------------	----------------	----------------	----------------	----------------	----------------	----------------	----------------	----------------	----------------	----------------	----------------	----------------	----------------	----------------	----------------	----------------	----------------	----------------	----------------	----------------	----------------	----------------	----------------	----------------	----------------	----------------	----------------	----------------	----------------	----------------	----------------	----------------	----------------	----------------	----------------	----------------	----------------	----------------	----------------	----------------	----------------	----------------	----------------	----------------	----------------	----------------	----------------	----------------	----------------	----------------	----------------	----------------	----------------	----------------	----------------	----------------	----------------	----------------	----------------	----------------	----------------	----------------	----------------	----------------	----------------	----------------	----------------	----------------	----------------	----------------	----------------	----------------	----------------	----------------	----------------	----------------	----------------	----------------	----------------	----------------	----------------	----------------	----------------	----------------	----------------	----------------	----------------	----------------	----------------	----------------	----------------	----------------	----------------	----------------	----------------	----------------	----------------	----------------	----------------	----------------	----------------	----------------	----------------	----------------	----------------	----------------	----------------	----------------	----------------	----------------	----------------	----------------	----------------	----------------	----------------	----------------	----------------	----------------	----------------	----------------	----------------	----------------	----------------	----------------	----------------	----------------	----------------	----------------	----------------	----------------	----------------	----------------	----------------	----------------	----------------	----------------	----------------	----------------	----------------	----------------	----------------	----------------	----------------	----------------	----------------	----------------	----------------	----------------	----------------	----------------	----------------	----------------	----------------	----------------	----------------	----------------	----------------	----------------	----------------	----------------	----------------	----------------	----------------	----------------	----------------	----------------	----------------	----------------	----------------	----------------	----------------	----------------	----------------	----------------	----------------	----------------	----------------	----------------	----------------	----------------	----------------	----------------	----------------	----------------	----------------	----------------	----------------	----------------	----------------	----------------	----------------	----------------	----------------	----------------	----------------	----------------	----------------	----------------	----------------	----------------	----------------	----------------	----------------	----------------	----------------	----------------	----------------	----------------	----------------	----------------	----------------	----------------	----------------	----------------	----------------	----------------	----------------	---------------



Table B-33. Model No. 33: 36 Chute, AR = 2.5,  $R_r^0 = 0.783$  Outer Suppressor;  $A/A_1 = 0.65$ ,  $R_r^1 = 0.674$  Inner Plug, Retracted.

$A_0 = 11.32$ ,  $\text{in.}^2$  at  $x = 12.11$   $\text{in.}$   
 $u_0 = 3043$   $\text{ft.}^2$   $\text{min.}$  (Chute Only)

Linear Scale Factor to 128  $\text{in.}^2$ , No. 1-35 and No. 44-59 at 3.45 (Chute Flow);

Data Point No.	Chute		Outlet		Exit		Mass Averages		Meteorological Conditions		Normalization Parameters		2400-ft S.S.: Data			
	$(\rho_0/\rho_1)^{1/2}$	$(T_0/T_1)^{1/2}$	$(\rho_0/\rho_1)^{1/2}$	$(T_0/T_1)^{1/2}$	$(\rho_0/\rho_1)^{1/2}$	$(T_0/T_1)^{1/2}$	$(\rho_0/\rho_1)^{1/2}$	$(T_0/T_1)^{1/2}$	$T_{DB}$ (°F)	$T_{WB}$ (°F)	$10 \log_{10}$ ( $V/A_0$ )	$10 \log_{10}$ $P_0(T_0/T_1)^{1/2}$	50° OASPL PWL	90° OASPL PWL	FWPL PWL	POASPL PWL
1	1.254	1.254	1.254	1.254	1.254	1.254	1.254	1.254	44	42	0.544	37.3	59.7	66.3	75.1	69.6
2	1.254	1.254	1.254	1.254	1.254	1.254	1.254	1.254	44	42	0.544	37.3	60.7	67.3	76.1	70.6
3	1.254	1.254	1.254	1.254	1.254	1.254	1.254	1.254	44	42	0.544	37.3	61.7	68.3	77.1	71.6
4	1.254	1.254	1.254	1.254	1.254	1.254	1.254	1.254	44	42	0.544	37.3	62.7	69.3	78.1	72.6
5	1.254	1.254	1.254	1.254	1.254	1.254	1.254	1.254	44	42	0.544	37.3	63.7	70.3	79.1	73.6
6	1.254	1.254	1.254	1.254	1.254	1.254	1.254	1.254	44	42	0.544	37.3	64.7	71.3	80.1	74.6
7	1.254	1.254	1.254	1.254	1.254	1.254	1.254	1.254	44	42	0.544	37.3	65.7	72.3	81.1	75.6
8	1.254	1.254	1.254	1.254	1.254	1.254	1.254	1.254	44	42	0.544	37.3	66.7	73.3	82.1	76.6
9	1.254	1.254	1.254	1.254	1.254	1.254	1.254	1.254	44	42	0.544	37.3	67.7	74.3	83.1	77.6
10	1.254	1.254	1.254	1.254	1.254	1.254	1.254	1.254	44	42	0.544	37.3	68.7	75.3	84.1	78.6
11	1.254	1.254	1.254	1.254	1.254	1.254	1.254	1.254	44	42	0.544	37.3	69.7	76.3	85.1	79.6
12	1.254	1.254	1.254	1.254	1.254	1.254	1.254	1.254	44	42	0.544	37.3	70.7	77.3	86.1	80.6
13	1.254	1.254	1.254	1.254	1.254	1.254	1.254	1.254	44	42	0.544	37.3	71.7	78.3	87.1	81.6
14	1.254	1.254	1.254	1.254	1.254	1.254	1.254	1.254	44	42	0.544	37.3	72.7	79.3	88.1	82.6
15	1.254	1.254	1.254	1.254	1.254	1.254	1.254	1.254	44	42	0.544	37.3	73.7	80.3	89.1	83.6
16	1.254	1.254	1.254	1.254	1.254	1.254	1.254	1.254	44	42	0.544	37.3	74.7	81.3	90.1	84.6
17	1.254	1.254	1.254	1.254	1.254	1.254	1.254	1.254	44	42	0.544	37.3	75.7	82.3	91.1	85.6
18	1.254	1.254	1.254	1.254	1.254	1.254	1.254	1.254	44	42	0.544	37.3	76.7	83.3	92.1	86.6
19	1.254	1.254	1.254	1.254	1.254	1.254	1.254	1.254	44	42	0.544	37.3	77.7	84.3	93.1	87.6
20	1.254	1.254	1.254	1.254	1.254	1.254	1.254	1.254	44	42	0.544	37.3	78.7	85.3	94.1	88.6
21	1.254	1.254	1.254	1.254	1.254	1.254	1.254	1.254	44	42	0.544	37.3	79.7	86.3	95.1	89.6
22	1.254	1.254	1.254	1.254	1.254	1.254	1.254	1.254	44	42	0.544	37.3	80.7	87.3	96.1	90.6
23	1.254	1.254	1.254	1.254	1.254	1.254	1.254	1.254	44	42	0.544	37.3	81.7	88.3	97.1	91.6
24	1.254	1.254	1.254	1.254	1.254	1.254	1.254	1.254	44	42	0.544	37.3	82.7	89.3	98.1	92.6
25	1.254	1.254	1.254	1.254	1.254	1.254	1.254	1.254	44	42	0.544	37.3	83.7	90.3	99.1	93.6
26	1.254	1.254	1.254	1.254	1.254	1.254	1.254	1.254	44	42	0.544	37.3	84.7	91.3	100.1	94.6
27	1.254	1.254	1.254	1.254	1.254	1.254	1.254	1.254	44	42	0.544	37.3	85.7	92.3	101.1	95.6
28	1.254	1.254	1.254	1.254	1.254	1.254	1.254	1.254	44	42	0.544	37.3	86.7	93.3	102.1	96.6
29	1.254	1.254	1.254	1.254	1.254	1.254	1.254	1.254	44	42	0.544	37.3	87.7	94.3	103.1	97.6
30	1.254	1.254	1.254	1.254	1.254	1.254	1.254	1.254	44	42	0.544	37.3	88.7	95.3	104.1	98.6
31	1.254	1.254	1.254	1.254	1.254	1.254	1.254	1.254	44	42	0.544	37.3	89.7	96.3	105.1	99.6
32	1.254	1.254	1.254	1.254	1.254	1.254	1.254	1.254	44	42	0.544	37.3	90.7	97.3	106.1	100.6
33	1.254	1.254	1.254	1.254	1.254	1.254	1.254	1.254	44	42	0.544	37.3	91.7	98.3	107.1	101.6
34	1.254	1.254	1.254	1.254	1.254	1.254	1.254	1.254	44	42	0.544	37.3	92.7	99.3	108.1	102.6
35	1.254	1.254	1.254	1.254	1.254	1.254	1.254	1.254	44	42	0.544	37.3	93.7	100.3	109.1	103.6
36	1.254	1.254	1.254	1.254	1.254	1.254	1.254	1.254	44	42	0.544	37.3	94.7	101.3	110.1	104.6
37	1.254	1.254	1.254	1.254	1.254	1.254	1.254	1.254	44	42	0.544	37.3	95.7	102.3	111.1	105.6
38	1.254	1.254	1.254	1.254	1.254	1.254	1.254	1.254	44	42	0.544	37.3	96.7	103.3	112.1	106.6
39	1.254	1.254	1.254	1.254	1.254	1.254	1.254	1.254	44	42	0.544	37.3	97.7	104.3	113.1	107.6
40	1.254	1.254	1.254	1.254	1.254	1.254	1.254	1.254	44	42	0.544	37.3	98.7	105.3	114.1	108.6
41	1.254	1.254	1.254	1.254	1.254	1.254	1.254	1.254	44	42	0.544	37.3	99.7	106.3	115.1	109.6
42	1.254	1.254	1.254	1.254	1.254	1.254	1.254	1.254	44	42	0.544	37.3	100.7	107.3	116.1	110.6
43	1.254	1.254	1.254	1.254	1.254	1.254	1.254	1.254	44	42	0.544	37.3	101.7	108.3	117.1	111.6
44	1.254	1.254	1.254	1.254	1.254	1.254	1.254	1.254	44	42	0.544	37.3	102.7	109.3	118.1	112.6
45	1.254	1.254	1.254	1.254	1.254	1.254	1.254	1.254	44	42	0.544	37.3	103.7	110.3	119.1	113.6
46	1.254	1.254	1.254	1.254	1.254	1.254	1.254	1.254	44	42	0.544	37.3	104.7	111.3	120.1	114.6
47	1.254	1.254	1.254	1.254	1.254	1.254	1.254	1.254	44	42	0.544	37.3	105.7	112.3	121.1	115.6
48	1.254	1.254	1.254	1.254	1.254	1.254	1.254	1.254	44	42	0.544	37.3	106.7	113.3	122.1	116.6
49	1.254	1.254	1.254	1.254	1.254	1.254	1.254	1.254	44	42	0.544	37.3	107.7	114.3	123.1	117.6
50	1.254	1.254	1.254	1.254	1.254	1.254	1.254	1.254	44	42	0.544	37.3	108.7	115.3	124.1	118.6
51	1.254	1.254	1.254	1.254	1.254	1.254	1.254	1.254	44	42	0.544	37.3	109.7	116.3	125.1	119.6
52	1.254	1.254	1.254	1.254	1.254	1.254	1.254	1.254	44	42	0.544	37.3	110.7	117.3	126.1	120.6
53	1.254	1.254	1.254	1.254	1.254	1.254	1.254	1.254	44	42	0.544	37.3	111.7	118.3	127.1	121.6
54	1.254	1.254	1.254	1.254	1.254	1.254	1.254	1.254	44	42	0.544	37.3	112.7	119.3	128.1	122.6
55	1.254	1.254	1.254	1.254	1.254	1.254	1.254	1.254	44	42	0.544	37.3	113.7	120.3	129.1	123.6
56	1.254	1.254	1.254	1.254	1.254	1.254	1.254	1.254	44	42	0.544	37.3	114.7	121.3	130.1	124.6
57	1.254	1.254	1.254	1.254	1.254	1.254	1.254	1.254	44	42	0.544	37.3	115.7	122.3	131.1	125.6
58	1.254	1.254	1.254	1.254	1.254	1.254	1.254	1.254	44	42	0.544	37.3	116.7	123.3	132.1	126.6
59	1.254	1.254	1.254	1.254	1.254	1.254	1.254	1.254	44	42	0.544	37.3	117.7	124.3	133.1	127.6
60	1.254	1.254	1.254	1.254	1.254	1.254	1.254	1.254	44	42	0.544	37.3	118.7	125.3	134.1	128.6
61	1.254	1.254	1.254	1.254	1.254	1.254	1.254	1.254	44	42	0.544	37.3	119.7	126.3	135.1	129.6
62	1.254	1.254	1.254	1.254	1.254	1.254	1.254	1.254	44	42	0.544	37.3	120.7	127.3	136.1	130.6
63	1.254	1.254	1.254	1.254	1.254	1.254	1.254	1.254	44	42	0.544	37.3	121.7	128.3	137.1	131.6
64	1.254	1.254	1.254	1.254	1.254	1.254	1.254	1.254	44	42	0.544	37.3	122.7	129.3	138.1	132.6
65	1.254	1.254	1.254	1.254	1.254	1.254	1.254	1.254	44	42	0.544	37.3	123.7	130.3	139.1	133.6
66	1.254	1.254	1.254	1.254	1.254	1.254	1.254	1.254	44	42	0.544	37.3	124.7	131.3	140.1	134.6
67	1.254	1.254	1.254	1.254	1.254	1.254	1.254	1.254	44	42	0.544	37.3	125.7	132.3	141.1	135.6
68	1.254	1.254	1.254	1.254	1.254	1.254	1.254	1.254	44	42	0.544	37.3	126.7	133.3	142.1	136.6
69	1.254	1.254	1.254	1.254	1.254	1.254	1.254	1.254	44	42	0.544	37.3	127.7	134.3	143.1	137.6
70	1.254	1.254	1.254	1.254	1.254	1.254	1.254	1.254	44	42	0.544	37.3	128.7	135.3	144.1	138.6
71	1.254	1.254	1.254													



Table B-35. Model No. 35: 36 Spoke, AR = 2.5,  $R_F^0 = 0.783$  Outer Suppressor;  $A_0/A_1 = 0.65$ ,  $R_F^1 = 0.674$   
Inner Plug, Retracted.

$A_0 = 11.11$  in.<sup>2</sup>,  $A_1 = 12.71$  in.<sup>2</sup> Linear Scale Factor to 338 in.<sup>2</sup> No. 1-15 and No. 44-59 at 3.45 (Dual Flow);  
No. 60-61 at 3.15 (Outer Only)

Data Point No.	Inner		Outer		Ratios		Mass Averages		Meteorological Conditions		Normalization Parameters		2400-ft S.L. Data			
	$(P_0/P_{01})_{0.1}$ (in. <sup>2</sup> )	$T_{01}$ (°K)	$(P_0/P_{01})_{0.1}$ (in. <sup>2</sup> )	$T_{01}$ (°K)	$\rho_0/\rho_1$	$M_0/M_1$	$(P_0/P_{01})_{0.1}$ (in. <sup>2</sup> )	$T_{01}$ (°K)	$T_{01}$ (°F)	$T_{01}$ (°F)	$10 \log_{10} (P_0/P_{01})_{0.1}$	$10 \log_{10} (T_{01}/T_{01}^0)$	OASPL PNL	50° PNL	OASPL PNL	90° PNL
1	1.884	523	1.553	704	1.0	0.5	1.74	579	1009	54	47	-0.438	59.0	66.0	64.9	73.4
2	1.412	525	1.499	465	1.3	0.5	1.791	638	1065	54	47	-0.124	61.0	69.4	68.4	77.0
3	1.783	532	1.674	491	1.5	0.6	1.872	685	1102	54	47	-0.102	62.9	71.6	70.7	80.2
4	1.786	546	1.736	513	2.0	0.6	1.876	853	1392	54	47	-0.033	62.9	71.6	70.7	80.2
5	1.412	546	1.407	450	1.0	0.6	1.882	795	1108	63	50	-0.033	65.4	66.6	65.7	74.3
6	1.644	577	1.623	512	1.5	0.8	1.882	924	1355	63	50	0.841	65.0	73.6	71.5	81.6
7	1.481	554	1.464	485	1.0	0.9	1.884	1149	1664	62	50	1.734	65.4	67.2	66.3	75.8
8	1.481	554	1.464	485	1.0	0.8	1.884	1149	1664	62	50	1.734	65.4	67.2	66.3	75.8
9	1.556	563	1.529	528	1.3	0.9	1.884	1209	1709	59	49	0.349	61.4	68.8	67.9	76.5
10	1.543	563	1.529	528	1.3	0.9	1.884	1209	1709	59	49	0.349	61.4	68.8	67.9	76.5
11	1.543	563	1.529	528	1.3	0.9	1.884	1209	1709	59	49	0.349	61.4	68.8	67.9	76.5
12	1.543	563	1.529	528	1.3	0.9	1.884	1209	1709	59	49	0.349	61.4	68.8	67.9	76.5
13	1.543	563	1.529	528	1.3	0.9	1.884	1209	1709	59	49	0.349	61.4	68.8	67.9	76.5
14	1.543	563	1.529	528	1.3	0.9	1.884	1209	1709	59	49	0.349	61.4	68.8	67.9	76.5
15	1.543	563	1.529	528	1.3	0.9	1.884	1209	1709	59	49	0.349	61.4	68.8	67.9	76.5
16	1.543	563	1.529	528	1.3	0.9	1.884	1209	1709	59	49	0.349	61.4	68.8	67.9	76.5
17	1.543	563	1.529	528	1.3	0.9	1.884	1209	1709	59	49	0.349	61.4	68.8	67.9	76.5
18	1.543	563	1.529	528	1.3	0.9	1.884	1209	1709	59	49	0.349	61.4	68.8	67.9	76.5
19	1.543	563	1.529	528	1.3	0.9	1.884	1209	1709	59	49	0.349	61.4	68.8	67.9	76.5
20	1.543	563	1.529	528	1.3	0.9	1.884	1209	1709	59	49	0.349	61.4	68.8	67.9	76.5
21	1.543	563	1.529	528	1.3	0.9	1.884	1209	1709	59	49	0.349	61.4	68.8	67.9	76.5
22	1.543	563	1.529	528	1.3	0.9	1.884	1209	1709	59	49	0.349	61.4	68.8	67.9	76.5
23	1.543	563	1.529	528	1.3	0.9	1.884	1209	1709	59	49	0.349	61.4	68.8	67.9	76.5
24	1.543	563	1.529	528	1.3	0.9	1.884	1209	1709	59	49	0.349	61.4	68.8	67.9	76.5
25	1.543	563	1.529	528	1.3	0.9	1.884	1209	1709	59	49	0.349	61.4	68.8	67.9	76.5
26	1.543	563	1.529	528	1.3	0.9	1.884	1209	1709	59	49	0.349	61.4	68.8	67.9	76.5
27	1.543	563	1.529	528	1.3	0.9	1.884	1209	1709	59	49	0.349	61.4	68.8	67.9	76.5
28	1.543	563	1.529	528	1.3	0.9	1.884	1209	1709	59	49	0.349	61.4	68.8	67.9	76.5
29	1.543	563	1.529	528	1.3	0.9	1.884	1209	1709	59	49	0.349	61.4	68.8	67.9	76.5
30	1.543	563	1.529	528	1.3	0.9	1.884	1209	1709	59	49	0.349	61.4	68.8	67.9	76.5
31	1.543	563	1.529	528	1.3	0.9	1.884	1209	1709	59	49	0.349	61.4	68.8	67.9	76.5
32	1.543	563	1.529	528	1.3	0.9	1.884	1209	1709	59	49	0.349	61.4	68.8	67.9	76.5
33	1.543	563	1.529	528	1.3	0.9	1.884	1209	1709	59	49	0.349	61.4	68.8	67.9	76.5
34	1.543	563	1.529	528	1.3	0.9	1.884	1209	1709	59	49	0.349	61.4	68.8	67.9	76.5
35	1.543	563	1.529	528	1.3	0.9	1.884	1209	1709	59	49	0.349	61.4	68.8	67.9	76.5
36	1.543	563	1.529	528	1.3	0.9	1.884	1209	1709	59	49	0.349	61.4	68.8	67.9	76.5
37	1.543	563	1.529	528	1.3	0.9	1.884	1209	1709	59	49	0.349	61.4	68.8	67.9	76.5
38	1.543	563	1.529	528	1.3	0.9	1.884	1209	1709	59	49	0.349	61.4	68.8	67.9	76.5
39	1.543	563	1.529	528	1.3	0.9	1.884	1209	1709	59	49	0.349	61.4	68.8	67.9	76.5
40	1.543	563	1.529	528	1.3	0.9	1.884	1209	1709	59	49	0.349	61.4	68.8	67.9	76.5
41	1.543	563	1.529	528	1.3	0.9	1.884	1209	1709	59	49	0.349	61.4	68.8	67.9	76.5
42	1.543	563	1.529	528	1.3	0.9	1.884	1209	1709	59	49	0.349	61.4	68.8	67.9	76.5
43	1.543	563	1.529	528	1.3	0.9	1.884	1209	1709	59	49	0.349	61.4	68.8	67.9	76.5
44	1.543	563	1.529	528	1.3	0.9	1.884	1209	1709	59	49	0.349	61.4	68.8	67.9	76.5
45	1.543	563	1.529	528	1.3	0.9	1.884	1209	1709	59	49	0.349	61.4	68.8	67.9	76.5
46	1.543	563	1.529	528	1.3	0.9	1.884	1209	1709	59	49	0.349	61.4	68.8	67.9	76.5
47	1.543	563	1.529	528	1.3	0.9	1.884	1209	1709	59	49	0.349	61.4	68.8	67.9	76.5
48	1.543	563	1.529	528	1.3	0.9	1.884	1209	1709	59	49	0.349	61.4	68.8	67.9	76.5
49	1.543	563	1.529	528	1.3	0.9	1.884	1209	1709	59	49	0.349	61.4	68.8	67.9	76.5
50	1.543	563	1.529	528	1.3	0.9	1.884	1209	1709	59	49	0.349	61.4	68.8	67.9	76.5
51	1.543	563	1.529	528	1.3	0.9	1.884	1209	1709	59	49	0.349	61.4	68.8	67.9	76.5
52	1.543	563	1.529	528	1.3	0.9	1.884	1209	1709	59	49	0.349	61.4	68.8	67.9	76.5
53	1.543	563	1.529	528	1.3	0.9	1.884	1209	1709	59	49	0.349	61.4	68.8	67.9	76.5
54	1.543	563	1.529	528	1.3	0.9	1.884	1209	1709	59	49	0.349	61.4	68.8	67.9	76.5
55	1.543	563	1.529	528	1.3	0.9	1.884	1209	1709	59	49	0.349	61.4	68.8	67.9	76.5
56	1.543	563	1.529	528	1.3	0.9	1.884	1209	1709	59	49	0.349	61.4	68.8	67.9	76.5
57	1.543	563	1.529	528	1.3	0.9	1.884	1209	1709	59	49	0.349	61.4	68.8	67.9	76.5
58	1.543	563	1.529	528	1.3	0.9	1.884	1209	1709	59	49	0.349	61.4	68.8	67.9	76.5
59	1.543	563	1.529	528	1.3	0.9	1.884	1209	1709	59	49	0.349	61.4	68.8	67.9	76.5
60	1.543	563	1.529	528	1.3	0.9	1.884	1209	1709	59	49	0.349	61.4	68.8	67.9	76.5
61	1.543	563	1.529	528	1.3	0.9	1.884	1209	1709	59	49	0.349	61.4	68.8	67.9	76.5
62	1.543	563	1.529	528	1.3	0.9	1.884	1209	1709	59	49	0.349	61.4	68.8	67.9	76.5
63	1.543	563	1.529	528	1.3	0.9	1.884	1209	1709	59	49	0.349	61.4	68.8	67.9	76.5
64	1.543	563	1.529	528	1.3	0.9	1.884	1209	1709	59	49	0.349	61.4	68.8	67.9	76.5
65	1.543	563	1.529	528	1.3	0.9	1.884	1209	1709	59	49	0.349	61.4	68.8	67.9	76.5
66	1.543	563	1.529	528	1.3	0.9	1.884	1209	1709	59	49	0.349	61.4	68.8	67.9	76.5
67	1.543	563	1.529	528	1.3	0.9	1.884	1209	1709	59	49	0.349	61.4	68.8	67.9	76.5
68	1.543	563	1.529	528	1.3	0.9	1.884	1209	1709	59	49	0.349	61.4	68.8	67.9	76.5
69	1.543	563	1.529	528	1.3	0.9	1.884	1209	1709	59	49	0.349	61.4	68.8	67.9	76.5
70	1.543	563	1.529	528	1.3	0.9	1.884	1209	1709	59	49	0.349	61.4	68.8	67.9	76.5

Table B-36. Model No. 36: 36 Chute, AR = 2.0,  $R^0 = 0.716$  Outer Suppressor;  $A/A_1 = 1.92$ ,  $R^1 = 0.779$  Inner Plug, Retracted with Acoustically Treated Secondary Ejector.

$A_0 = 21.76$ ,  $16.7$ ,  $16.7$ ,  $16.7$  in.  $2$  No. 9-37 at 3.09 (Dual Flow); No. 38-41 at 3.77 (Outer Only)

Data Point No.	Inlet		Outlet		Action		Mass Averages		Micrological Conditions		Normalization Parameters		2400-fr S.L. Data		POASFL	
	$(P_0/P_{01})_1$	$T_0/T_{01}$	$(P_0/P_{01})_2$	$T_0/T_{01}$	$V_0/V_{01}$	$V_0/V_{01}$	$(P_0/P_{01})_m$	$T_0/T_{01}$	$T_{01}/T_0$	$T_{01}/T_0$	$10 \log(P_0/P_{01})$	$10 \log(T_0/T_{01})$	OASFL	90°	PPNL	0
9	1.104	1.000	1.104	1.000	1.104	1.000	1.104	1.000	77	65	2.092	36.2	69	77.5	86.1	89.1
10	1.100	1.000	1.100	1.000	1.100	1.000	1.100	1.000	78	66	2.092	35.5	72	80.9	89.5	92.1
11	1.100	1.000	1.100	1.000	1.100	1.000	1.100	1.000	76	64	2.092	35.1	70.6	76.5	88.5	91.2
12	1.100	1.000	1.100	1.000	1.100	1.000	1.100	1.000	76	65	1.625	36.5	66.3	72.6	83.4	86.5
13	1.100	1.000	1.100	1.000	1.100	1.000	1.100	1.000	75	64	2.625	36.6	72.8	78.6	81.7	84.6
14	1.100	1.000	1.100	1.000	1.100	1.000	1.100	1.000	76	65	3.178	37.2	74.5	80.3	83.4	86.2
15	1.100	1.000	1.100	1.000	1.100	1.000	1.100	1.000	68	61	0.489	37.0	62.1	68.5	70.7	72.5
16	1.100	1.000	1.100	1.000	1.100	1.000	1.100	1.000	71	63	1.977	36.8	69.1	75.5	77.6	79.6
17	1.100	1.000	1.100	1.000	1.100	1.000	1.100	1.000	73	64	2.406	35.4	70.8	76.9	88.5	91.6
18	1.100	1.000	1.100	1.000	1.100	1.000	1.100	1.000	74	64	1.546	36.9	66.6	73.2	84.6	85.9
19	1.100	1.000	1.100	1.000	1.100	1.000	1.100	1.000	74	63	2.712	37.2	72.8	78.9	81.6	84.2
20	1.100	1.000	1.100	1.000	1.100	1.000	1.100	1.000	75	64	3.048	37.6	74.7	80.6	83.5	86.3
21	1.100	1.000	1.100	1.000	1.100	1.000	1.100	1.000	56	51	0.079	37.9	61.5	68.7	68.9	77.2
22	1.100	1.000	1.100	1.000	1.100	1.000	1.100	1.000	51	48	0.598	38.3	64.1	71.4	72.3	81.6
23	1.100	1.000	1.100	1.000	1.100	1.000	1.100	1.000	51	48	1.682	38.2	69.6	77.1	87.3	89.2
24	1.100	1.000	1.100	1.000	1.100	1.000	1.100	1.000	51	48	0.327	37.3	60.4	66.3	68.2	75.9
25	1.100	1.000	1.100	1.000	1.100	1.000	1.100	1.000	51	48	1.466	37.0	67.8	74.6	76.5	85.3
26	1.100	1.000	1.100	1.000	1.100	1.000	1.100	1.000	51	48	2.735	37.1	73.1	79.1	82.8	90.8
27	1.100	1.000	1.100	1.000	1.100	1.000	1.100	1.000	51	49	1.979	37.0	65.6	71.6	74.2	82.6
28	1.100	1.000	1.100	1.000	1.100	1.000	1.100	1.000	50	47	2.039	36.6	69.1	75.2	78.6	86.6
29	1.100	1.000	1.100	1.000	1.100	1.000	1.100	1.000	51	48	3.163	37.5	75.8	81.5	84.6	93.7
30	1.100	1.000	1.100	1.000	1.100	1.000	1.100	1.000	57	53	2.720	38.1	72.5	81.1	81.9	91.6
31	1.100	1.000	1.100	1.000	1.100	1.000	1.100	1.000	56	53	2.500	38.0	75.5	83.1	81.9	91.5
32	1.100	1.000	1.100	1.000	1.100	1.000	1.100	1.000	53	50	2.234	37.0	70.9	77.6	79.3	88.0
33	1.100	1.000	1.100	1.000	1.100	1.000	1.100	1.000	52	50	1.685	36.1	68.1	74.7	75.9	84.7
34	1.100	1.000	1.100	1.000	1.100	1.000	1.100	1.000	53	50	2.362	37.4	75.2	83.5	80.1	90.4
35	1.100	1.000	1.100	1.000	1.100	1.000	1.100	1.000	65	58	0.972	36.9	62.7	67.4	71.3	79.2
36	1.100	1.000	1.100	1.000	1.100	1.000	1.100	1.000	65	59	2.326	36.6	72.7	79.6	81.9	89.1
37	1.100	1.000	1.100	1.000	1.100	1.000	1.100	1.000	62	57	3.356	37.7	76.9	83.2	89.1	96.1
38	1.100	1.000	1.100	1.000	1.100	1.000	1.100	1.000	79	66	3.643	38.6	78.4	85.4	86.9	94.4
39	1.100	1.000	1.100	1.000	1.100	1.000	1.100	1.000	79	66	3.137	36.3	73.4	79.1	82.4	90.7
40	1.100	1.000	1.100	1.000	1.100	1.000	1.100	1.000	78	66	2.531	38.0	71.5	78.0	80.3	88.7
41	1.100	1.000	1.100	1.000	1.100	1.000	1.100	1.000	79	68	2.091	37.6	69.7	75.9	78.6	86.5

Table B-37. Model No. 37: Coannular-Noncoplanar Dual Plug Nozzle,  $R_T^0 = 0.853$ ,  $A_0/A_1 = 1.59$ ,  $R_T^1 = 0.800$  with Acoustically Treated Secondary Ejector.

$A_0 = 18.25 \text{ in.}^2$ ,  $A_1 = 11.15 \text{ in.}^2$  Linear Scale Factor to 318 in. $^2 = 1.18$

Data Point No.	Inner		Outer		Ratios		Mass Averages		Meteorological Conditions		Normalization Parameters		2400-ft S.L. Data			
	$(P/P_0)_1$	$T_1$	$(P/P_0)_2$	$T_2$	$U_0/U_1$	$U_0/U_2$	$T_0/T_1$	$T_0/T_2$	$T_{dry}$	$T_{wet}$	$10 \log_{10} (T_0/T_1)$	$10 \log_{10} (T_0/T_2)$	50°	90°	FPML	POASPL
12	2.962	843	3.950	1218	1.4	1.5	3.453	3.375	64	59	2.989	32.6	85	91.7	89.2	105.8
13	2.140	800	2.680	1153	1.5	1.6	2.121	1.947	60	57	2.437	32.6	75.1	87.7	87.2	100.9
20	2.280	890	3.140	1254	1.5	1.6	2.873	2.590	60	57	3.004	37.3	83.2	93.3	89.3	105.8
21	2.248	845	2.762	1194	1.2	1.3	1.751	1.574	69	61	0.044	37.9	69.4	74.1	72.8	80.3
22	2.248	845	2.762	1194	1.5	1.6	1.917	1.811	70	64	0.616	38.3	69.2	74.1	75.6	85.2
23	2.250	848	2.762	1194	2.0	2.1	2.283	2.037	68	60	1.615	38.3	74.8	81.6	80.9	93.7
24	2.250	848	2.762	1194	1.3	1.4	1.942	1.754	68	60	1.615	38.3	74.8	81.6	80.9	93.7
25	2.250	848	2.762	1194	1.5	1.6	2.188	1.947	65	60	1.972	38.3	75.5	82.8	81.2	90.6
26	2.250	848	2.762	1194	2.0	2.1	2.431	2.189	64	59	3.120	37.4	83.5	90.3	87.9	102.6
27	2.250	848	2.762	1194	1.6	1.7	2.806	2.554	62	57	2.649	38.2	81.8	88.5	86.5	95.4
31	2.250	848	2.762	1194	1.4	1.5	2.326	2.091	63	58	2.470	38.2	81.4	87.6	85.9	94.7
32	2.250	848	2.762	1194	1.4	1.5	2.366	2.145	62	57	2.182	37.1	76.6	83.1	82.9	91.1
33	2.250	848	2.762	1194	1.4	1.5	2.366	2.145	62	57	2.182	37.1	76.6	83.1	82.9	91.1
34	2.250	848	2.762	1194	2.0	2.1	2.255	1.992	62	57	2.291	36.2	76	84	82.8	91.5

Table B-38. Model No. 38: Coannular-Noncoplanar Dual Plug Nozzle,  $R_T^0 = 0.926$ ,  $A_0/A_1 = 0.71$ ,  $R_T^1 = 0.800$  with Acoustically Treated Ejector.

$A_0 = 8.61 \text{ in.}^2$ ,  $A_1 = 11.15 \text{ in.}^2$  Linear Scale Factor to 318 in. $^2 = 4.17$

Data Point No.	Inner		Outer		Ratios		Mass Averages		Meteorological Conditions		Normalization Parameters		2400-ft S.L. Data			
	$(P/P_0)_1$	$T_1$	$(P/P_0)_2$	$T_2$	$U_0/U_1$	$U_0/U_2$	$T_0/T_1$	$T_0/T_2$	$T_{dry}$	$T_{wet}$	$10 \log_{10} (T_0/T_1)$	$10 \log_{10} (T_0/T_2)$	50°	90°	FPML	POASPL
12	2.962	843	3.950	1218	1.4	1.5	3.453	3.375	55	53	2.989	39.9	85	91.4	88.3	103.5
13	2.140	800	2.680	1153	1.5	1.6	2.121	1.947	55	53	2.437	38.3	75.1	87.7	87.2	100.9
20	2.280	890	3.140	1254	1.5	1.6	2.873	2.590	55	53	3.004	38.3	83.2	93.3	89.3	105.8
21	2.248	845	2.762	1194	1.2	1.3	1.751	1.574	56	54	0.044	36.5	69.4	74.1	72.8	80.3
22	2.248	845	2.762	1194	1.5	1.6	1.917	1.811	55	53	0.616	36.2	69.2	74.1	75.6	85.2
23	2.250	848	2.762	1194	2.0	2.1	2.283	2.037	56	54	1.615	36.4	74.8	81.6	80.9	93.7
24	2.250	848	2.762	1194	1.3	1.4	1.942	1.754	56	54	1.615	36.4	74.8	81.6	80.9	93.7
25	2.250	848	2.762	1194	1.5	1.6	2.188	1.947	55	53	1.972	36.4	75.5	82.8	81.2	90.6
26	2.250	848	2.762	1194	2.0	2.1	2.431	2.189	54	54	3.120	37.4	83.5	90.3	87.9	102.6
27	2.250	848	2.762	1194	1.6	1.7	2.806	2.554	52	57	2.649	38.2	81.8	88.5	86.5	95.4
31	2.250	848	2.762	1194	1.4	1.5	2.326	2.091	53	58	2.470	38.2	81.4	87.6	85.9	94.7
32	2.250	848	2.762	1194	1.4	1.5	2.366	2.145	52	57	2.182	37.1	76.6	83.1	82.9	91.1
33	2.250	848	2.762	1194	1.4	1.5	2.366	2.145	52	57	2.182	37.1	76.6	83.1	82.9	91.1
34	2.250	848	2.762	1194	2.0	2.1	2.255	1.992	52	57	2.291	36.2	76	84	82.8	91.5

Table B-39. Model No. 39: Converging Plug, Single-Flow,  $R_r = 0.789$ .

$A_1 = 11.05 \text{ in.}^2$  Linear Scale Factor to 338 in. $^2 = 5.51$

Data Point No.	Inner		Free Stream	Meteorological Conditions		Normalization Parameters				2400-ft S.L. Data					
	$\frac{T_1}{(P_1/P_0)_1}$	$\frac{V_1}{(ft/sec)}$		$T_{Dry}$ ( $^{\circ}F$ )	$T_{Wet}$ ( $^{\circ}F$ )	$\frac{10 \log_{10} V/a_0}{}$	$\frac{10 \log_{10} P_g(T_0/T_{sm})^{w-1}}{}$	50° OASPL	50° PNL	90° OASPL	90° PNL	PPNL	$\theta$	POASPL	$\theta$
A22030	1.710	821	1185	42	37	0.026	37.6	67.6	72.0	73.7	79.6	83.3	130	78.8	130
A22040	1.934	934	1388	42	37	0.095	37.9	71.9	76.6	77.6	83.6	89.5	140	86.7	140
A22060	2.429	1197	1799	42	37	0.208	37.6	79.7	85.3	84.5	91.2	100.5	140	96.7	140
A22070	2.699	1335	1998	42	37	0.253	37.8	83.8	89.9	87.5	94.9	104.5	140	100.2	140
A22080	3.000	1487	2206	42	36	0.296	38.1	86.1	92.0	89.8	96.6	108.0	140	103.5	140
A22090	3.268	1628	2384	33	37	0.330	38.3	89.0	95.0	91.7	99.0	110.2	130	105.0	140
A22100	3.543	1794	2577	42	36	0.364	38.4	88.7	94.6	92.6	99.6	111.7	130	106.2	130
A22110	1.947	1542	1800	33	37	0.208	34.7	77.5	82.0	82.2	88.2	96.6	140	93.3	140
A22120	2.536	1693	2194	33	37	0.294	36.2	83.3	88.2	87.8	94.2	105.9	140	101.4	140
B22030	1.726	821	1194	49	39	0.030	37.7	68.2	73.0	71.6	77.4	80.5	120	75.8	140
B22040	1.933	929	1384	49	39	0.094	37.9	70.8	75.2	75.1	81.2	85.8	130	81.8	140
B22060	2.445	1194	1803	53	41	0.208	37.7	79.1	85.5	82.4	89.7	96.2	140	91.7	140
B22070	2.787	1337	2002	53	41	0.254	37.8	83.4	89.9	85.8	93.6	101.1	140	95.8	140
B22080	2.980	1481	2195	53	41	0.294	38.1	85.7	92.4	88.3	96.0	104.4	130	98.6	140
B22090	3.259	1634	2386	53	41	0.330	38.2	89.2	95.8	91.0	98.8	106.7	130	100.5	140
B22100	3.556	1792	2579	53	41	0.364	38.4	88.6	94.8	92.0	99.8	109.2	130	103.2	130
B22110	1.930	1524	1779	53	41	0.203	34.7	76.4	81.4	80.5	86.9	93.4	130	88.8	140
B22120	2.528	1682	2183	53	41	0.292	36.3	82.7	88.2	86.6	93.8	102.4	140	97.1	140
C22030	1.743	823	1206	47	38	0.034	37.7	73.7	78.5	71.5	76.5	78.0	110	71.7	110
C22040	1.944	934	1393	47	38	0.097	37.9	72.7	77.4	74.4	81.2	84.1	120	78.6	140
C22060	2.436	1202	1806	47	38	0.209	37.6	78.8	86.1	81.3	89.4	93.6	130	88.6	140
C22070	2.708	1338	2003	47	38	0.254	37.8	83.3	90.7	85.0	93.8	98.0	130	92.4	140
C22080	2.986	1485	2200	47	38	0.294	38.1	85.8	92.9	87.7	96.5	102.6	130	96.2	130
C22090	3.256	1627	2380	47	38	0.329	38.3	89.4	96.7	90.7	99.6	105.9	130	99.1	130
C22100	3.534	1790	2572	47	38	0.363	38.4	88.5	95.4	91.5	100.2	108.2	130	101.7	130
C22110	1.925	1534	1781	42	37	0.203	34.7	79.0	84.1	80.5	86.7	90.5	130	85.3	130
C22120	2.541	1683	2189	47	38	0.293	36.3	82.1	88.6	85.7	93.9	100.1	130	94.3	130

Table B-40. Model No. 40: Converging Plug, Single-Flow,  $R_r = 0.85$ .

$A_1 = 11.05 \text{ in.}^2$  Linear Scale Factor to 338 in.  $2 = 5.51$

Data Point No.	Inner		Free Stream	Meteorological Conditions		Normalization Parameters		2400-ft S.L. Data							
	$\frac{T_r}{T_o}$ ( $^{\circ}$ R)	$V_1$ (ft/sec)		$V_{\infty}$ (ft/sec)	$T_{dry}$ ( $^{\circ}$ F)	$T_{wet}$ ( $^{\circ}$ F)	$\frac{10 \log_{10} V/a_o}{V/a_o}$	$10 \log_{10} P_g(T_o/T_{ref})^{w-1}$	OASPL	50° PNL	OASPL	90° PNL	PPNL	$\theta$	POASPL
A21030	1.742	814	1198	0	56	0.031	37.7	66.7	71.5	71.8	77.3	81.0	130	77.9	140
A21040	1.952	927	1392	0	56	0.096	37.9	70.5	75.1	75.9	81.4	86.9	140	83.9	140
A21050	2.273	1084	1652	0	56	0.171	37.8	76.3	82.1	81.1	87.7	95.0	140	91.6	140
A21060	2.462	1196	1810	0	56	0.210	37.7	81.5	87.9	85.4	92.3	99.8	140	96.0	140
A21070	2.762	1335	2018	0	56	0.257	38.0	81.2	87.2	85.9	92.4	103.3	140	99.0	140
A21080	3.037	1473	2204	0	56	0.296	38.2	83.7	89.5	88.3	94.9	106.6	140	102.1	140
A21090	3.305	1618	2386	0	56	0.330	38.4	86.7	93.0	90.5	97.8	108.6	130	103.8	140
A21100	3.595	1789	2585	0	56	0.365	38.5	89.0	95.6	92.8	100.4	111.6	130	105.8	130
A21110	1.973	1538	1814	0	56	0.211	34.8	75.6	80.4	81.2	87.1	94.7	140	91.5	140
A21120	2.585	1678	2203	0	56	0.296	36.4	82.0	87.9	87.0	93.3	105.0	140	100.2	140
A21150	2.436	991	1636	0	56	0.166	38.7	80.9	87.6	83.6	90.8	96.6	140	92.9	140
A21160	2.076	1245	1683	0	56	0.178	36.5	74.6	79.2	80.3	86.1	93.6	140	90.4	140
A21170	1.772	1492	1650	0	56	0.170	34.6	72.9	77.8	79.3	85.2	90.9	130	87.4	140
A21190	1.624	1789	1646	0	56	0.169	33.2	72.6	77.2	78.8	84.5	89.8	130	86.3	140
A21210	4.077	1090	2081	0	56	0.271	41.7	90.8	97.1	92.3	99.4	108.9	140	104.4	140
A21220	3.337	1236	2084	0	56	0.271	39.7	87.5	94.0	89.5	96.7	106.4	140	102.0	140
A21230	2.638	1490	2093	0	56	0.273	37.1	82.0	87.8	86.3	92.7	104.0	140	99.8	140
A21240	2.253	1741	2095	0	56	0.274	35.2	80.1	85.8	85.8	92.7	101.9	140	97.4	140
B21030	1.744	813	1199	147	56	0.031	37.8	67.4	72.6	70.7	76.8	77.9	120	72.3	120
B21040	1.972	902	1382	147	56	0.093	38.1	70.8	75.9	74.6	80.3	84.8	130	80.5	140
B21050	2.271	986	1574	146	56	0.149	38.4	76.3	82.9	79.9	87.2	91.5	130	87.1	140
B21060	2.466	1084	1723	150	56	0.189	38.3	82.0	88.9	84.3	91.7	95.7	130	91.2	140
B21070	2.758	1330	2013	150	56	0.256	38.0	82.0	88.5	85.2	92.1	100.4	140	95.2	140
B21080	3.024	1466	2196	149	56	0.294	38.2	84.5	90.6	87.5	94.6	103.4	140	98.1	140
B21090	3.300	1614	2382	145	56	0.327	38.4	87.9	94.4	89.8	97.4	106.2	130	100.4	140
B21100	3.596	1781	2580	143	56	0.364	38.5	90.1	96.8	92.0	99.7	108.8	130	102.6	130
B21110	1.964	1524	1800	149	56	0.208	34.8	75.9	80.8	79.9	86.1	92.6	130	88.0	140
B21120	2.573	1672	2194	149	56	0.294	36.4	82.2	87.8	85.8	92.3	101.6	140	96.5	140
C21030	1.723	829	1199	283	38	0.031	37.7	72.4	77.2	69.7	74.0	77.4	70	72.4	50
C21040	1.943	939	1397	279	38	0.098	37.9	75.6	81.2	74.9	81.5	83.2	120	77.2	140
C21050	2.235	1093	1644	286	38	0.169	37.7	80.0	86.6	79.7	87.7	90.3	130	84.3	140
C21060	2.429	1202	1803	289	38	0.209	37.6	80.7	88.2	83.7	92.1	94.5	130	88.3	130
C21070	2.730	1325	2000	284	38	0.253	37.9	81.7	90.0	84.6	93.6	97.5	130	92.3	140
C21080	3.001	1479	2200	278	38	0.295	38.1	83.9	91.4	87.1	95.8	101.2	130	95.1	130
C21090	3.246	1639	2387	280	38	0.330	38.2	88.5	95.8	89.9	98.7	104.8	130	98.4	130
C21100	3.589	1776	2575	286	38	0.363	38.5	90.1	97.2	92.0	100.7	107.4	130	101.1	130
C21110	1.945	1548	1802	273	31	0.208	34.7	78.4	83.6	78.7	86.3	90.7	120	84.7	130
C21120	2.541	1687	2192	267	31	0.293	36.3	81.4	88.1	85.2	93.3	99.2	130	93.4	130
C21150	2.413	994	1630	266	38	0.165	38.7	83.4	92.1	84.7	93.0	94.0	130	87.3	130

Table E-40. Model No 40: Converging Plug, Single-Flow,  $K_r = 0.85$  (Concluded).

$A_1 = 11.12 \text{ in.}^2$  Linear Scale Factor to 338 in. = 5.50

Data Point No.	Inner		Free Stream	Meteorological Conditions	Normalization Parameters			2400-ft S.L. Data					
	$(P/P_0)_i$	$T_{ti} (^{\circ}R)$	$V_i$ (ft/sec)	$T_{dry} (^{\circ}F)$	$T_{wet} (^{\circ}F)$	$10 \log_{10} V/a_0$	$10 \log_{10} F_s(T_0/T_{sm})^{\omega-1}$	OASPL	PNL	90°	PNL	POASPL	$\theta$
C21160	1.966	1254	1631	45	38	0.165	36.1	77.7	81.7	77.1	84.4	87.8	130
C21170	1.755	1504	1645	36	31	0.169	34.5	77.1	81.5	77.3	84.4	87.4	120
C21190	1.607	1782	1655	38	31	0.171	32.9	76.7	81.2	77.1	83.8	86.9	120
C21210	4.057	1110	2098	38	31	0.274	41.6	92.8	99.5	93.6	101.9	105.6	140
C21220	3.304	1250	2089	38	31	0.272	39.6	89.2	96.7	89.2	98.1	101.6	140
C21230	2.608	1512	2097	38	31	0.274	37.0	81.4	88.9	85.0	93.4	98.7	140
C21240	2.231	1759	2075	38	31	0.274	35.1	80.4	87.5	84.2	92.1	97.5	130

Table B-41. Model No. 41: 36 Chute, AR = 2.5,  $R_r = 0.78$  Turbojet.

$A_1 = 11.12 \text{ in.}^2$  Linear Scale Factor to 338 in. = 5.50

Data Point No.	Inner		Free Stream	Meteorological Conditions	Normalization Parameters			2400-ft S.L. Data					
	$(P/P_0)_i$	$T_{ti} (^{\circ}R)$	$V_i$ (ft/sec)	$T_{dry} (^{\circ}F)$	$T_{wet} (^{\circ}F)$	$10 \log_{10} V/a_0$	$10 \log_{10} F_s(T_0/T_{sm})^{\omega-1}$	OASPL	PNL	90°	PNL	POASPL	$\theta$
A23030	1.735	816	1196	74	58	0.030	37.7	62.4	69.9	70.5	79.3	82.2	110
A23040	1.937	939	1404	74	58	0.100	37.9	65.6	73.6	73.5	82.8	86.0	120
A23050	2.452	1188	1803	74	58	0.208	37.7	70.9	79.3	78.4	87.9	92.5	120
A23070	2.731	1333	2007	74	58	0.255	37.9	73.4	82.0	80.9	90.5	94.9	120
A23090	3.264	1614	2372	73	58	0.328	38.3	76.8	85.9	84.5	93.7	98.4	120
A23100	3.573	1791	2582	73	58	0.364	38.5	78.2	85.9	86.1	95.1	99.5	140
A23110	1.951	1534	1798	74	58	0.207	34.7	69.1	77.2	77.5	87.0	91.7	120
A23120	2.547	1689	2195	74	58	0.294	36.3	73.9	82.1	81.3	90.8	96.0	120
B23030	1.737	816	1191	67	59	0.029	37.7	63.3	70.2	68.4	77.7	80.4	120
B23040	1.945	936	1396	67	59	0.097	37.9	68.1	75.9	71.9	81.3	84.8	120
B23050	2.454	1196	1807	67	59	0.209	37.7	72.6	81.6	77.4	87.4	92.1	120
B23070	2.716	1333	2001	67	59	0.254	37.9	74.4	83.8	79.3	89.2	94.2	120
B23090	3.268	1632	2387	74	59	0.330	38.3	78.0	87.7	83.2	93.0	98.0	120
B23100	3.566	1783	2574	74	59	0.363	38.5	79.7	89.4	84.4	94.0	99.1	120
B23110	1.955	1583	1802	67	59	0.208	34.7	71.2	79.5	76.3	86.0	90.7	120
B23120	2.549	1686	2194	74	59	0.294	36.3	75.1	83.8	80.1	90.1	95.2	120
C23030	1.708	823	1185	46	38	0.026	37.6	68.5	75.5	72.3	82.0	82.1	100
C23040	1.936	942	1396	46	38	0.097	37.8	77.6	81.2	79.5	86.2	87.2	110
C23060	2.432	1204	1806	46	38	0.209	37.6	75.5	83.4	78.6	90.3	92.5	120
C23070	2.699	1344	2004	46	38	0.254	37.8	75.1	84.0	80.6	92.4	95.2	130
C23090	3.246	1631	2380	40	38	0.329	38.2	77.5	87.8	84.0	95.4	98.6	130
C23100	3.535	1798	2578	40	38	0.363	38.4	79.9	90.0	85.8	97.3	100.8	120
C23110	1.937	1540	1793	38	31	0.206	34.7	76.1	82.7	77.5	88.8	91.4	120
C23120	2.531	1701	2197	40	38	0.294	36.2	75.6	84.0	81.5	93.1	95.8	120



Table B-42. Model No. 42: 36 Chute, AR = 2.5,  $R_r^0 = 0.78$  Outer Suppressor with Induced Flow Through  
 $A_o/A_i = 0.65$ ,  $R_i^1 = 0.674$  Inner Plug, Retracted.

$A_o = 11.12$ , in.<sup>2</sup>  $A_i = 17.21$  in.<sup>2</sup> Linear Scale Factor to 338 in.<sup>2</sup> = 5.50 (Outer Only)

Beta Point No.	Outer		Free Stream	Meteorological Conditions		Normalization Parameters		2400-ft S.L. Data					
	$(P_r/P_o)$	$T_{To}$ ( $^{\circ}$ R)	$V_o$ (ft/sec)	$T_{Dry}$ ( $^{\circ}$ F)	$T_{Wet}$ ( $^{\circ}$ F)	$V/a_o$	$10 \log 10 F_g(T_o/T_{ref})^{0.1}$	50°		90°		PNL	$\theta$ POASPL $\theta$
A24030	1.723	817	1190	77	61	0.028	37.7	61.7	69.3	70.3	79.0	91.8	120 72.9 120
A24040	1.948	928	1391	77	61	0.096	37.9	63.1	73.0	73.5	82.7	86.1	120 76.7 120
A24060	2.447	1180	1793	77	61	0.206	37.7	70.4	79.1	78.7	88.2	92.7	120 82.8 120
A24070	2.715	1300	1976	77	61	0.248	38.0	72.4	81.3	80.4	90.0	95.1	120 85.2 120
A24090	3.253	1614	2370	75	61	0.327	38.3	76.0	85.7	83.9	93.3	98.7	120 89.2 120
A24100	3.549	1774	2564	75	61	0.361	38.5	77.8	87.4	85.7	95.1	99.8	120 90.8 120
A24110	1.940	1527	1787	75	61	0.205	34.7	58.8	77.3	77.2	86.7	91.5	120 81.6 120
A24120	2.533	1673	2179	75	61	0.291	36.3	73.3	81.8	81.3	91.0	95.9	120 86.1 120
B24030	1.714	818	1186	69	60	0.026	37.6	63.6	70.8	68.7	78.3	80.6	120 71.0 120
B24040	1.943	928	1389	69	60	0.095	37.9	63.0	76.2	72.1	81.9	85.2	120 75.2 120
B24060	2.453	1185	1799	68	60	0.207	37.7	72.2	81.7	77.7	88.0	92.3	120 81.8 120
B24070	2.714	1330	1999	68	60	0.253	37.9	73.7	83.4	79.5	89.7	94.8	120 84.4 120
B24090	3.265	1616	2374	68	60	0.328	38.3	77.5	87.4	83.2	93.2	98.6	120 88.5 120
B24100	3.561	1793	2580	66	59	0.364	38.4	79.1	89.1	84.9	94.6	99.7	120 89.8 120
B24110	1.940	1523	1784	68	60	0.204	34.8	70.7	79.3	76.3	86.2	91.2	120 80.9 120
B24120	2.544	1679	2187	68	60	0.292	36.3	74.8	83.8	80.5	90.7	95.9	120 85.4 120
C24030	1.714	827	1192	36	30	0.029	37.6	68.7	75.9	72.9	82.8	82.9	100 73.4 120
C24040	1.930	944	1394	36	30	0.097	37.8	72.0	79.3	76.1	86.5	86.8	120 76.4 130
C24060	2.427	1203	1803	36	30	0.208	37.6	76.2	84.2	79.8	91.6	93.3	120 82.2 120
C24070	2.697	1342	2002	35	30	0.254	37.8	82.3	88.4	81.9	93.8	96.0	120 84.8 120
C24090	3.248	1639	2387	36	30	0.330	38.2	79.4	89.0	85.4	97.0	99.7	120 88.5 120
C24100	3.539	1797	2578	37	30	0.364	38.4	79.8	90.0	87.2	98.7	101.0	120 90.0 120
C24110	1.948	1546	1803	37	30	0.209	34.7	76.0	83.2	78.6	89.8	92.4	120 81.3 120
C24120	2.529	1698	2194	36	30	0.294	36.2	77.1	85.6	82.9	94.8	97.1	120 85.8 120

Table B-43. Model No. 43: 36 Chute, AR = 2.5,  $R_o^o = 0.78$  Outer Suppressor with Abrupt Step Over  $A_o/A_i = 0.65$ ,  $R_i^i = 0.674$  Inner Plug, Retracted.

$A_o = 11.12 \text{ in.}^2$  Linear Scale Factor to 338 in. $^2 = 5.50$  (Outer Only)

Data Point No.	Outer		Free Stream	Meteorological Conditions		Normalization Parameters		2400-ft S.L. Data					
	$(P_T/P_o)^o$	$T_{to}^o$ ( $^{\circ}\text{R}$ )	$V_o$ (ft/sec)	$T_{py}$ ( $^{\circ}\text{F}$ )	$T_{het}$ ( $^{\circ}\text{F}$ )	$10 \log_{10} V/a_o$	$10 \log_{10} P_c (T_o/T_c)^{u-1}$	OASPL 50° PNL	OASPL 90° PNL	PNL	$\theta$	POASPL	$\theta$
A25030	1.716	816	1185	76	61	0.026	37.7	62.0	69.6	70.0	79.0	81.7	120
A25040	1.930	910	1384	76	61	0.094	37.9	65.0	72.9	73.0	82.3	85.9	120
A25060	2.442	1192	1800	76	61	0.208	37.7	70.3	78.8	78.1	87.4	92.4	120
A25070	2.702	1328	1993	76	61	0.252	37.8	72.5	81.4	80.0	89.5	94.8	120
A25080	3.258	1620	2376	76	61	0.323	38.3	76.3	85.7	83.6	92.9	98.5	120
A25100	3.542	1769	2559	77	61	0.360	38.5	78.0	87.2	85.4	94.4	99.8	120
A25110	1.933	1533	1786	76	61	0.204	34.7	68.5	76.7	77.0	86.6	91.4	120
A25120	2.537	1678	2184	77	61	0.292	36.3	72.9	81.3	81.2	90.7	96.2	120
A25030	1.899	834	1187	38	33	0.027	37.6	64.4	71.9	70.4	80.1	80.9	120
A25040	1.931	945	1396	38	33	0.097	37.8	68.3	76.7	73.6	83.6	85.4	120
A25060	2.416	1195	1793	38	33	0.206	37.6	72.6	82.6	78.8	89.3	92.2	120
A25070	2.700	1348	2008	38	33	0.255	37.8	74.6	84.7	81.0	91.4	94.8	120
A25080	3.240	1641	2387	38	33	0.330	38.2	78.3	88.5	84.3	94.4	97.0	120
A25100	3.518	1801	2576	38	33	0.363	38.3	80.0	90.6	86.0	96.0	99.5	120
A25110	1.932	1537	1788	48	34	0.205	34.7	71.1	79.8	77.2	87.0	90.3	120
A25120	2.529	1701	2196	48	33	0.294	36.2	75.1	84.6	81.7	92.4	95.9	120
C25030	1.723	812	1200	40	33	0.032	37.6	69.9	76.5	72.3	82.1	82.3	120
C25040	1.928	945	1394	48	36	0.097	37.8	71.0	78.9	75.2	85.6	86.5	120
C25060	2.426	1204	1803	48	36	0.208	37.6	75.0	83.5	80.8	90.8	92.6	120
C25070	2.692	1344	2003	42	36	0.254	37.8	81.8	87.9	80.8	92.4	95.8	120
C25090	3.242	1645	2390	42	34	0.331	38.2	80.4	89.6	84.8	96.5	99.4	120
C25100	1.528	1811	2586	47	34	0.365	38.3	79.7	89.8	85.7	96.8	99.9	120
C25110	1.925	1555	1794	48	34	0.206	34.6	74.1	82.3	77.7	89.0	91.7	120
C25120	2.529	1704	2198	47	34	0.294	36.2	76.7	85.2	81.8	93.2	96.2	120



Table B-45. Model No. 45: 104 Elliptical Hole, AR = 2.8.

$A_2 = 13.03$  in. Linear Scale Factor to 118 in.  $\lambda = 3.06$

Data Point No.	Invert $(\frac{V}{V_0})_L$	$V_L$ (ft/sec)	Free Stream $V_\infty$ (ft/sec)	Meteorological Conditions		Normalization Parameters			2400-ft S.L. Data						
				$T_{air}$ (°F)	$T_{wet}$ (°F)	$\frac{10 \log 10}{V/\phi}$	$\frac{10 \log 10}{F_0(T_0/T_{ref})^{0.1}}$	50°		90°					
								OASPL	PWL	OASPL	PWL	PPHL	$\theta$	POASPL	$\theta$
A27090	3.239	1617	2389	70.0	58.0	0.331	38.2	78.6	82.6	84.3	90.6	97.9	140	95.5	140
A27110	1.944	1535	1794	0	0	0.206	34.7	68.1	72.3	75.4	84.6	88.1	110	80.6	140
A27120	3.162	1649	2202	70.0	58.0	0.295	36.3	74.9	78.7	81.1	88.9	92.7	130	89.8	140
A27130	0.073	641	1845	71.0	58.0	0.189	43.6	75.3	82.2	79.2	87.2	89.3	110	85.5	140
A27140	1.433	752	1815	71.0	58.0	0.167	42.2	72.1	78.3	77.6	85.9	88.3	120	83.7	140
A27150	2.411	983	1624	71.0	58.0	0.162	38.7	67.8	73.0	75.0	84.2	86.9	120	80.5	140
A27160	1.939	1222	1624	71.0	58.0	0.163	36.4	66.2	71.1	73.7	83.1	86.3	120	78.5	140
A27170	1.738	1462	1609	71.0	58.0	0.159	34.7	65.4	69.8	72.7	82.0	85.2	120	76.5	120
A27180	1.470	1665	1657	71.0	58.0	0.172	33.6	65.7	69.6	73.0	82.3	85.7	110	77.1	140
A27200	1.759	1664	1734	71.0	58.0	0.192	33.7	66.9	71.2	74.0	83.5	86.8	110	78.7	140
A27210	1.171	1205	799	70.0	58.0	-0.145	35.3	50.7	53.0	58.6	67.9	70.1	110	61.1	110
A27240	1.359	1254	1126	70.0	58.0	0.004	35.6	57.1	60.3	65.5	74.9	77.7	110	68.3	110
A27270	1.482	1273	1287	70.0	58.0	0.062	35.6	59.9	62.9	67.7	76.8	80.1	110	71.1	120
A27280	1.586	1309	1396	70.0	58.0	0.098	35.4	61.8	64.8	69.0	77.8	81.1	110	72.8	120
A27290	1.619	1415	1640	70.0	58.0	0.167	35.1	65.9	69.2	72.8	81.4	84.7	110	77.5	140
A27300	2.270	1685	2098	70.0	58.0	0.268	35.4	72.7	76.3	79.0	86.9	90.6	110	87.0	140
A27090	1.792	1627	2390	63.0	47.0	0.331	38.3	78.8	84.9	81.9	90.1	95.1	140	91.4	140
A27110	1.950	1543	1802	63.0	47.0	0.208	34.7	69.7	76.2	73.7	84.6	87.6	120	77.4	120
A27120	1.558	1687	2198	63.0	47.0	0.295	36.3	74.9	82.2	78.6	88.1	92.0	120	86.2	140
A27130	0.167	672	1645	60.0	45.5	0.169	43.8	75.3	84.1	77.1	86.2	88.6	120	82.2	140
A27140	1.445	739	1624	60.0	45.5	0.164	42.2	72.5	81.6	75.0	84.7	87.5	120	79.4	140
A27150	2.386	1001	1617	60.0	45.5	0.164	38.6	69.3	77.6	72.9	83.7	86.3	120	76.4	120
A27160	1.991	1353	1644	62.0	48.0	0.168	34.3	62.4	75.5	71.4	82.0	85.2	120	75.3	120
A27170	1.758	1496	1642	64.5	48.5	0.168	34.5	66.8	74.9	71.0	81.9	85.5	120	75.0	120
A27180	1.440	1686	1660	66.5	48.5	0.173	33.4	67.1	74.5	71.1	81.8	85.2	120	74.7	120
A27200	1.770	1693	1756	62.0	48.0	0.198	33.6	69.2	74.7	72.0	82.4	85.7	120	75.9	120
A27250	1.168	1199	791	64.5	48.5	0.169	35.3	56.0	60.8	58.6	67.6	69.7	110	60.4	110
A27260	1.257	1249	1121	64.5	48.5	0.002	35.7	55.7	62.4	63.4	74.0	76.6	100	65.4	120
A27270	1.455	1283	1283	64.0	44.5	0.055	35.6	60.3	67.0	66.2	77.2	79.9	110	69.3	120
A27280	1.594	1294	1398	64.0	44.5	0.098	35.5	62.3	69.5	68.0	78.9	82.0	120	71.4	120
A27190	1.525	1404	1637	64.0	46.5	0.167	35.1	67.3	75.5	71.4	82.5	85.8	120	75.1	120
A27200	1.272	1690	2092	63.0	47.0	0.271	35.5	72.8	80.3	76.9	86.6	90.1	120	82.8	140

Table B-46. Model No. 47: 4.0-Inch-Diameter Conical.

 $A_1 = 12.57 \text{ in.}^2$  Linear Scale Factor to 338 in.<sup>2</sup> = 5.17

Data Point No.	Inner		Free Stream	Metacological Conditions		Normalization Parameters		2400-ft S.L. Data					
	$(P_T/P_0)_i$	$T_{Ti}$ (°R)		$V_i$ (ft/sec)	$T_{Dry}$ (°F)	$T_{Wet}$ (°F)	$10 \log_{10} V/a_0$	$10 \log_{10} F_g(T_0/T_{gm})^{0.1}$	OASPL	PNL	90°	PPNL	$\theta$
A29120	2.545	1693		2197	30.0	27.5	0.294	36.3	86.7	93.3	91.7	99.8	130
A29300	2.281	1692		2079	30.0	27.5	0.270	35.4	83.6	89.3	89.6	97.1	130
A29310	2.472	1002		1657	30.0	27.5	0.172	38.8	87.0	93.7	88.3	96.4	130
A29320	3.004	999		1800	30.0	27.5	0.208	40.0	91.5	98.2	93.1	101.1	140
A29330	3.506	1001		1904	30.0	27.5	0.232	41.0	94.5	100.9	96.3	101.9	140
A29340	2.497	1407		1980	30.0	27.5	0.249	37.0	86.1	92.9	90.1	98.3	140
A29350	2.994	1411		2145	30.0	27.5	0.284	38.3	91.3	98.2	94.0	101.8	130
A29360	3.489	1386		2244	30.0	27.5	0.304	39.5	93.9	100.5	96.7	104.5	130
A29370	2.385	1799		2197	30.0	27.5	0.294	35.5	84.8	90.9	90.8	98.4	130
A29380	3.135	1692		2395	30.0	27.5	0.332	37.8	91.8	98.7	95.5	103.6	130
A29390	3.432	1707		2486	30.0	27.5	0.348	38.4	93.4	100.3	96.8	104.9	130
B29120	2.548	1689		2195	30.0	27.5	0.294	36.3	87.5	94.4	90.5	98.9	130
B29300	2.274	1690		2074	30.0	27.5	0.269	35.4	83.4	89.2	88.0	95.7	130
B29310	2.482	1002		1660	31.0	26.5	0.172	38.8	87.8	94.4	88.6	96.2	140
B29320	3.009	994		1797	27.5	25.0	0.207	40.0	93.7	99.6	94.4	104.4	140
B29330	3.496	1005		1906	27.5	25.0	0.233	41.0	95.9	101.7	96.3	103.9	140
B29340	2.484	1460		1971	31.0	26.5	0.247	37.0	87.2	94.2	89.1	97.4	140
B29350	2.985	1400		2134	27.5	25.0	0.282	38.3	93.7	100.2	94.0	101.9	130
B29360	3.478	1400		2253	27.5	25.0	0.305	39.4	96.6	102.4	97.8	105.3	130
B29370	2.395	1803		2203	30.0	27.5	0.295	35.5	85.4	91.8	89.7	97.7	130
B29380	3.141	1690		2396	30.0	27.5	0.332	37.8	95.3	101.8	95.7	103.4	130
B29390	3.444	1712		2492	27.5	25.0	0.349	38.4	96.1	102.4	97.3	104.8	130
C29120	2.544	1696		2199	32.0	28.5	0.295	36.3	87.2	94.5	89.9	99.0	130
C29300	2.279	1683		2071	32.0	28.5	0.269	35.4	82.9	89.5	87.1	95.6	130
C29310	2.500	1000		1664	32.0	26.5	0.174	38.8	88.7	95.7	88.3	96.4	130
C29320	3.002	999		1799	30.0	27.0	0.207	40.0	94.6	101.4	93.5	101.9	70
C29330	3.459	998		1892	30.0	27.0	0.229	40.9	97.4	103.4	96.6	104.6	80
C29340	2.492	1402		1975	32.0	26.5	0.248	37.0	87.3	94.8	88.7	97.8	130
C29350	2.986	1397		2132	31.0	26.5	0.281	38.4	93.6	100.6	94.0	102.7	130
C29360	3.448	1403		2250	30.0	27.0	0.305	39.4	96.8	103.0	96.6	105.1	130
C29370	2.390	1802		2200	32.0	28.5	0.295	35.5	84.9	92.0	88.9	97.7	130
C29380	3.127	1694		2387	32.0	28.5	0.330	37.8	94.1	100.9	95.6	104.1	130
C29390	3.438	1704		2484	30.0	27.0	0.348	38.4	97.0	103.4	97.1	105.8	130

## APPENDIX C

### GENERAL ELECTRIC AIR-ATTENUATION MODEL

The air-attenuation model used for JENOTS data was developed in 1973 by R.G. Fogg of General Electric (Reference 17). Mr. Fogg noticed that a linear extrapolation of the SAE/ARP 866 curves (Reference 13) or the prediction of Harris (Reference 15) tended to distort the spectral shape for frequencies above 20 kHz when the data was scaled or PWL was calculated as seen in Figures C-1 and C-2. He hypothesized that this distortion was the result of applying excessive air attenuation at the high frequencies. From Harris' data, it was clear that the molecular absorption diminished in percent of the total absorption as the frequency increased, leaving the classical absorption as the dominant attenuator. By curve-fitting the trends of the classical and molecular absorption with frequency at various humidities and a temperature such as in Figure C-3, a family of prediction curves as shown in Figure C-4 was developed. For comparison, a similar presentation from Harris (Reference 15) and Evans (Reference 20), is given in Figures C-5 and C-6, respectively.

Table C-1 is a listing of the computer program used to generate the correction factors. With the wet and dry bulb temperatures given in Appendix B, one can calculate the values of the air-attenuation corrections applied to the data presented in this report.

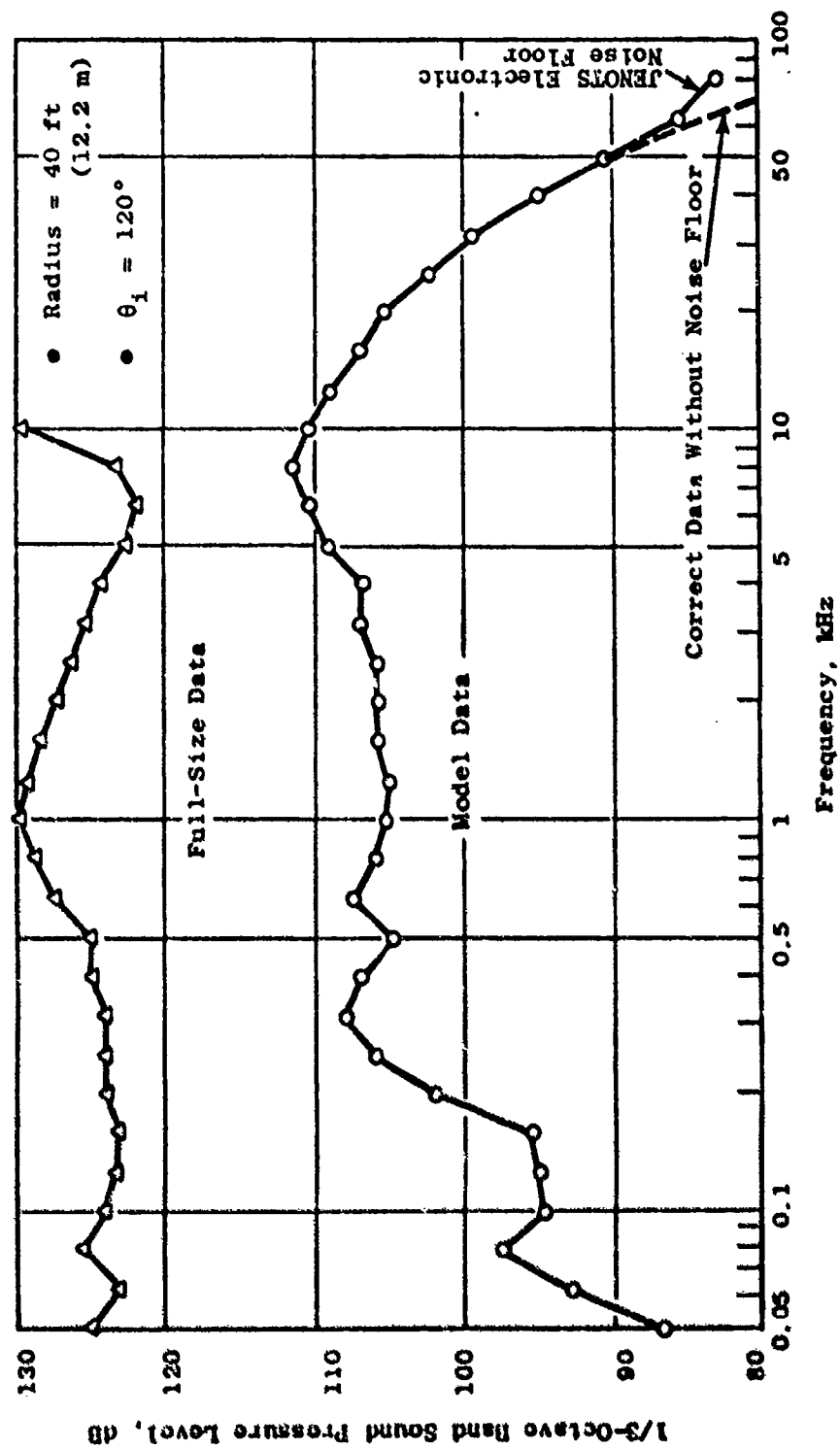


Figure C-1. JENOTS Data: SPL Spectra, FSDR Program Calculation.

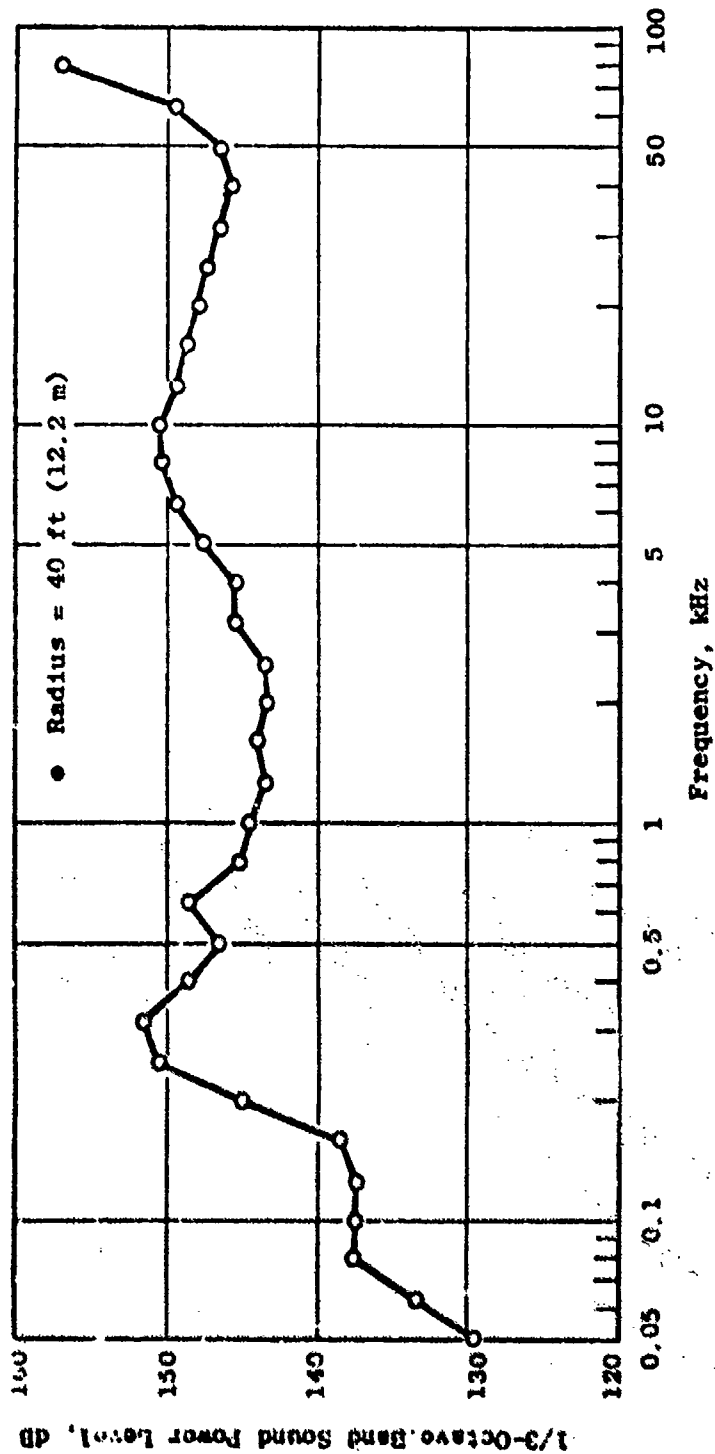


Figure C-2. JENOTS Data: SPL Spectra, FSDR Program Calculation.



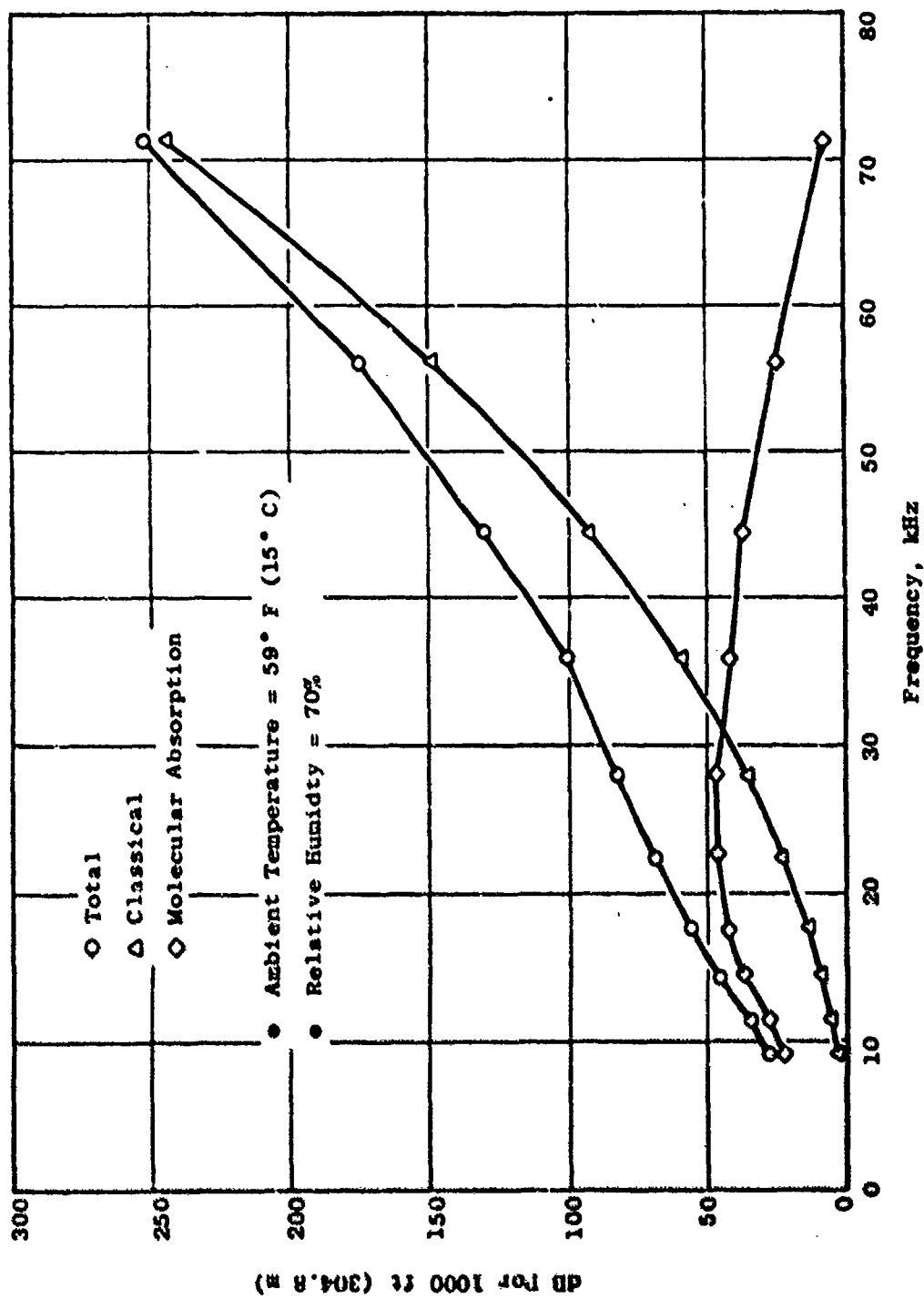


Figure C-3. Revised Atmospheric Correction Factors.

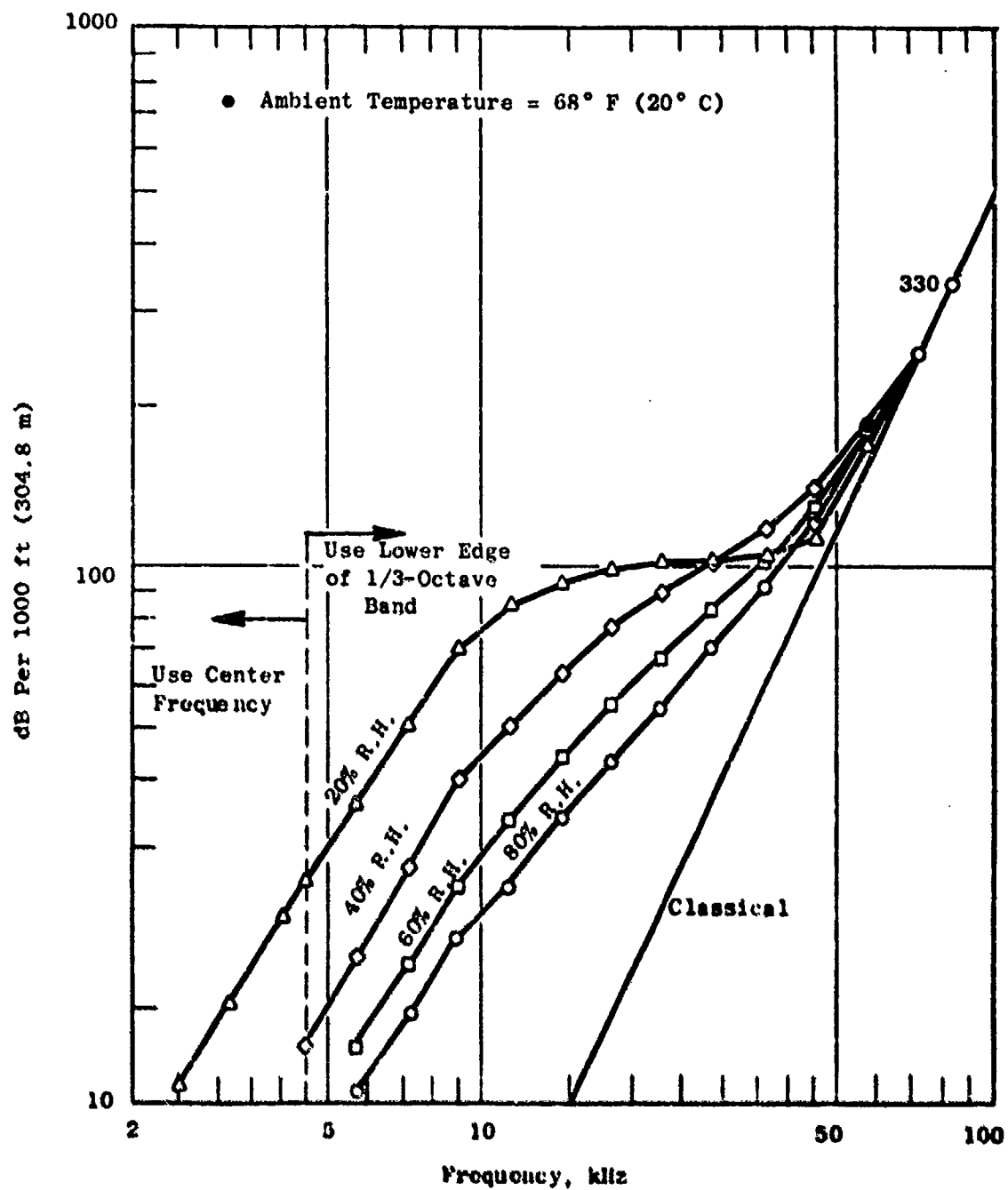


Figure C-4. Revised Atmospheric Absorption.

(Reference Figure 3.2, Page 3-3, "Harris Handbook of Noise")

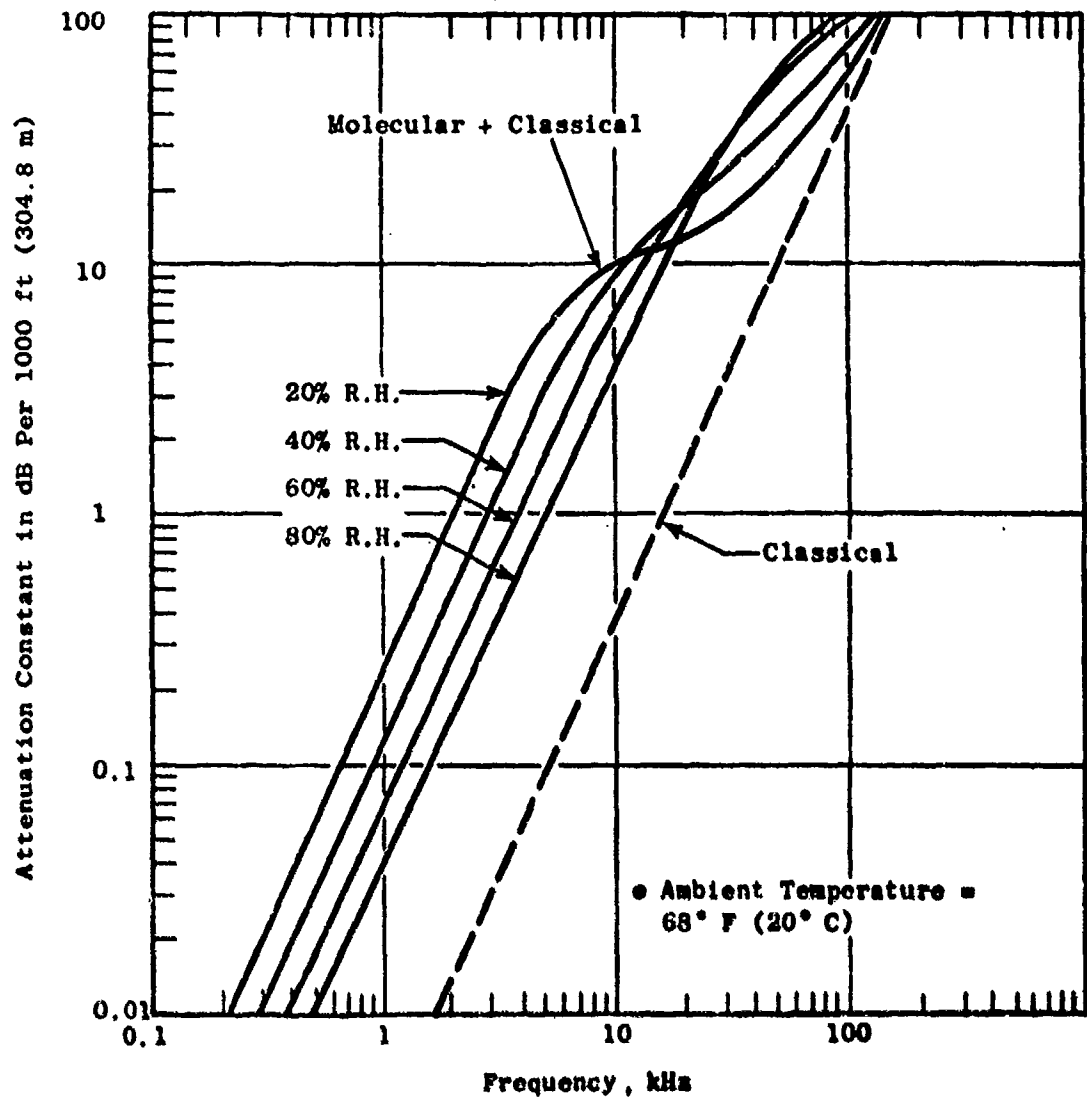


Figure C-5. Atmospheric Attenuation Factors.

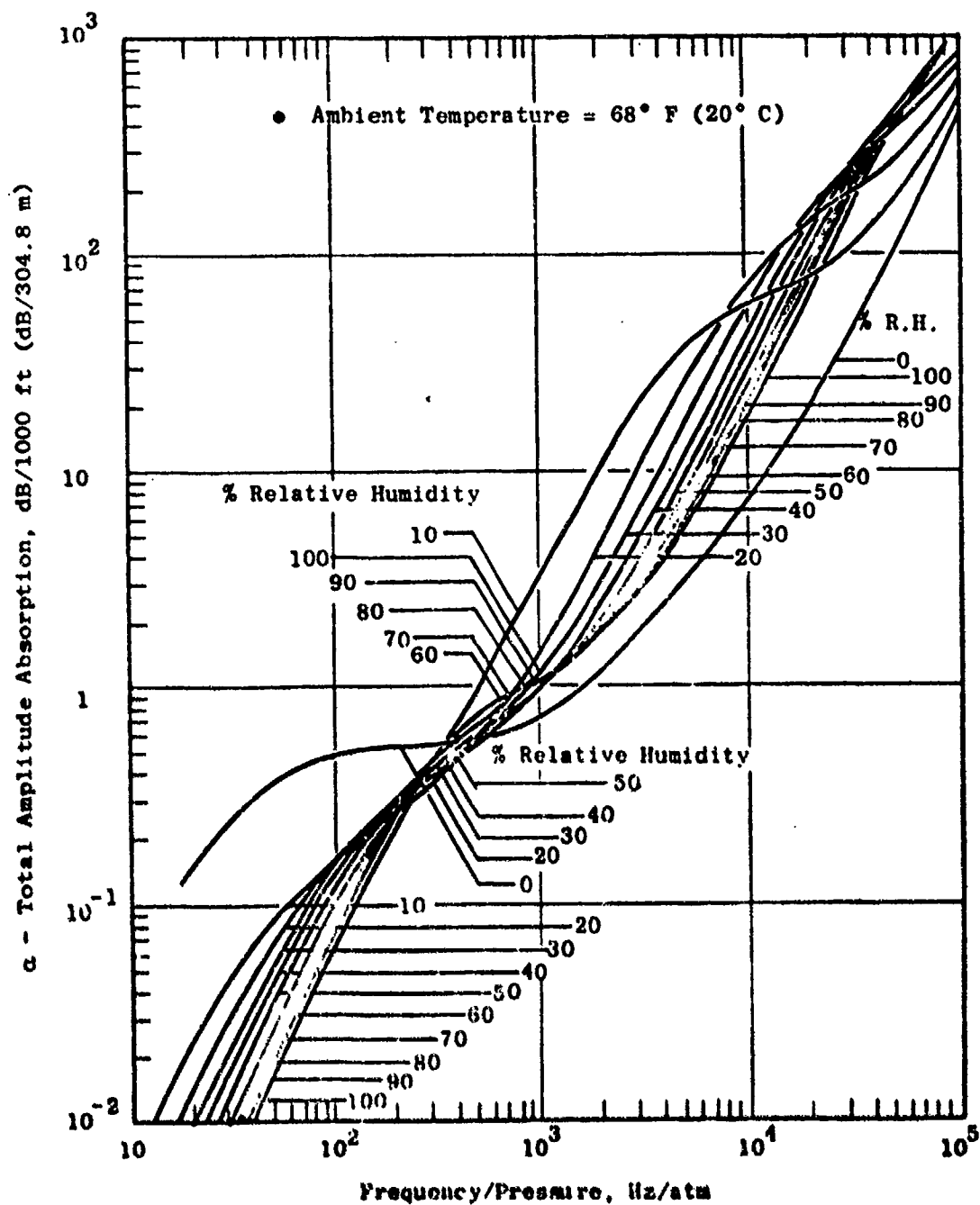


Figure C-6. Total Absorption of Sound in Air as a Function of Frequency.

Table 3-1. Listing of the GE Air-Attenuation Correction Computer Program.

```

10 REM THIS PROGRAM PROVIDES CORRECTION FACTORS AND INCREMENTAL
11 REM SPHERICAL AREAS FOR THE FAP FIELD CALCULATIONS. SEE TIME
12 REM SHARE PROGRAM "FARFLD". INPUT AMBIENT ATMOSPHERIC
13 REM CONDITIONS AND ARC RADIUS AT LINE 90. INPUT MICROPHONE
14 REM ANGLE LOCATIONS AT LINE 840.
30 DIM C(24),E(24),F(24),G(24),H(24),K(24),M(20),N(20)
31 DIM P(20),S(20),Z(20)
40 FOR I = 1 TO 24
50 READ F(I)
60 DATA 500,630,800,1000,1250,1600,2000,2500,3150,4000,
70 DATA 5000,6300,8000,10000,12500,16000,20000,25000,
71 DATA 31500,40000,50000,63000,80000,100000
72 NEXT I
75 REM "T1" IS WET BULB TEMPERATURE IN DEGREES F. "T3" IS
76 REM ATMOSPHERIC TEMPERATURE IN DEGREES F. "P1" IS ATMOSPHERIC
77 REM PRESSURE IN INCHES OF HG. "R2" IS SPHERICAL RADIUS IN FT.
80 READ T1,T3,P1,R2
90 DATA 33,40,29.921,1000
95 REM THE FOLLOWING CALCULATIONS ARE FOR ABSOLUTE HUMIDITY.
100 LET T2 = ((5/9)*(T1 - 32)) + 273.16
110 LET X1 = 647.27 - T2
111 READ L6,L7,B8,L9
112 DATA 3.2437814,5.86826E-3,1.1702379E-8
113 DATA 0.89
120 LET A5 = L6 + L7*X1 + L8*X1^3
130 LET A1 = 1 + 2.187846E-3*X1
140 LET A2 = (X1/T2)*(A5/A1)
141 READ C6,C7
142 DATA 218.167,14.6959
150 LET P = (C6/10*(A2)*C7
160 LET A3 = ((P1*0.49115)-P)*(T3 - T1)
170 LET P2 = P - ((A3)/(2755 - 1.28*T1))
171 READ C8,C9,C5,D6
172 DATA 144,460,85.7,16.02E3
180 LET A4 = ((P2*C8)/((T3 + C9)*C5))*D6
181 PRINT "AMBIENT TEMPERATURE =";T3;"DEGREES F"
182 PRINT "WET BULB TEMPERATURE =";T1;"DEGREES F"
183 PRINT "BAROMETRIC PRESSURE =";P1;"INCHES OF HG"
184 PRINT
185 PRINT "ABSOLUTE HUMIDITY (HA) =";A4;"GRAMS PER CUBIC METER"
187 LET D1 = P1/29.921
188 LET D2 = (T3 + 460)/519

```

Table C-1. Listing of the GE Air-Attenuation Correction Computer Program (Continued).

```

189 LET D3 = (SQR(D2))/D1
190 PRINT " IMPEDENCE CORRECTED TO STD. DAY =" ; D3*2.227525E-6
191 PRINT
192 PRINT
193 REM THE FOLLOWING CALCULATIONS ARE FOR ALPHA MOL MAX
200 REM H MOL MAX
205 READ F1,F2,F3,F4,F5,F6
210 FOR I = 1 TO 24
220 IF F(I) > 4000 THEN 227
225 LET A6 = F(I)
226 GO TO 230
227 LET A6 = B9*F(I)
230 LET H(I) = 0.028961*A6+0.51093
235 IF F(I) > 4000 THEN 250
240 LET A6 = F(I)
245 GO TO 260
250 LET A6 = B9*F(I)
260 LET C(I) = A6+0.00357451*EXP(0.0117537*T3)
261 IF A6 < 8900 THEN 266
263 DATA .15023777E02,.83707731E-02,.36541712E-06,.56857640E-11
264 DATA -0.31243498E-16,.0117537
265 LET C(I) = (F1+F2+A6+F3*A6+2+F4*A6+3+F5*A6+4)*EXP(F6*(T3-59))
266 IF F(I) > 4000 THEN 269
267 LET A6 = F(I)
268 GO TO 270
269 LET A6 = B9*F(I)
270 LET Y4 = 0.279129E-7*A6+2.05403
280 LET Y5 = 0.261933E-7*A6+2.05081
290 LET K(I) = Y5 + (Y4 - Y5)*(T3 - 32)/68
300 REM THE FOLLOWING CALCULATIONS ARE FOR ALPHA MOL OVER
301 REM ALPHA MOL MAX
305 LET A7 = A4/H(I)
310 IF A7 > 6.5 THEN 440
320 IF A7 < 1.0 THEN 380
330 LET Y1 = (0.16955546E-2*A7) - 0.35055924E-1
340 LET Y2 = (Y1*A7) + 0.20070773
350 LET Y3 = (Y2*A7) - 0.10581673E1
360 LET Z(I) = (Y3*A7) + 0.18009020E1
370 GO TO 450
380 LET Y1 = (0.74335316E1*A7) - 0.171860E2
390 LET Y2 = (Y1*A7) + 0.11814166E2
400 LET Y3 = (Y2*A7) - 0.23792759E1

```

Table C-1. Listing of the GE Air-Attenuation Correction Computer Program (Continued).

```

410 LET Y4 = (Y3*A7) + 0.13220157E1
420 LET Z(1) = (Y4*A7) + 0.5230581E-3
430 GP TO 450
440 LET Z(1) = 0.2
450 LET Z(1) = 0.001*INT(1000*Z(1) + 0.5)
460 LET E(1) = Z(1)*C(1)
470 REM THE FOLLOWING CALCULATIONS ARE FOR THE EGA CORRECTION
480 LET R1 = R2
510 LET C1 = (0.20411435E-20*R1) - 0.66703093E-16
520 LET C2 = (C1*R1) + 0.72854603E-12
530 LET C3 = (C2*R1) - 0.32650913E-8
540 LET C4 = (C3*R1) + 0.49614255E-5
550 LET C5 = (C4*R1) + 0.44663072E-2
560 LET G1 = (C5*R1) + 0.59387702
570 LET E1 = (0.16573369E-24*R1) - 0.46152934E-20
580 LET E2 = (E1*R1) + 0.32361609E-16
590 LET E3 = (E2*R1) + 0.39118972E-13
600 LET E4 = (E3*R1) - 0.10464995E-8
610 LET E5 = (E4*R1) + 0.29126338E-5
620 LET E6 = (E5*R1) - 0.54370996E-3
630 LET G2 = (E6*R1) + 0.59506112
650 IF R1 <= 4000 THEN 680
660 LET G1 = 5.010264
670 LET G2 = 15.44041 + 0.0001*(R1 - 4000)
680 IF F(1) = 63 THEN 720
690 IF F(1) >= 2000 THEN 740
700 LET Z1 = 0.2*((LOG(F(1)/62.5))/LOG(2))
710 GO TO 750
720 LET Z1 = 0
730 GO TO 750
740 LET Z1 = 1.0
750 LET G(1) = (Z1*(G1 - G2)) + G2
760 NEXT I
765 PRINT "CORRECTION FACTORS IN DB AT ARC RADIUS =" ; B2 ;
766 PRINT "FEET"
770 PRINT "FREQUENCY"; TAB(11); "CLASSICAL"; TAB(22);
771 PRINT "MOL.ABSORB."; TAB(36); "TOTAL ABSORB"; TAB(51);
772 PRINT "EGA"; TAB(63); "TOTAL CORR"
790 FOR I = 1 TO 24
802 PRINT F(1); TAB(8); K(1)*R2/1000; TAB(22); E(1)*R2/1000;
801 PRINT TAB(36); (K(1)+E(1))*R2/1000; TAB(51); G(1); TAB(63);
802 PRINT ((K(1)+E(1))*R2/1000)+G(1)

```

Table C-1. Listing of the GE Air-Attenuation Correction Computer Program (Concluded).

```

810 NEXT I
820 REM THE FOLLOWING CALCULATIONS ARE FOR STRIP AREA
821 PRINT
822 PRINT
825 PRINT "ANGLE LOCATION","STRIP AREA FOR";R2;
826 PRINT "FOOT SPHERICAL RADIUS"
827 PRINT "(DEGREES)","SQ. FT.,"
830 REM "M(I)" AND "N(I)" ARE ANGLES WHICH DEFINE THE ARC
831 REM ASSIGNED TO EACH MICROPHONE. "P(I)" IS THE
840 REM MICROPHONE LOCATION ANGLE.
845 READ F1,F2,F3,F4
846 DATA 1.5,3.1416,2,0.0174533
850 READ N
855 DATA 17
860 FOR I = 1 TO N
870 READ P(I)
875 NEXT I
880 DATA 0,10,20,30,40,50,60,70,80,90,100,110
881 DATA 120,130,140,150,160
895 FOR I = 1 TO N
900 LET M(I) = P(I) - (P(I) - P(I-1))/F3
910 LET N(I) = (P(I+1) - P(I))/F3 + P(I)
915 IF I = 1 THEN 917
916 GO TO 920
917 LET M(I) = P(I) - (P(I+1)-P(I))/F3
920 IF M(I) < 0 THEN 940
930 GO TO 950
940 LET M(I) = 0
950 IF N(I) > 180 THEN 970
954 IF I = N THEN 962
958 GO TO 980
960 GO TO 980
962 LET N(I) = P(I) + (P(I) - P(I-1))/F3
966 GO TO 980
970 LET N(I) = 180
980 LET S(I) = F1+F2+R2+F3*(COS(M(I)*F4) - COS(N(I)*F4))
990 PRINT P(I),S(I)
995 NEXT I
1000 END

```



## APPENDIX D

### 1.0 SUMMARY OF THE ELLIPSOIDAL MIRROR DEVELOPMENT

Ellipsoidal mirror (EM) measurements of axial source intensity distributions were made for selected data points during the Task 3 test program.

This appendix describes the ellipsoidal mirror technique as developed for Task 3. Section 1.1 describes the mirror configurations and test set-up. Section 1.2 discusses the mirror calibration. Section 1.3 discusses the data processing procedures and associated numerical techniques. Section 1.4 describes data analysis procedures. Section 2.0 is an evaluation of the ellipsoidal mirror technique and discusses theoretical limitations, data acquisition and data processing errors.

#### 1.1 MIRROR CONFIGURATION AND TEST SETUP

The ellipsoidal mirror is a directional microphone system in which an ellipsoidal dish (mirror) is used to focus acoustic radiation from a specific source region in a jet onto a microphone placed outside the flow. Figure D-1 shows a schematic representation of the system. The EM is mounted on a remotely driven cart on tracks parallel to the jet axis. Surveys of the jet are then accomplished by making continuous traverses along the length of the jet. A microphone is placed at the primary focus of the ellipse, and the secondary focus is placed on the jet centerline (and the mirror axis is fixed normal to the jet axis).

All of the EM source location data reported in References 8 and 12 were obtained with an 18-inch-diameter shallow-dish mirror (Figure D-2). In the Task 3 program, this mirror was used for testing at the JENOTS freejet facility, while a new 34.654-inch-diameter deep-dish mirror (Figure D-3) was used in the jet noise anechoic facility. A summary of physical and operating characteristics of the two systems was shown in Figure 3-17. The new deep-dish mirror was designed to have a larger diameter and increased working distance for improved low frequency performance. In addition, a different microphone orientation is used. With the 18-inch mirror, the microphone is inserted through the rear of the mirror and directed toward the source region. A "reverse mounting" fixture is used on the deep-dish mirror (Figure D-4), so that the microphone can be turned and directed back toward the mirror surface. This change was made to allow better resolution of high frequency data.

The setup of the 18-inch mirror at JENOTS is shown in Figure D-5, and the setup of the deep-dish mirror in the anechoic facility is shown in Figure D-6. Note that the picture in Figure D-6 was taken prior to installation of the reverse mounting fixture in the mirror.

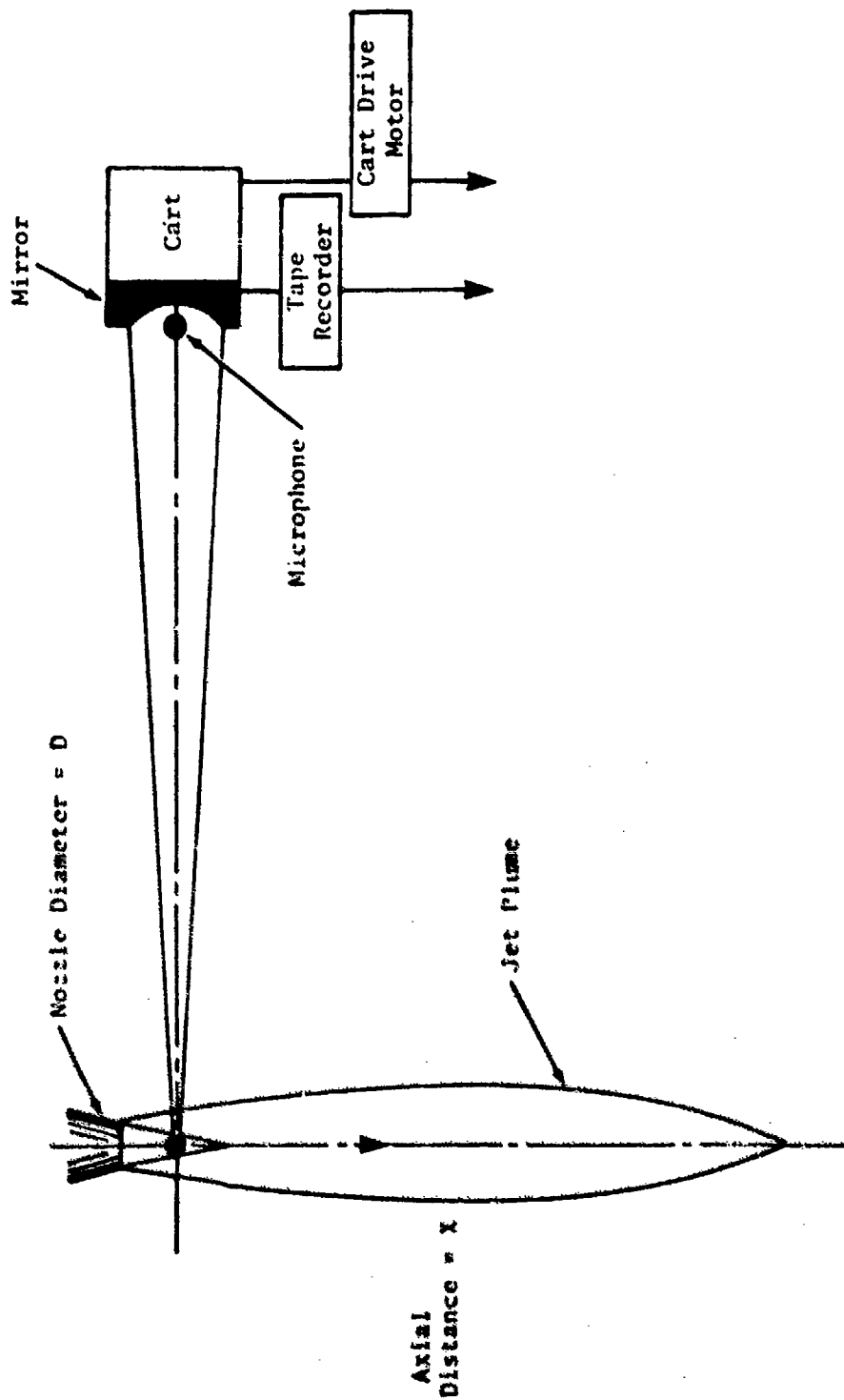


Figure D-1. Test Setup for Ellipsoidal Mirror Surveys.

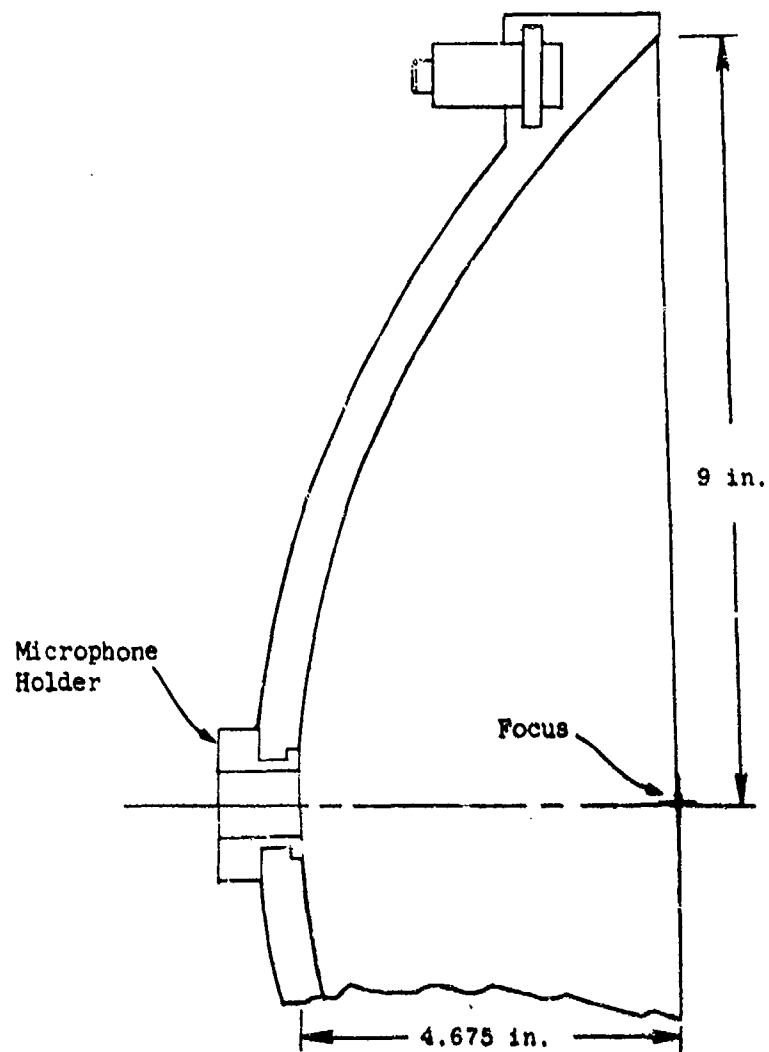
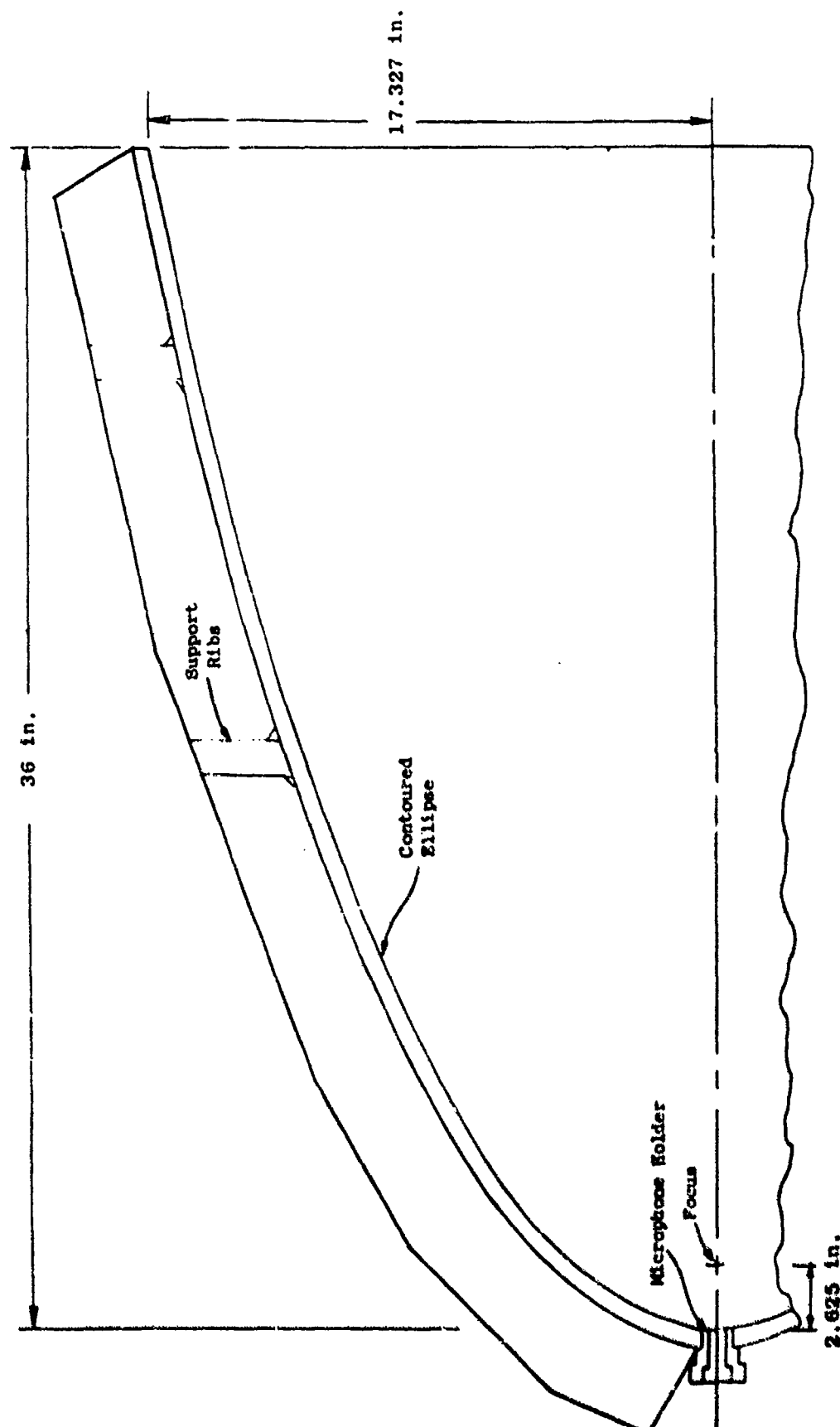


Figure D-2. 18-inch-Diameter Shallow-Dish EM with 9-foot Working Distance.



600

Figure D-3. 34.654-inch-Diameter Deep-Dish EM with 15-foot Working Distance.

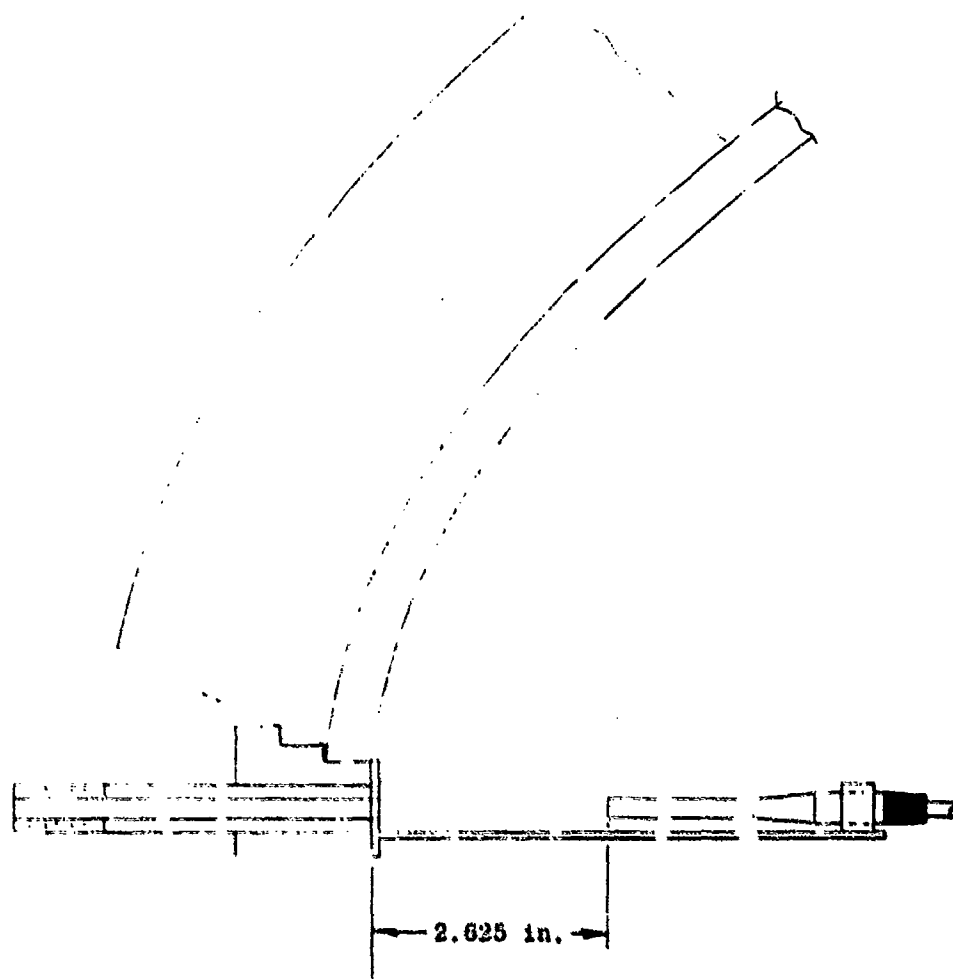


Figure D-4. "Reverse Mounting" Microphone Fixture for Deep-Dish Ellipsoidal Mirror.

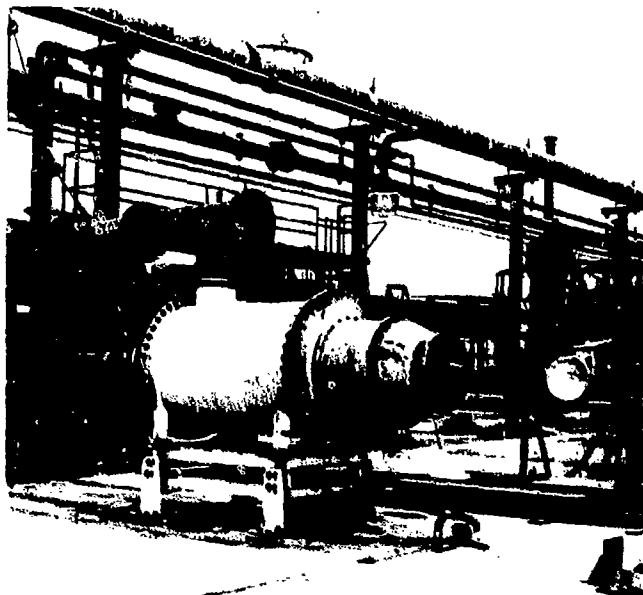


Figure D-5. Ellipsoidal Mirror Set-Up  
at JENOTS.

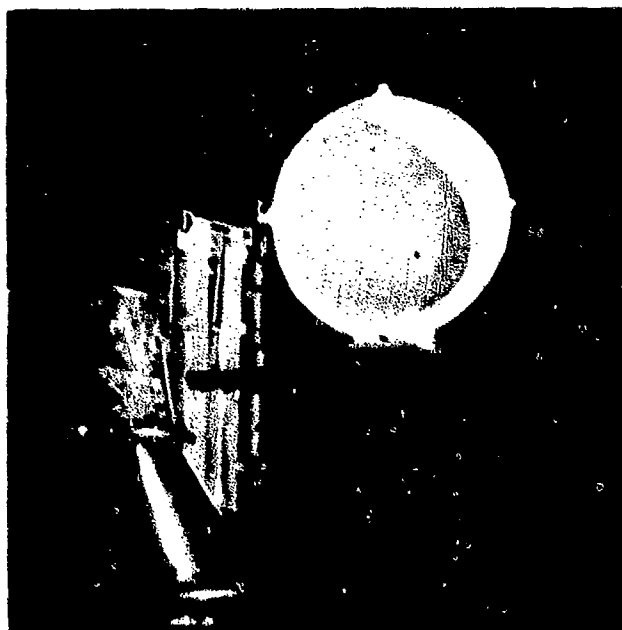


Figure D-6. Ellipsoidal Mirror Set-Up in  
the Anachoic Facility.

For each EM test point, data is recorded on magnetic tape over the full length of an "outbound" traverse. The microphone signal, a DC cart position signal and IRIG B-time code signal are all recorded using the standard acoustic data acquisition system for the particular facility (JENOTS or Anechoic).

## 1.2 MIRROR CALIBRATION

An ellipsoidal shape is used for the mirror surface because of its theoretical ability to resolve a point source of sound onto a microphone. The ellipse has the property that the tangent at any point makes equal angles with the two focal radii to that point. In the limit of high frequencies, with wavelengths very small relative to the mirror dimensions, acoustic radiation can be approximated as straight line rays and sound emanating from a source at one focal point would be reflected to the other focal point by any point on the surface. This focusing effect is characterized by the mirror gain, which theoretically increases with the square of frequency (6 dB/octave).

At lower frequencies, the wave character of sound becomes dominant, and resolution of source distributions by the mirror is limited by diffraction. The "point", which is resolved onto the microphone, spreads into a three-dimensional volume described by the frequency dependent diffraction pattern of the dish. A slice through the three-dimensional diffraction pattern along a plane parallel to the jet axis and normal to the mirror axis yields the window function. This function represents the sensitivity of the system to adjacent sources along the jet axis when the mirror is focused on a given point. The effect of diffraction is thus to smooth details and raise the overall level of measured distributions. The "width" of the window function is theoretically proportional to wavelength (inversely proportional to frequency).

The EM measurement of power spectral density at an arbitrary axial position in a jet can be expressed analytically in terms of a convolution integral:

$$p_m^2(x, f) = G(f) \int_a^{\infty} p_a^2(\xi, f) H(x - \xi, f) d\xi \quad (D-1)$$

where  $p_m^2$  and  $p_a^2$  are, respectively, the measured and actual values of mean square sound pressure,  $G$  is the mirror gain, and  $H$  is the diffraction window function. In order to obtain the true acoustic power distribution for a particular frequency, it is then necessary to solve (deconvolve) the integral equation for the excitation signal at each axial position, given knowledge of the system (mirror) characteristics and the response (measured) signal. Thus, each mirror must be calibrated to determine its gain and window function characteristics.

While the mirror gain is described by a single value for each frequency, the window function is actually a continuous function of distance from the focal point in the focal plane. The window function for a given frequency is mapped by placing a point source at the secondary focus of the mirror and translating it in the focal plane (normal to the mirror axis), or, conversely, by fixing the source and translating the mirror system. The gain is determined by fixing the point source at the secondary focus, and comparing measured levels of the primary focus with and without the mirror present. The algebraic difference (in dB) is the mirror gain.

Equation D-1 is strictly valid for discrete frequencies (1-Hz narrow-band). However, to maintain consistency with farfield acoustic data, it is desirable to analyze source location data in 1/3 octave bands, with the necessary approximations made in the formulation of equation D-1. Thus, a broadband source is required for mirror calibration, so that the window function and gain can be determined on a 1/3 octave band basis.

Both of the ellipsoidal mirrors were calibrated in the anechoic facility. The test setup for calibration of the 18-inch mirror is shown in Figures D-7 and D-8. The mirror was mounted on a remotely driven cart so that it could be traversed past the stationary noise source, a 1/2 inch diameter nozzle operating at sonic pressure ratio. The nozzle was positioned with its axis in the secondary focal plane of the mirror, normal to both the mirror axis and the vertical tracks on which the cart moved (Figure D-7). A reference microphone (for gain calibration) was placed in the same horizontal plane as the source, at the same displacement from the source as the mirror microphone and at 180° to the mirror axis (Figure D-8). The same basic setup was used for calibration of the deep-dish mirror.

Calibration data was obtained for both mirrors over the range 0.4 to 40 kHz. In each case, the mirror and reference microphone signals, the cart position and time code, were recorded over the full length of an "outbound" vertical traverse. The data from this traverse was then played back through the appropriate filters and analyzed to obtain 1/3-octave band gains and window functions. The results are summarized in Figures D-9 through D-12. The gain of the 18-inch mirror (Figure D-9) is seen to follow the theoretical 6 dB/octave increase over a wide range of frequencies. Figure D-10 shows the width of the window functions, defined as the distance between points at 50% of the peak value (3 dB down) on either side, as normalized by the wavelengths corresponding to 1/3 octave band center frequencies. Again, it is seen that the theoretical trend (constant normalized width) is followed over a wide range of frequencies. Calibration results for the deep-dish mirror (Figures D-11 and D-12), while not showing as good agreement with theoretical trends, do indicate higher gain and slightly narrower window functions relative to the 18-inch mirror.

### 1.3 DATA REDUCTION

Ellipsoidal mirror data reduction is accomplished as a two-stage procedure. The first step is a relatively straightforward conversion of raw



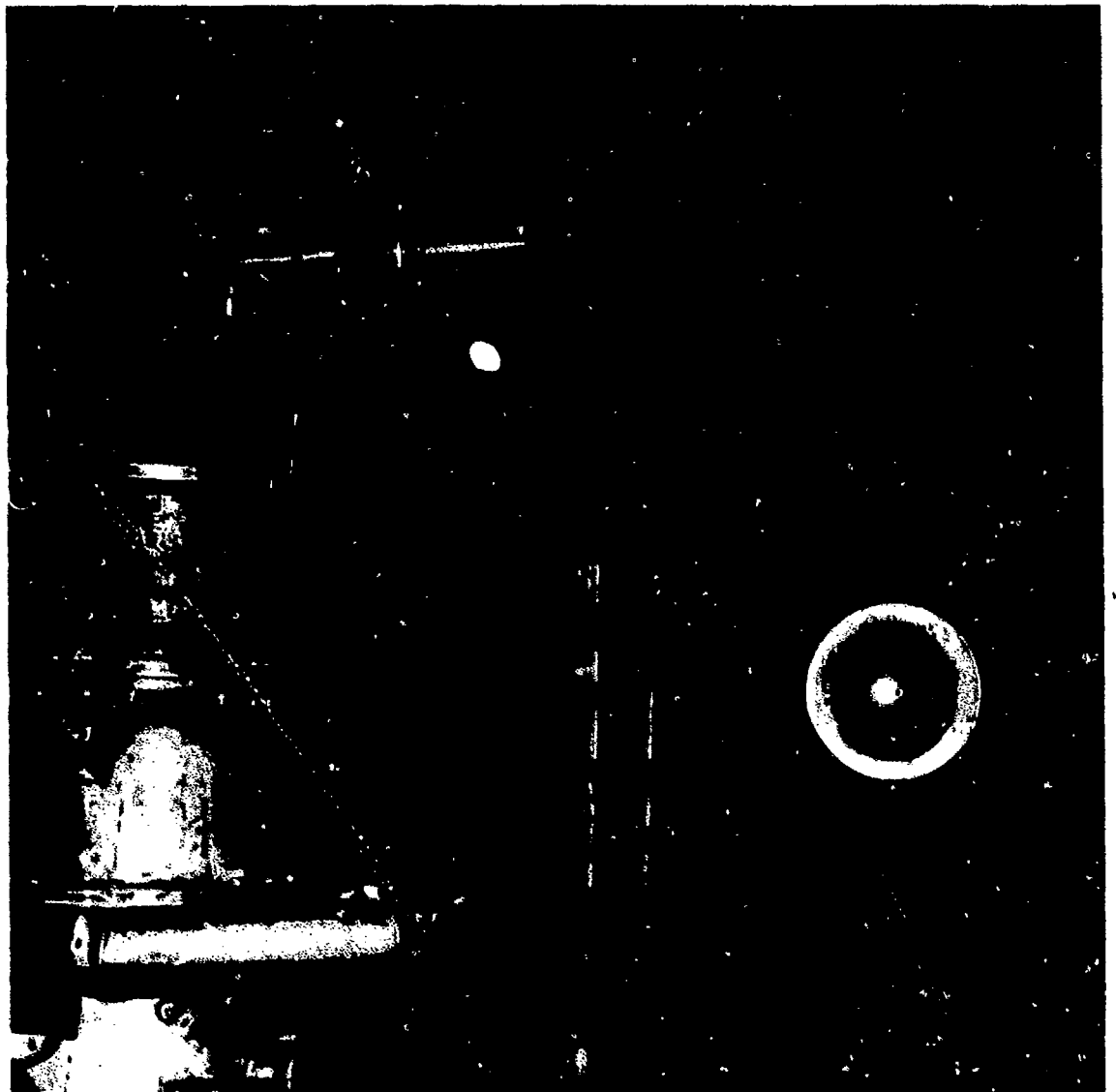


Figure D-7. Set-Up of Mirror and Noise Source for Calibration of 18-inch EM.

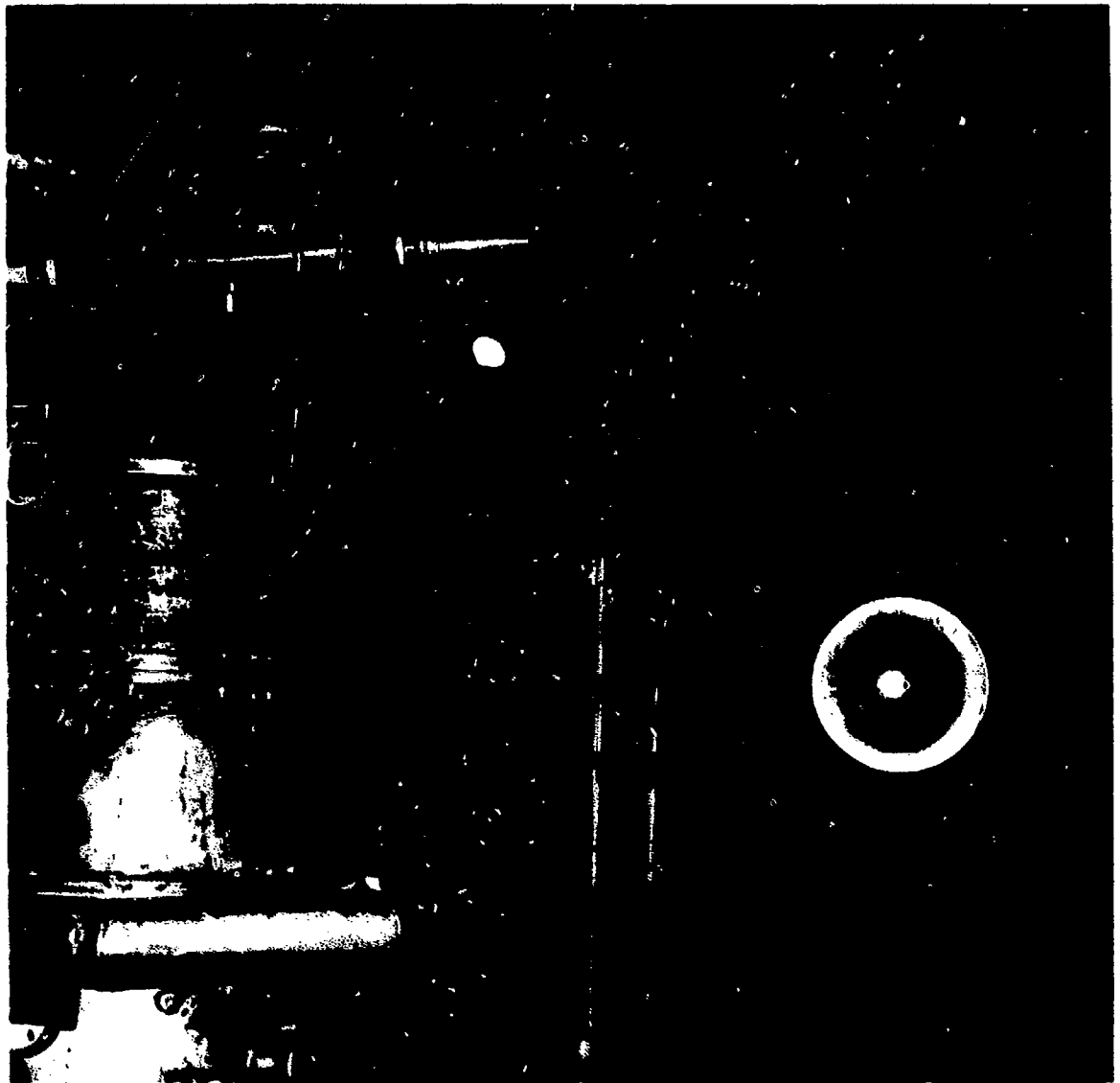


Figure D-7. Set-Up of Mirror and Noise Source for Calibration of 18-inch EM.

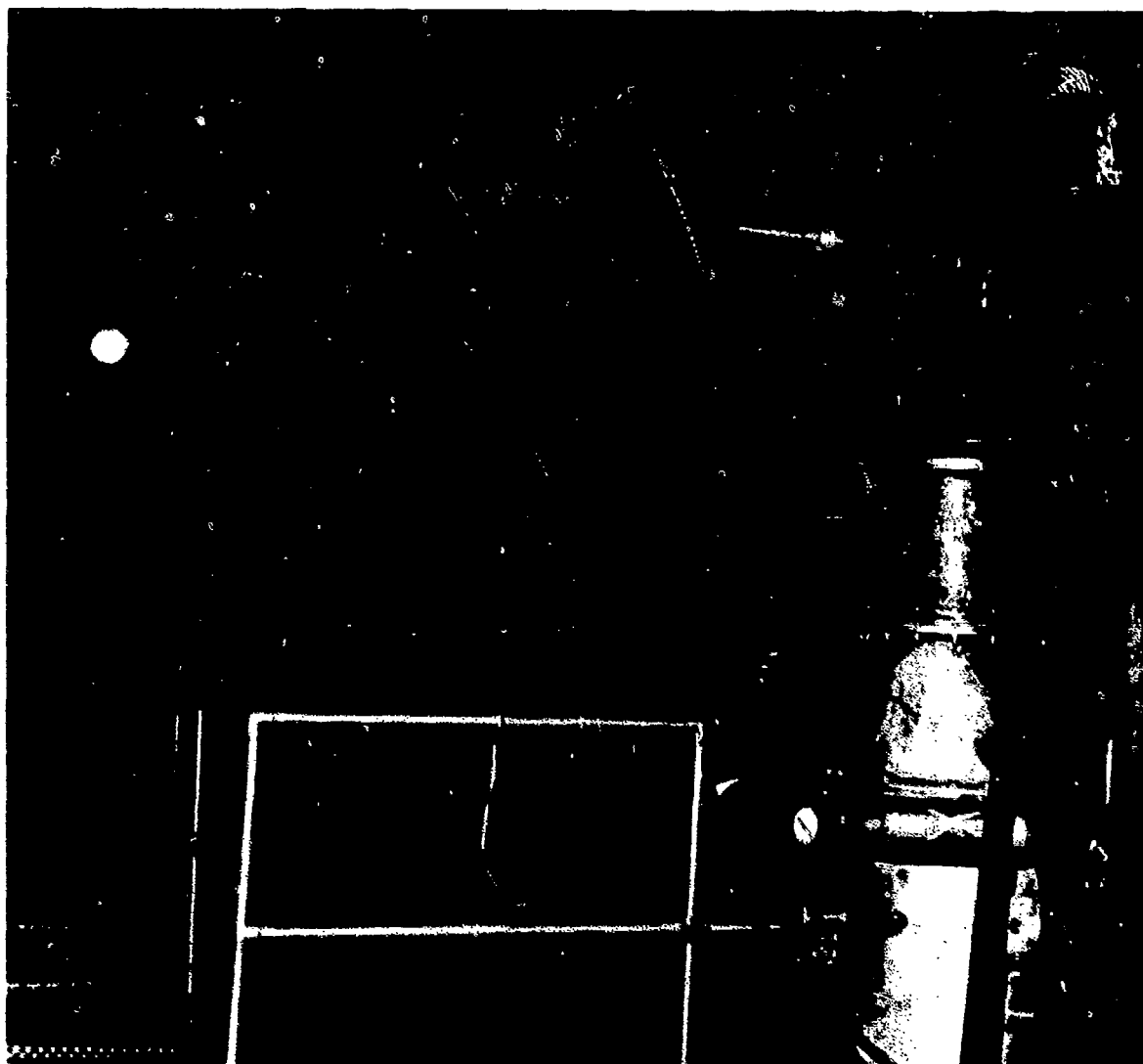


Figure D-8. Set-Up of Reference Microphone and Noise Source  
for Calibration of 18-inch EM.

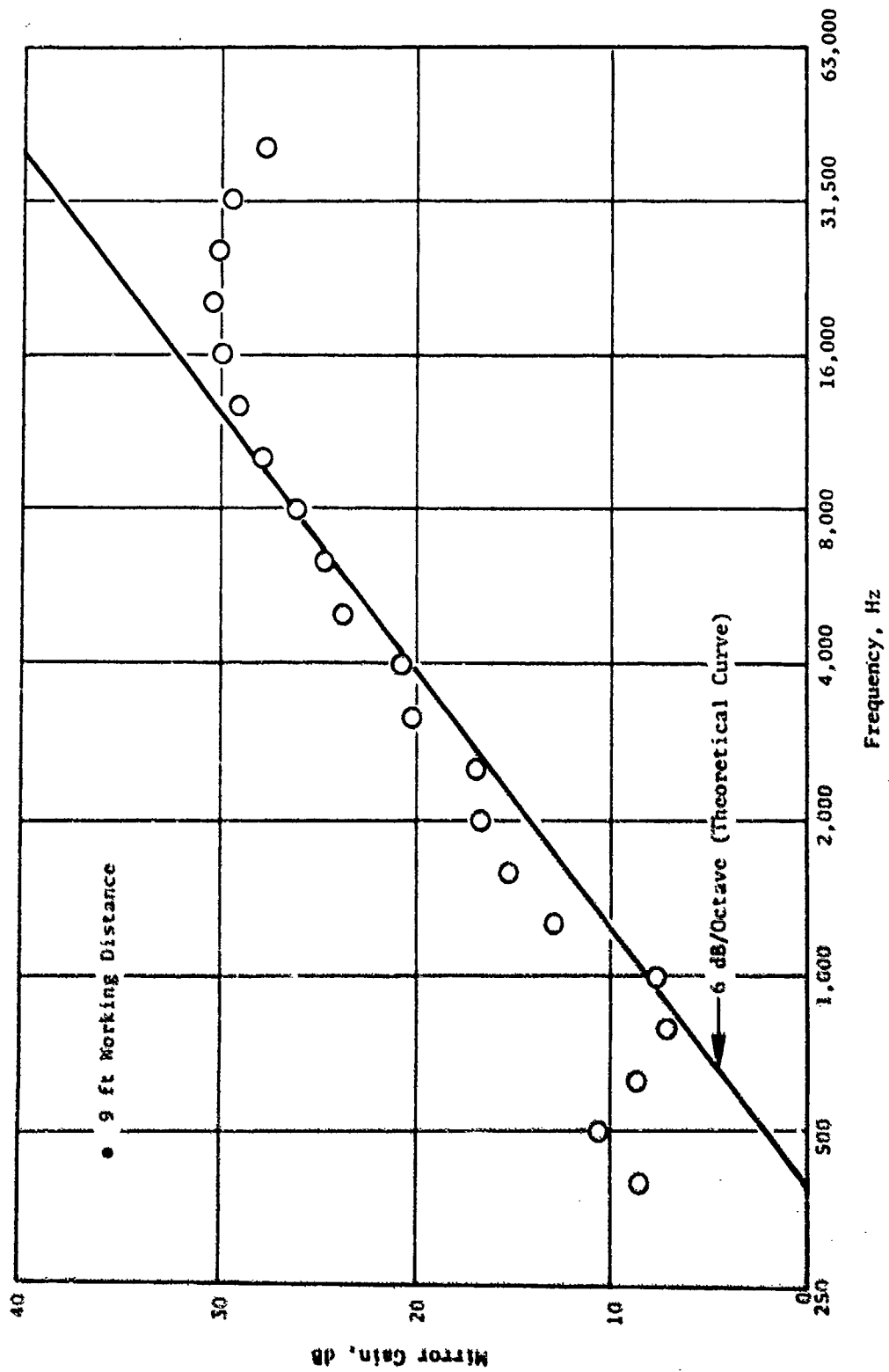


Figure D-9. Gain of the 18-inch-Diameter Ellipsoidal Mirror.

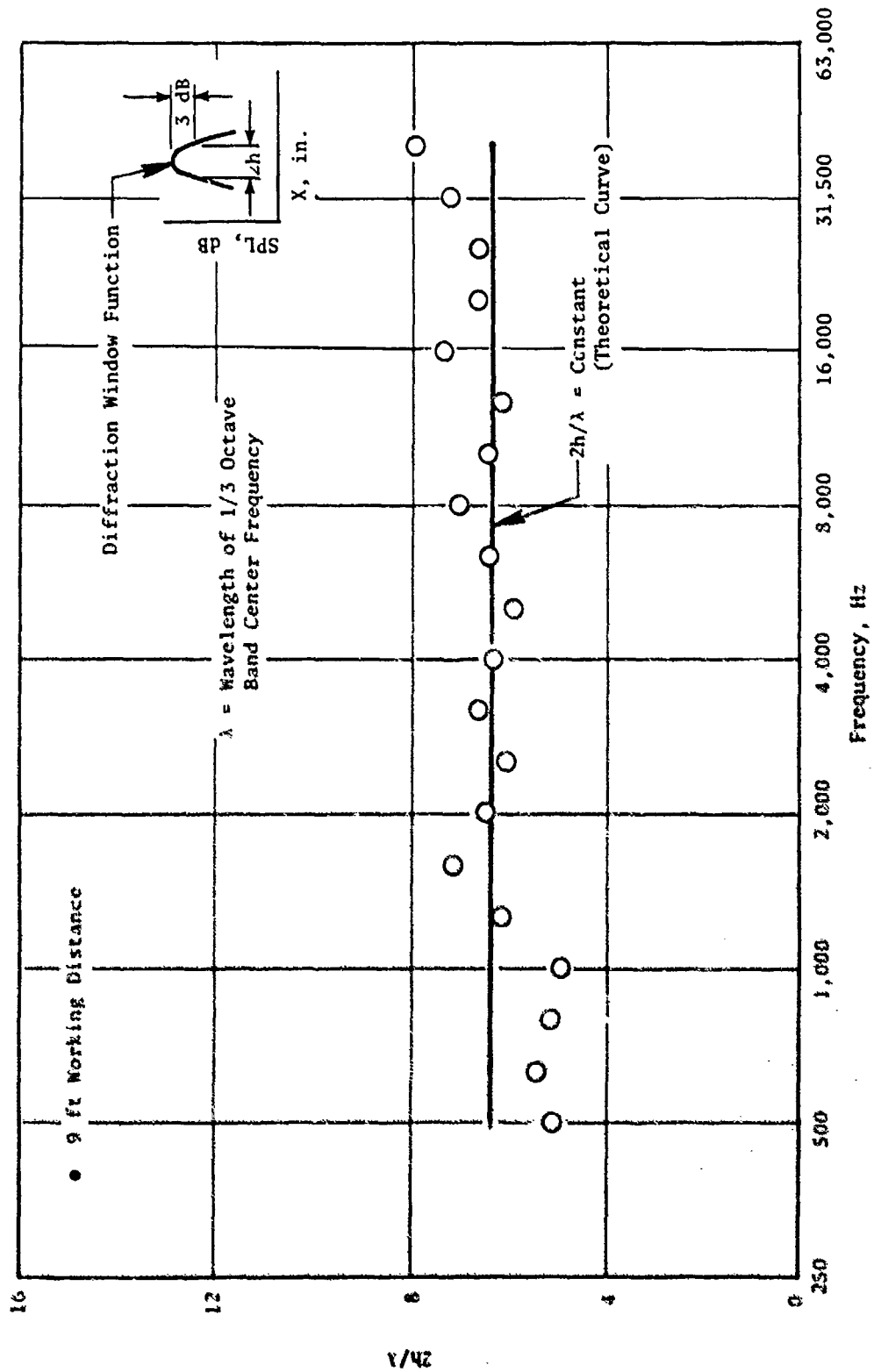


Figure D-10. Normalized Window Function Width for the 18-inch-Diameter Ellipsoidal Mirror.

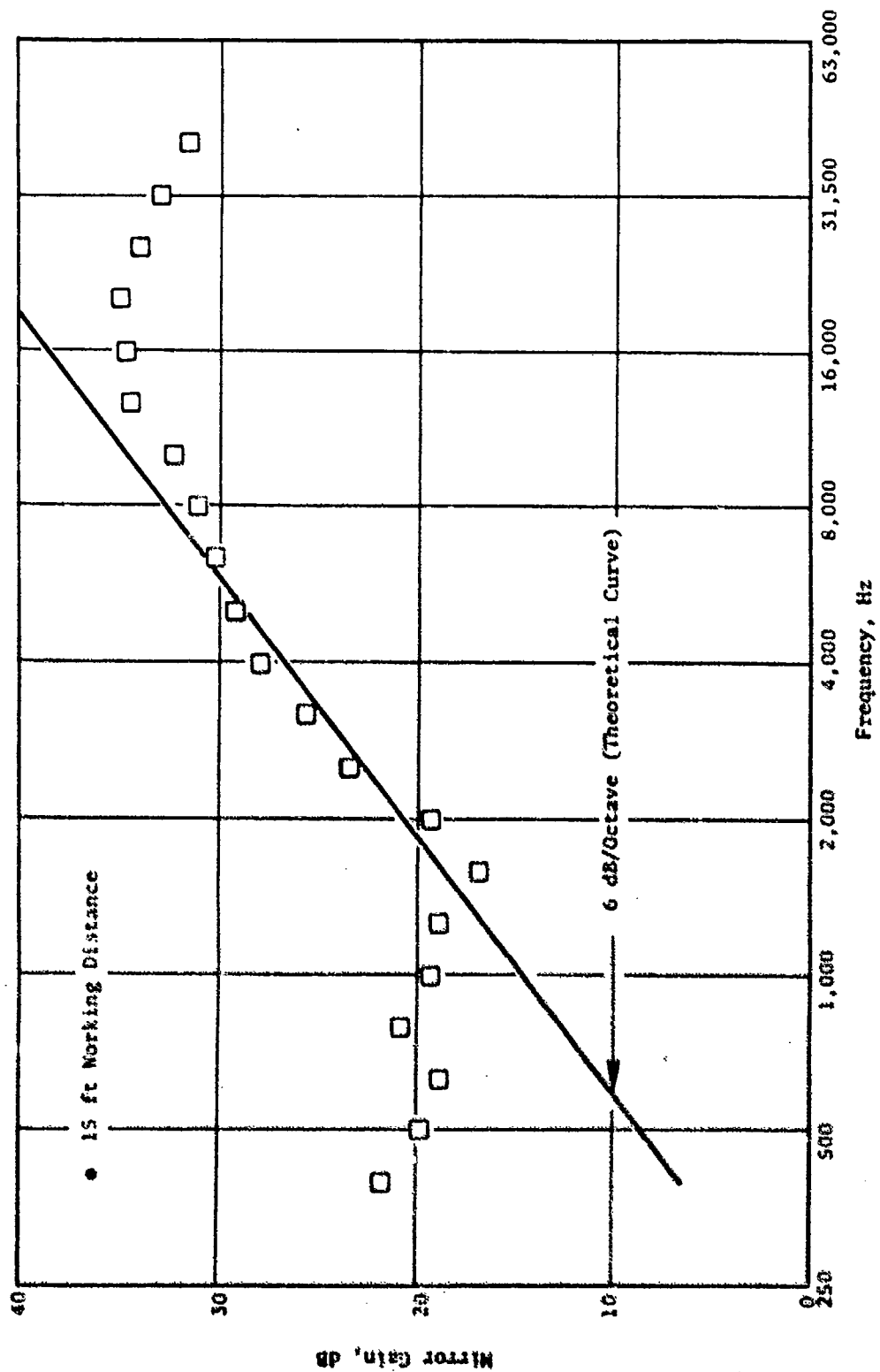


Figure D-11. Gain of the Deep-Dish Ellipsoidal Mirror.

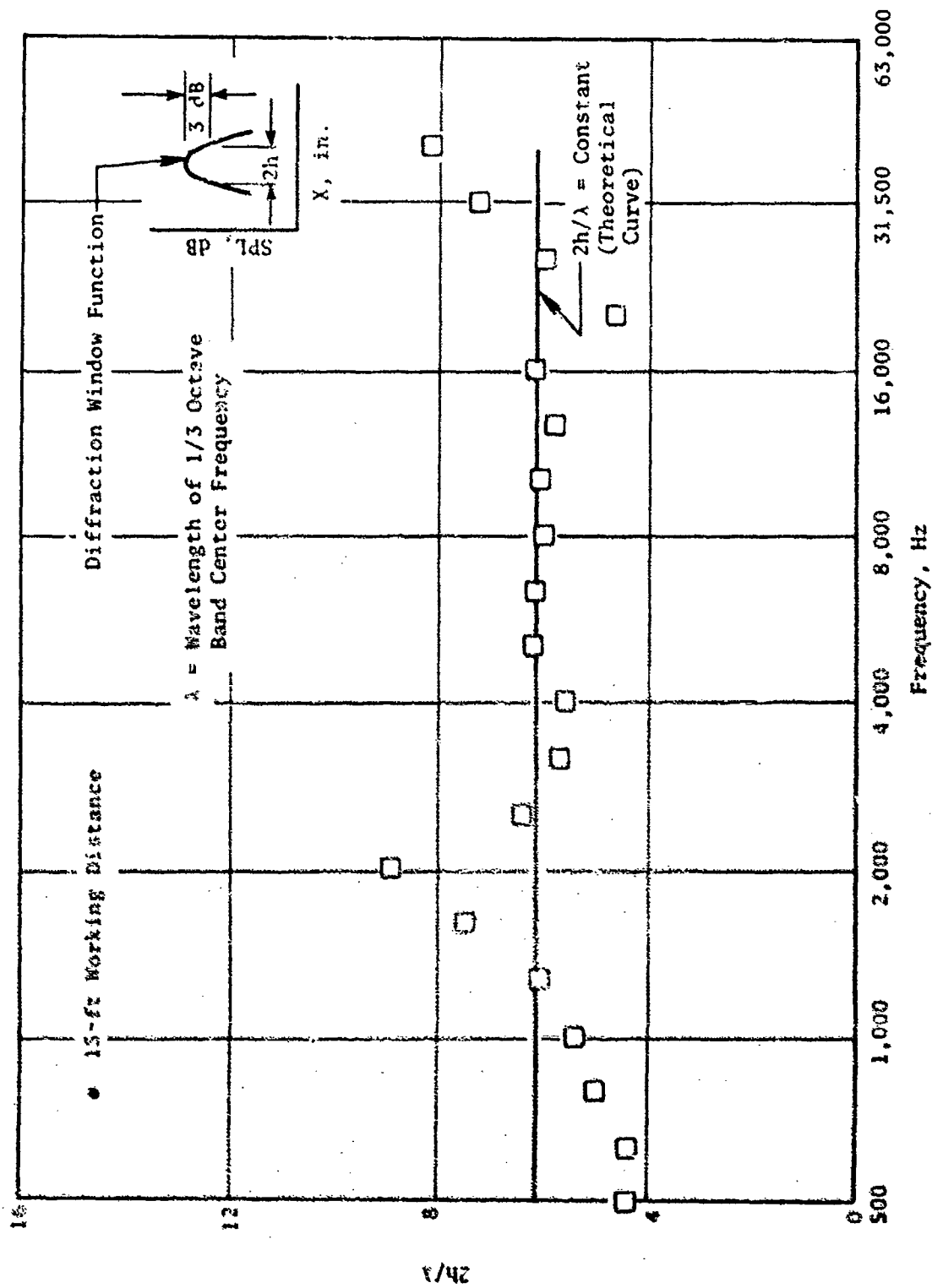


Figure B-12. Normalized Window Function Width for the Deep-Dish Ellipsoidal Mirror.

analog data to digitized spectral distributions. The second step involves numerical processing of these results to correct for the effects of mirror gain and diffraction window function.

### 1.3.1 One-third Octave Band Analysis

The initial stage of EM data reduction utilizes systems and procedures developed for handling of aircraft flyover noise data in the General Electric Acoustic Van (Figure D-13). The previously recorded EM microphone signal is played back through a Honeywell 7600 28-track recorder, set up for IRIG Wideband Group I operation. The playback signal is processed through a General Radio Model 1921 Real Time Analyzer coupled with a GE/PAC 30 mini-computer and a Terment 300 printer/tape punch. Accurate event location is possible through the use of a CGS Datametrics SP-425 Time Code Reader and a CGS Datametrics Time Code Comparator.

The data is resolved into twenty-four 1/3-octave bands and averaged over each of eighty consecutive discrete time stops, then digitized and corrected for nonlinear frequency response and gain or attenuation of the data acquisition system. The length of the time steps (integration time) and the frequency range to be covered can be specified, within certain limits, to suit the requirements of a particular test. Integration time, while remaining constant during processing of an individual data point, can be set for 1/8, 1/4, 1/2, 1, 2, 4, 8, 16 or 32 seconds. A relatively short integration time is required for accurate definition of the details of high frequency source regions near the nozzle exit, especially for suppressor nozzles. However, for lower frequencies, a longer time step is generally necessary in order to allow coverage of the entire source region within eighty steps and to assure reasonable accuracy in resolution of the data (Figure D-14). An additional consideration is that the uncertainty in locating true axial source position increases with increasing integration time since data is averaged over this interval. In order to accommodate both high and low frequency requirements, each data point is processed twice, using two different integration times. The exact values are determined from the desired spacing/coverage and the cart speed. Based on the system characteristics shown in Figure 3-17, integration times of 1 and 4 seconds are used for EM data from JENOTS (18-inch mirror), while 2 and 8-second times are used for data from the anechoic facility (deep-dish mirror). The frequency range for data reduction, while not as flexible as integration time, can be regulated. Data can be resolved with twenty-four 1/3-octave bands over a range of 50Hz-10K Hz, 100Hz-20K Hz or 200Hz - 40K Hz. The range of 200Hz - 40K Hz is used for EM data reduction.

During this stage of data reduction, a three-channel brush chart is also prepared for each data point, showing traces of mirror cart position, overall sound level and time code (Figure D-15). Through use of the time code, an average cart position can thus be determined for each of the digitized spectra.



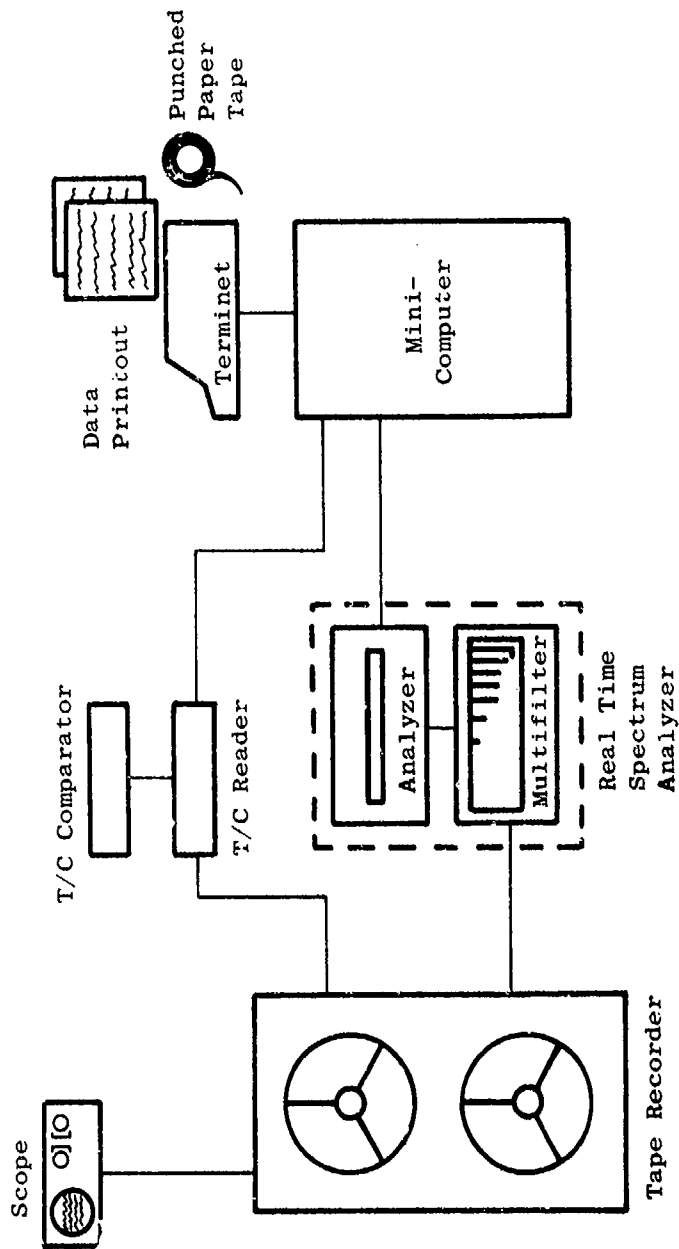


Figure D-13. Equipment Schematic for EM Data Processing - General Electric Acoustic Van.

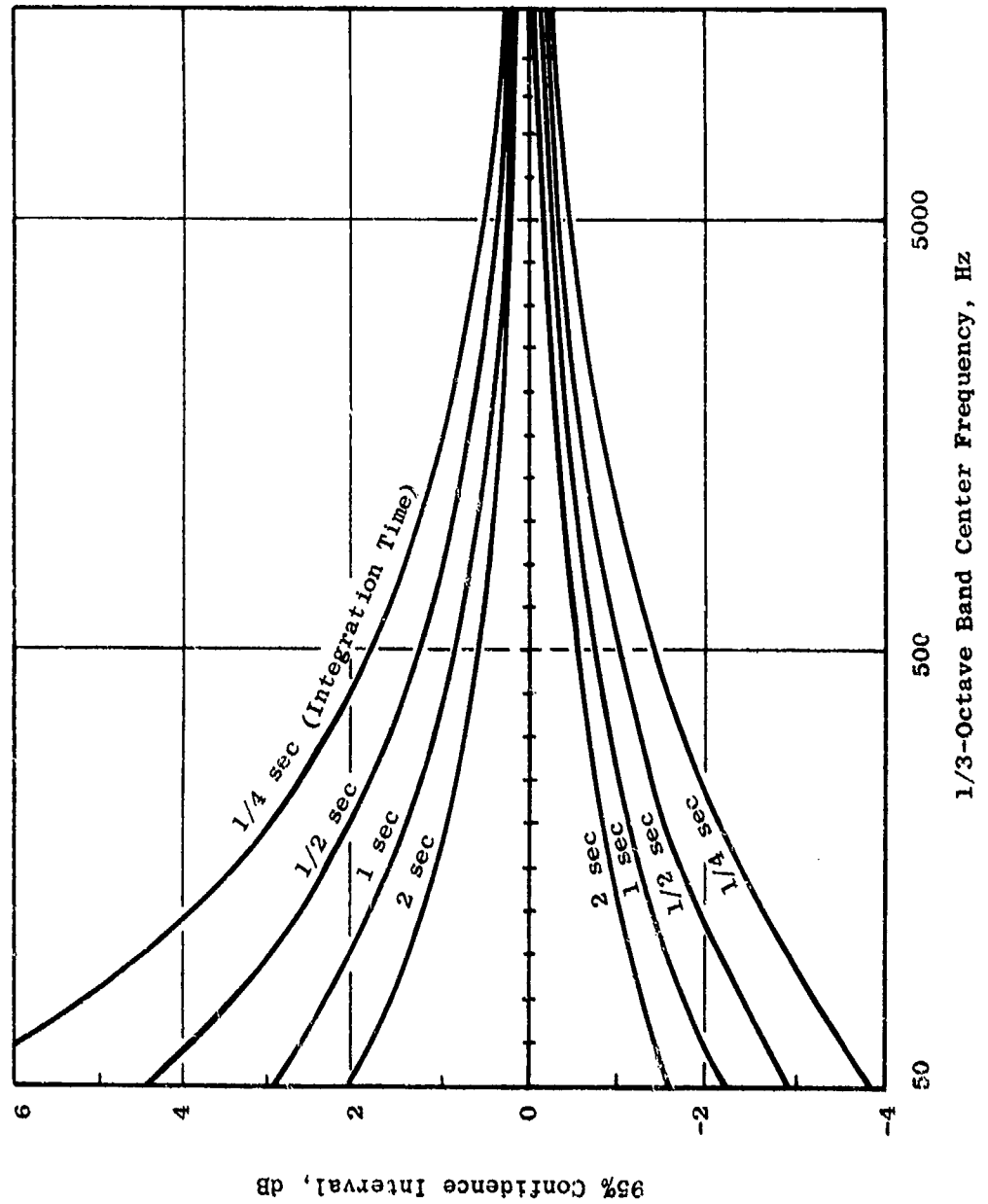


Figure D-14. 95% Confidence Interval Curves as a Function of Frequency and Integration Time.

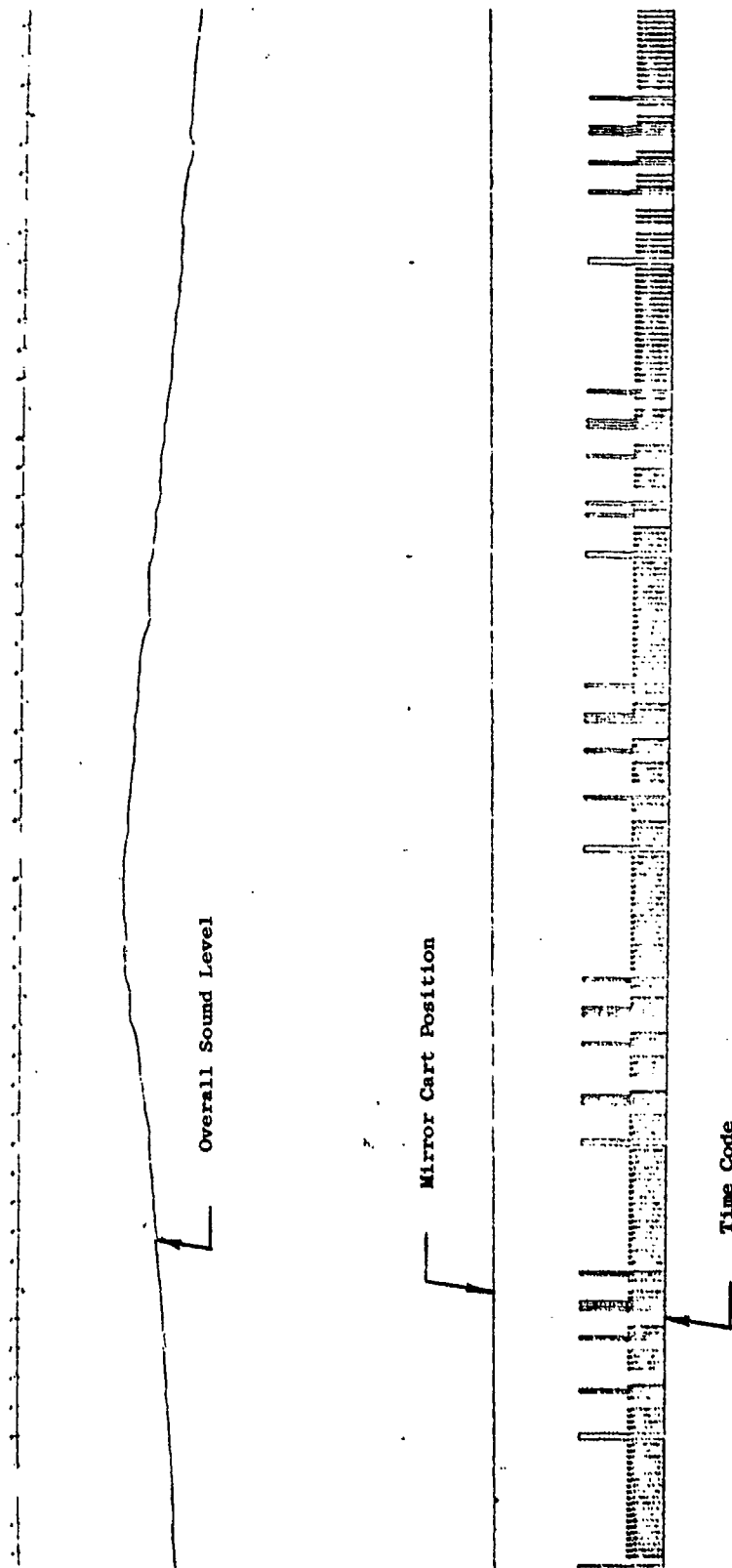


Figure D-15. Typical Brush Chart from EM Data Reduction.

### 1.3.2 Numerical Processing

The second stage of ellipsoidal mirror data reduction is the "correction" of the digitized source intensity distributions for the effects of mirror gain and diffraction window function.

Noise source intensity distributions obtained with a physical focusing device, such as the EM, are inevitably contaminated at lower frequencies by the effects of wave diffraction. However, if the window functions are known, the true source distribution can theoretically be determined from measurements with the use of a numerical deconvolution procedure. Since diffraction is a three-dimensional phenomenon, sources across the jet cross section, as well as along the axis, can be "heard" when the mirror is focused at a given point on the centerline. Thus, after deconvolution, the distributions represent total source contributions at each axial position (i.e., slice of jet measurements).

Recall that the actual and measured source intensity distributions, in terms of mean square sound pressures, are related by a convolution integral, equation D-1, which is formulated approximately for a 1/3-octave band. Due to the complexity of the problem, a numerical solution is mandatory. This reduces the continuous (in  $x$ ) physical problem to a system with a finite number of degrees of freedom. In a numerical solution of equation D-1. The definite integral is expressed as the summation of integrals between discrete points within the continuous domain. The integrand is then approximated by a polynomial over each individual sub-range (e.g., trapezoidal rule). This leads to a series of simultaneous linear algebraic equations for each frequency band:

$$m_1(f) = g(f) \sum_{j=1}^n h_{1j}(f) a_j(f) \quad (D-2)$$

In tensor notation, this is expressed as:

$$\underline{M}(f) = g(f) \underline{H}(f) \underline{A}(f) \quad (D-3)$$

where the vectors  $\underline{A}$  and  $\underline{M}$  represent the actual and measured signals, respectively, at discrete values of  $x$  while  $\underline{H}$  is the matrix of window function coefficients and the scalar  $g$  is the mirror gain.

A non-homogeneous set of simultaneous linear algebraic equations has a unique solution only when the equations are linearly independent (i.e., when none of the equations in the set can be expressed as linear combinations of the others). The solution can be expressed as:

$$\underline{A}(f) = \frac{1}{g(f)} \underline{H}^{-1}(f) \underline{M}(f) \quad (D-4)$$

although solutions are rarely obtained by direct matrix inversion due to the monumental number of calculations required. For a linearly dependent set, the determinant of the coefficient matrix is identically zero and the inverse, expressed as the adjoint matrix divided by the determinant, does not exist. In this case, there is no unique solution, and the matrix is termed singular.

Deconvolution problems which occur in practice are often quite difficult to solve because the systems of equations are ill-conditioned. In this case, the coefficient matrix is "almost singular," with the value of the determinant very close to zero. While solutions exist for these systems, they are extremely sensitive to small changes or errors in the data. Thus, measurement accuracy and choice of a deconvolution technique become critical. An indirect, iterative solution may fail to converge if small successive corrections result in large changes. Direct solutions can fail if accumulated roundoff errors become significant.

The mode of operation of the EM is to make continuous constant-speed traverses parallel to the jet axis. The data is then averaged over each of eighty consecutive, constant time interval, discrete steps. In analyzing results, the integrated spectrum for each interval is assumed to represent the mid-point. Since the cart moves at (approximately) constant speed, the equally spaced time intervals translate to constant axial spacing. Symmetry of the window function and equal spacing of the assumed measurement locations allow the matrix of window function coefficients to be reduced to a form:

$$\underline{H} = \begin{bmatrix} h_{11} & h_{12} & h_{13} & \dots & h_{1n} \\ h_{12} & h_{11} & h_{12} & \dots & h_{1(n-1)} \\ h_{13} & h_{12} & h_{11} & \dots & h_{1(n-2)} \\ \vdots & \vdots & \vdots & \ddots & \vdots \\ h_{1n} & h_{1(n-1)} & h_{1(n-2)} & \dots & h_{11} \end{bmatrix}$$

which is symmetric and has equal elements along any diagonal (Toeplitz matrix). In this case, the matrix is completely defined by its first row, resulting in considerable simplification of the numerical deconvolution procedure. It is apparent from examination of the simplified matrix that the set of equations will become ill-conditioned as the window function "width" increases relative to point spacing, and the magnitudes of the individual elements approach a common value. This point is illustrated by the following example.

Consider the set:

$$a_1 + 0.9 a_2 = 1.9$$

$$0.9 a_1 + a_2 = 1.9$$

The determinant of the coefficient matrix is  $|\underline{\underline{H}}| = 0.19$ , and the inverse is:

$$\underline{\underline{H}}^{-1} = \begin{bmatrix} 5.26316 & -4.73684 \\ -4.73684 & 5.26316 \end{bmatrix}$$

The solution is  $a_1 = 1.0$ ,  $a_2 = 1.0$ .

If the equations are altered slightly, to:

$$a_1 + 0.9 a_2 = 1.9$$

$$0.9 a_1 + a_2 = 1.899$$

The solution is now  $a_1 = 1.00474$ ,  $a_2 = 0.99474$ . This is a relatively small change. Now, consider the set of equations:

$$a_1 + 0.999 a_2 = 1.999$$

$$0.999 a_1 + a_2 = 1.999$$

In this case, the determinant is  $|\underline{\underline{H}}| = 0.001999$  and the inverse is:

$$\underline{\underline{H}}^{-1} = \begin{bmatrix} 500.25 & -499.75 \\ -499.75 & 500.25 \end{bmatrix}$$

The solution is again  $a_1 = 1.0$ ,  $a_2 = 1.0$ .

It is apparent from the magnitude of the elements of  $\underline{\underline{H}}^{-1}$  that any small changes in the right-hand-side terms (response signal) will be greatly magnified in the solution. Thus, when the equations are altered slightly to:

$$a_1 + 0.999 a_2 = 1.999$$

$$0.999 a_1 + a_2 = 1.998$$

the solution is now  $a_1 = 1.49975$ ,  $a_2 = 0.49975$ .

The major conclusion to be drawn from this discussion is that there is a practical limit to the width of window function which can be analytically "removed" from data. The critical dimension is the ratio of window function width (however defined) to point spacing. Thus, all other things being equal, it is as difficult to correct high frequency data at very close spacing as it is to correct low frequency data at wider spacings. There is no single magic number for the width-to-spacing ratio. Rather, it depends on the

degree of accuracy that is required in the calculation, the magnitude of errors and/or noise in the input data and the solution technique being used. The reported analytical error analysis provides further insight into this question.

A comparative study of numerical techniques for accomplishing the deconvolution of directional microphone data was made by Schlinker, et al. (Reference 30). Three different methods were considered:

1. Integral transform
2. Matrix inversion
3. Relaxation

Based on an evaluation in terms of resolution, sensitivity to noise and amount of computation, the relaxation procedure was found to be superior to the other techniques. Following a review of the results and recommendations of this study, the relaxation technique, which is actually an adaptation of the classical point Jacobi iterative method for solution of simultaneous linear algebraic equations, was chosen for use in processing source location data obtained with the ellipsoidal mirror.

The initial applications of relaxation to EM test data resulted in rather severe problems with non-converging solutions, for most frequency bands, due to ill-conditioning of the equations. In response to these problems, the solution algorithm was modified to limit the magnitude of corrections from one iteration to the next and to stop the iteration if and when the solution began to diverge. The incorporation of these modifications resulted in somewhat better convergence, although solutions still contained a relatively high degree of scatter. Another change was made by including a generalized relaxation factor in the iterative correction term. This allowed a solution to be obtained by over- (or under-) relaxation, if desired.

Since deconvolved data still exhibited a high degree of scatter, despite improvements made to the relaxation algorithm, alternative procedures were considered. A direct solution technique was discovered during the course of the error analysis, Appendix E. This method, due to Levinson (Reference 31), is applicable to symmetric, positive definite Toeplitz matrices. Although the window function matrix is symmetric and Toeplitz, it is not necessarily positive definite, even though all of the elements are positive. However, the potential savings in computation and the advantages of an "exact" solution suggested that this approach should be considered. A somewhat more efficient formulation of Levinson's recursion algorithm, presented as a FORTRAN subroutine in Reference 31, was evaluated after a coding error (in Reference 32) was found and corrected. The evaluation revealed that the technique did indeed require less computation than relaxation, while apparently producing much more accurate solutions. The latter fact was determined by "reconstructing" input data using equation D-3 from the known mirror gain and window function in combination with the deconvolved solution from each method. The actual input data was then compared with the two sets of "reconstructed"

data. However, it was found that solution obtained with the Levinson technique contained significantly more scatter than was found in solutions obtained by relaxation. Thus it became apparent that scatter was at least partially due to small fluctuations in the input data, which were magnified by the deconvolution, rather than just being the result at a non-converging solution. This meant that it should be possible to obtain more meaningful results by increasing point spacing to reduce the degree of ill-conditioning, or by applying a pre-smoothing procedure to lessen the impact of errors and/or noise in the input data.

Data which has been properly smoothed will be less influenced by random errors and should more nearly represent the underlying trends than will raw data. Thus, pre-smoothing of measured data can be expected to significantly reduce the scatter in deconvolved source distributions. It should be noted, however, that this is not a magic cure for "bad" data and that care must be exercised to avoid the loss of important details due to indiscriminate smoothing. Rather than being a standard procedure, smoothing should be used only when needed and when the point specifically required to desensitize the deconvolution with respect to small changes in data is too large for satisfactory definition of the measured distribution.

When the point spacing of sample EM data was doubled by averaging (combining) adjacent points, the slight improvement in scatter did not warrant the resultant loss of definition. Therefore, a study of smoothing procedures was undertaken. Source location measurements are resolved into 1/3 octave band spectra for several successive time steps, each step representing a discrete axial position in the jet. This spectral information is then recast as axial power distributions for given frequency bands. At this point the data is converted from dB to mean square sound pressure. It is these distributions of  $P^2$  versus  $x$  which must be smoothed.

There are several techniques available which could be used for pre-smoothing. In Reference 30, for example, data is numerically convolved with a smoothing operator prior to processing. Although such an approach would appear to merely result in the substitution of an analytical window function for the physical one, this type of procedure was nevertheless considered. However, an evaluation of the technique failed to show any significant lessening of scatter in the data. A great many smoothing techniques use some form of least squares estimation. A common approach is to fit a polynomial of relatively low degree (say a parabola) to a set of  $2N + 1$  data points ( $N$  five or seven). The ordinate of the approximating polynomial curve at the central point of the set is then taken as the new "corrected" value of that data point. Successive applications of this procedure, accomplished by indexing the set through the data one point at a time will result in a smoothed distribution. Further smoothing can be achieved by repeating the entire process. This technique was evaluated with over a dozen combinations of the three parameters:

1. Degree of the least squares polynomial
2. Number of points in the set
3. Number of passes through the data.



The results of this evaluation showed very significant improvements in scatter. The addition of increased point spacing, in combination with smoothing, did not have an appreciable effect. From the viewpoint of mathematical rigor, presmoothing is not a desirable step. However, as a practical matter, smoothing can be a useful technique for removing the effects of random errors from a set of data, and, in this way, can enhance the fidelity of deconvolved solutions. Also, the small changes in dB levels resulting from limited smoothing of the  $P^2$  distribution seem almost insignificant when compared to the potential magnitude of measurement and sampling errors.

The studies of smoothing and deconvolution techniques have led to the adoption of improved data reduction procedures. The best results have been obtained using 2-7-3 least-squares smoothing (second degree polynomial, seven points, three passes) in combination with the modified relaxation method. It has been found that, for the smoothing techniques under study, application of the Levinson technique still results in an acceptable level of scatter. It is considered preferable to use relaxation with least-squares smoothing, rather than attempting more extensive smoothing for use with the Levinson procedure.

#### 1.4 DATA ANALYSIS

Ellipsoidal mirror data can be interpreted as axial source intensity distributions for individual 1/3 octave bands, or as source spectra at discrete axial positions. The results are most readily summarized in terms of the axial location of the peak intensity for each frequency band. This is generally expressed by relating Strouhal Number (center frequency normalized by jet diameter and velocity,  $fD/V$ ) to normalized axial position ( $x/D$ ). Trends in the data can then be established by comparison of the summary plots between different nozzle configurations or operating conditions.

A typical data point for a conical converging nozzle was chosen for detailed examination as an illustration of EM data analysis. The sample case is a 3.56" conic nozzle operating statically at a velocity at 2253 ft/sec. This data was obtained on the JENOTS freejet facility with the 18-inch mirror, at a traverse speed approximately four times the value shown in Table 3-17. The data was processed at both 1/8 and 1-second integration times and deconvolved using 2-7-3 smoothing and modified relaxation. The data obtained with 1/8-second integration time is used to determine high frequency source distributions, while the 1-second data is used for low frequencies. The "dividing line" between the two is defined, case by case, from the results of the integral closure test. Far-field noise signatures are calculated from the two measured source distributions, and these predictions are then checked against actual farfield data to determine which gives the best results. The integral closure results (Figure D-16) indicate that the 1-second data should be used over the range 1 to 20 kHz.

Figures D-17 through D-20 show axial power distributions, obtained from 1-second integrations, for 1/3 octave bands centered at 16, 6.3, 2.5, and 1 kHz, respectively. In all four figures, the raw data and processed data,

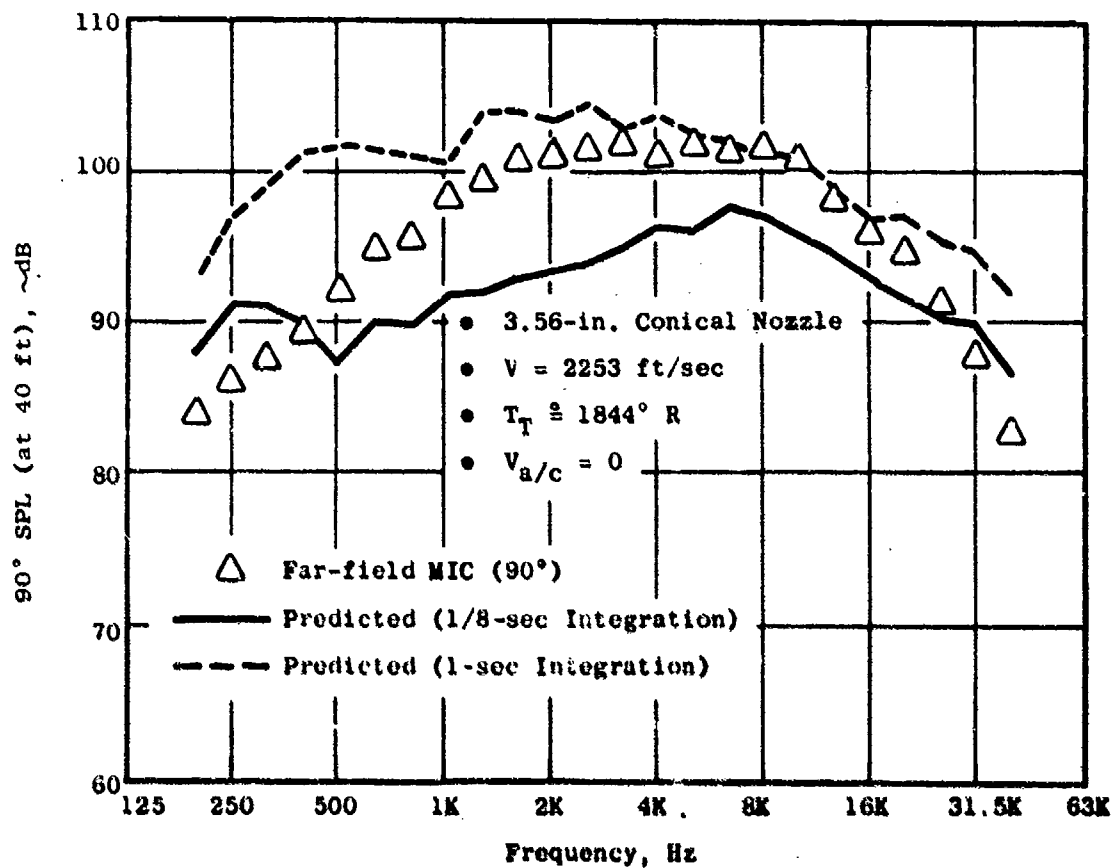


Figure D-16. Integral Closure Check for 3.56-Inch Conical Nozzle,  $V = 2253$  ft/sec,  $V_{a/c} = 0$ .

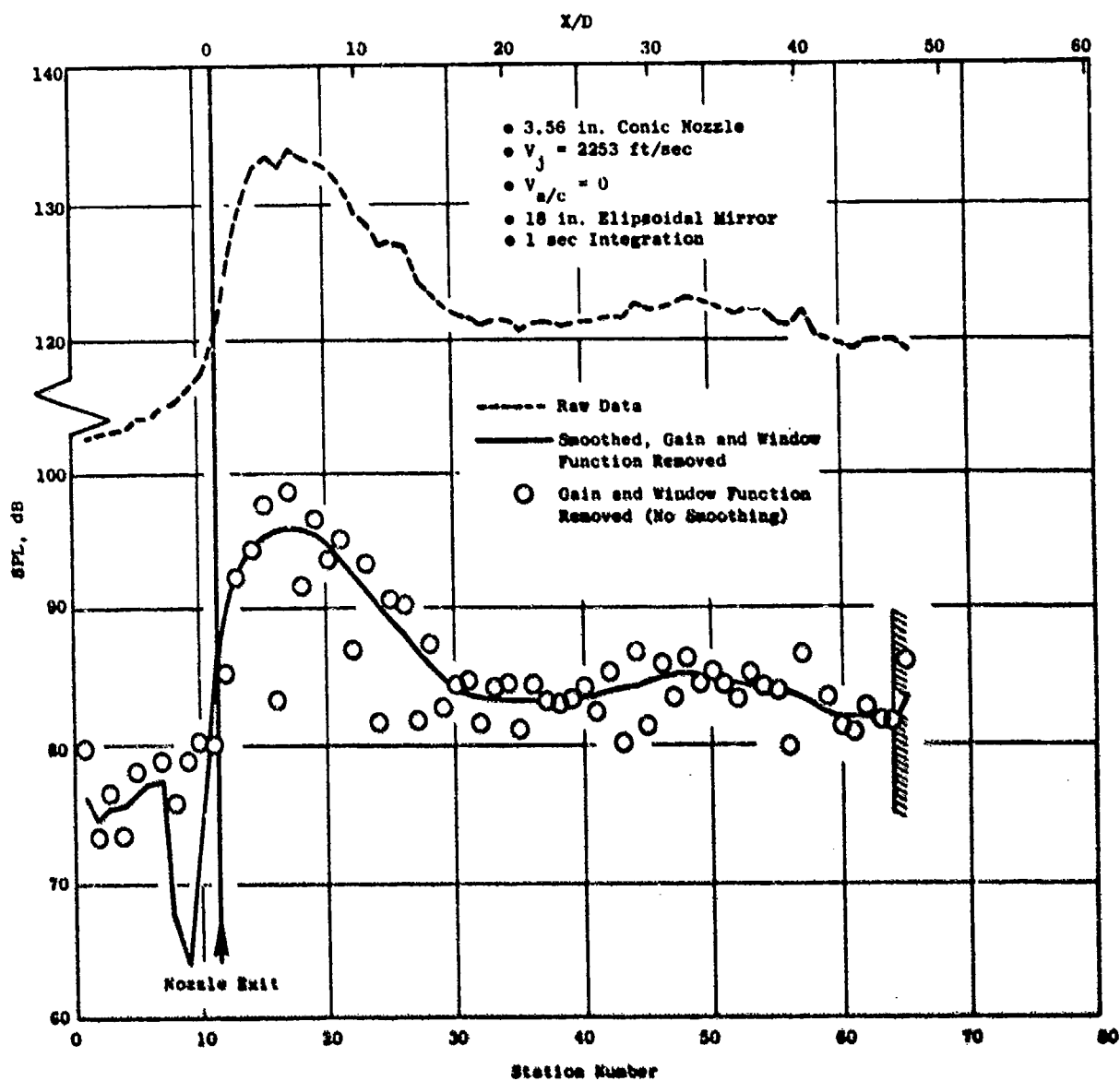


Figure D-17. Axial Distribution of Sound Source Intensity (16,000 Hz, 1/3 Octave Band).

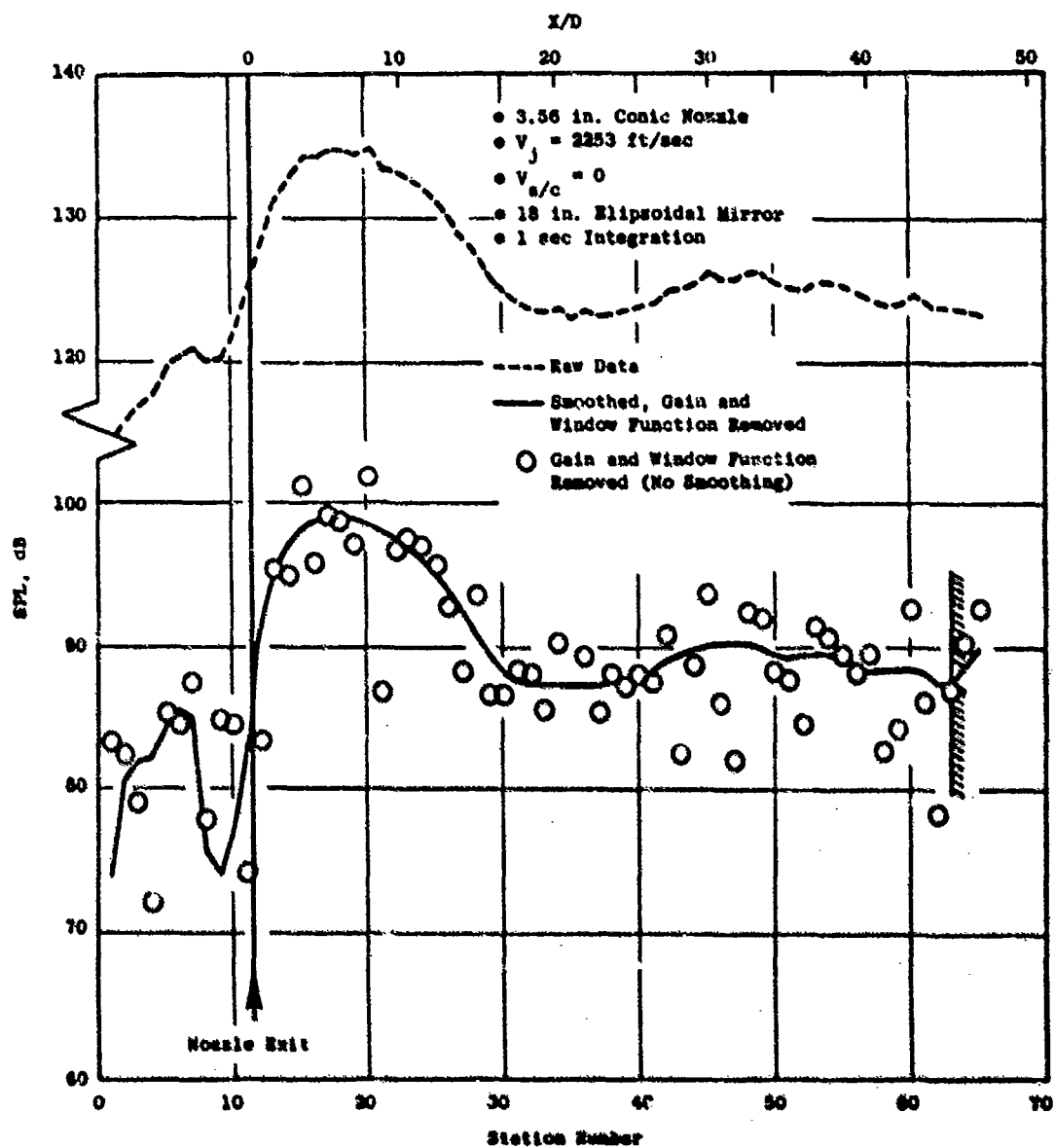


Figure D-18. Axial Distribution of Sound Source Intensity (6300 Hz, 1/3 Octave Band).

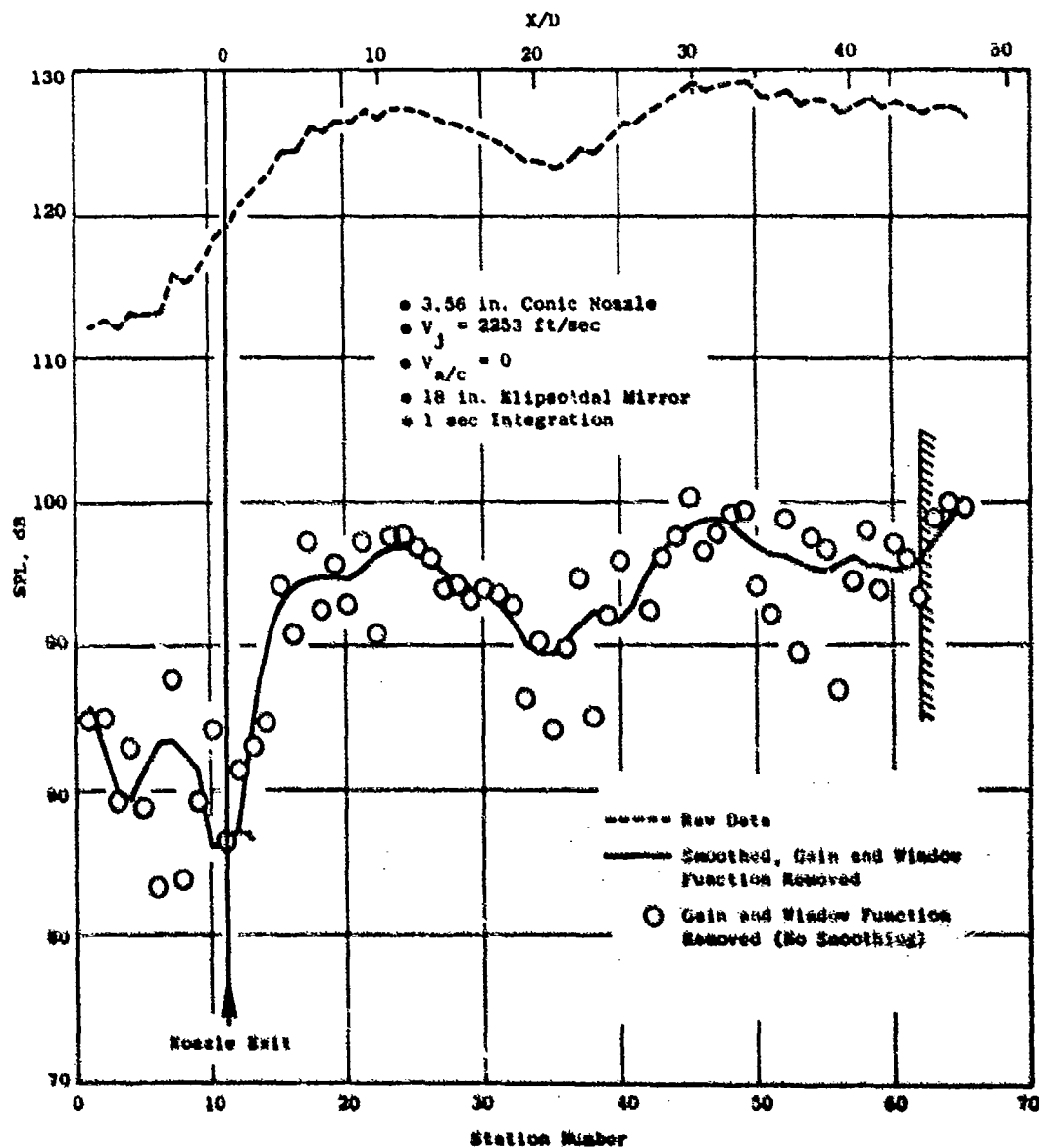


Figure D-19. Axis Distribution of Sound Source Intensity (2500 Hz, 1/3 Octave Band.

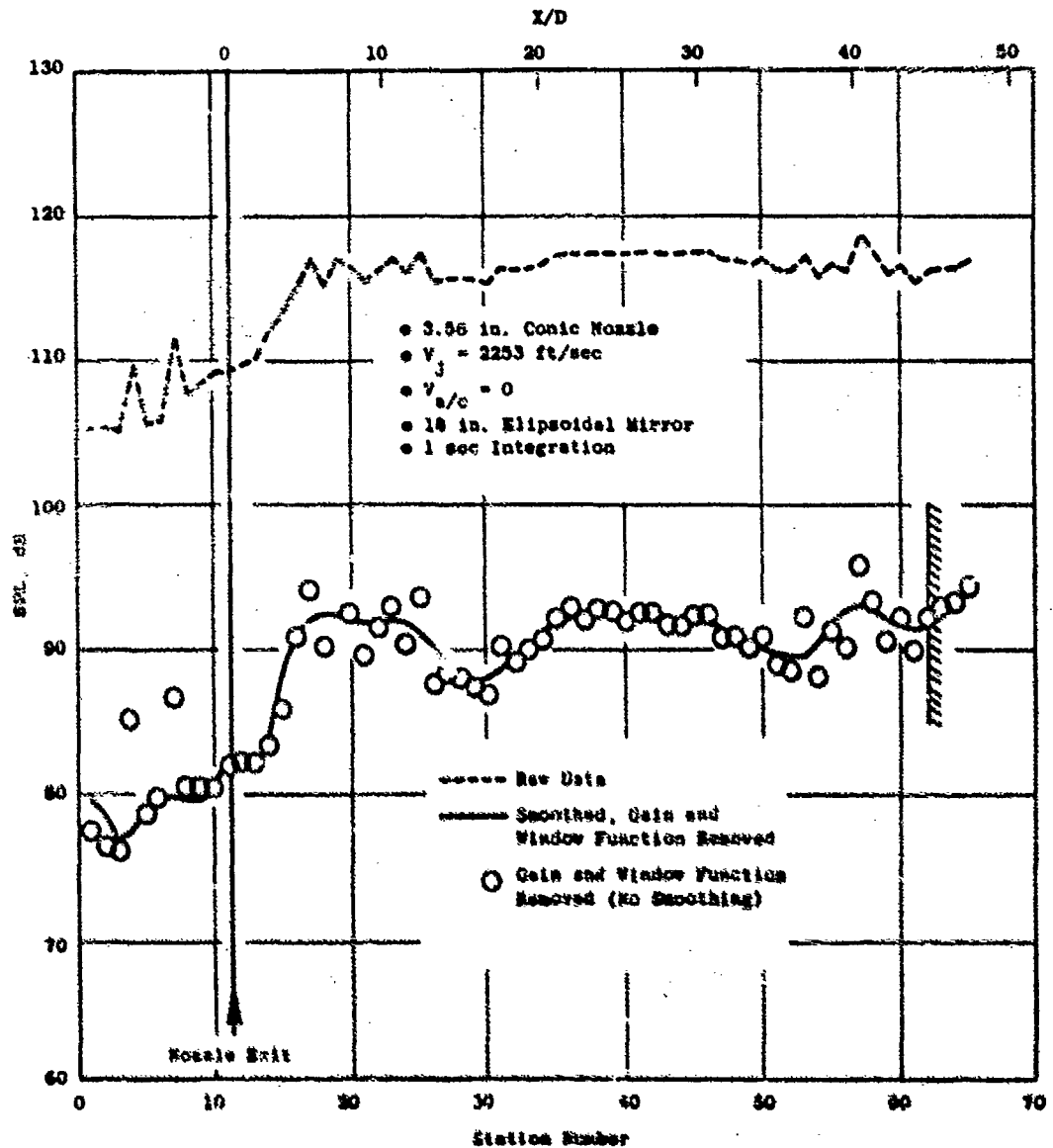


Figure D-20. Axial Distribution of Sound Source Intensity (1000 Hz, 1/3 Octave Band).

with and without presmoothing, are shown. The presmoothed data are seen to contain very little scatter, while retaining the basic trends of the unsmoothed data. As expected, the deconvolved distributions differ from the "as measured" distributions only in level, at higher frequencies, while the shapes of the curves are noticeably different at the two lowest frequencies. There are two distinct source regions apparent in the axial power distributions. At higher frequencies, the upstream region is dominant. With decreasing frequency, the peak source location (in the upstream region) moves downstream and the region broadens somewhat. At the same time, the downstream region is increasing in intensity to the point where the two sections are of approximately equal importance, with the downstream region barely dominant (Figure D-19). This phenomenon explains the seemingly discontinuous shift of the peak location to a high  $X/D$  at low frequencies (Strouhal numbers) in Figure D-21, which shows the peak and "3 dB down" curves for this case. It is interesting, and perhaps important, to note from Figure D-21 that the source intensity is still within 3 dB of the peak at  $X/D$  greater than 40 for Strouhal numbers below 0.4. The fictitious upturn at the "tail end" of the deconvolved source distributions (Figures D-17 through D-20) also results from the presence of additional sources downstream of the last measurement location. These indications of the sizable extent of the noise-producing region could have significant impact on practical, as well as theoretical, considerations of jet noise.

Typical spectra in the upstream and downstream source regions are shown in Figures D-22 and D-23, respectively. Each figure shows the "as measured" spectrum, as well as the deconvolved spectrum, with and without presmoothing. Also shown is the spectrum after smoothing and removal of mirror gain, but before deconvolution. Reductions in scatter in the deconvolved spectra, due to presmoothing, are obvious. These figures also illustrate the relative effects of mirror gain and window function on measured source spectra. Mirror gain increases with frequency (approximately as  $f^2$ ) while an apparent gain due to the window function has a reciprocal trend. Thus, it is necessary to make both corrections in order to obtain unbiased spectra.

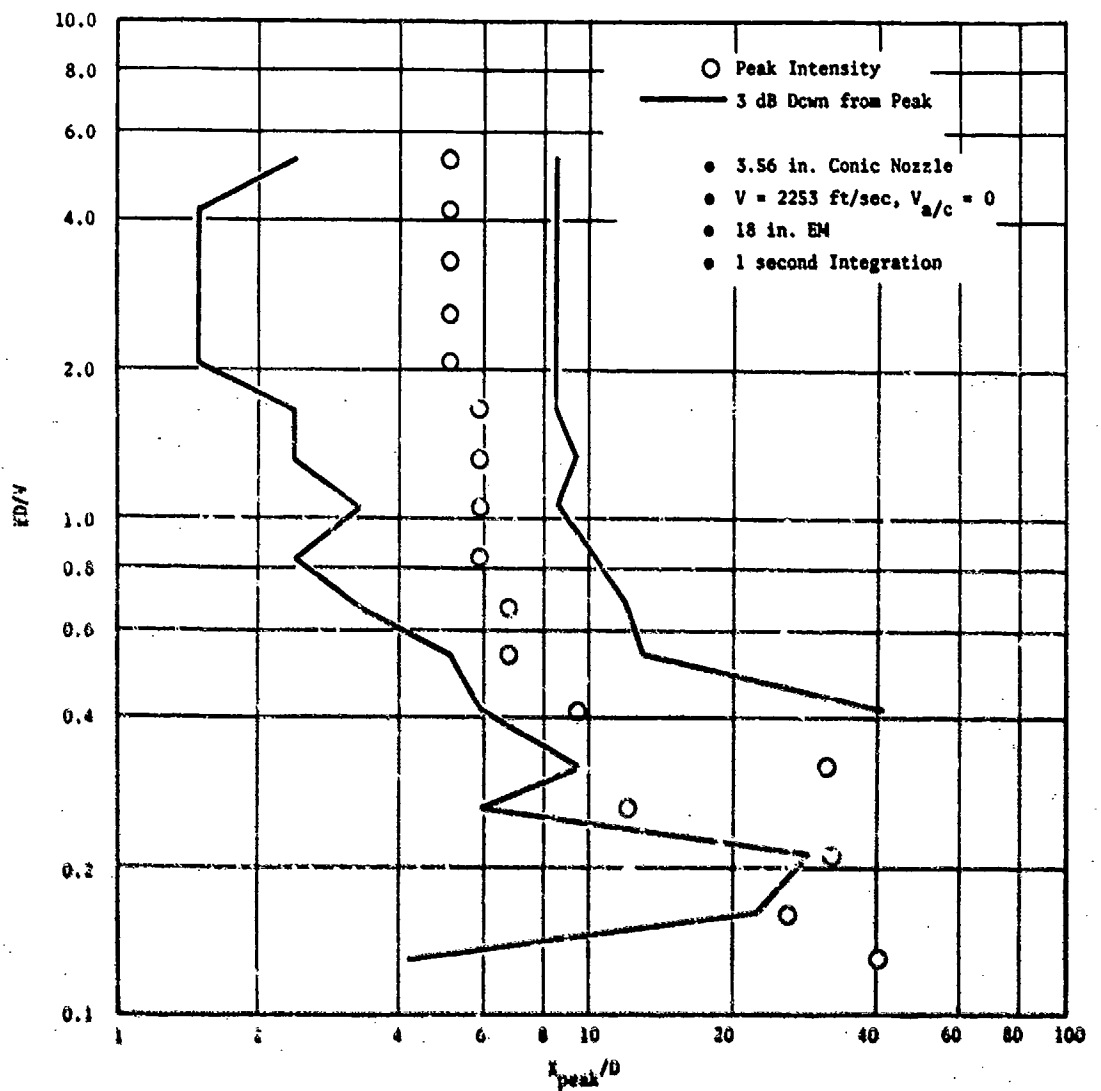


Figure D-21. Axial Location of Peak Sound Source Intensity.



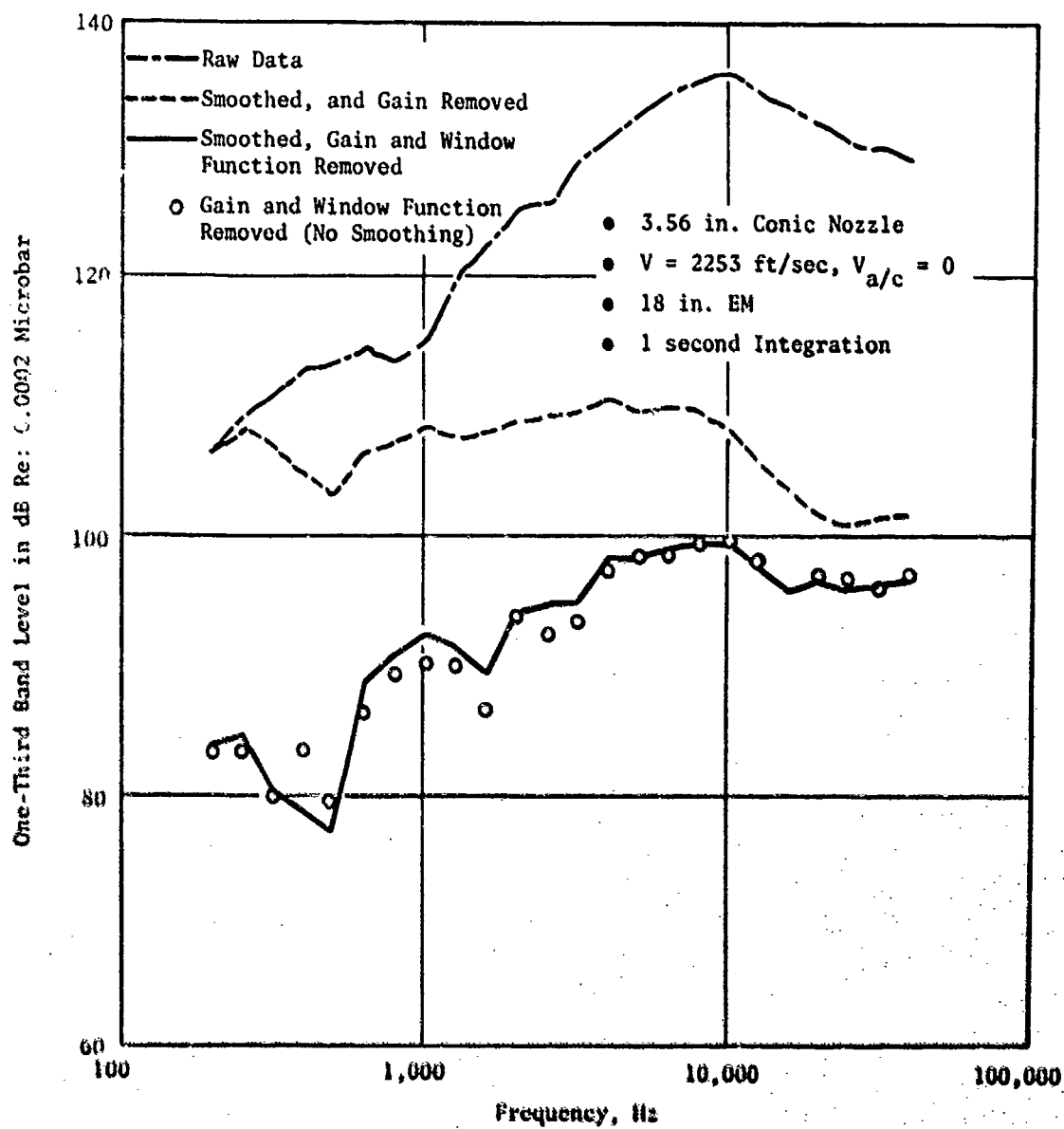


Figure D-22. Source Spectrum at Station 18 ( $x/D = 5.9$ ).

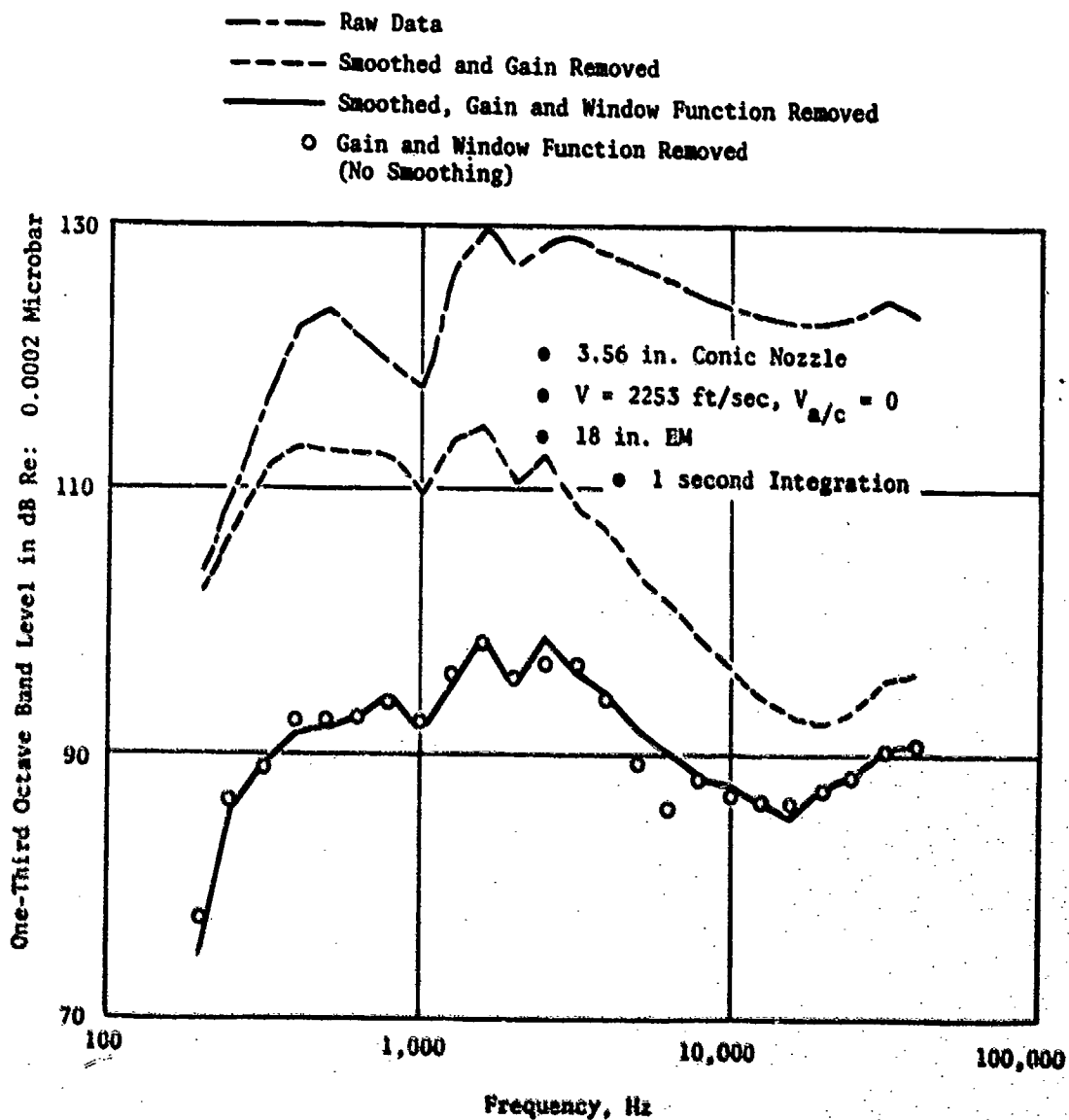


Figure D-23. Source Spectrum at Station 46 ( $x/D = 30.6$ ).

## 2.0 EVALUATION OF THE EM TECHNIQUE

As in the case of any measurement system, it is necessary to assess the potential limitations and sources of error in the application of the ellipsoidal mirror technique. These can be separated into three distinct areas:

1. Theoretical limitations
2. Data acquisition errors
3. Data processing errors and limitations

In the realm of theoretical limitations, there are several items to be considered. Since the EM senses farfield acoustic radiation, measurements are affected by propagation phenomena such as convection, refraction, and turbulence scattering. Thus, even though these effects are minimized by alignment of the mirror axis normal to the jet (source) axis, it is still only possible to define "apparent" source distributions. In addition, there are limitations to the range of frequencies over which the EM provides meaningful data. These are dependent on the exact physical characteristics of the system in use. There are two potential limits at low frequencies. One occurs when the ratio of working distance to wavelength falls too low and the mirror is operating in the acoustic nearfield. The other occurs when the ratio of aperture diameters to wavelength falls too low and the mirror is unable to focus incoming waves. At high frequencies, the system is limited by microphone frequency response/directivity and by the dimensional tolerances at the mirror. The latter limit is reached when deviation from either the theoretical mirror surface contour or the focal point location become appreciable fractions of wavelength. It should also be noted that, since the width of a 1/3 octave band is proportional to the contour frequency, the formulation of equation D-1 in terms of 1/3-octave bands may not be a valid approximation at higher frequencies due to the large bandwidths.

In addition to the real or potential problems generally associated with acoustic data acquisition, there are particular sources of error associated with the mode of operation of the EM. As described in Section 1.1, measurements are made while the mirror is slowly traversed parallel to the jet axis. In data reduction, the signal is resolved into 1/3 octave bands, averaged over discrete time steps and digitized. Since the EM is moving during these time steps, the digitized spectra represent averages over some distance. This limits the resolution capability of the mirror to the width of an individual time step. Since the averaging time must be long enough to allow for extraction of a statistically valid sample (Figure D-14), this distance can be decreased only by a reduction in the traverse speed. Mirror misalignment and improper location of the microphone (relative to the primary focal point) are also potential sources of error during data acquisition. If the mirror axis is not normal to the jet axis, the window function is affected, becoming increasingly skewed as the mirror is tilted. Similarly, the measured data is distorted if the microphone is not properly located at the focal point.

The major sources of error encountered in processing EM data are:

1. Statistical errors due to insufficient averaging time.
2. Enhancement of ambient or electronic noise, or of statistical measurement errors, due to an ill-conditioned window function matrix.
3. Limits on achievable resolution due to numerical instabilities in the solution of an ill-conditioned set of equations.
4. Errors induced by uncertainty in window function measurements.

A discussion of these errors is included in Appendix E, along with some simplified numerical examples.

## 2.1 INTEGRAL CLOSURE TEST

An important test of a source location technique is to see if a measured farfield noise signature can be calculated from the measured source distribution. This test, referred to as integral closure, does not guarantee that the source measurements are correct since a given farfield signature could be generated by any of a number of different source distributions. However, it does provide some confidence in the results and can be used to identify ranges of variables for which a given technique is definitely not valid. For example, the results of integral closure checks on EM measurements reported in Reference 12 showed that it is an extremely valuable tool for determining the proper choice of integration time and for evaluating the range of frequencies over which the EM appears to yield valid source location data.

The farfield signal is predicted by logarithmically summing (integrating) the deconvolved source intensities (dB per unit length) over the length of the jet for each 1/3-octave band, after inverse square law and air attenuation adjustments have been made to correct the data to standard day conditions at the desired farfield position. The formulation of Reference 33, with an extrapolation to frequencies above 10 kHz, is used to calculate air attenuation corrections. The 90° farfield microphone is always chosen for closure checks since measurements at this location are known to most accurately reflect source generation mechanisms.

An integral closure check of 18-inch mirror measurements on a conical converging nozzle was illustrated in Figure D-15. Although results vary from case to case, the overall conclusion drawn from integral closure checks is that, as a minimum, the deconvolved source distributions generally appear to be valid over the following range of frequencies:

<u>Mirror</u>	<u>Frequency Range</u>
18" shallow-dish	1 kHz $\leq$ f $\leq$ 20 kHz
34.654" deep-dish	500 Hz $\leq$ f $\leq$ 10 kHz

## 2.2 POINT SOURCE EXPERIMENT

The measurement of a point source is a critical test for any noise source location technique, since the results can be used to infer the accuracy of the method in defining discrete sources and in discriminating among adjacent distributed sources. Although the window function width indicates the inherent resolution of a particular device, it is possible to enhance this capability with the use of numerical deconvolution procedures. Thus, the performance of a given source location technique is strongly dependent on the adequacy of the data processing routines. In the idealized case where a closed form solution of equation D-1 is possible, the function representing the measured point source distribution is resolved identically to a Dirac delta function, which is the analytical representation of a point source. However, a numerical solution will only yield an approximation to this result. The width of this deconvolved distribution is an accurate measure of the resolution of the technique.

An evaluation of the ellipsoidal mirror technique was made, using data obtained during calibration testing of the deep dish mirror (Section 1.2). The measured 1/3-octave band source distributions were first fitted with least-squares polynomial curves to reduce the influence of random measurement errors. The modeled data were then deconvolved using a modified relaxation. Typical results, for the 4KHz 1/3 octave band, are shown in Figure D-24. Note the relatively minor adjustment of measured data points due to the introduction of the polynomial model. The deconvolved distribution, while not a delta function, shows a marked improvement in resolution relative to the "raw" data. The overall results, illustrated in Figure D-25, indicate that the achievable resolution is an approximately constant fraction of wavelength. The point source can be located (within 3 dB) with a tolerance of  $\pm 0.6 \lambda$ . While this is a five factor of improvement over the unprocessed results, it is not indicative of a precise measurement. For example, at 1 kHz, the error band is approximately  $\pm 8$  inches. The numerical study of the 18" mirror, which was conducted as part of the error analysis (Appendix E), indicates that it should be possible to achieve significantly better resolution than this with the proper numerical procedures. This indicates a need for further study to identify and implement a better numerical technique for deconvolution of ellipsoidal mirror data. It should also be noted here that it is still important to optimize a mirror design for a narrow window function, since, as a practical matter, precise numerical deconvolution is difficult to accomplish.

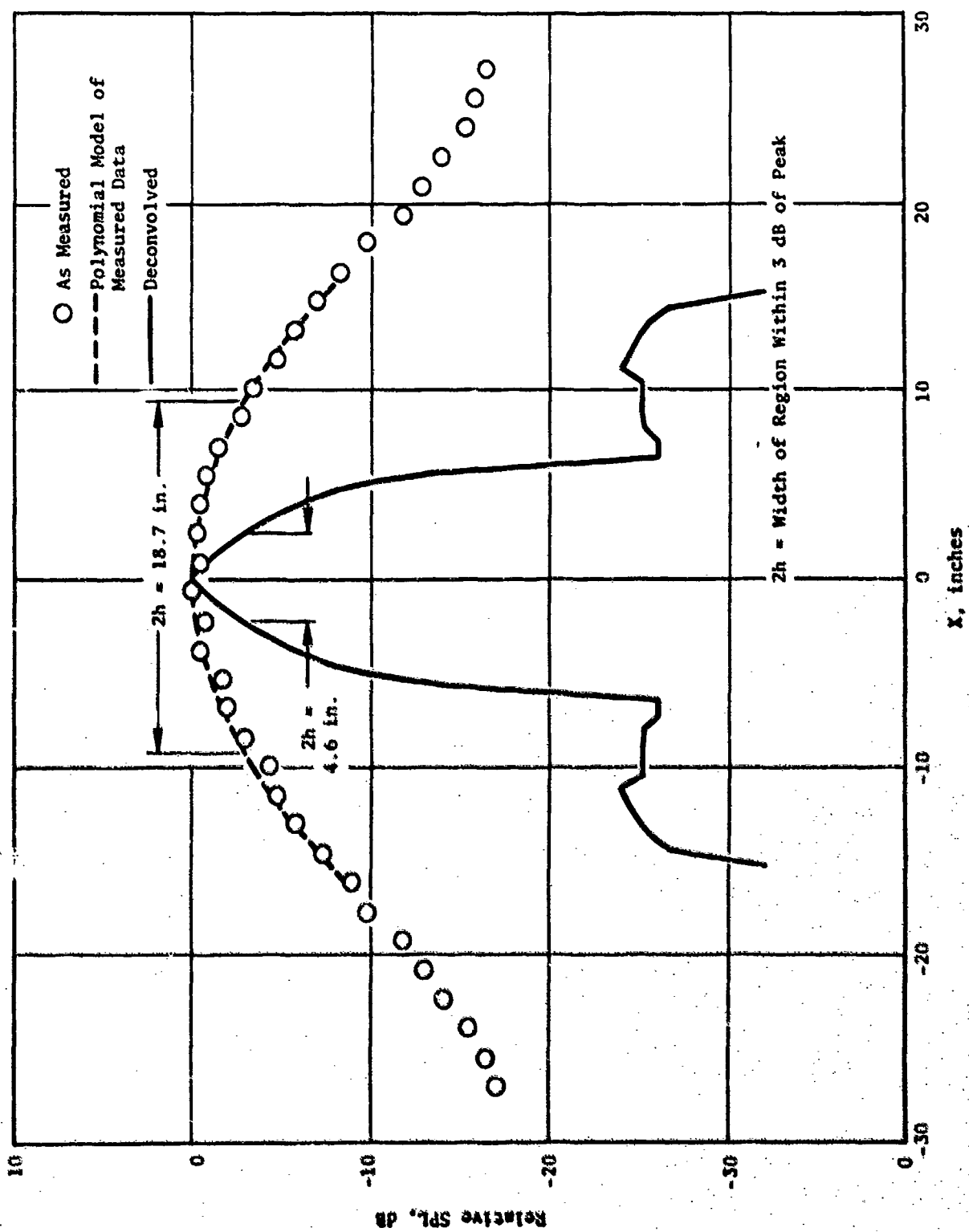


Figure D-24. Resolution of the Deep-Dish Ellipsoidal Mirror (Point Source Measurement), 4000 Hz.

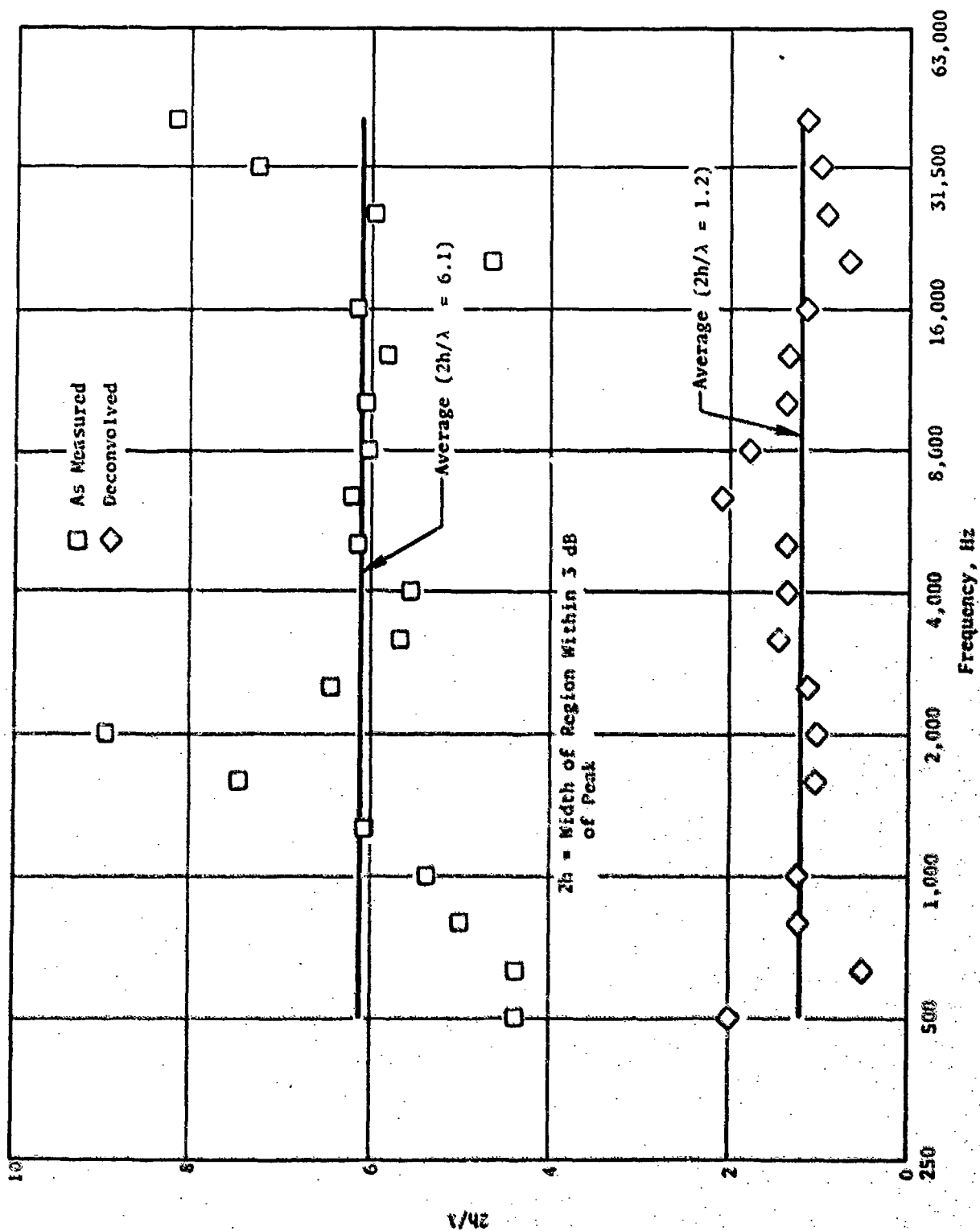


Figure D-25. Resolution of the Deep-Dish Ellipsoidal Mirror (Point Source Measurement).

## APPENDIX E

### ERROR ANALYSIS OF THE ELLIPSOIDAL MIRROR TECHNIQUE

#### 1. MODEL FOR ELLIPSOIDAL MIRROR ERROR ANALYSIS

An analysis is developed herein of the window function removal technique for the ellipsoidal mirror. This analysis is based on a model for the device that describes the way in which acoustic sources are combined by the mirror to yield the measurement values. The following assumptions are made in the construction of this model (see Figure E-1):

1. The jet is composed of N statistically independent acoustic pressure sources equispaced along a line, x.
2. The M-measurements are made along a line, y, parallel to x, with the same spacing as the sources.
3. The measurements are the mean square outputs from a filter of sufficiently narrow bandwidth that the acoustic response of the mirror may be assumed constant for any frequency in the filter band.
4. The quantities of interest are the mean square values of the pressure sources.

Using the geometry illustrated in Figure E-1, each measured pressure signal is equal to a linear combination of the pressure sources which may be seen by application of the superposition principle of acoustics. The weights are determined by the pressure response of the ellipsoidal mirror (EM). Thus:

$$a_m(t) = \sum_{n=1}^N b(m,n) P_n(t) \quad (E-1)$$

where  $a_m(t)$  is the  $m^{\text{th}}$  measured pressure signal

$P_n(t)$  is the  $n^{\text{th}}$  source pressure signal and

$b(m,n)$  is the pressure response of the EM between the  $m^{\text{th}}$  measurement position and the  $n^{\text{th}}$  source position.

The mean square pressure measurements, corresponding to the outputs of a single filter, a CR third octave analyzer for example, are given by:



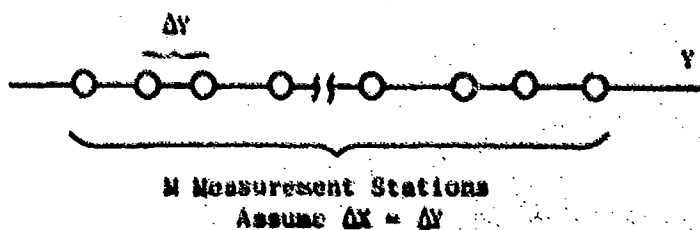
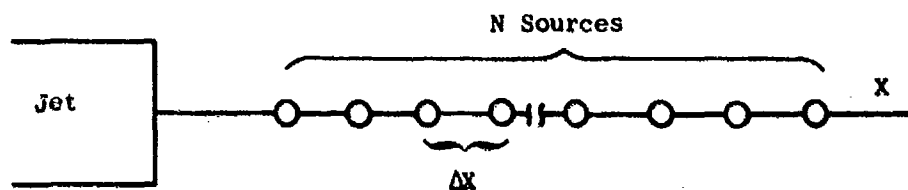


Figure E-1. Assumed Measurement Geometry.

$$S_m = \overline{|s_m(\cdot)|^2} = \sum_{n=1}^N \sum_{k=1}^N b(m,n) b^*(m,k) \overline{P_n P_k^*} \quad (E-2)$$

where \* indicates the complex conjugate.

Since the sources are assumed to be statistically independent,

$$\overline{P_n P_m^*} = P_n \delta(n-m)$$

where  $\delta(n)$  is the Kronecker delta function.

Then:

$$S_m = \sum_{n=1}^N \sum_{k=1}^N b(m,n) b^*(m,k) P_n \delta(n-k) = \sum_{n=1}^N |b(m,n)|^2 P_n \quad (E-3)$$

Finally, defining  $a(m,n)$  as the power response of the EM between measurement point  $m$  and source position  $n$ ,

$$a(m,n) = |b(m,n)|^2 \quad (E-4)$$

so that

$$S_m = \sum_{n=1}^N a(m,n) P_n \quad (E-5)$$

where  $S_m$  are the filter mean square pressure measurements

$P_n$  are the mean source strengths

and  $a(m,n)$  is the power response of the EM between  $m$  and  $n$ .

This may be written in matrix notation as

$$\underline{S} = \underline{A} \underline{P} \quad (E-6)$$

where  $\underline{S}$  is the vector of  $N$ -measured powers,  $\underline{P}$  is the vector of  $N$  source powers and  $\underline{A}$  is the matrix of power response values that performs the operations indicated in Equation E-5.

Since the pressure fluctuations in the jet are random, the measurements will also be random. To include random data effects in the model, a slight modification to the definition of  $\underline{S}$  and  $\underline{P}$  is necessary. With  $\underline{S}$  as the

vector of actual random measurements,  $\underline{P}$  as the vector of true source values, and  $\underline{\epsilon}$  as the vector of zero mean random variables representing the uncertainty in  $\underline{S}$ , the random data model becomes:

$$\underline{S} = \underline{A} \underline{P} + \underline{\epsilon} \quad (\text{E-7})$$

To obtain an estimate of the source distribution, which will be denoted as  $\hat{\underline{P}}$ , from the measurement vector  $\underline{S}$ , the Fisher theory of estimation will be employed. This method is detailed in Schweppe, Reference 32, and provides the unbiased estimate of  $\underline{P}$  with the minimum variance (statistical error) under the assumption that before the measurements are taken,  $\underline{P}$  is completely unknown. Under this assumption,  $\hat{\underline{P}}$  may be shown to be

$$\hat{\underline{P}} = (\underline{A}^T \underline{R}^{-1} \underline{A})^{-1} \underline{A}^T \underline{R}^{-1} \underline{S} \quad (\text{E-8})$$

The covariance matrix of  $\hat{\underline{P}}$ , defined as

$$\underline{K}_{\hat{\underline{P}}} = E \left\{ (\hat{\underline{P}} - \underline{P}) (\hat{\underline{P}} - \underline{P})^T \right\}$$

is then

$$\underline{K}_{\hat{\underline{P}}} = (\underline{A}^T \underline{R}^{-1} \underline{A})^{-1} \quad (\text{E-9})$$

where

$$\underline{R} \triangleq E \left\{ \underline{\epsilon} \underline{\epsilon}^T \right\}$$

is the covariance matrix of the statistical error,  $\underline{\epsilon}$ .

In general, to evaluate Equation E-8, one must know  $\underline{R}$ . However, if it is assumed that there are as many measurements as sources,  $N = M$ ,  $\underline{A}$  is a square matrix. Manipulating Equation E-8,

$$\hat{\underline{P}} = (\underline{A}^T \underline{R}^{-1} \underline{A})^{-1} \underline{A}^T \underline{R}^{-1} \underline{S} = \underline{A}^{-1} \underline{R} \underline{A}^{-T} \underline{A}^T \underline{R}^{-1} \underline{S} = \underline{A}^{-1} \underline{S} \quad (\text{E-10})$$

Thus for this case, knowledge of the error covariance matrix is not required and the estimate is formed by inverting the  $\underline{A}$  matrix. Under the above assumptions,  $\hat{\underline{P}}$  is unbiased and has minimum variance. In the following uncertainty analysis it will be assumed that  $\underline{A}$  is a square matrix.

## 2. TECHNIQUES FOR COMPUTING THE ESTIMATE AND INVERTIBILITY OF THE A MATRIX

To compute the estimate of the source distribution given in Equation (E-10) it is necessary to solve the equation

$$\underline{S} = A \hat{P} \quad (E-11)$$

where  $\underline{S}$  and  $A$  are given.

This may be done by:

- (1) Iterative approaches such as the Jacobi or Gauss-Seidel procedures.
- (2) Direct inversion of the  $A$  matrix.
- (3) Direct, closed form solution of Equation E-11, taking advantage of a special property of  $A$  yet to be discussed.

Care must be taken in the solution of Equation E-11 because of its typical size (80 x 80) and the fact that  $A$  will generally be ill-conditioned particularly for low frequency conditions.

The invertibility of a matrix can be parameterized by its condition number. The condition number is an indication of how much the perturbation of an element of  $A$  will affect the values of the elements of  $A^{-1}$ . If the condition number is large, small changes in  $A$ , such as those that occur because of numerical truncation and roundoff errors, will drastically affect the value of  $A^{-1}$ . Conversely, if the condition number is small, small perturbation of the elements of  $A$  will have only small effects on the elements of  $A^{-1}$ . Zwicky (Reference 34) suggests that if the condition number is less than 1000, a matrix is easily inverted, and if it is more than 1000 special techniques should be employed. Zwicky defines this condition number as

$$u = \frac{\lambda_{\max.}}{\lambda_{\min.}} \quad (E-12)$$

where  $\lambda_{\max.}$  is the maximum eigenvalue of  $A$  and  $\lambda_{\min.}$  is the minimum eigenvalue of  $A$ .

To examine the effect of this on the window function removal technique, consider the following approximate window function matrix:

$$A = (1-p) U + pI \quad (E-13)$$

where  $I$  is the identity matrix and  $U$  is a matrix of all 1's. Thus the approximate window function has the form:

$$A = \begin{bmatrix} 1 & (1-p) & (1-p) & \dots & (1-p) \\ (1-p) & 1 & (1-p) & \dots & (1-p) \\ \vdots & \vdots & \vdots & \ddots & \vdots \\ (1-p) & (1-p) & \dots & (1-p) & 1 \end{bmatrix} \quad (E-14)$$

It may be shown that the eigenvalues for this choice of A are:

$$\lambda = \begin{cases} p & \text{(there are } n-1 \text{ of these)} \\ n - p & (n-1) \end{cases} \quad (E-15)$$

Thus,

$$u = \frac{n - p (n-1)}{p} = \frac{n}{p} - (n-1) \quad (E-16)$$

The table below gives the value of  $u$  for various values of  $p$  with  $n = 80$ .

Condition Number for  $N = 80$

$u$	$p$
721	0.1
987	0.075
1521	0.05
3121	0.025
7921	0.01
15921	0.005

If the on and off diagonal elements of this matrix differ by less than 0.075, problems may be expected in computing  $A^{-1}$ .

Other observations can be made from the result in Equation E-16. For large  $n$  and small  $p$  (the case most relevant to ellipsoidal mirror window function removal),

$$u \approx \frac{N}{p} \quad (E-17)$$

Therefore, the condition number is nearly proportional to the order of A. The condition number can be improved by reducing the number of measurement locations. Also,  $p$  should be nearly proportional to the reciprocal of the beamwidth for specially broad window functions. Thus, the condition number should be proportional to the beamwidth of the mirror.

The Jacobi method is used to solve Equation (E-11) in the numerical processing of EM data. This method is in general use for solving equations of this type and is often recommended by numerical analysts. Direct inversion of the A matrix was examined in this study. Because of a general notion in numerical analysis that if one can directly compute  $A^{-1}$ , then the Jacobi and Gauss-Seidel methods will almost certainly work as well if they converge. Also,  $A^{-1}$  is required to evaluate some of the expressions to be developed later herein.

Two methods were evaluated for inverting the A-matrix. The first was a "Maximum Pivotal Gaussian Elimination" routine taken from Carnahan, Luther, and Wilkes (Reference 35) and the second was a program for inverting symmetric matrices based on the matrix inversion theorem in Appendix A of Schweppe (Reference 33). Both routines were able to obtain at least three place accuracy in the inverse, but only when the computations were performed using double precision arithmetic. Further precision was obtained by taking advantage of the superior word length of the CDC-7600 computer. The test case used in the evaluation was the inversion of the 1.25 KHz window function from the 18-inch ellipsoidal mirror at 0.375-inch spacing. The worst case conditions of the 1.25-KHz window function at 0.375-inch spacing and the 1.6 KHz window function at 0.125-inch spacing were also examined. The program based on the "Schweppe Theorem" ran in considerably less computer time (because the assumed symmetry of the window function was exploited) than the Maximum Pivotal program and for this reason was chosen as the preferred inversion procedure.

A method was also discovered for the direct solution of Equation E-11. This method uses the fact that if the A matrix is symmetric, then it is completely defined by its first row. This procedure was reported by Levinson, Reference 31. An evaluation of this approach was not made, but examination of the algorithm indicated that there may be a computational savings over the Jacobi iterative method. This, coupled with the advantage of obtaining an "exact" solution (over the "converged" approximation of the iterative method), suggests that the approach should be evaluated. A Fortran subroutine for performing the required calculations appears in Robinson, Reference 32.

The major conclusion of this section is that it should be possible to accurately solve Equation E-11 for measurement spacings as small as 0.125 inches if sufficient care is taken (such as use of double precision arithmetic) in writing the computation subroutines. While the Jacobi procedure should yield adequate results, a closed-form solution procedure is available and this should be evaluated.

### 3. ESTIMATOR VARIANCE AND BIAS

Under the assumptions that led to the model of Equation E-7 and estimator of Equation E-10, the estimate was unbiased and had covariance matrix:

$$K_p = A^{-1}RA^{-T} \quad (E-18)$$

where  $R$  was the covariance matrix of the measurements. An ideal source distribution measurement is defined as  $\underline{P}$ , based on a direct observation of the sources. Then

$$\underline{\hat{P}} = \underline{P} + \underline{\gamma} \quad (\text{E-19})$$

is defined, where  $\underline{\gamma}$  represents the uncertainty in  $\underline{\hat{P}}$  caused by finite observation time and bandwidth. One can do no better than a direct observation and therefore:

$$K_{\underline{\hat{P}}}^{\min.} = K_{\underline{P}} = E \{ \underline{\gamma} \underline{\gamma}^T \} \quad (\text{E-20})$$

represents the minimum possible variance achievable. In the simple model of Equation E-7, the measurement uncertainty,  $\underline{\epsilon}$ , is caused by the uncertainty in  $\underline{P}$ , and in going from Equation E-6 to Equation E-7 it is implied that

$$\underline{\epsilon} = A \underline{\gamma} \quad (\text{E-21})$$

Therefore, it follows that

$$R = A K_{\underline{P}} A^T \quad (\text{E-22})$$

and from Equation 18,

$$K_{\underline{\hat{P}}} = A^{-1} R A^{-T} = A^{-1} (A K_{\underline{P}} A^T) A^{-T} = K_{\underline{P}} \quad (\text{E-23})$$

Thus, independent of the window function, the estimate achieves the same variance as a perfect observation of the source distribution. If  $\underline{p}(t)$  is assumed to be a normally distributed random vector, then  $\underline{P}$  is a Chi-Square random vector. The variance of a measurement  $P_n$  is

$$\text{VAR} \{ \hat{P}_n \} = \frac{P_n^2}{BT} \quad (\text{E-24})$$

and a 95% confidence statement on  $P_n$  is:

"The true value of  $\hat{P}_n$  which is  $P_n$  must lie between  $\hat{P}_n (2 BT) / \chi_{0.025,n}^2$  and  $\hat{P}_n (2 BT) / \chi_{0.975,n}^2$  with 95% confidence where  $B$  is the bandwidth of the one-third-octave filter and  $T$  is the integration time."

The curves in Figure E-2 may be used to determine the plus and minus 95% confidence limits in dB for  $P_n$ .

Another effect must be considered to complete the analysis of the variance and bias of the estimate. Generally ambient noise will be present

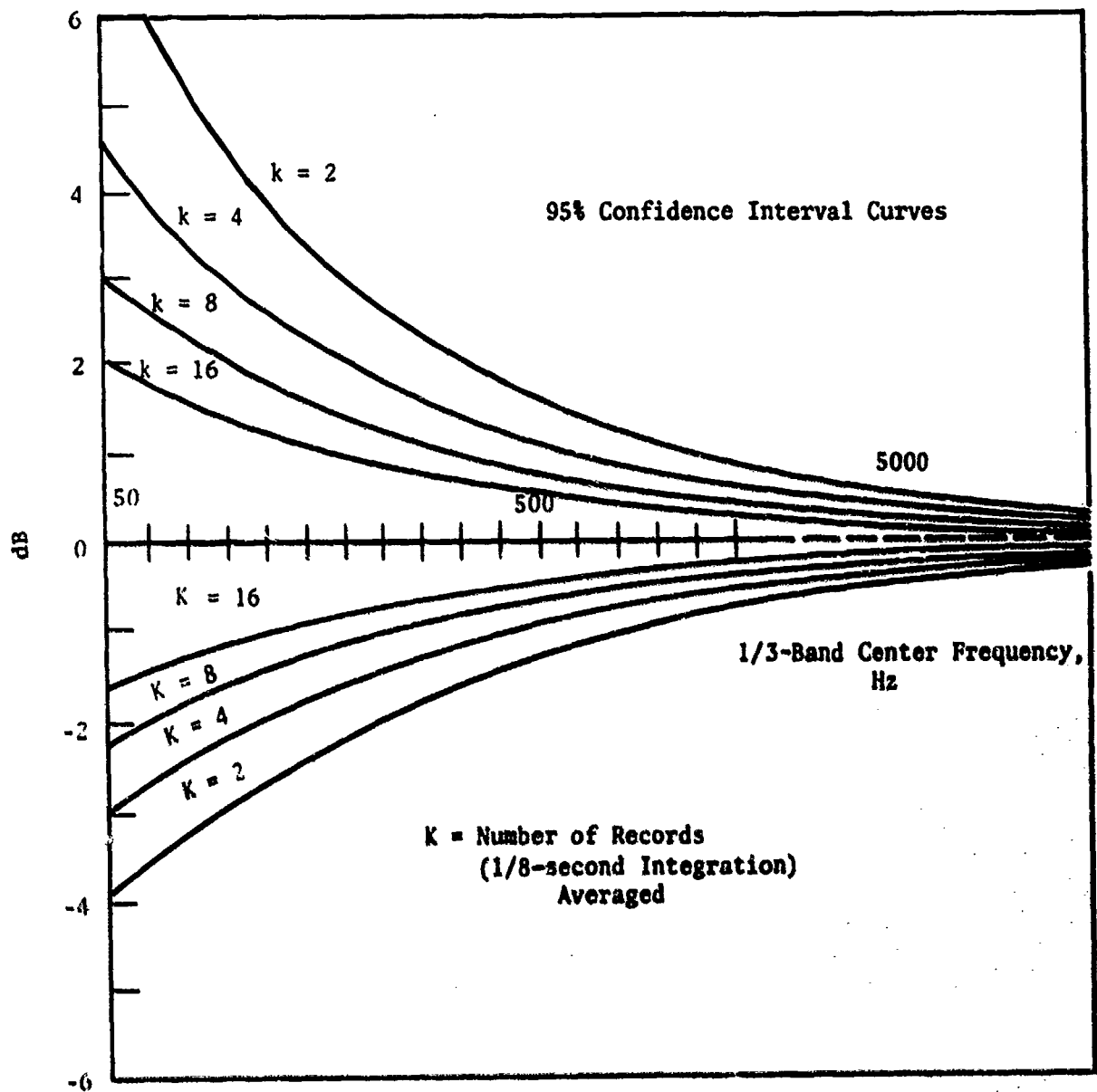


Figure E-2. 95% Confidence Interval Curves as a Function of Data Record Number.



in the enclosure in which measurements are made. In addition, instrument noise originating from the tape recorder, etc., will pollute the measurements. The effect of these noises is to add a bias error to the estimate as well as increase the variance. To evaluate these effects, the model is modified to include a vector of measurement noises  $\underline{W}$  which are assumed to be independent of the jet sources so that

$$E \left\{ \underline{\varepsilon} \underline{W}^T \right\} = 0 \quad (E-25)$$

The new model is

$$\underline{S} = \underline{A} \underline{P} + \underline{\varepsilon} + \underline{W} \quad (E-26)$$

Using

$$\hat{\underline{P}} = \underline{A}^{-1} \underline{S} \quad (E-27)$$

as the estimator for  $\underline{P}$ . Note that the expected value of  $\underline{P}$  is now

$$E \left\{ \hat{\underline{P}} \right\} = \underline{P} + \underline{A}^{-1} \underline{W} \quad (E-28)$$

Thus the estimate has the bias  $\underline{A}^{-1} \underline{W}$ . For the bias to be negligible,

$$\underline{P} \gg \underline{A}^{-1} \underline{W} \quad (E-29)$$

This says that the "estimated" source distribution with the ambient noise as an input to the estimator must be significantly less than the true source distribution. Equation E-29 suggests that the following procedure would be useful in evaluating the bias error in EM data:

1. Measure the ambient noise using the standard data recording procedure.
2. Use the data reduction program to obtain

$$\hat{\hat{\underline{P}}} = \underline{A}^{-1} \underline{W}$$

3. Compare  $\hat{\hat{\underline{P}}}$  to  $\hat{\underline{P}}$ 's obtained from the analysis of the jet data.  $\hat{\hat{\underline{P}}} \ll \hat{\underline{P}}$  means the bias error is negligible. (Here  $\ll$  means about 3 to 6 dB).

Bias in the estimate due to acoustic sources is difficult to bound because of the gross variations in the magnitude and sign of the elements of  $\underline{A}^{-1}$ . Such bounds have so far been too gross to be meaningful. A special and important case can be treated however. This is when the added noise

comes predominantly from the instrumentation (such as the tape recorder) and this dominates over the acoustic background noise. For this case it is reasonable to assume that

$$\underline{W} = \underline{U} W \quad (E-30)$$

or that the noise in each measurement has constant mean square value where  $\underline{u}$  is a vector of all "one's". For this case one must have

$$P_n \gg [A^{-1} \underline{U}]_n W \quad (E-31)$$

where  $[A^{-1} \underline{U}]_n$  can be seen to be the sum of the elements of the  $n$ th row of  $A^{-1}$ . Another way to write Equation E-31 is in terms of a Signal to Noise Ratio (SNR). This gives

$$SNR = 10 \log_{10} \left( \frac{P_n}{W} \right) \gg 10 \log_{10} [A^{-1} \underline{U}]_n \quad (E-32)$$

Some typical values of  $10 \log_{10} (A^{-1} \underline{u})_n$  are given in Table E-1. The bias error is more of a problem at the higher frequencies where the A matrix is well conditioned. As the A matrix becomes more singular, the sum of the elements of each row approaches zero and the sensitivity to bias error is reduced. The SNR given in Equation E-32 is not the recording SNR, but relates to the strength of the source distribution. The presence of bias error is best determined by the test given previously.

While the bias error might be small, the effect of ambient noise on the variance of the estimate may not be small. This effect may be determined by evaluating the variance of the estimator assuming the new model for the EM. With  $\underline{K}_W$  as the covariance matrix of  $\underline{W}$ ,

$$\begin{aligned} \underline{K}_P &= A^{-1} (A \underline{K}_P A^T + \underline{K}_W) A^{-T} \\ &+ \underline{K}_P + A^{-1} \underline{K}_W A^{-T} \end{aligned} \quad (E-33)$$

If as before, it is assumed that the measurement noises are uncorrelated and equal in magnitude,

$$\underline{K}_W = I \sigma_W^2 = I W^2/BT \quad (E-34)$$

where  $W$  is the mean square noise power in each measurement, and  $\underline{w}(t)$  is the assumed Gaussian noise vector. Thus

$$\underline{K}_P = \underline{K}_P + A^{-1} A^{-T} W^2/BT$$

Table E-1. Sum and Sum of Squares of Row Elements of Typical  $A^{-1}$  EM Matrices.

Frequency (Hz)	Distance Between Measurement	Sum of 40 <sup>th</sup> Row*		Sum of Squares of 40 <sup>th</sup> Row*	
		Actual	$10^* \log_{10}$	Actual	$5^* \log_{10}$
1,250	0.375	0.00292	-25.35	15269.8	20.9
1,600	0.125	0.00127	-28.90	83684.7	24.6
1,600	0.375	0.00446	-23.51	9298.4	19.8
1,600	0.5	0.00635	-21.97	5230.4	18.6
63,000	0.375	8.976	9.53	7633.0	19.4

\* The A-matrix was of dimension 80 x 80

and the individual estimate variances are

$$\text{VAR} \left\{ \hat{P}_n \right\} = \text{VAR} \left\{ \tilde{P}_n \right\} + [A^{-1}A^{-T}]_{n,n} W^2/BT \quad (\text{E-35})$$

where  $[A^{-1}A^{-T}]_{n,n}$  is the  $n$ th,  $n$ th diagonal element of  $A^{-1}A^{-T}$ . With the substitution used previously,

$$\text{VAR} \left\{ \tilde{P}_n \right\} = P_n^2/BT \quad (\text{E-36})$$

and,

$$P_n \gg [A^{-1}A^{-T}]_{n,n}^{1/2} W \quad (\text{E-37})$$

or in DB, the "Signal to Noise Ratio" defined as  $10 \log_{10} (P_n/W)$  must be

$$\text{SNR} \gg 5 \log_{10} \left\{ [A^{-1}A^{-T}]_{n,n} \right\} \quad (\text{E-38})$$

if the noise variance is not to dominate the source distribution variance. Note that  $[A^{-1}A^{-T}]_{n,n}$  is just the sum of the squares of the elements in the  $n$ th row of  $A^{-1}$  if  $A$  is symmetric. Thus while the sum of the elements of a row may be near zero, implying a low bias error, the sum of squares might be very high, implying a drastic increase in the variance of the estimator. Values of the right-hand side of Equation E-38 are tabulated in Table E-1 for some typical cases.

The best way to evaluate this error is to approximate  $P_n$  by  $\hat{P}_n$  and compare the value obtained from the estimation procedure with the ambient data before applying the analysis procedure. If the condition in Equation E-38 is satisfied, it is safe to use Figure E-2 to specify the confidence limits. If this condition is violated, the error in the estimate is probably much worse.

#### 4. ERRORS INDUCED BY WINDOW FUNCTION MEASUREMENT UNCERTAINTY

In the previous sections perfect knowledge of the  $A$  matrix (the matrix of window function values) has been assumed. However, in the case of the EM, the elements of  $A$  are determined by a series of measurements, containing uncertainty, followed by some sort of modeling procedure which hopefully reduces this uncertainty. The errors in the elements of  $A$  cause an error in the estimated value of  $\underline{P}$ ,  $\hat{P}$ . The purpose of this section is to evaluate the variance of  $\underline{P}$  due to this source of error. The simplifying assumption is made that there is no measurement uncertainty present, or that  $\underline{\epsilon} = \underline{0}$  in Equation E-7. A total variance including all of the effects may be determined by summing the variances of the individual effects.

Employing the above assumptions,

$$\underline{S} = A(\underline{w}_0) \underline{P} \quad (\text{E-39})$$

where  $\underline{w}_0$  is the vector of unique elements in the actual A matrix. The actual matrix used to estimate  $\underline{P}$  will have values of  $\underline{W}$  different from  $\underline{w}_0$ . Defining

$$\underline{W} = \underline{w}_0 + \delta \underline{W} \quad (\text{E-40})$$

and having as the estimate:

$$\hat{\underline{P}} = A^{-1}(\underline{W}) \underline{S} = A^{-1}(\underline{W}) A(\underline{w}_0) \underline{P} \quad (\text{E-41})$$

If  $\delta \underline{w}$  is assumed to be "small", the above may be linearized to find the perturbation in  $\underline{P}$ , which will be called  $\delta \underline{P}$ , caused by the error in  $\underline{W}$ ,  $\delta \underline{w}$ . Then

$$\hat{\underline{P}} = \hat{\underline{P}}_0 + \delta \hat{\underline{P}} \approx A^{-1}(\underline{w}_0) A(\underline{w}_0) \underline{P} + \underline{v}_w^T [A^{-1}(\underline{W}) A(\underline{w}_0) \underline{P}] \delta \underline{W} \Big|_{\underline{W}=\underline{w}_0} \quad (\text{E-42})$$

Observing that

$$\hat{\underline{P}}_0 = A^{-1}(\underline{w}_0) A(\underline{w}_0) \underline{P} = \underline{P} \quad (\text{E-43})$$

yields

$$\delta \hat{\underline{P}} = \underline{v}_w^T [A^{-1}(\underline{W}) A(\underline{w}_0) \underline{P}] \delta \underline{W} \Big|_{\underline{W}=\underline{w}_0} \quad (\text{E-44})$$

as the error in  $\hat{\underline{P}}$  due to a small error in  $\underline{W}$ . Since  $A^{-1}(\underline{W}) A(\underline{w}_0) \underline{P}_0$  is a vector,

$$\underline{v}_w^T [A^{-1}(\underline{W}) A(\underline{w}_0) \underline{P}_0] = \quad (\text{E-45})$$

$$\begin{bmatrix} \frac{\partial}{\partial w_1} (A^{-1}(\underline{W}) A(\underline{w}_0) \underline{P}_0)_1 & \dots & \frac{\partial}{\partial w_n} (A^{-1}(\underline{W}) A(\underline{w}_0) \underline{P}_0)_1 \\ \vdots & & \vdots \\ \frac{\partial}{\partial w_1} (A^{-1}(\underline{W}) A(\underline{w}_0) \underline{P}_0)_n & \dots & \frac{\partial}{\partial w_n} (A^{-1}(\underline{W}) A(\underline{w}_0) \underline{P}_0)_n \end{bmatrix}$$

Where  $(\quad)_k$  is the  $k^{\text{th}}$  row of the enclosed vector. Since  $\partial/\partial w_k (\quad)_1 = (\partial/\partial w_k (\quad))_1$ , and since

$$\frac{\partial}{\partial w_k} A^{-1}(\underline{w}) \Big|_{\underline{w}=\underline{w}_0} = -A^{-1}(\underline{w}_0) \left[ \frac{\partial}{\partial w_k} A(\underline{w}) \right] A^{-1}(\underline{w}_0) \Big|_{\underline{w}=\underline{w}_0} \quad (\text{E-46})$$

Then:

$$\begin{aligned} \underline{V}_{\underline{w}}^T [A^{-1}(\underline{w}) A(\underline{w}_0) \underline{P}_0] \Big|_{\underline{w}=\underline{w}_0} = \\ \left[ -A^{-1}(\underline{w}_0) \frac{\partial}{\partial w_1} [A(\underline{w})] \underline{P}_{0j} \dots -A^{-1}(\underline{w}_0) \frac{\partial}{\partial w_n} [A(\underline{w})] \underline{P}_0 \right] \\ = -A^{-1}(\underline{w}_0) \left[ \frac{\partial}{\partial w_1} [A(\underline{w})] \underline{P}_{0j} \dots \frac{\partial}{\partial w_n} [A(\underline{w})] \underline{P}_0 \right] \end{aligned} \quad (\text{E-47})$$

If it is assumed that  $A$  is a Toeplitz and symmetric matrix, then  $A(\underline{w})$  may be written

$$A(\underline{w}) = \begin{bmatrix} w(1) & \dots & \dots & w(n) \\ w(2), w(1) & w(2) & \dots & w(n-1) \\ \vdots & & \vdots & \\ w(n) & \dots & w(2) & w(1) \end{bmatrix} \quad (\text{E-48})$$

where  $\underline{w}$  is the defining row of the Toeplitz matrix. Thus

$$[A(\underline{w})]_{ij} = w(|i-j| + 1) \quad \begin{matrix} i = 1 \dots N \\ j = 1 \dots N \end{matrix} \quad (\text{E-49})$$

and

$$\left\{ \frac{\partial}{\partial w_k} A(\underline{w}) \right\}_{ij} = \delta(|i-j| + 1 - k)$$

If it is assumed that  $\delta \underline{w}$  represents a random error, and the model used for  $\underline{w}_0$  is such that

$$E(\underline{w}) = \underline{w}_0 \quad (\text{E-50})$$

Then the covariance matrix of the estimate due to the uncertainty in  $\underline{w}$  may be written

$$\underline{K}_{\hat{p}} = A^{-1}(\underline{w}_0) \phi \underline{K}_w \phi^T A^{-T}(\underline{w}_0) \quad (\text{E-51})$$

where  $\underline{K}_w$  is the covariance matrix of  $\underline{w}$  and

$$[\phi]_{ij} = \sum_{k=1}^N \delta(|i-k| + 1 - j) P_k \quad (\text{E-52})$$

The basic dependencies may be observed by examining the above.

The covariance of the estimation error is determined by the actual window function as embodied by  $A^{-1}(\underline{w}_0)$ , the measured source distribution as embodied by  $\phi$ , and the error in  $\underline{w}$  as embodied by  $\underline{K}_w$ . Equations E-51 and E-52 may be evaluated for any assumed set of conditions.

## 5. NUMERICAL EVALUATION STUDY

The equations developed in the previous four sections of this Appendix were evaluated for four cases closely related to the experimental conditions encountered with the 18-inch elliptical mirror. Measured window function data was used in the analysis and the variance of this was estimated by fitting a cubic polynomial through the data and using the variance of the resulting regression. Details of the test cases are given in Figure E-3.

The source distribution assumed in all cases was a point source of unit magnitude at the center of the source distribution line. Other source distributions can be derived from this case by application of the superposition theorem of acoustics.

The output of this numerical study was an estimate of the error in the measurement values after window function removal due to:

- Error in the determination of the true window function of the mirror.
- Statistical error due to the fact the source is random.

Thus this result indicates an upper limit on the mirror's performance since such error sources as:

- Alignment and positioning errors in mirror placement
- Background and measurement noise

Number of Source and Measurement Points: 80

Band Width = 1/3-Octave Centered about Frequency Shown in  
Table E-2

Integration Time Used in Data Reduction Process: 0.125 sec

Measurement Spacing - As Shown in Table E-2

Source Distribution - Point Source of Unit Magnitude at Source  
Location Number 40:

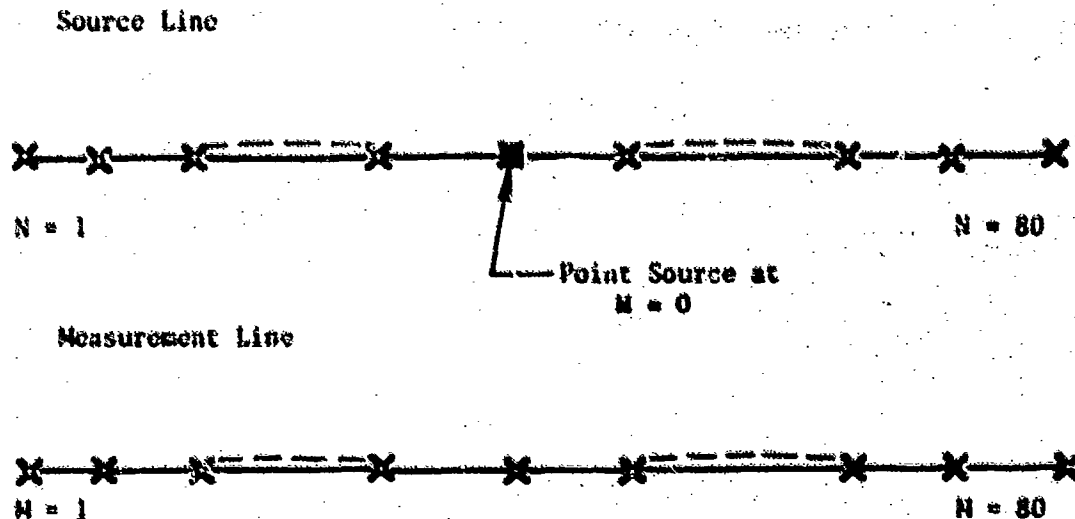


Figure E-3. Details of Test Cases Used in Numerical  
Analysis.



- Variation of mirror response with frequency within the bandwidth of the analysis filters
- Numerical "noise" errors in the data reduction process due to ill conditioning, etc.

are not included in this numerical evaluation.

In reducing this data, it was noted that the errors for the 80 source estimate points could be divided into two groups: the error at the source point and the errors at the other points where there was no source. The error at the source point represents the accuracy of determining the value of a strong source. The non-source point errors (which were all nearly the same magnitude) indicate the value of the "noise floor" of the measurement, and are thus a measure of the dynamic range of the procedure. Attempting to determine the strength of two sources whose magnitudes in dB differ by more than this noise floor value will result in the smaller of the two not being detected. The values obtained for the test cases are shown in Table E-2.

## 6. CONCLUSIONS

The following conclusions may be drawn from this study:

1. A small ellipsoidal mirror such as the 18" mirror developed for this program is capable of obtaining useful data when:
  - a. The source frequency is greater than 1000 Hz.
  - b. The source dynamic range is less than 25 dB
  - c. The source spacing is greater than 0.5 inch
  - d. The measurement accuracy required is less tight than  $\pm 2.5$  dB.
2. The window function removal procedure is very sensitive to any error. Especially those in:
  - a. The assumed shape of the window function. This includes measurement uncertainty in its determination, the mechanical repeatability of the mirror manipulation mechanism, and mathematical modeling errors.
  - b. The numerical procedure used to solve the estimation equation and the word length specified in the analysis.
  - c. Background and instrument noise.
3. The presence of errors in analyzed data may be difficult to detect due to high correlation between adjacent errors. Check procedures, like those suggested in this report, should be included in the data procedure to guarantee the quality of the data.

Table E-2. Theoretical Statistical Errors for a Single Point Source at Center of Measurement Set - 18-Inch Elliptical Mirror.

Frequency	Source Measurement Separation (inches)	Variance of Source Point	2 x Standard Deviation of Source Point	2 Standard Deviation Measurement Error (dB)
1600	0.125	0.014796	0.2433	(+0.95) (-1.2)
1600	0.375	0.01472	0.2427	(+0.95) (-1.2)
1600	0.5	0.014682	0.2423	(+0.95) (-1.2)
1250	0.375	0.044819	0.4234	(1.53) (-2.39)

Frequency	Source Measurement Separation (inches)	Typical Variance of Nonsource Point	2 x Standard Deviation of Nonsource Point	dB Below Source at 2 Standard Deviations
1600	0.125	$2.6577 \times 10^{-8}$	$3.26 \times 10^{-4}$	-34.9
1600	0.375	$2.7 \times 10^{-7}$	$1.04 \times 10^{-3}$	-29.8
1600	0.5	$4.99 \times 10^{-7}$	$1.41 \times 10^{-3}$	-28.5
1250	0.375	$1.406 \times 10^{-6}$	$2.037 \times 10^{-3}$	-26.2

## APPENDIX F

### 1.0 DATA REDUCTION PROCEDURES

#### DETAILED DATA REDUCTION PROCEDURES

A detailed description of the data reduction procedure is given in the following sections. All the constants and equations in this appendix are given in English units as actually used in the data reduction programs.

#### FLOW RATES

The mass flow through the outer nozzle was measured with a 1.248-in. throat diameter choked venturi meter, located as shown in Figure 4-2, Section 4.2. The flow rate was calculated using the equation

$$W_o = C_{DVo} \frac{K_{Vo} P_{TVo} A_{Vo}}{\sqrt{T_{TVo}}} \quad (F-1)$$

The critical flow factor,  $K_{Vo}$ , was calculated as a function of total pressure and temperature:

$$K_{Vo} = 0.5282 + a T_{TVo} + b T_{TVo}^2 + c T_{TVo}^3 + (1.86 \times 10^{-5}) P_{TVo} e^{-0.0067(T_{TVo} - 500.00)} \quad (F-2)$$

where

$$\begin{aligned} a &= 1.654 \times 10^{-5} \\ b &= -2.119 \times 10^{-8} \\ c &= 6.008 \times 10^{-12} \end{aligned}$$

where  $T_{TVo}$  and  $P_{TVo}$  are in °R and psia, respectively.

This equation was obtained by curve-fitting tabulated values in Reference 36.

The meter flow coefficient was calculated as a function of the throat Reynolds number using the following semiempirical relation:

$$C_{DVo} = 0.983 (-0.0691 RN^{-0.183}) \quad (F-3)$$

The 0.9983 factor in the equation is to account for the effects of sonic line distortion.

The meter total pressure,  $PT_{V_0}$ , was determined by measuring the static pressure,  $P_{V_0}$ , upstream of the venturi throat and calculating the total pressure as:

$$PT_{V_0} = P_{V_0} / 0.995 \quad (F-4)$$

The 0.9995 factor is the static-to-total pressure ratio for that Mach number based on the ratio of the area at the measurement plane to the meter throat area. The static pressure was measured by six taps, and each was sampled four times with dummy scanning valves during the taking of each data point. These 24 readings were averaged to determine the static pressure.

The meter total temperature,  $T_{V_0}$ , was determined using five platinum resistance thermometers located upstream of the venturi. Each thermometer was read twice and the readings averaged.

The mass flow through the inner nozzle was measured with either of two choked venturi meters located as shown on Figure 4-2, Section 4.2. The flow for high inner flow rates was measured using the 1.1398-in.-throat-diameter venturi. The flow for the low inner flow rate testing was measured with the 0.3985-in.-throat-diameter venturi. For both meters, the flow rate was calculated using the equation

$$W_1 = \frac{K_{V_1} P_{V_1}}{60.00 \sqrt{T_{V_1}}} \quad (F-5)$$

This equation is based on calibration of the meters made by the manufacturer. The  $K_{V_1}$  factors based from the calibration were

$$K_{V_1} = (-1.9153 \times 10^{-7}) P_{V_1}^2 + (1.10896 \times 10^{-3}) P_{V_1} + 32.29807 \quad (F-6)$$

for the 1.1398-in.-diameter meter, and

$$K_{V_1} = (-3.02076 \times 10^{-8}) P_{V_1}^2 + (9.49693 \times 10^{-5}) P_{V_1} + 3.93951 \quad (F-7)$$

for the 0.3985-in.-diameter meter.

The meter static pressure ( $P_{V_1}$ ) was measured upstream of the venturi throat with four static taps, each was read twice, and the eight numbers averaged. The venturi total temperatures were measured with three thermocouples (each read twice) located upstream of the meter.

### FLOW COEFFICIENTS

The flow coefficient of a nozzle is defined as the ratio of actual mass flow rate through the nozzle to the ideal isentropic flow rate at the temperature and pressure of the flow.

$$C_D = \frac{\text{measured } W}{\text{ideal } W} \quad (\text{F-8})$$

The ideal weight flow for the outer nozzle flow was calculated from the relation

$$W_{I_O} = \frac{K_O A_O P_{T_O}}{\sqrt{T_{T_O}}} \left( \frac{A^*}{A_O} \right) \quad (\text{F-9})$$

$A_O$  is the outer nozzle physical throat area and

$$K_O = 0.5282 + a T_{T_O} + b T_{T_O}^2 + c T_{T_O}^3 + (1.86 \times 10^{-5}) P_{T_O} e^{-0.0067(T_{T_O} - 500.00)}$$

where  $a$ ,  $b$ , and  $c$  are as given in the previous section, and  $T_{T_O}$  and  $P_{T_O}$  are in ° R and psia, respectively.

The nozzle temperature,  $T_{T_O}$ , and pressure,  $P_{T_O}$ , were measured upstream of the nozzle throat with multielement rakes. These rakes were placed downstream of choke plates and screens which provided a flow with no pressure profile distortion at the rakes to assure an accurate pressure measurement. The outer nozzle rakes contained eight total pressure probes, the readings of which were averaged to arrive at  $P_{T_O}$ , and two thermocouples, the readings of which were averaged. The inner nozzle rakes contained five Pitot tubes and one thermocouple.

For values of nozzle pressure ratio greater than 1.8929,  $A^*/A_O$  in the ideal weight flow equation is equal to one. For lower pressure ratios,  $A^*/A_O$  was calculated from the isentropic relationships

$$A^*/A_O = \frac{216}{125} M_O \left( 1 + \frac{M_O^2}{5} \right)^{-3} \quad (\text{F-10})$$

where

$$M_o = \left\{ 5 \left[ \left( \frac{P_{T_o}}{P_a} \right)^{0.28571} - 1 \right] \right\}^{1/2}$$

The inner nozzle ideal weight flow was calculated in identical fashion as the outer nozzle, but using the inner nozzle throat area, flow pressure, and temperature. For the low inner flow testing, the inner nozzle total pressures required to supply the low flow rates were generally lower than ambient pressure due to the pumping effect of the outer flow. In these cases, the ideal flow rate and flow coefficients are meaningless and were not calculated.

#### THRUST MEASUREMENTS

The thrust of the exhaust nozzles is defined as the axial exit momentum of the exhaust flow, plus the excess of exit pressure over ambient pressure times the exit area normal to the axis, minus the axial drag on the nozzle external surface; i.e.,

$$F = \int_{A_{\text{exit}}} d(WV)_{\text{axial}} + \int_{A_{\text{exit}}} (P - P_a) dA - D_{\text{external}}. \quad (F-11)$$

The external drag consists of both the pressure drag on the boattail surface and the axial component of skin friction. Figure F-11 shows a control volume applied to the test nozzles. Writing the momentum equation in the axial direction for this control volume demonstrates how the thrust was measured for the tests:

$$F = F_{LC} + F_{AS} + A_1(P_1 - P_a) + A_2(P_2 - P_a) + A_3(P_3 - P_a) + A_4(P_4 - P_a) \quad (F-12)$$

where  $F_{LC}$  is the axial force applied to the load cell and  $F_{AS}$  is the axial force applied at the boundary of the control volume by the air supply tubes. The static pressures  $P_1$ ,  $P_2$ ,  $P_3$ , and  $P_4$  were measured with two static taps  $180^\circ$  apart at each of the four areas (see Figure 4-11, Section 4.4.3). The force measuring system was calibrated by applying known forces and correlating this force against the load cell output, as previously described in Section 3.0. This calibration provided a linear relationship between the applied load and the load cell output in millivolts which was used to determine the load cell plus air supply tube force as follows:

$$\text{Applied Load} = a(mv) + b = F_{LC} + F_{AS} \quad (F-13)$$

where  $a$  and  $b$  are constants determined by the calibrations and  $mv$  is the load cell reading in millivolts. The load cell was sampled 48 times during the

taking of each point, the above calculation made for each sample, and the results averaged to yield the measured force.

An adjustment was made to the measured thrust to account for external friction drag on the cylindrical section upstream of the nozzle shroud. The axial force on this 8.0-in.-diameter section, which extended from the metric-break to the attach-point of the nozzle shrouds, was not included in the nozzle net thrust. The friction drag was calculated by the equation:

$$D_f = \frac{\gamma}{2} P_a M_a^2 A_c C_f \quad (F-14)$$

where  $A_c$  is the wetted surface area of the cylindrical piece 8.0 in. in diameter and 7.0 in. in length. The drag coefficient was calculated from

$$C_f = 0.288 (1 + 0.2 M_a^2)^{-0.5} (\log_{10} RN_x)^{-2.45} \quad (F-15)$$

where  $RN_x = 9.37 RN_a$ ;  $RN_a$  being the Reynolds number per foot based on the ambient stream Mach number, temperature, and pressure.

The thrust of the nozzles for this test was therefore given by:

$$F = F_{LC} + F_{AS} + A_1(P_1 - P_a) + A_2(P_2 - P_a) + A_3(P_3 - P_a) + A_4(P_4 - P_a) + D_f \quad (F-16)$$

or, substituting the equations by which  $F_{LC} + F_{AS}$  and  $D_f$  were calculated:

$$F = a(mv) + b + A_1(P_1 - P_a) + A_2(P_2 - P_a) + A_3(P_3 - P_a) + A_4(P_4 - P_a) + \frac{\gamma}{2} P_a M_a^2 A_c C_f$$

#### THRUST COEFFICIENT

The thrust coefficient is the ratio of the measured nozzle thrust to the ideal thrust of the inner duct flow plus the ideal thrust of the outer duct flow. The ideal thrust for each stream equals the actual mass flow rate times the ideal velocity; i.e., the velocity of the stream expanded isentropically from the total pressure to the ambient pressure. The equation for the thrust coefficient is thus:

$$C_T = \frac{F}{W_o V_{I_o} + W_1 V_{I_1}} \quad (F-17)$$

The ideal thrust for the nozzles was calculated using the dimensionless ideal-thrust function which is a function of only the nozzle pressure ratio.

$$\frac{W_I}{P_T} \frac{V_I}{A^*} = \gamma \left( \frac{2}{\gamma+1} \right)^{\frac{\gamma}{\gamma-1}} \left( \frac{\gamma+1}{\gamma-1} \right)^{1/2} \left[ 1 - (P_a/P_T)^{\frac{\gamma-1}{\gamma}} \right]^{1/2}$$

$$= 1.81163 \sqrt{1 - (P_a/P_T)^{0.28571}} \text{ for } \gamma = 1.4$$
(F-18)

The ideal thrust for the inner and outer streams was then:

$$W_I V_{I1} = C_{D1} P_{T1} A_1 \left( \frac{A_1^*}{A_1} \right) \left( \frac{W_{I1} V_{I1}}{P_{T1} A_1^*} \right)$$

$$W_O V_{I0} = C_{D0} P_{T0} A_0 \left( \frac{A_0^*}{A_1} \right) \left( \frac{W_{I0} V_{I0}}{P_{T0} A_0^*} \right)$$
(F-19)

For pressure ratios greater than 1.8929,  $A^*/A = 1.0$ . For pressure ratios less than this,  $A^*/A$  was calculated as described in the previous section on flow coefficients.

During much of the low inner flow rate testing, the total pressure of the inner nozzle flow was lower than ambient. In these cases, the ideal thrust of the inner nozzle was set equal to zero.

For the static thrust tests of the STA model, a dimensionless stream-thrust parameter was also calculated as:

$$f_9 = \frac{F + P_a A_9}{P_T A_9}$$
(F-20)

where  $A_9$  is the STA nozzle exit area.

#### PRESSURE DATA

Total pressures in the models and static pressures on the model surfaces were measured with scanning value/transducer arrangements. The individual static pressure readings were also nondimensionalized by the ambient pressure. Pressure forces on the aft-facing portions of the shroud, outer plug, inner plug, and suppressor bases were calculated by multiplying the difference between the static pressure at each tap and ambient pressure by an incremental projected area represented by the particular tap and summing the products, i.e.,

$$F_p + \sum (P - P_a) \Delta A$$
(F-21)



These pressure forces were also nondimensionalized by the total ideal thrust of the nozzle:

$$\frac{F_P}{W_i V_{I_i} + W_o V_{I_o}}$$

#### DETAILED MODEL DESCRIPTION

Geometric details of the annular, suppressed models are presented in Figures F-1 through F-15.



**Figure F-1. Geometric Details of Configuration SC-1, N = 20, Baseline Plug.**

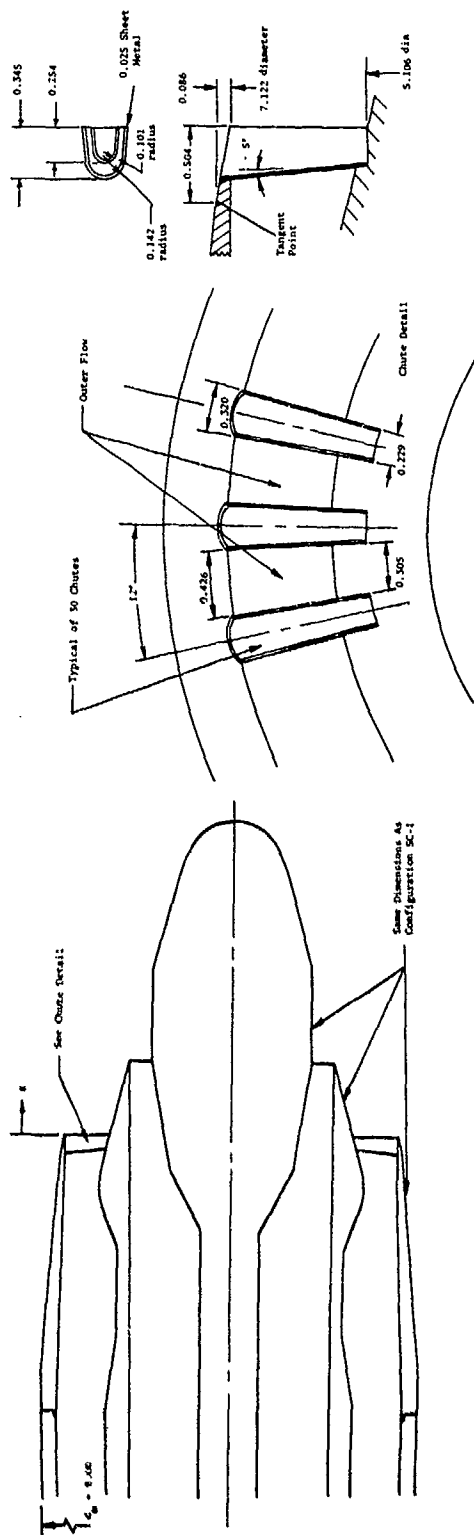
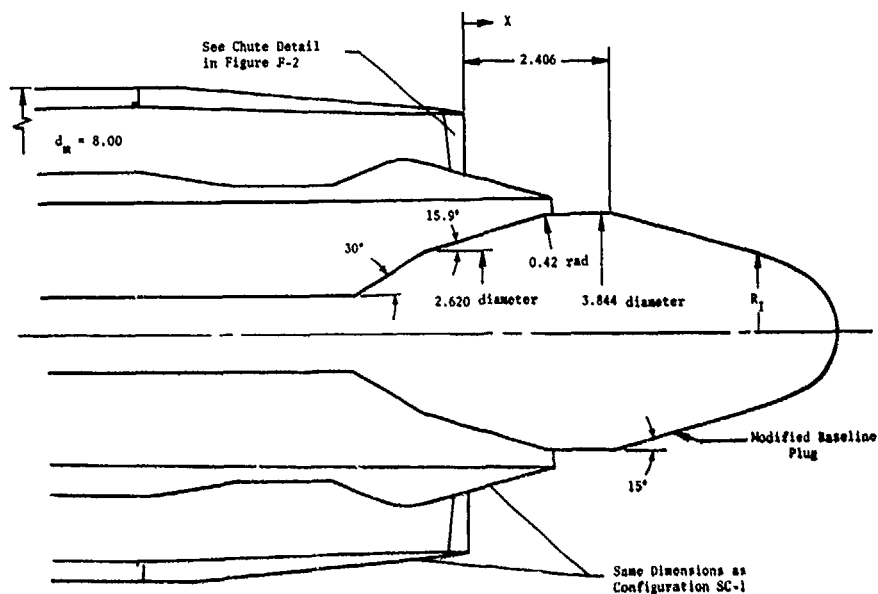


Figure F-2. Geometric Details of Configuration SC-2, N = 30, Baseline Plug.



Straight Line

Inner-Plug Geometry	
Axial Coordinate, $X/d_m$	Radial Coordinate, $R_i/d_m$
0.300	0.240
0.579	0.165
0.584	0.164
0.623	0.151
0.662	0.138
0.682	0.130
0.701	0.121
0.721	0.110
0.740	0.095
0.759	0.075
0.779	0.040
0.786	0

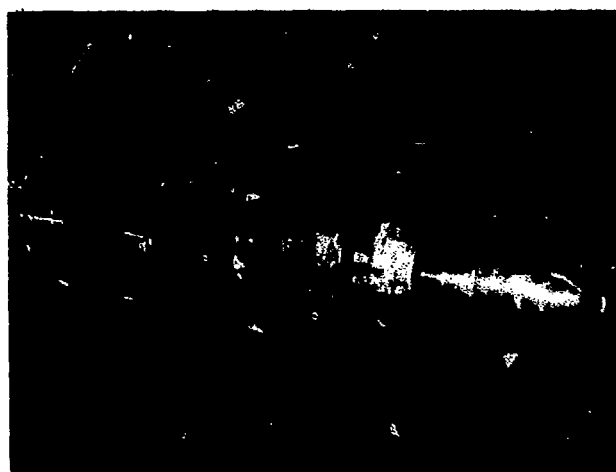


Figure F-3. Geometric Details of Configuration SC-3, Modified Baseline Plug.



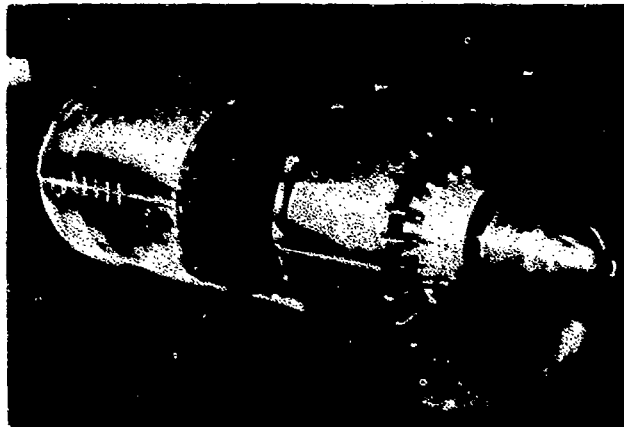
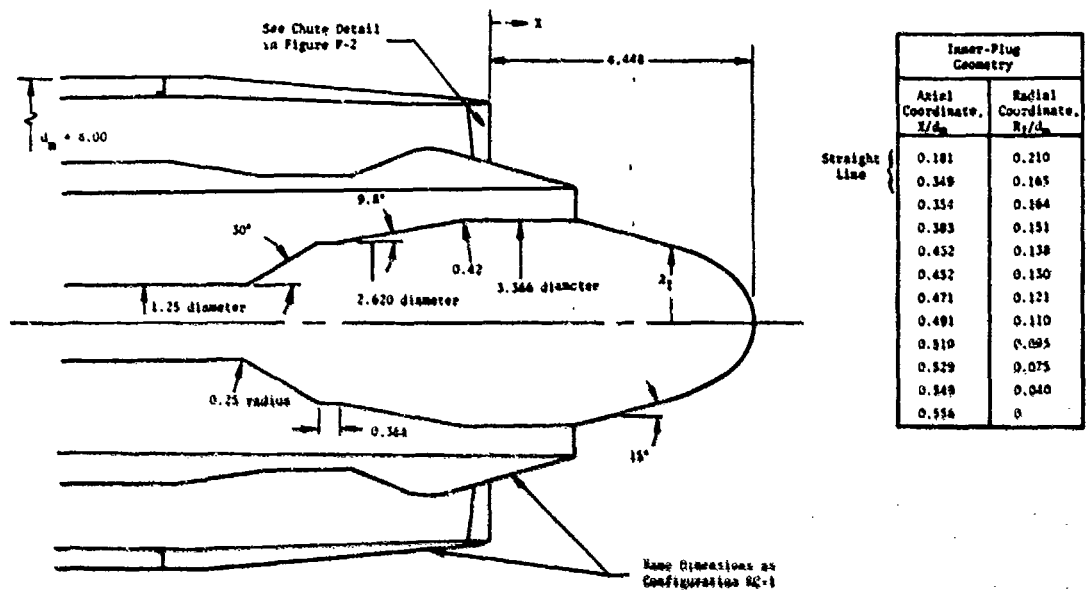


Figure F-5. Geometric Details of Configuration SC-5, N = 30, Forward Baseline Plug.

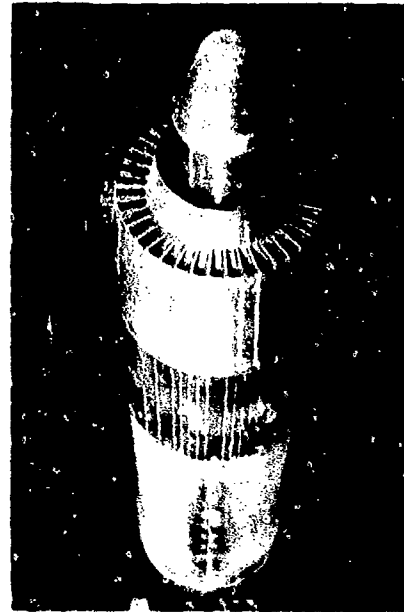
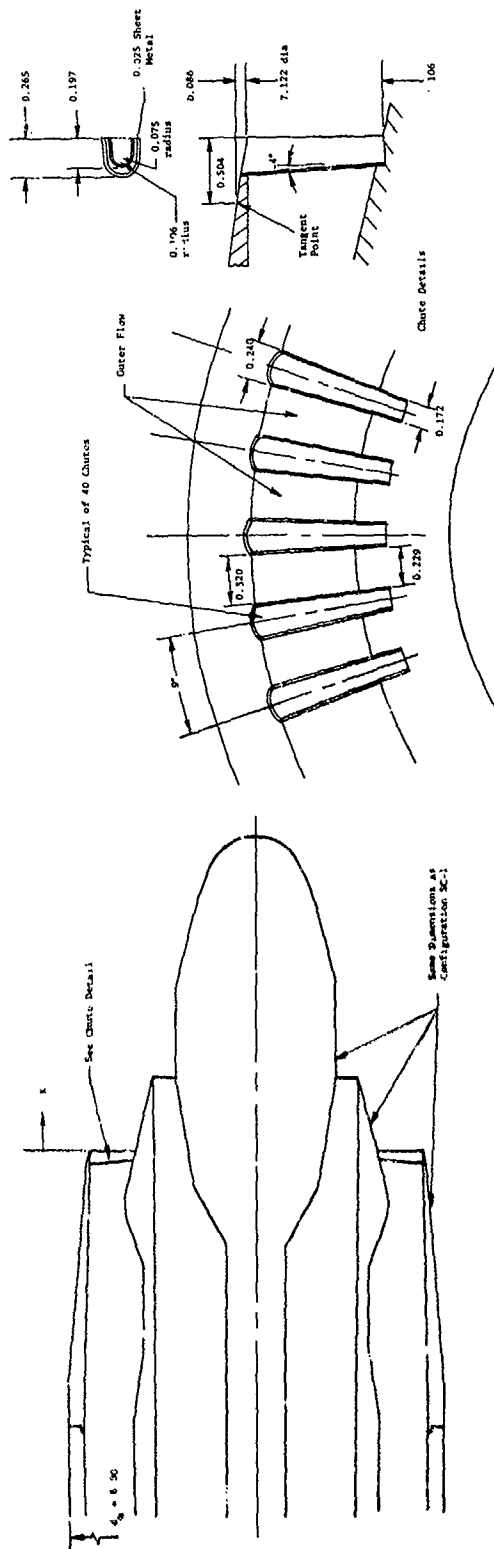


Figure F-6. Geometric Details of Configuration SC-6, N = 40, Baseline Plug.

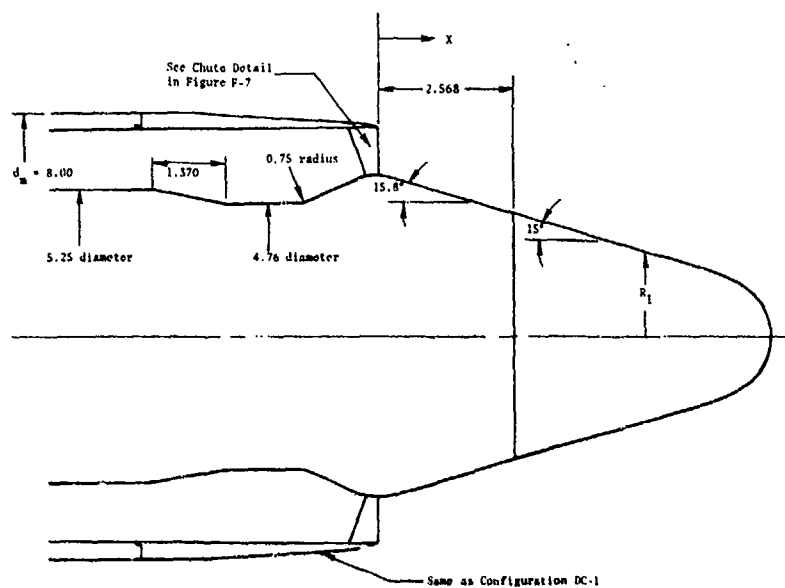


Outer Plug Geometry	Radial Coordinate, $\frac{R}{R_0}$	
	Actual Coordinate, $\frac{R}{R_0}$	Radial Coordinate, $\frac{R}{R_0}$
Straight Line	- 0.170	0.252
	- 0.044	0.159
	- 0.089	0.154
	- 0.029	0.187
Spiral Line	- 0.020	0.134
	- 0.070	0.159
	0	0.160
	0.010	0.159
Spiral Line	0.020	0.187
	0.029	0.155
	0.031	0.154
	0.160	0.282
Spiral Line	0.221	0.281

Inner-Clug Colum: 17	Actual Coordinate, 1/6 m	Radial Coordinate, 1/6 m
0.551	0.210	0.165
0.719	0.165	0.164
0.724	0.164	0.151
0.765	0.151	0.138
0.402	0.138	0.121
0.822	0.121	0.110
0.441	0.110	0.095
0.846	0.095	0.075
0.859	0.075	0.040
0.919	0.040	

**Figure F-7. Geometric Details of Configuration DC-1, AR = 1.5, Full Plug.**





Inner-Plug Geometry		
	Axial Coordinate, $X/d_m$	Radial Coordinate, $R_i/d_m$
Straight Line	- 0.170	0.298
	- 0.044	0.352
	- 0.039	0.354
	- 0.029	0.357
	- 0.020	0.358
	- 0.010	0.359
	0	0.360
	0.010	0.359
	0.020	0.357
	0.029	0.355
Straight Line	0.031	0.354
	0.286	0.282
	0.719	0.165
	0.724	0.164
	0.763	0.151
	0.802	0.138
	0.822	0.130
	0.841	0.121
	0.861	0.110
	0.880	0.095
	0.899	0.075
	0.919	0.040
	0.926	0

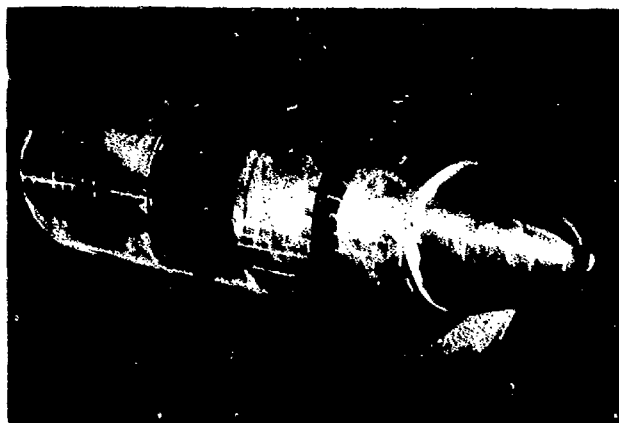
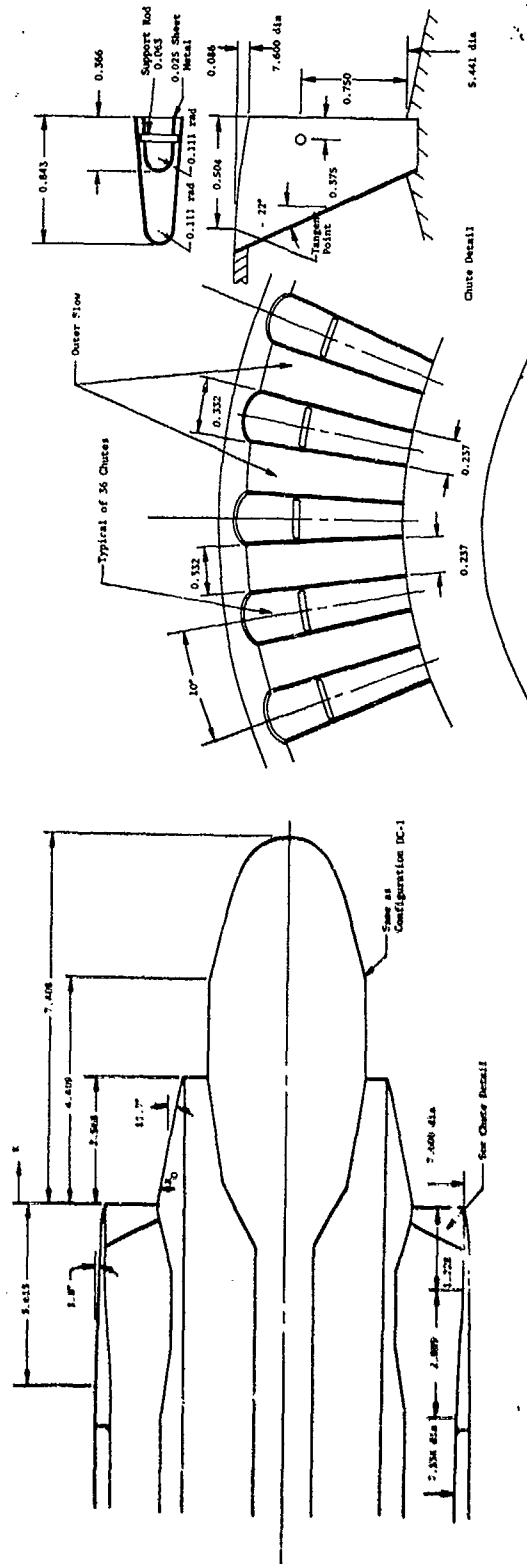


Figure F-8. Geometric Details of Configuration DC-2, AR = 1.5, Full Plug.



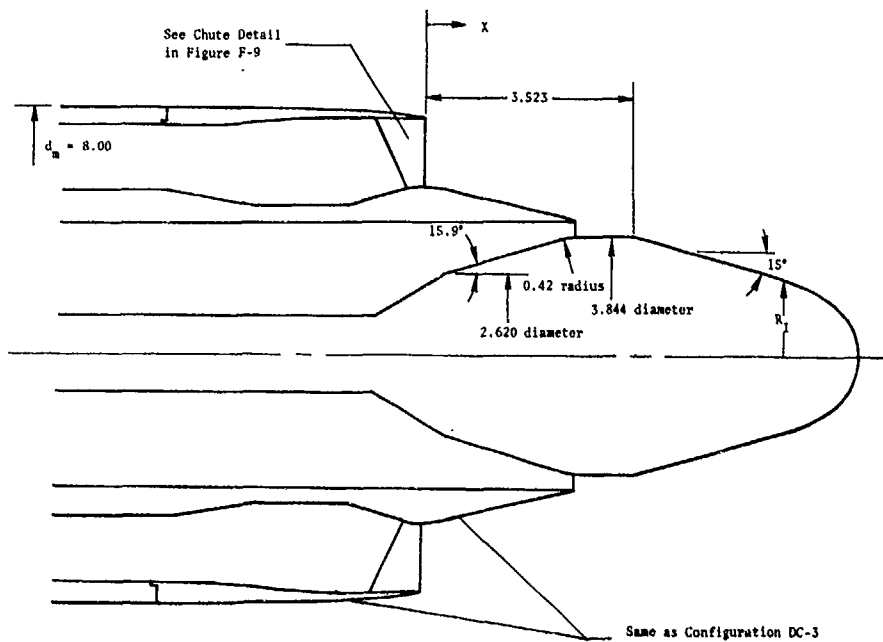
Outer-Plug Geometry	
Axis 1 Coordinate, $X/d_n$	Axis 1 Coordinate, $Y/d_n$
- 0.159	0.398
- 0.056	0.329
- 0.049	0.332
- 0.039	0.335
- 0.029	0.337
- 0.020	0.338
- 0.010	0.339
0	0.340
0.010	0.339
0.020	0.337
0.025	0.336
0.286	0.282
0.321	0.275

Straight Line

Straight Line



Figure F-9. Geometric Details of Configuration DC-3, AR = 2.0, Baseline Plug.



Inner-Plug Geometry	
Coordinate, $X/d_m$	Coordinate, $R_z/d_m$
0.440	0.240
0.719	0.165
0.724	0.164
0.763	0.151
0.802	0.138
0.822	0.130
0.841	0.121
0.861	0.110
0.880	0.095
0.899	0.075
0.919	0.040
0.926	0

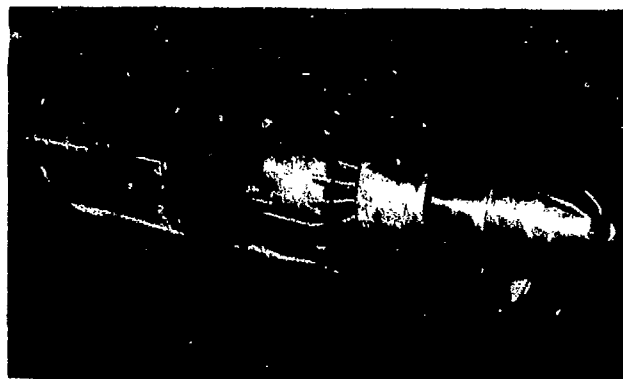
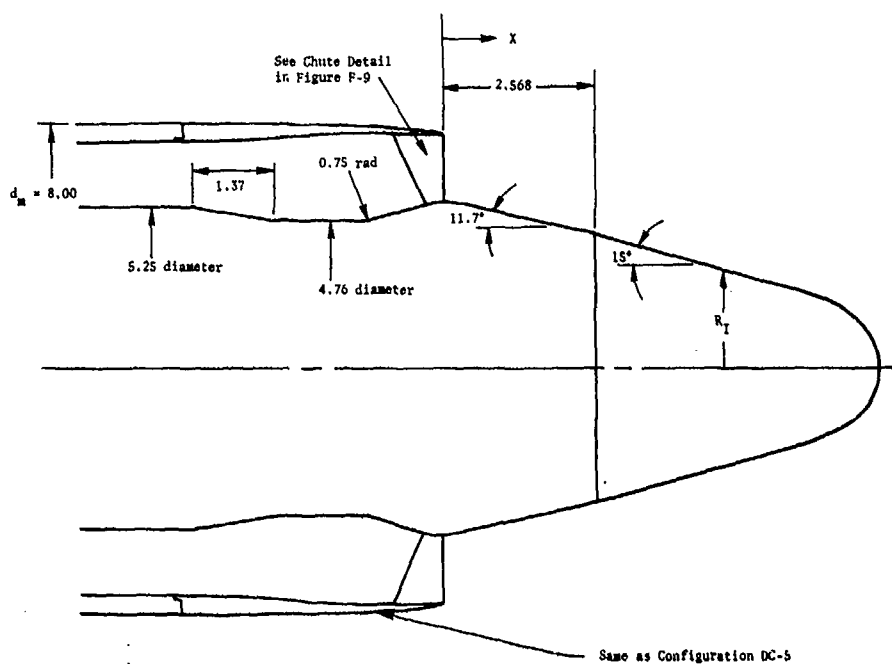


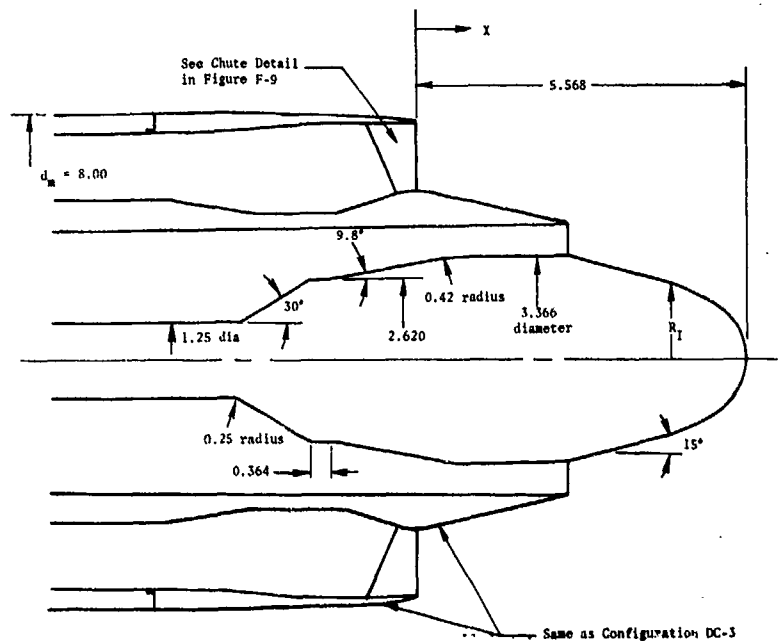
Figure F-10. Geometric Details of Configuration DC-4, AR = 2.0, Modified Baseline Plug.



Inner-Plug Geometry	
Axial Coordinates, $X/d_m$	Radial Coordinates, $R_r/d_m$
- 0.159	0.298
- 0.056	0.329
- 0.049	0.332
- 0.039	0.335
- 0.029	0.337
- 0.020	0.338
- 0.010	0.339
0	0.340
0.010	0.339
0.020	0.337
0.025	0.336
0.286	0.282
0.719	0.165
0.724	0.164
0.763	0.151
0.802	0.138
0.822	0.130
0.841	0.121
0.861	0.110
0.880	0.095
0.899	0.075
0.919	0.040
0.926	0



Figure F-11. Geometric Details of Configuration DC-5, AR = 2.0, Full Plug.



Inner-Plug Geometry	
Axial Coordinate, $X/d_m$	Radial Coordinate, $R_r/d_m$
0.321	0.210
0.489	0.165
0.494	0.164
0.533	0.151
0.572	0.138
0.592	0.130
0.611	0.121
0.631	0.110
0.650	0.095
0.669	0.075
0.689	0.040
0.696	0

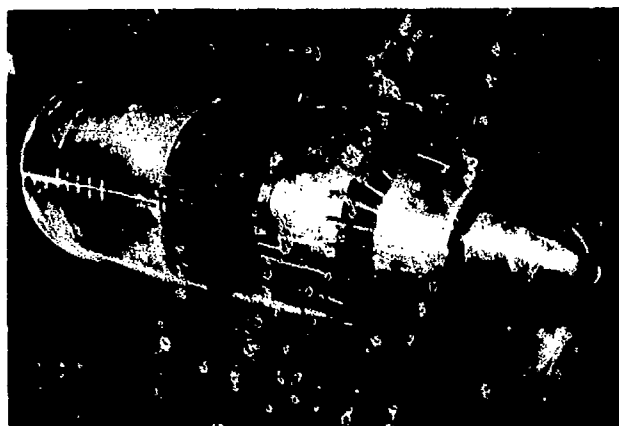


Figure F-12. Geometric Details of Configuration DC-6, AR = 2.0, Forward Plug.



673

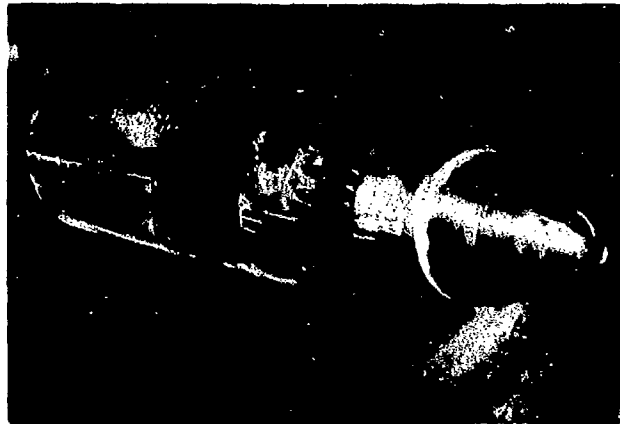
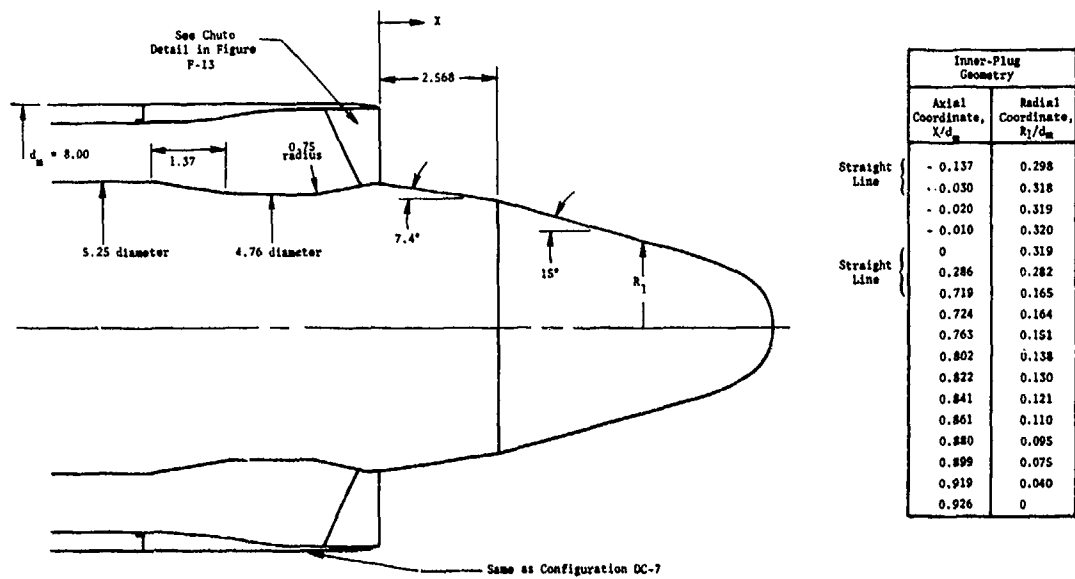


Figure F-14. Geometric Details of Configuration DC-8, AR = 2.5; Full Plug.

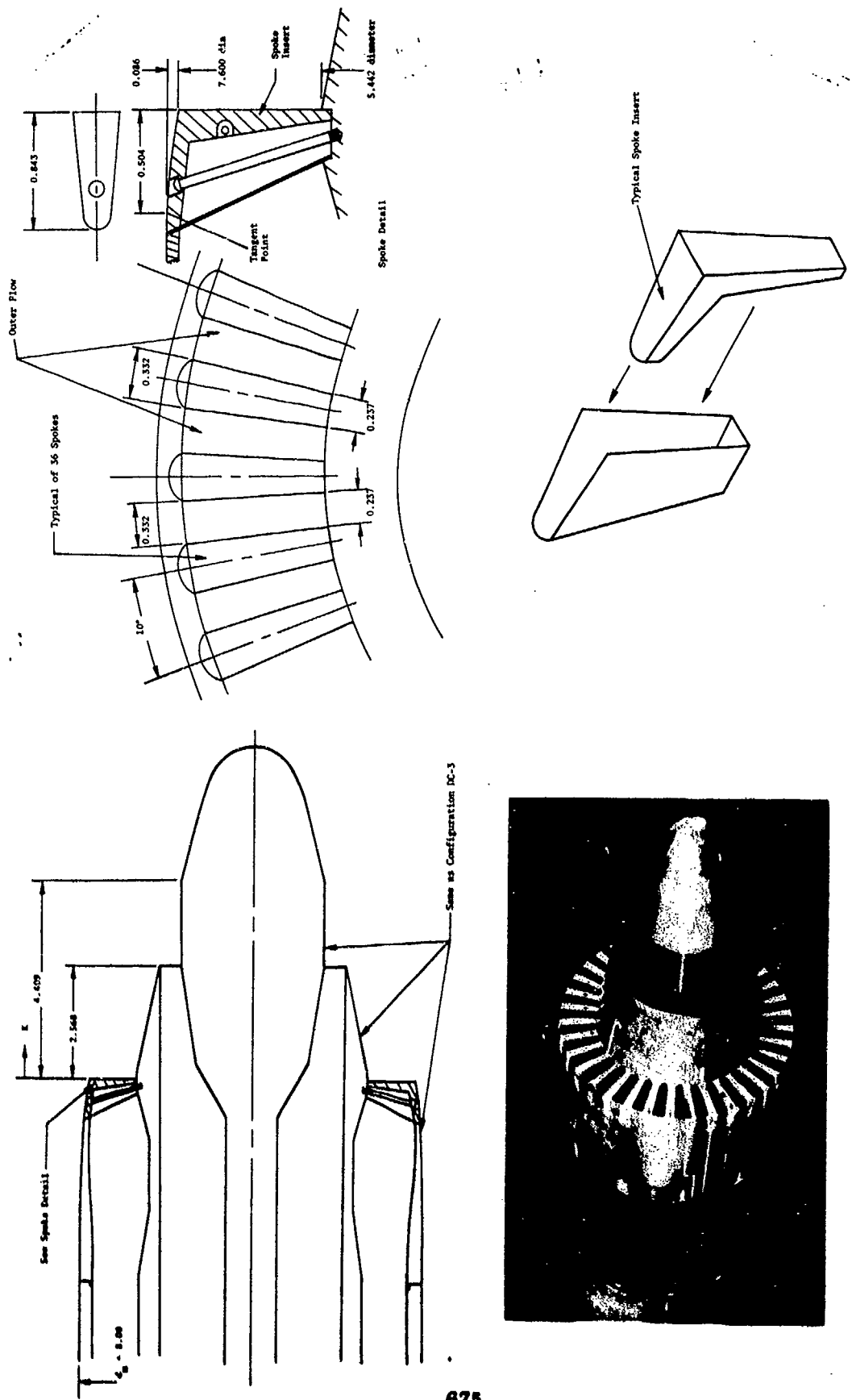


Figure F-15. Geometric Details of Configuration DC-3 (Spoke),  $N = 36$ ,  $AR = 2.0$ , Baseline Plug.

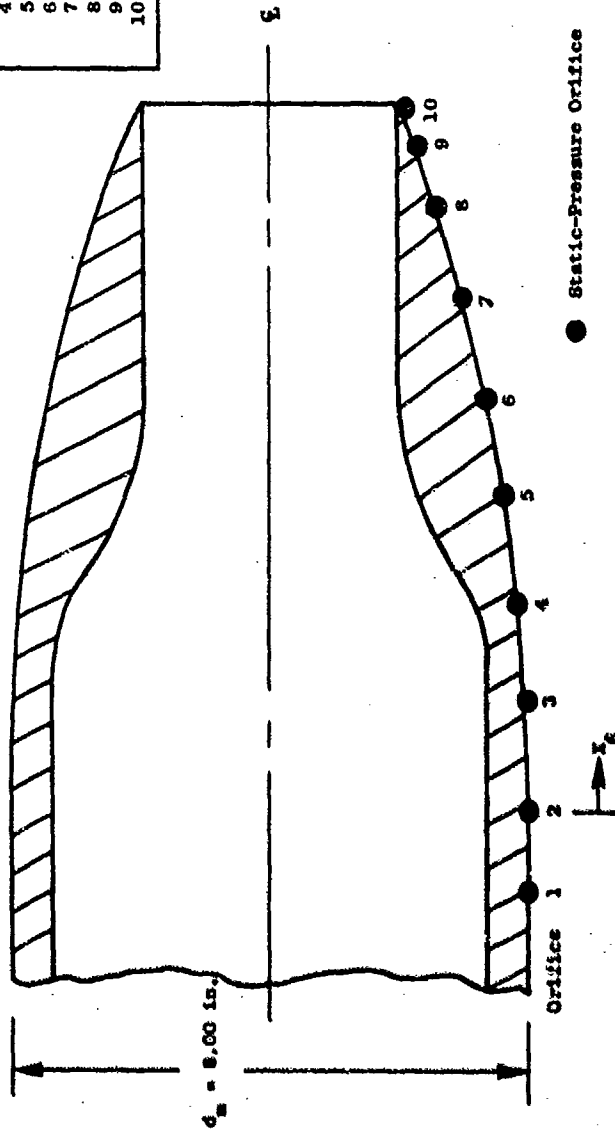


### INSTRUMENTATION LOCATION

Details of static pressure tap locations for all models tested are included in Figures F-16 through F-21.

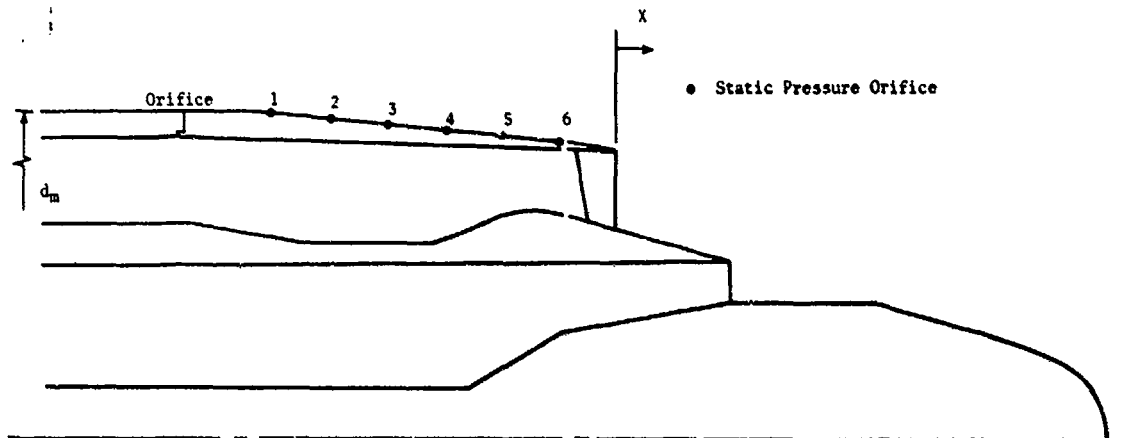
Static-Pressure Locations

Orifice	Axial Location, $X_p/d_m$	Circumferential Location, $\theta$ deg
1	-0.167	90, 180, 270
2	0	
3	0.193	
4	0.373	
5	0.566	
6	0.746	
7	0.927	
8	1.107	
9	1.197	
10	1.274	



● Static-Pressure Orifice

Figure F-16. Supersonic Tunnel Association (STA) Boattail Static-Pressure Instrumentation.



Shallow-Chute Nozzles

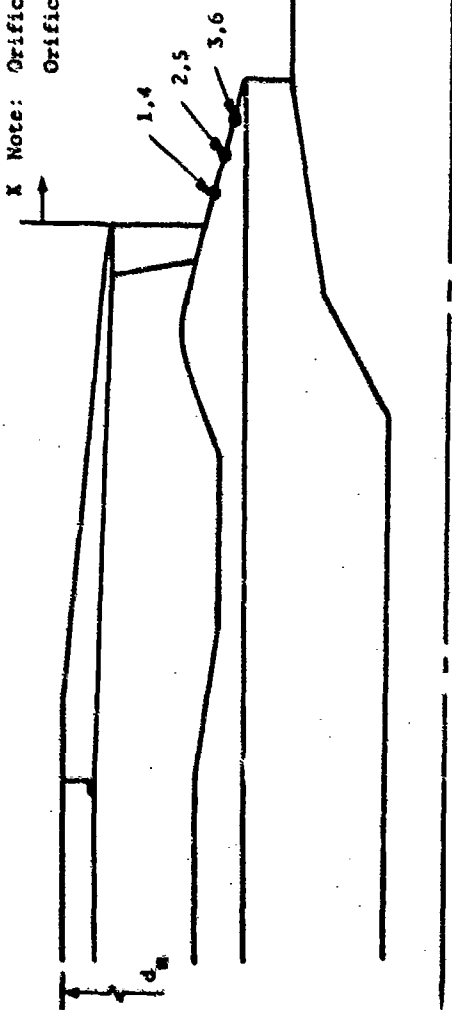
Orifice	SC-1		SC-2, SC-3, SC-4, SC-5		SC-6	
	Axial Location, $X/d_m$	Circumferential Location, $\theta$ degrees	Axial Location, $X/d_m$	Circumferential Location, $\theta$ degrees	Axial Location, $X/d_m$	Circumferential Location, $\theta$ degrees
1	- 0.554	108	- 0.554	108	- 0.554	168
2	- 0.461	0	- 0.461	348	- 0.461	351
3	- 0.369	18	- 0.369	12	- 0.369	9
4	- 0.276	36	- 0.276	24	- 0.276	18
5	- 0.184	252	- 0.184	252	- 0.184	252
6	- 0.091	126	- 0.071	132	- 0.061	135

Deep-Chute and Spoke Nozzles

Orifice	DC-1, DC-2		DC-3, DC-4, DC-5, DC-6, DC-7 (Spoke)		DC-7, DC-8	
	Axial Location, $X/d_m$	Circumferential Location, $\theta$ degrees	Axial Location, $X/d_m$	Circumferential Location, $\theta$ degrees	Axial Location, $X/d_m$	Circumferential Location, $\theta$ degrees
1	- 0.410	110	- 0.410	110	- 0.410	110
2	- 0.313	350	- 0.325	350	- 0.329	350
3	- 0.210	10	- 0.240	10	- 0.253	10
4	- 0.166	20	- 0.138	30	- 0.166	20
5	..	..	..	..	..	..
6	..	..	..	..	..	..

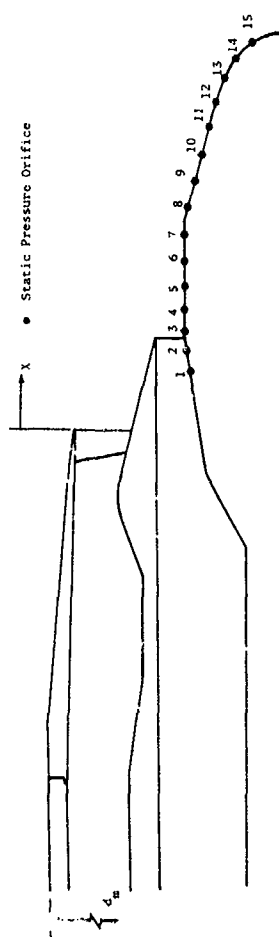
Figure F-17. Annular Nozzle Outer Shroud Static Pressures.

- Static Pressure Orifice
- X Note: Orifices 1, 2, & 3 in Line with Chutes
- Orifices 4, 5, & 6 Between Chutes



Shallow-Chute Nozzles										Deep-Chute and Spoke Nozzles	
SC-1			SC-2, SC-3, SC-4, SC-5		SC-6						
Orifice	Axial Location, $X/d_m$	Circumferential Location, $\theta$ degrees	Axial Location, $X/d_m$	Circumferential Location, $\theta$ degrees	Axial Location, $X/d_m$	Circumferential Location, $\theta$ degrees	Axial Location, $X/d_m$	Circumferential Location, $\theta$ degrees	Axial Location, $X/d_m$	Circumferential Location, $\theta$ degrees	
1	0.042	126	0.042	132	0.042	135	0.081	120			
2	0.088	252	0.088	252	0.088	261	0.163	260			
3	0.133	270	0.133	264	0.133	261	0.244	270			
4	0.042	54	0.042	48	0.042	63	0.081	60			
5	0.088	342	0.088	336	0.088	342	0.163	330			
6	0.133	162	0.133	156	0.133	162	0.244	160			

Figure F-18. Outer Plug Static Pressures.



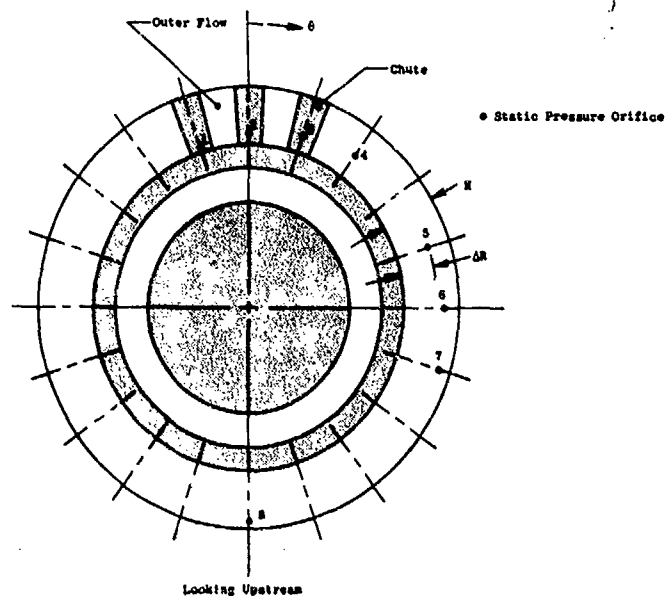
Shallow-Chute Nozzles

Orifice	SC-1, SC-2, SC-3, SC-4		SC-4		SC-5	
	Axial Location, $X/d_n$	Circumferential Location, $\theta$ Degrees	Axial Location, $X/d_n$	Circumferential Location, $\theta$ Degrees	Axial Location, $X/d_n$	Circumferential Location, $\theta$ Degrees
1	0.131	160	0.200	160	- 0.107	300
2	0.180	240	0.242	170	- 0.055	240
3	0.200	160	0.286	60	- 0.073	160
4	0.271	120	0.358	0	0.018	120
5	0.294	60	0.394	0	0.164	60
6	0.358	0	0.444	0	0.114	0
7	0.394	0	...	...	0.171	0
8	0.444	0	...	...	0.224	0
9	0.500	45	0.500	45	0.277	45
10	0.555	90	0.555	90	0.329	90
11	0.607	135	0.607	135	0.385	135
12	0.659	180	0.659	180	0.436	180
13	0.707	225	0.707	225	0.483	225
14	0.748	270	0.748	270	0.524	270
15	0.777	315	0.777	315	0.555	315

Deep-Chute and Spoke Nozzles

Orifice	DC-1, DC-3, DC-4, DC-7		DC-2, DC-5, DC-8		DC-6	
	Axial Location, X/d <sub>n</sub>	Circumferential Location, θ degrees	Axial Location, X/d <sub>n</sub>	Circumferential Location, θ degrees	Axial Location, X/d <sub>n</sub>	Circumferential Location, θ degrees
1	0.256	300	0.240	180	0.033	300
2	0.300	240	0.381	120	0.077	240
3	0.340	180	0.428	60	0.117	180
4	0.381	120	0.478	0	0.158	120
5	0.428	60	0.534	0	0.204	60
6	0.478	0	0.588	0	0.254	0
7	0.534	0	0.588	0	0.310	0
8	0.588	0	0.588	0	0.364	0
9	0.640	45	0.640	45	0.417	45
10	0.693	90	0.693	90	0.469	90
11	0.746	135	0.746	135	0.523	135
12	0.799	180	0.799	180	0.575	180
13	0.846	225	0.846	225	0.624	225
14	0.888	270	0.888	270	0.664	270
15	0.916	315	0.916	315	0.693	315

Figure F-19. Inner Plug Static Pressures.



Shallow-Chute Nozzle

Orifice	SC-1		SC-2, SC-3, SC-4, SC-5		SC-6	
	Radial Location, $\Delta R/H$	Circumferential Location, $\theta$ degrees	Radial Location, $\Delta R/H$	Circumferential Location, $\theta$ degrees	Radial Location, $\Delta R/H$	Circumferential Location, $\theta$ degrees
1	0.070	342	0.020	336	0	342
2	0.160	0	0.171	348	0.151	351
3	0.290	18	0.381	12	0.302	9
4	0.450	36	0.411	24	0.433	18
5	0.526	72	0.522	72	0.605	72
6	0.696	90	0.602	84	0.690	81
7	0.791	108	0.782	108	0.806	108
8	0.876	180	0.803	168	0.958	171
9	..	..	..	..	..	..
10	..	..	..	..	..	..

Deep-Chute and Spoke Nozzles

Orifice	DC-1, DC-2		DC-3, DC-4, DC-5, DC-6		DC-7, DC-8		DC-9 (Spoke)	
	Radial Location, $\Delta R/H$	Circumferential Location, $\theta$ degrees	Radial Location, $\Delta R/H$	Circumferential Location, $\theta$ degrees	Radial Location, $\Delta R/H$	Circumferential Location, $\theta$ degrees	Radial Location, $\Delta R/H$	Circumferential Location, $\theta$ degrees
1	0.025	348	0	348	0	348	..	..
2	0.210	350	0.126	350	0.154	351	0.126	350
3	0.287	10	0.255	10	0.311	10	0.255	10
4	0.401	20	0.424	20	0.475	20	0.424	20
5	0.607	30	0.554	30	0.593	30	0.554	30
6	0.753	60	0.734	60	0.768	60	0.734	60
7	0.858	110	0.811	110	0.865	110	0.830	110
8	0.941	170	0.912	170	1.046	170	..	..
9	0.987	210	0.981	210	0.983	210	..	..
10	0.970	180	0.918	180	0.905	180	..	..

Figure F-20. Suppressor Element Base Static Pressures.

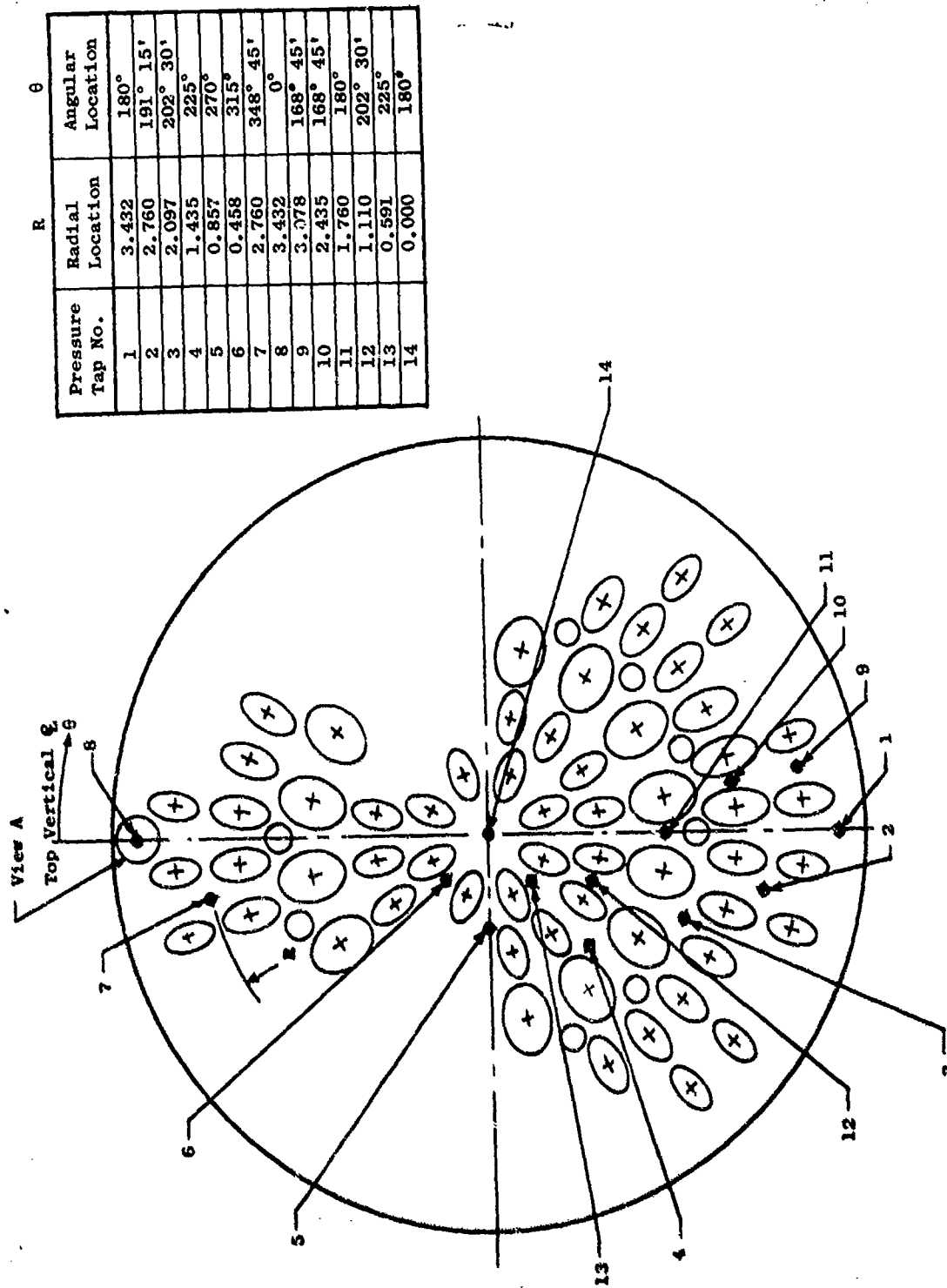


Figure F-21. 104-Tube Nozzle Instrumentation.

### ANNULAR SUPPRESSED-NOZZLE THRUST COEFFICIENTS

Annular suppressed-nozzle thrust coefficients are presented as a function of pressure ratio in Figures F-22 through F-36.



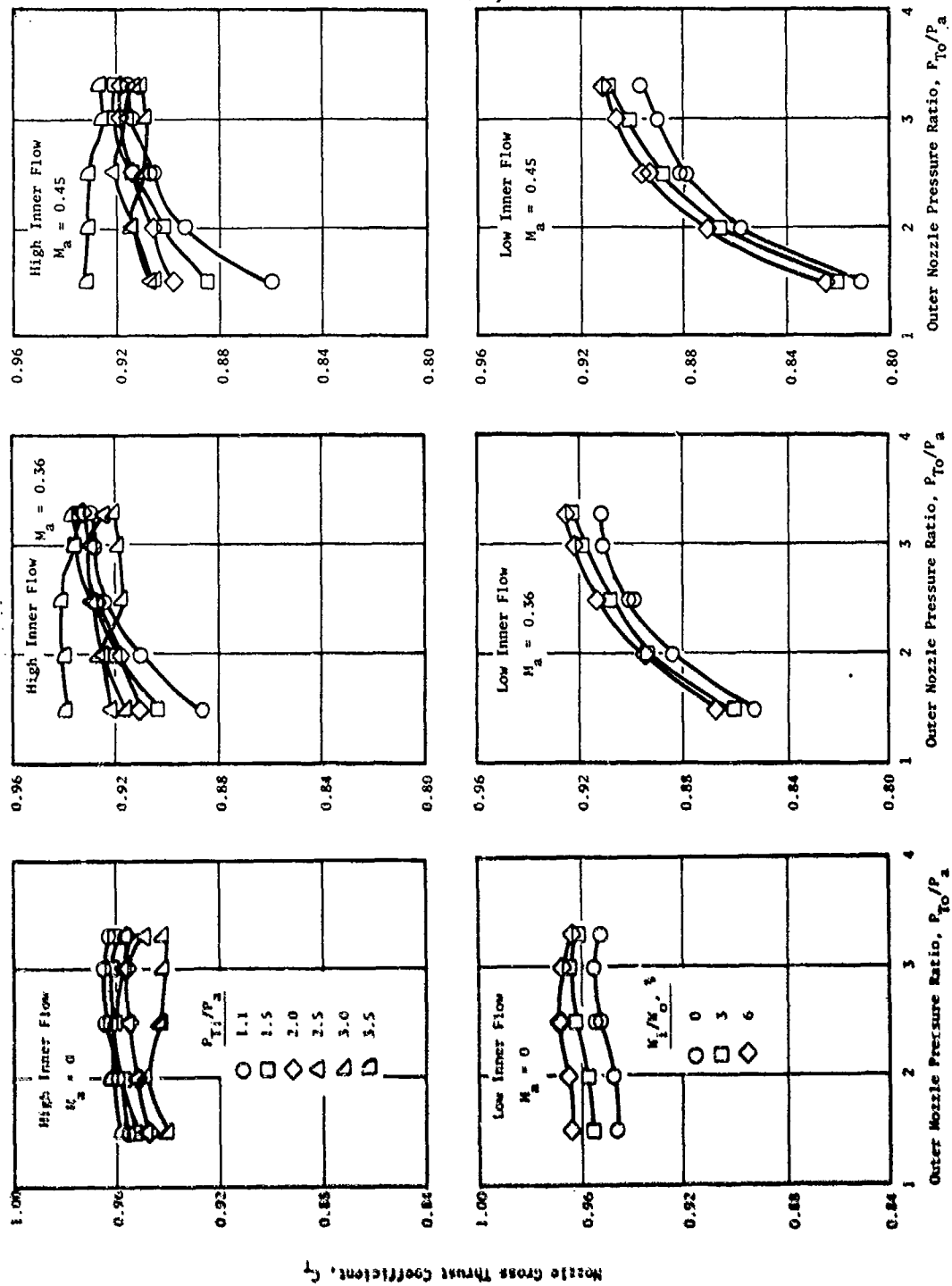


Figure F-22. Configuration SC-1 Performance.

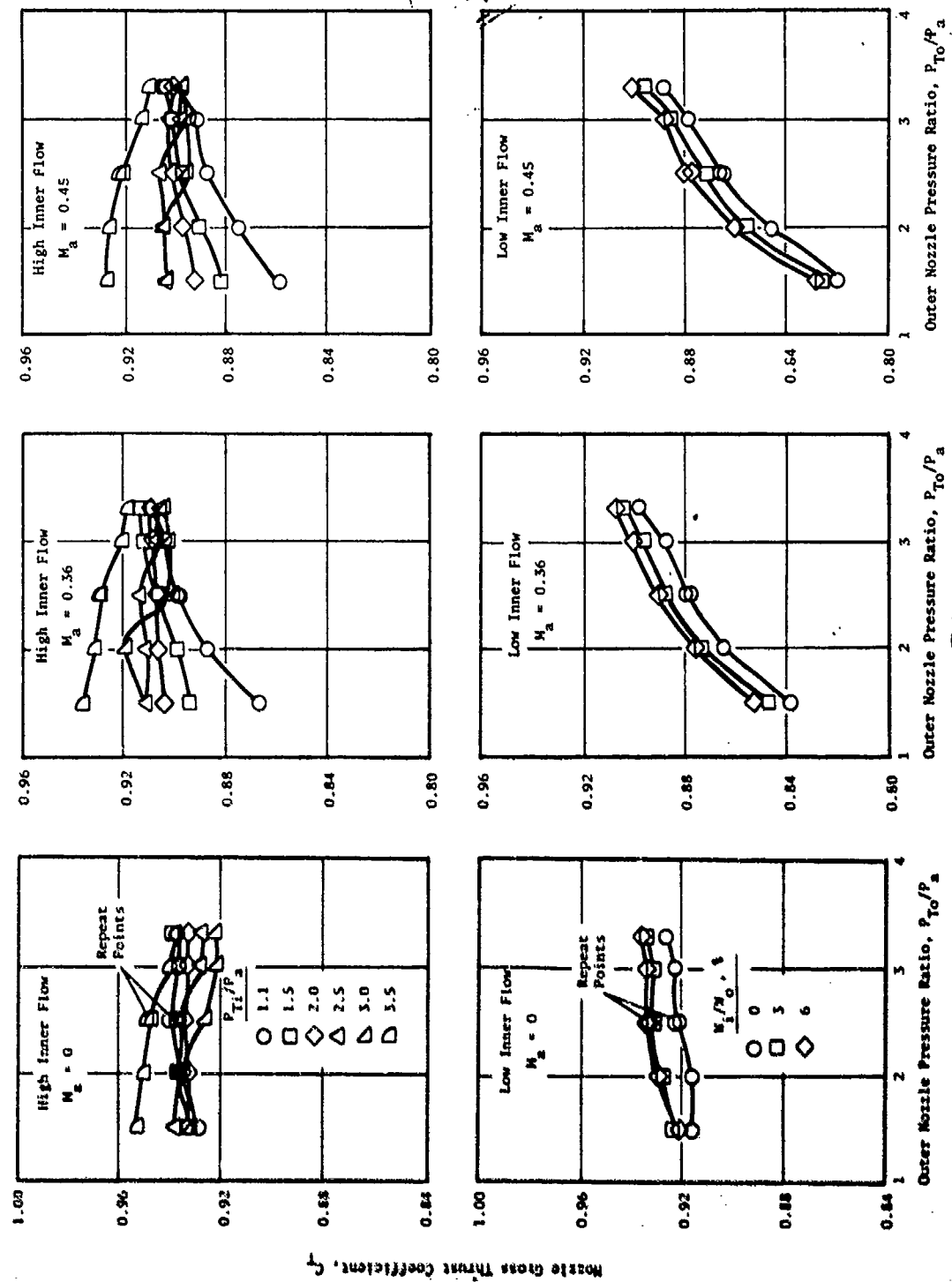


Figure F-23. Configuration SC-2 Performance.

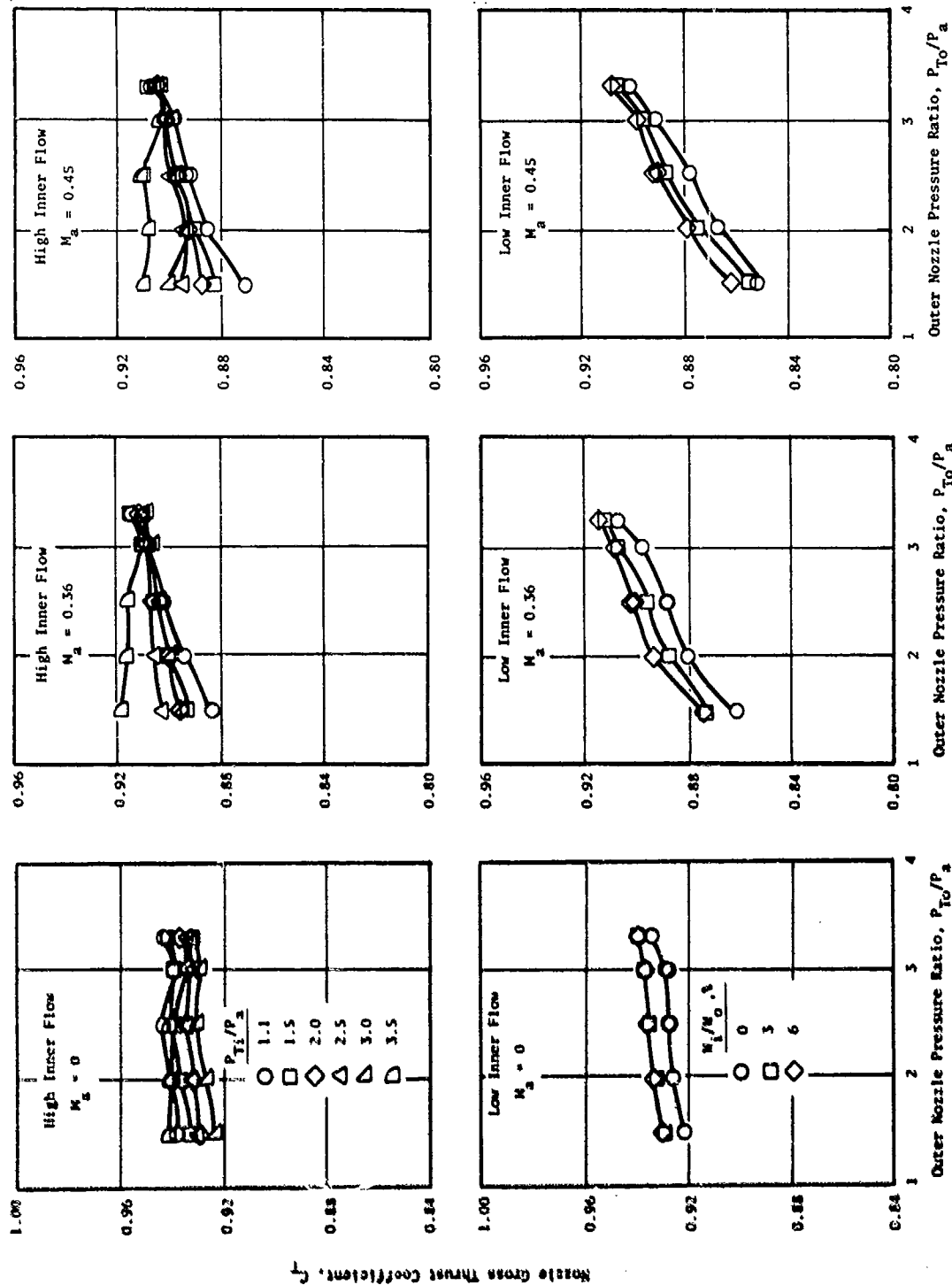


Figure F-24. Configuration SC-3 Performance.

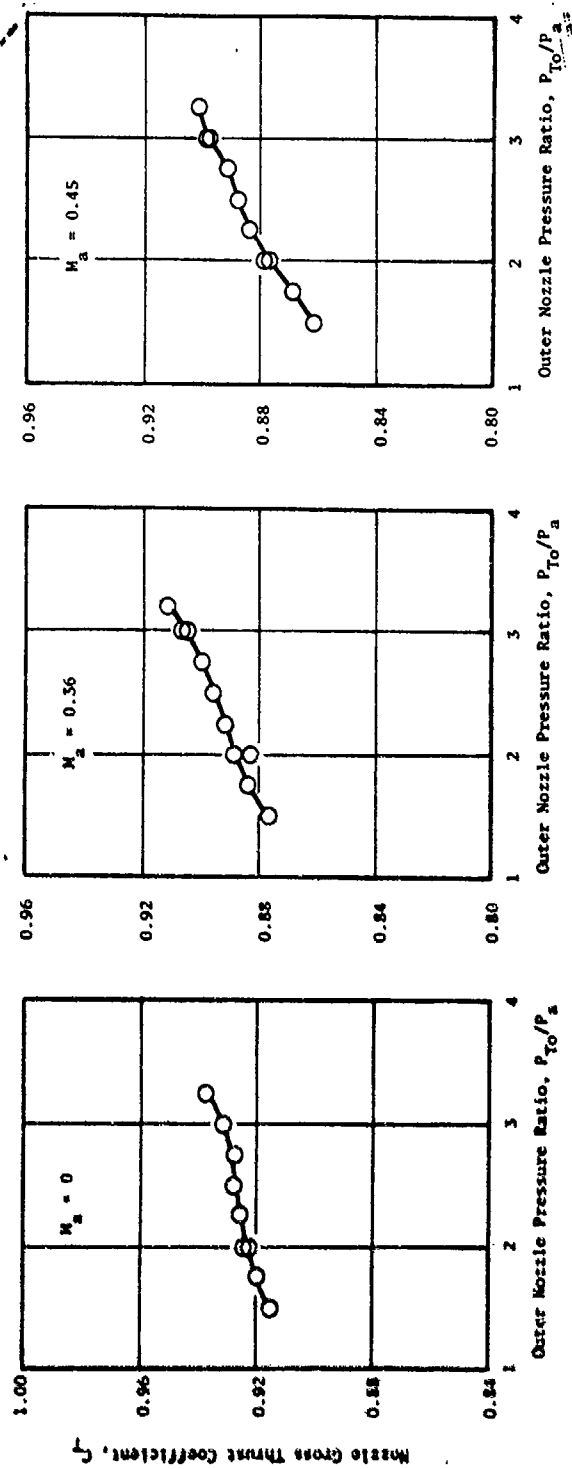


Figure F-25. Configuration SC-4 Performance.

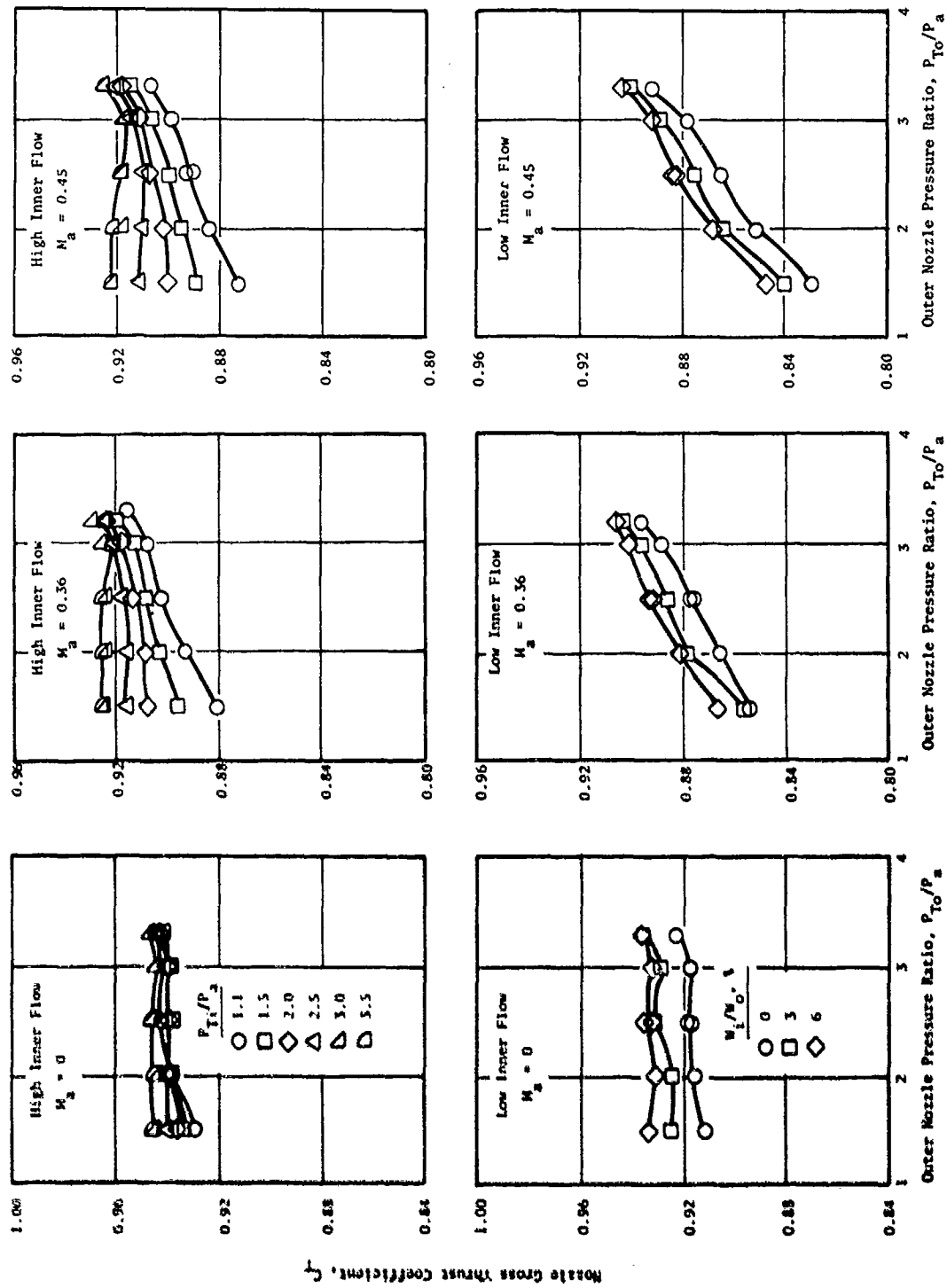


Figure F-26. Configuration SC-5 Performance.

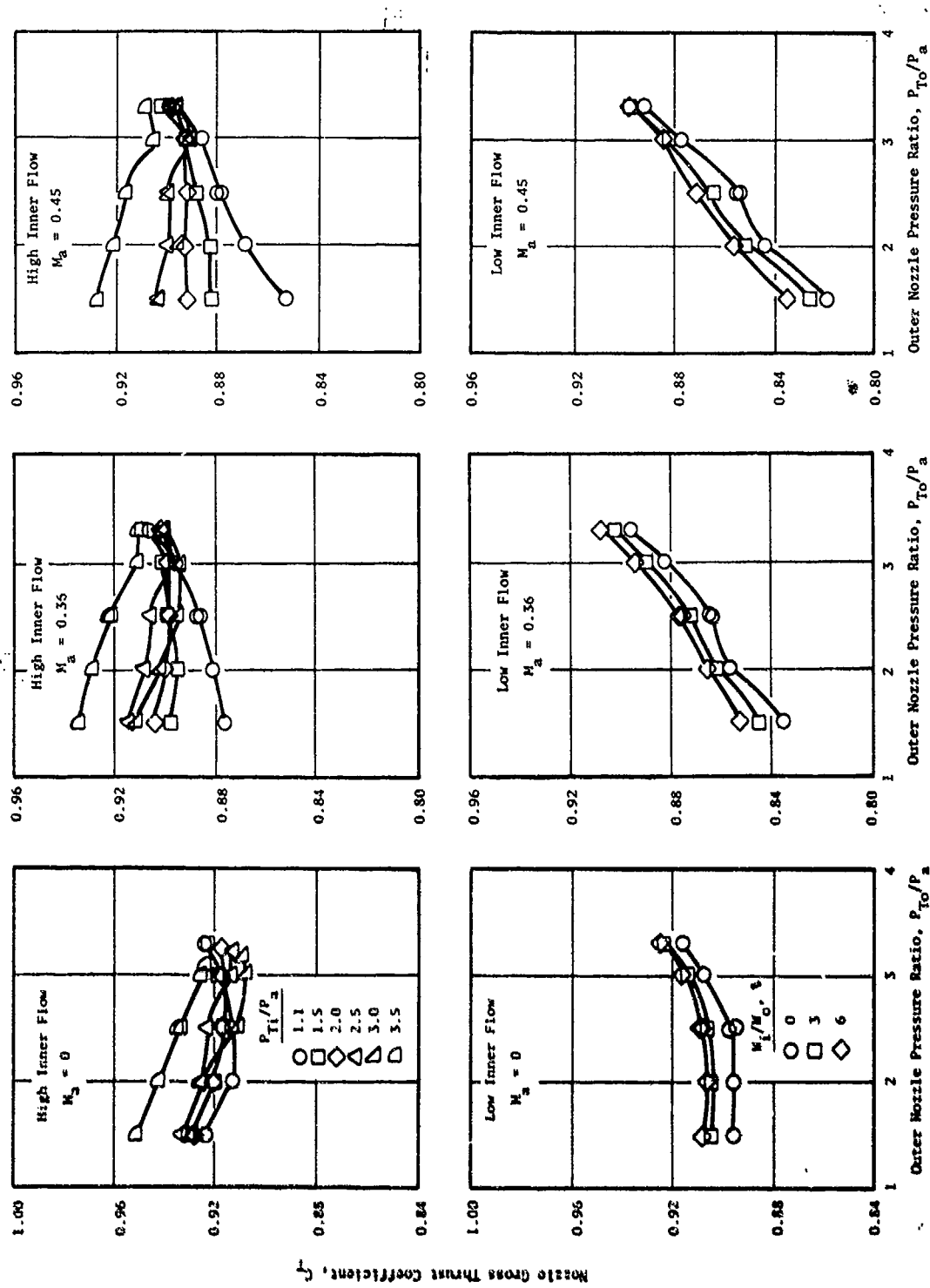


Figure F-27. Configuration SC-6 Performance.

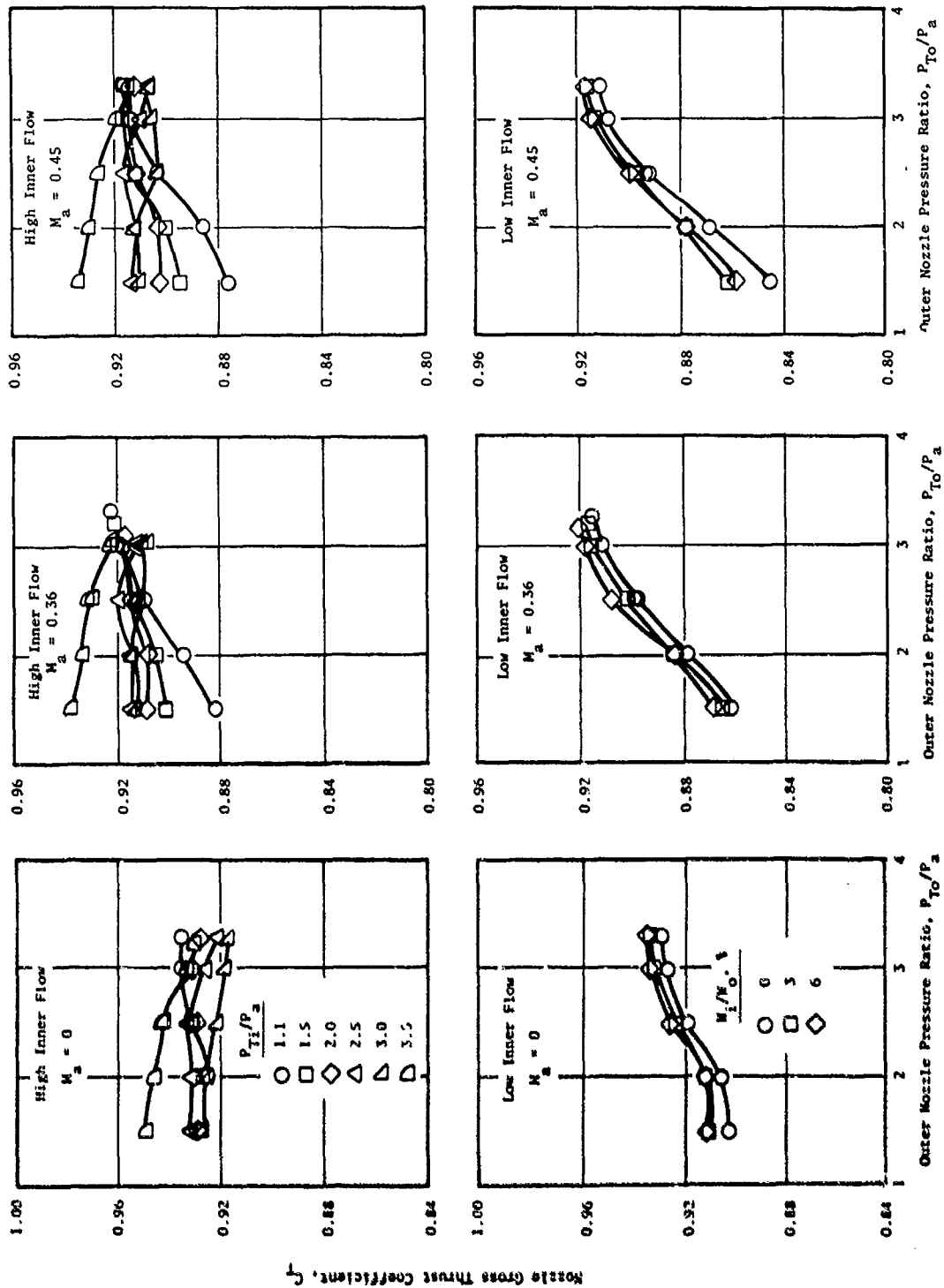


Figure F-28. Configuration DC-1 Performance.

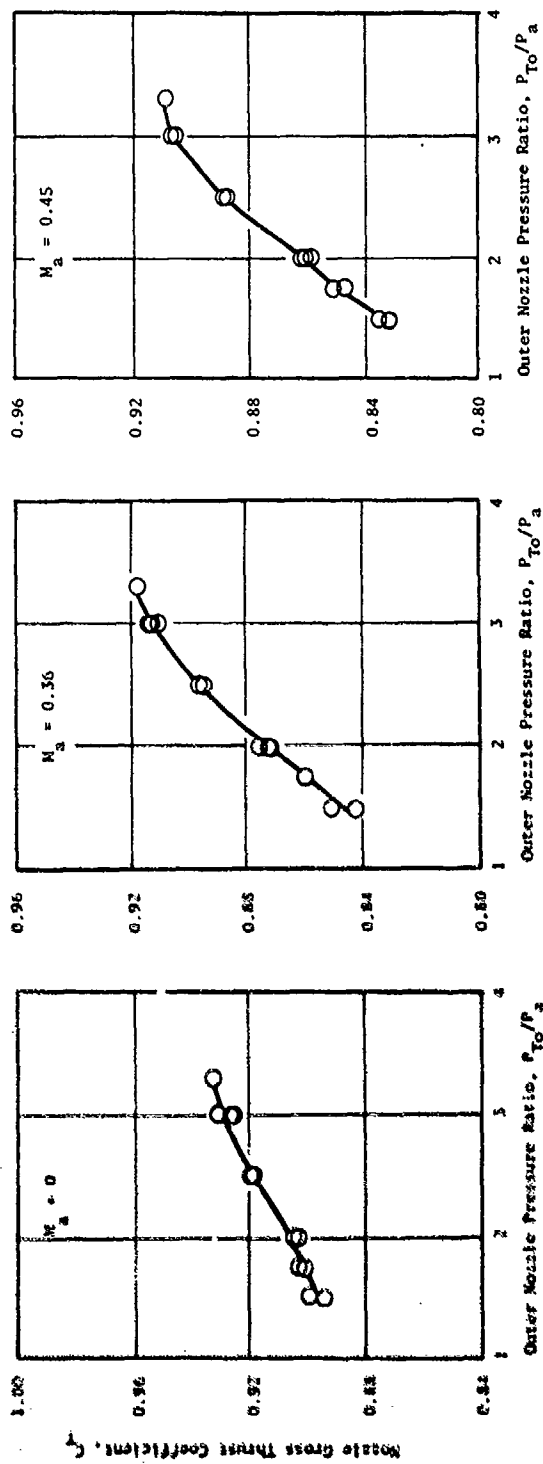


Figure F-29. Configuration DC-2 Performance.



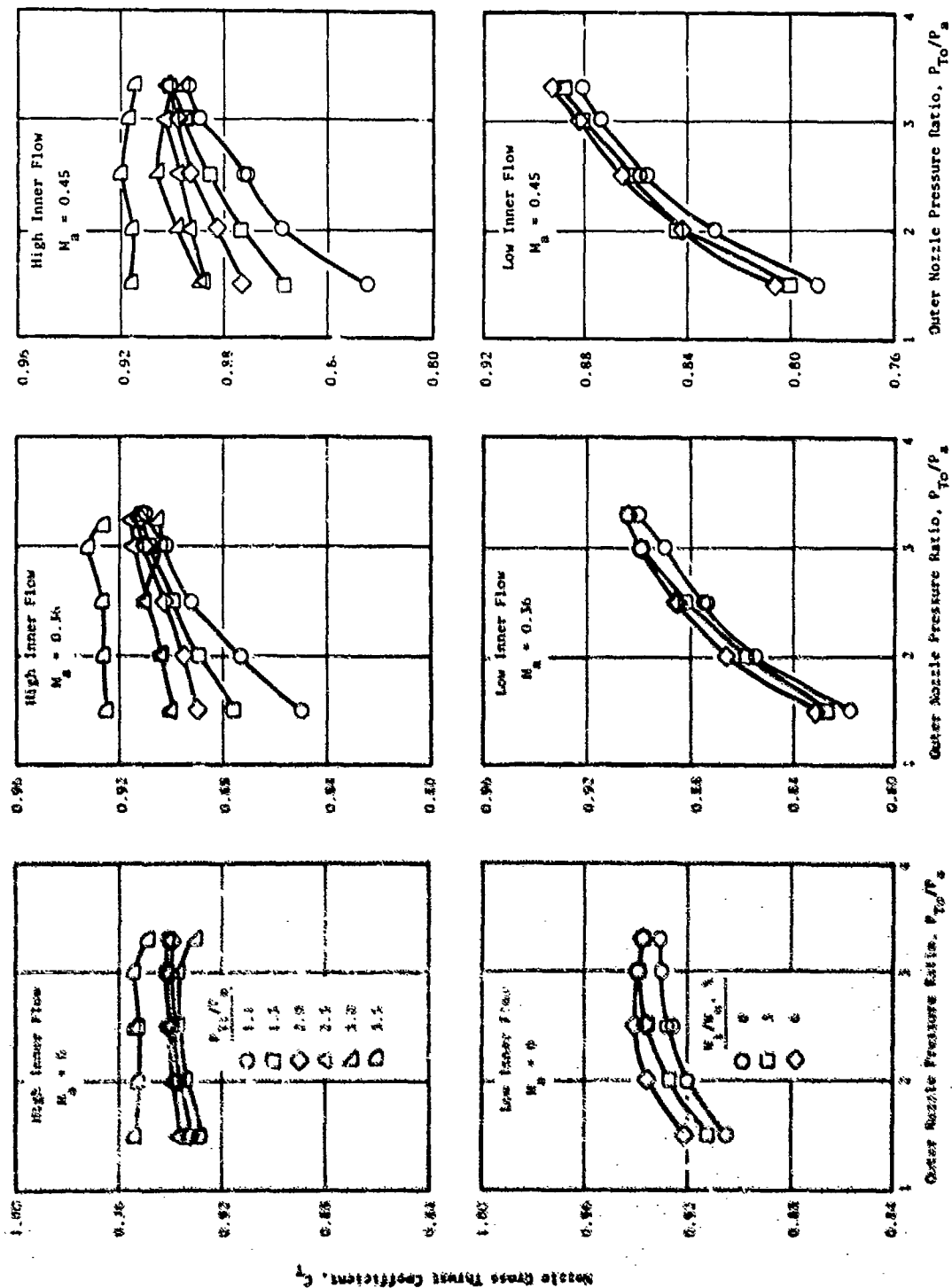


Figure F-30. Configuration DC-3 Performance.

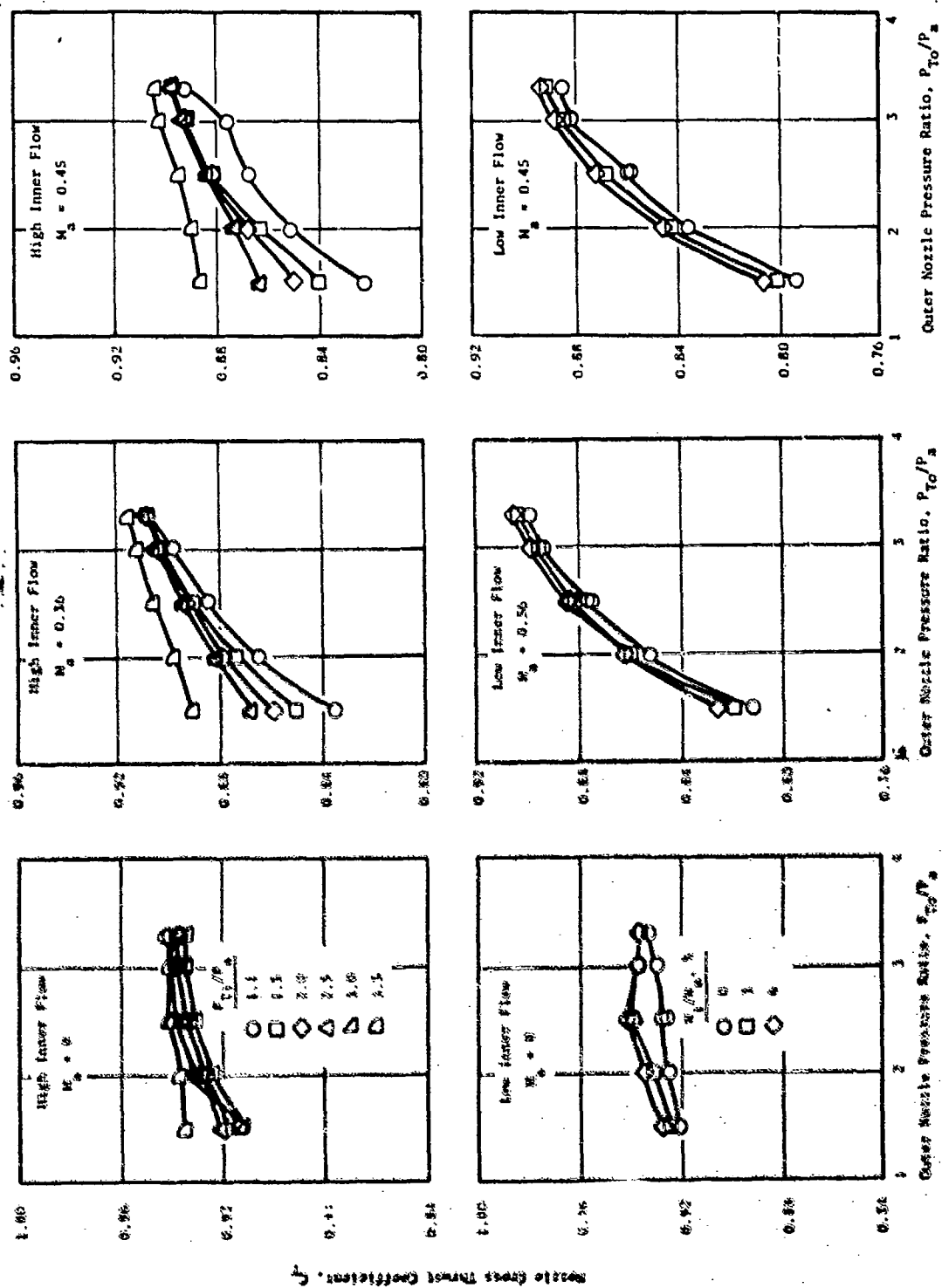


Figure P-31. Configuration DC-4 Performance.

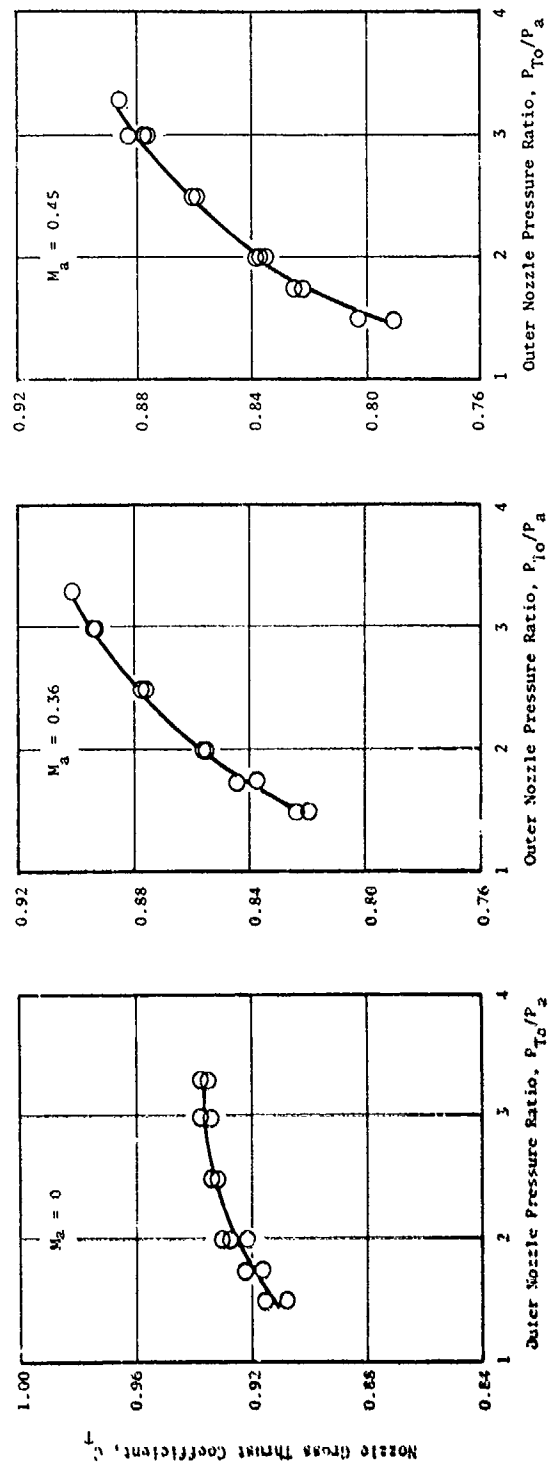


Figure F-32. Configuration DC-5 Performance.

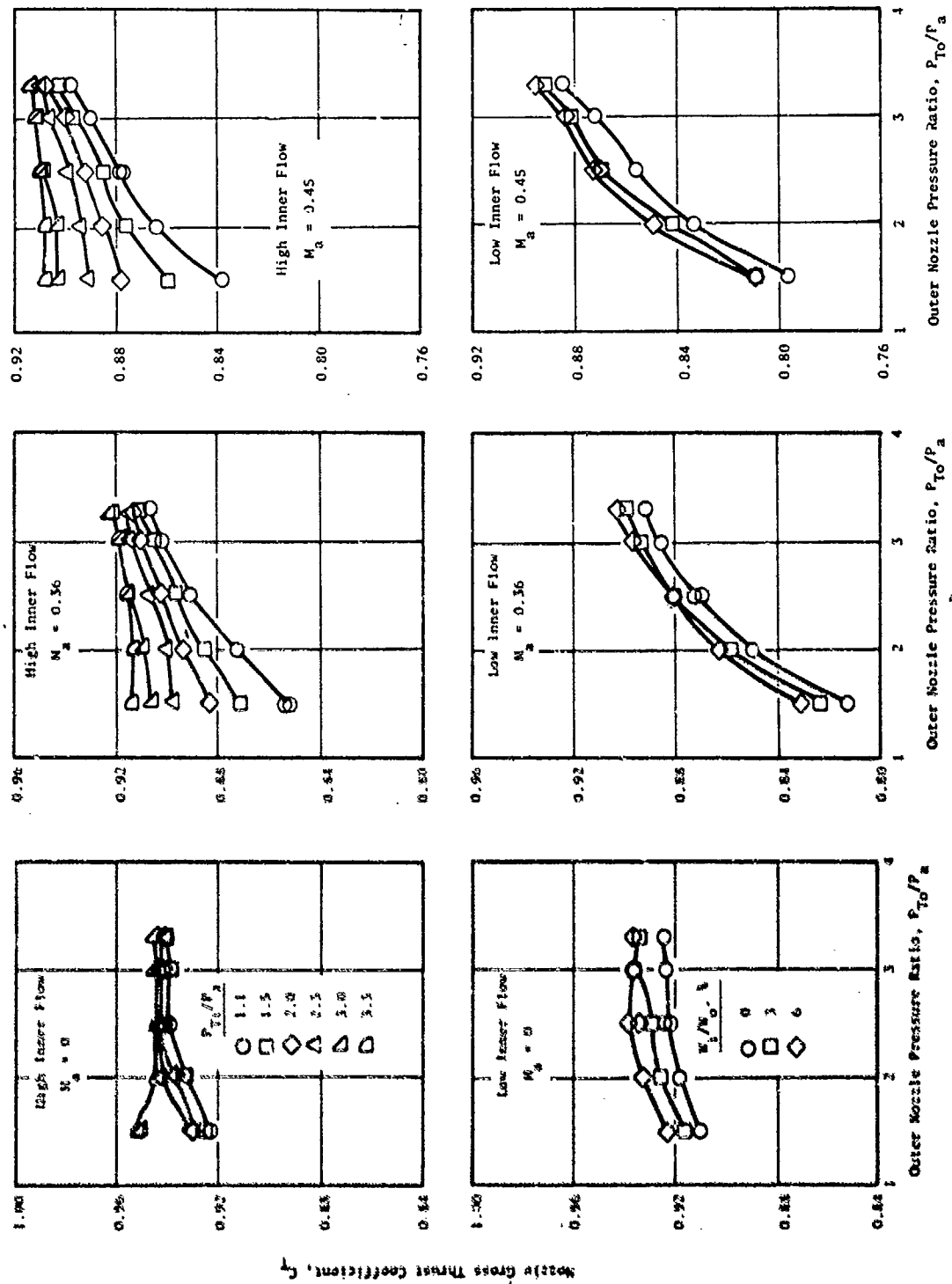


Figure F-33. Configuration DC-6 Performance.

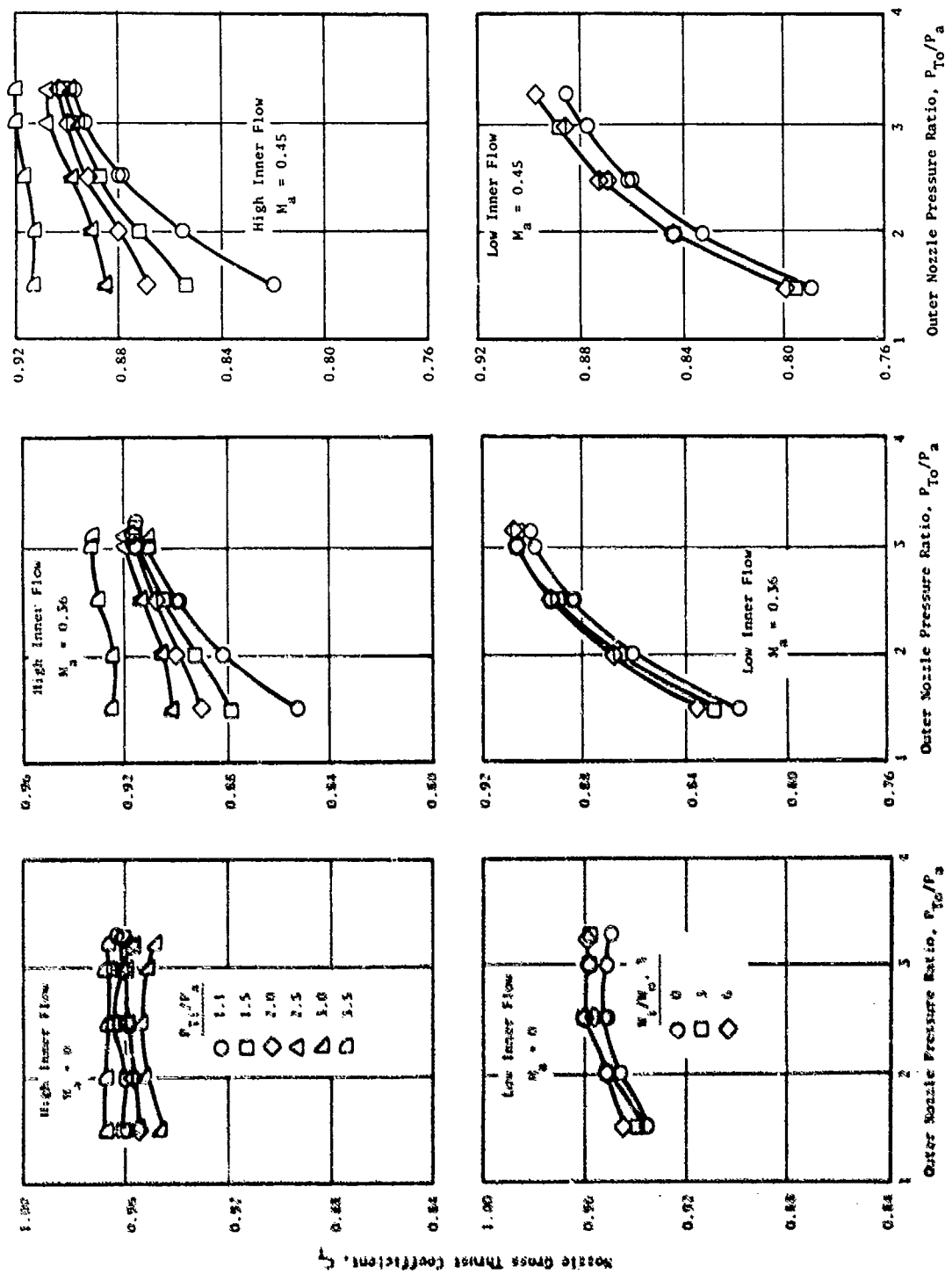


Figure F-34. Configuration DC-7 Performance.

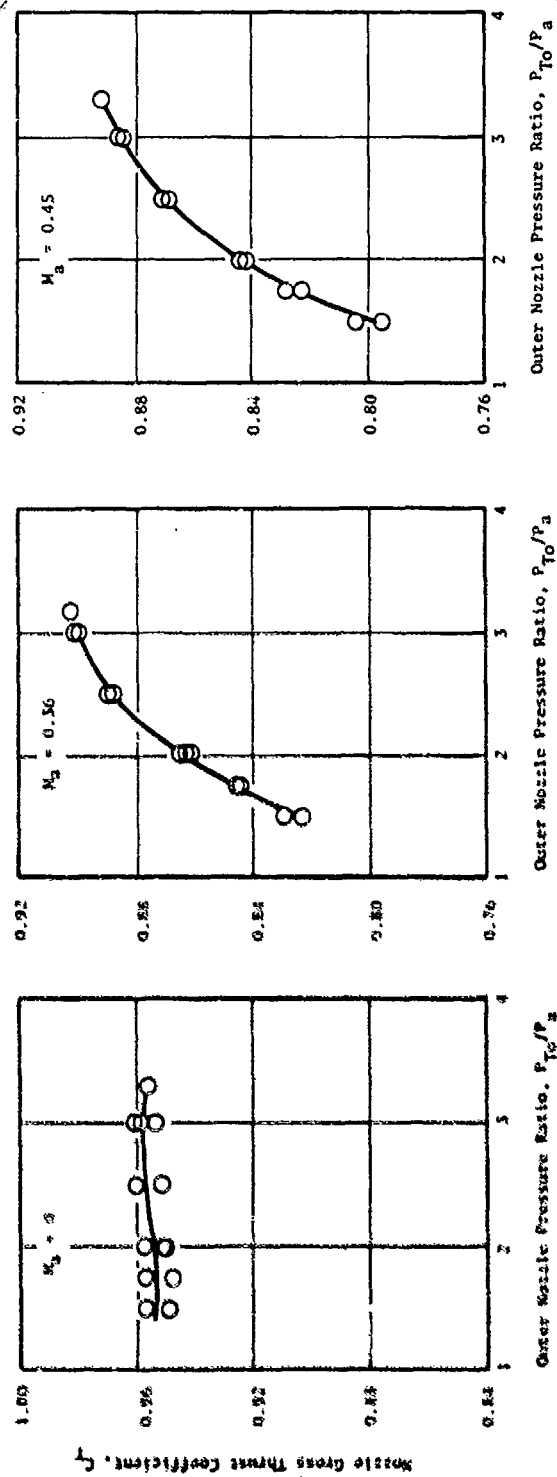


Figure F-35. Configuration DC-8 Performance.

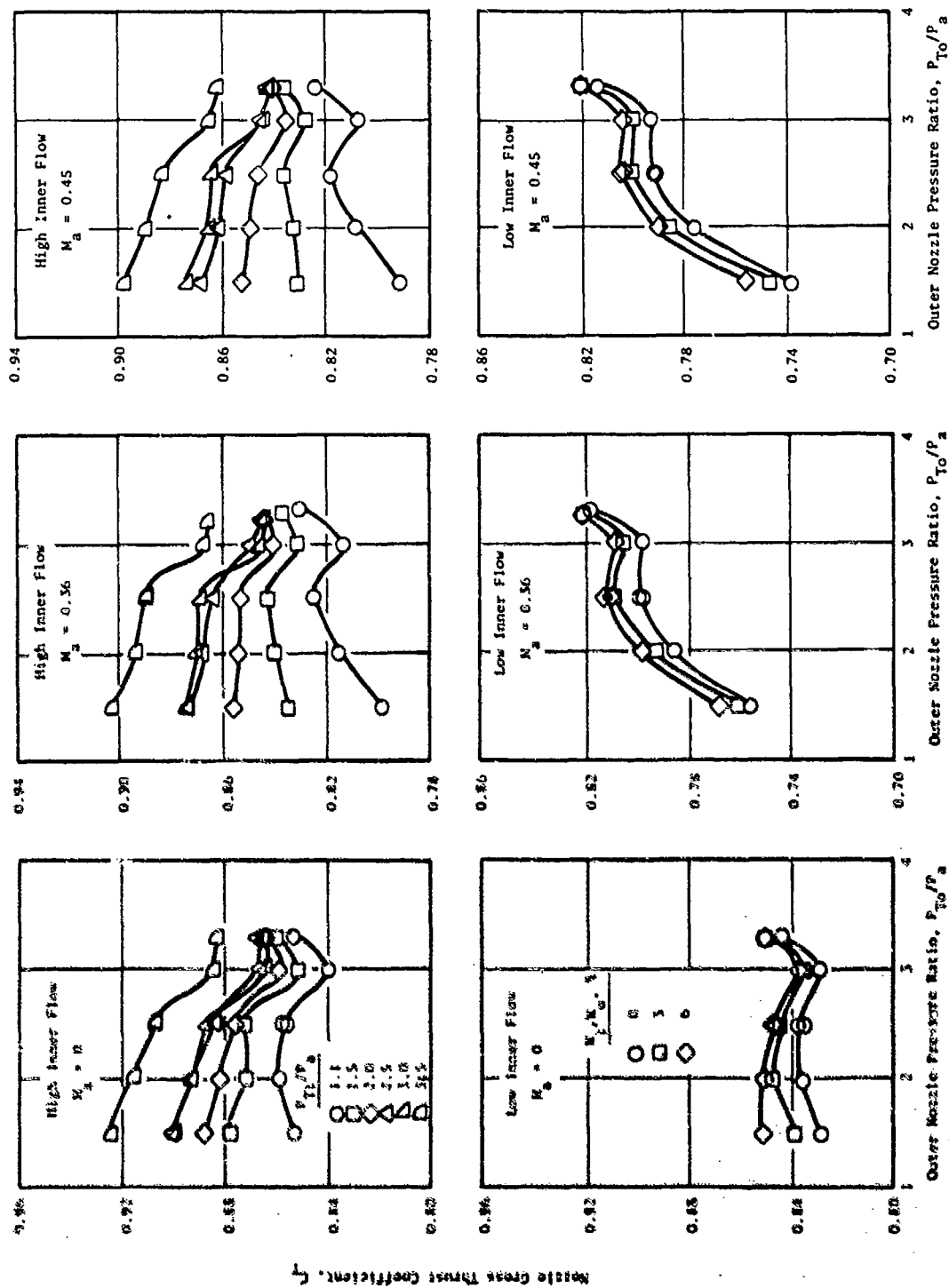


Figure F-36. Configuration DC-3 (Spoke) Performance.

## OFF-LINE DATA SUMMARY

This section includes a data summary for each point taken in the test program. Listed below are the parameters presented in the summary.

### Page 1 of data summary

D2	Inner nozzle venturi diameter, in.
MA	Tunnel Mach number
PTO/PA	Outer nozzle throat total-to-ambient pressure ratio
PTI/PA	Inner nozzle throat total-to-ambient pressure ratio
OMEGAT	Inner to outer nozzle flow ratio, $W_1/W_0$
CDO	Outer nozzle flow coefficient
CDI	Inner nozzle flow coefficient
CFNET1	Nozzle thrust coefficient based on sum of ideal thrusts of inner and outer streams, $(F-D)/(F_{I0} + F_{I1})$
CFNET2	Nozzle thrust coefficient based on outer stream ideal thrust, $(F-D)/F_{I0}$
F9	Nozzle exit stream thrust parameter

### Page 2 of data summary

DCS	Integrated suppressor base pressure drag divided by the sum of the ideal thrusts of the inner and outer streams, $D_{ch}/(F_{I0} + F_{I1})$
CDS	Suppressor base pressure drag coefficient referenced to free stream dynamic pressure and the model cross section area, $D_{ch}/q_a A_{max}$
DCSH	Integrated shroud axial boattail pressure drag referenced to the sum of the ideal thrusts of the inner and outer streams, $D_{sh}/(F_{I0} + F_{I1})$
CDSH	Integrated shroud axial boattail pressure drag coefficient referenced to free stream dynamic pressure and the model cross section area, $D_{sh}/q_a A_{max}$
DCPL,O	Integrated outer plug axial pressure force referenced to the sum of the inner and outer nozzle ideal thrust, $D_{PLO}/(F_{I0} + F_{I1})$
DCPL,I	Integrated inner plug axial pressure force referenced to the sum of inner and outer nozzle ideal thrust, $D_{PLI}/(F_{I0} + F_{I1})$
DCTOT	Summation of nozzle integrated axial pressure forces referenced to the sum of inner and outer nozzle ideal thrust, $DSC + DCSH + DCPL,O + DCPL,I$
PSUP/PA	Area averaged suppressor base pressure referenced to tunnel ambient pressure, $P/P_a$



STA CALIBRATION MODEL













**TABLE 1** **ALUMINUM COIL** **NO. 1** **TYPE** **PLATE** **CONFIGURATIONS** **SUPPRESSOR CONFIGURATION**

TABLE 1									
ALUMINUM COIL									
NO. 1									
TYPE									
PLATE									
CONFIGURATIONS									
SUPPRESSOR CONFIGURATION									
TABLE 1									
ALUMINUM COIL									
NO. 1									
TYPE									
PLATE									
CONFIGURATIONS									
SUPPRESSOR CONFIGURATION									
TABLE 1									
ALUMINUM COIL									
NO. 1									
TYPE									
PLATE									
CONFIGURATIONS									
SUPPRESSOR CONFIGURATION									
TABLE 1									
ALUMINUM COIL									
NO. 1									
TYPE									
PLATE									
CONFIGURATIONS									
SUPPRESSOR CONFIGURATION									
TABLE 1									
ALUMINUM COIL									
NO. 1									
TYPE									
PLATE									
CONFIGURATIONS									
SUPPRESSOR CONFIGURATION									
TABLE 1									
ALUMINUM COIL									
NO. 1									
TYPE									
PLATE									
CONFIGURATIONS									
SUPPRESSOR CONFIGURATION									
TABLE 1									
ALUMINUM COIL									
NO. 1									
TYPE									
PLATE									
CONFIGURATIONS									
SUPPRESSOR CONFIGURATION									
TABLE 1									
ALUMINUM COIL									
NO. 1									
TYPE									
PLATE									
CONFIGURATIONS									
SUPPRESSOR CONFIGURATION									
TABLE 1									
ALUMINUM COIL									
NO. 1									
TYPE									
PLATE									
CONFIGURATIONS									
SUPPRESSOR CONFIGURATION									
TABLE 1									
ALUMINUM COIL									
NO. 1									
TYPE									
PLATE									
CONFIGURATIONS									
SUPPRESSOR CONFIGURATION									
TABLE 1									
ALUMINUM COIL									
NO. 1									
TYPE									
PLATE									
CONFIGURATIONS									
SUPPRESSOR CONFIGURATION									
TABLE 1									
ALUMINUM COIL									
NO. 1									
TYPE									
PLATE									
CONFIGURATIONS									
SUPPRESSOR CONFIGURATION									
TABLE 1									
ALUMINUM COIL									
NO. 1									
TYPE									
PLATE									
CONFIGURATIONS									
SUPPRESSOR CONFIGURATION									
TABLE 1									
ALUMINUM COIL									
NO. 1									
TYPE									
PLATE									
CONFIGURATIONS									
SUPPRESSOR CONFIGURATION									
TABLE 1									
ALUMINUM COIL									
NO. 1									
TYPE									
PLATE									
CONFIGURATIONS									
SUPPRESSOR CONFIGURATION									
TABLE 1									
ALUMINUM COIL									
NO. 1									
TYPE									
PLATE									
CONFIGURATIONS									
SUPPRESSOR CONFIGURATION									
TABLE 1									
ALUMINUM COIL									
NO. 1									
TYPE									
PLATE									
CONFIGURATIONS									
SUPPRESSOR CONFIGURATION									
TABLE 1									
ALUMINUM COIL									
NO. 1									
TYPE									
PLATE									
CONFIGURATIONS									
SUPPRESSOR CONFIGURATION									



FACILITY		PROGRAM CODE		NOZZLE TYPE		STREAM		CONFIGURATIONS		SUPPRESSOR CONFIGURATION	
		2 INCH STA(OUTER STREAM ONLY)				PLIN					
THRUST PARAMETER		OUTER RADIUS RATIO		INNER RADIUS RATIO		DVG					
		0.0000		0.0000		1.2480					
REC	GE	USE	D2	WA	DTG/PA	FTI/PA	CMFAT	CON	CHI	CFNET1	CFNET2
3230	7000	70000	0.0000	-0.0000	1.0780	1.1460	0.0000	0.9915	9.9999	0.9746	0.9746
3231	7000	70000	0.0000	0.0100	2.9879	1.3169	0.0000	0.9905	9.9999	0.9799	0.9799
3232	7000	70000	0.0000	0.0215	3.9683	1.4804	0.0000	0.9931	9.9999	0.9785	0.9785
3233	7000	70000	0.0000	0.0308	3.9889	1.4797	0.0000	1.0067	9.9999	0.9767	0.9767
3234	7000	70000	0.0000	0.0433	2.5842	1.5168	0.0000	0.9940	9.9999	0.9932	0.9932
3235	7000	70000	0.0000	0.0517	1.8906	1.1494	0.0000	0.9884	9.9999	0.9978	0.9978
3242	7000	70000	0.0000	0.0170	1.0883	1.1502	0.0000	0.9939	1.0111	1.0111	1.0111
3243	7000	70000	0.0000	0.0072	2.9873	1.3159	0.0000	0.9952	9.9999	0.9890	0.9890
3244	7000	70000	0.0000	0.0264	3.5742	1.4800	0.0000	0.9959	9.9999	0.9806	0.9806
3245	7000	70000	0.0000	0.0483	3.9882	1.4901	0.0000	1.0043	9.9999	0.9809	0.9809
3246	7000	70000	0.0000	0.0500	2.5913	1.5171	0.0000	0.9978	9.9999	0.9878	0.9878
3247	7000	70000	0.0000	0.0748	1.9813	1.1497	0.0000	0.9914	9.9999	0.9959	0.9959
3248	7000	70000	0.0000	0.0058	1.9927	1.1501	0.0000	0.9903	9.9999	0.9904	0.9904
3249	7000	70000	0.0000	0.0144	2.9871	1.3157	0.0000	0.9854	9.9999	0.9922	0.9922
3250	7000	70000	0.0000	0.0307	3.9801	1.4819	0.0000	1.0034	9.9999	0.9757	0.9757
3251	7000	70000	0.0000	0.0297	5.0064	1.5444	0.0000	1.0101	9.9999	0.9665	0.9665
3252	7000	70000	0.0000	-0.0000	4.5716	1.5397	0.0000	1.0116	9.9999	0.9732	0.9732
3253	7000	70000	0.0000	-0.0000	2.9723	1.4763	0.0000	1.0053	9.9999	0.9840	0.9840
3254	7000	70000	0.0000	0.0176	2.9770	1.5131	0.0000	1.0011	9.9999	0.9883	0.9883
3255	7000	70000	0.0000	0.0058	1.9760	1.1473	0.0000	0.9931	9.9999	0.9994	0.9994
3256	7000	70000	0.0000	0.0052	1.9843	1.1495	0.0000	0.9899	9.9999	0.9986	0.9986
3257	7000	70000	0.0000	0.0277	2.9868	1.184	0.0000	0.9930	9.9999	0.9808	0.9808
3258	7000	70000	0.0000	0.0320	3.9814	1.4838	0.0000	0.9999	9.9999	0.9812	0.9812
3259	7000	70000	0.0000	0.0512	4.9993	1.5446	0.0000	1.0104	9.9999	0.9684	0.9684
3260	7000	70000	0.0000	0.0366	4.9843	1.5456	0.0000	1.0105	9.9999	0.9666	0.9666
3261	7000	70000	0.0000	0.0467	3.9837	1.4769	0.0000	1.0092	9.9999	0.9740	0.9740
3262	7000	70000	0.0000	0.0150	2.9838	1.3163	0.0000	1.0015	9.9999	0.9758	0.9758
3263	7000	70000	0.0000	0.0076	1.9820	1.1500	0.0000	0.9934	9.9999	0.9765	0.9765
3264	7000	70000	0.0000	0.0062	1.9825	1.1540	0.0000	0.9942	9.9999	0.9644	0.9644
3265	7000	70000	0.0000	0.0109	2.9884	1.3165	0.0000	0.9927	9.9999	0.9748	0.9748
3266	7000	70000	0.0000	0.0267	3.9595	1.4810	0.0000	1.0040	9.9999	0.9725	0.9725
3267	7000	70000	0.0000	0.0432	4.9413	1.6454	0.0000	1.0149	9.9999	0.9667	0.9667
3268	7000	70000	0.0000	0.0465	4.9413	1.6458	0.0000	1.0148	9.9999	0.9688	0.9688
3269	7000	70000	0.0000	0.0328	3.9428	1.4807	0.0000	1.0108	9.9999	0.9775	0.9775
3270	7000	70000	0.0000	0.0144	2.9616	1.3175	0.0000	0.9999	9.9999	0.9869	0.9869
3271	7000	70000	0.0000	0.0236	1.9793	1.1545	0.0000	0.9874	9.9999	0.9805	0.9805

MODEL SC-1, 20 SHALLOW CHUTES, AR = 1.75 BASELINE PLUG

FACILITY BX6X1 PROGRAM C031				NOZZLE TYPE				INNER-STEAM PLUG CONFIGURATIONS				SUPPRESSOR CONFIGURATION			
				DIAL FLOW (FAR)				BASELINE PLUG WITH BLEED				20-SPOKE, AREA RATIO = 1.75			
THRUST PARAMETERS				OUTER PACIUS P/TIO				INNER PACIUS P/TIO				C/N			
				0.0000				0.7700				1.2480			
PRG	CF	MASA	M	PA	PTD/PA	PTI/PA	OMEGA	C/N	CDI	CFM/FI	CFM/FI2	FO			
1209	0001	44530	0.398	0.021	1.400	0.579	0.000	0.971	9.999	0.946	0.946	1.149			
1210	0001	44530	0.398	0.022	1.404	0.586	0.020	0.971	9.997	0.955	0.955	1.150			
1211	0001	44530	0.398	0.020	1.405	0.598	0.020	0.970	9.999	0.964	0.964	1.150			
1212	0001	44530	0.398	0.021	1.389	0.566	0.000	0.966	9.999	0.947	0.947	1.149			
1213	0001	44530	0.398	0.040	1.591	0.421	0.000	0.965	9.999	0.957	0.957	1.170			
1214	0001	44530	0.398	0.032	1.591	0.421	0.000	0.965	9.999	0.954	0.954	1.170			
1215	0001	44530	0.398	0.054	2.492	0.556	0.000	0.967	9.999	0.964	0.964	1.174			
1216	0001	44530	0.398	0.044	2.492	0.577	0.000	0.967	9.999	0.962	0.962	1.174			
1217	0001	44530	0.398	0.053	2.494	1.003	0.000	0.966	9.999	0.968	0.968	1.178			
1218	0001	44530	0.398	0.040	2.497	0.566	0.000	0.966	9.999	0.966	0.966	1.181			
1219	0001	44530	0.398	0.053	3.005	0.976	0.000	0.964	9.999	0.964	0.964	1.181			
1220	0001	44530	0.398	0.055	3.005	1.012	0.000	0.964	9.999	0.967	0.967	1.183			
1221	0001	44530	0.398	0.057	3.017	1.017	0.000	0.966	9.999	0.967	0.967	1.183			
1222	0001	44530	0.398	0.056	3.320	0.979	0.000	0.965	9.999	0.961	0.961	1.182			
1223	0001	44530	0.398	0.055	3.315	1.021	0.000	0.965	9.999	0.963	0.963	1.184			
1224	0001	44530	0.398	0.027	1.405	1.114	0.000	0.969	9.999	0.955	0.955	1.182			
1225	0001	44530	0.398	0.027	1.405	1.114	0.000	0.969	9.999	0.957	0.957	1.182			
1226	0001	44530	0.398	0.044	1.405	1.509	0.000	0.968	9.999	0.968	0.968	1.204			
1227	0001	44530	0.398	0.050	1.497	2.504	0.000	0.968	9.999	0.968	0.968	1.204			
1228	0001	44530	0.398	0.052	1.498	3.009	0.000	0.969	9.999	0.968	0.968	1.204			
1229	0001	44530	0.398	0.043	1.407	3.450	0.000	0.968	9.999	0.968	0.968	1.204			
1230	0001	44530	0.398	0.042	1.407	3.450	0.000	0.968	9.999	0.968	0.968	1.204			
1231	0001	44530	0.398	0.048	1.985	1.509	0.000	0.968	9.999	0.968	0.968	1.204			
1232	0001	44530	0.398	0.054	1.985	2.000	0.000	0.968	9.999	0.968	0.968	1.204			
1233	0001	44530	0.398	0.055	1.985	2.501	0.000	0.968	9.999	0.968	0.968	1.204			
1234	0001	44530	0.398	0.057	1.985	3.001	0.000	0.968	9.999	0.968	0.968	1.204			
1235	0001	44530	0.398	0.057	1.985	3.501	0.000	0.968	9.999	0.968	0.968	1.204			
1236	0001	44530	0.398	0.051	2.487	1.117	0.000	0.968	9.999	0.968	0.968	1.204			
1237	0001	44530	0.398	0.052	2.487	1.607	0.000	0.968	9.999	0.968	0.968	1.204			
1238	0001	44530	0.398	0.054	2.487	2.000	0.000	0.968	9.999	0.968	0.968	1.204			
1239	0001	44530	0.398	0.057	2.487	2.503	0.000	0.968	9.999	0.968	0.968	1.204			
1240	0001	44530	0.398	0.054	2.487	3.003	0.000	0.968	9.999	0.968	0.968	1.204			
1241	0001	44530	0.398	0.062	2.487	3.500	0.000	0.968	9.999	0.968	0.968	1.204			
1242	0001	44530	0.398	0.056	2.487	1.113	0.000	0.968	9.999	0.968	0.968	1.204			
1243	0001	44530	0.398	0.056	2.487	1.607	0.000	0.968	9.999	0.968	0.968	1.204			
1244	0001	44530	0.398	0.056	2.487	2.000	0.000	0.968	9.999	0.968	0.968	1.204			
1245	0001	44530	0.398	0.056	2.487	2.503	0.000	0.968	9.999	0.968	0.968	1.204			
1246	0001	44530	0.398	0.062	2.487	3.003	0.000	0.968	9.999	0.968	0.968	1.204			
1247	0001	44530	0.398	0.062	2.487	3.503	0.000	0.968	9.999	0.968	0.968	1.204			
1248	0001	44530	0.398	0.057	3.293	1.117	0.000	0.968	9.999	0.968	0.968	1.204			
1249	0001	44530	0.398	0.060	3.293	1.607	0.000	0.968	9.999	0.968	0.968	1.204			
1250	0001	44530	0.398	0.060	3.293	2.000	0.000	0.968	9.999	0.968	0.968	1.204			
1251	0001	44530	0.398	0.062	3.293	2.503	0.000	0.968	9.999	0.968	0.968	1.204			
1252	0001	44530	0.398	0.064	3.293	3.003	0.000	0.968	9.999	0.968	0.968	1.204			
1253	0001	44530	0.398	0.067	3.293	3.503	0.000	0.968	9.999	0.968	0.968	1.204			

FACILITY	I PROGRAM CODE										JUG CONFIGURATIONS										SUPPRESSOR CONFIGURATION									
	NOZLE TYPE										PASSIVE PLUG WITH BLEED										20-SPOKE, AREA RATIO = 1.75									
	OUTER RADIUS RATIO										INNER RADIUS RATIO																			
NOZLE PARAMETERS										JUG										SUPPRESSOR										
REF	GE	MASSA	D2	VA	FT/DA	DT/DA	OMGAT	OC	COS	NCOS	COSH	DCPI, C	DCPI, I	DCOT, C	DCOT, PSUP/PA															
1209	0001	44530	0.398	0.021	1.490	0.979	0.000	-0.014	9.199	-0.001	0.637	-0.007	0.006	-0.017	0.984															
1210	0001	44530	0.398	0.022	1.492	0.982	0.000	-0.015	8.962	-0.001	0.533	-0.005	0.005	-0.016	0.986															
1211	0001	44530	0.399	0.020	1.455	0.978	0.000	-0.014	8.799	-0.001	0.710	-0.006	0.003	-0.018	0.986															
1212	0001	44530	0.398	0.023	1.588	0.964	0.000	-0.014	8.755	-0.000	0.540	-0.005	0.009	-0.012	0.975															
1213	0001	44530	0.398	0.043	1.691	0.981	0.000	-0.013	2.602	-0.000	0.081	-0.004	0.008	-0.009	0.976															
1214	0001	44530	0.398	0.027	1.691	1.200	0.000	-0.012	2.612	-0.001	0.249	-0.003	0.006	-0.011	0.977															
1215	0001	44530	0.398	0.054	2.492	0.952	0.000	-0.012	2.666	-0.000	0.104	-0.004	0.010	-0.007	0.970															
1216	0001	44530	0.398	0.054	2.490	0.977	0.000	-0.011	3.777	-0.001	0.200	-0.004	0.008	-0.007	0.971															
1217	0001	44530	0.398	0.053	2.494	1.103	0.000	-0.011	2.545	-0.000	0.058	-0.001	0.006	-0.006	0.972															
1218	0001	44530	0.398	0.063	2.497	0.944	0.000	-0.010	3.036	-0.001	0.170	-0.014	0.009	-0.016	0.947															
1219	0001	44530	0.398	0.052	2.608	0.974	0.000	-0.008	2.904	-0.000	0.178	-0.012	0.007	-0.015	0.959															
1220	0001	44530	0.398	0.053	2.605	1.012	0.000	-0.008	2.793	-0.000	0.144	-0.011	0.005	-0.016	0.969															
1221	0001	44530	0.398	0.057	3.317	0.937	0.000	-0.010	2.853	-0.000	0.154	-0.013	0.009	-0.015	0.964															
1222	0001	44530	0.398	0.058	3.320	0.979	0.000	-0.009	2.665	-0.000	0.137	-0.012	0.007	-0.015	0.965															
1223	0001	44530	0.398	0.055	3.315	1.021	0.000	-0.009	2.801	-0.001	0.137	-0.011	0.004	-0.016	0.967															
1224	0001	44530	1.140	0.022	1.494	1.114	0.000	-0.011	7.013	-0.001	0.594	-0.003	0.001	-0.014	0.987															
1225	0001	44530	1.140	0.027	1.493	1.502	0.000	-0.008	4.798	-0.001	0.404	-0.002	0.001	-0.012	0.987															
1226	0001	44530	1.140	0.046	1.493	2.032	0.000	-0.008	1.435	-0.000	0.012	-0.001	0.017	-0.027	0.988															
1227	0001	44530	1.140	0.050	1.497	2.504	0.000	-0.008	1.241	-0.000	0.057	-0.001	0.021	-0.027	0.988															
1228	0001	44530	1.140	0.052	1.496	3.037	0.000	-0.004	1.066	-0.000	0.076	-0.001	0.028	-0.033	0.988															
1229	0001	44530	1.140	0.052	1.497	3.468	0.000	-0.004	1.070	-0.000	0.087	-0.001	0.028	-0.033	0.988															
1230	0001	44530	1.140	0.042	1.565	1.114	0.000	-0.012	2.893	-0.001	0.161	-0.001	0.002	-0.010	0.980															
1231	0001	44530	1.140	0.048	1.686	1.509	0.000	-0.008	2.054	-0.000	0.102	-0.001	0.000	-0.010	0.981															
1232	0001	44530	1.140	0.054	1.989	2.099	0.000	-0.008	1.445	-0.000	0.077	-0.001	0.019	-0.027	0.982															
1233	0001	44530	1.140	0.055	1.992	2.591	0.000	-0.006	1.625	-0.000	0.114	-0.000	0.017	-0.023	0.981															
1234	0001	44530	1.140	0.057	1.984	3.021	0.000	-0.005	1.593	-0.000	0.095	-0.000	0.025	-0.031	0.981															
1235	0001	44530	1.140	0.058	1.992	3.505	0.000	-0.005	1.402	-0.000	0.117	-0.000	0.010	-0.014	0.992															
1236	0001	44530	1.140	0.051	2.494	1.117	0.000	-0.012	2.617	-0.000	0.123	-0.001	0.002	-0.007	0.974															
1237	0001	44530	1.140	0.052	2.497	1.507	0.000	-0.008	2.348	-0.000	0.111	-0.001	0.006	-0.007	0.975															
1238	0001	44530	1.140	0.054	2.491	1.989	0.000	-0.007	2.206	-0.000	0.112	-0.001	0.014	-0.021	0.975															
1239	0001	44530	1.140	0.057	2.494	2.593	0.000	-0.005	1.994	-0.000	0.150	-0.001	0.019	-0.025	0.975															
1240	0001	44530	1.140	0.056	2.495	3.003	0.000	-0.004	1.904	-0.000	0.127	-0.001	0.030	-0.035	0.975															
1241	0001	44530	1.140	0.062	2.494	3.505	0.000	-0.004	1.540	-0.000	0.129	-0.001	0.013	-0.017	0.977															
1242	0001	44530	1.140	0.056	2.496	1.113	0.000	-0.012	2.617	-0.001	0.153	-0.000	0.002	-0.017	0.971															
1243	0001	44530	1.140	0.056	2.494	1.510	0.000	-0.007	2.224	-0.001	0.158	-0.000	0.000	-0.014	0.973															
1244	0001	44530	1.140	0.059	2.494	2.000	0.000	-0.007	2.120	-0.000	0.159	-0.000	0.012	-0.026	0.972															
1245	0001	44530	1.140	0.060	2.497	2.597	0.000	-0.006	1.857	-0.000	0.155	-0.000	0.016	-0.029	0.974															
1246	0001	44530	1.140	0.053	2.607	3.008	0.000	-0.003	1.709	-0.000	0.143	-0.000	0.028	-0.039	0.974															
1247	0001	44530	1.140	0.065	3.005	3.494	0.000	-0.004	1.536	-0.000	0.142	-0.000	0.015	-0.025	0.975															
1248	0001	44530	1.140	0.057	3.293	1.117	0.000	-0.008	2.506	-0.000	0.154	-0.000	0.002	-0.016	0.969															
1249	0001	44530	1.140	0.060	3.293	1.509	0.000	-0.007	2.147	-0.000	0.147	-0.000	0.006	-0.007	0.971															
1250	0001	44530	1.140	0.060	3.297	2.000	0.000	-0.006	2.102	-0.000	0.157	-0.000	0.013	-0.027	0.970															
1251	0001	44530	1.140	0.062	3.299	2.591	0.000	-0.006	2.024	-0.000	0.149	-0.000	0.007	-0.021	0.970															
1252	0001	44530	1.140	0.064	3.298	3.004	0.000	-0.006	1.791	-0.000	0.156	-0.000	0.006	-0.023	0.972															
1253	0001	44530	1.140	0.067	3.296	3.502	0.000	-0.006	1.564	-0.000	0.151	-0.000	0.005	-0.024	0.973															

FACILITY	AL PROGRAM CODE	NOZZLE TYPE		INLET STREAM		SUPPRESSOR CONFIGURATION					
		GUAL FLOW (GAL)		PLUG CONFIGURATIONS		20-SPOKE, AREA RATIO = 1.75					
		THRUST PARAMETERS		OUTER DIAMETER RATIO		INNER DIAMETER RATIO					
		0.0000		0.7790		1.2480					
PDC	CF	NASA	D2	M2	PT/PA	PM/CA	C/D	COI	CEMET1	CEMET2	F0
1254	0001	44550	1.140	0.050	1.114	0.143	0.936	0.941	0.944	1.014	1.184
1255	0001	44550	1.140	0.050	1.114	0.143	0.936	0.941	0.944	1.014	1.184
1256	0001	44550	1.140	0.050	1.114	0.143	0.936	0.941	0.944	1.014	1.184
1257	0001	44550	1.140	0.050	1.114	0.143	0.936	0.941	0.944	1.014	1.184
1258	0001	44550	1.140	0.050	1.114	0.143	0.936	0.941	0.944	1.014	1.184
1259	0001	44550	1.140	0.050	1.114	0.143	0.936	0.941	0.944	1.014	1.184
1260	0001	44550	1.140	0.050	1.114	0.143	0.936	0.941	0.944	1.014	1.184
1261	0001	44550	1.140	0.050	1.114	0.143	0.936	0.941	0.944	1.014	1.184
1262	0001	44550	1.140	0.050	1.114	0.143	0.936	0.941	0.944	1.014	1.184
1263	0001	44550	1.140	0.050	1.114	0.143	0.936	0.941	0.944	1.014	1.184
1264	0001	44550	1.140	0.050	1.114	0.143	0.936	0.941	0.944	1.014	1.184
1265	0001	44550	1.140	0.050	1.114	0.143	0.936	0.941	0.944	1.014	1.184
1266	0001	44550	1.140	0.050	1.114	0.143	0.936	0.941	0.944	1.014	1.184
1267	0001	44550	1.140	0.050	1.114	0.143	0.936	0.941	0.944	1.014	1.184
1268	0001	44550	1.140	0.050	1.114	0.143	0.936	0.941	0.944	1.014	1.184
1269	0001	44550	1.140	0.050	1.114	0.143	0.936	0.941	0.944	1.014	1.184
1270	0001	44550	1.140	0.050	1.114	0.143	0.936	0.941	0.944	1.014	1.184
1271	0001	44550	1.140	0.050	1.114	0.143	0.936	0.941	0.944	1.014	1.184
1272	0001	44550	1.140	0.050	1.114	0.143	0.936	0.941	0.944	1.014	1.184
1273	0001	44550	1.140	0.050	1.114	0.143	0.936	0.941	0.944	1.014	1.184
1274	0001	44550	1.140	0.050	1.114	0.143	0.936	0.941	0.944	1.014	1.184
1275	0001	44550	1.140	0.050	1.114	0.143	0.936	0.941	0.944	1.014	1.184
1276	0001	44550	1.140	0.050	1.114	0.143	0.936	0.941	0.944	1.014	1.184
1277	0001	44550	1.140	0.050	1.114	0.143	0.936	0.941	0.944	1.014	1.184
1278	0001	44550	1.140	0.050	1.114	0.143	0.936	0.941	0.944	1.014	1.184
1279	0001	44550	1.140	0.050	1.114	0.143	0.936	0.941	0.944	1.014	1.184
1280	0001	44550	1.140	0.050	1.114	0.143	0.936	0.941	0.944	1.014	1.184
1281	0001	44550	1.140	0.050	1.114	0.143	0.936	0.941	0.944	1.014	1.184
1282	0001	44550	1.140	0.050	1.114	0.143	0.936	0.941	0.944	1.014	1.184
1283	0001	44550	1.140	0.050	1.114	0.143	0.936	0.941	0.944	1.014	1.184
1284	0001	44550	1.140	0.050	1.114	0.143	0.936	0.941	0.944	1.014	1.184
1285	0001	44550	1.140	0.050	1.114	0.143	0.936	0.941	0.944	1.014	1.184
1286	0001	44550	1.140	0.050	1.114	0.143	0.936	0.941	0.944	1.014	1.184
1287	0001	44550	1.140	0.050	1.114	0.143	0.936	0.941	0.944	1.014	1.184
1288	0001	44550	1.140	0.050	1.114	0.143	0.936	0.941	0.944	1.014	1.184
1289	0001	44550	1.140	0.050	1.114	0.143	0.936	0.941	0.944	1.014	1.184
1290	0001	44550	1.140	0.050	1.114	0.143	0.936	0.941	0.944	1.014	1.184
1291	0001	44550	1.140	0.050	1.114	0.143	0.936	0.941	0.944	1.014	1.184
1292	0001	44550	1.140	0.050	1.114	0.143	0.936	0.941	0.944	1.014	1.184
1293	0001	44550	1.140	0.050	1.114	0.143	0.936	0.941	0.944	1.014	1.184
1294	0001	44550	1.140	0.050	1.114	0.143	0.936	0.941	0.944	1.014	1.184
1295	0001	44550	1.140	0.050	1.114	0.143	0.936	0.941	0.944	1.014	1.184
1296	0001	44550	1.140	0.050	1.114	0.143	0.936	0.941	0.944	1.014	1.184
1297	0001	44550	1.140	0.050	1.114	0.143	0.936	0.941	0.944	1.014	1.184
1298	0001	44550	1.140	0.050	1.114	0.143	0.936	0.941	0.944	1.014	1.184
1299	0001	44550	1.140	0.050	1.114	0.143	0.936	0.941	0.944	1.014	1.184
1300	0001	44550	1.140	0.050	1.114	0.143	0.936	0.941	0.944	1.014	1.184

## FACILITY A PROGRAM C031

SUPPRESSOR CONFIGURATION  
20-SPOKE, AREA RATIO = 1.75INSTRUMENT  
PLUG CONFIGURATIONS  
BASELINE PLUG WITH GLEONOZZLE TYPE  
FIAL FL04 (FAN)

## FACILITY A PROGRAM C031

SUPPRESSOR CONFIGURATION  
20-SPOKE, AREA RATIO = 1.75INSTRUMENT  
PLUG CONFIGURATIONS  
BASELINE PLUG WITH GLEONOZZLE TYPE  
FIAL FL04 (FAN)

NOISE PARAMETERS		OUTER RADIUS RATIO		INNER RADIUS RATIO		INSTRUMENT		PLUG CONFIGURATIONS		SUPPRESSOR CONFIGURATION	
		0.0020		0.7790		1.7500					
PDC	GE	M4	PI/PA	PI/PA	PI/PA	PI/PA	PI/PA	PI/PA	PI/PA	PI/PA	PI/PA
1254	0001	44550	1.140	0.050	2.401	1.114	0.143	-0.019	2.075	-0.001	0.003
1255	0001	44550	1.140	0.050	2.401	1.114	0.143	-0.019	2.075	-0.001	0.003
1256	0001	44550	0.394	0.048	2.466	1.007	0.455	-0.006	1.792	-0.000	0.132
1257	0001	44550	0.394	0.048	2.466	1.007	0.455	-0.006	1.792	-0.000	0.132
1258	0001	44550	0.394	0.048	2.466	1.007	0.455	-0.006	1.792	-0.000	0.132
1259	0001	44550	0.394	0.048	2.466	1.007	0.455	-0.006	1.792	-0.000	0.132
1260	0001	44550	0.394	0.048	2.466	1.007	0.455	-0.006	1.792	-0.000	0.132
1261	0001	44550	0.394	0.048	2.466	1.007	0.455	-0.006	1.792	-0.000	0.132
1262	0001	44550	0.394	0.048	2.466	1.007	0.455	-0.006	1.792	-0.000	0.132
1263	0001	44550	0.394	0.048	2.466	1.007	0.455	-0.006	1.792	-0.000	0.132
1264	0001	44550	0.394	0.048	2.466	1.007	0.455	-0.006	1.792	-0.000	0.132
1265	0001	44550	0.394	0.048	2.466	1.007	0.455	-0.006	1.792	-0.000	0.132
1266	0001	44550	0.394	0.048	2.466	1.007	0.455	-0.006	1.792	-0.000	0.132
1267	0001	44550	0.394	0.048	2.466	1.007	0.455	-0.006	1.792	-0.000	0.132
1268	0001	44550	0.394	0.048	2.466	1.007	0.455	-0.006	1.792	-0.000	0.132
1269	0001	44550	0.394	0.048	2.466	1.007	0.455	-0.006	1.792	-0.000	0.132
1270	0001	44550	0.394	0.048	2.466	1.007	0.455	-0.006	1.792	-0.000	0.132
1271	0001	44550	0.394	0.048	2.466	1.007	0.455	-0.006	1.792	-0.000	0.132
1272	0001	44550	0.394	0.048	2.466	1.007	0.455	-0.006	1.792	-0.000	0.132
1273	0001	44550	0.394	0.048	2.466	1.007	0.455	-0.006	1.792	-0.000	0.132
1274	0001	44550	0.394	0.048	2.466	1.007	0.455	-0.006	1.792	-0.000	0.132
1275	0001	44550	0.394	0.048	2.466	1.007	0.455	-0.006	1.792	-0.000	0.132
1276	0001	44550	0.394	0.048	2.466	1.007	0.455	-0.006	1.792	-0.000	0.132
1277	0001	44550	0.394	0.048	2.466	1.007	0.455	-0.006	1.792	-0.000	0.132
1278	0001	44550	0.394	0.048	2.466	1.007	0.455	-0.006	1.792	-0.000	0.132
1279	0001	44550	0.394	0.048	2.466	1.007	0.455	-0.006	1.792	-0.000	0.132
1280	0001	44550	0.394	0.048	2.466	1.007	0.455	-0.006	1.792	-0.000	0.132
1281	0001	44550	0.394	0.048	2.466	1.007	0.455	-0.006	1.792	-0.000	0.132
1282	0001	44550	0.394	0.048	2.466	1.007	0.455	-0.006	1.792	-0.000	0.132
1283	0001	44550	0.394	0.048	2.466	1.007	0.455	-0.006	1.792	-0.000	0.132
1284	0001	44550	0.394	0.048	2.466	1.007	0.455	-0.006	1.792	-0.000	0.132
1285	0001	44550	0.394	0.048	2.466	1.007	0.455	-0.006	1.792	-0.000	0.132
1286	0001	44550	0.394	0.048	2.466	1.007	0.455	-0.006	1.792	-0.000	0.132
1287	0001	44550	0.394	0.048	2.466	1.007	0.455	-0.006	1.792	-0.000	0.132
1288	0001	44550	0.394	0.048	2.466	1.007	0.455	-0.006	1.792	-0.000	0.132
1289	0001	44550	0.394	0.048	2.466	1.007	0.455	-0.006	1.792	-0.000	0.132
1290	0001	44550	0.394	0.048	2.466	1.007	0.455	-0.006	1.792	-0.000	0.132
1291	0001	44550	0.394	0.048	2.466	1.007	0.455	-0.006	1.792	-0.000	0.132
1292	0001	44550	0.394	0.048	2.466	1.007	0.455	-0.006	1.792	-0.000	0.132
1293	0001	44550	0.394	0.048	2.466	1.007	0.455	-0.006	1.792	-0.000	0.132
1294	0001	44550	0.394	0.048	2.466	1.007	0.455	-0.006	1.792	-0.000	0.132
1295	0001	44550	0.394	0.048	2.466	1.007	0.455	-0.006	1.792	-0.000	0.132
1296	0001	44550	0.394	0.048	2.466	1.007	0.455	-0.006	1.792	-0.000	0.132
1297	0001	44550	0.394	0.048	2.466	1.007	0.455	-0.006	1.792	-0.000	0.132
1298	0001	44550	0.394	0.048	2.466	1.007	0.455	-0.006	1.792	-0.000	0.132
1299	0001	44550	0.394	0.048	2.466	1.007	0.455	-0.006	1.792	-0.000	0.132
1300	0001	44550	0.394	0.048	2.466	1.007	0.455	-0.006	1.792	-0.000	0.132

FACILITY A - 1 PROGRAM CODE		NOZZLE TYPE		INLET STREAM		SUPPRESSOR CONFIGURATION	
DUAL FLOW (FAC)		WASSELING PLUG WITH SCREEN		20-SOURCE, ADFA PATIN = 1.75			
THURST PARAMETERS		OUTLET PRESSURE RATIO		INLET PRESSURE RATIO		DVO	
QVC	CF	MASS	PZ	W	QVC/MASS	PZ/MASS	QVC/MASS
1300	0001	64550	1.140	0.448	3.204	0.278	0.949
1301	0001	64550	1.140	0.448	3.204	0.278	0.949
1302	0001	64550	1.140	0.448	3.204	0.278	0.949
1303	0001	64550	1.140	0.448	3.204	0.278	0.949
1304	0001	64550	1.140	0.448	3.204	0.278	0.949
1305	0001	64550	1.140	0.448	3.204	0.278	0.949
1306	0001	64550	1.140	0.448	3.204	0.278	0.949
1307	0001	64550	1.140	0.448	3.204	0.278	0.949
1308	0001	64550	1.140	0.448	3.204	0.278	0.949
1309	0001	64550	1.140	0.448	3.204	0.278	0.949
1310	0001	64550	1.140	0.448	3.204	0.278	0.949
1311	0001	64550	1.140	0.448	3.204	0.278	0.949
1312	0001	64550	1.140	0.448	3.204	0.278	0.949
1313	0001	64550	1.140	0.448	3.204	0.278	0.949
1314	0001	64550	1.140	0.448	3.204	0.278	0.949
1315	0001	64550	1.140	0.448	3.204	0.278	0.949
1316	0001	64550	1.140	0.448	3.204	0.278	0.949
1317	0001	64550	1.140	0.448	3.204	0.278	0.949
1318	0001	64550	1.140	0.448	3.204	0.278	0.949
1319	0001	64550	1.140	0.448	3.204	0.278	0.949
1320	0001	64550	1.140	0.448	3.204	0.278	0.949
1321	0001	64550	1.140	0.448	3.204	0.278	0.949
1322	0001	64550	1.140	0.448	3.204	0.278	0.949
1323	0001	64550	1.140	0.448	3.204	0.278	0.949
1324	0001	64550	1.140	0.448	3.204	0.278	0.949
1325	0001	64550	1.140	0.448	3.204	0.278	0.949
1326	0001	64550	1.140	0.448	3.204	0.278	0.949
1327	0001	64550	1.140	0.448	3.204	0.278	0.949
1328	0001	64550	1.140	0.448	3.204	0.278	0.949
1329	0001	64550	1.140	0.448	3.204	0.278	0.949
1330	0001	64550	1.140	0.448	3.204	0.278	0.949
1331	0001	64550	1.140	0.448	3.204	0.278	0.949
1332	0001	64550	1.140	0.448	3.204	0.278	0.949
1333	0001	64550	1.140	0.448	3.204	0.278	0.949
1334	0001	64550	1.140	0.448	3.204	0.278	0.949
1335	0001	64550	1.140	0.448	3.204	0.278	0.949
1336	0001	64550	1.140	0.448	3.204	0.278	0.949
1337	0001	64550	1.140	0.448	3.204	0.278	0.949
1338	0001	64550	1.140	0.448	3.204	0.278	0.949
1339	0001	64550	1.140	0.448	3.204	0.278	0.949
1340	0001	64550	1.140	0.448	3.204	0.278	0.949
1341	0001	64550	1.140	0.448	3.204	0.278	0.949
1342	0001	64550	1.140	0.448	3.204	0.278	0.949
1343	0001	64550	1.140	0.448	3.204	0.278	0.949
1344	0001	64550	1.140	0.448	3.204	0.278	0.949





[illegible][illegible]

MODEL SC-2, 30 SHALLOW CHUTES, AR = 1.75, BASELINE PLUG

FACILITY NO. [ ] PROGRAM CODE      MODEL TYPE      1954-1958M      PLUG CONFIGURATIONS      SUPPRESSOR CONCENTRATION  
 30-SPOKE, AREA RATIO = 1.75

INPUT: PAR PARAMETERS      RUTHERFORDS      IMAGE RADIUS      0.7790      DUTY      1.1480

PRC	RF	Q55A	Q3	FE	PIR200	PIR100	RMCA2	Q2	Q01	CEP11	CEP12	F9
1357	0002	45510	0.108	0.440	1.453	1.003	0.300	3.545	0.303	0.819	0.819	1.097
1358	0002	45510	0.108	0.440	1.453	1.003	0.300	3.545	0.303	0.819	0.819	1.097
1359	0002	45510	0.108	0.440	1.453	1.003	0.300	3.545	0.303	0.819	0.819	1.097
1360	0002	45510	0.108	0.440	1.453	1.003	0.300	3.545	0.303	0.819	0.819	1.097
1361	0002	45510	0.108	0.440	1.453	1.003	0.300	3.545	0.303	0.819	0.819	1.097
1362	0002	45510	0.108	0.440	1.453	1.003	0.300	3.545	0.303	0.819	0.819	1.097
1363	0002	45510	0.108	0.440	1.453	1.003	0.300	3.545	0.303	0.819	0.819	1.097
1364	0002	45510	0.108	0.440	1.453	1.003	0.300	3.545	0.303	0.819	0.819	1.097
1365	0002	45510	0.108	0.440	1.453	1.003	0.300	3.545	0.303	0.819	0.819	1.097
1366	0002	45510	0.108	0.440	1.453	1.003	0.300	3.545	0.303	0.819	0.819	1.097
1367	0002	45510	0.108	0.440	1.453	1.003	0.300	3.545	0.303	0.819	0.819	1.097
1368	0002	45510	0.108	0.440	1.453	1.003	0.300	3.545	0.303	0.819	0.819	1.097
1369	0002	45510	0.108	0.440	1.453	1.003	0.300	3.545	0.303	0.819	0.819	1.097
1370	0002	45510	0.108	0.440	1.453	1.003	0.300	3.545	0.303	0.819	0.819	1.097
1371	0002	45510	0.108	0.440	1.453	1.003	0.300	3.545	0.303	0.819	0.819	1.097
1372	0002	45510	0.108	0.440	1.453	1.003	0.300	3.545	0.303	0.819	0.819	1.097
1373	0002	45510	0.108	0.440	1.453	1.003	0.300	3.545	0.303	0.819	0.819	1.097
1374	0002	45510	0.108	0.440	1.453	1.003	0.300	3.545	0.303	0.819	0.819	1.097
1375	0002	45510	0.108	0.440	1.453	1.003	0.300	3.545	0.303	0.819	0.819	1.097
1376	0002	45510	0.108	0.440	1.453	1.003	0.300	3.545	0.303	0.819	0.819	1.097
1377	0002	45510	0.108	0.440	1.453	1.003	0.300	3.545	0.303	0.819	0.819	1.097
1378	0002	45510	0.108	0.440	1.453	1.003	0.300	3.545	0.303	0.819	0.819	1.097
1379	0002	45510	0.108	0.440	1.453	1.003	0.300	3.545	0.303	0.819	0.819	1.097
1380	0002	45510	0.108	0.440	1.453	1.003	0.300	3.545	0.303	0.819	0.819	1.097
1381	0002	45510	0.108	0.440	1.453	1.003	0.300	3.545	0.303	0.819	0.819	1.097
1382	0002	45510	0.108	0.440	1.453	1.003	0.300	3.545	0.303	0.819	0.819	1.097
1383	0002	45510	0.108	0.440	1.453	1.003	0.300	3.545	0.303	0.819	0.819	1.097
1384	0002	45510	0.108	0.440	1.453	1.003	0.300	3.545	0.303	0.819	0.819	1.097
1385	0002	45510	0.108	0.440	1.453	1.003	0.300	3.545	0.303	0.819	0.819	1.097
1386	0002	45510	0.108	0.440	1.453	1.003	0.300	3.545	0.303	0.819	0.819	1.097
1387	0002	45510	0.108	0.440	1.453	1.003	0.300	3.545	0.303	0.819	0.819	1.097
1388	0002	45510	0.108	0.440	1.453	1.003	0.300	3.545	0.303	0.819	0.819	1.097
1389	0002	45510	0.108	0.440	1.453	1.003	0.300	3.545	0.303	0.819	0.819	1.097
1390	0002	45510	0.108	0.440	1.453	1.003	0.300	3.545	0.303	0.819	0.819	1.097
1391	0002	45510	0.108	0.440	1.453	1.003	0.300	3.545	0.303	0.819	0.819	1.097
1392	0002	45510	0.108	0.440	1.453	1.003	0.300	3.545	0.303	0.819	0.819	1.097
1393	0002	45510	0.108	0.440	1.453	1.003	0.300	3.545	0.303	0.819	0.819	1.097
1394	0002	45510	0.108	0.440	1.453	1.003	0.300	3.545	0.303	0.819	0.819	1.097
1395	0002	45510	0.108	0.440	1.453	1.003	0.300	3.545	0.303	0.819	0.819	1.097
1396	0002	45510	0.108	0.440	1.453	1.003	0.300	3.545	0.303	0.819	0.819	1.097
1397	0002	45510	0.108	0.440	1.453	1.003	0.300	3.545	0.303	0.819	0.819	1.097
1398	0002	45510	0.108	0.440	1.453	1.003	0.300	3.545	0.303	0.819	0.819	1.097
1399	0002	45510	0.108	0.440	1.453	1.003	0.300	3.545	0.303	0.819	0.819	1.097
1400	0002	45510	0.108	0.440	1.453	1.003	0.300	3.545	0.303	0.819	0.819	1.097

[illegible]

720

[illegible]



[illegible]





MODEL SC-3, 30 SHALLOW CHUTES, AR = 1.75, REDUCED AREA

726



FACILITY 21 BONGHOM 0031		IN - STREAM		SUPPRESSOR CONFIGURATION	
MODEL TYPE		122 BLEED AREA WITH BLEED		32-SOPKE, AREA RATIO = 1.75	
DUAL, 122 BLEED		DUAL		DUAL	
OFFER RADIUS 0.0030		OFFER RADIUS 0.0030		OFFER RADIUS 0.0030	
INSTR. PARAMETERS		INSTR. PARAMETERS		INSTR. PARAMETERS	
LOC	CE	WAVE	Q2	Q1	Q0
1402	0003	45710	1.140	0.440	0.440
1403	0003	45710	1.140	0.440	0.440
1404	0003	45710	1.140	0.440	0.440
1405	0003	45710	1.140	0.440	0.440
1406	0003	45710	1.140	0.440	0.440
1407	0003	45710	1.140	0.440	0.440
1408	0003	45710	1.140	0.440	0.440
1409	0003	45710	1.140	0.440	0.440
1410	0003	45710	1.140	0.440	0.440
1411	0003	45710	1.140	0.440	0.440
1412	0003	45710	1.140	0.440	0.440
1413	0003	45710	1.140	0.440	0.440
1414	0003	45710	1.140	0.440	0.440
1415	0003	45710	1.140	0.440	0.440
1416	0003	45710	1.140	0.440	0.440
1417	0003	45710	1.140	0.440	0.440
1418	0003	45710	1.140	0.440	0.440
1419	0003	45710	1.140	0.440	0.440
1420	0003	45710	1.140	0.440	0.440
1421	0003	45710	1.140	0.440	0.440
1422	0003	45710	1.140	0.440	0.440
1423	0003	45710	1.140	0.440	0.440
1424	0003	45710	1.140	0.440	0.440
1425	0003	45710	1.140	0.440	0.440
1426	0003	45710	1.140	0.440	0.440
1427	0003	45710	1.140	0.440	0.440
1428	0003	45710	1.140	0.440	0.440
1429	0003	45710	1.140	0.440	0.440
1430	0003	45710	1.140	0.440	0.440
1431	0003	45710	1.140	0.440	0.440
1432	0003	45710	1.140	0.440	0.440
1433	0003	45710	1.140	0.440	0.440
1434	0003	45710	1.140	0.440	0.440
1435	0003	45710	1.140	0.440	0.440
1436	0003	45710	1.140	0.440	0.440
1437	0003	45710	1.140	0.440	0.440
1438	0003	45710	1.140	0.440	0.440
1439	0003	45710	1.140	0.440	0.440
1440	0003	45710	1.140	0.440	0.440
1441	0003	45710	1.140	0.440	0.440
1442	0003	45710	1.140	0.440	0.440
1443	0003	45710	1.140	0.440	0.440
1444	0003	45710	1.140	0.440	0.440
1445	0003	45710	1.140	0.440	0.440
1446	0003	45710	1.140	0.440	0.440











DATE: 04/24/87

TIME: 15:00

LOCATION: 11-175

CONF: 11-175

CONF: 11-175

CONF: 11-175

CONF: 11-175

CONF: 11-175

CONF: 11-175

CONF: 11-175

CONF: 11-175

CONF: 11-175

CONF: 11-175

CONF: 11-175

CONF: 11-175

CONF: 11-175

CONF: 11-175

CONF: 11-175

CONF: 11-175

CONF: 11-175

CONF: 11-175

CONF: 11-175

CONF: 11-175

CONF: 11-175

CONF: 11-175

CONF: 11-175

CONF: 11-175

CONF: 11-175

CONF: 11-175

CONF: 11-175

CONF: 11-175

CONF: 11-175

CONF: 11-175

CONF: 11-175

CONF: 11-175

CONF: 11-175

CONF: 11-175

CONF: 11-175

CONF: 11-175

CONF: 11-175

CONF: 11-175

CONF: 11-175

CONF: 11-175

CONF: 11-175

CONF: 11-175

CONF: 11-175

CONF: 11-175

CONF: 11-175

CONF: 11-175

CONF: 11-175

CONF: 11-175

CONF: 11-175

CONF: 11-175

CONF: 11-175

CONF: 11-175

CONF: 11-175

MODEL SC-4, 30 SHALLOW CHUTES, AR = 1.75, FULL PLUG





FACILITY		L PROGRAM COIL		NOZZLE TYPE		INLET		SUPPRESSOR CONFIGURATION	
				FULL FLOW LEAK		PLUG CONFIGURATIONS		30-SPRKE, AREA RATIO = 1.75	
						FULL PLUG W/O BLEED			
THROUST PARAMETERS				OUTER RADIUS RATIO		INNER RADIUS RATIO		DVT	
				0.0000		0.0000		1.2680	
CF	MSA	N2	WA	PT/PA	PT/PA	CFMGT	CDI	CFMGT1	CFMGT2
1552	0005	45830	0.398	2.772	1.221	0.000	0.971	0.999	0.899
1553	0005	45830	0.398	3.007	1.271	0.000	1.909	0.906	0.905
1554	0005	45830	0.398	3.232	1.342	0.000	2.970	0.911	0.911
1555	0005	45830	0.398	3.357	1.377	0.000	0.967	0.882	0.882
1556	0005	45830	0.398	3.355	1.392	0.000	0.573	0.904	0.904

FACILITY		L PROGRAM COIL		NOZZLE TYPE		INLET		SUPPRESSOR CONFIGURATION	
				FULL FLOW LEAK		PLUG CONFIGURATIONS		30-SPRKE, AREA RATIO = 1.75	
						FULL PLUG W/O BLEED			
THROUST PARAMETERS				OUTER RADIUS RATIO		INNER RADIUS RATIO		DVT	
				0.0000		0.0000		1.2680	
CF	MSA	N2	WA	PT/PA	PT/PA	CFMGT	CDI	CFMGT1	CFMGT2
1552	0005	45830	0.398	2.772	1.221	0.000	0.971	0.999	0.899
1553	0005	45830	0.398	3.007	1.271	0.000	1.909	0.906	0.905
1554	0005	45830	0.398	3.232	1.342	0.000	2.970	0.911	0.911
1555	0005	45830	0.398	3.357	1.377	0.000	0.967	0.882	0.882
1556	0005	45830	0.398	3.355	1.392	0.000	0.573	0.904	0.904

MODEL SC-5, 30 SHALLOW CHUTES, AR = 1.75, FORWARD PLUG

FACILITY -- 621 90024M C031		JETTABLE IFAS		IN. 2-STEP		PLUG CONFIGURATIONS		SUPPRESSOR CONFIGURATION	
DUAL FLOW IFAS		FORWARD PLUG WITH BLEED		30-SPRKE, ARFA RATIO = 1.75					
THRUJET PARALLEL-STEP		OUTER RADIUS RATIO		INNER RADIUS RATIO		DVO			
		0.0000		0.2700		1.2480			
ARC	CF	DATA	D2	MA	BIKARA	CMGAT	CDN	CDUET1	GENE12
2505	0004	45610	0.104	0.447	1.504	0.000	0.995	0.830	0.830
2506	0004	45610	0.104	0.447	1.504	0.000	0.995	0.830	0.830
2507	0004	45610	0.104	0.447	1.504	0.000	0.995	0.830	0.830
2508	0004	45610	0.104	0.447	1.504	0.000	0.995	0.830	0.830
2509	0004	45610	0.104	0.447	1.504	0.000	0.995	0.830	0.830
2510	0004	45610	0.104	0.447	1.504	0.000	0.995	0.830	0.830
2511	0004	45610	0.104	0.447	1.504	0.000	0.995	0.830	0.830
2512	0004	45610	0.104	0.447	1.504	0.000	0.995	0.830	0.830
2513	0004	45610	0.104	0.447	1.504	0.000	0.995	0.830	0.830
2514	0004	45610	0.104	0.447	1.504	0.000	0.995	0.830	0.830
2515	0004	45610	0.104	0.447	1.504	0.000	0.995	0.830	0.830
2516	0004	45610	0.104	0.447	1.504	0.000	0.995	0.830	0.830
2517	0004	45610	0.104	0.447	1.504	0.000	0.995	0.830	0.830
2518	0004	45610	0.104	0.447	1.504	0.000	0.995	0.830	0.830
2519	0004	45610	0.104	0.447	1.504	0.000	0.995	0.830	0.830
2520	0004	45610	0.104	0.447	1.504	0.000	0.995	0.830	0.830
2521	0004	45610	0.104	0.447	1.504	0.000	0.995	0.830	0.830
2522	0004	45610	0.104	0.447	1.504	0.000	0.995	0.830	0.830
2523	0004	45610	0.104	0.447	1.504	0.000	0.995	0.830	0.830
2524	0004	45610	0.104	0.447	1.504	0.000	0.995	0.830	0.830
2525	0004	45610	0.104	0.447	1.504	0.000	0.995	0.830	0.830
2526	0004	45610	0.104	0.447	1.504	0.000	0.995	0.830	0.830
2527	0004	45610	0.104	0.447	1.504	0.000	0.995	0.830	0.830
2528	0004	45610	0.104	0.447	1.504	0.000	0.995	0.830	0.830
2529	0004	45610	0.104	0.447	1.504	0.000	0.995	0.830	0.830
2530	0004	45610	0.104	0.447	1.504	0.000	0.995	0.830	0.830
2531	0004	45610	0.104	0.447	1.504	0.000	0.995	0.830	0.830
2532	0004	45610	0.104	0.447	1.504	0.000	0.995	0.830	0.830
2533	0004	45610	0.104	0.447	1.504	0.000	0.995	0.830	0.830
2534	0004	45610	0.104	0.447	1.504	0.000	0.995	0.830	0.830
2535	0004	45610	0.104	0.447	1.504	0.000	0.995	0.830	0.830
2536	0004	45610	0.104	0.447	1.504	0.000	0.995	0.830	0.830
2537	0004	45610	0.104	0.447	1.504	0.000	0.995	0.830	0.830
2538	0004	45610	0.104	0.447	1.504	0.000	0.995	0.830	0.830
2539	0004	45610	0.104	0.447	1.504	0.000	0.995	0.830	0.830
2540	0004	45610	0.104	0.447	1.504	0.000	0.995	0.830	0.830
2541	0004	45610	0.104	0.447	1.504	0.000	0.995	0.830	0.830
2542	0004	45610	0.104	0.447	1.504	0.000	0.995	0.830	0.830
2543	0004	45610	0.104	0.447	1.504	0.000	0.995	0.830	0.830
2544	0004	45610	0.104	0.447	1.504	0.000	0.995	0.830	0.830
2545	0004	45610	0.104	0.447	1.504	0.000	0.995	0.830	0.830
2546	0004	45610	0.104	0.447	1.504	0.000	0.995	0.830	0.830
2547	0004	45610	0.104	0.447	1.504	0.000	0.995	0.830	0.830
2548	0004	45610	0.104	0.447	1.504	0.000	0.995	0.830	0.830
2549	0004	45610	0.104	0.447	1.504	0.000	0.995	0.830	0.830















MODEL SC-6, 40 SHALLOW CHUTES, AR = 1.75, BASELINE PLUG

[illegible]







ACTIVITY - AXI PROGRAM CODE

IN - STEAM  
PI CONFIGURATIONS  
BASELINE PLUG WITH BLEED  
SUPPRESSOR CONFIGURATION  
40-SPOKE, AREA RATIO = 1.75

NOZZLE TYPE  
DUAL FLOW (F44)

NOZZLE PARAMETERS		OUTER RADIUS RATIO		INNER RADIUS RATIO		DWT	
		0.0000		0.7790		1.2480	
LOC	PL	W	PI/PA	PI/PA	PI/PA	W	PI/PA
1777	0004	46550	1.140	3.140	0.512	0.066	17.804
1778	0004	46550	1.140	3.067	0.510	0.064	17.804
1779	0004	46550	1.140	2.994	0.508	0.062	17.804
1780	0004	46550	1.140	2.921	0.506	0.060	17.804
1781	0004	46550	1.140	2.848	0.504	0.058	17.804
1782	0004	46550	1.140	2.775	0.502	0.056	17.804
1783	0004	46550	1.140	2.702	0.500	0.054	17.804
1784	0004	46550	1.140	2.629	0.498	0.052	17.804
1785	0004	46550	1.140	2.556	0.496	0.050	17.804
1786	0004	46550	1.140	2.483	0.494	0.048	17.804
1787	0004	46550	1.140	2.410	0.492	0.046	17.804
1788	0004	46550	1.140	2.337	0.490	0.044	17.804
1789	0004	46550	1.140	2.264	0.488	0.042	17.804
1790	0004	46550	1.140	2.191	0.486	0.040	17.804
1791	0004	46550	1.140	2.118	0.484	0.038	17.804
1792	0004	46550	1.140	2.045	0.482	0.036	17.804
1793	0004	46550	1.140	1.972	0.480	0.034	17.804
1794	0004	46550	1.140	1.899	0.478	0.032	17.804
1795	0004	46550	1.140	1.826	0.476	0.030	17.804
1796	0004	46550	1.140	1.753	0.474	0.028	17.804
1797	0004	46550	1.140	1.680	0.472	0.026	17.804
1798	0004	46550	1.140	1.607	0.470	0.024	17.804
1799	0004	46550	1.140	1.534	0.468	0.022	17.804
1800	0004	46550	1.140	1.461	0.466	0.020	17.804
1801	0004	46550	1.140	1.388	0.464	0.018	17.804
1802	0004	46550	1.140	1.315	0.462	0.016	17.804
1803	0004	46550	1.140	1.242	0.460	0.014	17.804
1804	0004	46550	1.140	1.169	0.458	0.012	17.804
1805	0004	46550	1.140	1.096	0.456	0.010	17.804
1806	0004	46550	1.140	1.023	0.454	0.008	17.804
1807	0004	46550	1.140	0.950	0.452	0.006	17.804
1808	0004	46550	1.140	0.877	0.450	0.004	17.804
1809	0004	46550	1.140	0.804	0.448	0.002	17.804
1810	0004	46550	1.140	0.731	0.446	0.000	17.804
1811	0004	46550	1.140	0.658	0.444	0.000	17.804
1812	0004	46550	1.140	0.585	0.442	0.000	17.804
1813	0004	46550	1.140	0.512	0.440	0.000	17.804
1814	0004	46550	1.140	0.439	0.438	0.000	17.804
1815	0004	46550	1.140	0.366	0.436	0.000	17.804
1816	0004	46550	1.140	0.293	0.434	0.000	17.804
1817	0004	46550	1.140	0.220	0.432	0.000	17.804
1818	0004	46550	1.140	0.147	0.430	0.000	17.804
1819	0004	46550	1.140	0.074	0.428	0.000	17.804
1820	0004	46550	1.140	0.001	0.426	0.000	17.804
1821	0004	46550	1.140	0.000	0.424	0.000	17.804



FACILITY: 1X1 POWER CO. 311

NOZZLE TYPE: 11

PI: 11

STREAM CONFIGURATIONS: 40-SPOKE, AREA RATIO = 1.75

BASELINE P.L.G. WITH BLEED

NOZZLE TYPE: 11

PI: 11

STREAM CONFIGURATIONS: 40-SPOKE, AREA RATIO = 1.75

DEAC	PARAMETERS	OUTER RADIUS RATIO	INNER RADIUS RATIO	NOZZLE TYPE	PI	STREAM CONFIGURATIONS	SUPPRESSOR CONFIGURATION
1822	0006 46550	1.140	0.000	1.122	0.7790	1.2490	0.000
1823	0006 46550	1.140	0.000	1.122	0.7790	1.2490	0.000
1824	0006 46550	1.140	0.000	1.122	0.7790	1.2490	0.000
1825	0006 46550	1.140	0.000	1.122	0.7790	1.2490	0.000
1826	0006 46550	1.140	0.000	1.122	0.7790	1.2490	0.000
1827	0006 46550	1.140	0.000	1.122	0.7790	1.2490	0.000
1828	0006 46550	1.140	0.000	1.122	0.7790	1.2490	0.000
1829	0006 46550	1.140	0.000	1.122	0.7790	1.2490	0.000
1830	0006 46550	1.140	0.000	1.122	0.7790	1.2490	0.000
1831	0006 46550	1.140	0.000	1.122	0.7790	1.2490	0.000
1832	0006 46550	1.140	0.000	1.122	0.7790	1.2490	0.000
1833	0006 46550	1.140	0.000	1.122	0.7790	1.2490	0.000
1834	0006 46550	1.140	0.000	1.122	0.7790	1.2490	0.000
1835	0006 46550	1.140	0.000	1.122	0.7790	1.2490	0.000
1836	0006 46550	1.140	0.000	1.122	0.7790	1.2490	0.000
1837	0006 46550	1.140	0.000	1.122	0.7790	1.2490	0.000
1838	0006 46550	1.140	0.000	1.122	0.7790	1.2490	0.000
1839	0006 46550	1.140	0.000	1.122	0.7790	1.2490	0.000
1840	0006 46550	1.140	0.000	1.122	0.7790	1.2490	0.000
1841	0006 46550	1.140	0.000	1.122	0.7790	1.2490	0.000
1842	0006 46550	1.140	0.000	1.122	0.7790	1.2490	0.000
1843	0006 46550	1.140	0.000	1.122	0.7790	1.2490	0.000
1844	0006 46550	1.140	0.000	1.122	0.7790	1.2490	0.000
1845	0006 46550	1.140	0.000	1.122	0.7790	1.2490	0.000
1846	0006 46550	1.140	0.000	1.122	0.7790	1.2490	0.000
1847	0006 46550	1.140	0.000	1.122	0.7790	1.2490	0.000
1848	0006 46550	1.140	0.000	1.122	0.7790	1.2490	0.000
1849	0006 46550	1.140	0.000	1.122	0.7790	1.2490	0.000
1850	0006 46550	1.140	0.000	1.122	0.7790	1.2490	0.000
1851	0006 46550	1.140	0.000	1.122	0.7790	1.2490	0.000
1852	0006 46550	1.140	0.000	1.122	0.7790	1.2490	0.000
1853	0006 46550	1.140	0.000	1.122	0.7790	1.2490	0.000
1854	0006 46550	1.140	0.000	1.122	0.7790	1.2490	0.000
1855	0006 46550	1.140	0.000	1.122	0.7790	1.2490	0.000
1856	0006 46550	1.140	0.000	1.122	0.7790	1.2490	0.000
1857	0006 46550	1.140	0.000	1.122	0.7790	1.2490	0.000
1858	0006 46550	1.140	0.000	1.122	0.7790	1.2490	0.000
1859	0006 46550	1.140	0.000	1.122	0.7790	1.2490	0.000
1860	0006 46550	1.140	0.000	1.122	0.7790	1.2490	0.000
1861	0006 46550	1.140	0.000	1.122	0.7790	1.2490	0.000
1862	0006 46550	1.140	0.000	1.122	0.7790	1.2490	0.000
1863	0006 46550	1.140	0.000	1.122	0.7790	1.2490	0.000
1864	0006 46550	1.140	0.000	1.122	0.7790	1.2490	0.000
1865	0006 46550	1.140	0.000	1.122	0.7790	1.2490	0.000
1866	0006 46550	1.140	0.000	1.122	0.7790	1.2490	0.000

FACILITY		X1 PROGRAM CODE		NOZZLE TYPE		IN-STREAM PL. CONFIGURATIONS		SUPPRESSOR CONFIGURATION			
		NOZAL FLOW (FAA)		PIUG WITH BLEED		40-SPRKE, AREA RATIO = 1.75					
TIMEST		PARAMETERS		OUTER RADIUS RATIO		INNER RADIUS RATIO		DVG			
		0.0000		C.7700		1.2480					
ENG	GE	NASA	D2	M4	PTN/PA	PTI/PA	24EGAT	COI	CFNFT1	CFNFT2	FQ
1667	0006	46550	1-150	0-360	3-012	2-535	C-448	0-993	0-897	1-271	1-156
1668	0006	46550	1-140	0-361	3-018	3-093	C-524	0-935	0-894	1-372	1-153
1669	0006	46550	1-140	0-361	3-015	3-526	C-625	0-995	0-911	1-513	1-170
1670	0006	46550	1-140	0-360	3-306	1-120	0-046	0-966	0-907	1-032	1-126
1671	0006	46550	1-140	0-361	3-252	1-531	C-214	0-879	0-909	1-032	1-150
1672	0006	46550	1-140	0-360	3-224	2-035	C-334	0-886	0-902	1-145	1-159
1673	0006	46550	1-140	0-361	3-270	2-536	C-519	0-993	0-900	1-242	1-157
1674	0006	46550	1-140	0-362	3-237	3-527	C-498	0-990	0-902	1-362	1-157
1675	0006	46550	1-140	0-362	3-237	3-527	C-582	0-966	0-911	1-457	1-169
1676	0006	46550	1-140	0-359	2-519	1-121	0-111	0-955	0-726	0-888	0-924
1677	0006	46550	1-140	0-360	2-515	3-520	0-748	0-995	0-921	1-708	1-183

FACILITY		6X3 PROGRAM CODE		NOZZLE TYPE		IN-STREAM CONFIGURATIONS		SUPPRESSOR CONFIGURATION			
		DUAL FLOW (FAA)		PIUG WITH BLEED		40-SPRKE, AREA RATIO = 1.75					
PARAMETERS		OUTER RADIUS RATIO		INNER RADIUS RATIO		DVG					
		0.0000		3.7790		1.2480					
ENG	GE	NASA	D2	M4	PTN/PA	PTI/PA	24EGAT	COI	CFNFT1	CFNFT2	FQ
1667	0006	46550	1-140	0-360	3-012	2-535	C-448	0-993	0-897	1-271	1-156
1668	0006	46550	1-140	0-361	3-018	3-093	C-524	0-935	0-894	1-372	1-153
1669	0006	46550	1-140	0-361	3-015	3-526	C-625	0-966	0-911	1-513	1-170
1670	0006	46550	1-140	0-360	3-306	1-120	0-046	0-995	0-907	1-032	1-126
1671	0006	46550	1-140	0-361	3-252	1-531	C-214	0-879	0-909	1-032	1-150
1672	0006	46550	1-140	0-360	3-224	2-035	C-334	0-886	0-902	1-145	1-159
1673	0006	46550	1-140	0-361	3-270	2-536	C-519	0-957	0-900	1-242	1-157
1674	0006	46550	1-140	0-362	3-237	3-527	C-498	0-990	0-902	1-362	1-169
1675	0006	46550	1-140	0-359	2-519	1-121	0-111	0-955	0-911	1-457	1-122
1676	0006	46550	1-140	0-360	2-515	3-520	0-748	0-966	0-921	1-708	1-183

MODEL DC-1, 36 DEEP CHUTES, AR = 1.5, BASELINE PLUG

755















MODEL DC-2, 36 DEEP CHUTES, AR = 1.5, FULL PLUG







MODEL DC-3, 36 DEEP CHUTES, AR = 2.0, BASELINE PLUG

FACILITY	CL PROGRAM CODE	NOZZLE TYPE	INLET CONFIGURATIONS		SUPPRESSOR CONFIGURATION						
			BASELINE PLUG WITH BLEED		36-CHUTE, AREA RATIO = 2.0						
			DUAL FLOW (FAA)								
THRUST PARAMETERS			OUTER RADIUS RATIO	INNER RADIUS RATIO	DVN						
			0.0030	0.7790	1.2480						
FDG	CF	MASA	Q2	MA	PTI/PA	QMGAT	CON	CDI	CFMET1	CFMET2	F9
2025	0008	48530	0.392	0.000	1.502	0.980	0.952	9.999	0.905	0.905	1.125
2026	0008	48530	0.392	0.000	1.504	0.986	0.950	9.999	0.912	0.912	1.126
2027	0008	48530	0.392	0.000	1.504	0.986	0.950	9.999	0.921	0.921	1.127
2028	0008	48530	0.392	0.010	2.004	0.974	0.944	9.999	0.920	0.920	1.138
2029	0008	48530	0.392	0.016	2.001	0.977	0.945	9.999	0.927	0.927	1.140
2030	0008	48530	0.392	0.005	1.999	1.000	0.959	10.119	0.935	0.935	1.143
2031	0008	48530	0.392	0.025	2.512	0.958	0.944	9.999	0.928	0.928	1.140
2032	0008	48530	0.392	0.041	2.505	0.957	0.946	9.999	0.936	0.936	1.144
2033	0008	48530	0.392	0.018	2.401	1.000	0.959	9.999	0.941	0.941	1.149
2034	0008	48530	0.392	0.016	3.011	0.965	0.948	9.999	0.930	0.930	1.145
2035	0008	48530	0.392	0.047	3.015	0.997	0.948	9.999	0.939	0.939	1.145
2036	0008	48530	0.392	0.042	3.015	1.079	0.948	9.999	0.936	0.936	1.148
2037	0008	48530	0.392	0.020	3.313	0.968	0.949	9.999	0.931	0.931	1.147
2038	0008	48530	0.392	0.035	3.313	1.008	0.949	9.999	0.937	0.937	1.147
2039	0008	48530	0.392	0.036	3.311	1.051	0.949	9.999	0.938	0.938	1.149
2040	0008	48530	0.392	0.028	2.507	0.967	0.945	9.999	0.926	0.926	1.140
2041	0008	48530	0.392	0.015	2.501	1.010	0.947	9.999	0.936	0.936	1.143
2042	0008	48530	0.392	0.007	1.522	1.111	0.951	1.027	0.928	0.928	1.148
2043	0008	48530	0.392	0.015	1.531	1.513	0.952	0.996	0.932	0.932	1.184
2044	0008	48530	0.392	0.021	1.501	2.008	0.952	0.993	0.932	0.932	1.190
2045	0008	48530	0.392	0.047	1.505	2.508	0.951	0.993	0.929	0.929	1.192
2046	0008	48530	0.392	0.039	1.502	3.073	0.952	0.996	0.933	0.933	1.198
2047	0008	48530	0.392	0.020	2.003	1.111	0.945	1.017	0.938	0.938	1.210
2048	0008	48530	0.392	0.021	1.502	1.508	0.946	0.996	0.937	0.937	1.187
2049	0008	48530	0.392	0.030	1.507	2.006	0.945	0.993	0.936	0.936	1.191
2050	0008	48530	0.392	0.030	2.003	2.514	0.945	0.993	0.939	0.939	1.193
2051	0008	48530	0.392	0.030	2.003	3.013	0.946	0.994	0.934	0.934	1.191
2052	0008	48530	0.392	0.045	2.307	3.518	0.944	0.997	0.932	0.932	1.208
2053	0008	48530	0.392	0.032	2.508	1.113	0.949	0.995	0.942	0.942	1.159
2054	0008	48530	0.392	0.021	2.503	1.512	0.948	0.993	0.940	0.940	1.182
2055	0008	48530	0.392	0.037	2.503	2.004	0.947	0.993	0.935	0.935	1.185
2056	0008	48530	0.392	0.047	2.507	2.507	0.947	0.994	0.941	0.941	1.188
2057	0008	48530	0.392	0.045	2.506	3.021	0.947	0.994	0.937	0.937	1.186
2058	0008	48530	0.392	0.046	2.513	3.511	0.944	0.996	0.952	0.952	1.201
2059	0008	48530	0.392	0.047	2.008	1.114	0.951	0.930	0.942	0.942	1.158
2060	0008	48530	0.392	0.041	3.307	1.515	0.949	0.993	0.941	0.941	1.178
2061	0008	48530	0.392	0.053	3.012	2.004	0.949	0.994	0.939	0.939	1.183
2062	0008	48530	0.392	0.051	3.016	2.515	0.949	0.994	0.941	0.941	1.185
2063	0008	48530	0.392	0.045	3.015	3.014	0.949	0.995	0.937	0.937	1.183
2064	0008	48530	0.392	0.052	3.012	3.518	0.949	0.996	0.954	0.954	1.201
2065	0008	48530	0.392	0.037	3.314	1.119	0.950	0.948	0.941	0.941	1.156
2066	0008	48530	0.392	0.037	3.314	1.119	0.950	0.948	0.941	0.941	1.156
2067	0008	48530	0.392	0.044	3.299	2.008	0.951	0.970	0.940	0.940	1.176
2068	0008	48530	0.392	0.044	3.299	2.008	0.951	0.993	0.939	0.939	1.183
2069	0008	48530	0.392	0.051	3.323	2.509	0.950	0.994	0.940	0.940	1.184

[illegible]

FACILITY - XI PROGRAM C031				WRTZLF TYPE		INP - STREAM		SUPPRESSOR CONFIGURATION	
				DUAL FLOW (FAA)		PL CONFIGURATIONS		36-CHUTE, AREA RATIO = 2.0	
				OUTER RADIUS RATIO		INNER RADIUS RATIO		DYN	
				0.0030		0.7790		1.2480	
TRUST PARAMETERS									
EDS	WASA	Q2	PA	PTD/PA	PTI/PA	OMEGAT	CDN	CFNET1	CFNET2
2070	0008 48530	1.142	0.053	3.327	3.018	0.492	0.950	0.930	1.373
2071	0008 48530	1.140	0.051	3.307	3.517	0.576	0.950	0.948	1.506
2072	0008 48530	1.140	0.012	2.509	1.112	0.150	0.945	0.990	1.155
2073	0008 48530	1.143	0.050	2.499	3.507	0.764	0.950	0.954	1.749
2074	0008 48530	0.398	0.446	1.504	0.000	0.000	0.970	0.790	1.079
2075	0008 48530	0.398	0.449	1.501	1.000	0.029	0.970	0.800	1.081
2076	0008 48530	0.398	0.447	1.503	1.000	0.059	0.969	0.806	0.813
2077	0008 48530	0.398	0.448	2.037	0.990	0.000	0.937	0.830	0.830
2078	0008 48530	0.398	0.447	2.037	1.006	0.029	0.939	0.845	0.847
2079	0008 48530	0.398	0.447	2.037	1.026	0.059	0.946	0.842	0.852
2080	0008 48530	0.398	0.448	2.515	0.945	0.000	0.943	0.856	1.086
2081	0008 48530	0.398	0.449	2.517	1.012	0.029	0.945	0.861	1.087
2082	0008 48530	0.398	0.448	3.008	0.984	0.000	0.948	0.874	1.088
2083	0008 48530	0.398	0.448	3.317	1.072	0.029	0.949	0.880	1.100
2084	0008 48530	0.398	0.448	3.008	1.066	0.059	0.952	0.882	1.103
2085	0008 48530	0.398	0.449	3.322	1.032	0.000	0.950	0.881	1.104
2086	0008 48530	0.398	0.448	3.322	1.032	0.029	0.949	0.888	1.105
2087	0008 48530	0.398	0.448	3.322	1.032	0.059	0.945	0.893	1.107
2088	0008 48530	0.398	0.448	2.513	0.984	0.000	0.943	0.859	1.087
2089	0008 48530	0.398	0.447	2.521	1.040	0.059	0.943	0.861	1.096
2090	0008 48530	1.140	0.447	1.501	1.113	0.441	0.950	0.925	1.101
2091	0008 48530	1.140	0.447	1.501	1.113	0.533	0.950	0.925	1.104
2092	0008 48530	1.142	0.447	1.502	1.516	0.743	0.968	0.873	1.155
2093	0008 48530	1.140	0.448	1.502	2.015	0.927	0.970	0.888	1.162
2094	0008 48530	1.140	0.449	1.503	3.022	1.115	0.969	0.905	1.161
2095	0008 48530	1.140	0.448	1.502	3.516	1.302	0.958	0.916	1.184
2096	0008 48530	1.142	0.448	2.010	1.112	0.180	0.945	0.916	1.184
2097	0008 48530	1.140	0.448	2.005	1.515	0.386	0.946	0.916	1.184
2098	0008 48530	1.140	0.448	2.005	2.016	0.545	0.946	0.916	1.184
2099	0008 48530	1.140	0.447	2.007	2.510	0.740	0.946	0.916	1.184
2100	0008 48530	1.140	0.448	2.007	3.020	0.940	0.946	0.916	1.184
2101	0008 48530	1.140	0.448	2.008	3.522	0.954	0.946	0.916	1.184
2102	0008 48530	1.140	0.447	2.523	1.113	0.171	0.945	0.916	1.184
2103	0008 48530	1.140	0.447	2.523	1.513	0.305	0.945	0.916	1.184
2104	0008 48530	1.140	0.447	2.523	2.014	0.535	0.945	0.916	1.184
2105	0008 48530	1.140	0.448	2.513	2.519	0.744	0.947	0.916	1.184
2106	0008 48530	1.140	0.448	2.513	3.018	0.952	0.947	0.916	1.184
2107	0008 48530	1.140	0.448	2.510	3.522	0.962	0.947	0.916	1.184
2108	0008 48530	1.140	0.448	2.510	3.522	0.962	0.947	0.916	1.184
2109	0008 48530	1.140	0.448	3.022	1.116	0.093	0.945	0.916	1.184
2110	0008 48530	1.140	0.448	3.013	1.517	0.250	0.949	0.916	1.184
2111	0008 48530	1.140	0.448	3.011	2.015	0.361	0.950	0.916	1.184
2112	0008 48530	1.140	0.448	3.022	2.513	0.450	0.948	0.916	1.184
2113	0008 48530	1.140	0.449	3.022	3.028	0.543	0.948	0.916	1.184
2114	0008 48530	1.140	0.450	3.527	3.525	0.832	0.947	0.916	1.184



FACILITY B		PROGRAM CODE		NOZZLE TYPE		INLET TREAM		SUPPRESSOR CONFIGURATION		
				PLUG CONFIGURATIONS		BASELINE PLUG WITH BLEED		36-CHUTE, AREA RATIO = 2.0		
THRUST PARAMETERS		EJECTOR RADIUS RATIO		JUMPER RADIUS RATIO		DND				
		0.3330		0.7790		1.7480				
PCG	CF	MA	PTN/PA	PTI/PA	CMFCAT	COO	CNI	CFNET1	CFNET2	F9
2115	0008	48530	1.140	2.448	1.116	0.940	0.670	0.894	0.915	1.111
2116	0008	48530	1.140	0.449	1.517	0.940	0.930	0.901	1.025	1.136
2117	0008	48530	1.140	0.449	3.313	0.940	0.994	0.903	1.135	1.147
2118	0008	48530	1.140	0.449	3.322	0.940	0.994	0.903	1.233	1.149
2119	0008	48530	1.140	0.450	3.325	0.940	0.995	0.896	1.321	1.143
2120	0008	48530	1.140	0.450	3.325	0.940	0.995	0.915	1.442	1.163
2121	0008	48530	1.140	0.449	2.523	0.940	0.810	0.873	0.913	1.100
2122	0008	48530	1.140	0.449	3.517	0.940	0.943	0.920	1.720	1.173
2123	0008	48530	0.104	0.449	1.641	0.940	0.849	0.866	0.817	1.092
2124	0008	48530	0.358	0.358	1.505	0.940	0.999	0.817	0.817	1.089
2125	0008	48530	0.398	0.358	1.503	0.940	0.999	0.827	0.827	1.091
2126	0008	48530	0.398	0.362	1.504	0.940	0.800	0.821	0.838	1.092
2127	0008	48530	0.398	0.362	2.011	0.940	0.999	0.854	0.854	1.097
2128	0008	48530	0.398	0.361	2.017	0.940	0.854	0.854	0.854	1.095
2129	0008	48530	0.398	0.362	2.017	0.940	0.854	0.854	0.854	1.103
2130	0008	48530	0.398	0.362	2.017	0.940	0.854	0.854	0.854	1.102
2131	0008	48530	0.398	0.362	2.527	0.940	0.854	0.885	0.885	1.104
2132	0008	48530	0.398	0.362	2.521	0.940	0.854	0.885	0.885	1.105
2133	0008	48530	0.398	0.361	2.007	0.940	0.854	0.890	0.890	1.112
2134	0008	48530	0.398	0.362	3.021	0.940	0.854	0.899	0.902	1.115
2135	0008	48530	0.398	0.362	3.021	0.940	0.854	0.899	0.912	1.117
2136	0008	48530	0.398	0.362	3.021	0.940	0.854	0.900	0.900	1.117
2137	0008	48530	0.398	0.361	3.021	0.940	0.854	0.904	0.908	1.117
2138	0008	48530	0.398	0.362	3.021	0.940	0.854	0.904	0.918	1.120
2139	0008	48530	0.398	0.362	2.517	0.940	0.854	0.874	0.874	1.102
2140	0008	48530	0.398	0.362	2.513	0.940	0.854	0.886	0.897	1.106
2141	0008	48530	0.398	0.361	2.513	0.940	0.854	0.875	0.875	1.104
2142	0008	48530	0.398	0.362	1.503	0.940	0.854	0.850	0.957	1.112
2143	0008	48530	0.398	0.361	1.501	0.940	0.854	0.876	1.345	1.154
2144	0008	48530	0.398	0.361	1.501	0.940	0.854	0.890	1.744	1.166
2145	0008	48530	0.398	0.362	1.502	0.940	0.854	0.900	2.122	1.171
2146	0008	48530	0.398	0.362	1.502	0.940	0.854	0.900	2.477	1.169
2147	0008	48530	0.398	0.362	1.504	0.940	0.854	0.925	2.523	1.190
2148	0008	48530	0.398	0.361	2.014	0.940	0.854	0.873	0.933	1.113
2149	0008	48530	0.398	0.362	2.009	0.940	0.854	0.873	0.873	1.150
2150	0008	48530	0.398	0.362	2.009	0.940	0.854	0.895	1.385	1.161
2151	0008	48530	0.398	0.362	2.017	0.940	0.854	0.904	1.603	1.166
2152	0008	48530	0.398	0.362	2.017	0.940	0.854	0.904	1.603	1.166
2153	0008	48530	0.398	0.362	2.017	0.940	0.854	0.904	1.603	1.166
2154	0008	48530	0.398	0.362	2.017	0.940	0.854	0.904	1.603	1.166
2155	0008	48530	0.398	0.362	2.017	0.940	0.854	0.904	1.603	1.166
2156	0008	48530	0.398	0.362	2.017	0.940	0.854	0.904	1.603	1.166
2157	0008	48530	0.398	0.362	2.017	0.940	0.854	0.904	1.603	1.166
2158	0008	48530	0.398	0.362	2.017	0.940	0.854	0.904	1.603	1.166
2159	0008	48530	0.398	0.362	2.017	0.940	0.854	0.904	1.603	1.166
2160	0008	48530	0.398	0.362	2.017	0.940	0.854	0.904	1.603	1.166

FACILITY			EL PROGRAM C031			MORZIE TYPE			IM' - STRFAM			SUPPRESSOR CONFIGURATION		
			DUAL FLOW LERAL			BASELINE PLUG WITH ALLED			26-CHUTE AREA RATIO = 2.0					
DINAG PARAMETERS			PIPER FARIUS PAVT3			JYMER RADIUS R4110			DVO					
			0.0030			0.7790			1.2480					
ORG	GE	WASA	N2	VA	PT/PA	PT/PA	PMEGAT	NCS	CNS	NCSH	CNSH	NCPL,N	DCPL,1	DCINT PSUP/PA
2115	0008	48550	1.140	2.468	3.328	1.114	0.077	-0.077	0.338	-0.004	0.024	-0.010	0.006	-0.085
2116	0008	48550	1.140	0.449	3.317	1.517	0.223	-0.069	0.379	-0.004	0.023	-0.005	0.003	-0.075
2117	0008	48550	1.140	0.449	3.310	2.214	0.328	-0.062	0.377	-0.004	0.023	-0.004	0.003	-0.075
2118	0008	48550	1.140	0.449	3.322	2.516	0.400	-0.057	0.376	-0.003	0.023	-0.003	0.014	-0.077
2119	0008	48550	1.140	0.450	3.325	3.324	0.491	-0.052	0.372	-0.003	0.022	-0.002	0.014	-0.077
2120	0008	48550	1.140	0.450	3.320	2.575	0.575	-0.048	0.370	-0.003	0.022	-0.001	0.013	-0.084
2121	0008	48550	1.140	0.448	3.324	1.114	0.124	-0.191	0.348	-0.007	0.023	-0.006	0.008	-0.065
2122	0008	48550	1.140	0.449	2.501	3.517	0.760	-0.055	0.333	-0.004	0.022	-0.000	0.015	-0.074
2123	0008	48550	0.398	2.447	2.517	1.941	0.059	-0.106	0.355	-0.007	0.023	-0.000	0.015	-0.074
2124	0008	48530	0.398	0.358	1.505	0.902	0.000	-0.133	0.276	-0.010	0.021	-0.018	0.010	-0.151
2125	0008	48530	0.398	0.359	1.502	0.909	0.029	-0.120	0.267	-0.010	0.020	-0.016	0.005	-0.150
2126	0008	48530	0.398	0.362	1.504	1.309	0.059	-0.128	0.262	-0.010	0.020	-0.015	0.002	-0.148
2127	0008	48530	0.398	0.362	2.011	0.289	0.006	-0.115	0.304	-0.007	0.024	-0.011	0.006	-0.124
2128	0008	48530	0.398	0.361	2.017	1.306	0.029	-0.112	0.403	-0.007	0.024	-0.011	0.006	-0.124
2129	0008	48530	0.398	0.352	2.006	1.774	0.059	-0.110	0.396	-0.007	0.024	-0.010	0.004	-0.123
2130	0008	48530	0.398	0.362	2.513	0.984	0.000	-0.096	0.474	-0.005	0.024	-0.013	0.007	-0.105
2131	0008	48530	0.398	0.362	2.570	1.712	0.029	-0.094	0.468	-0.005	0.025	-0.011	0.007	-0.103
2132	0008	48530	0.398	0.362	2.521	1.941	0.059	-0.092	0.468	-0.005	0.025	-0.011	0.007	-0.103
2133	0008	48530	0.398	0.361	3.007	0.980	0.000	-0.091	0.529	-0.004	0.027	-0.018	0.009	-0.094
2134	0008	48530	0.398	0.362	1.070	1.319	0.029	-0.079	0.519	-0.004	0.027	-0.015	0.005	-0.093
2135	0008	48530	0.398	0.362	3.021	1.959	0.059	-0.078	0.515	-0.004	0.027	-0.013	0.003	-0.091
2136	0008	48530	0.398	0.362	3.302	0.980	0.000	-0.070	0.516	-0.004	0.028	-0.018	0.009	-0.083
2137	0008	48530	0.398	0.361	3.296	1.227	0.029	-0.069	0.515	-0.004	0.026	-0.015	0.006	-0.082
2138	0008	48530	0.398	0.362	3.274	1.073	0.059	-0.069	0.511	-0.003	0.026	-0.013	0.003	-0.082
2139	0008	48530	0.398	0.362	2.517	0.984	0.000	-0.096	0.497	-0.003	0.026	-0.016	0.010	-0.107
2140	0008	48530	0.398	0.362	2.513	1.039	0.000	-0.092	0.470	-0.005	0.025	-0.011	0.004	-0.104
2141	0008	48530	0.398	0.361	2.510	0.983	0.000	-0.092	0.485	-0.005	0.027	-0.016	0.010	-0.107
2142	0008	48530	0.398	0.362	1.503	1.113	0.241	-0.110	0.250	-0.008	0.019	-0.007	0.004	-0.121
2143	0008	48530	0.398	0.361	1.501	1.510	0.532	-0.081	0.252	-0.006	0.019	-0.007	0.004	-0.121
2144	0008	48530	0.398	0.361	1.501	2.012	0.746	-0.063	0.250	-0.005	0.020	-0.005	0.003	-0.090
2145	0008	48530	0.398	0.362	1.502	2.520	0.933	-0.052	0.249	-0.004	0.020	-0.004	0.003	-0.082
2146	0008	48530	0.398	0.362	1.504	3.017	1.118	-0.045	0.249	-0.004	0.019	-0.004	0.017	-0.078
2147	0008	48530	0.398	0.362	1.504	3.510	1.304	-0.039	0.247	-0.003	0.019	-0.003	0.031	-0.082
2148	0008	48530	0.398	0.361	2.016	1.117	0.156	-0.101	0.386	-0.006	0.023	-0.006	0.032	-0.076
2149	0008	48530	0.398	0.362	2.008	1.512	0.386	-0.083	0.382	-0.005	0.023	-0.005	0.032	-0.076
2150	0008	48530	0.398	0.362	2.008	2.017	0.545	-0.069	0.381	-0.004	0.023	-0.005	0.032	-0.076
2151	0008	48530	0.398	0.363	2.010	2.524	0.683	-0.060	0.378	-0.004	0.023	-0.003	0.032	-0.076
2152	0008	48530	0.398	0.363	2.012	3.019	0.816	-0.053	0.376	-0.003	0.023	-0.002	0.031	-0.078
2153	0008	48530	0.398	0.363	2.000	3.513	0.951	-0.047	0.375	-0.003	0.023	-0.002	0.031	-0.078
2154	0008	48530	0.398	0.363	2.517	1.116	0.124	-0.088	0.451	-0.005	0.025	-0.008	0.003	-0.098
2155	0008	48530	0.398	0.363	2.519	1.515	0.306	-0.075	0.455	-0.004	0.025	-0.005	0.002	-0.098
2156	0008	48530	0.398	0.362	2.511	2.017	0.435	-0.065	0.452	-0.004	0.025	-0.004	0.013	-0.086
2157	0008	48530	0.398	0.362	2.511	2.519	0.545	-0.058	0.453	-0.003	0.025	-0.003	0.010	-0.075
2158	0008	48530	0.398	0.362	2.519	3.020	0.651	-0.052	0.449	-0.003	0.025	-0.002	0.012	-0.070
2159	0008	48530	0.398	0.363	2.527	3.520	0.760	-0.047	0.444	-0.003	0.024	-0.001	0.016	-0.068



FACILITY: XL PROGRAM C031 NOZZLE TYPE: SUPPRESSOR CONFIGURATION: 36-CHUTE, AREA RATIO = 2.0

THREAT PARAMETERS: INLET STREAM PLI CONFIGURATIONS: BASELINE PLUG WITH BLEED DVG 1.2480

ORF	CF	NASA	72	MA	PTO/PA	PTI/PA	OMF/GAT	CNN	CNI	CFNET1	CFNET2	F9
2160	0008	48550	1.140	0.362	3.019	1.114	0.250	0.949	0.758	0.902	0.930	1.120
2161	0008	48550	1.140	0.362	3.007	1.511	0.250	0.949	0.953	0.908	1.054	1.147
2162	0008	48550	1.140	0.363	3.013	2.523	0.250	0.950	0.994	0.910	1.181	1.157
2163	0008	48550	1.140	0.363	3.013	3.070	0.250	0.950	0.994	0.910	1.299	1.162
2164	0008	48550	1.140	0.363	3.017	3.522	0.250	0.950	0.994	0.910	1.394	1.153
2165	0008	48550	1.140	0.363	3.017	3.522	0.250	0.950	0.994	0.910	1.555	1.177
2166	0008	48550	1.140	0.363	3.017	3.522	0.250	0.950	0.994	0.910	1.634	1.125
2167	0008	48550	1.140	0.363	3.017	3.522	0.250	0.950	0.994	0.910	1.741	1.148
2168	0008	48550	1.140	0.362	3.275	2.530	0.250	0.950	0.994	0.910	1.158	1.157
2169	0008	48550	1.140	0.362	3.275	2.530	0.250	0.950	0.994	0.910	1.267	1.162
2170	0008	48550	1.140	0.362	3.275	3.017	0.250	0.950	0.994	0.905	1.349	1.152
2171	0008	48550	1.140	0.363	3.223	3.517	0.250	0.951	0.996	0.926	1.490	1.175

FACILITY: 1 PROGRAM C031 NOZZLE TYPE: SUPPRESSOR CONFIGURATION: 36-CHUTE, AREA RATIO = 2.0

THREAT PARAMETERS: INLET STREAM PLI CONFIGURATIONS: BASELINE PLUG WITH BLEED DVG 1.2480

ORF	CF	NASA	72	MA	PTO/PA	PTI/PA	OMF/GAT	CNN	CNI	CFNET1	CFNET2	F9
2160	0008	48550	1.140	0.362	3.019	1.114	0.250	0.949	0.758	0.902	0.930	1.120
2161	0008	48550	1.140	0.362	3.007	1.511	0.250	0.949	0.953	0.908	1.054	1.147
2162	0008	48550	1.140	0.363	3.013	2.523	0.250	0.950	0.994	0.910	1.181	1.157
2163	0008	48550	1.140	0.363	3.013	3.070	0.250	0.950	0.994	0.910	1.299	1.162
2164	0008	48550	1.140	0.363	3.017	3.522	0.250	0.950	0.994	0.910	1.394	1.153
2165	0008	48550	1.140	0.363	3.017	3.522	0.250	0.950	0.994	0.910	1.555	1.177
2166	0008	48550	1.140	0.363	3.017	3.522	0.250	0.950	0.994	0.910	1.634	1.125
2167	0008	48550	1.140	0.363	3.017	3.522	0.250	0.950	0.994	0.910	1.741	1.148
2168	0008	48550	1.140	0.362	3.275	2.530	0.250	0.950	0.994	0.910	1.158	1.157
2169	0008	48550	1.140	0.362	3.275	2.530	0.250	0.950	0.994	0.910	1.267	1.162
2170	0008	48550	1.140	0.362	3.275	3.017	0.250	0.950	0.994	0.905	1.349	1.152
2171	0008	48550	1.140	0.363	3.223	3.517	0.250	0.951	0.996	0.926	1.490	1.175

MODEL DC-4, 36 DEEP CHUTES, AR = 2.0, REDUCED AREA



卷之五 雜著

李 雲 龍 著 李 雲 龍 著

1. STAN  
PL. CONFUSATIONS  
1500 APCA WILLIAM ALFEE

SUPPRESSOR CONFIGURATION  
26-CHUTE, AREA RATIO = 2.0

[illegible]

FACILITY		PROGRAM		NOZZLE TYPE		IM		STREAM		SUPPRESSOR CONFIGURATION	
		1		2		3		4		5	
		FLOW (AA)		1/2 BLEED AREA WITH BLEED		1/2 BLEED AREA WITH BLEED		36-CHUTE, AREA RATIO = 2.0			
		OUTER RADIUS RATIO		INNER RADIUS RATIO		DVI					
		0.0030		0.3840		1.2480					
THRUST PARAMETERS											
STC	GE	MASA	O2	WA	PTI/PA	PTI/PA	OMFAT	CDI	CFNFT1	CFNFT2	F9
2217	0000	48750	1.140	0.449	3.31	3.029	0.264	0.951	0.909	0.896	1.125
2218	0000	48750	1.140	0.450	3.323	3.031	0.267	0.951	0.909	0.896	1.125
2219	0000	48750	1.140	0.448	2.911	1.114	0.075	0.947	0.923X	0.867	1.105
2220	0000	48750	1.140	0.448	2.911	1.114	0.075	0.947	0.923X	0.867	1.105
2221	0000	48750	1.140	0.448	2.911	1.114	0.075	0.947	0.923X	0.867	1.105
2222	0000	48750	1.140	0.448	2.911	1.114	0.075	0.947	0.923X	0.867	1.105
2223	0000	48750	1.140	0.448	2.911	1.114	0.075	0.947	0.923X	0.867	1.105
2224	0000	48750	1.140	0.448	2.911	1.114	0.075	0.947	0.923X	0.867	1.105
2225	0000	48750	1.140	0.448	2.911	1.114	0.075	0.947	0.923X	0.867	1.105
2226	0000	48750	1.140	0.448	2.911	1.114	0.075	0.947	0.923X	0.867	1.105
2227	0000	48750	1.140	0.448	2.911	1.114	0.075	0.947	0.923X	0.867	1.105
2228	0000	48750	1.140	0.448	2.911	1.114	0.075	0.947	0.923X	0.867	1.105
2229	0000	48750	1.140	0.448	2.911	1.114	0.075	0.947	0.923X	0.867	1.105
2230	0000	48750	1.140	0.448	2.911	1.114	0.075	0.947	0.923X	0.867	1.105
2231	0000	48750	1.140	0.448	2.911	1.114	0.075	0.947	0.923X	0.867	1.105
2232	0000	48750	1.140	0.448	2.911	1.114	0.075	0.947	0.923X	0.867	1.105
2233	0000	48750	1.140	0.448	2.911	1.114	0.075	0.947	0.923X	0.867	1.105
2234	0000	48750	1.140	0.448	2.911	1.114	0.075	0.947	0.923X	0.867	1.105
2235	0000	48750	1.140	0.448	2.911	1.114	0.075	0.947	0.923X	0.867	1.105
2236	0000	48750	1.140	0.448	2.911	1.114	0.075	0.947	0.923X	0.867	1.105
2237	0000	48750	1.140	0.448	2.911	1.114	0.075	0.947	0.923X	0.867	1.105
2238	0000	48750	1.140	0.448	2.911	1.114	0.075	0.947	0.923X	0.867	1.105
2239	0000	48750	1.140	0.448	2.911	1.114	0.075	0.947	0.923X	0.867	1.105
2240	0000	48750	1.140	0.448	2.911	1.114	0.075	0.947	0.923X	0.867	1.105
2241	0000	48750	1.140	0.448	2.911	1.114	0.075	0.947	0.923X	0.867	1.105
2242	0000	48750	1.140	0.448	2.911	1.114	0.075	0.947	0.923X	0.867	1.105
2243	0000	48750	1.140	0.448	2.911	1.114	0.075	0.947	0.923X	0.867	1.105
2244	0000	48750	1.140	0.448	2.911	1.114	0.075	0.947	0.923X	0.867	1.105
2245	0000	48750	1.140	0.448	2.911	1.114	0.075	0.947	0.923X	0.867	1.105
2246	0000	48750	1.140	0.448	2.911	1.114	0.075	0.947	0.923X	0.867	1.105
2247	0000	48750	1.140	0.448	2.911	1.114	0.075	0.947	0.923X	0.867	1.105
2248	0000	48750	1.140	0.448	2.911	1.114	0.075	0.947	0.923X	0.867	1.105
2249	0000	48750	1.140	0.448	2.911	1.114	0.075	0.947	0.923X	0.867	1.105
2250	0000	48750	1.140	0.448	2.911	1.114	0.075	0.947	0.923X	0.867	1.105
2251	0000	48750	1.140	0.448	2.911	1.114	0.075	0.947	0.923X	0.867	1.105
2252	0000	48750	1.140	0.448	2.911	1.114	0.075	0.947	0.923X	0.867	1.105
2253	0000	48750	1.140	0.448	2.911	1.114	0.075	0.947	0.923X	0.867	1.105
2254	0000	48750	1.140	0.448	2.911	1.114	0.075	0.947	0.923X	0.867	1.105
2255	0000	48750	1.140	0.448	2.911	1.114	0.075	0.947	0.923X	0.867	1.105
2256	0000	48750	1.140	0.448	2.911	1.114	0.075	0.947	0.923X	0.867	1.105
2257	0000	48750	1.140	0.448	2.911	1.114	0.075	0.947	0.923X	0.867	1.105
2258	0000	48750	1.140	0.448	2.911	1.114	0.075	0.947	0.923X	0.867	1.105
2259	0000	48750	1.140	0.448	2.911	1.114	0.075	0.947	0.923X	0.867	1.105
2260	0000	48750	1.140	0.448	2.911	1.114	0.075	0.947	0.923X	0.867	1.105
2261	0000	48750	1.140	0.448	2.911	1.114	0.075	0.947	0.923X	0.867	1.105
2262	0000	48750	1.140	0.448	2.911	1.114	0.075	0.947	0.923X	0.867	1.105





FACILITY		CL PROGRAM CODE		NOZZLE TYPE		1/2 PLEED AREA WITH BLUED		PLUG CONFIGURATIONS		STREAM		SUPPRESSOR CONFIGURATION	
												36-CHUTE AREA RATIO = 2.0	



FACILITY 1 (Program 001)		NOZZLE TYPE		STREAM		SUPPRESSOR CONFIGURATION	
DUAL FLOW (EAR)		1/2 RIFLED AREA WITH BLEED		PLU CONFIGURATIONS		36-CHUTE, AREA RATIO = 2.0	
INJECT PARAMETERS		OUTER RADIUS RATIO		INNER RADIUS RATIO		DVO	
		0.0000		0.0000		1.2480	
PC	CF	WASA	W2	PA	PTI/PA	DMFGAT	CFNET2
2100	0000	48750	1.140	0.072	3.001	0.194	0.999
2110	0000	48750	1.140	0.075	3.001	0.243	0.937
2120	0000	48750	1.140	0.078	3.001	0.293	0.866
2130	0000	48750	1.140	0.081	3.001	0.343	0.795
2140	0000	48750	1.140	0.084	3.001	0.393	0.724
2150	0000	48750	1.140	0.087	3.001	0.443	0.653
2160	0000	48750	1.140	0.090	3.001	0.493	0.582
2170	0000	48750	1.140	0.093	3.001	0.543	0.511
2180	0000	48750	1.140	0.096	3.001	0.593	0.440
2190	0000	48750	1.140	0.099	3.001	0.643	0.369
2200	0000	48750	1.140	0.102	3.001	0.693	0.298
2210	0000	48750	1.140	0.105	3.001	0.743	0.227
2220	0000	48750	1.140	0.108	3.001	0.793	0.156

FACILITY 2 (Program 001)		NOZZLE TYPE		STREAM		SUPPRESSOR CONFIGURATION	
DUAL FLOW (EAR)		1/2 RIFLED AREA WITH BLEED		PLU CONFIGURATIONS		36-CHUTE, AREA RATIO = 2.0	
INJECT PARAMETERS		OUTER RADIUS RATIO		INNER RADIUS RATIO		DVO	
		0.0000		0.0000		1.2480	
PC	CF	WASA	W2	PA	PTI/PA	DMFGAT	CFNET2
2100	0000	48750	1.140	0.072	3.001	0.194	0.999
2110	0000	48750	1.140	0.075	3.001	0.243	0.937
2120	0000	48750	1.140	0.078	3.001	0.293	0.866
2130	0000	48750	1.140	0.081	3.001	0.343	0.795
2140	0000	48750	1.140	0.084	3.001	0.393	0.724
2150	0000	48750	1.140	0.087	3.001	0.443	0.653
2160	0000	48750	1.140	0.090	3.001	0.493	0.582
2170	0000	48750	1.140	0.093	3.001	0.543	0.511
2180	0000	48750	1.140	0.096	3.001	0.593	0.440
2190	0000	48750	1.140	0.099	3.001	0.643	0.369
2200	0000	48750	1.140	0.102	3.001	0.693	0.298
2210	0000	48750	1.140	0.105	3.001	0.743	0.227
2220	0000	48750	1.140	0.108	3.001	0.793	0.156

MODEL DC-5, 36 DEEP CHUTES, AR = 2.0, FULL PLUG

FACILITY		PL PROGRAM CODE		NOZZLE TYPE		INLET-STREAM		SUPPRESSOR CONFIGURATION			
		RUBI CODE (EAS)		FULL		36-CHUTE, AREA RATIO = 2.0					
		CUIF. RADIUS RATIO		INNER RADIUS RATIO		DVD					
		0.0000		0.0000		1.2480					
THRUST PARAMETERS											
ENG	GF	MASS	OZ	W	PIG/PA	PII/PA	OMEGAT	CDI	CFNET1	CFNET2	F9
2654	4883	48830	0.394	0.019	1.504	1.179	0.000	9.999	0.907	0.907	1.162
2655	4883	48830	0.394	0.027	1.760	1.173	0.000	9.999	0.916	0.916	1.172
2656	4883	48830	0.394	0.033	2.001	1.178	0.000	9.999	0.921	0.921	1.169
2657	4883	48830	0.394	0.038	2.504	1.192	0.000	9.999	0.932	0.932	1.166
2658	4883	48830	0.394	0.046	3.010	1.224	0.000	9.999	0.934	0.934	1.166
2659	4883	48830	0.394	0.055	3.312	1.269	0.000	9.999	0.935	0.935	1.168
2660	4883	48830	0.394	0.064	3.502	1.295	0.000	9.999	0.933	0.933	1.168
2661	4883	48830	0.394	0.072	3.683	1.295	0.000	9.999	0.930	0.930	1.174
2662	4883	48830	0.394	0.085	3.863	1.217	0.000	9.999	0.916	0.916	1.166
2663	4883	48830	0.394	0.097	4.043	1.205	0.000	9.999	0.922	0.922	1.176
2664	4883	48830	0.394	0.107	4.223	1.210	0.000	9.999	0.928	0.928	1.170
2665	4883	48830	0.394	0.117	4.403	1.267	0.000	9.999	0.938	0.938	1.170
2666	4883	48830	0.394	0.127	4.583	1.267	0.000	9.999	0.922	0.922	1.108
2667	4883	48830	0.394	0.137	4.763	1.444	0.000	9.999	0.835	0.835	1.104
2668	4883	48830	0.394	0.147	4.943	1.417	0.000	9.999	0.860	0.860	1.106
2669	4883	48830	0.394	0.157	5.123	1.412	0.000	9.999	0.883	0.883	1.113
2670	4883	48830	0.394	0.167	5.303	1.421	0.000	9.999	0.886	0.886	1.120
2671	4883	48830	0.394	0.177	5.483	1.438	0.000	9.999	0.877	0.877	1.113
2672	4883	48830	0.394	0.187	5.663	1.453	0.000	9.999	0.859	0.859	1.105
2673	4883	48830	0.394	0.197	5.843	1.450	0.000	9.999	0.836	0.836	1.105
2674	4883	48830	0.394	0.207	6.023	1.476	0.000	9.999	0.825	0.825	1.110
2675	4883	48830	0.394	0.217	6.203	1.399	0.000	9.999	0.803	0.803	1.109
2676	4883	48830	0.394	0.227	6.383	1.367	0.000	9.999	0.838	0.838	1.106
2677	4883	48830	0.394	0.237	6.563	1.357	0.000	9.999	0.874	0.874	1.114
2678	4883	48830	0.394	0.247	6.743	1.083	0.000	9.999	0.824	0.824	1.121
2679	4883	48830	0.394	0.257	6.923	1.092	0.000	9.999	0.845	0.845	1.123
2680	4883	48830	0.394	0.267	7.103	1.104	0.000	9.999	0.857	0.857	1.119
2681	4883	48830	0.394	0.277	7.283	1.141	0.000	9.999	0.844	0.844	1.114
2682	4883	48830	0.394	0.287	7.463	1.141	0.000	9.999	0.895	0.895	1.131
2683	4883	48830	0.394	0.297	7.643	1.234	0.000	9.999	0.902	0.902	1.135
2684	4883	48830	0.394	0.307	7.823	1.782	0.000	9.999	0.893	0.893	1.128
2685	4883	48830	0.394	0.317	8.003	1.254	0.000	9.999	0.877	0.877	1.116
2686	4883	48830	0.394	0.327	8.183	1.254	0.000	9.999	0.854	0.854	1.116
2687	4883	48830	0.394	0.337	8.363	1.261	0.000	9.999	0.839	0.839	1.119
2688	4883	48830	0.394	0.347	8.543	1.262	0.000	9.999	0.820	0.820	1.117
2689	4883	48830	0.394	0.357	8.723	1.598	0.000	9.999	0.856	0.856	1.129
2690	4883	48830	0.394	0.367	8.903	2.015	0.000	9.999	0.894	0.894	1.124
2691	4883	48830	0.394	0.377	9.083	2.508	0.000	9.999	0.878	0.878	1.124
2692	4883	48830	0.394	0.387	9.263	2.508	0.000	9.999	0.878	0.878	1.124
2693	4883	48830	0.394	0.397	9.443	2.508	0.000	9.999	0.878	0.878	1.124



MODEL DC-6, 36 DEEP CHUTES, AR = 2.0, FORWARD PLUG

FACILITY 626X1 PROGRAM C031				INLET-STREAM PLUG CONFIGURATIONS				SUPPRESSOR CONFIGURATION			
				DUAL FLOW (FAA)				36-CHUTE, AREA RATIO = 2.0			
				OUTER RADIIUS RATIO				INNER RADIIUS RATIO			
				0.0000				0.7100			
THRUST PARAMETERS				DVO				1.2480			
40C	CF	4454	42	M	ATC/PA	PI/PA	OMEGAT	COO	COI	CFNET1	CFNET2
2321	0010	48610	0.398	0.023	1.500	0.984	0.000	0.952	0.999	0.910	0.910
2322	0010	48610	0.398	0.011	1.502	0.989	0.029	0.951	0.999	0.914	0.914
2323	0010	48610	0.398	0.019	1.504	0.995	0.059	0.950	0.999	0.923	0.923
2324	0010	48610	0.398	0.048	1.998	0.982	0.000	0.946	0.999	0.918	0.918
2327	0010	48610	0.398	0.026	1.997	0.990	0.029	0.946	0.999	0.925	0.925
2328	0010	48610	0.398	0.024	1.997	0.990	0.059	0.946	0.999	0.932	0.932
2329	0010	48610	0.398	0.041	2.496	0.977	0.000	0.949	0.999	0.922	0.922
2330	0010	48610	0.398	0.044	2.500	0.993	0.029	0.944	0.999	0.929	0.929
2331	0010	48610	0.398	0.050	2.507	1.008	0.059	0.945	1.435	0.933	0.939
2332	0010	48610	0.398	0.067	3.012	0.973	0.000	0.949	0.999	0.923	0.923
2333	0010	48610	0.398	0.052	3.012	0.998	0.029	0.946	0.999	0.935	0.935
2334	0010	48610	0.398	0.056	3.013	1.022	0.059	0.947	1.051	0.936	0.945
2335	0010	48610	0.398	0.066	3.309	0.968	0.000	0.949	0.999	0.924	0.924
2336	0010	48610	0.398	0.055	3.307	1.005	0.029	0.948	1.124	0.933	0.935
2337	0010	48610	0.398	0.057	3.309	1.033	0.059	0.949	0.999	0.936	0.946
2338	0010	48610	0.398	0.061	2.500	0.977	0.000	0.943	0.999	0.924	0.924
2339	0010	48610	0.398	0.052	2.499	1.008	0.059	0.947	1.497	0.938	0.943
2340	0010	48610	1.140	0.028	1.504	1.118	0.286	0.949	1.060	0.923	1.064
2341	0010	48610	1.140	0.054	1.502	1.518	0.545	0.951	0.989	0.925	1.179
2342	0010	48610	1.140	0.050	1.502	2.013	0.715	0.951	0.966	0.929	1.807
2343	0010	48610	1.140	0.024	1.501	2.514	0.919	0.952	0.967	0.930	2.171
2344	0010	48610	1.140	0.050	1.501	3.020	1.097	0.963	0.953	0.950	2.584
2345	0010	48610	1.140	0.054	1.502	3.514	1.277	0.944	0.954	0.952	2.965
2346	0010	48610	1.140	0.042	2.002	1.126	0.313	0.946	1.064	0.932	1.159
2347	0010	48610	1.140	0.023	1.994	1.517	0.393	0.946	0.990	0.931	1.223
2348	0010	48610	1.140	0.048	1.994	2.013	0.533	0.946	0.964	0.936	1.637
2349	0010	48610	1.140	0.051	1.998	2.518	0.663	0.944	0.963	0.942	1.655
2350	0010	48610	1.140	0.056	2.001	3.020	0.773	0.945	0.968	0.939	1.860
2351	0010	48610	1.140	0.062	2.500	3.518	0.931	0.943	0.965	0.944	2.083
2352	0010	48610	1.140	0.055	2.498	1.118	0.165	0.948	1.069	0.940	0.997
2353	0010	48610	1.140	0.051	2.493	1.515	0.313	0.943	0.985	0.940	1.147
2354	0010	48610	1.140	0.057	2.501	2.015	0.421	0.943	0.959	0.943	1.297
2355	0010	48610	1.140	0.040	2.499	2.514	0.529	0.948	0.967	0.943	1.445
2356	0010	48610	1.140	0.053	2.502	3.021	0.677	0.948	0.967	0.943	1.637
2357	0010	48610	1.140	0.048	2.498	3.514	0.843	0.948	0.967	0.943	1.860
2358	0010	48610	1.140	0.056	3.004	1.118	0.133	0.948	1.063	0.939	0.981
2359	0010	48610	1.140	0.056	3.004	1.517	0.262	0.948	0.989	0.938	1.176
2360	0010	48610	1.140	0.057	3.010	2.017	0.362	0.948	0.966	0.939	1.211
2361	0010	48610	1.140	0.066	3.011	2.516	0.440	0.949	0.967	0.941	1.324
2362	0010	48610	1.140	0.064	3.012	3.021	0.529	0.948	0.967	0.943	1.445
2363	0010	48610	1.140	0.061	3.002	3.521	0.617	0.952	0.968	0.943	1.558
2364	0010	48610	1.140	0.063	3.306	1.118	0.117	0.948	1.000	0.941	0.972
2365	0010	48610	1.140	0.058	3.289	1.522	0.239	0.949	0.985	0.940	1.177
2366	0010	48610	1.140	0.056	3.295	2.010	0.320	0.949	0.965	0.940	1.178
2367	0010	48610	1.140	0.062	3.307	2.512	0.399	0.950	0.967	0.941	1.278

FACILITY 60X61 PROGRAM C031															
NOZZLE TYPE															
DUAL FLOW (FAA)															
SUPPRESSOR CONFIGURATIONS															
36-CHUTE, AREA RATIO = 2.0															
ORIG. PARAMETERS															
OUTER RADIUS RATIO INNER RADIUS RATIO															
0.0000 0.7390															
DVO															
1.2480															
ROC	CS	MASA	R2	WA	R2/D2A	RT/D2A	OMEGAT	DCS	CDS	PCSM	CDSH	DCPL-D	DCPL-I	DELTOI	PSUM/PA
2323	0010	48630	0.398	0.023	1.500	0.984	0.000	-0.046	21.938	-0.001	0.282	-0.026	-0.002	-0.075	0.965
2324	0010	48630	0.398	0.011	1.502	0.939	0.029	-0.045	95.310	-0.001	1.337	-0.023	-0.001	-0.065	0.966
2325	0010	48630	0.398	0.019	1.504	0.995	0.059	-0.045	32.792	-0.000	0.308	-0.022	-0.001	-0.066	0.966
2326	0010	48630	0.398	0.046	1.958	0.932	0.030	-0.040	7.935	-0.000	0.049	-0.023	-0.000	-0.063	0.947
2327	0010	48630	0.398	0.024	1.907	0.990	0.079	-0.040	26.874	-0.000	0.314	-0.021	0.000	-0.061	0.948
2328	0010	48630	0.398	0.024	1.557	0.995	0.058	-0.040	31.398	-0.001	0.308	-0.021	0.002	-0.059	0.948
2329	0010	48630	0.398	0.041	2.456	0.977	0.000	-0.035	13.514	-0.000	0.125	-0.023	0.001	-0.058	0.935
2330	0010	48630	0.398	0.044	2.502	0.933	0.029	-0.034	11.322	-0.000	0.096	-0.020	0.001	-0.054	0.936
2331	0010	48630	0.398	0.050	2.507	1.008	0.059	-0.033	8.784	-0.000	0.066	-0.020	0.003	-0.051	0.937
2332	0010	48630	0.398	0.057	3.017	0.973	0.050	-0.030	11.823	-0.000	0.096	-0.025	0.002	-0.053	0.925
2333	0010	48630	0.398	0.052	3.012	0.994	0.079	-0.030	9.561	-0.000	0.076	-0.022	0.002	-0.050	0.927
2334	0010	48630	0.398	0.055	3.011	1.022	0.058	-0.030	8.496	-0.000	0.067	-0.021	0.004	-0.047	0.927
2335	0010	48630	0.398	0.064	3.305	0.968	0.000	-0.026	5.985	-0.000	0.055	-0.023	0.004	-0.046	0.926
2336	0010	48630	0.398	0.055	3.327	1.005	0.129	-0.026	8.558	-0.000	0.059	-0.021	0.002	-0.046	0.926
2337	0010	48630	0.398	0.057	3.359	1.033	0.055	-0.026	7.873	-0.000	0.059	-0.020	0.004	-0.042	0.926
2338	0010	48630	0.398	0.061	2.500	0.977	0.000	-0.035	13.638	-0.000	0.112	-0.023	0.001	-0.058	0.934
2339	0010	48630	0.398	0.057	2.456	1.008	0.059	-0.034	8.107	-0.000	0.063	-0.019	0.003	-0.050	0.936
2340	0010	48630	1.140	0.025	1.504	1.113	0.286	-0.040	19.892	-0.000	0.204	-0.023	0.004	-0.060	0.965
2341	0010	48630	1.140	0.054	1.502	1.518	0.545	-0.030	4.205	-0.000	0.024	-0.018	0.005	-0.044	0.965
2342	0010	48630	1.140	0.050	1.502	2.013	0.735	-0.024	4.566	-0.000	0.012	-0.015	0.000	-0.039	0.965
2343	0010	48630	1.140	0.054	1.501	2.514	0.919	-0.021	22.161	-0.000	0.419	-0.013	-0.003	-0.037	0.963
2344	0010	48630	1.140	0.050	1.504	3.020	1.097	-0.017	4.847	-0.000	0.049	-0.011	0.009	-0.019	0.965
2345	0010	48630	1.140	0.056	1.502	3.514	1.277	-0.015	3.963	-0.000	0.038	-0.009	0.000	-0.024	0.964
2346	0010	48630	1.140	0.062	2.002	1.124	0.210	-0.037	10.674	-0.000	0.091	-0.021	0.006	-0.052	0.947
2347	0010	48630	1.140	0.023	1.954	1.517	0.396	-0.032	37.095	-0.000	0.427	-0.020	0.005	-0.046	0.945
2348	0010	48630	1.140	0.064	1.954	2.013	0.533	-0.027	8.208	-0.000	0.079	-0.017	0.001	-0.037	0.945
2349	0010	48630	1.140	0.051	1.959	2.514	0.665	-0.023	7.323	-0.000	0.049	-0.014	0.001	-0.037	0.946
2350	0010	48630	1.140	0.052	2.001	3.020	0.799	-0.020	5.918	-0.000	0.047	-0.012	0.007	-0.026	0.946
2351	0010	48630	1.140	0.067	2.000	3.518	0.931	-0.018	4.915	-0.000	0.048	-0.011	0.001	-0.028	0.946
2352	0010	48630	1.140	0.055	2.458	1.119	0.165	-0.033	7.600	-0.000	0.042	-0.021	0.005	-0.028	0.934
2353	0010	48630	1.140	0.051	2.503	1.519	0.315	-0.029	8.758	-0.000	0.046	-0.019	0.007	-0.042	0.934
2354	0010	48630	1.140	0.057	2.501	2.015	0.423	-0.026	7.144	-0.000	0.059	-0.018	0.002	-0.062	0.933
2355	0010	48630	1.140	0.064	2.507	2.517	0.545	-0.024	6.447	-0.000	0.062	-0.014	0.003	-0.031	0.934
2356	0010	48630	1.140	0.053	3.018	3.018	0.665	-0.021	8.221	-0.000	0.062	-0.014	0.001	-0.031	0.934
2357	0010	48630	1.140	0.058	3.027	3.518	0.799	-0.021	8.221	-0.000	0.062	-0.014	0.001	-0.031	0.934
2358	0010	48630	1.140	0.054	3.027	4.021	0.919	-0.021	8.221	-0.000	0.062	-0.014	0.001	-0.031	0.934
2359	0010	48630	1.140	0.056	3.024	4.517	1.033	-0.029	32.918	-0.000	0.410	-0.021	0.005	-0.046	0.926
2360	0010	48630	1.140	0.057	3.010	5.017	1.113	-0.026	8.314	-0.000	0.080	-0.020	0.006	-0.041	0.926
2361	0010	48630	1.140	0.066	3.011	5.516	1.193	-0.021	8.028	-0.000	0.070	-0.019	0.002	-0.040	0.926
2362	0010	48630	1.140	0.064	3.012	6.012	1.273	-0.020	5.968	-0.000	0.056	-0.016	0.002	-0.036	0.926
2363	0010	48630	1.140	0.061	3.002	6.507	1.353	-0.020	6.202	-0.000	0.042	-0.014	0.001	-0.033	0.927
2364	0010	48630	1.140	0.063	3.006	7.001	1.433	-0.018	6.781	-0.000	0.067	-0.012	0.001	-0.030	0.927
2365	0010	48630	1.140	0.058	3.289	7.501	1.513	-0.025	6.447	-0.000	0.068	-0.020	0.006	-0.040	0.926
2366	0010	48630	1.140	0.056	3.295	8.001	1.593	-0.023	7.643	-0.000	0.036	-0.019	0.006	-0.036	0.926
2367	0010	48630	1.140	0.062	3.307	8.501	1.673	-0.021	8.174	-0.000	0.052	-0.017	0.002	-0.037	0.926
2368	0010	48630	1.140	0.062	3.307	9.001	1.753	-0.019	6.535	-0.000	0.060	-0.015	0.002	-0.033	0.927

FACILITY	JET PROGRAM CODE	NOZZLE TYPE		PLUG CONFIGURATIONS		SUPPRESSOR CONFIGURATION	
		DUAL FLOW (FAR)	FORWARD PLUG WITH BLEED	36-CHUTE, AREA RATIO = 2.0			
OUTER RADIUS RATIO INLET RADIUS RATIO DVO							
0.0009		0.3300		1.2480			
ARC	CR	MA	RT/TRA	CMCAT	COI	CMCF11	CMCF12
2769	0010	48650	1-140	0.068	3.315	3.020	0.480
2769	0010	48650	1-140	0.068	3.315	3.020	0.480
2770	0010	48650	1-140	0.068	2.502	1.122	0.167
2770	0010	48650	1-140	0.068	2.502	1.122	0.167
2771	0010	48650	1-140	0.068	2.496	3.513	0.346
2771	0010	48650	1-140	0.068	2.496	3.513	0.346
2772	0010	48650	1-140	0.068	3.602	3.513	0.530
2772	0010	48650	1-140	0.068	3.602	3.513	0.530
2773	0010	48650	1-140	0.068	3.602	3.513	0.530
2773	0010	48650	1-140	0.068	3.602	3.513	0.530
2774	0010	48650	1-140	0.068	1.500	1.002	0.020
2774	0010	48650	1-140	0.068	1.500	1.002	0.020
2775	0010	48650	1-140	0.068	1.500	1.002	0.020
2775	0010	48650	1-140	0.068	1.500	1.002	0.020
2776	0010	48650	1-140	0.068	2.003	1.051	0.059
2776	0010	48650	1-140	0.068	2.003	1.051	0.059
2777	0010	48650	1-140	0.068	2.005	1.011	0.029
2777	0010	48650	1-140	0.068	2.005	1.011	0.029
2778	0010	48650	1-140	0.068	3.046	1.021	0.059
2778	0010	48650	1-140	0.068	3.046	1.021	0.059
2779	0010	48650	1-140	0.068	2.508	0.986	0.000
2779	0010	48650	1-140	0.068	2.508	0.986	0.000
2780	0010	48650	1-140	0.068	2.508	0.986	0.000
2780	0010	48650	1-140	0.068	2.508	0.986	0.000
2781	0010	48650	1-140	0.068	2.508	0.986	0.000
2781	0010	48650	1-140	0.068	2.508	0.986	0.000
2782	0010	48650	1-140	0.068	2.508	0.986	0.000
2782	0010	48650	1-140	0.068	2.508	0.986	0.000
2783	0010	48650	1-140	0.068	2.508	0.986	0.000
2783	0010	48650	1-140	0.068	2.508	0.986	0.000
2784	0010	48650	1-140	0.068	2.508	0.986	0.000
2784	0010	48650	1-140	0.068	2.508	0.986	0.000
2785	0010	48650	1-140	0.068	2.508	0.986	0.000
2785	0010	48650	1-140	0.068	2.508	0.986	0.000
2786	0010	48650	1-140	0.068	2.508	0.986	0.000
2786	0010	48650	1-140	0.068	2.508	0.986	0.000
2787	0010	48650	1-140	0.068	2.508	0.986	0.000
2787	0010	48650	1-140	0.068	2.508	0.986	0.000
2788	0010	48650	1-140	0.068	2.508	0.986	0.000
2788	0010	48650	1-140	0.068	2.508	0.986	0.000
2789	0010	48650	1-140	0.068	2.508		



[illegible]



FACILITY			XI PROGRAM C031			NOZZLE TYPE			THI. - STREAM			SUPPRESSOR CONFIGURATION			
			DUAL FLOW (FA4)			FOPHARD PLUG WITH PLEED			36-CHUTE, AREA RATIO = 2.0						
DRAG PARAMETERS			OUTER RADIUS RATIO			INNER RADIUS RATIO			DYN						
			0.0000			0.7750			1.2480						
FC	CE	RASA	R2	HA	RH/RA	RI/RA	OMEGAT	UCS	CDS	DCSH	CUSH	DCPL-C	DCPL-I	DCIOT-PSUP/PA	
2413	CC10	48650	1.140	0.446	1.501	3.024	1.086	-0.055	0.197	-0.005	0.016	-0.006	0.016	-0.050	0.887
2414	CC10	48650	1.140	0.446	1.500	3.519	1.266	-0.048	0.137	-0.005	0.019	-0.006	0.007	-0.051	0.887
2415	CC10	48650	1.140	0.446	2.000	1.112	0.184	-0.115	0.285	-0.005	0.022	-0.005	0.017	-0.115	0.836
2416	CC10	48650	1.140	0.446	2.000	1.518	0.392	-0.095	0.287	-0.007	0.022	-0.007	0.016	-0.092	0.835
2417	CC10	48650	1.140	0.445	1.958	2.012	0.532	-0.081	0.290	-0.006	0.021	-0.007	0.009	-0.085	0.834
2418	CC10	48650	1.140	0.445	2.000	2.514	0.664	-0.071	0.290	-0.005	0.022	-0.006	0.006	-0.074	0.834
2419	CC10	48650	1.140	0.446	2.002	3.023	0.799	-0.062	0.286	-0.005	0.022	-0.005	0.011	-0.060	0.836
2420	CC10	48650	1.140	0.446	2.000	3.523	0.932	-0.055	0.284	-0.004	0.022	-0.003	0.006	-0.057	0.837
2421	CC10	48650	1.140	0.445	2.503	1.115	0.145	-0.102	0.355	-0.007	0.023	-0.011	0.014	-0.106	0.797
2422	CC10	48650	1.140	0.446	2.500	1.516	0.312	-0.089	0.360	-0.006	0.024	-0.010	0.014	-0.092	0.795
2423	CC10	48650	1.140	0.446	2.504	2.016	0.424	-0.079	0.357	-0.005	0.023	-0.009	0.009	-0.085	0.795
2424	CC10	48650	1.140	0.446	2.508	2.518	0.530	-0.071	0.357	-0.005	0.023	-0.007	0.007	-0.076	0.795
2425	CC10	48650	1.140	0.447	2.507	3.024	0.637	-0.063	0.351	-0.004	0.022	-0.006	0.003	-0.070	0.797
2426	CC10	48650	1.140	0.444	2.508	3.523	0.743	-0.057	0.347	-0.004	0.023	-0.004	0.006	-0.059	0.799
2427	CC10	48650	1.140	0.446	3.024	1.114	0.115	-0.092	0.393	-0.005	0.024	-0.011	0.012	-0.092	0.774
2428	CC10	48650	1.140	0.446	3.024	1.516	0.258	-0.079	0.394	-0.005	0.024	-0.011	0.013	-0.082	0.774
2429	CC10	48650	1.140	0.445	3.016	2.017	0.369	-0.065	0.392	-0.005	0.024	-0.008	0.006	-0.065	0.775
2430	CC10	48650	1.140	0.445	3.022	2.517	0.476	-0.058	0.389	-0.004	0.024	-0.006	0.006	-0.071	0.775
2431	CC10	48650	1.140	0.446	3.022	3.019	0.578	-0.055	0.391	-0.004	0.024	-0.006	0.004	-0.064	0.776
2432	CC10	48650	1.140	0.445	3.022	3.523	0.616	-0.055	0.389	-0.003	0.024	-0.005	0.004	-0.059	0.776
2433	CC10	48650	1.140	0.445	3.022	3.523	0.616	-0.055	0.389	-0.003	0.024	-0.005	0.004	-0.059	0.776
2434	CC10	48650	1.140	0.445	3.022	3.523	0.616	-0.055	0.389	-0.003	0.024	-0.005	0.004	-0.059	0.776
2435	CC10	48650	1.140	0.445	3.022	3.523	0.616	-0.055	0.389	-0.003	0.024	-0.005	0.004	-0.059	0.776
2436	CC10	48650	1.140	0.445	3.022	3.523	0.616	-0.055	0.389	-0.003	0.024	-0.005	0.004	-0.059	0.776
2437	CC10	48650	1.140	0.445	3.022	3.523	0.616	-0.055	0.389	-0.003	0.024	-0.005	0.004	-0.059	0.776
2438	CC10	48650	1.140	0.445	3.022	3.523	0.616	-0.055	0.389	-0.003	0.024	-0.005	0.004	-0.059	0.776
2439	CC10	48650	1.140	0.444	2.500	1.114	0.144	-0.102	0.366	-0.007	0.023	-0.010	0.013	-0.106	0.797
2440	CC10	48650	1.140	0.446	2.501	1.524	0.243	-0.057	0.347	-0.004	0.024	-0.014	0.005	-0.060	0.801
2441	CC10	48650	1.140	0.445	3.019	2.009	0.350	-0.071	0.395	-0.004	0.024	-0.010	0.007	-0.079	0.801
2442	CC10	48650	1.140	0.445	3.022	2.522	0.476	-0.057	0.395	-0.004	0.024	-0.010	0.007	-0.079	0.801
2443	CC10	48650	1.140	0.445	3.022	3.022	0.600	-0.057	0.395	-0.004	0.024	-0.010	0.007	-0.079	0.801
2444	CC10	48650	1.140	0.445	3.022	3.522	0.723	-0.057	0.395	-0.004	0.024	-0.010	0.007	-0.079	0.801
2445	CC10	48650	1.140	0.445	3.022	3.522	0.723	-0.057	0.395	-0.004	0.024	-0.010	0.007	-0.079	0.801
2446	CC10	48650	1.140	0.445	3.022	3.522	0.723	-0.057	0.395	-0.004	0.024	-0.010	0.007	-0.079	0.801
2447	CC10	48650	1.140	0.445	3.022	3.522	0.723	-0.057	0.395	-0.004	0.024	-0.010	0.007	-0.079	0.801
2448	CC10	48650	1.140	0.445	3.022	3.522	0.723	-0.057	0.395	-0.004	0.024	-0.010	0.007	-0.079	0.801
2449	CC10	48650	1.140	0.445	3.022	3.522	0.723	-0.057	0.395	-0.004	0.024	-0.010	0.007	-0.079	0.801
2450	CC10	48650	1.140	0.445	3.022	3.522	0.723	-0.057	0.395	-0.004	0.024	-0.010	0.007	-0.079	0.801
2451	CC10	48650	1.140	0.445	3.022	3.522	0.723	-0.057	0.395	-0.004	0.024	-0.010	0.007	-0.079	0.801
2452	CC10	48650	1.140	0.445	3.022	3.522	0.723	-0.057	0.395	-0.004	0.024	-0.010	0.007	-0.079	0.801
2453	CC10	48650	1.140	0.445	3.022	3.522	0.723	-0.057	0.395	-0.004	0.024	-0.010	0.007	-0.079	0.801
2454	CC10	48650	1.140	0.445	3.022	3.522	0.723	-0.057	0.395	-0.004	0.024	-0.010	0.007	-0.079	0.801
2455	CC10	48650	1.140	0.445	3.022	3.522	0.723	-0.057	0.395	-0.004	0.024	-0.010	0.007	-0.079	0.801
2456	CC10	48650	1.140	0.445	3.022	3.522	0.723	-0.057	0.395	-0.004	0.024	-0.010	0.007	-0.079	0.801
2457	CC10	48650	1.140	0.445	3.022	3.522	0.723	-0.057	0.395	-0.004	0.024	-0.010	0.007	-0.079	0.801

FACILITY		-071 PROGRAM CODE		1. A-STREAM PLUM CONFIGURATIONS										SUPPRESSOR CONFIGURATION	
				QUAL FLTM (FAS)										36-CHUTE, AREA RATIO = 2.0	
				OUTER RADIUS RATIO INNER RADIUS RATIO										DVM	
				0.0000 1.2480											
PARAMETER															
LOC	PL	WALL	DR	EL	FLY/PA	RT/PA	UMSCAT	CPD	CNI	CENET1	CENET2	EO	EO		
2458	0010	4850	0.170	0.140	2.517	0.984	0.070	0.947	0.999	0.870	0.870	0.870	1.099		
2458	0010	4850	0.204	0.160	2.515	1.028	0.089	0.947	0.975	0.881	0.881	0.881	1.104		
2463	0010	4850	0.240	0.160	2.508	1.073	0.112	0.947	0.999	0.880	0.880	0.880	1.108		
2461	0010	4850	0.276	0.160	1.506	1.517	0.534	0.965	0.985	0.871	1.342	1.151	1.151		
2462	0010	4850	0.312	0.160	1.506	2.026	0.727	0.965	0.966	0.883	1.709	1.153	1.153		
2463	0010	4850	0.348	0.160	1.506	2.533	0.907	0.966	0.966	0.883	2.082	1.157	1.157		
2464	0010	4850	0.384	0.160	1.502	3.040	1.086	0.966	0.967	0.906	2.451	1.161	1.161		
2465	0010	4850	0.420	0.160	2.016	1.124	0.191	0.946	0.977	0.872	0.943	1.118	1.118		
2466	0010	4850	0.456	0.160	2.016	1.631	0.390	0.945	0.982	0.885	1.157	1.148	1.148		
2468	0010	4850	0.528	0.160	2.012	2.028	0.531	0.947	0.965	0.893	1.370	1.152	1.152		
2469	0010	4850	0.564	0.160	2.012	2.530	0.644	0.946	0.967	0.900	1.577	1.153	1.153		
2470	0010	4850	0.600	0.160	2.014	3.025	0.794	0.945	0.967	0.909	1.791	1.159	1.159		
2471	0010	4850	0.636	0.160	2.011	3.528	0.927	0.944	0.967	0.913	2.005	1.162	1.162		
2472	0010	4850	0.672	0.160	2.514	1.119	0.148	0.947	0.965	0.890	0.938	1.119	1.119		
2473	0010	4850	0.708	0.160	2.512	1.614	0.312	0.947	0.983	0.896	1.090	1.145	1.145		
2474	0010	4850	0.744	0.160	2.512	2.020	0.424	0.948	0.966	0.902	1.241	1.150	1.150		
2475	0010	4850	0.780	0.160	2.524	2.522	0.520	0.944	0.966	0.907	1.389	1.149	1.149		
2476	0010	4850	0.816	0.160	2.516	3.021	0.614	0.947	0.967	0.915	1.542	1.157	1.157		
2477	0010	4850	0.852	0.160	3.005	1.123	0.172	0.949	0.934	0.901	0.939	1.123	1.123		
2478	0010	4850	0.888	0.160	3.005	1.622	0.260	0.948	0.980	0.906	1.059	1.148	1.148		
2479	0010	4850	0.924	0.160	3.017	2.027	0.441	0.947	0.966	0.914	1.289	1.153	1.153		
2480	0010	4850	0.960	0.160	3.018	2.527	0.529	0.948	0.967	0.919	1.406	1.157	1.157		
2481	0010	4850	1.000	0.160	3.016	3.027	0.617	0.949	0.968	0.919	1.518	1.159	1.159		
2482	0010	4850	1.040	0.160	2.501	1.112	0.144	0.948	0.956	0.876	0.922	1.109	1.109		
2483	0010	4850	1.080	0.160	2.501	1.612	0.264	0.948	0.968	0.908	1.082	1.122	1.122		
2484	0010	4850	1.120	0.160	2.507	2.020	0.313	0.949	0.960	0.890	0.939	1.122	1.122		
2485	0010	4850	1.160	0.160	2.511	2.527	0.424	0.948	0.966	0.897	1.094	1.147	1.147		
2486	0010	4850	1.200	0.160	2.514	3.024	0.520	0.948	0.966	0.902	1.244	1.149	1.149		
2487	0010	4850	1.240	0.160	2.514	3.520	0.614	0.947	0.967	0.908	1.391	1.152	1.152		
2488	0010	4850	1.280	0.160	2.515	4.024	0.708	0.947	0.968	0.915	1.543	1.157	1.157		
2489	0010	4850	1.320	0.160	3.013	1.123	0.170	0.948	0.969	0.916	1.691	1.160	1.160		
2490	0010	4850	1.360	0.160	3.025	1.623	0.262	0.948	0.969	0.927	1.841	1.166	1.166		
2491	0010	4850	1.400	0.160	3.008	2.027	0.356	0.949	0.981	0.906	1.060	1.148	1.148		
2492	0010	4850	1.440	0.160	3.008	2.532	0.443	0.949	0.967	0.915	1.291	1.155	1.155		
2493	0010	4850	1.480	0.160	3.016	3.040	0.531	0.949	0.967	0.915	1.409	1.158	1.158		
2494	0010	4850	1.520	0.160	3.017	3.542	0.616	0.949	0.969	0.915	1.517	1.159	1.159		
2495	0010	4850	1.560	0.160	3.225	1.121	0.107	0.949	0.901	0.906	0.939	1.128	1.128		
2496	0010	4850	1.600	0.160	3.265	1.625	0.240	0.949	0.979	0.911	1.048	1.151	1.151		
2497	0010	4850	1.640	0.160	3.222	2.030	0.331	0.948	0.966	0.913	1.156	1.153	1.153		
2498	0010	4850	1.680	0.160	3.216	2.533	0.414	0.951	0.967	0.916	1.260	1.156	1.156		
2499	0010	4850	1.720	0.160	3.237	3.038	0.493	0.951	0.967	0.923	1.367	1.162	1.162		
2500	0010	4850	1.760	0.160	3.258	3.520	0.569	0.949	0.968	0.920	1.458	1.159	1.159		





MODEL DC-7, 36 DEEP CHUTES, AR = 2.5, BASELINE PLUG

[illegible]















MODEL DC-8, 36 DEEP CHUTES, AR = 2.5, FULL PLUG

[illegible]



FACILITY 6X1 PROGRAM C031			NOZZLE TYPE			PI CONFIGURATIONS			SUPPRESSOR CONFIGURATION		
DUAL FLOW (EAA)			FULL AUG W/C BLEED			36-CHUTE AREA RATIO = 2.5					
DRAG PARAMETER			INNER RADIUS RATIO			DVC					
			0.0000			1.24R3					
PNG	GE	NASA	WA	PIR/PA	PTI/PA	OMEGAI	DCS	DCSH	CDS	DCSH	DCSH
2696	4983	49830	0.398	0.445	1.375	0.000	-0.178	0.253	-0.004	0.006	0.006
2697	4983	49830	0.398	0.445	1.375	0.000	-0.178	0.253	-0.004	0.006	0.006
2698	4983	49830	0.398	0.445	1.375	0.000	-0.178	0.253	-0.004	0.006	0.006
2699	4983	49830	0.398	0.445	1.375	0.000	-0.178	0.253	-0.004	0.006	0.006
2700	4983	49830	0.398	0.445	1.375	0.000	-0.178	0.253	-0.004	0.006	0.006
2701	4983	49830	0.398	0.445	1.375	0.000	-0.178	0.253	-0.004	0.006	0.006
2702	4983	49830	0.398	0.445	1.375	0.000	-0.178	0.253	-0.004	0.006	0.006
2703	4983	49830	0.398	0.445	1.375	0.000	-0.178	0.253	-0.004	0.006	0.006
2704	4983	49830	0.398	0.445	1.375	0.000	-0.178	0.253	-0.004	0.006	0.006
2705	4983	49830	0.398	0.445	1.375	0.000	-0.178	0.253	-0.004	0.006	0.006
2706	4983	49830	0.398	0.445	1.375	0.000	-0.178	0.253	-0.004	0.006	0.006
2707	4983	49830	0.398	0.445	1.375	0.000	-0.178	0.253	-0.004	0.006	0.006
2708	4983	49830	0.398	0.445	1.375	0.000	-0.178	0.253	-0.004	0.006	0.006
2709	4983	49830	0.398	0.445	1.375	0.000	-0.178	0.253	-0.004	0.006	0.006
2710	4983	49830	0.398	0.445	1.375	0.000	-0.178	0.253	-0.004	0.006	0.006
2711	4983	49830	0.398	0.445	1.375	0.000	-0.178	0.253	-0.004	0.006	0.006
2712	4983	49830	0.398	0.445	1.375	0.000	-0.178	0.253	-0.004	0.006	0.006
2713	4983	49830	0.398	0.445	1.375	0.000	-0.178	0.253	-0.004	0.006	0.006
2714	4983	49830	0.398	0.445	1.375	0.000	-0.178	0.253	-0.004	0.006	0.006
2715	4983	49830	0.398	0.445	1.375	0.000	-0.178	0.253	-0.004	0.006	0.006
2716	4983	49830	0.398	0.445	1.375	0.000	-0.178	0.253	-0.004	0.006	0.006
2717	4983	49830	0.398	0.445	1.375	0.000	-0.178	0.253	-0.004	0.006	0.006
2718	4983	49830	0.398	0.445	1.375	0.000	-0.178	0.253	-0.004	0.006	0.006
2719	4983	49830	0.398	0.445	1.375	0.000	-0.178	0.253	-0.004	0.006	0.006
2720	4983	49830	0.398	0.445	1.375	0.000	-0.178	0.253	-0.004	0.006	0.006
2721	4983	49830	0.398	0.445	1.375	0.000	-0.178	0.253	-0.004	0.006	0.006
2722	4983	49830	0.398	0.445	1.375	0.000	-0.178	0.253	-0.004	0.006	0.006
2723	4983	49830	0.398	0.445	1.375	0.000	-0.178	0.253	-0.004	0.006	0.006
2724	4983	49830	0.398	0.445	1.375	0.000	-0.178	0.253	-0.004	0.006	0.006
2725	4983	49830	0.398	0.445	1.375	0.000	-0.178	0.253	-0.004	0.006	0.006
2726	4983	49830	0.398	0.445	1.375	0.000	-0.178	0.253	-0.004	0.006	0.006
2727	4983	49830	0.398	0.445	1.375	0.000	-0.178	0.253	-0.004	0.006	0.006
2728	4983	49830	0.398	0.445	1.375	0.000	-0.178	0.253	-0.004	0.006	0.006
2729	4983	49830	0.398	0.445	1.375	0.000	-0.178	0.253	-0.004	0.006	0.006
2730	4983	49830	0.398	0.445	1.375	0.000	-0.178	0.253	-0.004	0.006	0.006
2731	4983	49830	0.398	0.445	1.375	0.000	-0.178	0.253	-0.004	0.006	0.006
2732	4983	49830	0.398	0.445	1.375	0.000	-0.178	0.253	-0.004	0.006	0.006
2733	4983	49830	0.398	0.445	1.375	0.000	-0.178	0.253	-0.004	0.006	0.006
2734	4983	49830	0.398	0.445	1.375	0.000	-0.178	0.253	-0.004	0.006	0.006

MODEL DC-3 (SPOKE), 36 SPOKES, AR = 2.0, BASELINE PLUG

















104-TUBE NOZZLE







8-LOBE NOZZLE

FACILITY: 201 PROGRAM COSL  
 MODEL TYPE: 1-STREAM  
 DISEY SUPPRESSOR (244)  
 CONFIGURATIONS: SUPPRESSOR CONFIGURATION

THROTT PARAMETERS		CUTER RADIUS RATIO		INNER RADIUS RATIO		OVO	
C, L, A, S, S		C, 0, 0, 0, 0		0, 0, 0, 0		1, 2, 6, 0	
NO	CLASS	D2	W4	PI/PSA	PI/PSA	CMCAT	COO
3177	1000 10000	0.000	0.000	1.407	1.075	0.000	1.006
3178	1000 10000	0.000	0.000	1.407	1.075	0.000	1.006
3179	1000 10000	0.000	0.000	1.407	1.075	0.000	1.006
3180	1000 10000	0.000	0.000	1.407	1.075	0.000	1.006
3181	1000 10000	0.000	0.000	1.407	1.075	0.000	1.006
3182	1000 10000	0.000	0.000	1.407	1.075	0.000	1.006
3183	1000 10000	0.000	0.000	1.407	1.075	0.000	1.006
3184	1000 10000	0.000	0.000	1.407	1.075	0.000	1.006
3185	1000 10000	0.000	0.000	1.407	1.075	0.000	1.006
3186	1000 10000	0.000	0.000	1.407	1.075	0.000	1.006
3187	1000 10000	0.000	0.000	1.407	1.075	0.000	1.006
3188	1000 10000	0.000	0.000	1.407	1.075	0.000	1.006
3189	1000 10000	0.000	0.000	1.407	1.075	0.000	1.006
3190	1000 10000	0.000	0.000	1.407	1.075	0.000	1.006
3191	1000 10000	0.000	0.000	1.407	1.075	0.000	1.006
3192	1000 10000	0.000	0.000	1.407	1.075	0.000	1.006
3193	1000 10000	0.000	0.000	1.407	1.075	0.000	1.006
3194	1000 10000	0.000	0.000	1.407	1.075	0.000	1.006
3195	1000 10000	0.000	0.000	1.407	1.075	0.000	1.006
3196	1000 10000	0.000	0.000	1.407	1.075	0.000	1.006
3197	1000 10000	0.000	0.000	1.407	1.075	0.000	1.006
3198	1000 10000	0.000	0.000	1.407	1.075	0.000	1.006
3199	1000 10000	0.000	0.000	1.407	1.075	0.000	1.006
3200	1000 10000	0.000	0.000	1.407	1.075	0.000	1.006
3201	1000 10000	0.000	0.000	1.407	1.075	0.000	1.006
3202	1000 10000	0.000	0.000	1.407	1.075	0.000	1.006
3203	1000 10000	0.000	0.000	1.407	1.075	0.000	1.006
3204	1000 10000	0.000	0.000	1.407	1.075	0.000	1.006
3205	1000 10000	0.000	0.000	1.407	1.075	0.000	1.006
3206	1000 10000	0.000	0.000	1.407	1.075	0.000	1.006
3207	1000 10000	0.000	0.000	1.407	1.075	0.000	1.006
3208	1000 10000	0.000	0.000	1.407	1.075	0.000	1.006
3209	1000 10000	0.000	0.000	1.407	1.075	0.000	1.006
3210	1000 10000	0.000	0.000	1.407	1.075	0.000	1.006
3211	1000 10000	0.000	0.000	1.407	1.075	0.000	1.006
3212	1000 10000	0.000	0.000	1.407	1.075	0.000	1.006
3213	1000 10000	0.000	0.000	1.407	1.075	0.000	1.006
3214	1000 10000	0.000	0.000	1.407	1.075	0.000	1.006
3215	1000 10000	0.000	0.000	1.407	1.075	0.000	1.006
3216	1000 10000	0.000	0.000	1.407	1.075	0.000	1.006
3217	1000 10000	0.000	0.000	1.407	1.075	0.000	1.006
3218	1000 10000	0.000	0.000	1.407	1.075	0.000	1.006
3219	1000 10000	0.000	0.000	1.407	1.075	0.000	1.006
3220	1000 10000	0.000	0.000	1.407	1.075	0.000	1.006
3221	1000 10000	0.000	0.000	1.407	1.075	0.000	1.006

MACLEAY & CO. 155, 157, 159, 161, 163, 165, 167, 169, 171, 173, 175, 177, 179, 181, 183, 185, 187, 189, 191, 193, 195, 197, 199, 201, 203, 205, 207, 209, 211, 213, 215, 217, 219, 221, 223, 225, 227, 229, 231, 233, 235, 237, 239, 241, 243, 245, 247, 249, 251, 253, 255, 257, 259, 261, 263, 265, 267, 269, 271, 273, 275, 277, 279, 281, 283, 285, 287, 289, 291, 293, 295, 297, 299, 301, 303, 305, 307, 309, 311, 313, 315, 317, 319, 321, 323, 325, 327, 329, 331, 333, 335, 337, 339, 341, 343, 345, 347, 349, 351, 353, 355, 357, 359, 361, 363, 365, 367, 369, 371, 373, 375, 377, 379, 381, 383, 385, 387, 389, 391, 393, 395, 397, 399, 401, 403, 405, 407, 409, 411, 413, 415, 417, 419, 421, 423, 425, 427, 429, 431, 433, 435, 437, 439, 441, 443, 445, 447, 449, 451, 453, 455, 457, 459, 461, 463, 465, 467, 469, 471, 473, 475, 477, 479, 481, 483, 485, 487, 489, 491, 493, 495, 497, 499, 501, 503, 505, 507, 509, 511, 513, 515, 517, 519, 521, 523, 525, 527, 529, 531, 533, 535, 537, 539, 541, 543, 545, 547, 549, 551, 553, 555, 557, 559, 561, 563, 565, 567, 569, 571, 573, 575, 577, 579, 581, 583, 585, 587, 589, 591, 593, 595, 597, 599, 601, 603, 605, 607, 609, 611, 613, 615, 617, 619, 621, 623, 625, 627, 629, 631, 633, 635, 637, 639, 641, 643, 645, 647, 649, 651, 653, 655, 657, 659, 661, 663, 665, 667, 669, 671, 673, 675, 677, 679, 681, 683, 685, 687, 689, 691, 693, 695, 697, 699, 701, 703, 705, 707, 709, 711, 713, 715, 717, 719, 721, 723, 725, 727, 729, 731, 733, 735, 737, 739, 741, 743, 745, 747, 749, 751, 753, 755, 757, 759, 761, 763, 765, 767, 769, 771, 773, 775, 777, 779, 781, 783, 785, 787, 789, 791, 793, 795, 797, 799, 801, 803, 805, 807, 809, 811, 813, 815, 817, 819, 821, 823, 825, 827, 829, 831, 833, 835, 837, 839, 841, 843, 845, 847, 849, 851, 853, 855, 857, 859, 861, 863, 865, 867, 869, 871, 873, 875, 877, 879, 881, 883, 885, 887, 889, 891, 893, 895, 897, 899, 901, 903, 905, 907, 909, 911, 913, 915, 917, 919, 921, 923, 925, 927, 929, 931, 933, 935, 937, 939, 941, 943, 945, 947, 949, 951, 953, 955, 957, 959, 961, 963, 965, 967, 969, 971, 973, 975, 977, 979, 981, 983, 985, 987, 989, 991, 993, 995, 997, 999, 1001, 1003, 1005, 1007, 1009, 1011, 1013, 1015, 1017, 1019, 1021, 1023, 1025, 1027, 1029, 1031, 1033, 1035, 1037, 1039, 1041, 1043, 1045, 1047, 1049, 1051, 1053, 1055, 1057, 1059, 1061, 1063, 1065, 1067, 1069, 1071, 1073, 1075, 1077, 1079, 1081, 1083, 1085, 1087, 1089, 1091, 1093, 1095, 1097, 1099, 1101, 1103, 1105, 1107, 1109, 1111, 1113, 1115, 1117, 1119, 1121, 1123, 1125, 1127, 1129, 1131, 1133, 1135, 1137, 1139, 1141, 1143, 1145, 1147, 1149, 1151, 1153, 1155, 1157, 1159, 1161, 1163, 1165, 1167, 1169, 1171, 1173, 1175, 1177, 1179, 1181, 1183, 1185, 1187, 1189, 1191, 1193, 1195, 1197, 1199, 1201, 1203, 1205, 1207, 1209, 1211, 1213, 1215, 1217, 1219, 1221, 1223, 1225, 1227, 1229, 1231, 1233, 1235, 1237, 1239, 1241, 1243, 1245, 1247, 1249, 1251, 1253, 1255, 1257, 1259, 1261, 1263, 1265, 1267, 1269, 1271, 1273, 1275, 1277, 1279, 1281, 1283, 1285, 1287, 1289, 1291, 1293, 1295, 1297, 1299, 1301, 1303, 1305, 1307, 1309, 1311, 1313, 1315, 1317, 1319, 1321, 1323, 1325, 1327, 1329, 1331, 1333, 1335, 1337, 1339, 1341, 1343, 1345, 1347, 1349, 1351, 1353, 1355, 1357, 1359, 1361, 1363, 1365, 1367, 1369, 1371, 1373, 1375, 1377, 1379, 1381, 1383, 1385, 1387, 1389, 1391, 1393, 1395, 1397, 1399, 1401, 1403, 1405, 1407, 1409, 1411, 1413, 1415, 1417, 1419, 1421, 1423, 1425, 1427, 1429, 1431, 1433, 1435, 1437, 1439, 1441, 1443, 1445, 1447, 1449, 1451, 1453, 1455, 1457, 1459, 1461, 1463, 1465, 1467, 1469, 1471, 1473, 1475, 1477, 1479, 1481, 1483, 1485, 1487, 1489, 1491, 1493, 1495, 1497, 1499, 1501, 1503, 1505, 1507, 1509, 1511, 1513, 1515, 1517, 1519, 1521, 1523, 1525, 1527, 1529, 1531, 1533, 1535, 1537, 1539, 1541, 1543, 1545, 1547, 1549, 1551, 1553, 1555, 1557, 1559, 1561, 1563, 1565, 1567, 1569, 1571, 1573, 1575, 1577, 1579, 1581, 1583, 1585, 1587, 1589, 1591, 1593, 1595, 1597, 1599, 1601, 1603, 1605, 1607, 1609, 1611, 1613, 1615, 1617, 1619, 1621, 1623, 1625, 1627, 1629, 1631, 1633, 1635, 1637, 1639, 1641, 1643, 1645, 1647, 1649, 1651, 1653, 1655, 16

DAYS	PARTICIPANTS	ENTER RESCURS RATIO	INAP RADIUS RATIO	0.0003	DWN	L-2460
3177	1000	10000	0.000	0.000	0.000	0.000
3178	1000	10000	0.000	0.000	0.000	0.000
3179	1000	10000	0.000	0.000	0.000	0.000
3180	1000	10000	0.000	0.000	0.000	0.000
3181	1000	10000	0.000	0.000	0.000	0.000
3182	1000	10000	0.000	0.000	0.000	0.000
3183	1000	10000	0.000	0.000	0.000	0.000
3184	1000	10000	0.000	0.000	0.000	0.000
3185	1000	10000	0.000	0.000	0.000	0.000
3186	1000	10000	0.000	0.000	0.000	0.000
3187	1000	10000	0.000	0.000	0.000	0.000
3188	1000	10000	0.000	0.000	0.000	0.000
3189	1000	10000	0.000	0.000	0.000	0.000
3190	1000	10000	0.000	0.000	0.000	0.000
3191	1000	10000	0.000	0.000	0.000	0.000
3192	1000	10000	0.000	0.000	0.000	0.000
3193	1000	10000	0.000	0.000	0.000	0.000
3194	1000	10000	0.000	0.000	0.000	0.000
3195	1000	10000	0.000	0.000	0.000	0.000
3196	1000	10000	0.000	0.000	0.000	0.000
3197	1000	10000	0.000	0.000	0.000	0.000
3198	1000	10000	0.000	0.000	0.000	0.000
3199	1000	10000	0.000	0.000	0.000	0.000
3200	1000	10000	0.000	0.000	0.000	0.000
3201	1000	10000	0.000	0.000	0.000	0.000
3202	1000	10000	0.000	0.000	0.000	0.000
3203	1000	10000	0.000	0.000	0.000	0.000
3204	1000	10000	0.000	0.000	0.000	0.000
3205	1000	10000	0.000	0.000	0.000	0.000
3206	1000	10000	0.000	0.000	0.000	0.000
3207	1000	10000	0.000	0.000	0.000	0.000
3208	1000	10000	0.000	0.000	0.000	0.000
3209	1000	10000	0.000	0.000	0.000	0.000
3210	1000	10000	0.000	0.000	0.000	0.000
3211	1000	10000	0.000	0.000	0.000	0.000
3212	1000	10000	0.000	0.000	0.000	0.000
3213	1000	10000	0.000	0.000	0.000	0.000
3214	1000	10000	0.000	0.000	0.000	0.000
3215	1000	10000	0.000	0.000	0.000	0.000
3216	1000	10000	0.000	0.000	0.000	0.000
3217	1000	10000	0.000	0.000	0.000	0.000
3218	1000	10000	0.000	0.000	0.000	0.000
3219	1000	10000	0.000	0.000	0.000	0.000
3220	1000	10000	0.000	0.000	0.000	0.000
3221	1000	10000	0.000	0.000	0.000	0.000



FACILITY 001 PROGRAM COIL									
NOZZLE TYPE					I-STREAM PLW CONFIGURATIONS				
DAILY SUPPRESSOR (GAS)					SUPPRESSOR CONFIGURATION				
THRUOUT PARAMETERS									
CUTER RADIUS RATIO					DVO				
C.0000					1.2480				
NOZ	GE	W314	D2	PA	PT/PA	OMEGAT	CDI	CFNET1	CFNET2
3222	1000	10000	0.000	0.357	2.500	1.247	0.000	0.912	0.912
3223	1000	10000	0.000	0.358	2.746	1.247	0.000	0.919	0.919
3224	1000	10000	0.000	0.358	2.507	1.249	0.000	0.914	0.914
3225	1000	10000	0.000	0.358	2.234	1.207	0.000	0.924	0.924
3226	1000	10000	0.000	0.359	2.003	1.185	0.000	0.926	0.926
3227	1000	10000	0.000	0.358	1.752	1.125	0.000	0.916	0.916
3228	1000	10000	0.000	0.358	1.444	1.082	0.000	0.912	0.912

FACILITY 431 PROGRAM COIL													
NOZZLE TYPE					I-STREAM PLW CONFIGURATIONS								
DAILY SUPPRESSOR (GAS)					SUPPRESSOR CONFIGURATION								
THRUOUT PARAMETERS													
CUTER RADIUS RATIO					DVO								
C.0000					1.2480								
NOZ	GE	W314	D2	PA	PT/PA	OMEGAT	DCS	DCSH	DCSH	DCPL+0	DCPL+1	DCTOT	PSUP/PA
3222	1000	10000	0.000	0.357	2.500	1.247	0.000	0.000	0.000	0.000	0.000	0.000	0.000
3223	1000	10000	0.000	0.358	2.746	1.287	0.000	0.000	0.000	0.000	0.000	0.000	0.000
3224	1000	10000	0.000	0.358	2.507	1.249	0.000	0.000	0.000	0.000	0.000	0.000	0.000
3225	1000	10000	0.000	0.358	2.234	1.207	0.000	0.000	0.000	0.000	0.000	0.000	0.000
3226	1000	10000	0.000	0.359	2.003	1.185	0.000	0.000	0.000	0.000	0.000	0.000	0.000
3227	1000	10000	0.000	0.358	1.752	1.125	0.000	0.000	0.000	0.000	0.000	0.000	0.000
3228	1000	10000	0.000	0.358	1.454	1.082	0.000	0.000	0.000	0.000	0.000	0.000	0.000

## REFERENCES

1. Lee, R., Kendall, R.M., et al., "Research Investigation of the Generation and Suppression of Jet Noise," General Electric Company, NOAS 59-6160-C, January 1961.
2. Simcox, C.S., et al., "SST Technology Follow-On Program - Phase I - A Summary of the SST Jet Noise Suppression Test Program," Boeing Company, FAA-SS-72-41, February 1972.
3. Brausch, J.F. and Doyle, V.L., "Summary of GE4/SST Acoustic Suppression Research, Supersonic Transport Noise Reduction Technology Program, Phase I," General Electric Company, FAA-SS-72-42, December 1972.
4. Stringas, E.J. and Kazin, S.B., "Supersonic Transport Noise Reduction Technology Program - Phase II," General Electric Company, FAA-SS-73-29-1, September 1975.
5. Atvars, J., et al., "SST Technology Follow-On Program - Phase II," Boeing Company, FAA-SS-73-11, March 1975.
6. Hawkins, R. and Hoch, R., "Studies into Concorde's Engine Noise Reduction," NATO, AGARD-CPP-131.
7. Mani, R. and Stringas, E.J., et. al., "High Velocity Jet Noise Source Location and Reduction - Task 2 - Theoretical Developments and Basic Experiments," General Electric Company, FAA-RD-76-79, II, May 1978.
8. Savell, C.T., Stringas, E.J., et al., "High Velocity Jet Noise Source Location and Reduction - Task 1, Activation of Facilities and Validation of Source Location Techniques," General Electric Company, FAA-RD-76-79, I, February 1977.
9. Savell, C.T. and Stringas, E.J., "High Velocity Jet Noise Source Location and Reduction - Task I Supplement - Certification of the General Electric Jet Noise Anechoic Test Facility," General Electric Company, FAA-RD-76-79, IA, February 1977.
10. Knott, P.R., Stringas E.J., et al., "Acoustic Tests of Duct-Burning Turbofan Jet Noise Simulation," General Electric Company, NASA Contract Report 2966, July 1978.
11. Knott, P.R., Blozy, J.T., and Staid, P.S., "Acoustic and Performance Investigation of Coannular Plug Nozzles," General Electric Company, NASA Contract NAS3-19777, May 1977 (to be published).
12. Clapper, W.S., Stringas, E.J., et al., "High Velocity Jet Noise Source Location and Reduction - Task 4 - Development/Evaluation of Techniques for In-Flight Investigations," General Electric Company, FAA-RD-76-79, IV, February 1977.

REFERENCES (Continued)

13. Anon., "Standard Values of Atmospheric Absorption as a Function of Temperature and Humidity for Use in Evaluating Aircraft Flyover Noise," SAE ARP 866, 1964.
14. Ibid., Proposed Revision to SAE ARP 866, October 1973.
15. Harris, C.M., "Absorption of Sound in Air in the Audio Frequency Range," JASA Vol. 35, 1963.
16. Knesner, H.O., "Interpretation of the Anomalous Sound Absorption in Air and Oxygen in Terms of Molecular Collisions," JASA Vol. 5, 1933.
17. Fogg, R.G., "Internal Memorandum," of the General Electric Aircraft Engine Group, Evendale, Ohio, December 1973.
18. Anon., "Acoustic Effects Produced by a Reflecting Plane," SAE AIR 876, October 1973.
19. Anon., "Jet Noise Predictions," SAE AIR 876, July 1965.
20. Evans., L.B., Bass, H.E., and Sutherland, L.C., "Atmospheric Absorption of Sound: Theoretical Predictions," Part 2, JASA, Vol. 51, 1972.
21. Knott, P.R., et al., "Supersonic Jet Exhaust Noise Investigation - Final Report," General Electric Company, AFAPL-TR-76-68, July 1976.
22. Knott, P.R., et al., "Supersonic Jet Exhaust Noise Investigation - Interim Report," General Electric Company, AFAPL-TR-74-25, June 1974.
23. Benzakein, M.J., and Knott, P.R., (editors), "Supersonic Jet Exhaust Noise - Final Report," General Electric Company, AFAPL-TR-72-52, August 1972.
24. "Prediction of Single Stream Shock Cell Noise," SAE ARP 876 (Proposed), April 1975.
25. Hoch, R.G., Duponchel, J.P., Cocking, B.J., and Bryce, W.D., "Studies of the Influence of Density on Jet Noise," Journal of Sound and Vibration, Vol. 28, No. 4, 1973, pp. 649-668.
26. Williams, T.J., Ali, M.R.M., and Anderson, J.S., "Noise and Flow Characteristics of Coaxial Jets," Journal of Mechanical Engineering Science, Vol. II, No. 2, April 1969, pp. 133-142.
27. Olson, W. and Friedman, R., "Jet Noise from Coaxial Nozzles Over a Wide Range of Geometric and Flow Parameters," AIAA Paper No. 74-43, 1974.

#### REFERENCES (Concluded)

28. Kazin, S.B., et al., "Core Engine Noise Control Program - Final Report," General Electric Company, FAA-RD-75-125, 1974.
29. Von Glahn, U., Groesbeck, D., and Goodykoontz, J., "Velocity Decay and Acoustic Characteristics of Various Nozzle Geometries with Forward Velocity," NASA TMX-68259, July 1973.
30. Schlinker, R.H., Peterson, R.A., and Kaplan, R.E., "Enhancement of Directional Microphone Measurements," AIAA Paper 73-1040, October 1973.
31. Levinson, N., "The Wiener RMS Error Criterion in Filter Design and Prediction," Journal of Mathematics and Physics, Vol. 25, 1946, pp. 261-278.
32. Robinson, E.A., Multichannel Time Series Analysis with Digital Computer Programs, Holden-Day, 1967.
33. Anon., "Standard Values of Atmospheric Absorption as a Function of Temperature and Humidity," SAE ARP 866A, March 1975.
34. Zwicky, E.E., Jr., "Solution of Linear Algebraic Equations," from the General Electric ABC Course Notes, 1972.
35. Carnahan, Luther, and Wilkes, Applied Numerical Analysis, Wiley, 1969.
36. Johnson, R.D., "Real-Gas Effects in Critical Flow Through Nozzles and Tabulated Thermodynamic Properties," NASA TN-D-2565, 1965.
37. Siegfried, R.G., and Kuchar, A.P., "A Standard for Exhaust Nozzle Tests," General Electric Company, ESAD Technical Brief 71006, April 6, 1971.
38. Harrington, D.E., Schloemer, J.J., Skebe, S.A., "Thrust Performance of Isolated 36-Chute Suppressor Plug Nozzles With and Without Ejectors at Mach Numbers from 0 to 0.45," NASA TMX-3298, October 1975.
39. Staid, Paul S., "Wind Tunnel Performance Tests of Coannular Plug Nozzles," NASA Contract NAS3-19777, April 1977.